THE LONG-LASTING QUEST FOR NUCLEAR INTERACTIONS: THE PAST, THE PRESENT AND THE FUTURE

EDITED BY: Laura Elisa Marcucci
PUBLISHED IN: Frontiers in Physics

frontiers Research Topics



frontiers

Frontiers eBook Copyright Statement

The copyright in the text of individual articles in this eBook is the property of their respective authors or their respective institutions or funders. The copyright in graphics and images within each article may be subject to copyright of other parties. In both cases this is subject to a license granted to Frontiers.

The compilation of articles constituting this eBook is the property of Frontiers.

Each article within this eBook, and the eBook itself, are published under the most recent version of the Creative Commons CC-BY licence. The version current at the date of publication of this eBook is CC-BY 4.0. If the CC-BY licence is updated, the licence granted by Frontiers is automatically updated to the new version.

When exercising any right under the CC-BY licence, Frontiers must be attributed as the original publisher of the article or eBook, as applicable.

Authors have the responsibility of ensuring that any graphics or other materials which are the property of others may be included in the CC-BY licence, but this should be checked before relying on the CC-BY licence to reproduce those materials. Any copyright notices relating to those materials must be complied with.

Copyright and source acknowledgement notices may not be removed and must be displayed in any copy, derivative work or partial copy which includes the elements in question.

All copyright, and all rights therein, are protected by national and international copyright laws. The above represents a summary only. For further information please read Frontiers' Conditions for Website Use and Copyright Statement, and the applicable CC-BY licence.

ISSN 1664-8714
ISBN 978-2-88966-348-4
DOI 10.3389/978-2-88966-348-4

About Frontiers

Frontiers is more than just an open-access publisher of scholarly articles: it is a pioneering approach to the world of academia, radically improving the way scholarly research is managed. The grand vision of Frontiers is a world where all people have an equal opportunity to seek, share and generate knowledge. Frontiers provides immediate and permanent online open access to all its publications, but this alone is not enough to realize our grand goals.

Frontiers Journal Series

The Frontiers Journal Series is a multi-tier and interdisciplinary set of open-access, online journals, promising a paradigm shift from the current review, selection and dissemination processes in academic publishing. All Frontiers journals are driven by researchers for researchers; therefore, they constitute a service to the scholarly community. At the same time, the Frontiers Journal Series operates on a revolutionary invention, the tiered publishing system, initially addressing specific communities of scholars, and gradually climbing up to broader public understanding, thus serving the interests of the lay society, too.

Dedication to Quality

Each Frontiers article is a landmark of the highest quality, thanks to genuinely collaborative interactions between authors and review editors, who include some of the world's best academicians. Research must be certified by peers before entering a stream of knowledge that may eventually reach the public - and shape society; therefore, Frontiers only applies the most rigorous and unbiased reviews.
Frontiers revolutionizes research publishing by freely delivering the most outstanding research, evaluated with no bias from both the academic and social point of view. By applying the most advanced information technologies, Frontiers is catapulting scholarly publishing into a new generation.

What are Frontiers Research Topics?

Frontiers Research Topics are very popular trademarks of the Frontiers Journals Series: they are collections of at least ten articles, all centered on a particular subject. With their unique mix of varied contributions from Original Research to Review Articles, Frontiers Research Topics unify the most influential researchers, the latest key findings and historical advances in a hot research area! Find out more on how to host your own Frontiers Research Topic or contribute to one as an author by contacting the Frontiers Editorial Office: frontiersin.org/about/contact

THE LONG-LASTING QUEST FOR NUCLEAR INTERACTIONS: THE PAST, THE PRESENT AND THE FUTURE

Topic Editor:
Laura Elisa Marcucci, University of Pisa, Italy

Citation: Marcucci, L. E., ed. (2021). The Long-Lasting Quest for Nuclear Interactions: The Past, the Present and the Future. Lausanne: Frontiers Media SA. doi: 10.3389/978-2-88966-348-4

Table of Contents

04 ***Editorial: The Long-Lasting Quest for Nuclear Interactions: The Past, the Present and the Future***
Laura E. Marcucci

07 ***High-Precision Nuclear Forces From Chiral EFT: State-of-the-Art, Challenges, and Outlook***
Evgeny Epelbaum, Hermann Krebs and Patrick Reinert

37 ***Nucleon-Nucleon Scattering Up to N^5LO in Chiral Effective Field Theory***
David Rodriguez Entem, Ruprecht Machleidt and Yevgen Nosyk

65 ***Analyzing the Nuclear Interaction: Challenges and New Ideas***
Andreas Ekström

80 ***Local Nucleon-Nucleon and Three-Nucleon Interactions Within Chiral Effective Field Theory***
Maria Piarulli and Ingo Tews

99 ***The Problem of Renormalization of Chiral Nuclear Forces***
U. van Kolck

120 ***NN Scattering and Nuclear Uncertainties***
Enrique Ruiz Arriola, Jose Enrique Amaro and Rodrigo Navarro Pérez

146 ***Hyperon-Nuclear Interactions From SU(3) Chiral Effective Field Theory***
Stefan Petschauer, Johann Haidenbauer, Norbert Kaiser, Ulf-G. Meißner and Wolfram Weise

181 ***Parity- and Time-Reversal-Violating Nuclear Forces***
Jordy de Vries, Evgeny Epelbaum, Luca Girlanda, Alex Gnech, Emanuele Mereghetti and Michele Viviani

220 ***Quark Models of the Nucleon–Nucleon Interaction***
Francisco Fernández, Pablo G. Ortega and David R. Entem

241 ***Lattice QCD and Baryon-Baryon Interactions: HAL QCD Method***
Sinya Aoki and Takumi Doi

268 ***Description of Four- and Five-Nucleon Systems by Solving Faddeev-Yakubovsky Equations in Configuration Space***
Rimantas Lazauskas and Jaume Carbonell

283 ***The Hyperspherical Harmonics Method: A Tool for Testing and Improving Nuclear Interaction Models***
Laura E. Marcucci, Jérémy Dohet-Eraly, Luca Girlanda, Alex Gnech, Alejandro Kievsky and Michele Viviani

304 ***Nuclear Forces in the Medium: Insight From the Equation of State***
Francesca Sammarruca and Randy Millerson

328 ***Implementing Chiral Three-Body Forces in Terms of Medium-Dependent Two-Body Forces***
Jeremy W. Holt, Mamiya Kawaguchi and Norbert Kaiser

348 ***Antiproton Physics***
Jean-Marc Richard

frontiers in Physics

EDITORIAL
published: 18 November 2020
doi: 10.3389/fphy.2020.609907

Editorial: The Long-Lasting Quest for Nuclear Interactions: The Past, the Present and the Future

Laura E. Marcucci[1,2]*

[1]Department of Physics "E. Fermi", University of Pisa, Pisa, Italy, [2]Sezione di Pisa, Istituto Nazionale di Fisica Nucleare, Pisa, Italy

Keywords: Nuclear interactions, two- and three-nucleon interactions, chiral effective field theory, lattice QCD, light nuclei, ab-initio methods

Editorial on the Research Topic

The long-lasting quest for nuclear interactions: the past, the present and the future

As it was stated when this Research Topic was launched, despite many years of intense research, our understanding of the force that holds the atomic nuclei together is still far from complete, and numerous crucial questions are yet to be answered. The theory of nuclear forces has a long and glorious history, as recently summarized in 1. In a nutshell, in the 1990s, meson-theoretic and pure phenomenological approaches were used to describe the nuclear interaction, with models which were able to reproduce the large set of two-nucleon ($2N$) experimental data available at that time (or more properly the phase-shifts arising from a partial wave analysis of these data) with a χ^2/datum close to unity [2, 3]. However, all these models were relegated in the world of phenomenology and no connection with the underlying theory of Quantum Chromodynamics (QCD) could be found.

At the beginning of the 1990s, we entered in a new still-ongoing phase: nuclear physicists "discovered" QCD and, more importantly, effective field theory (EFT). Following a seminal idea of Weinberg [4, 5], several groups developed nuclear interaction models within the so-called chiral EFT (χEFT), an EFT where the spontaneous breaking of QCD chiral symmetry plays a crucial role. The χEFT approach is reviewed and discussed at length in essentially all contributions to this Research Topic, as we will outline below. Due to lack of space, here we only mention that the accuracy nowadays reached by the chiral models for nuclear interactions is comparable to, if not even better than, the one reached by the "old" phenomenological models.

Let us quickly review the different contributions to this Research Topic. Four of the most active groups working to derive nuclear force within the χEFT approach are among the contributors to this Research Topic. In particular, Epelbaum et al. review the most recent achievements of the so-called Bochum group, focusing on a new generation of nuclear chiral forces derived using the recently proposed semi-local regularization method. The authors also describe the ongoing efforts by the Low-Energy Nuclear Physics International Collaboration (LENPIC) toward developing consistent two- and many-body forces, and discuss selected applications. The contribution of Entem et al. is a clear and thorough review of the latest work of the so-called Idaho group, which has developed χEFT-based potentials, from leading order up to next-to-next-to-next-to-next-to leading order (N4LO). The authors present also a discussion of the most recently developed N5LO contributions, and their effects on $2N$ scattering. In the contribution of Ekström we can find a discussion of the importance of careful model calibration and uncertainty quantification of theoretical predictions. To this aim, the author reviews how statistical computing and methods, such as Bayesian inference methods, can be used in conjunction with ab-initio methods for atomic nuclei, in order to construct χEFT-based nuclear potentials. Finally, Piarulli et al. review the efforts made by two different groups in applying the χEFT approach in coordinate space. This allows to derive chiral potential models which are local and suitable to be used in studies of nuclear structure with the

OPEN ACCESS

Edited and reviewed by:
Alex Hansen,
Norwegian University of Science and Technology, Norway

****Correspondence:***
Laura E. Marcucci
laura.elisa.marcucci@unipi.it

Specialty section:
This article was submitted to Nuclear Physics, a section of the journal Frontiers in Physics

Received: *24 September 2020*
Accepted: *05 October 2020*
Published: *18 November 2020*

Citation:
Marcucci LE (2020) Editorial: The Long-Lasting Quest for Nuclear Interactions: The Past, the Present and the Future. Front. Phys. 8:609907. doi: 10.3389/fphy.2020.609907

ab-initio methods based on Quantum Monte Carlo techniques. Selected results, ranging from light nuclei up to ^{16}O, as well as neutron matter, are also presented.

Two essential aspects of χEFT are also reviewed in the Research Topic. The first one is the problem of renormalization of chiral nuclear forces. In his contribution, Van Kolck summarizes the huge body of work done on this subject and describes alternative approaches which can be used to achieve renormalization order by order. The second essential aspect is the proper quantification of uncertainties on 2*N* phase shifts analysis and, consequently, on the 2*N* interactions. The work done in Granada in determining the 2*N* scattering database is reviewed by Arriola et al., who also discuss the impact of this database on the determination of the 2*N* force.

The χEFT approach can be suitably adapted to derive also more general baryon-baryon interactions. For instance, Petschauer et al. review the systematic derivation of hyperon-nuclear forces from the symmetries of QCD within non-relativistic SU(3) χEFT, and also discuss several applications, ranging from hyperon-nucleon scattering up to hyperon-nuclear few- and many-body systems, including hypernuclei and neutron star matter. The contribution of de Vries et al., instead, is about the parity-violating but time-reversal conserving, and the parity-violating and time-reversal-violating forces in nuclei. These forces are a tiny component of the total interaction between nucleons, but their study is extremely interesting, because they allow one to obtain information on fundamental symmetries using nuclear systems. In this contribution, the authors review how the above mentioned interactions are derived in χEFT, and discuss the effects of these forces on several few-nucleon observables.

Two papers are devoted to approaches alternative to χEFT used to derive nuclear interaction models. In the first one, Fernández et al. review the different quark models used to describe 2*N* and, more in general, baryon-baryon interaction. These models are non-perturbative QCD-inspired and retain quark and gluons as degrees of freedom. Special attention is devoted to the constituent quark model. This model has recently attracted large interest, because its description of the 2*N* interaction at short distances is qualitatively consistent with the lattice-QCD simulations near the physical quark masses. An example of nuclear interaction models derived from lattice-QCD simulations is presented by Aoki et al., who discuss the so-called HAL QCD method, and review the derivation of the central, tensor, and spin-orbit components present in the 2*N* force, and of the three-nucleon (3*N*) interaction.

The nuclear interaction models derived in χEFT reproduce with great accuracy 2*N* bound and scattering states. However, it is essential to know how they perform in reproducing other nuclear systems, starting from $A > 2$ light nuclei. In order to address this question, very accurate ab-initio methods are fundamental. In this Research Topic, the latest advances of two of these methods are reviewed: Lazauskas et al. discuss the application of the Faddeev-Yakubovsky equations in configuration space to the four- and five-nucleon systems; Marcucci et al. review the hyperspherical harmonics method and its latest results obtained with both local and non-local chiral potentials for three- and four-body nuclear bound and scattering systems. Together with the method based on the Faddeev-Yakubovsky equations in momentum space [6, 7], the presented methods are among the most accurate ones for bound and scattering $A = 3, 4$ nuclear systems.

In order to use chiral forces in larger nuclei up to nuclear matter, further work is necessary. Some issues related to the use of nuclear forces in the medium are discussed by Sammarruca et al. and Holt et al. In particular, Sammarruca et al. present a review of their recent studies of the equation of state for symmetric nuclear matter and pure neutron matter, using state-of-the-art chiral interactions. Holt et al. discuss the implementation of 3*N* forces in many-body nuclear structure and reaction studies, presenting an approach which employs a medium-dependent 2*N* interaction. The authors also discuss several applications.

We conclude this overview with the contribution of Richard, which is devoted to the physics of low-energy antiprotons and, most importantly in this context, its link with nuclear forces. In fact, a good understanding of antinucleon-nucleon and antinucleon-nucleus interactions is necessary in order to investigate important phenomena in astrophysics, as high-energy cosmic rays, or the matter-antimatter asymmetry in early Universe.

In conclusion, this Research Topic has collected the contributions of the researchers most active in the development and understanding of the nuclear interaction and some related topics, as those outlined above. At the end, we hope that this article collection will serve as a useful compendium for practitioners, who everyday apply nuclear potentials in their work and wish to learn about the most significant aspects in an efficient way.

AUTHOR CONTRIBUTIONS

The author confirms being the sole contributor of this work and approved it for publication.

ACKNOWLEDGMENTS

The author would like to warmly thank Prof. Ruprecht Machleidt for his deep insights and great support in proposing, managing, and reviewing large part of the editorial work. Last, but not least, the author would like to thank the many colleagues who have enthusiastically answered to the call of submission, and the many reviewers who, with great professionalism, have worked anonymously together with the authors to improve the submitted articles.

REFERENCES

1. Machleidt R. Historical perspective and future prospects for nuclear interactions. *Int J Mod Phys E* (2017) **26**(11):1730005. doi:10.1142/s0218301317300053

2. Machleidt R. High-precision, charge-dependent Bonn nucleon-nucleon potential. *Phys Rev C* (2001) **63**(2):024001. doi:10.1103/PhysRevC.63.024001

3. Wiringa RB, Stoks VGJ, Schiavilla R. Accurate nucleon-nucleon potential with charge-independence breaking. *Phys Rev C* (1995) **51**(1):38–51. doi:10.1103/PhysRevC.51.38

4. Weinberg S. Nuclear forces from chiral Lagrangians. *Phys Lett B* (1990) **251**(2): 288–92. doi:10.1016/0370-2693(90)90938-3
5. Weinberg S. Effective chiral Lagrangians for nucleon-pion interactions and nuclear forces. *Nucl Phys B* (1991) **363**(1):3–18. doi:10.1016/0550-3213(91)90231-L
6. Deltuva A, Fonseca A, Sauer P. Coulomb force effects in few-nucleon systems. *Few Body Syst* (2019) **60**(2):29. doi:10.1007/s00601-019-1496-x
7. Witała H, Golak J, Skibiński R, Topolnicki K, Epelbaum E, Hebeler K, et al. Application of semilocal coordinate-space regularized chiral forces to elastic Nd scattering and breakup. *Few Body Syst* (2019) **60**(1):19. doi:10.1007/s00601-019-1485-0

Conflict of Interest: The author declares that the research was conducted in the absence of any commercial or financial relationships that could be construed as a potential conflict of interest.

Copyright © 2020 Marcucci. This is an open-access article distributed under the terms of the Creative Commons Attribution License (CC BY). The use, distribution or reproduction in other forums is permitted, provided the original author(s) and the copyright owner(s) are credited and that the original publication in this journal is cited, in accordance with accepted academic practice. No use, distribution or reproduction is permitted which does not comply with these terms.

frontiers in Physics

REVIEW
published: 17 April 2020
doi: 10.3389/fphy.2020.00098

High-Precision Nuclear Forces From Chiral EFT: State-of-the-Art, Challenges, and Outlook

Evgeny Epelbaum, Hermann Krebs and Patrick Reinert*

Fakultät für Physik und Astronomie, Institut für Theoretische Physik II, Ruhr-Universität Bochum, Bochum, Germany

We review a new generation of nuclear forces derived in chiral effective field theory using the recently proposed semilocal regularization method. We outline the conceptual foundations of nuclear chiral effective field theory, discuss all steps needed to compute nuclear observables starting from the effective chiral Lagrangian and consider selected applications in the two- and few-nucleon sectors. We highlight key challenges in developing high-precision three-body forces, such as the need to maintain consistency between two- and many-body interactions and constraints placed by the chiral and gauge symmetries after regularization.

Keywords: nuclear forces, effective field theory, chiral perturbation theory, regularization, few-body systems

OPEN ACCESS

Edited by:
Ruprecht Machleidt, University of Idaho, United States

Reviewed by:
David Rodriguez Entem, University of Salamanca, Spain
Andreas Ekström, Chalmers University of Technology, Sweden

****Correspondence:***
Evgeny Epelbaum
evgeny.epelbaum@rub.de

Specialty section:
This article was submitted to Nuclear Physics, a section of the journal Frontiers in Physics

Received: *29 November 2019*
Accepted: *16 March 2020*
Published: *17 April 2020*

Citation:
Epelbaum E, Krebs H and Reinert P (2020) High-Precision Nuclear Forces From Chiral EFT: State-of-the-Art, Challenges, and Outlook. Front. Phys. 8:98. doi: 10.3389/fphy.2020.00098

1. INTRODUCTION

Almost 30 years ago, Weinberg put forward his groundbreaking idea to apply chiral perturbation theory (ChPT), the low-energy effective field theory (EFT) of QCD, to the derivation of nuclear interactions [1, 2]. This seminal work has revolutionized the whole field of nuclear physics by providing a solid theoretical basis and offering a systematically improvable approach to low-energy nuclear structure and reactions.

So where do we stand today in the implementation of the program initiated by Weinberg? Much has been learned about specific features of the nuclear interactions and currents and about the role of many-body forces from the point of view of the effective chiral Lagrangian, see Epelbaum [3], Epelbaum et al. [4], Machleidt and Entem [5], and Hammer et al. [6] for review articles covering different research areas, while some issues are still under debate [6, 7]. Meanwhile, the interactions derived in chiral EFT, sometimes referred to as "chiral forces," have largely replaced phenomenological potentials developed in the nineties of the last century. They are nowadays commonly used in *ab initio* nuclear structure calculations, see Epelbaum et al. [8], Piarulli et al. [9], Lonardoni et al. [10], Hagen et al. [11], Gebrerufael et al. [12], and Cipollone et al. [13] for recent examples using a variety of continuum *ab initio* methods and Epelbaum et al. [14], Elhatisari et al. [15], and Lähde and Meißner [16] for selected highlights from nuclear lattice simulations. With the most recent chiral nucleon-nucleon (NN) potentials [17] providing a nearly perfect description of the mutually consistent neutron-proton (np) and proton-proton (pp) scattering data below pion production threshold from the Granada-2013 database [18], the two-nucleon sector is already in a very good shape. On the other hand, three-nucleon forces (3NF) are much less understood at the quantitative level [19] and constitute an important frontier in nuclear physics [20].

In this article we focus on the latest generation of chiral nuclear forces based on an improved regularization approach [17, 21, 22], which allows one to maintain the long-range part of the interaction as will be described in section 4.1. We review our recent work along these lines in the two-nucleon sector, describe the ongoing efforts by the Low-Energy Nuclear Physics

International Collaboration (LENPIC) toward developing consistent[1] many-body forces and solving the structure and reactions of nuclei, and discuss selected applications. For selected recent studies along these lines by other groups, see Entem et al. [23], Gezerlis et al. [24], Piarulli et al. [25], Ekström et al. [26, 27], Li et al. [28], Lynn et al. [29], and Girlanda et al. [30], and references therein.

Our paper is organized as follows. In section 2, we outline the foundations of the employed theoretical framework. Section 3 gives an overview of various methods to derive nuclear forces and currents from the effective chiral Lagrangian. It also summarizes the available results for nuclear potentials derived using dimensional regularization (DR). In section 4, we present the improved semilocal regularization approach, which is utilized in the most accurate and precise NN potentials of Reinert et al. [17]. We also discuss the challenges that need to be addresses to construct *consistently regularized* 3NFs and exchange current operators beyond tree level, which are not restricted to any particular type of cutoff regularization. Section 5 is devoted to uncertainty quantification in chiral EFT. Selected results for the NN system, three-nucleon scattering and light nuclei are presented in section 6. We conclude with a short summary and outlook in section 7.

2. THE FRAMEWORK IN A NUTSHELL

Throughout this work, we restrict ourselves to the two-flavor case of the light up- and down-quarks and employ the simplest version of the effective chiral Lagrangian with pions and nucleons as the only active degrees of freedom. Contributions of the $\Delta(1232)$ isobar to the nuclear potentials are discussed in Ordonez et al. [31], Kaiser et al. [32], Krebs et al. [33], Epelbaum et al. [34, 35], and Krebs et al. [36]. The effective Lagrangian involves all possible interactions between pions and nucleons compatible with the symmetries of QCD and is organized in powers of derivatives and quark (or equivalently pion) masses. Pions correspond to the (pseudo) Nambu-Goldstone bosons of the spontaneously broken axial generators and thus transform nonlinearly with respect to chiral $\mathrm{SU}(2)_L \times \mathrm{SU}(2)_R$ transformations. The effective Lagrangian can be constructed in a straightforward way using covariantly transforming building blocks defined in terms of the pion fields [37, 38]. All applications reviewed in this paper rely on a non-relativistic treatment of the nucleon fields and make use of the heavy-baryon formalism to eliminate the nucleon mass m from the leading-order Lagrangian. The individual terms in the effective Lagrangian are multiplied by the corresponding coupling constants, commonly referred to as low-energy constants (LECs), which are not fixed by the symmetry and typically need to be determined from experimental data. The most accurate currently available nuclear potentials at fifth order in the chiral expansion, i.e., at $\mathrm{N^4LO}$, require input from the following effective Lagrangians (with each line containing the contributions with a fixed number of the nucleon fields)

$$\begin{aligned}\mathcal{L}_{\rm eff} &= \mathcal{L}_{\pi}^{(2)}(M_\pi, F_\pi) + \mathcal{L}_{\pi}^{(4)}(l_{1,\ldots,7}) \\ &+ \mathcal{L}_{\pi\rm N}^{(1)}(g_A) + \mathcal{L}_{\pi\rm N}^{(2)}(m, c_{1,\ldots,7}) + \mathcal{L}_{\pi\rm N}^{(3)}(d_{1,\ldots,23}) + \mathcal{L}_{\pi\rm N}^{(4)}(e_{1,\ldots,118}) \\ &+ \mathcal{L}_{\rm NN}^{(0)}(C_S, C_T) + \mathcal{L}_{\rm NN}^{(2)}(C_{1,\ldots,7}) + \mathcal{L}_{\rm NN}^{(4)}(D_{1,\ldots,12}) + \mathcal{L}_{\pi\rm NN}^{(1)}(D) + \ldots \\ &+ \mathcal{L}_{\rm NNN}^{(0)}(E) + \mathcal{L}_{\rm NNN}^{(2)}(E_{1,\ldots,10}), \end{aligned} \tag{1}$$

where M_π and F_π are the pion mass and decay constant[2], g_A is the nucleon axial-vector coupling while l_i, c_i, d_i, e_i, C_i, D, D_i, E, and E_i are further LECs. The superscript n of $\mathcal{L}^{(n)}$ denotes the number of derivatives and/or M_π-insertions and is sometimes referred to as the chiral dimension. Notice that we only show new LECs that appear in the corresponding Lagrangians and suppress the dependence on the LECs appearing at lower orders. The pionic Lagrangian can be found in Gasser and Leutwyler [39], $\mathcal{L}_{\pi\rm N}$ is given in Bernard et al. [40], and Fettes et al. [41], $\mathcal{L}_{\rm NN}^{(0)}$ was introduced in Weinberg [1, 2], $\mathcal{L}_{\rm NN}^{(2)}$ can be found in Epelbaum et al. [42], and Girlanda et al. [43], the minimal form of $\mathcal{L}_{\rm NN}^{(4)}$ is given in Reinert et al. [17], $\mathcal{L}_{\pi\rm NN}^{(1)}$ and $\mathcal{L}_{\rm NNN}^{(0)}$ are discussed in Epelbaum et al. [44] while $\mathcal{L}_{\rm NNN}^{(2)}$ was constructed in Girlanda et al. [45]. Notice further that the chiral symmetry breaking terms $\propto M_\pi^2$ are not shown explicitly in $\mathcal{L}_{\rm NN}$ and $\mathcal{L}_{\rm NNN}$. For calculations at the physical value of the quark masses, their contributions are absorbed into the LECs listed in Equation (1). We have, furthermore, restricted ourselves in this equation to isospin-invariant terms for the Lagrangians involving two and three nucleons. The single-nucleon Lagrangian $\mathcal{L}_{\pi\rm N}$ does involve isospin-breaking contributions due to the quark mass difference and can be extended to include virtual photon effects [46, 47]. The ellipses in the second-to-last line of Equation (1) refer to higher-order Lagrangians $\mathcal{L}_{\pi\rm NN}$, which have not been worked out yet and would be needed to finalize the derivation of the 3NF at $\mathrm{N^4LO}$.

The long-range parts of the nuclear forces emerge from pion exchange diagrams and can be derived from $\mathcal{L}_\pi$ and $\mathcal{L}_{\pi\rm N}$. Fortunately, only a very restricted set of (linear combinations of) LECs from these Lagrangians contributes to the $\pi N \to \pi N$ and $\pi N \to \pi\pi N$ scattering amplitudes, which enter as subprocesses when deriving the long-range nuclear interactions up to $\mathrm{N^4LO}$, namely $c_{1,\ldots,4}$ from $\mathcal{L}_{\pi\rm N}^{(2)}$, $d_1 + d_2$, $d_{3,5,18}$, and $d_{14} - d_{15}$ from $\mathcal{L}_{\pi\rm N}^{(3)}$ and $e_{14,\ldots,18}$ from $\mathcal{L}_{\pi\rm N}^{(4)}$. Here, we made use of the fact that the contributions from the LECs l_3, $e_{19,\ldots,22}$, and $e_{35,\ldots,38}$ can be absorbed into the appropriate shifts of the LECs c_i [48]. All these πN LECs can nowadays be reliably extracted by matching the πN scattering amplitude from the recent Roy-Steiner equation analysis [49] with ChPT at the subthreshold point [50], see also Siemens et al. [51] for an alternative strategy. Thus, *the long-range nuclear interactions are completely determined by the spontaneously broken approximate chiral symmetry of QCD and experimental/empirical information on the πN system in a parameter-free way*. The two- and three-nucleon interactions

[1] The precise meaning of consistency of many-body forces is defined in sections 2 and 4.2.

[2] Strictly speaking, M_π is to be understood as the pion mass to leading order in the chiral expansion while F_π and other parameters in the effective Lagrangian refer to the corresponding LECs in the chiral limit of vanishing light quark masses.

in the last two lines of Equation (1) parameterize the short-range part of the nuclear forces, and the corresponding LECs have to be determined from NN scattering and three- or more-nucleon observables.

In the single-nucleon sector, the effective Lagrangian $\mathcal{L}_\pi + \mathcal{L}_{\pi\mathrm{N}}$ can be used to systematically compute the scattering amplitude in perturbation theory by applying the chiral expansion, a simultaneous expansion in particles' external three-momenta $p \equiv |\vec{p}\,|$ and around the chiral limit $M_\pi \to 0$. The importance of every Feynman diagram is estimated by counting powers of the soft scales and applying the rules of naive dimensional analysis (NDA). The expansion parameter $Q \in \{p/\Lambda_\mathrm{b},\, M_\pi/\Lambda_\mathrm{b}\}$ is determined by the breakdown scale Λ_b, which may (optimistically) be expected to be of the order of the ρ-meson mass[3]. At every order in the chiral expansion only a finite number of Feynman diagrams need to be evaluated. For more details on ChPT in the 1N sector see the review article [53].

Contrary to the 1N case, the NN S-wave scattering amplitude exhibits poles in the near-threshold region corresponding to the bound state (deuteron) and the virtual state in the $^1\mathrm{S}_0$ channel, which signal the breakdown of perturbation theory. In this context, it was pointed out by Weinberg that the contributions of multi-nucleon ladder diagrams are enhanced compared to the estimation based on the chiral power counting due to the appearance of pinch singularities (in the $m \to \infty$ limit) [1, 2]. Weinberg also argued that the nucleon mass needs to be counted as $m \sim \Lambda_\mathrm{b}^2/M_\pi \gg \Lambda_\mathrm{b}$ in order to formally justify the need to perform a non-perturbative resummation of the ladder contributions. Given that the ladder diagrams are automatically resummed by solving the few-nucleon Schrödinger equation, Weinberg's chiral EFT approach to low-energy nuclear systems, perhaps not surprisingly, resembles the quantum mechanical A-body problem

$$\left[\left(\sum_{i=1}^{A}\frac{-\Delta_i}{2m}+\mathcal{O}\big(m^{-3}\big)\right)+V_\mathrm{2N}+V_\mathrm{3N}+V_\mathrm{4N}+\ldots\right]|\Psi\rangle = E|\Psi\rangle, \tag{2}$$

where Δ_i is the Laplace operator acting on the nucleon i. The nuclear potentials V_2N, V_3N, ... receive contributions from diagrams that cannot be reduced to ladder iterations and are calculable in a systematically improvable way within ChPT.

Among the many attractive features, the approach outlined above allows one to maintain *consistency* between nuclear forces and exchange current operators which are scheme-dependent quantities. To illustrate the meaning and importance of consistency consider the Feynman diagram on the left-hand side (l.h.s.) of the equality shown in **Figure 1** as an example. The corresponding (on-shell) contribution to the scattering amplitude features both a reducible (i.e., of a ladder-type) and irreducible pieces as visualized in the figure. Reducible contributions to the amplitude are resummed up to an infinite order when solving the Faddeev equation corresponding to Equation (2). In doing so, the diagrams corresponding to its zeroth and first iterations shown in the figure *must* match

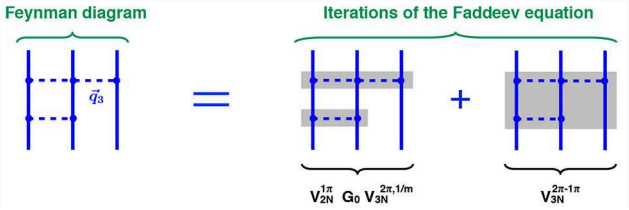


FIGURE 1 | Representation of the on-shell scattering amplitude from the one-pion-two-pion-exchange Feynman diagram **(left)** in terms of iterations of the Faddeev equation **(right)**. Gray-shaded rectangles visualize the corresponding two- and three-nucleon potentials $V_\mathrm{2N}^{1\pi}$, $V_\mathrm{3N}^{2\pi,\,1/m}$, and $V_\mathrm{3N}^{2\pi-1\pi}$ while G_0 denotes the free resolvent operator for non-relativistic nucleons.

the result obtained from the Feynman diagram when taken on the energy shell. The iterative contribution from the first graph on the right-hand side of the depicted equality, however, involves NN and 3N potentials, whose off-shell behavior is scheme dependent. Also the 3NF corresponding to the last diagram is scheme dependent (even on the energy shell) [54], and only a *consistent* choice of the involved two- and three-nucleon potentials guarantees the validity of matching for the scattering amplitude. This can indeed be verified explicitly using the expressions for the 3NFs $V_\mathrm{3N}^{2\pi,\,1/m}$ from Equations (4.9) to (4.11) of Bernard et al. [55] and $V_\mathrm{3N}^{2\pi-1\pi}$ from Equations (2.16) to (2.20) of Bernard et al. [54] and employing DR to evaluate loop integrals[4].

Clearly, DR is impractical for a numerical solution of the A-body problem and is usually replaced by cutoff regularization. Renormalization of the Schrödinger equation in the context of chiral EFT is a controversial and heavily debated topic, see Lepage [56], Pavon Valderrama and Ruiz Arriola [57], Nogga et al. [58], Birse [59], Epelbaum and Meißner, [60], Epelbaum and Gegelia [61], Long and Yang [62], Valderrama [63], Epelbaum et al. [7], and Hammer et al. [6] for a range of opinions. The essence of the problem is related to the non-renormalizable nature of the Lippmann-Schwinger (LS) equation for NN potentials truncated at a finite order in the chiral expansion. Except for a few cases, such as the leading-order (LO) equation in pionless EFT and in chiral EFT in spin-singlet channels, ultraviolet (UV) divergences emerging from the loop expansion of the scattering amplitude cannot be absorbed into redefinitions of parameters appearing in the truncated potentials [7, 64]. The problem can be avoided by treating the one-pion exchange (OPE) and higher-order contributions to the potential in perturbation theory using e.g., the systematic power counting scheme proposed by Kaplan et al. [65], but the resulting approach unfortunately fails to converge (at least) in certain spin-triplet channels [66, 67] (see also [68] for a recent discussion). A renormalizable framework with the one-pion exchange potential (OPEP) treated non-perturbatively was proposed in Epelbaum and Gegelia [69] (see also [70]), based on a manifestly Lorentz invariant form of the effective Lagrangian. This approach

[3] An upper bound for Λ_b is set by the scale $4\pi F_\pi$ emerging from pion loops [52].

[4] Notice that the contributions from diagrams shown in **Figure 1** are finite in DR.

requires a perturbative inclusion of higher-order contributions to the potential in order to maintain renormalizability (which may lead to convergence issues in some channels [71]) but has not been systematically explored beyond LO yet.

Throughout this work we employ a finite-cutoff version of nuclear chiral EFT in the formulation of Lepage [56], which is utilized in most of the applications available today. This is so far the only scheme, that has been advanced to high chiral orders and successfully applied to a broad range of few- and many-nucleon systems. Below, we briefly summarize the basic steps involved in the calculation of nuclear observables within this framework. In the following sections, all four steps outlined below will be discussed in detail.

i. *Derivation of nuclear forces and current operators from the effective chiral Lagrangian.* This can be achieved by separating out irreducible contributions to the A-nucleon scattering amplitude that cannot be generated by iterations of the dynamical equation using various methods outlined in section 3. The derivations are carried out in perturbation theory using the standard chiral power counting. In contrast to ChPT for the scattering amplitude, special efforts are needed to arrive at renormalized nuclear potentials. This requires that all UV divergences from *irreducible* loop diagrams are canceled by the corresponding counter terms. The renormalizability requirement imposes strong constraints on the unitary ambiguity of nuclear forces and currents [48, 72–75].

ii. *Introduction of a regulator for external (off-shell) momenta of the nucleons* in order to make the A-body Schrödinger equation well-behaved. Given the lack of counter terms needed to absorb all UV divergences from iterations of the dynamical equation with a truncated potential, the (momentum-space) cutoff Λ must not be set to arbitrarily high values but should be kept of the order of the breakdown scale, $\Lambda \sim \Lambda_b$ [7, 56, 61]. The accessible cutoff window is, in practice, further restricted by the need to avoid the appearance of spurious deeply bound states which provide a severe complication for applications beyond the NN system [76] and a preference for soft interactions in order to optimize convergence of *ab initio* many-body methods. Given the rather restricted available cutoff window, it is important to employ regulators that minimize the amount of finite-cutoff artifacts, see section 4 for discussion. While the regulator choice for V_{2N} still features a high degree of ambiguity, maintaining the relevant symmetries and consistency with *regularized* many-body forces and exchange currents beyond tree level represents a highly nontrivial task [77, 78] (see section 4 for an example and discussion).

iii. *Renormalization of the few-nucleon amplitude by fixing the short-range multi-nucleon interactions from low-energy experimental data* (see section 6 for details). This allows one to express the calculated scattering amplitude in terms of observable quantities instead of the *bare* LECs $C_{S,T}(\Lambda)$, $C_i(\Lambda)$, $D_i(\Lambda)$, $D(\Lambda)$, $E(\Lambda)$, $E_i(\Lambda)$, . . ., and amounts to implicit renormalization of the amplitude. Notice that in the pion and 1N sectors of ChPT, renormalization is usually carried out *explicitly* by splitting the bare LECs $l_i, d_i, e_i, \ldots$, into the (finite) renormalized ones and counter terms, e.g., $d_i = d_i^{\rm r}(\mu) + R_i(\mu)$. Here, μ denotes the renormalization scale while R_i are the corresponding counter terms, which diverge in the limit of a removed regulator (i.e., $\Lambda \to \infty$ in the cutoff regularization or the number of dimensions $d \to 4$ in DR). Such a splitting is not unique as reflected by the scale μ, and the appropriate choice of renormalization conditions is essential to maintain the desired power counting, i.e., to ensure the appropriate scaling behavior of renormalized contributions to the amplitude leading to a systematic and self-consistent scheme (see e.g., [79, 80]). In the few-nucleon sector, the non-perturbative resummation of pion-exchange potentials via Equation (2) can only be carried out numerically[5], which leaves the *implicit* renormalization outlined above as the only available option. Notice that contrary to the renormalized LECs $l_i^{\rm r}(\mu), d_i^{\rm r}(\mu), \ldots$, the bare LECs $C_{S,T}(\Lambda), C_i(\Lambda), \ldots$, must be re-determined at every order in the expansion.

iv. *Estimation of the truncation uncertainty and a-posteriori consistency checks of the obtained results.* These include, among others, testing the naturalness of the extracted LECs [17], making error plots for phase shifts as suggested in Lepage [56], and Grießhammer [81], verifying a reduced residual Λ-dependence of observables (within a specified cutoff range) upon including higher-order short-range interactions, see e.g., Figure 4 of Epelbaum [82], and confronting the contributions of many-body interactions and/or exchange currents with estimations based on the assumed power counting [83, 84]. Our approach to error analysis is outlined in section 5, while selected consistency checks are discussed in section 6.

Before closing this section, several remarks are in order. First, we emphasize that the approach outlined above is applicable at the physical quark masses. Quark mass dependence of nuclear observables can be studied more efficiently in the renormalizable chiral EFT framework of Epelbaum and Gegelia [69, 85], see also Baru et al. [86, 87], and Lähde et al. [88] for an alternative method. Secondly, the validity (in the EFT sense) of the finite-cutoff EFT formulation outlined above has been demonstrated numerically by means of the error plots [56, 89] and analytically [61] for toy-models with long-range interactions. It can also be easily verified in pionless EFT. For the case of exactly known non-singular long-range potentials, the employed approach reduces in the NN sector to the well-known modified effective range expansion [90]. The relation between the choice of renormalization conditions and power counting is discussed within pionless EFT in Epelbaum et al. [91][6]. That paper provides an explicit example of the choice of subtraction scheme (i.e., renormalization conditions), which leads to a self-consistent EFT approach for two particles with both a natural and unnaturally large scattering length, while respecting the NDA scaling of renormalized LECs. Notice that in all

[5] See, however, Kaplan [68] for analytical results in the chiral limit.

[6] For pionless EFT or chiral EFT with perturbative pions, the NN amplitude can be calculated analytically, and renormalization can be carried out explicitly.

applications reviewed in this article, few-nucleon short-range interactions are counted according to NDA. A number of authors advocate alternative approaches, in particular by inferring the importance of short-range operators from the requirement of Λ-independence of the scattering amplitude at arbitrarily large values of Λ as articulated in detail in Hammer et al. [6]. However, performing the loop expansion of the solution of the LS equation in spin-triplet channels for the resummed OPEP shows that the scattering amplitude is only *partially* renormalized in spite of the fact that it admits, in some cases, a finite $\Lambda \to \infty$ limit at a fixed energy [7]. The danger of choosing $\Lambda \gg \Lambda_b$ in such partially renormalized non-perturbative expressions is demonstrated using an exactly solvable model in Epelbaum and Gegelia [61].

3. CHIRAL PERTURBATION THEORY FOR NUCLEAR POTENTIALS

One method to decouple pion-nucleon and purely nucleonic subspaces of the Fock space, thereby reducing a quantum field theoretic problem to a quantum mechanical one, is the unitary transformation (UT) technique. Let η and λ be the projection operators onto the purely nucleonic subspace of the Fock space and the rest, respectively. The time-independent Schrödinger equation can be written in the form

$$\begin{pmatrix} \eta H \eta & \eta H \lambda \\ \lambda H \eta & \lambda H \lambda \end{pmatrix} \begin{pmatrix} \eta |\Psi\rangle \\ \lambda |\Psi\rangle \end{pmatrix} = E \begin{pmatrix} \eta |\Psi\rangle \\ \lambda |\Psi\rangle \end{pmatrix}, \tag{3}$$

where E denotes the eigenenergy of the πN system. The idea is to apply a UT to the Hamilton operator H in order to block diagonalize the matrix on the l.h.s. of Equation (3) leading to

$$\Big[U^\dagger H\, U\Big]\, U^\dagger |\Psi\rangle \,=\, E\, U^\dagger |\Psi\rangle. \tag{4}$$

The decoupling requirement is given by

$$\eta\, U^\dagger H\, U \lambda \,=\, \lambda\, U^\dagger H\, U\, \eta \,=\, 0. \tag{5}$$

To construct the UT U we first introduce a Møller operator Ω [92], which is defined by

$$|\Psi\rangle \,=\, \Omega\eta|\Psi\rangle \tag{6}$$

with the requirement

$$\Omega \,=\, \Omega\eta. \tag{7}$$

Here, $|\Psi\rangle$ refers to few-nucleon scattering states below pion production threshold. See Lindgre [93] for a discussion of the properties of the operator Ω. The Møller operator reproduces the original low-energy state out of projected state. By projecting Equation (6) onto the model space η one obtains the identity

$$\eta\Omega \,=\, \eta. \tag{8}$$

Using Equation (6), we can write the time-independent Schrödinger equation in the form

$$\big(E - H_0\big)\Omega\eta|\Psi\rangle = V|\Psi\rangle, \tag{9}$$

where H_0 denotes a free Hamiltonian. On the other hand, projecting the original Schrödinger equation Equation (3) onto the model space and applying on the resulting equation the operator Ω, we obtain

$$\big(E\Omega - \Omega H_0\big)\eta|\Psi\rangle = \Omega\eta V|\Psi\rangle. \tag{10}$$

Subtracting Equation (10) from Equation (9) leads to

$$\big[\Omega, H_0\big]\eta|\Psi\rangle = \big(V - \Omega\eta V\big)|\Psi\rangle = \big(V - \Omega\eta V\big)\Omega\eta|\Psi\rangle.$$

This way we obtain a non-linear equation for the Møller operator Ω

$$\big[\Omega, H_0\big] - V\Omega + \Omega V\Omega = 0. \tag{11}$$

Defining the operator A via $\Omega =: \eta + A$ with $A \,=\, \lambda A\eta$, as follows from Equations (7) and (8), we rewrite Equation (11) in the form

$$\lambda\big(H + \big[H, A\big] - AVA\big)\eta = 0. \tag{12}$$

The UT U was parameterized by Okubo [94] in terms of the operator A via

$$U \,=\, \begin{pmatrix} \eta\,(1 + A^\dagger A)^{-1/2} & -A^\dagger (1 + AA^\dagger)^{-1/2} \\ A(1 + A^\dagger A)^{-1/2} & \lambda(1 + AA^\dagger)^{-1/2} \end{pmatrix}. \tag{13}$$

The resulting transformed Hamiltonian

$$\eta\, U^\dagger H\, U\eta \,=\, (\Omega^\dagger\Omega)^{1/2}\eta H\, \Omega(\Omega^\dagger\Omega)^{-1/2}, \tag{14}$$

leads to the effective potential defined via

$$V_{\rm eff}^{\rm UT} :=\, \eta\, U^\dagger H\, U\eta - H_0. \tag{15}$$

Obviously, the Okubo transformation in Equation (13) is not the only possibility to obtain a block-diagonalized Hamiltonian. On top of the transformation U one can always apply e.g., a UT acting nontrivially on the η-space, thus leaving the Hamiltonian block-diagonal. This freedom has been exploited in a systematic manner to construct renormalizable/factorizable 3NFs and four-nucleon forces (4NFs) in chiral EFT in Epelbaum [72], Bernard et al. [54, 55], and Krebs et al. [48, 95].

To derive the potential $V_{\rm eff}^{\rm UT}$ from the effective chiral Lagrangian in Equation (1) one needs to solve the non-linear decoupling Equation (12) for the operator A. This can be done perturbatively using NDA [3] to count powers of three-momenta and pion masses, denoted collectively by Q. For the sake of definiteness, we restrict ourselves in the following to nuclear potentials in the absence of external sources. The extension to the current operators is straightforward and discussed in details in Krebs et al. [75]. The irreducible contributions of any connected Feynman diagram scale as Q^ν with $\nu \,=\, -2 +$

$\sum_i V_i \kappa_i$, where V_i denotes the number of vertices of type i and κ_i is the inverse mass dimension of the corresponding coupling constant, $\kappa_i = d_i + \frac{3}{2} n_i + p_i - 4$. Here, d_i is the number of derivatives and/or M_π-insertions, while n_i and p_i denote the number of nucleon and pion fields, respectively[7]. This particular form of the power counting allows one to formulate the chiral expansion in the form that is completely analogous to the expansion in powers of coupling constants. It is thus particularly well suited for algebraic approaches such as the method of UT. Once the operator A is available, one can perform the chiral expansion of Equation (14) to construct the effective potential order-by-order.

The chiral expansion of the nuclear forces is visualized in **Figure 2**. Below, we briefly discuss isospin symmetric contributions starting from the leading order (LO) Q^0. The only contributions at this order emerge from the OPEP and two contact interactions $\propto C_{S,T}$ [1, 2]. The first corrections at order Q^2 (NLO) involve the leading two-pion exchange potential (TPEP) [31, 96, 97] and 7 short range interactions $\propto C_i$. At order Q^3 ($\mathrm{N^2LO}$), further corrections to the TPEP $\propto c_i$ need to be taken into account [96]. At the same order one has the first non-vanishing contributions to the 3NF. They are given by the two-pion exchange diagram involving the LECs c_i and two shorter-range tree-level diagrams involving the LECs D and E [44, 98]. At order Q^4 ($\mathrm{N^3LO}$), the NN potential receives the contributions from the leading three-pion exchange [99–101], further corrections to the TPEP [102, 103] and 12 new short-range interactions $\propto D_i$ [17]. At the same order, there are various one-loop corrections to the 3NF [54, 55, 104] and the first contributions to the 4NFs [72, 73], which do not involve unknown parameters. Finally, at order Q^5 ($\mathrm{N^4LO}$), the NN potential receives corrections to the three-pion exchange $\propto c_i$ [101] and further contributions to the TPEP [105]. No additional unknown parameters appear in the isospin-conserving part of the NN force at this order. The 3NF also receives corrections at $\mathrm{N^4LO}$, most of which have already been worked out using DR [45, 48, 95]. Notice that the 3NF involves at this order a number of new short-range operators. Work is still in progress to derive the remaining 3NF and 4NF at $\mathrm{N^4LO}$. We further emphasize that all calculations mentioned above are carried out using DR or equivalent schemes.

The effective potential $V_{\rm eff}^{\rm UT}$ leads, by construction, to the same spectrum and on-shell scattering matrix as the original untransformed potential V [106, 107]. There are, however, other possibilities to define the effective potential without changing on-shell physics. One example is an energy-independent potential defined by

$$V_{\rm eff}^{\rm EI} = \eta V \Omega \eta. \tag{16}$$

The proof that $V_{\rm eff}^{\rm EI}$ of Equation (16) leads to the same spectrum is trivial:

$$\begin{aligned} \big(\eta H_0 \eta + \eta V \eta + \eta V \lambda\big)|\Psi\rangle &= E\,\eta|\Psi\rangle, \\ \big(\eta H_0 \eta + \eta V \eta + \eta V \lambda \Omega\big)\eta|\Psi\rangle &= E\,\eta|\Psi\rangle, \\ \big(\eta H_0 \eta + \eta V \Omega\eta\big)\eta|\Psi\rangle &= E\,\eta|\Psi\rangle, \end{aligned} \tag{17}$$

where we used Equations (6) and (8) in the first and second lines, respectively. Note that the potential $V_{\rm eff}^{\rm EI}$ is manifestly non-hermitian. However, due to its simplicity, it is widely used in the literature [92]. This example shows that there is a considerable freedom to define nuclear potentials. Nuclear forces and current operators constructed by the Bochum-Bonn group (see e.g., [17, 21, 22, 48, 54, 55, 73–75, 95, 97]), are obtained using the method of UT. The JLab-Pisa group utilizes a different approach by starting with the on-shell transfer matrix T and "inverting" it to obtain the effective potential (see e.g., [108–111]). This is carried out in perturbation theory by counting the nucleon mass via $m \sim \Lambda_{\rm b}$

$$T = T^{(0)} + T^{(1)} + T^{(2)} + \dots\,, \tag{18}$$

where the superscripts indicate the chiral order Q^n. The same counting scheme is used to organize the contributions to effective potential:

$$v = v^{(0)} + v^{(1)} + v^{(2)} + \dots\,. \tag{19}$$

The inversion of the LS equation is carried out iteratively to yield

$$v^{(0)} = T^{(0)}\,, \qquad v^{(1)} = T^{(1)} - v^{(0)} G_0 v^{(0)}\,, \qquad \dots\,. \tag{20}$$

Obviously, the knowledge of the on-shell transfer matrix is insufficient to perform the inversion, and one needs to specify its off-shell extension. Notice that the potentials constructed in this way are not necessarily hermitian, and thus there is no guarantee that they are unitarily equivalent to the ones derived using the UT technique. It should, however, always be possible to find a similarity transformation that relates one potential to another. This is exemplified with the potential $v_{2\pi}^{(3)}(\nu = 1)$ in Equation (20) of Pastore et al. [109], where ν is an arbitrary phase, which is manifestly non-hermitian. Using the similarity transformation in Equation (28) of that paper[8], it can be transformed to the hermitian potential $v_{2\pi}^{(3)}(\nu = 0)$, that is actually employed in the current version of the interactions developed by the JLab-Pisa group. With this choice, their potentials are unitarily equivalent to the ones of the Bochum-Bonn group.

4. REGULARIZATION

4.1. Semilocal Momentum-Space Regularization of the NN Potential

In this review article we focus on the semilocal regularization approach of the chiral nuclear potentials carried out in

[7] Alternatively (but equivalently), the chiral order ν of a connected, N-nucleon irreducible diagram with L loops can be expressed as $\nu = -4 + 2N + 2L + \sum_i V_i \Delta_i$ with $\Delta_i = d_i + n_i/2 - 2$.

[8] The claim in Pastore et al. [109] that the transformation e^{iU} in Equation (28) of that paper is unitary is incorrect since the operator $iU^{(1)}(\nu)$ from Equation (28) is not antihermitian.

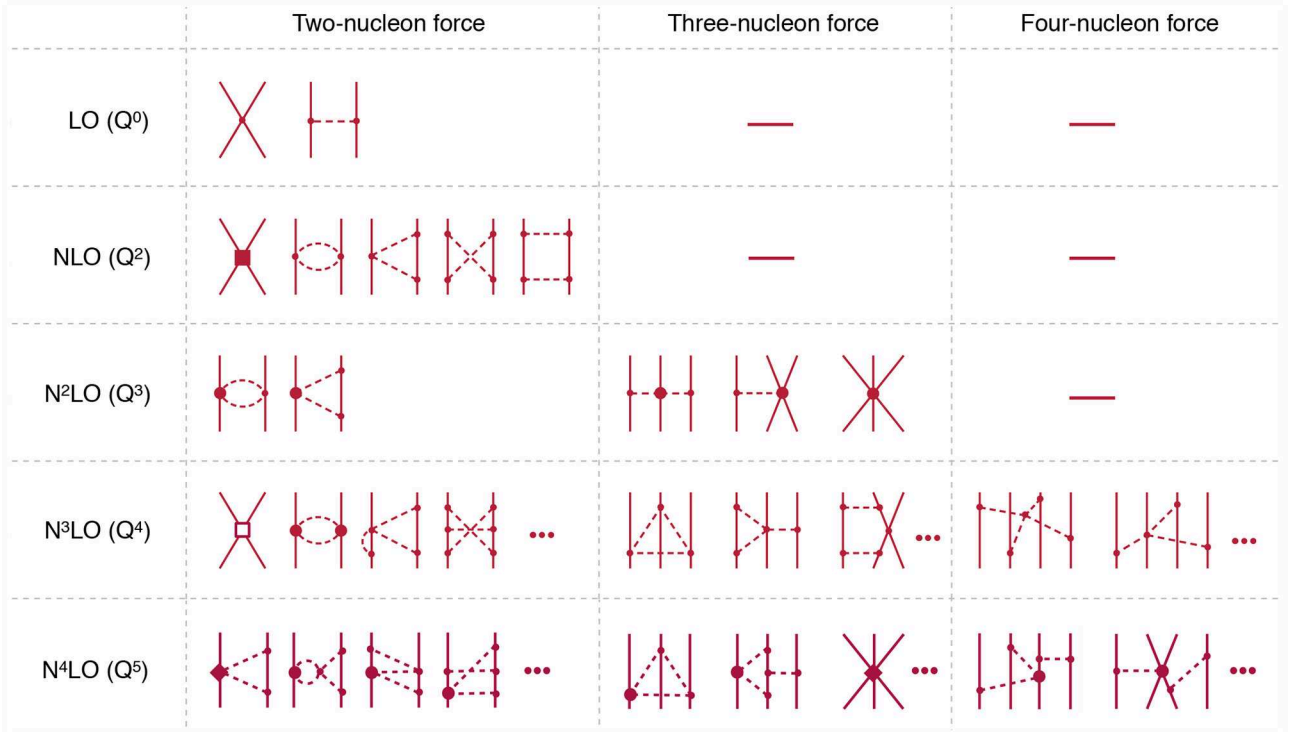


FIGURE 2 | Hierarchy of nuclear forces at increasing orders in chiral expansion in the Weinberg scheme. Solid and dashed lines refer to nucleons and pions, respectively. Solid dots, filled circles, filled squares, filled diamonds, and open squares refer to vertices from the Lagrangian in Equation (1) of dimension $\Delta = 0, 1, 2, 3,$ and 4, respectively.

momentum space [17]. For the purpose of regularization we will consider the two-nucleon interaction consisting of two distinct parts: the short-range contact interaction part and the long-range pion-exchange part. In this context, the term "semilocal" refers to the application of a nonlocal regulator for the former and a local regulator for the latter. In particular, the momentum-space matrix elements of the contact potential are multiplied by a simple nonlocal Gaussian regulator

$$\langle \vec{p}\,' | V_{\rm cont} | \vec{p}\,\rangle_{\rm reg} = \langle \vec{p}\,' | V_{\rm cont} | \vec{p}\,\rangle \, e^{-\frac{p'^2+p^2}{\Lambda^2}}. \qquad (21)$$

Here and in what follows, $p \equiv |\vec{p}\,|$ and $p' \equiv |\vec{p}\,'|$. Such kinds of nonlocal regulators (albeit with different powers of p, p', and Λ) have been and still are employed as the main method of regularization for the entire potential including the long-range interactions (see e.g., [23, 27, 112–115])[9].

However, in Epelbaum et al. [21, 22] it was shown that the amount of long-range cutoff artifacts can be significantly reduced by employing a local regulator for pion-exchange potentials. Notice that pion-exchange contributions, except for some relativistic corrections, give rise to local potentials. We *require* the regulator to preserve the long-range part of the interaction, which is unambiguously determined in chiral EFT. More precisely, for $\Lambda \gg M_\pi$, the regulator is required not to affect the large-distance behavior of the n-pion exchange potential $V_{n\pi}(r) \sim \exp(-nM_\pi r) f(r)$, with $f(r)$ being an irrational function, up to exponentially small corrections that vanish in the limit $\Lambda \to \infty$. Inspired by Rijken [118], this is achieved in our momentum-space approach by regularizing the static propagators of pions exchanged between different nucleons with a local Gaussian cutoff via

$$\frac{1}{l^2 + M_\pi^2} \to \frac{1}{l^2 + M_\pi^2} \, e^{-\frac{l^2+M_\pi^2}{\Lambda^2}}, \qquad (22)$$

with $l = |\vec{l}|$ and $\vec{l}$ denoting the three-momentum of the exchanged pion. The introduction of the Gaussian form factor in the pion propagators leads to properly regularized long-range potentials that are finite at short distances in coordinate space. In order to have a clean separation of the long-range pion-exchange potential from the short-range contact interactions, we made use of the available contact interactions to subtract out the remaining (finite) admixtures of short-range interactions [17]. The fixed coefficients of these subtractions are determined from the requirement that the corresponding coordinate-space potential and as many derivatives thereof as

[9]Notice that the aforementioned potentials (except the one of [112]) additionally employ spectral function regularization (SFR) [116, 117] of the TPEP in the form of a sharply cut-off spectral integral in order to suppress its remaining unphysical short-distance behavior. Notice, however, that the application of a nonlocal regulator $\exp(-(p^{2n} + p'^{2n})/\Lambda^{2n})$ with suitably chosen n is sufficient to arrive at UV-finite iterations of the potential.

allowed by power counting vanish at the origin. This convention leads to a qualitatively similar regularization as the coordinate-space regulator previously employed in Epelbaum et al. [21, 22].

Application of these ideas to the OPEP is straightforward and leads, in the limit of exact isospin symmetry, to

$$V_{\rm 2N,\,\Lambda}^{1\pi}(M_\pi) = -\frac{g_A^2}{4F_\pi^2}\,\boldsymbol{\tau}_1\cdot\boldsymbol{\tau}_2\left(\frac{\vec\sigma_1\cdot\vec q\,\vec\sigma_2\cdot\vec q}{q^2+M_\pi^2}+C(M_\pi)\,\vec\sigma_1\cdot\vec\sigma_2\right) e^{-\frac{q^2+M_\pi^2}{\Lambda^2}}, \tag{23}$$

where $q\equiv|\vec q\,|\equiv|\vec p\,'-\vec p\,|$ and $\vec\sigma_i$ ($\boldsymbol{\tau}_i$) are the Pauli spin (isospin) matrices of the i-th nucleon. Here, the static pion propagator has been regularized according to Equation (22) and a likewise-regularized LO contact interaction has been added to the OPEP. Its coefficient $C(M_\pi)$,

$$C(M_\pi) = -\frac{\Lambda\left(\Lambda^2-2M_\pi^2\right)+2\sqrt{\pi}M_\pi^3 e^{\frac{M_\pi^2}{\Lambda^2}}\,\mathrm{erfc}\left(\frac{M_\pi}{\Lambda}\right)}{3\Lambda^3}, \tag{24}$$

with erfc(z) denoting the complementary error function, is fixed by the requirement that the spin-spin part of the OPEP in coordinate space vanishes at the origin. For the regularization of the TPEP, we start with a generic three-dimensional loop integral $I(\vec q\,)$ arising in the derivation of the TPEP using e.g., the method of unitary transformation as detailed in the previous section or comparable approaches like time-ordered perturbation theory or S-matrix-based methods [96]. As discussed in Rijken [118], the pion energy denominators in the corresponding 1-loop expressions can always be rewritten into an integral over a mass parameter λ involving a product of two static pion propagators with mass $\sqrt{M_\pi^2+\lambda^2}$

$$I(\vec q\,) = \int_0^\infty d\lambda\int\frac{d^3l_1}{(2\pi)^3}\frac{d^3l_2}{(2\pi)^3}(2\pi)^3\delta(\vec q-\vec l_1-\vec l_2)\,\frac{1}{(l_1^2+M_\pi^2+\lambda^2)(l_2^2+M_\pi^2+\lambda^2)}\times\ldots, \tag{25}$$

where $\vec l_1$ and $\vec l_2$ denote the three-momenta of the exchanged pions and the ellipses refer to additional momentum-spin-isospin structures arising from the vertices of a particular diagram. With the pion propagators factorized in this a way, we can regularize them by applying the prescription specified in Equation (22) to each of them. Although the introduction of the regulator obviously affects the resulting expression for the TPEP, there is no need to rederive them explicitly. Indeed, the scalar functions accompanying the spin-isospin operators in the *unregularized* TPEP can be expressed using the dispersive representation

$$V_{\rm 2N}^{2\pi}(q) = \frac{2}{\pi}\int_{2M_\pi}^\infty \mu\,d\mu\,\frac{\rho(\mu)}{q^2+\mu^2}, \tag{26}$$

with the spectral functions $\rho(\mu)=\Im(V_{2\pi}(q))|_{q=0^+-i\mu}$ which are readily available up to N^{4}LO. For the explicit expressions of the TPEP, additional subtractions of short-range terms have to be performed to arrive at a convergent spectral integral in Equation (26) whose number depends on the chiral order of the contribution at hand. Introducing the pion propagator regulators in Equation (25), the regularized generic spectral integral of Equation (26) is replaced by

$$V_{\rm 2N,\Lambda}^{2\pi}(q) = e^{-\frac{q^2}{2\Lambda^2}}\,\frac{2}{\pi}\int_{2M_\pi}^\infty \mu\,d\mu\,\frac{\rho(\mu)}{q^2+\mu^2}\,e^{-\frac{\mu^2}{2\Lambda^2}}, \tag{27}$$

see Reinert et al. [17] for more details. The resulting potential $V_{\rm 2N,\Lambda}^{2\pi}(q)$ coinsides with the one obtained by explicitly evaluating the loop integral with regularized pion propagators up to a short-range function.

Expanding the exponentials in inverse powers of the cutoff in either Equation (23) or Equation (27), one observes that the regulator indeed does not affect the long-range part of the potential to any order, but generates an infinite series of short-range terms polynomial in q^2. Since an increasing number of contact interactions of this form with freely adjustable LECs become available with increasing chiral order, the perturbative restoration of cutoff-independence is also obvious in this scheme.

The expressions of the regularized and subtracted TPEP can be found in Reinert et al. [17]. Here we restrict ourselves to the example of the isospin-independent central part of the leading TPEP at NLO which is given by

$$W_{C,\,\Lambda}^{(2)}(q) = e^{-\frac{q^2}{2\Lambda^2}}\,\frac{2}{\pi}\int_{2M_\pi}^\infty\frac{d\mu}{\mu^3}\rho_C^{(2)}(\mu)\left(\frac{q^4}{\mu^2+q^2}+C_{C,1}^2(\mu)+C_{C,2}^2(\mu)\,q^2\right)e^{-\frac{\mu^2}{2\Lambda^2}}, \tag{28}$$

with the spectral function

$$\rho_C^{(2)}(\mu) = \frac{\sqrt{\mu^2-4M_\pi^2}}{768\pi F_\pi^4\,\mu}\left(4M_\pi^2(5g_A^4-4g_A^2-1)-\mu^2(23g_A^4-10g_A^2-1)+\frac{48g_A^4M_\pi^4}{4M_\pi^2-\mu^2}\right). \tag{29}$$

Two subtractions have been performed in order to render the unregularized spectral integral in Equation (28) convergent and according to our convention, we have additionally fixed the subtraction coefficients $C_{C,1}^2(\mu)$ and $C_{C,2}^2(\mu)$ by the requirement that $W_{C,\,\Lambda}^{(2)}(r)\Big|_{r=0} = \frac{d^2}{dr^2}W_{C,\,\Lambda}^{(2)}(r)\Big|_{r=0} = 0$. [The first derivative of $W_{C,\,\Lambda}^{(2)}(r)$ vanishes at the origin regardless of the subtraction coefficients]. **Figure 3** shows the ratio of the regularized and unregularized expressions in Equation (28) in coordinate space. As one can see, the behavior of the regularized potential is smoother when fixing the subtraction coefficients by the convention explained above. Also note that the potential with $C_{C,1}^2(\mu)=C_{C,2}^2(\mu)=0$ does not vanish at the origin[10].

4.2. Regularization and Consistency of Nuclear Forces

Having defined the regularization scheme in the NN sector, we now turn to regularization of the 3NF. The expressions for the

[10]This is not visible in **Figure 3** since the unregularized potential $W_{C,\infty}(r)$ is singular at $r=0$.

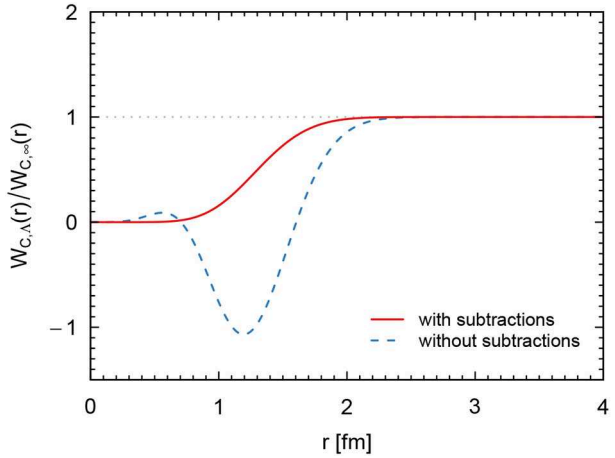


FIGURE 3 | Ratio of the regularized and unregularized central part of the leading TPEP in coordinate space for $C^2_{C,1}(\mu)$, $C^2_{C,2}(\mu)$ fixed as discussed in the text and $C^2_{C,1}(\mu) = C^2_{C,2}(\mu) = 0$.

3NFs described in section 3 have been worked out completely through N^{3}LO using DR. They are off-shell consistent with the unregularized NN interactions reviewed in that section in the way explained in section 2. To arrive at regularized 3NFs, it is tempting to apply some kind of multiplicative regulators to the expressions of the 3NF derived using DR. Such a naive approach, however, leads to a violation of the chiral symmetry at N^{3}LO and destroys the consistency between two- and three-nucleon forces after regularization.

To illustrate the problem consider the diagrams shown in **Figure 1**, which have already been discussed in section 2. The 3NF entering the first graph on the right-hand side (r.h.s.) is given by Bernard et al. [55]

$$V_{\rm 3N}^{2\pi,\,1/m} = i\frac{g_A^2}{32mF_\pi^4}\frac{\vec\sigma_1\cdot\vec q_1\,\vec\sigma_3\cdot\vec q_3}{(q_1^2+M_\pi^2)(q_3^2+M_\pi^2)}\boldsymbol\tau_1\cdot(\boldsymbol\tau_2\times\boldsymbol\tau_3)$$
$$(2\vec k_1\cdot\vec q_3+4\vec k_3\cdot\vec q_3+i\,[\vec q_1\times\vec q_3]\cdot\vec\sigma_2)\,, \qquad (30)$$

with $\vec q_i = \vec p\,'_i - \vec p_i$, $\vec k_i = 1/2(\vec p\,'_i - \vec p_i)$, and $\vec p_i$, $(\vec p\,'_i)$ the initial (final) momenta of the i-th nucleon. The complete expression for the relativistic corrections to the 3NF at N^{3}LO can be found in Bernard et al. [55]. We now consider the first iteration of $V_{\rm 3N}^{2\pi,\,1/m}$ with the static OPEP

$$V_{\rm 2N}^{1\pi} = -\left(\frac{g_A}{2F_\pi}\right)^2\boldsymbol\tau_1\cdot\boldsymbol\tau_2\frac{\vec\sigma_1\cdot\vec q\,\vec\sigma_2\cdot\vec q}{q^2+M_\pi^2} \qquad (31)$$

as shown by the first diagram on the r.h.s. of **Figure 1**. By simply counting the powers of momenta in the loop integration one observes that the loop integral is linearly divergent, which leads to a finite result in DR. As already pointed out in section 2, adding the DR expression for the 3NF $V_{\rm 3N}^{2\pi-1\pi}$ from Equations (2.16) to (2.20) of Bernard et al. [54] yields (on-shell) the same result as obtained from calculating the Feynman diagram on the l.h.s. of **Figure 1** as expected for consistent two- and three-nucleon forces.

We now repeat this exercise using the semilocally regularized nuclear potentials

$$V_{\rm 3N,\,\Lambda}^{2\pi,\,1/m} = V_{\rm 3N}^{2\pi,\,1/m}\,e^{-\frac{q_1^2+M_\pi^2}{\Lambda^2}}\,e^{-\frac{q_3^2+M_\pi^2}{\Lambda^2}}\,,$$
$$V_{\rm 2N,\,\Lambda}^{1\pi} = V_{\rm 2N}^{1\pi}\,e^{-\frac{q^2+M_\pi^2}{\Lambda^2}}\,, \qquad (32)$$

in the calculation of the first diagram on the r.h.s. of **Figure 2**. This leads to

$$V_{\rm 3N,\,\Lambda}^{2\pi,\,1/m}\,G_0\,V_{\rm 2N,\,\Lambda}^{1\pi} + V_{\rm 2N,\,\Lambda}^{1\pi}\,G_0\,V_{\rm 3N,\,\Lambda}^{2\pi,\,1/m}$$
$$= \Lambda\frac{g_A^4}{128\sqrt{2}\pi^{3/2}F_\pi^6}(\boldsymbol\tau_2\cdot\boldsymbol\tau_3-\boldsymbol\tau_1\cdot\boldsymbol\tau_3)\frac{\vec q_2\cdot\vec\sigma_2\vec q_3\cdot\vec\sigma_3}{q_3^2+M_\pi^2}$$
$$-\,\Lambda\frac{g_A^4}{96\sqrt{2}\pi^{3/2}F_\pi^6}\frac{\vec q_3\cdot\vec\sigma_3\vec q_3\cdot\vec\sigma_1\;\boldsymbol\tau_1\cdot\boldsymbol\tau_3}{q_3^2+M_\pi^2}+\ldots\,, \qquad (33)$$

where the ellipses refer to all permutations of the nucleon labels and terms finite in the $\Lambda\to\infty$-limit. The linear divergence $\propto \vec q_3\cdot\vec\sigma_3\vec q_3\cdot\vec\sigma_1$ is canceled by the D counter term in the second 3NF diagram at N^{2}LO in **Figure 2**. To cancel the linearly divergent contribution $\propto \vec q_2\cdot\vec\sigma_2$ one would, however, need to introduce a vertex in $\mathcal{L}^{(1)}_{\pi\rm NN}$ corresponding to a derivative-less coupling of the pion to the NN systems. Such vertices violate the chiral symmetry and, being suppressed by powers of M_π^2, cannot appear in $\mathcal{L}^{(1)}_{\pi\rm NN}$. As a consequence, this linear divergence can *not* be absorbed into redefinition of the LECs, and the amplitude on the r.h.s. of **Figure 1** can seemingly not be renormalized (i.e., made finite in the $\Lambda\to\infty$ limit). The r.h.s. of the shown equation, therefore, apparently cannot match the (renormalizable) on-shell scattering amplitude from the Feynman diagram on the l.h.s.. The problem can be traced back to mixing the DR when calculating the 3NF $V_{\rm 3N}^{2\pi-1\pi}$ with a cutoff regularization for the iterative contributions in Equation (33), see Krebs [77] for another example with the NN axial vector current operator at N^{3}LO. Indeed, recalculating the loop integral in $V_{\rm 3N}^{2\pi-1\pi}$ using the cutoff-regularized pion propagators leads to

$$V_{\rm 3N,\,\Lambda}^{2\pi-1\pi} = -\Lambda\frac{g_A^4}{128\sqrt{2}\pi^{3/2}F_\pi^6}(\boldsymbol\tau_2\cdot\boldsymbol\tau_3-\boldsymbol\tau_1\cdot\boldsymbol\tau_3)\frac{\vec q_2\cdot\vec\sigma_2\vec q_3\cdot\vec\sigma_3}{q_3^2+M_\pi^2}$$
$$-\Lambda\frac{g_A^4}{32\sqrt{2}\pi^{3/2}F_\pi^6}\frac{\vec q_3\cdot\vec\sigma_3\vec q_3\cdot\vec\sigma_1\;\boldsymbol\tau_1\cdot\boldsymbol\tau_3}{q_3^2+M_\pi^2}+\ldots\,, \qquad (34)$$

where the ellipses refer to the finite terms in the $\Lambda\to\infty$-limit. The problematic linear divergence cancels exactly and the agreement with the on-shell amplitude from the Feynman diagram is restored when both *consistently regularized* contributions on the r.h.s. of **Figure 1** are added together.

One may worry whether the regularization issues discussed above could also be relevant for NN interactions. Fortunately, this is not the case since the momentum structure of the NN contact interactions is not restricted by the chiral symmetry. UV divergences emerging from iterations of the LS equation can,

therefore, always be absorbed into redefinition of the bare LECs $C_{S,T}(\Lambda)$, $C_i\,(\Lambda)$, ...

In the considered example with the 3N amplitude, the consistently regularized 3NF could be obtained by simply recalculating $V_{\rm 3N}^{2\pi-1\pi}$ with all pion propagators being regularized according to Equation (22). This would indeed solve the problem with the cancelation of linear divergencies at N^{3}LO, but it would still lead to a violation of the chiral symmetry in diagrams involving three- and four-pion vertices, which depend on the parametrization of the pion field. For vertices involving up to four pion fields, this freedom is represented by a single real parameter α. In the effective chiral Lagrangian, all pion fields are collected in an SU(2) matrix $U(\boldsymbol{\pi})$, whose most general expression, expanded in powers of the pion fields, takes the form

$$U(\boldsymbol{\pi}) = 1 + \frac{i}{F}\boldsymbol{\pi}\cdot\boldsymbol{\tau} - \frac{1}{2F^2}(\boldsymbol{\pi}\cdot\boldsymbol{\tau})^2 - \alpha\frac{i}{F^3}(\boldsymbol{\pi}\cdot\boldsymbol{\tau})^3 + \left(\alpha - \frac{1}{8}\right)\frac{1}{F^4}(\boldsymbol{\pi}\cdot\boldsymbol{\tau})^4 + O(\boldsymbol{\pi}^5)\,. \tag{35}$$

Clearly, the on-shell amplitude must be independent of the arbitrary parameter α. Evaluating the 3NF and 4NF with the regularized pion propagators, however, leads to α-dependent expressions (for finite values of Λ). This shows, perhaps not surprisingly, that the simplistic approach by regularizing all pion propagators as described above violates the chiral symmetry. A possible solution of this problem is provided by the symmetry preserving higher derivative regularization method introduced by Slavnov [119], see also Djukanovic et al. [120] and Long and Mei [121] for recent applications in chiral EFT.

To summarize, we have shown that a naive regularization of the three- and more-nucleon forces by multiplying the expressions derived in DR with regulator functions leads to inconsistencies starting from N^{3}LO, see Krebs [77] for the same conclusion for two- and more-nucleon charge and current operators. This problem is by no means restricted to semilocal cutoffs. To derive many-body forces and currents regularized *consistently* with the NN potentials of Reinert et al. [17], the expressions for the 3NF of Bernard et al. [54, 55] and Krebs et al. [48], 4NF of Epelbaum [73], and exchange charge and current operators of Kölling et al. [74, 122] and Krebs et al. [75, 123] need to be recalculated using e.g., an appropriately chosen higher derivative regulator at the level of the effective Lagrangian.

5. TRUNCATION ERROR ANALYSIS

Estimating the uncertainty associated with truncations of the EFT expansion, which typically dominates the error budget (see section 6), is an important task – in particular since chiral EFT is being developed into a precision tool. In the past, truncation errors were often estimated in few-nucleon calculations from a residual cutoff dependence. This approach, however, suffers from several drawbacks and does not allow for a reliable estimation of truncation errors [113]. In Epelbaum et al. [21], we have formulated a simple algorithm to estimate the size of neglected higher-order terms based on the available information about the EFT expansion pattern for any given observable. To be specific, consider an arbitrary NN scattering observable X at the center of mass momentum p, which is calculated in chiral EFT up to the order Q^k

$$X(p) = X^{(0)} + \Delta X^{(2)} + \Delta X^{(3)} + \ldots + \Delta X^{(k)} + \Delta X^{(k+1)} + \ldots \equiv X^{(k)} + \delta X^{(k)}. \tag{36}$$

The corrections $\Delta X^{(i)}$, $\Delta X^{(i)} = \mathcal{O}\big(X^{(0)}Q^i\big)$, are assumed to be known explicitly up to the order $i = k$. The goal is to estimate the size of neglected higher-order terms $\delta X^{(k)} = \sum_{n>k}\Delta X^{(n)}$. We, furthermore, assume that the expansion parameter Q is given by

$$Q = \max\left(\frac{M_\pi^{\rm eff}}{\Lambda_{\rm b}},\ \frac{p}{\Lambda_{\rm b}}\right). \tag{37}$$

This simple ansatz is motivated by the expectation that at very low energies, the errors are dominated by the expansion around the chiral limit. The scale $M_\pi^{\rm eff}$, which will be specified below, is related to the pion mass and controls the convergence rate of the expansion around the chiral limit. At higher energies one would, on the other hand, expect the expansion to be dominated by powers of momenta. This simple picture is in qualitative agreement with the error plots for NN phase shifts [21], which show clearly the two different regimes mentioned above, see Epelbaum [82] for a discussion. It is less clear how to estimate the relevant momentum scale in bound-state observables.

The algorithm proposed by Epelbaum, Krebs and Meißner (EKM) in Epelbaum et al. [21] employs $M_\pi^{\rm eff} = M_\pi$ and $\Lambda_{\rm b} = 600$ MeV based on the estimation from the error plots. It also assumes the truncation error $\delta X^{(k)}$ to be dominated by the first neglected term. The truncation errors at orders Q^i, $0 \le i \le k$, are then estimated via

$$\delta X^{(0)} = Q^2|X^{(0)}|, \qquad \delta X^{(i)} = \max_{2\le j\le i}\left(Q^{i+1}|X^{(0)}|,\ Q^{i+1-j}|\Delta X^{(j)}|\right)\ \text{ for }\ i \ge 2\,, \tag{38}$$

subject to the additional constraint

$$\delta X^{(i)} \ge \max_{j,m=i,\ldots,k}\left(|X^{(j)} - X^{(m)}|\right), \tag{39}$$

which ensures that the estimated errors cannot be smaller than the known actual higher-order contributions. Notice that this relation leads, per construction, to overlapping errors at different orders. In Binder et al. [83], the method was adjusted to make it applicable to incomplete calculations of few-body observables based on NN interactions only. The EKM approach was applied to a broad range of low-energy reactions in the single-baryon [51, 124–126] as well as few- and many-nucleon [8, 22, 127–129] sectors. The robustness of this method and some alternative algorithms are discussed in Binder et al. [130]. The obvious drawback of the EKM approach is that the estimated uncertainties do not offer a statistical interpretation.

In Furnstahl et al. [131] and Melendez et al. [132, 133], a more general and statistically well-founded Bayesian approach was developed to calculate the probability distribution function (pdf)

for truncation errors in chiral EFT. The EKM approach was then shown to correspond to one particular choice of prior probability distribution for the coefficients in the chiral expansion of $X(p)$. In Furnstahl et al. [131], the EKM uncertainties for the np total cross section were found to be consistent with 68% degree-of-belief (DoB) intervals. The authors of that paper, furthermore, found using the semilocal coordinate-space regularized (SCS) potentials of Epelbaum et al. [21, 22] the assumed value of the breakdown scale of $\Lambda_b = 600$ MeV to be statistically consistent for not too soft regulator values, see also Melendez et al. [132] for a related discussion. Recently, a slightly modified version of the Bayesian approach developed in Furnstahl et al. [131] and Melendez et al. [132] was applied by the LENPIC Collaboration to study NN and 3N scattering [84]. Below, we briefly outline the Bayesian model $\bar{C}^{650}_{0.5-10}$ proposed in that paper, which will be employed throughout section 6. For more details on the Bayesian approach the reader is referred to the original publications [131, 132].

We begin with rewriting Equation (36) in terms of dimensionless expansion coefficients c_i by introducing a (generally dimensionfull) scale $X_{\rm ref}$ via

$$X = X_{\rm ref}\left(c_0 + c_2 Q^2 + c_3 Q^3 + c_4 Q^4 + \ldots\right), \qquad (40)$$

where[11]

$$X_{\rm ref} = \begin{cases} X_{\rm ref} = \max\left(|X^{(0)}|,\ Q^{-2}|\Delta X^{(2)}|\right) & \text{for} \quad k = 2\,, \\ X_{\rm ref} = \max\left(|X^{(0)}|,\ Q^{-2}|\Delta X^{(2)}|,\ Q^{-3}|\Delta X^{(3)}|\right) & \text{for} \quad k \geq 3\,. \end{cases} \qquad (41)$$

This choice of the reference scale was found in Epelbaum et al. [84] to be more robust for observables that depend on continuously varying parameters, as compared with the choice of $X_{\rm ref} = |X^{(0)}|$ adopted in Melendez et al. [132]. Alternatively, correlations between observables (and thus the coefficients c_i) evaluated at different values of continuously varying parameters can be taken into account using Gaussian processes [133]. Except for the coefficient $c_m = 1$, $m \in \{0, 2, 3\}$, used to set the scale $X_{\rm ref}$, the expansion coefficients c_i are assumed to be distributed according to some common pdf $\mathrm{pr}(c_i|\bar{c})$ with a hyperparameter $\bar{c}$. Performing marginalization over h chiral orders $k+1, \ldots, k+h$, which are assumed to dominate the truncation error, the probability distribution for the dimensionless residual $\Delta_k \equiv \sum_{n=k+1}^{\infty} c_n Q^n \simeq \sum_{n=k+1}^{k+h} c_n Q^n$ to take a value $\Delta_k = \Delta$, given the knowledge of $\{c_{i\leq k}\}$, is given by Melendez et al. [132]

$$\mathrm{pr}_h(\Delta|\{c_{i\leq k}\}) = \frac{\int_0^\infty d\bar{c}\,\mathrm{pr}_h(\Delta|\bar{c})\,\mathrm{pr}(\bar{c})\prod_{i\in A}\mathrm{pr}(c_i|\bar{c})}{\int_0^\infty d\bar{c}\,\mathrm{pr}(\bar{c})\prod_{i\in A}\mathrm{pr}(c_i|\bar{c})}\,, \qquad (42)$$

where the set A is defined as $A = \{n \in \mathbb{N}_0 \,|\, n \leq k \wedge n \neq 1 \wedge n \neq m\}$ and

$$\mathrm{pr}_h(\Delta|\bar{c}) \equiv \left[\prod_{i=k+1}^{k+h}\int_{-\infty}^{\infty} dc_i\,\mathrm{pr}(c_i|\bar{c})\right]\delta\left(\Delta - \sum_{j=k+1}^{k+h} c_j Q^j\right). \qquad (43)$$

[11] No meaningful uncertainty estimation can be carried out within the Bayesian approach at LO.

The model $\bar{C}^{650}_{0.5-10}$ utilizes the Gaussian prior of "set C" from Melendez et al. [132],

$$\mathrm{pr}(c_i|\bar{c}) = \frac{1}{\sqrt{2\pi}\bar{c}}\,e^{-c_i^2/(2\bar{c}^2)},$$
$$\mathrm{pr}(\bar{c}) = \frac{1}{\ln(\bar{c}_>/\bar{c}_<)}\,\frac{1}{\bar{c}}\,\theta(\bar{c}-\bar{c}_<)\,\theta(\bar{c}_>-\bar{c})\,, \qquad (44)$$

for which the integrals in Equation (42) can be performed analytically [132], and uses the values of $h = 10$, $\bar{c}_< = 0.5$ and $\bar{c}_> = 10$. Following Epelbaum [134], the scales that control the expansion parameter are set to $M_\pi^{\rm eff} = 200$ MeV and $\Lambda_b = 650$ MeV. The sensitivity of the estimated uncertainties to the choice of prior pdf is discussed in Epelbaum et al. [84], Furnstahl et al. [131], and Melendez et al. [132]. One generally finds minor dependence on the prior pdf if a sufficient amount of information on the coefficients c_i is available.

6. SELECTED RESULTS

6.1. The Two-Nucleon System

We now turn to the calculation of phase shifts and observables in the two-nucleon system. While the derivation and regularization of the nuclear forces have been outlined in the previous sections, we also need to specify the numerical values of all relevant physical quantities and LECs to perform actual calculations. For pion-exchange contributions to the potential, all LECs can be extracted from processes involving at most one nucleon, making it parameter-free. In the TPEP, we use the values of the πN LECs as determined recently by matching the πN scattering amplitude from chiral perturbation theory to a Roy-Steiner equations analysis of πN scattering data at the subthreshold point [50].

We account for the isospin-breaking effects due to the different pion masses in the OPEP and employ the physical masses of the charged and neutral pions $M_{\pi^\pm} = 139.57$ MeV and $M_{\pi^0} = 134.98$ MeV, while we use the isospin-averaged value of $M_\pi = 138.03$ MeV in the TPEP. We adopt an effective value of $g_A = 1.29$ for the nucleon axial coupling constant which is slightly larger than the current experimental average value of $g_A = 1.2723(23)$ [135] because it already accounts for the Goldberger-Treiman discrepancy (see [136] for a related discussion). The employed value of the pion decay constant is $F_\pi = 92.4$ MeV.

In contrast to the parameter-free long-range potential, the short-range contact interactions in the two-nucleon force have to be determined from experimental NN data. In order to achieve a proper reproduction of pp and, to a lesser extent, np scattering data, it is crucial to also include electromagnetic interactions between the nucleons. Although these interactions are accompanied by powers of a numerically small coupling constant $\alpha \sim 1/137$, they are enhanced at low energies and/or forward angles due to the infrared singularity of the photon propagator or, equivalently, due to their long-range nature. Here, we follow the treatment of the Nijmegen group [137] and include the so-called improved Coulomb potential [138], the magnetic-moment interaction [139] as well as the vacuum-polarization

potential [140] in the calculation of proton-proton observables. The magnetic moment interaction is also taken into account in neutron-proton scattering. To the best of our knowledge, these effects have been included in every partial-wave analysis (PWA) of or fit of a high-quality potential model from NN data since the Nijmegen PWA of Stoks et al. [137], so that differences in their predictions stem from modeling the strong interaction, the experimental input and/or details of the fitting procedure itself.

For scattering data we use the Granada-2013 database [18] which consists of experimental data for NN elastic scattering up to $E_{\rm lab} = 350$ MeV from 1950 up to 2013[12]. The database contains the data that have been found to be mutually compatible by means of a 3σ rejection criterion in the corresponding phase shift analysis of Navarro Pérez et al. [18]. The presence of very precisely measured proton-proton data in the database, such as those of Cox et al. [142], motivated us to introduce the $\mathrm{N^4LO^+}$ version of the potential. As the proper description of these data requires a precise reproduction of F-waves, the $\mathrm{N^4LO^+}$ potential adds the four leading F-wave contact interactions

$$\langle {}^S F_j,\, p' | V_{\rm cont} | {}^S F_j,\, p \rangle = E_{SFj}\, p^3 p'^3\,, \tag{45}$$

formally appearing at $\mathrm{N^5LO}$ and entering the ${}^3F_2$, ${}^1F_3$, ${}^3F_3$, and ${}^3F_4$ partial waves, to the $\mathrm{N^4LO}$ potential.

The fits have been performed for all cutoffs $\Lambda = 400, 450, 500,$ and 550 MeV as well as for all orders from LO up to $\mathrm{N^4LO^+}$[13]. When determining the values of the contact LECs, one has to decide up to which energy $E_{\rm lab}$ the experimental data should be taken into account. One is faced with the two competing features: on the one hand, the inclusion of as many data as possible is desirable from a data fitting point of view. On the other hand, the truncation errors for the chiral interactions become larger at high energies. We therefore chose the maximum energy $E_{\rm lab}$ of data to be included to be $E_{\rm max} = 260$ MeV for $\mathrm{N^4LO}$ and $\mathrm{N^4LO^+}$, while we reduced the energy to $E_{\rm max} = 25, 100, 125,$ and 200 MeV at the orders LO, NLO, $\mathrm{N^2LO}$, and $\mathrm{N^3LO}$, respectively. Notice that balancing the tradeoff between these two competing features can be handled using Bayesian methods (see e.g., [143]). From $\mathrm{N^3LO}$ on, we also adjust the deuteron binding energy B_d and the coherent neutron-proton scattering length $b_{\rm np}$ to reproduce their experimental values of $B_d = 2.224575(9)$ MeV [144] and $b_{\rm np} = -3.7405(9)$ fm [145].

Table 1 shows the reproduction of neutron-proton and proton-proton scattering data in terms of χ^2/datum values at all considered orders for the cutoff $\Lambda = 450$ MeV[14]. We employ a standard definition of the objective function in terms of a sum of squared residuals as detailed in Reinert et al. [17]. As expected, a clear order-by-order improvement in the description of the scattering data can be seen. **Table 1** also gives the number of adjustable parameters at each order which also includes isospin-breaking LECs contributing to the ${}^1S_0$ partial wave. It should be noted that no new contact interactions are added when going from NLO to $\mathrm{N^2LO}$ and that the observed improvement of the χ^2/datum values is entirely due to the $\mathrm{N^2LO}$ contributions to the parameter-free TPEP. A similar situation occurs when going from $\mathrm{N^3LO}$ to $\mathrm{N^4LO}$, although here we also allow for additional isospin-breaking of the C_{1S0} contact LEC splitting it into two independently adjustable parameters for the neutron-proton and proton-proton/neutron-neutron systems. These improvements demonstrate both the importance of the chiral TPEP in the nuclear force and the predictive power of chiral perturbation theory, which allows to use LECs extracted in one process for making parameter-free predictions for (parts of) another.

TABLE 1 | χ^2/datum for the description of the neutron-proton and proton-proton scattering data at various orders in the chiral expansion for $\Lambda = 450$ MeV.

E_{lab} bin	$\mathrm{LO}_{(3)}$	$\mathrm{NLO}_{(10)}$	$\mathrm{N^2LO}_{(10)}$	$\mathrm{N^3LO}_{(22)}$	$\mathrm{N^4LO}_{(23)}$	$\mathrm{N^4LO^+}_{(27)}$
Neutron–proton scattering data						
0–100	73	2.2	1.2	1.07	1.07	1.07
0–200	62	5.4	1.7	1.09	1.08	1.06
0–300	75	14	4.2	2.01	1.16	1.06
Proton-proton scattering data						
0–100	2290	10	2.2	0.90	0.88	0.86
0–200	1770	90	37	1.99	1.42	0.95
0–300	1380	90	41	3.43	1.67	1.00

The numbers in brackets after the order indicate the number of parameters entering the neutron-proton and proton-proton potentials.

Starting from $\mathrm{N^3LO}$, a satisfactory description of the neutron-proton data in the energy range of $E_{\rm lab} = 0 - 200$ MeV and the proton-proton data for $E_{\rm lab} = 0 - 100$ MeV is achieved. Although the $\mathrm{N^4LO}$ potential improves on this, especially at intermediate and higher energies, it does not achieve a χ^2/datum ~ 1 description of the proton-proton data for $E_{\rm lab} \geq 100$ MeV. In the intermediate region, this value is significantly affected by the already mentioned high-precision data which requires an accurate description of F-waves. At $\mathrm{N^4LO}$ the differential cross section data set of Cox et al. [142] at $E_{\rm lab} = 144.1$ MeV, although well described within the Bayesian truncation errors, yields a χ^2/datum value of 27.88.

The situation is much improved once we switch to the $\mathrm{N^4LO^+}$ potential and short-range interactions in F-waves are added. The description of scattering data at higher energies is generally improved and also the high-precision proton-proton data at intermediate energies is accurately reproduced leading to a χ^2/datum ~ 1 description of the complete scattering database. Throughout the orders LO $-$ $\mathrm{N^4LO}$ the χ^2/datum value for proton-proton scattering up to 200 or 300 MeV has been larger than the one for neutron-proton scattering. This is plausible as proton-proton data is in general more precise than neutron-proton data and because only isovector partial waves contribute to it and hence only roughly half of the total number of parameters. However, at $\mathrm{N^4LO^+}$, the reproduction of proton-proton data becomes very accurate while the slightly

[12]Strictly speaking, our database differs from the one of Navarro Pérez [18] by the omission of the data set from Daub et al. [141] (see [17] for more details).

[13]In our paper Reinert et al. [17], also the cutoff $\Lambda = 350$ MeV was considered. Given the sizable finite-Λ artifacts for this very soft cutoff choice, we do not consider this case in the following discussion.

[14]We have corrected the last figures in the values for χ^2/datum for np data in the $E_{\rm lab}$ bins of 0–100 and 0–200 MeV at $\mathrm{N^3LO}$ and $\mathrm{N^4LO^+}$ quoted in Table 3 of Reinert et al. [17].

larger χ^2/datum values for the neutron-proton data as compared to proton-proton data reflect the larger statistical fluctuations among different data sets. This can be seen as an indication for reaching the threshold where the model accuracy approaches the precision of the data. In fact, the description of the scattering data at N^{4}LO$^+$ and $\Lambda = 450$ MeV is comparable to or exceeds that of the high-quality semi-phenomenological potentials such as CD-Bonn [146], Nijm I, II [147], and Reid93 [147]. Thanks to the parameter-free effects of the TPEP this is achieved with only 27 adjustable short-range parameters instead of the $\sim 40 - 50$ parameters used in those potentials.

Indeed, due to the excellent description of the data, the obtained results at $\Lambda = 450$ MeV qualify to be considered a partial-wave analysis. In **Figures 4**, **5**, we show the obtained N^{4}LO$^+$ neutron-proton and proton-proton phase shifts for $\Lambda = 450$ MeV, respectively. We compare them to the 2013 Granada analysis [18] and in the case of neutron-proton scattering also to the corresponding 2008 analysis by Gross and Stadler [148]. Furthermore, we also show the predictions from the N^{4}LO$^+$ potential of Entem et al. [23] at the intermediate cutoff $\Lambda = 500$ MeV.

In general, there is good agreement between the shown N^{4}LO$^+$ phase shifts and the results obtained by the considered phase shift analyses. This is especially true for the case of proton-proton phase shifts which are more strongly constrained by the precise experimental data. Some discrepancies among the different results remain e.g., around the maximum of the $^3P_0$ phase shift where the N^{4}LO$^+$ prediction for the proton-proton phase is slightly larger than the ones of the Nijmegen and Granada PWAs, resulting in a $\sim 3\sigma$ deviation from the former at $E_{\rm lab} = 50$ MeV. On the other hand, our neutron-proton phase shifts fall in between the results of the two PWAs. The study of isospin-breaking effects in P-waves beyond the ones included in the two PWAs and the current version of the semilocal momentum-space regularized (SMS) interaction of Reinert et al. [17] is expected to shed some light on this issue. We can also compare our results at N^{4}LO$^+$ to the ones of Entem et al. [23]. Similar to the comparison with the PWAs, agreement with proton-proton phases is better than with neutron-proton ones. There are, however, notable differences in the $^3P_0$, $^3P_2$, and $^3D_2$ waves starting at low or intermediate energies. At higher energies around $E_{\rm lab} = 250 - 300$ MeV, a change in curvature of the phase shift as a function of energy is visible e.g., in the $^1P_1$ and $^3P_1$ waves, which is presumably caused by the regulator employed in Entem et al. [23]. The effects of regulator artifacts can be observed particularly well in the $^1G_4$, $^3H_4$, and ϵ_4 phase shifts and mixing angle shown in **Figure 5** since they do not involve any adjustable short-range parameters at N^{4}LO$^+$ but are solely determined by the long-range pion-exchange potential. Here, the local regulator of Equation (22) leads to an undistorted reproduction of the peripheral phase shifts.

Selected proton-proton scattering observables and their estimated truncation error at various orders are shown in **Figure 6** for $E_{\rm lab}$ around ~ 143 MeV. In particular, we show our predictions for the differential cross section at $E_{\rm lab} = 144.1$ MeV and compare them with two high-precision data sets, most notably the one of Cox et al. [142], which motivated the introduction of the N^{4}LO$^+$ potential as discussed above. The data are well described within the given truncation error for all considered orders, but the N^{4}LO$^+$ clearly allows for a proper quantitative description. Likewise, the reproduction of the spin observables in **Figure 6** is excellent already at N^{3}LO with a good convergence pattern. Notice however, that the error bands at lower orders for D (A) at the minimum (maximum) around $\Theta_{\rm CM} = 150^\circ$ do not overlap with the ones for N$^{\geq 3}$LO and are indeed underestimating the uncertainty. Here we find that the value of the observable in that particular angular region is notably shifted starting at N^{3}LO while lower-order corrections are small, such that the overall scale in Equation (41) is still underestimated. Using a more sophisticated Bayesian approach of Melendez et al. [133] would likely allow for a more reliable estimation of the truncation errors at LO-N^{2}LO in these particular cases.

There are various a posteriori checks that can be performed to test the self-consistency and quality of the fit. First, the values of the LECs have to be of natural size assuming the cutoff is kept below the hard scale. The expected sizes of the spectroscopic contact LECs can be estimated to be [21]

$$|\tilde{C}_i| \sim \frac{4\pi}{F_\pi^2}, \quad |C_i| \sim \frac{4\pi}{F_\pi^2 \Lambda_{\rm b}^2}, \quad |D_i| \sim \frac{4\pi}{F_\pi^2 \Lambda_{\rm b}^4}, \quad |E_i| \sim \frac{4\pi}{F_\pi^2 \Lambda_{\rm b}^6}, \tag{46}$$

where the LECs $\tilde{C}_i$, C_i, D_i, and E_i start to contribute at order Q^0, Q^2, Q^4, and Q^6, respectively. $\Lambda_{\rm b}$ is the breakdown scale of the chiral expansion discussed in section 5. Furthermore, the factor of 4π emerges from the angular integration of the partial-wave decomposition and has been included in the definition of the spectroscopic LECs. If we now divide the contact LECs obtained in the fit by their expected sizes in Equation (46), we consequently should obtain values of unit magnitude. **Figure 7** shows the absolute values of the LECs at N^{4}LO$^+$ in these natural units for all considered values of the cutoff Λ using $\Lambda_{\rm b} = 650$ MeV. As can be seen, all LECs are indeed of natural size with D_{1S0} and D_{3S1} being among the largest in magnitude. This is especially true for the softest cutoff $\Lambda = 400$ MeV, for which also most of the other-Q^4 LECs turn out to be slightly larger than at higher values of the cutoff. This indicates that at $\Lambda = 400$ MeV and below, finite-cutoff artifacts start to increase, leading to a lower effective breakdown scale compared to the other considered cutoffs. Notice further that the values for the Q^6 LECs E_i included at N^{4}LO$^+$ turn out to be of a perfectly natural size. Therefore, even though we have emphasized their importance in describing some high-precision proton-proton data and achieving a χ^2/datum ~ 1 description of the database, their actual contributions agree with the expectations from naive dimensional analysis (i.e., Weinberg) power counting, and there is no need to promote them to a lower order.

In addition to the absolute of the central values, **Figure 7** also shows the statistical uncertainties of the contact LECs as determined from the covariance matrix of the fit (expressed in their natural units). When going from $\tilde{C}_i$, C_i, D_i to E_i the statistical relative errors tend to increase. This is in accordance with the decreasing importance of higher-order contributions as predicted by power counting. One also notices that errors are smaller for LECs entering isovector partial waves, because

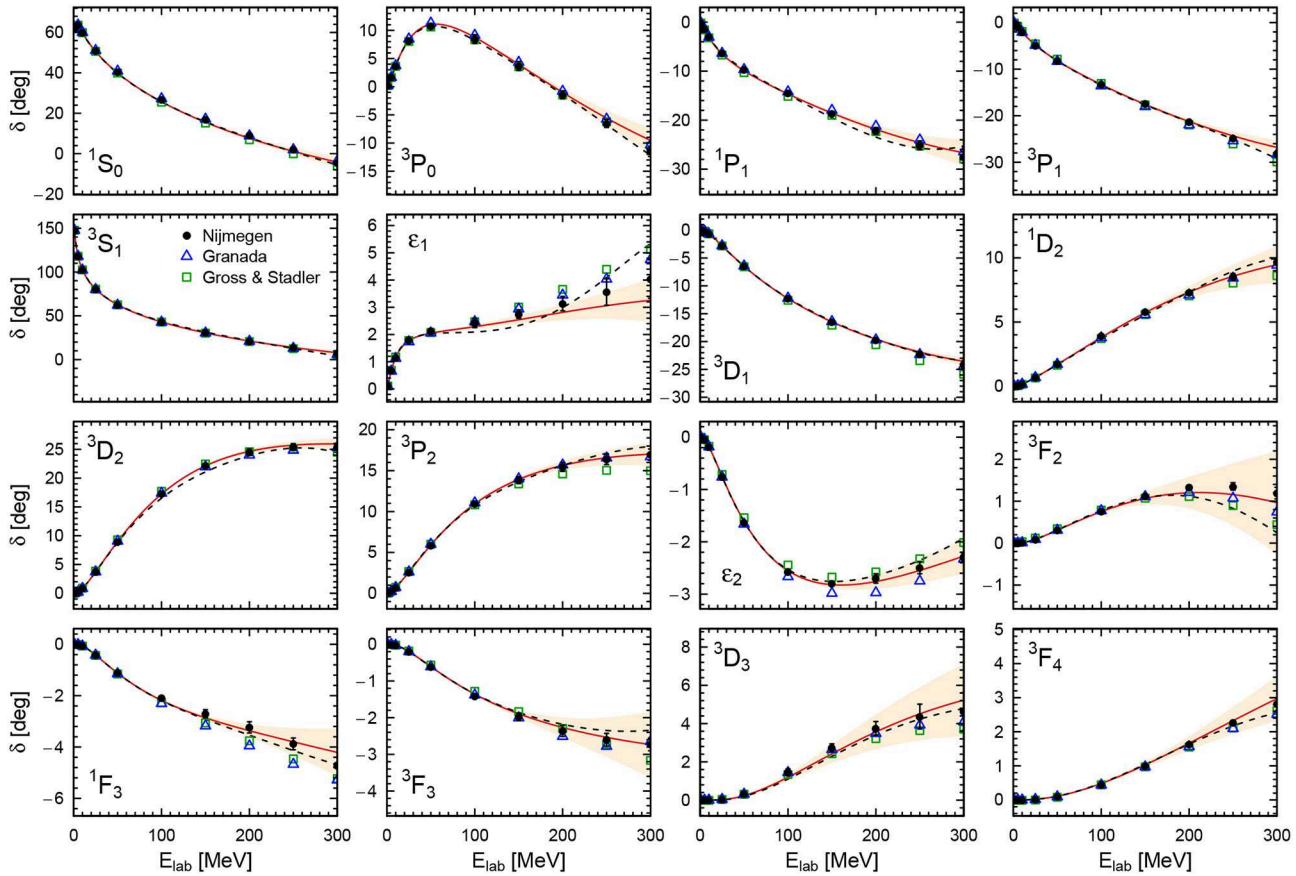


FIGURE 4 | Neutron-proton phase shifts with respect to Riccati-Bessel functions in comparison with the Nijmegen [137] (solid dots), the Granada [149] (blue open triangles), and Gross-Stadler [148] (green open squares) PWA. Red solid lines and peach-colored bands denote the central results and 68% DoB truncation errors at the order N^4LO^+ for the cutoff $\Lambda = 450$ MeV. Black dashed lines denote the result of the nonlocal N^4LO^+ potential of Entem et al. [23] for the cutoff $\Lambda = 500$ MeV. The shown uncertainties of the Nijmegen PWA correspond to systematic errors defined in Equation (32) of Epelbaum et al. [21].

these parameters are mainly constrained by the more precise proton-proton data. Since we perform a combined fit of neutron-proton and proton-proton data, the isovector partial waves are not only constrained by more precise data but also by more data in general compared to the isoscalar partial waves which have to be extracted from neutron-proton data alone. The covariance matrix also gives access to the correlations among the LECs. As to be expected, correlations mostly occur among LECs entering the same partial waves with the largest ones arising in the channels with the most parameters, namely in the $^1S_0$ and $^3S_1 - {}^3D_1$ channels. Nevertheless, all LECs are well-constrained as can already be seen by looking at the errors in **Figure 7**. We can further look at the largest eigenvalue of the covariance matrix of the natural LECs as a measure of how well-determined the parameters are. Throughout the considered range of the cutoff $\Lambda = 400 - 550$ MeV, the largest eigenvalue of the covariance matrix does not exceed 0.1 and is ~ 0.08 for $\Lambda = 450$ MeV.

From the point of view of data fitting, another check concerns the statistical assumptions underlying a χ^2 fit. One usually assumes that the residuals $r_i = (O_i^{\rm exp} - O_i^{\rm th})/\Delta O_i$ follow a normal distribution $\mathcal{N}(0,1)$ with zero mean and unit standard deviation. Here $O_i^{\rm exp}$ and ΔO_i are the experimental value and its error of an observable and $O_i^{\rm th}$ is its calculated "theoretical" value. If the assumptions on the normally-distributed residuals can be verified, this confirms that the data are described sufficiently well by the theoretical model. An easy and often employed check is the value of χ^2 per degree of freedom. For the N^4LO^+ fit with $\Lambda = 450$ MeV we get $\chi^2 = 4708.65$ in the fitting range of $E_{\rm lab} = 0 - 260$ MeV with the number of data $N_{\rm dat} = 4616$ and the number of parameters $N_{\rm par} = 27$. Consequently, we obtain $\chi^2/\nu = 1.026$ with $\nu = N_{\rm dat} - N_{\rm par}$. If the residuals are indeed normal-distributed then χ^2/ν should follow the χ^2-distribution and yields $\chi^2/\nu = 1 \pm \sqrt{2/\nu} = 1 \pm 0.021$ as the 68% confidence interval.

We can go one step beyond this simple check and plot the quantiles of the empirical distribution of residuals r_i that we obtain against the quantiles of the assumed normal distribution $\mathcal{N}(0,1)$. If they are the same, they should lie on the diagonal line $x = y$. In order to statistically quantify deviations from the diagonal, confidence bands have been derived with one of the most recent and most sensitive being the ones of the "tail-sensitive test" by Aldor-Noiman et al. [154]. This graphical

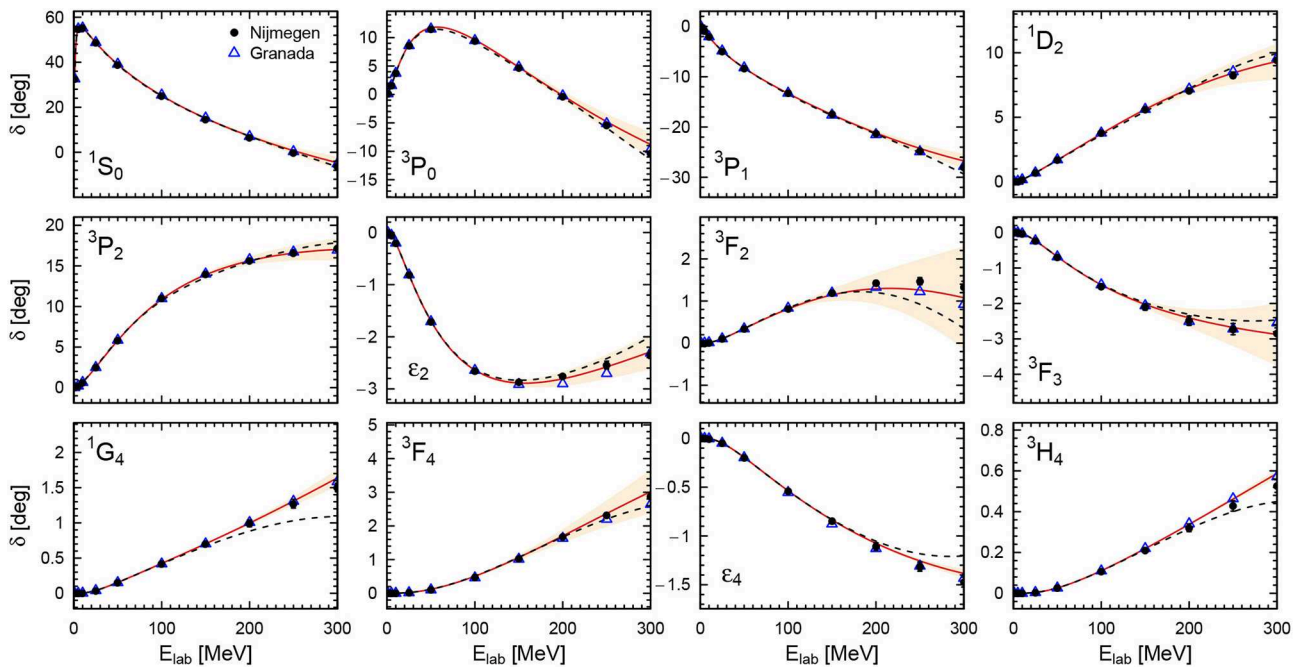


FIGURE 5 | Proton-proton phase shifts with respect to Coulomb wave functions in comparison with the Nijmegen [137] (solid dots) and the Granada [149] (blue open triangles) PWA. Red solid lines and peach-colored bands denote the central result and 68% DoB truncation errors at the order N^4LO^+ for the cutoff $\Lambda = 450$ MeV. Black dashed lines denote the result of the nonlocal N^4LO^+ potential of Entem et al. [23] for the cutoff $\Lambda = 500$ MeV. The shown uncertainties of the Nijmegen PWA correspond to systematic errors defined in Equation (32) of Epelbaum et al. [21].

test for normal-distributed residuals has been first applied to the analysis of nucleon-nucleon scattering by Navarro Pérez et al. [155]. **Figure 8** shows a rotated quantile-quantile plot for the N^4LO^+ residuals at $\Lambda = 450$ MeV where the theoretical quantiles have been subtracted from the empirical ones on the y-axis, turning the diagonal line into a horizontal one. As evident from the figure, the empirical distribution of residuals lies within the 68% confidence region of the tail-sensitive test signaling that the residuals are indeed normal-distributed. The quantile-quantile plot for the other values of the cutoff turn out to be overall similar, but perform slightly worse. For $\Lambda = 500$ MeV and $\Lambda = 550$ MeV the quantiles that are already close to the edge of the 68% confidence region in **Figure 8** cross these limits but still stay well within the 95% confidence region. The increased cutoff-artifacts at $\Lambda = 400$ MeV manifest themselves in a stronger deviation from normality as the plotted quantiles also cross the 95% confidence limits at the spike at $Q_{\rm th} = 2$ in **Figure 8**.

We now turn to the extended error analysis for observable predictions. While the truncation of the chiral expansion is clearly the dominant source of uncertainty at higher energies, other sources of uncertainty can become relevant at N^4LO^+. In particular we account for the following sources of uncertainty:

- *Statistical uncertainties of NN LECs:* As already mentioned, **Figure 7** shows the statistical errors of the contact LECs as determined from the covariance matrix of the fit. The uncertainties of the parameters can then be propagated from the covariance matrix to the observable of interest. While it is always possible to do this via a Monte Carlo sampling of the corresponding multivariate Gaussian probability distribution, it is computationally much more convenient to do a Taylor expansion of the desired observable with respect to the LECs and evaluate the moments of the LECs analytically. While a linear expansion is commonly employed, it has been argued in Carlsson et al. [114], that some observables require a second order expansion for an accurate reproduction of their uncertainties. In the case of large second-order contributions, the error bars become asymmetric and we usually give both the upper and lower error to accommodate for this possibility. Notice that in such a case, the probability density of the observable is not Gaussian and the quoted uncertainties do not necessarily correspond to a 68% degree-of-belief.
- *Statistical uncertainties of πN LECs:* In addition to the central values, the authors of Hoferichter et al. [50] also give the covariance matrix as determined from πN scattering data. Propagation of these uncertainties to NN observables is, however, less straightforward, because the values of the NN contact interactions depend on the values of πN LECs. We thus resort to some Monte Carlo sampling of the multivariate Gaussian probability distribution of the πN LECs given by their central values and their covariance matrix. For each of the sampled sets of LECs, we refit the NN contact LECs before calculating any observables. The uncertainty of a given observable can then be estimated in a standard way from the variance of the results calculated with different πN LEC

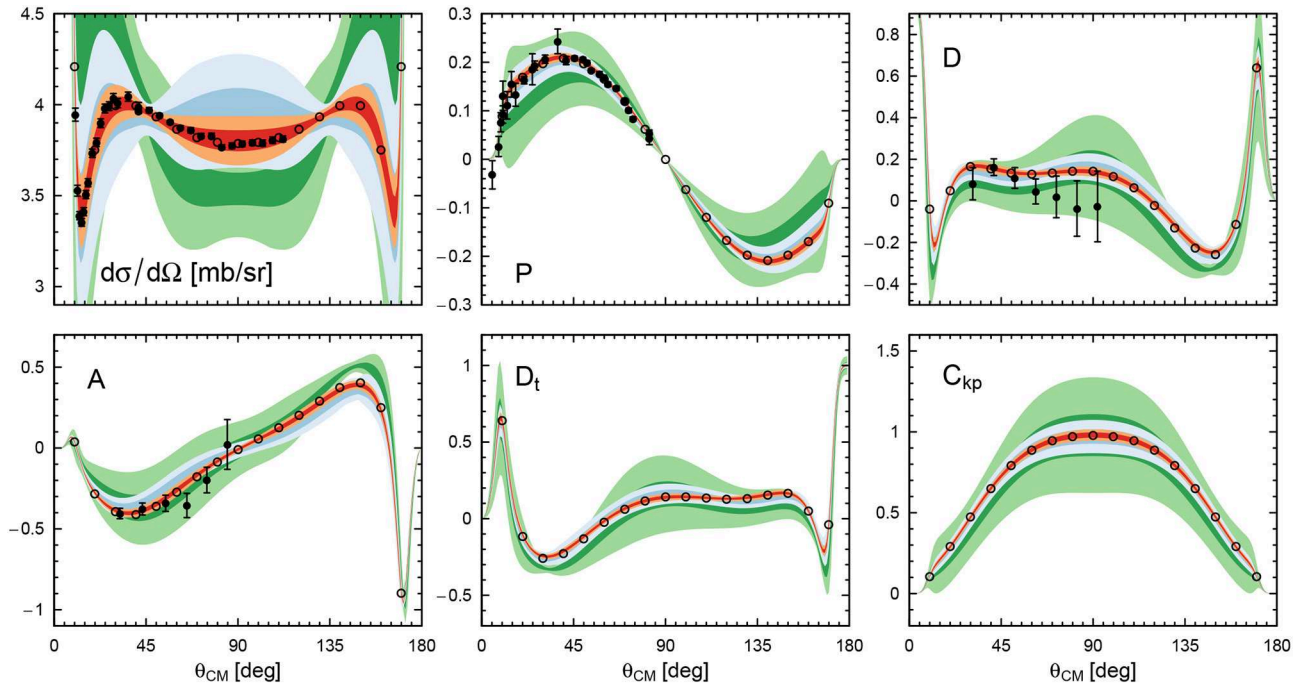


FIGURE 6 | Selected proton-proton observables around $E_{\rm lab} = 143$ MeV: Differential cross section $d\sigma/d\Omega$ at $E_{\rm lab} = 144.1$ MeV with experimental data taken from Cox et al. [142] and Jarvis et al. [150]. The data sets have been corrected for their estimated norms of 0.988 and 1.001, respectively. Analyzing power P at $E_{\rm lab} = 142$ MeV with experimental data taken from Taylor et al. [151]. The data have been floated and multiplied by an estimated norm of 0.942. Depolarization D, rotation parameter A, polarization transfer coefficient D_t, and spin-correlation parameter C_{kp} at $E_{\rm lab} = 143$ MeV with experimental data taken from Bird et al. [152] and Jarvis et al. [153]. The light- (dark-) shaded green, blue, and red bands depict the 68% (95%) DoB truncation errors at N^{2}LO, N^{3}LO, and N^{4}LO$^+$, respectively. Open circles show the predictions of the Nijmegen partial-wave analysis [137].

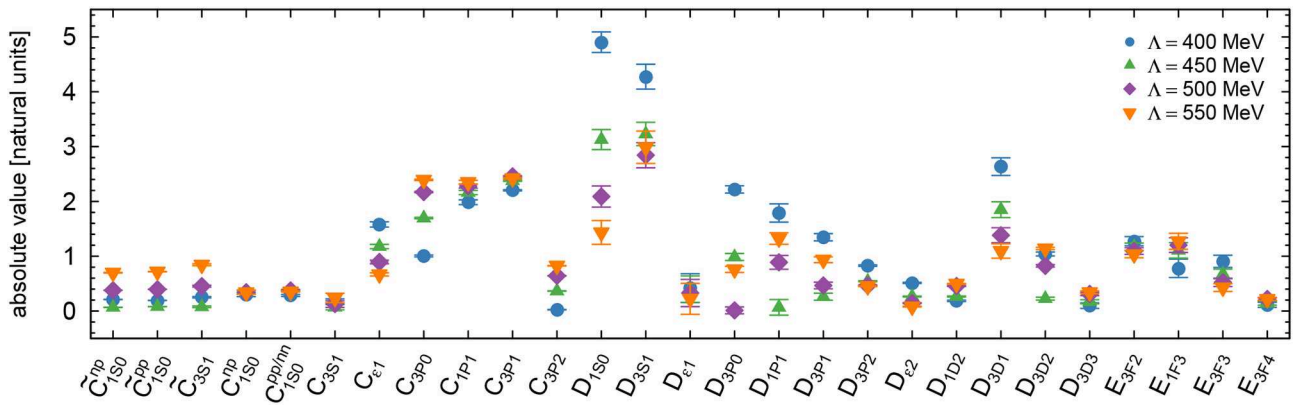


FIGURE 7 | Absolute values of the contact interaction LECs in natural units at the order N^{4}LO$^+$ for all considered cutoffs. Error bars represent the statistical errors of the LECs.

sets. Due to the need to refit the contact interactions for each sampled set of πN LECs and the computational overhead related to it, we have restricted the total number of such sets to 50. Although this is a quite low statistics for a Monte Carlo approach, it should give an idea of the order of magnitude of the uncertainty. It indeed turns out that the uncertainty related to the statistical error of the πN LECs is small compared to the other sources of uncertainty. However, the aforementioned approach does not probe the systematic errors in the determination of the πN LECs emerging from the truncation of the chiral expansion and thus does not represent the full uncertainty related to these LECs.

- *Uncertainty due to the choice of the maximum fit energy:* The extracted values of the contact LECs also depend on details of the fitting protocol. In particular, we probe the impact of the choice for the maximum laboratory energy

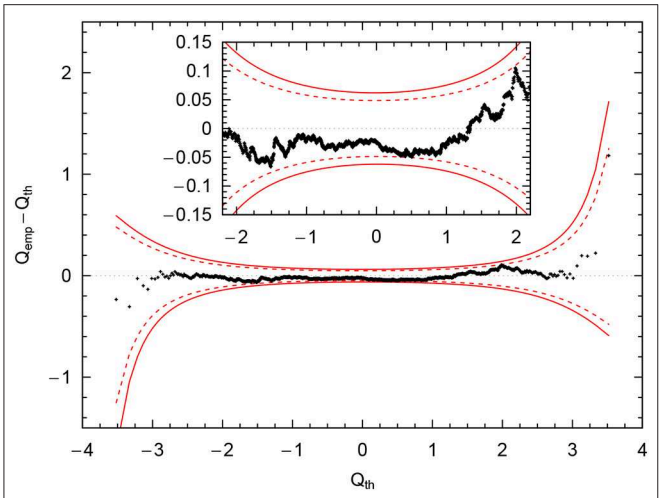


FIGURE 8 | Rotated Quantile–Quantile plot of the empirical quantiles at N^4LO^+ and $\Lambda = 450$ MeV vs. the quantiles of the normal distribution $\mathcal{N}(0, 1)$ Dotted (solid) red bands denote the 68% (95%) confidence bands of the tail-sensitive test by Aldor-Noiman et al. [154].

$E_{\max} = 260$ MeV up to which scattering data is included in the N^4LO^+ fit. This is achieved by performing additional fits with $E_{\max} = 220$ MeV and $E_{\max} = 300$ MeV and determining the maximum deviation of the observables from the $E_{\max} = 260$ MeV predictions. Unlike the aforementioned uncertainties, the error estimated via this simple procedure does not reflect any particular degree-of-belief.

As an example, **Figure 9** shows the neutron-proton total cross section and the corresponding uncertainties in the energy range $E_{\rm lab} = 0 - 300$ MeV. The plot on the left in **Figure 9** shows the ratio of our predictions using the N^4LO^+ potential at $\Lambda = 450$ MeV and the result of the Nijmegen partial-wave analysis [137]. In the right panel, the different relative errors stemming from the various sources discussed above are shown. For the case of the statistical errors of the NN contact interactions, second order effects and resulting asymmetries in the error bands turn out to be small for the total cross section, and the plotted uncertainty corresponds to the average of upper and lower statistical errors. As expected, the dominant contribution to the uncertainty at higher energies ($E_{\rm lab} > 100$ MeV) arises from the truncation of the chiral expansion. At lower energies, however, other sources of uncertainty become relevant and indeed both the statistical errors of the NN contact LECs and the uncertainty due to the maximum fitting energy are larger than the truncation error in the range of $E_{\rm lab} = 30 - 100$ MeV. When quantitatively comparing the different errors, one has to keep in mind that the uncertainty due to the maximum fitting energy does not correspond to a particular degree-of-belief. The uncertainty arising from the statistical errors of the πN LECs is found to be significantly smaller throughout the whole considered energy range and is negligible for the total cross section. Finally, we would like to comment on the origin of the existing kinks in the right-hand-side plot of **Figure 9**. In particular, the kink in the $E_{\max}$-error at around 200 MeV arises because of the maximum operation. Below 200 MeV, the error is dominated by the deviation of the $E_{\max} = 220$ MeV fit while it is given by the deviation of the $E_{\max} = 300$ MeV fit above 200 MeV. The second kink present in the truncation error, on the other hand, is caused by the transition of Q from $M_\pi^{\rm eff}/\Lambda_{\rm b}$ to $p/\Lambda_{\rm b}$.

Table 2 shows the deuteron properties as predicted by various high-quality potentials. Clearly, the error analysis can also be applied to the bound state properties of **Table 2**. However, the obtained uncertainties are only meaningful for a complete calculation of an unconstrained observable. This excludes the deuteron binding energy B_d (as it is a fitted quantity), the quadrupole moment Q and deuteron radius r_d (as meson exchange currents and relativistic corrections are not taken into account) as well as the D-state probability P_D (which is not observable). On the other hand, we can perform the uncertainty quantification for the asymptotic S-state normalization A_S and the asymptotic D/S-state ratio η for which we obtain at N^4LO^+ and for $\Lambda = 450$ MeV the values of $A_s = 0.8847^{(+3)}_{(-3)}(5)(0)(1)$ and $\eta = 0.02553^{(+11)}_{(-9)}(4)(3)(8)$, respectively. Here the first, second, third, and fourth error refer to the NN statistical, truncation, πN statistical, and $E_{\max}$ uncertainty, respectively. Notice that the quoted truncation errors estimated using the Bayesian model of section 5 are fairly similar to the ones given in Reinert et al. [17], which were obtained using the EKM method. On the other hand, the πN statistical uncertainties are much smaller than the corresponding errors quoted in Reinert et al. [17], where an attempt was made to also include systematic effects by using the values of these LECs determined in the physical region of πN scattering.

Finally, let us discuss the treatment of isospin-breaking effects in the two-nucleon interaction. Like all modern high-precision potentials, the SMS interactions include isospin-breaking in the OPEP due to the different physical pion masses $M_{\pi^\pm}$ and M_{π^0} and charge dependence of the short-range potential in the $^1S_0$ partial wave. These are the dominant and well-understood isospin-breaking effects necessary to arrive at e.g. a correct description of the charge-dependence of the $^1S_0$ scattering length. For the calculation of scattering observables in the two-nucleon system, the isospin-breaking due to long-range electromagnetic interactions is taken into account as discussed at the beginning of this section. This treatment of strong and electromagnetic isospin-breaking effects is identical to the Nijmegen PWA [137]. On the other hand, chiral EFT allows for a systematic inclusion of isospin-breaking effects beyond the ones previously considered. In fact, expressions for the leading isospin-breaking TPEP [161, 162], the subleading isospin-breaking TPEP [163], and irreducible $\pi\gamma$ exchange [164], which are (mostly) parameter-free in the two-nucleon system, have been available for some time. The long-standing question regarding the charge-dependence of the πNN coupling constant also re-emerges in a systematic treatment of isospin-breaking effects in the framework of chiral EFT. While the Nijmegen group did not find evidence for charge-dependence, the issue does not seem to be settled (see [165] for a recent

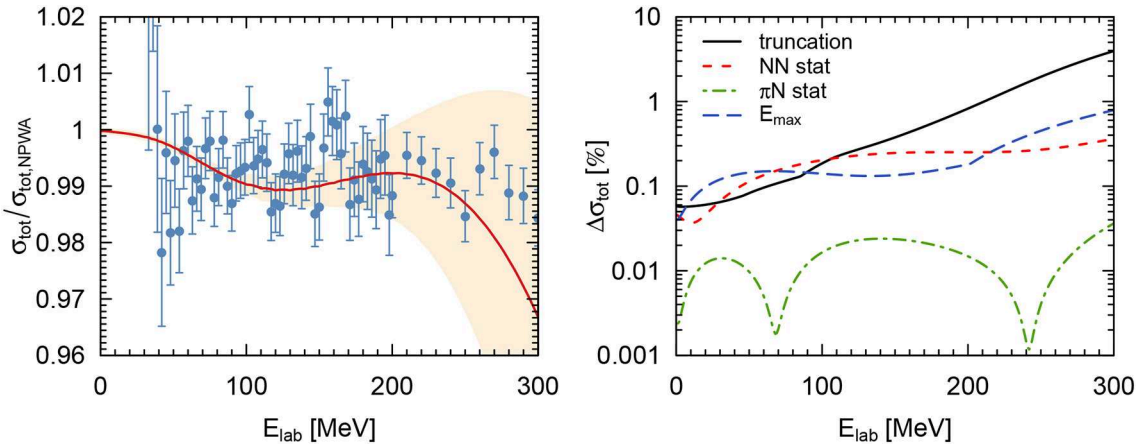


FIGURE 9 | Neutron-proton total cross section in the range of $E_{lab} = 0 - 300$ MeV. The plot on the left shows the results divided by the predictions of the Nijmegen PWA. The red line and peach-colored band show the central values and truncation errors (the 68% DoB interval) at the order N^4LO^+ and for $\Lambda = 450$ MeV. The experimental data are taken from Lisowski et al. [156] and have been corrected for their estimated norm of 0.999. The plot on the right shows the relative uncertainties as discussed in the text.

determination). Last but not least, charge-dependence in the short-range potential entering P-waves should also be taken into account starting from N^4LO [163].

6.2. Three-Nucleon Scattering

As discussed in the previous subsection, the N^4LO^+ SMS potentials of Reinert et al. [17] lead to excellent and in fact a nearly perfect description of np and pp scattering data below pion production threshold. Moreover, an order-by-order comparison of the results for various observables along with the Bayesian error analysis indicate a generally good convergence of the chiral expansion in the NN sector. On the other hand, a description of nucleon-deuteron elastic and breakup scattering data at a comparable level of accuracy is not available yet. Extensive calculations performed in the last decades using high-precision phenomenological NN potentials and 3NF models in the framework of the Faddeev equations [166] and using other *ab initio* methods [167] have revealed the following picture (see [19] and references therein):

- Calculations based on high-precision NN potentials alone (including the N^4LO^+ ones of [17]) tend to underestimate the ^{3}H and ^{3}He binding energy by ~ 0.5 MeV and generally lead to similar predictions in Nd scattering observables.
- At low energies, the resulting description of Nd data appears to be rather good apart from a few exceptions such as the underprediction of the nucleon analyzing power A_y, known as the A_y puzzle [168], and the discrepancy for the cross section for the symmetric space star deuteron breakup configuration [169]. 3NF effects in this energy range are found to be small in agreement with qualitative arguments based on the chiral power counting as explained below.
- Starting from $E_{\rm lab} \sim 50$ MeV, discrepancies between theory and experimental data set in and become large at $E_{\rm lab} \sim 200$ MeV and above. Except for the cross section, the inclusion of the phenomenological 3NFs like the Tucson-Melbourne (TM99) [170] and Urbana-IX [171] models does not globally reduce the discrepancies between theory and data [19]. Relativistic effects have also been studied, see Witała et al. [172] and references therein, and found to be small at energies below the pion production threshold.

TABLE 2 | Deuteron binding energy B_d, asymptotic S-state normalization A_S, asymptotic D/S-state ratio η, radius r_d, quadrupole moment Q, and D-state probability P_D as predicted by various high-quality potentials.

	Granada CD Bonn		EMN N^4LO^+ [23]	SMS N^4LO^+ [17]	Empirical
	[149]	[146]	$\Lambda = 500$ MeV	$\Lambda = 450$ MeV	
B_d (MeV)	2.2246*	2.2246*	2.2246*	2.2246*	2.224575(9) [144]
A_S (fm$^{-1/2}$)	0.8829	0.8846	0.8852	0.8847	0.8846(8) [157]
η	0.0249	0.0256	0.0258	0.0255	0.0256(4) [158]
r_d (fm)	1.965	1.966	1.973	1.966	1.97535(85)† [159]
Q (fm^2)	0.268	0.270	0.273	0.270	0.2859(3) [160]
P_D (%)	5.62	4.85	4.10	4.59	—

The binding energy has been calculated with the non-relativistic energy-momentum relation for the potentials of Entem et al. [23] and with the relativistic relation for the SMS potential of Reinert et al. [17] and the CD Bonn potential [146].

** The deuteron binding energy has been taken as input in the fit.*

† This value corresponds to the so-called deuteron structure radius, which is defined as a square root of the difference of the deuteron, proton and neutron mean square charge radii.

Assuming that the discrepancies between theory and experimental data in the 3N system are to be resolved by 3NFs, these findings demonstrate that the currently available phenomenological models do not provide an appropriate description of the 3NF. This should not come as a surprise given the enormously rich and complex spin-isospin-momentum structure of a most general 3NF [95, 173–175]. Here, chiral EFT offers a decisive advantage over more phenomenological

approaches by predicting the long-range part of the 3NF in a model-independent way, establishing a clear importance hierarchy of short-range terms and providing a solid theoretical framework for maintaining consistency between two- and three-nucleon forces and ensuring scheme independence of the calculated observables.

As already mentioned in section 3, three-body contributions to the nuclear Hamiltonian first appear at N^{2}LO in the chiral expansion and are, therefore, suppressed by Q^3 relative to the dominant pairwise NN interaction. It is instructive to estimate the expected magnitude of 3NF effects for various observables solely on the basis of the chiral power counting (i.e., using NDA). For ^{3}H and ^{4}He, one can use the typical expectation values of the NN potential energy of $\langle V_{\rm NN}\rangle_{^3{\rm H}} \sim 50$ MeV and $\langle V_{\rm NN}\rangle_{^4{\rm He}} \sim 100$ MeV [83], along with the estimation of the expansion parameter $Q \sim M_\pi^{\rm eff}/\Lambda_{\rm b}$ with $M_\pi^{\rm eff} = 200$ MeV and $\Lambda_{\rm b} = 650$ MeV, in order to estimate the expected 3NF contributions to the binding energy to be $\langle V_{\rm 3N}\rangle_{^3{\rm H}} \sim Q^3\langle V_{\rm NN}\rangle_{^3{\rm H}} \sim 1.5$ MeV and $\langle V_{\rm 3N}\rangle_{^4{\rm He}} \sim Q^3\langle V_{\rm NN}\rangle_{^4{\rm He}} \sim 3$ MeV. These qualitative estimations agree well with the actual underprediction of the ^{3}H and ^{4}He by the NN interactions alone which, using the AV18 [176], CD Bonn [146], N^{2}LO [113], and Idaho N^{3}LO [112] potentials as representative examples, amounts to 0.5 . . . 0.9 MeV and 2.1 . . . 4.1 MeV, respectively. The shallow nature of few-nucleon bound states indicates that there are large cancelations between the kinetic and potential energies. Because of this fine tuning, 3NF contributions to the binding energies are enhanced beyond the naive estimation of $Q^3 \sim 3\%$ and actually reach 10 . . . 15%. On the other hand, there is generally no reason to expect a similar enhancement for Nd scattering observables at low energy except for some fine-tuned polarization observables such as A_y. It is well known that tiny changes of the NN interaction in the triplet P-waves amount to large relative changes in the Nd A_y [168]. On the other hand, starting from $E_{\rm N} \sim 60$ MeV, the expansion parameter Q in Equation (37) is dominated by the momentum scale $p = \sqrt{2/3mE_{\rm N}}$ [84]. At e.g. the energies of $E_{\rm N} \sim 100$ MeV and $E_{\rm N} \sim 200$ MeV, the expansion parameter becomes $Q \sim 0.40$ and $Q \sim 0.55$, and the relative contributions of the 3NF to a generic scattering observable are expected to increase to ~ 6 and $\sim 16\%$, respectively. Clearly, these simplistic back-of-envelope estimations only yield qualitative insights into the role of the 3NF. Nevertheless, they agree remarkably well with the observed trend of discrepancies between theoretical predictions based solely on the NN interactions and experimental data, which tend to increase with energy. For further examples and a more quantitative analysis along this line of Nd scattering, selected properties of light and medium-mass nuclei and the equation of state of nuclear matter (see [83, 127, 130, 177]). We further emphasize that it is not entirely clear how to estimate the relevant momentum scale, that determines the expansion parameter in heavy nuclei, and how to quantify truncation errors for excited states (see [130] for an extended discussion).

As discussed in section 3 and visualized in **Figure 2**, the leading contributions to the 3NF at N^{2}LO emerge from the two-pion exchange, one-pion-exchange-contact and purely contact tree-level diagrams, leading to the well-known expressions [44, 98]

$$
\begin{aligned}
V_{\rm 3N} &= \frac{g_A^2}{8F_\pi^4}\,\frac{\vec\sigma_1\cdot\vec q_1\,\vec\sigma_3\cdot\vec q_3}{(\vec q_1^{\,2}+M_\pi^2)\,(\vec q_3^{\,2}+M_\pi^2)} \\
&\Big[\boldsymbol\tau_1\cdot\boldsymbol\tau_3\big(-4c_1M_\pi^2+2c_3\,\vec q_1\cdot\vec q_3\big)+c_4\boldsymbol\tau_1\times\boldsymbol\tau_3\cdot\boldsymbol\tau_2\,\vec q_1\times\vec q_3\cdot\vec\sigma_2\Big] \\
&-\frac{g_A\,D}{8F_\pi^2}\,\frac{\vec\sigma_3\cdot\vec q_3}{\vec q_3^{\,2}+M_\pi^2}\,\boldsymbol\tau_1\cdot\boldsymbol\tau_3\,\vec\sigma_1\cdot\vec q_3\;+\;\frac{1}{2}E\,\boldsymbol\tau_1\cdot\boldsymbol\tau_2\;+\;5\ \text{permutations}\,,
\end{aligned}
\tag{47}
$$

where $\vec q_i = \vec p_i\,' - \vec p_i$ with $\vec p_i\,'$ and $\vec p_i$ being the final and initial momenta of the nucleon i. The LECs D and E are usually expressed in terms of the corresponding dimensionless coefficients c_D and c_E via $D = c_D/(F_\pi^2\Lambda_\chi)$ and $E = c_E/(F_\pi^4\Lambda_\chi)$ [44]. In Epelbaum et al. [8] and [84], semilocal coordinate- and momentum-space regularized 3NF expressions in combination with the corresponding chiral NN potentials from Epelbaum et al. [21, 22] and Reinert et al. [17], respectively, were employed by the LENPIC Collaboration to analyze Nd scattering observables at N^{2}LO. The numerical implementation of the 3NF in the Faddeev equations is carried out in the partial wave basis. Partial wave decomposition (PWD) of a general 3NF can be carried out numerically using the machinery developed in Golak et al. [178] by performing five-dimensional angular integrations. Given the required number of partial waves and grid points for the four Jacobi momenta to reach converged results for Nd scattering observables, such a numerical PWD requires substantial computational resources. In Hebeler et al. [179], a more efficient approach was introduced, that exploits the local nature of the bulk of the 3NF.

To make predictions for few-nucleon observables, one first needs to determine the LECs c_D and c_E entering the 3NF. A broad range of few- and many-body observables including the binding energies and radii of ^{3}H, ^{4}He, and heavier nuclei, nucleon-deuteron doublet scattering length ^2a, n-α scattering, triton β-decay, and the saturation properties of nuclear matter have been proposed and employed in the past to determine these two LECs [9, 27, 29, 44, 180, 181]. A reliable determination of c_D, c_E is complicated by the existence of strong correlations between some of the low-energy observables (see e.g.,[182]), which originate from the large S-wave scattering lengths in the NN system. Furthermore, going beyond the 3N system may require, depending on the observable and the chiral order, the inclusion of 4NF and exchange current contributions. In Epelbaum et al. [8], we therefore, restricted ourselves to 3N observables in the determination of c_D, c_E. Specifically, we employed the ^{3}H binding energy of $B_{^3{\rm H}} = 8.482$ MeV to fix the LECs c_E for a given value of c_D. The remaining LEC c_D was determined by considering a number of observables including $^2a = 0.645 \pm 0.008$ fm [145], nd total cross section data from [183] and precisely measured pd differential cross section in the minimum region at $E_{\rm N} = 70$ MeV [184], 108 MeV [185], and 135 MeV [184]. In the left panel of **Figure 10**, we show the extracted values of c_D for the SCS interactions with the cutoff $R = 0.9$ fm. It is reassuring to see that the considered 3N observables lead to consistent values of c_D. In addition, these results show that the strongest constraint on c_D, given the experimental

and the estimated truncation uncertainty, is imposed by the pd differential cross section data at $E_N = 70$ MeV from Sekiguchi et al. [184] as visualized in the right panel of **Figure 10**. We also found no correlations between this observable and the ^{3}H binding energy. In particular, the resulting value of the LEC c_D is largely determined by the differential cross section and almost insensitive to a variation of the triton binding energy.

In Epelbaum et al. [84], we have analyzed Nd scattering observables using the most recent SMS NN potentials from Reinert et al. [17] in combination with the N^{2}LO 3NF regularized in the same way. Motivated by the experience with the SCS interactions [8], the LECs c_D and c_E were determined from the ^{3}H binding energy and the pd cross section minimum at $E_N = 70$ MeV. In **Figure 11**, we show, as a representative example, our N^{2}LO predictions for selected Nd scattering observables at $E_N = 135$ MeV, along with the experimental data and calculations based on the CD Bonn NN potential with and without the TM99 3NF model. As an important internal consistency check of the calculations, we have verified that the predictions obtained using different cutoff values are consistent with each other (within errors) (see Figure 5 of [84]).

It is reassuring to see that the experimental data are generally well described by the theory. On the other hand, while accurate, our predictions at N^{2}LO have obviously rather low precision at this energy. In fact, the N^{2}LO truncation errors are comparable with or even larger than the observed deviations between experimental data and calculations based on phenomenological high-precision NN and 3NF models, see the dotted and dashed-dotted lines in **Figure 11**. Based on the experience in the NN sector as discussed in section 6.1, it is conceivable that a high-precision description of Nd scattering data will require the chiral expansion of the 3NF to be pushed to (at least) N^{4}LO. At the energy of $E_N = 135$ MeV, the uncertainty bands at N^{4}LO are expected to become 4-5 times more narrow as compared with the N^{2}LO ones shown in **Figure 11**.

So where do we stand in terms of efforts to include 3NF corrections beyond N^{2}LO? As explained in section 4.2, the main obstacle for the inclusion of higher order contributions to the 3NF is the lack of their *consistently regularized* expressions. Starting from N^{3}LO, it is not sufficient anymore to naively regularize the available expressions for the 3NF from Bernard and Epelbaum [54, 55] and Krebs et al. [48, 95] derived using DR, since such an approach violates constraints imposed by the chiral symmetry. Rather, the N^{3}LO and N^{4}LO corrections to the 3NF need to be re-derived using the consistent finite-cutoff regularization approach. Work along these lines is in progress. Another challenge, that will have to be addressed at N^{4}LO, is the determination of the LECs appearing in the 3NF at this order. While the N^{3}LO contributions do not involve free parameters, the short-range part of the 3NF at N^{4}LO depends on 10 unknown LECs [45], from which 9 contribute to the isospin-1/2 channel and thus can, in principle, be determined in Nd scattering. Furthermore, the yet-to-be-derived one-pion-exchange-contact contributions to the 3NF at N^{4}LO will also involve unknown LECs. Given the still rather significant computational cost of solving the Faddeev equations in the 3N continuum, the complicated treatment of the Coulomb interaction [186] and the lack of partial wave analyses in the 3N sector, the determination of these LECs from 3N scattering data will certainly be a challenging task.

While a complete analysis of Nd scattering is currently not available beyond N^{2}LO, it is instructive to explore the role of subleading short-range 3NF interactions. In Girlanda et al. [30], it was shown within a hybrid phenomenological approach that the 3N contact operators at N^{4}LO can be tuned to reproduce the ^{3}H binding energy, nd scattering lengths, cross section and polarization observables of pd scattering at 2 MeV center-of-mass energy. The resulting models were shown to lead to a satisfactory description of pd polarization observables below the deuteron breakup. On the other hand, 3NF effects are expected to be much more visible at intermediate and higher energies. In Epelbaum et al. [84], we explored the impact of the short-range 3NF operators of the central and spin-orbit types proportional to the LECs E_1 and E_7, respectively,

$$V_{3N} = E_1\, \vec{q}_1^{\,2} \;+\; iE_7\, \vec{q}_1 \times (\vec{K}_1 - \vec{K}_2)\cdot(\vec{\sigma}_1 + \vec{\sigma}_2) \;+\; 5 \text{ permutations}\,, \tag{48}$$

where $\vec{K}_i = (\vec{p}_i\,' + \vec{p}_i)/2$. Parameterizing the dimension-full LECs E_1, E_7 in terms of the corresponding dimensionless parameters via $E_i = c_{E_i}/(F_\pi^4 \Lambda_\chi^3)$ with $\Lambda_\chi = 700$ MeV, we studied the impact of these N^{4}LO terms on selected Nd scattering observables for the fixed values of the LECs of $c_{E_i} = \pm 2$. Based on the experience in the NN sector and with the N^{2}LO 3NF, we expect the actual values of these LECs to lie well within this range. The expectation values of various contributions to the 3NF in the triton state indicate that the employed values $c_{E_7} = \pm 2$ may already overestimate the expected natural range of this LEC.

In order to compute the contributions of the c_{E_i}-terms to 3N observables in a meaningful way, one needs to perform (implicit) renormalization as explained in section 2. This was achieved in Epelbaum et al. [84] by simultaneously adjusting the values of the N^{2}LO LECs c_D, c_E to the triton binding energy and the cross section minimum at $E_N = 70$ MeV for all considered values of the LECs c_{E_i}. The calculations have been performed using the N^{4}LO$^+$ SMS NN potential from Reinert et al. [17] in combination with the SMS N^{2}LO 3NF. In **Figure 12**, we show the resulting predictions at the lowest considered energy of $E_N = 10$ MeV. The blue bands show the estimated truncation error at N^{3}LO, obtained by rescaling the N^{2}LO Bayesian truncation uncertainty with the expansion parameter Q[15], and visualize the expected impact of N^{4}LO terms. In agreement with the expectations, 3NF effects generally appear to be rather small at such low energies. This figure also provides a nice illustration of the fine tuned nature of the nucleon vector analyzing power A_y, which shows a strong sensitivity to small changes in the Hamiltonian. What has been traditionally referred to as the A_y-puzzle thus appears to be just a consequence of the fine-tuned nature of this observable, and the "puzzle" may be expected to be resolved by 3NF contributions beyond N^{2}LO (see also [30, 45] for a similar conclusion). While the A_y is

[15]We cannot estimate the N^{3}LO truncation error using the Bayesian approach described in section 5 since no complete N^{3}LO results are available for Nd scattering.

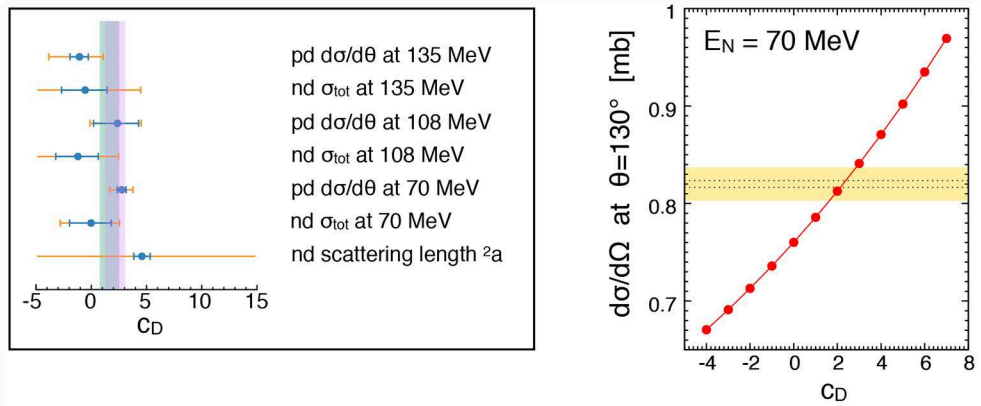


FIGURE 10 | (Left) Determination of the LEC c_D at N^{2}LO from selected Nd scattering observables. The smaller (blue) error bars correspond to the experimental uncertainty while the larger (orange) error bars also take into account the truncation error at N^{2}LO estimated using the EKM approach of Epelbaum et al. [21]. The green (violet) bands show standard error intervals of c_D resulting from a combined least squares single-parameter fit to all observables (to observables up to $E_N = 108$ MeV) using the orange error bars. **(Right)** Nd cross section in the minimum region ($\theta = 130^\circ$) at $E_N = 70$ MeV as function of the LEC c_D. For each c_D value, the LEC c_E is adjusted to the ^{3}H binding energy. Dotted lines show the statistical uncertainty of the experimental data from Sekiguchi et al. [184], while the yellow band also takes into account the quoted systematic uncertainty of 2%. All results are obtained using the N^{2}LO SCS NN potential from Epelbaum et al. [21] in combination with the N^{2}LO SCS 3NF for the coordinate-space cutoff $R = 0.9$ fm.

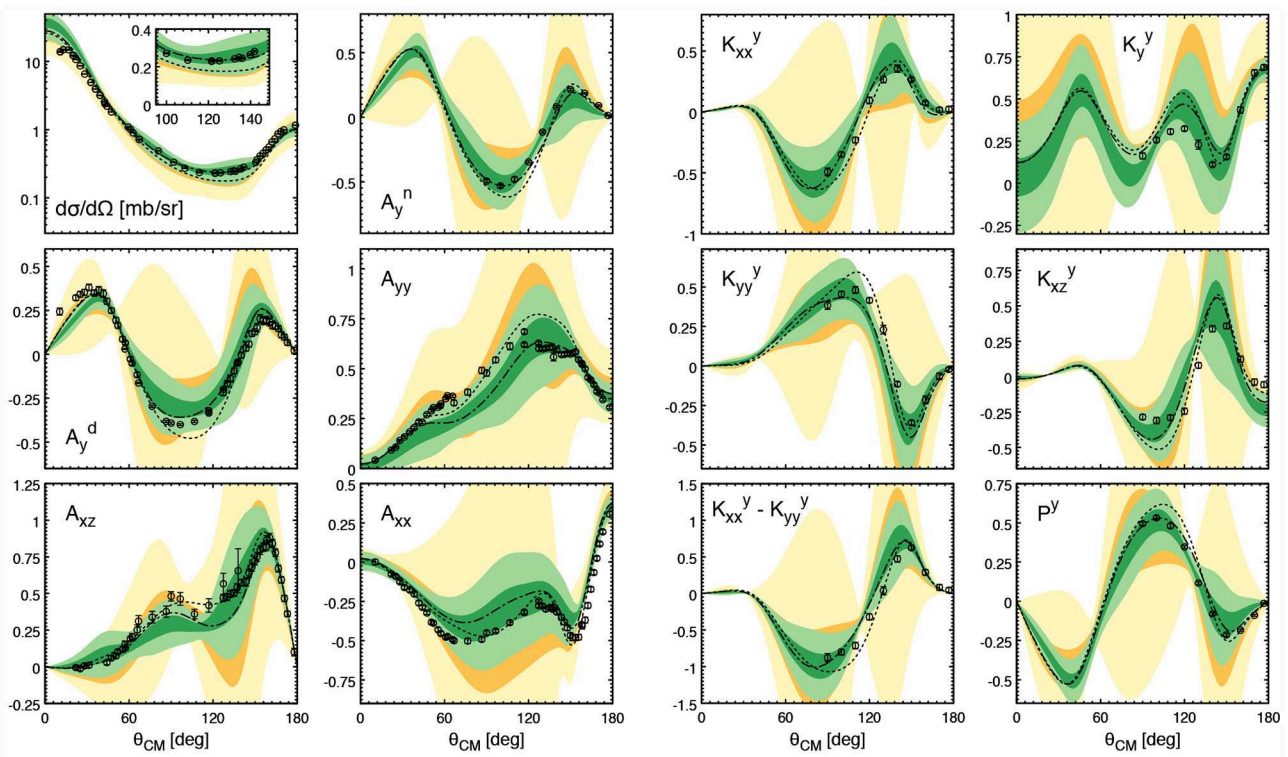


FIGURE 11 | Predictions for the differential cross section, nucleon and deuteron analyzing powers A_y^n and A_y^d, deuteron tensor analyzing powers A_{yy}, A_{xz}, A_{xx}, polarization transfer coefficients K_{xx}^y, K_y^y, K_{yy}^y, K_{xz}^y, $K_{xx}^y - K_{yy}^y$, and the induced polarization P^y in elastic Nd scattering at laboratory energy of $E_N = 135$ MeV at NLO (yellow bands) and N^{2}LO (green bands). The light- (dark-) shaded bands indicate 95% (68%) DoB intervals using the Bayesian model $\bar{C}^{650}_{0.5-10}$ introduced in section 5. Open circles are proton-deuteron data from Sekiguchi et al. [184]. The dotted (dashed-dotted) lines show the results based on the CD Bonn NN potential [146] (CD Bonn NN potential in combination with the Tucson-Melbourne 3NF [170]). All results are obtained using the N^{2}LO SMS NN potential from Reinert et al. [17] in combination with the N^{2}LO SMS 3NF for the momentum-space cutoff $\Lambda = 500$ MeV.

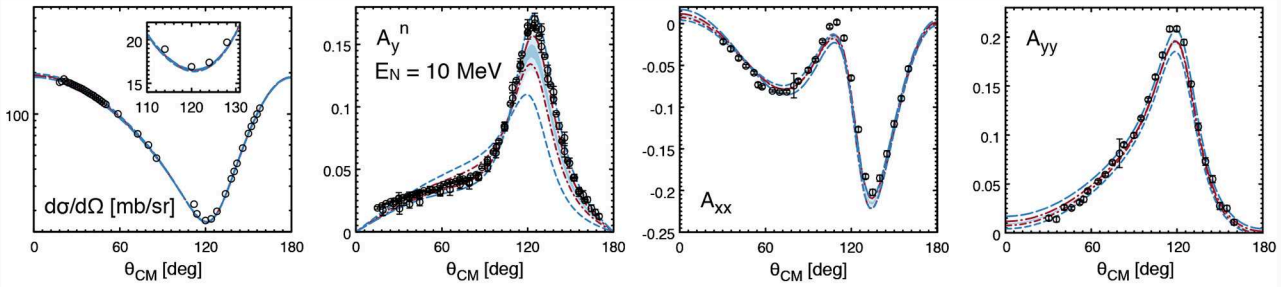


FIGURE 12 | Results for the differential cross section, nucleon analyzing powers A_y^n as well as deuteron tensor analyzing powers A_{xx} and A_{xx} in elastic nucleon-deuteron scattering at laboratory energy of $E_{\rm lab}^N = 10$ MeV based on the SMS NN potentials of Reinert et al. [17] at N^{4}LO$^+$ in combination with the SMS 3NF at N^{2}LO using $\Lambda = 450$ MeV. Blue light- (dark-) shaded bands show the expected truncation uncertainty for a *complete* N^{3}LO calculation and are obtained by multiplying the N^{2}LO truncation error corresponding to 95% (68%) DoB intervals for the model $\tilde{C}^{650}_{0.5-10}$ with the corresponding value of the expansion parameter Q. Short-dashed-dotted and long-dashed-dotted red lines show the impact of the N^{4}LO central short-range 3NF $\propto c_{E_1}$ with $c_{E_1} = -2$ and $c_{E_1} = 2$, respectively. Similarly, short-dashed and long-dashed blue lines show the impact of the N^{4}LO spin-orbit short-range 3NF $\propto c_{E_7}$ with $c_{E_7} = -2$ and $c_{E_7} = 2$, respectively. Open circles are neutron-deuteron data from Howell et al. [187] and proton-deuteron data from Sagara et al. [188], Rauprich et al. [189], and Sperisen et al. [190], corrected for the Coulomb effects (see [44] for details).

well-known to be particularly sensitive to spin-orbit types of 3NFs [191] such as the one proportional to c_{E_7}, our results also show an unexpectedly strong sensitivity to the subleading central interaction of the c_{E_1}-type.

At higher energies, the effects of the considered N^{4}LO 3NF terms become more significant as visualized in **Figure 13** for the case of selected spin-correlation parameters. More results for the cross section, vector and tensor analyzing powers and polarization transfer coefficients at $E_{\rm N} = 135$ MeV can be found in Epelbaum et al. [84]. It is comforting to see that the impact of the c_{E_i}-terms on Nd scattering observables is, in general, consistent with the estimated N^{3}LO truncation errors. One should, however, keep in mind that the employed Bayesian approach may, under certain circumstances, become unreliable. This is, in particular, the case for observables that depend on a continuously varying parameter in the kinematical regions where the LO results and higher-order corrections change sign (see [84] for a detailed discussion). One such failure of the Bayesian model is shown in **Figure 13** for the spin-correlation coefficient $C_{x,z}$ at $E_{\rm N} = 200$ MeV around $\theta = 120^\circ$. In such problematic cases, the approach proposed in Melendez et al. [133] and based on Gaussian processes is expected to provide more reliable estimations of the truncation uncertainty.

6.3. Light Nuclei

While no results for light nuclei using SMS chiral interactions are available yet, we briefly review here some recent highlights obtained by the LENPIC Collaboration using the SCS NN potentials of Epelbaum et al. [21, 22] with and without the corresponding 3NFs at N^{2}LO. In Binder et al. [83, 130], we have calculated the ground state energies and selected properties of light and medium-mass nuclei up to ^{48}Ca using the SCS NN interactions at various chiral orders. Specifically, $A = 3, 4$ nuclei were analyzed in the framework of the Faddeev-Yakubovsky equations while light p-shell nuclei were calculated using the No-Core Configuration Interaction (NCCI) method [193–195] and employing Similarity Renormalization Group (SRG) transformed interactions [196–199] to improve the convergence. The results for ^{16,24}O and ^{40,48}Ca were obtained within the coupled cluster and in-medium SRG group frameworks (see [12, 200–203] and references therein). A qualitatively similar convergence pattern was observed in all considered cases, namely a significant overbinding at LO, results close to the experimental values at NLO and N^{2}LO and underbinding at N^{3}LO and N^{4}LO. Notice that the strongly repulsive nature of the N^{3}LO contributions to the SCS NN interactions of Epelbaum et al. [21, 22] was shown to be caused by the employed unnaturally large values of the redundant short-range operators [17]. The SMS interactions of Reinert et al. [17] utilize a soft choice for these contact terms, which leads to more perturbative interactions at and beyond N^{3}LO. No large gap between the N^{2}LO and N^{3}LO results for the ground state energies is, therefore, expected for the new SMS NN interactions. The calculated charge radii of the considered medium-mass nuclei were found to show a systematic improvement with the chiral order, but remain underestimated using the NN interaction at the highest available order N^{4}LO$^+$.

In Epelbaum et al. [8], a *complete* N^{2}LO analysis of p-shell nuclei was presented by the LENPIC Collaboration using the SCS NN and 3N interactions. In **Figure 14**, we show the NLO and N^{2}LO results from that paper for nuclei up to $A = 16$. We emphasize that since the Hamiltonian has been completely determined in the NN and 3N system as described in sections 6.1 and 6.2, the ground-state energies shown in that figure are parameter-free predictions. In **Figure 14**, we have updated the corresponding figure from Epelbaum et al. [8] by replacing the truncation errors, that have been estimated in that paper using the EKM approach of Epelbaum et al. [21] and Binder et al. [130], with the Bayesian uncertainties calculated as described in section 5. The 68% DoB Bayesian truncation errors are similar to those quoted in Epelbaum et al. [8] at N^{2}LO but appear to be significantly larger at NLO. We also calculated in that

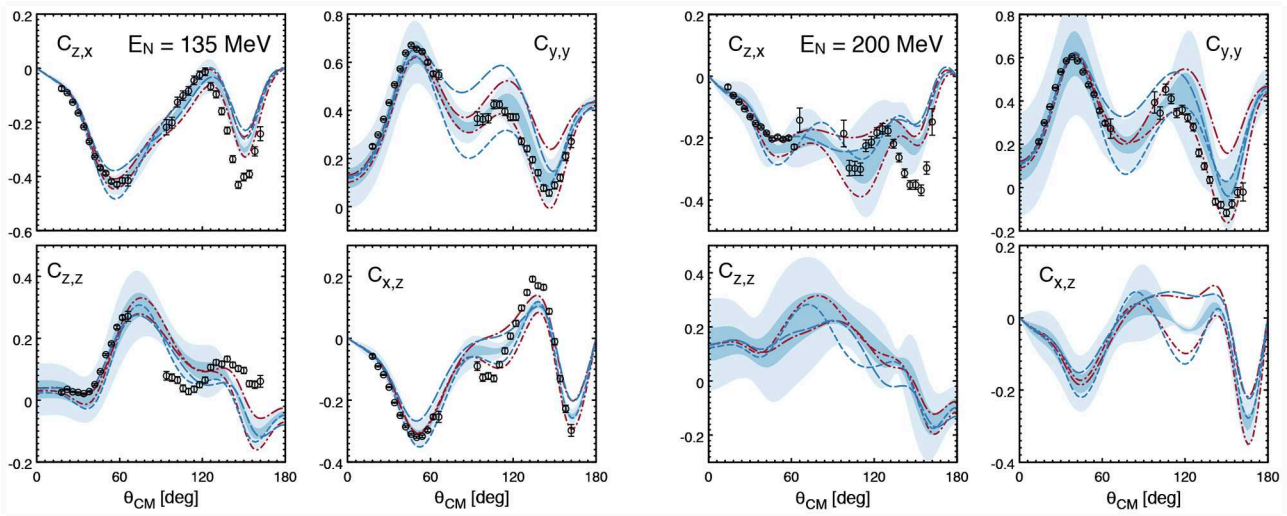


FIGURE 13 | Same as **Figure 12** but for the deuteron-nucleon spin-correlation parameters $C_{z,x}$, $C_{y,y}$, $C_{z,z}$, and $C_{x,z}$ for Nd elastic scattering at $E_N = 135$ MeV **(left)** and $E_N = 200$ MeV **(right)**. Open circles are proton-deuteron data from von Przewoski et al. [192].

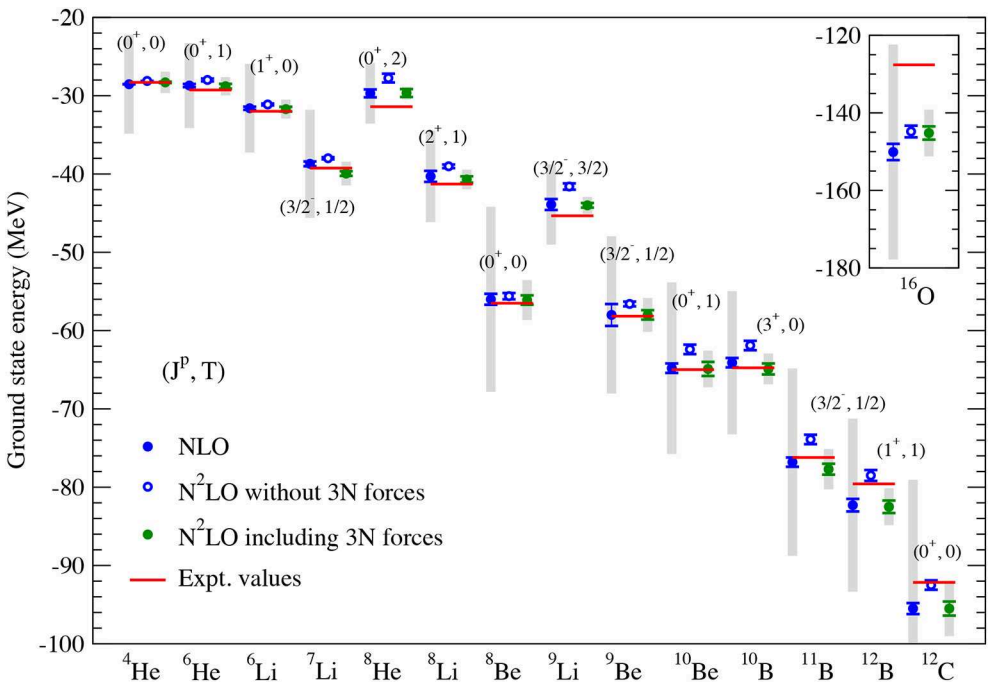


FIGURE 14 | Calculated ground state energies in MeV using chiral SCS NN interactions from Epelbaum et al. [8] in combination with the SCS 3NF at $R = 1.0$ fm (open and solid dots) in comparison with experimental values (red levels). For each nucleus the NLO and N^{2}LO results are the left and right symbols and bars, respectively. The open blue symbols correspond to incomplete calculations at N^{2}LO using NN-only interactions. Blue and green error bars indicate the NCCI extrapolation uncertainty and, where applicable, an estimate of the SRG dependence. The shaded bars indicate the truncation error at each chiral order corresponding to 68% DoB intervals using the Bayesian model $\tilde{C}^{650}_{0.5-10}$ with the expansion parameter $Q = M_\pi^{\text{eff}}/\Lambda_b$.

paper the excitation energies for selected states of $A = 6 - 12$ nuclei and the point-proton radius of ^{4}He. For almost all considered cases, adding the 3NF to the NN interaction was found to lead to a significant improvement in the description of experimental data. The predicted ground state energies of p-shell nuclei show a good agreement with the data except for ^{16}O, which appears to be overbound. Notice that the deviation between the predicted and experimental values of the ^{16}O binding energy is comparable to the 95% DoB Bayesian error at N^{2}LO. It will be very interesting to repeat the calculations for the newest SMS interactions and to extend them to higher orders and heavier nuclei.

7. SUMMARY AND OUTLOOK

In this review article we have presented a snapshot of the current state-of-the-art in low-energy nuclear theory with a focus on the latest generation of semilocal nuclear potentials from chiral EFT. We now summarize some of the key conclusions of our paper.

- We have presented a concise and self-contained introduction to the conceptual foundations of chiral effective field theory in the few-nucleon sector and described in some detail all steps needed to compute low-energy observables from the effective chiral Lagrangians (including error analysis). Special emphasis was given to clarify the notion of *consistency* of nuclear forces and current operators in terms of a perturbative matching to the unambiguously defined on-shell scattering amplitude. In particular, few-nucleon potentials from Epelbaum [73], Bernard et al. [54, 55], Krebs et al. [48, 95] and electroweak current operators from Kölling et al. [74, 122] and Krebs et al. [75, 123] at N^{3}LO and beyond, derived using DR, are off-shell consistent with each other provided DR is also used to compute loop integrals arising from iterations of the dynamical equations.
- We have reviewed the semilocal momentum-space regularized potentials of Reinert et al. [17], which are currently the most precise chiral EFT NN forces on the market. These are the only NN interactions derived in chiral EFT, which—from the statistical point of view—qualify to be regarded as PWA of NN data below pion production threshold (see section 6.1 for details). At the highest considered order N^{4}LO$^+$, these interactions describe the np and pp data from the self-consistent Granada-2013 database with a precision that is at least comparable to the one reached by modern phenomenological potentials with a much larger number of adjustable parameters. The significantly better description of the scattering data by the SMS N^{4}LO$^+$ interactions of Reinert et al. [17] as compared to the nonlocal potentials of Entem et al. [23] at the same chiral order, and their much smaller residual cutoff dependence (see Figure 17 of Reinert et al. [17]), can presumably be traced back to the improved semilocal regulator, which maintains the long-range part of the interaction as described in section 4.1. We also addressed in detail the issue of uncertainty quantification in the NN sector. In particular, we discussed statistical uncertainties of NN and πN LECs and their propagation to selected observables as well as uncertainty introduced by fixing the maximum fit energy in the determination of the NN LECs. We also estimated truncation errors at various chiral orders using the Bayesian model specified in section 5.
- Beyond the NN sector, calculations based on the SMS interactions have so far been carried out up to N^{2}LO [84]. The LECs c_D and c_E, which enter the 3NF at this order, have been determined from the ^{3}H binding energy and the very precise pd cross section data at $E_{\rm lab}^N = 70$ MeV from Sekiguchi et al. [184]. Using the employed Bayesian model to estimate truncation uncertainties, the predicted ground state energies of p-shell nuclei up to $A = 16$ are generally in a good agreement with the data. Also the predicted Nd scattering observables including the vector analyzing power A_y are consistent with experimental data within errors. We performed an additional test of the employed Bayesian model for truncation errors by exploring the impact of selected short-range 3NF terms at N^{4}LO on observables in Nd elastic scattering. Our results suggest that a high-precision description of Nd scattering data will likely require the chiral expansion of the 3NF to be pushed to N^{4}LO.
- The novel semilocal nuclear forces, derived in the finite-cutoff formulation of chiral EFT with short-range interactions counted according to NDA (i.e., the Weinberg scheme), have already been successfully confronted with few-nucleon data and passed a number of a-posteriori consistency checks as briefly summarized below:
  - Using the minimal basis of the order-Q^4 NN contact interactions as detailed in section 6, the LECs determined from the np and pp scattering data come out of a natural size (see **Figure 7**). The same is true for the LECs c_D and c_E entering the leading 3NF, as can be seen e.g., from the corresponding expectation values in the ^{3}H state [84].
  - The residual cutoff-dependence of NN phase shifts is strongly reduced at N^{3,4}LO as compared to N^{1,2}LO within the considered Λ-range (see e.g., Figure 4 of [82]).
  - There is a clear systematic improvement in the description of np and pp data with increasing chiral orders (see **Table 1**). At order Q^3 (i.e., N^{2}LO), this improvement results solely from taking into account the parameter-free subleading TPEP contributions. Notice that certain alternative power counting schemes suggest that some of the contact interactions that appear at order Q^4 in the Weinberg scheme are enhanced and should yield contributions to observables larger than the order-Q^3 TPEP (see e.g., Table 1 of [81]). The clear evidence of the chiral TPEP at orders Q^3 and Q^5 observed in Epelbaum et al. [21, 22] and Reinert et al. [17] does, however, not support such alternative scenarios.
  - The resulting convergence pattern of the EFT expansion for selected NN observables was scrutinized using Bayesian statistical methods (see section 5 for details). For not too soft cutoffs, the assumed breakdown scale of the EFT expansion of $\Lambda_{\rm b} \sim 600$ MeV [21] was found to be statistically consistent [131] (see also [84, 132] for a related discussion).
  - Scheme-dependence of nuclear potentials offers yet another way to perform nontrivial consistency checks of the theoretical framework by explicitly verifying (approximate) scheme-independence of observables. In the formulation we employ, scheme dependence of the nuclear forces first appears at N^{3}LO and manifests itself in their dependence on arbitrary real phases $\bar\beta_8$, $\bar\beta_9$, which parameterize the unitary ambiguity of the leading relativistic corrections [21, 74], and the appearance of three off-shell short-range operators in the ^{1}S$_0$ and ^{3}S$_1$-^{3}D$_1$ channels proportional to the LECs $D_{1S0}^{\rm off}$, $D_{3S1}^{\rm off}$, and $D_{\epsilon 1}^{\rm off}$ [17, 204, 205]. The SMS potentials of Reinert et al. [17] make use of the standard choice for $\bar\beta_{8,9}$ namely $\bar\beta_8 = -\bar\beta_9 = 1/4$, which minimizes the amount

of $1/m^2$-corrections to the OPEP, and employ $D^{\rm off}_{^1S_0} = D^{\rm off}_{^3S1} = D^{\rm off}_{\epsilon 1} = 0$. Different choices of these parameters lead to different off-shell behaviors of the potential. They are related to each other by unitary transformations which, however, also induce an infinite tower of higher-order terms beyond the order one is working. The residual dependence of observables on $\bar\beta_{8,9}$ and $D^{\rm off}_i$, therefore, probes the impact of neglected higher-order terms and should lie within the estimated truncation errors. We have redone the fits at N^{4}LO$^+$ for $\Lambda = 450$ MeV using alternative choices of $D^{\rm off}_i$ [17] and also developed a version of the potential with $\bar\beta_8 = \bar\beta_9 = 1/2$ [206]. The letter choice is motivated by the vanishing isoscalar exchange charge density operator at N^{3}LO. In all considered cases, we found negligibly small changes in observables in spite of strong changes at the interaction level.

– Calculations of three- and more-nucleon observables based on solely NN interactions are incomplete beyond second order. They do, however, provide information about the magnitude of the missing 3NF contributions by assessing the spread in results at different orders $Q^{\geq 3}$ and via a comparison of such incomplete predictions with experimental data. In Binder et al. [83], such an analysis was performed for Nd scattering observables and selected properties of light nuclei using the SCS NN interactions of Epelbaum et al. [21, 22]. The sizes of the 3NF contributions required to bring such incomplete results in agreement with experimental data were found to agree well with expectations based on Weinberg's power counting. Furthermore, recent calculations by the LENPIC Collaboration which include the leading 3NF [8, 84] show that the resulting N^{2}LO predictions for observables that have not been used in the determination of the LECs c_D, c_E are generally in a good agreement with the data (see section 6). No indications are found for enhanced contributions of the 3NF in general and of the c_D-term in particular as suggested in Birse [207].

To summarize, major progress has been achieved in recent years toward developing chiral EFT into a precision tool for low-energy nuclear physics. In the NN sector, the latest SMS interactions at fifth chiral order have already reached the accuracy at or even below permille level for low-energy observables such as e.g., the deuteron asymptotic S-state normalization A_S (see section 6.1 for details and further examples). The only essential missing step in the NN sector concerns the inclusion of isospin-breaking interactions up to fifth chiral order. Work along this line is in progress.

Pushing the precision frontier beyond the NN system opens exciting perspectives for low-energy nuclear theory and will allow one to confront chiral EFT with currently unsolved problems, such as a quantitative description of 3N scattering observables [19]. This, however, will require to address the two core challenges:

(i) Derivation of *consistent regularized* three- and four-nucleon forces and exchange charge and current operators at and beyond N^{3}LO as detailed in section 4.2. This issue has not been paid attention to in the recent calculations involving the 3NFs [208–211] and exchange electroweak currents [110, 212, 213] at N^{3}LO. As explained in section 4.2, using ad hoc regularization approaches at N^{3}LO and beyond generally leads to incorrect results for the scattering amplitude and other observables due to the appearance of uncontrolled short-range artifacts, which violate chiral symmetry and are not suppressed by inverse powers of Λ. This puts the findings of these studies into question.

(ii) Determination of the LECs in the 3NF at N^{4}LO. While the N^{3}LO contributions to the 3NF and 4NF do not involve unknown parameters, the N^{4}LO corrections to the 3NF involve 10 LEC accompanying purely short-range operators [45] and one or more LECs entering the one-pion-exchange-contact topology, which has not been worked out yet. As discussed in section 6.2, the determination of these LECs from 3N data will require a computationally challenging analysis.

As a first example of a precision calculation not restricted to NN scattering, we have recently determined the deuteron structure radius with an accuracy below the permille level, $r_{\rm str} = 1.9731^{+0.0013}_{-0.0018}$ fm, by pushing the chiral expansion of the electromagnetic exchange charge density beyond N^{3}LO and performing a thorough analysis of various types of uncertainty [206]. By combining the predicted value for $r_{\rm str}$ with the very accurate atomic data from isotope shift measurements, it was, for the first time, possible to extract the neutron charge radius from experimental data on light nuclei. This study was facilitated by the absence of loop contributions in the isoscalar exchange charge density at N^{3}LO [74, 122], which allowed for a trivial construction of the corresponding consistently regularized expressions for the charge operator. Rederivation of the contributions to 3NFs, 4NFs and exchange currents at and beyond N^{3}LO using a regulator, consistent with the one employed in Reinert et al. [17], would open the way for performing similar precision calculations for a broad class of low-energy few-nucleon reactions.

AUTHOR CONTRIBUTIONS

EE has lead the development of this review. All authors listed have made a substantial, direct and intellectual contribution to the work, and approved it for publication.

FUNDING

This work was supported by BMBF (Grant No. 05P18PCFP1) and by DFG through funds provided to the Sino-German CRC 110 110 Symmetries and the Emergence of Structure in QCD (Grant No. TRR110).

ACKNOWLEDGMENTS

We are grateful to Ashot Gasparyan, Jambul Gegelia, and Ulf-G. Meißner for a careful reading of the manuscript and useful comments and to all members of the LENPIC Collaboration for sharing their insights into the topics addressed in this review article. We also thank Pieter Maris for providing us with a source file of Figure 8 from Epelbaum et al. [8].

REFERENCES

1. Weinberg S. Nuclear forces from chiral Lagrangians. *Phys Lett B.* (1990) **251**:288. doi: 10.1016/0370-2693(90)90938-3
2. Weinberg S. Effective chiral Lagrangians for nucleon - pion interactions and nuclear forces. *Nucl Phys B.* (1991) **363**:3. doi: 10.1016/0550-3213(91)90231-L
3. Epelbaum E. Few-nucleon forces and systems in chiral effective field theory. *Prog Part Nucl Phys.* (2006) **57**:654. doi: 10.1016/j.ppnp.2005.09.002
4. Epelbaum E, Hammer HW, Meißner U-G. Modern theory of nuclear forces. *Rev Mod Phys.* (2009) **81**:1773. doi: 10.1103/RevModPhys.81.1773
5. Machleidt R, Entem DR. Chiral effective field theory and nuclear forces. *Phys Rept.* (2011) **503**:1. doi: 10.1016/j.physrep.2011.02.001
6. Hammer H-W, König S, van Kolck U. Nuclear effective field theory: status and perspectives. *arXiv: [preprint] arXiv:1906.12122 [nucl-th].*
7. Epelbaum E, Gasparyan AM, Gegelia J, Meißner U-G. How (not) to renormalize integral equations with singular potentials in effective field theory. *Eur Phys J A.* (2018) **54**:186. doi: 10.1140/epja/i2018-12632-1
8. Epelbaum E, Golak J, Hebeler K, Hüther T, Kamada H, Krebs H, et al. Few- and many-nucleon systems with semilocal coordinate-space regularized chiral two- and three-body forces. *Phys Rev C.* (2019) **99**:024313. doi: 10.1103/PhysRevC.99.024313
9. Piarulli M, Baroni A, Girlanda L, Kievsky A,Lovato A, Lus E, et al. Light-nuclei spectra from chiral dynamics. *Phys Rev Lett.* (2018) **120**:052503. doi: 10.1103/PhysRevLett.120.052503
10. Lonardoni D, Carlson J, Gandolfi S, Lynn JE, Schmidt KE, Schwenk A, Wang X. Properties of nuclei up to $A = 16$ using local chiral interactions. *Phys Rev Lett.* (2018) **120**: 122502 doi: 10.1103/PhysRevLett.120.122502
11. Hagen G, Jansen GR, Papenbrock T. Structure of ^{78}Ni from first principles computations. *Phys Rev Lett.* (2016) **117**: 172501 doi: 10.1103/PhysRevLett.117.172501
12. Gebrerufael E, Vobig K, Hergert H, Roth R. Ab initio description of open-shell nuclei: merging no-core shell model and in-medium similarity renormalization group. *Phys Rev Lett.* (2017) **118**:152503. doi: 10.1103/PhysRevLett.118.152503
13. Cipollone A, Barbieri C, Navratil P. Chiral three-nucleon forces and the evolution of correlations along the oxygen isotopic chain. *Phys Rev C.* (2015) **92**:014306. doi: 10.1103/PhysRevC.92.014306
14. Epelbaum E, Krebs H, Lee D, Meißner UG. Ab initio calculation of the Hoyle state. *Phys Rev Lett.* (2011) **106**:192501. doi: 10.1103/PhysRevLett.106.192501
15. Elhatisari S, Lee D, Rupak G, Epelbaum E, Krebs H, Lähde TA, et al. Ab initio alpha-alpha scattering. *Nature.* (2015) **528**:111. doi: 10.1038/nature16067
16. Lähde TA, Meißner UG. Nuclear lattice effective field theory : an introduction. *Lect Notes Phys.* (2019) **957**:1. doi: 10.1007/978-3-030-14189-9
17. Reinert P, Krebs H, Epelbaum E. Semilocal momentum-space regularized chiral two-nucleon potentials up to fifth order. *Eur Phys J A.* (2018) **54**:86. doi: 10.1140/epja/i2018-12516-4
18. Navarro Pérez R, Amaro JE, Ruiz Arriola E. Coarse-grained potential analysis of neutron-proton and proton-proton scattering below the pion production threshold. *Phys Rev C.* (2013) **88**:064002. doi: 10.1103/PhysRevC.88.064002
19. Kalantar-Nayestanaki N, Epelbaum E, Messchendorp JG, Nogga A. Signatures of three-nucleon interactions in few-nucleon systems. *Rept Prog Phys.* (2012) **75**:016301. doi: 10.1088/0034-4885/75/1/016301
20. Hammer HW, Nogga A, Schwenk A. Three-body forces: from cold atoms to nuclei. *Rev Mod Phys.* (2013) **85**:197. doi: 10.1103/RevModPhys.85.197
21. Epelbaum E, Krebs H, Meißner U-G. Improved chiral nucleon-nucleon potential up to next-to-next-to-next-to-leading order. *Eur Phys J A.* (2015) **51**:53. doi: 10.1140/epja/i2015-15053-8
22. Epelbaum E, Krebs H, Meißner U-G. Precision nucleon-nucleon potential at fifth order in the chiral expansion. *Phys Rev Lett.* (2015) **115**:122301. doi: 10.1103/PhysRevLett.115.122301
23. Entem DR, Machleidt R, Nosyk Y. High-quality two-nucleon potentials up to fifth order of the chiral expansion. *Phys Rev C.* (2017) **96**:024004. doi: 10.1103/PhysRevC.96.024004
24. Gezerlis A, Tews I, Epelbaum E, Freunek M, Gandolfi S, Hebeler K, et al. Local chiral effective field theory interactions and quantum Monte Carlo applications. *Phys Rev C.* (2014) **90**:054323. doi: 10.1103/PhysRevC.90.054323
25. Piarulli M, Girlanda L, Schiavilla R, Navarro Perez R, Amaro JE, Ruiz Arriola E. Minimally nonlocal nucleon-nucleon potentials with chiral two-pion exchange including Δ resonances. *Phys Rev C.* (2015) **91**:024003. doi: 10.1103/PhysRevC.91.024003
26. Ekström A, Baardsen G, Forssén C, Hagen G, Hjorth-Jensen M, Jansen GR, et al. Optimized chiral nucleon-nucleon interaction at next-to-next-to-leading order. *Phys Rev Lett.* (2013) **110**:192502. doi: 10.1103/PhysRevLett.110.192502
27. Ekström A, Jansen GR, Wendt KA, Hagen G, Papenbrock T, Carlsson BD, et al. Accurate nuclear radii and binding energies from a chiral interaction. *Phys Rev C.* (2015) **91**:051301. doi: 10.1103/PhysRevC.91.051301
28. Li N, Elhatisari S, Epelbaum E, Lee D, Lu BN, Meißner U-G. Neutron-proton scattering with lattice chiral effective field theory at next-to-next-to-next-to-leading order. *Phys Rev C.* (2018) **98**:044002. doi: 10.1103/PhysRevC.98.044002
29. Lynn JE, Tews I, Carlson J, Gandolfi S, Gezerlis A, Schmidt KE, Schwenk A. Quantum Monte Carlo calculations of light nuclei with local chiral two- and three-nucleon interactions. *Phys Rev C.* (2017) **96**:054007. doi: 10.1103/PhysRevC.96.054007
30. Girlanda L, Kievsky A, Viviani M, Marcucci LE. Short-range three-nucleon interaction from A=3 data and its hierarchical structure. *Phys Rev C.* (2019) **99**:054003. doi: 10.1103/PhysRevC.99.054003
31. Ordonez C, Ray L, van Kolck U. The two nucleon potential from chiral Lagrangians. *Phys Rev C.* (1996) **53**:2086. doi: 10.1103/PhysRevC.53.2086
32. Kaiser N, Gerstendorfer S, Weise W. Peripheral NN scattering: role of delta excitation, correlated two pion and vector meson exchange. *Nucl Phys A.* (1998) **637**:395. doi: 10.1016/S0375-9474(98)00234-6
33. Krebs H, Epelbaum E, Meißner U-G. Nuclear forces with Delta-excitations up to next-to-next-to-leading order. I. Peripheral nucleon-nucleon waves, *Eur Phys J A.* (2007) **32**:127. doi: 10.1140/epja/i2007-10372-y
34. Epelbaum E, Krebs H, Meißner U-G. Delta-excitations and the three-nucleon force. *Nucl Phys A.* (2008) **806**:65. doi: 10.1016/j.nuclphysa.2008.02.305
35. Epelbaum E, Krebs H, Meißner U-G. Isospin-breaking two-nucleon force with explicit Delta-excitations. *Phys Rev C.* (2008) **77**:034006. doi: 10.1103/PhysRevC.77.034006
36. Krebs H, Gasparyan AM, Epelbaum E. Three-nucleon force in chiral EFT with explicit $\Delta(1232)$ degrees of freedom: longest-range contributions at fourth order. *Phys Rev C.* (2018) **98**:014003. doi: 10.1103/PhysRevC.98.014003
37. Coleman SR, Wess J, Zumino B. Structure of phenomenological Lagrangians. 1. *Phys Rev.* (1969) **177**:2239 doi: 10.1103/PhysRev.177.2239
38. Callan CG Jr, Coleman SR, Wess J, Zumino B. Structure of phenomenological Lagrangians. 2. *Phys Rev.* (1969) **177**:2247. doi: 10.1103/PhysRev.177.2247
39. Gasser J, Leutwyler H. Chiral perturbation theory to one loop. *Ann Phys.* (1984) **158**:142. doi: 10.1016/0003-4916(84)90242-2
40. Bernard V, Kaiser N, Meißner U-G. Chiral dynamics in nucleons and nuclei. *Int J Mod Phys E.* (1995) **4**:193. doi: 10.1142/S0218301395000092

41. Fettes N, Meißner U-G, Mojzis M, Steininger S. The Chiral effective pion nucleon Lagrangian of order p^4. *Ann Phys.* (2000) **283**:273. doi: 10.1006/aphy.2000.6059
42. Epelbaum E, Meißner U-G, Glöckle W, Elster C. Resonance saturation for four nucleon operators. *Phys Rev C.* (2002) **65**:044001. doi: 10.1103/PhysRevC.65.044001
43. Girlanda L, Pastore S, Schiavilla R, Viviani M. Relativity constraints on the two-nucleon contact interaction. *Phys Rev C.* (2010) **81**:034005. doi: 10.1103/PhysRevC.81.034005
44. Epelbaum E, Nogga A, Glöckle W, Kamada H, Meißner U-G, Witała H. Three nucleon forces from chiral effective field theory. *Phys Rev C.* (2002) **66**:064001. doi: 10.1103/PhysRevC.66.064001
45. Girlanda L, Kievsky A, Viviani M. Subleading contributions to the three-nucleon contact interaction. *Phys Rev C.* (2011) **84**:014001. doi: 10.1103/PhysRevC.84.014001
46. Müller G, and Meißner U-G. Virtual photons in baryon chiral perturbation theory. *Nucl Phys B.* (1999) **556**:265. doi: 10.1016/S0550-3213(99)00339-9
47. Gasser J, Ivanov MA, Lipartia E, Mojzis M, Rusetsky A. Ground state energy of pionic hydrogen to one loop. *Eur Phys J C.* (2002) **26**:13. doi: 10.1007/s10052-002-1013-z
48. Krebs H, Gasparyan A, Epelbaum E. Chiral three-nucleon force at N^4LO I: Longest-range contributions. *Phys Rev C.* (2012) **85**:054006. doi: 10.1103/PhysRevC.85.054006
49. Hoferichter M, Ruiz de Elvira J, Kubis B, Meißner U-G. Roy-Steiner-equation analysis of pion-nucleon scattering. *Phys Rept.* (2016) **625**:1. doi: 10.1016/j.physrep.2016.02.002
50. Hoferichter M, Ruiz de Elvira J, Kubis B, Meißner U-G. Matching pion-nucleon Roy-Steiner equations to chiral perturbation theory. *Phys Rev Lett.* (2015) **115**:192301. doi: 10.1103/PhysRevLett.115.192301
51. Siemens D, Bernard V, Epelbaum E, Gasparyan AM, Krebs H, Meißner U-G. Elastic and inelastic pion-nucleon scattering to fourth order in chiral perturbation theory. *Phys Rev C.* (2017) **96**:055205. doi: 10.1103/PhysRevC.96.055205
52. Manohar A, Georgi H. Chiral quarks and the nonrelativistic Quark model. *Nucl Phys B.* (1984) **234**:189. doi: 10.1016/0550-3213(84)90231-1
53. Bernard V. Chiral perturbation theory and baryon properties. *Prog Part Nucl Phys.* (2008) **60**:82. doi: 10.1016/j.ppnp.2007.07.001
54. Bernard V, Epelbaum E, Krebs H, Meißner U-G. Subleading contributions to the chiral three-nucleon force. I. Long-range terms. *Phys Rev C.* (2008) **77**:064004. doi: 10.1103/PhysRevC.77.064004
55. Bernard V, Epelbaum E, Krebs H, Meißner U-G. Subleading contributions to the chiral three-nucleon force II: short-range terms and relativistic corrections. *Phys Rev C.* (2011) **84**:054001. doi: 10.1103/PhysRevC.84.054001
56. Lepage GP. How to renormalize the Schrödinger equation. *arXiv: nucl-th/9706029.*
57. Pavon Valderrama M, Ruiz Arriola E. Renormalization of NN-scattering with one pion exchange and boundary conditions. *Phys Rev C.* (2004) **70**:044006. doi: 10.1103/PhysRevC.70.044006
58. Nogga A, Timmermans RGE, van Kolck U. Renormalization of one-pion exchange and power counting. *Phys Rev C.* (2005) **72**:054006. doi: 10.1103/PhysRevC.72.054006
59. Birse MC. Power counting with one-pion exchange. *Phys Rev C.* (2006) **74**:014003. doi: 10.1103/PhysRevC.74.014003
60. Epelbaum E, Meißner UG. On the renormalization of the one-pion exchange potential and the consistency of Weinberg's power counting. *Few Body Syst.* (2013) **54**:2175. doi: 10.1007/s00601-012-0492-1
61. Epelbaum E, Gegelia J. Regularization, renormalization and 'peratization' in effective field theory for two nucleons. *Eur Phys J A.* (2009) **41**:341. doi: 10.1140/epja/i2009-10833-3
62. Long B, Yang CJ. Renormalizing chiral nuclear forces: triplet channels. *Phys Rev C.* (2012) **85**:034002. doi: 10.1103/PhysRevC.85.034002
63. Valderrama MP. Power counting and wilsonian renormalization in nuclear effective field theory. *Int J Mod Phys E.* (2016) **25**:1641007. doi: 10.1142/S021830131641007X
64. Savage MJ. Including pions *Pasadena 1998, Nuclear physics with effective field theory. *arXiv: nucl-th/9804034.* p. 247–67.
65. Kaplan DB, Savage MJ, Wise MB. A new expansion for nucleon-nucleon interactions. *Phys Lett B.* (1998) **424**:390 doi: 10.1016/S0370-2693(98)00210-X
66. Cohen TD, Hansen JM. Testing low-energy theorems in nucleon-nucleon scattering. *Phys Rev C.* (1999)**59**:3047 doi: 10.1103/PhysRevC.59.3047
67. Fleming S, Mehen T, Stewart IW. NNLO corrections to nucleon-nucleon scattering and perturbative pions. *Nucl Phys A.* (2000) **677**:313. doi: 10.1016/S0375-9474(00)00221-9
68. Kaplan DB. On the convergence of nuclear effective field theory with perturbative pions. *arXiv: [preprint] arXiv:1905.07485 [nucl-th].*
69. Epelbaum E, Gegelia J. Weinberg's approach to nucleon-nucleon scattering revisited. *Phys Lett B* . (2012)**716**:338. doi: 10.1016/j.physletb.2012.08.025
70. Baru V, Epelbaum E, Gegelia J, Ren XL. Towards baryon-baryon scattering in manifestly Lorentz-invariant formulation of SU(3) baryon chiral perturbation theory. *Phys Lett B.* (2019)**798**:134987. doi: 10.1016/j.physletb.2019.134987
71. Epelbaum E, Gasparyan AM, Gegelia J, Krebs H. $^1S_0$ nucleon-nucleon scattering in the modified Weinberg approach. *Eur Phys J A.* (2015)**51**:71. doi: 10.1140/epja/i2015-15071-6
72. Epelbaum E. Four-nucleon force in chiral effective field theory. *Phys Lett B.* (2006)**639**:456. doi: 10.1016/j.physletb.2006.06.046
73. Epelbaum E. Four-nucleon force using the method of unitary transformation. *Eur Phys J A.* (2007)**34**:197. doi: 10.1140/epja/i2007-10496-0
74. Kölling S, Epelbaum E, Krebs H, Meißner U-G. Two-nucleon electromagnetic current in chiral effective field theory: one-pion exchange and short-range contributions. *Phys Rev C.* (2011) **84**:054008. doi: 10.1103/PhysRevC.84.054008
75. Krebs H, Epelbaum E, Meißner UG. Nuclear axial current operators to fourth order in chiral effective field theory. *Ann Phys.* (2017) **378**:317. doi: 10.1016/j.aop.2017.01.021
76. Epelbaum E, Nogga A, Glöckle W, Kamada H, Mei UGßner, Witała H. Few nucleon systems with two nucleon forces from chiral effective field theory. *Eur Phys J A.* (2002) **15**:543. doi: 10.1140/epja/i2002-10048-2
77. Krebs H. Electroweak current operators in chiral effective field theory. *PoS CD.* (2019) **2018**:098 doi: 10.22323/1.317.0098
78. Epelbaum E. Towards high-precision nuclear forces from chiral effective field theory. *arXiv:1908.09349 [nucl-th].*
79. Gegelia J, Japaridze G, Wang XQ. Is heavy baryon approach necessary?. *J Phys G.* (2003) **29**:2303. doi: 10.1088/0954-3899/29/9/322
80. Fuchs T, Gegelia J, Japaridze G, Scherer S. Renormalization of relativistic baryon chiral perturbation theory and power counting. *Phys Rev D.* (2003) **68**:056005. doi: 10.1103/PhysRevD.68.056005
81. Grießhammer HW. Assessing theory uncertainties in EFT power countings from residual cutoff dependence. *PoS CD.* (2016) **15**:104. doi: 10.22323/1.253.0104
82. Epelbaum E. Nuclear chiral EFT in the precision era. *PoS CD.* (2016) **15**:014. doi: 10.22323/1.253.0014
83. Binder S, Calci A, Epelbaum E, Furnstahl RJ, Golak J, Hebeler K, et al. Few-nucleon systems with state-of-the-art chiral nucleon-nucleon forces. *Phys Rev C.* (2016) **93**:044002. doi: 10.1103/PhysRevC.93.044002
84. Epelbaum E, Golak J, Hebeler K, Kamada H, Krebs H, Meißner UG, et al. Towards high-order calculations of three-nucleon scattering in chiral effective field theory. *Eur Phys J A.* (2020) **56**:92. doi: 10.1140/epja/s10050-020-00102-2
85. Epelbaum E, Gegelia J. The two-nucleon problem in EFT reformulated: Pion and nucleon masses as soft and hard scales. *PoS CD.* (2013) **12**:090. doi: 10.22323/1.172.0090
86. Baru V, Epelbaum E, Filin AA, Gegelia J. Low-energy theorems for nucleon-nucleon scattering at unphysical pion masses. *Phys Rev C.* (2015) **92**:014001. doi: 10.1103/PhysRevC.92.014001
87. Baru V, Epelbaum E, Filin AA. Low-energy theorems for nucleon-nucleon scattering at $M_\pi = 450$ MeV. *Phys Rev C.* (2016) **94**:014001. doi: 10.1103/PhysRevC.94.014001
88. Lahde TA, Meißner UG, Epelbaum E. An update on fine-tunings in the triple-alpha process. *Eur Phys J A.* (2020) **56**:89. doi: 10.1140/epja/s10050-020-00093-0
89. Epelbaum E. Nuclear forces from chiral effective field theory: a primer. *arXiv: 1001.3229 [nucl-th].*

90. van Haeringen H, Kok LP. Modified effective range function. *Phys Rev A.* (1982) **26**:1218. doi: 10.1103/PhysRevA.26.1218
91. Epelbaum E, Gegelia J, Meißner UG. Wilsonian renormalization group versus subtractive renormalization in effective field theories for nucleon-nucleon scattering. *Nucl Phys B.* (2017) **925**:161. doi: 10.1016/j.nuclphysb.2017.10.008
92. Suzuki K, Okamoto R. Degenerate perturbation theory in quantum mechanics. *Prog Theor Phys.* (1983) **70**:439.
93. Lindgren I. The Rayleigh-Schrödinger perturbation and the linked-diagram theorem for a multi-configurational model space. *J Phys B.* (1974) **7**:2441.
94. Okubo S. Diagonalization of Hamiltonian and Tamm-Dancoff equation. *Prog Theor Phys.* (1954) **12**:603. doi: 10.1143/PTP.12.603
95. Krebs H, Gasparyan A, Epelbaum E. Chiral three-nucleon force at N^4LO II: intermediate-range contributions. *Phys Rev C.* (2013) **87**:054007. doi: 10.1103/PhysRevC.87.054007
96. Kaiser N, Brockmann R, Weise W. Peripheral nucleon-nucleon phase shifts and chiral symmetry. *Nucl Phys A.* (1997) **625**:758. doi: 10.1016/S0375-9474(97)00586-1
97. Epelbaum E, Glöckle W, Meißner U-G. Nuclear forces from chiral Lagrangians using the method of unitary transformation. 1. Formalism. *Nucl Phys A.* (1998) **637**:107. doi: 10.1016/S0375-9474(98)00220-6
98. van Kolck U. Few nucleon forces from chiral Lagrangians. *Phys Rev C.* (1994) **49**:2932. doi: 10.1103/PhysRevC.49.2932
99. Kaiser N. Chiral three pi exchange N N potentials: results for diagrams proportional to g_A^4 and g_A^6. *Phys Rev C.* (2000) **62**:024001. doi: 10.1103/PhysRevC.62.024001
100. Kaiser N. Chiral 3π exchange NN potentials: results for representation invariant classes of diagrams. *Phys Rev C.* (2000) **61**:014003. doi: 10.1103/PhysRevC.61.014003
101. Kaiser N. Chiral 3π exchange NN potentials: results for dominant next-to-leading order contributions. *Phys Rev C.* (2001) **63**:044010. doi: 10.1103/PhysRevC.63.044010
102. Kaiser N. Chiral 2π exchange NN potentials: two loop contributions. *Phys Rev C.* (2001) **64**:057001. doi: 10.1103/PhysRevC.64.057001
103. Kaiser N. Chiral 2π exchange NN potentials: relativistic $1/M^2$ corrections. *Phys Rev C.* (2002) **65**:017001. doi: 10.1103/PhysRevC.65.017001
104. Ishikawa S, Robilotta MR. Two-pion exchange three-nucleon potential: $\mathcal{O}(q^4)$ chiral expansion. *Phys Rev C.* (2007) **76**:014006. doi: 10.1103/PhysRevC.76.014006
105. Entem DR, Kaiser N, Machleidt R, Nosyk Y. Peripheral nucleon-nucleon scattering at fifth order of chiral perturbation theory. *Phys Rev C.* (2015) **91**:014002. doi: 10.1103/PhysRevC.91.014002
106. Epelbaum E, Glöckle W, Krüger A, Meißner U-G. Effective theory for the two nucleon system. *Nucl Phys A.* (1999) **645**:413. doi: 10.1016/S0375-9474(98)00585-5
107. Polyzou WN. Equivalent hamiltonians. *Phys Rev C.* (2010) **82**:014002. doi: 10.1103/PhysRevC.82.014002
108. Pastore S, Girlanda L, Schiavilla R, Viviani M, Wiringa RB. Electromagnetic currents and magnetic moments in (χ)EFT. *Phys Rev C.* (2009) **80**:034004. doi: 10.1103/PhysRevC.80.034004
109. Pastore S, Girlanda L, Schiavilla R, Viviani M. The two-nucleon electromagnetic charge operator in chiral effective field theory (χEFT) up to one loop. *Phys Rev C.* (2011) **84**:024001. doi: 10.1103/PhysRevC.84.024001
110. Piarulli M, Girlanda L, Marcucci LE, Pastore S, Schiavilla R, Viviani M. Electromagnetic structure of A = 2 and 3 nuclei in chiral effective field theory. *Phys Rev C.* (2013) **87**:014006. doi: 10.1103/PhysRevC.87.014006
111. Baroni A, Girlanda L, Pastore S, Schiavilla R, Viviani M. Nuclear axial currents in chiral effective field theory. *Phys Rev C.* (2016) **93**:015501. doi: 10.1103/PhysRevC.93.015501
112. Entem DR, Machleidt R. Accurate charge dependent nucleon nucleon potential at fourth order of chiral perturbation theory. *Phys Rev C.* (2003) **68**:041001. doi: 10.1103/PhysRevC.68.041001
113. Epelbaum E, Glöckle W, Meißner U-G. The two-nucleon system at next-to-next-to-next-to-leading order. *Nucl Phys A.* (2005) **747**:362. doi: 10.1016/j.nuclphysa.2004.09.107
114. Carlsson BD, Ekström A, Forssén C, Fahlin Strömberg D, Jansen GR, Lija O, et al. Uncertainty analysis and order-by-order optimization of chiral nuclear interactions. *Phys Rev X.* (2016) **6**:011019. doi: 10.1103/PhysRevX.6.011019
115. Ekström A, Hagen G, Morris TD, Papenbrock T, Schwartz PD. Δ isobars and nuclear saturation. *Phys Rev C.* (2018) **97**:024332. doi: 10.1103/PhysRevC.97.024332
116. Epelbaum E, Glöckle W, Meißner U-G. Improving the convergence of the chiral expansion for nuclear forces. 1. Peripheral phases. *Eur Phys J A.* (2004) **19**:125. doi: 10.1140/epja/i2003-10096-0
117. Epelbaum E, Glöckle W, Meißner U-G. Improving the convergence of the chiral expansion for nuclear forces. 2. Low phases and the deuteron. *Eur Phys J A.* (2004) **19**:401. doi: 10.1140/epja/i2003-10129-8
118. Rijken TA. Soft two pion exchange nucleon-nucleon potentials. *Ann Phys.* (1991) **208**:253. doi: 10.1016/0003-4916(91)90296-K
119. Slavnov AA. Invariant regularization of nonlinear chiral theories. *Nucl Phys B.* (1971) **31**:301. doi: 10.1016/0550-3213(71)90234-3
120. Djukanovic D, Schindler MR, Gegelia J, Scherer S. Improving the ultraviolet behavior in baryon chiral perturbation theory. *Phys Rev D.* (2005) **72**:045002. doi: 10.1103/PhysRevD.72.045002
121. Long B, Mei Y. Cutoff regulators in chiral nuclear effective field theory. *Phys Rev C.* (2016) **93**:044003. doi: 10.1103/PhysRevC.93.044003
122. Kölling S, Epelbaum E, Krebs H, Meißner U-G. Two-pion exchange electromagnetic current in chiral effective field theory using the method of unitary transformation. *Phys Rev C.* (2009) **80**:045502. doi: 10.1103/PhysRevC.80.045502
123. Krebs H, Epelbaum E, Meißner U-G. Nuclear electromagnetic currents to fourth order in chiral effective field theory. *Few Body Syst.* (2019) **60**:31. doi: 10.1007/s00601-019-1500-5
124. Siemens D, Bernard V, Epelbaum E, Gasparyan A, Krebs H, Meißner U-G. Elastic pion-nucleon scattering in chiral perturbation theory: a fresh look. *Phys Rev C.* (2016) **94**:014620. doi: 10.1103/PhysRevC.94.014620
125. Yao DL, Siemens D, Bernard V, Epelbaum E, Gasparyan AM, Gegelia J, et al. Pion-nucleon scattering in covariant baryon chiral perturbation theory with explicit Delta resonances. *JHEP.* (2016) **1605**:038. doi: 10.1007/JHEP05(2016)038
126. Hiller Blin AN, Sun ZF, Vicente Vacas MJ. Electromagnetic form factors of spin 1/2 doubly charmed baryons. *Phys Rev D.* (2018) **98**:054025. doi: 10.1103/PhysRevD.98.054025
127. Hu J, Zhang Y, Epelbaum E, Meißner U-G, Meng J. Nuclear matter properties with nucleon-nucleon forces up to fifth order in the chiral expansion. *Phys Rev C.* (2017) **96**:034307. doi: 10.1103/PhysRevC.96.034307
128. Skibiński R, Golak J, Topolnicki K, Witała H, Epelbaum E, Krebs H, et al. Testing semi-local chiral two-nucleon interaction in selected electroweak processes. *Phys Rev C.* (2016) **93**:064002. doi: 10.1103/PhysRevC.93.064002
129. Nevo Dinur N, Hernandez OJ, Bacca S, Barnea N, Ji C, Pastore S, et al. Zemach moments and radii of ^{2,3}H and ^{3,4}He. *Phys Rev C.* (2019) **99**:034004. doi: 10.1103/PhysRevC.99.034004
130. Binder S, Calci A, Epelbaum E, Furnstahl RJ, Golak J, Hebeler K, et al. Few-nucleon and many-nucleon systems with semilocal coordinate-space regularized chiral nucleon-nucleon forces. *Phys Rev C.* (2018) **98**:014002. doi: 10.1103/PhysRevC.98.014002
131. Furnstahl RJ, Klco N, Phillips DR, Wesolowski S. Quantifying truncation errors in effective field theory. *Phys Rev C.* (2015) **92**:024005. doi: 10.1103/PhysRevC.92.024005
132. Melendez JA, Wesolowski S, Furnstahl RJ. Bayesian truncation errors in chiral effective field theory: nucleon-nucleon observables. *Phys Rev C.* (2017) **96**:024003. doi: 10.1103/PhysRevC.96.024003
133. Melendez JA, Furnstahl RJ, Phillips DR, Pratola MT, Wesolowski S. Quantifying correlated truncation errors in effective field theory. *Phys Rev C.* (2019) **100**:044001. doi: 10.1103/PhysRevC.100.044001
134. Epelbaum E. High-precision nuclear forces: where do we stand?. In: *To Appear in Proceedings of the 9th International Workshop on Chiral Dynamics*. Durham, NC (2018).
135. Tanabashi M, Hagiwara K, Hikasa K, Nakamura K, Sumino Y, Takashi F, et al. Review of particle physics. *Phys Rev D.* (2018) **98**:030001. doi: 10.1103/PhysRevD.98.030001
136. Fettes N, Meißner U-G, Steininger S. Pion-nucleon scattering in chiral perturbation theory. 1. Isospin symmetric case. *Nucl Phys A.* (1998) **640**:199. doi: 10.1016/S0375-9474(98)00452-7 [hep-ph/9803266].
137. Stoks VGJ, Klomp RAM, Rentmeester MCM, de Swart JJ. Partial wave analaysis of all nucleon-nucleon scattering data below

350 MeV. *Phys Rev C.* (1993) **48**:792. doi: 10.1103/PhysRevC.48.792
138. Austen GJM,de Swart JJ. An improved coulomb potential. *Phys Rev Lett.* (1983) **50**:2039. doi: 10.1103/PhysRevLett.50.2039
139. Stoks VGJ,De Swart JJ. The magnetic moment interaction in nucleon-nucleon phase shift analyses. *Phys Rev C.* (1990) **42**:1235. doi: 10.1103/PhysRevC.42.1235
140. Durand L. Vacuum polarization effects in proton-proton scattering. *Phys Rev.* (1957) **108**:1597. doi: 10.1103/PhysRev.108.1597
141. Daub BH, Henzl V, Kovash MA, Matthews JL, Miller ZW, Shoniyozov K, Yang H. Measurements of the neutron-proton and neutron-carbon total cross section from 150 to 800 keV. *Phys Rev C.* (2013) **87**:014005. doi: 10.1103/PhysRevC.87.014005
142. Cox GF, Eaton GH, Van Zyl CP, Jarvis ON, Rose B. Measurements of the differential cross section and polarization in proton-proton scattering at about 143 MeV. *Nucl Phys B.* (1968) **4**:353. doi: 10.1016/0550-3213(68)90115-6
143. Wesolowski S, Furnstahl RJ, Melendez JA, Phillips DR. Exploring Bayesian parameter estimation for chiral effective field theory using nucleon–nucleon phase shifts. *J Phys G.* (2019) **46**:045102. doi: 10.1088/1361-6471/aaf5fc
144. Van Der Leun C, Alderliesten C. The deuteron binding energy. *Nucl Phys A.* (1982) **380**:261. doi: 10.1016/0375-9474(82)90105-1
145. Schoen K, Jacobson DL, Arif M, Huffman PR, Black TC, Snow WM, et al. Precision neutron interferometric measurements and updated evaluations of the *np* and *nd* coherent neutron scattering lengths. *Phys Rev C.* (2003) **67**:044005. doi: 10.1103/PhysRevC.67.044005
146. Machleidt R. The high precision, charge dependent Bonn nucleon-nucleon potential (CD-Bonn). *Phys Rev C.* (2001) **63**:024001. doi: 10.1103/PhysRevC.63.024001
147. Stoks VGJ, Klomp RAM, Terheggen CPF, de Swart JJ. Construction of high quality N N potential models. *Phys Rev C.* (1994) **49**:2950 doi: 10.1103/PhysRevC.49.2950
148. Gross F, Stadler A. Covariant spectator theory of np scattering: phase shifts obtained from precision fits to data below 350-MeV. *Phys Rev C.* (2008) **78**:014005. doi: 10.1103/PhysRevC.78.014005
149. Navarro Pérez R, Amaro JE, Ruiz Arriola E. Partial wave analysis of nucleon-nucleon scattering below pion production threshold. *Phys Rev C.* (2013) **88**:024002. doi: 10.1103/PhysRevC.88.024002
150. Jarvis ON, Whitehead C, Shah M. Small-angle proton - proton scattering cross-sections at 144 MeV. *Phys Lett.* (1971) **36B**:409. doi: 10.1016/0370-2693(71)90737-4
151. Taylor AE, Wood E, Bird L. Proton-proton scattering at 98 and 142 MeV. *Nucl Phys.* (1960) **16**:320.
152. Bird L, Christmas P, Taylor A, Wood E. De-polarization parameter in p-p scattering at 143 MeV. *Nucl Phys.* (1961) **27**:586.
153. Jarvis O, Rose B, Scanlon J, Wood E. A measurement of the Wolfenstein A parameter in p-p scattering at 143 MeV. *Nucl Phys.* (1963) **42**:294.
154. Aldor-Noiman S, Brown LD, Buja A, Rolke W, Stine RA. The power to see: a new graphical test of normality. *Am Stat.* (2013) **67**:249. doi: 10.1080/00031305.2013.847865
155. Navarro Pérez R, Amaro JE, Ruiz Arriola E. Statistical error analysis for phenomenological nucleon-nucleon potentials. *Phys Rev C.* (2014) **89**:064006. doi: 10.1103/PhysRevC.89.064006
156. Lisowski PW, Shamu RE, Auchampaugh GF, King NSP, Moore MS, Morgan GL, Singleton TS. Search for resonance structure in *np* total cross-section below 800 MeV. *Phys Rev Lett.* (1982) **49**:255. doi: 10.1103/PhysRevLett.49.255
157. Ericson TEO, Rosa-Clot M. The deuteron asymptotic *D* state as a probe of the nucleon-nucleon force. *Nucl Phys A.* (1983) **405**:497.
158. Rodning NL, Knutson LD. Asymptotic D-state to S-state ratio of the deuteron. *Phys Rev C.* (1990) **41**:898.
159. Huber A, Udem T, Gross B, Reichert J, Kourogi M, Pachucki K, et al. Hydrogen-deuterium S-1- S-2 isotope shift and the structure of the deuteron. *Phys Rev Lett.* (1998) **80**:468.
160. Bishop DM, Cheung LM. Quadrupole moment of the deuteron from a precise calculation of the electric field gradient in D-2. *Phys Rev A.* (1979) **20**:381.
161. Friar JL, van Kolck U. Charge independence breaking in the two pion exchange nucleon-nucleon force. *Phys Rev C.* (1999) **60**:034006.
162. Friar JL, van Kolck U, Payne GL, Coon SA. Charge symmetry breaking and the two pion exchange two nucleon interaction, *Phys Rev C.* (2003) **68**:024003. doi: 10.1103/PhysRevC.68.024003
163. Epelbaum E, Meißner U-G. Isospin-violating nucleon-nucleon forces using the method of unitary transformation. *Phys Rev C.* (2005) **72**:044001. doi: 10.1103/PhysRevC.72.044001
164. van Kolck U, Rentmeester MCM, Friar JL, Goldman JT, de Swart JJ. Electromagnetic corrections to the one pion exchange potential. *Phys Rev Lett.* (1998) **80**:4386. doi: 10.1103/PhysRevLett.80.4386
165. Navarro Pérez R, Amaro JE, Ruiz Arriola E. Precise determination of charge dependent pion-nucleon-nucleon coupling constants. *Phys Rev C.* (2017) **95**:064001. doi: 10.1103/PhysRevC.95.064001
166. Glöckle W, Witała H, Hüber D, Kamada H, Golak J. The three nucleon continuum: achievements, challenges and applications. *Phys Rept.* (1996) **274**:107.
167. Kievsky A, Viviani M, Rosati S, Huber D, Glöckle W, Kamada H, et al. Benchmark calculations for polarization observables in three nucleon scattering. *Phys Rev C.* (1998) **58**:3085. doi: 10.1103/PhysRevC.58.3085
168. Witała H, Glöckle W. The analysing power in elastic nucleon-deuteron scattering. *Nucl Phys A.* (1991) **528**:48.
169. Witała H, Glöckle W. On the discrepancies in the low energy neutron-deuteron breakup. *J Phys G.* (2010) **37**:064003. doi: 10.1088/0954-3899/37/6/064003
170. Coon SA, Han HK. Reworking the Tucson-Melbourne three nucleon potential. *Few Body Syst.* (2001) **30**:131. doi: 10.1007/s006010170022
171. Pudliner BS, Pandharipande VR, Carlson J, Wiringa RB. Quantum Monte Carlo calculations of A <= 6 nuclei. *Phys Rev Lett.* (1995) **74**:4396. doi: 10.1103/PhysRevLett.74.4396
172. Witała H, Golak J, Skibiński R, Glöckle W, Kamada H, Polyzou WN. Three-nucleon force in relativistic three-nucleon Faddeev calculations. *Phys Rev C.* (2011) **83**:044001. doi: 10.1103/PhysRevC.83.044001
173. Phillips DR, Schat C. Three-nucleon forces in the 1/Nc expansion. *Phys Rev C.* (2013) **88**:034002. doi: 10.1103/PhysRevC.88.034002
174. Epelbaum E, Gasparyan AM, Krebs H, Schat C. Three-nucleon force at large distances: Insights from chiral effective field theory and the large-N_c expansion. *Eur Phys J A.* (2015) **51**:26. doi: 10.1140/epja/i2015-15026-y
175. Topolnicki K. General operator form of the non-local three-nucleon force. *Eur Phys J A.* (2017) **53**:181. doi: 10.1140/epja/i2017-12376-4
176. Wiringa RB, Stoks VGJ, Schiavilla R. An accurate nucleon-nucleon potential with charge independence breaking. *Phys Rev C.* (1995) **51**:38. doi: 10.1103/PhysRevC.51.38
177. Hu J, Wei P, Zhang Y. Bayesian truncation errors in equations of state of nuclear matter with chiral nucleon-nucleon potentials. *Phys Lett B.* (2019) **798**:134982. doi: 10.1016/j.physletb.2019.134982
178. Golak J, Rozpedzik D, Skibinski R, TopolnickiK, Witała H, Glöckle W, et al. A new way to perform partial wave decompositions of few-nucleon forces. *Eur Phys J A.* (2010) **43**:241. doi: 10.1140/epja/i2009-10903-6
179. Hebeler K, Krebs H, Epelbaum E, Golak J, Skibiński R. Efficient calculation of chiral three-nucleon forces up to N3LO for ab initio studies. *Phys Rev C.* (2015) **91**:044001. doi: 10.1103/PhysRevC.91.044001
180. Navratil P, Gueorguiev VG, Vary JP, Ormand WE, Nogga A. Structure of A=10-13 nuclei with two plus three-nucleon interactions from chiral effective field theory. *Phys Rev Lett.* (2007) **99**:042501. doi: 10.1103/PhysRevLett.99.042501
181. Gazit D, Quaglioni S, Navratil P. Three-Nucleon low-energy constants from the consistency of interactions and currents in chiral effective field theory. *Phys Rev Lett.* (2009) **103**:102502. doi: 10.1103/PhysRevLett.103.102502
182. Platter L, Hammer H-W, Meißner U-G. On the correlation between the binding energies of the triton and the alpha-particle. *Phys Lett B.* (2005) **607**:254. doi: 10.1016/j.physletb.2004.12.068
183. Abfalterer WP, Bateman FB, Dietrich FS, Finlay RW, Haight RC, Morgan GL. Measurement of neutron total cross-sections up to 560-MeV. *Phys Rev C.* (2001) **63**:044608. doi: 10.1103/PhysRevC.63.044608

184. Sekiguchi K, Sakai H, Witała H, Glöckle W, Golak J, Hatano M, et al. Complete set of precise deuteron analyzing powers at intermediate energies: comparison with modern nuclear force predictions. *Phys Rev C.* (2002) **65**:034003. doi: 10.1103/PhysRevC.65.034003
185. Ermisch K, Amir-Ahmadi HR, van den Berg AM, Castelijns R, Davids B, Epelbaum E, et al. Systematic investigation of the elastic proton deuteron differential cross-section at intermediate-energies. *Phys Rev C.* (2003) **68**:051001. doi: 10.1103/PhysRevC.68.051001
186. Deltuva A, Fonseca AC, Sauer PU. Momentum-space treatment of coulomb interaction in three-nucleon reactions with two protons. *Phys Rev C.* (2005) **71**:054005. doi: 10.1103/PhysRevC.71.054005
187. Howell CR, Tornow W, Murphy K, Pfützner HG, Roberts ML, Anli L, et al. Comparisons of vector analyzing-power data and calculations for neutron-deuteron elastic scattering from 10 to 14 MeV. *Few Body Syst.* (1987) **2**:19.
188. Sagara K, Oguri H, Shimizu S, Maeda K, Nakamura H, Nakashima T, Morinobu S. Energy dependence of analyzing power A_y and cross section for $p + d$ scattering below 18 MeV. *Phys Rev C.* (1994) **50**:576.
189. Rauprich G, Hähn HJ, Karus M, Nießen P, Nyga KR,Oswald H, et al. Measurement of $D(\vec{p}, p)D$ elastic scattering at 10.0, 12.0, 14.1 and 16.5 MeV especially for small forward and extreme backward scattering angles. *Few Body Syst.* (1988) **5**:67.
190. Sperisen F, Grüebler W, König V, Schmelzbach PA, Elsener K,Jenny B, et al. Comparison of a nearly complete pd elastic scattering data set with Faddeev calculations. *Nucl Phys.* (1984) **A422**:81.
191. Kievsky A. Phenomenological spin orbit three-body force. *Phys Rev C.* (1999) **60**:034001. doi: 10.1103/PhysRevC.60.034001
192. von Przewoski B, Meyer HO, Balewski JT, Daehnick WW, Doskow J, Haeberli W, et al. Analyzing powers and spin correlation coefficients for p+d elastic scattering at 135-MeV and 200-MeV. *Phys Rev C.* (2006) **74**:064003. doi: 10.1103/PhysRevC.74.064003
193. Barrett BR, Navratil P, Vary JP. Ab initio no core shell model. *Prog Part Nucl Phys.* (2013) **69**:131. doi: 10.1016/j.ppnp.2012.10.003
194. Maris P, Vary JP, Shirokov AM. Ab initio no-core full configuration calculations of light nuclei. *Phys Rev C.* (2009) **79**:014308. doi: 10.1103/PhysRevC.79.014308
195. Maris P, Vary JP. Ab initio nuclear structure calculations of p-shell nuclei with JISP16. *Int J Mod Phys E.* (2013) **22**:1330016. doi: 10.1142/S0218301313300166
196. Glazek SD, Wilson KG. Renormalization of Hamiltonians. *Phys Rev D.* (1993) **48**:5863. doi: 10.1103/PhysRevD.48.5863
197. Wegner F. Flow equations for Hamiltonians. *Ann Phys.* (1994) **506**:77. doi: 10.1002/andp.19945060203
198. Bogner SK, Furnstahl RJ, Maris P, Perry RJ, Schwenk A, Vary JP. Convergence in the no-core shell model with low-momentum two-nucleon interactions. *Nucl Phys A.* (2008) **801**:21. doi: 10.1016/j.nuclphysa.2007.12.008
199. Bogner SK, Furnstahl RJ, Schwenk A. From low-momentum interactions to nuclear structure. *Prog Part Nucl Phys.* (2010) **65**:94. doi: 10.1016/j.ppnp.2010.03.001
200. Hagen G, Papenbrock T, Dean DJ, Schwenk A, Nogga A, Wloch M, Piecuch P. Coupled-cluster theory for three-body Hamiltonians. *Phys Rev C.* (2007) **76**:034302. doi: 10.1103/PhysRevC.76.034302
201. Roth R, Binder S, Vobig K, Calci A, Langhammer J, Navratil P. Ab initio calculations of medium-mass nuclei with normal-ordered chiral NN+3N interactions. *Phys Rev Lett.* (2012) **109**:052501. doi: 10.1103/PhysRevLett.109.052501
202. Binder S, Piecuch P, Calci A, Langhammer J, Navratil P, Roth R. Extension of coupled-cluster theory with a noniterative treatment of connected triply excited clusters to three-body Hamiltonians. *Phys Rev C.* (2013) **88**:054319. doi: 10.1103/PhysRevC.88.054319
203. Stroberg SR, Calci A, Hergert H, Holt JD, Bogner SK, Roth R, Schwenk A. A nucleus-dependent valence-space approach to nuclear structure. *Phys Rev Lett.* (2017) **118**:032502. doi: 10.1103/PhysRevLett.118.032502
204. Beane SR, Savage MJ. Rearranging pionless effective field theory. *Nucl Phys A.* (2001) **694**:511. doi: 10.1016/S0375-9474(01)01088-0
205. Furnstahl RJ, Hammer HW, Tirfessa N. Field redefinitions at finite density. *Nucl Phys A.* (2001) **689**:846. doi: 10.1016/S0375-9474(00)00687-4
206. Filin AA, Baru V, Epelbaum E, Krebs H, Möller D, Reinert P. Extraction of the neutron charge radius from a precision calculation of the deuteron structure radius. *Phys Rev Lett.* (2020) **124**:082501.
207. Birse MC. More effective theory of nuclear forces. *PoS CD* (2009) **09**:078. doi: 10.22323/1.086.0078
208. Golak J, Skibinski R, Topolnicki K, Witała H, Epelbaum E, Krebs H, et al. Low-energy neutron-deuteron reactions with N3LO chiral forces. *Eur Phys J A.* (2014) **50**:177. doi: 10.1140/epja/i2014-14177-7
209. Drischler C, Hebeler K, Schwenk A. Chiral interactions up to next-to-next-to-next-to-leading order and nuclear saturation. *Phys Rev Lett.* (2019) **122**:042501. doi: 10.1103/PhysRevLett.122.042501
210. Hoppe J, Drischler C, Hebeler K, Schwenk A, Simonis J. Probing chiral interactions up to next-to-next-to-next-to-leading order in medium-mass nuclei. *Phys Rev C.* (2019) **100**:024318. doi: 10.1103/PhysRevC.100.024318
211. Hüther T, Vobig K, Hebeler K, Machleidt R, Roth R. Family of chiral two-plus three-nucleon interactions for accurate nuclear structure studies. *arXiv: [preprint]. arXiv:1911.04955 [nucl-th].*
212. Baroni A, Girlanda L, Kievsky A, Marcucci LE, Schiavilla R, Viviani M. Tritium β-decay in chiral effective field theory. *Phys Rev C.* (2016) **94**:024003.
doi: 10.1103/PhysRevC.94.024003
213. Baroni A, Schiavilla R, Marcucci LE, Girlanda L, Kievsky A, Lovato A, et al. Local chiral interactions, the tritium Gamow-Teller matrix element, and the three-nucleon contact term. *Phys Rev C.* (2018) **98**:044003. doi: 10.1103/PhysRevC.98.044003

Conflict of Interest: The authors declare that the research was conducted in the absence of any commercial or financial relationships that could be construed as a potential conflict of interest.

Copyright © 2020 Epelbaum, Krebs and Reinert. This is an open-access article distributed under the terms of the Creative Commons Attribution License (CC BY). The use, distribution or reproduction in other forums is permitted, provided the original author(s) and the copyright owner(s) are credited and that the original publication in this journal is cited, in accordance with accepted academic practice. No use, distribution or reproduction is permitted which does not comply with these terms.

frontiers in Physics

REVIEW
published: 18 March 2020
doi: 10.3389/fphy.2020.00057

Nucleon-Nucleon Scattering Up to N^{5}LO in Chiral Effective Field Theory

David Rodriguez Entem[1,2]*, *Ruprecht Machleidt*[3] *and Yevgen Nosyk*[3]

[1] Department of Fundamental Physics, Faculty of Science, University of Salamanca, Salamanca, Spain, [2] Institute on Fundamental Physics and Mathematics (IUFFyM), University of Salamanca, Salamanca, Spain, [3] Department of Physics, University of Idaho, Moscow, ID, United States

During the past few decades a large effort has been made toward describing the *NN* interaction in the framework of chiral Effective Field Theory (EFT). The main idea is to exploit the symmetries of QCD to obtain an effective theory for low energy nuclear systems. In 2003, the first accurate charge-dependent *NN* potential in this scheme was developed and it has been applied to many ab-initio calculations, opening the possibility to study nuclear systems in a systematic and accurate way. It was shown that the fourth order (N^{3}LO) was necessary and sufficient to describe the *NN* scattering data with a χ^2/d.o.f on the order of so-called high precision potentials. However the systematics of chiral EFT also allow to relate two- and many-body interactions in a well-defined way. Since many-body forces make their first appearance at higher order, they are substantially smaller than their two-body counterparts, but may never-the-less be crucial for some processes. Thus, there are observables where they can have a big impact and, for example, there are indications that they solve the long standing A_y puzzle of *N-d* scattering. The last few years, have also seen substantial progress toward higher orders of chiral EFT which was motivated by the fact that only three-body forces of rather high order may solve some outstanding issues in microscopic nuclear structure and reactions. In this chapter we will review the latest contributions of the authors to development of chiral EFT based potentials up to N^{4}LO as well as first calculations conducted for *NN* scattering at N^{5}LO.

Keywords: nucleon-nucleon scattering, chiral effective field theory, EFT, nucleon-nucleon interaction, nucleon-nucleon potential

OPEN ACCESS

Edited by:
Nunzio Itaco,
University of Campania Luigi Vanvitelli, Italy

Reviewed by:
Michele Viviani,
National Institute of Nuclear Physics of Pisa, Italy
Daniel Phillips,
Ohio University, United States

***Correspondence:**
David Rodriguez Entem
entem@usal.es

Specialty section:
This article was submitted to Nuclear Physics, a section of the journal Frontiers in Physics

Received: *03 September 2019*
Accepted: *26 February 2020*
Published: *18 March 2020*

Citation:
Rodriguez Entem D, Machleidt R and Nosyk Y (2020) Nucleon-Nucleon Scattering Up to N^{5}LO in Chiral Effective Field Theory. Front. Phys. 8:57. doi: 10.3389/fphy.2020.00057

1. INTRODUCTION

The modern view of the *NN* interaction is given in the framework of Chiral Effective Field Theory (χEFT). The concept of an Effective Field Theory (EFT) is not a new one. The main idea is to identify the relevant degrees of freedom and symmetries for a certain system at a certain scale, and use this to find a Quantum Field Theory that is able to describe the system. However the traditional renormalization condition used to build theories like QCD is not required and a renormalization order by order is used instead. Nowadays, this approach is widely applied in different areas of physics.

In the case of strong interactions, we know that the fundamental theory is given by Quantum Chromodynamics (QCD). However for nuclear systems, the relevant degrees of freedom are not quarks and gluons, but nucleons and pions. Applying the EFT concept to nuclear systems allows to build theories for nucleons and pions that are consistent with the symmetries of the underlying theory. In the case of QCD, a very important property for low energy dynamics is that the original approximate chiral symmetry is broken spontaneously. This effect makes the pion come into play

as the pseudo-Goldstone boson of the theory, which naturally explains the low mass of the pion as compared to other scales in nuclear systems.

Chiral Perturbation Theory (ChPT) uses these ideas to determine observables making a perturbative expansion in the pion mass or some low energy external momenta. The Goldstone-boson character of the pion allows for this perturbative expansion, having always derivative couplings. ChPT was first applied to $\pi\pi$ systems [1] and πN systems [2] with quite some success. Chiral EFT is essentially based on ChPT, however in the case of the *NN* interaction this perturbative expansion is inadequate and non-perturbative resummations are needed. The complicate structure of the amplitudes makes it difficult to resum these contributions using the techniques of Unitarized ChPT that are applied in two-meson systems [3]. However first attempts to use similar techniques using the so called N/D method have been made [4].

The use of χEFT for the two-nucleon system was introduced by Weinberg in two seminal papers [5, 6]. Weinberg realized that reducible diagrams violate the chiral expansion and, therefore, proposed to determine the potential using the rules of ChPT and then insert it into a Schrödinger-like equation to conduct the non-perturbative resummation.

Soon after, the first nuclear potentials were obtained by Ordoñez and van Kolck [7–9]. These position-space potentials were developed up to next-to-next-to-leading order (N^{2}LO) and regularized by a cutoff function. Momentum-space potentials up to N^{2}LO using dimensional regularization were derived by the Bochum group [10, 11]. The simple and transparent momentum-space expressions obtained in this type of derivation [12] made chiral potentials more popular. However it was not until 2003 that χEFT reached high precision when the first chiral potential at N^{3}LO was developed by Entem and Machleidt [13, 14] that was able to describe the *NN* scattering data with a χ^2/d.o.f similar to what the high-precision potentials of the 90's had achieved [15–18].

Since then, many applications of N^{3}LO NN potentials together with chiral three-nucleon forces (3NFs) have been reported. These investigations include few-nucleon reactions [19–22], structure of light- and medium-mass nuclei [23–27] and infinite matter [28–33]. Although satisfactory predictions have been obtained in many cases, persistent problems continue to pose serious challenges, as the overbinding in medium mass nuclei [25] or the descriptions of charge and matter radii [34]. There is also the well-known A_y puzzle of nucleon-deuteron scattering [35]. In this case recent calculations including contact 3NFs at N^{4}LO have been shown to be able to solve the puzzle [36]. This suggests that one may have to proceed to the next higher order, namely, N^{4}LO, for the two-nucleon force.

Thus, during the past few years, chiral potentials up to N^{4}LO have been developed by the Idaho-Salamanca group [37] as well as the Bochum group [38].

In the whole chapter we will be referring to the so called Δ-less EFT, where Δ degrees of freedom have been integrated out. There are recent advances in the Δ-full theory [39, 40]. We refer the interested reader to contributions on this topic in the present monograph.

The chapter is organized as follows. In section 2 we review the most important aspects of χEFT for the two-nucleon system. In section 3 we apply the perturbative amplitude obtained to study peripheral *NN* scattering up to N^{5}LO. In section 4 we review *NN* potentials up to N^{4}LO. We conclude with a summary in section 5.

2. CHIRAL EFT FOR THE *NN* SYSTEM

2.1. Power Counting

In order to build an EFT for the two nucleon system, the Lagrangians for the involved degrees of freedom have to be constructed. However, there is an infinite number of terms in the Lagrangian compatible with the allowed symmetries. For this reason, it is necessary to order all terms by what we call power counting. Following power counting, the terms in the Lagrangian are arranged by order. Moreover, the diagrams representing an amplitude calculated from the Lagrangian are also of a well defined order. Since higher orders include loop diagrams that diverge, the power counting also needs to be such that all the infinities generated at a certain order can be reabsorbed into redefinitions of the coupling constants of the Lagrangian at the same order. With these ideas in mind Weinberg, proposed the so called Weinberg power counting which is based on naive dimensional analysis.

Following naive dimensional analysis, a nucleon propagator counts as Q^{-1}, where Q stands for a low momentum or pion mass, a pion propagator as Q^{-2}, each derivative or pion mass insertion counts as Q and each four momentum integration as Q^4. The power of a diagram is then given by the simple formula [5, 6, 14]

$$\nu = -2 + 2A - 2C + 2L + \sum_i \Delta_i \,, \tag{1}$$

where A is the number of nucleons involved, C the number of connected pieces, L the number of loops, and the sum runs over all vertexes i with Δ_i the index of the vertex given by

$$\Delta_i \equiv d_i + \frac{n_i}{2} - 2 \tag{2}$$

with d_i the number of derivatives or pion mass insertions (chiral dimension) and n_i the number of nucleon legs. In this way the contribution of a diagram goes as $(Q/\Lambda_b)^\nu$ with Λ_b the breakdown scale.

In the heavy-baryon formalism, an expansion in terms of Q/M_N is performed, with M_N denoting the nucleon mass. It is used for low energy nucleon systems and we will count these contributions as $Q/M_N \sim (Q/\Lambda_b)^2$ for reasons explained in Weinberg [5, 6].

An important property of chiral symmetry is that the index of the vertexes is always zero or positive $\Delta_i \geq 0$. This fact implies that for a fixed number of nucleons with $A \geq 2$ and considering diagrams with one connected piece, the power of a diagram is always bounded from below. This fact is crucial for the convergence of the chiral expansion.

A very important aspect of the EFT is that it relates two-body forces with many-body forces. We know that two-body forces

are the main contribution to nuclear forces, however, many-body forces should exist. If we consider lowest order diagrams with $L = 0$ and $\Delta_i = 0$, for an m-body force in an A-nucleon system, the number of separately connected pieces is $C = A - m + 1$, and so the power of the diagram is given by $\nu = 2m - 4$. This means that two-body forces ($m = 2$) appear at $\nu = 0$, three-body forces ($m = 3$) at $\nu = 2$, four-body ($m = 4$) at $\nu = 4$ and so on. So the power counting explains in a simple way the hierarchy of nuclear forces. In **Figure 1** we summarize this hierarchy up to N^{5}LO or sixth order of the chiral expansion.

2.2. The Lagrangian

We will limit ourselves to the Δ-less version of χEFT, and so the relevant degrees of freedom are pions and nucleons. The effective Lagrangian, subdivided in terms of the number of nucleon legs, is given by

$$\mathcal{L}_{\rm eff} = \mathcal{L}_{\pi\pi} + \mathcal{L}_{\pi N} + \mathcal{L}_{NN} + \dots, \tag{3}$$

where $\mathcal{L}_{\pi\pi}$ stands for the Lagrangian that deals with pion dynamics, $\mathcal{L}_{\pi N}$ the interaction between pions and a nucleon, and $\mathcal{L}_{NN}$ contains four nucleon legs and no pion fields. The ellipsis stands for terms that involve two nucleons plus pions and three or more nucleons with or without pions, not relevant for the two nucleon sector.

All the pieces in the Lagrangian are then organized in terms of the chiral dimension (number of derivatives/pion mass insertions) of increasing order

$$\begin{aligned}
\mathcal{L}_{\pi\pi} &= \mathcal{L}^{(2)}_{\pi\pi} + \mathcal{L}^{(4)}_{\pi\pi} + \dots, && (4)\\
\mathcal{L}_{\pi N} &= \mathcal{L}^{(1)}_{\pi N} + \mathcal{L}^{(2)}_{\pi N} + \mathcal{L}^{(3)}_{\pi N} + \mathcal{L}^{(4)}_{\pi N} + \mathcal{L}^{(5)}_{\pi N} + \dots, && (5)\\
\mathcal{L}_{NN} &= \mathcal{L}^{(0)}_{NN} + \mathcal{L}^{(2)}_{NN} + \mathcal{L}^{(4)}_{NN} + \dots, && (6)
\end{aligned}$$

where the superscript refers to the chiral dimension and the ellipsis refers to terms of higher dimensions. We use the heavy-baryon formulation of the Lagrangians, the explicit expressions of which can be found in Machleidt and Entem [14] and Krebs et al. [41]. Notice that only in the *NN* case the chiral dimension is the same as the index Δ_i.

2.3. The Scattering Amplitude

Having the Lagrangian, we can now calculate the *NN* scattering amplitude. The *NN* amplitude has contributions from irreducible as well as reducible diagrams. The reducible diagrams are those that we can separate into two diagrams by cutting only nucleon lines. In covariant perturbation theory the separation is well defined, however when we apply a three-dimensional reduction of the Bethe-Salpeter equation it depends on the way this reduction is performed. See Machleidt and Entem [14] for a discussion on this point. We will come back to this when we define the potential.

The amplitude for diagrams involving pions is organized in terms of the number of pions exchanged by the two nucleons

$$V_\pi = V_{1\pi} + V_{2\pi} + V_{3\pi} + \dots \tag{7}$$

Then each piece is divided in terms of the power counting described previously as

$$\begin{aligned}
V_{1\pi} &= V^{(0)}_{1\pi} + V^{(2)}_{1\pi} + V^{(3)}_{1\pi} + V^{(4)}_{1\pi} + V^{(5)}_{1\pi} + V^{(6)}_{1\pi} + \dots, && (8)\\
V_{2\pi} &= V^{(2)}_{2\pi} + V^{(3)}_{2\pi} + V^{(4)}_{2\pi} + V^{(5)}_{2\pi} + V^{(6)}_{2\pi} + \dots, && (9)\\
V_{3\pi} &= V^{(4)}_{3\pi} + V^{(5)}_{3\pi} + V^{(6)}_{3\pi} + \dots, && (10)
\end{aligned}$$

where the superscript denotes the order ν.

Besides these diagrams, contributions coming from Lagrangian $\mathcal{L}_{NN}$ are also present. These contributions are contact-like contributions and take into account the unknown short-distance dynamics. They are again organized using the power counting

$$V_{\rm ct} = V^{(0)}_{\rm ct} + V^{(2)}_{\rm ct} + V^{(4)}_{\rm ct} + V^{(6)}_{\rm ct} + \dots, \tag{11}$$

where the superscript is the order ν. Due to symmetry requirements these contributions come only in even powers.

Then the order by order contributions are given by

$$\begin{aligned}
V_{\rm LO} \equiv V^{(0)}_\pi + V^{(0)}_{\rm ct} &= V^{(0)}_{\rm ct} + V^{(0)}_{1\pi}, && (12)\\
V_{\rm NLO} \equiv V_{\rm LO} + V^{(2)}_\pi + V^{(2)}_{\rm ct} &= V_{\rm LO} + V^{(2)}_{\rm ct} + V^{(2)}_{1\pi} + V^{(2)}_{2\pi}, && (13)\\
V_{\rm NNLO} \equiv V_{\rm NLO} + V^{(3)}_\pi &= V_{\rm NLO} + V^{(3)}_{1\pi} + V^{(3)}_{2\pi}, && (14)\\
V_{\rm N^3LO} \equiv V_{\rm NNLO} + V^{(4)}_\pi + V^{(4)}_{\rm ct} &= V_{\rm NNLO} + V^{(4)}_{\rm ct} + V^{(4)}_{1\pi}\\
&\quad + V^{(4)}_{2\pi} + V^{(4)}_{3\pi}, && (15)\\
V_{\rm N^4LO} \equiv V_{\rm N^3LO} + V^{(5)}_\pi &= V_{\rm N^3LO} + V^{(5)}_{1\pi} + V^{(5)}_{2\pi}\\
&\quad + V^{(5)}_{3\pi}, && (16)\\
V_{\rm N^5LO} \equiv V_{\rm N^4LO} + V^{(6)}_\pi + V^{(6)}_{\rm ct} &= V_{\rm N^4LO} + V^{(6)}_{\rm ct} + V^{(6)}_{1\pi}\\
&\quad + V^{(6)}_{2\pi} + V^{(6)}_{3\pi}, && (17)
\end{aligned}$$

where LO stands for leading order, NLO next-to-leading order, etc.

For the presentation of amplitudes we will use the following decomposition

$$\begin{aligned}
V(\vec{p}\,',\vec{p}) = &\quad V_C \;+\vec{\tau}_1\cdot\vec{\tau}_2\, W_C\\
&+ \left[\, V_S \;+\vec{\tau}_1\cdot\vec{\tau}_2\, W_S \;\right] \vec{\sigma}_1\cdot\vec{\sigma}_2\\
&+ \left[\, V_{LS} + \vec{\tau}_1\cdot\vec{\tau}_2\, W_{LS}\right] \left(-i\vec{S}\cdot(\vec{q}\times\vec{k})\right)\\
&+ \left[\, V_T \;+\vec{\tau}_1\cdot\vec{\tau}_2\, W_T \;\right] \vec{\sigma}_1\cdot\vec{q}\;\vec{\sigma}_2\cdot\vec{q}\\
&+ \left[\, V_{\sigma L} + \vec{\tau}_1\cdot\vec{\tau}_2\, W_{\sigma L}\right] \vec{\sigma}_1\cdot(\vec{q}\times\vec{k})\;\vec{\sigma}_2\cdot(\vec{q}\times\vec{k}), \qquad (18)
\end{aligned}$$

where $\vec{p}\,'$ and $\vec{p}$ denote the final and initial nucleon momenta in the center-of-mass system (CMS), respectively. Moreover, $\vec{q} = \vec{p}\,' - \vec{p}$ is the momentum transfer, $\vec{k} = (\vec{p}\,' + \vec{p})/2$ the average momentum, and $\vec{S} = (\vec{\sigma}_1 + \vec{\sigma}_2)/2$ the total spin, with $\vec{\sigma}_{1,2}$ and $\vec{\tau}_{1,2}$ the spin and isospin operators, of nucleon 1 and 2, respectively. For on-shell scattering, V_α and W_α ($\alpha = C, S, LS, T, \sigma L$) can be expressed as functions of $q = |\vec{q}\,|$ and $p = |\vec{p}\,'| = |\vec{p}\,|$, only.

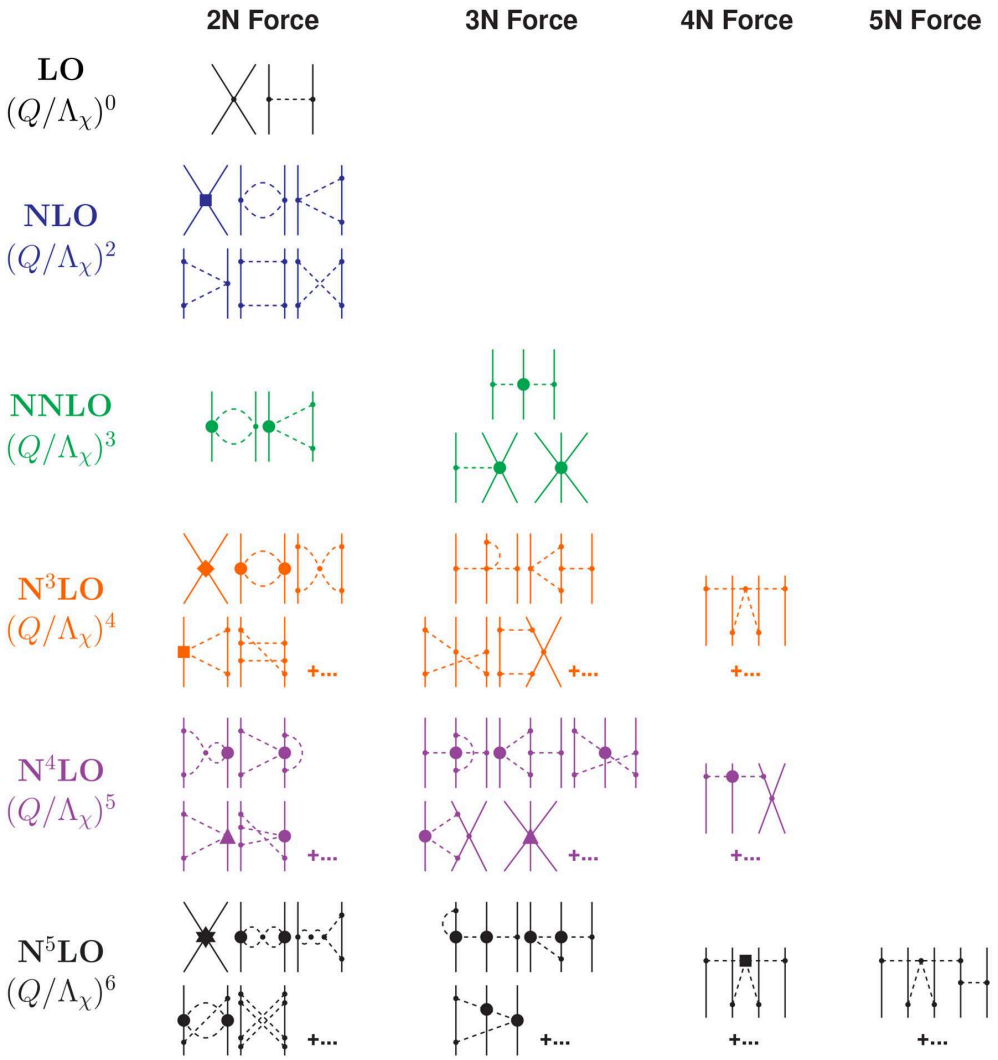


FIGURE 1 | Hierarchy of nuclear forces up to N^{5}LO or sixth order of the chiral expansion. Only some representative diagrams are included. Small dots, large solid dots, solid squares, triangles, diamonds, and stars denote vertexes of index $\Delta_i = 0, 1, 2, 3, 4$, and 6, respectively. Reprinted figure with permission from Entem et al. [37], copyright (2017) by the American Physical Society.

2.4. Pion-Exchange Contributions

We now specify the contributions coming from pion exchanges which provide the long-range interactions. Contributions at LO, NLO, and NNLO are diagrammatically given by the graphs in **Figure 2**.

2.4.1. Leading Order

The leading order (LO) is just the charge-independent one-pion-exchange (OPE). The expression is given by

$$V_{1\pi}^{(0)} = -\frac{g_A^2}{4f_\pi^2}\vec{\tau}_1\cdot\vec{\tau}_2\frac{\vec{\sigma}_1\cdot\vec{q}\;\vec{\sigma}_2\cdot\vec{q}}{q^2+m_\pi^2}\,, \tag{19}$$

where g_A, f_π, and m_π denoted the axial-vector coupling constant, pion-decay constant, and the pion mass, respectively. There are corrections at higher orders that renormalize the coupling constant. They are taken into account by using $g_A/f_\pi = g_{\pi N}/M_N$, with $g_{\pi N}$ the πNN coupling constant. Numerical values are given in **Table 1**. Note that, on-shell, there are no relativistic corrections.

Charge dependence is taken into account using

$$V_{1\pi}^{(np)}(\vec{p}',\vec{p}) = -V_{1\pi}(m_{\pi^0}) + (-1)^{I+1}2V_{1\pi}(m_{\pi^\pm})\,, \tag{20}$$

$$V_{1\pi}^{(pp/nn)}(\vec{p}',\vec{p}) = V_{1\pi}(m_{\pi^0})\,, \tag{21}$$

with I the isospin of the two-nucleon system and

$$V_{1\pi}(m_\pi) = -\frac{g_A^2}{4f_\pi^2}\frac{\vec{\sigma}_1\cdot\vec{q}\;\vec{\sigma}_2\cdot\vec{q}}{q^2+m_\pi^2}\,; \tag{22}$$

m_{π^0} denotes the mass of the neutral pion and $m_{\pi^\pm}$ the one of the charged pion. The charge dependence is an NLO effect [14], but

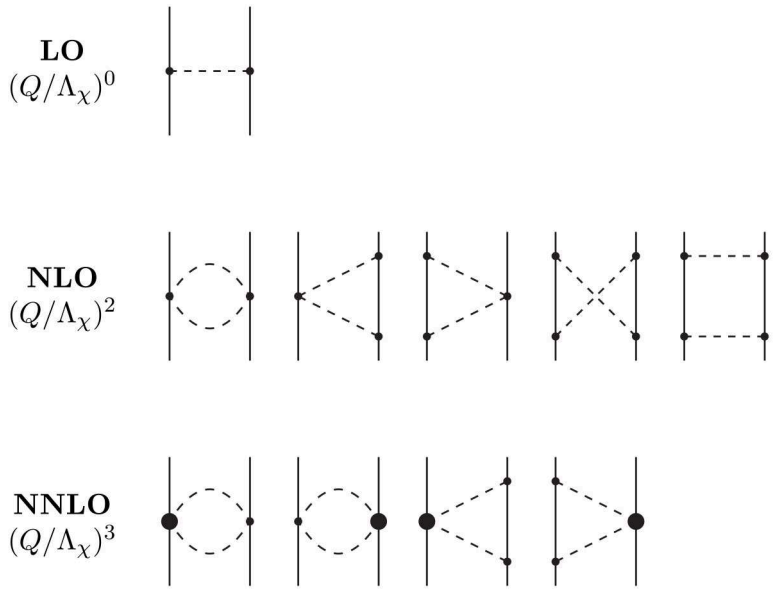


FIGURE 2 | LO, NLO, and NNLO contributions to the *NN* interaction. Solid lines represent nucleons and dashed lines pions. Small dots and large solid dots represent vertices with index $\Delta_i = 0$ and 1, respectively. Reprinted figure with permission from Entem et al. [46], copyright (2015) by the American Physical Society.

we include it already at leading order to make comparison with phase-shifts more meaningful.

2.4.2. Next-to-Leading Order

The NLO contributions appear at order $\nu = 2$. Symmetry requirements make the contributions at $\nu = 1$ vanish. In the past, the expressions for these diagrams as obtained in dimensional regularization were used [14]. Here, we apply the so-called spectral-function regularization (SFR) [42]. The potentials are obtained using dispersion relations from the imaginary part of the amplitude in the left-hand cut. However a cut-off $\tilde{\Lambda}$ is used in the dispersion relation to constrain the potentials to the low-energy region where χEFT is applicable.

The contribution is given by

$$W_C = \frac{L(\tilde{\Lambda};q)}{384\pi^2 f_\pi^4}\left[4m_\pi^2(1+4g_A^2-5g_A^4)+q^2(1+10g_A^2-23g_A^4) - \frac{48g_A^4 m_\pi^4}{w^2}\right], \quad (23)$$

$$V_T = -\frac{1}{q^2}V_S = -\frac{3g_A^4}{64\pi^2 f_\pi^4}L(\tilde{\Lambda};q), \quad (24)$$

with

$$w = \sqrt{4m_\pi^2+q^2}, \quad (25)$$

$$L(\tilde{\Lambda};q) = \frac{w}{2q}\ln\frac{\tilde{\Lambda}^2(2m_\pi^2+q^2)-2m_\pi^2 q^2+\tilde{\Lambda}\sqrt{\tilde{\Lambda}^2-4m_\pi^2}\,q\,w}{2m_\pi^2(\tilde{\Lambda}^2+q^2)}, \quad (26)$$

which agrees with the dimensional regularization expressions [14] when replacing $L(\tilde{\Lambda};q)$ by $L(q)$. In fact,

$$\lim_{\tilde{\Lambda}\to\infty} L(\tilde{\Lambda};q) = L(q). \quad (27)$$

2.4.3. Next-to-Next-to-Leading Order

Here the diagrams that contribute include a vertex with $\Delta_i = 1$ which is represented by a large solid dot in **Figure 2**. The NNLO contribution is

$$V_C = \frac{3g_A^2}{16\pi f_\pi^4}\left[2m_\pi^2(c_3-2c_1)+c_3q^2\right](2m_\pi^2+q^2)A(\tilde{\Lambda};q), \quad (28)$$

$$W_T = -\frac{1}{q^2}W_S = -\frac{g_A^2}{32\pi f_\pi^4}c_4 w^2 A(\tilde{\Lambda};q), \quad (29)$$

with

$$A(\tilde{\Lambda};q) = \frac{1}{2q}\arctan\frac{q(\tilde{\Lambda}-2m_\pi)}{q^2+2\tilde{\Lambda}m_\pi}. \quad (30)$$

As in the case of the NLO contribution, dimensional regularization is recovered when using

$$\lim_{\tilde{\Lambda}\to\infty} A(\tilde{\Lambda};q) = \frac{1}{2q}\arctan\frac{q}{2m_\pi}. \quad (31)$$

Notice that, here, we demote the relativistic corrections of the NLO diagrams to N^{3}LO, while in Machleidt and Entem [14] they were counted NNLO.

2.4.4. N^{3}LO Contributions

At this order the first 3π exchange contributions appear. However it was shown in Kaiser [43, 44] that they give negligible

TABLE 1 | Basic constants used throughout this review article.

Quantity	Value
Axial-vector coupling constant g_A	1.29
Pion-decay constant f_π	92.4 MeV
Charged-pion mass $m_{\pi^\pm}$	139.5702 MeV
Neutral-pion mass m_{π^0}	134.9766 MeV
Average pion-mass m_π	138.0390 MeV
Proton mass M_p	938.2720 MeV
Neutron mass M_n	939.5654 MeV
Average nucleon-mass M_N	938.9183 MeV

contributions for peripheral waves and, therefore, we leave them out.

There are three types of contributions given by the three classes represented in **Figure 3**. The first one is the football diagram (a). The contribution is [45],

$$V_C = \frac{3}{16\pi^2 f_\pi^4}\left[\left(\frac{c_2}{6}w^2 + c_3(2m_\pi^2+q^2) - 4c_1 m_\pi^2\right)^2 + \frac{c_2^2}{45}w^4\right] L(\tilde{\Lambda};q)\,, \tag{32}$$

$$W_T = -\frac{1}{q^2}W_S = \frac{c_4^2}{96\pi^2 f_\pi^4} w^2 L(\tilde{\Lambda};q)\,. \tag{33}$$

The second class (b) corresponds to the 2π-exchange two-loop diagrams.

Here as well as for the N^{4}LO expressions (see below), we state contributions in terms of their spectral functions, from which the momentum-space amplitudes $V_\alpha(q)$ and $W_\alpha(q)$ are obtained via the subtracted dispersion integrals:

$$V_{C,S}(q) = -\frac{2q^6}{\pi}\int_{nm_\pi}^{\tilde{\Lambda}} d\mu\, \frac{\mathrm{Im}\, V_{C,S}(i\mu)}{\mu^5(\mu^2+q^2)}\,,$$
$$V_T(q) = \frac{2q^4}{\pi}\int_{nm_\pi}^{\tilde{\Lambda}} d\mu\, \frac{\mathrm{Im}\, V_T(i\mu)}{\mu^3(\mu^2+q^2)}\,, \tag{34}$$

and similarly for $W_{C,S,T}$. The thresholds are given by $n = 2$ for two-pion exchange and $n = 3$ for three-pion exchange. For $\tilde{\Lambda} \to \infty$ the above dispersion integrals yield the finite parts of loop-functions as in dimensional regularization, while for finite $\tilde{\Lambda} >> nm_\pi$ we employ the method known as spectral-function regularization (SFR). The purpose of the finite scale $\tilde{\Lambda}$ is to constrain the imaginary parts to the low-momentum region where chiral effective field theory is applicable.

The spectral functions for class (b) are given by [45, 46]

$$\mathrm{Im}\, V_C = \frac{3g_A^4(2m_\pi^2-\mu^2)}{\pi\mu(4f_\pi)^6}\left[(m_\pi^2-2\mu^2)\left(2m_\pi + \frac{2m_\pi^2-\mu^2}{2\mu}\ln\frac{\mu+2m_\pi}{\mu-2m_\pi}\right) + 4g_A^2 m_\pi(2m_\pi^2-\mu^2)\right], \tag{35}$$

$$\mathrm{Im}\, V_S = \mu^2\,\mathrm{Im}\, V_T = \frac{g_A^2\mu\kappa^3}{8\pi f_\pi^4}\left(\bar{d}_{15}-\bar{d}_{14}\right) + \frac{2g_A^6\mu\kappa^3}{(8\pi f_\pi^2)^3}\int_0^1 dx(1-x^2)\left[\frac{1}{6} - \frac{m_\pi^2}{\kappa^2x^2} + \left(1+\frac{m_\pi^2}{\kappa^2x^2}\right)^{3/2}\ln\frac{\kappa x+\sqrt{m_\pi^2+\kappa^2x^2}}{m_\pi}\right], \tag{36}$$

$$\mathrm{Im}\, W_C = \frac{2\kappa}{3\mu(8\pi f_\pi^2)^3}\int_0^1 dx\left[g_A^2(\mu^2-2m_\pi^2)+2(1-g_A^2)\kappa^2x^2\right] \times\left\{96\pi^2 f_\pi^2\left[(2m_\pi^2-\mu^2)(\bar{d}_1+\bar{d}_2) - 2\kappa^2x^2\bar{d}_3 + 4m_\pi^2\bar{d}_5\right] + \left[4m_\pi^2(1+2g_A^2)-\mu^2(1+5g_A^2)\right]\frac{\kappa}{\mu}\ln\frac{\mu+2\kappa}{2m_\pi} + \frac{\mu^2}{12}(5+13g_A^2) - 2m_\pi^2(1+2g_A^2) + g_A^4\left(\mu^2-2\kappa^2x^2-2m_\pi^2\right)\left[\frac{5}{6}+\frac{m_\pi^2}{\kappa^2x^2} - \left(1+\frac{m_\pi^2}{\kappa^2x^2}\right)^{3/2}\ln\frac{\kappa x+\sqrt{m_\pi^2+\kappa^2x^2}}{m_\pi}\right] - 3\kappa^2x^2 + 6\kappa x\sqrt{m_\pi^2+\kappa^2x^2}\ln\frac{\kappa x+\sqrt{m_\pi^2+\kappa^2x^2}}{m_\pi}\right\}, \tag{37}$$

$$\mathrm{Im}\, W_S = \mu^2\,\mathrm{Im}\, W_T(i\mu) = \frac{g_A^4(4m_\pi^2-\mu^2)}{\pi(4f_\pi)^6}\left[\left(m_\pi^2-\frac{\mu^2}{4}\right)\ln\frac{\mu+2m_\pi}{\mu-2m_\pi} + (1+2g_A^2)\mu m_\pi\right], \tag{38}$$

where $\kappa = \sqrt{\mu^2/4 - m_\pi^2}$. Here and below all imaginary parts are evaluated at $i\mu$, because that is where they are needed for the calculation of the SFR integrals.

Finally the relativistic corrections of the NLO diagrams corresponding to class (c) are given by [14]

$$V_C = \frac{3g_A^4}{128\pi f_\pi^4 M_N}\left[\frac{m_\pi^5}{2w^2} + (2m_\pi^2+q^2)(q^2-m_\pi^2)A(\tilde{\Lambda};q)\right], \tag{39}$$

$$W_C = \frac{g_A^2}{64\pi f_\pi^4 M_N}\left\{\frac{3g_A^2 m_\pi^5}{2\omega^2} + \left[g_A^2(3m_\pi^2+2q^2) - 2m_\pi^2 - q^2\right](2m_\pi^2-q^2)A(\tilde{\Lambda};q)\right\}, \tag{40}$$

$$V_T = -\frac{1}{q^2}V_S = \frac{3g_A^4}{256\pi f_\pi^4 M_N}(5m_\pi^2+2q^2)A(\tilde{\Lambda};q)\,, \tag{41}$$

$$W_T = -\frac{1}{q^2}W_S = \frac{g_A^2}{128\pi f_\pi^4 M_N}\left[g_A^2(3m_\pi^2+q^2) - w^2\right]A(\tilde{\Lambda};q), \tag{42}$$

$$V_{LS} = \frac{3g_A^4}{32\pi f_\pi^4 M_N}(2m_\pi^2+q^2)A(\tilde{\Lambda};q)\,, \tag{43}$$

$$W_{LS} = \frac{g_A^2(1-g_A^2)}{32\pi f_\pi^4 M_N}w^2 A(\tilde{\Lambda};q)\,. \tag{44}$$

2.4.5. N^{4}LO Contributions

The 2π-exchange contributions at N^{4}LO have three different classes of diagrams shown in **Figure 4**. The contributions of

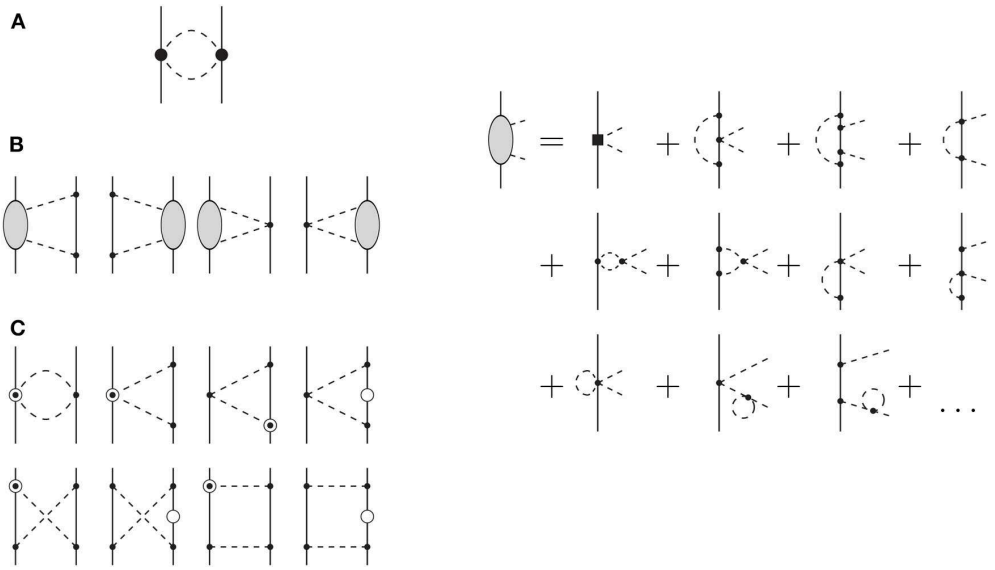


FIGURE 3 | N^{3}LO 2π-exchange contributions to the *NN* interaction. The same notation as in **Figure 2** is use. Solid squares represent vertices with index $\Delta_i = 2$. Open circles and open circles with a dot inside are relativistic $1/M_N$ corrections to propagators and the vertex with one derivative, respectively. The leading one-loop πN amplitude is represented by a shaded oval. Adapted figure with permission from Entem et al. [46], copyright (2015) by the American Physical Society. **(A)** Football diagram, **(B)** two-loop diagrams, and **(C)** relativistic corrections to one loop diagrams.

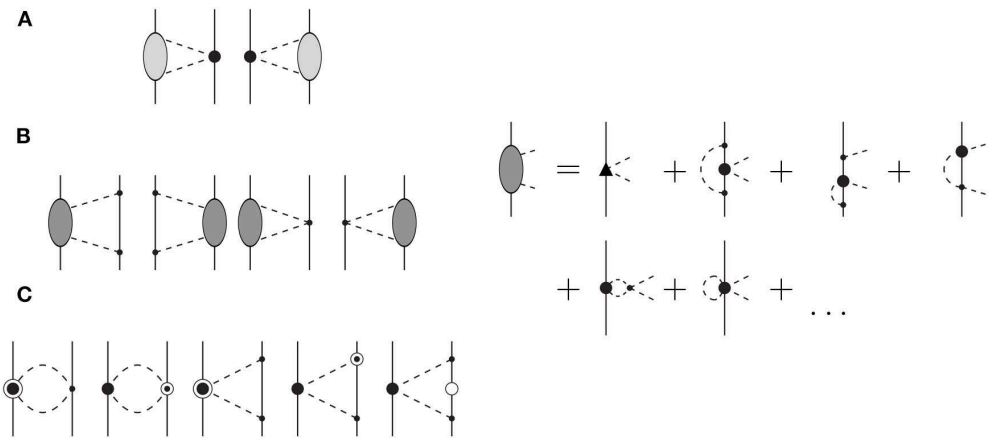


FIGURE 4 | N^{4}LO 2π-exchange contributions to the *NN* interaction. The same notation as in **Figure 3** is used. Open circles with a large solid dot inside refers to the $1/M_N$ corrections to vertexes with two derivatives. Solid triangles represent vertices with index $\Delta_i = 3$. The subleading one-loop πN amplitude is represented by a dark-shaded oval. Adapted figure with permission from Entem et al. [46], copyright (2015) by the American Physical Society. **(A,B)** Two-loop diagrams, and **(C)** relativistic corrections to one loop diagrams.

class (a) and (b) are given in terms of spectral functions and Equation (34).

The spectral functions for class (a) are obtained by integrating the product of the leading one-loop πN amplitude and the subleading chiral $\pi\pi NN$ vertex proportional to c_i over the Lorentz-invariant 2π-phase space. The result for the non-vanishing amplitudes is given by [46]

$$\begin{aligned}
\mathrm{Im}V_C \;=\; & -\frac{m_\pi^5}{(4f_\pi)^6\pi^2}\left\{g_A^2\sqrt{u^2-4}\left(5-2u^2-\frac{2}{u^2}\right)\right.\\
& \left.\Big[24c_1+c_2(u^2-4)+6c_3(u^2-2)\Big]\ln\frac{u+2}{u-2}\right.\\
& +\frac{8}{u}\Big[3\big(4c_1+c_3(u^2-2)\big)(4g_A^4u^2-10g_A^4+1)\\
& +c_2(6g_A^4u^2-10g_A^4-3)\Big]B(u)\\
& +\sqrt{u^2-4}\left[3(2-u^2)\big(4c_1+c_3(u^2-2)\big)\right.\\
& +c_2(7u^2-6-u^4)+\frac{4g_A^2}{u}(2u^2-1)\\
& \left.\times\Big[4(6c_1-c_2-3c_3)+(c_2+6c_3)u^2\Big]\right.\\
& +4g_A^4\left(\frac{32}{u+2}(2c_1+c_3)+\frac{64}{3u}(6c_1+c_2-3c_3)\right.
\end{aligned}$$

$$+14c_3 - 5c_2 - 92c_1 + \frac{8u}{3}(18c_3 - 5c_2) + \frac{u^2}{6}(36c_1 + 13c_2 - 156c_3) + \frac{u^4}{6}(2c_2 + 9c_3)\Big)\Big]\Big\}, \quad (45)$$

$$\mathrm{Im}W_S = \mu^2\,\mathrm{Im}W_T = \frac{c_4\,g_A^2 m_\pi^5}{(4f_\pi)^6\pi^2}\Big\{8g_A^2 u(5-u^2)B(u) + \frac{1}{3}(u^2-4)^{5/2}\ln\frac{u+2}{u-2} + \frac{u}{3}\sqrt{u^2-4}\Big[g_A^2(30u-u^3-64) - 4u^2 + 16\Big]\Big\}, \quad (46)$$

with the dimensionless variable $u = \mu/m_\pi > 2$ and the logarithmic function

$$B(u) = \ln\frac{u+\sqrt{u^2-4}}{2}. \quad (47)$$

Class (b) is obtained in the same way but multiplying the one-loop πN amplitude proportional to c_i (see [41] for details) and the leading-order chiral πN amplitude. The result is [46]

$$\mathrm{Im}V_S = \mu^2\,\mathrm{Im}V_T = \frac{g_A^4 m_\pi^5 (c_3 - c_4)u}{(4f_\pi)^6\pi^2}\Big\{\sqrt{u^2-4}\,(u^3 - 30u + 64) + 24(u^2-5)B(u)\Big\}, \quad (48)$$

$$\mathrm{Im}W_S = \mu^2\,\mathrm{Im}W_T = \frac{g_A^2 m_\pi^5}{(4f_\pi)^6\pi^2}(4-u^2)\Big\{\frac{c_4}{3}\Big[\sqrt{u^2-4}\,(2u^2-8)B(u) + 4u(2+9g_A^2) - \frac{5u^3}{3}\Big] + 2\bar{e}_{17}(8\pi f_\pi)^2(u^3-2u)\Big\} \quad (49)$$

$$\mathrm{Im}V_C = \frac{g_A^2 m_\pi^5}{(4f_\pi)^6\pi^2}(u^2-2)\Big(\frac{1}{u^2}-2\Big)\Big\{2\sqrt{u^2-4}\Big[24c_1 + c_2(u^2-4) + 6c_3(u^2-2)\Big]B(u) + u\Big[c_2\Big(8 - \frac{5u^2}{3}\Big) + 6c_3(2-u^2) - 24c_1\Big]\Big\} + \frac{3g_A^2 m_\pi^5}{(2f_\pi)^4 u}(2-u^2)^3\,\bar{e}_{14}, \quad (50)$$

$$\mathrm{Im}W_C = -\frac{c_1 m_\pi^5}{(2f_\pi)^6\pi^2}\Big\{\frac{3g_A^2+1}{8}\sqrt{u^2-4}\,(2-u^2) + \Big(\frac{3g_A^2+1}{u} - 2g_A^2\,u\Big)B(u)\Big\} - \frac{c_2 m_\pi^5}{(2f_\pi)^6\pi^2}\Big\{\frac{1}{96}\sqrt{u^2-4}\Big[7u^2 - 6 - u^4 + g_A^2(5u^2-6-2u^4)\Big] + \frac{1}{4u}(g_A^2u^2 - 1 - g_A^2)B(u)\Big\} - \frac{c_3 m_\pi^5}{(4f_\pi)^6\pi^2}\Big\{\frac{2}{9}\sqrt{u^2-4}\Big[3(7u^2-6-u^4) + 4g_A^2\Big(\frac{32}{u} - 12 - 20u + 7u^2 - u^4\Big) + g_A^4\Big(114 - \frac{512}{u} + 368u - 169u^2 + 7u^4 + \frac{192}{u+2}\Big)\Big] + \frac{16}{3u}\Big[g_A^4(6u^4 - 30u^2 + 35) + g_A^2(6u^2-8) - 3\Big]B(u)\Big\} - \frac{c_4 g_A^2 m_\pi^5}{(4f_\pi)^6\pi^2}\Big\{\frac{2}{9}\sqrt{u^2-4}\Big[30 - \frac{128}{u} + 80u - 13u^2 - 2u^4 + g_A^2\Big(\frac{512}{u} - 114 - 368u + 169u^2 - 7u^4 - \frac{192}{u+2}\Big)\Big] + \frac{16}{3u}\Big[5 - 3u^2 + g_A^2(30u^2 - 35 - 6u^4)\Big]B(u)\Big\}. \quad (51)$$

where the only two independent LEC's $\bar{e}_{14}$ and $\bar{e}_{17}$ have been used to give the final result.

Finally class (c) consists of the relativistic corrections of the NNLO 2π-exchange. The contributions are proportional to c_i/M_N. They read [45]

$$W_C = -\frac{c_4}{192\pi^2 M_N f_\pi^4}\left[g_A^2(8m_\pi^2 + 5q^2) + w^2\right]q^2\,L(\tilde{\Lambda};q), \quad (52)$$

$$V_C = \frac{g_A^2\,L(\tilde{\Lambda};q)}{32\pi^2 M_N f_\pi^4}\left[(6c_3 - c_2)q^4 + 4(3c_3 - c_2 - 6c_1)q^2 m_\pi^2 + 6(2c_3 - c_2)m_\pi^4 - 24(2c_1 + c_3)m_\pi^6 w^{-2}\right], \quad (53)$$

$$W_T = -\frac{1}{q^2}W_S = \frac{c_4}{192\pi^2 M_N f_\pi^4}\left[w^2 - g_A^2(16m_\pi^2 + 7q^2)\right]L(\tilde{\Lambda};q), \quad (54)$$

$$V_{LS} = \frac{c_2\,g_A^2}{8\pi^2 M_N f_\pi^4}\,w^2 L(\tilde{\Lambda};q), \quad (55)$$

$$W_{LS} = -\frac{c_4}{48\pi^2 M_N f_\pi^4}\left[g_A^2(8m_\pi^2 + 5q^2) + w^2\right]L(\tilde{\Lambda};q), \quad (56)$$

The 3π-exchange contributions at order N^{4}LO are shown in **Figure 5**. The spectral functions have been calculated first in Kaiser [47] where the classification scheme applied in **Figure 5** was introduced. Class XI vanishes while class X and part of class XIV give negligible contributions. Thus, we include in our calculations only class XII and XIII, and the V_S contribution of class XIV. In Kaiser [47], the spectral functions were presented in terms of integrals over the invariant mass of a pion pair. These integrals have been solved analytically in Entem et al. [46], and the spectral functions are given by

$$\mathrm{Im}\,V_S^{(\mathrm{XII})} = -\frac{g_A^2 c_4 m_\pi^5}{(4f_\pi)^6\pi^2 u^3}\Big[\frac{y}{12}(u-1)(100u^3 - 27 - 50u - 151u^2 + 185u^4 - 14u^5 - 7u^6) + 4\,D(u)\,(2 + 10u^2 - 9u^4)\Big], \quad (57)$$

$$\mathrm{Im}\,V_T^{(\mathrm{XII})} = \frac{1}{\mu^2}\,\mathrm{Im}\,V_S^{(\mathrm{XII})} - \frac{g_A^2 c_4 m_\pi^3}{(4f_\pi)^6\pi^2 u^5}\Big[\frac{y}{6}(u-1)$$

$$
\begin{aligned}
&(u^6+2u^5-39u^4-12u^3+65u^2-50u-27)\\
&+8\,D(u)\,(3u^4-10u^2+2)\Big]\,, \qquad (58)\\
\mathrm{Im}\,W_S^{(\mathrm{XII})} &= -\frac{g_A^2 m_\pi^5}{(4f_\pi)^6\pi^2 u^3}\Big\{y\,(u-1)\Big[\frac{4c_1 u}{3}\Big(u^3+2u^2-u+4\Big)\\
&+\frac{c_2}{72}\Big(u^6+2u^5-39u^4-12u^3+65u^2-50u-27\Big)\\
&+\frac{c_3}{12}\Big(u^6+2u^5-31u^4+4u^3+57u^2-18u-27\Big)\\
&+\frac{c_4}{72}\Big(7u^6+14u^5-185u^4-100u^3+151u^2+50u+27\Big)\Big]\\
&+D(u)\Big[16c_1(4u^2-1-u^4)+\frac{2c_2}{3}\Big(2-10u^2+3u^4\Big)\\
&+4c_3u^2(u^2-2)+\frac{2c_4}{3}\Big(9u^4-10u^2-2\Big)\Big]\Big\}\,, \qquad (59)\\
\mathrm{Im}\,W_T^{(\mathrm{XII})} &= \frac{1}{\mu^2}\,\mathrm{Im}\,W_S^{(\mathrm{XII})}-\frac{g_A^2 m_\pi^3}{(4f_\pi)^6\pi^2 u^5}\Big\{y\,(u-1)\Big[\frac{16c_1 u}{3}\\
&\Big(2+u-2u^2-u^3\Big)+\frac{c_2}{36}\Big(73u^4-6u^5-3u^6+44u^3\\
&-43u^2-50u-27\Big)+\frac{c_3}{2}\Big(19u^4-2u^5-u^6\\
&+4u^3-9u^2-6u-9\Big)+\frac{c_4}{36}\Big(39u^4-2u^5-u^6\\
&+12u^3-65u^2+50u+27\Big)\Big]+4\,D(u)\Big[8c_1(u^4-1)\\
&+c_2\Big(\frac{2}{3}-u^4\Big)-2c_3u^4+\frac{c_4}{3}\Big(10u^2-2-3u^4\Big)\Big]\Big\}\,, \qquad (60)\\
\mathrm{Im}\,W_C^{(\mathrm{XIII})} &= -\frac{g_A^4 c_4 m_\pi^5}{(4f_\pi)^6\pi^2}\Big[\frac{8y}{3}(u-1)(u-4-2u^2-u^3)\\
&+32\,D(u)\Big(u^3-4u+\frac{1}{u}\Big)\Big]\,, \qquad (61)\\
\mathrm{Im}\,V_S^{(\mathrm{XIII})} &= -\frac{g_A^4 c_4 m_\pi^5}{(4f_\pi)^6\pi^2 u^3}\Big[\frac{y}{24}(u-1)(37u^6+74u^5\\
&-251u^4-268u^3+349u^2-58u-135)\\
&+2\,D(u)\,(39u^4-2-52u^2-6u^6)\Big]\,, \qquad (62)\\
\mathrm{Im}\,V_T^{(\mathrm{XIII})} &= \frac{1}{\mu^2}\,\mathrm{Im}\,V_S^{(\mathrm{XIII})}-\frac{g_A^4 c_4 m_\pi^3}{(4f_\pi)^6\pi^2 u^5}\Big[\frac{y}{12}(u-1)(5u^6\\
&+10u^5-3u^4-252u^3\\
&-443u^2-58u-135)+4\,D(u)\,(3u^4+22u^2-2)\Big]\,, \qquad (63)\\
\mathrm{Im}\,W_S^{(\mathrm{XIII})} &= -\frac{g_A^4 m_\pi^5}{(4f_\pi)^6\pi^2 u^3}\Big\{y\,(u-1)\Big[2c_1u(5u^3+10u^2-5u-4)\\
&+\frac{c_2}{48}\Big(135+58u-277u^2-36u^3+147u^4-10u^5-5u^6\Big)\\
&+\frac{c_3}{8}\Big(7u^6+14u^5-145u^4-20u^3+111u^2+18u+27\Big)\\
&+\frac{c_4}{6}\Big(44u^3+37u^4-14u^5-7u^6-3u^2-18u-27\Big)\Big]\\
&+D(u)\Big[24c_1(1+4u^2-3u^4)+c_2(2+2u^2-3u^4)\\
&+6c_3u^2(3u^2-2)+8c_4u^2(u^4-5u^2+5)\Big]\Big\}\,, \qquad (64)\\
\mathrm{Im}\,W_T^{(\mathrm{XIII})} &= \frac{1}{\mu^2}\,\mathrm{Im}\,W_S^{(\mathrm{XIII})}-\frac{g_A^4 m_\pi^3}{(4f_\pi)^6\pi^2 u^5}\Big\{y\,(u-1)\\
&\Big[4c_1u(5u^3+10u^2+7u-4)+\frac{c_2}{24}\Big(135+58u\\
&+227u^2+204u^3+27u^4-10u^5-5u^6\Big)\\
&+\frac{c_3}{4}\Big(27+18u-9u^2-68u^3-121u^4+14u^5+7u^6\Big)\\
&+c_4(4u^3+19u^4-2u^5-u^6-9u^2-6u-9)\Big]\\
&+2\,D(u)\Big[24c_1(1-3u^4)+c_2(2-10u^2-3u^4)\\
&+6c_3u^2(3u^2+2)-8c_4u^4\Big]\Big\}\,, \qquad (65)\\
\mathrm{Im}\,V_S^{(\mathrm{XIV})} &= -\frac{g_A^4 c_4 m_\pi^5}{(4f_\pi)^6\pi^2 u^3}\Big[\frac{y}{24}(u-1)(637u^2-58u-135+116u^3\\
&-491u^4-22u^5-11u^6)\\
&+2\,D(u)\,(6u^6-9u^4+8u^2-2)\Big]\,, \qquad (66)
\end{aligned}
$$

where $y=\sqrt{(u-3)(u+1)}$ and $D(u)=\ln[(u-1+y)/2]$ with $u=\mu/m_\pi>3$.

2.4.6. Going Beyond N^{4}LO

The next order is N^{5}LO or sixth order. At this order, no complete calculation exists; however, the presumed dominant contributions have been evaluated in Entem et al. [48].

As before, we will state contributions in terms of their spectral functions, from which the momentum-space amplitudes $V_\alpha(q)$ and $W_\alpha(q)$ are obtained via subtracted dispersion integrals which, for N^{5}LO read:

$$
\begin{aligned}
V_{C,S}(q) &= \frac{2q^8}{\pi}\int_{nm_\pi}^{\tilde{\Lambda}} d\mu\,\frac{\mathrm{Im}\,V_{C,S}(i\mu)}{\mu^7(\mu^2+q^2)}\,,\\
V_T(q) &= -\frac{2q^6}{\pi}\int_{nm_\pi}^{\tilde{\Lambda}} d\mu\,\frac{\mathrm{Im}\,V_T(i\mu)}{\mu^5(\mu^2+q^2)}\,, \qquad (67)
\end{aligned}
$$

and similarly for $W_{C,S,T}$. The thresholds are given by $n=2$ for two-pion exchange and $n=3$ for three-pion exchange.

The 2π-exchange at N^{5}LO is given by the diagrams of **Figure 6**. There are three different classes. Class (a) is obtained from the subleading one loop πN amplitude folded with the subleading $\pi\pi NN$ vertex proportional to c_i. The results for the non-vanishing spectral functions are

$$
\begin{aligned}
\mathrm{Im}V_C=&\frac{m_\pi^6\sqrt{u^2-4}}{(8\pi f_\pi^2)^3}\Big(\frac{1}{u^2}-2\Big)\Big[(c_2+6c_3)u^2+4(6c_1-c_2-3c_3)\Big]\\
&\Big\{2c_1u+\frac{c_2u}{36}(5u^2-24)+\frac{c_3u}{2}(u^2-2)+\Big[c_3(2-u^2)\\
&+\frac{c_2}{6}(4-u^2)-4c_1\Big]\sqrt{u^2-4}\,B(u)\Big\}\\
&+\frac{m_\pi^6\sqrt{u^2-4}}{8\pi f_\pi^4 u}\Big\{\Big[4c_1+c_3(u^2-2)\Big]\\
&\Big[\bar{e}_{15}(u^4-6u^2+8)+6\bar{e}_{14}(u^2-2)^2+\frac{3\bar{e}_{16}}{10}(u^2-4)^2\Big]
\end{aligned}
$$

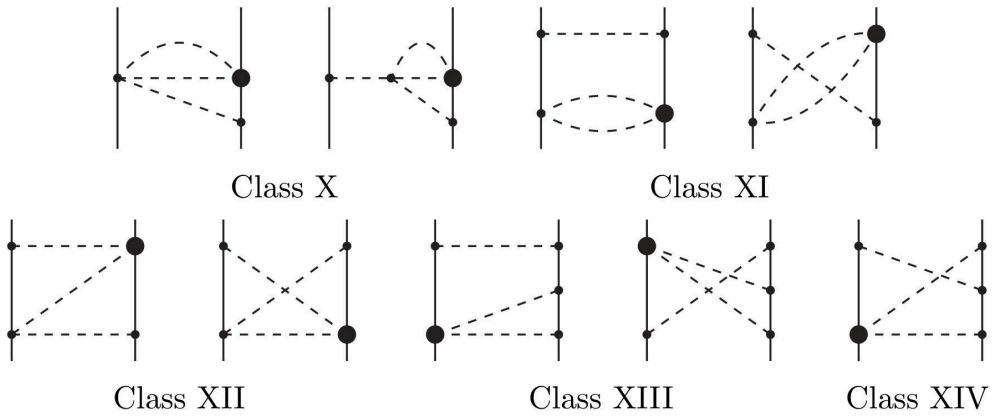


FIGURE 5 | N^{4}LO 3π-exchange contributions to the *NN* interaction. The classification scheme of Kaiser [47] is applied. The same notation as in **Figure 2** is use. Reprinted figure with permission from Entem et al. [46], copyright (2015) by the American Physical Society.

$$+c_2(u^2-4)\left[\frac{3\bar{e}_{15}}{10}(u^4-6u^2+8)+\bar{e}_{14}(u^2-2)^2 +\frac{3\bar{e}_{16}}{28}(u^2-4)^2\right]\Bigg\}, \quad (68)$$

$$\mathrm{Im}W_S=\frac{c_4^2m_\pi^6(u^2-4)}{9(8\pi f_\pi^2)^3}\Bigg\{u\sqrt{u^2-4}\left[\frac{5u^2}{6}-4+\frac{2g_A^2}{15}(2u^2-23)\right] -(u^2-4)^2B(u) +6g_A^2u\int_0^1dx\left(x-\frac{1}{x}\right)\left[4+(u^2-4)x^2\right]^{3/2} \ln\frac{x\sqrt{u^2-4}+\sqrt{4+(u^2-4)x^2}}{2}\Bigg\} +\frac{c_4m_\pi^6u(u^2-4)^{3/2}}{240\pi f_\pi^4}\left[10\bar{e}_{17}(2-u^2)+\bar{e}_{18}(4-u^2)\right] =\mu^2\,\mathrm{Im}W_T\,, \quad (69)$$

with the dimensionless variable $u=\mu/m_\pi>2$ and the logarithmic function $B(u)$ defined in Equation (47). We give the result in terms of the independent pion LEC's $\bar{e}_{14}$ and $\bar{e}_{18}$.

Class (b) is obtained from the leading one-loop πN amplitude folded by itself. The result is

$$\mathrm{Im}V_C=\frac{m_\pi^6\sqrt{u^2-4}}{(4f_\pi)^8\pi^3u}\Bigg\{-\frac{3}{70}(5u^2+8)(u^2-4)^2 +3g_A^2(1-2u^2)\left[1+\frac{2-u^2}{4u}\ln\frac{u+2}{u-2}\right] \times\left[u-\frac{u^3}{2}+\frac{4B(u)}{\sqrt{u^2-4}}\right]+g_A^4\left[\frac{32(3-2u^2)}{\sqrt{u^2-4}}B(u) +3(2u^2-1)^2\left(\frac{u^2-2}{u}\ln\frac{u+2}{u-2}+\frac{(u^2-2)^2}{8u^2} \left(\pi^2-\ln^2\frac{u+2}{u-2}\right)\right)-\frac{2258}{35}+24u +\frac{5336u^2}{105}-12u^3-\frac{2216u^4}{105}+\frac{18u^6}{35}\right] +g_A^6(2u^2-1)\left(1+\frac{2-u^2}{4u}\ln\frac{u+2}{u-2}\right) \left[46u-3u^3-96+\frac{64}{u+2}+\frac{24(5-2u^2)}{\sqrt{u^2-4}}B(u)\right] +\frac{64g_A^8}{9}\left[\frac{3119u^2}{70}-\frac{71u^6}{1120}-\frac{197u^4}{70}-\frac{85u^3}{8}+\frac{97u}{4} -\frac{582}{7}-\frac{16}{u+2}+\frac{8}{(u+2)^2}+\frac{6u^4-60u^2+105}{\sqrt{u^2-4}}B(u)\right]\Bigg\}, \quad (70)$$

$$\mathrm{Im}W_S=\frac{g_A^4m_\pi^6\sqrt{u^2-4}}{(4f_\pi)^8\pi^3u}\Bigg\{\frac{u^2-4}{48}\left[4u+(4-u^2)\ln\frac{u+2}{u-2}\right]^2 -\frac{\pi^2}{48}(u^2-4)^3+g_A^2u\left[(u^2-4)\ln\frac{u+2}{u-2}-4u\right] \left[\frac{5u}{4}-\frac{u^3}{24}-\frac{8}{3}+\frac{5-u^2}{\sqrt{u^2-4}}B(u)\right]+\frac{32g_A^4u^2}{27}\left[\frac{u^4}{40} +\frac{13u^2}{10}+\frac{11u}{2}-\frac{118}{5}-\frac{8}{u+2}+\frac{3(10-u^2)}{\sqrt{u^2-4}}B(u)\right]\Bigg\} =\mu^2\mathrm{Im}W_T\,, \quad (71)$$

$$\mathrm{Im}V_S=\frac{g_A^8m_\pi^6u\sqrt{u^2-4}}{3(4f_\pi)^8\pi^5}\int_0^1dx\,(x^2-1)\Bigg\{(u^2-4)x \left[\frac{48\pi^2f_\pi^2}{g_A^4}(\bar{d}_{14}-\bar{d}_{15})-\frac{1}{6}\right]+\frac{4}{x} -\frac{\left[4+(u^2-4)x^2\right]^{3/2}}{x^2\sqrt{u^2-4}}\ln\frac{x\sqrt{u^2-4}+\sqrt{4+(u^2-4)x^2}}{2}\Bigg\}^2 =\mu^2\mathrm{Im}V_T\,, \quad (72)$$

$$\mathrm{Im}W_C=-\frac{m_\pi^6(u^2-4)^{5/2}}{(4f_\pi)^8(3\pi u)^3}\left[2+4g_A^2-\frac{u^2}{2}(1+5g_A^2)\right]^2+ \frac{m_\pi^6(u^2-4)^{3/2}}{9(4f_\pi)^8\pi^5u}\int_0^1dx\,x^2\Bigg\{\frac{3x^2}{2}(4-u^2) +3x\sqrt{u^2-4}\sqrt{4+(u^2-4)x^2} \ln\frac{x\sqrt{u^2-4}+\sqrt{4+(u^2-4)x^2}}{2}+g_A^4\Big[(4-u^2)x^2 +2u^2-4\Big]\left[\frac{5}{6}+\frac{4}{(u^2-4)x^2}-\left(1+\frac{4}{(u^2-4)x^2}\right)^{3/2}\right.$$

$$\ln\frac{x\sqrt{u^2-4}+\sqrt{4+(u^2-4)x^2}}{2}\Big]$$
$$+\Big[4(1+2g_A^2)-u^2(1+5g_A^2)\Big]\sqrt{u^2-4}\,\frac{B(u)}{u}+\frac{u^2}{6}$$
$$(5+13g_A^2)-4(1+2g_A^2)+96\pi^2 f_\pi^2\Big[(4-2u^2)(\bar{d}_1+\bar{d}_2)$$
$$+(4-u^2)x^2\bar{d}_3+8\bar{d}_5\Big]\Big\}^2. \quad (73)$$

Class (c) is obtained from the leading two-loop πN amplitude with the tree-level πN amplitude. The two-loop πN amplitude has not been evaluated and we omit this class of diagrams.

The next contribution is the $1/M_N^2$ correction to the leading one-loop chiral 2π-exchange diagrams. They were given in Kaiser [49] and are shown in **Figure 7**. The explicit expressions are

$$V_C = \frac{g_A^4}{32\pi^2 M_N^2 f_\pi^4}\Big[L(\tilde{\Lambda};q)\Big(2m_\pi^4+q^4-8m_\pi^6 w^{-2}$$
$$-2m_\pi^8 w^{-4}\Big)-\frac{m_\pi^6}{2w^2}\Big], \quad (74)$$

$$W_C = \frac{1}{192\pi^2 M_N^2 f_\pi^4}\Big\{L(\tilde{\Lambda};q)\Big[g_A^2\Big(2k^2(8m_\pi^2+5q^2)$$
$$+12m_\pi^6 w^{-2}-3q^4-6m_\pi^2 q^2-6m_\pi^4\Big)$$
$$+g_A^4\Big(k^2(16m_\pi^4 w^{-2}-20m_\pi^2-7q^2)-16m_\pi^8 w^{-4}$$
$$-12m_\pi^6 w^{-2}+4m_\pi^4 q^2 w^{-2}+5q^4+6m_\pi^2 q^2+6m_\pi^4\Big)$$
$$+k^2 w^2\Big]-\frac{4g_A^4 m_\pi^6}{w^2}\Big\}, \quad (75)$$

$$V_T = -\frac{1}{q^2}V_S = \frac{g_A^4 L(\tilde{\Lambda};q)}{32\pi^2 M_N^2 f_\pi^4}\Big(k^2+\frac{5}{8}q^2+m_\pi^4 w^{-2}\Big), \quad (76)$$

$$W_T = -\frac{1}{q^2}W_S = \frac{L(\tilde{\Lambda};q)}{1536\pi^2 M_N^2 f_\pi^4}\Big[g_A^4\Big(28m_\pi^2+17q^2$$
$$+16m_\pi^4 w^{-2}\Big)-2g_A^2(16m_\pi^2+7q^2)+w^2\Big], \quad (77)$$

$$V_{LS} = \frac{g_A^4 L(\tilde{\Lambda};q)}{128\pi^2 M_N^2 f_\pi^4}\Big(11q^2+32m_\pi^4 w^{-2}\Big), \quad (78)$$

$$W_{LS} = \frac{L(\tilde{\Lambda};q)}{256\pi^2 M_N^2 f_\pi^4}\Big[2g_A^2(8m_\pi^2+3q^2)$$
$$+\frac{g_A^4}{3}\Big(16m_\pi^4 w^{-2}-11q^2-36m_\pi^2\Big)-w^2\Big], \quad (79)$$

$$V_{\sigma L} = \frac{g_A^4 L(\tilde{\Lambda};q)}{32\pi^2 M_N^2 f_\pi^4}, \quad (80)$$

The next contribution is given by 3π-exchange contributions. There are several classes of diagrams as shown in **Figure 8**. The class (a) diagrams are proportional to c_i^2. We use the same notation as in Kaiser [47] and Entem et al. [46].

Class XIa:

$$\mathrm{Im}W_C = \frac{g_A^2 c_4^2 m_\pi^6}{6(4\pi f_\pi^2)^3}\int_2^{u-1} dw\,(w^2-4)^{3/2}\sqrt{\lambda(w)}, \quad (81)$$

$$\mathrm{Im}V_S = \frac{g_A^2 c_4^2 m_\pi^6}{6(8\pi f_\pi^2)^3}\int_2^{u-1} dw\,\frac{(w^2-4)^{3/2}}{u^4\sqrt{\lambda(w)}}$$
$$\Big[w^8-4(1+u^2)w^6+2w^4(3+5u^2)$$
$$+4w^2(2u^6-5u^4-2u^2-1)-(u^2-1)^3$$
$$(5u^2+1)\Big], \quad (82)$$

$$\mathrm{Im}(\mu^2 V_T - V_S) = \frac{g_A^2 c_4^2 m_\pi^6}{6(8\pi f_\pi^2)^3}\int_2^{u-1} dw\,(w^2-4)^{3/2}\sqrt{\lambda(w)}$$
$$\Big[\frac{(w^2-1)^2}{u^4}+1-\frac{2}{u^2}(7w^2+1)\Big], \quad (83)$$

with the kinematical function $\lambda(w)=w^4+u^4+1-2(w^2u^2+w^2+u^2)$. The dimensionless integration variable w is the invariant mass of a pion-pair divided by m_π.

Class XIIa:

$$\mathrm{Im}V_C = \frac{g_A^2 c_4^2 m_\pi^6}{8960\pi f_\pi^6}(u-3)^3\Big[u^3+9u^2+12u-3-\frac{3}{u}\Big], \quad (84)$$

$$\mathrm{Im}W_C = \frac{2g_A^2 c_4^2 m_\pi^6 u^2}{(4\pi f_\pi^2)^3}\iint_{z^2<1} d\omega_1 d\omega_2\, k_1 k_2\sqrt{1-z^2}\,\arcsin(z), \quad (85)$$

$$\mathrm{Im}V_S = \frac{g_A^2 c_4^2 m_\pi^6}{(4\pi f_\pi^2)^3}\iint_{z^2<1} d\omega_1 d\omega_2\,\Big\{2\omega_1^2(\omega_2^2-9\omega_2 u+9u^2+1)$$
$$+3\omega_1\big[\omega_2(1+8u^2)-6u-6u^3\big]$$
$$+\frac{1}{4}(9u^4+18u^2+5)+\frac{2zk_2}{k_1}\Big[\omega_1^3(4u-\omega_2)$$
$$+\omega_1^2(7\omega_2 u-2-2u^2)-2\omega_1(2u+\omega_2)$$
$$+2+2u^2-4\omega_2 u\Big]+\frac{3\arcsin(z)}{k_1 k_2\sqrt{1-z^2}}$$
$$\Big[2\omega_1^3 u(u^2+1-2\omega_2 u)+\omega_1^2\Big(\omega_2 u(7+11u^2)$$
$$-5\omega_2^2 u^2-1-4u^2-3u^4\Big)+\frac{\omega_1}{4}$$
$$\Big(6u^5+12u^3-2u-\omega_2(5+16u^2+15u^4)\Big)$$
$$+\frac{(1-u^4)(u^2+3)}{8}\Big]\Big\}, \quad (86)$$

$$\mathrm{Im}(\mu^2 V_T - V_S) = \frac{g_A^2 c_4^2 m_\pi^6}{(4\pi f_\pi^2)^3}\iint_{z^2<1} d\omega_1 d\omega_2$$
$$\Big\{4\omega_1^2(\omega_2^2+6u^2+2-10\omega_2 u)+6u^2(1+u^2)$$
$$+2\omega_1\big[3\omega_2(1+7u^2)-18u^3-10u\big]$$
$$+\frac{2zk_2}{k_1}\Big[\omega_1^3(7u-2\omega_2)+u^2-\omega_2 u$$
$$+\omega_1^2(13\omega_2 u-3-10u^2)+\omega_1(2+3u^2)(u-2\omega_2)\Big]$$

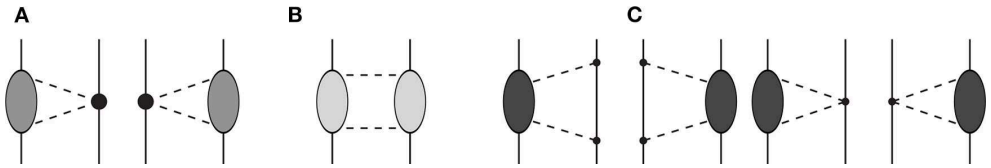


FIGURE 6 | N^{5}LO 2π-exchange contributions to the *NN* interaction. There are three classes of diagrams. Class **(A)** is obtained from the subleading one loop πN amplitude folded with the subleading $\pi\pi NN$ vertex proportional to c_i. Class **(B)** is obtained from the leading one-loop πN amplitude folded by itself. Class **(C)** is obtained from the leading two-loop πN amplitude (represented by a black oval) with the tree-level πN amplitude. Other notation as in **Figure 6**. Adapted figure with permission from Entem et al. [48], copyright (2015) by the American Physical Society.

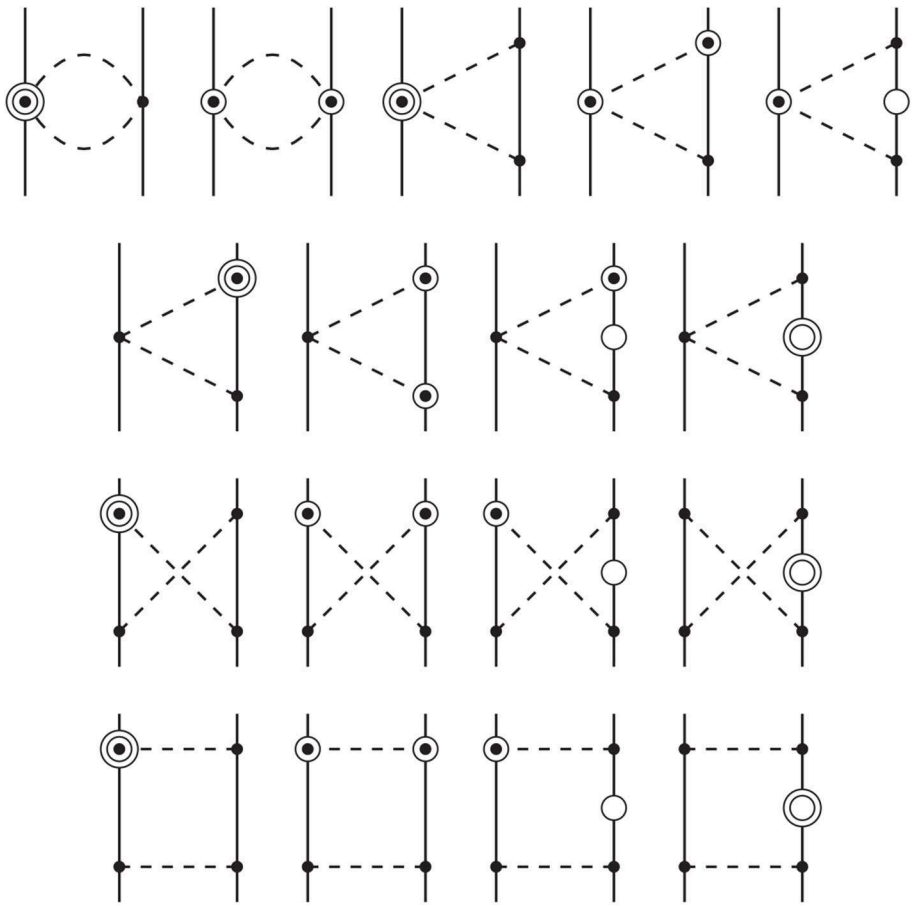


FIGURE 7 | N^{5}LO 2π exchange contributions to the *NN* interaction coming from $1/M_N^2$ corrections to the NLO chiral 2π-exchange diagrams. Notation as in **Figure 3**. Two open circles refers to $1/M_N^2$ corrections to propagators and vertices as in the case of one open circle. Reprinted figure with permission from Entem et al. [48], copyright (2015) by the American Physical Society.

$$+\frac{3\arcsin(z)}{k_1k_2\sqrt{1-z^2}}\times(u^2-2\omega_1u+1)(u^2-2\omega_2u+1)$$
$$\left[\frac{\omega_1}{2}(6u-5\omega_2)-\frac{u^2}{2}-2\omega_1^2\right]\Bigg\}, \qquad (87)$$

with the magnitudes of pion-momenta divided by m_π, and their scalar-product given by:

$$k_1=\sqrt{\omega_1^2-1}\,, \qquad k_2=\sqrt{\omega_2^2-1}\,,$$

$$z\,k_1k_2=\omega_1\omega_2-u(\omega_1+\omega_2)+\frac{u^2+1}{2}\,. \qquad (88)$$

The upper/lower limits of the ω_2-integration are $\omega_2^\pm=\frac{1}{2}(u-\omega_1\pm k_1\sqrt{u^2-2\omega_1u-3}/\sqrt{u^2-2\omega_1u+1}\,)$ with ω_1 in the range $1<\omega_1<(u^2-3)/2u$.

The contributions to $\mathrm{Im}W_S$ and $\mathrm{Im}(\mu^2W_T-W_S)$ are split into three pieces according to their dependence on the isoscalar/isovector low-energy constants $c_{1,3}$ and c_4:

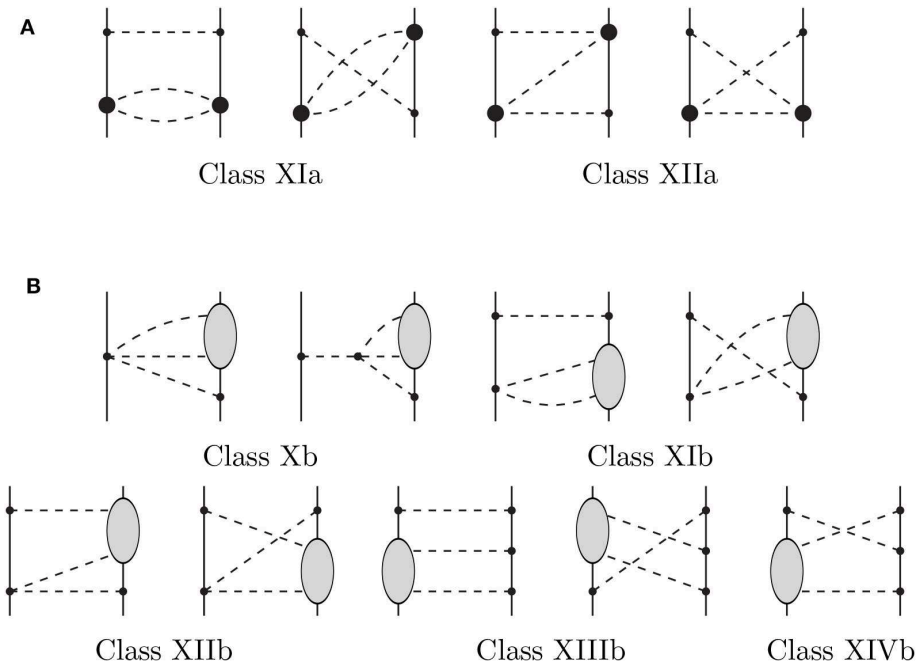


FIGURE 8 | N^{5}LO 3π-exchange contributions to the *NN* interaction. **(A)** Diagrams proportional to c_i^2. **(B)** Diagrams involving the one-loop πN amplitude. Notation as in **Figure 3**. Reprinted figure with permission from Entem et al. [48], copyright (2015) by the American Physical Society.

$$\begin{aligned}\mathrm{Im}W_S &= \frac{g_A^2 m_\pi^6 (u-3)^2}{2240\pi f_\pi^6}\left\{7c_1^2\left(\frac{4}{3}+\frac{3}{u}-\frac{2}{3u^2}-\frac{1}{u^3}\right)\right.\\ &+c_1c_3\left(\frac{2u^2}{3}+4u-\frac{2}{3}-\frac{5}{u}-\frac{2}{3u^2}-\frac{1}{u^3}\right)\\ &\left.+c_3^2\left(\frac{3u^2}{4}+\frac{u}{8}-\frac{5}{2}-\frac{3}{u}+\frac{19}{12u^2}+\frac{19}{8u^3}\right)\right\}, \quad (89)\end{aligned}$$

$$\begin{aligned}\mathrm{Im}(\mu^2 W_T - W_S) &= \frac{g_A^2 m_\pi^6 (u-3)}{1120\pi f_\pi^6}\left\{7c_1^2\left(\frac{1}{3u}+\frac{1}{u^2}+\frac{3}{u^3}-2u-1\right)\right.\\ &+c_1c_3\left(13u+4-5u^2-\frac{5u^3}{3}+\frac{1}{3u}+\frac{1}{u^2}+\frac{3}{u^3}\right)\\ &\left.+\frac{c_3^2}{8}\left(23u^2-\frac{u^5}{3}-u^4-4u^3-8u-3+\right.\right.\\ &\left.\left.\frac{8}{3u}-\frac{19}{u^2}-\frac{57}{u^3}\right)\right\}, \quad (90)\end{aligned}$$

$$\begin{aligned}\mathrm{Im}W_S &= \frac{g_A^2 c_4 m_\pi^6}{1120\pi f_\pi^6}(u-3)^2\left\{c_1\left(u^2+6u\right.\right.\\ &\left.-1-\frac{15}{2u}-\frac{1}{u^2}-\frac{3}{2u^3}\right)+\frac{c_3}{4}\left(\frac{2u^4}{9}+\frac{4u^3}{3}+\\ &\left.\frac{u^2}{3}-\frac{25u}{6}+\frac{6}{u}+\frac{1}{u^2}+\frac{3}{2u^3}\right)\right\}, \quad (91)\end{aligned}$$

$$\begin{aligned}\mathrm{Im}(\mu^2 W_T - W_S) &= \frac{g_A^2 c_4 m_\pi^6}{1120\pi f_\pi^6}(u-3)^3\left\{c_1\left(\frac{1}{u^2}+\frac{1}{u^3}-\frac{u}{3}-3-\frac{4}{u}\right)\right.\\ &\left.+\frac{c_3}{4}\left(\frac{u^3}{9}+u^2+\frac{5u}{3}+\frac{8}{3}+\frac{11}{3u}-\frac{1}{u^2}-\frac{1}{u^3}\right)\right\}, \quad (92)\end{aligned}$$

$$\begin{aligned}\mathrm{Im}W_S &= \frac{g_A^2 c_4^2 m_\pi^6}{8960\pi f_\pi^6}(u-3)^2\left(\frac{25u}{12}-\frac{u^4}{9}-\frac{2u^3}{3}\right.\\ &\left.-\frac{u^2}{6}-\frac{3}{u}-\frac{1}{2u^2}-\frac{3}{4u^3}\right), \quad (93)\\ \mathrm{Im}(\mu^2 W_T - W_S) &= \frac{g_A^2 c_4^2 m_\pi^6}{8960\pi f_\pi^6}(u-3)^3\left(\frac{1}{2u^2}+\frac{1}{2u^3}-\frac{u^3}{18}\right.\\ &\left.-\frac{u^2}{2}-\frac{5u}{6}-\frac{4}{3}-\frac{11}{6u}\right). \quad (94)\end{aligned}$$

The next contribution is given by class (b). Each diagram includes the one-loop πN amplitude. Not all the contributions could be treated; only those contributions that are independent of the pion-nucleon CMS energy in the loop or linearly dependent could be included. The contributions are in general small. The omitted contributions are typically an order of magnitude smaller.

Class Xb:

$$\mathrm{Im}W_S = \frac{g_A^2 m_\pi^6}{(4f_\pi)^8\pi^5}\int_2^{u-1} dw\,\frac{4G(w)}{27w^2u^4}\left[(w^2-4)\lambda(w)\right]^{3/2}, \quad (95)$$

$$\mathrm{Im}(\mu^2 W_T - W_S) = \frac{g_A^2 m_\pi^6}{(4f_\pi)^8\pi^5}\int_2^{u-1} dw\,\frac{4G(w)}{9w^2u^4}(w^2-4)^{3/2}\sqrt{\lambda(w)}\,\frac{3u^2+1}{u^2-1}\left[u^4-(w^2-1)^2\right]. \quad (96)$$

Class XIb:

$$\mathrm{Im}W_S = \frac{g_A^2 m_\pi^6}{(4f_\pi)^8\pi^5}\int_2^{u-1} dw\,\frac{8G(w)}{27w^2u^4}(w^2-4)^{3/2}$$

$$\sqrt{\lambda(w)}\Big[2u^2(1+7w^2)-u^4-(w^2-1)^2\Big], \quad (97)$$

$$\mathrm{Im}(\mu^2 W_T - W_S) = \frac{g_A^2 m_\pi^6}{(4f_\pi)^8\pi^5}\int_2^{u-1} dw\,\frac{8G(w)}{9w^2u^4}\frac{(w^2-4)^{3/2}}{\sqrt{\lambda(w)}}$$
$$(u^2+1-w^2)^2\Big[2w^2(1+3u^2)-w^4-(u^2-1)^2\Big]. \quad (98)$$

Class XIIb:

$$\mathrm{Im}W_S = \frac{g_A^2 m_\pi^6}{9f_\pi^8(4\pi)^5}\iint_{z^2<1} d\omega_1 d\omega_2\, G(w)\Big[(\omega_1^2+\omega_2^2-2)$$
$$(1-3z^2)-5k_1k_2z\Big], \quad (99)$$

$$\mathrm{Im}(\mu^2 W_T - W_S) = -\frac{g_A^2 m_\pi^6}{3f_\pi^8(4\pi)^5}\iint_{z^2<1} d\omega_1 d\omega_2\, G(w)\omega_1\omega_2$$
$$\left[5+2z\left(\frac{k_1}{k_2}+\frac{k_2}{k_1}\right)\right], \quad (100)$$

setting $w=\sqrt{1+u^2-2u\omega_1}$.

Class XIIIb:

$$\mathrm{Im}V_S = \frac{g_A^4 m_\pi^6}{(4f_\pi)^8\pi^3u^3}\int_2^{u-1} dw\,2G(w)\lambda(w)(2-w^2), \quad (101)$$

$$\mathrm{Im}(\mu^2 V_T - V_S) = \frac{g_A^4 m_\pi^6}{(4f_\pi)^8\pi^3u^3}\int_2^{u-1} dw\,4G(w)(2-w^2)$$
$$(1+u^2-w^2)^2, \quad (102)$$

$$\mathrm{Im}W_S = \frac{g_A^4 m_\pi^6}{3f_\pi^8(4\pi)^5}\iint_{z^2<1} d\omega_1 d\omega_2\, G(w)\Big\{u(\omega_1+4\omega_2)-$$
$$2-\frac{\omega_1^2+8\omega_2^2}{3}+z^2(\omega_1^2+4\omega_2^2-5) \quad (103)$$
$$+\frac{zk_2}{k_1}(4u\omega_1+\omega_1^2-5)+\frac{zk_1}{k_2}(u\omega_2+\omega_2^2-2)$$
$$+\frac{\arcsin(z)}{\sqrt{1-z^2}}\left[\frac{k_1}{k_2}(1-u\omega_2)+z(1-u\omega_1)\right]\Big\},$$

$$\mathrm{Im}(\mu^2 W_T - W_S) = \frac{g_A^4 m_\pi^6}{f_\pi^8(4\pi)^5}\iint_{z^2<1} d\omega_1 d\omega_2\,\frac{2\omega_1}{3}G(w)$$
$$\Big\{\frac{2\omega_2}{k_1^2}\Big[\omega_1(u-\omega_2)-1\Big]+u+2\omega_2$$
$$+\frac{zk_1\omega_2}{k_2}+\frac{zk_2}{k_1}(4u+\omega_1)+\omega_1\Big(\frac{2zk_2}{k_1}\Big)^2 \quad (104)$$
$$+\frac{\arcsin(z)}{k_1k_2\sqrt{1-z^2}}\Big[(1+u^2)\Big(\omega_1+\omega_2-\frac{u}{2}\Big)$$
$$-2u\omega_1\omega_2\Big]\Big\},$$

setting again $w=\sqrt{1+u^2-2u\omega_1}$.

Class XIVb:

$$\mathrm{Im}V_S = \frac{g_A^4 m_\pi^6}{(4f_\pi)^8\pi^3u^3}\int_2^{u-1} dw\,\frac{G(w)}{2}\,\lambda(w)$$
$$\Big[u^2+w^2+4(u^2-1)w^{-2}-5\Big], \quad (105)$$

$$\mathrm{Im}(\mu^2 V_T - V_S) = \frac{g_A^4 m_\pi^6}{(4f_\pi)^8\pi^3u^3}\int_2^{u-1} dw\,G(w)(w^2-1-u^2)$$
$$\Big[w^4-2w^2(3+u^2)+(u^2-1)^2(1+4w^{-2})\Big]. \quad (106)$$

where the auxiliary function $G(w)$ is defined as

$$G(w) = \left[1+2g_A^2-\frac{w^2}{4}(1+5g_A^2)\right]\frac{\sqrt{w^2-4}}{w}\ln\frac{w+\sqrt{w^2-4}}{2}$$
$$+\frac{w^2}{24}(5+13g_A^2)-1-2g_A^2+48\pi^2f_\pi^2$$
$$\Big[(2-w^2)(\bar{d}_1+\bar{d}_2)+4\bar{d}_5\Big]. \quad (107)$$

Finally 4π-exchange diagrams occur for the first time at N^{5}LO. These diagrams are three loop diagrams with only leading vertices. As mentioned before, three-pion exchanges with just leading order vertices turned out to be negligible. For that reason, we expect the leading four-pion exchanges to be even smaller, and we leave them out.

2.5. *NN* Contact Terms

Contact terms are given by the *NN* piece of the Lagrangian Equation (6). They start at order $\nu = 0$ with non-derivatives terms given by [5]

$$V_{\rm ct}^{(0)}(\vec{p}',\vec{p}) = C_S + C_T\,\vec{\sigma}_1\cdot\vec{\sigma}_2\,. \quad (108)$$

They contribute to *S* waves, only.

The next order is $\nu = 2$ (NNLO), which introduces seven new contact terms, given by [11]

$$V_{\rm ct}^{(2)}(\vec{p}',\vec{p}) = C_1\,q^2 + C_2\,k^2$$
$$+\left(C_3\,q^2+C_4\,k^2\right)\vec{\sigma}_1\cdot\vec{\sigma}_2$$
$$+C_5\left(-i\vec{S}\cdot(\vec{q}\times\vec{k})\right)$$
$$+C_6\,(\vec{\sigma}_1\cdot\vec{q})\,(\vec{\sigma}_2\cdot\vec{q})$$
$$+C_7\,(\vec{\sigma}_1\cdot\vec{k})\,(\vec{\sigma}_2\cdot\vec{k})\,. \quad (109)$$

The next order is $\nu = 4$ (N^{3}LO) which has 15 contributions given by

$$V_{\rm ct}^{(4)}(\vec{p}',\vec{p}) = D_1\,q^4 + D_2\,k^4 + D_3\,q^2k^2 + D_4\,(\vec{q}\times\vec{k})^2$$
$$+\left(D_5\,q^4+D_6\,k^4+D_7\,q^2k^2+D_8\,(\vec{q}\times\vec{k})^2\right)\vec{\sigma}_1\cdot\vec{\sigma}_2$$
$$+\left(D_9\,q^2+D_{10}\,k^2\right)\left(-i\vec{S}\cdot(\vec{q}\times\vec{k})\right)$$
$$+\left(D_{11}\,q^2+D_{12}\,k^2\right)(\vec{\sigma}_1\cdot\vec{q})\,(\vec{\sigma}_2\cdot\vec{q})$$
$$+\left(D_{13}\,q^2+D_{14}\,k^2\right)(\vec{\sigma}_1\cdot\vec{k})\,(\vec{\sigma}_2\cdot\vec{k})$$
$$+D_{15}\left(\vec{\sigma}_1\cdot(\vec{q}\times\vec{k})\;\vec{\sigma}_2\cdot(\vec{q}\times\vec{k})\right), \quad (110)$$

We note that, on shell, there are only 12 independent operators. The redundancy on-shell has been shown to generate large correlations. Reinert et al. [38] and Wesolowski et al. [50]

claim that removal of the three (on-shell) redundant operators improves the fit.

The partial wave decomposition of all these terms can be found in Machleidt and Entem [14]. Contact contributions are polynomials in external momenta and they only give contributions to partial waves with $L \leq \nu/2$.

3. PERIPHERAL *NN* SCATTERING

Peripheral *NN* scattering is of special interest since it is less sensitive to the short distance dynamics. A way to study it is to consider partial waves with high angular momentum, since the centrifugal barrier prevents sensitivity to short distance forces.

In the framework of EFT, the short distance physics is mimicked by the contact terms. In momentum space, they are given by polynomial terms in external momenta. This has the property that they don't give contributions to all partial waves, but only to angular momenta $L \leq \frac{\nu}{2}$. This means that, for example at N^{5}LO, there are only contributions up to F-waves.

Peripheral *NN* scattering was already considered at NNLO [12], N^{3}LO [51], N^{4}LO [46], and N^{5}LO [48]. Here, we will review the most important results.

One important aspect of peripheral waves is that the interaction is weaker and perturbative calculations can be performed, so avoiding all the problems posed by singular interactions in the Lippmann-Schwinger equation. For these reasons, it can be viewed as a clean probe of chiral dynamics in the *NN* sector.

The calculation is conducted by using the K matrix perturbatively as

$$K(\vec{p}\,',\vec{p}) \;=\; V_\pi(\vec{p}\,',\vec{p}) + V_{2\pi,\mathrm{it}}(\vec{p}\,',\vec{p}) \qquad (111)$$

with $V_\pi(\vec{p}\,',\vec{p})$ the χEFT amplitude where the iteration of OPE has been subtracted, and $V_{2\pi,\mathrm{it}}(\vec{p}\,',\vec{p})$ representing the once iterated OPE given by

$$V_{2\pi,\mathrm{it}}(\vec{p}',\vec{p}) = \mathcal{P}\int d^3p'' \frac{M_N^2}{E_{p''}} \frac{V_{1\pi}(\vec{p}',\vec{p}'')\, V_{1\pi}(\vec{p}'',\vec{p})}{p^2 - p''^2}\,, \qquad (112)$$

where $\mathcal{P}$ denotes the principal value integral and $E_{p''} = \sqrt{M_N^2 + p''^2}$.

There is no unique way to subtract the iterative part of OPE. The prescription given by Equation (112) is slightly different from the one used in Kaiser et al. [12]. The difference between them is reabsorbed in a redefinition of the irreducible part. See Appendix C of Machleidt and Entem [14] for more details.

Now the order by order calculation is conducted as follows. At LO only OPE is included in V_π and no iteration is included. At NLO V_π up to order $\nu = 2$ is included and $V_{2\pi,\mathrm{it}}$ is included. Higher orders (NNLO, N^{3}LO, etc) include V_π up to this order and the once iterated OPE. N^{3}LO and higher orders should also include the twice iterated OPE contribution. However the difference between the once iterated OPE and the infinitely iterated OPE is very small and can not be identified on the scale of the figures. For this reason, we omit iterations of OPE beyond what is contained in $V_{2\pi,\mathrm{it}}$.

3.1. Fifth-Order (N^{4}LO) Results

The contributions at NNLO [12] and N^{3}LO [51] are in general too attractive, especially when the c_i LEC's obtained from πN scattering are used.

We analyze now the contributions at N^{4}LO. In **Figure 9** we show results for selected F and G waves. Curve (1) gives the results for the N^{3}LO calculation. Curve (2) adds the relativistic corrections (proportional to c_i/M_N) of the NNLO terms. In curve (3), the 2π-exchange two-loop contributions of class (a) (**Figure 4** and section 2.4.5) are added. Curve (4) adds the two-loop contribution of class (b). Finally curve (5) adds 3π-exchange contributions giving the final result at N^{4}LO. In all calculations a SFR cutoff $\tilde{\Lambda} = 1.5$ GeV is used.

One can see that 3π-exchange contributions are significantly smaller than 2π-exchanges which can be interpreted as a convergence in regard to the number of pions exchanged. The 3π contribution is the sum of individual contributions that can be sizable but they add up to a small final result.

The c_i/M_N and two-loop contributions are mainly repulsive which helps to overcome the excess of attraction at N^{3}LO. An exception is the $^1F_3$ partial wave where the two-loop contribution of class (b) gives attraction, resulting in too much attraction for the whole N^{4}LO contribution at higher energies.

For F and G waves (except $^1F_3$) the final N^{4}LO result is in very good agreement with the empirical phase-shifts. An interesting case is the $^3G_5$ that is a problem at N^{3}LO [51]; however, the final result at N^{4}LO is in almost perfect agreement with the phase-shift analysis.

Here we have used $\tilde{\Lambda} = 1.5$ GeV. It is interesting to note that other potentials constructed from dispersion relations like the Stony Brook [52] and the Paris [53] potentials cut the dispersion integral at $\mu^2 = 50m_\pi^2$ which is equivalent to a SFR cut-off of $\tilde{\Lambda} \sim 1$ GeV. In **Figures 10**, **11** we show the impact of the SFR cutoff on the results at different orders. In general the variations for N^{3}LO are large and always too attractive while at N^{4}LO variations are smaller and close to the data. We also include lower orders to compare the relative size of the order-by-order contributions. One would expect a convergence pattern going from NNLO to N^{3}LO and further to N^{4}LO; however, this is not the case as seen in **Figures 10**, **11**.

Concerning the LECs used, note that in the calculations of this subsection, the "KH" set of LECs shown in **Table 2** was applied, while in the calculations of the next subsection the "GW" set is employed.

3.2. Going Beyond Fifth Order

As mentioned before there is no complete calculation at sixth order (N^{5}LO). However a study of peripheral *NN* scattering with the expected dominant contributions was performed in Entem et al. [48]. We present here the results at this order.

For N^{5}LO we consider G and higher waves, since they are not affected by contact terms at this order. In **Figure 12**, we show how individual groups of diagrams contribute to two G waves. Curve (1) represents the N^{4}LO result. Curve (2) adds the N^{5}LO 2π-exchange contributions of class (a) and curve (3) adds also class (b) (**Figure 6** and Section 2.4.6). 3π-exchange (**Figure 8**) of class (a) are included in curve (4) and class (b) is contained in

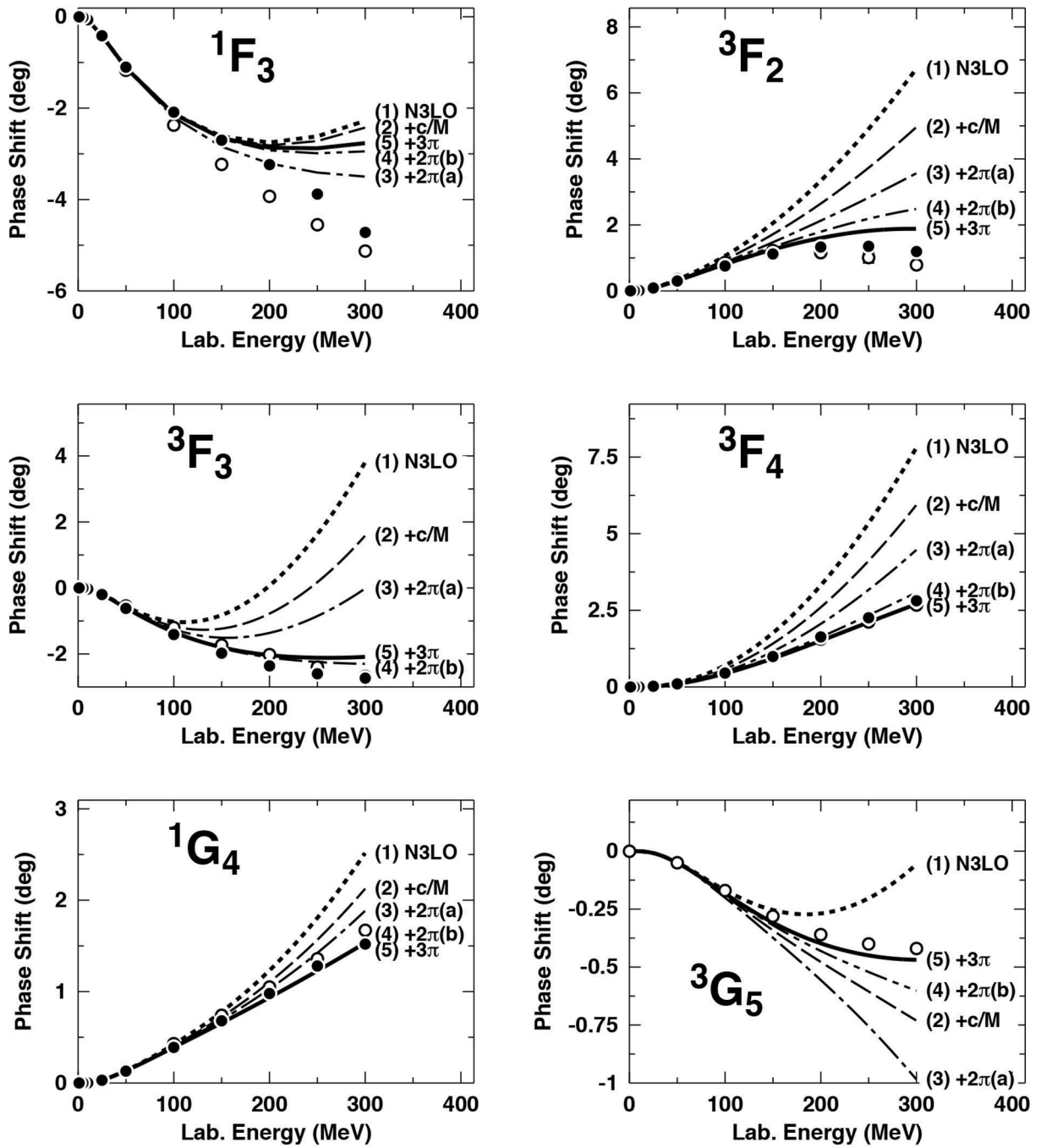


FIGURE 9 | Effect of individual fifth-order contributions to the neutron-proton phase shifts of some selected peripheral partial waves. The individual contributions are added up successively in the order given in parentheses next to each curve. In all cases an SFR cut-off $\tilde{\Lambda} = 1.5$ GeV is used. Curve (1) is N^{3}LO and curve (5) the complete N^{4}LO. The filled and open circles represent the results from the Nijmegen multi-energy *np* phase-shift analysis [93] and the VPI-GWU single-energy *np* analysis SM99 [91], respectively. Reprinted figure with permission from Entem et al. [46], copyright (2015) by the American Physical Society.

curve (5). The final result at N^{5}LO is given by curve (6) which includes the $1/M_N^2$ corrections. In all cases a SFR cutoff $\tilde{\Lambda} = 800$ MeV is used.

The two-loop 2π-exchange class (a) (**Figure 6**) generates a strong repulsive central force, while the spin-spin and tensor forces provided by this class are negligible. The fact that this class produces a relatively large contribution is not unexpected, since it is proportional to c_i^2. The 2π-exchange contribution class (b) creates a moderately repulsive central force and a noticeable tensor force, as the impact on $^3G_5$ demonstrates.

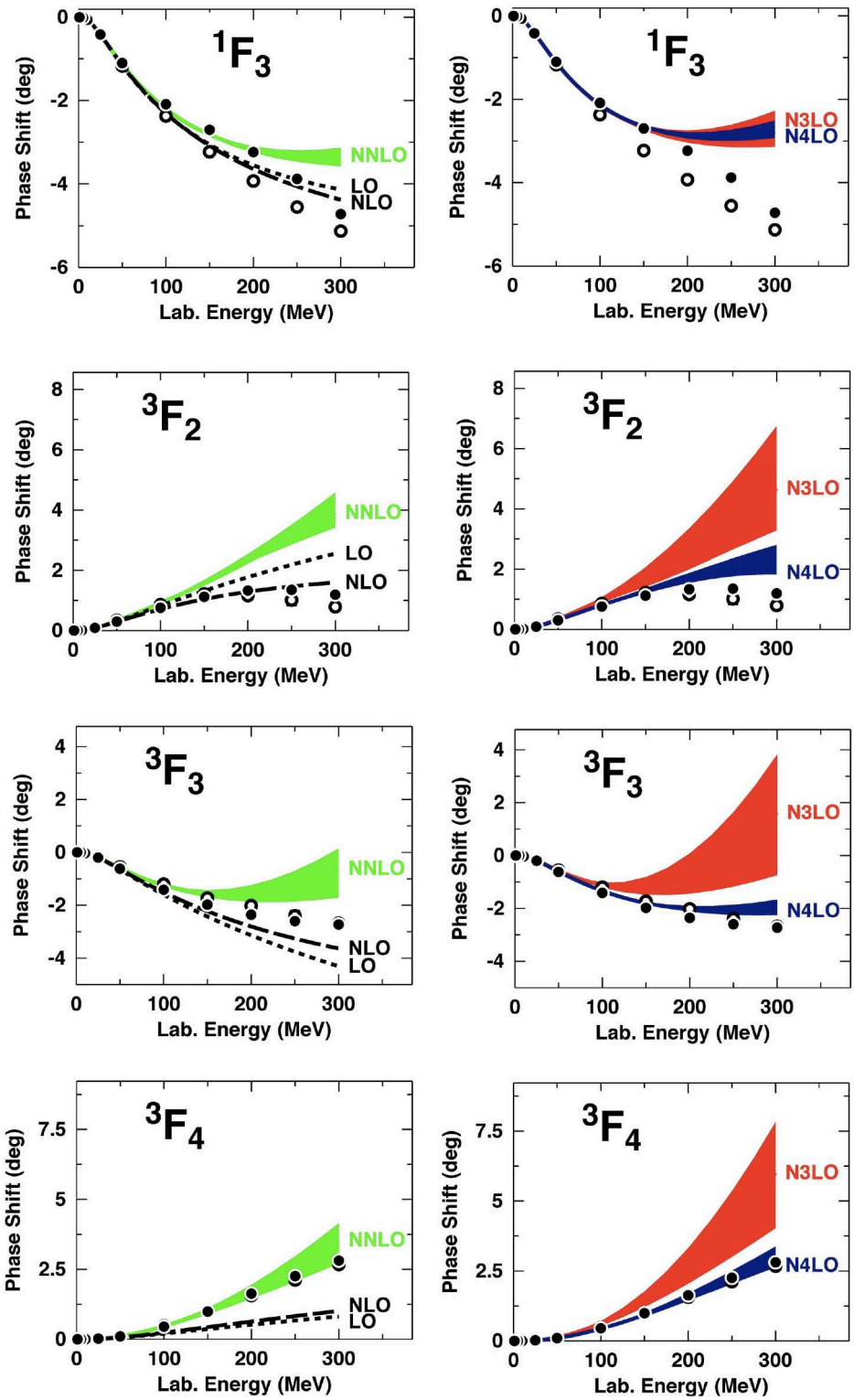


FIGURE 10 | Phase-shifts of neutron-proton scattering at various orders as denoted. The shaded bands show the sensitivity of the contributions to the SFR cut-off $\tilde{\Lambda}$ which is varied over the range 0.7–1.5 GeV. Filled and open circles as in **Figure 9**. Reprinted figure with permission from Entem et al. [46], copyright (2015) by the American Physical Society.

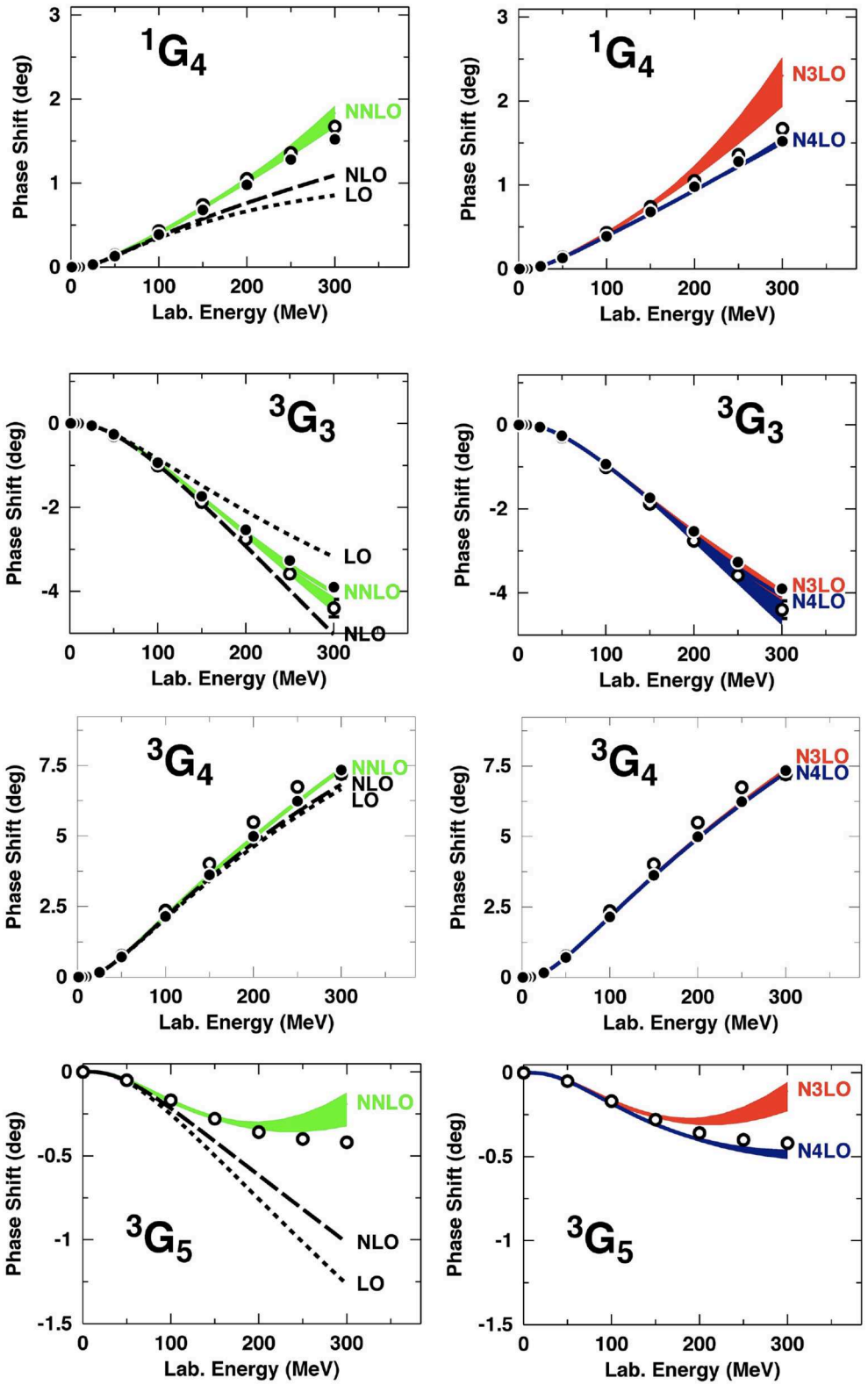


FIGURE 11 | Same as **Figure 10**, but for *G* waves. Reprinted figure with permission from Entem et al. [46], copyright (2015) by the American Physical Society.

TABLE 2 | Low-energy constants as determined in Krebs et al. [41].

	GW	KH
c_1	–1.13	–0.75
c_2	3.69	3.49
c_3	–5.51	–4.77
c_4	3.71	3.34
$\tilde{d}_1 + \tilde{d}_2$	5.57	6.21
$\tilde{d}_3$	–5.35	–6.83
$\tilde{d}_5$	0.02	0.78
$\tilde{d}_{14} - \tilde{d}_{15}$	–10.26	–12.02
$\tilde{e}_{14}$	1.75	1.52
$\tilde{e}_{15}$	–5.80	–10.41
$\tilde{e}_{16}$	1.76	6.08
$\tilde{e}_{17}$	–0.58	–0.37
$\tilde{e}_{18}$	0.96	3.26

The c_i, $\tilde{d}_i$, and $\tilde{e}_i$ are the LECs of the second, third, and fourth order πN Lagrangian given in Krebs et al. [41] and are in units of GeV^{-1}, GeV^{-2}, and GeV^{-3}, respectively. GW refers to the LECs obtained fitting to the George Washington University partial wave analysis from Arndt et al. [54], while KH refers to the Karlsruhe-Helsinki analysis from Koch [55].

The 3π-exchange class (a) (**Figure 8**) is negligible in $^1G_4$, but noticeable in $^3G_5$ and, therefore, it should not be neglected. This contribution is proportional to c_i^2, which suggests a non-negligible size but it is typically smaller than the corresponding 2π-exchange contribution class (a). The 3π-exchange class (b) contribution turns out to be negligible [see the difference between curve (4) and (5) in **Figure 12**]. This may not be unexpected since it is a three-loop contribution with only leading-order vertexes. Finally the relativistic $1/M_N^2$ corrections to the leading 2π-exchange have a small but non-negligible impact, particularly in $^3G_5$.

The predictions for G and H waves are shown in **Figure 13**, with shaded bands corresponding to a variation of the SFR cut-off $\tilde{\Lambda}$ over the range 700–900 MeV. The N^{5}LO contribution shows a moderately repulsive effect, reducing further the excess attraction at N^{3}LO. The N^{5}LO result is, in general, substantially smaller than the N^{4}LO one, indicating a signature of convergence. At N^{5}LO, there is excellent agreement with the data.

Concerning the values for the LECs, let us note again that, in this subsection, the "GW" set of LECs shown in **Table 2** was used, while in the calculations of the previous subsection the "KH" set was applied.

Figure 13 includes only the three highest orders. However, a comparison between all orders is also of interest. Therefore, we show in **Figure 14** the contributions to phase shifts through all six chiral orders from LO to N^{5}LO. Note that the difference between the LO prediction (one-pion-exchange) and the data (filled and open circles) is to be provided by two- and three-pion exchanges, i.e., the intermediate-range part of the nuclear force. How well that is accomplished is a crucial test for any theory of nuclear forces. NLO produces only a small contribution, but NNLO (denoted by N2LO in the figure) creates substantial intermediate-range attraction (most clearly seen in $^1G_4$, $^3G_5$, and $^3H_6$). In fact, NNLO is the largest contribution among all orders. This is due to the one-loop 2π-exchange (2PE) triangle diagram which involves one $\pi\pi NN$-contact vertex proportional to c_i. This vertex represents correlated 2PE as well as intermediate $\Delta(1232)$-isobar excitation. It is well-known from the traditional meson theory of nuclear forces that these two features are crucial for a realistic and quantitative 2PE model. Consequently, the one-loop 2π-exchange at NNLO is attractive and assumes a realistic size describing the intermediate-range attraction of the nuclear force about right. At N^{3}LO, more one-loop 2PE is added by the bubble diagram with two c_i-vertices, a contribution that seemingly is overestimating the attraction. This attractive surplus is then compensated by the prevailingly repulsive two-loop 2π- and 3π-exchanges that occur at N^{4}LO and N^{5}LO.

In this context, it is worth to note that also in conventional meson theory the one-loop models for the 2PE contribution always show some excess of attraction. In conventional meson theory, the surplus attraction is reduced by heavy-meson exchange (ρ- and ω-exchange) which, however, has no place in chiral effective field theory (as a finite-range contribution). Instead, in the latter approach, two-loop 2π- and 3π-exchanges provide the corrective action.

4. *NN* POTENTIALS UP TO N^{4}LO

The starting point of all ab-initio calculations of nuclear systems is the *NN* potential. For that reason, it is necessary to define a potential.

We define the *NN* potential as the sum of the irreducible *NN* diagrams discussed in previous sections, which are calculated perturbatively. However, in reality, the *NN* system is characterized by the presence of a shallow bound state (the deuteron) and large (*S*-wave) scattering lengths that cannot be obtained perturbatively. Therefore, the potential has to be applied in a scattering equation to obtain the *NN* amplitude. Since our approach is in principal covariant (with relativity taken into account perturbatively), a proper equation would be the Bethe-Salpeter equation. However, it is more convenient, to use one of the three-dimensional reductions of that equation. We use the Blankenbeclar-Sugar (BbS) version of the equation [56] which reads

$$T(\vec{p}\,',\vec{p}) = V(\vec{p}\,',\vec{p}) + \int \frac{d^3p''}{(2\pi)^3} V(\vec{p}\,',\vec{p}\,'') \frac{M_N^2}{E_{p''}} \frac{1}{p^2 - p''^2 + i\epsilon} T(\vec{p}\,'',\vec{p}\,), \tag{113}$$

where V is the potential and $E_{p''} = \sqrt{M_N^2 + p''^2}$. Since this is a relativistic equation, it includes relativistic kinematical corrections to all orders.

If we now define

$$\hat{V}(\vec{p}\,',\vec{p}) = \frac{1}{(2\pi)^3} \sqrt{\frac{M_N}{E_{p'}}} V(\vec{p}\,',\vec{p}) \sqrt{\frac{M_N}{E_p}} \tag{114}$$

$$\hat{T}(\vec{p}\,',\vec{p}) = \frac{1}{(2\pi)^3} \sqrt{\frac{M_N}{E_{p'}}} T(\vec{p}\,',\vec{p}) \sqrt{\frac{M_N}{E_p}}, \tag{115}$$

TABLE 3 | The πN LECs as determined in the Roy-Steiner-equation analysis of πN scattering conducted in Hoferichter et al. [86].

	NNLO	N^{3}LO	N^{4}LO
c_1	−0.74 (2)	−1.07 (2)	−1.10 (3)
c_2	–	3.20 (3)	3.57 (4)
c_3	−3.61 (5)	−5.32 (5)	−5.54 (6)
c_4	2.44 (3)	3.56 (3)	4.17 (4)
$\tilde{d}_1 + \tilde{d}_2$	–	1.04 (6)	6.18 (8)
$\tilde{d}_3$	–	−0.48 (2)	−8.91 (9)
$\tilde{d}_5$	–	0.14 (5)	0.86 (5)
$\tilde{d}_{14} - \tilde{d}_{15}$	–	−1.90 (6)	−12.18 (12)
$\tilde{e}_{14}$	–	–	1.18 (4)
$\tilde{e}_{17}$	–	–	−0.18 (6)

The c_i, $\tilde{d}_i$, and $\tilde{e}_i$ are the LECs of the second, third, and fourth order πN Lagrangian Krebs et al. [41] and are in units of GeV^{-1}, GeV^{-2}, and GeV^{-3}, respectively. The uncertainties in the last digits are given in parentheses after the values.

the BbS equation becomes

$$\hat{T}(\vec{p}\,',\vec{p}) = \hat{V}(\vec{p}\,',\vec{p}) + \int d^3p''\,\hat{V}(\vec{p}\,',\vec{p}\,'')\frac{1}{p^2 - p''^2 + i\epsilon}\hat{T}(\vec{p}\,'',\vec{p})\,, \tag{116}$$

which is the Lippmann-Schwinger equation and $\hat{V}$ can be used like a non-relativistic potential. All the technical details to solve the Lippmann-Schwinger equation, including the case where the Coulomb interaction is included, can be found in Machleidt [18].

The amplitude V and the potential $\hat{V}$ are built order-by-order following the Equations (12–16) with two exceptions. We add to $V_{\mathrm{N^3LO}}$ the $1/M_N$ corrections of the NNLO 2π-exchange proportional to c_i. This c_i/M_N correction is formally an N^{4}LO contribution, however, in Entem et al. [46] it was shown that the football diagram proportional to c_i^2 at N^{3}LO was unrealistically attractive, while the c_i/M_N correction is large and repulsive. Therefore, it makes sense to group these diagrams together to arrive at a more realistic intermediate-range attraction at N^{3}LO.

The other exception is to include, at N^{4}LO, the four F-wave contacts that formally appear at N^{5}LO, cf. Equation (17). This ensures an optimal fit of the NN data for the potential of the highest order to be constructed.

4.1. Regularization

The potential $\hat{V}$ obtained previously is in most cases singular. Singular potentials are those that diverges in momentum space when the momentum goes to infinity, being more singular than $1/r^2$ in coordinate space. For this reason they cannot be included in a Lippmann-Schwinger equation without further manipulation. The practical way to solve this problem is to cut the potential at a certain scale Λ by multiplying with a regulator function $f(p', p)$

$$\hat{V}(\vec{p}\,',\vec{p}) \to f(p',p)\hat{V}(\vec{p}\,',\vec{p}) \tag{117}$$

where the function $f(p', p)$ can be taken to be

$$f(p',p) = \exp[-(p'/\Lambda)^{2n} - (p/\Lambda)^{2n}]. \tag{118}$$

This regularization allows to obtain finite results, however renormalization requires to have regularization independent results. The implicit assumption in Weinberg's proposal [5, 6] was that the same contact interactions that renormalize loop diagrams would also renormalize the iterative loops of the (infinite) resummation in the Lippmann-Schwinger equation. This is not necessarily true and has given rise to a comprehensive discussion about non-perturbative renormalization. This is one of the key issues where the EFT community is divided, mainly, in two different points of view, one with the cut-off scale below the hard-scale of the EFT, and the other with a value above (let's say, infinity). This topic has been discussed by many authors [4, 57–76], and we refer the interested reader to contributions about this topic in the monograph. However, using cutoffs in the order of 450 − 550 MeV (first point of view) has been shown to give mild regularization dependence and to be phenomenologically successful at N^{3}LO [77], although renormalization is not so clear.

The parameter n is usually chosen in such a way that the corrections induced by the regulator are of an order that is higher than the given order. We choose $n = 2$ for 3PE and 2PE and $n = 4$ for OPE (except in LO and NLO, where we use $n = 2$ for OPE). For contacts of order ν, we choose $2n > \nu$.

4.2. Charge Dependence

In order to fit the np and pp databases, charge dependence has to be included. All orders include the charge dependence due to pion mass splitting in the one-pion exchange as was already discussed. Charge dependence is most important in the $^1S_0$ partial wave at low energies, particularly in the scattering lengths. The charge dependence from OPE cannot explain it all. The remainder is accounted for by treating the $^1S_0$ LO contact term parameter $\tilde{C}_{^1S_0} \equiv 4\pi(C_s - 3C_T)$ in a charge-dependent way. So, we distinguish between $\tilde{C}^{(pp)}_{^1S_0}$, $\tilde{C}^{(np)}_{^1S_0}$ and $\tilde{C}^{(nn)}_{^1S_0}$. For pp at any order, the relativistic Coulomb interaction is included [78, 79]. Finally at N^{3}LO and N^{4}LO, we take into account irreducible π-γ exchange [80], which affects only the np potential. Also, the charge-dependent effects from n-p mass splitting are taking into account by using the correct values for the nucleon masses.

For a detailed discussion of possible sources for charge dependence of the NN interaction, see Machleidt and Entem [14].

4.3. Fitting Procedure

Potentials from LO to N^{4}LO were constructed by Entem et al. [37]. [For alternative chiral potential constructions (see [38, 81–85]). Three cutoff values were considered, namely $\Lambda = 450, 500,$ and 550 MeV. Taking charge dependence into account, each potential comes in three versions: pp, np, and nn.

The pion exchange contribution, V_π, is fixed by the πN LECs for which we use the values from the very accurate analysis by Hoferichter et al. [86], **Table 3**. However, the short-range part given by V_{ct} has to be determined from NN scattering. This was done by fitting the NN potentials to the NN database. The database includes all NN data below 350 MeV laboratory energy published in refereed physics journals between January 1955 and December 2016 that are not discarded when applying the Nijmegen rejection criteria [79]. There are alternative criteria

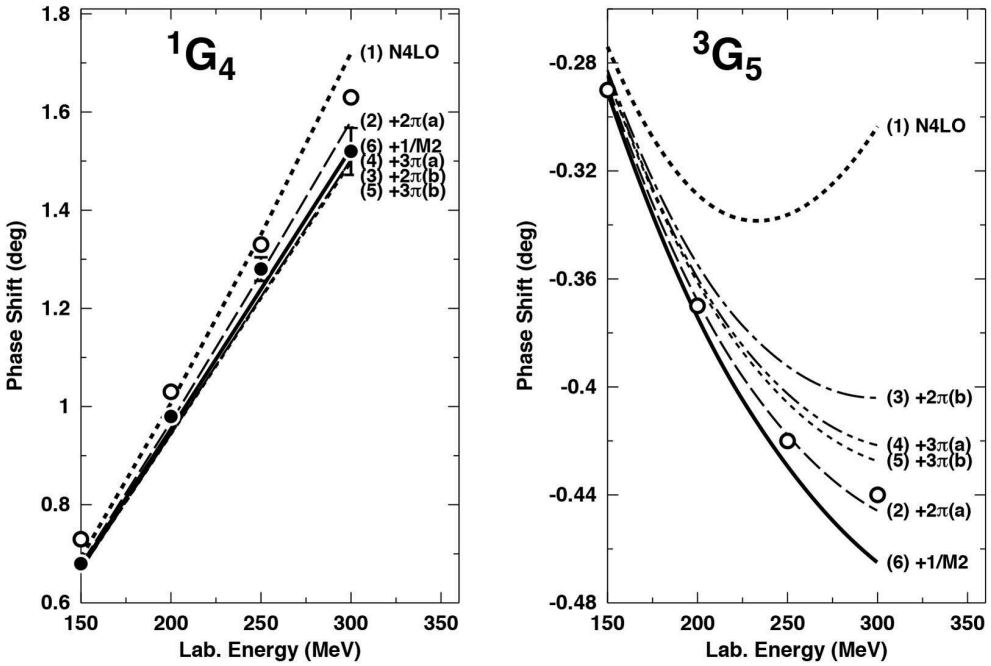


FIGURE 12 | Effect of individual N^{5}LO contributions to the neutron-proton phase-shifts of two *G* waves. Contributions are added up successively starting from the N^{4}LO result (1) to the final N^{5}LO result (6). A SFR cutoff $\tilde{\Lambda} = 800$ MeV is used. The filled and open circles represent the results from the Nijmegen multienergy *np* phase-shift analysis [93] and the GWU *np* analysis SP07 [94], respectively. Reprinted figure with permission from Entem et al. [48], copyright (2015) by the American Physical Society.

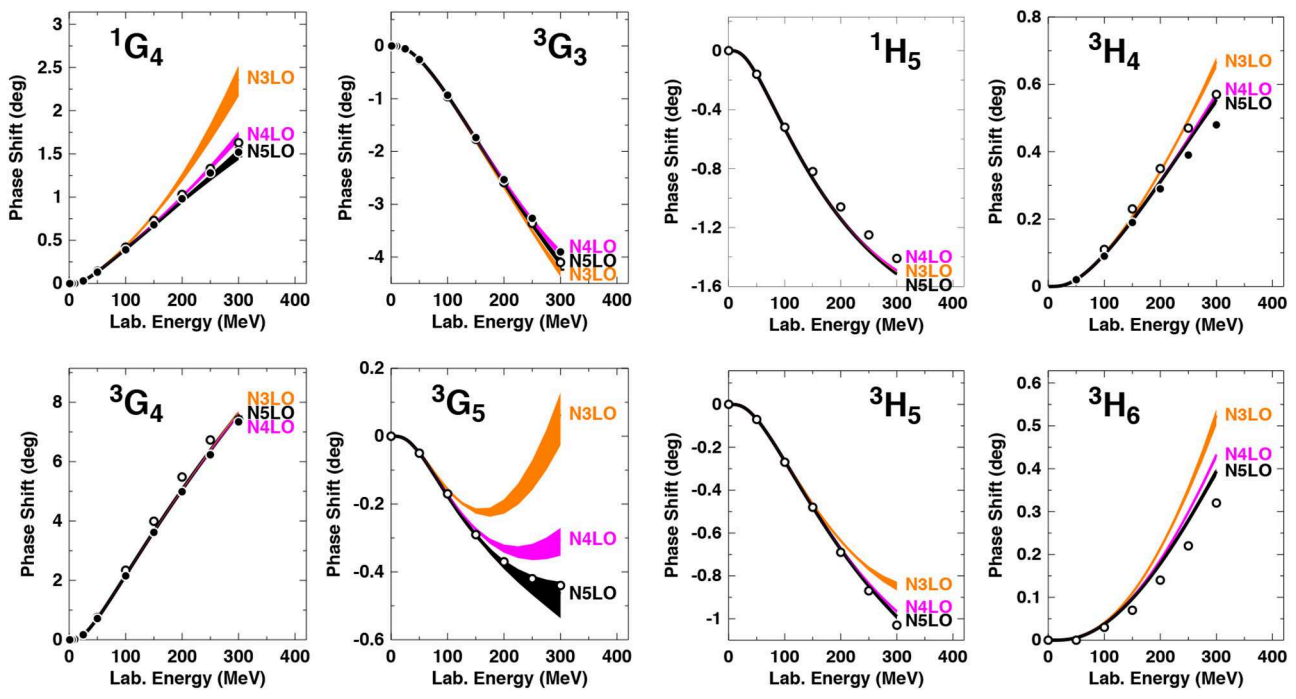


FIGURE 13 | Phase-shifts of *np* scattering in *G* and *H* waves at various orders as denoted. The shaded bands show the variations of the predictions when the SFR cut-off $\tilde{\Lambda}$ is changed over the range 700 to 900 MeV. Empirical phase-shifts as in **Figure 12**. Reprinted figure with permission from Entem et al. [48], copyright (2015) by the American Physical Society.

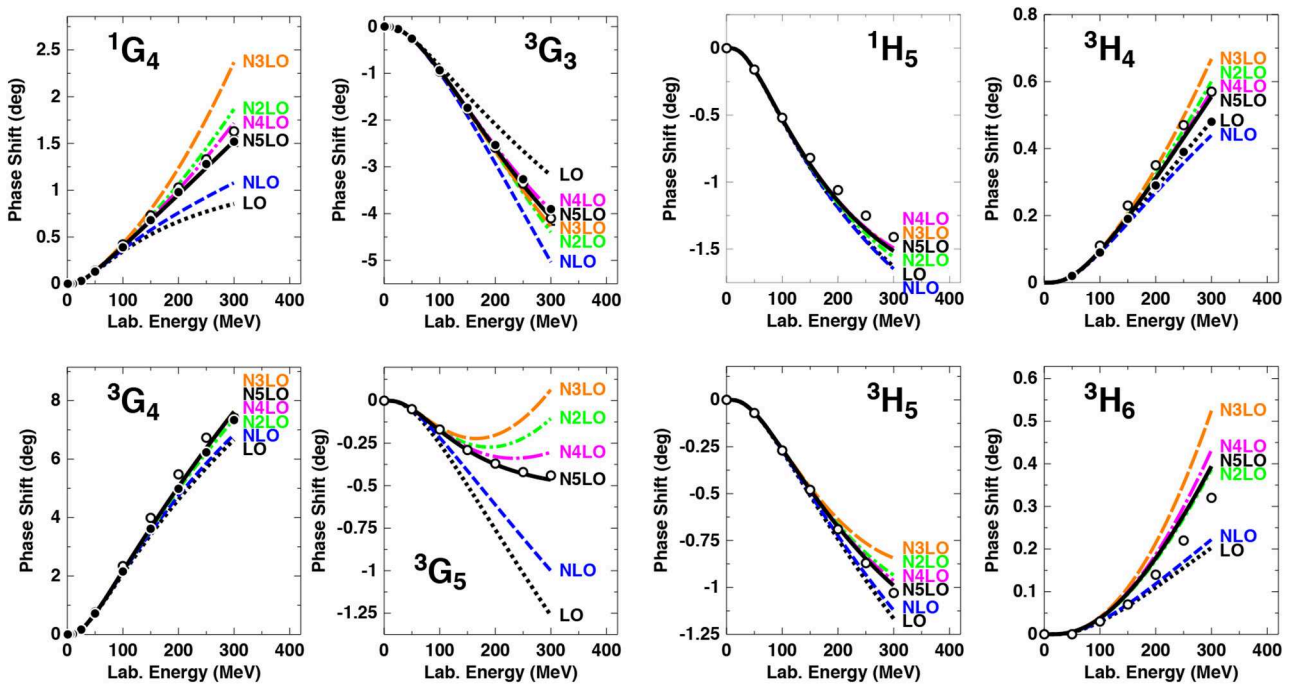


FIGURE 14 | Phase-shifts of *np* scattering in *G* and *H* waves at all orders from LO to N^{5}LO. A SFR cut-off $\tilde{\Lambda} = 800$ MeV is used. Empirical phase-shifts as in **Figure 12**. Reprinted figure with permission from Entem et al. [48], copyright (2015) by the American Physical Society.

[87] which have been applied, e.g., in the Granada database [88], however we continue to use the Nijmegen criteria to be consistent with the pre-2000 part of our database.

The database finally consists of 3072 *pp* scattering data and 3569 *np* data. The 2013 Granada *NN* database [88] consists of 2996 *pp* and 3717 *np* data. The larger number of *pp* data in our base is mainly due to the inclusion of 140 *pp* data from The EDDA Collaboration [89] which are left out in the Granada base. On the other hand, the Granada base contains 148 more *np* data, which is a consequence of the modified rejection criteria applied by the Granada group, which allows for the survival of a few more *np* data.

In the fitting procedure, only data below 290 MeV were taken into account. One starts with the *pp* potential, since the *pp* data are more accurate than the *np* data. First, a fit to the *pp* phase-shifts is made, and then a rough minimization of the χ^2 is performed by using the Nijmegen error matrix [90]. In the end, the potential is fitted directly to the scattering data. For this the SAID software package [91] that includes all electromagnetic contributions necessary for the calculation of *NN* observables at low energy is used.

Then the $I = 1$ *np* potential is fixed by starting from the *pp* potential and applying charge dependence. For the $^1S_0$ part of the *np* potential, the $\tilde{C}_{^1S_0}^{(np)}$ LEC is adjusted to the *np* scattering length. The $I = 0$ part is then fitted in a similar way as the $I = 1$ part. After the $I = 0$ fit, some small variations of the $I = 1$ parameters were allowed to obtain a minimal over-all χ^2.

The *nn* potential is obtained from the *pp* one by leaving out Coulomb, replacing the proton mass by the neutron mass, and fitting the $\tilde{C}_{^1S_0}^{(nn)}$ LEC to the $^1S_0$ *nn* scattering length.

The above procedure is basically the same as used in the construction of the so called high-precision potentials of the 1990s [15, 16, 18], which all have χ^2/datum $\approx$ 1. This differs from the procedure applied in the recent construction of the NNLO$_{\rm sat}$ potential [83] where *NN* data up to 35 MeV and the ground-state energies and radii of nuclei up to ^{16}O are taken into account to fix simultaneously the two- and three-nucleon forces. Our procedure also differs from the construction of some recent chiral *NN* potentials by the Bochum group [81, 82], where only phase-shifts are fitted. However, in their most recent potential constructions, the Bochum group [38] does apply a procedure where the fitted potentials are directly confronted with the *NN* data.

4.4. Results for *NN* Scattering

The χ^2/datum for the reproduction of the *NN* data is given in **Table 4**. For the close to 5000 *pp* plus *np* data below 290 MeV (pion-production threshold), the χ^2/datum is 51.4 at NLO and 6.3 at NNLO, which is of special relevance since the number of *NN* contact terms is the same for both orders. The improvement comes entirely from a better description of the 2PE at NNLO. At N^{3}LO, the χ^2/datum further improves to 1.63. It, finally, reaches 1.15 at N^{4}LO, in acordance with high precision potentials, showing a great convergence pattern.

np phase shifts are displayed in **Figure 15**, which reflect the same features as the χ^2, namely, an excellent convergence when going from NNLO to N^{3}LO and, finally, to N^{4}LO.

TABLE 4 | χ^2/datum for the fit of the 2016 *NN* data base by *NN* potentials at various orders of chiral EFT ($\Lambda = 500$ MeV in all cases).

T_{lab} bin (MeV)	No. of data	LO	NLO	NNLO	N^{3}LO	N^{4}LO
			Proton-proton			
0–100	795	520	18.9	2.28	1.18	1.09
0–190	1206	430	43.6	4.64	1.69	1.12
0–290	2132	360	70.8	7.60	2.09	1.21
			Neutron-proton			
0–100	1180	114	7.2	1.38	0.93	0.94
0–190	1697	96	23.1	2.29	1.10	1.06
0–290	2721	94	36.7	5.28	1.27	1.10
			pp* plus *np			
0–100	1975	283	11.9	1.74	1.03	1.00
0–190	2903	235	31.6	3.27	1.35	1.08
0–290	4853	206	51.5	6.30	1.63	1.15

From Entem et al. [37].

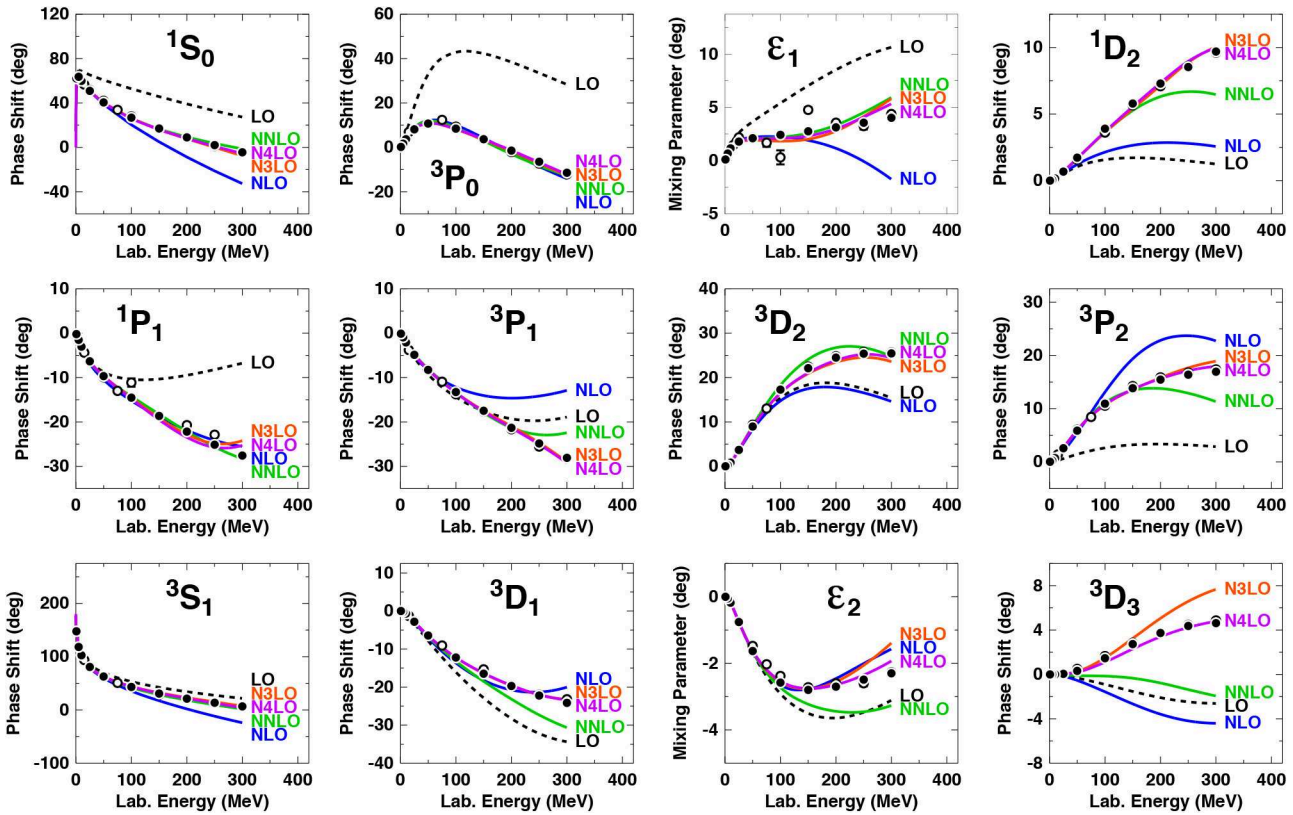


FIGURE 15 | Chiral expansion of neutron-proton scattering as represented by the phase shifts in *S*, *P*, and *D* waves and mixing parameters ϵ_1 and ϵ_2. Five orders ranging from LO to N^{4}LO are shown as denoted. A cutoff $\Lambda = 500$ MeV is applied in all cases. The filled and open circles represent the results from the Nijmegen multi-energy *np* phase-shift analysis [93] and the GWU single-energy *np* analysis SP07 [95], respectively. Reprinted figure with permission from Entem et al. [37], copyright (2017) by the American Physical Society.

However, at LO and NLO there are large discrepancies between the predictions and the empirical phase shifts as to be expected from the corresponding χ^2 values. This fact renders applications of the LO and NLO nuclear forces useless for any realistic calculation (but they could be used to demonstrate truncation errors).

It is important to be aware of the regulator dependence of the *NN* phase shifts and scattering observables. For this reason, potentials with cutoffs $\Lambda = 450, 500$, and 550 MeV were constructed. We show in **Figure 16** the phase shifts at NNLO (green curves, left panel) and N^{4}LO (purple curves, right panel) for potentials with varying cutoffs. As

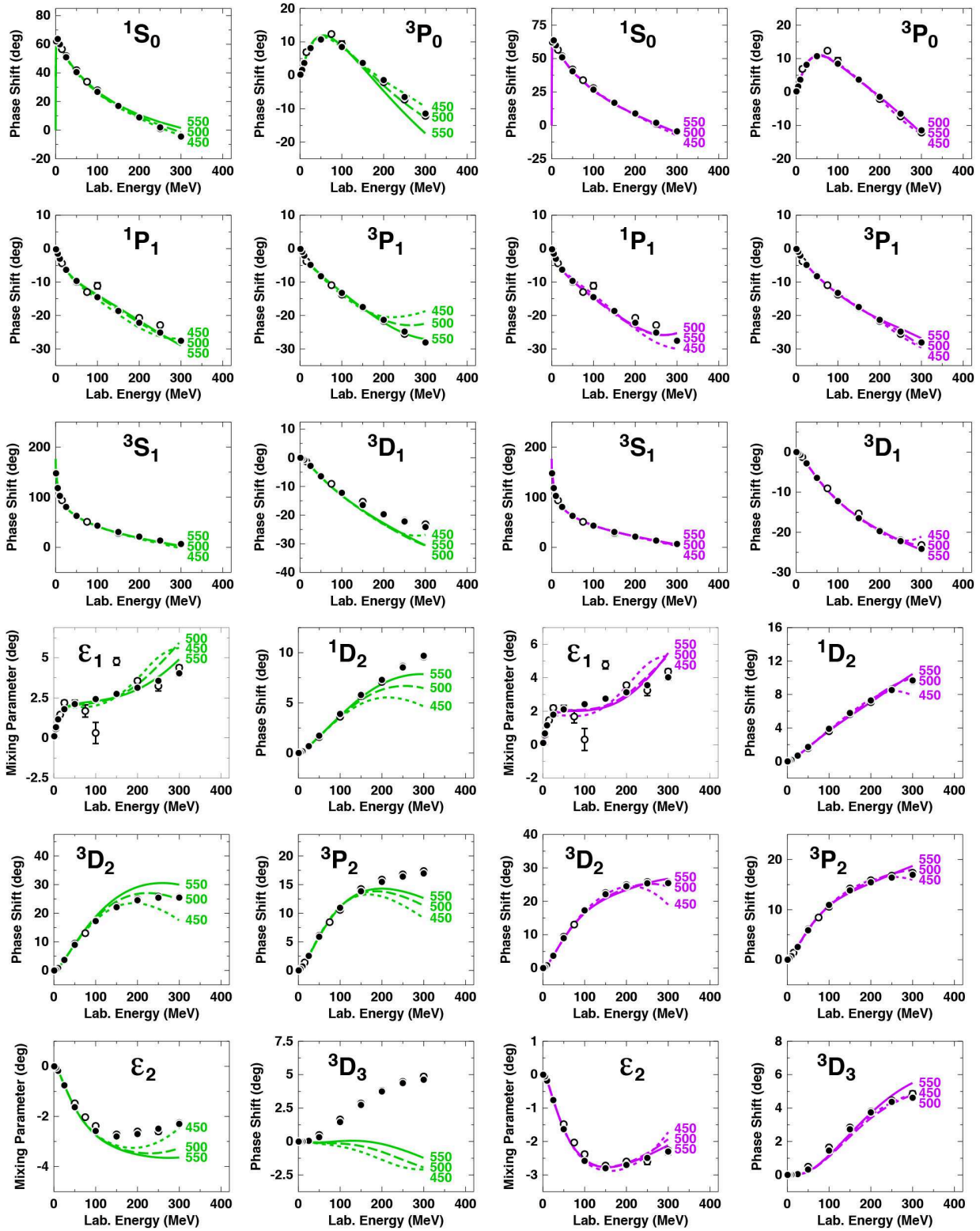


FIGURE 16 | Cutoff variations of the *np* phase shifts at NNLO (left side, green lines) and N^{4}LO (right side, purple lines). Dotted, dashed, and solid lines represent the results obtained with cutoff parameter $\Lambda = 450$, 500, and 550 MeV, respectively, as also indicated by the curve labels. Note that, at N^{4}LO, the cases 500 and 550 MeV cannot be distinguished on the scale of the figures for most partial waves. Filled and open circles as in **Figure 15**. Reprinted figure with permission from Entem et al. [37], copyright (2017) by the American Physical Society.

TABLE 5 | Two- and three-nucleon bound-state properties as predicted by *NN* potentials at various orders of chiral EFT ($\Lambda = 500$ MeV in all cases).

	LO	NLO	NNLO	N^{3}LO	N^{4}LO	Empirical[a]
Deuteron						
B_d (MeV)	2.224575	2.224575	2.224575	2.224575	2.224575	2.224575(9)
A_S (fm$^{-1/2}$)	0.8526	0.8828	0.8844	0.8853	0.8852	0.8846(9)
η	0.0302	0.0262	0.0257	0.0257	0.0258	0.0256(4)
r_{str} (fm)	1.911	1.971	1.968	1.970	1.973	1.97507(78)
Q (fm^2)	0.310	0.273	0.273	0.271	0.273	0.2859(3)
P_D (%)	7.29	3.40	4.49	4.15	4.10	–
Triton						
B_t (MeV)	11.09	8.31	8.21	8.09	8.08	8.48

(Deuteron: Binding energy B_d, asymptotic S state A_S, asymptotic D/S state η, structure radius r_{str}, quadrupole moment Q, D-state probability P_D; the predicted r_{str} and Q are without meson-exchange current contributions and relativistic corrections. Triton: Binding energy B_t.) B_d is fitted, all other quantities are predictions.
[a]See Table XVIII of Machleidt [18] for references; the empirical value for r_{str} is from Jentschura et al. [92].

TABLE 6 | χ^2/datum for the fit of the *pp* plus *np* data up to 190 MeV and two- and three-nucleon bound-state properties as produced by *NN* potentials at NNLO and N^{4}LO applying different values for the cutoff parameter Λ.

	NNLO			N^{4}LO		
Λ(MeV)	450	500	550	450	500	550
χ^2/datum pp & np						
0–190 MeV (2903 data)	4.12	3.27	3.32	1.17	1.08	1.25
Deuteron						
B_d (MeV)	2.224575	2.224575	2.224575	2.224575	2.224575	2.224575
A_S (fm$^{-1/2}$)	0.8847	0.8844	0.8843	0.8852	0.8852	0.8851
η	0.0255	0.0257	0.0258	0.0254	0.0258	0.0257
r_{str} (fm)	1.967	1.968	1.968	1.966	1.973	1.971
Q (fm^2)	0.269	0.273	0.275	0.269	0.273	0.271
P_D (%)	3.95	4.49	4.87	4.38	4.10	4.13
Triton						
B_t (MeV)	8.35	8.21	8.10	8.04	8.08	8.12

*For some of the notation, see **Table 5**, where also empirical information on the deuteron and triton can be found.*

expected, the cutoff dependence diminishes with increasing order, being very small at N^{4}LO. The cutoff window we selected is motivated by the fact that for values $\Lambda \leq 450$ MeV cutoff artifacts start to appear above 200 MeV as seen in the $^1D_2$ and $^3D_2$ partial waves. The upper limit is given by the fact that the breakdown scale occurs around $\Lambda_b \sim 600$ MeV [82].

4.5. Deuteron and Triton

The deuteron binding energy is fitted at all orders to the empirical value of 2.224575 MeV using the nonderivative contact term in the $^3S_1$ partial wave. Different observables of the deuteron and triton are given at all orders in **Table 5**. Notice that only the deuteron binding energy is fitted while all other observables are predictions. It is interesting to notice that already at NNLO all properties are close to the empirical values and vary little when going to higher orders, as one would expect, since they are low energy observables.

The triton binding energy is also given. A 34-channel charge dependent Faddeev calculation using only two-nucleon forces is used. The results show a smooth and steady convergence order by order toward a value around 8.1 MeV, giving some space to three-nucleon forces. The low deuteron D-state probabilities and the high triton binding energy predictions are due to the softness of the potentials.

In **Table 6**, we demonstrate, for order NNLO and N^{4}LO, the cutoff dependence of the χ^2/datum, the deuteron properties, and the triton binding energy. One observes a mild regulator dependence for most quantities. The exception is the deuteron D-state probability which, however, is not an observable. Linked to this (via the strength of tensor force) is the triton binding energy. This is due to the off-shell behavior of the two-nucleon force. This can be compensated by corresponding changes in the three-nucleon force.

5. SUMMARY

The past 25 years have seen great progress in our understanding of nuclear forces in terms of low-energy QCD. Key to this development was the realization that low-energy QCD

is equivalent to an effective field theory which allows for a perturbative expansion that has become known as chiral perturbation theory. In this framework, two- and many-body forces emerge together and the empirical fact that nuclear many-body forces are substantially weaker than the two-nucleon force is explained naturally.

The main focus of this review, was on the two-nucleon force. We presented the order-by-order development from LO ($\sim Q^0$) to N^{5}LO ($\sim Q^6$). Using low-energy constants (LECs) determined from πN scattering, our predictions for peripheral partial waves are parameter-free, except for the spectral function cutoff that regularizes the dispersion integrals which determine the *NN* amplitudes. This spectral-function regularization ensures that the calculated contributions are restricted to the long- and intermediate range, where chiral effective field theory is applicable. Specifically, we have calculated perturbative *NN* scattering in peripheral partial-waves, which is dominated by one-, two-, and three-pion exchanges ruled by chiral symmetry. The order-by-order convergence is slow, but is ultimately achieved at N^{5}LO, where predictions are in perfect agreement with empirical phase shifts.

Besides this, we have also discussed the construction of complete (i.e., including the lower partial waves) chiral *NN* potentials through all orders up to N^{4}LO. The construction may be perceived as consistent, because the same power counting scheme as well as the same cutoff procedures are applied in all orders. The potential of the highest order (N^{4}LO) reproduces the *NN* data below pion-production threshold with a χ^2/datum of 1.15. This is among the highest precisions ever accomplished with any chiral *NN* potential to date. The *NN* potentials presented may serve as a solid basis for systematic *ab initio* calculations of nuclear structure and reactions that allow for a comprehensive error analysis. In particular, the order by order development of the potentials will make possible a reliable determination of the truncation error at each order.

In summary, this review presents the most comprehensive investigation of the implications of chiral symmetry for the *NN* system. The results provide the ultimate confirmation that chiral EFT is an adequate theory for nuclear forces.

AUTHOR CONTRIBUTIONS

All authors listed have made a substantial, direct and intellectual contribution to the work, and approved it for publication.

FUNDING

This work has been funded by Ministerio de Economía, Industria y Competitividad under Contract No. FPA2016-77177-C2-2-P, by the U.S. Department of Energy, Office of Science, Office of Basic Energy Sciences, under Award Number DEFG02-03ER41270 and by the European Union's Horizon 2020 research and innovation programme under grant agreement No. 824093.

REFERENCES

1. Gasser J, Leutwyler H. Chiral perturbation theory to one loop. *Ann Phys.* (1984) **158**:142–210. doi: 10.1016/0003-4916(84)90242-2
2. Gasser J, Sainio ME, Švarc A. Nucleons with chiral loops. *Nucl Phys B.* (1988) **307**:779–853. doi: 10.1016/0550-3213(88)90108-3
3. Oller JA, Oset E. N/D description of two meson amplitudes and chiral symmetry. *Phys Rev D.* (1999) **60**:074023. doi: 10.1103/PhysRevD.60.074023
4. Entem DR, Oller JA. The N/D method with non-perturbative left-hand-cut discontinuity and the S01 NN partial wave. *Phys Lett B.* (2017) **773**:498–504. doi: 10.1016/j.physletb.2017.09.012
5. Weinberg S. Nuclear forces from chiral lagrangians. *Phys Lett B.* (1990) **251**:288–92. doi: 10.1016/0370-2693(90)90938-3
6. Weinberg S. Effective chiral lagrangians for nucleon-pion interactions and nuclear forces. *Nucl Phys B.* (1991) **363**:3–18. doi: 10.1016/0550-3213(91)90231-L
7. Ordóñez C, van Kolck U. Chiral lagrangians and nuclear forces. *Phys Lett B.* (1992) **291**:459–64. doi: 10.1016/0370-2693(92)91404-W
8. Ordóñez C, Ray L, van Kolck U. Nucleon-nucleon potential from an effective chiral Lagrangian. *Phys Rev Lett.* (1994) **72**:1982–5. doi: 10.1103/PhysRevLett.72.1982
9. Ordóñez C, Ray L, van Kolck U. Two-nucleon potential from chiral Lagrangians. *Phys Rev C.* (1996) **53**:2086–105. doi: 10.1103/PhysRevC.53.2086
10. Epelbaoum E, Glöckle W, Meißner UG. Nuclear forces from chiral Lagrangians using the method of unitary transformation (I): formalism. *Nucl Phys A.* (1998) **637**:107–34. doi: 10.1016/S0375-9474(98)00220-6
11. Epelbaum E, Glöckle W, Meißner UG. Nuclear forces from chiral Lagrangians using the method of unitary transformation II: the two-nucleon system. *Nucl Phys A.* (2000) **671**:295–331. doi: 10.1016/S0375-9474(99)00821-0
12. Kaiser N, Brockmann R, Weise W. Peripheral nucleon-nucleon phase shifts and chiral symmetry. *Nucl Phys A.* (1997) **625**:758–88. doi: 10.1016/S0375-9474(97)00586-1
13. Entem DR, Machleidt R. Accurate charge-dependent nucleon-nucleon potential at fourth order of chiral perturbation theory. *Phys Rev C.* (2003) **68**:041001. doi: 10.1103/PhysRevC.68.041001
14. Machleidt R, Entem DR. Chiral effective field theory and nuclear forces. *Phys Rep.* (2011) **503**:1–75. doi: 10.1016/j.physrep.2011.02.001
15. Stoks VGJ, Klomp RAM, Terheggen CPF, de Swart JJ. Construction of high-quality NN potential models. *Phys Rev C.* (1994) **49**:2950–62. doi: 10.1103/PhysRevC.49.2950
16. Wiringa RB, Stoks VGJ, Schiavilla R. Accurate nucleon-nucleon potential with charge-independence breaking. *Phys Rev C.* (1995) **51**:38–51. doi: 10.1103/PhysRevC.51.38
17. Machleidt R, Sammarruca F, Song Y. Nonlocal nature of the nuclear force and its impact on nuclear structure. *Phys Rev C.* (1996) **53**:R1483–7. doi: 10.1103/PhysRevC.53.R1483
18. Machleidt R. High-precision, charge-dependent Bonn nucleon-nucleon potential. *Phys Rev C.* (2001) **63**:024001. doi: 10.1103/PhysRevC.63.024001
19. Epelbaum E, Nogga A, Glöckle W, Kamada H, Meißner UG, Witała H. Three-nucleon forces from chiral effective field theory. *Phys Rev C.* (2002) **66**:064001. doi: 10.1103/PhysRevC.66.064001
20. Navrátil P, Roth R, Quaglioni S. Ab initio many-body calculations of nucleon scattering on ^{4}He, ^{7}Li, ^{7}Be, ^{12}C, and ^{16}O. *Phys Rev C.* (2010) **82**:034609. doi: 10.1103/PhysRevC.82.034609
21. Viviani M, Girlanda L, Kievsky A, Marcucci LE. Effect of three-nucleon interactions in p-^{3}He elastic scattering. *Phys Rev Lett.* (2013) **111**:172302. doi: 10.1103/PhysRevLett.111.172302

22. Golak J, Skibinski R, Topolnicki K, Witala H, Epelbaum E, Krebs H, et al. Low-energy neutron-deuteron reactions with N 3 LO chiral forces. *Eur Phys J A*. (2014) **50**:177. doi: 10.1140/epja/i2014-14177-7
23. Barrett BR, Navrátil P, Vary JP. *Ab initio* no core shell model. *Prog Part Nucl Phys*. (2013) **69**:131–81. doi: 10.1016/j.ppnp.2012.10.003
24. Hergert H, Bogner SK, Binder S, Calci A, Langhammer J, Roth R, et al. In-medium similarity renormalization group with chiral two- plus three-nucleon interactions. *Phys Rev C*. (2013) **87**:034307. doi: 10.1103/PhysRevC.87.034307
25. Binder S, Langhammer J, Calci A, Roth R. *Ab initio* path to heavy nuclei. *Phys Lett B*. (2014) **736**:119–23. doi: 10.1016/j.physletb.2014.07.010
26. Hagen G, Papenbrock T, Hjorth-Jensen M, Dean DJ. Coupled-cluster computations of atomic nuclei. *Rep Prog Phys*. (2014) **77**:096302. doi: 10.1088/0034-4885/77/9/096302
27. Simonis J, Stroberg SR, Hebeler K, Holt JD, Schwenk A. Saturation with chiral interactions and consequences for finite nuclei. *Phys Rev C*. (2017) **96**:014303. doi: 10.1103/PhysRevC.96.014303
28. Hebeler K, Schwenk A. Chiral three-nucleon forces and neutron matter. *Phys Rev C*. (2010) **82**:014314. doi: 10.1103/PhysRevC.82.014314
29. Hebeler K, Bogner SK, Furnstahl RJ, Nogga A, Schwenk A. Improved nuclear matter calculations from chiral low-momentum interactions. *Phys Rev C*. (2011) **83**:031301. doi: 10.1103/PhysRevC.83.031301
30. Hagen G, Papenbrock T, Ekström A, Wendt KA, Baardsen G, Gandolfi S, et al. Coupled-cluster calculations of nucleonic matter. *Phys Rev C*. (2014) **89**:014319. doi: 10.1103/PhysRevC.89.014319
31. Coraggio L, Holt JW, Itaco N, Machleidt R, Sammarruca F. Reduced regulator dependence of neutron-matter predictions with perturbative chiral interactions. *Phys Rev C*. (2013) **87**:014322. doi: 10.1103/PhysRevC.87.014322
32. Coraggio L, Holt JW, Itaco N, Machleidt R, Marcucci LE, Sammarruca F. Nuclear-matter equation of state with consistent two- and three-body perturbative chiral interactions. *Phys Rev C*. (2014) **89**:044321. doi: 10.1103/PhysRevC.89.044321
33. Sammarruca F, Coraggio L, Holt JW, Itaco N, Machleidt R, Marcucci LE. Toward order-by-order calculations of the nuclear and neutron matter equations of state in chiral effective field theory. *Phys Rev C*. (2015) **91**:054311. doi: 10.1103/PhysRevC.91.054311
34. Lapoux V, Somà V, Barbieri C, Hergert H, Holt JD, Stroberg SR. Radii and binding energies in oxygen isotopes: a challenge for nuclear forces. *Phys Rev Lett*. (2016) **117**:052501. doi: 10.1103/PhysRevLett.117.052501
35. Entem DR, Machleidt R, Witała H. Chiral NN model and A_y puzzle. *Phys Rev C*. (2002) **65**:064005. doi: 10.1103/PhysRevC.65.064005
36. Girlanda L, Kievsky A, Viviani M, Marcucci LE. Short-range three-nucleon interaction from $A = 3$ data and its hierarchical structure. *Phys Rev C*. (2019) **99**:054003. doi: 10.1103/PhysRevC.99.054003
37. Entem DR, Machleidt R, Nosyk Y. High-quality two-nucleon potentials up to fifth order of the chiral expansion. *Phys Rev C*. (2017) **96**:024004. doi: 10.1103/PhysRevC.96.024004
38. Reinert P, Krebs H, Epelbaum E. Semilocal momentum-space regularized chiral two-nucleon potentials up to fifth order. *Eur Phys J A*. (2018) **54**:86. doi: 10.1140/epja/i2018-12516-4
39. Piarulli M, Baroni A, Girlanda L, Kievsky A, Lovato A, Lusk E, et al. Light-nuclei spectra from chiral dynamics. *Phys Rev Lett*. (2018) **120**:052503. doi: 10.1103/PhysRevLett.120.052503
40. Ekström A, Hagen G, Morris TD, Papenbrock T, Schwartz PD. Δ isobars and nuclear saturation. *Phys Rev C*. (2018) **97**:024332. doi: 10.1103/PhysRevC.97.024332
41. Krebs H, Gasparyan A, Epelbaum E. Chiral three-nucleon force at N^{4}LO: Longest-range contributions. *Phys Rev C*. (2012) **85**:054006. doi: 10.1103/PhysRevC.85.054006
42. Epelbaum E, Glöckle W, Meißner UG. Improving the convergence of the chiral expansion for nuclear forces - I: Peripheral phases. *Eur Phys J A*. (2004) **19**:125–37. doi: 10.1140/epja/i2003-10096-0
43. Kaiser N. Chiral 3π-exchange NN potentials: results for representation-invariant classes of diagrams. *Phys Rev C*. (1999) **61**:014003. doi: 10.1103/PhysRevC.61.014003
44. Kaiser N. Chiral 3π-exchange NN potentials: results for diagrams proportional to g_A^4 and g_A^6. *Phys Rev C*. (2000) **62**:024001. doi: 10.1103/PhysRevC.62.024001
45. Kaiser N. Chiral 2π-exchange NN potentials: two-loop contributions. *Phys Rev C*. (2001) **64**:057001. doi: 10.1103/PhysRevC.64.057001
46. Entem DR, Kaiser N, Machleidt R, Nosyk Y. Peripheral nucleon-nucleon scattering at fifth order of chiral perturbation theory. *Phys Rev C*. (2015) **91**:014002. doi: 10.1103/PhysRevC.91.014002
47. Kaiser N. Chiral 3π-exchange NN potentials: results for dominant next-to-leading-order contributions. *Phys Rev C*. (2001) **63**:044010. doi: 10.1103/PhysRevC.63.044010
48. Entem DR, Kaiser N, Machleidt R, Nosyk Y. Dominant contributions to the nucleon-nucleon interaction at sixth order of chiral perturbation theory. *Phys Rev C*. (2015) **92**:064001. doi: 10.1103/PhysRevC.92.064001
49. Kaiser N. Chiral 2π-exchange NN potentials: relativistic $1/M^2$ corrections. *Phys Rev C*. (2001) **65**:017001.
50. Wesolowski S, Furnstahl RJ, Melendez JA, Phillips DR. Exploring Bayesian parameter estimation for chiral effective field theory using nucleon–nucleon phase shifts. *J Phys G Nucl Part Phys*. (2019) 46:045102. doi: 10.1088/1361-6471/aaf5fc
51. Entem DR, Machleidt R. Chiral 2π exchange at fourth order and peripheral NN scattering. *Phys Rev C*. (2002) **66**:014002. doi: 10.1103/PhysRevC.66.014002
52. Jackson AD, Riska DO, Verwest B. Meson exchange model for the nucleon-nucleon interaction. *Nucl Phys A*. (1975) **249**:397–444. doi: 10.1016/0375-9474(75)90666-1
53. Lacombe M, Loiseau B, Richard JM, Mau RV, Côté J, Pirès P, et al. Parametrization of the Paris $N - N$ potential. *Phys Rev C*. (1980) **21**:861–73. doi: 10.1103/PhysRevC.21.861
54. Arndt RA, Briscoe WJ, Strakovsky II, Workman RL. Extended partial-wave analysis of πN scattering data. *Phys Rev C*. (2006) **74**:045205. doi: 10.1103/PhysRevC.74.045205
55. Koch R. A calculation of low-energy πN partial waves based on fixed-t analyticity. *Nucl Phys A*. (1986) **448**:707–31. doi: 10.1016/0375-9474(86)90438-0
56. Blankenbecler R, Sugar R. Linear integral equations for relativistic multichannel scattering. *Phys Rev*. (1966) **142**:1051–9. doi: 10.1103/PhysRev.142.1051
57. Kaplan DB, Savage MJ, Wise MB. A new expansion for nucleon-nucleon interactions. *Phys Lett B*. (1998) **424**:390–6. doi: 10.1016/S0370-2693(98)00210-X
58. Birse MC, McGovern JA, Richardson KG. A renormalisation-group treatment of two-body scattering. *Phys Lett B*. (1999) **464**:169–76. doi: 10.1016/S0370-2693(99)00991-0
59. Fleming S, Mehen T, Stewart IW. NNLO corrections to nucleon-nucleon scattering and perturbative pions. *Nucl Phys A*. (2000) **677**:313–66. doi: 10.1016/S0375-9474(00)00221-9
60. Oller JA. Nucleon-nucleon interactions from effective field theory. *Nucl Phys A*. (2003) **725**:85–115. doi: 10.1016/S0375-9474(03)01448-9
61. Nieves J. Renormalization of the 1S0 one-pion-exchange {NN} interaction in presence of derivative contact interactions. *Phys Lett B*. (2003) **568**:109–17. doi: 10.1016/j.physletb.2003.05.009
62. Gegelia J, Scherer S. Effective field theory approach to the nucleon-nucleon interaction revisited. *Int J Mod Phys A*. (2006) **21**:1079–89. doi: 10.1142/S0217751X06025237
63. Valderrama MP, Arriola ER. Renormalization of singlet NN-scattering with one pion exchange and boundary conditions. *Phys Lett B*. (2004) **580**:149–56. doi: 10.1016/j.physletb.2003.11.037
64. Valderrama MP, Arriola ER. Renormalization of the deuteron with one pion exchange. *Phys Rev C*. (2005) **72**:054002. doi: 10.1103/PhysRevC.72.054002
65. Harada K, Inoue K, Kubo H. Wilsonian {RG} and redundant operators in nonrelativistic effective field theory. *Phys Lett B*. (2006) **636**:305–9. doi: 10.1016/j.physletb.2006.03.072
66. Nogga A, Timmermans RGE, Kolck Uv. Renormalization of one-pion exchange and power counting. *Phys Rev C*. (2005) **72**:054006. doi: 10.1103/PhysRevC.72.054006
67. Mondejar J, Soto J. The nucleon-nucleon potential beyond the static approximation. *Eur Phys J A*. (2007) **32**:77–85. doi: 10.1140/epja/i2006-10357-4

68. Pavón Valderrama M. Perturbative renormalizability of chiral two-pion exchange in nucleon-nucleon scattering. *Phys Rev C*. (2011) **83**:024003. doi: 10.1103/PhysRevC.83.024003
69. Frederico T, Timóteo VS, Tomio L. Renormalization of the one-pion-exchange interaction. *Nucl Phys A*. (1999) **653**:209–21. doi: 10.1016/S0375-9474(99)00234-1
70. Valderrama P, Ruiz Arriola ME. Renormalization of the *NN* interaction with a chiral two-pion exchange potential: central phases and the deuteron. *Phys Rev C*. (2006) **74**:054001. doi: 10.1103/PhysRevC.74.054001
71. Yang CJ, Elster C, Phillips DR. Subtractive renormalization of the *NN* interaction in chiral effective theory up to next-to-next-to-leading order: *S* waves. *Phys Rev C*. (2009) **80**:044002. doi: 10.1103/PhysRevC.80.034002
72. Long B, Yang CJ. Renormalizing chiral nuclear forces: triplet channels. *Phys Rev C*. (2012) **85**:034002. doi: 10.1103/PhysRevC.85.034002
73. Entem DR, Arriola ER, Valderrama MP, Machleidt R. Renormalization of chiral two-pion exchange *NN* interactions: momentum space versus coordinate space. *Phys Rev C*. (2008) **77**:044006. doi: 10.1103/PhysRevC.77.044006
74. Zeoli C, Machleidt R, Entem DR. Infinite-cutoff renormalization of the chiral nucleon–nucleon interaction up to N3LO. *Few-Body Syst*. (2013) **54**:2191–205. doi: 10.1007/s00601-012-0481-4
75. Behrendt J, Epelbaum E, Gegelia J, Meißner UG, Nogga A. Two-nucleon scattering in a modified Weinberg approach with a symmetry-preserving regularization. *Eur Phys J A*. (2016) **88**:296. doi: 10.1140/epja/i2016-16296-5
76. Sánchez MS, Yang CJ, Long B, van Kolck U. Two-nucleon $^1S_0$ amplitude zero in chiral effective field theory. *Phys Rev C*. (2018) **97**:024001. doi: 10.1103/PhysRevC.97.024001
77. Marji E, Canul A, MacPherson Q, Winzer R, Zeoli C, Entem DR, et al. Nonperturbative renormalization of the chiral nucleon-nucleon interaction up to next-to-next-to-leading order. *Phys Rev C*. (2013) **88**:054002. doi: 10.1103/PhysRevC.88.054002
78. Austen GJM, de Swart JJ. Improved coulomb potential. *Phys Rev Lett*. (1983) **50**:2039–42. doi: 10.1103/PhysRevLett.50.2039
79. Bergervoet JR, van Campen PC, van der Sanden WA, de Swart JJ. Phase shift analysis of 0–30 MeV pp scattering data. *Phys Rev C*. (1988) **38**:15–50. doi: 10.1103/PhysRevC.38.15
80. van Kolck U, Rentmeester MCM, Friar JL, Goldman T, de Swart JJ. Electromagnetic corrections to the one-pion-exchange potential. *Phys Rev Lett*. (1998) **80**:4386–9. doi: 10.1103/PhysRevLett.80.4386
81. Epelbaum E, Krebs H, Meißner UG. Precision nucleon-nucleon potential at fifth order in the chiral expansion. *Phys Rev Lett*. (2015) **115**:122301. doi: 10.1103/PhysRevLett.115.122301
82. Epelbaum E, Krebs H, Meißner UG. Improved chiral nucleon-nucleon potential up to next-to-next-to-next-to-leading order. *Eur Phys J A*. (2015) **51**:53. doi: 10.1140/epja/i2015-15053-8
83. Ekström A, Jansen GR, Wendt KA, Hagen G, Papenbrock T, Carlsson BD, et al. Accurate nuclear radii and binding energies from a chiral interaction. *Phys Rev C*. (2015) **91**:051301. doi: 10.1103/PhysRevC.91.051301
84. Piarulli M, Girlanda L, Schiavilla R, Navarro Pérez R, Amaro JE, Ruiz Arriola E. Minimally nonlocal nucleon-nucleon potentials with chiral two-pion exchange including Δ resonances. *Phys Rev C*. (2015) **91**:024003. doi: 10.1103/PhysRevC.91.024003
85. Piarulli M, Girlanda L, Schiavilla R, Kievsky A, Lovato A, Marcucci LE, et al. Local chiral potentials with Δ-intermediate states and the structure of light nuclei. *Phys Rev C*. (2016) **94**:054007. doi: 10.1103/PhysRevC.94.054007
86. Hoferichter M, Ruiz de Elvira J, Kubis B, Meißner UG. Matching pion-nucleon roy-steiner equations to chiral perturbation theory. *Phys Rev Lett*. (2015) **115**:192301. doi: 10.1103/PhysRevLett.115.192301
87. Gross F, Stadler A. Covariant spectator theory of *np* scattering: phase shifts obtained from precision fits to data below 350 MeV. *Phys Rev C*. (2008) **78**:014005. doi: 10.1103/PhysRevC.78.014005
88. Pérez RN, Amaro JE, Arriola ER. Coarse-grained potential analysis of neutron-proton and proton-proton scattering below the pion production threshold. *Phys Rev C*. (2013) **88**:064002. doi: 10.1103/PhysRevC.88.064002
89. The EDDA Collaboration. A precision measurement of PP elastic scattering cross-sections at intermediate energies. *Eur Phys J A*. (2004) **22**:125–48. doi: 10.1140/epja/i2004-10011-3
90. Stoks V, de Swart JJ. Comparison of potential models with the pp scattering data below 350 MeV. *Phys Rev C*. (1993) **47**:761–7. doi: 10.1103/PhysRevC.47.761
91. Arndt RA, Strakovsky II, Workman RL. Updated analysis of NN elastic scattering data to 1.6 GeV. *Phys Rev C*. (1994) **50**:2731–41. doi: 10.1103/PhysRevC.50.2731
92. Jentschura UD, Matveev A, Parthey CG, Alnis J, Pohl R, Udem T, et al. Hydrogen-deuterium isotope shift: from the $1S-2S$-transition frequency to the proton-deuteron charge-radius difference. *Phys Rev A*. (2011) **83**:042505. doi: 10.1103/PhysRevA.83.042505
93. Stoks VGJ, Klomp RAM, Rentmeester MCM, de Swart JJ. Partial-wave analysis of all nucleon-nucleon scattering data below 350 MeV. *Phys Rev C*. (1993) **48**:792–815. doi: 10.1103/PhysRevC.48.792
94. Briscoe WJ, Strakovsky II, Workman RL. *SAID Partial-Wave Analysis Facility*. Data Analysis Center, The George Washington University. (Unpublished) (2007).
95. Arndt RA, Briscoe WJ, Strakovsky II, Workman RL. Updated analysis of *NN* elastic scattering to 3 GeV. *Phys Rev C*. (2007) **76**:025209. doi: 10.1103/PhysRevC.76.025209

Conflict of Interest: The authors declare that the research was conducted in the absence of any commercial or financial relationships that could be construed as a potential conflict of interest.

Copyright © 2020 Rodriguez Entem, Machleidt and Nosyk. This is an open-access article distributed under the terms of the Creative Commons Attribution License (CC BY). The use, distribution or reproduction in other forums is permitted, provided the original author(s) and the copyright owner(s) are credited and that the original publication in this journal is cited, in accordance with accepted academic practice. No use, distribution or reproduction is permitted which does not comply with these terms.

frontiers in Physics

REVIEW
published: 25 February 2020
doi: 10.3389/fphy.2020.00029

Analyzing the Nuclear Interaction: Challenges and New Ideas

*Andreas Ekström**

Department of Physics, Chalmers University of Technology, Gothenburg, Sweden

This review presents some of the challenges in constructing models of atomic nuclei starting from theoretical descriptions of the strong interaction between nucleons. The focus is on statistical computing and methods for analyzing the link between bulk properties of atomic nuclei, such as radii and binding energies, and the underlying microscopic description of the nuclear interaction. The importance of careful model calibration and uncertainty quantification of theoretical predictions is highlighted.

Keywords: nuclear interactions, chiral effective field theory, model calibration, uncertainty quantification, optimization, Bayesian parameter estimation

1. INTRODUCTION

The *ab initio* approach to describe atomic nuclei and nuclear matter is grounded in a theoretical description of the interaction between the constituent protons and neutrons. The long-term goal with this course of action is to construct models to describe and analyze the properties of nuclear systems with maximum predictive power. It is of course well-known that the elementary particles of the strongly interacting sector of the Standard Model are quarks and gluons, not protons and neutrons. However, since the relevant momentum scales of typical nuclear structure phenomena are low enough to not resolve the internal degrees of freedoms of nucleons, it is reasonable to model the nucleus as a collection of strongly interacting and point-like nucleons. This idea has inspired significant efforts aimed at developing algorithms and mathematical approaches for solving the many-nucleon Schrödinger equation in a bottom-up fashion and with as few uncontrolled approximations as possible (see e.g., references [1–10]), as well as a multitude of theoretical descriptions of the interaction between nucleons, at various levels of phenomenology (see e.g., references [11, 12], and references [13–15]) for comprehensive reviews on (chiral) effective field theory (EFT) methods. Reference [16] also offers a historical account of various approaches to understand the nuclear interaction.

Currently, *ab initio* modeling of atomic nuclei faces two main challenges:

- We have limited knowledge about the details of the interaction between nucleons, which in turn limits our ability to predict nuclear properties.
- Given a microscopic description of the interaction between nucleons inside a nucleus, a quantum-mechanical solution of the nuclear many-body problem is exacerbated by the curse of dimensionality.

There is however continuous progress on both frontiers, and attempts at quantifying the uncertainty of model predictions are beginning to emerge in the community. Rapid algorithmic advances in combination with a dramatic increase in available computational resources make it possible to employ several complementary mathematical methods for solving the nuclear Schrödinger equation. We can nowadays generate numerical representations of microscopic many-nucleon wavefunctions, for selected medium-mass and heavy-mass nuclei, with a rather impressive precision. Although several observables remain beyond the

OPEN ACCESS

Edited by:
Laura Elisa Marcucci,
University of Pisa, Italy

Reviewed by:
Maria Piarulli,
Washington University in St. Louis, United States
Giuseppina Orlandini,
University of Trento, Italy

***Correspondence:**
Andreas Ekström
andreas.ekstrom@chalmers.se

Specialty section:
This article was submitted to Nuclear Physics, a section of the journal Frontiers in Physics

Received: *04 December 2019*
Accepted: *31 January 2020*
Published: *25 February 2020*

Citation:
Ekström A (2020) Analyzing the Nuclear Interaction: Challenges and New Ideas. Front. Phys. 8:29. doi: 10.3389/fphy.2020.00029

reach of state-of-the-art models, e.g., most properties associated with highly collective states, we can still describe certain classes of observables rather well, such as total ground-state binding energies and radii, and sometimes low-energy excitation spectra. We are thus capable of analyzing experimentally relevant nuclei directly in terms of a quantum mechanical description of the interaction between its constituent nucleons. Indeed, the list of, sometimes glaring, discrepancies between theory and experiment furnish some of the most interesting nuclear physics questions at the moment (see e.g., references [17–23]). Many of these efforts are aimed at understanding the nuclear binding mechanism, the location of the neutron dripline, the existence of shell-closures and magic numbers in exotic systems, and the emergence of nuclear saturation.

State-of-the-art theoretical analyses of experimental data indicate a large and non-negligible systematic uncertainty in the description of bulk nuclear observables (see e.g., reference [24]). Given the high-precision of modern many-body methods, much of this uncertainty can be traced to the description of the interaction potential. Although there exists *ab initio* models that describe nuclei rather well, albeit in a limited domain, it is less clear why other models sometimes fail. Indeed, the $\mathrm{NNLO_{sat}}$ interaction potential [25] reproduces several key experimental binding energies and charge radii for nuclei up to mass $A \sim 50$ [23, 26–28], while the so-called 1.8/2.0 (EM) interaction potential [29, 30] reproduces binding energies and low-energy spectra up to mass $A \sim 100$ [26, 31–35] while radii are underestimated. The origin of the differences between these potentials is unknown. It is of course the role of nuclear theory to close the gap between theory and experiment by developing and refining the theoretical underpinnings of the model. But given the complex nature of atomic nuclei, there is significant value in trying to quantify, or estimate, the detailed structure of the observed theoretical uncertainty. This might provide important clues about where we should focus our efforts. There exists well-defined statistical inference methods that can provide additional guidance, and several ongoing projects are currently focused on applying statistical computing methods in the field of *ab initio* modeling. The topic of uncertainty quantification in nuclear physics has been discussed at a series of workshops on Information and Statistics in Nuclear Experiment and Theory (ISNET). Recent developments in this field are documented in the associated focus issue published in Journal of Physics G [36]. A second focus issue has just been announced, and the first few papers are already published.

In sections 2 and 3 of this paper I will review a selection of recent results and often applied methods for calibrating *ab initio* models. In sections 4 and 5 I will discuss some of the recently emerging strategies for making progress using statistical computing and Bayesian inference methods. The aim is to provide an overview of selected accomplishments in the field of statistical inference and statistical computing with *ab initio* models of atomic nuclei. Hopefully, this paper can serve as a brief introduction to practitioners who wish to learn about ongoing developments and possible future directions.

As a final remark, in this paper I will try to consistently use the word *model* when referring to *any* current method for theoretically describing the properties of atomic nuclei, including descriptions that claim to be building on more fundamental underpinnings, such as EFT. One can certainly make a finer distinction between models, EFTs, and theories. As outlined in reference [37]; theories provide a unified framework, categorization, and the joint language used for discussions; EFTs capture physics at a given momentum scale; and models can be used to study aspects of a theory, increase understanding, and provide intuition.

2. *AB INITIO* MODELS OF NUCLEAR MANY-BODY SYSTEMS

An *ab initio* model is here defined as a description that is based on a state $|\Psi\rangle$ that solve the many-nucleon Schrödinger equation

$$[\hat{T} + \hat{V}(\vec{\alpha})]|\Psi\rangle = E|\Psi\rangle. \quad (1)$$

In this schematic representation, $\hat{T}$ is the total kinetic energy operator for the A-nucleon system, $\hat{V}(\vec{\alpha})$ is the potential energy operator for the interaction between the nucleons, and E is the total energy of the system in the state represented by $|\Psi\rangle$. The potential operator term depends on a set of parameters $\vec{\alpha}$ that governs the strengths of the various interaction pieces in the potential. In the context of EFT, these parameters are often referred to as low-energy constants (LECs). Given a particular expression for the potential $\hat{V}$, with numerical values for the parameter vector $\vec{\alpha}$, and a mathematical method to solve Equation (1) for e.g., the state $|\Psi\rangle$ with lowest energy, it is in principle possible to quantitatively compute the expectation value for any observable $\hat{\mathcal{O}}$ with respect to this state, e.g., its charge radius. Of course the trustworthiness of the result and its level of agreement with experimental data can vary dramatically between different models, i.e., combinations of potentials and many-body methods.

I will denote an *ab initio* model with $M(\vec{\alpha}, \vec{x})$. It is defined as the combination of a definite expression for the potential $\hat{V}(\vec{\alpha})$, and a method for solving the Schrödinger equation. The vector $\vec{x}$ is a set of control inputs that specify all necessary settings, such as nucleon numbers, which observable to compute, values of the fundamental physical constants, and algorithmic settings for the mathematical method used for solving Equation (1). Once a set of numerical values for $\vec{\alpha}$ has been determined, a subset of the control inputs $\vec{x}$ of the model can be varied to make model predictions, preferably at some physical setting, for e.g., exotic nuclei where we cannot easily make measurements. Provided that the form of the potential operator $\hat{V}$ and relevant physical constants remain the same, and the model parameters $\vec{\alpha}$ were calibrated carefully, it is of course possible to transfer the vector $\vec{\alpha}$ between *ab initio* models based on different methods for solving the many-nucleon Schrödinger equation. This is also in line with a physical interpretation of the parameters $\vec{\alpha}$ that elevate them to a status beyond being simple tunable parameters inherent to a specific model with the sole purpose of achieving a good fit to calibration data. This will be discussed further in section 3.

One of the most exciting developments in nuclear theory is that we nowadays have access to a range of methods for solving Equation (1) with very high numerical precision for selected isotopes and observables. This gives us the opportunity to compare model predictions with experimental data to learn more about the elusive structure of the interaction between nucleons. However, such an analyses require careful statistical interpretation of the theoretical results. In particular a sensible estimate of the uncertainty associated with a theoretical prediction. Indeed, only with reliable theoretical errors is it possible to infer the significance of a disagreement between experiment and theory, which in turn may hint at new physics.

2.1. Chiral Potentials and the Strong Interaction Between Nucleons

On a fundamental level, the atomic nucleus is a quantum mechanical and self-bound system of interacting nucleons. In turn these particles are composed of three quarks whose mutual interactions are described well by the Standard Model of particle physics. As such, starting from the Standard Model it should be possible to account for all observed phenomena also in atomic nuclei, besides possible signals of beyond Standard Model physics. However, to theoretically understand the emergence of nuclei from the Standard Model is an open problem, and linking the quantitative predictions of atomic nuclei to the dynamics of quarks and gluons is a central challenge in low-energy nuclear theory. Although, viewing the atomic nucleus as a (color-singlet) composite multi-quark system is not the most economical choice. Indeed, the strong interaction, which is the most important component for nuclear binding and well-described by quantum chromodynamics (QCD), is non-perturbative in the low-energy region inhabited by atomic nuclei. Non-perturbative Monte Carlo sampling of the quantum fields of QCD amounts to a computational problem of tremendous proportions. This strategy, referred to as lattice QCD, is expected to require at least exascale resources for a realistic analysis of even the lightest multi-nucleon systems. Without any unforeseen disruptive technology, this approach will not provide an operational method for routine analyses of nuclei. For the cases where numerically converged results can be obtained, lattice QCD offers a unique computational laboratory for theoretical studies of QCD in a low-energy setting (see e.g., references [38, 39]).

The description of nuclei should nevertheless build on QCD, or the Standard Model in general. A turning point in the development of QCD-based descriptions of the nuclear interaction came when EFTs of QCD [40] arrived also to many-nucleon physics [41]. An EFT formulates the dynamics between low-energy degrees of freedom, e.g., nucleons and pions, in harmony with some assumed symmetries of an underlying theory, e.g., QCD, and any high-energy dynamics, e.g., quark-gluon interactions, are integrated out of the theory. The resulting chiral effective Lagrangian models the low-energy interactions between two or more nucleons in terms of pion exchanges between nucleons and the high-energy dynamics is incorporated as zero-ranged contact interactions. This approach introduces several model parameters referred to as low energy constants (LECs). They were denoted with $\vec{\alpha}$ above, and play a central role during the model calibration discussed below. The notion of high- and low-energy scales in EFT requires the presence of at least two scales in the physical system under study. An EFT formally exploits this scale separation to expand observables in powers of the low-energy (soft) scale over the high-energy (hard) scale, and in chiral EFT the resulting ratio is often denoted

$$Q = \frac{\max[m_\pi, k]}{\Lambda_b} \tag{2}$$

where, in the case of chiral EFT, the soft scales are m_π and k, the pion mass and a typical external momentum scale, respectively. The hard scale is denoted Λ_b and is set by the e.g., the nucleon mass M_N. Depending on the system under study, one can always try to exploit existing scale separations to construct other kinds of EFTs in nuclear physics, e.g., pion-less EFT [42], vibrational EFT [43], or chiral perturbation theory (the prototypical EFT of QCD) [44]. In the following, I will only discuss results from *ab initio* models based on chiral EFT, i.e., a pion-full EFT, but many of the methods can be generally applied.

In chiral EFT, the nuclear interaction potential V is analyzed as an order-by-order expansion in terms of Q^ν and organized following the principles of an underlying power counting (PC). Terms at a higher chiral expansion-orders ν should be less important than terms at a lower orders. Potentials expanded to higher orders are expected to describe data better. Higher chiral orders contain more involved pion exchanges and polynomial nucleon-contacts of increasing exponential dimension, and therefore more undetermined model parameters $\vec{\alpha}$ to handle during the calibration stage. To provide some detail about the chiral potentials: the leading-order (LO) typically consists of the familiar one-pion exchange interaction plus a nucleonic contact-potential. The structure of the contact potential, and the exact treatment of sub-leading orders vary depending on the PC. Still, typical chiral potentials include at most contributions up to a handful of chiral orders, e.g., next-to-next-leading order (NNLO) and next-to-next-to-next-to-leading order (N3LO), and the total number of LECs, i.e., undetermined model parameters, range between ∼10 and 20, sometimes a few more, at such chiral orders. Several important contributions to the two-, three-, and four-nucleon interactions at higher orders in the chiral expansion have also been worked out [45–50]. At N5LO, a new set of 26 contact LECs appear, bringing the total number of contacts to 50. Some of the unique advantages of chiral EFT descriptions of the nuclear interaction are the natural emergence of two-, three-, and many-nucleon interactions [51–55], the consistent formulation of quantum currents, e.g., with respect to electroweak operators [56–62], and a clear connection with the pion-nucleon Lagrangian which makes it possible to link nuclei with low-energy pion-nucleon scattering processes [63]. For a detailed account of chiral EFT potentials (see references [13–15]).

To ensure steady progress toward a realistic *ab initio* model for atomic nuclei, we need to critically examine and evaluate the quality and predictive power of different theoretical approaches and model predictions. To this end it is crucial to equip all

quantitative theoretical results with uncertainties, and this is where another advantageous aspect of EFT comes into play. It promises to deliver a handle on the systematic uncertainty of a theoretical prediction. Indeed, on a high level the EFT expansion for an observable $\mathcal{O}$ can be written

$$\mathcal{O} = \mathcal{O}_0 \sum_{\nu=0}^{\infty} c_\nu Q^\nu, \tag{3}$$

where $\mathcal{O}_0$ is the first term in the above expansion, and c_ν are dimensionless expansion coefficients. Here, and in the following, the LO result ($\mathcal{O}_0$) was pulled out in front of the sum to set the overall scale. One could equally well use the experimental value for $\mathcal{O}$ or the highest-order calculation to set the scale of the observable expansion. If we are dealing with an EFT, one should expect the expansion coefficients to be of natural size such that predictions at successive chiral orders are smaller by a factor of Q. See also references [64, 65] for discussions on how to assess the convergence of data. In an actual calculation, the order-by-order description of $\mathcal{O}$ is truncated at some finite order k, which induces a truncation error δ_k in the prediction. The underlying EFT description then, in principle, allows us to determine the formal structure of the truncation error

$$\delta_k = \mathcal{O}_0 \sum_{\nu=k+1}^{\infty} c_\nu Q^\nu. \tag{4}$$

This type of handle on the theoretical uncertainty in a prediction is not present in purely phenomenological descriptions of the nuclear interaction, such as the Argonne V18 potential [11] or the CD-Bonn potential [12]. Despite all of the promised advantages of chiral EFT, it should be pointed out that much work remains to be done regarding the analysis and theoretical underpinnings of chiral EFT, in particular the formulation of a PC that, arguably, fulfills the field theoretic requirements for an EFT of QCD (see e.g., references [66–73]), for various views on this topic. Indeed, one cannot yet confidently claim that the uncertainty estimates in *ab initio* predictions of nuclear observables based on proposed chiral EFT interactions are linked to missing physics at the level of the effective Lagrangian. The details of the PC, regularization approach, and chosen maximum chiral order k in Equation (3), are some of many possible choices that give rise to the rich landscape of different chiral interactions in nuclear theory. Although there is a flurry of activity, and far from clear which is the best way to proceed, there is tremendous overarching value to organize the model analysis according to the fundamental ideas and expectations of EFT, most importantly the promise of order-by-order improvement.

3. MODEL CALIBRATION

The goal of model calibration is to learn about the parameter of the model using a pool of calibration data. This can mean many different things depending on the situation, and in this section I will discuss a few representative model calibration examples from *ab initio* nuclear theory.

Assume that we have a model $M(\vec{\alpha}; \vec{x})$ that consists of a method for solving the Schrödinger equation and some theoretical description of the nuclear interaction, e.g., a particular interaction potential from chiral EFT, and we do not know the permissible values for $\vec{\alpha}$. The vector $\vec{\alpha} = [\alpha_1, \alpha_2, \ldots, \alpha_N]$ denotes the N physically relevant and adjustable calibration parameters of model M, and the vector $\vec{x}$ denotes the set of control inputs. The adjustable parameters of interest will typically correspond to the LECs of the nuclear interaction potential, and the vector $\vec{x}$ will contain e.g., proton- and neutron-numbers, observable type, or some kinematical setting. In principle the model might contain additional adjustable parameters that for some reasons can be considered as constants. For instance, we typically do not consider the pion mass as a calibration parameter, although the variation of such fundamental properties can also play an important role (see e.g., references [74, 75]). The choice of many-body method will depend on which class of observables is targeted, either during prediction or calibration. For instance, coupled-cluster theory will perform very well for nuclei in the vicinity of closed shells and Faddeev integration will be able to access the positive energy spectrum of the three-nucleon Hamiltonian. Throughout, I will implicitly assume that the model is realized only on a computer, i.e., M is defined through some computer code, and there is no stochastic element present in the output. This means that each time the model is evaluated with the same input and settings, we will basically get the same result.

To calibrate the parameters, suppose that we have a set of n experimental observations compiled in a data vector $D = [z_1, z_2, \ldots, z_n]$. They correspond to particular settings $\vec{x}_1, \vec{x}_2, \ldots, \vec{x}_n$ of the control variables, to produce model outputs for e.g., ground-state energies for light nuclei or scattering cross sections at selected scattering momenta. We can link the data points to the model outputs via the following relation

$$z_i = M(\vec{\alpha}, \vec{x}_i) + \delta(\vec{x}_i) + \varepsilon_i. \tag{5}$$

This expression relates the reality of measurement with our model, and includes a so-called model discrepancy term δ, that depends on the control variable $\vec{x}_i$. The measurement error is denoted with ε_i. In cases where the measurement is accompanied with *zero* uncertainty, something that is highly unlikely of course, the model discrepancy term represents the entire difference between the model and reality. The theoretical discrepancy δ is not physics *per se*, but should rather be interpreted as a random variable of statistical origin, informed via domain knowledge.

The model discrepancy term can be partitioned into at least three terms

$$\delta(\vec{x}_i) = \delta_{\text{interaction}}(\vec{x}_i) + \delta_{\text{many-body}}(\vec{x}_i) + \delta_{\text{numerical}}(\vec{x}_i), \tag{6}$$

and they represent the neglected or missing physics in the theoretical description of the nuclear interaction, neglected or missing many-body correlations in the mathematical solution of the many-body Schrödinger equation, and any numerical errors arising due to algorithmic approximations in the implementation of the computer model, respectively. We are currently most interested in understanding $\delta_{\text{interaction}}$ in situations where we,

to a good approximation, can neglect $\delta_{\text{many-body}}$ and $\delta_{\text{numerical}}$. Thus, in most of the literature, the dominant part of the model discrepancy originates from the chiral EFT description of the nuclear interaction. It should be pointed out that the discrepancy term of the many-body method can be quite large for many types of observables. However, *ab initio* methods are often applied wisely, and there exists plenty of domain knowledge regarding which many-body methods that are best suited for different kinds of observables. Yet, it is not easy to set bounds on this discrepancy *a priori*. Comparison between several complementary *ab initio* models provides important validation [76–78]. Although challenging, it would be of great value to quantify the many-body discrepancy more carefully. Finally, the last term in Equation (6) is currently not the dominant part of the discrepancy, provided that the computer code has been benchmarked.

Two related questions immediately arise: (i) what is the impact of the discrepancy term $\delta(\vec{x}_i)$ on the inference about the model parameters $\vec{\alpha}$? and (ii) what happens if we neglect all sources of model discrepancy during model calibration?

Let us consider the second question, since it is easier and also sheds light on the first one. Ignoring $\delta(\vec{x}_i)$ in Equation (5) leaves us with the following expression

$$z_i = M(\vec{\alpha}, \vec{x}_i) + \varepsilon_i. \tag{7}$$

This is the conventional starting point in nuclear model calibration. If one also assumes that the measurement errors ε_i have finite variance, then the principle of maximum entropy dictates that the likelihood of the data is normally distributed. For independent errors, this leads to the canonical expression for the likelihood

$$\begin{aligned} P(D|\vec{\alpha}, M, \sigma) &= \prod_{i=1}^{n} \frac{1}{\sqrt{2\pi}\sigma_i} \exp\left\{ -\frac{(z_i - M(\vec{\alpha}, \vec{x}_i))^2}{2\sigma_i^2} \right\} \\ &= \left[\prod_{i=1}^{n} \frac{1}{\sqrt{2\pi}\sigma_i} \right] \exp\left\{ -\frac{1}{2} \sum_{j=1}^{n} \frac{(z_j - M(\vec{\alpha}, x_j))^2}{\sigma_j^2} \right\} \\ &= \left[\prod_{i=1}^{n} \frac{1}{\sqrt{2\pi}\sigma_i} \right] \exp\left\{ -\frac{1}{2} \chi^2(\vec{\alpha}) \right\}. \end{aligned} \tag{8}$$

Here, the notation $P(X|Y)$ denotes the probability density function (pdf) of X conditioned on Y. The structure of the likelihood remains the same for correlated measurement errors, although one must employ the full covariance matrix instead of only the diagonal terms σ_j^2 to represent the variance of the data. Model calibration in *ab initio* nuclear theory is typically formulated as a maximum likelihood problem. This boils down to finding the optimal, or best-fitting, parameters $\vec{\alpha}_\star$ that minimize the exponent in Equation (8). We are thus facing a mathematical optimization (minimization) problem

$$\vec{\alpha}_\star = \underset{\vec{\alpha} \in \Omega}{\arg\min}\ \chi^2(\vec{\alpha}), \tag{9}$$

of finding the point that fulfills $\chi^2(\vec{\alpha}_\star) \leq \chi^2(\vec{\alpha})$ for all $\vec{\alpha} \in \Omega$, where Ω represents the parameter domain. In general, this is an intractable problem unless we have detailed information about $\vec{\alpha}$ or that the parameter domain is discrete and contains a finite number of points. In reality, we are trying to find *local* minimizers to $\chi^2(\vec{\alpha})$, i.e., points $\vec{\alpha}_\star$ for which $\chi^2(\vec{\alpha}_\star) \leq \chi^2(\vec{\alpha})$ for all $\vec{\alpha} \in \Omega$ close to $\vec{\alpha}_\star$.

For *ab initio* models, optimization of the likelihood function typically proceeds in several steps [11, 12, 79–82]. First, the parameters, i.e., the LECs in chiral EFT, are calibrated such that the model optimally reproduces nucleon-nucleon scattering phase-shifts from published partial-wave analyses [83, 84]. This typically yield model parameters confined to some narrow range of values. Although each scattering phase-shift only depends on a limited subset of the entire vector of model parameters $\vec{\alpha}$, this stage still benefits from using mathematical optimization algorithms, such as the derivate-free algorithm called pounders [85, 86]. In a next step, the results from the phase-shift optimization serves as the starting point for a second round of parameter optimization where all model parameters are varied to best reproduce thousands of nucleon-nucleon scattering cross sections up to scattering energies in the vicinity of the pion-production threshold.

Minimizing the χ^2 in Equation (8) for nucleon-nucleon interaction potentials with respect to nucleon-nucleon scattering data[1] has been the workhorse of model calibration in nuclear theory for decades[2]. Since long, the figure of merit for a nuclear interaction potential has been the χ^2-per-datum value. If this value is close to unity for some particular parameterization $\vec{\alpha}_\star$, then the corresponding potential is dubbed to be "high-precision." This is beginning to change. Only for models M, where the model-discrepancy is in fact negligible this approach can be justified. Otherwise, chasing a low χ^2 leads down the path of significant over-fitting, with unreliable predictions as a consequence. For the calculation of nucleon-nucleon scattering phase shifts and cross sections it is valid to ignore $\delta_{\text{many-body}}$ and $\delta_{\text{numerical}}$ since the corresponding equations are can be solved more or less numerically exactly. However, since we clearly cannot claim to have a zero-valued $\delta_{\text{interaction}}$ term, the χ^2-per-datum with respect to nucleon-nucleon scattering data is not the optimal measure to guide future efforts in nuclear theory. Before and during the development of *ab initio* many-body methods and EFT principles, when it was very unclear how to understand the concept of model discrepancy in nuclear theory, it was certainly more warranted to benchmark nuclear potentials based solely on a straightforward χ^2 value.

State-of-the-art interaction potentials also contain three-nucleon force terms. Although some of the parameters in chiral EFT are shared between two- and three-nucleon terms, there exists a subset of parameters inherent only to the three-nucleon interaction. Such parameters must be determined using observables from $A > 2$ systems. Arguably, all parameters

[1] A recent compilation of scattering data that is typically employed for this is provided in reference [84].

[2] The χ^2 function employed for nucleon-nucleon scattering data is slightly more involved to encompass partially correlated measurements (see e.g., [87]).

of a chiral potential should be optimized simultaneously to a joint dataset D. The easiest approach is to employ also e.g., the binding energies and charge radii of ^{3,4}He and ^{3}H. Unfortunately, there exists a universal correlation between the binding energies of ^{3}H and ^{4}He, the so-called Tjon line [88]. Also the radii and binding energies exhibit a strong correlation. Altogether, this reduces the information content of this data. Fortunately, it was demonstrated in reference [89] that the beta decay of ^{3}H can add valuable, although limited [90], information about the parameters in the three-nucleon interaction, and this has been employed in several works, as indicated by the long list of citations of reference [89]. Recently, selected three-nucleon scattering observables have been added to the pool of calibration data [91, 92], however not routinely since it is still computationally quite costly to evaluate the *ab initio* models for such observables. There are indications that it is necessary to include also data from nuclei heavier than ^{4}He to learn about the parameters in *ab initio* models. This is discussed in section 3.2.

Ignoring the $\delta_{\text{interaction}}$ discrepancy terms during model calibration can have serious consequences. Most importantly, this reduces the LECs to tuning parameters without *any* physical meaning. Indeed, in the strive to replicate the data at any cost, the numerical values can be driven far away from the *true* values of the model. At some point, continued tuning of the parameters induces over-fitting and the model will pick up on the noise in the data. Naturally, this leads to poor predictive power. With increasing amounts of data, the optimization process will converge with increasing certainty to false values for $\vec{\alpha}$. A pedagogical introduction to the statistics of model discrepancies and a physics example is provided in reference [93].

A total model discrepancy, according to Equation (6), was included in *ab initio* model calibration for the first time in reference [80]. The parameters in a set of chiral interactions at LO, NLO, and NNLO were optimized using nucleon-nucleon, and pion-nucleon scattering data. The terms in the three-nucleon interaction were simultaneously informed using bound-state observables from $A = 2, 3$ nuclei. The details of the analysis and results can be found in the original paper. The discrepancy terms were interpreted as uncorrelated errors and added in quadrature with the data uncertainties, leading to a slight modification of the corresponding χ^2 function

$$\chi^2 = \sum_{j=1}^{n} \frac{(z_j - M(\vec{\alpha}, x_j))^2}{\sigma^2_{\text{data},J} + \sigma^2_{\text{interaction},j} + \sigma^2_{\text{many-body},j} + \sigma^2_{\text{numerical},j}}. \tag{10}$$

The interaction discrepancy was constructed from the EFT assumption that the external momenta flowing through the interaction diagrams scale as some power corresponding to the truncation of the chiral expansion, in accordance with Equation (4). The intrinsic scale of this error was solved for self-consistently by requiring that the χ^2-per-datum should approach unity providing that the model error is correctly estimated. This implicitly assumes a correct estimate of the number of statistical degrees of freedom. Something that cannot be easily estimated for non-linear χ^2 functions [94].

To summarize, although the inclusion of model discrepancies is preferred, it is not without problems. To blindly include a term $\delta(\vec{x}_i)$ to capture model discrepancies in the process of model calibration can lead to statistical confounding between $\vec{\alpha}$ and a general discrepancy function $\delta(\cdot)$ [93]. This means that the model parameters and the discrepancy term are not identifiable and we only recover a some joint pdf for the two components. Indeed, for any $\vec{\alpha}$ there is a $\delta(\cdot)$ given by the difference between model and reality. To make progress requires us to specify some *a priori* ranges for $\vec{\alpha}$ and/or $\delta(\cdot)$. Or in the language of Bayesian inference, we need to specify the prior pdf for the model parameters and the theory uncertainties. This is partly related to approaches where one augments the χ^2 function with a penalty term to constrain the values of the model parameters (see e.g., reference [95]). For EFT descriptions of the nuclear interaction one can argue that the LECs should maintain values of order unity, if expressed in units of the breakdown scale, and the discrepancy could follow the pattern of Equation (4). To adequately represent the discrepancy term in nuclear models is ongoing research, and it appears advantageous to reformulate model calibration as a Bayesian inference problem, see section 4.

3.1. Hessian Error Analysis

At the optimum parameter point $\vec{\alpha}_\star$, a Taylor expansion of the χ^2 function to second order gives

$$\chi^2(\vec{\alpha}_\star + \Delta\vec{\alpha}) \approx \chi^2(\vec{\alpha}_\star) + \frac{1}{2}(\Delta\vec{\alpha})^T H(\Delta\vec{\alpha}), \quad \text{where} \quad H_{ij} = \left.\frac{\partial^2\chi^2(\vec{\alpha})}{\partial\alpha_i\partial\alpha_j}\right|_{\vec{\alpha}=\vec{\alpha}_\star}, \tag{11}$$

where H denotes a Hessian matrix, the inverse of which is proportional to the covariance matrix for the model parameters [96]. Contracting the parameter-Jacobian of any model prediction with this covariance matrix yields the standard error propagation result of the parameter uncertainties. For the conventional χ^2 function, the parameter covariances reflect the impact of the experimental uncertainties on the precision of the optimum and predicted observables. Sometimes, this is referred to as statistical uncertainties, which is a bit confusing since all uncertainties are statistical in nature. See **Figure 1** for an example result of applying a parameter covariance matrix to obtain the joint pdf for the ^{4}He ground-state energy and the ^{2}H point-proton radius, two important few-nucleon observables. This particular result is taken from reference [80], where in fact a model discrepancy term $\delta(\cdot)$ was incorporated during the optimization, thus in this particular case the covariances reflect more than just the measurement noise. See e.g., references [97–102] for details about statistical error analysis and illuminating examples of forward error propagation in *ab initio* nuclear theory.

To extract the covariance matrix requires computation of the second-order derivatives of the χ^2 function with respect to the model parameters. The general process of numerically differentiating an *ab initio* model with respect to $\vec{\alpha}$ is significantly simplified, and numerically much more precise, with the use of automatic differentiation (AD) [80]. This corresponds

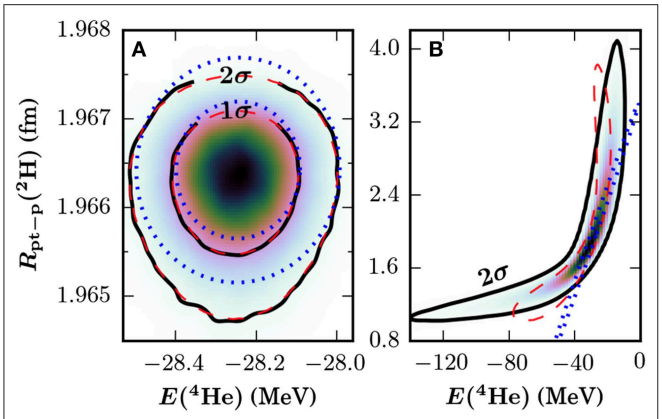


FIGURE 1 | Joint distribution for the ground-state energy of ^{4}He (x-axis) and the point-proton radius of ^{2}H (y-axis) for **(A)** the chiral potential NNLO$_{\mathrm{sim}}$ and **(B)** the chiral potential NNLO$_{\mathrm{sep}}$ (see reference [80]). Contour lines for the distributions are shown as black solid lines, while blue dotted (red dashed) contours are obtained assuming a linear (quadratic) dependence on the LECs for the observables.

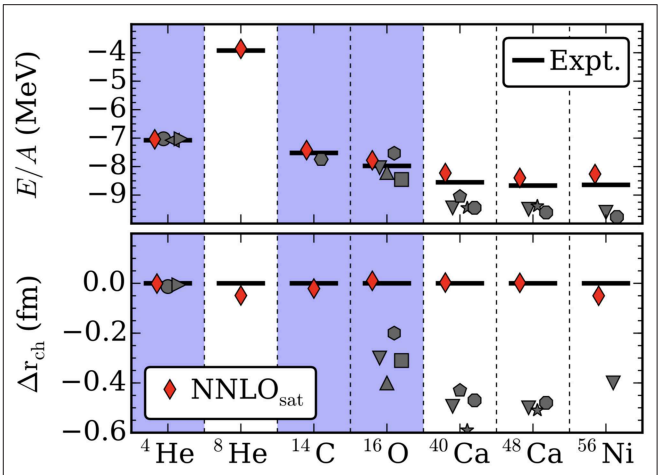


FIGURE 2 | Ground-state energies per nucleon (top) and differences between theoretical and experimental charge radii (bottom) for selected light and medium-mass nuclei and results from ab initio computations. The red diamonds mark results based on the chiral interaction NNLO$_{\mathrm{sat}}$. The blue columns indicate which nuclei where included in the optimization of the LECs in NNLO$_{\mathrm{sat}}$, while the white columns are predictions. Gray symbols indicate other chiral interactions.

to applying the chain rule of differentiation on a function represented as a computer code. It relies on the principle that any computer code, no matter how complicated always executes a set of elementary arithmetic operations on a finite set of elementary functions (exponentiation, logarithmization, etc). To implement AD requires modification of the original computer code, e.g., operator overloading via third-party libraries. Once implemented, AD also enables application of more advanced derivative-based optimization algorithms and Markov chain Monte Carlo methods [103] with the computer model M. An alternative, and derivative-free approach, to computing the Hessian matrix for forward error propagation is to employ Lagrange multipliers [104]. This method is more robust, but also more computationally demanding to carry out. From a practical and computational perspective, if one considers to use Lagrange multipliers, one should also look into performing a Bayesian analysis (see section 4).

3.2. Selecting Calibration Data

It is preferable to use data corresponding to observables that are computationally cheap to evaluate, and if possible with model settings corresponding to low $\delta(\vec{x})_{\mathrm{many-body}}$ discrepancies. One should also strive to include data with highly complementary information content that constrain a maximum amount of linearly independent combinations of model parameters.

The conventional approach to calibrate *ab initio* models is to use only data from $A \lesssim 4$ nuclei, as was discussed above. It was observed in reference [25] that the additional inclusion of ground-state energies and charge radii of selected carbon and oxygen isotopes dramatically increases the predictive power of models for bulk properties of nuclei up to the medium-mass nickel region (see **Figure 2**). This calibration strategy led to the construction of the so-called NNLO$_{\mathrm{sat}}$ interaction. The strategy to include data from selected $A > 4$ nuclei was also used in the construction of the Illinois 3NF presented in reference [105].

From a quantitative perspective, the advent of models capable of accurate predictions is of course an important step forward and has proven very useful [26, 27, 106, 107].

The major drawback of any model based on the NNLO$_{\mathrm{sat}}$ interaction is the lack of quantified theoretical uncertainties. This is quite common also for *ab initio* models based on other interaction potentials. At the moment, the best we can do is to estimate the truncation error using Equation (4). This requires additional and sub-leading chiral-order potentials using the same optimization protocol, e.g., LO$_{\mathrm{sat}}$ and NLO$_{\mathrm{sat}}$, which do not exist. The calibration of such models require an even more careful inclusion of model discrepancies. This is discussed more in section 4. One can certainly argue that it becomes even more important to quantify the theory errors for models that we strongly believe will make accurate predictions, like the ones based on the NNLO$_{\mathrm{sat}}$ interaction. Otherwise we are limited in our ability to assess discrepancies with respect to experiment. This argument applies equally well to models based on e.g., the 1.8/2.0 interaction from reference [29, 30] which typically yield good predictions for binding energies and low-energy spectra. In reference [26], the prediction from *ab initio* models based on different interactions, NNLO$_{\mathrm{sat}}$ and the 1.8/2.0 interactions amongst other, were compared to estimate the overall theoretical uncertainty.

It is difficult to judge the degree of over-fitting to finite nuclei in NNLO$_{\mathrm{sat}}$. It was noted during calibration that this interaction fails to reproduce experimental nucleon-nucleon scattering cross sections for scattering momenta larger than $\sim m_\pi$. Enforcing a good reproduction of all scattering data up to e.g., the pion-production threshold most likely corresponds to over-fitting in the $A = 2$ sector. It is the role of the model discrepancy term, with appropriate priors, to balance this.

One clearly gains predictive power regarding saturation properties by including additional medium-mass data during the calibration stage. This was also observed in a lattice EFT analysis of the nuclear binding mechanism [108]. The related topic of possibly emergent nuclear phenomena like saturation, binding, and deformation of atomic nuclei is discussed further in reference [109]. Although the inclusion of a model discrepancy term while calibrating to heavier-mass data will be important, it does not solve the underlying problem of having a systematically uncertain model. It was noted in references [110–112] that the explicit inclusion of the Δ isobar in the chiral description of the nuclear interaction dramatically improves the description of nuclei while also reproducing nucleon-nucleon scattering data. A possibly fruitful way forward is to employ improved models, i.e., with explicit inclusion of the Δ isobar, that are calibrated using also data from selected heavy-mass nuclei, while systematically accounting for model discrepancies. Furthermore, it will be interesting to se how much additional information is contained in three-nucleon scattering data [91, 92, 113].

4. BAYESIAN INFERENCE

The previous section introduced the concept of model calibration and the fundamental expression in Equation (5) that relates a model with measured data. In this section I will outline the Bayesian strategy for learning about the model parameters and some existing estimates of the discrepancy term. The overarching goal is still to calibrate an *ab initio* model $M(\vec{\alpha}, \vec{x})$, and reliably predict properties of atomic nuclei. However, instead of finding a single point $\vec{\alpha}_\star$ in parameter space that maximizes the likelihood for the data, we can use Bayes' theorem to relate the data likelihood to a pdf for the model parameters themselves

$$P(\vec{\alpha}|D, M, I) = \frac{P(D|\vec{\alpha}, M, I)P(\vec{\alpha}|M, I)}{P(D|M, I)}, \tag{12}$$

where $P(\vec{\alpha}|M, I)$ denotes the prior pdf for the parameters, $P(D|\vec{\alpha}, M, I)$ denotes the likelihood of the data, the denominator $P(D|M, I)$ denotes the marginal likelihood of the data, and $P(\vec{\alpha}|D, M, I)$ denotes the sought-after posterior pdf of the model parameters. The additional I represents any other information at hand.

The Bayesian reformulation of the inference problem can at first sight appear as a subtle point, and it is easy to overlook the fundamental difference between computing the pdf for the parameters and maximizing the likelihood, i.e., frequentist inference. From a practical perspective, it is clearly advantageous to obtain a pdf for the model parameters $P(\vec{\alpha}|D, M)$. This quantity is also intuitively straightforward to interpret compared to frequentist interval estimates that might contain the true value of the unknown model parameters, e.g., confidence intervals. The prior pdf $P(\vec{\alpha}|M, I)$ for the parameters $\vec{\alpha}$ given a model M offers up front possibility to incorporate any prior knowledge (or belief) about the parameters, before we look at the data. In the case of *ab initio* modeling, an underlying EFT-description of the nuclear interaction embodies substantial prior knowledge, such as the typical magnitude of the model parameters as well as a handle on the systematic uncertainty. The Bayesian requirement of prior specification also ensures full transparency regarding the assumptions that goes into the analysis.

The existence of priors in Bayesian inference is sometimes criticized and one can argue that the scientific method should let the data speak for itself, without the explicit insertion of subjective prior belief. Inference about model parameters in terms of hypothesis tests or confidence intervals, derived from the frequency of the data, is referred to as frequentist inference. Note however that the likelihood rests on initial subjective choice(s) regarding the data model. In this review, I will maintain a practical perspective, and just recognize the usefulness of the Bayesian approach to encode prior information about the model parameters and the model discrepancy terms. Which is also required in order to handle possible confounding between the discrepancy and the model parameters [93]. Either way, it is difficult to avoid subjective choices in statistical inference involving uncertainties and limited data. In fact, one can even argue that only *subjective* probabilities exist [114].

Bayesian model calibration, sometimes called Bayesian parameter estimation, is currently emerging in *ab initio* modeling [115–117]. To get some intuition about this topic, let us look at Bayesian parameter estimation in its most simple version. This amounts to assuming a (bounded) uniform prior pdf for the model parameters $\vec{\alpha}$, i.e.,

$$P(\vec{\alpha}|M, I) \sim \mathcal{U}(\vec{a}, \vec{b}) \tag{13}$$

and adopting a data likelihood as in Equation (8). In practice, what remains is to explicitly evaluate $P(\vec{\alpha}|D, M, I)$ in Equation (12) by computing the product of the two terms in the numerator. The denominator can be neglected since it does not explicitly depend on $\vec{\alpha}$. This marginal likelihood does however matter for absolute normalization of the posterior pdf. The evaluation of the posterior can be done via brute force evaluation in some simple cases, but for computationally expensive models and/or high-dimensional parameter space typically more clever strategies are required, such as Markov chain Monte Carlo. With uniform priors, the point for the maximum posterior coincides exactly with the point obtained using maximum likelihood methods, which for normal likelihood distributions is nothing but least-squares.

The advantages of Bayesian parameter estimations becomes apparent once we include non-uniform prior knowledge, and in most cases we know a bit more about the parameters than what a simple uniform pdf reflects. The general strategies for application of Bayesian methods to calibrate EFTs are pedagogically outlined in reference [116]. To exemplify the use of priors and some of the related techniques, let us assume a Gaussian prior with zero mean for the model parameters $\vec{\alpha} = [\alpha_1, \alpha_2, \ldots, \alpha_N]$, i.e.,

$$P(\vec{\alpha}|\bar{a}, M, I) = \left(\frac{1}{\sqrt{2\pi}\bar{a}}\right)^N \exp\left(-\frac{\vec{\alpha}^2}{2\bar{a}^2}\right), \tag{14}$$

where the parameter $\bar{a}^2$ denotes the prior variance. This is not an unreasonable prior for the model parameters in chiral EFT. The impact of this parameter prior is to penalize model parameters

that are too large, which would typically signal over-fitting. For situations where there exist a large amount of precise data, the prior specification for the parameters matter less. Nevertheless, the question remains, what value should we pick for $\bar{a}$? This can be dealt with straightforwardly by marginalizing over $\bar{a}$, i.e., we express the prior for the parameters as

$$P(\vec{\alpha}|M,I) = \int \mathrm{d}\bar{a}\, P(\vec{\alpha}|\bar{a},M,I)P(\bar{a}|M,I), \tag{15}$$

which only forces us to specify a prior for the variance for our belief about the model parameters, here we could choose a rather broad range if we like. With appropriate analytical form for the prior on $\bar{a}$, it is even possible to carry out this marginalization step analytically. See reference [117] for illuminating examples about the impact of different priors in model calibration with scattering-phase shifts.

4.1. Prediction and Calibration Including Model Discrepancies

Observables computed with potentials from chiral EFT should exhibit a pattern where contributions from successive orders $\nu = 0, 1, 2, 3, \ldots$ are smaller by factors Q^ν. This is reflected in Equation (3). Therefore, the expansion coefficients $\{c_\nu\}$ should remain of natural size, a clear example of a situation where we have prior knowledge[3]. Given a series of model calculations of the observable $\mathcal{O}$, up to the chiral order $\nu = k$, i.e., $\mathcal{O}_0, \mathcal{O}_1, \ldots, \mathcal{O}_k$, and an estimate of the factor Q, it is straightforward to extract the coefficients $[c_0, c_1, \ldots, c_k]$. It was shown in references [118, 119] how to extract a pdf for the EFT truncation error δ_k in Equation (4) using this information. First, we factor out the overall scale, and define

$$\tilde{\delta}_k = \delta_k/\mathcal{O}_0 \tag{16}$$

as the overall dimensionless truncation error. We now seek an expression for $P(\tilde{\delta}_k|c_0, c_1, \ldots, c_k)$ given the known values for the first $k+1$ coefficients. It turns out that for independent, bounded, and uniform prior pdfs for the expansion coefficients, the integrals can be solved analytically if one also approximates $\tilde{\delta}_k$ with the leading term. Thus, we assume

$$\tilde{\delta}_k \approx \tilde{\delta}_k^{(1)} = c_{k+1}Q^{k+1}, \tag{17}$$

The posterior pdf $P(\tilde{\delta}_k^{(1)}|c_0, c_1, \ldots, c_k)$ is given in reference [119] (Equation 22), and explicitly derived in the appendix of reference [118]. This posterior pdf is the complete inference about $\tilde{\delta}_k^{(1)}$. If the pdf is multi-modal or otherwise non-trivial one should use it in its entirety in forward analyses. However, we can sometimes use a so-called degree of belief (DOB) value to quantify the width of a pdf. This is the probability p%, expressed in percent, that the value of an uncertain variable η, distributed according to the pdf $P(\eta)$, falls within an interval $[a, b]$. This interval is then referred to as a credible interval with p% DOB, where

$$p\% = \int_a^b P(\eta)\ \mathrm{d}\eta. \tag{18}$$

The posterior pdf for $\tilde{\delta}_k^{(1)}$ is not Gaussian, however it is symmetric and have zero mean. Therefore, we can define a smallest interval $[-d_k^{(p)}, +d_k^{(p)}]$ that captures p% of the probability mass

$$p\% = \int_{-d_k^{(p)}}^{+d_k^{(p)}} P(\tilde{\delta}_k^1|c_0, c_1, \ldots, c_k)\ \mathrm{d}\tilde{\delta}_k^{(1)}, \tag{19}$$

and solve for $d_k^{(p)}$. This will define the width of the credible interval within which the next term in the EFT expansion will fall with p% DOB, i.e., an estimate of the truncation error. The expression is derived in references [118, 119], and given by

$$d_k^{(p)} = \max(|c_0|, |c_1|, \ldots, |c_k|)Q^{k+1}\frac{n_c+1}{n_c}p\%, \text{if } p\% \leq n_c/(n_c+1), \tag{20}$$

where n_c denotes the number of available coefficients. Thus, with $n_c/(n_c+1) \times 100\%$ DOB, the EFT truncation error for the observable $\mathcal{O}$, in dimensionful units, is straightforwardly estimated by $\mathcal{O}_0 \times \max(|c_0|, |c_1|, \ldots, |c_k|)Q^{k+1}$. This estimate also corresponds to the prescription employed in reference [120]. This *a posteriori* truncation error estimate essentially boils down to guessing the largest number that one can expect based on a series of numbers drawn from the same underlying distribution. For example, given only one ($n_c = 1$) expansion parameter c_0, we have a 50% DOB that we have encountered the largest coefficient in the series. This procedure has been applied to estimate the truncation error in several *ab initio* model calculations, see the long list of papers that are citing references [119, 120].

The procedure for estimating the EFT truncation error, i.e., part of the model discrepancy, requires an estimate of the high-energy scale Λ_b of the underlying EFT. For the models discussed here, the results are based on chiral EFT, for which the naive estimate of Λ_b is roughly $M_N \sim 1$ GeV. This was analyzed more carefully for semi-local chiral potentials [45, 120] in reference [121]. The posterior pdf for Λ_b indicated that a more probable value is $\Lambda_b \approx 500$ MeV. This value was also used for the breakdown scale in the truncation error analysis of nucleon-nucleon scattering phase shifts from the Δ-full models at LO,NLO, and NNLO chiral orders in reference [110]. The results are presented in **Figure 3**. This result also strengthens the observation made earlier, that the inclusion of the Δ degree of freedom tend to improve model descriptions of nuclear systems. This is more clearly seen when employing the same potentials to make model predictions for the ground-state-energies and charge radii of selected finite nuclei (see **Figure 4**), and the energy per nucleon in symmetric nuclear matter (see **Figure 5**).

The model predictions for the nuclear matter indicate that the Δ-full models on average agree better with experimental energies and radii. The uncertainty bands for the predictions were extracted under the additional assumption that the relevant

[3]The wording; prior knowledge vs. prior expectation, or even prior belief, signals the level of subjective certainty or source for the prior.

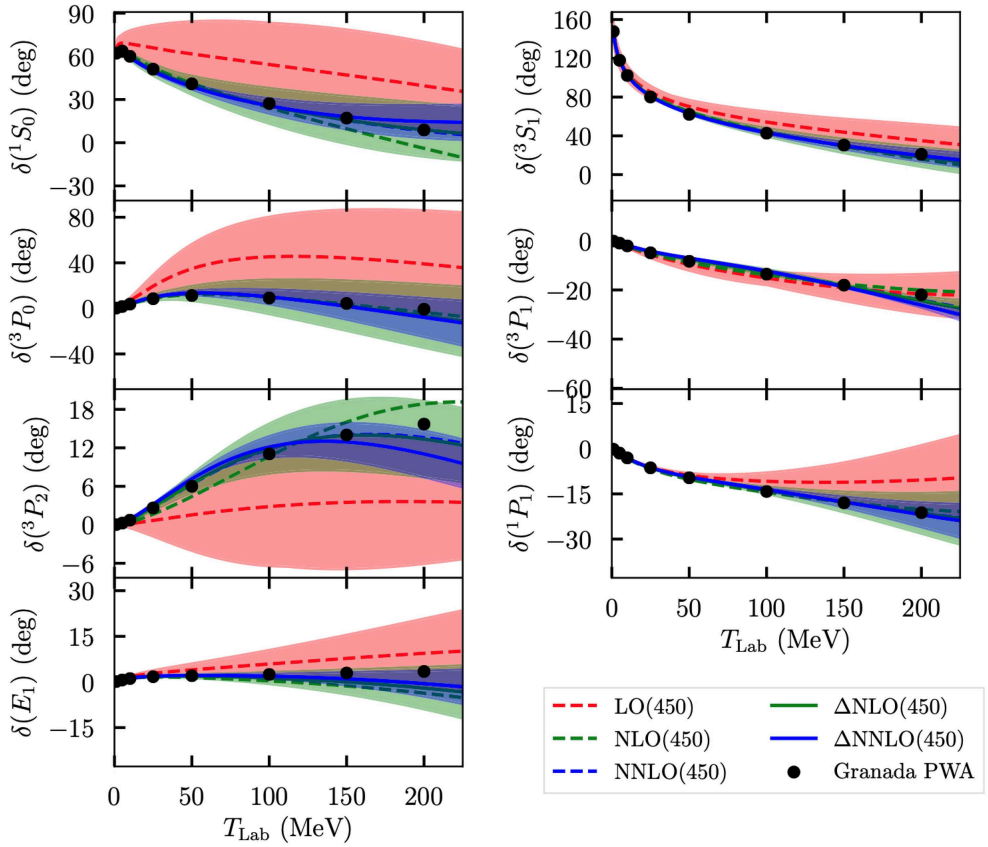


FIGURE 3 | Neutron-proton scattering phase shifts computed with models based on Δ-full and Δ-less chiral interaction potentials. The bands indicate the limits of the expected DOB intervals at each chiral order ν. The black dots represent the values from the Granada partial wave analysis [84].

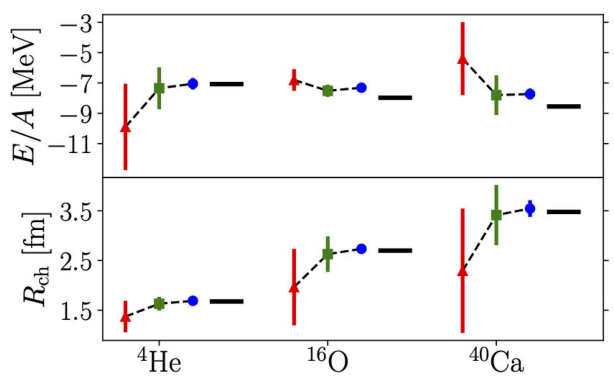


FIGURE 4 | Ground-state energy (negative of binding energy) per nucleon and charge radii for selected nuclei computed with coupled cluster theory and the Δ-full potential ΔNNLO(450). For each nucleus, from left to right as follows: LO (red triangle), NLO (green square), and NNLO (blue circle). The black horizontal bars are data. Vertical bars estimate uncertainties from the order-by-order EFT truncation errors.

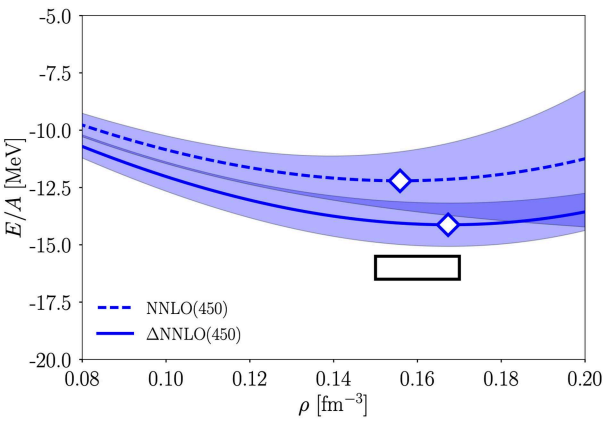


FIGURE 5 | Coupled-cluster based model prediction of the energy per nucleon (in MeV) in symmetric nuclear matter using an NNLO potential with (solid line) and without (dashed line) the Δ isobar. Both interactions employ a momentum regulator-cutoff $\Lambda = 450$ MeV. The shaded areas indicate the estimated EFT-truncation errors. The diamonds mark the saturation point and the black rectangle indicates the region $E/A = -16 \pm 0.5$ MeV and $\rho = 0.16 \pm 0.01$ fm^{-3}.

soft-scales for finite and infinite nuclear systems are given by the pion mass and the Fermi momentum, respectively. Although these are rough estimates of the soft scales, it is important to note that the the truncation error in Equation (20) only holds up to factors of order unity. A comparison of theoretical error estimates based on different statistical methods provide additional validation. The Bayesian method for estimating the truncation error and the model errors estimated using the

modified χ^2-function in Equation (10) are quite different in nature. Nevertheless, a comparison of the theoretical errors in nucleon-nucleon cross sections at high scattering-energies agree very well for these methods [80, 119]. The link between the two approaches for estimating the model uncertainties is discussed further in reference [117]. A complete Bayesian parameter estimation including model discrepancy will hopefully reveal more details about the structure of the chiral EFT error.

At the moment, most model discrepancies in *ab initio* modeling based on chiral EFT are extracted *a posteriori* using predictions based on calibrated models. This is possible based on the expectation that the predictions might follow an EFT pattern. This of course remains to be validated on theoretical grounds. However, under the assumption that the interaction potential actually gives rise to an EFT pattern for the observable, we can build on Equation (4) to include a discrepancy term in the likelihood for calibrating *ab initio* models. See reference [122] for a discussion about correlated truncation errors in nucleon-nucleon scattering observables following this line of thought, where it is also observed that the expansion parameters behave largely as expected.

5. SUMMARY AND OUTLOOK

Statistical representation of a sound model discrepancy term is certainly challenging. Still, the assumption of zero model discrepancy is a rather extreme position. Almost any reasonable guess is better than nothing in order to avoid false values for the model parameters and to minimize over-fitting.

The importance of acknowledging model discrepancies is neatly summarized in the famous quote of George E. P. Box: "Essentially, all models are wrong, but some are useful" [123], with the additional comment in reference [93]: "But a model that is wrong can only be useful if we acknowledge the fact that it is wrong."

Fortunately, most of the *ab initio* models of atomic nuclei are built on methods from EFT, which by construction promises extra information about the expected impact of the neglected or missing physics in theoretical predictions. Bayesian inference is a natural choice for accounting for model discrepancies and prior knowledge, especially when the priors have a physical basis. Indeed, extracting the posterior pdf for the model parameters via Bayesian inference methods makes it possible to abandon the notion of having *a single* parameterization of a particular interaction potential and instead build models based on a continuous pdf of parameters. Developments along these lines are already taking place in e.g., density functional theory for atomic nuclei [124].

At the moment, most theoretical analyses of atomic nuclei proceed in the following fashion. Given a potential $V(\vec{\alpha}_\star)$, optimized to reproduce some set of calibration data D, we setup a model $M(\vec{\alpha}_\star, \vec{x})$ to analyze an experimental result corresponding to the control setting $\vec{x}_i$, i.e., we evaluate $M(\vec{\alpha}_\star, \vec{x}_i)$. In a few cases we propagate uncertainties originating from the measurement errors present in the data vector D, and sometimes we estimate the EFT truncation error using a series of models at different chiral orders. This takes a lot of effort. Indeed, *ab initio* nuclear models are represented by complex computer codes, implemented via years of dedicated work by several people, and computationally expensive to evaluate. On top of that, to understand the underlying nuclear interaction is, arguably, one of the most difficult problems in all physics. Still, we would like to answer questions like: how much should we trust a model prediction? is the model M over-fitted? why is it not agreeing with observed data, and how do we understand this discrepancy?

We should strive to use Bayesian methods for calibrating our models $M(\vec{\alpha}, \vec{x})$ to obtain posterior pdfs $P(\vec{\alpha}|M, D, I)$ for the parameters. Subsequent evaluations of an observable $\mathcal{O}_i$, corresponding to setting the model control variable to $\vec{x}_i$, should be marginalized over the parameter posterior pdf to produce a posterior predictive pdf

$$P(\mathcal{O}_i|M, \vec{x}_i, D) = \int \mathrm{d}\vec{\alpha}\ P(\mathcal{O}_i|\vec{\alpha}, M, \vec{x}_i, D)P(\vec{\alpha}|M, D). \qquad (21)$$

This quantity will best reflect our state of knowledge, and is quite meaningful to compare with data. Various marginalizations with respect to subsets of the parameters can provide better insights into the qualities of the *ab initio* model. Bayesian inference also allows us to compare different models via the computation of Bayes factors [125], which in turn enables us to address questions like: which PC in chiral EFT has the strongest support by data? It is also theoretically straightforward to compute the posterior predictive pdf averaged over a set of different models $\mathcal{M} = [M_1, M_2, \ldots, M_3]$ [126], each weighted by their probability of being true, in the finite space spanned by $\mathcal{M}$, given data D.

5.1. The Computational Challenge

There are several challenges connected with the outlook presented above: working out the theoretical underpinnings of chiral EFT, specifying prior information, formulating model discrepancy terms, and performing challenging Markov Chain Monte Carlo evaluation of complicated posterior pdfs. From a practical point of view, handling, the computational complexity is the most difficult one. Indeed, evaluating models of medium- and heavy-mass atomic nuclei typically requires vast high-performance computing resources. This clearly puts the feasibility of the Bayesian scenario presented above into question. Without any unforeseen disruptive computer technologies or dramatic algorithmic advances, it will be necessary to employ, where possible, fast emulators that accurately mimic the response of the original *ab initio* models. This is where we can draw from advances in machine learning. Possibly useful methods are e.g., Gaussian process regression and artificial neural networks. Both of these approaches can be challenging since they introduce hyperparameters that require additional optimization. Although it can be difficult to assess how well such methods will work, there exist several examples of useful surrogate interpolation and extrapolation in nuclear modeling (see e.g., references [122, 124, 127–131]). A new method called eigenvector continuation [132] turns out to be a promising tool for accurate extrapolation

and fast emulation of nuclear properties [133]. In a recent paper [134], this method proved capable of emulating (with a root mean squared error of 1%) more than one million solutions of an *ab initio* model for the ground-state energy and radius of ^{16}O in one hour on a standard laptop. An equivalent set of exact *ab initio* coupled-cluster computations would require 20 years.

AUTHOR CONTRIBUTIONS

The author has made a substantial contribution to the work, and approved it for publication.

FUNDING

This work was supported by the European Research Council (ERC) under the European Unions Horizon 2020 research and innovation programme (Grant agreement No. 758027).

ACKNOWLEDGMENTS

I would like to thank all my collaborators for fruitful discussions and for sharing their insights during our joint work on the topics presented here.

REFERENCES

1. Dickhoff WH, Barbieri C. Self-consistent Green's function method for nuclei and nuclear matter. *Prog Part Nucl Phys.* (2004) **52**:377–496. doi: 10.1016/j.ppnp.2004.02.038
2. Lee D. Lattice simulations for few- and many-body systems. *Prog Part Nucl Phys.* (2009) **63**:117–54. doi: 10.1016/j.ppnp.2008.12.001
3. Bogner SK, Furnstahl RJ, Schwenk A. From low-momentum interactions to nuclear structure. *Prog Part Nucl Phys.* (2010) **65**:94–147. doi: 10.1016/j.ppnp.2010.03.001
4. Barrett BR, Navrátil P, Vary JP. Ab initio no core shell model. *Prog Part Nucl Phys.* (2013) **69**:131–81. doi: 10.1016/j.ppnp.2012.10.003
5. Carbone A, Cipollone A, Barbieri C, Rios A, Polls A. Self-consistent Green's functions formalism with three-body interactions. *Phys Rev C.* (2013) **88**:054326. doi: 10.1103/PhysRevC.88.054326
6. Hagen G, Papenbrock T, Hjorth-Jensen M, Dean DJ. Coupled-cluster computations of atomic nuclei. *Rep Prog Phys.* (2014) **77**:096302. doi: 10.1088/0034-4885/77/9/096302
7. Hergert H, Bogner SK, Morris TD, Binder S, Calci A, Langhammer J, et al. *Ab initio* multireference in-medium similarity renormalization group calculations of even calcium and nickel isotopes. *Phys Rev C.* (2014) **90**:041302. doi: 10.1103/PhysRevC.90.041302
8. Carlson J, Gandolfi S, Pederiva F, Pieper SC, Schiavilla R, Schmidt KE, et al. Quantum Monte Carlo methods for nuclear physics. *Rev Mod Phys.* (2015) **87**:1067–118. doi: 10.1103/RevModPhys.87.1067
9. Barnea N, Leidemann W, Orlandini G. Ground state wave functions in the hyperspherical formalism for nuclei with A>4. *Nucl Phys A.* (1999) **650**:427–42. doi: 10.1016/S0375-9474(99)00113-X
10. Glöckle W, Witala H, Hüber D, Kamada H, Golak J. The three-nucleon continuum: achievements, challenges and applications. *Phys Rep.* (1996) **274**:107–285. doi: 10.1016/0370-1573(95)00085-2
11. Wiringa RB, Stoks VGJ, Schiavilla R. Accurate nucleon-nucleon potential with charge-independence breaking. *Phys Rev C.* (1995) **51**:38–51.
12. Machleidt R. High-precision, charge-dependent Bonn nucleon-nucleon potential. *Phys Rev C.* (2001) **63**:024001. doi: 10.1103/PhysRevC.63.024001
13. Kolck UV. Effective field theory of nuclear forces. *Prog Part Nucl Phys.* (1999) **43**:337–418.
14. Epelbaum E, Hammer HW, Meißner UG. Modern theory of nuclear forces. *Rev Mod Phys.* (2009) 81:1773–825. doi: 10.1103/RevModPhys.81.1773
15. Machleidt R, Entem DR. Chiral effective field theory and nuclear forces. *Phys Rep.* (2011) **503**:1–75. doi: 10.1016/j.physrep.2011.02.001
16. Machleidt R. 2. In: *The Meson Theory of Nuclear Forces and Nuclear Structure*. Boston, MA: Springer US (1989). p. 189–376. doi: 10.1007/978-1-4613-9907-0_2
17. Elhatisari S, Lee D, Rupak G, Epelbaum E, Krebs H, Lähde TA, et al. *Ab initio* alpha–alpha scattering. *Nature.* (2015) **528**:111–4. doi: 10.1038/nature16067
18. Rosenbusch M, Ascher P, Atanasov D, Barbieri C, Beck D, Blaum K, et al. Probing the $N = 32$ shell closure below the magic proton number $Z = 20$: mass measurements of the exotic isotopes ^{52,53}K. *Phys Rev Lett.* (2015) **114**:202501. doi: 10.1103/PhysRevLett.114.202501
19. Lapoux V, Somà V, Barbieri C, Hergert H, Holt JD, Stroberg SR. Radii and binding energies in oxygen isotopes: a challenge for nuclear forces. *Phys Rev Lett.* (2016) **117**:052501. doi: 10.1103/PhysRevLett.117.052501
20. Lu BN, Li N, Elhatisari S, Lee D, Epelbaum E, Meißner UG. Essential elements for nuclear binding. *Phys Lett B.* (2019) **797**:134863. doi: 10.1016/j.physletb.2019.134863
21. Taniuchi R, Santamaria C, Doornenbal P, Obertelli A, Yoneda K, Authelet G, et al. 78Ni revealed as a doubly magic stronghold against nuclear deformation. *Nature.* (2019) **569**:53–8. doi: 10.1038/s41586-019-1155-x
22. Gysbers P, Hagen G, Holt JD, Jansen GR, Morris TD, Navrátil P, et al. Discrepancy between experimental and theoretical β-decay rates resolved from first principles. *Nat Phys.* (2019) **15**:428–31. doi: 10.1038/s41567-019-0450-7
23. Somá V, Navrátil P, Raimondi F, Barbieri C, Duguet T. Novel chiral Hamiltonian and observables in light and medium-mass nuclei. *Phys Rev C.* (2020) **101**:014318. doi: 10.1103/PhysRevC.101.014318
24. Binder S, Langhammer J, Calci A, Roth R. *Ab initio* path to heavy nuclei. *Phys Lett B.* (2014) **736**:119–23. doi: 10.1016/j.physletb.2014.07.010
25. Ekström A, Jansen GR, Wendt KA, Hagen G, Papenbrock T, Carlsson BD, et al. Accurate nuclear radii and binding energies from a chiral interaction. *Phys Rev C.* (2015) **91**:051301. doi: 10.1103/PhysRevC.91.051301
26. Hagen G, Ekström A, Forssén C, Jansen GR, Nazarewicz W, Papenbrock T, et al. Neutron and weak-charge distributions of the ^{48}Ca nucleus. *Nat Phys.* (2016) **12**:186. doi: 10.1038/nphys3529
27. Garcia Ruiz RF, Bissell ML, Blaum K, Ekström A, Frömmgen N, Hagen G, et al. Unexpectedly large charge radii of neutron-rich calcium isotopes. *Nat Phys.* (2016) **12**:594–8. doi: 10.1038/nphys3645
28. Duguet T, Somà V, Lecluse S, Barbieri C, Navrátil P. *Ab initio* calculation of the potential bubble nucleus ^{34}Si. *Phys Rev C.* (2017) **95**:034319. doi: 10.1103/PhysRevC.95.034319
29. Nogga A, Bogner SK, Schwenk A. Low-momentum interaction in few-nucleon systems. *Phys Rev C.* (2004) **70**:061002. doi: 10.1103/PhysRevC.70.061002
30. Hebeler K, Bogner SK, Furnstahl RJ, Nogga A, Schwenk A. Improved nuclear matter calculations from chiral low-momentum interactions. *Phys Rev C.* (2011) **83**:031301. doi: 10.1103/PhysRevC.83.031301
31. Hagen G, Jansen GR, Papenbrock T. Structure of ^{78}Ni from first-principles computations. *Phys Rev Lett.* (2016) **117**:172501. doi: 10.1103/PhysRevLett.117.172501
32. Morris TD, Simonis J, Stroberg SR, Stumpf C, Hagen G, Holt JD, et al. Structure of the lightest tin isotopes. *Phys Rev Lett.* (2018) **120**:152503. doi: 10.1103/PhysRevLett.120.152503
33. Simonis J, Stroberg SR, Hebeler K, Holt JD, Schwenk A. Saturation with chiral interactions and consequences for finite nuclei. *Phys Rev C.* (2017) **96**:014303. doi: 10.1103/PhysRevC.96.014303
34. Liu HN, Obertelli A, Doornenbal P, Bertulani CA, Hagen G, Holt JD, et al. How robust is the $N = 34$ subshell closure? First spectroscopy of ^{52}Ar. *Phys Rev Lett.* (2019) **122**:072502. doi: 10.1103/PhysRevLett.122.072502
35. Holt JD, Stroberg SR, Schwenk A, Simonis J. *Ab initio* limits of atomic nuclei. *arXiv [Preprint]* arXiv:1905.10475 (2019).

36. Ireland DG, Nazarewicz W. Enhancing the interaction between nuclear experiment and theory through information and statistics. *J Phys G Nucl Part Phys.* (2015) **42**:030301. doi: 10.1088/0954-3899/42/3/030301
37. Hartmann S. Effective field theories, reductionism and scientific explanation. *Stud Hist Philos Sci B Stud Hist Philos Mod Phys.* (2001) **32**:267–304. doi: 10.1016/S1355-2198(01)00005-3
38. Barnea N, Contessi L, Gazit D, Pederiva F, van Kolck U. Effective field theory for lattice nuclei. *Phys Rev Lett.* (2015) **114**:052501. doi: 10.1103/PhysRevLett.114.052501
39. Chang CC, Nicholson AN, Rinaldi E, Berkowitz E, Garron N, Brantley DA, et al. A per-cent-level determination of the nucleon axial coupling from quantum chromodynamics. *Nat Publ. Group.* (2018) **558**:91–4. doi: 10.1038/s41586-018-0161-8
40. Weinberg S. Phenomenological Lagrangians. *Phys A Stat Mech Appl.* (1979) **96**:327–40.
41. Weinberg S. Nuclear forces from chiral lagrangians. *Phys Lett B.* (1990) **251**:288–92.
42. Bedaque PF, van Kolck U. Effective field theory for few-nucleon systems. *Annu Rev Nucl Part Sci.* (2002) **52**:339–96. doi: 10.1146/annurev.nucl.52.050102.090637
43. Papenbrock T. Effective theory for deformed nuclei. *Nucl Phys A.* (2011) **852**:36–60. doi: 10.1016/j.nuclphysa.2010.12.013
44. Gasser J, Leutwyler H. Chiral perturbation theory to one loop. *Ann Phys.* (1984) **158**:142–210.
45. Epelbaum E, Krebs H, Meißner UG. Precision nucleon-nucleon potential at fifth order in the chiral expansion. *Phys Rev Lett.* (2015) **115**:122301. doi: 10.1103/PhysRevLett.115.122301
46. Epelbaum E. Four-nucleon force in chiral effective field theory. *Phys Lett B.* (2006) **639**:456–61. doi: 10.1016/j.physletb.2006.06.046
47. Krebs H, Gasparyan A, Epelbaum E. Chiral three-nucleon force at N^4LO: longest-range contributions. *Phys Rev C.* (2012) **85**:054006. doi: 10.1103/PhysRevC.85.054006
48. Krebs H, Gasparyan A, Epelbaum E. Chiral three-nucleon force at N^4LO. II. Intermediate-range contributions. *Phys Rev C.* (2013) **87**:054007. doi: 10.1103/PhysRevC.87.054007
49. Entem DR, Kaiser N, Machleidt R, Nosyk Y. Peripheral nucleon-nucleon scattering at fifth order of chiral perturbation theory. *Phys Rev C.* (2015) **91**:014002. doi: 10.1103/PhysRevC.91.014002
50. Entem DR, Kaiser N, Machleidt R, Nosyk Y. Dominant contributions to the nucleon-nucleon interaction at sixth order of chiral perturbation theory. *Phys Rev C.* (2015) **92**:064001. doi: 10.1103/PhysRevC.92.064001
51. van Kolck U. Few-nucleon forces from chiral Lagrangians. *Phys Rev C.* (1994) **49**:2932–41.
52. Epelbaum E, Nogga A, Glöckle W, Kamada H, Meißner UG, Witała H. Three-nucleon forces from chiral effective field theory. *Phys Rev C.* (2002) **66**:064001. doi: 10.1103/PhysRevC.66.064001
53. Bernard V, Epelbaum E, Krebs H, Meißner UG. Subleading contributions to the chiral three-nucleon force: long-range terms. *Phys Rev C.* (2008) **77**:064004. doi: 10.1103/PhysRevC.77.064004
54. Bernard V, Epelbaum E, Krebs H, Meißner UG. Subleading contributions to the chiral three-nucleon force. II. Short-range terms and relativistic corrections. *Phys Rev C.* (2011) **84**:054001. doi: 10.1103/PhysRevC.84.054001
55. Girlanda L, Kievsky A, Viviani M. Subleading contributions to the three-nucleon contact interaction. *Phys Rev C.* (2011) **84**:014001. doi: 10.1103/PhysRevC.84.014001
56. Park TS, Min DP, Rho M. Chiral dynamics and heavy-fermion formalism in nuclei: exchange axial currents. *Phys Rep.* (1993) **233**:341–95.
57. Park TS, Min DP, Rho M. Chiral Lagrangian approach to exchange vector currents in nuclei. *Nucl Phys A.* (1996) **596**:515–52.
58. Krebs H, Epelbaum E, Meißner UG. Nuclear axial current operators to fourth order in chiral effective field theory. *Ann Phys.* (2017) **378**:317–95. doi: 10.1016/j.aop.2017.01.021
59. Baroni A, Girlanda L, Pastore S, Schiavilla R, Viviani M. Nuclear axial currents in chiral effective field theory. *Phys Rev C.* (2016) **93**:015501. doi: 10.1103/PhysRevC.93.015501
60. Kölling S, Epelbaum E, Krebs H, Meißner UG. Two-nucleon electromagnetic current in chiral effective field theory: one-pion exchange and short-range contributions. *Phys Rev C.* (2011) **84**:054008. doi: 10.1103/PhysRevC.84.054008
61. Pastore S, Girlanda L, Schiavilla R, Viviani M, Wiringa RB. Electromagnetic currents and magnetic moments in chiral effective field theory (χEFT). *Phys Rev C.* (2009) **80**:034004. doi: 10.1103/PhysRevC.80.034004
62. Piarulli M, Girlanda L, Marcucci LE, Pastore S, Schiavilla R, Viviani M. Electromagnetic structure of $A = 2$ and 3 nuclei in chiral effective field theory. *Phys Rev C.* (2013) **87**:014006. doi: 10.1103/PhysRevC.87.014006
63. Hoferichter M, de Elvira JR, Kubis B, Meißner UG. Roy-Steiner-equation analysis of pion-nucleon scattering. *Phys Rep.* (2016) **625**:1–88. doi: 10.1016/j.physrep.2016.02.002
64. Lepage P. How to renormalize the Schrodinger equation. *arXiv [Preprint]* arXiv:nucl-th/9706029 (1997).
65. Grieshammer H. *Assessing Theory Uncertainties in EFT Power Countings From Residual Cutoff Dependence. Vol. 253 of The 8th International Workshop on Chiral Dynamics, CD2015g. Proceedings of Science* (Pisa) (2015). doi: 10.22323/1.253.0104
66. Nogga A, Timmermans RGE, Kolck UV. Renormalization of one-pion exchange and power counting. *Phys Rev C.* (2005) **72**:054006. doi: 10.1103/PhysRevC.72.054006
67. Pavón Valderrama M, Arriola ER. Renormalization of the *NN* interaction with a chiral two-pion-exchange potential: central phases and the deuteron. *Phys Rev C.* (2006) **74**:054001. doi: 10.1103/PhysRevC.74.054001
68. Long B, Yang CJ. Renormalizing chiral nuclear forces: triplet channels. *Phys Rev C.* (2012) **85**:034002. doi: 10.1103/PhysRevC.85.034002
69. Epelbaum E, Meißner UG. On the renormalization of the one–pion exchange potential and the consistency of Weinberg's power counting. *Few Body Syst.* (2013) **54**:2175–90. doi: 10.1007/s00601-012-0492-1
70. Dyhdalo A, Furnstahl RJ, Hebeler K, Tews I. Regulator artifacts in uniform matter for chiral interactions. *Phys Rev C.* (2016) **94**:034001. doi: 10.1103/PhysRevC.94.034001
71. Sánchez MS, Yang CJ, Long B, van Kolck U. Two-nucleon $^1S_0$ amplitude zero in chiral effective field theory. *Phys Rev C.* (2018) **97**:024001. doi: 10.1103/PhysRevC.97.024001
72. Epelbaum E, Gasparyan AM, Gegelia J, Meißner UG. How (not) to renormalize integral equations with singular potentials in effective field theory. *Eur Phys J A.* (2018) **54**:186. doi: 10.1140/epja/i2018-12632-1
73. Yang CJ. Do we know how to count powers in pionless and pionful effective field theory? *arXiv [Preprint]* arXiv:1905.12510 (2019).
74. Flambaum VV, Wiringa RB. Dependence of nuclear binding on hadronic mass variation. *Phys Rev C.* (2007) **76**:054002. doi: 10.1103/PhysRevC.76.054002
75. Epelbaum E, Krebs H, Lähde TA, Lee D, Meißner UG. Viability of carbon-based life as a function of the light quark mass. *Phys Rev Lett.* (2013) **110**:112502. doi: 10.1103/PhysRevLett.110.112502
76. Kamada H, Nogga A, Glöckle W, Hiyama E, Kamimura M, Varga K, et al. Benchmark test calculation of a four-nucleon bound state. *Phys Rev C.* (2001) **64**:044001. doi: 10.1103/PhysRevC.64.044001
77. Hebeler K, Holt JD, Menéndez J, Schwenk A. Nuclear forces and their impact on neutron-rich nuclei and neutron-rich matter. *Annu Rev Nucl Part Sci.* (2015) **65**:457–84. doi: 10.1146/annurev-nucl-102313-025446
78. Hergert H. In-medium similarity renormalization group for closed and open-shell nuclei. *Phys Script.* (2016) **92**:023002. doi: 10.1088/1402-4896/92/2/023002
79. Entem DR, Machleidt R. Accurate charge-dependent nucleon-nucleon potential at fourth order of chiral perturbation theory. *Phys Rev C.* (2003) **68**:041001. doi: 10.1103/PhysRevC.68.041001
80. Carlsson BD, Ekström A, Forssén C, Strömberg DF, Jansen GR, Lilja O, et al. Uncertainty analysis and order-by-order optimization of chiral nuclear interactions. *Phys Rev X.* (2016) **6**:011019. doi: 10.1103/PhysRevX.6.011019
81. Piarulli M, Girlanda L, Schiavilla R, Pérez RN, Amaro JE, Arriola ER. Minimally nonlocal nucleon-nucleon potentials with chiral two-pion exchange including Δ resonances. *Phys Rev C.* (2015) **91**:024003. doi: 10.1103/PhysRevC.91.024003
82. Reinert P, Krebs H, Epelbaum E. Semilocal momentum-space regularized chiral two-nucleon potentials up to fifth order. *Eur Phys J A.* (2018) **54**:86. doi: 10.1140/epja/i2018-12516-4

83. Stoks VGJ, Klomp RAM, Rentmeester MCM, de Swart JJ. Partial-wave analysis of all nucleon-nucleon scattering data below 350 MeV. *Phys Rev C.* (1993) **48**:792–815. doi: 10.1103/PhysRevC.48.792
84. Pérez RN, Amaro JE, Arriola ER. Coarse-grained potential analysis of neutron-proton and proton-proton scattering below the pion production threshold. *Phys Rev C.* (2013) **88**:064002. doi: 10.1103/PhysRevC.88.064002
85. Wild SM. Solving derivative-free nonlinear least squares problems with POUNDERS. In: Terlaky T, Anjos MF, Ahmed S, editors. *Advances and Trends in Optimization With Engineering Applications.* SIAM (2017). p. 529–40.
86. Ekström A, Baardsen G, Forssén C, Hagen G, Hjorth-Jensen M, Jansen GR, et al. Optimized chiral nucleon-nucleon interaction at next-to-next-to-leading order. *Phys Rev Lett.* (2013) **110**:192502. doi: 10.1103/PhysRevLett.110.192502
87. Bergervoet JR, van Campen PC, van der Sanden WA, de Swart JJ. Phase shift analysis of 0–30 MeV pp scattering data. *Phys Rev C.* (1988) **38**:15–50.
88. Tjon JA. Bound states of 4He with local interactions. *Phys Lett B.* (1975) **56**:217–20.
89. Gazit D, Quaglioni S, Navrátil P. Three-nucleon low-energy constants from the consistency of interactions and currents in chiral effective field theory. *Phys Rev Lett.* (2009) **103**:102502. doi: 10.1103/PhysRevLett.103.102502
90. Klos P, Carbone A, Hebeler K, Menéndez J, Schwenk A. Uncertainties in constraining low-energy constants from 3H β decay. *Eur Phys J A.* (2017) **53**:168. doi: 10.1140/epja/i2017-12357-7
91. Epelbaum E, Golak J, Hebeler K, Hüther T, Kamada H, Krebs H, et al. Few- and many-nucleon systems with semilocal coordinate-space regularized chiral two- and three-body forces. *Phys Rev C.* (2019) **99**:024313. doi: 10.1103/PhysRevC.99.024313
92. Girlanda L, Kievsky A, Viviani M, Marcucci LE. Short-range three-nucleon interaction from $A = 3$ data and its hierarchical structure. *Phys Rev C.* (2019) **99**:054003. doi: 10.1103/PhysRevC.99.054003
93. Brynjarsdóttir J, O'Hagan A. Learning about physical parameters: the importance of model discrepancy. *Inv Probl.* (2014) **30**:114007. doi: 10.1088/0266-5611/30/11/114007
94. Andrae R, Schulze-Hartung T, Melchior P. Dos and don'ts of reduced Chi-squared. *arXiv [Preprint]* arXiv:1012.3754 (2010).
95. Furnstahl RJ, Phillips DR, Wesolowski S. A recipe for EFT uncertainty quantification in nuclear physics. *J Phys G Nucl Part Phys.* (2015) **42**:034028. doi: 10.1088/0954-3899/42/3/034028
96. Dobaczewski J, Nazarewicz W, Reinhard PG. Error estimates of theoretical models: a guide. *J Phys G Nucl Part Phys.* (2014) **41**:074001. doi: 10.1088/0954-3899/41/7/074001
97. Ekström A, Carlsson BD, Wendt KA, Forssén C, Jensen MH, Machleidt R, et al. Statistical uncertainties of a chiral interaction at next-to-next-to leading order. *J Phys G.* (2015) **42**:034003. doi: 10.1088/0954-3899/42/3/034003
98. Navarro Pérez R, Amaro JE, Ruiz Arriola E, Maris P, Vary JP. Statistical error propagation in ab initio no-core full configuration calculations of light nuclei. *Phys Rev C.* (2015) **92**:064003. doi: 10.1103/PhysRevC.92.064003
99. Navarro Pérez R, Amaro JE, Ruiz Arriola E. Statistical error analysis for phenomenological nucleon-nucleon potentials. *Phys Rev C.* (2014) **89**:064006. doi: 10.1103/PhysRevC.89.064006
100. Acharya B, Carlsson BD, Ekström A, Forssén C, Platter L. Uncertainty quantification for proton-proton fusion in chiral effective field theory. *Phys Lett B.* (2016) **760**:584–9. doi: 10.1016/j.physletb.2016.07.032
101. Acharya B, Ekström A, Platter L. Effective-field-theory predictions of the muon-deuteron capture rate. *Phys Rev C.* (2018) **98**:065506. doi: 10.1103/PhysRevC.98.065506
102. Hernandez OJ, Ekström A, Dinur NN, Ji C, Bacca S, Barnea N. The deuteron-radius puzzle is alive: a new analysis of nuclear structure uncertainties. *Phys Lett B.* (2018) **778**:377–83. doi: 10.1016/j.physletb.2018.01.043
103. Brooks S, Gelman A, Jones G, Meng XL. *Handbook of Markov Chain Monte Carlo*. Boca Raton, FL; London; New York, NY: CRC Press (2011).
104. Carlsson BD. Quantifying statistical uncertainties in ab initio nuclear physics using Lagrange multipliers. *Phys Rev C.* (2017) **95**:034002. doi: 10.1103/PhysRevC.95.034002
105. Pieper SC, Pandharipande VR, Wiringa RB, Carlson J. Realistic models of pion-exchange three-nucleon interactions. *Phys Rev C.* (2001) **64**:014001. doi: 10.1103/PhysRevC.64.014001
106. Rotureau J, Danielewicz P, Hagen G, Jansen GR, Nunes FM. Microscopic optical potentials for calcium isotopes. *Phys Rev C.* (2018) **98**:044625. doi: 10.1103/PhysRevC.98.044625
107. Idini A, Barbieri C, Navrátil P. *Ab initio* optical potentials and nucleon scattering on medium mass nuclei. *Phys Rev Lett.* (2019) **123**:092501. doi: 10.1103/PhysRevLett.123.092501
108. Elhatisari S, Li N, Rokash A, Alarcón JM, Du D, Klein N, et al. Nuclear binding near a quantum phase transition. *Phys Rev Lett.* (2016) **117**:132501. doi: 10.1103/PhysRevLett.117.132501
109. Hagen G, Hjorth-Jensen M, Jansen GR, Papenbrock T. Emergent properties of nuclei from *ab initio* coupled-cluster calculations. *Phys Scr.* (2016) **91**:063006. doi: 10.1088/0031-8949/91/6/063006
110. Ekström A, Hagen G, Morris TD, Papenbrock T, Schwartz PD. Δ isobars and nuclear saturation. *Phys Rev C.* (2018) **97**:024332. doi: 10.1103/PhysRevC.97.024332
111. Piarulli M, Baroni A, Girlanda L, Kievsky A, Lovato A, Lusk E, et al. Light-nuclei spectra from chiral dynamics. *Phys Rev Lett.* (2018) **120**:052503. doi: 10.1103/PhysRevLett.120.052503
112. Logoteta D, Bombaci I, Kievsky A. Nuclear matter properties from local chiral interactions with Δ isobar intermediate states. *Phys Rev C.* (2016) **94**:064001. doi: 10.1103/PhysRevC.94.064001
113. Kalantar-Nayestanaki N, Epelbaum E, Messchendorp JG, Nogga A. Signatures of three-nucleon interactions in few-nucleon systems. *Rep Prog Phys.* (2011) **75**:016301. doi: 10.1088/0034-4885/75/1/016301
114. de Finetti B. *Theory of Probability: A Critical Introductory Treatment*. New York, NY: John Wiley and Sons Ltd. (2017).
115. Schindler MR, Phillips DR. Bayesian methods for parameter estimation in effective field theories. *Ann Phys.* (2009) **324**:682–708. doi: 10.1016/j.aop.2008.09.003
116. Wesolowski S, Klco N, Furnstahl RJ, Phillips DR, liya AT. Bayesian parameter estimation for effective field theories. *J Phys G Nucl Part Phys.* (2016) **43**:074001. doi: 10.1088/0954-3899/43/7/074001
117. Wesolowski S, Furnstahl RJ, Melendez JA, Phillips DR. Exploring Bayesian parameter estimation for chiral effective field theory using nucleon–nucleon phase shifts. *J Phys G Nucl Part Phys.* (2019) **46**:045102. doi: 10.1088/1361-6471/aaf5fc
118. Cacciari M, Houdeau N. Meaningful characterisation of perturbative theoretical uncertainties. *J High Energy Phys.* (2011) **2011**:39. doi: 10.1007/JHEP09(2011)039
119. Furnstahl RJ, Klco N, Phillips DR, Wesolowski S. Quantifying truncation errors in effective field theory. *Phys Rev C.* (2015) **92**:024005. doi: 10.1103/PhysRevC.92.024005
120. Epelbaum E, Krebs H, Meißner UG. Improved chiral nucleon-nucleon potential up to next-to-next-to-next-to-leading order. *Eur Phys J A.* (2015) **51**:53. doi: 10.1140/epja/i2015-15053-8
121. Melendez JA, Wesolowski S, Furnstahl RJ. Bayesian truncation errors in chiral effective field theory: Nucleon-nucleon observables. *Phys Rev C.* (2017) **96**:024003. doi: 10.1103/PhysRevC.96.024003
122. Melendez JA, Furnstahl RJ, Phillips DR, Pratola MT, Wesolowski S. Quantifying correlated truncation errors in effective field theory. *Phys Rev C.* (2019) **100**:044001. doi: 10.1103/PhysRevC.100.044001
123. Box GE, Draper NR. *Empirical Model-Building and Response Surfaces*. New York, NY: John Wiley & Sons (1987).
124. Neufcourt L, Cao Y, Nazarewicz W, Olsen E, Viens F. Neutron drip line in the Ca region from Bayesian model averaging. *Phys Rev Lett.* (2019) **122**:062502. doi: 10.1103/PhysRevLett.122.062502
125. Gelman A, Carlin JB, Stern HS, Dunson DB, Vehtari A, Rubin DB. *Bayesian Data Analysis*, 3rd ed. Chapman Hall/CRC Texts in Statistical Science. Boca Raton, FL; London; New York, NY: Taylor Francis (2013).
126. Hoeting JA, Madigan D, Raftery AE, Volinsky CT. Bayesian model averaging: a tutorial. *Stat Sci.* (1999) **14**:382–401.
127. Ekström A, Forssén C, Dimitrakakis C, Dubhashi D, Johansson HT, Muhammad AS, et al. Bayesian optimization in *ab initio* nuclear physics. *J Phys G Nucl Part Phys.* (2019) **46**:095101. doi: 10.1088/1361-6471/ab2b14
128. Negoita GA, Vary JP, Luecke GR, Maris P, Shirokov AM, Shin IJ, et al. Deep learning: extrapolation tool for *ab initio* nuclear

theory. *Phys Rev C.* (2019) **99**:054308. doi: 10.1103/PhysRevC.99.054308
129. Jiang WG, Hagen G, Papenbrock T. Extrapolation of nuclear structure observables with artificial neural networks. *Phys Rev C.* (2019) **100**:054326. doi: 10.1103/PhysRevC.100.054326
130. Neufcourt L, Cao Y, Nazarewicz W, Viens F. Bayesian approach to model-based extrapolation of nuclear observables. *Phys Rev C.* (2018) **98**:034318. doi: 10.1103/PhysRevC.98.034318
131. McDonnell JD, Schunck N, Higdon D, Sarich J, Wild SM, Nazarewicz W. Uncertainty uantification for nuclear density functional theory and information content of new measurements. *Phys Rev Lett.* (2015) **114**:122501. doi: 10.1103/PhysRevLett.114.122501
132. Frame D, He R, Ipsen I, Lee D, Lee D, Rrapaj E. Eigenvector continuation with subspace learning. *Phys Rev Lett.* (2018) **121**:032501. doi: 10.1103/PhysRevLett.121.032501
133. König S, Ekström A, Hebeler K, Lee D, Schwenk A. Eigenvector continuation as an efficient and accurate emulator for uncertainty quantification. *arXiv [Preprint]* arXiv:1909.08446 (2019).
134. Ekström A, Hagen G. Global sensitivity analysis of bulk properties of an atomic nucleus. *Phys Rev Lett.* (2019) **123**:252501. doi: 10.1103/PhysRevLett.123.252501

Conflict of Interest: The author declares that the research was conducted in the absence of any commercial or financial relationships that could be construed as a potential conflict of interest.

Copyright © 2020 Ekström. This is an open-access article distributed under the terms of the Creative Commons Attribution License (CC BY). The use, distribution or reproduction in other forums is permitted, provided the original author(s) and the copyright owner(s) are credited and that the original publication in this journal is cited, in accordance with accepted academic practice. No use, distribution or reproduction is permitted which does not comply with these terms.

frontiers in Physics

REVIEW
published: 30 January 2020
doi: 10.3389/fphy.2019.00245

Local Nucleon-Nucleon and Three-Nucleon Interactions Within Chiral Effective Field Theory

Maria Piarulli[1]* *and Ingo Tews*[2]

[1] Physics Department, Washington University, St. Louis, MO, United States, [2] Los Alamos National Laboratory, Theoretical Division, Los Alamos, NM, United States

To obtain an understanding of the structure and reactions of nuclear systems from first principles has been a long-standing goal of nuclear physics. In this respect, few- and many-body systems provide a unique laboratory for studying nuclear interactions. During the past decades, the development of accurate representations of the nuclear force has undergone substantial progress. Particular emphasis has been devoted to chiral effective field theory (EFT), a low-energy effective representation of quantum chromodynamics (QCD). Within chiral EFT, many studies have been carried out dealing with the construction of both the nucleon-nucleon (*NN*) and three-nucleon (3*N*) interactions. The aim of the present article is to give a detailed overview of the chiral interaction models that are local in configuration space, and show recent results for nuclear systems obtained by employing these local chiral forces.

Keywords: nuclear interactions, chiral effective field theory, local interactions, three-body forces, *ab-initio* calculations

OPEN ACCESS

Edited by:
Ruprecht Machleidt,
University of Idaho, United States

Reviewed by:
David Rodriguez Entem,
University of Salamanca, Spain
Norbert Kaiser,
Technical University of Munich, Germany

***Correspondence:**
Maria Piarulli
mpiarulli@physics.wustl.edu

Specialty section:
This article was submitted to Nuclear Physics, a section of the journal Frontiers in Physics

Received: *30 September 2019*
Accepted: *20 December 2019*
Published: *30 January 2020*

Citation:
Piarulli M and Tews I (2020) Local Nucleon-Nucleon and Three-Nucleon Interactions Within Chiral Effective Field Theory. Front. Phys. 7:245. doi: 10.3389/fphy.2019.00245

1. INTRODUCTION

The last few decades have marked the emergence of the *basic model* of nuclear theory in which nuclear systems—particularly atomic nuclei and infinite nucleonic matter—can be described as a collection of point-like particles, the nucleons, interacting with each other in terms of two- and many-body effective interactions, and with external electroweak probes via effective current operators. This approach, in conjunction with a computational method of choice to solve the many-body Schrödinger equation, can then be used to study the structure and dynamics of nuclear systems in a fully microscopic way, which is commonly referred to as *ab-initio* calculations. Examples of such calculations are based on the no-core shell model (NCSM) [1, 2], the coupled cluster (CC) [3, 4] or hyperspherical harmonics (HH) [5] expansions, similarity renormalization group (SRG) approaches [6, 7], self-consistent Green's function techniques [8, 9], quantum Monte Carlo (QMC) methods [10], and nuclear lattice effective field theory (NLEFT) [11]. Although significant progress has been made in recent years, these ab-initio techniques remain challenging and their domain of applicability is, at present, limited to provide quantitative description of light and medium-mass nuclei [1, 4, 7–10, 12] and their reactions [13–16]. A special but related challenge is the development of microscopic models that include continuum couplings which are mandatory to describe, for instance, weakly bound nuclear systems [17, 18].

One might argue that nucleons are not the fundamental building blocks of the nuclear systems at hand, and that one should instead start from Quantum Chromodynamics (QCD). QCD provides the theoretical framework to describe strong interactions which governs the dynamics and properties of quarks and gluons. However, while strong interactions are weak and perturbative

at high energies, i.e., short distances (asymptotic freedom), quarks are strongly interacting at low energies or long distances, of relevance for nuclear physics, which makes a non-perturbative treatment necessary. In addition, at these energies quarks are confined into colorless objects called hadrons (baryons, consisting of three quarks, e.g., the nucleon, and mesons consisting of a quark and an anti-quark, e.g., the pion). Hence, while QCD is responsible for the complex inter-nucleon forces in nuclear systems, which can be thought of as residual interactions among quarks, a description in terms of nucleon degrees of freedom is particularly valid at sufficiently low energies.

How the interactions among nucleons emerge from the fundamental theory, QCD, has kept nuclear theorists occupied for many decades. Since QCD is non-perturbative at low energies of interest in nuclear systems, one may try to solve QCD with brute computing power on a discretized Euclidean space-time lattice (known as lattice QCD) However, in spite of many advances [19–22], lattice QCD calculations are still limited to small nucleon numbers and/or large pion masses, and hence, at the present time, can only be used to address a limited set of representative key-issues.

As a consequence, most theoretical studies of nuclear systems have to resort to using the basic model of nuclear theory, i.e., assuming pointlike nucleons to be the relevant degrees of freedom instead of quarks. In this review, we will briefly introduce this basic model and discuss the current state-of-the-art for nuclear interactions, chiral effective field theory (EFT). We will then focus on a particular subclass of chiral EFT interactions, local chiral EFT interactions, intended for the use in QMC methods.

The review is structured as follows. In section 2, we discuss the general features of nuclear interactions starting with the phenomenological ones and moving to those obtained in chiral EFT. In section 3, we provide many details about the theoretical derivation of local interactions in both delta-full and delta-less chiral EFT, i.e., when explicitly including the delta resonance or not. In section 4, we briefly discuss finite cutoff and regulator artifacts that can appear in calculations with local interactions. Finally, in section 5, we report selected results for light and medium-mass nuclei and the equation of state of pure neutron matter using QMC methods.

2. NUCLEAR HAMILTONIANS

The basic model of nuclear theory assumes that a nuclear system can be described by a non-relativistic Hamiltonian that contains interactions among nucleons, i.e., protons and neutrons. The individual nucleons mostly interact via two-body (*NN*) interactions. However, nucleons can also interact via three-body (3*N*) and higher many-body interactions. The way these many-body interactions appear is 2-fold. First, nucleons are compound particles and, hence, treating them as point-like particles induces effective many-body interactions even if only two-quark interactions were to be considered. This is similar to describing tides on Earth, where the three-body system given by Earth, Moon, and Sun is relevant, even though gravity is only a two-body force. Second, since quarks themselves can have multi-quark interactions, this immediately leads to the appearance of "true" 3*N* forces among nucleons, where, for example, single quarks in each of the three nucleons interact with each other.

The resulting Hamiltonian can then be written as a sum of the non-relativistic one-body kinetic energy ($\mathcal{T}_i$), *NN* interactions between particle *i* and *j* (V_{ij}), 3*N* interactions between particle *i*, *j*, and *k* (V_{ijk}), and additional many-body interactions, and provides a good approximation for interacting nucleons in a given nuclear system:

$$\mathcal{H} = \sum_i \mathcal{T}_i + \sum_{i<j} V_{ij} + \sum_{i<j<k} V_{ijk} + \cdots . \tag{1}$$

There are indications that four-body interactions may contribute at the level of only ∼100 keV in ^{4}He [23] or pure neutron matter [24], and therefore are negligible compared to *NN* and 3*N* interactions. Hence, current formulations of the basic model do not typically include them (see e.g., [10]).

In order to derive two- and three-body nuclear forces, one has to take into account some general considerations, specify the theoretical framework in which such interactions are formulated, and the experimental inputs necessary to determine possible unknown parameters of the theory.

2.1. General Considerations for Nuclear Interactions

To accurately describe nuclear systems that are governed by QCD, nuclear interactions need to obey all the relevant symmetries of QCD. Hence, nuclear potentials need to have the following properties (we will focus on *NN* forces here, but the statements remain true for all parts of the interaction):

- V is hermitian, because the Hamiltonian is hermitian,
- V is symmetric under the permutation of identical particles, i.e., $V_{ij} = V_{ji}$,
- V is translationally and rotationally invariant,
- V is invariant under translations in time, i.e., time-independent,
- V is Lorentz invariant (for non-relativistic interactions this reduces to Galilean invariance),
- V is invariant under parity transformations and time reversal,
- V has to conserve baryon and lepton number,
- V has to be approximately isospin symmetric and charge independent,
- and V has to include the properties of spontaneously and explicitly broken chiral symmetry.

Chiral symmetry is a symmetry of the QCD Lagrangian with massless quarks under independent rotations of left- and right-handed quarks. Considering only u and d quarks, this symmetry can be written as $SU(2)_L \times SU(2)_R$. This expression contains two symmetries: the first (vector) one represents isospin symmetry, i.e., symmetry under the exchange of u and d quarks, and the second (axial) one is the so-called chiral symmetry. These two symmetries imply degenerate fermions under isospin and spin-parity transformations. While isospin symmetry is approximately fulfilled in nature, i.e., the neutron and proton have similar

masses, nucleons with spin $1/2^+$ and $1/2^-$ have very different masses (940 vs. 1,535 MeV). This signals that chiral symmetry is broken in nature.

In fact, chiral symmetry is broken 2-fold. First, it is broken spontaneously, leading to the formation of Goldstone bosons, that can be identified with the pions. Second, chiral symmetry is also explicitly broken by the finite quark masses, which leads to the pion being pseudo-Goldstone bosons with finite but small mass. In contrast, isospin symmetry remains a good symmetry, because the ratio $(m_d - m_u)/\Lambda_{\rm QCD}$ is very small, where $m_u \simeq 2.4$ MeV and $m_d \simeq 4.8$ MeV.

These symmetries only allow certain operator structures for nuclear interactions. Galilean invariance, for instance, implies that nuclear interactions depend only on relative momenta between two nucleons, $\mathbf{p} = \mathbf{p}_i - \mathbf{p}_j$, while symmetry under parity transformations implies that nuclear interactions cannot be linear in $\mathbf{p}$, and charge independence requires that the nuclear interactions can be written as

$$V = V_{\mathbb{1}} \cdot \mathbb{1} + V_\tau \, \boldsymbol{\tau}_i \cdot \boldsymbol{\tau}_j \,, \tag{2}$$

and so on. In addition, the spin dependencies are included through operators like $1, \boldsymbol{\sigma}_i \cdot \boldsymbol{\sigma}_j$, spin-orbit interactions given by $\mathbf{L} \cdot \mathbf{S}$ with $\mathbf{L} = \mathbf{r} \times \mathbf{p}$, where $\mathbf{r} = \mathbf{r}_i - \mathbf{r}_j$, or tensor interactions with the tensor operator $S_{ij}(\mathbf{r}) = \boldsymbol{\sigma}_i \cdot \hat{\mathbf{r}} \, \boldsymbol{\sigma}_j \cdot \hat{\mathbf{r}} - \boldsymbol{\sigma}_i \cdot \boldsymbol{\sigma}_j$. As a consequence, interactions typically have a spin-isospin operator structure given by

$$\mathcal{O}_V = \{\mathbb{1}, \boldsymbol{\sigma}_i \cdot \boldsymbol{\sigma}_j, \mathbf{L} \cdot \mathbf{S}, S_{ij}\} \times \{\mathbb{1}, \boldsymbol{\tau}_i \cdot \boldsymbol{\tau}_j\} \,, \tag{3}$$

where the individual operators carry momentum-dependent functions consistent with all required symmetries.

2.2. Phenomenological Interactions

Historically, *NN* interactions were derived using phenomenological insight. They were characterized by a long-range component characterizing the interaction for inter-nucleon separations $r \gtrsim 1/m_\pi$, due to one-pion exchange (OPE) [25], and intermediate- and short-range components describing the interactions at 1 fm $\lesssim r \lesssim$ 2 fm and $r \lesssim 1$ fm, respectively. The intermediate- and short-range components were included to simulate intermediate-range attraction as well as short-range repulsion.

Up to the mid-1990's, nuclear interactions were based almost exclusively on meson-exchange phenomenology. Interactions of the mid-1990's [26–28] were constrained by fitting nucleon-nucleon (*NN*) elastic scattering data up to laboratory energies of 350 MeV, with χ^2/datum $\simeq 1$ relative to the database available at the time [29]. Two well-known and still widely used examples in this class are the Argonne v_{18} (AV18) [27] and CD-Bonn [28] interactions. These are so-called *phenomenological* interactions.

Already in the 1980's, accurate three-body calculations showed that contemporary *NN* interactions alone did not provide sufficient binding to reproduce experimental numbers for nuclei with nucleon number $A = 3$, ^{3}H and ^{3}He [30]. This realization was later on extended to the spectra (ground and low-lying excited states) of light p-shell nuclei, for instance, in calculations based on quantum Monte Carlo (QMC) methods [31] and in no-core shell-model (NCSM) studies [32]. Consequently, the basic model with only *NN* interactions fit to scattering data, without the inclusion of a three-nucleon (3*N*) interaction, was found to be unsatisfactory. However, because of the composite nature of the nucleon and, in particular, the dominant role of the Δ resonance, a spin-3/2, isospin-3/2 nucleon resonance, in pion-nucleon scattering, many-body interactions arise quite naturally in meson-exchange phenomenology.

For example, the Illinois 3*N* interaction [33] consists of a dominant two-pion exchange (TPE)—the Fujita-Miyazawa interaction [34]—and smaller multi-pion exchange components resulting from the excitation of intermediate Δ's. The most recent version, Illinois-7 (IL7) [35], also contains phenomenological isospin-dependent central terms. The parameters characterizing this 3*N* potential have been determined by fitting the low-lying spectra of nuclei in the mass range $A = 3$–10. The resulting AV18+IL7 Hamiltonian, generally utilized with QMC methods, then leads to predictions of 100 ground- and excited-state energies up to $A = 12$, including the ^{12}C ground- and Hoyle-state energies, in good agreement with the corresponding experimental values [10]. However, when used to compute the neutron-star equation of state, these interactions do not provide sufficient repulsion to guarantee the stability of the observed neutron stars with masses larger than two solar masses against gravitational collapse [36]. Thus, in the context of the phenomenological nuclear interactions, we do not have a Hamiltonian that can predict the properties of all nuclear systems, from *NN* scattering to dense nuclear and neutron matter.

Furthermore, high-precision phenomenological potentials suffer from several limitations, most notably the missing connection with the low-energy QCD, and hence, the absence of a guiding principle for the construction of interactions. As a consequence, phenomenological interactions do not provide rigorous schemes to consistently derive two- and three-body forces and compatible electroweak currents. In addition, there is no clear way to properly assess the theoretical uncertainty associated with the nuclear potentials and currents.

2.3. Chiral Effective Field Theory

These drawbacks were addressed when a new phase in the evolution of the basic model began in the early 1990's with the emergence of chiral effective field theory (EFT) [37–39].

Chiral EFT is a low-energy effective theory of QCD based on the choice of baryons as effective degrees of freedom: in chiral EFT one chooses pions and nucleons. At typical momenta in nuclei, $p \sim m_\pi \sim \mathcal{O}(100\,\text{MeV})$, this choice is accurate, because shorter-range structures, e.g., the quark substructure, or heavier meson exchanges, e.g., exchanges of the ρ-meson, are not resolved, and can be absorbed in short-range nucleon contact interactions. This *separation of scales* between typical momenta p and scales of the same order, i.e., the pion mass $m_\pi \sim 140$ MeV, and larger scales, e.g., the mass of the ρ, $m_\rho \sim 770$ MeV, can then be used to systematically derive an effective and most general scheme accommodating all possible interactions among the relevant degrees of freedom consistent with the symmetries

of QCD. In some modern approaches, the choice of degrees of freedom also includes the Δ isobar (delta-full chiral EFT), because the Δ-nucleon mass splitting is only 300 MeV$\sim 2\, m_\pi$.

The starting point in chiral EFT is the most general Lagrangian in terms of the chosen degrees of freedom, which contains all allowed interaction mechanisms in accordance with the considerations in section 2.1. As a consequence, this Lagrangian contains an infinite number of terms and needs to be truncated using a given power-counting scheme. Most chiral interactions used in nuclear structure calculations are based on Weinberg power counting, which itself is based on naive dimensional analysis of interaction contributions. Within Weinberg power counting, the interactions are expanded in powers of the typical momentum p over the breakdown scale Λ_b, $Q = p/\Lambda_b$, where the breakdown scale denotes momenta at which the short distance structure becomes important and cannot be neglected and absorbed into contact interactions anymore (see [40–43] for recent review articles). It is worthwhile mentioning that alternative power-counting schemes have been also suggested as in Kaplan et al. [44, 45], Nogga et al. [46], Pavon Valderrama and Ruiz Arriola [47], Long and Yang [48], and van Kolck [49].

This expansion defines an order by order scheme, defined by the power ν of the expansion scale Q in each interaction contribution: leading order (LO) for $\nu = 0$, next-to-leading order (NLO) for $\nu = 2$, next-to-next-to-leading order (N^{2}LO) for $\nu = 3$ and so on. Similarly as for nuclear interactions, such a scheme can also be developed for electroweak currents. Therefore, chiral EFT provides a rigorous scheme to systematically construct many-body forces and consistent electroweak currents, and tools to estimate their uncertainties [50–55]. From this perspective, it can be justifiably argued that chiral EFT has put the basic model on a more fundamental basis, by providing a link between QCD with all its symmetries, and the strong and electroweak interactions in nuclei.

Figure 1 shows the state of the art of chiral contributions to the *NN* and 3*N* interactions in the delta-less and delta-full chiral EFT. Higher many-body forces, such as four-nucleon (4*N*) or five-nucleon (5*N*) interactions, can naturally also be derived within this framework [42], but they will not be discussed here. Nuclear forces in chiral EFT are separated into pion-exchange contributions and contact terms. Pion-exchange contributions represent the long- and intermediate-range parts of nuclear interactions and contain all chiral physics. Contact terms, on the other hand, encode the unresolved short-range physics and their strength is specified by unknown low-energy constants (LECs), that need to be adjusted to experimental data.

At LO, besides the already mentioned OPE potential, there are two *NN* contact terms with no momentum dependence that contribute only to the *S*-wave. They are identified by the four-nucleon-leg diagram with a momentum-independent vertex denoted by a small dot in the first row of **Figure 1**. The interaction at LO is a very simple approximation, but already takes into account some of the important features of the *NN* force. For instance, the OPE generates the tensor component of the nuclear force known to be crucial to properly describe the two-nucleon bound state (deuteron).

The leading *NN* two-pion-exchange (TPE) contributions appear at NLO. Diagrams involving virtual excitations of the Δ-isobars [56–59] also appear at NLO in the delta-full chiral-EFT approach. Most importantly, seven new momentum-dependent contact terms can be constructed at this order, which are denoted by the four-nucleon-leg graph with a solid square in the second row of **Figure 1**. These additional contact terms are important to correctly describe *NN* scattering in the *S*- and *P*-waves. More details about these contributions are presented in the next sections. Another important contribution at NLO is the leading 3*N* force, which can be described by the well-known Fujita-Miyazawa diagram [34], which involves intermediate excitation of the Δ-isobars between three nucleons. While this contribution has to be considered in the Δ-full approach, it can be shown that the net contribution of 3*N* forces vanishes in the delta-less chiral EFT [39, 49] at this order.

At next order, N^{2}LO, the sub-leading *NN* TPE diagrams contain vertices (large solid dots) proportional to the so-called c_i coefficients. The values of these parameters can be obtained by pion-nucleon (πN) [60–67] or *NN* scattering data [41]. In the delta-less chiral EFT, these coefficients mimic the effect of the Δ-isobar (or some other meson resonances) through a mechanism known as resonance saturation. Hence, they are enhanced in magnitude and found to be "unnaturally" large. The explicit inclusion of the Δ isobar in the delta-full theory reduces the strength of the c_i's and promotes the corresponding contributions to a lower order (see gray arrows in **Figure 1**). As a consequence, the convergence of the expansion in the delta-full theory improves considerably at these orders. In the delta-full approach, additional sub-leading TPE contributions appear that have also been worked out at this order [60].

In addition to the *NN* sector, additional 3*N* diagrams appear at N^{2}LO in both approaches. They involve a 3*N* TPE, a OPE-contact interaction, and a true 3*N* contact diagram. The 3*N* TPE potential also involves the c_i parameters already present in the TPE *NN* force. As in the case of the *NN* force, these contributions absorb the presence of the Δ-isobar in the delta-less approach, while some of their strength is promoted to lower order in the form of the already discussed Fujita-Miyazawa diagram in the delta-full approach. The OPE-contact and 3*N* contact diagrams include two purely three-body LECs that have to be adjusted to $A \geq 3$ data. Finally, the are no additional diagrams due to Δ contributions to the 3*N* force at N2LO [68].

At higher orders, the number of contributions to the *NN* force dramatically increases. In **Figure 1** only a few representative diagrams are displayed. For instance, at N^{3}LO more TPE contributions occur—in both delta-less and delta-full chiral EFT—involving leading two-loop and relativistic corrections. In addition, leading three-pion (3π) exchange contributions arise at this order but they are found to be negligible. The main feature at N^{3}LO is the presence of additional contact interactions represented by the four-nucleon-leg with a solid diamond. Since these interactions are $\sim p^4, p'^4$, they have a relevant impact up to the *D* waves. Their full operator structure will be discussed in the next section. Additional complicated 3*N* diagrams appear at N^{3}LO, as well as the first contributions to four-nucleon forces (4*N*). We will not discuss these diagrams here and refer the reader to Bernard et al. [69, 70] and Epelbaum [71, 72]. For additional contributions at N^{4}LO and N^{5}LO, we refer the interested reader

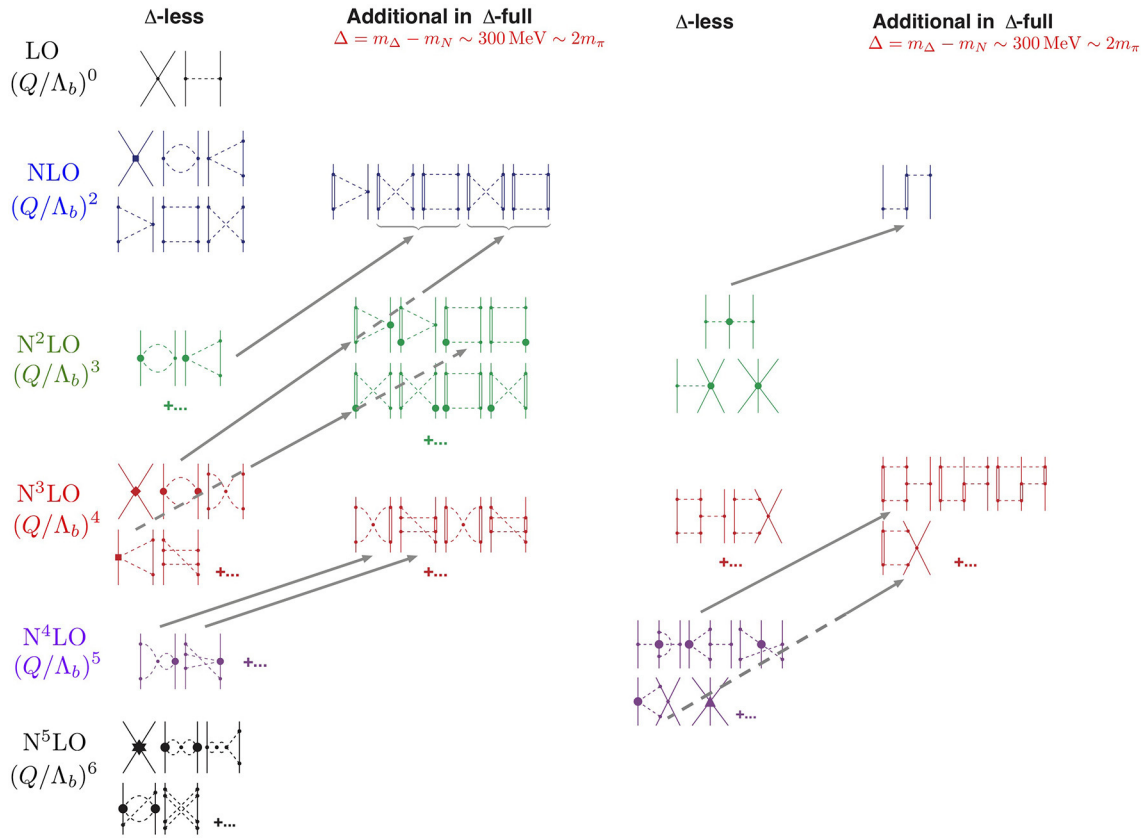


FIGURE 1 | Chiral contributions to the *NN* and 3*N* interactions in the delta-less and delta-full chiral EFT based on Weinberg power counting. Solid lines represent nucleons, dashed lines represent pions, and double lines represent the Δ isobar. Gray arrows indicate the shift of individual contributions within the two power-counting schemes when explicit Δ's are accounted for. Figure adapted from Machleidt and Entem [41] and Machleidt and Sammarruca [42] under the Creative Commons CCBY license.

to Entem et al. [73], Epelbaum et al. [74], Reinert et al. [75], and Entem et al. [76].

An important aspect of nuclear interactions (and currents) in the basic model is that they suffer from ultraviolet (UV) divergences which need to be removed by a proper regularization and renormalization procedure. There are two sources of UV divergences that require regularization: first, UV divergences appear in loop corrections, and second when solving the Schrödinger or Lippmann-Schwinger equations or when calculating matrix elements involving nuclear currents. Loop divergences can be treated via dimensional regularization (DR) or spectral-function regularization (SFR), where the latter is implemented through the inclusion of a finite cutoff in the spectral functions. To cure divergences when solving the Schrödinger or Lippmann-Schwinger equations, the nuclear potential is multiplied by regulator functions that remove large-momentum contributions above a chosen cutoff scale. The regularization of the potential (and current) operators is followed by a renormalization procedure, i.e., dependencies on the regularization scheme and cutoff are reabsorbed, order by order, by the LECs entering the potential (and currents).

Nucleon-nucleon scattering has been extensively studied in chiral EFT in the past two decades following the pioneering work by Weinberg [37–39] and Ordonez et al. [58]. In particular, *NN* potentials at N^{3}LO in the chiral expansion are available since the early 2000's [77, 78] and have served as a basis for numerous *ab initio* calculations of nuclear structure and reactions. Recently, accurate and precise chiral EFT potentials up to fifth order in the chiral expansion, i.e., N^{4}LO, have been developed [73–76], and provide an extremely accurate description of *NN* data bases up to laboratory energies of 300 MeV with a χ^2 per datum close to one. These databases have been provided by the Nijmegen group [26, 29], the VPI/GWU group [79], and more recently the Granada group [80–82]. In the standard optimization procedure, the *NN* potentials are first constrained through fits to neutron-proton (*np*) and proton-proton (*pp*) phase shifts, and then refined by minimizing the total χ^2 obtained from a direct comparison with the *NN* scattering data. However, new optimization schemes are being explored in Carlsson et al. [83] and Ekström et al. [84]. For instance, the optimization strategy of the N2LO$_{\rm sat}$ interaction of Ekström et al. [84] is based on a simultaneous fit of the two- and three-nucleon forces to low-energy *NN* data, the deuteron binding energy, and binding energies and charge radii of hydrogen, helium, carbon, and oxygen isotopes using consistent *NN* and 3*N* interactions at N^{2}LO. However, despite the good description of properties of ^{16}O and ^{40}Ca, the *NN* component of this interaction shows deficiencies in

reproducing the *pp* and *np* scattering data even at very low energy.

Three-nucleon forces and their impact on nuclear structure and reactions has become an important frontier in nuclear physics, see Kalantar-Nayestanaki et al. [85] and Hammer et al. [86] for review articles. As shown in **Figure 1**, chiral contributions to the 3*N* interaction have been derived up to N4LO in the chiral expansion [69, 70, 87–89]. However, few- and many-nucleon calculations are, with very few exceptions, still limited to chiral 3*N* forces at N^{2}LO. At this order, as we have mentioned above, 3*N* forces are characterized by the presence of two unknown LECs that have to be determined. The two LECs—namely c_D in the OPE-contact and c_E in the 3*N* contact interaction– have been constrained either by fitting exclusively strong-interaction observables [90–93] or by relying on a combination of strong- and weak-interaction observables [94–96]. This last approach is made possible by the relation between c_D in the OPE-contact interaction and the LEC in the *NN* contact axial current [94, 95, Schiavilla, private communication], established in chiral EFT [97]. This connection allows one to use nuclear properties governed by either strong or weak interactions to constrain simultaneously the 3*N* interaction and *NN* axial current.

As chiral EFT is a low-momentum expansion of nuclear interactions, many of the chiral interactions available in the literature are formulated in momentum space and have the feature of being strongly non-local in coordinate space. This makes them not well-suited for certain numerical algorithms, for example QMC methods. In this context, an interaction is local if it depends solely on the momentum transfer $\mathbf{q} = \mathbf{p} - \mathbf{p}'$, which Fourier transforms to dependencies on $\mathbf{r}$. However, interactions in momentum-space can also depend on the momentum scale $\mathbf{k} = (\mathbf{p}' + \mathbf{p})/2$, which Fourier transform to derivatives in coordinate space. These $\mathbf{k}$ dependencies, and thus non-localities, come about because of (i) the specific functional choice made to regularize the momentum space potentials in terms of the two momentum scales $\mathbf{p}$ and $\mathbf{p}'$, and (ii) contact interactions that explicitly depend on $\mathbf{k}$.

QMC methods, for example variational (VMC) and Green's Function Monte Carlo (GFMC) [10, 98] techniques, provide reliable solutions of the many-body Schrödinger equation—presently for up to $A = 12$ nucleons—with full account of the complexity of the many-body, spin- and isospin-dependent correlations induced by nuclear interactions. The sampling of configuration space in VMC and GFMC simulations gives access to many important properties of light nuclei, such as spectra, form factors, transitions, low-energy scattering, and response functions. Auxiliary Field Diffusion Monte Carlo (AFDMC) [10, 98] uses Monte Carlo techniques to additionally sample the spin-isospin degrees of freedom, enabling studies of, for example, nuclei up to $A = 16$ [99, 100] and neutron matter [90, 91, 101–103, Piarulli et al., private communication] that is so critical to determining the structure of neutron stars. QMC simulations have surely proved to be very valuable in attacking many nuclear-structure problems over the last three decades but require local chiral interactions as input. Therefore, there is a need to develop local chiral interactions for the use in QMC methods in order combine these accurate many-body methods with systematic nuclear interactions and to test to what extent the chiral EFT framework impacts our knowledge of few- and many-body systems.

3. LOCAL HAMILTONIANS

3.1. Local Two-Nucleon Interactions

A major thrust of our work is based on the theoretical derivation, optimization, and implementation of chiral interactions suitable for QMC methods. In recent years, local configuration-space chiral *NN* interactions have been derived by two groups [104–107]. In this section, we will introduce these two families of interactions, that are either derived in the delta-less [104, 105] or delta-full [106, 107] approach. We begin by introducing general features of both approaches and then describe the specifics. We will be stating general considerations in momentum-space, where $\mathbf{q}$ dependencies indicate local parts of interactions and $\mathbf{k}$ dependencies indicate non-localities, and then switch to coordinate-space where interactions are local if they only depend on the relative distance $\mathbf{r} = \mathbf{r}_i - \mathbf{r}_j$. Fourier transformations connect interactions in momentum- and coordinate-space, with $\mathbf{q}$ and $\mathbf{r}$ being associated variables, while $\mathbf{k}$ leads to appearances of gradient terms.

As discussed before, nuclear interactions can generally be separated into different interaction channels depending on their operator structure. Obviously, chiral interactions can also be separated into long-range physics, mediated by pion-exchange interactions, and short-range physics, which is described by a set of operators consistent with all symmetries and accompanied by LECs adjusted to reproduce experimental data:

$$V(\mathbf{q},\mathbf{k}) = V_{\rm cont}(\mathbf{q},\mathbf{k}) + V_{\pi}(\mathbf{q},\mathbf{k})\,. \tag{4}$$

Each of these components can then be expanded in chiral order ν as discussed before:

$$V_i = \sum_{\nu} V_i^{(\nu)} = V_i^{(0)} + V_i^{(2)} + V_i^{(3)} + V_i^{(4)} + \dots\,. \tag{5}$$

At LO, $\nu = 0$, both delta-less and delta-full chiral EFT have the same operator structure. At this order, only the leading contact interactions as well as the one-pion exchange (OPE) interaction contribute (see **Figure 1**). Generally, pion-exchange interaction can be written as

$$\begin{aligned} V_\pi \;=\; & V_{C,\pi} + \boldsymbol{\tau}_i\cdot\boldsymbol{\tau}_j W_C + \left(V_S + \boldsymbol{\tau}_i\cdot\boldsymbol{\tau}_j W_S\right)\boldsymbol{\sigma}_i\cdot\boldsymbol{\sigma}_j \\ & + \left(V_T + \boldsymbol{\tau}_i\cdot\boldsymbol{\tau}_j W_T\right)\boldsymbol{\sigma}_i\cdot\mathbf{q}\,\boldsymbol{\sigma}_j\cdot\mathbf{q} \\ & + \left(V_{LS} + \boldsymbol{\tau}_i\cdot\boldsymbol{\tau}_j W_{LS}\right) i(\boldsymbol{\sigma}_i+\boldsymbol{\sigma}_j)\cdot\mathbf{q}\times\mathbf{k} \\ & + \left(V_{\sigma L} + \boldsymbol{\tau}_i\cdot\boldsymbol{\tau}_j W_{\sigma L}\right)\boldsymbol{\sigma}_i\cdot\mathbf{q}\times\mathbf{k}\;\;\boldsymbol{\sigma}_j\cdot\mathbf{q}\times\mathbf{k}\,, \end{aligned} \tag{6}$$

with central, spin, tensor, spin-orbit and quadratic spin-orbit components, respectively. In the local chiral interactions discussed in this review, the spin-orbit and quadratic spin-orbit

terms are not included as they are of higher order. The one-pion exchange interaction is given in momentum space as

$$V_{\rm OPE}^{(0)}(\mathbf{q}) = -\frac{g_A^2}{4f_\pi^2}\frac{\boldsymbol{\sigma}_i\cdot\mathbf{q}\boldsymbol{\sigma}_j\cdot\mathbf{q}}{q^2+m_\pi^2}\boldsymbol{\tau}_i\cdot\boldsymbol{\tau}_j\,, \tag{7}$$

where g_A, $f_\pi = 92.4$ MeV, and m_π denote the axial-vector coupling constant of the nucleon, the pion decay constant, and the pion mass, respectively. As a consequence, the OPE contributes to the W_T channel.

Including isospin-symmetry breaking effects induced by the mass difference between charged and neutral pions, the OPE interaction can be rewritten as

$$\begin{aligned} V_{\rm OPE}^{(0)}(\mathbf{q}) = &\left[v_{\sigma\tau}^{\pi,\rm LO}(q)\,\boldsymbol{\sigma}_i\cdot\boldsymbol{\sigma}_j + v_{t\tau}^{\pi,\rm LO}(q)\,S_{ij}(\mathbf{q})\right]\boldsymbol{\tau}_i\cdot\boldsymbol{\tau}_j \\ &+\left[v_{\sigma T}^{\pi,\rm LO}(q)\,\boldsymbol{\sigma}_i\cdot\boldsymbol{\sigma}_j + v_{tT}^{\pi,\rm LO}(q)\,S_{ij}(\mathbf{q})\right]T_{ij}\,, \end{aligned} \tag{8}$$

with the tensor operator $S_{ij}(\mathbf{q})$ in momentum space, $S_{ij}(\mathbf{q}) = 3\,\boldsymbol{\sigma}_i\cdot\mathbf{q}\;\boldsymbol{\sigma}_j\cdot\mathbf{q} - q^2\,\boldsymbol{\sigma}_i\cdot\boldsymbol{\sigma}_j$, and the isotensor operator $T_{ij} = 3\,\tau_{iz}\tau_{jz} - \boldsymbol{\tau}_i\cdot\boldsymbol{\tau}_j$. Hence, when including isospin-symmetry breaking, the OPE adds to the W_S and W_T parts of Equation (6). The functions, $v_{\sigma\tau}^{\pi,\rm LO}(q)$, $v_{t\tau}^{\pi,\rm LO}(q)$, $v_{\sigma T}^{\pi,\rm LO}(q)$, and $v_{tT}^{\pi,\rm LO}(q)$ are defined as

$$\begin{aligned} v_{\sigma\tau}^{\pi,\rm LO}(q) &= \frac{Y_0(q)+2\,Y_+(q)}{3}\,, v_{t\tau}^{\pi,\rm LO}(q) = \frac{T_0(q)+2\,T_+(q)}{3} \\ v_{\sigma T}^{\pi,\rm LO}(q) &= \frac{Y_0(q)-Y_+(q)}{3}\,, v_{tT}^{\pi,\rm LO}(q) = \frac{T_0(q)-T_+(q)}{3}\,, \end{aligned} \tag{9}$$

with $Y_\alpha(q)$ and $T_\alpha(q)$ given by

$$Y_\alpha(q) = -\frac{g_A^2}{3\,(2f_\pi)^2}\frac{q^2}{q^2+m_{\pi_\alpha}^2}\,, T_\alpha(q) = -\frac{g_A^2}{3\,(2f_\pi)^2}\frac{1}{q^2+m_{\pi_\alpha}^2}. \tag{10}$$

Here, m_{π_α} denotes the neutral (m_{π_0}) and charged ($m_{\pi_\pm}$) pion masses. When Fourier-transformed, the coordinate-space OPE is given by

$$\begin{aligned} v^{\pi,\rm LO}(\mathbf{r}) = &\left[v_{\sigma\tau}^{\pi,\rm LO}(r)\,\boldsymbol{\sigma}_i\cdot\boldsymbol{\sigma}_j + v_{t\tau}^{\pi,\rm LO}(r)\,S_{ij}(\mathbf{r})\right]\boldsymbol{\tau}_i\cdot\boldsymbol{\tau}_j \\ &+\left[v_{\sigma T}^{\pi,\rm LO}(r)\,\boldsymbol{\sigma}_i\cdot\boldsymbol{\sigma}_j + v_{tT}^{\pi,\rm LO}(r)\,S_{ij}\right]T_{ij} \end{aligned} \tag{11}$$

where the individual functions can be obtained from Equation (9) with $q\to r$ and with the functions $Y_\alpha(r)$ and $T_\alpha(r)$ given by

$$Y_\alpha(r) = \frac{g_A^2}{12\,\pi}\frac{m_{\pi_\alpha}^3}{(2f_\pi)^2}\frac{e^{-x_\alpha}}{x_\alpha}\,,\quad T_\alpha(r) = Y_\alpha(r)\left(1+\frac{3}{x_\alpha}+\frac{3}{x_\alpha^2}\right). \tag{12}$$

Here, $x_\alpha = m_{\pi_\alpha} r$. Note that Equation (11) only holds in the case $r > 0$. In addition, upon Fourier transformation a δ-function appears, which has been dropped from Equation (11), because it can be reabsorbed in the short-range contact terms at LO, which we will discuss next.

The LO contact interactions are momentum-independent and can be described by the most general operator set allowed by all symmetries:

$$\begin{aligned} V_{\rm cont}^{\rm LO}(\mathbf{q},\mathbf{k}) = V_{\rm cont}^{\rm LO} = &\alpha_1\mathbb{1} + \alpha_2\,\boldsymbol{\sigma}_i\cdot\boldsymbol{\sigma}_j + \alpha_3\,\boldsymbol{\tau}_i\cdot\boldsymbol{\tau}_j \\ &+\alpha_4\,\boldsymbol{\sigma}_i\cdot\boldsymbol{\sigma}_j\,\boldsymbol{\tau}_i\cdot\boldsymbol{\tau}_j\,. \end{aligned} \tag{13}$$

As these terms describe the interactions of nucleons, i.e., fermions, these interactions are used between anti-symmetrized wave functions. One can define the anti-symmetrized interaction $V_{\rm as} = 1/2\,(V - \mathcal{A}[V])$ by applying the anti-symmetrizer, given by

$$\begin{aligned} \mathcal{A}[V(\mathbf{q},\mathbf{k})] = &\frac{1}{4}(1+\boldsymbol{\sigma}_i\cdot\boldsymbol{\sigma}_j)(1+\boldsymbol{\tau}_i\cdot\boldsymbol{\tau}_j) \\ &\times V\left(\mathbf{q}\to-2\mathbf{k},\mathbf{k}\to-\frac{1}{2}\mathbf{q}\right). \end{aligned} \tag{14}$$

One then finds

$$\begin{aligned} V_{\rm cont,as}^{(0)} &= \frac{1}{2}\left(1-\frac{1}{4}(1+\boldsymbol{\sigma}_i\cdot\boldsymbol{\sigma}_j)(1+\boldsymbol{\tau}_i\cdot\boldsymbol{\tau}_j)\right)V_{\rm cont}^{(0)} \\ &= \left(\frac{3}{8}\alpha_1-\frac{3}{8}\alpha_2-\frac{3}{8}\alpha_3-\frac{9}{8}\alpha_4\right) \\ &\quad+\left(-\frac{1}{8}\alpha_1+\frac{5}{8}\alpha_2-\frac{3}{8}\alpha_3+\frac{3}{8}\alpha_4\right)\boldsymbol{\sigma}_i\cdot\boldsymbol{\sigma}_j \\ &\quad+\left(-\frac{1}{8}\alpha_1-\frac{3}{8}\alpha_2+\frac{5}{8}\alpha_3+\frac{3}{8}\alpha_4\right)\boldsymbol{\tau}_i\cdot\boldsymbol{\tau}_j \\ &\quad+\left(-\frac{1}{8}\alpha_1+\frac{1}{8}\alpha_2+\frac{1}{8}\alpha_3+\frac{3}{8}\alpha_4\right)\boldsymbol{\sigma}_i\cdot\boldsymbol{\sigma}_j\,\boldsymbol{\tau}_i\cdot\boldsymbol{\tau}_j \\ &= \tilde{C}_S+\tilde{C}_T\,\boldsymbol{\sigma}_i\cdot\boldsymbol{\sigma}_j+\left(-\frac{2}{3}\tilde{C}_S-\tilde{C}_T\right)\boldsymbol{\tau}_i\cdot\boldsymbol{\tau}_j \\ &\quad+\left(-\frac{1}{3}\tilde{C}_S\right)\boldsymbol{\sigma}_i\cdot\boldsymbol{\sigma}_j\,\boldsymbol{\tau}_i\cdot\boldsymbol{\tau}_j\,. \end{aligned} \tag{15}$$

It follows immediately that only two out of these four couplings are linearly independent, describing the two possible S-wave scattering channels. The two commonly chosen LO contact operators are

$$V_{\rm cont}^{(0)} = C_S + C_T\boldsymbol{\sigma}_i\cdot\boldsymbol{\sigma}_j\,, \tag{16}$$

but in principle any different two of the four contact interactions can be chosen and lead to the same physical description for fermionic systems. This is analogous to Fierz ambiguities and in the following we will call this freedom to choose operators Fierz rearrangement freedom.

Additionally, there are isospin breaking corrections to the LO contact interactions that have to be taken into account. These are due to different masses of u and d quarks, and account for differences in neutron-neutron (nn), np, and pp S-wave scattering lengths:

$$V_{\rm cont,\,CIB}(\mathbf{r}) = C_{\rm CIB}\frac{1+4\boldsymbol{\tau}_i^3\boldsymbol{\tau}_j^3}{2}\frac{1-\boldsymbol{\sigma}_i\cdot\boldsymbol{\sigma}_k}{4}\,, \tag{17}$$

$$V_{\rm cont,\,CSB}(\mathbf{r}) = C_{\rm CSB}(\boldsymbol{\tau}_i^3+\boldsymbol{\tau}_j^3)\frac{1-\boldsymbol{\sigma}_i\cdot\boldsymbol{\sigma}_k}{4}\,. \tag{18}$$

At higher orders, the description of the potential changes depending on the choice of delta-less or delta-full approach. In the following, we will describe both approaches as pursued by individual research groups.

3.1.1. Without Delta Isobars

At NLO in chiral EFT, additional momentum-dependent contact interactions as well as TPE interactions appear. For the TPE, we give the expressions within the spectral-function representation (SFR) as detailed in Epelbaum et al. [108], with spectral functions ρ_i and η_i:

$$V_{C,\pi}(r) = \frac{1}{2\pi^2 r}\int_{2M_\pi}^{\tilde{\Lambda}} d\mu\, \mu\, e^{-\mu r}\, \rho_C(\mu)\,, \tag{19}$$

$$V_S(r) = -\frac{1}{6\pi^2 r}\int_{2M_\pi}^{\tilde{\Lambda}} d\mu\, \mu\, e^{-\mu r}\left(\mu^2\rho_T(\mu) - 3\rho_S(\mu)\right), \tag{20}$$

$$V_T(r) = -\frac{1}{6\pi^2 r^3}\int_{2M_\pi}^{\tilde{\Lambda}} d\mu\, \mu\, e^{-\mu r}\, \rho_T(\mu)\,(3+3\mu r+\mu^2 r^2)\,. \tag{21}$$

Here, $\tilde{\Lambda}$ is the SFR cutoff. Similar expressions are valid for W_C, W_S, and W_T in terms of η_C, η_S, and η_T. The TPE spectral functions at NLO are given by Kaiser et al. [109]

$$\rho_T^{(2)}(\mu) = \frac{1}{\mu^2}\,\rho_S^{(2)}(\mu) = \frac{3g_A^4}{128\pi f_\pi^4}\,\frac{\sqrt{\mu^2-4m_\pi^2}}{\mu}\,, \tag{22}$$

$$\eta_C^{(2)}(\mu) = \frac{1}{768\pi f_\pi^4}\,\frac{\sqrt{\mu^2-4m_\pi^2}}{\mu}\Bigg(4m_\pi^2(5g_A^4-4g_A^2-1) - \mu^2(23g_A^4-10g_A^2-1) + \frac{48g_A^4m_\pi^4}{4m_\pi^2-\mu^2}\Bigg)\,. \tag{23}$$

For the NLO contact interactions, the most general set of operators is given by

$$\begin{aligned} V_{\rm cont}^{\rm NLO}(\mathbf{q},\mathbf{k}) = {}& \gamma_1\, q^2 + \gamma_2\, q^2\, \boldsymbol{\sigma}_i\cdot\boldsymbol{\sigma}_j + \gamma_3\, q^2\, \boldsymbol{\tau}_i\cdot\boldsymbol{\tau}_j + \gamma_4\, q^2 \boldsymbol{\sigma}_i\cdot\boldsymbol{\sigma}_j\boldsymbol{\tau}_i\cdot\boldsymbol{\tau}_j \\ & + \gamma_5\, k^2 + \gamma_6\, k^2\, \boldsymbol{\sigma}_i\cdot\boldsymbol{\sigma}_j + \gamma_7\, k^2\, \boldsymbol{\tau}_i\cdot\boldsymbol{\tau}_j + \gamma_8\, k^2 \boldsymbol{\sigma}_i\cdot\boldsymbol{\sigma}_j\boldsymbol{\tau}_i\cdot\boldsymbol{\tau}_j \\ & + \gamma_9\,(\boldsymbol{\sigma}_i+\boldsymbol{\sigma}_j)(\mathbf{q}\times\mathbf{k}) + \gamma_{10}\,(\boldsymbol{\sigma}_i+\boldsymbol{\sigma}_j)(\mathbf{q}\times\mathbf{k})\boldsymbol{\tau}_i\cdot\boldsymbol{\tau}_j \\ & + \gamma_{11}(\boldsymbol{\sigma}_i\cdot\mathbf{q})(\boldsymbol{\sigma}_j\cdot\mathbf{q}) + \gamma_{12}(\boldsymbol{\sigma}_i\cdot\mathbf{q})(\boldsymbol{\sigma}_j\cdot\mathbf{q})\boldsymbol{\tau}_i\cdot\boldsymbol{\tau}_j \\ & + \gamma_{13}(\boldsymbol{\sigma}_i\cdot\mathbf{k})(\boldsymbol{\sigma}_j\cdot\mathbf{k}) + \gamma_{14}(\boldsymbol{\sigma}_i\cdot\mathbf{k})(\boldsymbol{\sigma}_j\cdot\mathbf{k})\boldsymbol{\tau}_i\cdot\boldsymbol{\tau}_j\,. \end{aligned} \tag{24}$$

Using the same arguments as for the LO contact interactions, only 7 out of these 14 operators are linearly independent. To construct local interactions, one typically chooses the 6 local operators (proportional to γ_1-γ_4, γ_{11}, and γ_{12}) as well as the spin-orbit operator (proportional to γ_9):

$$\begin{aligned} V_{\rm cont}^{(2)} = {}& C_1\, q^2 + C_2\, q^2\, \boldsymbol{\tau}_i\cdot\boldsymbol{\tau}_j + \left(C_3\, q^2 + C_4\, q^2\, \boldsymbol{\tau}_i\cdot\boldsymbol{\tau}_j\right)\boldsymbol{\sigma}_i\cdot\boldsymbol{\sigma}_j + \\ & + i\,\frac{C_5}{2}\,(\boldsymbol{\sigma}_i\boldsymbol{\sigma}_j)\cdot(\mathbf{q}\times\mathbf{k}) + C_6\,(\boldsymbol{\sigma}_i\cdot\mathbf{q})(\boldsymbol{\sigma}_j\cdot\mathbf{q}) \\ & + C_7\,(\boldsymbol{\sigma}_i\cdot\mathbf{q})(\boldsymbol{\sigma}_j\cdot\mathbf{q})\,\boldsymbol{\tau}_i\cdot\boldsymbol{\tau}_j\,. \end{aligned} \tag{25}$$

In coordinate space, this translates to

$$\begin{aligned} V_{\rm cont}^{(2)}(\mathbf{r}) = {}& -(C_1 + C_2\,\boldsymbol{\tau}_i\cdot\boldsymbol{\tau}_j)\Delta\delta(\mathbf{r}) - (C_3 + C_4\,\boldsymbol{\tau}_i\cdot\boldsymbol{\tau}_j)\,\boldsymbol{\sigma}_i\cdot\boldsymbol{\sigma}_j\Delta\delta(\mathbf{r}) \\ & + \frac{C_5}{2}\,\frac{\partial_r\delta(\mathbf{r})}{r}\mathbf{L}\cdot\mathbf{S} + (C_6 + C_7\,\boldsymbol{\tau}_i\cdot\boldsymbol{\tau}_j) \\ & \times\left[(\boldsymbol{\sigma}_i\cdot\hat{\mathbf{r}})(\boldsymbol{\sigma}_j\cdot\hat{\mathbf{r}})\left(\frac{\partial_r\delta(\mathbf{r})}{r} - \partial_r^2\delta(\mathbf{r})\right) - \boldsymbol{\sigma}_i\cdot\boldsymbol{\sigma}_j\frac{\partial_r\delta(\mathbf{r})}{r}\right]. \end{aligned} \tag{26}$$

At N^{2}LO, the subleading TPE interactions appear. The spectral functions for these at N^{2}LO read

$$\rho_C^{(3)}(\mu) = -\frac{3g_A^2}{64\mu f_\pi^4}\,(2m_\pi^2-\mu^2)\left(2m_\pi^2(2c_1-c_3)+c_3\mu^2\right), \tag{27}$$

$$\eta_T^{(3)}(\mu) = \frac{1}{\mu^2}\,\eta_S^{(3)}(\mu) = -\frac{g_A^2}{128\mu f_\pi^4}\,c_4(4m_\pi^2-\mu^2)\,, \tag{28}$$

where the c_i denote the previously mentioned LECs of the subleading pion-nucleon vertices. For the N^{2}LO TPE, one can solve Equations (19–21):

$$\begin{aligned} W_S^{(3)}(r) = {}& \frac{g_A^2}{48\pi^2 f_\pi^4}\,\frac{e^{-2x}}{r^6}\,c_4\,(1+x)(3+3x+2x^2) \\ & - \frac{g_A^2}{384\pi^2 f_\pi^4}\,\frac{e^{-y}}{r^6}\,c_4\left(24+24y+12y^2+4y^3+y^4 \right. \\ & \left. - 4x^2(2+2y+y^2)\right), \end{aligned} \tag{29}$$

$$\begin{aligned} W_T^{(3)}(r) = {}& -\frac{g_A^2}{48\pi^2 f_\pi^4}\,\frac{e^{-2x}}{r^6}\,c_4\,(1+x)(3+3x+x^2) \\ & + \frac{g_A^2}{768\pi^2 f_\pi^4}\,\frac{e^{-y}}{r^6}\,c_4\left(48+48y+24y^2+7y^3+y^4 \right. \\ & \left. - 4x^2(8+5y+y^2)\right), \end{aligned} \tag{30}$$

and

$$\begin{aligned} V_{C,\pi}^{(3)}(r) = {}& \frac{3g_A^2}{32\pi^2 f_\pi^4}\,\frac{e^{-2x}}{r^6}\Big[2c_1\,x^2(1+x)^2 + c_3(6+12x+10x^2 \\ & + 4x^3+x^4)\Big] - \frac{3g_A^2}{128\pi^2 f_\pi^4}\,\frac{e^{-y}}{r^6}\Big[4c_1x^2\Big(2+y(2+y)-2x^2\Big) \\ & + c_3\Big(24+y(24+12y+4y^2+y^3) - 4x^2(2+2y \\ & + y^2) + 4x^4\Big)\Big], \end{aligned} \tag{31}$$

where $x \equiv m_\pi r$ and $y \equiv \tilde{\Lambda} r$.

The relativistic $1/m_N$ corrections, with m_N being the nucleon mass, have been omitted here since, in the counting employed here, they would appear at N^{3}LO, provided the nucleon mass is counted according to $Q/m_N \sim Q^2/\Lambda_b^2$ as suggested in Weinberg [38].

The delta-less chiral EFT approach has been used to construct local interactions up to N^{2}LO. At next higher order, N^{3}LO, contact interactions cannot be written down in a purely local fashion, as only 8 out of 30 possible operators are local. A possible way forward is the definition of "maximally local" N^{3}LO potentials, which has been pursued in the delta-full approach and will be discussed in the next section.

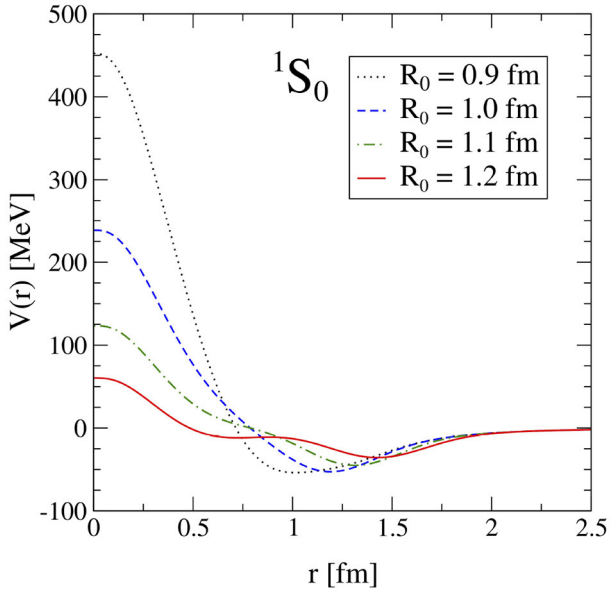


FIGURE 2 | Local delta-less chiral potential in the $^1S_0$ partial wave at N^{2}LO. The smaller the coordinate-space cutoff R_0, the smaller is the short-range repulsive core. Figure taken from Gezerlis et al. [105] under the Creative Commons CCBY license.

Finally, it is necessary to specify a regulator scheme. For the delta-less local interactions of Gezerlis et al. [104, 105], the following long- and short-range regulators are used:

$$f_{\rm long}(r) = \left(1 - e^{-\left(\frac{r}{R_0}\right)^{n_1}}\right)^{n_2} , \quad f_{\rm short}(r) = \frac{n}{4\pi\, R_0^3\, \Gamma\left(\frac{3}{n}\right)}\, e^{-\left(\frac{r}{R_0}\right)^{n}} . \tag{32}$$

The long-range regulator multiplies each function $Y(r)$, while the short-range regulator replaces all δ functions. The regulator functions depend on the cutoff scale R_0, that determines how long- and short-range physics are separated. For a smaller cutoff R_0 (i.e., for a larger momentum-space cutoff), the interactions is probed at shorter distances, and typically shows stronger short-range repulsion. We show the delta-less local chiral interactions in the $^1S_0$ channel in **Figure 2** for different values of the cutoff. Introducing a local regulator function leads to the appearance of regulator artifacts that brake Fierz-rearrangement freedom. We will address this topic in detail in section 4.1.

3.1.2. With Delta Isobars

In the delta-full local chiral interactions, coordinate-space expressions for the TPE terms at NLO and N^{2}LO are obtained by using the spectral function representation [108, 109] but with dimensional regularization (DR) [59]. This implies taking the cutoff $\tilde{\Lambda}$ in Equations (19–21) to infinity ($\tilde{\Lambda} \to \infty$). Consequently, the terms depending on the variable y in Equations (29–31) vanish. For the relevant radial functions involved in the one- and two-delta diagrams up to N^{2}LO, we refer the interested reader to **Appendix A** (**Supplementary Material**).

The singularities at the origin of the OPE and TPE components are regularized by cutoff functions of the form

$$f^{\Delta}_{\rm long}(r) = 1 - \frac{1}{(r/R_{\rm L})^6\, e^{(r-R_{\rm L})/a_{\rm L}} + 1} , \tag{33}$$

where three values for the radius $R_{\rm L}$ are considered: $R_{\rm L} = (0.8, 1.0, 1.2)$ fm with the diffuseness $a_{\rm L}$ fixed at $a_{\rm L} = R_{\rm L}/2$ in each case.

Another difference between the delta-less and delta-full coordinate-space interactions lies in the operator structure of their short-range components. In the delta-full potentials, selected contact terms at N^{3}LO are also retained in addition to the LO and NLO contributions given in Equations (16) and (26). The contact potential at order N3LO, $V^{\rm N3LO}_{\rm cont}(q,k)$, which involves four gradients acting on the nucleon fields, is expressed in terms of 15 independent operators [41] after considering the Fierz rearrangement freedom. Its standard parametrization, adopted in momentum-space potentials, is given by

$$\begin{aligned} V^{\rm N3LO}_{\rm cont}(q,k) &= \tilde{D}_1\, q^4 + \tilde{D}_2\, k^4 + \tilde{D}_3\, q^2\, k^2 + \tilde{D}_4\, (\mathbf{k}\times\mathbf{q})^2 \\ &+ \Big[\tilde{D}_5\, q^4 + \tilde{D}_6\, k^4 + \tilde{D}_7\, q^2 k^2 \\ &+ \tilde{D}_8\, (\mathbf{k}\times\mathbf{q})^2\Big]\, \boldsymbol{\sigma}_i\cdot\boldsymbol{\sigma}_j + i\,(\tilde{D}_9\, q^2 + \tilde{D}_{10}\, k^2)\, \mathbf{S}\cdot(\mathbf{k}\times\mathbf{q}) \\ &+ (\tilde{D}_{11}\, q^2 + \tilde{D}_{12}\, k^2)\, S_{ij}(\mathbf{k}) + (\tilde{D}_{13}\, q^2 + \tilde{D}_{14}\, k^2)\, S_{ij}(\mathbf{k}) \\ &+ \tilde{D}_{15}\, [\boldsymbol{\sigma}_i\cdot(\mathbf{k}\times\mathbf{q})\, \boldsymbol{\sigma}_j\cdot(\mathbf{k}\times\mathbf{q})] . \end{aligned} \tag{34}$$

However terms proportional to k^2 and k^4 in those expressions, upon Fourier transformation, would lead to gradient operators in coordinate-space ($\mathbf{p} \longrightarrow -i\boldsymbol{\nabla}$ is the relative momentum operator), making the *NN* potential strongly non-local.

The number of non-localities can be reduced by reconsidering the Fierz rearrangement freedom. However, some of these non-local terms still persist at N^{3}LO leading to the definition of "minimally non-local" contact interactions:

$$\begin{aligned} V^{\rm N3LO}_{\rm cont}(q,k) &= D_1\, q^4 + D_2\, q^4\, \boldsymbol{\tau}_i\cdot\boldsymbol{\tau}_j + D_3\, q^4\, \boldsymbol{\sigma}_i\cdot\boldsymbol{\sigma}_j + D_4\, q^4\, \boldsymbol{\sigma}_i\cdot\boldsymbol{\sigma}_j\, \boldsymbol{\tau}_i\cdot\boldsymbol{\tau}_j \\ &+ D_5\, q^2\, S_{ij}(\mathbf{q}) + D_6\, q^2\, S_{ij}(\mathbf{q})\, \boldsymbol{\tau}_i\cdot\boldsymbol{\tau}_j + iD_7\, q^2\, \mathbf{S}\cdot(\mathbf{k}\times\mathbf{q}) \\ &+ i\, D_8\, q^2\, \mathbf{S}\cdot(\mathbf{k}\times\mathbf{q})\, \boldsymbol{\tau}_i\cdot\boldsymbol{\tau}_j + D_9\, [\mathbf{S}\cdot(\mathbf{k}\times\mathbf{q})]^2 + D_{10}\, (\mathbf{k}\times\mathbf{q})^2 \\ &+ D_{11}\, (\mathbf{k}\times\mathbf{q})^2\, \boldsymbol{\sigma}_i\cdot\boldsymbol{\sigma}_j + D_{12}\, q^2 k^2 + D_{13}\, q^2 k^2 \boldsymbol{\sigma}_i\cdot\boldsymbol{\sigma}_j \\ &+ D_{14}\, k^2\, S_{ij}(\mathbf{q}) + D_{15}\, k^2\, S_{ij}(\mathbf{q})\, \boldsymbol{\tau}_i\cdot\boldsymbol{\tau}_j . \end{aligned} \tag{35}$$

In coordinate space, this reads as

$$\begin{aligned} V^{(3)}_{\rm cont}(\mathbf{r}) &= \left[\sum_{l=1}^{11} v^l_{\rm S}(r)\, O^l_{ij}\right] + \{\, v^p_{\rm S}(r) + v^{p\sigma}_{\rm S}(r)\, \boldsymbol{\sigma}_i\cdot\boldsymbol{\sigma}_j \\ &+ v^{pt}_{\rm S}(r)\, S_{ij}(\mathbf{r}) + v^{pt\tau}_{\rm S}(r)\, S_{ij}(\mathbf{r})\, \boldsymbol{\tau}_i\cdot\boldsymbol{\tau}_j\ ,\ \mathbf{p}^2\,\} , \end{aligned} \tag{36}$$

where

$$\begin{aligned} O^{l=1,\ldots,11}_{ij} &= \{\mathbf{1}\,,\ \boldsymbol{\tau}_i\cdot\boldsymbol{\tau}_j\,,\ \boldsymbol{\sigma}_i\cdot\boldsymbol{\sigma}_j\,,\ \boldsymbol{\sigma}_i\cdot\boldsymbol{\sigma}_j\, \boldsymbol{\tau}_i\cdot\boldsymbol{\tau}_j\,, S_{ij}\,,\ S_{ij}\, \boldsymbol{\tau}_i\cdot\boldsymbol{\tau}_j\,, \\ &\mathbf{L}\cdot\mathbf{S}\,,\ \mathbf{L}\cdot\mathbf{S}\, \boldsymbol{\tau}_i\cdot\boldsymbol{\tau}_j\,,\ (\mathbf{L}\cdot\mathbf{S})^2\,,\ \mathbf{L}^2\,,\ \mathbf{L}^2\, \boldsymbol{\sigma}_i\cdot\boldsymbol{\sigma}_j\}\,, \end{aligned} \tag{37}$$

referred to as $c, \tau, \sigma, \sigma\tau, t, t\tau$ for the first six operators, and $b, b\tau, bb, q, q\sigma$ for the remaining five operators. The four additional terms, denoted as $p, p\sigma, pt$, and $pt\tau$, in the anti-commutator of Equation (36) are $\mathbf{p}^2$-dependent. For the definition of the radial functions $v_S^l(r)$ as well as those multiplying the $\mathbf{p}^2$-terms, we refer the reader to **Appendix A**.

A comment is now in order. The strict adherence to power counting would require the inclusion of additional one-loop as well as two-loop TPE and three-pion exchange contributions at N^{3}LO. For the time being, these contributions have been neglected, since part of their strength is promoted at lower orders due to the inclusion of the Δ resonance, and some of the remaining diagrams are also known to be small (see e.g., [41]). Furthermore, it is the D_i LEC's at N^{3}LO that are critical for a good reproduction of phase shifts in lower partial waves, particularly D-waves, and a good fit to the *NN* database. However, the consistency between the long- and short-range part at higher orders in the delta-full chiral EFT is work in progress.

The local versions of these "minimally non-local" *NN* potentials have been defined by dropping the terms proportional to $\mathbf{p}^2$ in the anti-commutator when the optimization procedure for estimating the LECs is carried out [107]. In Piarulli et al. [107] we observed that the inclusion of the $\mathbf{p}^2$-dependent terms would have improved the fits to the database in the laboratory energy range up to 200 MeV only marginally. However, apart from the small improvement that the $\mathbf{p}^2$-dependent terms would bring to the total χ^2 in the fit to the *NN* scattering data, the effect of these terms on nuclear observables has not been studied.

Lastly, the delta-full local interactions contain additional isospin breaking terms at NLO. They are parameterized by the following operators

$$O_{ij}^{l=12,\ldots,16} = \{\tau_i^z + \tau_j^z,\ T_{ij},\ \boldsymbol{\sigma}_i \cdot \boldsymbol{\sigma}_j T_{ij},\ S_{ij}\, T_{ij},\ \mathbf{L}\cdot\mathbf{S}\, T_{ij}\}\,, \quad (38)$$

referred to as $\tau z, T, \sigma T, tT, bT$. The radial functions multiplying these operators are also reported in **Appendix A**.

The short-range part of these potentials involve the local regulator given in Equation (32) with $n = 2$,

$$f^{\Delta}_{\rm short}(r) = \frac{1}{\pi^{3/2} R_S^3} e^{-(r/R_S)^2}, \quad (39)$$

where we consider, in combination with $R_L = (0.8, 1.0, 1.2)$ fm, $R_S = (0.6, 0.7, 0.8)$ fm, corresponding to typical momentum-space cutoffs $\Lambda_S = 2/R_S$ ranging from about 660 MeV down to 500 MeV. Hereafter, we will denote the potential with cutoffs $(R_L, R_S) = (1.2, 0.8)$ fm as model *a*, that with $(1.0, 0.7)$ fm as model *b*, and that with $(0.8, 0.6)$ fm as model *c*.

There are 26 LECs in the definition of the delta-full local interactions. Of these, 20 LECs describe the charge-independent part of the interaction: 2 at LO (Q^0), 7 at NLO (Q^2), and 11 at N^{3}LO (Q^4). The remaining 6 LECs describe its charge-dependent part: 2 at LO (one each from CIB and CSB), and 4 at NLO from CIB. The optimization procedure to fix these 26 LECs uses *pp* and *np* scattering data (including normalizations), as assembled in the Granada database [80], the *NN* scattering length, and the deuteron binding energy. The minimization of the χ^2 objective function with respect to the LECs is carried out with the Practical Optimization Using no Derivatives (for Squares) routine, POUNDerS [110]. For each of three different sets of cutoff radii (R_S, R_L), two classes of local interactions have been developed, which only differ in the range of laboratory energy over which the fits were carried out, either 0–125 MeV in class I or 0–200 MeV in class II. The χ^2/datum achieved by the fits in class I (II) was $\lesssim 1.1 (\lesssim 1.4)$ for a total of about 2,700 (3,700) data points. In the literature, we are referring to these *NN* interactions generically as the Norfolk potentials (NV2s), and designate those in class I as NV2-Ia, NV2-Ib, and NV2-Ic, and those in class II as NV2-IIa, NV2-IIb, and NV2-IIc.

The NV2 interactions were found to provide insufficient attraction in calculations of the ground-state energies of nuclei with $A = 3$–6 [107]. To remedy this and similar shortcomings, 3*N* interactions at N^{2}LO have to be included in both approaches. This will be described in the next section.

3.2. Local Three-Nucleon Interactions

Three-nucleon forces are very important ingredients for the correct description of physical systems. They naturally appear within chiral EFT and are consistent with the *NN* sector. The exact description of the 3*N* interactions depends on the choice of delta-less vs. delta-full approach. In the following, we review 3*N* forces in both approaches.

3.2.1. Without Delta Isobars

In the delta-less chiral EFT approach, the leading 3*N* contributions appear at N^{2}LO in the power counting. They an be separated into three topologies: (i) a long-range TPE interaction named V_C depending on the pion-nucleon LECs c_1, c_3, and c_4, that already appear in the *NN* sector, (ii) a one-pion-exchange–contact interaction V_D dependent on a new LEC c_D, and (iii) a 3N contact interaction V_E dependent in a new LEC c_E. The LECs c_D and c_E solely describe 3*N* physics and need to be adjusted to properties of $A \geq 3$ systems. In momentum space, these interactions are defined as

$$V_C = \frac{1}{2}\left(\frac{g_A}{2f_\pi}\right)^2 \sum_{\pi(ijk)} \frac{\boldsymbol{\sigma}_i \cdot \mathbf{q}_i\, \boldsymbol{\sigma}_k \cdot \mathbf{q}_k}{(q_i^2 + m_\pi^2)(q_k^2 + m_\pi^2)} F_{ijk}^{\alpha\beta}\, \boldsymbol{\tau}_i^\alpha\, \boldsymbol{\tau}_k^\beta\,, \quad (40)$$

$$V_D = -\frac{g_A}{8f_\pi^2}\frac{c_D}{f_\pi^2 \Lambda_\chi} \sum_{\pi(ijk)} \frac{\boldsymbol{\sigma}_k \cdot \mathbf{q}_k}{q_k^2 + m_\pi^2}\, \boldsymbol{\sigma}_i \cdot \mathbf{q}_k\, \boldsymbol{\tau}_i \cdot \boldsymbol{\tau}_k\,, \quad (41)$$

$$V_E = \frac{c_E}{2f_\pi^4 \Lambda_\chi} \sum_{\pi(ijk)} \boldsymbol{\tau}_i \cdot \boldsymbol{\tau}_k\,, \quad (42)$$

where we sum over all permutations of the particles *i*, *j*, and *k*, where the first pion carries a momentum $\mathbf{q}_i$ from nucleon i to j, while the second pion carries $\mathbf{q}_k$ from j to k, and where $F_{ijk}^{\alpha\beta}$ is given by

$$F_{ijk}^{\alpha\beta} = \delta^{\alpha\beta}\left[-\frac{4c_1 m_\pi^2}{f_\pi^2} + \frac{2c_3}{f_\pi^2}\,\mathbf{q}_i \cdot \mathbf{q}_k\right] + \sum_\gamma \frac{c_4}{f_\pi^2} \varepsilon^{\alpha\beta\gamma}\, \boldsymbol{\tau}_j^\gamma\, \boldsymbol{\sigma}_j \cdot (\mathbf{q}_i \times \mathbf{q}_k)\,. \quad (43)$$

As one can easily see, all of these interactions are local, as long as local regulator functions are applied. To obtain expressions in coordinate space, these interactions have to be Fourier transformed. For the part of V_C proportional to c_1, we find

$$V_{C,c_1}^{ijk} = -\frac{c_1 m_\pi^2 g_A^2}{2f_\pi^4} \sum_{\pi(ijk)} \boldsymbol{\tau}_i \cdot \boldsymbol{\tau}_k \int \frac{d^3q_i}{(2\pi)^3} \frac{\boldsymbol{\sigma}_i \cdot \mathbf{q}_i}{q_i^2 + m_\pi^2} e^{i\mathbf{q}_i \cdot \mathbf{r}_{ij}} \int \frac{d^3q_k}{(2\pi)^3} \frac{\boldsymbol{\sigma}_k \cdot \mathbf{q}_k}{q_k^2 + m_\pi^2} e^{i\mathbf{q}_k \cdot \mathbf{r}_{kj}} . \quad (44)$$

This results in

$$V_{C,c_1}^{ijk} = \frac{c_1 m_\pi^6 g_A^2}{2f_\pi^4 (4\pi)^2} \sum_{\pi(ijk)} \boldsymbol{\tau}_i \cdot \boldsymbol{\tau}_k \, \boldsymbol{\sigma}_i \cdot \hat{\mathbf{r}}_{ij} \, \boldsymbol{\sigma}_k \cdot \hat{\mathbf{r}}_{kj} \, U(r_{ij}) Y(r_{ij}) U(r_{kj}) Y(r_{kj}) , \quad (45)$$

where we have used

$$\int \frac{d^3q_i}{(2\pi)^3} \frac{\boldsymbol{\sigma}_i \cdot \mathbf{q}_i}{q_i^2 + m_\pi^2} e^{i\mathbf{q}_i \cdot \mathbf{r}_{ij}} = -i \, \sigma_i^\alpha \, \partial^\alpha \frac{e^{-m_\pi r_{ij}}}{4\pi r_{ij}} = i \frac{m_\pi^2}{4\pi} \sigma_i^\alpha \hat{r}_{ij}^\alpha \, U(r_{ij}) Y(r_{ij}) , \quad (46)$$

and

$$Y(r) = \frac{\exp(-m_\pi \cdot r)}{m_\pi r} , \quad U(r) = 1 + \frac{1}{m_\pi r} . \quad (47)$$

For the other parts of V_C we find

$$V_{C,c_3} = \frac{g_A^2 m_\pi^6 c_3}{2304\pi^2 f_\pi^4} \sum_{\pi(ijk)} \{\boldsymbol{\tau}_i \cdot \boldsymbol{\tau}_k, \boldsymbol{\tau}_k \cdot \boldsymbol{\tau}_j\} \{\mathcal{X}_{ik}(\mathbf{r}_{ik}), \mathcal{X}_{kj}(\mathbf{r}_{kj})\} , \quad (48)$$

$$V_{C,c_4} = -\frac{g_A^2 m_\pi^6 c_4}{4608\pi^2 f_\pi^4} \sum_{\pi(ijk)} [\boldsymbol{\tau}_i \cdot \boldsymbol{\tau}_k, \boldsymbol{\tau}_k \cdot \boldsymbol{\tau}_j] [\mathcal{X}_{ik}(\mathbf{r}_{ik}), \mathcal{X}_{kj}(\mathbf{r}_{kj})] , \quad (49)$$

where

$$\mathcal{X}_{ij}(\mathbf{r}) = X_{ij}(\mathbf{r}) - \frac{4\pi}{m_\pi^3} \delta(\mathbf{r}) \boldsymbol{\sigma}_i \cdot \boldsymbol{\sigma}_j , \quad X_{ij}(\mathbf{r}) = \left(S_{ij}(\mathbf{r}) T(r) + \boldsymbol{\sigma}_i \cdot \boldsymbol{\sigma}_j Y(r) \right) , \quad (50)$$

and

$$T(r) = \left(1 + \frac{3}{m_\pi r} + \frac{3}{m_\pi^2 r^2} \right) Y(r) . \quad (51)$$

For the one-pion-exchange–contact part V_D we find

$$V_D^{ijk} = \frac{g_A}{24 f_\pi^2} \frac{c_D}{f_\pi^2 \Lambda_\chi} \sum_{\pi(ijk)} \boldsymbol{\tau}_i \cdot \boldsymbol{\tau}_k \left[\frac{m_\pi^3}{4\pi} \delta(\mathbf{r}_{ij}) X_{ik}(\mathbf{r}_{kj}) - \boldsymbol{\sigma}_i \cdot \boldsymbol{\sigma}_k \, \delta(\mathbf{r}_{ij}) \delta(\mathbf{r}_{kj}) \right] , \quad (52)$$

and for the three-nucleon–contact interaction V_E we find

$$V_E = \frac{c_E}{2 f_\pi^4 \Lambda_\chi} \sum_{\pi(ijk)} \boldsymbol{\tau}_i \cdot \boldsymbol{\tau}_k \delta(\mathbf{r}_{ij}) \delta(\mathbf{r}_{kj}) . \quad (53)$$

To regularize these 3N topologies, we choose consistent regulators with the NN sector, i.e., we replace δ functions by $f_{\text{short}}(r)$ and multiply Yukawa functions with $f_{\text{long}}(r)$. The cutoff scale for 3N interactions does not necessarily have to be the same as for the NN sector, and we call it R_{3N} in the following.

To adjust the appearing 3N couplings to experimental data, one should select few-body observables that are uncorrelated. In the delta-less approach, these observables have been chosen to be the ^{4}He binding energy and n-α scattering P wave phase shifts (see **Figure 3**), where we show parameter curves for the 3N LECs for different 3N cutoffs R_{3N}, chosen similar to R_0, and for different parameterizations that we will discuss in the next section. Stars in the parameter curves mark fits that also describe neutron-alpha scattering, shown in the right panel. For more details, see Lynn et al. [91].

3.2.2. With Delta Isobars

In the delta-full chiral EFT approach, the structure of the 3N force at N^{2}LO is similar to the 3N force in the delta-less approach. We still have the three topologies V_C, V_D, and V_E at N^{2}LO but, in addition, the well-known Fujita-Miyazawa interaction [34] (V_Δ), which in the delta-less approach is absorbed by V_C, appears already at NLO in the power counting. In momentum space, it reads as

$$V_\Delta^{ijk} = -\frac{g_A^2 h_A^2}{16 f_\pi^4} \frac{1}{m_{\Delta N} (q_i^2 + m_\pi^2)(q_k^2 + m_\pi^2)} \Big[\boldsymbol{\sigma}_k \cdot \mathbf{q}_k \, \mathbf{S}_j^\dagger \cdot \mathbf{q}_k \, \mathbf{S}_j \cdot \mathbf{q}_i \, \boldsymbol{\sigma}_i \cdot \mathbf{q}_i \, \boldsymbol{\tau}_k \cdot \mathbf{T}_j^\dagger \, \mathbf{T}_j \cdot \boldsymbol{\tau}_i \quad (54)$$

$$- \boldsymbol{\sigma}_i \cdot \mathbf{q}_i \, \mathbf{S}_j^\dagger \cdot \mathbf{q}_i \, \mathbf{S}_j \cdot \mathbf{q}_k \, \boldsymbol{\sigma}_k \cdot \mathbf{q}_k \, \boldsymbol{\tau}_i \cdot \mathbf{T}_j^\dagger \, \mathbf{T}_j \cdot \boldsymbol{\tau}_k \Big] , \quad (55)$$

where S, $S^\dagger$ and T, $T^\dagger$ are the transition spin and isospin operators: The operator S (T) converts a spin (isospin) 1/2 into a spin (isospin) 3/2 particle.

The configuration-space expression follows from

$$V_\Delta^{ijk} = -\frac{g_A^2 h_A^2}{16 \cdot 144 \, \pi^2} \frac{m_\pi^6}{m_{\Delta N} f_\pi^4} \left[X_{jk}^{II\,\dagger} X_{ji}^{II} \, \mathbf{T}_j^\dagger \cdot \boldsymbol{\tau}_k \, \mathbf{T}_j \cdot \boldsymbol{\tau}_i + X_{ji}^{II\,\dagger} X_{jk}^{II} \, \mathbf{T}_j^\dagger \cdot \boldsymbol{\tau}_i \, \mathbf{T}_j \cdot \boldsymbol{\tau}_k \right] , \quad (56)$$

where the following definitions have been introduced:

$$X_{ij}^{II} = T(r_{ij}) \, S_{ij}^{II} + Y(r_{ij}) \, \mathbf{S}_i \cdot \boldsymbol{\sigma}_j , \quad S_{ij}^{II} = 3 \, \mathbf{S}_i \cdot \hat{\mathbf{r}}_{ij} \, \boldsymbol{\sigma}_j \cdot \hat{\mathbf{r}}_{ij} - \mathbf{S}_i \cdot \boldsymbol{\sigma}_j \quad (57)$$

and the dimensionless functions $Y(r)$ and $T(r)$ defined before. The term $[\cdots]$ in Equation (56) can be written as

$$[\cdots] = \frac{1}{2} \Big[\left(X_{jk}^{II\,\dagger} X_{ji}^{II} + \text{h.c.} \right) \left(\mathbf{T}_j^\dagger \cdot \boldsymbol{\tau}_k \, \mathbf{T}_j \cdot \boldsymbol{\tau}_i + \text{h.c.} \right) + \left(X_{jk}^{II\,\dagger} X_{ji}^{II} - \text{h.c.} \right) \left(\mathbf{T}_j^\dagger \cdot \boldsymbol{\tau}_k \, \mathbf{T}_j \cdot \boldsymbol{\tau}_i - \text{h.c.} \right) \Big] , \quad (58)$$

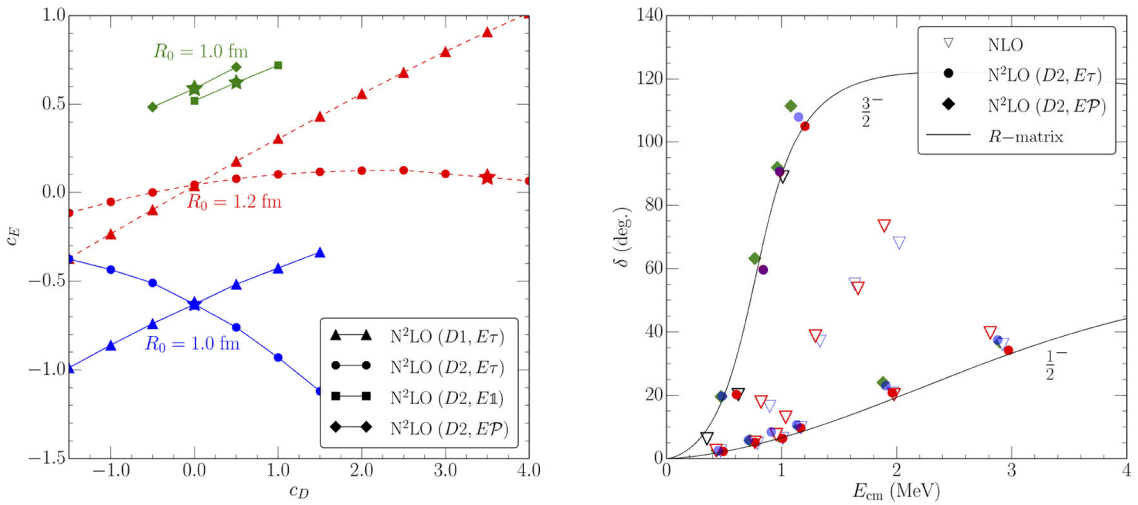


FIGURE 3 | (Left) Parameter curves for the LECs c_D and c_E for the binding energy of ^{4}He for different cutoffs and 3*N* parameterizations discussed in section 4. **(Right)** Reproduction of n-α *P* wave phase shifts at NLO and at N^{2}LO for the parameter combinations marked by a star in the left panel. Figures taken from Lynn et al. [91] under the Creative Commons CCBY license.

and the transition-spin and transition-isospin operators can be eliminated using the identities

$$X^{II\dagger}_{jk}\, X^{II}_{ji} + \text{h.c.} = \frac{2}{3}\Big\{X_{jk}\,,\, X_{ji}\Big\}\,, \tag{59}$$

$$X^{II\dagger}_{jk}\, X^{II}_{ji} - \text{h.c.} = -\frac{1}{3}\Big[X_{jk}\,,\, X_{ji}\Big]\,, \tag{60}$$

$$\mathbf{T}^\dagger_j \cdot \boldsymbol{\tau}_k\, \mathbf{T}_j \cdot \boldsymbol{\tau}_i + \text{h.c.} = \frac{2}{3}\Big\{\boldsymbol{\tau}_j \cdot \boldsymbol{\tau}_k\,,\, \boldsymbol{\tau}_j \cdot \boldsymbol{\tau}_i\Big\}\,, \tag{61}$$

$$\mathbf{T}^\dagger_j \cdot \boldsymbol{\tau}_k\, \mathbf{T}_j \cdot \boldsymbol{\tau}_i - \text{h.c.} = -\frac{1}{3}\Big[\boldsymbol{\tau}_j \cdot \boldsymbol{\tau}_k\,,\, \boldsymbol{\tau}_j \cdot \boldsymbol{\tau}_i\Big]\,, \tag{62}$$

to obtain

$$V^{ijk}_{\Delta} = -\frac{g_A^2 h_A^2}{72\cdot 144\,\pi^2}\,\frac{m_\pi^6}{m_{\Delta N} f_\pi^4}\Bigg[\Big\{X_{ij}\,,\, X_{jk}\Big\}\Big\{\boldsymbol{\tau}_i \cdot \boldsymbol{\tau}_j\,,\, \boldsymbol{\tau}_j \cdot \boldsymbol{\tau}_k\Big\} + \frac{1}{4}\Big[X_{ij}\,,\, X_{jk}\Big]\Big[\boldsymbol{\tau}_i \cdot \boldsymbol{\tau}_j\,,\, \boldsymbol{\tau}_j \cdot \boldsymbol{\tau}_k\Big]\Bigg]\,, \tag{63}$$

where the function X_{ij} was defined in the previous section. In the definitions above, the $\delta(\mathbf{r})$-function terms have been dropped.

In analogy to the 3*N* delta-less chiral EFT, we regularize the 3*N* contributions in the delta-full chiral EFT by replacing the δ functions with $f^{\Delta}_{\rm short}(r)$ and multiplying the Yukawa functions with $f^{\Delta}_{\rm long}(r)$. Note that the implementation of V_C and V_D in the delta-full chiral EFT does not retain the terms proportional to $\boldsymbol{\sigma}_i \cdot \boldsymbol{\sigma}_j$ in the definition of $\mathcal{X}_{ik}$, in Equations (50) and (52). They can be reabsorbed in the redefinition of the short-range contact terms.

In the delta-full chiral EFT, two different sets for the values of c_D and c_E were obtained, leading to two different parametrization of the 3*N* interaction [93, 96]. In the first, these LECs were determined by simultaneously reproducing the experimental trinucleon ground-state energies and neutron-deuteron (*nd*) doublet scattering length, as shown in the left panel of **Figure 4**. In the second set, these c_D and c_E were constrained by fitting, in addition to the trinucleon energies, the empirical value of the Gamow-Teller matrix element in tritium β decay [96], see right panel of **Figure 4**. Because of the much reduced correlation between binding energies and the GT matrix element, the second fit procedure leads to a more robust determination of c_D and c_E then attained in the first one. Note that these observables have been calculated with hyperspherical-harmonics (HH) expansion methods [5] as described in Piarulli et al. [93], Gazit et al. [94], Marcucci et al. [95], and Baroni et al. [96].

4. FINITE CUTOFF AND REGULATOR ARTIFACTS

The derivations of local interactions in the last sections did not include any of the local regulator functions that necessarily have to be applied to the interactions to make them suitable for the use in nuclear many-body methods. Generally, when introducing a regulator function, terms beyond the order at which one is working are affected. Hence, the use of such regulator functions with finite values for the cutoff leads to the appearance of regulator artifacts, that might influence calculations of many-body observables. In this section, we will address the different regulator artifacts that can appear in calculations with local interactions.

4.1. Violation of Fierz-Rearrangement Freedom

The first regulator artifact for local interactions affects short-range operators. In previous sections we had shown how only half of the operators at each order are linearly independent due to their insertion between

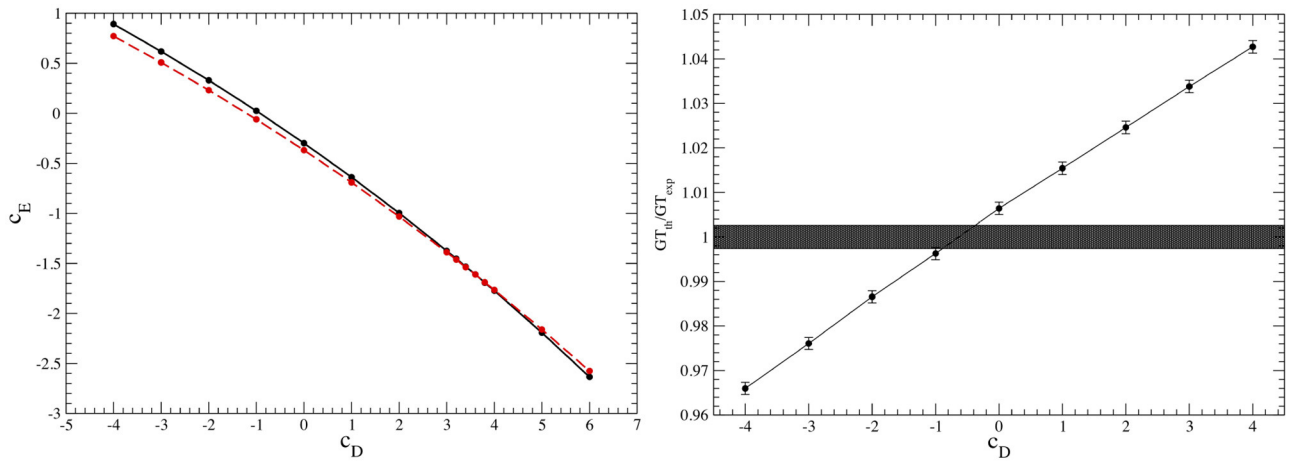


FIGURE 4 | (Left) The c_D-c_E trajectories obtained by fitting the experimental trinucleon binding energies (solid line) and *nd* doublet scattering length (dashed line) (the intercept of these two lines gives the c_D and c_E values that reproduce these two observables simultaneously). Figure taken from Piarulli et al. [93] under the Creative Commons CCBY license. **(Right)** The calculated ratio GT_{th}/GT_{exp} as function of c_D (solid line; each point on his line reproduces the trinucleon binding energies). Figure taken from Baroni et al. [96] under the Creative Commons CCBY license.

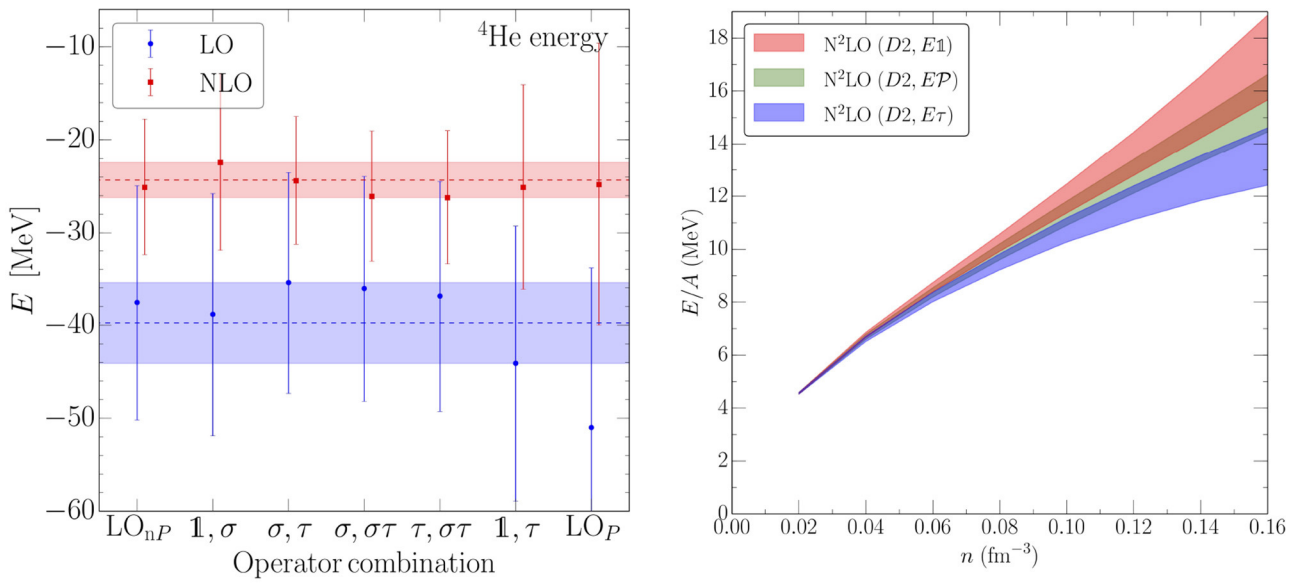


FIGURE 5 | (Left) Ground-state energies of ^{4}He at LO and NLO for different LO operator choices. Figure taken from Huth et al. [111] under the Creative Commons CCBY license. **(Right)** Regulator artifacts in pure neutron matter due to the violation of the Fierz rearrangement freedom for the 3*N* contact interactions. The three different bands correspond to three different operator choices, where the green band projects the 3*N* interaction on triples with $S = 1/2$ and $T = 1/2$. Figure taken from Lynn et al. [91] under the Creative Commons CCBY license.

antisymmetric fermionic states (see e.g., Equation 15). However, this argument changes when a regulator function is applied. The discussion in this section will follow Huth et al. [111].

In general, a regulator function can depend on two momentum scales, $f_R(\mathbf{q}, \mathbf{k})$. Local regulators, on the other hand, only depend on $\mathbf{q}$, $f_{R,\text{loc}}(\mathbf{q})$. The derivation of Equation (15) remains valid if the regulator function commutes with the anti-symmetrizer and, hence, reduces to a simple pre-factor in Equation (15), i.e., when

$$f_R(\mathbf{q}, \mathbf{k}) = f_R\left(-2\mathbf{k}, -\frac{1}{2}\mathbf{q}\right). \tag{64}$$

We can immediately see, that a purely local regulator can never fulfill this condition while typical non-local regulators of the

form [76–78, 83, 84]

$$f_R(\mathbf{p},\mathbf{p}') = \exp\left[-\left(\frac{\mathbf{p}}{\Lambda}\right)^{2n}\right]\exp\left[-\left(\frac{\mathbf{p}'}{\Lambda}\right)^{2n}\right], \quad (65)$$

do. As a consequence,

$$\begin{aligned} V^{(0,\mathrm{loc})}_{\mathrm{cont,as}} &= \frac{1}{2}\left(1-\frac{\mathcal{P}^{\mathrm{m}}}{4}(1+\boldsymbol{\sigma}_i\cdot\boldsymbol{\sigma}_j)(1+\boldsymbol{\tau}_i\cdot\boldsymbol{\tau}_j)\right)V^{(0)}_{\mathrm{cont}} f_R(\mathbf{q}) \\ &= \mathbb{1}\left(\frac{C_{\mathbb{1}}}{2}f_R(\mathbf{q}) - \frac{1}{8}\left(C_{\mathbb{1}}+3C_\sigma+3C_\tau+9C_{\sigma\tau}\right)f_R(2\mathbf{k})\right) \\ &+ \boldsymbol{\sigma}_i\cdot\boldsymbol{\sigma}_j\left(\frac{C_\sigma}{2}f_R(\mathbf{q}) - \frac{1}{8}\left(C_{\mathbb{1}}-C_\sigma+3C_\tau-3C_{\sigma\tau}\right)f_R(2\mathbf{k})\right) \\ &+ \boldsymbol{\tau}_i\cdot\boldsymbol{\tau}_j\left(\frac{C_\tau}{2}f_R(\mathbf{q}) - \frac{1}{8}\left(C_{\mathbb{1}}+3C_\sigma-C_\tau-3C_{\sigma\tau}\right)f_R(2\mathbf{k})\right) \\ &+ \boldsymbol{\sigma}_i\cdot\boldsymbol{\sigma}_j\boldsymbol{\tau}_i\cdot\boldsymbol{\tau}_j\left(\frac{C_{\sigma\tau}}{2}f_R(\mathbf{q}) - \frac{1}{8}\left(C_{\mathbb{1}}-C_\sigma-C_\tau+C_{\sigma\tau}\right)f_R(2\mathbf{k})\right), \end{aligned} \quad (66)$$

and the Fierz-rearrangement freedom is violated. For general regulator functions as defined in the previous sections, this leads to

$$\begin{aligned} V^{(0,\mathrm{loc})}_{\mathrm{cont,as}} = &\left(\tilde{C}_S+\tilde{C}_T\boldsymbol{\sigma}_i\cdot\boldsymbol{\sigma}_j+\left(-\frac{2}{3}\tilde{C}_S-\tilde{C}_T\right)\boldsymbol{\tau}_i\cdot\boldsymbol{\tau}_j\right. \\ &\left.+\left(-\frac{1}{3}\tilde{C}_S\right)\boldsymbol{\sigma}_i\cdot\boldsymbol{\sigma}_j\boldsymbol{\tau}_i\cdot\boldsymbol{\tau}_j\right)f_R(\mathbf{q}) + V^f_{\mathrm{corr}}(\mathbf{p}\cdot\mathbf{p}'), \end{aligned} \quad (67)$$

where $V^f_{\mathrm{corr}}(\mathbf{p}\cdot\mathbf{p}')$ captures all the regulator artifacts that are of higher-order in the EFT. It depends on the functional form of the regulator and the cutoff value. One can also see, that the corrections can be angle-dependent, which leads to a mixing of different partial waves. As a consequence, when applying these regulators to a three-neutron system, for example, pure contact interactions, that otherwise would vanish due to the Pauli principle, start to contribute. This mixing of partial waves complicates the fitting procedure, increases theoretical uncertainties, and makes calculated observables dependent on the operator structure that was chosen.

In **Figure 5** we show results for the ^{4}He ground-state energy for different LO operator choices. As one can see, the ground-state energies can vary by ∼10 MeV at LO, depending on the operator choice. However, when going to higher order and including subleading contact operators, regulator artifacts get partially absorbed and corrected. Then, only higher-order artifacts remain, which improves the situation considerably, as can be seen for the NLO results. In this case, the spread originating from different choices of LO operators reduces to ∼4 MeV.

A similar effect appears in the 3N sector, where the V_E contact interaction suffers from a similar violation of the Fierz freedom when local regulators are applied. While 3*N* forces are typically fit to symmetric systems where this dependence can then be approximately accounted for, in triples with $S = 3/2$ or $T = 3/2$ (where typically no 3*N* contact force can contribute due to the Pauli principle) regulator artifacts appear, and lead to a finite contribution from 3*N* contact interactions that depend on the operator choice. We show this behavior in **Figure 5** in the right panel in the case of pure neutron matter, where all triples have T = 3/2. The three different bands explore three choices for the 3*N* contact operators. At nuclear saturation density, we find that the regulator artifacts introduce a spread of ∼5 MeV. Unfortunately, higher-order correction terms only appear at N^{4}LO and, to date, are not systematically included in any calculation.

Finally, we mention that the finite cutoff also introduces an ambiguity in the V_D term, that depends on the choice of the initial spin-isospin structure when Fourier transforming:

$$\begin{aligned} V^{ijk}_{D,1} = &\frac{g_A}{24f_\pi^2}\frac{c_D}{f_\pi^2\Lambda_\chi}\sum_{\pi(ijk)}\boldsymbol{\tau}_i\cdot\boldsymbol{\tau}_k\left[\frac{m_\pi^3}{4\pi}\,\delta(\mathbf{r}_{ij})X_{ik}(\mathbf{r}_{kj})\right. \\ &\left.-\boldsymbol{\sigma}_i\cdot\boldsymbol{\sigma}_k\,\delta(\mathbf{r}_{ij})\delta(\mathbf{r}_{kj})\right], \\ V^{ijk}_{D,2} = &\frac{g_A}{24f_\pi^2}\frac{c_D}{f_\pi^2\Lambda_\chi}\sum_{\pi(ijk)}\boldsymbol{\tau}_i\cdot\boldsymbol{\tau}_k\left[\frac{m_\pi^3}{4\pi}\,\delta(\mathbf{r}_{ij})X_{ik}(\mathbf{r}_{ik})\right. \\ &\left.-\boldsymbol{\sigma}_i\cdot\boldsymbol{\sigma}_k\,\delta(\mathbf{r}_{ij})\delta(\mathbf{r}_{ik})\right]. \end{aligned} \quad (68)$$

Both expressions are identical for true δ functions (infinite cutoff) but differ when a finite cutoff is applied.

4.2. Weaker Pion Exchanges

A second regulator artifact for local regulators affects the pion exchanges. In Tews et al. [90] it was shown that locally regulated pion exchanges lead to less 3*N* repulsion than non-locally regulated pion exchanges. At the Hartree-Fock level, for a typical cutoff of 2.5fm^{-1}, when applying non-local regulators ≈ 97% of the infinite cutoff result is recovered, while local regulators only recover ≈ 60%. To reproduce the momentum-space results, the cutoff has to be considerably increased.

Local regulators for pion exchanges have been investigated in detail in Dyhdalo et al. [112] in both the *NN* and 3*N* sector. The fact that the contribution due to pion exchanges is weaker for local than for non-local regulator functions is easy to understand in the Hartree-Fock approximation. At the Hartree-Fock level, there are both a direct and an exchange term. The momentum transfer $\mathbf{q} = \mathbf{p} - \mathbf{p}'$ vanishes in the direct term because $\mathbf{p} = \mathbf{p}'$, but it is $\mathbf{q} = 2\mathbf{p}$ in the exchange term because $\mathbf{p} = -\mathbf{p}'$. A typical local regulator of the form $\exp\left(-\left(\frac{q}{\Lambda}\right)^n\right)$, thus, evaluates to 1 in the direct term, but to $\exp\left(-\left(\frac{p}{\Lambda/2}\right)^n\right)$ in the exchange term. Therefore, compared to non-local regulators for which both terms are identical, $\exp\left(-\left(\frac{p}{\Lambda}\right)^n\right)$, local regulators have a very different behavior. In particular, local regulators have an effectively lower cutoff in the exchange channel. In the Hartree-Fock approximation, where the direct term vanishes for spin-dependent interactions like pion exchanges, only the exchange term contributes and, hence, is weaker for local than for non-local regulators.

While the situation is more complicated when abandoning the Hartree-Fock approximation, this reasoning qualitatively

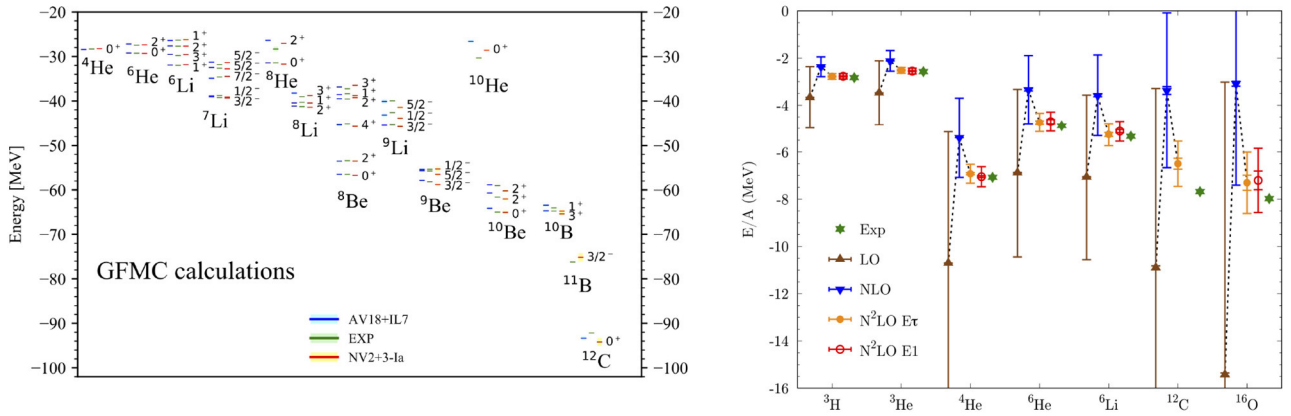


FIGURE 6 | (Left) Spectra of light nuclei up to ^{12}C obtained with GFMC with chiral interactions obtained in the delta-full approach (red) compared to experimental data (green) and GFMC calculations with phenomenological interactions (blue). Figure taken from Piarulli et al. [93] under the Creative Commons CCBY license. **(Right)** Ground-state energies for nuclei up to ^{16}O at different orders in the chiral expansion for AFDMC calculations with local interactions in the delta-less approach. Reprinted from Lonardoni et al. [99] with permission from the American Physical Society.

remains valid and locally regulated pion exchanges are weaker than non-locally regulated pion exchanges.

5. SELECTED RESULTS

In this section, we will briefly show the successes of Quantum Monte Carlo calculations with local chiral interactions for light atomic nuclei and infinite matter.

5.1. Light Nuclei

Local chiral interactions, both in the delta-less and delta-full approach, have been used to successfully describe properties of light nuclei using QMC methods. In **Figure 6**, we show GFMC results for ground- and excited states for nuclei up to ^{12}C within the delta-full approach compared to experimental data. In addition, the results obtained with chiral EFT are compared to results with phenomenological interactions. The results clearly show that chiral interactions describe spectra of light nuclei with great success and are compatible to the accuracy of phenomenological interaction in these systems. In addition, we also show ground-state energies obtained in the AFDMC method for nuclei up to ^{16}O for delta-less chiral interactions. Results are given at LO, NLO, and N^{2}LO for two different 3*N* parameterizations to explore regulator artifacts. Again, chiral interactions agree well with experimental results, which are shown as green points.

In addition to energies, local chiral interactions describe charge radii well. In **Figure 7**, we present order-by-order AFDMC results for the charge radii of nuclei up to ^{16}O, compared to experiment. Again, the description is accurate. In addition, as mentioned before, delta-less chiral interactions have been adjusted to reproduce neutron-alpha scattering phase shifts (see **Figure 3**). While *NN* interactions alone cannot reproduce the *P* wave splitting in this system (NLO calculations in **Figure 3**), chiral Hamiltonians at N^{2}LO, including 3*N* interactions, reproduce the neutron-α *P* wave scattering phase shifts accurately.

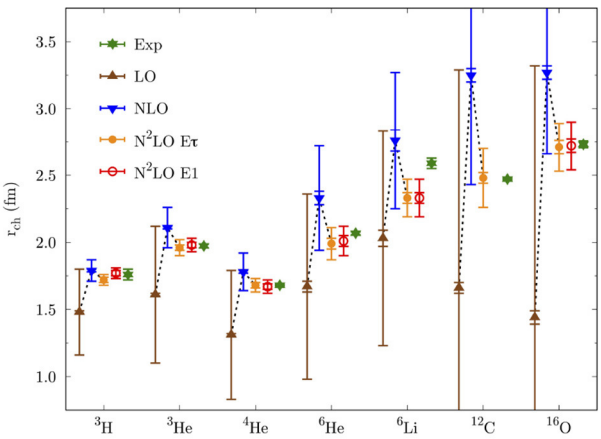


FIGURE 7 | Same as **Figure 6** (right) but for radii of nuclei up to ^{16}O. Reprinted from Lonardoni et al. [99] with permission from the American Physical Society.

5.2. Infinite Matter

In addition to properties of atomic nuclei, local chiral interactions have been used to study infinite matter, and in particular, pure neutron matter. In the right panel of **Figure 3**, we have already shown results for the energy per particle of pure neutron matter. Results are shown for three Hamiltonians at N^{2}LO, that explore the uncertainty due to regulator artifacts and the truncation of the chiral series. While uncertainties in pure neutron matter are enhanced due to the local regulator artifacts discussed before, indicated by the differences between the three bands, the resulting neutron-matter equation of state (EOS) is consistent with other ab initio determinations within uncertainties.

These calculations have been successfully used to study the EOS of neutron stars, and it has been found that the resulting equations of state are consistent with astrophysical observations of pulsar masses. The EOS have also been used to study gravitational waves from neutron-star mergers [102, 113, 114].

6. CONCLUSION AND OUTLOOK

The quest to understand properties of nuclear systems in terms of forces acting between the nucleons has been considered one of the most challenging efforts of nuclear theory. During the past quarter century, particular emphasis has been devoted to the systematic framework provided by chiral EFT. This approach allows for a consistent description of the two- and many-body interactions and ensuing many-body currents, and a quantification of the theoretical uncertainty due to the truncation error in the chiral expansion.

In this review, we have presented a comprehensive description of the two families of local chiral interactions that have been developed for the use in QMC methods: one within the delta-less and one within the delta-full approach. We provided many details about the theoretical derivation and optimization of these nuclear models addressing their similarities and differences. For completeness, we also presented selected QMC results for light nuclei and neutron matter. These results show that the combination of local chiral EFT interactions with powerful QMC many-body methods can accurately describe ground- and excited-state energies, radii of nuclei up to ^{16}O, and n-α scattering, as well as the equation of state of neutron matter.

These local chiral interactions have also been used to calculate the distribution of nucleons in a nucleus in both momentum and coordinate space which are related to experimental observations [99, 100, 115, 116], in benchmark calculations of the energy per particle of pure neutron matter as a function of the baryon density [103] and in studies of neutrinoless double-beta decays [117].

In future, local chiral interactions will continue to serve as input for precise QMC methods to systematically study, for example, electroweak reactions, along the lines of Pastore et al. [118], Marcucci et al. [119], Lovato et al. [120, 121], Pastore et al. [122], Schiavilla et al. [123], and Pastore et al. [124] and infinite matter also at finite proton fractions.

Improvements to the interactions that reduce uncertainties due to the scheme and scale dependence of the interactions, e.g., the inclusion of higher orders in the chiral expansion in both the NN and $3N$ sectors, will provide exciting prospects and permit precision studies of many nuclear systems.

AUTHOR CONTRIBUTIONS

All authors listed have made a substantial, direct and intellectual contribution to the work, and approved it for publication.

FUNDING

This work was supported by the US Department of Energy, Office of Science, Office of Nuclear Physics, under Contract DE-AC52-06NA25396 (IT), the FRIB Theory Alliance award DE-SC0013617 (MP), the Los Alamos National Laboratory (LANL) LDRD program, and the NUCLEI SciDAC and INCITE programs. Part of this research used resources of the Argonne Leadership Computing Facility at Argonne National Laboratory, the Los Alamos Open Supercomputing via the Institutional Computing (IC) program, and the National Energy Research Scientific Computing Center (NERSC), which was supported by the U.S. Department of Energy, Office of Science, under contract No. DE-AC02-05CH11231.

ACKNOWLEDGMENTS

We thank our collaborators A. Baroni, J. Carlson, E. Epelbaum, S. Gandolfi, A. Gezerlis, L. Girlanda, K. Hebeler, L. Huth, A. Kievsky, D. Lonardoni, A. Lovato, J. E. Lynn, L. E. Marcucci, A. Nogga, S. Pastore, R. Schiavilla, K. E. Schmidt, A. Schwenk, M. Viviani, and R. B. Wiringa for their contributions to the studies presented in this work.

SUPPLEMENTARY MATERIAL

The Supplementary Material for this article can be found online at: https://www.frontiersin.org/articles/10.3389/fphy.2019.00245/full#supplementary-material

REFERENCES

1. Barrett BR, Navratil P, Vary JP. *Ab initio* no core shell model. *Prog Part Nucl Phys.* (2013) **69**:131–81. doi: 10.1016/j.ppnp.2012.10.003
2. Jurgenson ED, Maris P, Furnstahl RJ, Navratil P, Ormand WE, Vary JP. Structure of *p*-shell nuclei using three-nucleon interactions evolved with the similarity renormalization group. *Phys Rev.* (2013) **C87**:054312. doi: 10.1103/PhysRevC.87.054312
3. Hagen G, Papenbrock T, Ekström A, Wendt KA, Baardsen G, Gandolfi S, et al. Coupled-cluster calculations of nucleonic matter. *Phys Rev.* (2014) **C89**:014319. doi: 10.1103/PhysRevC.89.014319
4. Hagen G, Papenbrock T, Hjorth-Jensen M, Dean DJ. Coupled-cluster computations of atomic nuclei. *Rept Prog Phys.* (2014) **77**:096302. doi: 10.1088/0034-4885/77/9/096302
5. Kievsky A, Rosati S, Viviani M, Marcucci LE, Girlanda L. A High-precision variational approach to three- and four-nucleon bound and zero-energy scattering states. *J Phys.* (2008) **G35**:063101. doi: 10.1088/0954-3899/35/6/063101
6. Bogner SK, Furnstahl RJ, Schwenk A. From low-momentum interactions to nuclear structure. *Prog Part Nucl Phys.* (2010) **65**:94–147. doi: 10.1016/j.ppnp.2010.03.001
7. Hergert H, Bogner SK, Binder S, Calci A, Langhammer J, Roth R, et al. In-medium similarity renormalization group with chiral two- plus three-nucleon interactions. *Phys Rev.* (2013) **C87**:034307. doi: 10.1103/PhysRevC.87.034307
8. Dickhoff WH, Barbieri C. Self-consistent Green's function method for nuclei and nuclear matter. *Prog Part Nucl Phys.* (2004) **52**:377–496. doi: 10.1016/j.ppnp.2004.02.038

9. Soma V, Barbieri C, Duguet T. *Ab-initio* Gorkov-Green's function calculations of open-shell nuclei. *Phys Rev.* (2013) **C87**:011303. doi: 10.1103/PhysRevC.87.011303
10. Carlson J, Gandolfi S, Pederiva F, Pieper SC, Schiavilla R, Schmidt KE, et al. Quantum Monte Carlo methods for nuclear physics. *Rev Mod Phys.* (2015) **87**:1067. doi: 10.1103/RevModPhys.87.1067
11. Lähde TA, Epelbaum E, Krebs H, Lee D, Meißner UG, Rupak G. Lattice effective field theory for medium-mass nuclei. *Phys Lett.* (2014) **B732**:110–5. doi: 10.1016/j.physletb.2014.03.023
12. Hagen G, Ekström A, Forssén C, Jansen GR, Nazarewicz W, Papenbrock T, et al. Neutron and weak-charge distributions of the ^{48}Ca nucleus. *Nat Phys.* (2015) **12**:186–90. doi: 10.1038/nphys3529
13. Lovato A, Gandolfi S, Carlson J, Pieper SC, Schiavilla R. Neutral weak current two-body contributions in inclusive scattering from ^{12}C. *Phys Rev Lett.* (2014) **112**:182502. doi: 10.1103/PhysRevLett.112.182502
14. Lovato A, Rocco N, Schiavilla R. Muon capture in nuclei: an ab initio approach based on Green's function Monte Carlo methods. *Phys Rev.* (2019) C100:035502. doi: 10.1103/PhysRevC.100.035502
15. Hupin G, Quaglioni S, Navrátil P. Unified description of ^{6}Li structure and deuterium-^{4}He dynamics with chiral two- and three-nucleon forces. *Phys Rev Lett.* (2015) **114**:212502. doi: 10.1103/PhysRevLett.114.212502
16. Elhatisari S, Lee D, Rupak G, Epelbaum E, Krebs H, Lähde TA, et al. *Ab initio* alpha-alpha scattering. *Nature.* (2015) **528**:111. doi: 10.1038/nature16067
17. Fossez K, Rotureau J, Michel N, Nazarewicz W. Continuum effects in neutron-drip-line oxygen isotopes. *Phys Rev.* (2017) **C96**:024308. doi: 10.1103/PhysRevC.96.024308
18. Fossez K, Rotureau J, Nazarewicz W. Energy spectrum of neutron-rich helium isotopes: complex made simple. *Phys Rev.* (2018) **C98**:061302. doi: 10.1103/PhysRevC.98.061302
19. Inoue T, Aoki S, Doi T, Hatsuda T, Ikeda Y, Ishii N, et al. Equation of state for nucleonic matter and its quark mass dependence from the nuclear force in lattice QCD. *Phys Rev Lett.* (2013) **111**:112503. doi: 10.1103/PhysRevLett.111.112503
20. Beane SR, Chang E, Cohen S, Detmold W, Lin HW, Orginos K, et al. Magnetic moments of light nuclei from lattice quantum chromodynamics. *Phys Rev Lett.* (2014) **113**:252001. doi: 10.1103/PhysRevLett.113.252001
21. Orginos K, Parreno A, Savage MJ, Beane SR, Chang E, Detmold W. Two nucleon systems at $m_\pi \sim 450$ MeV from lattice QCD. *Phys Rev.* (2015) **D92**:114512. doi: 10.1103/PhysRevD.92.114512
22. Savage MJ, Shanahan PE, Tiburzi BC, Wagman ML, Winter F, Beane SR, et al. Proton-proton fusion and tritium β decay from lattice quantum chromodynamics. *Phys Rev Lett.* (2017) **119**:062002. doi: 10.1103/PhysRevLett.119.062002
23. Rozpedzik D, Golak J, Skibinski R, Witala H, Glockle W, Epelbaum E, et al. A first estimation of chiral four-nucleon force effects in He-4. *Acta Phys Polon.* (2006) **B37**:2889–904.
24. Krüger T, Tews I, Hebeler K, Schwenk A. Neutron matter from chiral effective field theory interactions. *Phys Rev.* (2013) **C88**:025802. doi: 10.1103/PhysRevC.88.025802
25. Yukawa H. On the interaction of elementary particles I. *Proc Phys Math Soc Jap.* (1935) **17**:48–57. doi: 10.1143/PTPS.1.1
26. Stoks VGJ, Klomp RAM, Terheggen CPF, de Swart JJ. Construction of high quality NN potential models. *Phys Rev.* (1994) **C49**:2950–62. doi: 10.1103/PhysRevC.49.2950
27. Wiringa RB, Stoks VGJ, Schiavilla R. An accurate nucleon-nucleon potential with charge independence breaking. *Phys Rev.* (1995) **C51**:38–51. doi: 10.1103/PhysRevC.51.38
28. Machleidt R. The High precision, charge dependent Bonn nucleon-nucleon potential (CD-Bonn). *Phys Rev.* (2001) **C63**:024001. doi: 10.1103/PhysRevC.63.024001
29. Stoks VGJ, Klomp RAM, Rentmeester MCM, de Swart JJ. Partial wave analaysis of all nucleon-nucleon scattering data below 350-MeV. *Phys Rev.* (1993) **C48**:792–815. doi: 10.1103/PhysRevC.48.792
30. Friar JL, Gibson BF, Payne GL. Recent progress in understanding trinucleon properties. *Ann Rev Nucl Part Sci.* (1984) **34**:403–33. doi: 10.1146/annurev.ns.34.120184.002155
31. Pudliner BS, Pandharipande VR, Carlson J, Pieper SC, Wiringa RB. Quantum Monte Carlo calculations of nuclei with A <= 7. *Phys Rev.* (1997) **C56**:1720–50. doi: 10.1103/PhysRevC.56.1720
32. Navratil P, Vary JP, Barrett BR. Large basis ab initio no-core shell model and its application to C-12. *Phys Rev.* (2000) **C62**:054311. doi: 10.1103/PhysRevC.62.054311
33. Pieper SC, Pandharipande VR, Wiringa RB, Carlson J. Realistic models of pion exchange three nucleon interactions. *Phys Rev.* (2001) **C64**:014001. doi: 10.1103/PhysRevC.64.014001
34. Fujita J, Miyazawa H. Pion theory of three-body forces. *Prog Theor Phys.* (1957) **17**:360–5. doi: 10.1143/PTP.17.360
35. Pieper SC. The Illinois extension to the Fujita-Miyazawa three-nucleon force. *AIP Conf. Proc.* (2008) **1011**:143–52. doi: 10.1063/1.2932280
36. Maris P, Vary JP, Gandolfi S, Carlson J, Pieper SC. Properties of trapped neutrons interacting with realistic nuclear Hamiltonians. *Phys Rev.* (2013) **C87**:054318. doi: 10.1103/PhysRevC.87.054318
37. Weinberg S. Nuclear forces from chiral Lagrangians. *Phys Lett.* (1990) **B251**:288–92. doi: 10.1016/0370-2693(90)90938-3
38. Weinberg S. Effective chiral Lagrangians for nucleon–pion interactions and nuclear forces. *Nucl Phys.* (1991) **B363**:3–18. doi: 10.1016/0550-3213(91)90231-L
39. Weinberg S. Three body interactions among nucleons and pions. *Phys Lett.* (1992) **B295**:114–21. doi: 10.1016/0370-2693(92)90099-P
40. Epelbaum E, Hammer HW, Meissner UG. Modern theory of nuclear forces. *Rev Mod Phys.* (2009) **81**:1773–825. doi: 10.1103/RevModPhys.81.1773
41. Machleidt R, Entem DR. Chiral effective field theory and nuclear forces. *Phys Rept.* (2011) **503**:1–75. doi: 10.1016/j.physrep.2011.02.001
42. Machleidt R, Sammarruca F. Chiral EFT based nuclear forces: achievements and challenges. *Phys Scripta.* (2016) **91**:083007. doi: 10.1088/0031-8949/91/8/083007
43. Machleidt R. Historical perspective and future prospects for nuclear interactions. *Int J Mod Phys.* (2017) **E26**:1730005. doi: 10.1142/S0218301317300053
44. Kaplan DB, Savage MJ, Wise MB. A new expansion for nucleon-nucleon interactions. *Phys Lett.* (1998) **B424**:390–6. doi: 10.1016/S0370-2693(98)00210-X
45. Kaplan DB, Savage MJ, Wise MB. Two nucleon systems from effective field theory. *Nucl Phys.* (1998) **B534**:329–55. doi: 10.1016/S0550-3213(98)00440-4
46. Nogga A, Timmermans RGE, van Kolck U. Renormalization of one-pion exchange and power counting. *Phys Rev.* (2005) **C72**:054006. doi: 10.1103/PhysRevC.72.054006
47. Pavon Valderrama M, Ruiz Arriola E. Renormalization of NN interaction with chiral two pion exchange potential. central phases and the deuteron. *Phys Rev.* (2006) **C74**:054001. doi: 10.1103/PhysRevC.74.054001
48. Long B, Yang CJ. Renormalizing chiral nuclear forces: triplet channels. *Phys Rev.* (2012) **C85**:034002. doi: 10.1103/PhysRevC.85.034002
49. van Kolck U. Few nucleon forces from chiral Lagrangians. *Phys Rev.* (1994) **C49**:2932–41. doi: 10.1103/PhysRevC.49.2932
50. Furnstahl RJ, Phillips DR, Wesolowski S. A recipe for EFT uncertainty quantification in nuclear physics. *J Phys.* (2015) **G42**:034028. doi: 10.1088/0954-3899/42/3/034028
51. Epelbaum E, Krebs H, Meißner UG. Improved chiral nucleon-nucleon potential up to next-to-next-to-next-to-leading order. *Eur Phys J.* (2015) **A51**:53. doi: 10.1140/epja/i2015-15053-8
52. Furnstahl RJ, Klco N, Phillips DR, Wesolowski S. Quantifying truncation errors in effective field theory. *Phys Rev.* (2015) **C92**:024005. doi: 10.1103/PhysRevC.92.024005
53. Wesolowski S, Klco N, Furnstahl RJ, Phillips DR, Thapaliya A. Bayesian parameter estimation for effective field theories. *J Phys.* (2016) **G43**:074001. doi: 10.1088/0954-3899/43/7/074001
54. Melendez JA, Wesolowski S, Furnstahl RJ. Bayesian truncation errors in chiral effective field theory: nucleon-nucleon observables. *Phys Rev.* (2017) **C96**:024003. doi: 10.1103/PhysRevC.96.024003
55. Wesolowski S, Furnstahl RJ, Melendez JA, Phillips DR. Exploring Bayesian parameter estimation for chiral effective field theory using nucleon-nucleon phase shifts. *J Phys.* (2019) **46**:045102. doi: 10.1088/1361-6471/aaf5fc

56. Ordonez C, Ray L, van Kolck U. Nucleon-nucleon potential from an effective chiral Lagrangian. *Phys Rev Lett.* (1994) **72**:1982–5. doi: 10.1103/PhysRevLett.72.1982
57. Ordonez C, van Kolck U. Chiral Lagrangians and nuclear forces. *Phys Lett.* (1992) **B291**:459–64. doi: 10.1016/0370-2693(92)91404-W
58. Ordonez C, Ray L, van Kolck U. The two nucleon potential from chiral Lagrangians. *Phys Rev.* (1996) **C53**:2086–105. doi: 10.1103/PhysRevC.53.2086
59. Kaiser N, Gerstendorfer S, Weise W. Peripheral NN scattering: role of delta excitation, correlated two pion and vector meson exchange. *Nucl Phys.* (1998) **A637**:395–420. doi: 10.1016/S0375-9474(98)00234-6
60. Krebs H, Epelbaum E, Meissner UG. Nuclear forces with Delta-excitations up to next-to-next-to-leading order. I. Peripheral nucleon-nucleon waves. *Eur Phys J.* (2007) **A32**:127–37. doi: 10.1140/epja/i2007-10372-y
61. Ditsche C, Hoferichter M, Kubis B, Meissner UG. Roy-Steiner equations for pion-nucleon scattering. *JHEP.* (2012) **6**:43. doi: 10.1007/JHEP06(2012)043
62. Hoferichter M, Ruiz de Elvira J, Kubis B, Meißner UG. High-precision determination of the Pion-nucleon σ term from Roy-Steiner equations. *Phys Rev Lett.* (2015) **115**:092301. doi: 10.1103/PhysRevLett.115.092301
63. Hoferichter M, Ruiz de Elvira J, Kubis B, Meißner UG. Roy–Steiner-equation analysis of pion–nucleon scattering. *Phys Rept.* (2016) **625**:1–88. doi: 10.1016/j.physrep.2016.02.002
64. Hoferichter M, Ruiz de Elvira J, Kubis B, Meißner UG. Matching pion-nucleon Roy-Steiner equations to chiral perturbation theory. *Phys Rev Lett.* (2015) **115**:192301. doi: 10.1103/PhysRevLett.115.192301
65. Siemens D, Bernard V, Epelbaum E, Gasparyan A, Krebs H, Meißner UG. Elastic pion-nucleon scattering in chiral perturbation theory: a fresh look. *Phys Rev C.* (2016) **94**:014620. doi: 10.1103/PhysRevC.94.014620
66. Siemens D, Ruiz de Elvira J, Epelbaum E, Hoferichter M, Krebs H, Kubis B, et al. Reconciling threshold and subthreshold expansions for Pion–nucleon scattering. *Phys Lett.* (2017) **B770**:27–34. doi: 10.1016/j.physletb.2017.04.039
67. Yao DL, Siemens D, Bernard V, Epelbaum E, Gasparyan AM, Gegelia J, et al. Pion-nucleon scattering in covariant baryon chiral perturbation theory with explicit Delta resonances. *JHEP.* (2016) **5**:38. doi: 10.1007/JHEP05(2016)038
68. Epelbaum E, Krebs H, Meissner UG. Delta-excitations and the three-nucleon force. *Nucl Phys.* (2008) **A806**:65–78. doi: 10.1016/j.nuclphysa.2008.02.305
69. Bernard V, Epelbaum E, Krebs H, Meissner UG. Subleading contributions to the chiral three-nucleon force. I. Long-range terms. *Phys Rev.* (2008) **C77**:064004. doi: 10.1103/PhysRevC.77.064004
70. Bernard V, Epelbaum E, Krebs H, Meissner UG. Subleading contributions to the chiral three-nucleon force II: short-range terms and relativistic corrections. *Phys Rev.* (2011) **C84**:054001. doi: 10.1103/PhysRevC.84.054001
71. Epelbaum E. Four-nucleon force in chiral effective field theory. *Phys Lett.* (2006) **B639**:456–61. doi: 10.1016/j.physletb.2006.06.046
72. Epelbaum E. Four-nucleon force using the method of unitary transformation. *Eur Phys J.* (2007) **A34**:197–214. doi: 10.1140/epja/i2007-10496-0
73. Entem DR, Kaiser N, Machleidt R, Nosyk Y. Dominant contributions to the nucleon-nucleon interaction at sixth order of chiral perturbation theory. *Phys Rev.* (2015) **C92**:064001. doi: 10.1103/PhysRevC.92.064001
74. Epelbaum E, Krebs H, Meißner UG. Precision nucleon-nucleon potential at fifth order in the chiral expansion. *Phys Rev Lett.* (2015) **115**:122301. doi: 10.1103/PhysRevLett.115.122301
75. Reinert P, Krebs H, Epelbaum E. Semilocal momentum-space regularized chiral two-nucleon potentials up to fifth order. *Eur Phys J.* (2018) **A54**:86. doi: 10.1140/epja/i2018-12516-4
76. Entem DR, Machleidt R, Nosyk Y. High-quality two-nucleon potentials up to fifth order of the chiral expansion. *Phys Rev.* (2017) **C96**:024004. doi: 10.1103/PhysRevC.96.024004
77. Entem DR, Machleidt R. Accurate charge dependent nucleon-nucleon potential at fourth order of chiral perturbation theory. *Phys Rev.* (2003) **C68**:041001. doi: 10.1103/PhysRevC.68.041001
78. Epelbaum E, Glockle W, Meissner UG. The two-nucleon system at next-to-next-to-next-to-leading order. *Nucl Phys.* (2005) **A747**:362–424. doi: 10.1016/j.nuclphysa.2004.09.107
79. Arndt RA, Briscoe WJ, Strakovsky II, Workman RL. Updated analysis of NN elastic scattering to 3-GeV. *Phys Rev.* (2007) **C76**:025209. doi: 10.1103/PhysRevC.76.025209
80. Navarro Pérez R, Amaro JE, Ruiz Arriola E. Coarse-grained potential analysis of neutron-proton and proton-proton scattering below the pion production threshold. *Phys Rev.* (2013) **C88**:064002. doi: 10.1103/PhysRevC.88.064002 [Erratum: Phys. Rev.C91,no.2,029901(2015)].
81. Navarro Pérez R, Amaro JE, Ruiz Arriola E. Coarse grained NN potential with chiral two Pion exchange. *Phys Rev.* (2014) **C89**:024004. doi: 10.1103/PhysRevC.89.024004
82. Navarro Perez R, Amaro JE, Ruiz Arriola E. Statistical error analysis for phenomenological nucleon-nucleon potentials. *Phys Rev.* (2014) **C89**:064006. doi: 10.1103/PhysRevC.89.064006
83. Carlsson BD, Ekström A, Forssén C, Strömberg DF, Jansen GR, Lilja O, et al. Uncertainty analysis and order-by-order optimization of chiral nuclear interactions. *Phys Rev.* (2016) **X6**:011019. doi: 10.1103/PhysRevX.6.011019
84. Ekström A, Jansen GR, Wendt KA, Hagen G, Papenbrock T, Carlsson BD, et al. Accurate nuclear radii and binding energies from a chiral interaction. *Phys Rev.* (2015) **C91**:051301. doi: 10.1103/PhysRevC.91.051301
85. Kalantar-Nayestanaki N, Epelbaum E, Messchendorp JG, Nogga A. Signatures of three-nucleon interactions in few-nucleon systems. *Rept Prog Phys.* (2012) **75**:016301. doi: 10.1088/0034-4885/75/1/016301
86. Hammer HW, Nogga A, Schwenk A. Three-body forces: from cold atoms to nuclei. *Rev Mod Phys.* (2013) **85**:197. doi: 10.1103/RevModPhys.85.197
87. Krebs H, Gasparyan A, Epelbaum E. Chiral three-nucleon force at N^4LO I: longest-range contributions. *Phys Rev.* (2012) **C85**:054006. doi: 10.1103/PhysRevC.85.054006
88. Krebs H, Gasparyan A, Epelbaum E. Chiral three-nucleon force at N^4LO II: intermediate-range contributions. *Phys Rev.* (2013) **C87**:054007. doi: 10.1103/PhysRevC.87.054007
89. Girlanda L, Kievsky A, Viviani M. Subleading contributions to the three-nucleon contact interaction. *Phys Rev.* (2011) **C84**:014001. doi: 10.1103/PhysRevC.84.014001
90. Tews I, Gandolfi S, Gezerlis A, Schwenk A. Quantum Monte Carlo calculations of neutron matter with chiral three-body forces. *Phys Rev.* (2016) **C93**:024305. doi: 10.1103/PhysRevC.93.024305
91. Lynn JE, Tews I, Carlson J, Gandolfi S, Gezerlis A, Schmidt KE, et al. Chiral three-nucleon interactions in light nuclei, neutron-α scattering, and neutron matter. *Phys Rev Lett.* (2016) **116**:062501. doi: 10.1103/PhysRevLett.116.062501
92. Lynn JE, Tews I, Carlson J, Gandolfi S, Gezerlis A, Schmidt KE, et al. Quantum Monte Carlo calculations of light nuclei with local chiral two- and three-nucleon interactions. *Phys Rev.* (2017) **C96**:054007. doi: 10.1103/PhysRevC.96.054007
93. Piarulli M, Baroni A, Girlanda L, Kievsky A, Lovato A, Lusk E, et al. Light-nuclei spectra from chiral dynamics. *Phys Rev Lett.* (2018) **120**:052503. doi: 10.1103/PhysRevLett.120.052503
94. Gazit D, Quaglioni S, Navratil P. Three-nucleon low-energy constants from the consistency of interactions and currents in chiral effective field theory. *Phys Rev Lett.* (2009) **103**:102502. doi: 10.1103/PhysRevLett.103.102502
95. Marcucci LE, Kievsky A, Rosati S, Schiavilla R, Viviani M. Chiral effective field theory predictions for muon capture on deuteron and ^{3}*He*. *Phys Rev Lett.* (2012) **108**:052502. doi: 10.1103/PhysRevLett.108.052502
96. Baroni A, Schiavilla R, Marcucci LE, Girlanda L, Kievsky A, Lovato A, et al. Local chiral interactions, the tritium Gamow-Teller matrix element, and the three-nucleon contact term. *Phys Rev.* (2018) **C98**:044003. doi: 10.1103/PhysRevC.98.044003
97. Gardestig A, Phillips DR. How low-energy weak reactions can constrain three-nucleon forces and the neutron-neutron scattering length. *Phys Rev Lett.* (2006) **96**:232301. doi: 10.1103/PhysRevLett.96.232301
98. Lynn JE, Tews I, Gandolfi S, Lovato A. Quantum Monte Carlo methods in nuclear physics: recent advances. *Ann Rev Nucl Part Sci.* (2019) **69**:279–305. doi: 10.1146/annurev-nucl-101918-023600
99. Lonardoni D, Gandolfi S, Lynn JE, Petrie C, Carlson J, Schmidt KE, et al. Auxiliary field diffusion Monte Carlo calculations of light and medium-mass nuclei with local chiral interactions. *Phys Rev.* (2018) **C97**:044318. doi: 10.1103/PhysRevC.97.044318
100. Lonardoni D, Gandolfi S, Wang XB, Carlson J. Single- and two-nucleon momentum distributions for local chiral interactions. *Phys Rev.* (2018) **C98**:014322. doi: 10.1103/PhysRevC.98.014322

101. Tews I, Carlson J, Gandolfi S, Reddy S. Constraining the speed of sound inside neutron stars with chiral effective field theory interactions and observations. *Astrophys J.* (2018) **860**:149. doi: 10.3847/1538-4357/aac267
102. Tews I, Margueron J, Reddy S. Critical examination of constraints on the equation of state of dense matter obtained from GW170817. *Phys Rev.* (2018) **C98**:045804. doi: 10.1103/PhysRevC.98.045804
103. Piarulli M, Bombaci I, Logoteta D, Lovato A, Wiringa RB. Benchmark calculations of pure neutron matter with realistic nucleon-nucleon interactions. *arXiv:1908.04426* [Preprint]. (2019). Available online at: https://arxiv.org/abs/1908.04426
104. Gezerlis A, Tews I, Epelbaum E, Gandolfi S, Hebeler K, Nogga A, et al. Quantum Monte Carlo calculations with chiral effective field theory interactions. *Phys Rev Lett.* (2013) **111**:032501. doi: 10.1103/PhysRevLett.111.032501
105. Gezerlis A, Tews I, Epelbaum E, Freunek M, Gandolfi S, Hebeler K, et al. Local chiral effective field theory interactions and quantum Monte Carlo applications. *Phys Rev.* (2014) **C90**:054323. doi: 10.1103/PhysRevC.90.054323
106. Piarulli M, Girlanda L, Schiavilla R, Navarro Pérez R, Amaro JE, Ruiz Arriola E. Minimally nonlocal nucleon-nucleon potentials with chiral two-pion exchange including Δ resonances. *Phys Rev.* (2015) **C91**:024003. doi: 10.1103/PhysRevC.91.024003
107. Piarulli M, Girlanda L, Schiavilla R, Kievsky A, Lovato A, Marcucci LE, et al. Local chiral potentials with Δ-intermediate states and the structure of light nuclei. *Phys Rev.* (2016) **C94**:054007. doi: 10.1103/PhysRevC.94.054007
108. Epelbaum E, Gloeckle W, Meissner UG. Improving the convergence of the chiral expansion for nuclear forces. 1. Peripheral phases. *Eur Phys J.* (2004) **A19**:125–37. doi: 10.1140/epja/i2003-10096-0
109. Kaiser N, Brockmann R, Weise W. Peripheral nucleon-nucleon phase shifts and chiral symmetry. *Nucl Phys.* (1997) **A625**:758–88. doi: 10.1016/S0375-9474(97)00586-1
110. Kortelainen M, Lesinski T, Moré J, Nazarewicz W, Sarich J, Schunck N, et al. Nuclear energy density optimization. *Phys Rev C.* (2010) **82**:024313. doi: 10.1103/PhysRevC.82.024313
111. Huth L, Tews I, Lynn JE, Schwenk A. Analyzing the Fierz rearrangement freedom for local chiral two-nucleon potentials. *Phys Rev.* (2017) **C96**:054003. doi: 10.1103/PhysRevC.96.054003
112. Dyhdalo A, Furnstahl RJ, Hebeler K, Tews I. Regulator artifacts in uniform matter for chiral interactions. *Phys Rev.* (2016) **C94**:034001. doi: 10.1103/PhysRevC.94.034001
113. Tews I, Margueron J, Reddy S. Confronting gravitational-wave observations with modern nuclear physics constraints. *Eur Phys J.* (2019) **A55**:97. doi: 10.1140/epja/i2019-12774-6
114. Capano CD, Tews I, Brown SM, Margalit B, De S, Kumar S, et al. GW170817: stringent constraints on neutron-star radii from multimessenger observations and nuclear theory. *arXiv:1908.10352*. (2019).
115. Cruz-Torres R, Lonardoni D, Weiss R, Barnea N, Higinbotham DW, Piasetzky E, et al. Scale and scheme independence and position-momentum equivalence of nuclear short-range correlations. *arXiv:1907.03658*. (2019).
116. Lynn JE, Lonardoni D, Carlson J, Chen JW, Detmold W, Gandolfi S, et al. *Ab initio* short-range-correlation scaling factors from light to medium-mass nuclei. *arXiv:1903.12587*. (2019).
117. Cirigliano V, Dekens W, De Vries J, Graesser ML, Mereghetti E, Pastore S, et al. A renormalized approach to neutrinoless double-beta decay. *Phys Rev.* (2019) 5:055504. doi: 10.1103/PhysRevC.100.055504
118. Pastore S, Pieper SC, Schiavilla R, Wiringa RB. Quantum Monte Carlo calculations of electromagnetic moments and transitions in A $\leq$ 9 nuclei with meson-exchange currents derived from chiral effective field theory. *Phys Rev.* (2013) **C87**:035503. doi: 10.1103/PhysRevC.87.035503
119. Marcucci LE, Gross F, Pena MT, Piarulli M, Schiavilla R, Sick I, et al. Electromagnetic structure of few-nucleon ground states. *J Phys.* (2016) **G43**:023002. doi: 10.1088/0954-3899/43/2/023002
120. Lovato A, Gandolfi S, Carlson J, Pieper SC, Schiavilla R. Electromagnetic response of ^{12}C: a first-principles calculation. *Phys Rev Lett.* (2016) **117**:082501. doi: 10.1103/PhysRevLett.117.082501
121. Lovato A, Gandolfi S, Carlson J, Lusk E, Pieper SC, Schiavilla R. Quantum Monte Carlo calculation of neutral-current $\nu - ^{12}C$ inclusive quasielastic scattering. *Phys Rev.* (2018) **C97**:022502. doi: 10.1103/PhysRevC.97.022502
122. Pastore S, Baroni A, Carlson J, Gandolfi S, Pieper SC, Schiavilla R, et al. Quantum Monte Carlo calculations of weak transitions in $A = 6 - 10$ nuclei. *Phys Rev.* (2018) **C97**:022501. doi: 10.1103/PhysRevC.97.022501
123. Schiavilla R, Baroni A, Pastore S, Piarulli M, Girlanda L, Kievsky A, et al. Local chiral interactions and magnetic structure of few-nucleon systems. *Phys Rev.* (2019) **C99**:034005. doi: 10.1103/PhysRevC.99.034005
124. Pastore S, Carlson J, Gandolfi S, Schiavilla R, Wiringa RB. Quasielastic lepton scattering and back-to-back nucleons in the short-time approximation. *arXiv:1909.06400* [Preprint]. (2019). Available online at: https://arxiv.org/abs/1909.06400

Conflict of Interest: The authors declare that the research was conducted in the absence of any commercial or financial relationships that could be construed as a potential conflict of interest.

Copyright © 2020 Piarulli and Tews. This is an open-access article distributed under the terms of the Creative Commons Attribution License (CC BY). The use, distribution or reproduction in other forums is permitted, provided the original author(s) and the copyright owner(s) are credited and that the original publication in this journal is cited, in accordance with accepted academic practice. No use, distribution or reproduction is permitted which does not comply with these terms.

frontiers in Physics

REVIEW
published: 05 May 2020
doi: 10.3389/fphy.2020.00079

The Problem of Renormalization of Chiral Nuclear Forces

U. van Kolck [1,2]*

[1] Université Paris-Saclay, CNRS/IN2P3, IJCLab, Orsay, France, [2] Department of Physics, University of Arizona, Tucson, AZ, United States

Ever since quantum field theory was first applied to the derivation of nuclear forces in the mid-twentieth century, the renormalization of pion exchange with realistic couplings has presented a challenge. The implementation of effective field theories (EFTs) in the 1990s promised a solution to this problem but unexpected obstacles were encountered. The response of the nuclear community has been to focus on "chiral potentials" with regulators chosen to produce a good description of data. Meanwhile, a successful EFT without explicit pion exchange—Pionless EFT—has been formulated where renormalization is achieved order by order in a systematic expansion of low-energy nuclear observables. I describe how lessons from Pionless EFT are being applied to the construction of a properly renormalized Chiral EFT.

Keywords: effective field theory, renormalization, nuclear physics, singular potentials, pion exchange

OPEN ACCESS

Edited by:
Ruprecht Machleidt,
University of Idaho, United States

Reviewed by:
Enrique Ruiz Arriola,
University of Granada, Spain
Daniel Phillips,
Ohio University, United States

****Correspondence:***
U. van Kolck
vankolck@ipno.in2p3.fr

Specialty section:
This article was submitted to Nuclear Physics, a section of the journal Frontiers in Physics

Received: *29 October 2019*
Accepted: *06 March 2020*
Published: *05 May 2020*

Citation:
van Kolck U (2020) The Problem of Renormalization of Chiral Nuclear Forces. Front. Phys. 8:79. doi: 10.3389/fphy.2020.00079

1. INTRODUCTION

In the aftermath of the solution of the "problem of infinities" in Quantum Electrodynamics (QED), an intense quest set in to renormalize nuclear forces, where pion exchange replaced the photon exchange responsible for atomic forces. (For an early example, see reference [1].) It was quickly understood that the only relativistic pion-nucleon coupling that is renormalizable is pseudoscalar [2]. However, pseudoscalar coupling differs from pseudovector coupling by a large nucleon-pair term, which was found to be in conflict with pion phenomenology [3]. For the favored pseudovector coupling, the description of two-nucleon data depended sensitively on the high-momentum (or short-distance) cutoff (see, for example, reference [4]). Efforts moved toward the investigation of various prescriptions for handling short-range effects, including specific cocktails of (usually single-)heavier-meson exchange, form factors with *ad hoc* shapes, and/or boundary conditions at some finite distance. Nuclear theory acquired an increasingly phenomenological character. Typically, the non-relativistic Schrödinger equation was solved with a two-nucleon ($2N$) potential including one-pion exchange, some approximation to two-pion exchange, and a more or less arbitrary short-range form, with sufficiently many parameters to fit data to the desired accuracy. The end result was that potentials including quite different physics could produce very good parameterizations of $2N$ data up to around the pion-production threshold, while typically underpredicting three- and more-nucleon binding by more than 10%. A serious difficulty was to infer a satisfactory form of three-nucleon ($3N$) forces and, for reactions, $2N$ currents. Reference [5] recounts some of this history.

In contrast, by the mid-1970s renormalizable quantum field theories had won the day in particle physics, leading to the formulation of Quantum Chromodynamics (QCD) as the theory of strong interactions. Out of the attempts to make predictions for QCD at low energies and to understand how the Standard Model (SM) can arise from a more fundamental theory, the concept of effective field theory (EFT) was born [6]. An EFT comprises all the interactions among relevant degrees of

freedom that are allowed by symmetries, including an arbitrary number of fields and derivatives. For predictions, contributions to observables must be ordered according to their expected size. This "power counting" allows for an *a priori* error estimate from neglected higher-order contributions. At each order in the expansion, only a finite number of "low-energy constants" (LECs)—the interaction strengths—appear. In a consistent power counting, they are sufficient to ensure that any dependence on the regulator can be made arbitrarily small by taking the cutoff large. Thus, EFTs are renormalizable in the modern sense that at each order a finite number of parameters generate results for observables that are independent of details of the arbitrary regularization procedure.

A successful EFT, Chiral Perturbation Theory (ChPT), was developed in the 1980s to handle interactions among pions and one nucleon below the characteristic QCD scale $M_{\rm QCD} \sim 1$ GeV [7, 8]. Requiring renormalization in a perturbative expansion, a consistent power counting was developed based on "naive dimensional analysis" (NDA) [9]. Taking the typical external momentum in a reaction to be of the order of the pion mass, $Q \sim m_\pi \ll M_{\rm QCD}$, observables are expanded in a series of powers of $Q/M_{\rm QCD}$ times calculable functions of Q/m_π. When Weinberg remarked [10, 11] that ChPT, now generalized as "Chiral EFT" (ChEFT), could be used to derive nuclear forces, he identified an infrared enhancement in nuclear amplitudes by the nucleon mass $m_N = \mathcal{O}(M_{\rm QCD})$, which can lead to the failure of perturbation theory—a good thing since nuclei are bound states and resonances. He proposed that the ChPT power counting could still be applied to the nuclear potential, defined as the sum of diagrams lacking an explicit enhancement. Then, the Lippmann-Schwinger equation, or equivalently the Schrödinger equation, would be solved with a truncated "chiral potential."

The potential defined by Weinberg contains pion exchange diagrams where all LECs are fixed, at least in principle, from ChPT. But it also includes shorter-range interactions with LECs that can only be determined in nuclear systems. Implicit in Weinberg's proposal was that the short-range LECs would not contain an *implicit* enhancement. This would be the case if the solution of the dynamical equation does not generate cutoff dependence beyond that which can be compensated by the LECs already present up to that order according to NDA.

Whether this assumption is true was not immediately clear. NDA says that the potential at leading order (LO) consists of two non-derivative, chirally symmetric contact interactions together with one-pion exchange (OPE). More-pion exchange should come at higher orders together with more-derivative contact interactions. Non-perturbative pion exchange prevents an analytical solution even at the 2N level. The first numerical solution of a chiral potential in the 2N system [12, 13] tested renormalizability of the amplitude: a variation from 0.5 to 1 GeV in the cutoff of a local Gaussian regulator seemed to be compensated by a refitting of the LECs at hand. However, the fitting procedure was cumbersome as an over-complete set of interactions was used and the local regulator mixed different partial waves, limiting the range of cutoffs that could be explored. Since then a large variety of chiral potentials have been developed (for reviews, see for example references [14, 15]). A landmark was a 2N potential [16] that was perceived to match the accuracy of phenomenological potentials (for a recent comparison between chiral 2N potentials and data, see reference [17]). Chiral potentials have become the favorite input to "*ab initio*" methods, which provide numerically controlled solutions of the Schrödinger equation for multi-nucleon systems.

Unfortunately, pretty early on the first evidence appeared [18] that Weinberg's prescription does not provide amplitudes, and thus observables, that are renormalized order by order. In the 2N $^1S_0$ channel at LO, a semi-analytical argument shows that there remains a logarithmic dependence on the cutoff proportional to the average quark mass. The only way to eliminate it, at least with a momentum- or coordinate-space cutoff, is to include at LO a non-derivative, chirally *breaking* contact interaction, which according to NDA should appear two orders down the expansion, that is, at next-to-next-to-leading order (N^{2}LO)[1]. More dramatically, it was later shown [20, 21] that oscillatory cutoff dependence appears at LO in waves where OPE is attractive, singular, and accounted for non-perturbatively. A chirally symmetric LEC is needed for renormalization in each wave, but again NDA assigns those in partial waves beyond S to higher orders. Similar problems afflict processes with external probes [22].

As I describe in section 3, the origin of these problems is the renormalization of attractive singular potentials [23, 24]. NDA might fail because exact solutions of the Schrödinger equation depend on the cutoff differently than perturbative solutions. The LECs needed for the renormalization of the amplitude are enhanced by implicit powers of $M_{\rm QCD}$.

How to account for this? In response to the renormalization failure of Weinberg's power counting a simpler nuclear EFT [25–27] was developed in the late 1990s. In this "Pionless EFT" pions are integrated out and only contact interactions remain. The effects of loops in the Lippmann-Schwinger equation are much easier to see, including the m_N enhancement and a further enhancement of 4π [26, 27] that was not pointed out by Weinberg. The lessons of Pionless EFT for ChEFT are summarized in section 2.

The first attempt to fix power counting using the insights from Pionless EFT was initiated [28, 29] at the same time as the main elements of the power counting of Pionless EFT were being understood. Valid for sufficiently small values of the pion mass and external momenta, this version of ChEFT treats pion exchange in perturbation theory, removing the renormalization problems mentioned above. Unfortunately, in the 2N system at physical pion mass one cannot go in this way to momenta much beyond those of Pionless EFT [30]. The alternative is *partly* perturbative pions: OPE is iterated only in the low partial waves where it is sufficiently strong, together with the contact interactions whose LECs are necessary

[1] A note on notation: It has become usual in the nuclear community to refer to a subleading chiral potential of order $n \geq 2$ as "N^{n-1}LO," because with Weinberg's power counting the parity- and time-reversal-invariant potential of order $n = 1$ vanishes [19]. However, this usage is too provincial to accommodate experience with other observables and power countings in ChEFT or other EFTs. Here, a correction of order n in the expansion is denoted as N^{n}LO, whether it is non-zero or not.

for LO renormalization [20]. All subleading pion exchanges, together with the remaining contact interactions, are treated in perturbation theory [31]. This approach is discussed in section 4, including what little has been done to confront it with data.

Section 5 offers the conclusion that this approach solves the renormalization woes of nuclear forces while accounting for the long-range interactions from pion exchange systematically. Although they differ in detail from the field-theoretical renormalization described below, renormalization-group analyses of the Schrödinger equation [22, 32–34] support this picture. How it can meet the accuracy requirements of the nuclear community remains to be seen. My emphasis here is on the *internal consistency* of ChEFT. I expand on the renormalization issues summarized in reference [35], but I refer the reader to the latter for a more complete review of ChEFT and its relation to other nuclear EFTs.

2. SAY WHAT?

As reviewed in reference [35], defining the nuclear potential as the sum of "irreducible" diagrams without the m_N infrared (IR) enhancement does indeed ensure that the *cutoff-independent* parts of pion-exchange diagrams can be ordered according to ChPT power counting. These components of the pion-exchange potentials are in general non-analytic functions of momenta and pion mass that can be calculated in terms of pion-baryon interactions.

The ChPT power counting is designed for processes where the typical external momentum is comparable to the pion mass, $Q \sim m_\pi$. A (relativistic) pion propagator scales as Q^{-2}. In contrast, a nucleon is heavy compared to Q and thus non-relativistic. Moreover, energies and three-momenta being comparable, nucleon recoil is suppressed by one power of $Q/m_N = \mathcal{O}(Q/M_{\rm QCD})$—that is, the nucleon is static, its propagator scaling as Q^{-1}. Because the Delta-nucleon mass difference is (at physical quark masses) only about twice the pion mass, a Delta propagator scales in the same way. In integrals from the loops that make up the potential one picks poles from the pion propagators, typically resulting in factors of $(4\pi)^{-2}$. They combine with factors of the pion decay constant $f_\pi \simeq 92$ MeV from the pion-baryon interactions to produce inverse factors of $4\pi f_\pi = \mathcal{O}(M_{\rm QCD})$. The power counting explicitly relies on an estimate, NDA [9], of the factors of 4π that distinguish between f_π and the breakdown scale $M_{\rm QCD}$, which appears in interactions with derivatives and powers of the pion mass. In summary, the ChPT rules (in momentum space) are:

$$\text{(pion) loop integral} \sim (4\pi)^{-2} Q^4 , \tag{1}$$

$$\text{baryon, pion propagator} \sim Q^{-1}, Q^{-2} , \tag{2}$$

$$\text{vertex} \sim Q^d f_\pi^{2-b-f} M_{\rm QCD}^{2-d-f/2} , \tag{3}$$

where d, b, and f are the numbers of derivatives/pion masses, pion fields, and baryon fields, respectively, in an interaction.

The expected size of any diagram can be found using the identities $I = L - 1 + \sum_i V_i$ and $2I + E = \sum_i V_i (b_i + f_i)$ involving the number of loops (L), internal (external) lines I (E), and vertices (V_i) having a set of values $d = d_i$, $b = b_i$, and $f = f_i$. In particular,

$$2N \text{ potential} \sim 4\pi m_N^{-1} M_{NN}^{-1} \left(Q M_{\rm QCD}^{-1} \right)^\mu , \tag{4}$$

where [28, 29]

$$M_{NN} \equiv \frac{16\pi f_\pi^2}{g_A^2 m_N} = \mathcal{O}(f_\pi) \tag{5}$$

in terms of the pion-nucleon axial-vector coupling $g_A \simeq 1.27$ and [11]

$$\mu \equiv 2L + \sum_i V_i (d_i + f_i/2 - 2) . \tag{6}$$

Because every additional loop (without increase in the number of derivatives/pion masses at vertices) leads to a relative factor $\mathcal{O}(Q^2/M_{\rm QCD}^2)$, one gets the well-known ordering where p-pion exchange starts at $\mu = 2(p-1)$. Note that the NLO correction vanishes due to parity and time-reversal symmetries [19].

This power counting applies to diagrams that make up the long-range potential. Yet physics, as opposed to metaphysics, is about observables. The meaning of Equation (4) is that it indirectly orders the contributions to *amplitudes*. For the direct link, we need to consider as well "reducible" diagrams where intermediate states contain only nucleons. One picks poles from the non-relativistic nucleon propagators, for which energies are of the order of recoil—in those diagrams, one cannot approximate nucleons as static. (This of course has nothing to do with relativistic corrections, as sometimes misstated in the literature.) These poles lead not only to an m_N enhancement [10, 11], but typically also to different powers of $(4\pi)^{-1}$. Experience with Pionless EFT [35, 36], where these are all the loops one needs to deal with, shows that the factors associated with reducible loops are

$$\text{nucleon propagator} \sim m_N Q^{-2} , \tag{7}$$

$$\text{reducible loop integral} \sim (4\pi m_N)^{-1} Q^5 . \tag{8}$$

When one inserts the order-μ potential into a $2N$ diagram we need one extra reducible loop with two nucleon propagators (compare **Figures 1A,B**), leading to a relative factor $(Q/M_{NN})(Q/M_{\rm QCD})^\mu$. This amount to an IR enhancement of $4\pi m_N/Q$ over the factor that arises from Equations (1) and (2). As a consequence, the series in the LO potential fails to converge for $Q \sim M_{NN}$. This is what makes ChEFT different for $A \geq 2$ nucleons compared to ChPT for $A \leq 1$.

The factor of 4π in the IR enhancement had not been recognized before Pionless EFT was developed, but it is important to understand the failure of perturbation theory *for pions*. The exact solution of the LO potential for $Q \sim M_{NN}$ can give rise to a binding energy per nucleon

$$\frac{B_A}{A} \sim \frac{M_{NN}^2}{M_{\rm QCD}} \sim \frac{f_\pi}{4\pi} \sim 10 \text{ MeV} . \tag{9}$$

This is somewhat larger than observed for light nuclei, indicating a certain amount of fine tuning in the $2N$ interactions. But it is on

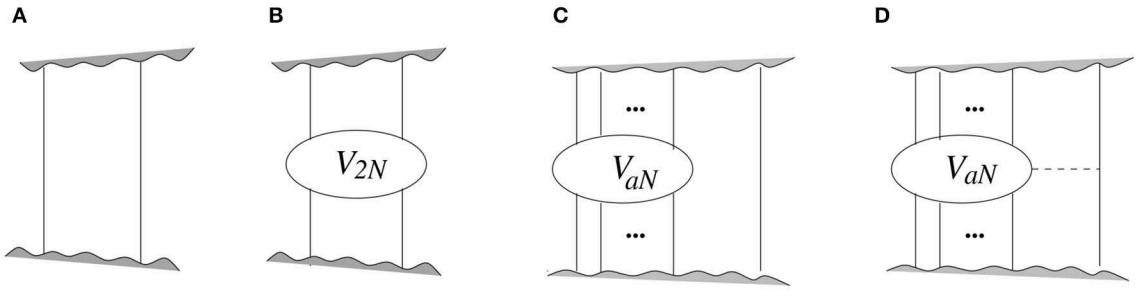


FIGURE 1 | Some diagrams discussed in the text. Inside a diagram, **(A)** two nucleons (solid lines) propagate; **(B)** two nucleons interact through the 2*N* potential (blob); **(C)** *a* nucleons interact through the *aN* potential (blob), while another nucleon propagates; and **(D)** $a+1$ nucleons interact through the $(a+1)N$ potential formed from the *aN* potential and the exchange of a pion (dashed line).

the right ballpark for heavier nuclei, so chiral symmetry together with the IR enhancement provides a natural explanation [36] for the shallowness of nuclei compared to $M_{\rm QCD}$, $B_A/A \ll M_{\rm QCD}$, long considered a mystery.

The same factor of 4π has implications for the natural size of few-body forces, which were recognized by Friar [37]. To see this, consider connecting a nucleon with OPE to an *aN* potential to make an $(a+1)N$ potential, without changing the number of derivatives, pion masses, and loops in the *aN* potential. (See **Figures 1C,D**. For example, take the crossed-box two-pion exchange 2*N* potential and connect one of the intermediate nucleons to the third nucleon.) The additional nucleon propagator inside the *aN* potential and the additional OPE combine for a factor of $4\pi m_N^{-1} M_{NN}^{-1} Q^{-1}$. At the same time, at the amplitude level we are adding a reducible loop and one propagator for the extra nucleon, that is, another factor $(4\pi)^{-1}Q^3$. The contribution of the $(a+1)N$ potential to the amplitude is, overall, of $\mathcal{O}(Q^2 m_N^{-1} M_{NN}^{-1})$ compared to that of its "parent" *aN* potential. For $Q \sim M_{NN}$, the suppression from connecting a nucleon is thus of $\mathcal{O}(Q/M_{\rm QCD})$, or one order in the expansion of the potential [37]. In contrast, missing the 4π in the IR enhancement would give an additional $(4\pi)^{-1} = \mathcal{O}(M_{NN}/M_{\rm QCD})$, or a suppression of $(Q/M_{\rm QCD})^2$ [11, 19, 38, 39]. In either case a hierarchy of many-body forces arises, with perturbative 3*N* forces coming after the leading 2*N* forces. Unfortunately, existing calculations do not question the additional suppression of $(4\pi)^{-1}$.

Note that when connecting the additional nucleon we might not be able to maintain the number of derivatives or pion masses. In particular, for the leading *aN* force, this can only be done with an intermediate Delta isobar—for 3*N*, that is the Fujita-Myiazawa force [40], which has been argued to be important for convergence of the chiral expansion [41]. Keeping this in mind, a contribution to the (connected) *aN* potential scales as

$$aN \text{ potential} \sim (4\pi m_N^{-1} M_{NN}^{-1})^{a-1} Q^{2-a} \left(\frac{Q}{M_{\rm QCD}^{-1}}\right)^{\mu} . \qquad (10)$$

To estimate the respective contributions to the *AN* amplitude, one can first consider the LO ($\mu = 0$), 2*N* potential: to produce a connected diagram, we need at least $A-1$ 2*N* interactions linked by $A-2$ propagators. Next, one insertion of a subleading *aN* potential between two LO amplitudes comes with $A+a-2$ propagators and $A+a$ loops. Another insertion of the same subleading potential takes *a* additional propagators and $a-1$ additional loops, and so on. The rules (7), (8) imply that an *aN* potential of index μ gives, at $Q \sim M_{NN}$,

$$AN \text{ amplitude} \sim (4\pi)^{A-1} m_N^{-1} M_{NN}^{5-3A} \left(\frac{Q}{M_{\rm QCD}^{-1}}\right)^{n\nu} , \qquad (11)$$

where

$$\nu \equiv \mu + a - 2 \qquad (12)$$

and *n* is the order in perturbation theory. While ν is the perturbative cost of one insertion of a subleading potential characterized by μ (6) and *a*, *n* insertions cost $n\nu$ as indicated by the power of $Q/M_{\rm QCD}$ in Equation (11). The presence of $a-2$ [instead of $2(a-2)$] in ν reflects the suppression by $(4\pi)^{-1}$ [instead of $(4\pi)^{-2}$] in more-nucleon forces. A sample of pion-range diagrams that contributes at various values of ν is shown in **Figure 2** (see reference [35] for more details).

The *n* in Equation (11) encodes the perturbative character of any subleading interaction. A common fallacy is that the mere definition of a potential means that the corresponding dynamical (Lippmann-Schwinger or Schrödinger) equation must be solved exactly. On the contrary, if there is a sense in which a subleading potential can be treated non-perturbatively, then it should also be possible to include it in distorted-wave perturbation theory, where the distortion is caused by the LO potential. If that is not the case, then at least part of that "subleading" potential is not subleading. Such a consistency test is almost completely ignored in the community. The one exception I am aware of is reference [42], where it is shown that this test is not met by most available chiral potentials.

"But surely," you might be reasoning, "a subleading potential can be treated non-perturbatively." That is certainly the case for a regular subleading potential, but not necessarily for a singular potential, for which neither the perturbative series nor the exact solution of the dynamical equation are well-defined without (potentially distinct) counterterms. So far I have been glossing over the cutoff dependence that usually arises in loops and is, of course, present in the LECs. A regulator is nothing

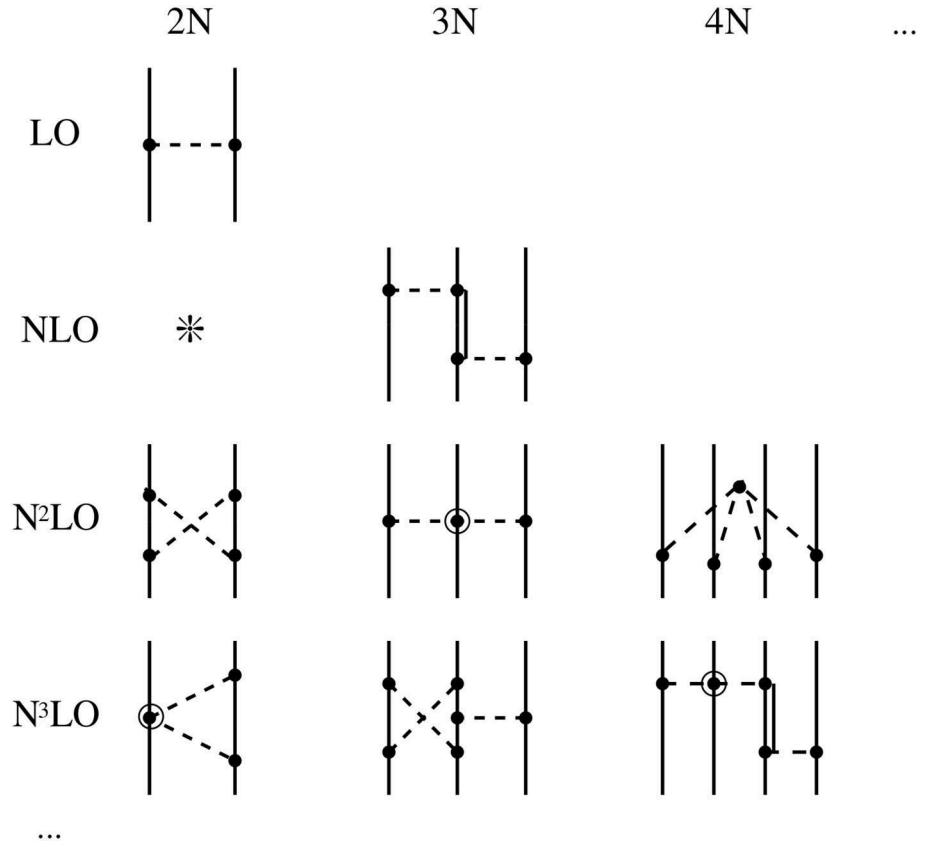


FIGURE 2 | Sample of pion-range diagrams in the *aN* nuclear potential ordered according to the expected size of their contributions to the amplitude (Equation 12). N$^{\nu}$LO denotes relative $\mathcal{O}(Q^{\nu}/M_{\rm QCD}^{\nu})$. A solid (double) line stands for a nucleon (nucleon excitation), while a dashed line, for a pion. A circle (circled circle) represents an interaction with $d + f/2 - 2 = 0\ (= 1)$.

but a way to split short-range physics between loops and LECs. If we increase a momentum cutoff Λ (or decrease a coordinate cutoff $R \sim \Lambda^{-1}$), we account, correctly or incorrectly, for more short-range physics through the loops of the Lippmann-Schwinger equation. As long as $\Lambda \gtrsim M_{\rm QCD}$, we can compensate by changing the LECs present at the same order, without increasing the relative truncation error of $\mathcal{O}(Q/M_{\rm QCD})$. The crucial point is that only the combination of the two effects matter, and physics enters through the fitting of as many observables as LECs—observables which are either calculated in the underlying theory (when we speak of "matching" the EFT to the underlying theory) or measured experimentally. This process of renormalization is essential for *amplitudes* to be free of detailed assumptions about short-range physics, and in general only the sum of all contributions at a given order—loops and LECs ensuring renormalization—can be said to be perturbative or not.

If all we needed was to eliminate the cutoff-dependent parts of pion exchange in the potential, the LECs for the job would be given by NDA, by construction [9]. It is crucial to realize, though, that reducible loops introduce further cutoff dependence, which we need eliminate as well. The potential itself has to depend on the cutoff so that observables do not. The LECs that renormalize this part of the $A \geq 2$ problem will not in general satisfy NDA. We examine this aspect of renormalization next.

3. RENORMALIZATION OF SINGULAR POTENTIALS

The difficulty we face is that EFT potentials are singular and, because of additional derivatives and loops, they get more and more singular as the order of the EFT expansion increases. Singularities are apparent already in the LO ($\mu = 0$, $a = 2$) pion-range potential, OPE: labeling the two nucleons 1 and 2,

$$V_{\rm OPE}(\vec{r}) = \frac{\boldsymbol{\tau}_1 \cdot \boldsymbol{\tau}_2}{m_N M_{NN}} \left[\frac{e^{-m_\pi r}}{r^3} \left(1 + m_\pi r + \frac{m_\pi^2 r^2}{3} \right) S_{12}(\hat{r}) + \left(m_\pi^2 \frac{e^{-m_\pi r}}{r} - 4\pi\,\delta(\vec{r}) \right) \frac{\vec{\sigma}_1 \cdot \vec{\sigma}_2}{3} \right], \quad (13)$$

where $\vec{r} = r\hat{r}$ is the relative position, $\vec{\sigma}_i$ ($\boldsymbol{\tau}_i$) is the spin (isospin) Pauli matrix for nucleon i, and

$$S_{12}(\hat{r}) = 3\,\vec{\sigma}_1 \cdot \hat{r}\,\vec{\sigma}_2 \cdot \hat{r} - \vec{\sigma}_1 \cdot \vec{\sigma}_2 \quad (14)$$

is the spin-tensor operator. While the delta function contributes only to S waves, the tensor potential is non-vanishing for total

spin $s = 1$ and can mix waves with orbital angular momentum $l = j \pm 1$. It is attractive in some uncoupled waves like $^3P_0$ and $^3D_2$, and in one of the eigenchannels of each coupled wave. The regular Yukawa potential is attractive in isovector (isoscalar) channels for $s = 0$ ($s = 1$). More-pion exchange leads to more singular terms, p-pion exchange containing for example terms $\propto r^{-(2p+1)}$ in addition to delta functions and their derivatives.

For $Q \sim M_{NN}$ OPE is expected to be non-perturbative by the argument of the previous section. It has been known for a long time (see e.g., the review [43]) that attractive singular potentials, treated exactly, do not fully determine the solution of the Schrödinger equation [44]. This is a manifestation that renormalization of a singular potential requires contact terms that naturally exist in EFT [23, 24]. In contrast, pion-range corrections to OPE are expected to be perturbative according to the power counting embodied in Equations (11) and (12). From an EFT perspective, additional contact interactions are needed to make these corrections well-defined [31].

The issue I address in this section is how many, and which, contact interactions must be present for the renormalization of specific singular potentials. For simplicity, I consider central potentials; we return to the nuclear potential in section 4.

3.1. Non-perturbative Renormalization

Renormalization is usually discussed at the level of loops in Feynman diagrams for the Lippmann-Schwinger equation in momentum space, but it can also be formulated in terms of the Schrödinger equation in coordinate space. In the latter, which is more familiar to many, renormalization deals with distances on the order of those where the EFT breaks down, which I will call $R_{\rm und}$. The fall off of the potential at much larger distances is not important, as it affects instead the near-threshold behavior. For definiteness, let us take a central two-body potential

$$V_{\rm L}(r) = -\frac{\alpha}{2\mu r^n} \tag{15}$$

in the center-of-mass frame, where μ is the reduced mass, α is a constant with mass dimension $2-n$, and $n > 0$ is an integer. The long-range potential is characterized by an intrinsic distance scale $r_0 \equiv |\alpha|^{1/(n-2)}$. For $n = 2$ the action is scale invariant.

In the radial Schrödinger equation the potential is supplemented by the centrifugal barrier with orbital angular momentum l, $l(l+1)/(2\mu r^2)$. The uncertainty principle implies the kinetic term scales similarly, as $1/(2\mu r^2)$. For $0 < n < 2$ the potential is relatively small at small distances and the corresponding behavior of the wavefunction is determined by l: we find ourselves in the familiar situation where one solution, labeled regular, behaves as r^l for small r, while the other, labeled irregular and discarded, as $r^{-(l+1)}$. In contrast, for $n = 2$ and $|\alpha|$ is sufficiently large, or for $n \geq 3$, $V_{\rm L}(r)$ dominates at small distances. If $\alpha < 0$, the strong repulsion prevents any short-range approach; one can again keep just the regular solution, from which the scattering amplitude can be calculated. But when the potential is attractive, $\alpha > 0$, observables are sensitive to short-distance physics and renormalization is needed.

To see this in detail, consider first $n \geq 3$ at zero energy. For $r \lesssim [l(l+1)]^{-1/(n-2)} r_0$, where $V_{\rm L}(r)$ dominates, the Schrödinger equation becomes an ordinary Bessel equation, and the solution is a combination of spherical Bessel functions. Both solutions are equally irregular as $r \to 0$ [44]. One can write the wavefunction in the l wave at small distances as

$$\psi_l(r) \propto r^{n/4-1} \cos\left(\frac{\sqrt{\alpha}\, r^{1-n/2}}{n/2-1} + \phi_l\right) + \dots , \tag{16}$$

where ϕ_l is a phase that determines the relative importance of the two irregular solutions and is *not* fixed by the long-range potential $V_{\rm L}$. This is in strong contrast with the repulsive case, where the solutions are regular and irregular modified Bessel functions, which respectively decrease and increase exponentially as r decreases.

The case $n = 2$ is borderline singular, the character of the solution depending on the relative size of α and a combination of $l(l+1)$ with a number $\mathcal{O}(1)$ coming from the kinetic repulsion. It turns out that the critical value is $\alpha_l = (l+1/2)^2$. For $l \geq l_\alpha \equiv \sqrt{\alpha} - 1/2$, repulsion wins; one solution is more singular than the other and can again be discarded [45]. For $l < l_\alpha$ the situation is similar to $n \geq 3$: Equation (16) holds with $\sqrt{\alpha}\, r^{1-n/2}/(n/2-1) \to \sqrt{\alpha - \alpha_l}\, \ln(r/r_0)$, where r_0 is an arbitrary dimensionful parameter and $\phi_l = \phi_l(r_0)$. This is an example of an anomaly [46, 47] where the scale invariance of the classical system is broken by the renormalization of the quantum system.

Equation (16) is the quantum version of the "fall to the center" in a classical singular potential [45, 48]. The phases ϕ_l determine the asymptotic behavior of the wavefunction, from which the zero-energy scattering amplitude is extracted. For example, the S-wave scattering length is well-defined for a pure $n \geq 4$ potential [48] and given for $n = 4$ by

$$a_0 = \sqrt{\alpha}\, \tan\phi_0 \,. \tag{17}$$

If one imposes a particular value on $\psi_l(R)$ at a chosen distance R—for example, that the wavefunction $\psi_l(R) = 0$—the phases are fixed. However, a different value of R leads to different phases. In EFT, this arbitrariness is replaced by the values of LECs. The minimal set of contact interactions is determined by demanding renormalizability.

3.1.1. *S* Wave

Let us look into the S wave first. Choosing a sharp cutoff in coordinate space at R, we replace the potential (15) by [23]

$$V(r) = V_{\rm S}(R)\,\theta(R-r) + V_{\rm L}(r)\,\theta(r-R)\,. \tag{18}$$

The depth $V_{\rm S}(R)$ of the spherical well is related to the LEC C_0 of a contact interaction,

$$C_0\,\delta(\vec{r}) = \frac{C_0}{4\pi r^2}\,\delta(r) \to \frac{3C_0(R)}{4\pi R^3}\,\theta(R-r) \equiv V_{\rm S}(R)\,\theta(R-r)\,. \tag{19}$$

A solution of the Schrödinger equation for the augmented potential requires the matching of the logarithmic derivatives of outside and regular spherical-well wavefunctions at $r = R$,

$$\sqrt{-2\mu R^2 V_{\rm S}(R)}\, \cot\sqrt{-2\mu R^2 V_{\rm S}(R)} = r\frac{\partial}{\partial r} \ln\left(r\psi_0(r)\right)\Big|_{r=R} . \tag{20}$$

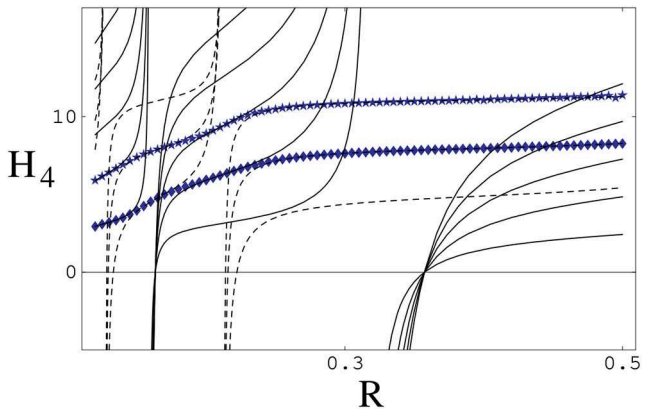


FIGURE 3 | Dependence of $H_4 \equiv \sqrt{-2\mu R^2 V_S(R)}$ for $n = 4$ on R (in units of r_0). Two analytical approximations, Equation (21) (solid lines) and Equation (22) (dashed lines), are shown together with a numerical solution of Equation (20) (bold lines) that interpolates between them. Reprinted figure with permission from reference [23]. Copyright (2001) by the American Physical Society.

When $n = 2$ and $\alpha \leq \alpha_0$, or $n = 1$, we can solve this equation with $V_S(R) = 0$ if the admixture of the most singular external solution tends to zero as $R \to 0$. Thus the amplitude is renormalized properly without a contact interaction as long as we retain only the least singular wavefunction behavior, the prescription offered in reference [45].

For $n = 2$ and $\alpha > \alpha_0$, or for $n \geq 3$, because the two external solutions differ only by a phase, the contact interaction is necessary. Substituting the wavefunction (16) into Equation (20), yields a transcendental equation linking ϕ_0 to $V_S(R)$ [23]. Two approximate solutions are

$$\sqrt{-2\mu R^2 V_S(R)} \simeq m\pi \left\{ 1 - \left[1 - \frac{n}{4} + \sqrt{\alpha}\, R^{1-n/2} \tan\left(\frac{2\sqrt{\alpha}}{n-2} R^{1-n/2} + \phi_0 \right) \right]^{-1} \right\}, \quad (21)$$

when the right-hand side of Equation (20) is large, and

$$\sqrt{-2\mu R^2 V_S(R)} \simeq \frac{(1+2m)\pi}{2} - \frac{2}{(1+2m)\pi} \left[\frac{n}{4} - \sqrt{\alpha} R^{1-n/2} \tan\left(\frac{2\sqrt{\alpha}}{n-2} R^{1-n/2} + \phi_0 \right) \right], \quad (22)$$

when it is small, where in both cases m is an integer. Now one can keep the scattering amplitude at zero energy fixed at its experimental value by adjusting $2\mu R^2 V_S(R)$, which displays an periodic dependence on a power of the cutoff [23, 24, 49–54]. For $n = 2$, the dependence is periodic in $\ln R$, characteristic of a limit cycle and a remaining *discrete* scale invariance. (For discussions of limit cycles, see references [55, 56].) The $n \geq 3$ oscillation indicates a generalized limit cycle. The case $n = 4$ is displayed in **Figure 3** [23].

Having renormalized zero-energy scattering, an important question is whether the problem is well-defined also at finite energy $E \equiv k^2/(2\mu)$. That this is the case can be shown [23] with the WKB approximation, which applies to the region where the wavelength is small compared to the characteristic distance over which the potential varies appreciably. For distances where $|V_L(r)| \gg E$, one recovers Equation (16) for the wavefunction, up to energy-dependent corrections that are determined by Equation (16) itself. In the absence of a short-range interaction, decrease in R would lead to the repeated appearance of low-energy bound states due to the unstoppable growth in attraction, a phenomenon reflected in the never-ending oscillations of the wavefunction [48]. With $V_S(R)$ preventing this collapse and ensuring the description of *one* low-energy datum, bound states can accrete only from negative energies, converging to finite values as R decreases. How many of the bound states are within the region of validity of the EFT depends, of course, on the scales in the problem: the very low-energy spectrum will be affected by the long-distance tail of the potential while states with binding energies $\gtrsim (2\mu R_{\rm und}^2)^{-1}$ are irrelevant for the distances of interest. For $n = 2$ and $\alpha > \alpha_0$, which is equivalent [57] to the three-boson system with short-range interactions at unitarity, the bound states form a geometric tower ("Efimov states" [58]) that signals the remaining discrete scale invariance stemming from the limit cycle in the contact interaction [59, 60]. While the existence of the tower is a consequence of the symmetry, its position is fixed by the LEC. It is remarkable that it is the proper renormalization of the EFT that underlies the "Efimov physics" intensely explored with cold atoms [61].

A particularly simple example of singular potential is the delta function itself. In this case the external potential vanishes and the external zero-energy wavefunction is replaced by

$$\psi_0(r) \propto r^{-1} \left(1 - \frac{r}{a_0} + \dots \right), \quad (23)$$

where a_0 determines the ratio between irregular and regular solutions and is nothing but the scattering length. The solution for Equation (20) can be written explicitly,

$$V_S(R) = -\frac{1}{2\mu R^2} \left[(1+2m)^2 \frac{\pi^2}{4} + \frac{2R}{a_0} + \dots \right], \quad (24)$$

where m is an integer. It is apparent how a cutoff-dependent $C_0(R) \propto R$ softens the delta function. The scattering length enters in the smaller R^2 term. Of course, a similar result is obtained for a momentum cutoff $\Lambda \sim R^{-1}$ [27].

A subtlety arises when a regular potential with $n = 1$ in Equation (15) is present together with the delta function, as is the case for OPE. By itself, the long-range potential needs no regularization; with the delta function, a new cutoff dependence emerges in the irregular solution [24, 62]:

$$\psi_0(r) \propto r^{-1} \left\{ 1 - r \left[\frac{1}{\bar{a}_0} + \alpha \left(\ln \frac{r}{R_\star} - 1 \right) \right] + \dots \right\}, \quad (25)$$

where $\bar{a}_0$ and $R_\star$ are length scales that enter the zero-energy scattering amplitude. Instead of Equation (24),

$$V_{\rm S}(R) = -\frac{1}{2\mu R^2}\left[(1+2m)^2\,\frac{\pi^2}{4} + 2R\left(\frac{1}{\bar{a}_0} + \alpha\,\ln\frac{R}{R_\star}\right) + \ldots\right]. \tag{26}$$

The main difference is the appearance of the $\ln R$ with a coefficient $\propto \alpha$.

In both these cases, where the outside potential is not singular, it is easy to see that the amplitude at finite energy is well-defined. The energy enters both internal and external wavefunctions as $(kr)^2$ and can only affect the depth of the spherical well by a term of $\mathcal{O}(R^0)$, an effect that disappears as R decreases. The multiple branches in Equations (24) and (26) are a consequence of the fact that a spherical well can have multiple bound states. The zero-energy amplitude is essentially determined by the shallowest state, and we can choose different well depths to place any one state at the desired position. Deeper states have energies $\propto (2\mu R^2)^{-1}$ and, again, are beyond the regime of the EFT for $R \lesssim R_{\rm und}$. Differently from long-range singular potentials, the three-dimensional delta function supports a single bound or virtual state.

3.1.2. Higher Partial Waves

We can now look at higher partial waves. Amplitudes in these waves have additional powers of $\vec{p}\,'\cdot\vec{p}$, where $\vec{p}$ ($\vec{p}\,'$) is the relative incoming (outgoing) nucleon momentum. Just as for k^2 in the S wave, in the absence of a long-range potential, dimensional analysis implies that $\vec{p}\,'\cdot\vec{p}$ must come together with R^2: the no-derivative contact interaction contributes in the small-R limit only to the S wave. For the $n=1$ external potential, the $l \geq 1$ phase shifts then converge as $R \to 0$. A long-range singular potential of the type (15) contains an intrinsic scale r_0 and $\vec{p}\,'\cdot\vec{p}$ comes in general with a factor r_0^2 and does not disappear as $R \to 0$. There is a phase ϕ_l in Equation (16) for every l, which can only be fixed by higher-derivative interactions.

To see this, let us first stick to the potential (18). The $k=0$ matching equation that generalizes Equation (20) is

$$\begin{aligned} R_l(R) &\equiv \sqrt{-2\mu R^2 V_{\rm S}(R)}\,\frac{j_{l+1}(\sqrt{-2\mu R^2 V_{\rm S}(R)})}{j_l(\sqrt{-2\mu R^2 V_{\rm S}(R)})} \\ &= l+1 - r\frac{\partial}{\partial r}\ln\left(r\psi_l(r)\right)\Big|_{r=R}, \end{aligned} \tag{27}$$

where j_l is the spherical Bessel function of the first kind. Using the recurrence relation for Bessel functions,

$$R_l(R) = 2l+1 + \frac{2\mu R^2 V_{\rm S}(R)}{R_{l-1}(R)}. \tag{28}$$

In the absence of an external potential, the external wavefunction is a combination of the regular j_l and the irregular y_l, the spherical Bessel function of the second kind. By direct calculation we find that at small R

$$R_l(R) = 2l+1 + \mathcal{O}(R^{2l+1}/a_l), \tag{29}$$

where a_l is the l-wave scattering "length" (e.g., volume for $l=1$), the zero-energy limit of the ratio of the y_l and j_l coefficients. Using $R_0(0)=1$ in Equation (28) gives

$$R_1(0) = 3 - \left[(2n+1)\frac{\pi}{2}\right]^2. \tag{30}$$

which implies, together with Equation (29), that $a_1 = \mathcal{O}(R^3)$. The argument repeats for $l \geq 2$ with different finite pieces, leading to $a_l = \mathcal{O}(R^{2l+1})$. As anticipated by dimensional analysis, the effect of the non-derivative contact interaction disappears from $l \geq 1$ waves as $R \to 0$. A similar argument for a regular outside potential leads to the same conclusion. For the argument with a delta-shell regularization, see reference [63].

In contrast, when the external potential is attractive and singular with $n \geq 3$,

$$R_l(R) = l+1-\frac{n}{4} + \sqrt{\alpha}\,R^{1-n/2}\tan\left(\frac{\sqrt{\alpha}}{n/2-1}R^{1-n/2} + \phi_l\right). \tag{31}$$

Matching in the S wave makes ϕ_0 R-independent. Since $2\mu R^2 V_{\rm S}(R)$ is approximately cutoff independent as can be seen from either of the two approximate solutions (21) and (22), Equation (28) gives

$$R_1(R) = 3 - \Delta_1(R), \tag{32}$$

where $\Delta_1(R \ll r_0)$ is finite. Comparison with Equation (31) then shows that $\phi_1 \propto R^{1-n/2}$. Continuing to larger l we find

$$\phi_l(R \ll r_0) = -\frac{\sqrt{\alpha}}{n/2-1}R^{1-n/2}. \tag{33}$$

The phases are thus angular-momentum and energy independent [63] in this limit, *but cutoff dependent* [48].

What is needed for renormalization is a single contact interaction with a minimum number of derivatives in each wave, with LECs C'_{2l}. The interaction is non-local, for example for $l=1$,

$$\frac{C'_2}{4\pi r^2}\left(\frac{\partial\delta(r)}{\partial r}\right)\frac{\partial}{\partial r'}\Big|_{r'=0} \to \frac{C'_2(R)}{4\pi R^3}\left[\frac{2}{r}\,\theta(R-r) - \delta(r-R)\right]\frac{\partial}{\partial r'}\Big|_{r'=R}, \tag{34}$$

where $C'_2(R)$ is determined so as to keep the phase ϕ_1, and thus one P-wave low-energy datum, fixed. The contact interactions are all determined by the underlying interactions, but without additional dynamical assumptions we do not know how they relate to each other. Model independence requires we keep them free.

3.1.3. Implications

Much of the above had been understood without EFT. The use of boundary conditions, for example, goes back at least to the work of Breit [64]. In EFT, a boundary condition corresponds to a specific regulator. At the two-body level, in the S wave we have simply traded the dependence in R by that of $V_{\rm S}(R)$. Renormalization means that, as far as observables are concerned, the regulator choice is irrelevant (within the error of the truncation); only the unobservable cutoff dependence of the

LECs depends on the regulator. What matters is that a LEC encodes one parameter. The LO EFT in coordinate space is in the spirit of atomic Quantum-Defect Theory, where the interaction of far-away electrons with an ionic core or molecule is solved for exactly and a few parameters ("defects") account for short-range interactions [65].

The model independence of the EFT is manifest in the fact that the same two-body contact interactions that renormalize the two-body problem contribute to other processes. For example, the three-boson system was considered in reference [54], where binding energies and the particle-dimer scattering length were calculated. Convergence was observed in a range of cutoffs, with asymptotic values representing model-independent predictions. The role of D and higher waves in these results was, however, not discussed.

The contact interactions can also be seen as providing a self-adjoint extension of the Hamiltonian. As stressed in reference [66], the so-called deficiency index for a singular potential is (∞, ∞), i.e., an infinite number of parameters—the phases ϕ_l in Equation (16) for all values of l—are needed to determine the self-adjoint extension uniquely. In the EFT this translates into the existence of an infinite number of contact interactions, one with the minimal number of derivatives for each wave (of course, the EFT contains also contact interactions with an arbitrary number of derivatives).

While mathematically the problem looks hopeless, on physical grounds this is clearly a red herring. As remarked in reference [20], increasing l strengthens the centrifugal barrier and shrinks the distances $r \lesssim [l(l+1)]^{-1/(n-2)} r_0$ where the attractive $n \geq 3$ potential takes over. The distance of closest approach at momentum k can be estimated from the point where the energy is comparable to the centrifugal barrier, or $r \gtrsim [l(l+1)]^{1/2} k^{-1}$. For $k \lesssim M_{\rm und}$, the breakdown scale, we are only interested in distances $r \gtrsim R_{\rm und} \sim [l(l+1)]^{1/2} M_{\rm und}^{-1}$. We might then expect that only in waves with $l \lesssim l_{\rm cr}$ does a singular potential need to be treated exactly and Equation (16) apply, where [32]

$$l_{\rm cr}\left(l_{\rm cr}+1\right) \sim \frac{r_0}{R_{\rm und}} \,. \tag{35}$$

A more precise semi-analytical estimate comes from the investigation of the critical strength α where a Bessel series solution of the Schrödinger equation exhibits a square-root branch point characteristic of non-perturbative behavior. For $n = 3$ [32], it is described pretty well for large l by the estimates above. For $n = 2$, consideration of the first two orders in the perturbative expansion suggests $l_{\rm cr} = (\pi|\alpha| - 2)/4$ [31]. An attractive singular potential defined with a step function at $l_{\rm cr}$ has a finite deficiency index $(l_{\rm cr}, l_{\rm cr})$.

The situation is different in the case of $n = 1$. The potential is larger than both centrifugal barrier and kinetic repulsion for $r \gtrsim n^2(l)\, r_0$, where $n(l)$ is $\mathcal{O}(1)$ for $l = 0$ and grows as l for large l. Balance among these terms leads to bound states of sizes $r_n \sim 2n^2 r_0$ and binding energies $B_n \sim \alpha^2/(8\mu n^2)$. (Taking as an example the Coulomb interaction, where $\alpha = 2\mu\alpha_{\rm e}$ in terms of the fine-structure constant $\alpha_{\rm e}$, we get the proper result $B \sim \mu\alpha_{\rm e}^2/(2n^2)$ if we interpret n as the principal quantum number.) These estimates are in any case affected by the long-range tail of the potential, which we are not considering in this section. But at distances $R_{\rm und} \lesssim r \lesssim r_0$, we expect $l_{\rm cr} \approx 1$: while the S wave might be non-perturbative and perhaps require a short-range potential (26) to generate a bound state at the observed location, higher waves should be perturbative.

3.2. Perturbative Corrections

EFT provides a framework where we can systematically incorporate corrections to the leading interactions, which can be checked with the method developed in reference [67]. We pair subleading long-range interactions with the subleading short-range interactions needed for renormalization order by order. As stressed in reference [68], renormalization at a given order contains clues about the relative importance of higher corrections. Just as a negative power of R indicates at least one missing LEC, so positive powers of R point to the order before at least one new LEC should appear. If the error in an observable not used in the fit of LECs at $\mathrm{N}^i\mathrm{LO}$ (with some integer i) scales as a positive power of the coordinate cutoff, say R^x, then we may expect that corrections appear at $\mathrm{N}^{i+j}\mathrm{LO}$, where $j \leq x$ is an integer (not necessarily the largest integer). This constraint comes from the demand that the regulator error should not exceed the truncation error when $R \lesssim R_{\rm und}$. (It does not exclude the presence of a LEC at a lower order than that estimated by the cutoff dependence, corresponding to boundary conditions of the RG equation [22].) We will see examples below.

The next renormalization challenge arises from the more-singular corrections to the long-range potential. An almost automatic reflex is to simply add the correction to the LO potential, as Weinberg prescribed, and solve the Schrödinger equation. For a regular potential, adding a regular correction that is small everywhere can be done in perturbation theory, but it can also be done by solving the Schrödinger equation exactly. For a more-singular correction, however, the perturbing potential will be larger than the LO potential at sufficiently small r. One risks destroying the systematic character of the EFT unless one keeps R relatively large. Whether this risk materializes needs to be checked explicitly. As we will see, renormalization requires distorted-wave perturbation theory around the LO solution [20, 31]. Implications for nuclear interactions are discussed in section 4.1.

3.2.1. Distorted-Wave Perturbation

A pedagogical toy model that nicely illustrates the need for perturbation theory on singular corrections was presented in reference [69]. The model consists of two separable, regular potentials, one of range $m_{\rm L}^{-1}$, the other of range $m_{\rm S}^{-1} \ll m_{\rm L}^{-1}$. Because the potentials are separable, exact answers can be found for the effective-range parameters. The potential parameters are fine-tuned so that each potential separately produces a natural scattering length, that is, $a_0 \sim m_{\rm L}^{-1}$ ($a_0 \sim m_{\rm S}^{-1}$) in the absence of the short-range (long-range) potential. Next, the short-range potential is expanded in powers of $k/m_{\rm S}$, creating a series of singular interactions. While for $k \sim m_{\rm L}$ the long-range potential is non-perturbative, the singular corrections should be treated in distorted-wave perturbation theory. Lo and behold, the results up

to N^{2}LO obtained with a standard subtraction scheme are found to reproduce the exact results. In contrast, when a truncation of the expanded short-range potential is solved exactly, similar to the "peratization" of Fermi theory [70, 71], one can no longer take a large momentum cutoff. Reference [69] concludes that removing the cutoff dependence is impossible, which is indeed true when one insists on iterating subleading corrections.

The situation is not significantly different for the case of interest in nuclear physics where not only corrections, but also the LO potential is singular. Again, the simplest example is provided by the delta function without external potential, $V_{\rm L}(R) = 0$ in Equation (18). As discussed above, the energy dependence first affects the matching between internal and external wavefunctions at relative $\mathcal{O}(k^2R^2)$. The ratio of irregular and regular solutions, which determines $k\cot\delta_0(k)$ where $\delta_0(k)$ is the S-wave phase shift, starts at $\mathcal{O}(R)$. Thus, at LO

$$k\cot\delta_0(k) = -\frac{1}{a_0}\left(1+\mathcal{O}(Ra_0k^2)\right) , \tag{36}$$

which means that the fractional error in δ_0 is

$$\frac{\Delta\delta_0(k)}{\delta_0(k)} = \mathcal{O}(Ra_0k^2) . \tag{37}$$

For example, the effective range $r_0 \sim R$. This again can be easily obtained with a momentum regulator [27]. In ChEFT, where away from the chiral limit the delta function is accompanied in the singlet S wave by the Yukawa potential, the situation is not substantially different [24]. Aside the $\mathcal{O}(\alpha R\ln R)$ dependence in Equation (26), the argument does not change and Equation (37) still holds with $a_0 \to \bar{a}_0$. Despite the presence of pions, the error is still $\propto R$. It can be removed in first-order perturbation theory by a two-derivative contact interaction

$$\delta V_{\rm S} = C_2\left\{\left[\nabla^2\delta(\vec{r})\right] + 2\left[\vec{\nabla}\delta(\vec{r})\right]\cdot\vec{\nabla} + 2\delta(\vec{r})\nabla^2\right\} , \tag{38}$$

whose LEC $C_2(R) \propto R^2$ fixes $r_0 \sim R_{\rm und}$. For $R \lesssim R_{\rm und}$, this contact interaction is an NLO correction to the LO interaction with LEC C_0. This is in fact one of the elements in the power counting in Pionless EFT [35]. Note that, if we were to impose that C_2/C_0 scaled with $R_{\rm und}^2$ as implied by NDA, we would obtain an effective range that scaled the same way, in contrast to what one obtains for typical short-range potentials [27]. Once again, renormalization automatically enforces a general property of short-range interactions.

But what if we solved the Schrödinger equation exactly following Weinberg's prescription? In the simpler case without a long-range potential, it has been shown explicitly [72–74] that this can be done in a renormalized way only if $r_0 \lesssim R$, which is arbitrarily small. In other words, the two-derivative contact interaction is non-perturbatively renormalizable only if the theory satisfies a "Wigner bound" [75] $r_0 \geq 0$. In contrast, when the two-derivative contact interaction is treated in perturbation theory, at second order and higher, which contain loops involving two or more powers of C_2, four- and higher-derivative contact interactions appear to guarantee renormalization. When we resum the two-derivative contact interaction we generate diagrams with an arbitrary number of loops, but lack the counterterms to remove the cutoff dependence. A calculator committed to exact solutions might be tempted to eschew renormalization (and thus model independence) and live with a relatively large R. Still, such stubbornness in resumming what needs no resummation might be rewarded by results that are *worse* than those of the perturbative expansion. An example is provided by a calculation [76] of the S-wave scattering phase shifts for a harmonically trapped unitary system, where the regulator was implemented in the form of a maximum number of shells. One can see explicitly how in first-order perturbation theory the derivatives in Equation (38) give a contribution to the NLO energy which is proportional to the LO energy, apart from a shift in the LO LEC. The result of resumming the NLO interaction is not only cutoff dependent but also gives rise to a larger violation of unitarity than even NLO.

Note that one can introduce an auxiliary "dimeron" field in the EFT Lagrangian [77] whose kinetic term provides an energy-dependent correction to the potential. Exploiting the redundancy of interactions in the enlarged Lagrangian, one can remove the momentum-dependent corrections (38). Renormalization changes with an energy-dependent potential and, in particular, a resummation does not restrict r_0. However, unless there is evidence for $r_0 \gg R_{\rm und}$, this is still an NLO correction and the resummation does not affect observables up to higher-order terms [27].

Resummation of subleading interactions can lead to an even more paradoxical situation. The problem is that subleading singular potentials are not in general attractive in all the same waves as OPE. If the corrections are iterated together with OPE, the cutoff behavior of the amplitude will change completely: channels that required a counterterm at LO may not require, or even tolerate, one at subleading order [24]. Take a wave where the LO potential is singular with a power n and attractive, thus requiring a counterterm, but the subleading potential is repulsive (strength α') with a power $n' > n$. The exact solution of the Schrödinger equation for the sum of the external potentials is now dominated at short distances by the irregular solution of the subleading potential, which grows exponentially as r decreases. Matching to the short-range potential $V_{\rm S}$ will force a non-vanishing irregular solution, which in turn leads to an exponentially *increasing* dependence of the fractional phase shift error in R, $\propto R^{1+n'/2}\exp[2\sqrt{-\alpha'}\,R^{1-n'/2}/(n'/2-1)]$ [24]. The only solution is to remove the LO LEC at subleading order! There is hardly a way to keep the systematic expansion of the EFT.

Another toy model [78] illustrates this paradox. This time the underlying potential consists of a *repulsive* r^{-3} component associated with a mass $m_{\rm L}$ together with an attractive r^{-3} from a heavier $m_{\rm S} \gg m_{\rm L}$, as well as less singular terms. Its exact S-wave results are compared to those of a potential consisting of the repulsive r^{-3} potential plus a delta-function interaction. Parameters are chosen so that the repulsive potential is non-perturbative. Despite the fact that the phase shifts of the repulsive component are well-defined by themselves, reference [78] includes the delta function non-perturbatively, fixing it to reproduce the scattering length of the underlying potential. For

$R^{-1} \lesssim m_S$ the phase shifts are in reasonably good agreement with those of the underlying potential. However, agreement deteriorates as R decreases. Disregarding conceptual differences in renormalization of attractive and repulsive singular potentials [23, 24], reference [78] concludes that cutoff dependence cannot be removed in general, rather than in the particular case of resumming the subleading delta function. In response, reference [79] included the $2n$-derivative delta functions, which account for the short-range potential, at $N^{2(n+1)}LO$ in perturbation theory. Calculations up to N^8LO show convergence to the exact phase shifts up to at least $k \sim 2m_L$ without significant restriction on R. (Reference [80] nevertheless points to some ambiguity in the values of the NLO phase shifts, apparently implying that it is suffcient reason to abandon renormalization.)

Thus the singular nature of the potentials that we want to treat in an EFT expansion of the amplitude requires the use of perturbation theory on corrections, as implied by the power counting of section 2. This in fact ensures small changes in amplitudes after renormalization [31]. But then one might wonder to which extent the singular nature of the LO potential affects the order of the corrections. As we have seen, when the only singular part of the LO potential is a delta function, the first correction comes at NLO. When the outside potential is singular and attractive, the situation is different. For an LO singular attraction, one finds [24] that after fixing the phase ϕ_0 the S-wave phase shifts scale as

$$\frac{\Delta\delta_0(k)}{\delta_0(k)} \propto R^{1+n/2} . \tag{39}$$

This means that corrections are expected at (or before) N^2LO for $n = 2, 3$, N^3LO for $n = 4, 5$, *etc.*. It is unclear why the results reported in reference [54] indicate higher sensitivity to R than given by Equation (39).

Now, the power counting for nuclear interactions in section 2 says that at N^2LO there are corrections to the long-range potential with an $r^{-(n+2)}$ singularity. The additional singularity can be removed in first-order perturbation theory by additional contact interactions with two derivatives. This can be shown relatively simply in a toy model where a $\pm r^{-4}$ potential is added to an $n = 2$ attractive LO potential [31]. The analysis was carried out in momentum space with a sharp cutoff Λ. At N^2LO, where the $\pm r^{-4}$ potential is considered as a first-order perturbation, two forms of additional, oscillating cutoff dependence appear: one proportional to Λ^2, reflecting the stronger singularity of the perturbing potential, the other proportional to k^2. In the S-wave, a two-derivative potential (38) is sufficient, together with an N^2LO shift in the C_0 of Equation (19), to remove the two additional divergences. This argument can presumably be continued at higher orders and repeated for $l \geq 1$ waves by considering interactions of type (34) with two more derivatives. One tentatively concludes that NDA holds in distorted-wave perturbation once it has been corrected at LO.

3.2.2. Simple Perturbation

In partial waves $l \gtrsim l_{cr}$ where the LO potential is perturbative and particles are free in zeroth approximation, corrections are included in simple perturbation theory. The first task in this case is to quantify the angular-momentum suppression for the long-range potentials so as to establish the orders they come in. The second need is to find the orders the associated contact interactions appear at.

For the $\mu = 0$ long-range potential, rules (7) and (8) indicate that a contact interaction is needed for renormalization at nth order in perturbation theory, where $n \geq 2l + 1$. This is consistent with the inference from the residual cutoff dependence of the non-derivative contact interaction. As we saw in section 3.1.2, l-wave scattering "lengths" a_l are induced through matching at finite R. Just as for the S-wave effective range, they can be made arbitrarily small by taking $R \to 0$. However, the higher power of R, R^{2l+1}, suggests that contact interactions in higher waves enter in perturbation theory at $N^{2l+1}LO$ or lower, another element of Pionless EFT power counting [35].

The increased singularity of subleading potentials asks for counterterms at lower orders in perturbation theory. The first-order perturbative correction due to subleading potentials involving pion loops is renormalized with LECs assigned by NDA. Making further general statements about the order contact interactions are needed is cumbersome without an explicit angular-momentum suppression factor.

If one were to solve the Schrödinger equation exactly in one of these waves, renormalization would require a LEC, which then determines the asymptotic properties of the wavefunction. The tail of the non-perturbative wavefunction can be reproduced with increasing accuracy as the order of perturbation theory increases [23]. Being a series in α, the perturbative expansion cannot reproduce the oscillations found in Equation (16), which are tied to the non-analytic dependence $\sqrt{\alpha}$. This is no problem because, by definition of l_{cr}, these oscillations take place at distances smaller than those probed by the EFT. Their effects can be "averaged out" and appear through contact interactions at subleading orders. If one wants to save all the perturbative work by sticking to a non-perturbative solution, one loses some predictive power at LO but, because it is a single LEC (in one wave), this is perhaps acceptable. Alternatively, one could simply not include the LEC if l is sufficiently high for oscillations to happen below R, which might be limited in numerical calculations anyway. In this case R is in the region where perturbation theory works and the result will be relatively insensitive to R. Unnecessary iteration in high waves is thus relatively harmless, other than obscuring the systematic EFT expansion.

4. RENORMALIZATION OF CHIRAL EFT

By this point in the manuscript it should be clear how to proceed with ChEFT in the nuclear sector. The power counting of ChPT is based on NDA, which comes from demanding that the EFT expansion be renormalized order by order so as to ensure model independence. In the more general ChEFT we continue to insist on model independence, but now LO is non-perturbative. The results of the previous section apply to pion-exchange potentials, where the spin-isospin factors and

the exponential fall-off at large $m_\pi r$ do not substantially affect renormalization. Perhaps not surprisingly in hindsight, NDA is violated.

Since the OPE tensor force is singular and attractive in an infinite number of channels, the first task (section 4.1) is to estimate up to which relative angular momentum l OPE needs to be considered at LO. In sections 4.2 and 4.3 renormalized results for, respectively, two and more nucleons are described.

4.1. Partly Perturbative Pions

The simple power counting of Equations (7) and (8) does not capture factors of l^{-1}, just as it misses other dimensionless factors. More realistically, OPE in the radial Schrödinger equation is an expansion in $Q/M_{NN}^{(l,s)}$, where $M_{NN}^{(0,s)} \sim M_{NN}$ but $M_{NN}^{(l,s)}$ increases with l depending in general also on the spin s. Once $M_{NN}^{(l_{\rm cr}^{(s)},s)} \sim M_{\rm QCD}$, OPE is perturbative. What do we know about $M_{NN}^{(l,s)}$ and $l_{\rm cr}^{(s)}$?

The bold suggestion was made in references [28, 29] that $l_{\rm cr}^{(s)} \approx 0$, so that pion exchange would be amenable to perturbation theory in *all* waves. The estimate in Equation (5) assumed NDA for the one-nucleon quantities $m_N = \mathcal{O}(M_{\rm QCD})$, $f_\pi = \mathcal{O}(M_{\rm QCD}/(4\pi))$, and $g_A = \mathcal{O}(1)$, plus neglected any dimensionless factors. Numerically, $M_{NN} \simeq 290$ MeV. What if the various spin/isospin factors and other numbers floating around, each of $\mathcal{O}(1)$, conspire to make OPE more perturbative, so that M_{NN} is effectively comparable to $M_{\rm QCD}$?

In that case, at LO ChEFT would be formally the same as Pionless EFT [35, 36], where the binding of light nuclei rests on the shoulders of non-derivative $2N$ and $3N$ contact interactions [81, 82]. But because pions are explicit, the range of validity of the EFT is enlarged—at least near the chiral limit where integrating out pions becomes a very restrictive condition. An attractive feature of this proposal is that it could potentially explain why Pionless EFT works better than expected, for example for binding energies [35].

This proposal also neatly solves the renormalization issues of the last section. OPE is now an NLO effect of relative $\mathcal{O}(Q/M_{NN})$, so no problems associated with its singularity emerge. Being perturbative, it brings NLO cutoff dependence only to S waves. Because at LO the external potential vanishes, Equation (36) requires at NLO one chirally symmetric two-derivative contact interaction in each S wave. Then $Q \sim m_\pi$ implies the concomitant presence of a chiral-symmetry-breaking non-derivative interaction with LEC proportional to the quark masses, $m_\pi^2 D_2$. In the background of an LO wavefunction of the type (23), OPE generates an $m_\pi^2 \ln \Lambda$ cutoff dependence which can be absorbed in D_2. The $2N$ amplitude is renormalized and in good agreement [28, 29, 83] with the Nijmegen partial-wave analysis (PWA) [84] up to $Q \sim m_\pi$.

Alas, calculations at $\mathcal{O}(Q^2/M_{NN}^2)$ have shown [30, 85] that in the low, spin-triplet partial waves, where the OPE tensor force is attractive, the expansion fails for $Q \sim 100$ MeV. In partial waves with $l = j \gg 1$, where counterterms are needed only at a very large number of loops $L \geq 2l$, the breakdown of perturbation theory

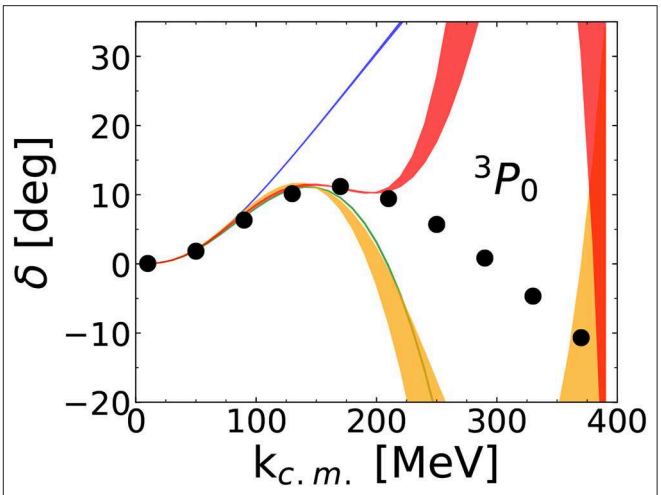


FIGURE 4 | Two-nucleon $^3P_0$ phase shift δ as function of the center-of-mass momentum $k_{\rm c.m.}$. The NLO (blue), N^{2}LO (green), N^{3}LO (orange), and N^{4}LO (red) bands from a perturbative treatment of pion exchange correspond to cutoff variation from 0.8 to 2.4 GeV. (LO in a perturbative expansion vanishes for this channel.) The empirical phase shifts from the SAID program [88] (solid circles) are shown for comparison. Reprinted figure with permission from reference [87]. Copyright (2019) by the American Physical Society.

was estimated in the chiral limit to be at a critical momentum [86]

$$p_{\rm cr} \approx \frac{l^3}{\sqrt{27}|2(-1)^l + 1|} M_{NN} \,. \tag{40}$$

If we impose $p_{\rm cr} \sim M_{\rm QCD}$, we get $l_{\rm cr}^{(1)} \approx 2.5$. The radius of convergence of the perturbative series is not as large in waves with $l = j \pm 1$. In both cases the first few orders were found [86] not to be representative of the large-order convergence. For low partial waves counterterms enter already at low orders. When they were assigned arbitrary but natural values, all waves except $^3S_1$-$^3D_1$, $^3P_0$, and perhaps $^3P_1$ were found to converge up to $p_{\rm cr} \approx M_{NN}$. An example of failure, $^3P_0$, is given in **Figure 4** [87], where OPE is NLO, n-iterated OPE N^{n}LO, leading two-pion exchange (TPE) N^{3}LO, and subleading TPE N^{4}LO. The LECs are assumed to be given by NDA instead of being introduced only at the order where they are first needed for renormalization. These signs of the breakdown of perturbative pions are consistent with an expansion in $Q/M_{NN}^{(l,1)}$ with $M_{NN}^{(l\approx 1,1)} \sim f_\pi$ as indicated by NDA.

It seems inevitable that pions must be treated non-perturbatively in the low partial waves if we want to go beyond Pionless EFT at physical quark masses. Still, based on the general arguments of section 3.1.3 we expect pions to be perturbative for sufficiently high partial waves. The $n = 3$ tensor force, for which $r_0 \sim M_{NN}^{-1}$, does not vanish for spin $s = 1$. Equation (35) with $R_{\rm und} \sim [l(l+1)]^{1/2} M_{\rm QCD}^{-1}$ provides an estimate $l_{\rm cr}^{(1)} \approx 2$ for the critical angular momentum in attractive triplet waves. This conclusion is made firmer by a generalization to the tensor potential of the analysis of the onset of square-root branch points in the Bessel series solution of the Schrödinger equation [32]. Given that the strength of OPE is fixed by M_{NN}, it translates

TABLE 1 | Estimate of the critical values $p_{\rm cr}$ of the relative momentum in the lowest 2*N* triplet channels above which the OPE tensor force cannot be treated perturbatively [32].

Partial wave	$p_{\rm cr}$/MeV
$^3S_1$-$^3D_1$	66
$^3P_0$	182
$^3P_1$	365
$^3P_2$-$^3F_2$	470
$^3D_2$	403
$^3D_3$-$^3G_3$	382
$^3F_3$	2860
$^3F_4$-$^3H_4$	2330
$^3G_4$	1870

into an upper bound on the critical momentum $p_{\rm cr}$, including repulsive waves. The results, listed in **Table 1**, are obtained in the chiral limit; a realistic pion mass could affect the smaller values by factors of $\mathcal{O}(1)$ but is not expected to be important for the larger values. They indicate that OPE in $^3S_1$-$^3D_1$ and $^3P_0$ likely fails to converge already below M_{NN}. In contrast, OPE in high waves, such as *F* and higher, converges beyond $M_{\rm QCD}$. The gray zone is the *D* and *P* waves other than $^3P_0$. Given the low values of $p_{\rm cr}$ on the scale set by $M_{\rm QCD}$, one might conclude that $l_{\rm cr}^{(1)} \approx 3$. An analysis of spin-triplet phase shifts where OPE and TPE are removed in distorted-wave perturbation [89] supports this conclusion.

A different but closely related estimate for $l_{\rm cr}^{(1)}$ comes from the cutoff values where the first bound state crosses threshold in the absence of contact interactions. The very early work on ChEFT and much of its phenomenological improvements, which continue to this day, have used Weinberg's prescription. Unfortunately this prescription assigns to triplet waves a single non-derivative contact interaction at LO, which is incapable to determine more than one phase in a model-independent way. In particular, for a separable regulator the contact interaction contributes only to the *S* wave. Spurious low-energy bound states can be kept at bay at LO in the $^3S_1$-$^3D_1$ coupled channel [62, 90–93], but only in this channel [20, 21]. In triplet waves where OPE is repulsive there is no need for counterterms at LO [20, 94], but without them bound states repeatedly cross threshold in attractive waves and lead to wild variations in the phase shifts at energies within the realm of ChEFT [20, 21, 93, 95]. With a super-Gaussian separable regulator, bound states first emerge at, roughly, $\Lambda \sim 0.5$, 1, 2, 4, and 6 GeV in respectively $^3S_1$-$^3D_1$, $^3P_0$, $^3D_2$, $^3P_2$-$^3F_2$, and $^3D_3$-$^3G_3$ channels [20, 93]. Except for $^3D_3$-$^3G_3$, this sequence is similar to that of the attractive channels in **Table 1**. The lowest two channels would display shallow states when $\Lambda \sim M_{\rm QCD}$, indicating that OPE is non-perturbative, while the higher waves are less clear—numerical experimentation suggested [20] their effects were not negligible, which can be understood from the results of reference [32].

Perhaps even more seriously, in Weinberg's scheme more-pion exchange and other contact interactions, which should be treated perturbatively, are not. This leads to the pathologies discussed in section 3.2. Indeed, renormalization problems have been reported [21, 96–100] within Weinberg's prescription also for higher-order potentials. These renormalization failures prevent taking a momentum-space cutoff at the breakdown scale $M_{\rm QCD}$ or higher. A "physical cutoff" $\Lambda_{\rm phys} \lesssim 1$ GeV, before $^3P_0$ would develop a bound state [20], is needed, and results are sensitive to the choice of regulator. No wonder then that much effort in phenomenology with chiral potentials has been dedicated to finding the "best" regulator. The limitation to small cutoffs leads to startling dependence on what should be equivalent forms of interactions in the Lagrangian, see for example reference [101].

One concludes that, while it seems well-established that to handle triplet waves beyond M_{NN} pions are non-perturbative in at least $^3S_1$-$^3D_1$ and $^3P_0$, there is some uncertainty as to the partial wave up to which this is so. Part of the uncertainty comes from the presence of LECs in lowest orders of the amplitude, which require a closer comparison with data (section 4.2). What is clear is that there is an angular-momentum suppression. The perturbative expressions in reference [86] suggest

$$M_{NN}^{(l,1)} \sim l^2 M_{NN} \,, \tag{41}$$

apart from an overall suppression of l^2. In contrast, the analyses of reference [32] leads to $l^2 \to [l(l+1)]^{3/2}$.

Singlet channels are somewhat simpler, but not devoid of subtleties. Since the tensor force vanishes for $s = 0$, OPE has $n = 1$ and $r_0 \sim M_{NN}/m_\pi^2$. The general argument from section 3.1.3 indicates that only in the *S* wave should we expect non-perturbative effects, $l_{\rm cr}^{(0)} \approx 1$. In higher waves, the OPE potential dominates over kinetic and centrifugal repulsion only at large distances, and there the exponential fall-off of OPE leads to further suppression.

The perturbative convergence of the $l \geq 1$ channels was studied in reference [102]. This is particularly easy because the Yukawa potential is well-defined for an arbitrary number of loops. The phase shifts are seen to converge quickly already for $^1P_1$, and faster as *l* increases. The suppression factor $M_{NN}^{(l,0)}$ can be estimated from the critical strength $M_{NN\,{\rm cr}}^{-1}$ needed to generate a zero-energy bound state in the corresponding *l* wave, shown in **Table 2**. There are two sequences of channels that alternate because of the factor of -3 in the ratio between isospin singlet and triplet: if we multiply the isosinglet entries in **Table 2** the results form a single monotonous sequence. Assuming $Q \sim m_\pi$, we find that in each sequence increasing *l* by 2 roughly suppresses OPE by one order in the expansion, starting with $^1P_1$ at NLO and $^1D_2$ at N^{2}LO. Moreover,

$$M_{NN}^{(l,0)} \sim \left[l(l+1)+1\right] M_{NN} \,, \tag{42}$$

in the isosinglet waves, with a factor 3 larger in isotriplets.

If one insists on the full solution for the Yukawa potential in higher partial waves, there are no renormalization problems [20, 94], as the potential is regular. In the *S* wave, however, interference with the delta function leads to an unexpected violation of NDA. As first noticed in reference [18] and confirmed many times since—for example, references [62,

TABLE 2 | Estimate of the critical strength M_{NNcr}^{-1} of the Yukawa potential in the lowest $2N$ singlet channels above which OPE cannot be treated perturbatively [102].

Partial wave	M_{NN}/M_{NNcr}
$^1P_1$	−6.4
$^1D_2$	45.8
$^1F_3$	−27.9
$^1G_4$	133.1
$^1H_5$	−64.6
$^1I_6$	265.9
$^1J_7$	−116.4
$^1K_8$	440.0
$^1L_9$	−183.3
$^1M_{10}$	667.4
$^1N_{11}$	−265.4

96, 103]— cutoff dependence proportional to m_π^2 emerges through the $\ln R$ term in Equation (26). Renormalization therefore requires the non-derivative chiral-symmetry-breaking interaction with LEC $m_\pi^2 D_2$. With Weinberg's prescription, where this LEC is missed at LO, the cutoff dependence can be seen in the $2N$ system only if quark masses are varied, as one does to match lattice QCD results. From the perspective of phenomenology, the main effect of the absence of the $m_\pi^2 D_2$ contact interaction is in processes sensitive to its associated pion interactions, which are generated by the way chiral symmetry is broken explicitly in QCD. Regardless of its phenomenological (ir)relevance, this is the simplest example where the renormalization of observables in ChEFT is not guaranteed by NDA.

Clearly, dimensionless factors stemming from spin and isospin make the transition from non-perturbative to perturbative OPE somewhat fuzzy. Moreover, virtually nothing has been done to estimate the angular-momentum suppression for multiple-pion exchange. Multiple-pion exchange is amenable to perturbation theory in all waves, but presumably further suppressed in higher waves. That is sufficient to start comparing with data.

4.2. Two Nucleons

Let us now take a closer look at how a renormalized approach works at the $2N$ level. I continue to consider $Q \sim m_\pi \sim M_{NN}$. Since the OPE tensor force survives in the chiral limit, if we take $m_\pi \lesssim M_{NN}$ we can perform an additional expansion around the chiral limit [62], but such an expansion in m_π/M_{NN} has not been fully explored.

Leading order at the $2N$ level consists of the exact solution of the Schrödinger equation up to $l_{\rm cr}^{(s)}$ with OPE and the required counterterms, not all of which were accounted for by NDA:

- Two non-derivative, chirally symmetric contact interactions with LECs $C_{0(s)}$, one for each S wave ($s = 0, 1$). They are needed to renormalize OPE even in the chiral limit, and were anticipated [10, 11] to appear at LO already on the basis of NDA, which estimates $C_{0(s)} \sim 4\pi/(m_N M_{NN})$.
- A non-derivative, chiral-symmetry-breaking contact interaction with LEC $m_\pi^2 D_{2(0)}$ if OPE is treated non-perturbatively in the $^1S_0$ channel. This LEC is $D_{2(0)} \sim C_{0(0)}/M_{\rm QCD}^2$ on the basis of NDA, and thus N^{2}LO. Renormalization of non-perturbative OPE instead requires $D_{2(0)} \sim C_{0(0)}/M_{NN}^2$ [18].
- One chirally symmetric contact interaction with the minimum number of derivatives for each wave where attractive tensor OPE is iterated. The most dramatic effect is in $^3P_0$, where a contact interaction $C'_{2(1)}\vec{p}\,' \cdot \vec{p}$ with $C'_{2(1)} \sim C_{0(1)}/M_{NN}^2$ is needed [20]. NDA would give instead $C'_{2(1)} \sim C_{0(1)}/M_{\rm QCD}^2$. The two-order enhancement comes from the running of pion exchange, and similar enhancements apply for the LECs in other attractive, singular waves where OPE is non-perturbative.

These counterterms are schematically displayed in **Table 3**, assuming $l_{\rm cr}^{(1)} = 3$.

Results can be found in references [20, 62, 93, 95] for cutoff values as high as 10 GeV in super-Gaussian separable regulators. In comparison with the Nijmegen PWA, one finds:

- In the $^3S_1$-$^3D_1$ coupled channels, where Weinberg's prescription is consistent with renormalization, phase shifts come out well with one fitted LEC. Results improve for $\Lambda \gtrsim M_{\rm QCD}$; even the mixing angle, which is somewhat overpredicted with a small $\Lambda \sim 500$ MeV, agrees with the Nijmegen PWA to within 1° up to a laboratory energy $E_{\rm lab} \simeq 200$ MeV for $\Lambda \gtrsim 4$ GeV. When the scattering length is used to fix the LEC, the deuteron binding energy is $B_2^{\rm LO} \simeq 2.0$ MeV, which is essentially the same as for lower cutoffs [106].
- For low uncoupled, attractive triplet channels ($^3P_0$, $^3D_2$) iterating pions with one fitted LEC works equally well. As an example, **Figure 5** [20] shows $^3P_0$, which comes out much better than in Weinberg's prescription with $\Lambda \sim 500$ MeV (compare this also with **Figure 4** where pions are treated perturbatively). The vanishing of the amplitude beyond $E_{\rm lab} \simeq 200$ MeV can be described, because attraction from OPE is compensated by the contact interaction. Again, agreement improves with increasing cutoff.
- For low coupled triplet channels ($^3P_2$-$^3F_2$, $^3D_3$-$^3G_3$)—see **Figure 5** [20] again for an example—iterated pions with the associated LEC do not improve significantly over Weinberg's prescription with $\Lambda \sim 500$ MeV. While $^3D_3$ is much better, changing from repulsion to attraction, $^3P_2$ goes from underprediction to considerable overprediction.
- In triplet channels without free parameters ($^3P_1$, $^3F_3$, $^3F_4$-$^3H_4$, $^3G_4$) iterated pions tend to work well, whether they are expected to be perturbative or not. In these channels results are the same as in Weinberg's prescription; there is not much change as $\Lambda \gtrsim M_{\rm QCD}$.
- In $l \geq 1$ singlet channels ($^1P_1$, $^1D_2$, $^1F_3$, $^1G_4$), iterated pions undershoot data except in $^1F_3$. Again results essentially agree with Weinberg's prescription at small $\Lambda \sim 500$ MeV.
- In $^1S_0$, the phase shifts resemble those of Pionless EFT, where after the fast rise due to the existence of a virtual state, they remain essentially flat as $E_{\rm lab}$ increases. Weinberg's

TABLE 3 | Schematic momentum dependence of the lowest-order contact interactions in the 2*N* system up to *D* waves, according to references [20, 31, 62, 68, 104, 105].

	$^1S_0$	$^3S_1$	ϵ_1	$^3P_0$, $^3P_2$	$^1P_1$, $^3P_1$	ϵ_2	$^3D_2$, $^3D_3$
LO	1	1		$p'p$			p'^2p^2
NLO	p'^2+p^2						
N^{2}LO	p'^4+p^4	p'^2+p^2	p^2	$p'p\,(p'^2+p^2)$	$p'p$	$p'pp^2$	$p'^2p^2\,(p'^2+p^2)$
N^{3}LO	p'^6+p^6						

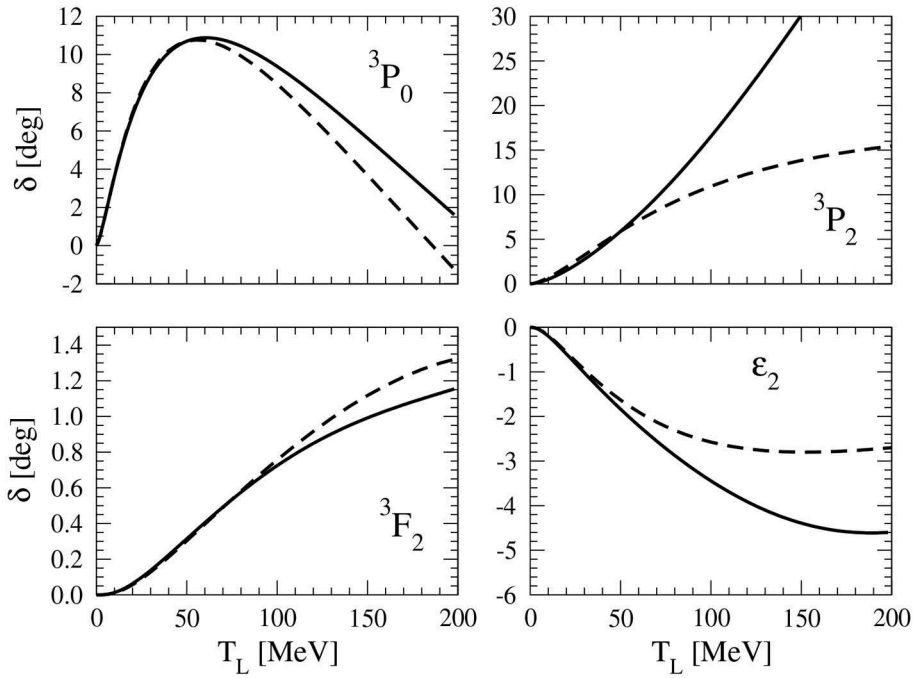


FIGURE 5 | Two-nucleon $^3P_0$ and $^3P_2$-$^3F_2$ phase shifts (δ) and mixing angle (ε_2) as functions of the laboratory energy T_L. The LO results (solid lines) at a cutoff $\Lambda = 3.94$ GeV are compared with the Nijmegen PWA [84] (dashed lines). Reprinted figure with permission from reference [20]. Copyright (2005) by the American Physical Society.

prescription applies, and renormalization allows us to increase the cutoff beyond $M_{\rm QCD}$, but agreement with the Nijmegen PWA deteriorates as we do so.

Thus, a renormalized approach where the regulator is unimportant gives a qualitative guide to 2*N* data at LO, which is slightly better than Weinberg's prescription with specific regulators and small momentum-cutoff parameters. It has been shown recently [107] that, with a non-separable regulator, a specific combination of the four possible spin-isospin non-derivative contact interactions that yields only one $^3S_1$-$^3D_1$ bound state simultaneously prevents bound states in other channels. While this is not true for an arbitrary regulator, it does allow to extend LO results with Weinberg's prescription to higher cutoff values, in general improving agreement with the Nijmegen PWA. However, results are not clearly better than the renormalized approach, particularly in the $^3P_0$ channel which lacks the repulsion to produce the amplitude zero.

In addition to simple perturbative corrections in higher partial waves, one needs to account in subleading orders for potential corrections *via* distorted-wave perturbation theory in the lowest partial waves. The residual Λ^{-1} dependence of the LO amplitude means that at NLO—relative $\mathcal{O}(Q/M_{\rm QCD})$—there is also:

- A two-derivative, chirally symmetric contact interaction with LEC $C_{2(0)}$ in the $^1S_0$ channel. In order to render cutoff effects on the effective range no larger than N^{2}LO, $C_{2(0)} \sim C_{0(0)}/(M_{NN}M_{\rm QCD})$ [68]. NDA gives instead $C_{2(0)} \sim C_{0(0)}/M_{\rm QCD}^2$, or N^{2}LO (confusingly denoted NLO in the nuclear community), which produces a short-range contribution to the effective range smaller than pion's by two powers of the expansion parameter. Yet, only about half of the $^1S_0$ effective range comes from OPE.

The cutoff dependence in other channels is milder, in agreement with the discussion of section 3.2. The NLO interaction is shown in the second line of **Table 3**. At NLO in the amplitude, the NLO interaction should be included in first order in the distorted-wave expansion.

At higher orders, corrections to the long-range potential enter according to the power counting of section 2. Barring unforeseen renormalization issues, at $\mathcal{O}(Q^\mu/M_{\rm QCD}^\mu)$ we need

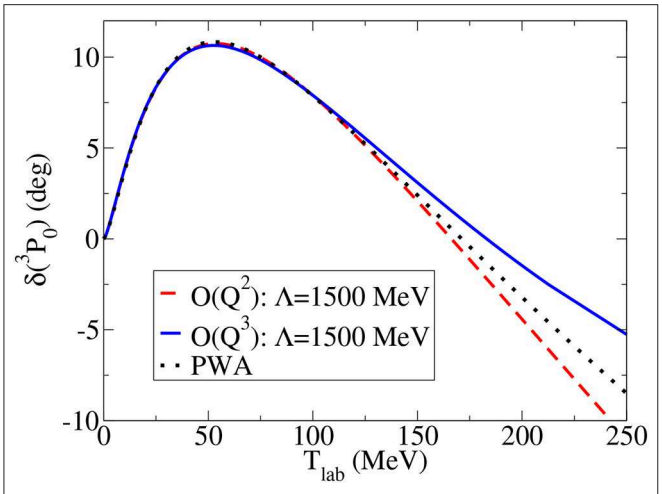


FIGURE 6 | Two-nucleon $^3P_0$ phase shift $\delta(^3P_0)$ as function of the laboratory energy $T_{\rm lab}$. The N^{2}LO (red dashed line) and N^{3}LO (blue solid line) results at a cutoff $\Lambda = 1.5$ GeV are compared with the Nijmegen PWA [84] (black points). Reprinted figure with permission from reference [104]. Copyright (2011) by the American Physical Society.

to include LECs with up to μ derivatives more than the LECs appearing at LO [31], except in the $^1S_0$ channel where the Yukawa/delta-function interference takes place. The momentum structures of the LECs up to N^{3}LO are shown in **Table 3**, again under the assumption $l_{\rm cr}^{(1)} = 3$. They are:

- In each triplet channel where attractive OPE is iterated at LO ($^3S_1$-$^3D_1$, $^3P_0$, *etc.*), a contact interaction with two derivatives more than the contact interaction at LO [104, 105]. While for $^3S_1$-$^3D_1$ this coincides with NDA, for other channels NDA would say these contact interactions only appear at N^{4}LO or higher.
- Contact interactions with two derivatives [68] for singlet ($^1P_1$) and triplet P waves where OPE is repulsive ($^3P_1$). This is the NDA scaling.
- Four- and six-derivative contact interactions in the $^1S_0$ channel at N^{2}LO and N^{3}LO, respectively [68]. Again, NDA would have these contact interactions at N^{4}LO or higher.

Up to N^{3}LO in the amplitude, their contributions are included in first order in the distorted-wave expansion. Meanwhile, the NLO interaction must be included in second and third orders, either by itself or with one N^{2}LO interaction.

The phase shifts have been calculated up to N^{3}LO along these lines in references [68, 104, 105], together with Deltaless TPE:

- In the $^3S_1$-$^3D_1$ coupled channels, where LO already yielded very good results at LO, results improve only marginally at N^{2,3}LO.
- In $^3P_0$, which was also relatively well-described at LO, results improve quite a bit around the maximum phase shift at N^{2}LO. Not much improvement, if any, is seen at N^{3}LO. Results from reference [104] are shown in **Figure 6**, to be compared with LO in **Figure 5**. Other uncoupled, attractive triplet channels ($^3D_2$ *etc.*) were not calculated.
- The coupled $^3P_2$-$^3F_2$ wave with OPE iterated at LO shows no real improvement at N^{2}LO, and only mildly better agreement with the Nijmegen PWA at N^{3}LO. No results are available for higher coupled triplet channels ($^3D_3$-$^3G_3$ *etc.*).
- In $^3P_1$, which works well at LO with no free parameter, results deteriorate at N^{2,3}LO. Higher repulsive triplet channels ($^3F_3$ *etc.*) were not considered.
- In $^1P_1$, agreement with the Nijmegen PWA improves at N^{2,3}LO, although results are very sensitive to the pion-nucleon parameters that enter the $\mu = 3$ TPE. Higher singlet partial waves were not studied.
- The $^1S_0$ phase shift improves considerably at NLO but is still not very close to the Nijmegen PWA. N^{2}LO improves further, but the zero of the amplitude is still poorly described.

Overall, there is some improvement at N^{2}LO but not much at N^{3}LO. This is perhaps an indication that a better description of the pion-nucleon subamplitude with an explicit Delta isobar is needed.

Note that subleading corrections have also been calculated in references [108, 109] with a slightly different accounting of higher orders. For example, TPE is taken to start three orders higher than OPE, which is contrary to the power counting of section 2 and difficult to conciliate with the power counting used in ChPT. Still, results are generically not much different from those described above. A third power-counting variant has been proposed [32] with similar features. It has not been tested in detail, perhaps because no clear prescription is given for handling the LO cutoff dependence in a channel like $^3P_0$ where a counterterm is assigned relative $\mathcal{O}(Q^{1/2}/M_{\rm QCD}^{1/2})$. Reference [67] discusses these alternatives.

The main phenomenological shortcomings of the renormalized approach are $^3P_1$, $^3P_2$ and singlet partial waves. For most of these channels, subsequent work indicates OPE might be perturbative. Equation (42) shows that OPE should be included in $^1P_1$ at NLO, in $^1D_2$ at N^{2}LO, and so on. On the basis of NDA, contact interactions with the minimal number of derivatives are expected at respectively N^{2}LO, N^{4}LO, and so on. Under the assumption that the angular-momentum suppression of TPE is the same as OPE, reference [87] provided evidence that the perturbative expansion converges for singlet waves up to $k \approx 300$ MeV and N^{4}LO without explicit Delta isobars. Reference [87] goes further by showing that under NDA for the LECs also triplet waves converge in the same range, except for $^3P_0$ and possibly $^3D_3$. For illustration, results for the $^3P_2$-$^3F_2$ coupled channels are shown in **Figure 7** [87], which should be compared to **Figure 5** where OPE was treated non-perturbatively at LO. The maximum momentum $k \approx 300$ MeV seems tied to the absence of an explicit Delta isobar [87] but no similar calculation is available in Deltaful ChEFT. Earlier studies [110–112], which indicated that pions are perturbative in high waves, sometimes included Deltas but did not take into account the IR enhancement in iterated pion exchange. Clearly a more comprehensive study of higher orders with Deltas is needed to confront this renormalized approach with phenomenology.

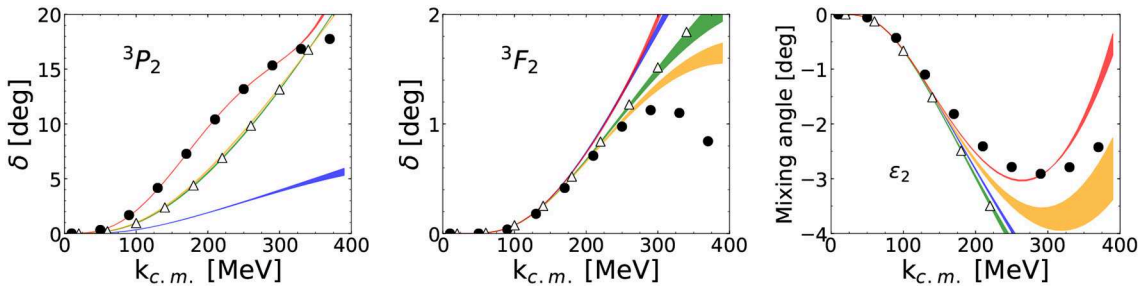


FIGURE 7 | Two-nucleon $^3P_2$-$^3F_2$ phase shifts (δ) and mixing angle (ε_2) as functions of the center-of-mass momentum $k_{\text{c.m.}}$. The NLO (blue), N^{2}LO (green), N^{3}LO (orange), and N^{4}LO (red) bands from a perturbative treatment of pion exchange correspond to cutoff variation from 0.8 to 4.8 GeV. N^{2}LO results for $\Lambda \to \infty$ are also shown (triangles) (LO in a perturbative expansion vanishes for these channels.) The empirical phase shifts from the SAID program [88] (solid circles) are shown for comparison. Reprinted figure with permission from reference [87]. Copyright (2019) by the American Physical Society.

The situation is particularly unsatisfactory in the $^1S_0$ channel, where LO—same as in Weinberg's prescription at fixed pion mass—is far off, just as in Pionless EFT [35]. In particular, the Nijmegen PWA displays a zero at a relative low momentum $k_0 \simeq 340$ MeV, which is absent at LO. It is possible that the inclusion of an explicit Delta isobar (separated in mass from the nucleon by ∼300 MeV) improves the convergence in this region, as a large part of the central potential moves from N^{3}LO to N^{2}LO. However, the expansion will in any case converge at best very slowly for $k \gtrsim k_0$, as all subleading orders have to conspire to cancel against LO. Since numerically $k_0 \sim M_{NN}$, only for a fully perturbative-pion approach is this of no concern. Note that also $^3S_1$ and $^3P_0$ have amplitude zeros at relatively low energies, but in both cases they arise at LO from the combination of non-perturbative OPE and contact interactions need for renormalization.

The $^1S_0$ channel is special also for the presence of an unnaturally shallow virtual state that requires a fine-tuning of the short-range interaction. It is the interference between the non-derivative contact interaction and the Yukawa potential that causes a violation of NDA in this channel. It also leads to the piling up of higher-order counterterms seen in **Table 3**. Given the uniqueness of this channel, it is perhaps not surprising that power counting might require refinement. In reference [113] it was shown that short-range interactions show strong energy dependence. To ameliorate the expansion in $^1S_0$, it was suggested in references [62, 114] that the chirally symmetric two-derivative interaction with LEC $C_{2(0)}$ should be promoted from NLO to LO, following an earlier suggestions for Pionless EFT [115] and ChEFT with purely perturbative pions [116]. To avoid the Wigner bound, this is done through a dibaryon field [77] whose kinetic term is taken to be LO together with its residual mass. This promotion induces promotions at higher orders of the contact interactions with more derivatives. Results of course improve at LO and further at NLO, but not at N^{2}LO, in particular near k_0. In reference [117] it was then proposed—similarly to an earlier attempt [118]—that the zero be included at LO by a combination of dibaryon field and contact interaction (or alternatively two dibaryon fields, the kinetic term of one of which is higher order). Again this induces the promotion of contact interactions with more derivatives at higher orders. Phase shifts come out great

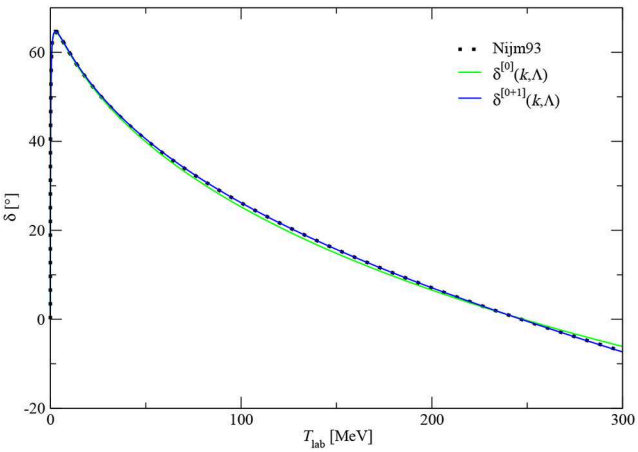


FIGURE 8 | Two-nucleon $^1S_0$ phase shift δ as function of the laboratory energy T_{lab} in an expansion that incorporates the amplitude zero at LO. The LO (green) and NLO (blue) bands correspond to cutoff variation from 0.6 to 2 GeV. The results from the Nijm93 potential [119] (black squares) are shown for comparison. Reprinted figure with permission from reference [117]. Copyright (2018) by the American Physical Society.

at LO and essentially on the nose at NLO, even beyond k_0 (see **Figure 8**). Unfortunately these reorganizations of the expansion produce energy-dependent potentials at LO, which complicate few-body calculations.

A further proposed reorganization of ChEFT arises from treating selected relativistic corrections, which are small for the momenta of interest, as LO—see, for example, reference [120]. A modified nucleon propagator ensures less dependence on the regulator, but a $^3P_0$ LEC still has to be promoted compared to NDA, as in the purely non-relativistic context [20]. By resumming higher-order terms into LO whether they are relativistic corrections or not, one can soften the large-momentum behavior of loops and alter the cutoff dependence. This is no different than picking a regulator, which effectively includes an infinite number of higher-derivative interactions. Results then depend on the corresponding cutoff parameter Λ. Renormalization exchanges this dependence for the minimal number of parameters allowed without dynamical assumptions.

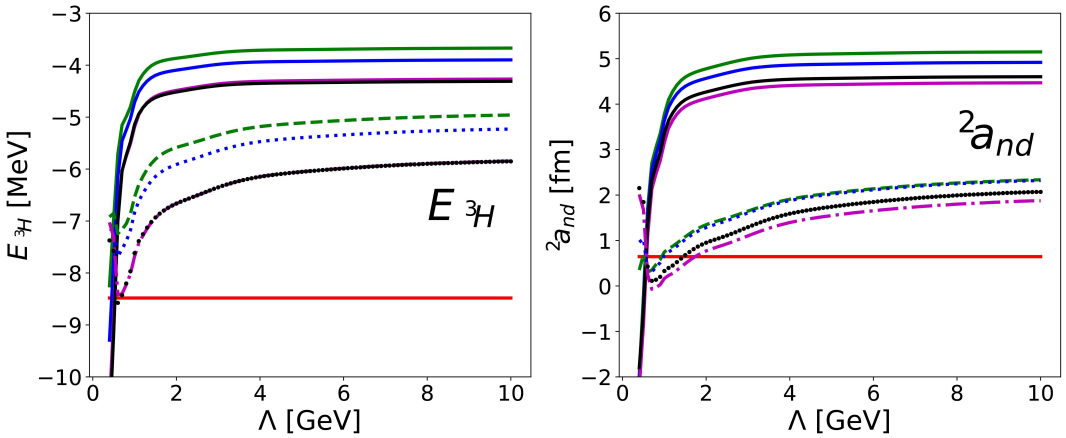


FIGURE 9 | Triton binding energy $E_{^3H}$ and doublet neutron-deuteron scattering length $^2a_{nd}$ as functions of the cutoff Λ. Results at LO (solid lines) and NLO (dashed and dotted lines) for various 2*N* fitting procedures are compared with experiment (horizontal red lines). Reprinted figure with permission from reference [93]. Copyright (2019) by the American Physical Society.

Achieving cutoff independence with a resummation of a selected interaction merely replaces Λ by the mass parameter characterizing this interaction, call it M'. If $M' \ll M_{\rm QCD}$ is inferred from data, this resummation is justified because the interaction is not of higher order. However, when resumming relativistic corrections $M' \gtrsim m_N$: it corresponds to one fixed cutoff value and convergence cannot be used to demote interactions that are needed for renormalization without resummation. As long as no LECs are promoted or demoted, a resummation of higher-order corrections is safe. There is growing interest in the development of a covariant version of ChEFT, which could perhaps be used as input to relativistic formulations of nuclear physics [121, 122].

4.3. More Nucleons

There is not much known about renormalized ChEFT beyond 2*N*. The power counting of section 2 shows that the 3*N* force is expected to start at NLO from two-pion exchange when Delta isobars are included explicitly, and at N^{2}LO when they are not. The crucial issue is whether shorter-range interactions are enhanced as in the 2*N* system. Such an enhancement does take place in Pionless EFT [81] and it has been suggested for ChEFT on phenomenological grounds in reference [123].

In calculations for more than two nucleons in the renormalized approach, one needs to truncate the LO 2*N* potential for $l \lesssim l_{\rm cr}^{(s)}$, which is reminiscent of the truncation in total 2*N* angular momentum typically invoked in solutions of the Faddeev and Faddeev-Yakubovski equations for 3*N* and 4*N* systems with phenomenological potentials. As we have seen the optimal values for $l_{\rm cr}^{(0,1)}$ are uncertain and the l dependence of $M_{NN}^{(l,s)}$ is not fully determined. Of course, as in the 2*N* system, subleading orders should be treated in distorted-wave perturbation theory.

Existing calculations are limited to the 3*N* system and took $l_{\rm cr}^{(0,1)} = 3$. At LO [20, 93] and, without explicit Deltas, also at NLO [93], observables converge as the cutoff increases to at least 10 GeV without 3*N* forces (see **Figure 9**) [93]. The triton binding energy is $B_3^{\rm LO} \simeq 4$ MeV and $B_3^{\rm NLO} \simeq 6$ MeV, quite different from results for a low cutoff in Weinberg's prescription, $\simeq 11$ MeV ($\simeq 6.5$ MeV) at LO (N^{2}LO) [106]. Results were shown not to change significantly when waves beyond $l_{\rm cr} = 3$ were included. Conversely, if it turns out that $l_{\rm cr}^{(0,1)} < 3$, results might change quantitatively, but qualitative statements should stand. In particular, one concludes there is no renormalization justification in ChEFT to take the non-derivative 3*N* contact interaction as LO. Most likely the same conclusion holds for higher-body forces, but no calculations have been carried out.

The tendency for underbinding at LO seen in the deuteron and triton seems to persist for symmetric nuclear matter. In a cutoff-converged Brueckner pair approximation [124], nuclear matter was found to saturate, but with significant underbinding. This is in contrast to Weinberg's prescription, where Deltaless [125] or Deltaful [126] potentials of $\mathcal{O}(1)$ and $\mathcal{O}(Q^2/M_{\rm QCD}^2)$ do not yield saturation within the EFT domain. Yet higher potentials do lead to saturation with this prescription [125–127]. Although usually presented as a success, the emperor has no clothes: it means that, if nuclear matter is within the regime of ChEFT, interactions that are formally of higher order according to NDA must actually be LO to balance against other LO interactions. Presumably it is the extra repulsion from $^3P_0$ in a renormalized approach that saturates nuclear matter. It is not clear how saturation in Chiral EFT would relate, if it can be related at all, to the proposal of reference [128] where saturation arises from the 3*N* parameter that appears at LO in Pionless EFT. What is clear is, more EFT calculations beyond the 2*N* system are sorely needed!

5. CONCLUSION

The longstanding problem of renormalization of chiral nuclear forces has been solved at the 2*N* and 3*N* levels. Perhaps not surprising in hindsight, this solution is a middle ground between Weinberg's original prescription and Kaplan, Savage, and Wise's suggestion of fully perturbative pions. One-pion exchange is iterated in lower waves together with the necessary contact interactions, while all corrections are included in distorted-wave perturbation theory.

That is not to say that the *best* solution has been found. Issues remain regarding exactly how strong the angular-momentum suppression is and where the non-perturbative/perturbative boundary lies. Whether the ordering of few-body forces holds similar surprises is also unknown. A high-quality fit to 2*N* data is missing, and there are very few studies of heavier systems. The extent to which Weinberg's phenomenologically successful prescription with a low cutoff can be reproduced remains an open question, although the first step in grounding it on a renormalized approach has been made [42]. Fortunately, there is still plenty to learn.

AUTHOR CONTRIBUTIONS

The author confirms being the sole contributor of this work and has approved it for publication.

ACKNOWLEDGMENTS

I thank Manolo Pavón Valderrama for useful discussions and Jaber Balal Habashi for comments on the manuscript. This material was based upon work supported in part by the U.S. Department of Energy, Office of Science, Office of Nuclear Physics, under award DE-FG02-04ER41338 and by the European Union Research and Innovation program Horizon 2020 under grant No. 654002.

REFERENCES

1. Watson KM, Lepore JV. Radiative corrections to nuclear forces in the pseudoscalar meson theory. *Phys Rev.* (1949) **76**:1157. doi: 10.1103/PhysRev.76.1157
2. Matthews PT, Salam A. The renormalization of meson theories. *Rev Mod Phys.* (1951) **23**:311. doi: 10.1103/RevModPhys.23.311
3. Marshak RE. *Meson Physics*. New York, NY: Dover (1952).
4. Gartenhaus S. Two-nucleon potential from the cut-off Yukawa theory. *Phys Rev.* (1955) **100**:900. doi: 10.1103/PhysRev.100.900
5. Machleidt R. Historical perspective and future prospects for nuclear interactions. *Int J Mod Phys E.* (2017) **26**:1730005. doi: 10.1142/S0218301317300053
6. Weinberg S. What is quantum field theory, and what did we think it was? In: Cao T, editor. *Conceptual Foundations of Quantum Field Theory*. Cambridge: Cambridge University Press (1999). doi: 10.1017/CBO9780511470813.020
7. Weinberg S. Phenomenological Lagrangians. *Physica A.* (1979) **96**:327. doi: 10.1016/0378-4371(79)90223-1
8. Gasser J, Leutwyler H. Chiral perturbation theory to one loop. *Ann Phys.* (1984) **158**:142. doi: 10.1016/0003-4916(84)90242-2
9. Manohar A, Georgi H. Chiral quarks and the nonrelativistic quark model. *Nucl Phys B.* (1984) **234**:189. doi: 10.1016/0550-3213(84)90231-1
10. Weinberg S. Nuclear forces from chiral Lagrangians. *Phys Lett B.* (1990) **251**:288. doi: 10.1016/0370-2693(90)90938-3
11. Weinberg S. Effective chiral Lagrangians for nucleon pion interactions and nuclear forces. *Nucl Phys B.* (1991) **363**:3. doi: 10.1016/0550-3213(91)90231-L
12. Ordóñez C, Ray L, van Kolck U. Nucleon-nucleon potential from an effective chiral Lagrangian. *Phys Rev Lett.* (1994) **72**:1982. doi: 10.1103/PhysRevLett.72.1982
13. Ordóñez C, Ray L, van Kolck U. The two nucleon potential from chiral Lagrangians. *Phys Rev C.* (1996) **53**:2086. doi: 10.1103/PhysRevC.53.2086
14. Epelbaum E, Hammer HW, Meißner UG. Modern theory of nuclear forces. *Rev Mod Phys.* (2009) **81**:1773. doi: 10.1103/RevModPhys.81.1773
15. Machleidt R, Entem DR. Chiral effective field theory and nuclear forces. *Phys Rept.* (2011) **503**:1. doi: 10.1016/j.physrep.2011.02.001
16. Entem DR, Machleidt R. Accurate charge dependent nucleon nucleon potential at fourth order of chiral perturbation theory. *Phys Rev C.* (2003) **68**:041001. doi: 10.1103/PhysRevC.68.041001
17. Navarro Pérez R, Ruiz Arriola E. Uncertainty quantification and falsification of chiral nuclear potentials. *arXiv.* 1907.04032.
18. Kaplan DB, Savage MJ, Wise MB. Nucleon nucleon scattering from effective field theory. *Nucl Phys B.* (1996) **478**:629. doi: 10.1016/0550-3213(96)00357-4
19. Ordóñez C, van Kolck U. Chiral Lagrangians and nuclear forces. *Phys Lett B.* (1992) **291**:459. doi: 10.1016/0370-2693(92)91404-W
20. Nogga A, Timmermans RGE, van Kolck U. Renormalization of one-pion exchange and power counting. *Phys Rev C.* (2005) **72**:054006. doi: 10.1103/PhysRevC.72.054006
21. Pavón Valderrama M, Ruiz Arriola E. Renormalization of NN interaction with chiral two pion exchange potential: non-central phases. *Phys Rev C.* (2006) **74**:064004. doi: 10.1103/PhysRevC.74.064004
22. Pavón Valderrama M, Phillips DR. Power counting of contact-range currents in effective field theory. *Phys Rev Lett.* (2015) **114**:082502. doi: 10.1103/PhysRevLett.114.082502
23. Beane SR, Bedaque PF, Childress L, Kryjevski A, McGuire J, van Kolck U. Singular potentials and limit cycles. *Phys Rev A.* (2001) **64**:042103. doi: 10.1103/PhysRevA.64.042103
24. Pavón Valderrama M, Ruiz Arriola E. Renormalization group analysis of boundary conditions in potential scattering. *Ann Phys.* (2008) **323**:1037. doi: 10.1016/j.aop.2007.08.003
25. Bedaque PF, van Kolck U. Nucleon deuteron scattering from an effective field theory. *Phys Lett B.* (1998) **428**:221. doi: 10.1016/S0370-2693(98)00430-4
26. van Kolck U. Nucleon-nucleon interaction and isospin violation. *Lect Notes Phys.* (1998) **513**:62. doi: 10.1007/BFb0104898
27. van Kolck U. Effective field theory of short-range forces. *Nucl Phys A.* (1999) **645**:273. doi: 10.1016/S0375-9474(98)00612-5
28. Kaplan DB, Savage MJ, Wise MB. A new expansion for nucleon-nucleon interactions. *Phys Lett B.* (1998) **424**:390. doi: 10.1016/S0370-2693(98)00210-X
29. Kaplan DB, Savage MJ, Wise MB. Two nucleon systems from effective field theory. *Nucl Phys B.* (1998) **534**:329. doi: 10.1016/S0550-3213(98)00440-4
30. Fleming S, Mehen T, Stewart IW. NNLO corrections to nucleon-nucleon scattering and perturbative pions. *Nucl Phys A.* (2000) **677**:313. doi: 10.1016/S0375-9474(00)00221-9
31. Long B, van Kolck U. Renormalization of singular potentials and power counting. *Ann Phys.* (2008) **323**:1304. doi: 10.1016/j.aop.2008.01.003
32. Birse MC. Power counting with one-pion exchange. *Phys Rev C.* (2006) **74**:014003. doi: 10.1103/PhysRevC.74.014003
33. Birse MC. The renormalisation group and nuclear forces. *Phil Trans R Soc Lond A.* (2011) **369**:2662. doi: 10.1098/rsta.2010.0381

34. Pavón Valderrama M. Power counting and wilsonian renormalization in nuclear effective field theory. *Int J Mod Phys E.* (2016) **25**:1641007. doi: 10.1142/S021830131641007X
35. Hammer HW, König S, van Kolck U. Nuclear effective field theory: status and perspectives. *arXiv*. 1906.12122.
36. Bedaque PF, van Kolck U. Effective field theory for few nucleon systems. *Ann Rev Nucl Part Sci.* (2002) **52**:339. doi: 10.1146/annurev.nucl.52.050102.090637
37. Friar JL. Dimensional power counting in nuclei. *Few Body Syst.* (1997) **22**:161. doi: 10.1007/s006010050059
38. Weinberg S. Three body interactions among nucleons and pions. *Phys Lett B.* (1992) **295**:114. doi: 10.1016/0370-2693(92)90099-P
39. van Kolck U. Few nucleon forces from chiral Lagrangians. *Phys Rev C.* (1994) **49**:2932. doi: 10.1103/PhysRevC.49.2932
40. Fujita J, Miyazawa H. Pion theory of three-body forces. *Prog Theor Phys.* (1957) **17**:360. doi: 10.1143/PTP.17.360
41. Pandharipande VR, Phillips DR, van Kolck U. Delta effects in pion-nucleon scattering and the strength of the two-pion-exchange three-nucleon interaction. *Phys Rev C.* (2005) **71**:064002. doi: 10.1103/PhysRevC.71.064002
42. Pavón Valderrama M. Scattering amplitudes versus potentials in nuclear effective field theory: is there a potential compromise? *arXiv.* 1902.08172.
43. Frank W, Land DJ, Spector RM. Singular potentials. *Rev Mod Phys.* (1971) **43**:36. doi: 10.1103/RevModPhys.43.36
44. Case KM. Singular potentials. *Phys Rev.* (1950) **80**:797. doi: 10.1103/PhysRev.80.797
45. Landau LD, Lifshitz EM. *Quantum Mechanics*. London: Pergamon Press (1965).
46. Camblong HE, Ordóñez CR. Anomaly in conformal quantum mechanics: from molecular physics to black holes. *Phys Rev D.* (2003) **68**:125013. doi: 10.1103/PhysRevD.68.125013
47. Camblong HE, Ordóñez CR. Renormalization in conformal quantum mechanics. *Phys Lett A.* (2005) **345**:22. doi: 10.1016/j.physleta.2005.06.110
48. Perelomov AM, Popov VS. Collapse onto scattering centre in quantum mechanics. *Teor Mat Fiz.* (1970) **4**:48. doi: 10.1007/BF01246666
49. Bawin M, Coon SA. The singular inverse square potential, limit cycles and selfadjoint extensions. *Phys Rev A.* (2003) **67**:042712. doi: 10.1103/PhysRevA.67.042712
50. Braaten E, Phillips D. The renormalization group limit cycle for the $1/r^2$ potential. *Phys Rev A.* (2004) **70**:052111. doi: 10.1103/PhysRevA.70.052111
51. Alberg M, Bawin M, Brau F. Renormalization of the singular attractive $1/r^4$ potential. *Phys Rev A.* (2005) **71**:022108. doi: 10.1103/PhysRevA.71.022108
52. Hammer HW, Swingle BG. On the limit cycle for the $1/r^2$ potential in momentum space. *Ann Phys.* (2006) **321**:306. doi: 10.1016/j.aop.2005.04.017
53. Bouaziz D, Bawin M. Singular inverse-square potential: renormalization and self-adjoint extensions for medium to weak coupling. *Phys Rev A.* (2014) **89**:022113. doi: 10.1103/PhysRevA.89.022113
54. Odell D, Deltuva A, Bonilla J, Platter L. Renormalization of a finite range inverse cube potential. *Phys Rev C.* (2019) **100**:054001. doi: 10.1103/PhysRevC.100.054001
55. Hammer HW, Platter L. Efimov physics from a renormalization group perspective. *Phil Trans R Soc Lond A.* (2011) **369**:2679. doi: 10.1098/rsta.2011.0001
56. Bulycheva KM, Gorsky AS. Limit cycles in renormalization group dynamics. *Phys Usp.* (2014) **57**:171. doi: 10.3367/UFNe.0184.201402g.0182
57. Efimov VN. Weakly-bound states of 3 resonantly-interacting particles. *Sov J Nucl Phys.* (1971) **12**:589.
58. Efimov V. Energy levels arising form the resonant two-body forces in a three-body system. *Phys Lett B.* (1970) **33**:563. doi: 10.1016/0370-2693(70)90349-7
59. Bedaque PF, Hammer HW, van Kolck U. Renormalization of the three-body system with short range interactions. *Phys Rev Lett.* (1999) **82**:463. doi: 10.1103/PhysRevLett.82.463
60. Bedaque PF, Hammer HW, van Kolck U. The three boson system with short range interactions. *Nucl Phys A.* (1999) **646**:444. doi: 10.1016/S0375-9474(98)00650-2
61. Braaten E, Hammer HW. Universality in few-body systems with large scattering length. *Phys Rept.* (2006) **428**:259. doi: 10.1016/j.physrep.2006.03.001
62. Beane SR, Bedaque PF, Savage MJ, van Kolck U. Towards a perturbative theory of nuclear forces. *Nucl Phys A.* (2002) **700**:377. doi: 10.1016/S0375-9474(01)01324-0
63. Pavón Valderrama M, Ruiz Arriola E. Renormalization of chiral two pion exchange NN interactions with Delta-excitations: correlations in the partial wave expansion. *Phys Rev C.* (2011) **83**:044002. doi: 10.1103/PhysRevC.83.044002
64. Breit G. The scattering of slow neutrons by bound protons. 1. Methods of calculation. *Phys Rev.* (1947) **71**:215. doi: 10.1103/PhysRev.71.215
65. Greene CH, Rau ARP, Fano U. General form of quantum-defect theory. II. *Phys Rev A.* (1982) **26**:2441. doi: 10.1103/PhysRevA.26.2441
66. Behncke H. Some remarks on singular attractive potentials. *Nuovo Cim A.* (1968) **55**:780. doi: 10.1007/BF02819574
67. Grießhammer HW. Assessing theory uncertainties in EFT power countings from residual cutoff dependence. *PoS CD.* (2016) **15**:104. doi: 10.22323/1.253.0104
68. Long B, Yang CJ. Short-range nuclear forces in singlet channels. *Phys Rev C.* (2012) **86**:024001. doi: 10.1103/PhysRevC.86.024001
69. Epelbaum E, Gegelia J. Regularization, renormalization and 'peratization' in effective field theory for two nucleons. *Eur Phys J A.* (2009) **41**:341. doi: 10.1140/epja/i2009-10833-3
70. Feinberg G, Pais A. A field theory of weak interactions. I. *Phys Rev.* (1963) **131**:2724. doi: 10.1103/PhysRev.131.2724
71. Feinberg G, Pais A. A field theory of weak interactions. II. *Phys Rev.* (1964) **133**:B477. doi: 10.1103/PhysRev.133.B477
72. Phillips DR, Cohen TD. How short is too short? Constraining contact interactions in nucleon-nucleon scattering. *Phys Lett B.* (1997) **390**:7. doi: 10.1016/S0370-2693(96)01411-6
73. Phillips DR, Beane SR, Cohen TD. Nonperturbative regularization and renormalization: simple examples from nonrelativistic quantum mechanics. *Ann Phys.* (1998) **263**:255. doi: 10.1006/aphy.1997.5771
74. Beane SR, Cohen TD, Phillips DR. The potential of effective field theory in NN scattering. *Nucl Phys A.* (1998) **632**:445. doi: 10.1016/S0375-9474(98)00007-4
75. Wigner EP. Lower limit for the energy derivative of the scattering phase shift. *Phys Rev.* (1955) **98**:145. doi: 10.1103/PhysRev.98.145
76. Stetcu I, Rotureau J, Barrett BR, van Kolck U. An effective field theory approach to two trapped particles. *Ann Phys.* (2010) **325**:1644. doi: 10.1016/j.aop.2010.02.008
77. Kaplan DB. More effective field theory for nonrelativistic scattering. *Nucl Phys B.* (1997) **494**:471. doi: 10.1016/S0550-3213(97)00178-8
78. Epelbaum E, Gasparyan AM, Gegelia J, Meißner UG. How (not) to renormalize integral equations with singular potentials in effective field theory. *Eur Phys J A.* (2018) **54**:186. doi: 10.1140/epja/i2018-12632-1
79. Pavón Valderrama M. Comment on "How (not) to renormalize integral equations with singular potentials in effective field theory". *Eur Phys J A.* (2019) **55**:55. doi: 10.1140/epja/i2019-12703-9
80. Epelbaum E, Gasparyan AM, Gegelia J, Meißner UG. Reply to Comment on "How (not) to renormalize integral equations with singular potentials in effective field theory". *Eur Phys J A.* (2019) **55**:56. doi: 10.1140/epja/i2019-12751-1
81. Bedaque PF, Hammer HW, van Kolck U. Effective theory of the triton. *Nucl Phys A.* (2000) **676**:357. doi: 10.1016/S0375-9474(00)00205-0
82. König S, Grießhammer HW, Hammer HW, van Kolck U. Nuclear physics around the unitarity limit. *Phys Rev Lett.* (2017) **118**:202501. doi: 10.1103/PhysRevLett.118.202501
83. Soto J, Tarrús J. Effective field theory with dibaryon degrees of freedom. *Phys Rev C.* (2008) **78**:024003. doi: 10.1103/PhysRevC.78.024003
84. Stoks VGJ, Klomp RAM, Rentmeester MCM, de Swart JJ. Partial wave analysis of all nucleon-nucleon scattering data below 350-MeV. *Phys Rev C.* (1993) **48**:792. doi: 10.1103/PhysRevC.48.792
85. Cohen TD, Hansen JM. The predictive power of effective field theory in NN scattering: 3S1-3D1 mixing at next-to-next-to leading order. nucl-th/9908049.
86. Kaplan DB. On the convergence of nuclear effective field theory with perturbative pions. *arXiv*. 1905.07485
87. Wu S, Long B. Perturbative *NN* scattering in chiral effective field theory. *Phys Rev C.* (2019) **99**:024003. doi: 10.1103/PhysRevC.99.024003

88. *The SAID Program at the George Washington University*. Available online at: http://gwdac.phys.gwu.edu/
89. Birse MC. Deconstructing triplet nucleon-nucleon scattering. *Phys Rev C.* (2007) **76**:034002. doi: 10.1103/PhysRevC.76.034002
90. Frederico T, Timóteo VS, Tomio L. Renormalization of the one pion exchange interaction. *Nucl Phys A.* (1999) **653**:209. doi: 10.1016/S0375-9474(99)00234-1
91. Pavón Valderrama M, Ruiz Arriola E. Renormalization of the deuteron with one pion exchange. *Phys Rev C.* (2005) **72**:054002. doi: 10.1103/PhysRevC.72.054002
92. Yang CJ, Elster C, Phillips DR. Subtractive renormalization of the NN scattering amplitude at leading order in chiral effective theory. *Phys Rev C.* (2008) **77**:014002. doi: 10.1103/PhysRevC.77.014002
93. Song YH, Lazauskas R, van Kolck U. Triton binding energy and neutron-deuteron scattering up to next-to-leading order in chiral effective field theory. *Phys Rev C.* (2017) **96**:024002. doi: 10.1103/PhysRevC.96.024002
94. Eiras D, Soto J. Renormalizing the Lippmann-Schwinger equation for the one pion exchange potential. *Eur Phys J A.* (2003) **17**:89. doi: 10.1140/epja/i2002-10138-1
95. Epelbaum E, Meißner UG. On the renormalization of the one-pion exchange potential and the consistency of Weinberg's power counting. *Few Body Syst.* (2013) **54**:2175. doi: 10.1007/s00601-012-0492-1
96. Pavón Valderrama M, Ruiz Arriola E. Renormalization of NN interaction with chiral two pion exchange potential. central phases and the deuteron. *Phys Rev C.* (2006) **74**:054001. doi: 10.1103/PhysRevC.74.054001
97. Entem DR, Ruiz Arriola E, Pavón Valderrama M, Machleidt R. Renormalization of chiral two-pion exchange NN interactions. Momentum versus coordinate space. *Phys Rev C.* (2008) **77**:044006. doi: 10.1103/PhysRevC.77.044006
98. Yang CJ, Elster C, Phillips DR. Subtractive renormalization of the chiral potentials up to next-to-next-to-leading order in higher NN partial waves. *Phys Rev C.* (2009) **80**:034002. doi: 10.1103/PhysRevC.80.034002
99. Yang CJ, Elster C, Phillips DR. Subtractive renormalization of the NN interaction in chiral effective theory up to next-to-next-to-leading order: S waves. *Phys Rev C.* (2009) **80**:044002. doi: 10.1103/PhysRevC.80.044002
100. Zeoli C, Machleidt R, Entem DR. Infinite-cutoff renormalization of the chiral nucleon-nucleon interaction at N^3LO. *Few Body Syst.* (2013) **54**:2191. doi: 10.1007/s00601-012-0481-4
101. Lynn JE, Tews I, Carlson J, Gandolfi S, Gezerlis A, Schmidt KE, et al. Chiral three-nucleon interactions in light nuclei, neutron-α scattering, and neutron matter. *Phys Rev Lett.* (2016) **116**:062501. doi: 10.1103/PhysRevLett.116.062501
102. Pavón Valderrama M, Sánchez Sánchez M, Yang CJ, Long B, Carbonell J, van Kolck U. Power counting in peripheral partial waves: the singlet channels. *Phys Rev C.* (2017) **95**:054001. doi: 10.1103/PhysRevC.95.054001
103. Pavón Valderrama M, Ruiz Arriola E. Renormalization of singlet NN scattering with one pion exchange and boundary conditions. *Phys Lett B.* (2004) **580**:149. doi: 10.1016/j.physletb.2003.11.037
104. Long B, Yang CJ. Renormalizing chiral nuclear forces: a case study of 3P0. *Phys Rev C.* (2011) **84**:057001. doi: 10.1103/PhysRevC.84.057001
105. Long B, Yang CJ. Renormalizing chiral nuclear forces: triplet channels. *Phys Rev C.* (2012) **85**:034002. doi: 10.1103/PhysRevC.85.034002
106. Lynn JE, Tews I, Carlson J, Gandolfi S, Gezerlis A, Schmidt KE, et al. Quantum Monte Carlo calculations of light nuclei with local chiral two- and three-nucleon interactions. *Phys Rev C.* (2017) **96**:054007. doi: 10.1103/PhysRevC.96.054007
107. Tews I, Huth L, Schwenk A. Large-cutoff behavior of local chiral effective field theory interactions. *Phys Rev C.* (2018) **98**:024001. doi: 10.1103/PhysRevC.98.024001
108. Pavón Valderrama M. Perturbative renormalizability of chiral two pion exchange in nucleon-nucleon scattering. *Phys Rev C.* (2011) **83**:024003. doi: 10.1103/PhysRevC.83.024003
109. Pavón Valderrama M. Perturbative renormalizability of chiral two pion exchange in nucleon-nucleon scattering: P- and D-waves. *Phys Rev C.* (2011) **84**:064002. doi: 10.1103/PhysRevC.84.064002
110. Kaiser N, Brockmann R, Weise W. Peripheral nucleon-nucleon phase shifts and chiral symmetry. *Nucl Phys A.* (1997) **625**:758. doi: 10.1016/S0375-9474(97)00586-1
111. Ballot JL, Robilotta MR, da Rocha CA. NN scattering: chiral predictions for asymptotic observables. *Phys Rev C.* (1998) **57**:1574. doi: 10.1103/PhysRevC.57.1574
112. Kaiser N, Gerstendorfer S, Weise W. Peripheral NN scattering: role of delta excitation, correlated two pion and vector meson exchange. *Nucl Phys A.* (1998) **637**:395. doi: 10.1016/S0375-9474(98)00234-6
113. Birse MC. Deconstructing $^1S_0$ nucleon-nucleon scattering. *Eur Phys J A.* (2010) **46**:231. doi: 10.1140/epja/i2010-11034-9
114. Long B. Improved convergence of chiral effective field theory for 1S0 of NN scattering. *Phys Rev C.* (2013) **88**:014002. doi: 10.1103/PhysRevC.88.014002
115. Beane SR, Savage MJ. Rearranging pionless effective field theory. *Nucl Phys A.* (2001) **694**:511. doi: 10.1016/S0375-9474(01)01088-0
116. Ando SI, Hyun CH. Effective range corrections from effective field theory with di-baryon fields and perturbative pions. *Phys Rev C.* (2012) **86**:024002. doi: 10.1103/PhysRevC.86.024002
117. Sánchez Sánchez M, Yang CJ, Long B, van Kolck U. Two-nucleon $^1S_0$ amplitude zero in chiral effective field theory. *Phys Rev C.* (2018) **97**:024001. doi: 10.1103/PhysRevC.97.024001
118. Lutz M. Effective chiral theory of nucleon-nucleon scattering. *Nucl Phys A.* (2000) **677**:241. doi: 10.1016/S0375-9474(00)00206-2
119. Stoks VGJ, Klomp RAM, Terheggen CPF, de Swart JJ. Construction of high quality N N potential models. *Phys Rev C.* (1994) **49**:2950. doi: 10.1103/PhysRevC.49.2950
120. Behrendt J, Epelbaum E, Gegelia J, Meißner UG, Nogga A. Two-nucleon scattering in a modified Weinberg approach with a symmetry-preserving regularization. *Eur Phys J A.* (2016) **52**:296. doi: 10.1140/epja/i2016-16296-5
121. Ren XL, Li KW, Geng LS, Long BW, Ring P, Meng J. Leading order relativistic chiral nucleon-nucleon interaction. *Chin Phys C.* (2018) **42**:014103. doi: 10.1088/1674-1137/42/1/014103
122. Ren XL, Li KW, Geng LS, Meng J. Relativistic chiral description of the $^1S_0$ nucleon-nucleon scattering. *arXiv*. 1712.10083
123. Kievsky A, Viviani M, Gattobigio M, Girlanda L. Implications of Efimov physics for the description of three and four nucleons in chiral effective field theory. *Phys Rev C.* (2017) **95**:024001. doi: 10.1103/PhysRevC.95.024001
124. Machleidt R, Liu P, Entem DR, Ruiz Arriola E. Renormalization of the leading-order chiral nucleon-nucleon interaction and bulk properties of nuclear matter. *Phys Rev C.* (2010) **81**:024001. doi: 10.1103/PhysRevC.81.024001
125. Sammarruca F, Marcucci LE, Coraggio L, Holt JW, Itaco N, Machleidt R. Nuclear and neutron matter equations of state from high-quality potentials up to fifth order of the chiral expansion. *arXiv*. 1807.06640
126. Ekström A, Hagen G, Morris TD, Papenbrock T, Schwartz PD. Δ isobars and nuclear saturation. *Phys Rev C.* (2018) **97**:024332. doi: 10.1103/PhysRevC.97.024332
127. Drischler C, Hebeler K, Schwenk A. Chiral interactions up to next-to-next-to-next-to-leading order and nuclear saturation. *Phys Rev Lett.* (2019) **122**:042501. doi: 10.1103/PhysRevLett.122.042501
128. van Kolck U. Unitarity and discrete scale invariance. *Few Body Syst.* (2017) **58**:112. doi: 10.1007/s00601-017-1271-9

Conflict of Interest: The author declares that the research was conducted in the absence of any commercial or financial relationships that could be construed as a potential conflict of interest.

Copyright © 2020 van Kolck. This is an open-access article distributed under the terms of the Creative Commons Attribution License (CC BY). The use, distribution or reproduction in other forums is permitted, provided the original author(s) and the copyright owner(s) are credited and that the original publication in this journal is cited, in accordance with accepted academic practice. No use, distribution or reproduction is permitted which does not comply with these terms.

frontiers in Physics

REVIEW
published: 28 January 2020
doi: 10.3389/fphy.2020.00001

NN Scattering and Nuclear Uncertainties

Enrique Ruiz Arriola[1]*, *Jose Enrique Amaro*[1]* and *Rodrigo Navarro Pérez*[2]

[1] Departamento de Física Atómica, Molecular y Nuclear and Instituto Carlos I de Física Teórica y Computacional, Universidad de Granada, Granada, Spain, [2] Department of Physics, San Diego State University, San Diego, CA, United States

Ab initio calculations in Nuclear physics for atomic nuclei require a specific knowledge of the interactions among their constituents, protons and neutrons. In particular, NN interactions can be constrained down to scale resolutions of $\Delta r \sim 0.6$ fm from the study of phase shifts below the pion production threshold. However, this allows for ambiguities and uncertainties which have an impact on finite nuclei, nuclear- and neutron-matter properties. On the other hand the nuclear many body problem is intrinsically difficult and the computational cost increases with numerical precision and number of nucleons. However, it is unclear what the physical precision should be for these calculations. In this contribution we review much of the work done in Granada to encompass both the uncertainties stemming from the NN scattering database in light nuclei such as triton and alpha particle and the numerical precision required by the solution method.

Keywords: nucleon-nucleon interaction, scattering data, uncertainty quantification, nuclear binding, effective interactions, statistical analysis

OPEN ACCESS

Edited by:
Ruprecht Machleidt,
University of Idaho, United States

Reviewed by:
Victor Mokeev,
Thomas Jefferson National Accelerator Facility, United States
Roelof Bijker,
National Autonomous University of Mexico, Mexico

***Correspondence:**
Enrique Ruiz Arriola
earriola@ugr.es
Jose Enrique Amaro
amaro@ugr.es

Specialty section:
This article was submitted to Nuclear Physics, a section of the journal Frontiers in Physics

Received: *21 November 2019*
Accepted: *06 January 2020*
Published: *28 January 2020*

Citation:
Ruiz Arriola E, Amaro JE and Navarro Pérez R (2020) NN Scattering and Nuclear Uncertainties. Front. Phys. 8:1. doi: 10.3389/fphy.2020.00001

1. INTRODUCTION

One of the main goals in Theoretical Nuclear Physics for many years has been to achieve a sufficiently accurate *ab initio* solution of the Nuclear Many Body Problem from a reductionist perspective. Within the present context this means starting with the forces among the hadronic constituents, protons and neutrons, and solving the corresponding quantum mechanical problem. While this has been widely and openly recognized as an extremely difficult problem, it already represents a simplification as compared to the fundamental problem where the constituents are quarks and gluons building the nucleons and the interactions are deduced from the gauge principle in QCD. The nuclear problem schematically comprises two main steps (i) the determination of the basic interactions from spectroscopy and reactions at the few body level and (ii) a precise method of solution of the inferred interactions for the many body problem. The predictive power of the theory corresponds therefore to the relation between the input (nuclear two-, three-, four-body, and so on, forces) and the output nuclear binding energies, form factors and nuclear reactions, and the corresponding uncertainties.

The seminal paper of Yukawa [1] established the first theoretical evidence that the nuclear force has a finite range by the particle exchange mechanism. The first determination of the tensor force and its consequences for the deuteron were analyzed by Bethe [2, 3]. The first χ^2 statistical analyzes of NN scattering data below pion production threshold started in the mid fifties [4] (an account up to 1966 can be traced from Arndt and Macgregor [5]). A modified χ^2 method was introduced [6] in order to include data without absolute normalization. The steady increase along the years in the number of scattering data with better precision generated incompatibilities and hence different criteria had to be introduced [7–9] to discard inconsistent data. For a comprehensive review up to 1977 see [10–13]. For a historical presentation before 1989 we recommend Machleidt [14].

Error analysis of NN phase-shifts for several partial waves became first possible when the Nijmegen group [15] carried out a partial wave analysis (PWA) fitting about 4,000 experimental np and pp data, after rejecting about 1,000 inconsistent data with a 3σ criterion. The analysis resulted in a value $\chi^2/\text{dof} \sim 1$. In the fit the potential was an energy dependent square well of radius 1.4 fm, plus one-pion-exchange (OPE) and charge-dependent (CD) contributions starting at 1.4 fm, and a one-boson-exchange (OBE) piece operating below 2–2.5 fm. Unfortunately, the required energy dependence becomes messy for nuclear structure calculations. In the next decade a variety of NN (energy independent) potentials appeared in the literature fitting a large body of scattering data with $\chi^2/\text{dof} \sim 1$ [15–19], but surprisingly error estimates on potential parameters were not made. While all these modern potentials share the *local* OPE and CD tail and include electromagnetic effects, the unknown short range components of these potentials display a variety of forms and shapes: local potentials [16], non-local ones with angular momentum dependence [17], energy dependence [15], or momentum dependence [16, 18, 19]. While in principle $p-$, $L-$, and $E-$non-localities are equivalent on-shell (see e.g., Amghar and Desplanques [20] for a proof in a $1/M_N$ expansion) they reflect truly different physical effects and generally one should consider them as independent quantities. Any specific choice results in a bias and hence becomes a source of systematic errors.

Error propagation from nucleon-nucleon data to three- and four-nucleon binding energies was pioneered in Adam et al. [21]. A rudimentary method based on coarse grained NN interactions was proposed [22, 23] providing a first guess for error on bindings in nuclei and neutron and nuclear matter. The Granada analysis of the triton using hyper-spherical harmonics method was performed in Navarro Perez et al. [24]. The triton and the alpha particle were analyzed by solving the Faddeev equations for ^{3}H and the Yakubovsky equations for ^{4}He in [25], and in *ab initio* no-core full configuration calculations [26]. Theoretical uncertainties in the elastic nucleon-deuteron scattering observables were calculated in Skibinski et al. [27].

While the history of the NN force and its applications to nuclear physics is rather long, uncertainty quantification has not been addressed seriously until recently (see e.g., [28] for a review prefacing a full volume of the ISNET community). There are several reasons why we think that stressing this aspect of the theory may be particularly useful and fruitful. One obvious one is to provide sensible error estimates in the theoretical calculations. The traditional way was to try out several schemes and compare the different results. Another, less obvious reason, is to address the many body nuclear problem within the realistic physical accuracy, rather than the computational accuracy as it has been the customary approach up to now. This applies in particular to the a priori accuracy of the solution of the nuclear many body problem, which may eventually be relaxed as to facilitate calculations not addressed before. However, this may occur at a high price; it is not unthinkable that any realistic attempt to quantify the theoretical uncertainties may end up with a lack of predictive power on the side of the theory.

We distinguish as usual in error analyses two sources of uncertainties: statistical errors stemming from the data uncertainties for a *fixed* form of the potential, and systematic errors arising from the *different* most-likely forms of the potentials. Assuming they are independent, the total uncertainty corresponds to adding both uncertainties in quadrature. In what follows it is advantageous to take the viewpoint of considering any of the different potentials as an independent but possibly *biased* way to determine the scattering amplitudes and/or phase-shifts. Because the biases introduced in all single potential are independent on each other, a randomization of systematic errors makes sense.

A prerequisite for such an analysis is to discern as much as possible between statistical and systematic uncertainties. The former correspond to the proper propagation of the experimental input while the latter is concerned with the model or scheme dependence of the calculation procedure. Systematic errors may include the genuine bias to describe the physics and truncation errors which are related to the approximate way the calculation is carried out. At the present stage, the model bias is the largest source of uncertainty.

After many years of tremendous efforts and steady progress, state of the art calculations suggest that considerable success can be expected if one includes the current knowledge of the two-, three-body forces and a variety of many body techniques are applied. Going beyond four-body forces has never been tried out, partly because of technical difficulties but also because of the appearance of $\alpha-$clustering, based on the large stability and compactness of the ^{4}He nucleus, suggests that five body forces are marginal[1].

As already said, a credible quantification of the accuracy of the theory requires a judicious determination of all sources of error in the final results, including both the experimental information needed to pin down the interactions as well as the convergence of the numerical procedure used to solve the many body problem. Given the formidable computational effort needed to implement accurately many body calculations—even for light nuclei—an *a priori* determination of the errors induced from input data would very helpful. This would set an useful accuracy goal and a limit beyond which all refinements in the numerics would not improve the *theoretical* accuracy of the output. The purpose of the present work is to review estimates on such limiting accuracy based on the imperfect knowledge of the basic two body interactions.

Unfortunately, the situation we face in strong interactions in general and in nuclear physics in particular is to compare and validate inaccurate theories on the basis of accurate data. No theoretical predictions outperforming experimental measurements in accuracy are easily found. To make our point and concern more clear let us take for instance the case of nuclear binding energies from a *semi-empirical* point of view, where a direct reference to nuclear forces is mostly avoided. Bindings are experimentally known to high accuracy, $\Delta B = 0.01 - 10$ KeV, whereas liquid-drop model inspired mass fit formulas yield a lower theoretical accuracy $\Delta B = 0.6$ MeV (see e.g., Toivanen et al. [29] and references therein). This suggests that already

[1] Actually there are no purely contact interactions beyond four body ones for fields with $(n, p, \uparrow, \downarrow)$ degrees of freedom.

within such a simple picture the phenomenological theory is generally *not expected* to be more accurate in its predictions than experiment. Actually, according to the standard $\chi^2/\text{dof} \sim 1$ criterion the previous results show that the theory is literally *incompatible* with data, and thus not even an error analysis based on uncertainty propagation may be undertaken. The situation is presumably less optimistic for the *ab initio* approach based entirely on the knowledge of (multiparticle) nuclear forces and a skillful solution of the nuclear many body problem. This provides a motivation to quantify the accuracy needed to solve the many body problem.

2. STATEMENT OF THE PROBLEM

Let us be more specific on the meaning of uncertainty quantification in nuclear physics. From a Hamiltonian describing A-nucleons, H_A, with kinetic energy $T = \sum_{i=1}^{A} p_i^2/2M$ and multi-nucleon forces V_{nN},

$$H_A = T + V_{2N} + V_{3N} + V_{4N} + \ldots, \tag{1}$$

where

$$V_{2N} = \sum_{i<j} V_{ij}\,, \quad V_{3N} = \sum_{i<j<k} V_{ijk}\,, \quad V_{4N} = \sum_{i<j<k<l} V_{ijkl} \quad \ldots \tag{2}$$

one proceeds to solve the Schrödinger equation

$$H_A \Psi_n = E_{n,A} \Psi_n. \tag{3}$$

In the absence of useful and accurate QCD-*ab initio* determinations, phenomenological V_{2N} interactions are *adjusted* to NN scattering data and the deuteron, ^{2}H ($A = 2$), binding energy, while V_{3N} enter into the ^{3}H and ^{3}He ($A = 3$), bindings, V_{4N} in ^{4}He (A = 4), and so on. Thus, the theoretical predictive power flow is expected to be from light to heavy nuclei. For instance, in the case of the binding energy the problem of error propagation based on NN force variations corresponds to

$$V_{NN} = \bar{V}_{NN} \pm \Delta V_{NN} \to E_n(A) = \bar{E}_n(A) \pm \Delta E_n(A) \tag{4}$$

The meaning of the variation ΔV_{NN} is a bit subtle, since there are variations which are (scattering) equivalent and hence do not change the scattering observables.

We are interested firstly in the NN scattering problem [30]. Quite generally we will consider non-relativistic scattering of two particles with masses m_1 and m_2 where $H = H_0 + V$ and $H_0 = p^2/2\mu$ is the kinetic energy and $\mu = m_1 m_2/(m_1 + m_2)$ the reduced mass (we drop "*NN*" for simplicity). The S-matrix is defined as a boundary condition problem for $E \geq 0$

$$S(E + i\epsilon) = 1 - 2\pi i \delta(E - H_0) T(E + i\epsilon) \tag{5}$$

where we have introduced the T-matrix which satisfies the scattering equation in operator form,

$$\begin{aligned} T(E) &= V + V G_0(E) T(E) \\ &= V + V G_0(E) V + \cdots = V(1 - G_0(E) V)^{-1} \end{aligned} \tag{6}$$

where in the second equality we write the exact summation of the perturbative series. Other (complex) energy values are defined by analytical continuation. The T-matrix satisfies the reflection property $T(E + i\epsilon)^\dagger = T(E - i\epsilon)$ if $V = V^\dagger$ in Equation (6) and hence the unitarity condition, $S(E + i\epsilon) S(E + i\epsilon)^\dagger = 1$, follows also from $V = V^\dagger$ in Equation (6). The phase-shift is defined in terms of the eigenvalues of the S-matrix, so that $S\varphi_\alpha = e^{2i\delta_\alpha}\varphi_\alpha$ and for rotational invariant interactions (we neglect spin to ease the notation) the scattering amplitude $M(\mathbf{p}', \mathbf{p})$ is given by

$$\begin{aligned} M(\mathbf{p}', \mathbf{p}) &= \sum_{lm} 4\pi\, Y_{lm}(\mathbf{p}) Y_{lm}(\mathbf{p}') \frac{e^{i\delta_l(p)} \sin\delta_l(p)}{p} \\ &= -\frac{2\mu}{4\pi} \langle \vec{p}\,' | T(E + i\epsilon) | \vec{p} \rangle \Big|_{E_p = E_{p'} = E} \end{aligned} \tag{7}$$

with $Y_{lm}(\mathbf{p})$ the spherical harmonics and in our convention $d\sigma/d\Omega = |M(\mathbf{p}', \mathbf{p})|^2$ the differential cross section. Any *NN* unitary transformation, U, transforms the Hamiltonian and hence the potential as $V \to \tilde{V} = UHU^\dagger - H_0$. For an infinitesimal transformation $U = 1 + i\eta + \ldots$, where η is a small self-adjoint two-body operator, the scattering equivalent variation corresponds to the change $\Delta V = i[\eta, H]$. To see the effect on scattering, start with the LS equation in the form $T^{-1} = V^{-1} - G_0$ which upon a variation of the potential produces a variation of the T-matrix $\Delta T = TV^{-1}\Delta V V^{-1} T$ and after some manipulation one gets

$$-i\Delta T = (1 + TG_0)\eta G_0^{-1} - G_0^{-1}\eta(1 + G_0 T) \tag{8}$$

so that sandwiching this expression between plane waves gives

$$\begin{aligned} \Delta\langle \vec{k}\,' | T(E + i\epsilon) | \vec{k} \rangle = &-i(E - E_{k'} + i\epsilon)\langle k' | \eta(1 + G_0 T) | k \rangle \\ &+ i(E - E_k + i\epsilon)\langle k' | (1 + TG_0)\eta | k \rangle \end{aligned} \tag{9}$$

which vanishes in the on-shell limit $E_k = E_{k'} = E$ and $\epsilon \to 0$. Thus,

$$\Delta V = i[\eta, H] \implies \Delta\langle \vec{k}\,' | T(E + i\epsilon) | \vec{k} \rangle \Big|_{E_k = E_{k'} = E} = 0 \tag{10}$$

or equivalently for finite unitary transformations, using Equation (7), $\delta_{l,H}(p) = \delta_{l,UHU^\dagger}(p)$.

Given this general ambiguity the long lasting problem has been to decide which is the proper representation of the NN interaction based on NN scattering data. This is in essence the so-called inverse scattering problem which has been studied extensively in the past (see e.g., Chadan and Sabatier [31] and Newton [32] for reviews)] and requires additional strong assumptions to fix the particular form of the potential. For instance, assuming a *local* potential and *complete* knowledge of the phase-shifts in each partial wave it is possible to determine the solution uniquely provided the binding energies and long distance behavior of the corresponding bound states wave functions allocated by the potential are known. Clearly, these inverse scattering ambiguities have an impact on the solution of the many body problem, as was documented long time ago in nuclear matter [33] and in the triton and alpha particles [34],

just to mention two prominent examples (see Srivastava and Sprung [35] for a review).

Much of the arbitrariness is reduced by invoking an underlying theoretical description in terms of hadronic degrees of freedom, which allows to compute $V_{NN}(\vec{x})$ in terms of one-, two-,..., pion exchanges. which in turn may be related to the πN scattering process, involving coupling constants for vertex interactions. At present such a picture seems to hold down to NN separations of about the elementary radius, $r_c = 1.8$ fm, below which composite and finite size effects start playing a role That means that, essentially, variations of the NN potential of are restricted at least to $\Delta V_{NN}(\vec{x}) = 0$ for $r \geq r_c \approx 1.8$ fm.

3. THE NN POTENTIAL

3.1. The Concept of a Potential

In order to properly formulate the uncertainties of the potentials it would be adequate to review first the meaning of a potential in nuclear physics. This is of utmost importance but also intriguing. On the one hand the potential is not an observable but on the other hand to our knowledge it is not practical to carry out *ab initio* calculations in Nuclear Physics at the hadronic level without potentials. Ultimately, one hopes to be able to provide a direct link between the uncertainties in the input data and propagate them to the output of the many body problem. As said, this is only possible by using non-observable nuclear potentials as intermediate steps.

From a classical (and macroscopic) point of view, potential and force can be measured directly by just determining the separation static energy between two infinitely heavy sources. Such a definition admits a direct extension to the quantum mechanical microscopic case and specifically to the NN interaction assuming interpolating composite local nucleon fields made out of three quarks. In essence, this is the approach followed in recent years in lattice QCD where many of the traditionally assumed features of the NN interaction seem to be confirmed [36–38]. A major drawback of this approach is that such a calculation determines the static NN energy which would become a physical observable if nucleons were infinitely heavy. The quantum mechanical problem needs adding kinetic energy contributions. Moreover, the fact that low energy NN scattering provides unnaturally large cross sections corresponds to an extreme fine tuning which is beyond the present lattice capabilities.

3.2. The Tensorial Structure

Assuming isospin invariance for the moment, the most general form of the NN interaction can be written as Okubo et al. [39]

$$\begin{aligned} V(\mathbf{p}',\mathbf{p}) = \; & V_C \; + \vec{\tau}_1\cdot\vec{\tau}_2\, W_C + \left[\, V_S \; + \vec{\tau}_1\cdot\vec{\tau}_2\, W_S \;\right] \vec{\sigma}_1\cdot\vec{\sigma}_2 \\ & - i\vec{S}\cdot(\mathbf{q}\times\mathbf{P})\left[\, V_{LS} + \vec{\tau}_1\cdot\vec{\tau}_2\, W_{LS}\right] \\ & + \left[\, V_T \; + \vec{\tau}_1\cdot\vec{\tau}_2\, W_T \;\right] \vec{\sigma}_1\cdot\mathbf{q}\;\vec{\sigma}_2\cdot\mathbf{q} \\ & + \left[\, V_Q + \vec{\tau}_1\cdot\vec{\tau}_2\, W_Q \right] \vec{\sigma}_1\cdot(\mathbf{q}\times\mathbf{P})\;\vec{\sigma}_2\cdot(\mathbf{q}\times\mathbf{P}) \\ & + \left[\, V_P + \vec{\tau}_1\cdot\vec{\tau}_2\, W_P \right] \vec{\sigma}_1\cdot\mathbf{P}\;\vec{\sigma}_2\cdot\mathbf{P}\,, \end{aligned} \tag{11}$$

where $\mathbf{p}'$ and $\mathbf{p}$ denote the final and initial nucleon momenta in the CMS, respectively. Moreover, $\mathbf{q} = \mathbf{p}' - \mathbf{p}$ is the momentum transfer, $\mathbf{P} = (\mathbf{p}' + \mathbf{p})/2$ the average momentum, and $\vec{S} = (\vec{\sigma}_1 + \vec{\sigma}_2)/2$ the total spin, with $\vec{\sigma}_{1,2}$ and $\vec{\tau}_{1,2}$ the spin and isospin operators, of nucleon 1 and 2, respectively.

The scalar functions appearing in the potential, Equation (11), depend on *both* initial and final momentum $\mathbf{p}$ and $\mathbf{p}'$ respectively. Because of rotational invariance we may thus form three independent invariants, such as p, p' and also $\mathbf{q}\cdot\mathbf{P}$ (which vanishes on-shell). Transforming to coordinate space in the variable $\mathbf{r}$, conjugate to q, we have

$$V(\mathbf{r},\mathbf{P}) = \int \frac{d^3q}{(2\pi)^3} e^{i\mathbf{q}\cdot\mathbf{r}} \langle \mathbf{P} + \tfrac{1}{2}\mathbf{q}|V|\mathbf{P} - \tfrac{1}{2}\mathbf{q}\rangle, \tag{12}$$

where we take $\langle \mathbf{P} + \frac{1}{2}\mathbf{q}|V|\mathbf{P} - \frac{1}{2}\mathbf{q}\rangle \equiv V(\mathbf{p}',\mathbf{p})$. The case where these functions depend *only* on the momentum transfer $\mathbf{q} = \mathbf{p}' - \mathbf{p}$ corresponds in coordinate space to a *local* potential, $V(\mathbf{r},\mathbf{P}) = V(\mathbf{r})$. Local potentials are appealing because they provide physical insight besides being directly manageable by means of a Schrödinger equation in configuration space. Moreover, attaching a field theoretical interpretation to the interaction, locality must be satisfied by heavy and point-like elementary nucleons which act as static sources, so that in this case the potential becomes the static energy between nucleons which is an unique observable defined by

$$E_{NN}(r) = V_{NN}(r) + 2M_N + \mathcal{O}(M_N^{-1}), \tag{13}$$

where we assume $M_N \gg m_\pi, E$. Non-localities are expected to be weak because $P/M_N \ll 1$, and should have a larger influence at short distances (see e.g., Piarulli et al. [40] for an explicit implementation). The finite mass effects generate some ambiguity in the definition of the potential and, as we will see, are the largest source of uncertainties in nuclear physics. In any case, there is some freedom that can be used advantageously to *choose*—by means of suitable unitary transformations [41]—a convenient form of the potential to simplify the solution of the two-body problem, and to simplify a particular scheme of the many body problem. We remind, however, that this choice may be a source of bias and hence of systematic uncertainty.

3.3. Operator Basis

In our analysis we will be using potentials which become local in the partial wave basis. While the use of local potentials is very appealing since the whole analysis simplifies tremendously, the truth is that their use at all distances is questionable for extended particles. However, the range of non-locality is determined by the interaction and our analysis (see below) supports that on a scale $\Delta r \sim 0.6$ fm non-locality is not essential.

The potential is written as a sum of functions multiplied by each operator

$$V(r) = \sum_{n=1,23} V_n(r) O^n \tag{14}$$

The first 14 operators are charge independent and correspond to the ones used in the Argonne v_{14} potential

$$\begin{aligned} O^{n=1,14} =& 1, \tau_1\cdot\tau_2,\ \sigma_1\cdot\sigma_2, (\sigma_1\cdot\sigma_2)(\tau_1\cdot\tau_2),\ S_{12}, S_{12}(\tau_1\cdot\tau_2), \\ & \mathbf{L}\cdot\mathbf{S}, \mathbf{L}\cdot\mathbf{S}(\tau_1\cdot\tau_2), L^2, L^2(\tau_1\cdot\tau_2),\ L^2(\sigma_1\cdot\sigma_2), \\ & L^2(\sigma_1\cdot\sigma_2)(\tau_1\cdot\tau_2),\ (\mathbf{L}\cdot\mathbf{S})^2, (\mathbf{L}\cdot\mathbf{S})^2(\tau_1\cdot\tau_2). \end{aligned} \tag{15}$$

These 14 components are denoted by c, τ, σ, $\sigma\tau$, t, $t\tau$, ls, $ls\tau$, $l2$, $l2\tau$, $l2\sigma$, $l2\sigma\tau$, $ls2$, and $ls2\tau$. The remaining CD operators are

$$\begin{aligned} O^{n=15,21} =& T_{12}, (\sigma_1\cdot\sigma_2)T_{12}, S_{12}T_{12}, (\tau_{z1}+\tau_{z2}), \\ & (\sigma_1\cdot\sigma_2)(\tau_{z1}+\tau_{z2}), L^2T_{12}, L^2(\sigma_1\cdot\sigma_2)T_{12}, \\ & \mathbf{L}\cdot\mathbf{S}T_{12}, (\mathbf{L}\cdot\mathbf{S})^2T_{12} \end{aligned} \tag{16}$$

and are labeled as T, σT,tT, τz,$\sigma\tau z$, $l2T$, $l2\sigma T$, lsT, and $ls2T$. The first five were introduced by Wiringa et al. [17]; the following two were included in Navarro Pérez et al. [42] to restrict CD to the $^1S_0$ partial wave by following certain linear dependence relations between V_T, $V_{\sigma T}$, V_{l2T}, and $V_{l2\sigma T}$. The last two terms are required for the CD on the $^3P_0$, $^3P_1$, and $^3P_2$ partial waves. To incorporate CD on P waves two more operators need to be added to the basis we used previously getting a total of 23 operators O^n.

As in our previous analysis we set $V_{tT} = V_{\tau z} = V_{\sigma\tau z} = 0$ to exclude CD on the tensor terms and charge asymmetries. To restrict CD to the S and P waves parameters the remaining potential functions must follow

$$48V_{l2T} = -5V_T + 3V_{\sigma T} + 12V_{lsT} - 48V_{ls2T} \tag{17}$$

$$48V_{\sigma l2T} = V_T - 7V_{\sigma T} + 4V_{lsT} - 16V_{ls2T} \tag{18}$$

The algebraic relation between the operator basis in momentum space and in configuration space is explicitly given in Navarro Perez and Ruiz Arriola [43] and several examples are displayed.

3.4. The Long Range Contributions

As mentioned above, the potential becomes an observable within a QFT setup for infinitely heavy hadronic sources. For the finite mass case one may use instead a perturbative matching procedure between a QFT with hadronic (and electro-magnetic fields) fields and the quantum mechanical problem, which should work at sufficiently long distances. The hadronic QFT calculable contribution is separated into two pieces, the strong (pion exchange) piece and the purely EM piece,

$$V_{\rm QFT} = V_\pi(r) + V_{\rm EM}(r)\,. \tag{19}$$

The CD-OPE potential in the long range part of the interaction is the same as the one used by the Nijmegen group on their 1993 PWA [15] and reads

$$V_{m,\rm OPE}(r) = f^2\left(\frac{m}{m_{\pi^\pm}}\right)^2 \frac{1}{3} m\left[Y_m(r)\sigma_1\cdot\sigma_2 + T_m(r)S_{1,2}\right] \tag{20}$$

being f the pion coupling constant, σ_1 and σ_2 the single nucleon Pauli matrices, $S_{1,2}$ the tensor operator, $Y_m(r)$ and $T_m(r)$ the usual Yukawa and tensor functions,

$$Y_m(r) = \frac{e^{-mr}}{mr},$$

$$T_m(r) = \left(1 + \frac{3}{mr} + \frac{3}{(mr)^2}\right)\frac{e^{-mr}}{mr}. \tag{21}$$

CD is introduced by the difference between the charged $m_{\pi^\pm}$ and neutral m_{π^0} pion mass by setting

$$\begin{aligned} V_{\rm OPE,}{}_{pp}(r) &= V_{m_{\pi^0},\rm OPE}(r), \\ V_{\rm OPE,}{}_{np}(r) &= -V_{m_{\pi^0},\rm OPE}(r) + (-)^{(T+1)}2V_{m_{\pi^\pm},\rm OPE}(r). \end{aligned} \tag{22}$$

The neutron-proton electromagnetic potential includes only a magnetic moment interaction

$$V_{\rm EM,np}(r) = V_{\rm MM,np}(r) = -\frac{\alpha\mu_n}{2M_n r^3}\left(\frac{\mu_p S_{1,2}}{2M_p} + \frac{\mathbf{L}\cdot\mathbf{S}}{\mu_{np}}\right), \tag{23}$$

where μ_n and μ_p are the neutron and proton magnetic moments, M_n the neutron mass, M_p the proton one and $\mathbf{L}\cdot\mathbf{S}$ is the spin orbit operator. The EM terms in the proton-proton channel include one and two photon exchange, vacuum polarization and magnetic moment,

$$V_{\rm EM,pp}(r) = V_{\rm C1}(r) + V_{\rm C2}(r) + V_{\rm VP}(r) + V_{\rm MM,pp}(r) \tag{24}$$

where

$$V_{\rm C1}(r) = \frac{\alpha'}{r}, \tag{25}$$

$$V_{\rm C2}(r) = -\frac{\alpha\alpha'}{M_p r^2}, \tag{26}$$

$$V_{\rm VP}(r) = \frac{2\alpha\alpha'}{3\pi r}\int_1^\infty e^{-2m_e rx}\left(1+\frac{1}{2x^2}\right)\frac{\sqrt{x^2-1}}{x^2}dx, \tag{27}$$

$$V_{\rm MM,pp}(r) = -\frac{\alpha}{4M_p^2 r^3}\left[\mu_p^2 S_{1,2} + 2(4\mu_p - 1)\mathbf{L}\cdot\mathbf{S}\right]. \tag{28}$$

Note that these potentials are *only* used above $r_c = 3$ fm and thus form factors accounting for the finite size of the nucleon can be set to one. Energy dependence is present through the parameter

$$\alpha' = \alpha\frac{1 + 2k^2/M_p^2}{\sqrt{1 + k^2/M_p^2}}, \tag{29}$$

where k is the center of mass momentum and α the fine structure constant. **Table 1** lists the values used for the fundamental constants in our calculations and typically used since the benchmarking Nijmegen analysis.

3.5. Short Range Contributions

The short range contributions are fundamentally unknown and, despite some lattice QCD efforts [36–38, 44], can only be determined indirectly and phenomenologically, mostly from NN scattering. Along the years some experience has been gathered about the size, shape, and range of the potentials in the bulk, at least in configuration space, so that refinements are made by a χ^2 minimization to pp and np scattering data (see below). Besides, the analysis of scattering data allows to obtain information on

TABLE 1 | Values of fundamental constants used.

Constant	Value	Units
$\hbar c$	197.327053	MeV fm
m_{π^0}	134.9739	MeV/c^2
$m_{\pi^\pm}$	139.5675	MeV/c^2
M_p	938.27231	MeV/c^2
M_n	939.56563	MeV/c^2
m_e	0.510999	MeV/c^2
α^{-1}	137.035989	
f^2	0.075	
μ_p	2.7928474	μ_0
μ_n	−1.9130427	μ_0

the lowest distance where the long range contributions can be trusted. We anticipate that they may be assumed to be valid for $r_c \geq 1.8$ fm when OPE and TPE contributions are included. This coincides *a fortiori* with the distance above which protons interact by Coulomb force as point-like particles, and also with the typical distance between nucleons in nuclear matter, $d = \rho^{-1/3} = 1.8$ fm for $\rho = 0.17\,\text{fm}^{-3}$.

Finally, there is the issue on *which* and *how many* parameters are needed to describe the short range force in a satisfactory manner. The primary 2013 Granada analysis has been carried out in terms of the so-called coarse grained potentials [45]. The coarse grain procedure *samples* the interaction with an optimal grain size, corresponding roughly to the reduced de Broglie wavelength $\Delta r = \hbar/p$. For the maximum LAB energy, 350 MeV, this corresponds to $\Delta r = 0.6$ fm. Thus, we do not need to sample the potential functions $V_i(r)$ at *all* points, but rather in a grid of points, $V_i(r_n)$ given by $r_n = n\Delta r$. We consider the $V_i(r_n)$ values as fitting parameters. The particular interpolations between these points are not physically relevant, because shorter scales than Δr cannot be probed by the scattering process below a maximal $p = \sqrt{T_{\rm LAB} M_N/2} \sim 2\,\text{fm}^{-1}$.

The number of grid points depends on the cut distance, r_c, above which the functional form of the potential is known and corresponds to $N = r_c/\Delta r$. Thus, the simplest case corresponds to $r_c = 1.8$ fm and $N = 3$ grid points for any radial component, $V_i(r_n)$, in the operator basis. In the partial wave basis some refinements can be incorporated since the centrifugal barrier limits the sampling points below the barrier in the classically forbidden region, so that the estimate is Fernandez-Soler and Ruiz Arriola [46] and Ruiz Arriola and Ruiz de Elvira [47],

$$N_{\rm Par} \sim \frac{1}{2}(p_{\rm CM}^{\rm max} r_c)^2\, g_S\, g_T\,, \tag{30}$$

where g_S and g_T are spin and isospin degeneracy factors. The counting of parameters for pp and np [48] yields about 40 "grained" points r_n in the fit carried up to a maximum energy $T_{\rm LAB} \leq 350$ MeV. This *a priori* estimate coincides in the bulk with the number of parameters which have traditionally been needed to fit data satisfactorily in the past. The previous argument suggests that including more parameters is not expected to improve significantly the fits to scattering data, but rather increase the correlations among the $V_i(r_n)$ parameters.

There are many possible ways to describe the interaction at the "grained" points. The simplest is to consider Dirac delta-shells located at the sampled points [49, 50]

$$V(r)|_{\rm Short} = \Delta r \sum_{i,n} O_i V_i(r_n)\delta(r - r_n) \qquad r \leq r_c \tag{31}$$

We refer to Navarro Perez et al. [51] for a pedagogical presentation of coarse grained interactions which solve the Schrödinger equation by a discretized form [49, 50] of the variable phase approach of Calogero [52]. This delta-shells decomposition implies a similar one at the partial waves level, so that one may use the partial wave strengths $V^{JS}_{LL'}(r_n)$ as fitting parameters. This choice is rather convenient for least squares minimization as the low angular momentum partial wave components of the potential are largely uncorrelated, substantially speeding up the minimum search [53, 54]. The transformation matrix from the $V_i(r_n)$ to the $V^{JS}_{LL'}(r_n)$ basis can be found in Navarro Pérez et al. [42].

4. PARTIAL WAVE ANALYSIS

The NN scattering amplitude has five independent complex components which are a function of energy and scattering angle [55],

$$\begin{aligned} M =& a + m(\sigma_1\cdot\mathbf{n})(\sigma_2\cdot\mathbf{n}) + (g-h)(\sigma_1\cdot\mathbf{m})(\sigma_2\cdot\mathbf{m}) \\ &+(g+h)(\sigma_1\cdot\mathbf{l})(\sigma_2\cdot\mathbf{l}) + c(\sigma_1+\sigma_2)\cdot\mathbf{n}. \end{aligned} \tag{32}$$

We use the three unit vectors ($\mathbf{k}_f$ and $\mathbf{k}_i$ are relative final and initial momenta),

$$\mathbf{l} = \frac{\mathbf{k}_f + \mathbf{k}_i}{|\mathbf{k}_f + \mathbf{k}_i|}\,, \qquad \mathbf{m} = \frac{\mathbf{k}_f - \mathbf{k}_i}{|\mathbf{k}_f - \mathbf{k}_i|}\,, \qquad \mathbf{n} = \frac{\mathbf{k}_f \wedge \mathbf{k}_i}{|\mathbf{k}_f \wedge \mathbf{k}_i|}\,. \tag{33}$$

For this amplitude the total spin S is conserved and in this case the partial wave expansion reads,

$$\begin{aligned} M^s_{m'_s,m_s}(\theta) =& \frac{1}{2ik}\sum_{J,l',l}\sqrt{4\pi(2l+1)}\,Y^{l'}_{m'_s-m_s}(\theta,0) \\ &\times C^{l',S,J}_{m_s-m'_s,m'_s,m_s}\, i^{l-l'}(\mathbf{S}^{J,S}_{l,l'} - \delta_{l',l})C^{l,S,J}_{0,m_s,m_s}, \end{aligned} \tag{34}$$

where $\mathbf{S}$ is the unitary coupled channel S-matrix, and the $C's$ are Clebsch-Gordan coefficients, $C^{l,S,J}_{m,m_s,M} = \langle lmSM_s|JM\rangle$. The spins of the nucleon pair can be coupled to total spin $S = 0, 1$ and hence $J = L \pm 1$ for unnatural parity, $(-1)^{L+1}$ states and $J = L$ for natural parity states. This amplitudes contains all measurable physical information and the relation to observable quantities such as differential cross sections and polarization asymmetries can be found in Hoshizaki [56] and Bystricky et al. [57].

In the Stapp-Ypsilantis-Metropolis (SYM) representation [4] the S-matrix is written in terms of the *nuclear-bar phase shifts* $\bar\delta_{j\pm1}$ and $\bar\epsilon_j$. Dropping the bars for simplicity and denoting the phase shifts as $\delta^{J,s}_{l,l'}$, for the singlet ($s = 0, l = l' = J$) and triplet uncoupled ($s = 1, l = l' = J$) channels the S matrix is simply

$e^{2i\delta^{J,s}_{l,l}}$, in the triplet coupled channel ($s=1, l=J\pm 1, l'=J\pm 1$) it reads

$$S^J = \begin{pmatrix} e^{2i\delta^{J,1}_{J-1}}\cos 2\epsilon_J & ie^{i(\delta^{J,1}_{J-1}+\delta^{J,1}_{J+1})}\sin 2\epsilon_J \\ ie^{i(\delta^{J,1}_{J-1}+\delta^{J,1}_{J+1})}\sin 2\epsilon_J & e^{2i\delta^{J,1}_{J+1}}\cos 2\epsilon_J \end{pmatrix}, \tag{35}$$

with ϵ_J the mixing angle.

The partial wave expansion provides an indirect way to find out the range of nuclear forces by truncating the expansion. According to the standard semi-classical argument (see e.g., [58]), for an impact parameter $b=(J+1/2)/p$ (p is the CM momentum) the no-scattering condition corresponds to $b \geq a$, so that $|\delta_{J_{\max}}| \leq \Delta\delta_{J_{\max}}$ where maximal angular momentum is provided by $J_{\max} \approx pa$ with a the range of the force. For the Yukawa OPE interaction the exponential fall-off of the potential also means a similar behavior for the phase-shifts, so typically one takes S, P, D, and F waves as *active* if the condition is $J+1/2 \approx pr_c$ with r_c the separation distance.

We will review briefly the basics of scattering from a NN potential for completeness and to provide our notation. Details may be found in standard textbooks on scattering theory (see e.g., [59]). The generalization of the well-known Rayleigh expansion for spin S is

$$e^{i\mathbf{k}\cdot\mathbf{x}}\chi_{SM_s} = 4\pi\sum_{l,m} i^l j_l(kr) Y^*_{l,m}(\hat{\mathbf{k}}) \sum_{J,M}\langle lmSM_s|JM\rangle \mathcal{Y}_{lSJM}(\hat{\mathbf{x}}), \tag{36}$$

where χ_{SM_s} is an eigenspinor with spin quantum numbers (S, M_s), and the functions $\mathcal{Y}_{lSJM}(\hat{\mathbf{x}})$ are the couplings of the spherical harmonics with the spinors χ_{SM_s} to total angular momentum J,

$$\mathcal{Y}_{lSJM}(\hat{\mathbf{x}}) = \sum_{m',M'_s}\langle lm'SM'_s|JM\rangle Y_{l,m'}(\hat{\mathbf{x}})\,\chi_{SM'_s}\,. \tag{37}$$

The local (but angular momentum dependent) NN potential described in the previous section conserves spin S and total angular momentum J, but not the orbital angular momentum L. Therefore, the scattering wave function for spin S is expanded as

$$\Psi_{\mathbf{k},SM_s}(\mathbf{x}) = 4\pi\sum_{lmJM} i^l Y^*_{l,m}(\hat{\mathbf{k}})\langle lmSM_s|JM\rangle \sum_{l'}\frac{u^{SJ}_{l'l}(r)}{kr}\mathcal{Y}_{l'SJM}(\hat{\mathbf{x}})\,. \tag{38}$$

where the reduced radial wave functions $u^{SJ}_{l'l}(r)$ satisfy the coupled channel differential equations

$$\left[-\frac{d^2}{dr^2}+\frac{l'(l'+1)}{r^2}-k^2\right]u^{SJ}_{l'l} + \sum_{l''}U^{SJ}_{l',l''}(r)u^{SJ}_{l''l} = 0 \tag{39}$$

and the reduced potential is defined as $U(r)=2\mu V(r)$. For regular potentials the boundary condition at the origin reads

$$u^{SJ}_{l'l}(r) \sim r^{l'+1} \qquad (r\to 0) \tag{40}$$

The integration of the equations can advantageously be done using the delta shell representation of the NN potential taking $\Delta r = 0.6$ fm for $r \leq r_c$ (the coarse-grained and unknown part) and $\Delta r = 0.1$ fm for $r \geq r_c$ (the known field theoretical part). The complete set of equations including Coulomb forces is provided in Navarro Pérez et al. [42]. The scattering boundary condition

$$\Psi_{S,m_s}(\vec{x}) \to e^{i\vec{k}\cdot\vec{x}}\chi_{S,m_s} + \frac{e^{ikr}}{r}\sum_{m_{s'}=-S}^{S} M_{m_S,m_{S'}}\chi_{S,m'_s} \tag{41}$$

implies a similar asymptotic condition for the reduced radial wave functions. For the uncoupled case, $l=J$, one has for $r\sim R \gg 1/m_\pi$

$$u_J(r) \equiv u_{JJ}(r) \to \hat{j}_J(kr) - \cot\delta_J(k)\hat{y}_J(kr) \tag{42}$$

where $\hat{j}_J(x)=xj_J(x)$ and $\hat{y}_J(x)=xy_J(x)$ are the reduced spherical Bessel functions of order J and $\delta_J=\delta^{1J}_J, \delta^{0J}_J$. In the coupled triplet case, $S=1$, the four wave functions $u_{l'l}(r)$, with $l', l = J-1, J+1$, are coupled in pairs. The pair

$$v_{\alpha J} = u_{J-1,J-1} \qquad w_{\alpha J} = u_{J+1,J-1} \tag{43}$$

verifies the coupled equations

$$\left[-\frac{d^2}{dr^2}+\frac{J(J-1)}{r^2}-k^2\right]v_{\alpha J} + U^{SJ}_{J-1,J-1}(r)v_{\alpha J} + U^{SJ}_{J-1,J+1}(r)w_{\alpha J} = 0 \tag{44}$$

$$\left[-\frac{d^2}{dr^2}+\frac{(J+1)(J+2)}{r^2}-k^2\right]w_{\alpha J} + U^{SJ}_{J+1,J+1}(r)w_{\alpha J} + U^{SJ}_{J+1,J-1}(r)v_{\alpha J} = 0 \tag{45}$$

On the other hand the pair

$$w_{\beta J} = u_{J+1,J+1} \qquad v_{\beta J} = u_{J-1,J+1} \tag{46}$$

verifies the same coupled equations by changing $\alpha \to \beta$. This is equivalent to say that the system (44, 45) has two linearly independent solutions that we label as α and β solutions. Their asymptotic behavior can be expressed in terms of the eigen phase shifts as,

$$v_{\alpha J}(r) \to \hat{j}_{J-1}(kr)\cot\delta^{1J}_{J-1} - \hat{y}_{j-1}(kr) \tag{47}$$

$$w_{\alpha J}(r) \to \tan\epsilon_J\left[\hat{j}_{j+1}(kr)\cot\delta^{1J}_{J-1} - \hat{y}_{j+1}(kr)\right] \tag{48}$$

$$v_{\beta J}(r) \to -\tan\epsilon\left[\hat{j}_{j-1}(kr)\cot\delta^{1J}_{J+1} - \hat{y}_{j-1}(kr)\right] \tag{49}$$

$$w_{\beta J}(r) \to \hat{j}_{j+1}(kr)\cot\delta^{1J}_{J+1} - \hat{y}_{j+1}(kr) \tag{50}$$

This is known as the Blatt-Biedenharn (BB) parameterization in terms of the *eigen phase shifts* $\delta^{1j}_{j\pm1}$ and ϵ_j. These are related to the nuclear-bar phase shifts by the following equations

$$\delta^{1J}_{J-1} + \delta^{1J}_{J+1} = \bar{\delta}^{1J}_{J-1} + \bar{\delta}^{1J}_{J+1} \tag{51}$$

$$\sin(\bar{\delta}^{1J}_{J-1} - \bar{\delta}^{1J}_{J+1}) = \frac{\tan 2\bar{\epsilon}_J}{\tan 2\epsilon_J} \tag{52}$$

$$\sin(\delta^{1J}_{J-1} - \delta^{1J}_{J+1}) = \frac{\sin 2\bar{\epsilon}_J}{\sin 2\epsilon_J} \tag{53}$$

Unless otherwise stated, in this work the phase shifts will always be assumed to be the nuclear-bar ones. The Coulomb force is included exactly by replacing in the previous formulas the Bessel functions j_l and y_l by Coulomb functions F_l and G_l [59]. The inclusion of magnetic moments effect is complicated by their $1/r^3$ behavior requiring about 1,000 partial waves [42].

5. STATISTICS

The statistical treatment we follow here is quite standard, and we list for the benefit of the newcomer to the field the main steps to be discussed in the following subsections. We first address the existing scattering data and then we formulate the nature of the problem and the standard χ^2 approach searching for the most likely potential. This requires discriminating between consistent and inconsistent data, something which can be formulated in terms of a self-consistent selection problem. After this, a direct statistically satisfactory result can be deduced and, more importantly, error propagation may legitimately be carried out in terms of the corresponding covariance matrix implementing statistical correlations. This allows in particular to determine the scattering phase-shifts with error bars reflecting directly the experimental uncertainties. More generally, it allows to transport these experimental errors to any observable based on the nucleon-nucleon potential. We will call these the statistical errors.

5.1. Scattering Data

Once we have defined the potential model and the scattering formalism we may proceed to determine the potential parameters $V_i(r_n)$ from the available np and pp scattering data and from the corresponding scattering observables which are obtained from the scattering amplitude [56, 57] (see also **Tables 2**, **3** below for the notation). The compilation of the existing published data since 1950 till 2013 is described in detail in Navarro Pérez et al. [42] and comprises 8,124 fitting data including 7,709 experimental measurements and 415 normalizations provided by the experimentalists.

5.2. Statement of the Problem

The finite amount, precision and limited energy range of the data as well as the many different observables calls for a standard statistical χ^2-fit analysis [62, 63]. This approach is subjected to assumptions and applicability conditions that can only be checked *a posteriori* in order to guarantee the self-consistency of the analysis. Indeed, scattering experiments deal with counting Poisson statistics and for moderately large number of counts a normal distribution is expected. Thus, one hopes that a satisfactory theoretical description $O_i^{\rm th}$ can predict a set of N independent observed data O_i given an experimental uncertainty ΔO_i as

$$O_i = O_i^{\rm th} + \xi_i \Delta O_i \tag{54}$$

TABLE 2 | Contributions to the total χ^2 for different pp observables [60, 61].

Observable	Code	N_{pp}	χ^2_{pp}	χ^2_{pp}/N_{pp}
$d\sigma/d\Omega$	DSG	935	903.5	0.97
A_{yy}	AYY	312	339.0	1.09
D	D	104	135.1	1.30
P	P	807	832.4	1.03
A_{zz}	AZZ	51	47.4	0.93
R	R	110	112.8	1.03
A	A	79	70.5	0.89
A_{xx}	AXX	271	250.7	0.92
C_{kp}	CKP	2	3.1	1.57
R'	RP	29	11.9	0.41
$M_{s'0sn}$	MSSN	18	13.1	0.73
$N_{s'0kn}$	MSKN	18	8.5	0.47
A_{zx}	AZX	264	250.6	0.95
A'	AP	6	0.8	0.14

We use the notation of Hoshizaki [56] and Bystricky et al. [57].

TABLE 3 | Contributions to the total χ^2 for different np observables [60, 61].

Observable	Code	N_{np}	χ^2_{np}	χ^2_{np}/N_{np}
$d\sigma/d\Omega$	DSG	1712	1803.4	1.05
D_t	DT	88	83.7	0.95
A_{yy}	AYY	119	96.0	0.81
D	D	29	37.1	1.28
P	P	977	941.7	0.96
A_{zz}	AZZ	89	108.1	1.21
R	R	5	4.5	0.91
R_t	RT	76	72.2	0.95
R'_t	RPT	4	1.4	0.35
A_t	AT	75	77.0	1.03
$D_{0s''0k}$	D0SK	29	44.0	1.52
$N_{0s''kn}$	NSKN	29	25.5	0.88
$N_{0s''sn}$	NSSN	30	20.3	0.68
N_{0nkk}	NNKK	18	13.5	0.75
A	A	6	2.9	0.49
σ	SGT	411	500.2	1.22
$\Delta\sigma_T$	SGTT	20	26.3	1.31
$\Delta\sigma_L$	SGTL	16	18.4	1.15

We use the notation of Hoshizaki [56] and Bystricky et al. [57].

with $i = 1, \ldots, N$ and ξ_i are independent random *normal* variables with vanishing mean value $\langle \xi_i \rangle = 0$ and unit variance $\langle \xi_i \xi_j \rangle = \delta_{ij}$, implying that $\langle O_i \rangle = O_i^{\rm th}$. Establishing the validity of Equation (54) is of utmost importance since it provides a basis for the statistical interpretation of the error analysis.

5.3. The Least Squares Minimization

If the ξ_i are independent normal variables,then $\sum_{i=1}^{\nu} \xi_i^2$ represents a χ^2 distribution with ν degrees of freedom. Thus, under this *hypothesis* we may consider the standard χ^2 method,

which in our case is defined as

$$\chi^2[V_k(r_n)] = \sum_{i=1}^{N_{\rm Dat}} \left[\frac{O_i^{\rm exp} - O_i^{\rm th}(V_k(r_n))}{\Delta O_i^{\rm exp}} \right]^2 \tag{55}$$

where $O_i^{\rm exp}$ is the experimental observable, $\Delta O_i^{\rm exp}$ its estimated uncertainty and $O_i^{\rm th}(V_k(r_n))$ are the theoretical results which depend on the fitting parameters $V_k(r_n)$, the values of the potentials at the sampled points r_n. The least squares minimization has always a solution which may be a global or a local minimum, namely

$$\chi^2_{\rm min} = \min_{V_k(r_n)} \chi^2[V_k(r_n)] \equiv \chi^2[\bar{V}_k(r_n)] \tag{56}$$

where $\bar{V}_k(r_n)$ the minimizing parameters. Basically, this minimization eliminates $N_{\rm Par}$ parameters from the $N_{\rm Dat}$ data and we are left with $\nu = N_{\rm Dat} - N_{\rm Par}$ degrees of freedom. The important aspect here is the *statistical significance* of the procedure. This can be checked *a posteriori* by looking at the residuals

$$R_i = \frac{O_i^{\rm exp} - O_i^{\rm th}|_{\rm min}}{\Delta O_i^{\rm exp}} \tag{57}$$

where $O_i^{\rm th}|_{\rm min} = O_i^{\rm th}(\bar{V}_k(r_n))$. According to the assumption underlying the χ^2-method, the set of variables $R_1, \ldots, R_{N_{\rm par}}$ should be distributed as normal variables, i.e., they should look as $N_{\rm Par}$ variables extracted from a normal distribution $N(0,1)$. For a finite sample the veracity of this hypothesis can only be established in probabilistic terms, so that we may estimate how likely or unlikely would it be to accept of reject the starting normality assumption. Technically, this can be done in a variety of ways (see e.g., [53, 54, 64]), but the most popular measure of goodness of a fit is the χ^2-test which requires that the fit is accepted if

$$\frac{\chi^2_{\rm min}}{\nu} = 1 \pm \sqrt{\frac{2}{\nu}} \tag{58}$$

with $\nu = N_{\rm Dat} - N_{\rm Par}$. More elaborate tests may be applied and we refer to Navarro Perez et al. [53, 54, 64] for further details. In practice this means that for $N_{\rm Dat} = 8000$ and $N_{\rm Par} = 50$ we should get $\chi^2_{\rm min}/\nu = 1 \pm 0.016$ in order to validate Equation (54). Note that this is *very different* than the loose claims in the literature where $\chi^2/\nu \approx 1$ qualifies for a good fit, complemented with a visual inspection of the phase shifts. We emphasize that *looking similar* is not the same as *statistical consistency*. In fact, a direct fit to the full database with our model gives $\chi^2_{\rm min}/\nu = 1.41$ which is 25σ away from the expected value. This clearly indicates either a bad model, inconsistent data, or both. A statistical measure of the probability that the theory is plausible is given by the p-value; assuming that the normality of residuals is correct it corresponds to the probability of obtaining results at least as extreme as the results actually observed [62, 63]. Thus, the probability of having $\chi^2_{\rm min}/\nu = 1.41$ for $\nu \sim 7000$ is $p = 10^{-20}$, which clearly rules out that the theory describes the data within fluctuations.

5.4. Inconsistent vs. Consistent Data

The determination of theoretical uncertainties requires as a prerequisite the compatibility or consistency of all data. This is a strong condition which is not always fulfilled, particularly when the number of data becomes large. Most often, different experiments have different sources of errors and are mutually incompatible. Thus, while any statistical analysis benefits from a large amount of data, a side effect is the proliferation of inconsistent data. In that case it is obvious that no model will be able to simultaneously describe all the data in a satisfactory manner. To appreciate this point more clearly, assume two experiments which yield the measurements $O_{\rm exp1} \pm \Delta O_{\rm exp1}$ and $O_{\rm exp2} \pm \Delta O_{\rm exp2}$. If the theoretical estimate is $O_{\rm th}$, we have

$$\chi^2 = \left[\frac{O_{\rm exp1} - O_{\rm th}}{\Delta O_{\rm exp1}} \right]^2 + \left[\frac{O_{\rm exp2} - O_{\rm th}}{\Delta O_{\rm exp2}} \right]^2 \tag{59}$$

Minimizing respect to $O_{\rm th}$ we get

$$\chi^2_{\rm min} = \frac{(O_{\rm exp1} - O_{\rm exp2})^2}{\Delta O^2_{\rm exp1} + \Delta O^2_{\rm exp2}} \tag{60}$$

which becomes larger than 1 for $|O_{\rm exp1} - O_{\rm exp2}| \geq \sqrt{\Delta O^2_{\rm exp1} + \Delta O^2_{\rm exp2}}$, in which case we have two *inconsistent* measurements. The important question is whether both measurements are wrong or just only one. The term wrong here does not necessarily mean an incorrect measurement; it suffices if *one* or *both* errors $\Delta O_{\rm exp1}$ and $\Delta O_{\rm exp2}$ are unrealistically small. In case of a discrepancy one may re-analyze the experiment or simply ask the experts, an unfeasible strategy for the experiments performed in the time span 1950–2013 comprising the analysis. The advantage of the statistical method is that, for a large number of experiments, the systematic errors are also randomized and one may rule out some experiments in a kind of majority vote argument.

The case discussed previously corresponds to two different measurements of the *same* observable, say the differential cross section at the same energy and angle, and the generalization to any number of experiments is straightforward. However, in the case of experiments with close kinematics there is no simple way to decide between inconsistent data unless some continuity and smooth behavior is assumed in order to intertwine the two measurements. Here is where the *model* enters and statistical methods will never tell us if a given model is correct but rather if the model is inconsistent with the data. This is a kind of circular argument which can only be avoided by looking for models which congregate as many data as possible in a consistent way. Clearly, following this criterion, once one finds a good model, any improvement of the model should describe *more data* in a statistically significant fashion. The great advantage is that if there are reasons to intertwine theoretically the different measurements of all possible observables one may discuss the data consistency in a generalized way and be able to select between different observables.

5.5. Self-Consistent Data Selection

The self-consistent criterion for data selection was proposed by Gross and Stadler [19] and implemented in Navarro Pérez et al. [45]. The way data have been selected proceeds according to the following procedure:

1. Fit the model to all data. If $\chi^2/\nu < 1$ you can stop. If not proceed further.
2. Remove data sets with improbably high or low χ^2 (3σ criterion).
3. Refit parameters for the remaining data.
4. Re-apply 3σ criterion to all data.
5. Repeat until no more data are excluded or recovered.

The effect of the selection criterion with our model is to go from $\chi^2/\nu|_{\rm all} = 1.41$ to $\chi^2/\nu|_{\rm selected} = 1.05$ with a reduction in the number of data from $N_{\rm Data} = 8173$ to $N_{\rm Data} = 6713$. While this seems a drastic rejection it is the largest self-consistent fit to date below 350 MeV. For this number of data this is *not* a minor improvement; in terms of a normality test, it makes the difference in p-value between having $p = 10^{-20}$ or $p = 0.68$.

5.6. Fitting Results

The set of 32 scattering observables which we use for the fits comprises a total of about 7000 selected measurements. It is interesting to decompose the contributions to the total χ^2 both in terms of the fitted observables as well as in different energy bins. The separation is carried out explicitly in **Tables 2**, **3** for pp and np scattering observables respectively and for the latest fit which includes also the pion-nucleon coupling constants [60, 61] (see below). As we can see the size of the contributions χ^2/N are at similar levels for most observables. Note that observables with a considerable larger or smaller χ^2/N are also observables with a small number of data and therefore larger statistical fluctuations are expected (we remind that for N *independent data* we expect $\chi^2/N \approx 1 \pm \sqrt{2/N}$.

Likewise, we can also break up the contributions in order to see the significance of different energy intervals, see **Table 4**. We find that, in agreement with the Nijmegen analysis (see [65, 66] for comparisons with previous potentials), there is a relatively large degree of uniformity in describing data at different energy bins. We note also that the fit in the low energy region below 2 MeV gives the largest values for χ^2/N.

From the optimal fitting parameters $V^\alpha(r_n)$ with $\alpha = {}^1S_0, {}^3P_0, {}^3S_1, {}^3D_1, E_1, \ldots$ being the different partial waves in a given pp or np channel, we define $(\lambda_n)^\alpha = 2\mu_{ab} V^\alpha(r_n)\Delta r$ which has units of fm^{-1} and $ab = pp, np$. In **Table 5** we show the corresponding numerical values. It would be nice to see whether something can be said about the nn interaction. However, one remarkable feature of this and similar analyses is the fact that with the exception of S-waves the short distance parameters can be chosen to coincide in the pp and np systems with common partial waves. The fact that to this date it is not possible to do it for S-waves precludes to predict the nn interaction from the combined *np* and *pp* fit (see however a theoretical discussion in Calle Cordon et al. [67]).

TABLE 4 | The χ^2 results of the main combined *pp* and *np* partial-wave analysis [60, 61] for the 10 single-energy bins in the range $0 < T_{\rm LAB} < 350$ MeV.

Bin (MeV)	N_{pp}	χ^2_{pp}	χ^2_{pp}/N_{pp}	N_{np}	χ^2_{np}	χ^2_{np}/N_{np}	N	χ^2	$\chi^2/N\|_{\rm fit}$	$\chi^2/N\|_{\rm th}$
0.0–0.5	103	107.2	1.04	46	88.2	1.92	149	195.4	1.31	1 ± 0.11
0.5–2	82	58.8	0.72	50	92.8	1.86	132	151.5	1.15	1 ± 0.12
2–8	92	80.1	0.87	122	151.0	1.24	214	231.0	1.08	1 ± 0.10
8–17	124	100.3	0.81	229	183.9	0.80	353	284.1	0.80	1 ± 0.08
17–35	111	85.5	0.77	346	324.2	0.94	457	409.7	0.90	1 ± 0.07
35–75	261	231.2	0.89	513	559.7	1.09	774	790.9	1.02	1 ± 0.05
75–125	152	154.8	1.02	399	445.2	1.12	551	600.0	1.09	1 ± 0.06
125–183	301	300.5	1.00	372	381.7	1.03	673	682.2	1.01	1 ± 0.05
183–290	882	905.0	1.03	858	841.4	0.98	1740	1746.4	1.00	1 ± 0.03
290–350	898	956.1	1.06	798	808.1	1.01	1696	1764.1	1.04	1 ± 0.03

We compare the fit $\chi^2/N|_{fit}$ with the theoretical expectation $\chi^2/N|_{th} = 1 \pm \sqrt{2/N}$.

TABLE 5 | Fitting delta-shell parameters $(\lambda_n)^{JS}_{l,l'}$ (in fm^{-1}) with their errors for all states in the *JS* channel for a fit with isospin symmetry breaking on the ${}^1S_0$ partial wave parameters only and the pion-nucleon coupling constants f_0^2, f_p^2, and f_c^2 as fitting parameters We take $N = 5$ equidistant points with $\Delta r = 0.6$ fm.

Wave	λ_1	λ_2	λ_3	λ_4	λ_5
${}^1S_{0\rm np}$	1.16(6)	-0.77(2)	-0.15(1)	–	-0.024(1)
${}^1S_{0\rm pp}$	1.31(2)	-0.716(5)	-0.192(2)	–	-0.0205(4)
${}^3P_0$	–	0.94(2)	-0.319(7)	-0.062(3)	-0.023(1)
${}^1P_1$	–	1.20(2)	–	0.075(2)	–
${}^3P_1$	–	1.354(5)	–	0.0570(5)	–
${}^3S_1$	1.79(7)	-0.47(1)	–	-0.072(2)	–
ε_1	–	-1.65(2)	-0.33(2)	-0.233(7)	-0.018(3)
${}^3D_1$	–	–	0.40(1)	0.070(9)	0.021(3)
${}^1D_2$	–	-0.20(1)	-0.206(3)	–	-0.0187(3)
${}^3D_2$	–	-1.01(3)	-0.17(2)	-0.237(6)	-0.016(2)
${}^3P_2$	–	-0.482(1)	–	-0.0289(7)	-0.0037(4)
ε_2	–	0.32(2)	0.190(4)	0.050(2)	0.0127(6)
${}^3F_2$	–	3.50(6)	-0.229(5)	–	-0.0140(5)
${}^1F_3$	–	–	0.12(2)	0.089(8)	–
${}^3D_3$	–	0.54(2)	–	–	–

$f_{\rm p}^2$	f_0^2	$f_{\rm c}^2$
0.0764(4)	0.0779(8)	0.0758(4)

– indicates that the corresponding fitting $(\lambda_n)^{JS}_{l,l'} = 0$. The lowest part of the table shows the resulting OPE coupling constants with errors.

5.7. Covariance Matrix Error Analysis and Statistical Correlations

After the data selection and fitting, error propagation becomes applicable. Here we show the results for the conventional covariance error analysis which assumes small errors and where one first determines the uncertainty in the fitting parameters $V_i(r_n)$ which will be labeled generically as λ_i for ease of notation[2].

[2]The bootstrap approach based on the MonteCarlo method [45, 68] will be discussed below.

Expanding around the minimum values, $\bar{\lambda}_i$ has

$$\chi^2 = \chi^2_{\rm min} + \sum_{ij=1}^{N_P} (\lambda_i - \bar{\lambda}_i)(\lambda_j - \bar{\lambda}_j)\mathcal{E}^{-1}_{ij} + \cdots \tag{61}$$

where the $N_P \times N_P$ error matrix is defined as the inverse of the Hessian matrix evaluated at the minimum

$$\mathcal{E}^{-1}_{ij} = \frac{1}{2}\frac{\partial^2 \chi^2}{\partial\lambda_i \partial\lambda_j}\Big|_{\lambda_i=\bar{\lambda}_i} \tag{62}$$

The correlation matrix between the fitting parameters λ_i and λ_j is given by

$$\mathcal{C}_{ij} = \frac{\mathcal{E}_{ij}}{\sqrt{\mathcal{E}_{ii}\mathcal{E}_{jj}}} \tag{63}$$

We compute the error of the parameter λ_i as

$$\Delta\lambda_i \equiv \sqrt{\mathcal{E}_{ii}}. \tag{64}$$

Error propagation of an observable depending on the fitting parameters $G = G(\lambda_1, \ldots, \lambda_P)$ is computed as

$$(\Delta G)^2 = \sum_{ij} \frac{\partial G}{\partial\lambda_i}\frac{\partial G}{\partial\lambda_j}\Big|_{\lambda_k=\lambda_{k,0}} \mathcal{E}_{ij}. \tag{65}$$

The correlation matrix, Equation (63), has been evaluated in Navarro Perez et al. [53, 54] where it has been found that for the potentials *in the partial wave basis* $V^{JS}_{l,l'}(r_n)$ the different points r_n are largely correlated within a given partial wave, whereas *different* partial waves are largely uncorrelated. This information allows to substantially speed up the minimum search as movements in the multidimensional space are thus independent and the approaching path to the minimum operates stepwise [53, 54].

5.8. Phase-Shifts

The first useful application of error propagation regards scattering amplitudes and phase shifts. Extensive tables for the selected values $T_{\rm LAB} = 1, 5, 10, 25, 50, 100, 150, 200, 250, 300, 350$ MeV have traditionally been presented since the Nijmegen analysis as representative of the fits. These energy values corresponds to a grid of almost equidistant CM momenta $p = \sqrt{T_{\rm LAB} M_N/2}$ between 0 and 2 fm^{-1}.

For illustration, **Figure 1** compares, for low angular momentum, the phase shifts of the primary PWA in Navarro Pérez et al. [42] from a fit with *fixed* pion coupling constant, f^2 (blue bands), and the most recent ones [60] (red band) from a fit with charge symmetry breaking on the $^3P_0$, $^3P_1$, and $^3P_2$ partial waves *and* in the pion coupling constants f_0^2, f_p^2, and f_c^2.

6. DETERMINATION OF YUKAWA COUPLING CONSTANTS

The first determination of the coupling constant was carried out in 1940 by Bethe who obtained the value $f^2 = 0.077 - 0.080$ from the study of deuteron properties [3] and very close to the currently accepted value (see **Table 1**). Subsequent determinations based on a variety of processes can be traced from recent compilations [69, 70]. A recent historical account has been given by Matsinos [71] where some newer determinations can be consulted according to his own eligibility criterium. For completeness we also quote recent studies based on pion-deuteron scattering [72, 73] or on the analysis of Roy equations for πN [74] where an upgrade of the corresponding scattering data is considered.

We note that what follows is a brief summary of the results presented in our previous papers where many more details may be found regarding the most influential observables, the dependence on the cut-off radius r_c, the inclusion of two-pion exchange contributions or the energy range used in the fit or the evolution with the numerical values and precision along the years [60, 61].

The πNN coupling constant is defined as the pion-nucleon-nucleon vertex when the three particles are on the mass shell. The corresponding potentials would be

$$V_{pp\to pp}(r) = f^2_{\pi^0 pp} V_{m_{\pi^0}}(r), \tag{66}$$

$$V_{np\to np}(r) = V_{pn\to pn}(r) = -f_{\pi^0 nn} f_{\pi^0 pp} V_{m_{\pi^0}}(r) \tag{67}$$

$$V_{pn\to np}(r) = V_{np\to pn}(r) = f_{\pi^- pn} f_{\pi^+ np}\, V_{m_{\pi^\pm}}(r) \tag{68}$$

$$V_{nn\to nn}(r) = f^2_{\pi^0 nn} V_{m_{\pi^0}}(r), \tag{69}$$

There exist four pion nucleon coupling constants, $f_{\pi^0 pp}$, $-f_{\pi^0 nn}$, $f_{\pi^+ pn}/\sqrt{2}$, and $f_{\pi^- np}/\sqrt{2}$ which coincide with f when up and down quark masses are identical and the electron charge is zero. In NN interactions we have access to the combinations,

$$\begin{aligned} f_n^2 &= f_{\pi^0 nn} f_{\pi^0 nn}, \\ f_p^2 &= f_{\pi^0 pp} f_{\pi^0 pp}, \\ f_0^2 &= -f_{\pi^0 nn} f_{\pi^0 pp}, \\ 2f_c^2 &= f_{\pi^- pn} f_{\pi^+ np}. \end{aligned} \tag{70}$$

While there is no reason why the pion-nucleon-nucleon coupling constants should be identical in the real world, one expects that the small differences might be pinned down from a sufficiently large number of independent and mutually consistent data. Note that from np and pp analysis we would obtain f_p^2, f_0^2, and f_c^2 we may deduce the nn coupling using the previous equations $f_n = -f_0^2/f_p$. We try to find out how many data would be needed by recalling that electroweak corrections scale with the fine structure constant $\alpha = 1/137$ and the light quark mass differences. Thus,

$$\frac{\delta g}{g} = \mathcal{O}\left(\alpha, \frac{m_u - m_d}{\Lambda_{\rm QCD}}\right) = \mathcal{O}\left(\alpha, \frac{M_p - M_n}{\Lambda_{\rm QCD}}\right) \tag{71}$$

for the relative change around a mean value. These are naturally at the $1 - 2\%$ level, a small effect. The question is on how many independent measurements N are needed to achieve this desired accuracy. According to the central limit theorem, for N

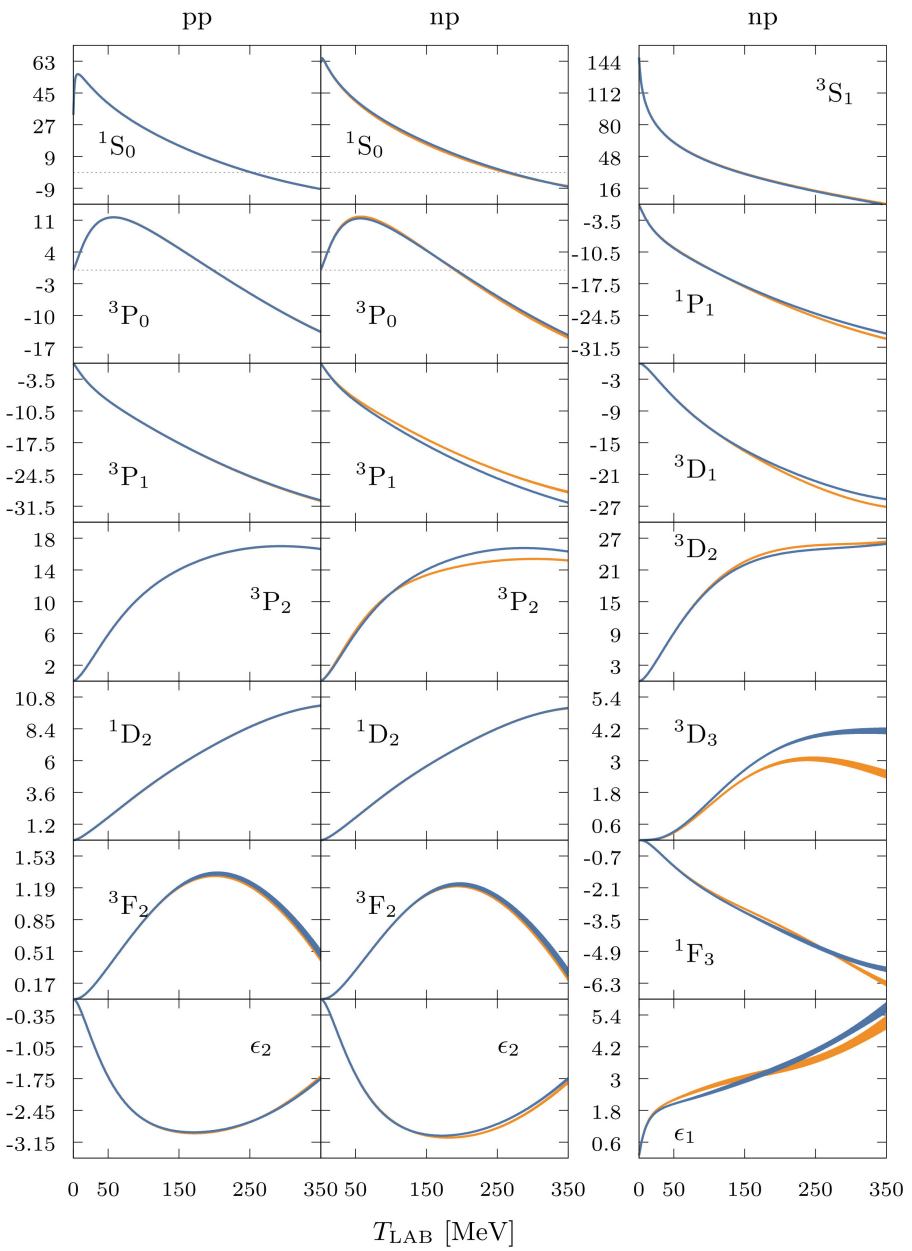


FIGURE 1 | (Color online) Phase shifts obtained from a partial waves analysis to pp and np data and statistical uncertainties. Blue band from Navarro Pérez et al. [42] from a fit with *fixed* f^2 and orange band [60] from a fit with charge symmetry breaking on the $^3P_0$, $^3P_1$, and $^3P_2$ partial waves *and* in the coupling constants f_0^2, f_p^2, and f_c^2.

direct independent measurements the relative standard deviation scales as

$$\frac{\Delta g}{g} = \mathcal{O}\left(\frac{1}{\sqrt{N}}\right)$$

and $\delta g \sim \Delta g$ for $N = 7000 - 10000$. We cannot carry out these direct measurements of g but we can proceed indirectly by considering a set of mutually consistent NN scattering measurements The most recent analysis [60, 61] based on the Granada-2013 database comprises 6713 published data. This allows: (i) to reduce the error bars, as expected and (ii) to discriminate between the three coupling constants (see **Table 6**). When charge dependence in $^1S_0$, P waves is allowed one has

$$f_p^2 = 0.0761(4), \quad f_0^2 = 0.0790(9), \quad f_c^2 = 0.0772(5), \qquad (72)$$

The most remarkable consequence is that from the point of view of the strong interaction neutrons interact more strongly than protons.

7. SYSTEMATIC VS. STATISTICAL ERRORS: THE 6 GRANADA POTENTIALS

Within the phenomenological approach the estimation of systematic errors can be addressed by using different representations of the mid-range function below the separation distance r_c while keeping the long range potential and the NN database. To this end we have analyzed 6 different potentials in Navarro Pérez et al. [75] which have been fitted to the *same* Granada 2013 database and have the *same* long distance components of the potential. First we have checked that the 6 Granada potentials are statistically acceptable. In fact, as it has been stressed in our previous works [53, 54] one can globally slightly enlarge the experimental uncertainties by the so-called Birge factor [76] provided the residuals verify a normality test. After this re-scaling the p-value becomes 0.68 for a 1σ confidence level and hence all potentials become statistically equivalent. The results are summarized in **Table 7**. Thus, the overall spread between the various phenomenological models with $\chi^2/\text{dof} \sim 1$ provides an estimate of the scale of the systematic uncertainty. A direct way of illustrating quantitatively the situation is by analyzing the corresponding phase shifts in the different analyses.

Thus, for each energy and partial wave, one evaluates the phaseshifts $\delta^{(1)}, \ldots, \delta^{(N)}$ for a representative set of high-precision NN potentials $V^{(1)}, \ldots, V^{(N)}$, and computes the average $\overline{\delta}$ and standard deviation

$$\Delta\delta = \text{Std}\,\delta = \sqrt{\frac{1}{N-1}\sum_{i=1}^{N}\left(\delta^{(i)} - \overline{\delta}\right)^2} \tag{73}$$

as a measure of the systematic uncertainty of the phaseshifts. In **Figure 2** we show the results for four different situations. To provide some historical perspective, we show in the upper left panel the averaged phase shifts, i.e., the absolute (mean-square) errors for np partial wave phase shifts due to the different potentials fitting scattering data with $\chi^2/\text{dof} \sim 1$ [15–19] as a function of the LAB energy, namely (CD Bonn) [78], Nijmegen (Nijm-I and Nijm-II) [15], Argonne AV18 [17], Reid (Reid93) [79], and the covariant spectator model [19]. As one naturally expects the average uncertainties grow with energy and decrease with the relative angular momentum which semi-classically corresponds to probing an impact parameter

$$b = \frac{L + 1/2}{p} \tag{74}$$

where p is the CM momentum, $p = \sqrt{M_N E_{\text{LAB}}/2}$, making peripheral waves to be mostly determined from OPE. These analyses stop at the pion production threshold so that one probes distances larger than

$$b_{\min} \sim 1/\Lambda = 0.5\text{fm}, \qquad \Lambda = \sqrt{m_\pi M_N}. \tag{75}$$

Note that the bumps or bulges at low energy in $^1S_0$ and $^3S_1$ channels in the top left panel are due to a unique potential which is an outlier at low energies. In particular, the authors believe that the outlier behavior is due to the use of an interpolating function used to approximate the potential between the values of laboratory energy at which phaseshifts are usually tabulated.

In the upper right panel of **Figure 2** we show the errors obtained via the standard covariance-matrix method explained above and including correlations in the fitting parameters for the primary Granada 2013 analysis [45] which corresponds to the DS-OPE potential. Thirdly, in the lower left panel we show the case of the np phase shifts for the 6 Granada potentials [45, 75, 77]. Finally, in lower right panel we present the uncertainties for all the 7 pre-Granada potentials and the 6 Granada potentials simultaneously.

TABLE 6 | The pion-nucleon coupling constants f_p^2, f_0^2, and f_c^2 determined from different fits to the Granada-2013 database and their characteristics.

f_p^2	f_0^2	f_c^2	CD-waves	χ^2_{pp}	χ^2_{np}	χ^2	N_{Dat}	N_{Par}	χ^2/ν
0.075	Idem	Idem	$^1S_0$	2997.29	3957.57	6954.86	6720	46	1.042
0.0763(1)	Idem	Idem	$^1S_0$	2995.20	3952.85	6947.05	6720	47	1.041
0.0764(4)	0.0779(8)	0.0758(4)	$^1S_0$	2994.41	3950.42	6944.83	6720	49	1.041
0.0761(4)	0.0790(9)	0.0772(5)	$^1S_0$, P	2979.37	3876.13	6855.50	6741	55	1.025

We indicate the partial waves where charge dependence is allowed.

TABLE 7 | Granada potentials summary.

Potential	N_{Par}	N_{np}	N_{pp}	χ^2_{np}	χ^2_{pp}	χ^2/d.o.f.	p-value	Normality	Birge factor
DS-OPE	46	2996	3717	3051.64	3958.08	1.05	0.32	Yes	1.03
DS-χTPE	33	2996	3716	3177.43	4058.28	1.08	0.50	Yes	1.04
DS-ΔBO	31	3001	3718	3396.67	4076.43	1.12	0.24	Yes	1.06
Gauss-OPE	42	2995	3717	3115.16	4048.35	1.07	0.33	Yes	1.04
Gauss-χTPE	31	2995	3717	3177.22	4135.02	1.09	0.23	Yes	1.05
Gauss-ΔBO	30	2995	3717	3349.89	4277.58	1.14	0.20	Yes	1.07

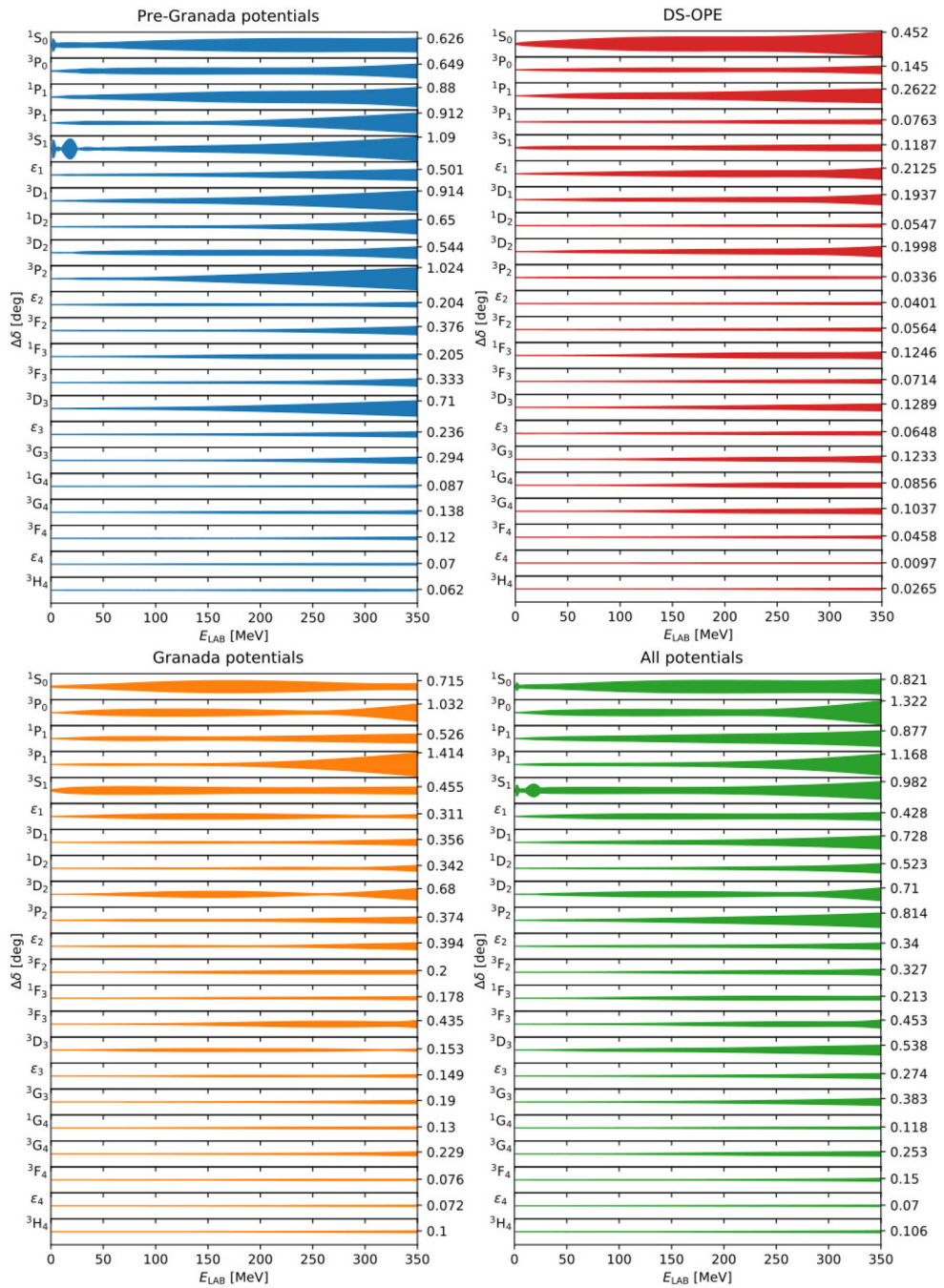


FIGURE 2 | Uncertainties (in degrees, right axis) for partial wave np phase shifts with $J \leq 4$ (left axis) for different potentials fitting scattering data with χ^2/dof ~ 1 as a function of the LAB energy (in MeV). (Upper left) Averaged errors for pre-Granada potentials [15–19]. (Upper right) Statistical errors for the primary Granada 2013 χ^2 analysis [45]. (Lower left) The averaged errors for the 6 Granada potentials [45, 75, 77]. (Lower right) Averaged errors for all 13=7 pre-Granada and the 6 Granada potentials.

In Navarro Pérez et al. [75] we found similar statistical errors in all the Granada potentials, which are statistically validated with the *same* Granada-2013 database, i.e., if the phase-shift for potential $V^{(i)}$ in a given partial wave is $\delta^{(i)} \pm \Delta\delta^{(i)}_{\rm stat}$, then

$$\Delta\delta^{(1)}_{\rm stat} \sim \cdots \sim \Delta\delta^{(6)}_{\rm stat}\,, \tag{76}$$

However, we also found that the standard deviation of systematic errors obeys

$$\Delta\delta_{\rm sys} \equiv {\rm Std}(\delta^{(1)},\ldots,\delta^{(6)}) \gg \Delta\delta^{(i)}_{\rm stat}\,. \tag{77}$$

In all the potentials, the tails *above* $r = 3$ fm (including CD-OPE and all electromagnetic effects) are the *same*, thus the discrepancies between the potentials at short distances dominate the uncertainties, rather than the np and pp experimental data themselves. This conclusion holds also when all high quality potentials are considered [75]. This counter-intuitive result relies not only on the specific forms of potentials which treat the mid– and short-range behavior of the interaction differently but also on the fact that the fits are mainly done to scattering amplitudes rather than to the phase-shifts themselves.

8. LOW ENERGY BEHAVIOR

8.1. Low Energy Parameters

The effective range expansion was proposed by Bethe [80] in order to provide a model independent characterization of the scattering at low energies where the shape of the potential is largely irrelevant. The extension to higher partial waves reads (see e.g., [81])

$$k^{2l+1}M_l(k) \equiv k^{2l+1}\cot\delta_l(k) = -\frac{1}{\alpha_l}+\frac{1}{2}r_l k^2 + v_{2,l}k^4 + v_{3,l}k^6 + \cdots \tag{78}$$

where α_l is the scattering length, r_l the effective range and $v_{i,l}$ the curvature parameters. In the case of coupled channels due to the tensor force one has that $\mathbf{S}^{JS} = (\mathbf{M}^{JS} - i\mathbf{1})(\mathbf{M}^{JS} + i\mathbf{1})^{-1}$ with $(\mathbf{M}^{JS})^\dagger = \mathbf{M}^{JS}$ a hermitian coupled channel matrix (also known as the K-matrix). At the level of partial waves the multi-pion exchange diagrams generate left hand cuts in the complex s-plane, which arise in addition to the NN elastic right cut and the πNN, $2\pi NN$ etc., pion production cuts. At low energies for $|p| \le m_\pi/2$ we have [82]

$$p^{l+l'+1}M^{JS}_{l,l'}(p) = -(\alpha^{-1})^{JS}_{l,l'} + \frac{1}{2}(r)^{JS}_{l,l'}p^2 + (v)^{JS}_{l,l'}p^4 + \ldots \tag{79}$$

which is the coupled channels effective range expansion. While at lowest orders explicit formulas where available in terms of wave functions, larger order and partial waves become rather cumbersome and no practical formula exists.

Fortunately, the variable S-matrix approach of Calogero [52] offers a unique way to extract low-energy threshold parameters for a given NN potential which was extended to coupled channels [82] and applied to the Reid93 and NijmII potentials up to $J \le 5$. For the 6 Granada potentials these have also been extracted and we have found that the systematic uncertainties are generally at least an order of magnitude larger than statistical uncertainties [75]. In **Table 8** where we provide the low energy parameters for ($J \le 2$).

8.2. Low Energy Constants

Alternatively, one may use effective interactions derived from a low momentum interaction where the coefficients can be identified with the phenomenological counter-terms of chiral effective field theory. To obtain such counter-terms we express the momentum space NN potential in the partial wave basis

$$v^{JS}_{l',l}(p',p) = (4\pi)^2\int_0^\infty dr\, r^2\, j_{l'}(p'r)j_l(pr)V^{JS}_{l'l}(r) \tag{80}$$

and use the Taylor expansion of the spherical Bessel function to get an expansion for the potential in each partial wave. Keeping terms up to fourth order $\mathcal{O}(p^4, p'^4, p^3p', pp'^3, p^2p'^2)$ corresponds to keeping only *S*-, *P*-, and *D*-waves along with *S*-*D* and *P*-*F* mixing parameters. Using the normalization and spectroscopic notation of Epelbaum et al. [84] one gets

$$\begin{aligned}
v^{JS}_{00}(p',p) &= \widetilde{C}^{JS}_{00} + C^{JS}_{00}(p^2+p'^2) + D^{1\ JS}_{00}(p^4+p'^4) + D^{2\ JS}_{00}p^2p'^2 + \cdots\\
v^{JS}_{11}(p',p) &= pp'C^{JS}_{11} + pp'(p^2+p'^2)D^{JS}_{11} + \cdots\\
v^{JS}_{22}(p',p) &= p^2p'^2D^{JS}_{22} + \cdots
\end{aligned}$$

TABLE 8 | Low energy threshold np parameters for all partial waves with $j \le 2$.

Wave	α	r_0	v_2	v_3	v_4
$^1S_0$	−23.735(6)	2.673(9)	−0.50(1)	3.87(2)	−19.6(1)
	−23.735(16)	2.68(3)	−0.48(2)	3.9(1)	−19.6(5)
$^3P_0$	−2.531(6)	3.71(2)	0.93(1)	3.99(3)	−8.11(5)
	−2.5(1)	3.7(4)	0.9(5)	3.9(1)	−8.2(9)
$^1P_1$	2.759(6)	−6.54(2)	−1.84(5)	0.41(2)	8.39(9)
	2.78(3)	−6.46(9)	−1.7(2)	0.5(2)	8.0(3)
$^3P_1$	1.536(1)	−8.50(1)	0.02(1)	−1.05(2)	0.56(1)
	1.52(1)	−8.6(1)	−0.06(7)	−0.9(2)	0.1(5)
$^3S_1$	5.435(2)	1.852(2)	−0.122(3)	1.429(7)	−7.60(3)
	5.42(1)	1.84(1)	−0.14(1)	1.46(3)	−7.7(2)
ϵ_1	1.630(6)	0.400(3)	−0.266(5)	1.47(1)	−7.28(2)
	1.61(2)	0.39(2)	−0.29(3)	1.47(2)	−7.35(9)
$^3D_1$	6.46(1)	−3.540(8)	−3.70(2)	1.14(2)	−2.77(2)
	6.43(4)	−3.57(2)	−3.77(4)	1.11(5)	−2.7(1)
$^1D_2$	−1.376	15.04(2)	16.68(6)	−13.5(1)	35.4(1)
	−1.379(6)	15.00(9)	16.7(2)	−12.9(4)	36.2(14)
$^3D_2$	−7.400(4)	2.858(3)	2.382(9)	−1.04(2)	1.74(2)
	−7.39(1)	2.87(1)	2.41(3)	−0.96(5)	1.75(8)
$^3P_2$	−0.290(2)	−8.19(1)	−6.57(5)	−5.5(2)	−12.2(3)
	−0.288(5)	−8.3(2)	−6.8(7)	−6.1(19)	−12.7(26)
ϵ_2	1.609(1)	−15.68(2)	−24.91(8)	−21.9(3)	−64.1(7)
	1.604(6)	−15.8(2)	−25.2(7)	−23.0(29)	−66.2(69)
$^3F_2$	−0.971	−5.74(2)	−23.26(8)	−79.5(4)	−113.0(16)
	−0.971(5)	−5.7(1)	−23.3(6)	−80.1(33)	−117.2(121)

The central value and statistical *error bars are given on the first line of each partial wave and correspond to the mean and standard deviation of a population of* 1020 *parameters calculated with the Monte Carlo family of potential parameters described in Navarro Pérez et al. [83] using the DS-OPE potential [42, 45]. The second line quotes the systematic uncertainties, the central value and error bars correspond to the mean and standard deviation of the 9 realistic potentials NijmII [16], Reid93 [16], AV18 [17], DS-OPE [42, 45], DS-χTPE [48, 77], Gauss-OPE [53], Gauss-χTPE, DS-ΔBO, and Gauss-ΔBO. For each partial wave we show the scattering length α and the effective range r_0, both in fm$^{l+l'+1}$, as well as the curvature parameters v_2 in fm$^{l+l'+3}$, v_3 in fm$^{l+l'+5}$, and v_4 in fm$^{l+l'+5}$. For the coupled channels we use the nuclear bar representation of the S matrix. Uncertainties smaller than* 10^{-3} *are not quoted.*

$$v_{20}^{JS}(p',p) = p'^2 C_{20}^{JS} + p'^2 p^2 D_{20}^{1\,JS} + p'^4 D_{20}^{2\,JS} + \dots$$
$$v_{31}^{JS}(p',p) = p'^3 p D_{31}^{JS} + \cdots \quad (81)$$

and each counter-term can be expressed as a radial momentum of the NN potential in a specific partial wave. Different methods have been proposed to quantify some of the uncertainties in these quantities [85, 86]. Using the statistical uncertainties method and the corresponding systematic error estimates [87], the results are summarized in **Table 9** for the 6 Granada potentials.

8.3. Scale Dependence and Correlations

While one normally uses a *fixed* value for the maximum energy in the fits (which in most NN studies has been 350 MeV), one may analyze the consequences of varying this fitting energy [88]. Denoting Λ as the (running) maximal momentum it is clear that the fitting potential will change as Λ is varied. Actually, these parameters may be mapped [54] into the so-called counter-terms which characterize the effective theories at small momenta [89]. We determined the two-body Skyrme force parameters arising from the NN interaction as a function of the maximal momentum in the fit. We found general agreement with the so-called $V_{\rm lowk}$ interactions based on high quality potentials after high energy components have been integrated out [90, 91].

In line with our remarks in section 5.7 let us note that, one major outcome of Navarro Pérez et al. [54] has been the fact that the counter-terms corresponding to volume integrals including OPE above 3 fm are weakly correlated, whereas those including OPE+TPE above 1.8 fm have larger but still moderate correlations. Thus, counter-terms in the partial waves basis would be efficient fitting parameters, unlike in the cartesian basis. As we have already discussed, using uncorrelated fitting parameters has the practical consequence of reducing the computational determination of the least squares minimization.

9. CHIRAL VS. NON-CHIRAL POTENTIALS

In common with the analysis presented in the previous sections, much of the early work on phase-shift analysis was undertaken long before the advent of QCD, so the NN potentials were at most considered to be derivable from Quantum Field Theory in purely hadronic terms. This implies in particular the One-Pion-Exchange potential, which has survived over the years, and the Two-Pion-Exchange which has been changing depending on the computational scheme since the first attempts in the early 50's (see e.g., Machleidt [14] for a historical review, in particular about the meson exchange picture).

TABLE 9 | Potential integrals in different partial waves.

	DqS-OPE	DS-χTPE	DS-Born	Gauss-OPE	Gauss-χTPE	Gauss-Born	Compilation
$\widetilde{C}_{^1S_0}$	–0.141(1)	–0.135(2)	–0.128(2)	–0.121(5)	–0.113(9)	–0.133(3)	–0.13(1)
$C_{^1S_0}$	4.17(2)	4.12(2)	4.04(1)	4.20(2)	4.16(2)	4.18(1)	4.15(6)
$D^1_{^1S_0}$	–448.8(11)	443.7(5)	–441.5(3)	–447.0(10)	–446.7(2)	–446.3(2)	–445.7(26)
$D^2_{^1S_0}$	–134.6(3)	–133.1(1)	–132.46(4)	–134.1(3)	–134.02(7)	–133.90(7)	–133.7(8)
$\widetilde{C}_{^3S_1}$	–0.064(2)	–0.038(1)	–0.039(1)	–0.070(2)	–0.019(6)	–0.038(4)	–0.045(19)
$C_{^3S_1}$	3.79(1)	3.55(1)	3.52(1)	4.09(2)	3.785(9)	3.724(9)	3.7(2)
$D^1_{^3S_1}$	–510.7(3)	–504.7(4)	–504.1(2)	–516.7(6)	–509.7(1)	–508.2(1)	–509.0(46)
$D^2_{^3S_1}$	–153.2(1)	–151.4(1)	–151.22(6)	–155.0(2)	–152.90(3)	–152.47(3)	–152.7(14)
$C_{^1P_1}$	6.44(2)	6.54(1)	6.464(6)	6.37(2)	6.529(7)	6.488(7)	6.47(6)
$D_{^1P_1}$	–594.9(2)	–592.1(2)	–590.21(6)	–594.5(2)	-597.83(7)	-596.25(7)	-594.3(28)
$C_{^3P_1}$	3.738(2)	3.659(3)	3.633(3)	3.762(6)	3.677(3)	3.599(1)	3.68(6)
$D_{^3P_1}$	–253.29(5)	–249.8(2)	–249.62(7)	–254.23(9)	-251.0(2)	-251.06(2)	-251.5(19)
$C_{^3P_0}$	–4.911(8)	–4.882(5)	–4.897(3)	–4.944(6)	–4.802(8)	–4.883(2)	–4.89(5)
$D_{^3P_0}$	347.0(2)	343.6(2)	344.62(6)	345.8(1)	345.02(3)	346.25(2)	345.4(12)
$C_{^3P_2}$	–0.445(2)	–0.434(3)	–0.426(2)	–0.426(2)	–0.448(1)	–0.427(1)	–0.43(1)
$D_{^3P_2}$	–10.62(7)	–9.7(2)	-9.45(6)	–11.55(4)	–9.939(8)	–9.631(7)	–10.1(8)
$D_{^1D_2}$	–70.92(3)	–70.66(6)	–70.52(3)	–70.58(3)	-7-1.109(7)	–71.074(5)	–70.8(3)
$D_{^3D_2}$	–367.8(2)	–364.39(7)	–364.54(4)	–367.19(8)	–367.10(2)	–366.99(1)	-366.3(15)
$D_{^3D_1}$	205.8(2)	204.25(7)	204.26(4)	204.4(1)	205.17(3)	205.21(3)	204.9(6)
$D_{^3D_3}$	0.55(1)	0.87(6)	0.90(4)	–0.32(9)	0.26(3)	0.51(3)	0.46(45)
C_{ϵ_1}	–8.36(2)	–8.500(4)	–8.492(4)	–8.35(1)	–8.404(4)	–8.399(5)	–8.42(7)
$D^1_{\epsilon_1}$	1012.6(6)	1005.5(1)	1006.23(6)	1010.5(3)	1011.83(5)	1012.71(6)	1009.9(32)
$D^2_{\epsilon_1}$	434.0(3)	430.94(4)	431.24(3)	433.1(1)	433.64(2)	434.02(2)	432.8(14)
D_{ϵ_2}	84.18(4)	83.29(1)	83.398(7)	84.25(3)	83.660(5)	83.818(8)	83.8(4)

Errors quoted for each potential are statistical; errors in the last column are systematic and correspond to the sample standard deviation of the six previous columns. See main text for details on the calculation of systematic errors. Units are: $\widetilde{C}$'s are in 10^4 GeV^{-2}, C's are in 10^4 GeV^{-4}, and D's are in 10^4 GeV^{-6}.

After the appearance of QCD as a fundamental theory of strong interactions there emerged dedicated studies on the underlying quark dynamics in terms of quark cluster models, particularly concerning the origin of the nuclear core (see e.g., [92–94] and references therein). Despite the numerous attempts it is fair to say that these investigations did provide some microscopic and quantitative understanding of the short range components of the interaction but did not offer an alternative to the conventional partial wave analysis. Current QCD potentials determined on the lattice [36–38, 44], are still less precise than phenomenological ones.

In the early 90's Weinberg [95] (see e.g., [96–98] for comprehensive reviews and references therein) proposed an Effective Field Theory (EFT) approach to NN scattering based on chiral symmetry directly inspired by QCD features, where the spontaneous breakdown of chiral symmetry underlies the would-be Goldstone boson nature of the pion. As compared to the phenomenological approaches, the attractive pattern of such an EFT was also the natural hierarchy of n-body forces and the possibility of making an *a priori* estimate of the systematic uncertainties in terms of a power counting to different orders. This happened at about the time when the phenomenological approach harvested its great success when the Nijmegen group obtained for the first time a statistically acceptable $\chi^2/\nu \sim 1$ by fitting and selecting np+pp scattering data. Comprehensive fits to data with chiral interactions have been made using the N2LO chiral potentials [99] to the Nijmegen database [15] for pp [100] and for pp+np [101] and the N3LO chiral potential [102] to the enlarged database [18] for np [103]. The newest generation of chiral potentials have already provided fits to the Granada-2013 database [40, 48, 77, 104–108].

9.1. Statistical Issues

Very recently chiral potentials to sixth order in the chiral expansion have been been claimed by the Bochum group to outperform the non-chiral potentials on the basis of the Granada-2013 database [107]. This was a major achievement of the chiral approach (see also [108] for a momentum space approach of the Idaho-Salamanca group). Another great advantage of the chiral approach is that the number of fitting parameters is substantially smaller than in the phenomenological approach. In no case, however, have the authors taken seriously the available statistical tests to verify *a posteriori* the normality of residuals.

Within the uncertainty quantification context, a critical analysis with an eye on the future developments has been put forward in Ruiz Arriola et al. [109] and Navarro Perez and Ruiz Arriola [43]. It has been suggested that a further order in the expansion, namely N5LO, might quite likely achieve the desired statistical consistency. At the present state, however, there are still some pending, hopefully manageable, issues which need to be resolved before the validation of the chiral approach to NN scattering can be declared without reservations.

9.2. The Chiral Tensorial Structure

For instance, the tensorial structure of the force requires phenomenologically that all allowed NN components should contribute to some extent to the total NN potential. Chiral perturbation theory proposes a hierarchy among the different components so that the chiral W_Q component vanishes to N4LO, unlike all the phenomenological analyses so far [43]. In addition, the number of independent parameters in a scheme where W_Q would be non-vanishing becomes comparable to the phenomenological potentials.

9.3. Peripheral Waves

One of the reasons why the coupling constants discussed in section 6 can be pinned down so accurately [60, 61] is given by the fact that long distant physics is rather well-determined. From that point of view one expects that peripheral waves are rather sensitive to the shape of the potential and hence become independent of the short range components. This also provides a method to validate other analyses and in particular chiral potentials. A very vivid way of presenting the discrepancy is by comparing the phase-shifts in terms of the impact parameter variable [110] (see Equation 74) for every partial wave

$$\xi^{\rm N4LO}(b) = \left. \frac{\delta_l^{\rm N4LO} - {\rm Mean}(\delta_l)}{{\rm Std}(\delta_l)} \right|_{l+1/2=bp}, \qquad (82)$$

which provides a measure of the discrepancy with respect to a set of phase-shifts (see **Figure 2** for a plot of different sets). The conclusion of Simo et al. [110] is quite unequivocal: In the range 2 fm $\leq b \leq$ 5 fm the $\delta^{\rm N4LO}$ differ by more than 3σ when compared to the primary Granada 2013 analysis for F, G, and H waves, and become 1σ compatible with the spread of the 13 high quality potentials.

9.4. Perturbation Theory for Higher Partial Waves

The long distance character of chiral potentials suggests that one may determine the high peripheral partial waves in perturbation theory, as done explicitly in Entem et al. [111]. Actually, the low energy parameters discussed above in section 8.1 probe the longest distance features of a given partial wave. Going to N2LO one sees that, while there is some rough agreement between the perturbative and the full low energy parameters, the detailed comparison including both statistical and systematic errors do not agree. Using the perturbative version of the variable phase approach, a perturbative evaluation [43] in the context of chiral TPE (N2LO in the chiral expansion) was also undertaken and shown *not* to converge to the exact result within uncertainties, even at the largest angular momenta and hence for the most peripheral waves.

9.5. Coarse Graining Chiral Potentials

Chiral potentials can be combined with coarse graining in a statistically consistent way [48, 48, 77, 104]. This allows for a reduction of parameters to about 30 since the separation distance can be made as small as $r_c = 1.8$ fm without spoiling the statistical analysis. This approach assumes the chiral power counting for the potential *above* r_c but not in the coarse grained region so that the all the potential components (including the chirally missing W_Q) are non-vanishing, and taking $f^2 = 0.0075$ has provided natural values for the chiral constants $(c_1, c_3, c_4) =$

$(-0.41 \pm 1.08, -4.66 \pm 0.60, 4.31 \pm 0.17)\text{GeV}^{-1}$ for $T_{\rm LAB} \leq$ 350MeV [48, 77].

In contrast, the canonical (Weinberg) power counting scheme applies to the *full* potential and only to at least N5LO provides all non-vanishing tensorial components ($W_Q = 0$ at N4LO), in which case the number of parameters becomes comparable with the phenomenological approach. As emphasized in Navarro Perez and Ruiz Arriola [43], the end of the chiral road-map in NN scattering based on the power counting will definitely occur when such a scheme becomes reliable enough to select and fit scattering data, without explicit reference to the phenomenological approach.

10. BINDING IN LIGHT NUCLEI: ERROR PROPAGATION

Much of the previous analysis may be used to analyze the impact of NN scattering uncertainties to binding energies. A precursor of this type of calculations was carried out in Adam et al. [21] where estimates on binding uncertainties were carried out using a statistical regularization of phases and a direct solution of the inverse scattering problem.

10.1. On-Shell vs. Off-Shell

NN Scattering data describe only the behavior of nucleons on-shell, i.e., with $E_p = \sqrt{p^2 + M^2}$ in the relativistic case. However, nuclear structure calculations usually need also the corresponding off-shell components so that when going from the NN scattering data to the binding energy calculation some extra information would be needed [35]. This ambiguity can be used in fact to our benefit, since ideally one would determine the off-shellness from the determination of the finite nuclei properties. The successful attempts by Vary et al. are a good demonstration of that [112, 113]

10.2. Computational vs. Physical Precision

Let us review the sources of numerical precision in the solution of the quantum-mechanical problem. In the simplest NN case, where we usually solve numerically the two-body Schrödinger equation, the precision is fixed by the precision in the wave function. In the positive energy situation corresponding to a scattering state we are rather interested in the determination of the scattering phase-shifts.

Within the few-body community there has been a trend to determine the quantum mechanical solution with an increasing pre-defined precision, say, a 1%. This is a pure conventional precision which has been a goal *per se* and, of course, good precision is not disturbing provided the computational cost does not scale up to an unbearable limit where the calculation becomes unfeasible. However, this does not correspond to the *physical* precision where all necessary effects are taken into account and which determines in fact the predictive power of the theory.

10.3. Monte Carlo Method

The normality property of the residuals has been exploited to extract the effective interaction parameters and corresponding counter-terms [54] and to replicate via Monte Carlo bootstrap simulation as a mean to gather more robust information on the uncertainty characteristics of fitting parameters [83]. We stress that the verification of normality, Equation (54), is essential for a meaningful propagation of the statistical error, since the uncertainty inherited from the fitted scattering data $\Delta O_i^{\rm exp}$ corresponds to a genuine statistical fluctuation. This allows to determine the 1σ error of the parameters $\mathbf{p} = \mathbf{p}_0 \pm \Delta\mathbf{p}^{\rm stat}$ and hence the error in the potential

$$V_{NN} = V_{NN}(\mathbf{p}_0) \pm \Delta V_{NN}^{\rm stat} \tag{83}$$

which generates in turn the error in the NN phase-shifs $\delta = \delta(\mathbf{p_0}) \pm \Delta\delta^{\rm stat}$ and mixing angles. Once the NN-potential is determined the few body problem can be solved for the binding energy,

$$\left[\sum_i T_i + \sum_{i<j} V_{NN}(ij)\right]\Psi = E_A\Psi \tag{84}$$

where

$$E_A = E_A(\mathbf{p}_0) \pm \Delta E_A^{\rm stat}\,. \tag{85}$$

Direct methods to determine $\Delta\mathbf{p}^{\rm stat}$, $\Delta V_{NN}^{\rm stat}$ and $\Delta E_A^{\rm stat}$ proceed either by the standard error matrix or Monte Carlo methods (see e.g., [68]). In Navarro Pérez et al. [83] we have shown that the latter method is more convenient for large number of fitting parameters (typically $N_P = 40 - 60$), and consists of generating a sufficiently large sample drawn from a multivariate normal probability distribution

$$P(p_1, p_2, \ldots, p_P) = \frac{1}{\sqrt{(2\pi)^{N_P}\det\mathcal{E}}} e^{-\frac{1}{2}(\mathbf{p}-\mathbf{p}_0)^T\mathcal{E}^{-1}(\mathbf{p}-\mathbf{p}_0)}, \tag{86}$$

where $\mathcal{E}_{ij} = (\partial^2\chi/\partial p_i\partial p_j)^{-1}$ is the error matrix. We generate M samples $\mathbf{p}_\alpha \in P$ with $\alpha = 1, \ldots, M$, and compute $V_{NN}(\mathbf{p}_\alpha)$ from which the corresponding scattering phase shifts $\delta(\mathbf{p}_\alpha)$ and binding energies $E_A(\mathbf{p}_\alpha)$ can be determined. Of course, one drawback of the MonteCarlo propagation method is that the object function, in this case the energy, needs to be evaluated a sufficiently large number of times which may be unduly time consuming. An analysis of statistical errors at the phase shift level shows that $M = 25$ may be sufficient to reproduce consistently the covariance matrix uncertainties from the MonteCarlo method.

10.4. The Deuteron

The deuteron is the simplest bound nuclear np system for which the theory has long been developed [114]. Its quantum numbers $J^P = 1^+$ correspond to the coupled ${}^3S_1 - {}^3D_1$ channel with reduced wave functions $u(r)$ and $w(r)$ respectively, so that we solve the bound state problem with $E_d = -B_d = -\gamma^2/2\mu_{np}$, i.e., with $p = i\gamma$. At long distances

$$u(r) \to A_S e^{-\gamma r}, \qquad w(r) \to \eta A_S e^{-\gamma r}\left[1 + \frac{3}{\gamma r} + \frac{3}{(\gamma r)^2}\right] \tag{87}$$

For normalized states we list in **Table 10** the asymptotic D/S ratio η, asymptotic S-wave amplitude A_S, mean squared matter radius r_m, quadrupole moment Q_D, D-wave probability P_D and inverse matter radius $\langle r^{-1} \rangle$ for some high quality potentials compared with two Granada potentials, DS-OPE [45], DS-TPE [77]. The PWA analysis indeed uses its binding energy as a fitting parameter, so that the quoted uncertainties are purely statistical. Unlike r_m, Q_D, or P_D which require (small) meson exchange currents corrections before being compared to experimental data, A_S and η are purely hadronic. As we see, both the DS-OPE [77] DS-TPE [77] provide *smaller* uncertainties than the experimental/recommended values for A_S and η. To our knowledge, this is an unprecedented situation in Nuclear Physics. Similar trends are also observed for the corresponding deuteron charge, magnetic and quadrupole form factors (see e.g., [121] for a review) where DS-OPE [45] and DS-TPE [77, 122] generate tiny uncertainties and offer an opportunity to discriminate meson exchange currents contributions.

10.5. Binding Energies for A = 3,4 Systems

The primary Granada DS-OPE potential which was used to fit and select np+pp scattering data uses Dirac delta-shells which are too singular in configuration space or have too long momentum tails, for instance in the deuteron [26], to be handled in few body calculations. Actually, this was the reason to design smooth SOG (Sum of Gaussian) potentials [53, 75] referenced in section 7.

In Navarro Perez et al. [24] the triton binding energy was evaluated for the SOG-OPE Granada potential using the hyperspherical harmonics method with $M \sim 200$ MonteCarlo replicas, and statistical distributions where also obtained yielding $\Delta E_t = 12$ KeV. One motivation for such a calculation was to determine if the computational accuracy was unnecessarily better than the statistical accuracy inherited from the NN scattering data. Our points are illustrated in **Table 11** from Navarro Perez et al. [24] where the numerical convergence regarding the number of partial waves is displayed. The error estimate clearly marks where the accuracy of the numerical calculation is larger than the physical accuracy.

The statistical uncertainty of experimental NN scattering data have also been propagated into the binding energy of ^{3}H and ^{4}He using the no-core full configuration method in a sufficiently large harmonic oscillator basis. The error analysis [26] yields $\Delta B_t = 15$ KeV and $\Delta B_\alpha = 55$ KeV.

Similar patterns occur when solving the Faddeev equations for ^{3}H and the Yakubovsky equations for ^{4}He respectively [25]. We check that in practice about $M = 30$ samples prove enough for a reliable error estimate within the MonteCarlo method, giving $\Delta B_t = 12$ KeV and $\Delta B_\alpha = 50$ KeV whereas, again, the computational accuracy is better, $\Delta B_t^{\rm num} = 1$ KeV and $\Delta B_\alpha^{\rm num} = 20$ KeV.

Results for the 3N and 4N binding energies for various NN potentials using the Faddeev equations for ^{3}H and the Yakubovsky equations for ^{4}He are listed in **Table 12** where we see a systematic underbinding with respect to the experimental values. A popular interpretation of this disagreement suggests that the influence of three- and four-body forces has been neglected. However, the contribution of three body forces depends on the definition of two body forces as we will discuss next.

10.6. The Tjon Line

Much of the error analysis which can and has been carried out in Nuclear Physics is probably best exemplified by the so called Tjon

TABLE 11 | Triton binding energy convergence for the hyper-spherical harmonics method [24] in the number of channels, N_c, classified according to the orbital angular momentum of the pair $L_{\rm Pair}$ and the spectator $l_{\rm spectator}$ in the triton as the number of total accumulated channels, $N_{\rm Total}$, is increased.

N_c	$L_{\rm Pair}$ $l_{\rm Spectator}$	$N_{\rm Total}$	Energy (MeV)
3	Ss	3	Unbound
+2	Sd+Ds	5	–7.0117
+10	Pp	15	–6.4377
+8	Dd	23	–7.4109
+4	Pf+Fp	27	–7.4956
+10	Ff	37	–7.5654
+2	Dg+Gd	39	–7.6178
+8	Gg	47	–7.6502
+4	Fh+Hf	51	–7.6508
+10	Hh	61	–7.6510

The potential used was Monte Carlo generated. A horizontal line is drawn when the change in E_t is smaller than the statistical uncertainty $\Delta B_t = 15(1)$ keV.

TABLE 10 | Deuteron static properties compared with empirical/recommended values [115–120] and high-quality potentials calculations, DS-OPE [45], DS-TPE [77], Nijm I [16], Nijm II [16], Reid93 [16], AV18 [17], CD-Bonn [18].

	Emp./Rec.	DS-OPE	DS-TPE	Nijm I	Nijm II	Reid93	AV18	CD-Bonn
E_d(MeV)	2.224575(9)	Input	Input	Input	Input	Input	Input	Input
η	0.0256(5)	0.02493(8)	0.02473(4)	0.02534	0.02521	0.02514	0.0250	0.0256
A_S(fm$^{1/2}$)	0.8845(8)	0.8829(4)	0.8854(2)	0.8841	0.8845	0.8853	0.8850	0.8846
r_m(fm)	1.971(6)	1.9645(9)	1.9689(4)	1.9666	1.9675	1.9686	1.967	1.966
Q_D(fm^2)	0.2859(3)	0.2679(9)	0.2658(5)	0.2719	0.2707	0.2703	0.270	0.270
P_D	5.67(4)	5.62(5)	5.30(3)	5.664	5.635	5.699	5.76	4.85
$\langle r^{-1} \rangle$(fm^{-1})		0.4540(5)	0.4542(2)		0.4502	0.4515		

We list binding energy E_d, asymptotic D/S ratio η, asymptotic S-wave amplitude A_S, mean squared matter radius r_m, quadrupole moment Q_D, D-wave probability P_D, and inverse matter radius $\langle r^{-1} \rangle$.

TABLE 12 | 3N and 4N binding energies for various NN potentials using the Faddeev equations for ^{3}H and the Yakubovsky equations for ^{4}He respectively [25, 123].

Potential	Exp.	SOG-OPE	CD Bonn	AV18	Nijm I	Nijm II	Nijm93
^{3}H [MeV]	−8.4820(1)	−7.660(12)	−8.012	−7.623	−7.736	−7.654	−7.668
^{4}He [MeV]	−28.2957(1)	−24.760(47)	−26.26	−24.28	−24.98	−24.56	−24.53

Errors in SOG-OPE are statistical.

line [34], a linear but empirical correlation between the triton and α-particle binding energies of the form

$$B_\alpha = aB_t + c \tag{88}$$

where a, c depend on a family of NN potentials which have the *same* NN scattering phase shifts and deuteron properties. Thus, the slope may be schematically be written as $a = (\partial B_\alpha/\partial B_t)|_{B_d}$. This empirical feature [124, 125] comparing between phase-equivalent potentials has been corroborated by many calculations ever since [123, 126, 127]. It is remarkable that such a simple property has no obvious explanation. One clue would be the fact that the deuteron binding energy, $B_d = 2.2$ MeV, is small compared to the triton and alpha bindings [128]. For small B_d the alpha binding energy then would scale as $B_\alpha = aB_t + bB_d + \mathcal{O}(B_d^2)$. The points along this line in the plane (B_t, B_α) correspond to potentials with the same phase-shifts, verifying $\Delta B_\alpha = a\Delta B_t$ The points along a perpendicular line, $\Delta B_\alpha = -1/a\Delta B_t$ should correspond to potentials with very different phase-shifts. In particular the difference may be generated by a unitary transformation of the NN potential, $V_2 \to UV_2U^\dagger$, so that the bindings depend on U but the coefficients a and b do not depend on U [123]. On the other hand, a unitary transformation of the *two-body* potential implies a change in multi-nucleon forces, V_3, V_4, etc. and, one may actually fit E_t with a suitable V_3 and E_α with a suitable V_4 yielding for $V_4 = 0$ in the so-called on-shell limit the formula $B_\alpha = 4B_t - 3B_d$ which works well [129, 130].

Phase equivalent interactions produce a Tjon slope which is typically about $\Delta B_\alpha/\Delta B_t \sim 5 - 6$ both in the Faddeev-Yakubovsky [126] and in the no-core shell model [131]. For the Faddeev-Yakubovsky solutions of ^{3}H-^{4}He the results from five high quality potentials, i.e., with $\chi^2/\nu \sim 1$ at their time and the Granada SOG-OPE, in **Table 12** give $B_\alpha = 4.73B_t - 5.26B_d$. For a sample of SOG-OPE potentials the statistical bootstrap analysis with $M = 30$ gives $B_\alpha = 4.8(1)B_t - 5.4(3)B_d$, where the central values reflect the actual scattering data and the uncertainties reflect the truly phase-inequivalent fluctuations. The extrapolation predicts the experimental binding of the alpha particle within uncertainties [25], since

$$\Delta B_\alpha^2|_{\rm stat} = (\Delta a)^2 B_t^2 + (\Delta b)^2 B_d^2 \tag{89}$$

so that $\Delta B_\alpha|_{\rm stat} \sim 1$MeV. Interestingly, this suggests a marginal effect of four body forces, for which independent estimates using approximate wave functions [132] give similar numbers, $B_\alpha|_{4N} \sim -100$ KeV (see also Epelbaum [133] for a chiral scheme where this is argued to overestimate the result). Thus, we see that since $B_\alpha|_{4N} \sim \Delta B_\alpha^{\rm stat}$ the four-body force might be unobservable. While this is good news from the theoretical point of view, more detailed calculations might be needed to confirm this feature. Finally, let us also mention that along these lines, theoretical uncertainties of the elastic nucleon-deuteron scattering observables have been undertaken [27].

11. EFFECTIVE NUCLEAR INTERACTIONS

11.1. Moshinsky-Skyrme Parameters

Power expansions in momentum space of effective interactions were introduced by Moshinsky [134] and Skyrme [135] to provide significant simplifications to the nuclear many body problem in comparison with the *ab initio* approach, in which it is customary to employ phenomenological interactions fitted to NN scattering data to solve the nuclear many body problem. As a consequence of such simplifications effective interactions, also called Skyrme forces, have been extensively used in mean field calculations [136–139]. Within this framework the effective force is deduced from the elementary NN interaction and encodes the relevant physical properties in terms of a small set of parameters. However, there is not a unique determination of the Skyrme force and different fitting strategies result in different effective potentials (see e.g., [140] and [141]). This diversity of effective interactions within the various available schemes signals a source of statistical and systematic uncertainties that remain to be quantified. Fortunately the parameters determining a Skyrme force can be extracted from phenomenological interactions [88, 142] and uncertainties can be propagated accordingly [54]. At the two body level the Moshinsky-Skyrme potential in momentum representation reads

$$\begin{aligned} V_\Lambda(\mathbf{p}', \mathbf{p}) &= \int d^3x e^{-i\mathbf{x}\cdot(\mathbf{p}'-\mathbf{p})} \hat{V}(\mathbf{x}) \\ &= t_0(1 + x_0P_\sigma) + \frac{t_1}{2}(1 + x_1P_\sigma)(\mathbf{p}'^2 + \mathbf{p}^2) \\ &+ t_2(1 + x_2P_\sigma)\mathbf{p}' \cdot \mathbf{p} + 2iW_0\mathbf{S} \cdot (\mathbf{p}' \times \mathbf{p}) \\ &+ \frac{t_T}{2}\left[\sigma_1 \cdot \mathbf{p}\,\sigma_2 \cdot \mathbf{p} + \sigma_1 \cdot \mathbf{p}'\,\sigma_2 \cdot \mathbf{p}'\right. \\ &\left. -\frac{1}{3}\sigma_1 \cdot \sigma_2(\mathbf{p}'^2 + \mathbf{p}^2)\right] \\ &+ \frac{t_U}{2}\left[\sigma_1 \cdot \mathbf{p}\,\sigma_2 \cdot \mathbf{p}' + \sigma_1 \cdot \mathbf{p}'\,\sigma_2 \cdot \mathbf{p} - \frac{2}{3}\sigma_1 \cdot \sigma_2\mathbf{p}' \cdot \mathbf{p}\right] \\ &+ \mathcal{O}(p^4) \end{aligned} \tag{90}$$

where $P_\sigma = (1 + \sigma_1 \cdot \sigma_2)/2$ is the spin exchange operator with $P_\sigma = -1$ for spin singlet $S = 0$ and $P_\sigma = 1$ for spin triplet $S = 1$ states. These parameters correspond to radial moments of volume integrals of the potentials $\int_0^\infty d^3x r^n V_i(r)$ which are increasingly insensitive to short distances.

As mentioned above different nuclear data can be used to constrain the Skyrme potential. The usual approach is to fit parameters of Equation (90) to doubly closed shell nuclei and nuclear matter saturation properties [136–139]. In Ruiz Arriola [142] the parameters were determined from just NN threshold properties such as scattering lengths, effective ranges

and volumes without explicitly taking into account the finite range of the NN interaction; while in Navarro Perez et al. [88] the parameters were computed directly from a local interaction in coordinate space that reproduces NN elastic scattering data. In Navarro Pérez et al. [54] the latter approach was used to propagate *statistical* uncertainties into the Skyrme parameters. The quantification of the *systematic* uncertainties, which arise from the different representations of the NN interaction was discussed in Navarro Perez et al. [87]. The results, summarized in **Table 13** clearly show, again, the dominance of systematic vs statistical errors.

11.2. Error Estimates for Heavy Nuclei and Nuclear Matter

Within the Skyrme effective interactions approach one can find a simple estimate of systematic errors due to the two body interaction uncertainty using (for a review see [139])

$$\frac{\Delta B}{A} = \frac{3}{8A}\Delta t_0 \int d^3x\, \rho(x)^2, \tag{91}$$

For nuclear matter at saturation, $\rho_0 = 0.17\text{fm}^{-3}$, our $\Delta t_0 = 75\text{MeV fm}^3$ implies

$$\frac{\Delta B}{A} = \frac{3}{8}\Delta t_0 \rho_0 = 2.4\text{MeV}. \tag{92}$$

We may implement finite size effects in light-heavy nuclei by using a Fermi-type shape for the matter density

$$\rho(r) = C/(1 + e^{(r-R)/a}) \tag{93}$$

with $R = r_0 A^{\frac{1}{3}}$, $r_0 = 1.1\,\text{fm}$ and $a = 0.7\,\text{fm}$, Normalizing to the total number of particles $A = \int d^3x\rho(x)$ we get values in the range

$$\Delta B_A/A = 0.4 - 1.6\text{MeV}, \tag{94}$$

depending on the value of A for $4 \leq A \leq 208$.

12. COARSE GRAINED POTENTIAL RESULTS

Besides the aspect of uncertainty quantification which is the focus of the present work, we believe that the very idea of coarse graining proves useful in nuclear physics. This requires that special methods have to be developed for delta–shells interaction, which in our view are the most flexible ones which allow for selecting and fitting the largest NN database to date, but cannot be plugged directly in conventional computing codes dealing with nuclear structure and reactions, and hence smooth potentials (such as the SOG-Granada type potentials) need to be defined *after* the data selection process. This is similar to what happened with the energy dependence needed by the Nijmegen group which also led to subsequent high quality interactions. We discuss here some simple examples where delta-shells may be used *directly*.

12.1. Repulsive vs. Structural Core

Besides the well-accepted OPE mechanism for long distances and the mid-range attraction which is needed for nuclear binding, one of the traditional and well-accepted properties of the nuclear potential is the existence of a nuclear strongly repulsive core at about 0.5 fm. While this feature guarantees the stability of nuclei and nuclear matter against collapse it also complicates the solution of the many body problem, since the relative NN wave function must vanish below the core, therefore introducing a very strong short range correlation. At a practical level the existence of the core implies a vanishing of the wave function at about the core location, but something else is needed to determine the wave function below the core radius. The question is whether the repulsive core is indispensable from the analysis of collision experiments. However, in order to resolve the core in NN elastic scattering one needs a wavelength which corresponds to energies where there is a substantial in-elasticity and hence a complex optical potential is needed in order to deal with the absorption due to inelastic processes such as $NN \to NN\pi$. This point has been analyzed in Fernandez-Soler and Ruiz Arriola [46] and it has been

TABLE 13 | Moshinsky-Skyrme parameters for the renormalization scale $\Lambda = 400$ MeV.

	DS-OPE	DS-χTPE	DS-Born	Gauss-OPE	Gauss-χTPE	Gauss-Born	Compilation
t_0	–626.8(64)	–529.6(53)	–509.0(55)	–584.4(157)	–406.1(289)	–521.8(152)	-529.6(751)
x_0	–0.38(2)	–0.56(1)	–0.54(1)	–0.26(2)	–0.71(8)	–0.55(4)	–0.50(16)
t_1	948.1(30)	913.6(22)	900.1(17)	987.4(29)	945.5(18)	941.3(16)	939.3(304)
x_1	–0.048(3)	–0.074(3)	–0.068(3)	–0.013(3)	–0.047(3)	–0.058(2)	–0.051(22)
t_2	2462.6(56)	2490.0(39)	2462.1(25)	2441.3(56)	2490.1(24)	2466.8(26)	2468.8(187)
x_2	–0.8686(6)	–0.8750(8)	–0.8753(6)	–0.8630(8)	–0.8729(6)	–0.8785(3)	–0.872(6)
W_0	107.7(4)	100.8(3)	96.2(3)	105.0(5)	109.3(7)	94.3(2)	102.2(61)
t_U	1278.6(12)	1260.3(5)	1257.0(4)	1285.6(12)	1254.9(9)	1249.3(3)	1264.3(144)
t_T	–4220.9(87)	–4292.8(23)	–4289.0(21)	–4385.6(99)	–4271.8(51)	–4319.5(58)	–4296.6(545)

Errors quoted for each potential are statistical; errors in the last column are systematic and correspond to the sample standard deviation of the six previous columns. See main text for details on the calculation of systematic errors. Units are: t_0 in MeVfm^3, t_1, t_2, W_0, t_U, t_T in MeVfm^5, and x_0, x_1, x_2 are dimensionless.

found that there exist two solutions, one corresponding to the usual repulsive core and the other one related to the so-called structural core, reminiscent of the composite character of the nucleon.

12.2. Coarse Graining Short Range Correlations

The Bethe-Goldstone equation [143, 144] has been a way to describe short range correlations between nucleons inside the nucleus. In the nuclear medium the interaction produces no scattering due to the Pauli principle. Instead the relative wave function of a pair is modified in presence of the two-body interaction, generating high-momentum components above the Fermi momentum, $p > p_F$. Using the delta-shell potential allows to simplify the problem of computing these high momentum components arising in an interacting nucleon pair in nuclear matter. This coarse graining of the Bethe-Goldstone equation has been explored in Ruiz Simo et al. [145, 146] for back-to-back nucleons, with total center of mass momentum equal to zero. The formalism still has to be extended to other values of the center of mass.

12.3. Error Analysis of Nuclear Matrix Elements

The expected errors of harmonic oscillator nuclear matrix elements coming from the uncertainty on the NN interaction have been estimated in Amaro et al. [147] for the coarse grained (GR) interaction fitted to NN scattering data, with several prescriptions for the long-part of the interaction, including one pion exchange and chiral two-pion exchange interactions.

12.4. Shell Model Estimates

In a previous calculation [51], we showed how our approach is competitive not only as a way of determining the phase shifts but also compared to more sophisticated approaches to Nuclear Structure [148]. We computed the ground state energy of several closed-shell nuclei by using oscillator wave functions. In the case of ^{4}He, ^{16}O, and ^{40}Ca nuclei, our calculation reproduces the experiment at the $20-30\%$-level provided the phase-shifts are fitted up to energy $E \leq 100$MeV [51]. This is a tolerable accuracy as we just intend to make a first estimate on the systematic uncertainties and then compute the change in the binding energy. For the $A = 3, 4$ nuclei we use the simple formulas,

$$\Delta B(^3\mathrm{H}) = \langle \Delta V_2 \rangle_{^3\mathrm{H}} = 3\langle 1s| \frac{1}{2}\left(\Delta V_{^1S_0} + \Delta V_{^3S_1}\right)|1s\rangle, \quad (95)$$

$$\Delta B(^4\mathrm{He}) = \langle \Delta V_2 \rangle_{^4\mathrm{He}} = 6\langle 1s| \frac{1}{2}\left(\Delta V_{^1S_0} + \Delta V_{^3S_1}\right)|1s\rangle, \quad (96)$$

where $|1s\rangle$ is the Harmonic oscillator relative wave function with the corresponding oscillator parameter b fixed to reproduce the physical charge radius. The factors in front of the matrix elements are Talmi-Moshinsky coefficients corresponding in this particular case to the number of pairs interacting through a relative s-wave. Errors in the potential ΔV are computed by adding individual contributions $(\Delta\lambda_n)^{JS}_{l,l'}$ in quadrature. By propagating the potential errors to Equation (95) we find

$$\frac{\Delta B(3)}{3} = 0.07 - 0.085\mathrm{MeV} \quad (97)$$

depending on the fitting cut-off LAB energy, 100–350 MeV respectively, overestimating the Faddeev estimates given above. For the $\alpha-$particle Equation (96) yields

$$\frac{\Delta B(4)}{4} = 0.10 - 0.13\mathrm{MeV}. \quad (98)$$

More generally, for heavier double-closed shell nuclei one has along the lines of Navarro Perez et al. [51]

$$\Delta B(A) = \sum_{nlSJ} g_{nlJS} \langle nl|\Delta V^{JST}|nl\rangle \quad (99)$$

where g_{nlJS} depends on the Talmi-Moshinsky brackets. For ^{16}O and ^{40}Ca, we find

$$\frac{\Delta B(^{16}\mathrm{O})}{16} = 0.26\,\mathrm{MeV} \qquad \frac{\Delta B(^{40}\mathrm{Ca})}{40} = 0.32\mathrm{MeV}. \quad (100)$$

These systematic estimates using shell model are of the same order to the ones obtained above in the Skyrme interaction.

13. OUTLOOK

Despite the many years elapsed since the first NN partial wave analysis in 1957 and the huge theoretical and experimental efforts carried out, the nuclear force is poorly known still where it is most needed, namely in the mid-range regime which is relevant for *ab initio* calculation of nuclear binding energies. This is the explanation behind the relatively large uncertainties found in large scale calculations. During many years there has been a conformist attitude regarding these uncertainties, and in most papers a purely computational approach has prevailed, validating theoretical frameworks just on their numerical performance. Only in recent years the issue of uncertainties has been taken seriously, as it is actually the key to establish the predictive power of the theory. Clearly, the level of ambiguity we are dealing with in the evaluation of nuclear uncertainties of all sorts, statistical, systematic, and computational requires a rigorous treatment. In this work we have reviewed this topic from the perspective of the impact of the Granada NN database on the determination of the NN force and its consequences on nuclear binding.

The main theoretical obstacle has to do with the great difficulty in providing a unique definition of the nuclear potential just from data. Quantum field theory at the hadronic level implies the existence of a long range interaction dominated by pion exchanges as the lightest particles and reduces the ambiguity. Lattice calculations of potentials may identify them with static energies assuming heavy quark-composite sources but their accuracy is at present not satisfactory. Chiral perturbation theory provides in addition several schemes based on a power

counting which, while not fully satisfactory, may be and have been implemented in the NN sector and extended to multi-nucleon forces. The consistency among chiral multi-nucleon forces is theoretically very appealing and the use of potentials is possibly the only practical path toward a satisfactory solution of the nuclear many body problem. It should be stressed that the EFT point of view is the most suitable one since in principle one gets rid of the model dependence with *a priori* uncertainty estimates. However, a more detailed analysis reveals that there are issues regarding the necessary regularization of the theory, which effectively model the mid-range regime of the NN interaction. Moreover, the indispensability of the chiral scheme for NN scattering data remains to be proven, not to speak about its suitability for fitting and selecting a NN database itself. At a phenomenological level at the present stage the determination of the NN interaction below 1.8 fm (up to a phase equivalent unitary transformation) remains so far connected to a combination of an abundance of data in a variety of kinematics and observables with the corresponding experimental errors.

In our view, this unfortunate situation on the side of the hadronic theory will likely not necessarily improve neither with more and better experimental measurements nor with larger computational facilities, but with a better understanding on the essence of hadronic interactions and their range of applicability.

AUTHOR CONTRIBUTIONS

All authors listed have made a substantial, direct and intellectual contribution to the work, and approved it for publication.

FUNDING

This work was supported by the Spanish MINECO and European FEDER funds (grant FIS2017-85053-C2-1-P) and Junta de Andalucía (grant FQM-225).

ACKNOWLEDGMENTS

We thank Ignacio Ruiz Simó, James Vary, Pieter Maris, Eduardo Garrido, Andreas Nogga, Rocco Schiavilla, Maria Piarulli, Pedro Fernández Soler, Jacobo Ruiz de Elvira, Varese Salvador Timoteo, and Sergio Szpigel for collaboration on different issues discussed in this paper.

REFERENCES

1. Yukawa H. On the interaction of elementary particles. *Proc Phys Math Soc Jpn.* (1935) **17**:48–57.
2. Bethe HA. The meson theory of nuclear forces I. General theory. *Phys Rev.* (1940) **57**:260–72. doi: 10.1103/PhysRev.57.260
3. Bethe H. The meson theory of nuclear forces. Part 2. Theory of the deuteron. *Phys Rev.* (1940) **57**:390–413. doi: 10.1103/PhysRev.57.390
4. Stapp H, Ypsilantis T, Metropolis N. Phase shift analysis of 310-MeV proton proton scattering experiments. *Phys Rev.* (1957) **105**:302–10. doi: 10.1103/PhysRev.105.302
5. Arndt R, Macgregor M. Chi-squared minimization techniques. *Methods Comput Phys.* (1966) **6**:253.
6. Perring J. Nucleon-nucleon phase shifts at 142 mev. *Nucl Phys.* (1963) **42**:306–12.
7. Arndt RA, MacGregor MH. Determination of the nucleon-nucleon elastic-scattering matrix. iv. comparison of energy-dependent and energy-independent phase-shift analyses. *Phys Rev.* (1966) **141**:873.
8. MacGregor MH, Arndt RA, Wright RM. Determination of the nucleon-nucleon scattering matrix. VII. (p, p) analysis from 0 to 400 MeV. *Phys Rev.* (1968) **169**:1128–48. doi: 10.1103/PhysRev.169.1128
9. Arndt R, Roper L. The use of partial-wave representations in the planning of scattering measurements. application to 330 mev n p scattering. *Nucl Phys.* (1972) **B50**:285–300. doi: 10.1016/S0550-3213(72)80019-1
10. Mac Gregor MH, Moravcsik MJ, Stapp HP. Nucleon-nucleon scattering experiments and their phenomenological analysis. *Annu Rev Nucl Part Sci.* (1960) **10**:291–352. doi: 10.1146/annurev.ns.10.120160.001451
11. Breit G. Aspects of nucleon-nucleon scattering theory. *Rev Mod Phys.* (1962) **34**:766–812. doi: 10.1103/RevModPhys.34.766
12. Signell P. The nuclear potential. In: Baranger M, Vogt E, editors. *Advances in Nuclear Physics*. New York, NY: Springer (1969). p. 223–94.
13. de Swart JJ, Nagels MM. The nucleon-nucleon interaction. *Fortsch Phys.* (1978) **26**:215. doi: 10.1002/prop.19780260402
14. Machleidt R. The Meson theory of nuclear forces and nuclear structure. *Adv Nucl Phys.* (1989) **19**:189–376.
15. Stoks V, Kompl R, Rentmeester M, de Swart J. Partial wave analaysis of all nucleon-nucleon scattering data below 350-MeV. *Phys Rev.* (1993) **C48**:792–815. doi: 10.1103/PhysRevC.48.792
16. Stoks V, Klomp R, Terheggen C, de Swart J. Construction of high quality N N potential models. *Phys Rev.* (1994) **C49**:2950–62. doi: 10.1103/PhysRevC.49.2950
17. Wiringa RB, Stoks V, Schiavilla R. An Accurate nucleon-nucleon potential with charge independence breaking. *Phys Rev.* (1995) **C51**:38–51. doi: 10.1103/PhysRevC.51.38
18. Machleidt R. The High precision, charge dependent Bonn nucleon-nucleon potential (CD-Bonn). *Phys Rev.* (2001) **C63**:024001. doi: 10.1103/PhysRevC.63.024001
19. Gross F, Stadler A. Covariant spectator theory of np scattering: Phase shifts obtained from precision fits to data below 350-MeV. *Phys Rev.* (2008) **C78**:014005. doi: 10.1103/PhysRevC.78.014005
20. Amghar A, Desplanques B. Are all models of the N N interaction independent of each other? *Nucl Phys.* (1995) **A585**:657–92. doi: 10.1016/0375-9474(94)00781-H
21. Adam RM, Fiedeldey H, Sofianos SA, Leeb H. Error propagation from nucleon-nucleon data to three- and four-nucleon binding energies. *Nucl Phys.* (1993) **A559**:157–72. doi: 10.1016/0375-9474(93)90184-Y
22. Navarro Perez R, Amaro JE, Ruiz Arriola E. Error estimates on nuclear binding energies from nucleon-nucleon uncertainties. *arXiv [Preprint]* arXiv:1202.6624 (2012).
23. Navarro Perez R, Amaro JE, Ruiz Arriola E. Nuclear binding energies and NN uncertainties. In: *Sixth International Conference on Quarks and Nuclear Physics* (2012). p. 145. doi: 10.22323/1.157.0145
24. Navarro Perez R, Garrido E, Amaro JE, Ruiz Arriola E. Triton binding energy with realistic statistical uncertainties. *Phys Rev.* (2014) **C90**:047001. doi: 10.1103/PhysRevC.90.047001
25. Navarro Perez R, Nogga A, Amaro JE, Ruiz Arriola E. Binding in light nuclei: statistical NN uncertainties vs Computational accuracy. *J Phys Conf Ser.* (2016) **742**:012001. doi: 10.1088/1742-6596/742/1/012001
26. Navarro Pérez R, Amaro JE, Ruiz Arriola E, Maris P, Vary JP. Statistical error propagation in *ab initio* no-core full configuration calculations of light nuclei. *Phys Rev.* (2015) **C92**:064003. doi: 10.1103/PhysRevC.92.064003

27. Skibinski R, Volkotrub Yu, Golak J, Topolnicki K, Witala H. Theoretical uncertainties of the elastic nucleon-deuteron scattering observables. *Phys Rev.* (2018) **C98**:014001. doi: 10.1103/PhysRevC.98.014001
28. Dobaczewski J, Nazarewicz W, Reinhard PG. Error estimates of theoretical models: a guide. *J Phys.* (2014) **G41**:074001. doi: 10.1088/0954-3899/41/7/074001
29. Toivanen J, Dobaczewski J, Kortelainen M, Mizuyama K. Error analysis of nuclear mass fits. *Phys Rev.* (2008) **C78**:034306. doi: 10.1103/PhysRevC.78.034306
30. Landau RH. *Quantum Mechanics II: A Second Course in Quantum Theory*. New York, NY: John Wiley & Sons (2008).
31. Chadan K, Sabatier PC. *Inverse Problems in Quantum Scattering Theory*. Springer Science & Business Media (2012).
32. Newton RG. *Inverse Schrödinger Scattering in Three Dimensions*. New York, NY: Springer Science & Business Media (2012).
33. Coester F, Cohen S, Day B, Vincent CM. Variation in nuclear-matter binding energies with phase-shift-equivalent two-body potentials. *Phys Rev.* (1970) **C1**:769–76. doi: 10.1103/PhysRevC.1.769
34. Tjon JA. Bound states of 4 He with local interactions. *Phys Lett.* (1975) **56B**:217–20. doi: 10.1016/0370-2693(75)90378-0
35. Srivastava M, Sprung DW. Off-shell behavior of the nucleon-nucleon interaction. In: *Advances in Nuclear Physics*. Springer (1975). p. 121–218.
36. Aoki S, Hatsuda T, Ishii N. Theoretical foundation of the nuclear force in QCD and its applications to central and tensor forces in quenched lattice QCD simulations. *Prog Theor Phys.* (2010) **123**:89–128. doi: 10.1143/PTP.123.89
37. Aoki S. Hadron interactions in lattice QCD. *Prog Part Nucl Phys.* (2011) **66**:687–726. doi: 10.1016/j.ppnp.2011.07.001
38. Aoki S. Nucleon-nucleon interactions via Lattice QCD: methodology. *Eur Phys J.* (2013) **A49**:81. doi: 10.1140/epja/i2013-13081-0
39. Okubo S, Marshak RE. Velocity dependence of the two-nucleon interaction. *Ann Phys.* (1958) **4**:166–79.
40. Piarulli M, Girlanda L, Schiavilla R, Navarro Pérez R, Amaro JE, Ruiz Arriola E. Minimally nonlocal nucleon-nucleon potentials with chiral two-pion exchange including Δ resonances. *Phys Rev.* (2015) **C91**:024003. doi: 10.1103/PhysRevC.91.024003
41. Amghar A, Desplanques B. More about the comparison of local and nonlocal NN interaction models. *Nucl Phys.* (2003) **A714**:502–34. doi: 10.1016/S0375-9474(02)01375-1
42. Navarro Pérez R, Amaro JE, Ruiz Arriola E. Coarse-grained potential analysis of neutron-proton and proton-proton scattering below the pion production threshold. *Phys Rev.* (2013) **C88**:064002. doi: 10.1103/PhysRevC.88.064002
43. Navarro Pérez R, Ruiz Arriola E. Uncertainty quantification and falsification of Chiral Nuclear Potentials (2019).
44. Walker-Loud A. Nuclear physics review. In: *31st International Symposium on Lattice Field Theory - LATTICE 2013*. (2014). p. 013. doi: 10.22323/1.187.0013
45. Navarro Pérez R, Amaro JE, Ruiz Arriola E. Partial wave analysis of nucleon-nucleon scattering below pion production threshold. *Phys Rev.* (2013) **C88**:024002. doi: 10.1103/PhysRevC.88.024002
46. Fernandez-Soler P, Ruiz Arriola E. Coarse graining of NN inelastic interactions up to 3 GeV: repulsive versus structural core. *Phys Rev.* (2017) **C96**:014004. doi: 10.1103/PhysRevC.96.014004
47. Ruiz Arriola E, Ruiz de Elvira J. Coarse graining hadronic scattering. In: *9th International Workshop on Chiral Dynamics (CD18)*. Durham, NC (2019).
48. Navarro Perez R, Amaro JE, Ruiz Arriola E. Partial wave analysis of chiral NN interactions. *Few Body Syst.* (2014) **55**:983–7. doi: 10.1007/s00601-014-0817-3
49. Aviles JB. Delta-function model for the two-nucleon interaction. *Phys Rev.* (1972) **C6**:1467–84. doi: 10.1103/PhysRevC.6.1467
50. Entem DR, Ruiz Arriola E, Pavon Valderrama M, Machleidt R. Renormalization of chiral two-pion exchange NN interactions. momentum versus coordinate space. *Phys Rev.* (2008) **C77**:044006. doi: 10.1103/PhysRevC.77.044006
51. Navarro Perez R, Amaro JE, Ruiz Arriola E. Coarse graining nuclear interactions. *Prog Part Nucl Phys.* (2012) **67**:359–64. doi: 10.1016/j.ppnp.2011.12.044
52. Calogero F. *Variable Phase Approach to Potential Scattering by F Calogero*, Vol. 35. New York, NY: Elsevier (1967).
53. Navarro Perez R, Amaro JE, Ruiz Arriola E. Statistical error analysis for phenomenological nucleon-nucleon potentials. *Phys Rev.* (2014) **C89**:064006. doi: 10.1103/PhysRevC.89.064006
54. Navarro Pérez R, Amaro JE, Ruiz Arriola E. Error analysis of nuclear forces and effective interactions. *J Phys.* (2015) **G42**:034013. doi: 10.1088/0954-3899/42/3/034013
55. Puzikov L, Ryndin R, Smorodinsky J. Construction of the scattering matrix of a two-nucleon system. *Nucl Phys.* (1957) **3**:436–45.
56. Hoshizaki N. Formalism of nucleon-nucleon scattering. *Prog Theor Phys Suppl.* (1969) **42**:107–59. doi: 10.1143/PTPS.42.107
57. Bystricky J, Lehar F, Winternitz P. Formalism of nucleon-nucleon elastic scattering experiments. *J Phys.* (1978) **39**:1. doi: 10.1051/jphys:019780039010100
58. Binstock J, Bryan R. Test of peripherality for n-n scattering. *Phys Rev.* (1971) **D4**:1341–52. doi: 10.1103/PhysRevD.4.1341
59. Goldberger ML, Watson KM. *Collision Theory*. New York, NY: Courier Corporation (2004).
60. Navarro Pérez R, Amaro JE, Ruiz Arriola E. Precise determination of charge dependent pion-nucleon-nucleon coupling constants. *Phys Rev.* (2017) **C95**:064001. doi: 10.1103/PhysRevC.95.064001
61. Ruiz Arriola E, Amaro JE, Navarro Pérez R. Three pion nucleon coupling constants. *Mod Phys Lett.* (2016) **A31**:1630027. doi: 10.1142/S0217732316300275
62. Evans MJ, Rosenthal JS. *Probability and Statistics: The Science of Uncertainty*. New York, NY: Macmillan (2004).
63. Eadie WT, Drijard D, James FE. *Statistical Methods in Experimental Physics*. Amsterdam: North-Holland1 (1971).
64. Navarro Pérez R, Ruiz Arriola E, Ruiz de Elvira J. Self-consistent statistical error analysis of $\pi\pi$ scattering. *Phys Rev.* (2015) **D91**:074014. doi: 10.1103/PhysRevD.91.074014
65. Stoks V, de Swart JJ. Comparison of potential models with the pp scattering data below 350 MeV. *Phys Rev.* (1993) **C47**:761–7. doi: 10.1103/PhysRevC.47.761
66. Stoks VGJ, de Swart JJ. Comparison of potential models with the n p scattering data below 350-MeV. *Phys Rev.* (1995) **C52**:1698–701. doi: 10.1103/PhysRevC.52.1698
67. Calle Cordon A, Pavon Valderrama M, Ruiz Arriola E. Nucleon-nucleon interaction, charge symmetry breaking and renormalization. *Phys Rev.* (2012) **C85**:024002. doi: 10.1103/PhysRevC.85.024002
68. Nieves J, Ruiz Arriola E. Error estimates for pi pi scattering threshold parameters in chiral perturbation theory to two loops. *Eur Phys J.* (2000) **A8**:377–84. doi: 10.1007/s10050-000-4511-0
69. de Swart J, Rentmeester M, Timmermans R. The Status of the pion - nucleon coupling constant. *PiN Newslett.* (1997) **13**:96–107.
70. Sainio M. Pion nucleon coupling constant: working group summary. *PiN Newslett.* (1999) **15**:156–61.
71. Matsinos E. A brief history of the pion-nucleon coupling constant. *arXiv [Preprint]* arXiv:1901.01204 (2019).
72. Baru V, Hanhart C, Hoferichter M, Kubis B, Nogga A, Phillips DR. Precision calculation of the π^- deuteron scattering length and its impact on threshold π N scattering. *Phys Lett.* (2011) **B694**:473–7. doi: 10.1016/j.physletb.2010.10.028
73. Baru V, Hanhart C, Hoferichter M, Kubis B, Nogga A, Phillips DR. Precision calculation of threshold pi d scattering, pi N scattering lengths, and the GMO sum rule. *Nucl Phys.* (2011) **A872**:69–116. doi: 10.1016/j.nuclphysa.2011.09.015
74. Hoferichter M, Ruiz de Elvira J, Kubis B, Meißner UG. Roy–Steiner-equation analysis of pion–nucleon scattering. *Phys Rept.* (2016) **625**:1–88. doi: 10.1016/j.physrep.2016.02.002
75. Navarro Pérez R, Amaro JE, Ruiz Arriola E. The low-energy structure of the nucleon–nucleon interaction: statistical versus systematic uncertainties. *J Phys.* (2016) **G43**:114001. doi: 10.1088/0954-3899/43/11/114001
76. Birge RT. The calculation of errors by the method of least squares. *Phys Rev.* (1932) **40**:207.
77. Navarro Pérez R, Amaro JE, Ruiz Arriola E. Coarse grained NN potential with Chiral Two Pion Exchange. *Phys Rev.* (2014) **C89**:024004. doi: 10.1103/PhysRevC.89.024004

78. Machleidt R, Sammarruca F, Song Y. The non-local nature of the nuclear force and its impact on nuclear structure. *Phys Rev.* (1996) **C53**:1483–7. doi: 10.1103/PhysRevC.53.1483
79. Friar JL, Payne GL, Stoks VGJ, de Swart JJ. Triton calculations with the new Nijmegen potentials. *Phys Lett.* (1993) **B311**:4. doi: 10.1016/0370-2693(93)90523-K
80. Bethe HA. Theory of the effective range in nuclear scattering. *Phys Rev.* (1949) **76**:38–50. doi: 10.1103/PhysRev.76.38
81. Madsen LB. Effective range theory. *Am J Phys.* (2002) **70**:811–4. doi: 10.1119/1.1473644
82. Pavon Valderrama M, Ruiz Arriola E. Low-energy NN scattering at next-to-next-to-next-to-next-to-leading order for partial waves with $j \leq 5$. *Phys Rev.* (2005) **C72**:044007. doi: 10.1103/PhysRevC.72.044007
83. Navarro Pérez R, Amaro JE, Ruiz Arriola E. Bootstrapping the statistical uncertainties of NN scattering data. *Phys Lett.* (2014) **B738**:155–9. doi: 10.1016/j.physletb.2014.09.035
84. Epelbaum E, Glockle W, Meissner UG. The Two-nucleon system at next-to-next-to-next-to-leading order. *Nucl Phys.* (2005) **A747**:362–424. doi: 10.1016/j.nuclphysa.2004.09.107
85. Epelbaum E, Krebs H, Meißner UG. Improved chiral nucleon-nucleon potential up to next-to-next-to-next-to-leading order. *Eur Phys J.* (2015) **A51**:53. doi: 10.1140/epja/i2015-15053-8
86. Furnstahl RJ, Klco N, Phillips DR, Wesolowski S. Quantifying truncation errors in effective field theory. *Phys Rev.* (2015) **C92**:024005. doi: 10.1103/PhysRevC.92.024005
87. Navarro Perez R, Amaro JE, Ruiz Arriola E. Uncertainty quantification of effective nuclear interactions. *Int J Mod Phys.* (2016) **E25**:1641009. doi: 10.1142/S0218301316410093
88. Navarro Perez R, Amaro JE, Ruiz Arriola E. Effective interactions in the delta-shells potential. *Few Body Syst.* (2013) **54**:1487–90. doi: 10.1007/s00601-012-0537-5
89. Ruiz Arriola E. Low scale aturation of effective NN interactions and their symmetries. *Symmetry* (2016) **8**:42. doi: 10.3390/sym8060042
90. Bogner S, Kuo T, Schwenk A. Model independent low momentum nucleon interaction from phase shift equivalence. *Phys Rept.* (2003) **386**:1–27. doi: 10.1016/j.physrep.2003.07.001
91. Bogner S, Furnstahl R, Schwenk A. From low-momentum interactions to nuclear structure. *Prog Part Nucl Phys.* (2010) **65**:94–147. doi: 10.1016/j.ppnp.2010.03.001
92. Oka M, Yazaki K. Baryon baryon interaction from quark model viewpoint. *Int Rev Nucl Phys.* (1984) **1**:489–567. doi: 10.1142/9789814415132_0006
93. Alvarez-Estrada RF, Fernandez F, Sanchez-Gomez JL, Vento V. Models of hadron structure based on quantum chromodynamics. *Lect Notes Phys.* (1986) **259**:1–294.
94. Valcarce A, Garcilazo H, Fernandez F, Gonzalez P. Quark-model study of few-baryon systems. *Rept Prog Phys.* (2005) **68**:965–1042. doi: 10.1088/0034-4885/68/5/R01
95. Weinberg S. Nuclear forces from chiral Lagrangians. *Phys Lett.* (1990) **B251**:288–92. doi: 10.1016/0370-2693(90)90938-3
96. Bedaque PF, van Kolck U. Effective field theory for few nucleon systems. *Ann Rev Nucl Part Sci.* (2002) **52**:339–96. doi: 10.1146/annurev.nucl.52.050102.090637
97. Epelbaum E, Hammer HW, Meissner UG. Modern theory of nuclear forces. *Rev Mod Phys.* (2009) **81**:1773–825. doi: 10.1103/RevModPhys.81.1773
98. Machleidt R, Entem DR. Chiral effective field theory and nuclear forces. *Phys Rept.* (2011) **503**:1–75. doi: 10.1016/j.physrep.2011.02.001
99. Kaiser N, Brockmann R, Weise W. Peripheral nucleon-nucleon phase shifts and chiral symmetry. *Nucl Phys.* (1997) **A625**:758–88. doi: 10.1016/S0375-9474(97)00586-1
100. Rentmeester MCM, Timmermans RGE, Friar JL, de Swart JJ. Chiral two pion exchange and proton proton partial wave analysis. *Phys Rev Lett.* (1999) **82**:4992–5. doi: 10.1103/PhysRevLett.82.4992
101. Rentmeester MCM, Timmermans RGE, de Swart JJ. Determination of the chiral coupling constants c(3) and c(4) in new pp and np partial wave analyses. *Phys Rev.* (2003) **C67**:044001. doi: 10.1103/PhysRevC.67.044001
102. Entem DR, Machleidt R. Chiral 2pi exchange at order four and peripheral NN scattering. *Phys Rev.* (2002) **C66**:014002. doi: 10.1103/PhysRevC.66.014002
103. Entem DR, Machleidt R. Accurate charge dependent nucleon nucleon potential at fourth order of chiral perturbation theory. *Phys. Rev.* (2003) **C68**:041001. doi: 10.1103/PhysRevC.68.041001
104. Navarro Pérez R, Amaro JE, Ruiz Arriola E. Low energy chiral two pion exchange potential with statistical uncertainties. *Phys Rev.* (2015) **C91**:054002. doi: 10.1103/PhysRevC.91.054002
105. Carlsson BD, Ekström A, Forssén C, Strömberg DF, Jansen GR, Lilja O, et al. Uncertainty analysis and order-by-order optimization of chiral nuclear interactions. *Phys Rev.* (2016) **X6**:011019. doi: 10.1103/PhysRevX.6.011019
106. Piarulli M, Girlanda L, Schiavilla R, Kievsky A, Lovato A, Marcucci LE, et al. Local chiral potentials with Δ-intermediate states and the structure of light nuclei. *Phys Rev.* (2016) **C94**:054007. doi: 10.1103/PhysRevC.94.054007
107. Reinert P, Krebs H, Epelbaum E. Semilocal momentum-space regularized chiral two-nucleon potentials up to fifth order. *Eur Phys J.* (2018) **A54**:86. doi: 10.1140/epja/i2018-12516-4
108. Entem DR, Machleidt R, Nosyk Y. High-quality two-nucleon potentials up to fifth order of the chiral expansion. *Phys Rev.* (2017) **C96**:024004. doi: 10.1103/PhysRevC.96.024004
109. Ruiz Arriola E, Amaro JE, Navarro Perez R. The falsification of chiral nuclear forces. *EPJ Web Conf.* (2017) **137**:09006. doi: 10.1051/epjconf/201713709006
110. Simo IR, Amaro JE, Ruiz Arriola E, Navarro Pérez R. Low energy peripheral scaling in nucleon–nucleon scattering and uncertainty quantification. *J Phys.* (2018) **G45**:035107. doi: 10.1088/1361-6471/aaabd2
111. Entem DR, Kaiser N, Machleidt R, Nosyk Y. Peripheral nucleon-nucleon scattering at fifth order of chiral perturbation theory. *Phys Rev.* (2015) **C91**:014002. doi: 10.1103/PhysRevC.91.014002
112. Shirokov AM, Vary JP, Mazur AI, Weber TA. Realistic Nuclear Hamiltonian: 'Ab exitu' approach. *Phys Lett.* (2007) **B644**:33–7. doi: 10.1016/j.physletb.2006.10.066
113. Johnson CW. Many-body fits of phase-equivalent effective interactions. *Phys Rev.* (2010) **C82**:031303. doi: 10.1103/PhysRevC.82.031303
114. Blatt JM, Weisskopf VF. *Theoretical Nuclear Physics.* New York, NY: Springer (1952). doi: 10.1007/978-1-4612-9959-2
115. Leun CVD, Alderliesten C. The deuteron binding energy. *Nucl Phys.* (1982) **A380**:261–9. doi: 10.1016/0375-9474(82)90105-1
116. Borbély I, Grüebler W, König V, Schmelzbach PA, Mukhamedzhanov AM. Determination of the deuteron s-state asymptotic normalization by continuation of p-d elastic cross section to the transfer pole. *Phys Lett.* (1985) **160B**:17–20. doi: 10.1016/0370-2693(85)91459-5
117. Rodning NL, Knutson LD. Asymptotic D-state to S-state ratio of the deuteron. *Phys Rev.* (1990) **C41**:898–909. doi: 10.1103/PhysRevC.41.898
118. Klarsfeld S, Martorell J, Oteo JA, Nishimura M, Sprung DWL. Determination of the deuteron mean square radius. *Nucl Phys.* (1986) **A456**:373–96. doi: 10.1016/0375-9474(86)90400-8
119. Bishop DM, Cheung LM. Quadrupole moment of the deuteron from a precise calculation of the electric field gradient in D-2. *Phys Rev.* (1979) **A20**:381–4. doi: 10.1103/PhysRevA.20.381
120. de Swart JJ, Terheggen CPF, Stoks VGJ. The Low-energy n p scattering parameters and the deuteron. In: *3rd International Symposium on Dubna Deuteron 95.* Dubna (1995).
121. Gilman R, Gross F. Electromagnetic structure of the deuteron. *J Phys G* (2002) **28**:R37. doi: 10.1088/0954-3899/28/4/201
122. Navarro Perez R, Amaro JE, Ruiz Arriola E. Nucleon-nucleon chiral two pion exchange potential vs coarse grained interactions. In: *Presented by R. Navarro Perez at the The 7th International Workshop on Chiral Dynamics.* Newport News, VA (2013). p. 104. doi: 10.22323/1.172.0104
123. Nogga A, Kamada H, Gloeckle W. Modern nuclear force predictions for the alpha particle. *Phys Rev Lett.* (2000) **85**:944–7. doi: 10.1103/PhysRevLett.85.944
124. Perne R, Kroger H. Tjon line in few-body systems. *Phys Rev.* (1979) **C20**:340–4. doi: 10.1103/PhysRevC.20.340

125. Tjon JA. The three and four nucleon systems (theory). *Nucl Phys.* (1981) **A353**:47–60. doi: 10.1016/0375-9474(81)90698-9
126. Nogga A, Bogner SK, Schwenk A. Low-momentum interaction in few-nucleon systems. *Phys Rev.* (2004) **C70**:061002. doi: 10.1103/PhysRevC.70.061002
127. Klein N, Elhatisari S, Lähde TA, Lee D, Meißner UG. The Tjon band in nuclear lattice effective field theory. *Eur Phys J.* (2018) **A54**:121. doi: 10.1140/epja/i2018-12553-y
128. Delfino A, Frederico T, Timoteo VS, Tomio L. The Few scales of nuclei and nuclear matter. *Phys Lett.* (2006) **B634**:185. doi: 10.1016/j.physletb.2006.01.046
129. Ruiz Arriola E, Szpigel S, Timoteo VS. Fixed points of the similarity renormalization group and the nuclear many-body problem. *Few Body Syst.* (2014) **55**:971–5. doi: 10.1007/s00601-014-0858-7
130. Ruiz Arriola E, Szpigel S, Timóteo VS. Fixed points of the SRG evolution and the on-shell limit of the nuclear force. *Ann Phys.* (2016) **371**:398–436. doi: 10.1016/j.aop.2016.06.002
131. Shirokov AM, Kulikov VA, Mazur AI, Vary JP, Maris P. Deuteron-equivalent and phase-equivalent interactions within light nuclei. *Phys Rev.* (2012) **C85**:034004. doi: 10.1103/PhysRevC.85.034004
132. Rozpedzik D, Golak J, Skibinski R, Witala H, Glockle W, Epelbaum E, et al. A first estimation of chiral four-nucleon force effects in He-4. *Acta Phys Pol.* (2006) **B37**:2889–904. Available online at: https://www.actaphys.uj.edu.pl/R/37/10/2889/pdf
133. Epelbaum E. Four-nucleon force using the method of unitary transformation. *Eur Phys J.* (2007) **A34**:197–214. doi: 10.1140/epja/i2007-10496-0
134. Moshinsky M. Short range forces and nuclear shell theory. *Nucl Phys.* (1958) **8**:19–40.
135. Skyrme T. The effective nuclear potential. *Nucl Phys.* (1958) **9**:615–34.
136. Vautherin D, Brink DM. Hartree-Fock calculations with Skyrme's interaction. 1. Spherical nuclei. *Phys Rev.* (1972) **C5**:626–47. doi: 10.1103/PhysRevC.5.626
137. Negele JW, Vautherin D. Density-matrix expansion for an effective nuclear hamiltonian. *Phys Rev.* (1972) **C5**:1472–93. doi: 10.1103/PhysRevC.5.1472
138. Chabanat E, Meyer J, Bonche P, Schaeffer R, Haensel P. A Skyrme parametrization from subnuclear to neutron star densities. *Nucl Phys.* (1997) **A627**:710–46. doi: 10.1016/S0375-9474(97)00596-4
139. Bender M, Heenen PH, Reinhard PG. Self-consistent mean-field models for nuclear structure. *Rev Mod Phys.* (2003) **75**:121–80. doi: 10.1103/RevModPhys.75.121
140. Friedrich J, Reinhard PG. Skyrme-force parametrization: least-squares fit to nuclear ground-state properties. *Phys Rev.* (1986) **C33**:335–51. doi: 10.1103/PhysRevC.33.335
141. Klupfel P, Reinhard PG, Burvenich TJ, Maruhn JA. Variations on a theme by Skyrme: a systematic study of adjustments of model parameters. *Phys Rev.* (2009) **C79**:034310. doi: 10.1103/PhysRevC.79.034310
142. Ruiz Arriola E. Low scale saturation of effective NN interactions and their symmetries (2010).
143. Bethe HA. Nuclear many-body problem. *Phys Rev.* (1956) **103**:1353–90. doi: 10.1103/PhysRev.103.1353
144. Goldstone J. Derivation of the brueckner many-body theory. *Proc R Soc Lond.* (1957) **A239**:267–79. doi: 10.1098/rspa.1957.0037
145. Ruiz Simo I, Navarro Perez R, Amaro JE, Ruiz Arriola E. Coarse grained short-range correlations. *Phys Rev.* (2017) **C95**:054003. doi: 10.1103/PhysRevC.95.054003
146. Ruiz Simo I, Navarro Pérez R, Amaro JE, Ruiz Arriola E. Coarse graining the Bethe–Goldstone equation: nucleon–nucleon high-momentum components. *Phys Rev.* (2017) **C96**:054006. doi: 10.1103/PhysRevC.96.054006
147. Amaro JE, Navarro Perez R, Ruiz Arriola E. Error analysis of nuclear matrix elements. *Few Body Syst.* (2014) **55**:977–81. doi: 10.1007/s00601-013-0756-4
148. Neff T, Feldmeier H. Tensor correlations in the unitary correlation operator method. *Nucl Phys.* (2003) **A713**:311–71. doi: 10.1016/S0375-9474(02)01307-6

Conflict of Interest: The authors declare that the research was conducted in the absence of any commercial or financial relationships that could be construed as a potential conflict of interest.

Copyright © 2020 Ruiz Arriola, Amaro and Navarro Pérez. This is an open-access article distributed under the terms of the Creative Commons Attribution License (CC BY). The use, distribution or reproduction in other forums is permitted, provided the original author(s) and the copyright owner(s) are credited and that the original publication in this journal is cited, in accordance with accepted academic practice. No use, distribution or reproduction is permitted which does not comply with these terms.

frontiers in Physics

REVIEW
published: 25 February 2020
doi: 10.3389/fphy.2020.00012

Hyperon-Nuclear Interactions From SU(3) Chiral Effective Field Theory

Stefan Petschauer[1,2]*, *Johann Haidenbauer*[3], *Norbert Kaiser*[2], *Ulf-G. Meißner*[4,3,5] *and Wolfram Weise*[2]

[1] TNG Technology Consulting GmbH, Unterföhring, Germany, [2] Physik Department, Technische Universität München, Garching, Germany, [3] Institute for Advanced Simulation and Jülich Center for Hadron Physics, Institut für Kernphysik, Forschungszentrum Jülich, Jülich, Germany, [4] Helmholtz-Institut für Strahlen- und Kernphysik and Bethe Center for Theoretical Physics, Universität Bonn, Bonn, Germany, [5] Tbilisi State University, Tbilisi, Georgia

The interaction between hyperons and nucleons has a wide range of applications in strangeness nuclear physics and is a topic of continuing great interest. These interactions are not only important for hyperon-nucleon scattering but also essential as basic input to studies of hyperon-nuclear few- and many-body systems including hypernuclei and neutron star matter. We review the systematic derivation and construction of such baryonic forces from the symmetries of quantum chromodynamics within non-relativistic SU(3) chiral effective field theory. Several applications of the resulting potentials are presented for topics of current interest in strangeness nuclear physics.

Keywords: chiral Lagrangian, effective field theory, hyperon-nucleon interaction, flavor SU(3) symmetry, strangeness nuclear physics

OPEN ACCESS

Edited by:
Ruprecht Machleidt,
University of Idaho, United States

Reviewed by:
Theodoros Gaitanos,
Aristotle University of Thessaloniki, Greece
Francesca Gulminelli,
University of Caen Normandy, France

***Correspondence:**
Stefan Petschauer
stefan.petschauer@tngtech.com

Specialty section:
This article was submitted to Nuclear Physics, a section of the journal Frontiers in Physics

Received: *13 October 2019*
Accepted: *13 January 2020*
Published: *25 February 2020*

Citation:
Petschauer S, Haidenbauer J, Kaiser N, Meißner U-G and Weise W (2020) Hyperon-Nuclear Interactions From SU(3) Chiral Effective Field Theory. Front. Phys. 8:12. doi: 10.3389/fphy.2020.00012

1. INTRODUCTION

Strangeness nuclear physics is an important topic of ongoing research, addressing for example scattering of baryons including strangeness, properties of hypernuclei, or strangeness in infinite nuclear matter and in neutron star matter. The theoretical foundation for such investigations are interaction potentials between nucleons and strange baryons such as the Λ hyperon.

Nuclear many-body systems are (mainly) governed by the strong interaction, described at the fundamental level by *quantum chromodynamics* (QCD). The elementary degrees of freedom of QCD are quarks and gluons. However, in the low-energy regime of QCD quarks and gluons are confined into colorless hadrons. This is the region where (hyper-)nuclear systems are formed. In this region QCD cannot be solved in a perturbative way. Lattice QCD is approaching this problem via large-scale numerical simulations: the (Euclidean) space-time is discretized and QCD is solved on a finite grid [1–4]. Since the seminal work of Weinberg [5, 6] *chiral effective field theory* (χEFT) has become a powerful tool for calculating systematically the strong interaction dynamics for low-energy hadronic processes [7–9]. Chiral EFT employs the same symmetries and symmetry breaking patterns at low-energies as QCD, but it uses the proper degrees of freedom, namely hadrons instead of quarks and gluons. In combination with an appropriate expansion in small external momenta, the results can be improved systematically, by going to higher order in the power counting, and at the same time theoretical errors can be estimated. Furthermore, two- and three-baryon forces can be constructed in a consistent fashion. The unresolved short-distance dynamics is encoded in χEFT in contact terms, with a priori unknown low-energy constants (LECs).

The *NN* interaction is empirically known to very high precision. Corresponding two-nucleon potentials have been derived to high accuracy in phenomenological approaches [10–12]. Nowadays the systematic theory to construct nuclear forces is χEFT [13, 14]. (Note however that there are still debates about the Weinberg power counting schemes and how it is employed in practice [15–17]).

In contrast, the *YN* interaction is presently not known in such detail. The scarce experimental data (about 35 data points for low-energy total cross sections) do not allow for a unique determination of the hyperon-nucleon interaction. The limited accuracy of the *YN* scattering data does not permit a unique phase shift analysis. However, at experimental facilities such as J-PARC in Japan or later at FAIR in Germany, a significant amount of beam time will be devoted to strangeness nuclear physics. Various phenomenological approaches have been employed to describe the *YN* interaction, in particular boson-exchange models [18–23] or quark models [24–26]. However, given the poor experimental data base, these interactions differ considerably from each other. Obviously there is a need for a more systematic investigation based on the underlying theory of the strong interaction, QCD. Some aspects of *YN* scattering and hyperon mass shifts in nuclear matter using EFT methods have been covered in Savage and Wise [27] and Korpa et al. [28]. The *YN* interaction has been investigated at leading order (LO) in SU(3) χEFT [29–31] by extending the very successful χEFT framework for the nucleonic sector [13, 14] to the strangeness sector. This work has been extended to next-to-leading order (NLO) in Petschauer and Kaiser [32], Haidenbauer et al. [33, 34] where an excellent description of the strangeness -1 sector has been achieved, comparable to most advanced phenomenological hyperon-nucleon interaction models. An extension to systems with more strangeness has been done in Haidenbauer et al. [35, 36] and Haidenbauer and Meißner [37]. Systems including decuplet baryons have been investigated in Haidenbauer et al. [38] at leading order in non-relativistic χEFT. Recently calculations within leading order covariant χEFT have been performed for *YN* interactions in the strangeness sector [39–43] with comparable results (see also [44]). It is worth to briefly discuss the differences between the covariant and the heavy-baryon approach. In the latter, due to the expansion in the inverse of the baryon masses, some terms are relegated to higher orders. Also, it can happen that the analytic structure is distorted in the strict heavy-baryon limit. This can easily be remedied by including the kinetic energy term in the baryon propagator [45]. In what follows, we will present results based on the heavy-baryon approach.

Numerous advanced few- and many-body techniques have been developed to employ such phenomenological or chiral interactions, in order to calculate the properties of nuclear systems with and without strangeness. For example, systems with three or four particles can be reliably treated by Faddeev-Yakubovsky theory [46–49], somewhat heavier (hyper)nuclei with approaches like the no-core-shell model [50–55]. In the nucleonic sector many-body approaches such as Quantum Monte Carlo calculations [56–58], or nuclear lattice simulations [59–61] have been successfully applied and can be extended to the strangeness sector. Furthermore, nuclear matter is well described by many-body perturbation theory with chiral low-momentum interactions [62–64]. Concerning Λ and Σ hyperons in nuclear matter, specific long-range processes related to two-pion exchange between hyperons and nucleons in the nuclear medium have been studied in Kaiser and Weise [65] and Kaiser [66]. Conventional Brueckner theory [67–69] at first order in the hole-line expansion, the so-called Bruecker-Hartree-Fock approximation, has been widely applied to calculations of hypernuclear matter [20, 24, 70, 71] employing phenomenological two-body potentials. This approach is also used in investigations of neutron star matter [72–74]. Recently, corresponding calculations of the properties of hyperons in nuclear matter have been also performed with chiral *YN* interaction potentials [37, 75, 76].

Employing the high precision *NN* interactions described above, even "simple" nuclear systems such as triton cannot be described satisfactorily with two-body interactions alone. The introduction of three-nucleon forces (3NF) substantially improves this situation [77–80] and also in the context of infinite nuclear matter 3NF are essential to achieve saturation of nuclear matter. These 3NF are introduced either phenomenologically, such as the families of Tuscon-Melbourne [81, 82], Brazilian [83], or Urbana-Illinois [84, 85] 3NF, or constructed according to the basic principles of χEFT [78, 86–94]. Within an EFT approach, 3NF arise naturally and consistently together with two-nucleon forces. Chiral three-nucleon forces are important in order to get saturation of nuclear matter from chiral low-momentum two-body interactions treated in many-body perturbation theory [63]. In the strangeness sectors the situation is similar: Three-baryon forces (3BF), especially the ΛNN interaction, seem to be important for a satisfactorily description of hypernuclei and hypernuclear matter [58, 95–103]. Especially in the context of neutron stars, 3BF are frequently discussed. The observation of two-solar-mass neutron stars [104, 105] sets strong constraints on the stiffness of the equation-of-state (EoS) of dense baryonic matter [106–110]. The analysis of recently observed gravitational wave signals from a two merging neutron stars [111, 112] provides further conditions, by constraining the tidal deformability of neutron star matter.

A naive introduction of Λ-hyperons as an additional baryonic degree of freedom would soften the EoS such that it is not possible to stabilize a two-solar-mass neutron star against gravitational collapse [113]. To solve this so-called *hyperon puzzle*, several *ad-hoc* mechanisms have so far been invoked, e.g., through vector meson exchange [114, 115], multi-Pomeron exchange [116] or a suitably adjusted repulsive ΛNN three-body interaction [117–119]. Clearly, a more systematic approach to the three-baryon interaction within χEFT is needed, to estimate whether the 3BF can provide the necessary repulsion and thus keep the equation-of-state sufficiently stiff. A first step in this direction was done in Petschauer et al. [120], where the leading 3BFs have been derived within SU(3) χEFT. The corresponding low-energy constants have been estimated by decuplet saturation in Petschauer et al. [121]. The effect of these estimated 3BF has been investigated in Petschauer et al. [121] and Kohno [122].

In this review article we present, on a basic level, the emergence of nuclear interactions in the strangeness sector from the perspective of (heavy-baryon) chiral effective field theory. After a brief introduction to SU(3) χEFT in section 2, we present how the interaction between hyperons and nucleons is derived at NLO from these basic principles for two-baryon interactions (section 3) and for three-baryon interactions (section 4). In section 5, applications of these potentials are briefly

reviewed for *YN* scattering, infinite nuclear matter, hypernuclei, and neutron star matter.

2. SU(3) CHIRAL EFFECTIVE FIELD THEORY

An *effective field theory* (EFT) is a low-energy approximation to a more fundamental theory. Physical quantities can be calculated in terms of a low-energy expansion in powers of small energies and momenta over some characteristic large scale. The basic idea of an EFT is to include the relevant degrees of freedom explicitly, while heavier (frozen) degrees of freedom are integrated out. An effective Lagrangian is obtained by constructing the most general Lagrangian including the active degrees of freedom, that is consistent with the symmetries of the underlying fundamental theory [6]. At a given order in the expansion, the theory is characterized by a finite number of coupling constants, called *low-energy constants* (LECs). The LECs encode the unresolved short-distance dynamics and furthermore allow for an order-by-order renormalization of the theory. These constants are a priori unknown, but once determined from one experiment or from the underlying theory, predictions for physical observables can be made. However, due to the low-energy expansion and the truncation of degrees of freedom, an EFT has only a limited range of validity.

The underlying theory of *chiral effective field theory* is quantum chromodynamics. QCD is characterized by two important properties. For high energies the (running) coupling strength of QCD becomes weak, hence a perturbative approach in the high-energy regime of QCD is possible. This famous feature is called *asymptotic freedom* of QCD and originates from the non-Abelian structure of QCD. However, at low energies and momenta the coupling strength of QCD is of order one, and a perturbative approach is no longer possible. This is the region of *non-perturbative QCD*, in which we are interested in. Several strategies to approach this regime have been developed, such as lattice simulations, Dyson-Schwinger equations, QCD sum rules or chiral perturbation theory. The second important feature of QCD is the so-called *color confinement*: isolated quarks and gluons are not observed in nature, but only color-singlet objects. These color-neutral particles, the hadrons, are the active degrees of freedom in χEFT.

But already before QCD was established, the ideas of an effective field theory were used in the context of the strong interaction. In the 60's the Ward identities related to spontaneously broken chiral symmetry were explored by using current algebra methods (e.g., [123]). The group-theoretical foundations for constructing phenomenological Lagrangians in the presence of spontaneous symmetry breaking have been developed by Weinberg [5], Coleman et al. [124], and Callan et al. [125]. With Weinberg's seminal paper [6] it became clear how to systematically construct an EFT and generate loop corrections to tree level results. This method was improved later by Gasser and Leutwyler [7, 126]. A systematic introduction of nucleons as degrees of freedom was done by Gasser et al. [8]. They showed that a fully relativistic treatment of nucleons is problematic, as the nucleon mass does not vanish in the chiral limit and thus adds an extra scale. A solution for this problem was proposed by Jenkins and Manohar [127] by considering baryons as heavy static sources. This approach was further developed using a systematic path-integral framework in Bernard et al. [128]. The nucleon-nucleon interaction and related topics were considered by Weinberg [86]. Nowadays χEFT is used as a powerful tool for calculating systematically the strong interaction dynamics of hadronic processes, such as the accurate description of nuclear forces [13, 14].

In this section, we give a short introduction to the underlying symmetries of QCD and their breaking pattern. The basic concepts of χEFT are explained, especially the explicit degrees of freedom and the connection to the symmetries of QCD. We state in more detail how the chiral Lagrangian can be constructed from basic principles. However, it is beyond the scope of this work to give a detailed introduction to χEFT and QCD. Rather we will introduce only the concepts necessary for the derivation of hyperon-nuclear forces. We follow [9, 13, 14, 129–131] and refer the reader for more details to these references (and references therein).

2.1. Low-Energy Quantum Chromodynamics

Let us start the discussion with the QCD Lagrangian

$$\mathscr{L}_{\mathrm{QCD}} = \sum_{f=u,d,s,c,b,t} \bar{q}_f \left(\mathrm{i} \not{D} - m_f \right) q_f - \frac{1}{4} G_{\mu\nu,a} G_a^{\mu\nu} \,, \tag{1}$$

with the six quark flavors f and the gluonic field-strength tensor $G_{\mu\nu,a}(x)$. The gauge covariant derivative is defined by $D_\mu = \mathbb{1}\partial_\mu - \mathrm{i}g A_\mu^a \frac{\lambda_a}{2}$, where $A_\mu^a(x)$ are the gluon fields and λ_a the Gell-Mann matrices. The QCD Lagrangian is symmetric under the local color gauge symmetry, under global Lorentz transformations, and the discrete symmetries parity, charge conjugation, and time reversal. In the following we will introduce the so-called *chiral symmetry*, an approximate global continuous symmetry of the QCD Lagrangian. The chiral symmetry is essential for chiral effective field theory. In view of the application to low energies, we divide the quarks into three light quarks u, d, s and three heavy quarks c, b, t, since the quark masses fulfill a hierarchical ordering:

$$m_u, m_d, m_s \ll 1 \text{ GeV} \leq m_c, m_b, m_t \,. \tag{2}$$

At energies and momenta well below 1 GeV, the heavy quarks can be treated effectively as static. Therefore, the light quarks are the only active degrees of freedom of QCD for the low-energy region we are interested in. In the following we approximate the QCD Lagrangian by using only the three light quarks. Compared to characteristic hadronic scales, such as the nucleon mass ($M_N \approx$ 939 MeV), the light quark masses are small. Therefore, a good starting point for our discussion of low-energy QCD are massless quarks $m_u = m_d = m_s = 0$, which is referred to as the *chiral limit*. The QCD Lagrangian becomes in the chiral limit

$$\mathscr{L}_{\mathrm{QCD}}^0 = \sum_{f=u,d,s} \bar{q}_f \mathrm{i} \not{D} q_f - \frac{1}{4} G_{\mu\nu,a} G_a^{\mu\nu} \,. \tag{3}$$

Now each quark field $q_f(x)$ is decomposed into its *chiral components*

$$q_{f,\mathrm{L}} = P_\mathrm{L}\, q_f\,, \qquad q_{f,\mathrm{R}} = P_\mathrm{R}\, q_f\,. \tag{4}$$

using the left- and right-handed projection operators

$$P_\mathrm{L} = \frac{1}{2}\left(1-\gamma_5\right)\,, \qquad P_\mathrm{R} = \frac{1}{2}\left(1+\gamma_5\right)\,, \tag{5}$$

with the chirality matrix γ_5. These projectors are called left- and right-handed since in the chiral limit they project the free quark fields on helicity eigenstates, $\hat{h}\, q_{L,R} = \pm\, q_{L,R}$, with $\hat{h} = \vec{\sigma}\cdot\vec{p}\,/\,|\vec{p}\,|$. For massless free fermions helicity is equal to chirality.

Collecting the three quark-flavor fields $q = (q_u, q_d, q_s)$ and equivalently for the left and right handed components, we can express the QCD Lagrangian in the chiral limit as

$$\mathscr{L}^0_\mathrm{QCD} = \bar{q}_\mathrm{R}\mathrm{i}\not{D} q_\mathrm{R} + \bar{q}_\mathrm{L}\mathrm{i}\not{D} q_\mathrm{L} - \frac{1}{4} G_{\mu\nu,a} G_a^{\mu\nu}\,. \tag{6}$$

Obviously the right- and left-handed components of the massless quarks are separated. The Lagrangian is invariant under a global transformation

$$q_\mathrm{L} \to L\, q_\mathrm{L}\,, \quad q_\mathrm{R} \to R\, q_\mathrm{R}\,, \tag{7}$$

with *independent* unitary 3×3 matrices L and R acting in flavor space. This means that $\mathscr{L}^0_\mathrm{QCD}$ possesses (at the classical, unquantized level) a global $\mathrm{U}(3)_\mathrm{L} \times \mathrm{U}(3)_\mathrm{R}$ symmetry, isomorphic to a global $\mathrm{SU}(3)_\mathrm{L} \times \mathrm{U}(1)_\mathrm{L} \times \mathrm{SU}(3)_\mathrm{R} \times \mathrm{U}(1)_\mathrm{R}$ symmetry. $U(1)_\mathrm{L} \times \mathrm{U}(1)_\mathrm{R}$ are often rewritten into a vector and an axial-vector part $U(1)_\mathrm{V} \times \mathrm{U}(1)_\mathrm{A}$, named after the transformation behavior of the corresponding conserved currents under parity transformation. The flavor-singlet vector current originates from rotations of the left- and right-handed quark fields with the same phase ("$V = L + R$") and the corresponding conserved charge is the *baryon number*. After quantization, the conservation of the flavor-singlet axial vector current, with transformations of left- an right-handed quark fields with opposite phase ("$A = L - R$"), gets broken due to the so-called Adler-Bell-Jackiw anomaly [132, 133]. The symmetry group $\mathrm{SU}(3)_\mathrm{L} \times \mathrm{SU}(3)_\mathrm{R}$ refers to the *chiral symmetry*. Similarly the conserved currents can be rewritten into flavor-octet vector and flavor-octet axial-vector currents, where the vector currents correspond to the diagonal subgroup $\mathrm{SU}(3)_\mathrm{V}$ of $\mathrm{SU}(3)_\mathrm{L} \times \mathrm{SU}(3)_\mathrm{R}$ with $L = R$.

After the introduction of small *non-vanishing quark masses*, the quark mass term of the QCD Lagrangian Equation (1) can be expressed as

$$\mathscr{L}_M = -\bar{q}Mq = -\left(\bar{q}_\mathrm{R}Mq_\mathrm{L} + \bar{q}_\mathrm{L}Mq_\mathrm{R}\right)\,, \tag{8}$$

with the diagonal quark mass matrix $M = \mathrm{diag}(m_u, m_d, m_s)$. Left- and right-handed quark fields are mixed in $\mathscr{L}_M$ and the chiral symmetry is explicitly broken. The baryon number is still conserved, but the flavor-octet vector and axial-vector currents are no longer conserved. The axial-vector current is not conserved for any small quark masses. However, the flavor-octet vector current remains conserved, if the quark masses are equal, $m_u = m_d = m_s$, referred to as the *(flavor) SU(3) limit*.

Another crucial aspect of QCD is the so-called *spontaneous chiral symmetry breaking*. The chiral symmetry of the Lagrangian is not a symmetry of the ground state of the system, the QCD vacuum. The structure of the hadron spectrum allows to conclude that the chiral symmetry $\mathrm{SU}(3)_\mathrm{L} \times \mathrm{SU}(3)_\mathrm{R}$ is spontaneously broken to its vectorial subgroup $\mathrm{SU}(3)_\mathrm{V}$, the so-called *Nambu-Goldstone realization* of the chiral symmetry. The spontaneous breaking of chiral symmetry can be characterized by a non-vanishing *chiral quark condensate* $\langle\bar{q}q\rangle \neq 0$, i.e., the vacuum involves strong correlations of scalar quark-antiquark pairs.

The eight Goldstone bosons corresponding to the spontaneous symmetry breaking of the chiral symmetry are identified with the eight lightest hadrons, the pseudoscalar mesons $(\pi^\pm, \pi^0, K^\pm, K^0, \bar{K}^0, \eta)$. They are pseudoscalar particles, due to the parity transformation behavior of the flavor-octet axial-vector currents. The explicit chiral symmetry breaking due to non-vanishing quark masses leads to non-zero masses of the pseudoscalar mesons. However, there is a substantial mass gap, between the masses of the pseudoscalar mesons and the lightest hadrons of the remaining hadronic spectrum. For non-vanishing but equal quark masses, $\mathrm{SU}(3)_\mathrm{V}$ remains a symmetry of the ground state. In this context $\mathrm{SU}(3)_\mathrm{V}$ is often called the flavor group SU(3), which provides the basis for the classification of low-lying hadrons in multiplets. In the following we will consider the so-called *isospin symmetric limit*, with $m_u = m_d \neq m_s$. The remaining symmetry is the SU(2) isospin symmetry. An essential feature of low-energy QCD is, that the pseudoscalar mesons *interact weakly* at low energies. This is a direct consequence of their Goldstone-boson nature. This feature allows for the construction of a low-energy effective field theory enabling a systematic expansion in small momenta and quark masses.

Let us introduce one more tool for the systematic development of χEFT called the *external-field method*. The chiral symmetry gives rise to so-called *chiral Ward identities*: relations between the divergence of Green functions that include a symmetry current (vector or axial-vector currents) to linear combinations of Green functions. Even if the symmetry is explicitly broken, Ward identities related to the symmetry breaking term exist. The chiral Ward identities do not rely on perturbation theory, but are also valid in the non-perturbative region of QCD. The external-field method is an elegant way to formally combine all chiral Ward identities in terms of invariance properties of a generating functional. Following the procedure of Gasser and Leutwyler [7, 126] we introduce (color neutral) *external fields*, $s(x)$, $p(x)$, $v_\mu(x)$, $a_\mu(x)$, of the form of Hermitian 3×3 matrices that couple to scalar, pseudoscalar, vector, and axial-vector currents of quarks:

$$\begin{aligned}\mathscr{L} &= \mathscr{L}^0_\mathrm{QCD} + \mathscr{L}_\mathrm{ext} \\ &= \mathscr{L}^0_\mathrm{QCD} + \bar{q}\gamma^\mu(v_\mu + \gamma_5 a_\mu)q - \bar{q}(s - \mathrm{i}\gamma_5 p)q\,.\end{aligned} \tag{9}$$

All chiral Ward identities are encoded in the corresponding generating functional, if the global chiral symmetry $\mathrm{SU}(3)_\mathrm{L} \times \mathrm{SU}(3)_\mathrm{R}$ of $\mathscr{L}^0_\mathrm{QCD}$ is promoted to a *local gauge symmetry* of

TABLE 1 | Transformation properties of the external fields under parity and charge conjugation.

	v^μ	a^μ	s	p
P	$P^\mu{}_\nu\, v^\nu$	$-P^\mu{}_\nu a^\nu$	s	$-p$
C	$-v^{\mu\top}$	$a^{\mu\top}$	$s^\top$	$p^\top$

For P a change of the spatial arguments $(t,\vec{x}) \to (t,-\vec{x})$ is implied and we defined the matrix $P^\mu_\nu = \mathrm{diag}(+1,-1,-1,-1)$.

$\mathscr{L}$ [134]. Since $\mathscr{L}^0_{\mathrm{QCD}}$ is only invariant under the global chiral symmetry, the external fields have to fulfill a suitable transformation behavior:

$$\begin{aligned} v_\mu + a_\mu &\to R(v_\mu + a_\mu)R^\dagger + \mathrm{i}\, R\partial_\mu R^\dagger\,, \\ v_\mu - a_\mu &\to L(v_\mu - a_\mu)L^\dagger + \mathrm{i}\, L\partial_\mu L^\dagger\,, \\ s + \mathrm{i}\, p &\to R\left(s + \mathrm{i}\, p\right) L^\dagger\,, \\ s - \mathrm{i}\, p &\to L\left(s - \mathrm{i}\, p\right) R^\dagger\,, \end{aligned} \tag{10}$$

where $L(x)$ and $R(x)$ are (independent) space-time-dependent elements of $\mathrm{SU(3)_L}$ and $\mathrm{SU(3)_R}$.

Furthermore, we still require the full Lagrangian $\mathscr{L}$ to be invariant under P, C, and T. As the transformation properties of the quarks are well-known, the transformation behavior of the external fields can be determined and is displayed in **Table 1**. Time reversal symmetry is not considered explicitly, since it is automatically fulfilled due to the *CPT* theorem.

Another central aspect of the external-field method is the addition of terms to the three-flavor QCD Lagrangian in the chiral limit, $\mathscr{L}^0_{\mathrm{QCD}}$. Non-vanishing current quark masses and therefore the *explicit breaking* of chiral symmetry can be included by setting the scalar field equal to the quark mass matrix, $s(x) = M = \mathrm{diag}\,(m_u, m_d, m_s)$. Similarly *electroweak interactions* can be introduced through appropriate external vector and axial vector fields. This feature is important, to systematically include explicit chiral symmetry breaking or couplings to electroweak gauge fields into the chiral effective Lagrangian.

2.2. Explicit Degrees of Freedom

In the low-energy regime of QCD, hadrons are the observable states. The active degrees of freedom of χEFT are identified as the pseudoscalar Goldstone-boson octet. The soft scale of the low-energy expansion is given by the small external momenta and the small masses of the pseudo-Goldstone bosons, while the large scale is a typical hadronic scale of about 1 GeV. The effective Lagrangian has to fulfill the same symmetry properties as QCD: invariance under Lorentz and parity transformations, charge conjugation and time reversal symmetry. Especially the chiral symmetry and its spontaneous symmetry breaking has to be incorporated. Using the external-field method, the *same* external fields v, a, s, p as in Equation (9), with the same transformation behavior, are included in the effective Lagrangian.

As the QCD vacuum is approximately invariant under the flavor symmetry group SU(3), one expects the hadrons to organize themselves in multiplets of irreducible representations of SU(3). The pseudoscalar mesons form an octet (cf. **Figure 1**).

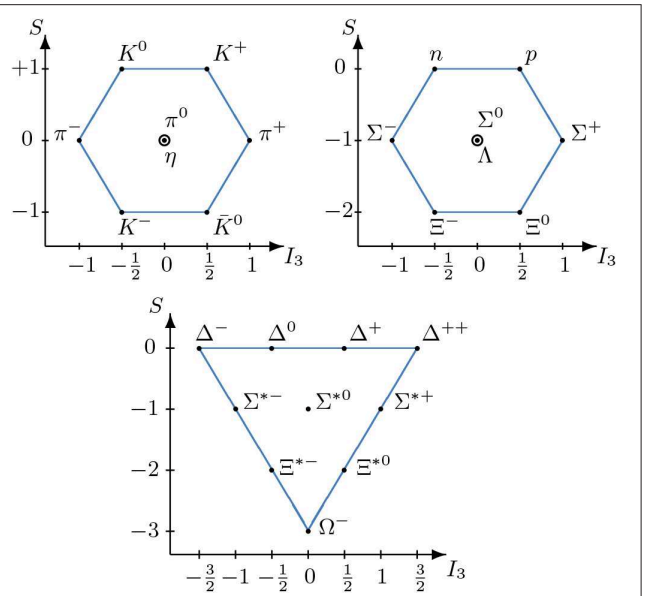


FIGURE 1 | Pseudoscalar meson octet ($J^P = 0^-$), baryon octet ($J^P = 1/2^+$), and baryon decuplet ($J^P = 3/2^+$).

The members of the octet are characterized by the strangeness quantum number S and the third component I_3 of the isospin. The symbol η stands for the octet component (η_8). As an approximation we identify η_8 with the physical η, ignoring possible mixing with the singlet state η_1. For the lowest-lying baryons one finds an octet and a decuplet (see also **Figure 1**). In the following we summarize how these explicit degrees of freedom are included in the chiral Lagrangian in the standard non-linear realization of chiral symmetry [124, 125].

The chiral symmetry group $\mathrm{SU(3)_L \times SU(3)_R}$ is spontaneously broken to its diagonal subgroup $\mathrm{SU(3)_V}$. Therefore, the *Goldstone-boson octet* should transform under $\mathrm{SU(3)_L \times SU(3)_R}$ such that an irreducible **8**-representation results for $\mathrm{SU(3)_V}$. A convenient choice to describe the pseudoscalar mesons under these conditions is a unitary 3×3 matrix $U(x)$ in flavor space, which fulfills

$$U^\dagger U = 1\,, \qquad \det U = 1\,. \tag{11}$$

The transformation behavior under chiral symmetry reads

$$U \to RUL^\dagger\,, \tag{12}$$

where $L(x)$, $R(x)$ are elements of $\mathrm{SU(3)_{L,R}}$. An explicit parametrization of $U(x)$ in terms of the pseudoscalar mesons is given by

$$U(x) = \exp\left[\mathrm{i}\,\phi(x)/f_0\right]\,, \tag{13}$$

with the traceless Hermitian matrix

$$\phi(x) = \sum_{a=1}^{8} \phi_a(x)\lambda_a$$

$$= \begin{pmatrix} \pi^0 + \frac{1}{\sqrt{3}}\eta & \sqrt{2}\pi^+ & \sqrt{2}K^+ \\ \sqrt{2}\pi^- & -\pi^0 + \frac{1}{\sqrt{3}}\eta & \sqrt{2}K^0 \\ \sqrt{2}K^- & \sqrt{2}\bar{K}^0 & -\frac{2}{\sqrt{3}}\eta \end{pmatrix} . \tag{14}$$

The constant f_0 is the *decay constant* of the pseudoscalar Goldstone bosons in the chiral limit. For a transformation of the subgroup $\mathrm{SU(3)_V}$ with $L = R = V$, the meson matrix U transforms as

$$U \to VUV^\dagger , \tag{15}$$

i.e., the mesons $\phi_a(x)$ transform in the adjoint (irreducible) **8**-representation of SU(3). The parity transformation behavior of the pseudoscalar mesons is $\phi_a(t,\vec{x}) \overset{P}{\to} -\phi_a(t,-\vec{x})$ or, equivalently, $U(t,\vec{x}) \overset{P}{\to} U^\dagger(t,-\vec{x})$. Under charge conjugation the particle fields are mapped to antiparticle fields, leading to $U \overset{C}{\to} U^\top$.

The *octet baryons* are described by Dirac spinor fields and represented in a traceless 3×3 matrix $B(x)$ in flavor space,

$$B = \sum_{a=1}^{8} \frac{B_a \lambda_a}{\sqrt{2}} = \begin{pmatrix} \frac{1}{\sqrt{2}}\Sigma^0 + \frac{1}{\sqrt{6}}\Lambda & \Sigma^+ & p \\ \Sigma^- & -\frac{1}{\sqrt{2}}\Sigma^0 + \frac{1}{\sqrt{6}}\Lambda & n \\ \Xi^- & \Xi^0 & -\frac{2}{\sqrt{6}}\Lambda \end{pmatrix} . \tag{16}$$

We use the convenient [135] non-linear realization of chiral symmetry for the baryons, which lifts the well-known flavor transformations to the chiral symmetry group. The matrix $B(x)$ transforms under the chiral symmetry group $\mathrm{SU(3)_L} \times \mathrm{SU(3)_R}$ as

$$B \to KBK^\dagger , \tag{17}$$

with the SU(3)-valued compensator field

$$K(L,R,U) = \sqrt{LU^\dagger R^\dagger} R \sqrt{U} . \tag{18}$$

Note that $K(L,R,U)$ also depends on the meson matrix U. The square root of the meson matrix,

$$u = \sqrt{U} , \tag{19}$$

transforms as $u \to \sqrt{RUL^\dagger} = RuK^\dagger = KuL^\dagger$. For transformations under the subgroup $\mathrm{SU(3)_V}$ the baryons transform as an octet, i.e., the adjoint representation of SU(3):

$$B \to VBV^\dagger . \tag{20}$$

The octet-baryon fields transform under parity and charge conjugation as $B_a(t,\vec{x}) \overset{P}{\to} \gamma^0 B_a(t,-\vec{x})$ and $B_{\alpha,a} \overset{C}{\to} C_{\alpha\beta}\bar{B}_{\beta,a}$ with the Dirac-spinor indices α, β, and with $C = \mathrm{i}\gamma^2\gamma^0$.

A natural choice to represent the *decuplet baryons* is a totally symmetric three-index tensor T. It transforms under the chiral symmetry $\mathrm{SU(3)_L} \times \mathrm{SU(3)_R}$ as

$$T_{abc} \to K_{ad} K_{be} K_{cf} T_{def} , \tag{21}$$

with the compensator field $K(L,R,U)$ of Equation (18). For an $\mathrm{SU(3)_V}$ transformation the decuplet fields transform as an irreducible representation of SU(3):

$$T_{abc} \to V_{ad} V_{be} V_{cf} T_{def} . \tag{22}$$

The physical fields are assigned to the following components of the totally antisymmetric tensor:

$$\begin{aligned} &T^{111} = \Delta^{++} , T^{112} = \tfrac{1}{\sqrt{3}}\Delta^+ , T^{122} = \tfrac{1}{\sqrt{3}}\Delta^0 , T^{222} = \Delta^- , \\ &T^{113} = \tfrac{1}{\sqrt{3}}\Sigma^{*+} , \; T^{123} = \tfrac{1}{\sqrt{6}}\Sigma^{*0} , \; T^{223} = \tfrac{1}{\sqrt{3}}\Sigma^{*-} , \\ &T^{133} = \tfrac{1}{\sqrt{3}}\Xi^{*0} , \; T^{233} = \tfrac{1}{\sqrt{3}}\Xi^{*-} , \\ &T^{333} = \Omega^- . \end{aligned} \tag{23}$$

Since decuplet baryons are spin-3/2 particles, each component is expressed through *Rarita-Schwinger fields*. Within the scope of this article, decuplet baryons are only used for estimating LECs via decuplet resonance saturation. In that case it is sufficient to treat them in their non-relativistic form, where no complications with the Rarita-Schwinger formalism arise.

Now the representation of the explicit degrees of freedom and their transformation behavior are established. Together with the external fields the construction of the chiral effective Lagrangian is straightforward.

2.3. Construction of the Chiral Lagrangian

The chiral Lagrangian can be ordered according to the number of baryon fields:

$$\mathscr{L}_{\mathrm{eff}} = \mathscr{L}_\phi + \mathscr{L}_B + \mathscr{L}_{BB} + \mathscr{L}_{BBB} + \dots , \tag{24}$$

where $\mathscr{L}_\phi$ denotes the purely mesonic part of the Lagrangian. Each part is organized in the number of small momenta (i.e., derivatives) or small meson masses, e.g.,

$$\mathscr{L}_\phi = \mathscr{L}_\phi^{(2)} + \mathscr{L}_\phi^{(4)} + \mathscr{L}_\phi^{(6)} + \dots . \tag{25}$$

$\mathscr{L}_\phi$ has been constructed to $\mathcal{O}(q^6)$ in Fearing and Scherer [136] and Bijnens et al. [137]. The chiral Lagrangian for the baryon-number-one sector has been investigated in various works. The chiral effective pion-nucleon Lagrangian of order $\mathcal{O}(q^4)$ has been constructed in Fettes et al. [138]. The three-flavor Lorentz invariant chiral meson-baryon Lagrangians $\mathscr{L}_B$ at order $\mathcal{O}(q^2)$ and $\mathcal{O}(q^3)$ have been first formulated in Krause [139] and were later completed in Oller et al. [140] and Frink and Meißner [141]. Concerning the nucleon-nucleon contact terms, the relativistically invariant contact Lagrangian at order $\mathcal{O}(q^2)$ for two flavors (without any external fields) has been constructed in Girlanda et al. [142]. The baryon-baryon interaction Lagrangian

$\mathscr{L}_{BB}$ has been considered up to NLO in Savage and Wise [27], Polinder et al. [29], and Petschauer and Kaiser [32]. Furthermore the leading three-baryon contact interaction Lagrangian $\mathscr{L}_{BBB}$ has been derived in Petschauer et al. [120].

We follow closely Petschauer and Kaiser [32] to summarize the basic procedure for constructing systematically the three-flavor chiral effective Lagrangian [124, 125] with the inclusion of external fields [7, 126]. The effective chiral Lagrangian has to fulfill all discrete and continuous symmetries of the strong interaction. Therefore, it has to be invariant under parity (P), charge conjugation (C), Hermitian conjugation (H), and the proper, orthochronous Lorentz transformations. Time reversal symmetry is then automatically fulfilled via the *CPT* theorem. Especially *local* chiral symmetry has to be fulfilled. A common way to construct the chiral Lagrangian is to define so-called *building blocks*, from which the effective Lagrangian can be determined as an invariant polynomial. Considering the chiral transformation properties, a convenient choice for the building blocks is

$$\begin{aligned} u_\mu &= \mathrm{i}\left[u^\dagger\left(\partial_\mu - \mathrm{i}\, r_\mu\right) u - u\left(\partial_\mu - \mathrm{i}\, l_\mu\right) u^\dagger\right], \\ \chi_\pm &= u^\dagger \chi u^\dagger \pm u \chi^\dagger u, \\ f^\pm_{\mu\nu} &= u f^{\mathrm{L}}_{\mu\nu} u^\dagger \pm u^\dagger f^{\mathrm{R}}_{\mu\nu} u, \end{aligned} \tag{26}$$

with the combination

$$\chi = 2B_0\left(s + \mathrm{i}\, p\right), \tag{27}$$

containing the new parameter B_0 and the external scalar and pseudoscalar fields. One defines external field strength tensors by

$$\begin{aligned} f^{\mathrm{R}}_{\mu\nu} &= \partial_\mu r_\nu - \partial_\nu r_\mu - \mathrm{i}\left[r_\mu, r_\nu\right], \\ f^{\mathrm{L}}_{\mu\nu} &= \partial_\mu l_\nu - \partial_\nu l_\mu - \mathrm{i}\left[l_\mu, l_\nu\right], \end{aligned} \tag{28}$$

where the fields

$$r_\mu = v_\mu + a_\mu, \quad l_\mu = v_\mu - a_\mu, \tag{29}$$

describe right handed and left handed external vector fields. In the absence of flavor singlet couplings one can assume $\langle a_\mu \rangle = \langle v_\mu \rangle = 0$, where $\langle \dots \rangle$ denotes the flavor trace. Therefore, the fields u_μ and $f^\pm_{\mu\nu}$ in Equation (26) are all traceless.

Using the *transformation behavior* of the pseudoscalar mesons and octet baryons in Equations (12) and (17), and the transformation properties of the external fields in Equation (10), one can determine the transformation behavior of the building blocks. All building blocks A, and therefore all products of these, transform according to the adjoint (octet) representation of SU(3), i.e., $A \to KAK^\dagger$. Note that traces of products of such building blocks are invariant under local chiral symmetry, since $K^\dagger K = \mathbb{1}$. The chiral covariant derivative of such a building block A is given by

$$D_\mu A = \partial_\mu A + \left[\Gamma_\mu, A\right], \tag{30}$$

with the chiral connection

$$\Gamma_\mu = \frac{1}{2}\left[u^\dagger\left(\partial_\mu - \mathrm{i}\, r_\mu\right) u + u\left(\partial_\mu - \mathrm{i}\, l_\mu\right) u^\dagger\right]. \tag{31}$$

The covariant derivative transforms homogeneously under the chiral group as $D_\mu A \to K\left(D_\mu A\right) K^\dagger$. The chiral covariant derivative of the baryon field B is given by Equation (30) as well.

A Lorentz-covariant *power counting scheme* has been introduced by Krause [139]. Due to the large baryon mass M_0 in the chiral limit, a time-derivative acting on a baryon field B cannot be counted as small. Only baryon three-momenta are small on typical chiral scales. This leads to the following counting rules for baryon fields and their covariant derivatives,

$$B,\ \bar{B},\ D_\mu B \sim \mathcal{O}\left(q^0\right), \qquad \left(\mathrm{i}\not{D} - M_0\right) B \sim \mathcal{O}\left(q\right). \tag{32}$$

The chiral dimension of the chiral building blocks and baryon bilinears $\bar{B}\Gamma B$ are given in **Table 2**. A covariant derivative acting on a building block (but not on B) raises the chiral dimension by one.

A building block A transforms under parity, charge conjugation and Hermitian conjugation as

$$A^P = (-1)^p A, \quad A^C = (-1)^c A^\top, \quad A^\dagger = (-1)^h A, \tag{33}$$

with the exponents (modulo two) $p, c, h \in \{0, 1\}$ given in **Table 2A**, and $\top$ denotes the transpose of a (flavor) matrix. A sign change of the spatial argument, $(t, \vec{x}) \to (t, -\vec{x})$, is implied in the fields in case of parity transformation P. Lorentz indices transform with the matrix $P^\mu{}_\nu = \mathrm{diag}(+1, -1, -1, -1)$ under parity transformation, e.g., $(u^\mu)^P = (-1)^p P^\mu{}_\nu u^\nu$. The transformation behavior of commutators and anticommutators of two building blocks $A_1,\ A_2$ is the same as for building block and should therefore be used instead of simple products, e.g.,

$$\begin{aligned} [A_1, A_2]^C_\pm &= (-1)^{c_1+c_2}(A_1^\top A_2^\top \pm A_2^\top A_1^\top) \\ &= \pm(-1)^{c_1+c_2}[A_1, A_2]^\top_\pm. \end{aligned} \tag{34}$$

The behavior under Hermitian conjugation is the same.

The basis elements of the Dirac algebra forming the baryon bilinears transform as

$$\begin{aligned} \gamma_0\Gamma\gamma_0 &= (-1)^{p_\Gamma}\Gamma, \quad C^{-1}\Gamma C = (-1)^{c_\Gamma}\Gamma^\top, \\ \gamma_0\Gamma^\dagger\gamma_0 &= (-1)^{h_\Gamma}\Gamma, \end{aligned} \tag{35}$$

where the exponents $p_\Gamma, c_\Gamma, h_\Gamma \in \{0, 1\}$ can be found in **Table 2B**. As before, Lorentz indices of baryon bilinears transform with the matrix $P^\mu{}_\nu$ under parity.

Due to the identity

$$\left[D_\mu, D_\nu\right] A = \frac{1}{4}\left[\left[u_\mu, u_\nu\right], A\right] - \frac{\mathrm{i}}{2}\left[f^+_{\mu\nu}, A\right] \tag{36}$$

it is sufficient to use only totally symmetrized products of covariant derivatives, $D^{\alpha\beta\gamma\cdots}A$, for any building block A (or baryon field B). Moreover, because of the relation

$$D_\nu u_\mu - D_\mu u_\nu = f^-_{\mu\nu}, \tag{37}$$

only the symmetrized covariant derivative acting on u_μ need to be taken into account,

$$h_{\mu\nu} = D_\mu u_\nu + D_\nu u_\mu. \tag{38}$$

TABLE 2 | Behavior under parity, charge conjugation, and Hermitian conjugation as well as the chiral dimensions of chiral building blocks and baryon bilinears $\bar{B}\Gamma B$ [140].

(A) Chiral building blocks

	p	c	h	$\mathcal{O}$
u_μ	1	0	0	$\mathcal{O}(q^1)$
$f^+_{\mu\nu}$	0	1	0	$\mathcal{O}(q^2)$
$f^-_{\mu\nu}$	1	0	0	$\mathcal{O}(q^2)$
χ_+	0	0	0	$\mathcal{O}(q^2)$
χ_-	1	0	1	$\mathcal{O}(q^2)$

(B) Baryon bilinears $\bar{B}\Gamma B$

Γ	p	c	h	$\mathcal{O}$
$\mathbb{1}$	0	0	0	$\mathcal{O}(q^0)$
γ_5	1	0	1	$\mathcal{O}(q^1)$
γ_μ	0	1	0	$\mathcal{O}(q^0)$
$\gamma_5\gamma_\mu$	1	0	0	$\mathcal{O}(q^0)$
$\sigma_{\mu\nu}$	0	1	0	$\mathcal{O}(q^0)$

Finally, the chiral effective Lagrangian can be constructed by taking traces (and products of traces) of different polynomials in the building blocks, so that they are invariant under chiral symmetry, Lorentz transformations, C and P.

2.3.1. Leading-Order Meson Lagrangian

As a first example, we show the leading-order purely mesonic Lagrangian. From the general construction principles discussed above, one obtains for the leading-order effective Lagrangian

$$\mathscr{L}_\phi^{(2)} = \frac{f_0^2}{4}\langle u_\mu u^\mu + \chi_+\rangle\,. \tag{39}$$

Note that there is no contribution of order $\mathcal{O}(q^0)$. This is consistent with the vanishing interaction of the Goldstone bosons in the chiral limit at zero momenta.

Before we continue with the meson-baryon interaction Lagrangian, let us elaborate on the leading chiral Lagrangian in the purely mesonic sector without external fields, but with non-vanishing quark masses in the isospin limit: $v^\mu(x) = a^\mu(x) = p(x) = 0$ and $s(x) = M = \mathrm{diag}\,(m, m, m_s)$. Inserting the definitions of the building blocks, Equation (39) becomes with these restrictions:

$$\mathscr{L}_\phi^{(2)} = \frac{f_0^2}{4}\langle \partial_\mu U \partial^\mu U^\dagger\rangle + \frac{1}{2}B_0 f_0^2\langle MU^\dagger + UM\rangle\,. \tag{40}$$

The physical decay constants $f_\pi \neq f_K \neq f_\eta$ differ from the decay constant of the pseudoscalar Goldstone bosons in the chiral limit f_0 in terms of order (m, m_s): $f_\phi = f_0\{1 + \mathcal{O}(m, m_s)\}$. The constant B_0 is related to the chiral quark condensate. Already from this leading-order Lagrangian famous relations such as the (reformulated) Gell-Mann–Oakes–Renner relations

$$\begin{aligned} m_\pi^2 &= 2mB_0 + \mathcal{O}(m_q^2)\,,\\ m_K^2 &= (m + m_s)\,B_0 + \mathcal{O}(m_q^2)\,,\\ m_\eta^2 &= \frac{2}{3}(m + 2m_s)\,B_0 + \mathcal{O}(m_q^2)\,, \end{aligned} \tag{41}$$

or the Gell-Mann–Okubo mass formula, $4m_K^2 = 3m_\eta^2 + m_\pi^2$, can be derived systematically.

2.3.2. Leading-Order Meson-Baryon Interaction Lagrangian

The leading-order meson-baryon interaction Lagrangian $\mathscr{L}_{\mathrm{B}}^{(1)}$ is of order $\mathcal{O}(q)$ and reads[1]

$$\begin{aligned} \mathscr{L}_{\mathrm{B}}^{(1)} =& \langle \bar{B}\left(i\not{D} - M_{\mathrm{B}}\right)B\rangle + \frac{D}{2}\langle \bar{B}\gamma^\mu\gamma_5\{u_\mu, B\}\rangle\\ &+ \frac{F}{2}\langle \bar{B}\gamma^\mu\gamma_5\left[u_\mu, B\right]\rangle\,. \end{aligned} \tag{42}$$

The constant M_{B} is the mass of the baryon octet in the chiral limit. The two new constants D and F are called axial-vector coupling constants. Their values can be obtained from semi-leptonic hyperon decays and are roughly $D \approx 0.8$ and $F \approx 0.5$ [143]. The sum of the two constants is related to the axial-vector coupling constant of nucleons, $g_{\mathrm{A}} = D + F = 1.27$, obtained from neutron beta decay. At lowest order the pion-nucleon coupling constant $g_{\pi N}$ is connected to the axial-vector coupling constant by the Goldberger-Treiman relation, $g_{\pi N} f_\pi = g_{\mathrm{A}} M_N$. The covariant derivative in Equation (42) includes the field Γ_μ, which leads to a vertex between two octet baryons and two mesons, whereas the terms containing u_μ lead to a vertex between two octet baryons and one meson. Different octet-baryon masses appear first in $\mathscr{L}_{\mathrm{B}}^{(2)}$ due to explicit chiral symmetry breaking and renormalization and lead to corrections linear in the quark masses:

$$M_i = M_{\mathrm{B}} + \mathcal{O}(m, m_s)\,. \tag{43}$$

2.4. Weinberg Power Counting Scheme

As stated before, an effective field theory has an infinite number of terms in the effective Lagrangian and for a fixed process an infinite number of diagrams contribute. Therefore, it is crucial to have a power counting scheme, to assign the importance of a term. Then, to a certain order in the power counting, only a *finite number* of terms contribute and the observables can be calculated to a given accuracy.

First, let us discuss the power counting scheme of χEFT in the pure meson sector, i.e., only the pseudoscalar Goldstone bosons are explicit degrees of freedom. The *chiral dimension* ν of a Feynman diagram represents the order in the low-momentum expansion, $(q/\Lambda_\chi)^\nu$. The symbol q is generic for a small external meson momentum or a small meson mass. The scale of chiral

[1]Note that an overall plus sign in front of the constants D and F is chosen, consistent with the conventions in SU(2) χEFT [13].

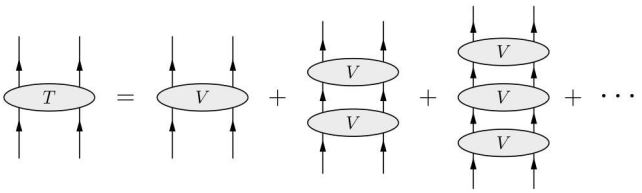


FIGURE 2 | Graphical representation of the Lippmann-Schwinger equation.

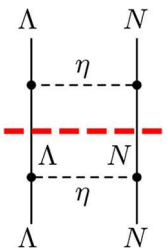


FIGURE 3 | Example of a planar box diagram. It contains an reducible part equivalent to the iteration of two one-meson exchange diagrams, as generated by the Lippmann-Schwinger equation. Additionally it contains a genuine irreducible contribution that is part of the effective potential.

symmetry breaking Λ_χ is often estimated as $4\pi f_\pi \approx 1$ GeV or as the mass of the lowest-lying resonance, $M_\rho \approx 770$ MeV. A simple dimensional analysis leads to the following expression for the chiral dimension of a connected Feynman diagram [6]:

$$\nu = 2 + 2L + \sum_i \nu_i \Delta_i \,, \qquad \Delta_i = d_i - 2 \,. \tag{44}$$

The number of Goldstone boson loops is denoted by L and ν_i is the number of vertices with vertex dimension Δ_i. The symbol d_i stands for the number of derivatives or meson mass insertions at the vertex, i.e., the vertex originates from a term of the Lagrangian of the order $\mathcal{O}(q^{d_i})$.

With the introduction of baryons in the chiral effective Lagrangian, the power counting is more complicated. The large baryon mass comes as an extra scale and destroys the one-to-one correspondence between the loop and the small momentum expansion. Jenkins and Manohar used methods from heavy-quark effective field theory to solve this problem [127]. Basically they considered baryons as heavy, static sources. This leads to a description of the baryons in the extreme non-relativistic limit with an expansion in powers of the inverse baryon mass, called heavy-baryon chiral perturbation theory.

Furthermore, in the two-baryon sector, additional features arise. Reducible Feynman diagrams are enhanced due to the presence of small kinetic energy denominators resulting from purely baryonic intermediate states. These graphs hint at the non-perturbative aspects in few-body problems, such as the existence of shallow bound states, and must be summed up to all orders. As suggested by Weinberg [86, 87], the baryons can be treated non-relativistically and the power counting scheme can be applied to an effective potential V, that contains only irreducible Feynman diagrams. Terms with the inverse baryon mass M_B^{-1} may be

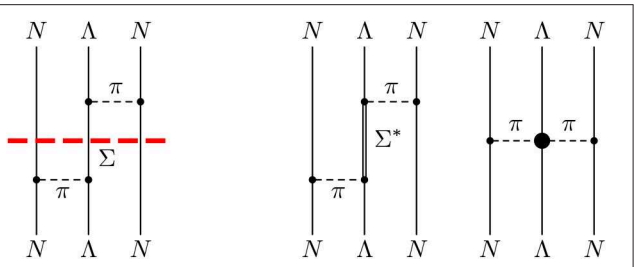


FIGURE 4 | Examples for reducible **(left)** and irreducible **(right)** three-baryon interactions for ΛNN. The thick dashed line cuts the reducible diagram in two two-body interaction parts.

counted as

$$\frac{q}{M_\mathrm{B}} \propto \left(\frac{q}{\Lambda_\chi}\right)^2 . \tag{45}$$

The resulting effective potential is the input for quantum mechanical few-body calculations. In case of the baryon-baryon interaction the effective potential is inserted into the Lippmann-Schwinger equation and solved for bound and scattering states. This is graphically shown in **Figures 2**, **3**. The T-matrix is obtained from the infinite series of ladder diagrams with the effective potential V. In this way the omitted reducible diagrams are regained. In the many-body sector, e.g., Faddeev (or Yakubovsky) equations are typically solved within a coupled-channel approach. In a similar way reducible diagrams such as on the left-hand side of **Figure 4**, are generated automatically and are not part of the effective potential. One should distinguish such iterated two-body interactions, from irreducible three-baryon forces, as shown on the right-hand side of **Figure 4**.

After these considerations, a consistent power counting scheme for the effective potential V is possible. The soft scale q in the low-momentum expansion $(q/\Lambda_\chi)^\nu$ denotes now small external meson four-momenta, small external baryon three-momenta or the small meson masses. Naive dimensional analysis leads to the generalization of Equation (44):

$$\nu = 2 - B + 2L + \sum_i \nu_i \Delta_i \,, \quad \Delta_i = d_i + \frac{1}{2} b_i - 2 \,, \tag{46}$$

where B is the number of external baryons and b_i is the number of internal baryon lines at the considered vertex. However, Equation (46) has an unwanted dependence on the baryon number, due to the normalization of baryon states. Such an effect can be avoided by assigning the chiral dimension to the transition operator instead of the matrix elements. This leads to the addition of $3B-6$ to the formula for the chiral dimension, which leaves the $B = 2$ case unaltered, and one obtains (see for example [9, 13, 14, 130])

$$\nu = -4 + 2B + 2L + \sum_i \nu_i \Delta_i \,, \quad \Delta_i = d_i + \frac{1}{2} b_i - 2 \,. \tag{47}$$

Following this scheme one arrives at the hierarchy of baryonic forces shown in **Figure 5**. The leading-order ($\nu = 0$) potential

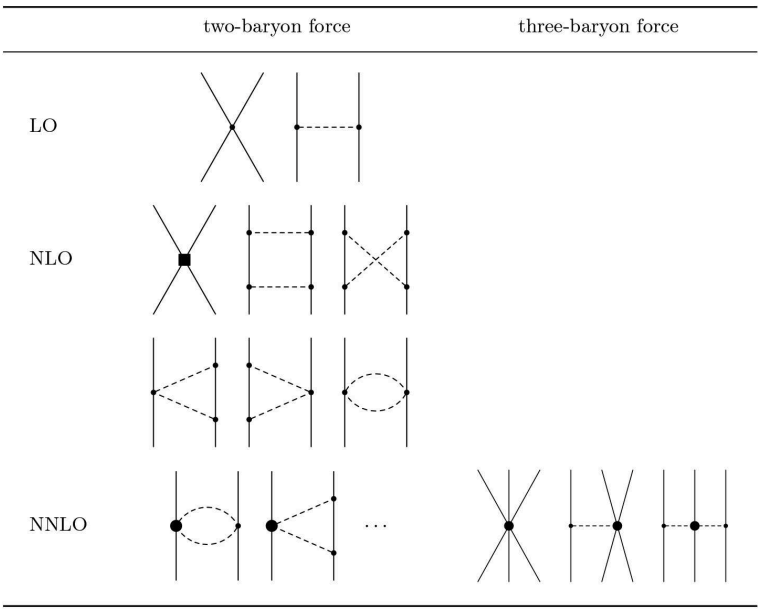


FIGURE 5 | Hierarchy of baryonic forces. Solid lines are baryons, dashed lines are pseudoscalar mesons. Solid dots, filled circles, and squares denote vertices with $\Delta_i = 0, 1,$ and 2, respectively.

is given by one-meson-exchange diagrams and non-derivative four-baryon contact terms. At next-to-leading order ($\nu = 2$) higher order contact terms and two-meson-exchange diagrams with intermediate octet baryons contribute. Finally, at next-to-next-to-leading order ($\nu = 3$) the three-baryon forces start to contribute. Diagrams that lead to mass and coupling constant renormalization are not shown.

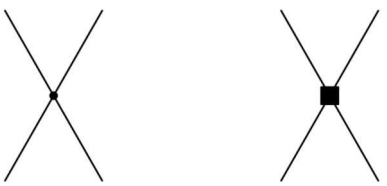


FIGURE 6 | Leading-order and next-to-leading-order baryon-baryon contact vertices.

3. BARYON-BARYON INTERACTION POTENTIALS

This section is devoted to the baryon-baryon interaction potentials up to next-to-leading order, constructed from the diagrams shown in **Figure 5**. Contributions arise from contact interaction, one- and two-Goldstone-boson exchange. The constructed potentials serve not only as input for the description of baryon-baryon scattering, but are also basis for few- and many-body calculations. We give also a brief introduction to common meson-exchange models and the difference to interaction potentials from χEFT.

3.1. Baryon-Baryon Contact Terms

The chiral Lagrangian necessary for the contact vertices shown in **Figure 6** can be constructed straightforwardly according to the principles outlined in section 2. For pure baryon-baryon scattering processes, no pseudoscalar mesons are involved in the contact vertices and almost all external fields can be dropped. Covariant derivatives D_μ reduce to ordinary derivatives ∂_μ. The only surviving external field is χ_+, which is responsible for the inclusion of quark masses into the chiral Lagrangian:

$$\frac{\chi_+}{2} = \chi = 2B_0 \begin{pmatrix} m_u & 0 & 0 \\ 0 & m_d & 0 \\ 0 & 0 & m_s \end{pmatrix} \approx \begin{pmatrix} m_\pi^2 & 0 & 0 \\ 0 & m_\pi^2 & 0 \\ 0 & 0 & 2m_K^2 - m_\pi^2 \end{pmatrix}, \tag{48}$$

where in the last step the Gell-Mann–Oakes–Renner relations, Equation (41), have been used. In flavor space the possible terms are of the schematic form

$$\langle \bar{B}B\bar{B}B \rangle\,,\ \langle \bar{B}\bar{B}BB \rangle\,,\ \langle \bar{B}B \rangle \langle \bar{B}B \rangle\,,\ \langle \bar{B}\bar{B} \rangle \langle BB \rangle\,, \tag{49}$$

and terms where the field χ is inserted such as

$$\langle \bar{B}\chi B\bar{B}B \rangle\,,\ \langle \bar{B}B\chi \bar{B}B \rangle\,,\ \langle \bar{B}\chi B \rangle \langle \bar{B}B \rangle\,,\ \ldots \tag{50}$$

where in both cases appropriate structures in Dirac space have to be inserted. For the case of the non-relativistic power counting it would also be sufficient, to insert the corresponding structures

in spin-momentum space. The terms involving χ lead to explicit SU(3) symmetry breaking at NLO linear in the quark masses. A set of linearly independent Lagrangian terms up to $\mathcal{O}(q^2)$ for pure baryon-baryon interaction in non-relativistic power counting can be found in Petschauer and Kaiser [32].

After a non-relativistic expansion up to $\mathcal{O}(q^2)$ the four-baryon contact Lagrangian leads to potentials in spin and momentum space. A convenient operator basis is given by [29]:

$$\begin{aligned}
P_1 &= \mathbb{1}\,,\\
P_2 &= \vec{\sigma}_1\cdot\vec{\sigma}_2\,,\\
P_3 &= (\vec{\sigma}_1\cdot\vec{q}\,)(\vec{\sigma}_2\cdot\vec{q}\,) - \frac{1}{3}(\vec{\sigma}_1\cdot\vec{\sigma}_2)\vec{q}^{\,2}\,,\\
P_4 &= \frac{\mathrm{i}}{2}(\vec{\sigma}_1+\vec{\sigma}_2)\cdot\vec{n}\,,\\
P_5 &= (\vec{\sigma}_1\cdot\vec{n}\,)(\vec{\sigma}_2\cdot\vec{n}\,)\,,\\
P_6 &= \frac{\mathrm{i}}{2}(\vec{\sigma}_1-\vec{\sigma}_2)\cdot\vec{n}\,,\\
P_7 &= (\vec{\sigma}_1\cdot\vec{k}\,)(\vec{\sigma}_2\cdot\vec{q}\,) + (\vec{\sigma}_1\cdot\vec{q}\,)(\vec{\sigma}_2\cdot\vec{k}\,)\,,\\
P_8 &= (\vec{\sigma}_1\cdot\vec{k}\,)(\vec{\sigma}_2\cdot\vec{q}\,) - (\vec{\sigma}_1\cdot\vec{q}\,)(\vec{\sigma}_2\cdot\vec{k}\,)\,,
\end{aligned} \tag{51}$$

with $\vec{\sigma}_{1,2}$ the Pauli spin matrices and with the vectors

$$\vec{k} = \frac{1}{2}(\vec{p}_f+\vec{p}_i)\,,\quad \vec{q} = \vec{p}_f-\vec{p}_i\,,\quad \vec{n} = \vec{p}_i\times\vec{p}_f\,. \tag{52}$$

The momenta $\vec{p}_f$ and $\vec{p}_i$ are the initial and final state momenta in the center-of-mass frame. In order to obtain the minimal set of Lagrangian terms in the non-relativistic power counting of Petschauer and Kaiser [32], the potentials have been decomposed into partial waves. The formulas for the partial wave projection of a general interaction $V = \sum_{j=1}^{8} V_j P_j$ can be found in the appendix of Polinder et al. [29]. For each partial wave one produces a non-square matrix which connects the Lagrangian constants with the different baryon-baryon channels. Lagrangian terms are considered as redundant if their omission does not lower the rank of this matrix. For the determination of the potential not only direct contributions have to be considered, but also additional structures from exchanged final state baryons, where the negative spin-exchange operator $-P^{(\sigma)} = -\frac{1}{2}(\mathbb{1}+\vec{\sigma}_1\cdot\vec{\sigma}_2)$ is applied. In the end 6 momentum-independent terms at LO contribute, and are therefore only visible in $^1S_0$ and $^3S_1$ partial waves. At NLO 22 terms contribute that contain only baryon fields and derivatives, and are therefore SU(3) symmetric. The other 12 terms at NLO include the diagonal matrix χ and produce explicit SU(3) symmetry breaking.

In **Table 3**, the non-vanishing transitions projected onto partial waves in the isospin basis are shown (cf. [29–32]). The pertinent constants are redefined according to the relevant irreducible SU(3) representations. This comes about in the following way. Baryons form a flavor octet and the tensor product of two baryons decomposes into irreducible representations as follows:

$$\mathbf{8}\otimes\mathbf{8} = \mathbf{27}_s\oplus\mathbf{10}_a\oplus\mathbf{10}_a^*\oplus\mathbf{8}_s\oplus\mathbf{8}_a\oplus\mathbf{1}_s\,, \tag{53}$$

where the irreducible representations $\mathbf{27}_s$, $\mathbf{8}_s$, $\mathbf{1}_s$ are symmetric and $\mathbf{10}_a$, $\mathbf{10}_a^*$, $\mathbf{8}_a$ are antisymmetric with respect to the exchange of both baryons. Due to the generalized Pauli principle, the symmetric flavor representations $\mathbf{27}_s$, $\mathbf{8}_s$, $\mathbf{1}_s$ have to combine with the space-spin antisymmetric partial waves $^1S_0$, $^3P_0$, $^3P_1$, $^3P_2$, ... ($L+S$ even). The antisymmetric flavor representations $\mathbf{10}_a$, $\mathbf{10}_a^*$, $\mathbf{8}_a$ combine with the space-spin symmetric partial waves $^3S_1$, $^1P_1$, $^3D_1 \leftrightarrow {}^3S_1$, ... ($L+S$ odd). Transitions can only occur between equal irreducible representations. Hence, transitions between space-spin antisymmetric partial waves up to $\mathcal{O}(q^2)$ involve the 15 constants $\tilde{c}_{^1S_0}^{27,8s,1}$, $c_{^1S_0}^{27,8s,1}$, $c_{^3P_0}^{27,8s,1}$, $c_{^3P_1}^{27,8s,1}$, and $c_{^3P_2}^{27,8s,1}$, whereas transitions between space-spin symmetric partial waves involve the 12 constants $\tilde{c}_{^3S_1}^{8a,10,10^*}$, $c_{^3S_1}^{8a,10,10^*}$, $c_{^1P_1}^{8a,10,10^*}$, and $c_{^3D_1\text{-}^3S_1}^{8a,10,10^*}$. The constants with a tilde denote leading-order constants, whereas the ones without tilde are at NLO. The spin singlet-triplet transitions $^1P_1 \leftrightarrow {}^3P_1$ is perfectly allowed by SU(3) symmetry since it is related to transitions between the irreducible representations $\mathbf{8}_a$ and $\mathbf{8}_s$. Such a transition originated from the antisymmetric spin-orbit operator P_6 and its Fierz-transformed counterpart P_8 and the single corresponding low-energy constant is denoted by c^{8as}. In case of the *NN* interaction such transitions are forbidden by isospin symmetry. The constants $\tilde{c}_{^1S_0}^{27,8s,1}$ and $\tilde{c}_{^3S_1}^{8a,10,10^*}$ fulfill the same SU(3) relations as the constants $c_{^1S_0}^{27,8s,1}$ and $c_{^3S_1}^{8a,10,10^*}$ in **Table 3**. SU(3) breaking terms linear in the quark masses appears only in the S-waves, $^1S_0$, $^3S_1$, and are proportional $m_K^2 - m_\pi^2$. The corresponding 12 constants are $c_\chi^{1,\ldots,12}$. The SU(3) symmetry relations in **Table 3** can also be derived by group theoretical considerations [29, 144–146]. Clearly, for the SU(3)-breaking part this is not possible and these contributions have to be derived from the chiral Lagrangian.

In order to obtain the complete partial-wave projected potentials, some entries in **Table 3** have to be multiplied with additional momentum factors. The leading order constants $\tilde{c}_j^i$ receive no further factor. For the next-to-leading-order constants (without tilde and without χ) the contributions to the partial waves $^1S_0$, $^3S_1$ have to be multiplied with a factor $p_i^2+p_f^2$. The contribution to the partial waves $^1S_0$, $^3S_1$ from constants c_χ^j has to be multiplied with $(m_K^2-m_\pi^2)$. The partial waves $^3P_0$, $^3P_1$, $^3P_2$, $^1P_1$, $^1P_1 \leftrightarrow {}^3P_1$ get multiplied with the factor $p_i p_f$. The entries for $^3S_1 \to {}^3D_1$ and $^3D_1 \to {}^3S_1$ have to be multiplied with p_i^2 and p_f^2, respectively. For example, one obtains for the *NN* interaction in the $^1S_0$ partial wave:

$$\begin{aligned}
&\langle NN,{}^1S_0|\hat{V}|NN,{}^1S_0\rangle\\
&\qquad = \tilde{c}_{^1S_0}^{27} + c_{^1S_0}^{27}(p_i^2+p_f^2) + \frac{1}{2}c_\chi^1(m_K^2-m_\pi^2)\,,
\end{aligned} \tag{54}$$

or for the $\Xi N \to \Sigma\Sigma$ interaction with total isospin $I=0$ in the $^1P_1 \to {}^3P_1$ partial wave:

$$\langle\Sigma\Sigma,{}^3P_1|\hat{V}|\Xi N,{}^1P_1\rangle = 2\sqrt{3}c^{8as}p_i p_f\,. \tag{55}$$

When restricting to the *NN* channel the well-known two leading and seven next-to-leading order low-energy constants

TABLE 3 | SU(3) relations of pure baryon-baryon contact terms for non-vanishing partial waves up to $\mathcal{O}(q^2)$ in non-relativistic power counting for channels described by strangeness S and total isospin I [32].

S	I	Transition	$j \in \{^1S_0, ^3P_0, ^3P_1, ^3P_2\}$	$j \in \{^3S_1, ^1P_1, ^3S_1 \leftrightarrow ^3D_1\}$	$^1P_1 \to ^3P_1$	$^3P_1 \to ^1P_1$	$^1S_0\ \chi$	$^3S_1\ \chi$
0	0	NN→ NN	0	$c_j^{10^*}$	0	0	0	$\frac{c_\chi^7}{2}$
	1	NN→ NN	c_j^{27}	0	0	0	$\frac{c_\chi^1}{2}$	0
-1	$\frac{1}{2}$	$\Lambda N \to \Lambda N$	$\frac{1}{10}(9c_j^{27} + c_j^{8s})$	$\frac{1}{2}(c_j^{10^*} + c_j^{8a})$	$-c^{8as}$	$-c^{8as}$	c_χ^2	c_χ^8
	$\frac{1}{2}$	$\Lambda N \to \Sigma N$	$-\frac{3}{10}(c_j^{27} - c_j^{8s})$	$\frac{1}{2}(c_j^{10^*} - c_j^{8a})$	$-3c^{8as}$	c^{8as}	$-c_\chi^3$	$-c_\chi^9$
	$\frac{1}{2}$	$\Sigma N \to \Sigma N$	$\frac{1}{10}(c_j^{27} + 9c_j^{8s})$	$\frac{1}{2}(c_j^{10^*} + c_j^{8a})$	$3c^{8as}$	$3c^{8as}$	c_χ^4	c_χ^{10}
	$\frac{3}{2}$	$\Sigma N \to \Sigma N$	c_j^{27}	c_j^{10}	0	0	$\frac{c_\chi^1}{4}$	$-\frac{c_\chi^7}{4}$
-2	0	$\Lambda\Lambda \to \Lambda\Lambda$	$\frac{1}{40}(5c_j^1 + 27c_j^{27} + 8c_j^{8s})$	0	0	0	$\frac{c_\chi^5}{2}$	0
	0	$\Lambda\Lambda \to \Xi N$	$\frac{1}{20}(5c_j^1 - 9c_j^{27} + 4c_j^{8s})$	0	0	$2c^{8as}$	$\frac{3c_\chi^1}{4} - 3c_\chi^2 - c_\chi^3 + \frac{3c_\chi^5}{4}$	0
	0	$\Lambda\Lambda \to \Sigma\Sigma$	$-\frac{\sqrt{3}}{40}(5c_j^1 + 3c_j^{27} - 8c_j^{8s})$	0	0	0	0	0
	0	$\Xi N \to \Xi N$	$\frac{1}{10}(5c_j^1 + 3c_j^{27} + 2c_j^{8s})$	c_j^{8a}	$2c^{8as}$	$2c^{8as}$	$\frac{2c_\chi^1}{3} - 3c_\chi^2 + \frac{c_\chi^4}{3} + \frac{9c_\chi^5}{8}$	c_χ^{11}
	0	$\Xi N \to \Sigma\Sigma$	$\frac{\sqrt{3}}{20}(-5c_j^1 + c_j^{27} + 4c_j^{8s})$	0	$2\sqrt{3}c^{8as}$	0	$-\frac{c_\chi^1}{4\sqrt{3}} + \sqrt{3}c_\chi^3 + \frac{c_\chi^4}{\sqrt{3}}$	0
	0	$\Sigma\Sigma \to \Sigma\Sigma$	$\frac{1}{40}(15c_j^1 + c_j^{27} + 24c_j^{8s})$	0	0	0	0	0
	1	$\Xi N \to \Xi N$	$\frac{1}{5}(2c_j^{27} + 3c_j^{8s})$	$\frac{1}{3}(c_j^{10} + c_j^{10^*} + c_j^{8a})$	$-2c^{8as}$	$-2c^{8as}$	c_χ^6	c_χ^{12}
	1	$\Xi N \to \Sigma\Sigma$	0	$\frac{1}{3\sqrt{2}}(c_j^{10} + c_j^{10^*} - 2c_j^{8a})$	0	$2\sqrt{2}c^{8as}$	0	$\sqrt{2}c_\chi^{10} - \frac{c_\chi^7}{2\sqrt{2}} - \sqrt{2}c_\chi^9$
	1	$\Xi N \to \Sigma\Lambda$	$\frac{\sqrt{6}}{5}(c_j^{27} - c_j^{8s})$	$\frac{1}{\sqrt{6}}(c_j^{10} - c_j^{10^*})$	$2\sqrt{\frac{2}{3}}c^{8as}$	0	$-\frac{1}{3}\sqrt{\frac{2}{3}}c_\chi^1 + \sqrt{\frac{3}{2}}c_\chi^2 - \frac{c_\chi^4}{3\sqrt{6}} - \sqrt{\frac{2}{3}}c_\chi^6$	$\frac{c_\chi^{10}}{\sqrt{6}} + \sqrt{\frac{2}{3}}c_\chi^{12} + \frac{c_\chi^7}{2\sqrt{6}} - \sqrt{\frac{3}{2}}c_\chi^8 + \sqrt{\frac{2}{3}}c_\chi^9$
	1	$\Sigma\Lambda \to \Sigma\Lambda$	$\frac{1}{5}(3c_j^{27} + 2c_j^{8s})$	$\frac{1}{2}(c_j^{10} + c_j^{10^*})$	0	0	$-\frac{c_\chi^1}{9} + \frac{4c_\chi^3}{3} + \frac{4c_\chi^4}{9} + \frac{2c_\chi^6}{3}$	$\frac{4c_\chi^{10}}{3} + \frac{2c_\chi^{12}}{3} - \frac{c_\chi^7}{3} - \frac{4c_\chi^9}{3}$
	1	$\Sigma\Lambda \to \Sigma\Sigma$	0	$\frac{1}{2\sqrt{3}}(c_j^{10} - c_j^{10^*})$	0	$\frac{4}{\sqrt{3}}c^{8as}$	0	0
	1	$\Sigma\Sigma \to \Sigma\Sigma$	0	$\frac{1}{6}(c_j^{10} + c_j^{10^*} + 4c_j^{8a})$	0	0	0	0
	2	$\Sigma\Sigma \to \Sigma\Sigma$	c_j^{27}	0	0	0	0	0
-3	$\frac{1}{2}$	$\Xi\Lambda \to \Xi\Lambda$	$\frac{1}{10}(9c_j^{27} + c_j^{8s})$	$\frac{1}{2}(c_j^{10} + c_j^{8a})$	$-c^{8as}$	$-c^{8as}$	$-\frac{55c_\chi^1}{72} + 2c_\chi^2 + \frac{7c_\chi^3}{6} + \frac{c_\chi^4}{18} + \frac{3c_\chi^5}{32} + \frac{c_\chi^6}{12}$	$\frac{11c_\chi^{10}}{12} + \frac{3c_\chi^{11}}{4} + \frac{25c_\chi^{12}}{12} + \frac{5c_\chi^7}{24} - \frac{7c_\chi^8}{4} - \frac{c_\chi^9}{6}$
	$\frac{1}{2}$	$\Xi\Lambda \to \Xi\Sigma$	$-\frac{3}{10}(c_j^{27} - c_j^{8s})$	$\frac{1}{2}(c_j^{10} - c_j^{8a})$	$-3c^{8as}$	c^{8as}	$\frac{11c_\chi^1}{24} - \frac{3c_\chi^2}{2} - \frac{c_\chi^3}{2} - \frac{c_\chi^4}{3} + \frac{9c_\chi^5}{32} + \frac{c_\chi^6}{4}$	$\frac{9c_\chi^{10}}{4} - \frac{3c_\chi^{11}}{4} + \frac{5c_\chi^{12}}{4} - \frac{c_\chi^7}{8} - \frac{3c_\chi^8}{4} - \frac{c_\chi^9}{2}$
	$\frac{1}{2}$	$\Xi\Sigma \to \Xi\Sigma$	$\frac{1}{10}(c_j^{27} + 9c_j^{8s})$	$\frac{1}{2}(c_j^{10} + c_j^{8a})$	$3c^{8as}$	$3c^{8as}$	$\frac{11c_\chi^1}{24} - 3c_\chi^2 + \frac{5c_\chi^3}{2} + \frac{c_\chi^4}{6} + \frac{27c_\chi^5}{32} + \frac{3c_\chi^6}{4}$	$\frac{5c_\chi^{10}}{4} + \frac{3c_\chi^{11}}{4} + \frac{3c_\chi^{12}}{4} - \frac{c_\chi^7}{8} - \frac{3c_\chi^8}{4} - \frac{3c_\chi^9}{2}$
	$\frac{3}{2}$	$\Xi\Sigma \to \Xi\Sigma$	c_j^{27}	$c_j^{10^*}$	0	0	$-\frac{2c_\chi^1}{3} + \frac{3c_\chi^2}{2} + c_\chi^3 + \frac{c_\chi^4}{6}$	$\frac{3c_\chi^{10}}{2} - c_\chi^7 + \frac{3c_\chi^8}{2} - 3c_\chi^9$
-4	0	$\Xi\Xi \to \Xi\Xi$	0	c_j^{10}	0	0	0	$5c_\chi^{10} + 4c_\chi^{12} - 3c_\chi^8 - 2c_\chi^9$
	1	$\Xi\Xi \to \Xi\Xi$	c_j^{27}	0	0	0	$-\frac{4c_\chi^1}{3} + 3c_\chi^2 + 2c_\chi^3 + \frac{c_\chi^4}{3}$	0

of Epelbaum et al. [147] are recovered, which contribute to the partial waves ${}^1S_0$, ${}^3S_1$, ${}^1P_1$, ${}^3P_0$, ${}^3P_1$, ${}^3P_2$, ${}^3S_1 \leftrightarrow {}^3D_1$.

Note, that the SU(3) relations in **Table 3** are general relations that have to be fulfilled by the baryon-baryon potential in the SU(3) limit, i.e., $m_\pi = m_K = m_\eta$. This feature can be used as a check for the inclusion of the loop diagrams. Another feature is, that the SU(3) relations contain only a few constants in each partial wave. For example, in the ${}^1S_0$ partial wave only the constants $\tilde{c}^{27}_{{}^1S_0}$, $\tilde{c}^{8s}_{{}^1S_0}$, $\tilde{c}^{1}_{{}^1S_0}$ are present. If these constants are fixed in some of the baryons channels, predictions for other channels can be made. This has, for instance, been used in Haidenbauer et al. [35], where the existence of $\Sigma\Sigma$, $\Sigma\Xi$ and $\Xi\Xi$ bound states has been studied within SU(3) χEFT.

3.2. One- and Two-Meson-Exchange Contributions

In the last section, we have addressed the short-range part of the baryon-baryon interaction via contact terms. Let us now analyze the long- and mid-range part of the interaction, generated by one- and two-meson-exchange as determined in Haidenbauer et al. [33]. The contributing diagrams up to NLO are shown in **Figure 5**, which displays the hierarchy of baryonic forces.

The vertices, necessary for the construction of these diagrams stem from the leading-order meson-baryon interaction Lagrangian $\mathscr{L}^{(1)}_{\mathrm{B}}$ in Equation (42). The vertex between two baryons and one meson emerges from the part

$$\begin{aligned}&\frac{D}{2}\langle\bar{B}\gamma^\mu\gamma_5\{u_\mu,B\}\rangle+\frac{F}{2}\langle\bar{B}\gamma^\mu\gamma_5\left[u_\mu,B\right]\rangle\\&=-\frac{1}{2f_0}\sum_{i,j,k=1}^{8}N_{B_iB_j\phi_k}(\bar{B}_i\gamma^\mu\gamma_5B_j)(\partial_\mu\phi_k)+\mathcal{O}(\phi^3)\,,\end{aligned}\tag{56}$$

where we have used $u_\mu = -\frac{1}{f_0}\partial_\mu\phi+\mathcal{O}(\phi^3)$ and have rewritten the pertinent part of the Lagrangian in terms of the physical meson and baryon fields

$$\begin{aligned}\phi_i &\in \left\{\pi^0,\pi^+,\pi^-,K^+,K^-,K^0,\bar{K}^0,\eta\right\}\,,\\B_i &\in \left\{n,p,\Sigma^0,\Sigma^+,\Sigma^-,\Lambda,\Xi^0,\Xi^-\right\}\,.\end{aligned}\tag{57}$$

The factors $N_{B_iB_j\phi_k}$ are linear combinations of the axial vector coupling constants D and F with certain SU(3) coefficients. These factors vary for different combinations of the involved baryons and mesons and can be obtained easily by multiplying out the baryon and meson flavor matrices. In a similar way, we obtain the (Weinberg-Tomozawa) vertex between two baryons and two mesons from the covariant derivative in $\mathscr{L}^{(1)}_{\mathrm{B}}$, leading to

$$\begin{aligned}&\langle\bar{B}\mathrm{i}\gamma^\mu\left[\Gamma_\mu,B\right]\rangle\\&=\frac{\mathrm{i}}{8f_0^2}\sum_{i,j,k,l=1}^{8}N_{B_i\phi_kB_j\phi_l}(\bar{B}_i\gamma^\mu B_j)(\phi_k\partial_\mu\phi_l)+\mathcal{O}(\phi^4)\,,\end{aligned}\tag{58}$$

where $\Gamma_\mu = \frac{1}{8f_0^2}[\phi,\partial_\mu\phi]+\mathcal{O}(\phi^4)$ was used.

The calculation of the baryon-baryon potentials is done in the center-of-mass frame and in the isospin limit $m_u = m_d$. To obtain the contribution of the Feynman diagrams to the non-relativistic potential, we perform an expansion in the inverse baryon mass $1/M_{\mathrm{B}}$. If loops are involved, the integrand is expanded before integrating over the loop momenta. This produces results that are equivalent to the usual heavy-baryon formalism. In the case of the two-meson-exchange diagrams at one-loop level, ultraviolet divergences are treated by dimensional regularization, which introduces a scale λ. In dimensional regularization divergences are isolated as terms proportional to

$$R = \frac{2}{d-4}+\gamma_{\mathrm{E}}-1-\ln(4\pi)\,,\tag{59}$$

with $d \neq 4$ the space-time dimension and the Euler-Mascheroni constant $\gamma_{\mathrm{E}} \approx 0.5772$. These terms can be absorbed by the contact terms.

According to Equations (56) and (58) the vertices have the same form for different combinations of baryons and mesons, just their prefactors change. Therefore, the one- and two-pseudoscalar-meson exchange potentials can be given by a master formula, where the proper masses of the exchanged mesons have to be inserted, and which has to be multiplied with an appropriate SU(3) factor N. In the following we will present the analytic formulas for the one- and two-meson-exchange diagrams, introduced in Haidenbauer et al. [33]. The pertinent SU(3) factors will be displayed next to the considered Feynman diagram (cf. **Figure 7**). The results will be given in terms of a central potential (V_{C}), a spin-spin potential ($\vec{\sigma}_1\cdot\vec{\sigma}_2\,V_S$) and a tensor-type potential ($\vec{\sigma}_1\cdot\vec{q}\,\vec{\sigma}_2\cdot\vec{q}\,V_T$). The momentum transfer is $q = \left|\vec{p}_f-\vec{p}_i\right|$, with $\vec{p}_i$ and $\vec{p}_f$ the initial and final state momenta in the center-of-mass frame.

Note that the presented results apply only to direct diagrams. This is for example the case for the leading-order one-eta exchange in the Λn interaction, i.e., for $\Lambda(\vec{p}_i)n(-\vec{p}_i) \xrightarrow{\eta} \Lambda(\vec{p}_f)n(-\vec{p}_f)$. An example of a crossed diagram is the one-kaon exchange in the process $\Lambda(\vec{p}_i)n(-\vec{p}_i) \xrightarrow{K} n(-\vec{p}_f)\Lambda(\vec{p}_f)$, where the nucleon and the hyperon in the final state are interchanged and strangeness is exchanged. In such cases, $\vec{p}_f$ is replaced by $-\vec{p}_f$ and the momentum transfer in the potentials is $q = \left|\vec{p}_f+\vec{p}_i\right|$. Due to the exchange of fermions in the final states a minus sign arises, and additionally the spin-exchange operator $P^{(\sigma)} = \frac{1}{2}(\mathbb{1}+\vec{\sigma}_1\cdot\vec{\sigma}_2)$ has to be applied. The remaining structure of the potentials stays the same (see also the discussion in section 4).

The leading-order contribution comes from the *one-meson exchange* diagram in **Figure 7A**. It contributes only to the tensor-type potential:

$$V_{\mathrm{T}}^{\mathrm{ome}}(q) = -\frac{N}{4f_0^2}\frac{1}{q^2+m^2-\mathrm{i}\epsilon}\,.\tag{60}$$

The symbol $\bar{M}$ in the SU(3) coefficient N denotes the charge-conjugated meson of meson M in particle basis (e.g., $\pi^+ \leftrightarrow \pi^-$).

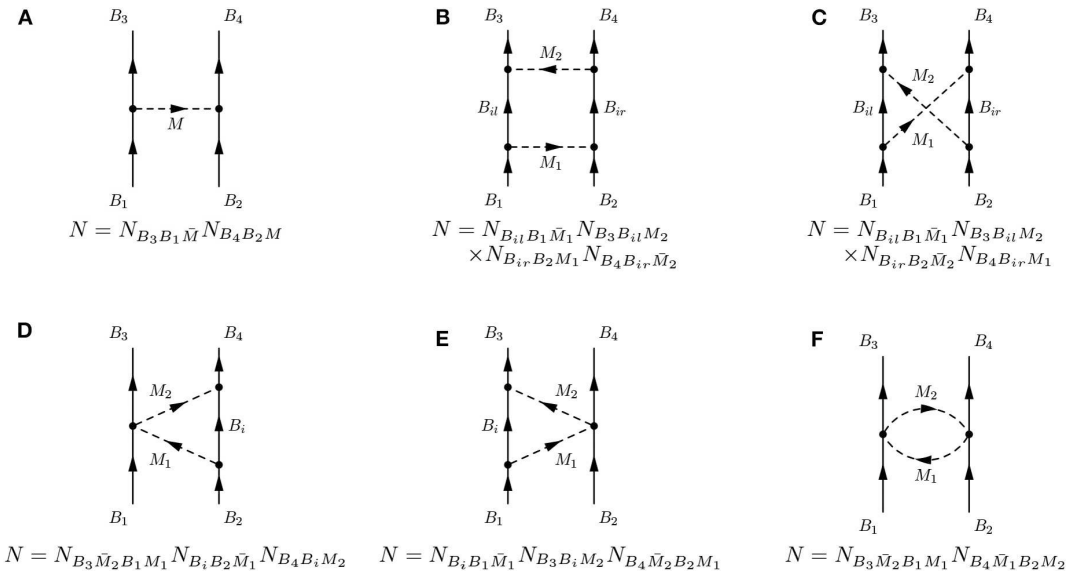


FIGURE 7 | One- and two-meson-exchange contributions and corresponding SU(3) factors. **(A)** One-meson exchange, **(B)** planar box, **(C)** crossed box, **(D)** left triangle, **(E)** right triangle, and **(F)** football diagram.

At next-to-leading order the two-meson exchange diagrams start to contribute. The *planar box* in **Figure 7B** contains an irreducible part and a reducible part coming from the iteration of the one-meson exchange to second order. Inserting the potential into the Lippmann-Schwinger equation generates the reducible part; it is therefore not part of the potential (see also section 2.4). The irreducible part is obtained from the residues at the poles of the meson propagators, disregarding the (far distant) poles of the baryon propagators. With the masses of the two exchanged mesons set to m_1 and m_2, the irreducible potentials can be written in closed analytical form,

$$
\begin{aligned}
V_{\text{irr, C}}^{\text{planar box}}(q) = \frac{N}{3072\pi^2 f_0^4} \Bigg\{ & \frac{5}{3} q^2 \\
& + \frac{\left(m_1^2 - m_2^2\right)^2}{q^2} + 16\left(m_1^2 + m_2^2\right) \\
& + \left[23q^2 + 45\left(m_1^2 + m_2^2\right)\right] \left(R + 2\ln\frac{\sqrt{m_1 m_2}}{\lambda}\right) \\
& + \frac{m_1^2 - m_2^2}{q^4} \Bigg[12q^4 + \left(m_1^2 - m_2^2\right)^2 \\
& \qquad - 9q^2\left(m_1^2 + m_2^2\right) \Bigg] \ln\frac{m_1}{m_2} \\
& + \frac{2}{w^2(q)} \Bigg[23q^4 - \frac{\left(m_1^2 - m_2^2\right)^4}{q^4} + 56\left(m_1^2 + m_2^2\right) q^2 \\
& \qquad + 8\frac{m_1^2 + m_2^2}{q^2}\left(m_1^2 - m_2^2\right)^2 \\
& \qquad + 2\left(21m_1^4 + 22m_1^2 m_2^2 + 21m_2^4\right) \Bigg] L(q) \Bigg\}, \qquad (61)
\end{aligned}
$$

$$
\begin{aligned}
V_{\text{irr, T}}^{\text{planar box}}(q) &= -\frac{1}{q^2} V_{\text{irr, S}}^{\text{planar box}}(q) \\
&= -\frac{N}{128\pi^2 f_0^4} \Bigg[L(q) - \frac{1}{2} - \frac{m_1^2 - m_2^2}{2q^2} \ln\frac{m_1}{m_2} \\
&\qquad + \frac{R}{2} + \ln\frac{\sqrt{m_1 m_2}}{\lambda} \Bigg] \qquad (62)
\end{aligned}
$$

where we have defined the functions

$$
\begin{aligned}
w(q) &= \frac{1}{q}\sqrt{\left(q^2 + (m_1 + m_2)^2\right)\left(q^2 + (m_1 - m_2)^2\right)}, \\
L(q) &= \frac{w(q)}{2q} \ln\frac{\left[q w(q) + q^2\right]^2 - \left(m_1^2 - m_2^2\right)^2}{4 m_1 m_2 q^2}. \qquad (63)
\end{aligned}
$$

The relation between the spin-spin and tensor-type potential follows from the identity $(\vec{\sigma}_1 \times \vec{q}\,) \cdot (\vec{\sigma}_2 \times \vec{q}\,) = q^2 \vec{\sigma}_1 \cdot \vec{\sigma}_2 - (\vec{\sigma}_1 \cdot \vec{q}\,)(\vec{\sigma}_2 \cdot \vec{q}\,)$.

One should note that all potentials shown above are finite also in the limit $q \to 0$. Terms proportional to $1/q^2$ or $1/q^4$ are canceled by opposite terms in the functions $L(q)$ and $w(q)$ in the limit of small q. For numerical calculations it is advantageous to perform an expansion of the potentials in a power series for small q in order to implement directly this cancellation. For equal meson masses the expressions for the potentials reduce to the results in Kaiser et al. [148]. This is the case for the *NN* interaction of Epelbaum et al. [147, 149,

150] and Entem and Machleidt [151] based on χEFT, where only contributions from two-pion exchange need to be taken into account.

In actual applications of these potentials such as in Haidenbauer et al. [33], only the non-polynomial part of Equations (61) and (62) is taken into account, i.e., the pieces proportional to $L(q)$ and to $1/q^2$ and $1/q^4$. The polynomial part is equivalent to the LO and NLO contact terms and, therefore, does not need to be considered. The contributions proportional to the divergence R are likewise omitted. Their effect is absorbed by the contact terms or a renormalization of the coupling constants, see, e.g., the corresponding discussion in Appendix A of Epelbaum et al. [149] for the *NN* case.

These statements above apply also to the other contributions to the potential described below.

The *crossed box* diagrams in **Figure 7C** contribute to the central, spin-spin, and tensor-type potentials. The similar structure with some differences in the kinematics of the planar and crossed box diagram leads to relations between them. Obviously, the crossed box has no iterated part. The potentials of the crossed box are equal to the potentials of the irreducible part of the planar box, up to a sign in the central potential:

$$\begin{aligned} V_{\mathrm{C}}^{\text{crossed box}}(q) &= -V_{\mathrm{C,\,irr}}^{\text{planar box}}(q)\,, \\ V_{\mathrm{T}}^{\text{crossed box}}(q) &= -\frac{1}{q^2} V_{\mathrm{S}}^{\text{crossed box}}(q) = V_{\mathrm{T,\,irr}}^{\text{planar box}}(q)\,. \end{aligned} \tag{64}$$

The two *triangle* diagrams, **Figures 7D,E**, constitute potentials, that are of equal form with different SU(3) factors N. The corresponding central potential reads

$$\begin{aligned} V_{\mathrm{C}}^{\text{triangle}}(q) = -\frac{N}{3072\pi^2 f_0^4} \Bigg\{ & -2\left(m_1^2+m_2^2\right) \\ & + \frac{\left(m_1^2-m_2^2\right)^2}{q^2} - \frac{13}{3}q^2 \\ & + \left[8\left(m_1^2+m_2^2\right) - \frac{2\left(m_1^2-m_2^2\right)^2}{q^2} + 10q^2\right] L\left(q\right) \\ & + \frac{m_1^2-m_2^2}{q^4}\left[\left(m_1^2-m_2^2\right)^2 - 3\left(m_1^2+m_2^2\right)q^2\right] \ln\frac{m_1}{m_2} \\ & + \left[9\left(m_1^2+m_2^2\right)+5q^2\right]\left(R + 2\ln\frac{\sqrt{m_1 m_2}}{\lambda}\right) \Bigg\}. \end{aligned} \tag{65}$$

The *football* diagrams in **Figure 7F** also contributes only to the central potential. One finds

$$\begin{aligned} V_{\mathrm{C}}^{\text{football}}(q) = \frac{N}{3072\pi^2 f_0^4} \Bigg\{ & -2\left(m_1^2+m_2^2\right) \\ & - \frac{\left(m_1^2-m_2^2\right)^2}{2q^2} - \frac{5}{6}q^2 + w^2\left(q\right) L\left(q\right) \\ & + \frac{1}{2}\left[3\left(m_1^2+m_2^2\right)+q^2\right]\left(R + 2\ln\frac{\sqrt{m_1 m_2}}{\lambda}\right) \\ & - \frac{m_1^2-m_2^2}{2q^4}\left[\left(m_1^2-m_2^2\right)^2 + 3\left(m_1^2+m_2^2\right)q^2\right] \ln\frac{m_1}{m_2} \Bigg\}. \end{aligned} \tag{66}$$

3.3. Meson-Exchange Models

Earlier investigations of the baryon-baryon interactions has been done within phenomenological meson-exchange potentials such as the Jülich [18, 19, 21], Nijmegen [20, 22, 23], or Ehime [152, 153] potentials. As we use two of them for comparison, we give a brief introduction to these type of models.

Conventional meson-exchange models of the *YN* interaction are usually also based on the assumption of SU(3) flavor symmetry for the occurring coupling constants, and in some cases even on the SU(6) symmetry of the quark model [18, 19]. In the derivation of the meson-exchange contributions one follows essentially the same procedure as outlined in section 3.2 for the case of pseudoscalar mesons. Besides the lowest pseudoscalar-meson multiplet also the exchanges of vector mesons (ρ, ω, K^*), of scalar mesons (σ ($f_0(500)$),...), or even of axial-vector mesons ($a_1(1270)$,...) [22, 23] are included. The spin-space structure of the corresponding Lagrangians that enter into Equation (42) and subsequently into Equation (56) differ and, accordingly, the final expressions for the corresponding contributions to the *YN* interaction potentials differ too. Details can be found in Holzenkamp et al. [18] and Rijken et al. [20, 22]. We want to emphasize that even for pseudoscalar mesons the final result for the interaction potentials differs, in general, from the expression given in Equation (60). Contrary to the chiral EFT approach, recoil, and relativistic corrections are often kept in meson-exchange models because no power counting rules are applied. Moreover, in case of the Jülich potential pseudoscalar coupling is assumed for the meson-baryon interaction Lagrangian for the pseudoscalar mesons instead of the pseudovector coupling (Equation 42) dictated by chiral symmetry. Note that in some *YN* potentials of the Jülich group [18, 19] contributions from two-meson exchanges are included. The ESC08 and ESC16 potentials [22, 23] include likewise contributions from two-meson exchange, in particular, so-called meson-pair diagrams analog to the ones shown in **Figures 7D–F**.

The major conceptual difference between the various meson-exchange models consists in the treatment of the scalar-meson sector. This simply reflects the fact that, unlike for pseudoscalar and vector mesons, so far there is no general agreement about what are the actual members of the lowest lying scalar-meson SU(3) multiplet. Therefore, besides the question of the masses of the exchange particles it also remains unclear whether and how the relations for the coupling constants should be specified. As a consequence, different prescriptions for describing the scalar sector, whose contributions play a crucial role in any baryon-baryon interaction at intermediate ranges, were adopted by the various authors who published meson-exchange models of the *YN* interaction. For example, the Nijmegen group views this interaction as being generated by genuine scalar-meson exchange. In their models NSC97 [20] and ESC08 (ESC16) [22, 23] a scalar SU(3) nonet is exchanged—namely, two isospin-0 mesons [an $\epsilon(760)$ and the $f_0(980)$] an isospin-1 meson ($a_0(980)$)

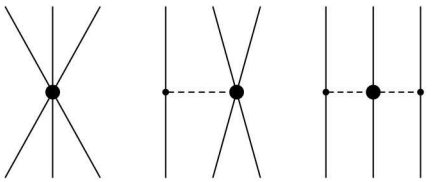


FIGURE 8 | Leading three-baryon interactions: contact term, one-meson exchange, and two-meson exchange. Filled circles and solid dots denote vertices with $\Delta_i = 1$ and $\Delta_i = 0$, respectively.

and an isospin-1/2 strange meson κ with a mass of 1,000 MeV. In the initial *YN* models of the Jülich group [18, 19] a σ (with a mass of $\approx$ 550 MeV) is included which is viewed as arising from correlated $\pi\pi$ exchange. In practice, however, the coupling strength of this fictitious σ to the baryons is treated as a free parameter and fitted to the data. In the latest meson-exchange *YN* potential presented by the Jülich group [21] a microscopic model of correlated $\pi\pi$ and $K\bar{K}$ exchange [154] is utilized to fix the contributions in the scalar-isoscalar (σ) and vector-isovector (ρ) channels.

Let us mention for completeness that meson-exchange models are typically equipped with phenomenological form factors in order to cut off the potential for large momenta (short distances). For example, in case of the *YN* models of the Jülich group the interaction is supplemented with form factors for each meson-baryon-baryon vertex (cf. [18, 19] for details). Those form factors are meant to take into account the extended hadron structure and are parameterized in the conventional monopole or dipole form. In case of the Nijmegen potentials a Gaussian form factor is used. In addition there is some additional sophisticated short-range phenomenology that controls the interaction at short distances [22, 23].

4. THREE-BARYON INTERACTION POTENTIALS

Three-nucleon forces are an essential ingredient for a proper description of nuclei and nuclear matter with low-momentum two-body interactions. Similarly, three-baryon forces, especially the ΛNN interaction, are expected to play an important role in nuclear systems with strangeness. Their introduction in calculations of light hypernuclei seems to be required. Furthermore, the introduction of 3BF is traded as a possible solution to the hyperon puzzle (see section 1). However, so far only phenomenological 3BF have been employed. In this section we present the leading irreducible three-baryon interactions from SU(3) chiral effective field theory as derived in Petschauer et al. [120]. We show the minimal effective Lagrangian required for the pertinent vertices. Furthermore the estimation of the corresponding LECs through decuplet saturation and an effective density-dependent two-baryon potential will be covered [121].

According to the power counting in Equation (47) the 3BF arise formally at NNLO in the chiral expansion, as can be seen from the hierarchy of baryonic forces in **Figure 5**. Three types of diagrams contribute: three-baryon contact terms, one-meson and two-meson exchange diagrams (cf. **Figure 8**). Note that a two-meson exchange diagram, such as in **Figure 8**, with a (leading order) Weinberg-Tomozawa vertex in the middle, would formally be a NLO contribution. However, as in the nucleonic sector, this contribution is kinematically suppressed due to the fact that the involved meson energies are differences of baryon kinetic energies. Anyway, parts of these NNLO contributions get promoted to NLO by the introduction of intermediate decuplet baryons, so that it becomes appropriate to use these three-body interactions together with the NLO two-body interaction of section 3. As already stated, the irreducible contributions to the chiral potential are presented. In contrast to typical phenomenological calculations, diagrams as on the left side of **Figure 4** do not lead to a genuine three-body potential, but are an iteration of the two-baryon potential. Such diagrams will be incorporated automatically when solving, e.g., the Faddeev (or Yakubovsky) equations within a coupled-channel approach. The three-body potentials derived from SU(3) χEFT are expected to shed light on the effect of 3BFs in hypernuclear systems. Especially in calculations about light hypernuclei these potentials can be implemented within reliable few-body techniques [48, 49, 51, 52].

4.1. Contact Interaction

In the following we consider the leading three-baryon contact interaction. Following the discussion in section 2.3 the corresponding Lagrangian can be constructed. The inclusion of external fields is not necessary, as we are interested in the purely baryonic contact term. One ends up with the following possible structures in flavor space [120]

$$\begin{aligned}
&\langle \bar{B}\bar{B}\bar{B}BBB\rangle\,,\ \langle \bar{B}\bar{B}B\bar{B}BB\rangle\,,\ \langle \bar{B}\bar{B}BB\bar{B}B\rangle\,,\\
&\langle \bar{B}B\bar{B}B\bar{B}B\rangle\,,\ \langle \bar{B}\bar{B}B\bar{B}B\rangle\langle \bar{B}B\rangle\,,\ \langle \bar{B}B\bar{B}B\rangle\langle \bar{B}B\rangle\,,\\
&\langle \bar{B}\bar{B}\bar{B}BB\rangle\langle BB\rangle\,,\ \langle \bar{B}\bar{B}\bar{B}\rangle\langle BBB\rangle\,,\ \langle \bar{B}\bar{B}B\rangle\langle B\bar{B}B\rangle\,,\\
&\langle \bar{B}B\rangle\langle \bar{B}B\rangle\langle \bar{B}B\rangle\,,\ \langle \bar{B}\bar{B}\rangle\langle \bar{B}B\rangle\langle BB\rangle\,,
\end{aligned} \tag{67}$$

with possible Dirac structures

$$\begin{aligned}
&\mathbb{1}\otimes\mathbb{1}\otimes\mathbb{1}\,,\ \mathbb{1}\otimes\gamma_5\gamma^\mu\otimes\gamma_5\gamma_\mu\,,\ \gamma_5\gamma^\mu\otimes\mathbb{1}\otimes\gamma_5\gamma_\mu\,,\\
&\gamma_5\gamma^\mu\otimes\gamma_5\gamma_\mu\otimes\mathbb{1}\,,\ \gamma_5\gamma_\mu\otimes \mathrm{i}\,\sigma^{\mu\nu}\otimes\gamma_5\gamma_\nu\,,
\end{aligned} \tag{68}$$

leading to the following operators in the three-body spin space

$$\mathbb{1}\,,\ \vec{\sigma}_1\cdot\vec{\sigma}_2\,,\ \vec{\sigma}_1\cdot\vec{\sigma}_3\,,\ \vec{\sigma}_2\cdot\vec{\sigma}_3\,,\ \mathrm{i}\,\vec{\sigma}_1\cdot(\vec{\sigma}_2\times\vec{\sigma}_3)\,. \tag{69}$$

All combinations of these possibilities leads to a (largely overcomplete) set of terms for the leading covariant Lagrangian. Note that in Petschauer et al. [120] the starting point is a covariant Lagrangian, but the minimal non-relativistic Lagrangian is the goal. Hence, only Dirac structures leading to independent (non-relativistic) spin operators are relevant.

Let us consider the process $B_1B_2B_3 \to B_4B_5B_6$, where the B_i are baryons in the particle basis, $B_i \in \{n, p, \Lambda, \Sigma^+, \Sigma^0, \Sigma^-, \Xi^0, \Xi^-\}$. The contact potential V has to be derived within a threefold spin space for this process.

The operators in spin-space 1 is defined to act between the two-component Pauli spinors of B_1 and B_4. In the same way, spin-space 2 belongs to B_2 and B_5, and spin-space 3 to B_3 and B_6. For a fixed spin configuration the potential can be calculated from

$$\chi^{(1)\dagger}_{B_4}\chi^{(2)\dagger}_{B_5}\chi^{(3)\dagger}_{B_6}\, V\, \chi^{(1)}_{B_1}\chi^{(2)}_{B_2}\chi^{(3)}_{B_3}\,, \tag{70}$$

where the superscript of a spinor denotes the spin space and the subscript denotes the baryon to which the spinor belongs. The potential is obtained as $V = -\langle B_4B_5B_6|\ \mathscr{L}\ |B_1B_2B_3\rangle$, where the contact Lagrangian $\mathscr{L}$ has to be inserted, and the 36 Wick contractions need to be performed. The number 36 corresponds to the 3! × 3! possibilities to arrange the three initial and three final baryons into Dirac bilinears. One obtains six direct terms, where the baryon bilinears combine the baryon pairs 1–4, 2–5, and 3–6, as shown in Equation (70). For the other 30 Wick contractions, the resulting potential is not fitting to the form of Equation (70), because the wrong baryon pairs are connected in a separate spin space. Hence, an appropriate exchange of the spin wave functions in the final state has to be performed. This is achieved by multiplying the potential with the well-known spin-exchange operators $P^{(\sigma)}_{ij} = \frac{1}{2}(\mathbb{1} + \vec{\sigma}_i \cdot \vec{\sigma}_j)$. Furthermore, additional minus signs arise from the interchange of anti-commuting baryon fields. The full potential is then obtained by adding up all 36 contributions to the potential. One obtains a potential that fulfills automatically the generalized Pauli principle and that is fully anti-symmetrized.

In order to obtain a minimal set of Lagrangian terms of the final potential matrix have been eliminated until the rank of the final potential matrix (consisting of multiple Lagrangian terms and the spin structures in Equation 69) matches the number of terms in the Lagrangian. The minimal non-relativistic six-baryon contact Lagrangian is [120]

$$\begin{aligned}
\mathscr{L} = &- C_1\langle \bar{B}_a\bar{B}_b\bar{B}_cB_aB_bB_c\rangle \\
&+ C_2\langle \bar{B}_a\bar{B}_b\bar{B}_aB_c\bar{B}_cB_bB_c\rangle \\
&- C_3\langle \bar{B}_a\bar{B}_b\bar{B}_aB_bB_c\bar{B}_cB_c\rangle \\
&+ C_4\langle \bar{B}_aB_a\bar{B}_bB_bB_c\bar{B}_cB_c\rangle \\
&- C_5\langle \bar{B}_a\bar{B}_bB_aB_b\rangle\ \langle \bar{B}_cB_c\rangle \\
&- C_6\Big(\langle \bar{B}_a\bar{B}_b\bar{B}_cB_a(\sigma^iB)_b(\sigma^iB)_c\rangle \\
&\qquad + \langle \bar{B}_c\bar{B}_b\bar{B}_a(\sigma^iB)_c(\sigma^iB)_bB_a\rangle\Big) \\
&+ C_7\Big(\langle \bar{B}_a\bar{B}_bB_a\bar{B}_c(\sigma^iB)_b(\sigma^iB)_c\rangle \\
&\qquad + \langle \bar{B}_c\bar{B}_b(\sigma^iB)_c\bar{B}_a(\sigma^iB)_bB_a\rangle\Big) \\
&- C_8\Big(\langle \bar{B}_a\bar{B}_bB_a(\sigma^iB)_b\bar{B}_c(\sigma^iB)_c\rangle \\
&\qquad + \langle \bar{B}_b\bar{B}_a(\sigma^iB)_bB_a\bar{B}_c(\sigma^iB)_c\rangle\Big) \\
&+ C_9\langle \bar{B}_aB_a\bar{B}_b(\sigma^iB)_b\bar{B}_c(\sigma^iB)_c\rangle \\
&- C_{10}\Big(\langle \bar{B}_a\bar{B}_bB_a(\sigma^iB)_b\rangle\ \langle \bar{B}_c(\sigma^iB)_c\rangle \\
&\qquad + \langle \bar{B}_b\bar{B}_a(\sigma^iB)_bB_a\rangle\ \langle \bar{B}_c(\sigma^iB)_c\rangle\Big) \\
&- C_{11}\langle \bar{B}_a\bar{B}_b\bar{B}_c(\sigma^iB)_aB_b(\sigma^iB)_c\rangle \\
&+ C_{12}\langle \bar{B}_a\bar{B}_b(\sigma^iB)_a\bar{B}_cB_b(\sigma^iB)_c\rangle \\
&- C_{13}\langle \bar{B}_a\bar{B}_b(\sigma^iB)_a(\sigma^iB)_b\bar{B}_cB_c\rangle \\
&- C_{14}\langle \bar{B}_a\bar{B}_b(\sigma^iB)_a(\sigma^iB)_b\rangle\ \langle \bar{B}_cB_c\rangle \\
&- \mathrm{i}\,\epsilon^{ijk}C_{15}\langle \bar{B}_a\bar{B}_b\bar{B}_c(\sigma^iB)_a(\sigma^jB)_b(\sigma^kB)_c\rangle \\
&+ \mathrm{i}\,\epsilon^{ijk}C_{16}\langle \bar{B}_a\bar{B}_b(\sigma^iB)_a\bar{B}_c(\sigma^jB)_b(\sigma^kB)_c\rangle \\
&- \mathrm{i}\,\epsilon^{ijk}C_{17}\langle \bar{B}_a\bar{B}_b(\sigma^iB)_a(\sigma^jB)_b\bar{B}_c(\sigma^kB)_c\rangle \\
&+ \mathrm{i}\,\epsilon^{ijk}C_{18}\langle \bar{B}_a(\sigma^iB)_a\bar{B}_b(\sigma^jB)_b\bar{B}_c(\sigma^kB)_c\rangle\,,
\end{aligned} \tag{71}$$

with vector indices i, j, k and two-component spinor indices a, b, c. In total 18 low-energy constants $C_1 \ldots C_{18}$ are present. The low-energy constant E of the six-nucleon contact term (cf. [78]) can be expressed through these LECs by $E = 2(C_4 - C_9)$.

As in the two-body sector, group theoretical considerations can deliver valuable constrains on the resulting potentials. In flavor space the three octet baryons form the 512-dimensional tensor product $\mathbf{8} \otimes \mathbf{8} \otimes \mathbf{8}$, which decomposes into the following irreducible SU(3) representations

$$\begin{aligned}
&\mathbf{8} \otimes \mathbf{8} \otimes \mathbf{8} = \\
&\quad \mathbf{64} \oplus (\mathbf{35} \oplus \overline{\mathbf{35}})_2 \oplus \mathbf{27}_6 \oplus (\mathbf{10} \oplus \overline{\mathbf{10}})_4 \oplus \mathbf{8}_8 \oplus \mathbf{1}_2\,,
\end{aligned} \tag{72}$$

TABLE 4 | Irreducible representations for three-baryon states with strangeness S and isospin I in partial waves $|^{2S+1}L_J\rangle$, with the total spin $S = \frac{1}{2}, \frac{3}{2}$, the angular momentum $L = 0$, and the total angular momentum $J = \frac{1}{2}, \frac{3}{2}$ [120].

States	(S,I)	$2^{\mathbf{S}}_{\mathbf{1/2}}$	$4^{\mathbf{S}}_{\mathbf{3/2}}$
NNN	$(0, \frac{1}{2})$	$\overline{\mathbf{35}}$	
ΛNN, ΣNN	$(-1,0)$	$\overline{\mathbf{10}}, \overline{\mathbf{35}}$	$\overline{\mathbf{10}}_a$
ΛNN, ΣNN	$(-1,1)$	$\mathbf{27}, \overline{\mathbf{35}}$	$\mathbf{27}_a$
ΣNN	$(-1,2)$	$\mathbf{35}$	
$\Lambda\Lambda N$, $\Sigma\Lambda N$, $\Sigma\Sigma N$, ΞNN	$(-2, \frac{1}{2})$	$\mathbf{8}, \overline{\mathbf{10}}, \mathbf{27}, \overline{\mathbf{35}}$	$\mathbf{8}_a, \overline{\mathbf{10}}_a, \mathbf{27}_a$
$\Sigma\Lambda N$, $\Sigma\Sigma N$, ΞNN	$(-2, \frac{3}{2})$	$\mathbf{10}, \mathbf{27}, \mathbf{35}, \overline{\mathbf{35}}$	$\mathbf{10}_a, \mathbf{27}_a$
$\Sigma\Sigma N$	$(-2, \frac{5}{2})$	$\mathbf{35}$	
$\Lambda\Lambda\Lambda$, $\Sigma\Sigma\Lambda$, $\Sigma\Sigma\Sigma$, $\Xi\Lambda N$, $\Xi\Sigma N$	$(-3,0)$	$\mathbf{8}, \mathbf{27}$	$\mathbf{1}_a, \mathbf{8}_a, \mathbf{27}_a$
$\Sigma\Lambda\Lambda$, $\Sigma\Sigma\Lambda$, $\Sigma\Sigma\Sigma$, $\Xi\Lambda N$, $\Xi\Sigma N$	$(-3,1)$	$\mathbf{8}, \mathbf{10}, \overline{\mathbf{10}}, \mathbf{27}, \mathbf{35}, \overline{\mathbf{35}}$	$\mathbf{8}_a, \mathbf{10}_a, \overline{\mathbf{10}}_a, \mathbf{27}_a$
$\Sigma\Sigma\Lambda$, $\Sigma\Sigma\Sigma$, $\Xi\Sigma N$	$(-3,2)$	$\mathbf{27}, \mathbf{35}, \overline{\mathbf{35}}$	$\mathbf{27}_a$
$\Xi\Lambda\Lambda$, $\Xi\Sigma\Lambda$, $\Xi\Sigma\Sigma$, $\Xi\Xi N$	$(-4, \frac{1}{2})$	$\mathbf{8}, \mathbf{10}, \mathbf{27}, \mathbf{35}$	$\mathbf{8}_a, \mathbf{10}_a, \mathbf{27}_a$
$\Xi\Sigma\Lambda$, $\Xi\Sigma\Sigma$, $\Xi\Xi N$	$(-4, \frac{3}{2})$	$\overline{\mathbf{10}}, \mathbf{27}, \mathbf{35}, \overline{\mathbf{35}}$	$\overline{\mathbf{10}}_a, \mathbf{27}_a$
$\Xi\Sigma\Sigma$	$(-4, \frac{5}{2})$	$\overline{\mathbf{35}}$	
$\Xi\Xi\Lambda$, $\Xi\Xi\Sigma$	$(-5,0)$	$\mathbf{10}, \mathbf{35}$	$\mathbf{10}_a$
$\Xi\Xi\Lambda$, $\Xi\Xi\Sigma$	$(-5,1)$	$\mathbf{27}, \mathbf{35}$	$\mathbf{27}_a$
$\Xi\Xi\Sigma$	$(-5,2)$	$\overline{\mathbf{35}}$	
$\Xi\Xi\Xi$	$(-6, \frac{1}{2})$	$\mathbf{35}$	

where the multiplicity of an irreducible representations is denoted by subscripts. In spin space one obtain for the product of three doublets

$$\mathbf{2} \otimes \mathbf{2} \otimes \mathbf{2} = \mathbf{2}_2 \oplus \mathbf{4}\,. \tag{73}$$

Transitions are only allowed between irreducible representations of the same type. Analogous to Dover and Feshbach [145] for the two-baryon sector, the contributions of different irreducible representations to three-baryon multiplets in **Table 4** can be established. At leading order only transitions between *S*-waves are possible, since the potentials are momentum-independent. Due to the Pauli principle the totally symmetric spin-quartet **4** must combine with the totally antisymmetric part of $\mathbf{8} \otimes \mathbf{8} \otimes \mathbf{8}$ in flavor space,

$$\mathrm{Alt}_3(\mathbf{8}) = \mathbf{56}_a = \mathbf{27}_a + \mathbf{10}_a + \overline{\mathbf{10}}_a + \mathbf{8}_a + \mathbf{1}_a\,. \tag{74}$$

It follows, that these totally antisymmetric irreducible representations are present only in states with total spin 3/2. The totally symmetric part of $\mathbf{8} \otimes \mathbf{8} \otimes \mathbf{8}$ leads to

$$\mathrm{Sym}_3(\mathbf{8}) = \mathbf{120}_s = \mathbf{64}_s + \mathbf{27}_s + \mathbf{10}_s + \overline{\mathbf{10}}_s + \mathbf{8}_s + \mathbf{1}_s\,. \tag{75}$$

However, the totally symmetric flavor part has no totally antisymmetric counterpart in spin space, hence these representations do not contribute to the potential. In **Table 4**, these restrictions obtained by the generalized Pauli principle have already be incorporated. The potentials of Petschauer et al. [120] (decomposed in isospin basis and partial waves) fulfill the restrictions of **Table 4**. For example the combination of LECs related to the representation $\overline{\mathbf{35}}$ is present in the *NNN* interaction as well as in the $\Xi\Xi\Sigma$ $(-5, 2)$ interaction.

4.2. One-Meson Exchange Component

The meson-baryon couplings in the one-meson exchange diagram of **Figure 8** emerges from the leading-order chiral Lagrangian $\mathscr{L}_{\mathrm{B}}^{(1)}$ (see Equation 56). The other vertex involves four baryon fields and one pseudoscalar-meson field. In Petschauer et al. [120], an overcomplete set of terms for the corresponding Lagrangian has been constructed. In order to obtain the complete minimal Lagrangian from the overcomplete set of terms, the matrix elements of the process $B_1B_2 \to B_3B_4\phi_1$ has been considered in Petschauer et al. [120]. The corresponding spin operators in the potential are

$$\vec{\sigma}_1 \cdot \vec{q}\,, \quad \vec{\sigma}_2 \cdot \vec{q}\,, \quad \mathrm{i}\,(\vec{\sigma}_1 \times \vec{\sigma}_2) \cdot \vec{q}\,, \tag{76}$$

where $\vec{q}$ denotes the momentum of the emitted meson. Redundant term are removed until the rank of the potential matrix formed by all transitions and spin operators matches the number of terms in the Lagrangian. One ends up with the minimal non-relativistic chiral Lagrangian

$$\begin{aligned}
\mathscr{L} = {} & D_1/f_0 \langle \bar{B}_a (\nabla^i \phi) B_a \bar{B}_b (\sigma^i B)_b \rangle \\
& + D_2/f_0 \Big(\langle \bar{B}_a B_a (\nabla^i \phi) \bar{B}_b (\sigma^i B)_b \rangle \\
& \qquad + \langle \bar{B}_a B_a \bar{B}_b (\sigma^i B)_b (\nabla^i \phi) \rangle \Big) \\
& + D_3/f_0 \langle \bar{B}_b (\nabla^i \phi) (\sigma^i B)_b \bar{B}_a B_a \rangle \\
& - D_4/f_0 \Big(\langle \bar{B}_a (\nabla^i \phi) \bar{B}_b B_a (\sigma^i B)_b \rangle \\
& \qquad + \langle \bar{B}_b \bar{B}_a (\sigma^i B)_b (\nabla^i \phi) B_a \rangle \Big) \\
& - D_5/f_0 \Big(\langle \bar{B}_a \bar{B}_b (\nabla^i \phi) B_a (\sigma^i B)_b \rangle \\
& \qquad + \langle \bar{B}_b \bar{B}_a (\nabla^i \phi) (\sigma^i B)_b B_a \rangle \Big) \\
& - D_6/f_0 \Big(\langle \bar{B}_b (\nabla^i \phi) \bar{B}_a (\sigma^i B)_b B_a \rangle \\
& \qquad + \langle \bar{B}_a \bar{B}_b B_a (\nabla^i \phi) (\sigma^i B)_b \rangle \Big) \\
& - D_7/f_0 \Big(\langle \bar{B}_a \bar{B}_b B_a (\sigma^i B)_b (\nabla^i \phi) \rangle \\
& \qquad + \langle \bar{B}_b \bar{B}_a (\sigma^i B)_b B_a (\nabla^i \phi) \rangle \Big) \\
& + D_8/f_0 \langle \bar{B}_a (\nabla^i \phi) B_a \rangle \langle \bar{B}_b (\sigma^i B)_b \rangle \\
& + D_9/f_0 \langle \bar{B}_a B_a (\nabla^i \phi) \rangle \langle \bar{B}_b (\sigma^i B)_b \rangle \\
& + D_{10}/f_0 \langle \bar{B}_b (\nabla^i \phi) (\sigma^i B)_b \rangle \langle \bar{B}_a B_a \rangle \\
& + \mathrm{i}\,\epsilon^{ijk} D_{11}/f_0 \langle \bar{B}_a (\sigma^i B)_a (\nabla^k \phi) \bar{B}_b (\sigma^j B)_b \rangle \\
& - \mathrm{i}\,\epsilon^{ijk} D_{12}/f_0 \Big(\langle \bar{B}_a (\nabla^k \phi) \bar{B}_b (\sigma^i B)_a (\sigma^j B)_b \rangle \\
& \qquad - \langle \bar{B}_b \bar{B}_a (\sigma^j B)_b (\nabla^k \phi) (\sigma^i B)_a \rangle \Big) \\
& - \mathrm{i}\,\epsilon^{ijk} D_{13}/f_0 \langle \bar{B}_a \bar{B}_b (\nabla^k \phi) (\sigma^i B)_a (\sigma^j B)_b \rangle \\
& - \mathrm{i}\,\epsilon^{ijk} D_{14}/f_0 \langle \bar{B}_a \bar{B}_b (\sigma^i B)_a (\sigma^j B)_b (\nabla^k \phi) \rangle\,,
\end{aligned} \tag{77}$$

with two-component spinor indices *a* and *b* and 3-vector indices *i*, *j*, and *k*. For all possible strangeness sectors $S = -4 \ldots 0$ one obtains in total 14 low-energy constants $D_1 \ldots D_{14}$. The low-energy constant of the corresponding vertex in the nucleonic sector *D* is related to the LECs above by $D = 4(D_1 - D_3 + D_8 - D_{10})$.[2]

To obtain the 3BF one-meson-exchange diagram, the generic one-meson-exchange diagram in **Figure 9A** can be investigated.

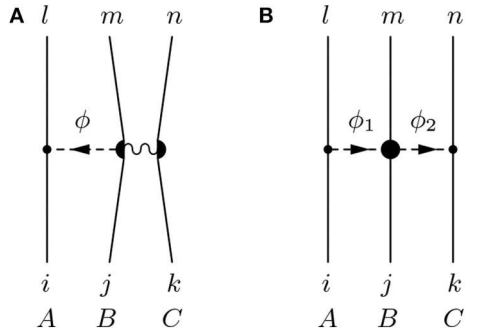


FIGURE 9 | Generic meson-exchange diagrams. The wiggly line symbolized the four-baryon contact vertex, to illustrate the baryon bilinears. **(A)** Generic one-meson exchange diagram. **(B)** Generic two-meson exchange diagram.

[2]This LEC *D* has not to be confused with the axial-vector coupling constant *D* in Equation (56).

It involves the baryons i, j, k in the initial state, the baryons l, m, n in the final state and an exchanged meson ϕ. The contact vertex on the right is pictorially separated into two parts to indicate that baryon j–m and k–n are in the same bilinear. The spin spaces corresponding to the baryon bilinears are denoted by A, B, C.

On obtains a generic potential of the form

$$V = \frac{1}{2f_0^2}\frac{\vec{\sigma}_A\cdot\vec{q}_{li}}{\vec{q}_{li}^{\,2}+m_\phi^2}\left(N_1\vec{\sigma}_C\cdot\vec{q}_{li}+N_2\mathrm{i}\,(\vec{\sigma}_B\times\vec{\sigma}_C)\cdot\vec{q}_{li}\right), \quad (78)$$

with the momentum transfer $\vec{q}_{li} = \vec{p}_l - \vec{p}_i$ carried by the exchanged meson. The constants N_1 and N_2 are linear combinations of low-energy constants.

The complete one-meson exchange three-baryon potential for the process $B_1B_2B_3 \to B_4B_5B_6$ is finally obtained by summing up the 36 permutations of initial-state and final-state baryons for a fixed meson and by summing over all mesons $\phi \in \{\pi^0,\pi^+,\pi^-,K^+,K^-,K^0,\bar{K}^0,\eta\}$. Additional minus signs arise from interchanging fermions and some diagrams need to be multiplied by spin exchange operators in order to be consistent with the form set up in Equation (70). As defined before, the baryons B_1, B_2, and B_3 belong to the spin-spaces 1, 2, and 3, respectively.

4.3. Two-Meson Exchange Component

The two-meson exchange diagram of **Figure 8** includes the vertex arising from the Lagrangian in Equation (56). Furthermore the well-known $\mathcal{O}(q^2)$ meson-baryon Lagrangian [139] is necessary. For the two-meson exchange diagram of **Figure 8** we need in addition to the Lagrangian in Equation (56) the well-known $\mathcal{O}(q^2)$ meson-baryon Lagrangian [139]. The relevant terms are [140]

$$\begin{aligned}\mathscr{L} = {} & b_D\langle\bar{B}\{\chi_+,B\}\rangle + b_F\langle\bar{B}[\chi_+,B]\rangle + b_0\langle\bar{B}B\rangle\langle\chi_+\rangle \\ & + b_1\langle\bar{B}[u^\mu,[u_\mu,B]]\rangle + b_2\langle\bar{B}\{u^\mu,\{u_\mu,B\}\}\rangle \\ & + b_3\langle\bar{B}\{u^\mu,[u_\mu,B]\}\rangle + b_4\langle\bar{B}B\rangle\langle u^\mu u_\mu\rangle \\ & + \mathrm{i}d_1\langle\bar{B}\{[u^\mu,u^\nu],\sigma_{\mu\nu}B\}\rangle \\ & + \mathrm{i}d_2\langle\bar{B}[[u^\mu,u^\nu],\sigma_{\mu\nu}B]\rangle \\ & + \mathrm{i}d_3\langle\bar{B}u^\mu\rangle\langle u^\nu\sigma_{\mu\nu}B\rangle, \end{aligned} \quad (79)$$

with $u_\mu = -\frac{1}{f_0}\partial_\mu\phi + \mathcal{O}(\phi^3)$ and $\chi_+ = 2\chi - \frac{1}{4f_0^2}\{\phi,\{\phi,\chi\}\} + \mathcal{O}(\phi^4)$, where

$$\chi = \begin{pmatrix} m_\pi^2 & 0 & 0 \\ 0 & m_\pi^2 & 0 \\ 0 & 0 & 2m_K^2 - m_\pi^2 \end{pmatrix}. \quad (80)$$

The terms proportional to b_D, b_F, b_0 break explicitly SU(3) flavor symmetry, because of different meson masses $m_K \neq m_\pi$. The LECs of Equation (79) are related to the conventional LECs of the nucleonic sector by [155, 156]

$$\begin{aligned} c_1 &= \frac{1}{2}(2b_0 + b_D + b_F), \\ c_3 &= b_1 + b_2 + b_3 + 2b_4, \\ c_4 &= 4(d_1 + d_2). \end{aligned} \quad (81)$$

To obtain the potential of the two-meson exchange diagram of **Figure 8**, the generic diagram of **Figure 9B** can be considered. It includes the baryons i, j, k in the initial state, the baryons l, m, n in the final state, and two exchanged mesons ϕ_1 and ϕ_2. The spin spaces corresponding to the baryon bilinears are denoted by A, B, C and they are aligned with the three initial baryons. The momentum transfers carried by the virtual mesons are $\vec{q}_{li} = \vec{p}_l - \vec{p}_i$ and $\vec{q}_{nk} = \vec{p}_n - \vec{p}_k$. One obtains the generic transition amplitude

$$\begin{aligned} V = {} & -\frac{1}{4f_0^4}\frac{\vec{\sigma}_A\cdot\vec{q}_{li}\,\vec{\sigma}_C\cdot\vec{q}_{nk}}{(\vec{q}_{li}^{\,2}+m_{\phi_1}^2)(\vec{q}_{nk}^{\,2}+m_{\phi_2}^2)} \\ & \times\left(N_1' + N_2'\,\vec{q}_{li}\cdot\vec{q}_{nk} + N_3'\,\mathrm{i}\,(\vec{q}_{li}\times\vec{q}_{nk})\cdot\vec{\sigma}_B\right), \end{aligned} \quad (82)$$

with N_i' linear combinations of the low-energy constants of the three involved vertices. The complete three-body potential for a transition $B_1B_2B_3 \to B_4B_5B_6$ can be calculated by summing up the contributions of all 18 distinguable Feynman diagrams and by summing over all possible exchanged mesons. If the baryon lines are not in the configuration 1–4, 2–5, and 3–6 additional (negative) spin-exchange operators have to be included.

4.4. ΛNN Three-Baryon Potentials

In order to give a concrete example the explicit expression for the ΛNN three-body potentials in spin-, isospin-, and momentum-space are presented for the contact interaction and one- and two-pion exchange contributions [120]. The potentials are calculated in the particle basis and afterwards rewritten into isospin operators.

The ΛNN contact interaction is described by the following potential

$$\begin{aligned} V_{\mathrm{ct}}^{\Lambda NN} = {} & C_1'\,(\mathbb{1} - \vec{\sigma}_2\cdot\vec{\sigma}_3)(3 + \vec{\tau}_2\cdot\vec{\tau}_3) \\ & + C_2'\,\vec{\sigma}_1\cdot(\vec{\sigma}_2 + \vec{\sigma}_3)\,(\mathbb{1} - \vec{\tau}_2\cdot\vec{\tau}_3) \\ & + C_3'\,(3 + \vec{\sigma}_2\cdot\vec{\sigma}_3)(\mathbb{1} - \vec{\tau}_2\cdot\vec{\tau}_3), \end{aligned} \quad (83)$$

where the primed constants are linear combinations of $C_1 \ldots C_{18}$ of Equation (71). The symbols $\vec{\sigma}$ and $\vec{\tau}$ denote the usual Pauli matrices in spin and isospin space. The constant C_1' appears only in the transition with total isospin $I = 1$. The constants C_2' and C_3' contribute for total isospin $I = 0$.

For the ΛNN one-pion exchange three-body potentials, various diagrams are absent due to the vanishing $\Lambda\Lambda\pi$-vertex, which is forbidden by isospin symmetry. One obtains the following potential

$$\begin{aligned} V_{\mathrm{OPE}}^{\Lambda NN} = {} & -\frac{g_A}{2f_0^2} \\ & \times\left(\frac{\vec{\sigma}_2\cdot\vec{q}_{52}}{\vec{q}_{52}^{\,2}+m_\pi^2}\vec{\tau}_2\cdot\vec{\tau}_3\Big[(D_1'\vec{\sigma}_1 + D_2'\vec{\sigma}_3)\cdot\vec{q}_{52}\Big]\right. \\ & + \frac{\vec{\sigma}_3\cdot\vec{q}_{63}}{\vec{q}_{63}^{\,2}+m_\pi^2}\vec{\tau}_2\cdot\vec{\tau}_3\Big[(D_1'\vec{\sigma}_1 + D_2'\vec{\sigma}_2)\cdot\vec{q}_{63}\Big] \\ & \left. + P_{23}^{(\sigma)}P_{23}^{(\tau)}P_{13}^{(\sigma)}\frac{\vec{\sigma}_2\cdot\vec{q}_{62}}{\vec{q}_{62}^{\,2}+m_\pi^2}\vec{\tau}_2\cdot\vec{\tau}_3\right. \end{aligned}$$

$$\times \Big[-\frac{D_1'+D_2'}{2}(\vec{\sigma}_1+\vec{\sigma}_3)\cdot\vec{q}_{62} + \frac{D_1'-D_2'}{2}\,\mathrm{i}\,(\vec{\sigma}_3\times\vec{\sigma}_1)\cdot\vec{q}_{62}\Big] + P_{23}^{(\sigma)}P_{23}^{(\tau)}P_{12}^{(\sigma)}\frac{\vec{\sigma}_3\cdot\vec{q}_{53}}{\vec{q}_{53}^{\,2}+m_\pi^2}\vec{\tau}_2\cdot\vec{\tau}_3 \times \Big[-\frac{D_1'+D_2'}{2}(\vec{\sigma}_1+\vec{\sigma}_2)\cdot\vec{q}_{53} - \frac{D_1'-D_2'}{2}\,\mathrm{i}\,(\vec{\sigma}_1\times\vec{\sigma}_2)\cdot\vec{q}_{53}\Big]\Big), \quad (84)$$

with only two constants D_1' and D_2', which are linear combinations of the constants $D_1 \ldots D_{14}$. Exchange operators in spin space $P_{ij}^{(\sigma)} = \frac{1}{2}(\mathbb{1} + \vec{\sigma}_i\cdot\vec{\sigma}_j)$ and in isospin space $P_{ij}^{(\tau)} = \frac{1}{2}(\mathbb{1} + \vec{\tau}_i\cdot\vec{\tau}_j)$ have been introduced.

The ΛNN three-body interaction generated by two-pion exchange is given by

$$V_{\mathrm{TPE}}^{\Lambda NN} = \frac{g_A^2}{3f_0^4}\frac{\vec{\sigma}_3\cdot\vec{q}_{63}\,\vec{\sigma}_2\cdot\vec{q}_{52}}{(\vec{q}_{63}^{\,2}+m_\pi^2)(\vec{q}_{52}^{\,2}+m_\pi^2)}\vec{\tau}_2\cdot\vec{\tau}_3 \times\Big(-(3b_0+b_D)m_\pi^2+(2b_2+3b_4)\,\vec{q}_{63}\cdot\vec{q}_{52}\Big) - P_{23}^{(\sigma)}P_{23}^{(\tau)}\frac{g_A^2}{3f_0^4}\frac{\vec{\sigma}_3\cdot\vec{q}_{53}\,\vec{\sigma}_2\cdot\vec{q}_{62}}{(\vec{q}_{53}^{\,2}+m_\pi^2)(\vec{q}_{62}^{\,2}+m_\pi^2)}\vec{\tau}_2\cdot\vec{\tau}_3 \times\Big(-(3b_0+b_D)m_\pi^2+(2b_2+3b_4)\,\vec{q}_{53}\cdot\vec{q}_{62}\Big). \quad (85)$$

Due to the vanishing of the $\Lambda\Lambda\pi$ vertex, only those two diagrams contribute, where the (final and initial) Λ hyperon are attached to the central baryon line.

4.5. Three-Baryon Force Through Decuplet Saturation

Low-energy two- and three-body interactions derived from SU(2) χEFT are used consistently in combination with each other in nuclear few- and many-body calculations. The a priori unknown low-energy constants are fitted, for example, to NN scattering data and $3N$ observables such as 3-body binding energies [78]. Some of these LECs are, however, large compared to their order of magnitude as expected from the hierarchy of nuclear forces in **Figure 5**. This feature has its physical origin in strong couplings of the πN-system to the low-lying $\Delta(1232)$-resonance. It is therefore, natural to include the $\Delta(1232)$-isobar as an explicit degree of freedom in the chiral Lagrangian (cf. [157–159]). The small mass difference between nucleons and deltas (293 MeV) introduces a small scale, which can be included consistently in the chiral power counting scheme and the hierarchy of nuclear forces. The dominant parts of the three-nucleon interaction mediated by two-pion exchange at NNLO are then promoted to NLO through the delta contributions. The appearance of the inverse mass splitting explains the large numerical values of the corresponding LECs [13, 160].

In SU(3) χEFT the situation is similar. In systems with strangeness $S = -1$ like ΛNN, resonances such as the spin-3/2 $\Sigma^*(1385)$-resonance play a similar role as the Δ in the NNN system, as depicted in **Figure 4** on the right side. The small decuplet-octet mass splitting (in the chiral limit), $\Delta := M_{10} - M_8$, is counted together with external momenta and meson masses as $\mathcal{O}(q)$ and thus parts of the NNLO three-baryon interaction are promoted to NLO by the explicit inclusion of the baryon decuplet, as illustrated in **Figure 10**. It is therefore likewise compelling to treat the three-baryon interaction together with the NLO hyperon-nucleon interaction of section 3. Note that in the nucleonic sector, only the two-pion exchange diagram with an intermediate Δ-isobar is allowed. Other diagrams are forbidden due to the Pauli principle, as we will show later. For three flavors more particles are involved and, in general, also the other diagrams (contact and one-meson exchange) with intermediate decuplet baryons in **Figure 10** appear.

The large number of unknown LECs presented in the previous subsections is related to the multitude of three-baryon multiplets, with strangeness ranging from 0 to -6. For selected processes only a small subset of these constants contributes as has been exemplified for the ΛNN three-body interaction. In this section we present the estimation of these LECs by resonance saturation as done in Petschauer et al. [121].

The leading-order non-relativistic interaction Lagrangian between octet and decuplet baryons (see, e.g., [161]) is

$$\mathscr{L} = \frac{C}{f_0}\sum_{a,b,c,d,e=1}^{3}\epsilon_{abc}\Big(\bar{T}_{ade}\vec{S}^{\,\dagger}\cdot\Big(\vec{\nabla}\phi_{db}\Big)B_{ec} + \bar{B}_{ce}\vec{S}\cdot\Big(\vec{\nabla}\phi_{bd}\Big)T_{ade}\Big), \quad (86)$$

where the decuplet baryons are represented by the totally symmetric three-index tensor T (cf. Equation 23). At this order only a single LEC C appears. Typically the (large-N_c) value $C = \frac{3}{4}g_A \approx 1$ is used, as it leads to a decay width $\Gamma(\Delta \to \pi N) = 110.6$ MeV that is in good agreement with the empirical value of $\Gamma(\Delta \to \pi N) = (115 \pm 5)$ MeV [158]. The spin $\frac{1}{2}$ to $\frac{3}{2}$ transition operators $\vec{S}$ connect the two-component spinors of octet baryons with the four-component spinors of decuplet baryons (see e.g., [162]). In their explicit form they are given as 2×4 transition matrices

$$S_1 = \begin{pmatrix} -\frac{1}{\sqrt{2}} & 0 & \frac{1}{\sqrt{6}} & 0 \\ 0 & -\frac{1}{\sqrt{6}} & 0 & \frac{1}{\sqrt{2}} \end{pmatrix},\quad S_2 = \begin{pmatrix} -\frac{i}{\sqrt{2}} & 0 & -\frac{i}{\sqrt{6}} & 0 \\ 0 & -\frac{i}{\sqrt{6}} & 0 & -\frac{i}{\sqrt{2}} \end{pmatrix},\quad S_3 = \begin{pmatrix} 0 & \sqrt{\frac{2}{3}} & 0 & 0 \\ 0 & 0 & \sqrt{\frac{2}{3}} & 0 \end{pmatrix}. \quad (87)$$

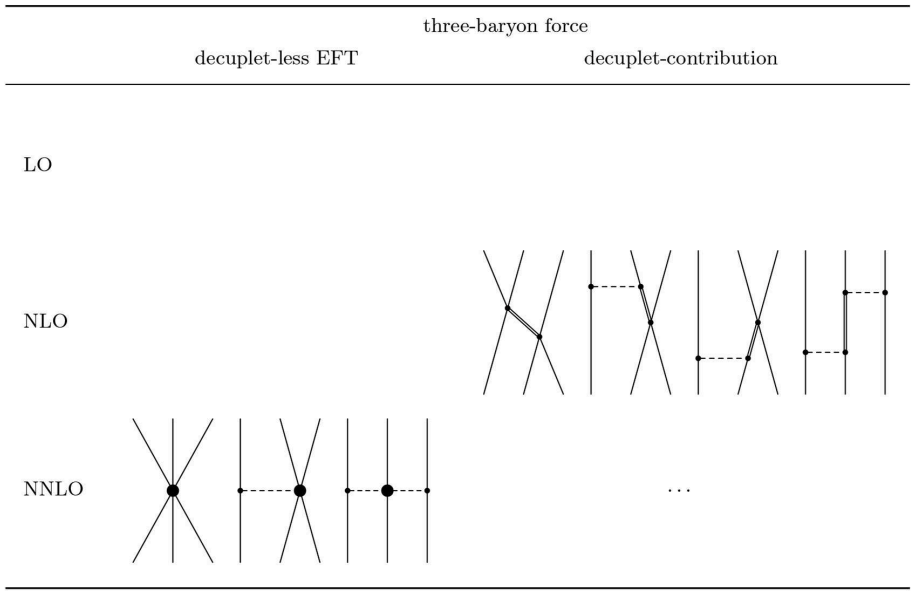


FIGURE 10 | Hierarchy of three-baryon forces with explicit introduction of the baryon decuplet (represented by double lines).

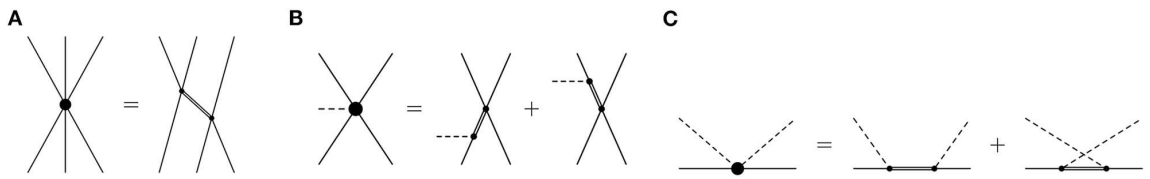


FIGURE 11 | Saturation via decuplet resonances. **(A)** Saturation of the six-baryon contact interaction. **(B)** Saturation of the $BB \to BB\phi$ vertex. **(C)** Saturation of the NLO baryon-meson vertex.

These operators fulfill the relation $S_i S_j^\dagger = \frac{1}{3}(2\delta_{ij} - \mathrm{i}\epsilon_{ijk}\sigma_k)$.

A non-relativistic B^*BBB Lagrangian with a minimal set of terms is given by [121]:

$$\begin{aligned}\mathscr{L} = \quad & H_1 \sum_{\substack{a,b,c,\\ d,e,f=1}}^{3} \epsilon_{abc}\Big[\left(\bar{T}_{ade}\vec{S}^\dagger B_{db}\right)\cdot\left(\bar{B}_{fc}\vec{\sigma}B_{ef}\right) \\ & \qquad + \left(\bar{B}_{bd}\vec{S}\,T_{ade}\right)\cdot\left(\bar{B}_{fe}\vec{\sigma}B_{cf}\right)\Big] \\ & + H_2 \sum_{\substack{a,b,c,\\ d,e,f=1}}^{3} \epsilon_{abc}\Big[\left(\bar{T}_{ade}\vec{S}^\dagger B_{fb}\right)\cdot\left(\bar{B}_{dc}\vec{\sigma}B_{ef}\right) \\ & \qquad + \left(\bar{B}_{bf}\vec{S}\,T_{ade}\right)\cdot\left(\bar{B}_{fe}\vec{\sigma}B_{cd}\right)\Big], \end{aligned} \tag{88}$$

with the LECs H_1 and H_2. Again one can employ group theory to justify the number of two constants for a transition $BB \to B^*B$. In flavor space the two initial octet baryons form the tensor product $\mathbf{8}\otimes\mathbf{8}$, and in spin space they form the product $\mathbf{2}\otimes\mathbf{2}$. These tensor products can be decomposed into irreducible representations:

$$\mathbf{8}\otimes\mathbf{8} = \underbrace{\mathbf{27}\oplus\mathbf{8}_s\oplus\mathbf{1}}_{\text{symmetric}} \oplus \underbrace{\mathbf{10}\oplus\mathbf{10}^*\oplus\mathbf{8}_a}_{\text{antisymmetric}},$$

$$\mathbf{2}\otimes\mathbf{2} = \mathbf{1}_a \oplus \mathbf{3}_s\,. \tag{89}$$

In the final state, having a decuplet and an octet baryon, the situation is similar:

$$\begin{aligned}\mathbf{10}\otimes\mathbf{8} &= \mathbf{35}\oplus\mathbf{27}\oplus\mathbf{10}\oplus\mathbf{8}\,, \\ \mathbf{4}\otimes\mathbf{2} &= \mathbf{3}\oplus\mathbf{5}\,. \end{aligned} \tag{90}$$

As seen in the previous sections, at leading order only S-wave transitions occur, as no momenta are involved. Transitions are only allowed between the same types of irreducible (flavor and spin) representations. Therefore, in spin space the representation **3** has to be chosen. Because of the Pauli principle in the initial state, the symmetric **3** in spin space combines with the antisymmetric representations $\mathbf{10}, \mathbf{10}^*, \mathbf{8}_a$ in flavor space. But only **10** and $\mathbf{8}_a$ have a counterpart in the final state flavor space. This number of two allowed transitions matches the number of two LECs in the minimal Lagrangian. Another interesting observation can be made from Equations (89) and (90). For NN states only the representations **27** and $\mathbf{10}^*$ can contribute, as can be seen, e.g., in **Table 3**. But these representations combine either with the wrong spin, or have no counterpart in the final state.

Therefore, $NN \rightarrow \Delta N$ transitions in S-waves are not allowed because of the Pauli principle.

Having the above two interaction types at hand, one can estimate the low-energy constants of the leading three-baryon interaction by decuplet saturation using the diagrams shown in **Figure 10**. At this order, where no loops are involved, one just needs to evaluate the diagrams with an intermediate decuplet baryon and the diagrams without decuplet baryons and compare them with each other.

In order to estimate the LECs of the six-baryon contact Lagrangian of Equation (71), one can consider the process $B_1B_2B_3 \rightarrow B_4B_5B_6$ as depicted in **Figure 11A**. The left side of **Figure 11A** has already been introduced in the previous subsection and can be obtained by performing all 36 Wick contractions. For the diagrams on right side of **Figure 11A** the procedure is similar. After summing over all intermediate decuplet baryons B^*, the full three-body potential of all possible combinations of baryons on the left side of **Figure 11A** can be compared with the ones on the right side. In the end the 18 LECs of the six-baryon contact Lagrangian $C_1, \ldots, C_{18}$ of Equation (71) can be expressed as linear combinations of the combinations H_1^2, H_2^2 and H_1H_2 and are proportional to the inverse average decuplet-octet baryon mass splitting $1/\Delta$ [121].

Since we are at the leading order only tree-level diagrams are involved and we can estimate the LECs of the one-meson-exchange part of the three-baryon forces already on the level of the vertices, as depicted in **Figure 11B**. We consider the transition matrix elements of the process $B_1B_2 \rightarrow B_3B_4\phi$ and start with the left side of **Figure 11B**. After doing all possible Wick contractions, summing over all intermediate decuplet baryons, and comparing the left side of **Figure 11B** with the right hand side for all combinations of baryons and mesons, the LECs can be estimated. The LECs of the minimal non-relativistic chiral Lagrangian for the four-baryon vertex including one meson of Equation (77) $D_1, \ldots, D_{14}$ are then proportional to C/Δ and to linear combinations of H_1 and H_2 [121].

The last class of diagrams is the three-body interaction with two-meson exchange. As done for the one-meson exchange, the unknown LECs can be saturated directly on the level of the vertex and one can consider the process $B_1\phi_1 \rightarrow B_2\phi_2$ as shown in **Figure 11C**. A direct comparison of the transition matrix elements for all combinations of baryons and mesons after summing over all intermediate decuplet baryons B^* leads to the following contributions to the LECs of the meson-baryon Lagrangian in Equation (79):

$$\begin{aligned} &b_D = 0\,,\ b_F = 0\,,\ b_0 = 0\,,\\ &b_1 = \frac{7C^2}{36\Delta}\,,\ b_2 = \frac{C^2}{4\Delta}\,,\ b_3 = -\frac{C^2}{3\Delta}\,,\ b_4 = -\frac{C^2}{2\Delta}\,,\\ &d_1 = \frac{C^2}{12\Delta}\,,\ d_2 = \frac{C^2}{36\Delta}\,,\ d_3 = -\frac{C^2}{6\Delta}\,, \end{aligned} \tag{91}$$

These findings are consistent with the $\Delta(1232)$ contribution to the LECs c_1, c_3, c_4 (see Equation 81) in the nucleonic sector [157, 160]:

$$c_1 = 0\,, \qquad c_3 = -2c_4 = -\frac{g_A^2}{2\Delta}\,. \tag{92}$$

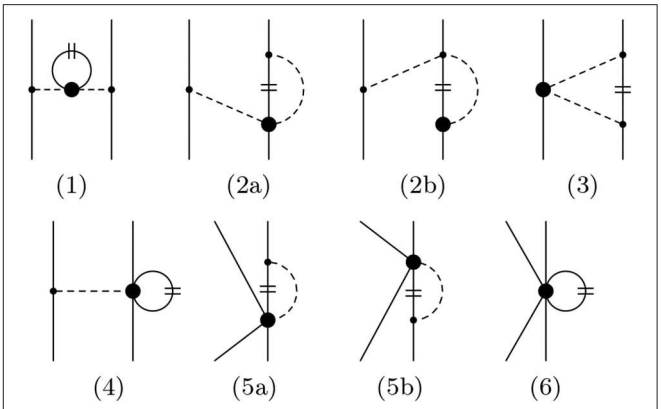


FIGURE 12 | Effective two-baryon interaction from genuine three-baryon forces. Contributions arise from two-pion exchange (1), (2a), (2b), (3), one-pion exchange (4), (5a), (5b), and the contact interaction (6).

Employing the LECs obtained via decuplet saturation, the constants of the ΛNN interaction (contact interaction, one-pion and two-pion exchange) of section 4.4 can be evaluated:

$$\begin{aligned} &C_1' = C_3' = \frac{(H_1 + 3H_2)^2}{72\Delta}\,, \quad C_2' = 0\,,\\ &D_1' = 0\,, \quad D_2' = \frac{2C(H_1 + 3H_2)}{9\Delta}\,,\\ &3b_0 + b_D = 0\,, \quad 2b_2 + 3b_4 = -\frac{C^2}{\Delta}\,. \end{aligned} \tag{93}$$

Obviously, the only unknown constant here is the combination $H' = H_1 + 3H_2$. It is also interesting to see, that the (positive) sign of the constants C_i' for the contact interaction is already fixed, independently of the values of the two LECs H_1 and H_2.

4.6. Effective In-medium Two-Baryon Interaction

In this subsection we summarize how the effect of three-body force in the presence of a (hyper)nuclear medium can be incorporated in an effective baryon-baryon potential. In Holt et al. [163], the density-dependent corrections to the NN interaction have been calculated from the leading chiral three-nucleon forces. This work has been extended to the strangeness sector in Petschauer et al. [121]. In order to obtain an effective baryon-baryon interaction from the irreducible 3BFs in **Figure 8**, two baryon lines have been closed, which represents diagrammatically the sum over occupied states within the Fermi sea. Such a "medium insertion" is symbolized by short double lines on a baryon propagator. All types of diagrams arising this way are shown in **Figure 12**.

In Petschauer et al. [121], the calculation is restricted to the contact term and to the contributions from one- and two-pion exchange processes, as they are expected to be dominant. When computing the diagrams of **Figure 8** the medium insertion corresponds to a factor $-2\pi\delta(k_0)\theta(k_f - |\vec{k}|)$. Furthermore, an additional minus sign comes from a closed fermion loop. The

effective two-body interaction can also be calculated from the expressions for the three-baryon potentials of Petschauer et al. [120] via the relation

$$V_{12} = \sum_B \mathrm{tr}_{\sigma_3} \int_{|\vec{k}|\leq k_f^B} \frac{\mathrm{d}^3 k}{(2\pi)^3} V_{123}\,, \tag{94}$$

where tr_{σ_3} denotes the spin trace over the third particle and where a summation over all baryon species B in the Fermi sea (with Fermi momentum k_f^B) is done.

As an example of such an effective interaction, we display the effective ΛN interaction in nuclear matter (with $\rho_p \neq \rho_n$) derived in Petschauer et al. [121]. It is determined from two-pion-exchange, one-pion-exchange and contact ΛNN three-body forces. Only the expressions for the Λn potential are shown as the Λp potential can be obtained just by interchanging the Fermi momenta k_f^p with k_f^n (or the densities ρ_p with ρ_n) in the expressions for Λn. In the following formulas the sum over the contributions from the protons and neutrons in the Fermi sea is already employed. Furthermore, the values of the LECs are already estimated via decuplet saturation (see section 4.5). The topologies (1), (2a), and (2b) vanish here because of the non-existence of an isospin-symmetric $\Lambda\Lambda\pi$ vertex. One obtains the density-dependent Λn potential in a nuclear medium

$$\begin{aligned} V_{\Lambda n}^{\mathrm{med},\pi\pi} = \frac{C^2 g_A^2}{12\pi^2 f_0^4 \Delta} \Bigg\{ & \\ \frac{1}{4}\Big[\frac{8}{3}(k_f^{n\,3} + 2k_f^{p\,3}) - 4(q^2+2m^2)\tilde{\Gamma}_0(p) - 2q^2\tilde{\Gamma}_1(p) & \\ + (q^2+2m^2)^2 \tilde{G}_0(p,q)\Big] & \\ + \frac{\mathrm{i}}{2}(\vec{q}\times\vec{p}\,)\cdot\vec{\sigma}_2\Big(2\tilde{\Gamma}_0(p) + 2\tilde{\Gamma}_1(p) & \\ - (q^2+2m^2)(\tilde{G}_0(p,q) + 2\tilde{G}_1(p,q))\Big)\Bigg\}\,, & \end{aligned} \tag{95}$$

$$V_{\Lambda n}^{\mathrm{med},\pi} = \frac{g_A C H'}{54\pi^2 f_0^2 \Delta}\big(2(k_f^{n\,3} + 2k_f^{p\,3}) - 3m^2\tilde{\Gamma}_0(p)\big)\,, \tag{96}$$

$$V_{\Lambda n}^{\mathrm{med,ct}} = \frac{H'^2}{18\Delta}(\rho_n + 2\rho_p)\,. \tag{97}$$

The different topologies related to two-pion exchange [(1), (2a), (2b), (3)] and one-pion exchange [(4), (5a), (5b)] have already been combined in $V^{\mathrm{med},\pi\pi}$ and $V^{\mathrm{med},\pi}$, respectively. The density and momentum dependent loop functions $\tilde{\Gamma}_i(p)$ and $\tilde{G}_i(p,q)$ can be found in Petschauer et al. [121]. The only spin-dependent term is the one proportional to $\vec{\sigma}_2 = \frac{1}{2}(\vec{\sigma}_1 + \vec{\sigma}_2) - \frac{1}{2}(\vec{\sigma}_1 - \vec{\sigma}_2)$ and therefore one recognizes a symmetric and an antisymmetric spin-orbit potential of equal but opposite strength.

5. APPLICATIONS

5.1. Hyperon-Nucleon and Hyperon-Hyperon Scattering

With the hyperon-nucleon potentials outlined in section 3 hyperon-nucleon scattering processes can be investigated. The very successful approach to the nucleon-nucleon interaction of Epelbaum et al. [147, 149, 150] within SU(2) χEFT, has been extended to the leading-order baryon-baryon interaction in Polinder et al. [29, 30] and Haidenbauer and Meißner [31] by the Bonn-Jülich group. In Haidenbauer et al. [33, 35, 36], this approach has been extended to next-to-leading order in SU(3) chiral effective field theory. As mentioned in section 2.4, the chiral power counting is applied to the potential, where only two-particle irreducible diagrams contribute. These potentials are then inserted into a regularized Lippmann-Schwinger equation to obtain the reaction amplitude (or T-matrix). In contrast to the NN interaction, the Lippmann-Schwinger equation for the YN interaction involves not only coupled partial waves, but also coupled two-baryon channels. The coupled-channel Lippmann-Schwinger equation in the particle basis reads after partial-wave decomposition (see also **Figure 2**)

$$\begin{aligned} T_{\nu''\nu'}^{\rho''\rho',J}(k'',k';\sqrt{s}) = V_{\nu''\nu'}^{\rho''\rho',J}(k'',k') & \\ + \sum_{\rho,\nu}\int_0^\infty \frac{\mathrm{d}k\,k^2}{(2\pi)^3}\, V_{\nu''\nu}^{\rho''\rho,J}(k'',k) & \\ \times \frac{2\mu_\nu}{k_\nu^2 - k^2 + \mathrm{i}\epsilon} T_{\nu\nu'}^{\rho\rho',J}(k,k';\sqrt{s})\,, & \end{aligned} \tag{98}$$

where J denotes the conserved total angular momentum. The coupled two-particle channels ($\Lambda p, \Sigma^+ n, \Sigma^0 p, \ldots$) are labeled by ν, and the partial waves ($^1S_0, ^3P_0, \ldots$) by ρ. Furthermore, μ_ν is the reduced baryon mass in channel ν. In Haidenbauer et al. [33], a non-relativistic scattering equation has been chosen to ensure that the potential can also be applied consistently to Faddeev and Faddeev-Yakubovsky calculations in the few-body sector, and to (hyper-) nuclear matter calculations within the conventional Brueckner-Hartree-Fock formalism (see section 5.2). Nevertheless, the relativistic relation between the on-shell momentum k_ν and the center-of-mass energy has been used, $\sqrt{s} = \sqrt{M_{B_1,\nu}^2 + k_\nu^2} + \sqrt{M_{B_2,\nu}^2 + k_\nu^2}$, in order to get the two-particle thresholds at their correct positions. The physical baryon masses have been used in the Lippmann-Schwinger equation, which introduces some additional SU(3) symmetry breaking. Relativistic kinematics has also been used to relate the laboratory momentum p_{lab} of the hyperon to the center-of-mass energy $\sqrt{s}$. The Coulomb interaction has been implemented by the use of the Vincent-Phatak method [147, 164]. Similar to the nucleonic sector at NLO [147], a regulator function of the form $f_R(\Lambda) = \exp[-(k'^4 + k^4)/\Lambda^4]$ is employed to cut off the high-energy components of the potential. For higher orders in the chiral power counting, higher powers than 4 in the exponent of f_R have to be used. This ensures that the regulator introduces only contributions, that are beyond the given order. The cutoff Λ is varied in the range (500 ... 700) MeV, i.e., comparable to what was used for the NN interaction in Epelbaum et al.

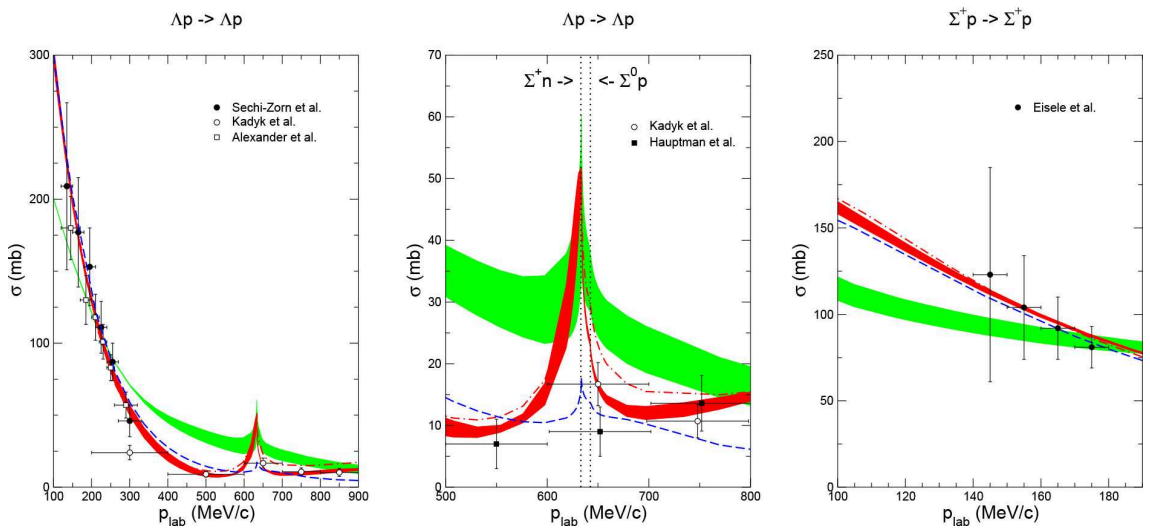


FIGURE 13 | Total cross section σ as a function of p_{lab}. The red (dark) band shows the chiral EFT results to NLO for variations of the cutoff in the range $\Lambda = (500 \ldots 650)$ MeV [33], while the green (light) band are results to LO for $\Lambda = (550 \ldots 700)$ MeV [29]. The dashed curves are the result of the Jülich '04 meson-exchange potential [21], the dash-dotted curves of the Nijmegen NSC97f potential [20].

[147]. The resulting bands represent the cutoff dependence, after readjusting the contact parameters, and thus could be viewed as a lower bound on the theoretical uncertainty. Recently, improved schemes to estimate the theoretical uncertainty were proposed and applied to the *NN* interaction [165–168]. Some illustrative results for *YN* scattering based on the method by Epelbaum et al. [166, 168] have been included in Haidenbauer et al. [34]. However, such schemes require higher orders than NLO in the chiral power counting if one wants to address questions like the convergence of the expansion.

The partial-wave contributions of the meson-exchange diagrams are obtained by employing the partial-wave decomposition formulas of Polinder et al. [29]. For further remarks on the employed approximations and the fitting strategy we refer the reader to Haidenbauer et al. [33]. As can be seen in **Table 3**, one gets for the *YN* contact terms five independent LO constants, acting in the *S*-waves, eight additional constants at NLO in the *S*-waves, and nine NLO constant acting in the *P*-waves. The contact terms represent the unresolved short-distance dynamics, and the corresponding low-energy constants are fitted to the "standard" set of 36 *YN* empirical data points [169–174]. The hypertriton ($^3_\Lambda$H) binding energy has been chosen as a further input. It determines the relative strength of the spin-singlet and spin-triplet *S*-wave contributions of the Λp interaction. Due to the sparse and inaccurate experimental data, the obtained fit of the low-energy constants is not unique. For instance, the *YN* data can be described equally well with a repulsive or an attractive interaction in the $^3S_1$ partial wave of the ΣN interaction with isospin $I = 3/2$. However, recent calculations from lattice QCD [3, 4] suggest a repulsive $^3S_1$ phase shift in the ΣN $I = 3/2$ channel, hence the repulsive solution has been adopted. Furthermore, this is consistent with empirical information from Σ^--production on nuclei, which point to a repulsive Σ-nucleus potential (see also section 5.2).

In the following we present some of the results of Haidenbauer et al. [33]. For comparison, results of the Jülich '04 [21] and the Nijmegen [20] meson-exchange models are also shown in the figures. In **Figure 13**, the total cross sections as functions of p_{lab} for various *YN* interactions are presented. The experimental data is well reproduced at NLO. Especially the results in the Λp channel are in line with the data points (also at higher energies) and the energy dependence in the $\Sigma^+ p$ channel is significantly improved at NLO. It is also interesting to note that the NLO results are now closer to the phenomenological Jülich '04 model than at LO. One expects the theoretical uncertainties to become smaller, when going to higher order in the chiral power counting. This is reflected in the fact, that the bands at NLO are considerably smaller than at LO. These bands represent only the cutoff dependence and therefore constitute a lower bound on the theoretical error.

In **Table 5**, the scattering lengths and effective range parameters for the Λp and $\Sigma^+ p$ interactions in the $^1S_0$ and $^3S_1$ partial waves are given. Result for LO [29] and NLO χEFT [33], for the Jülich '04 model [21] and for the Nijmegen NSC97f potential [20] are shown. The NLO Λp scattering lengths are larger than for the LO calculation, and closer to the values obtained by the meson-exchange models. The triplet $\Sigma^+ p$ scattering length is positive in the LO as well as the NLO calculation, which indicates a repulsive interaction in this channel. Also given in **Table 5** is the hypertriton binding energy, calculated with the corresponding chiral potentials. As stated before, the hypertriton binding energy was part of the fitting procedure and values close to the experimental value could be achieved. The predictions for the $^3_\Lambda H$ binding energy are based on the Faddeev equations in momentum space, as described in

TABLE 5 | The *YN* singlet (*s*) and triplet (*t*) scattering length *a* and effective range *r* (in fm) and the hypertriton binding energy E_B (in MeV) [33].

	NLO						LO	Jül '04	NSC97f
Λ **[MeV]**	**450**	**500**	**550**	**600**	**650**	**700**	**600**		
$a_s^{\Lambda p}$	−2.90	−2.91	−2.91	−2.91	−2.90	−2.90	−1.91	−2.56	−2.60
$r_s^{\Lambda p}$	2.64	2.86	2.84	2.78	2.65	2.56	1.40	2.74	3.05
$a_t^{\Lambda p}$	−1.70	−1.61	−1.52	−1.54	−1.51	−1.48	−1.23	−1.67	−1.72
$r_t^{\Lambda p}$	3.44	3.05	2.83	2.72	2.64	2.62	2.13	2.93	3.32
$a_s^{\Sigma^+ p}$	−3.58	−3.59	−3.60	−3.56	−3.46	−3.49	−2.32	−3.60	−4.35
$r_s^{\Sigma^+ p}$	3.49	3.59	3.56	3.54	3.53	3.45	3.60	3.24	3.16
$a_t^{\Sigma^+ p}$	0.48	0.49	0.49	0.49	0.48	0.49	0.65	0.31	−0.25
$r_t^{\Sigma^+ p}$	−4.98	−5.18	−5.03	−5.08	−5.41	−5.18	−2.78	−12.2	−28.9
$({}^3_\Lambda\mathrm{H})$ E_B	−2.39	−2.33	−2.30	−2.30	−2.30	−2.32	−2.34	−2.27	−2.30

The binding energies for the hypertriton are calculated using the Idaho-N3LO NN potential [151]. The experimental value for the ${}^3_\Lambda$H binding energy is −2.354(50) MeV.

Nogga [49, 175]. Note that genuine (irreducible) three-baryon interactions were not included in this calculation. However, in the employed coupled-channel formalism, effects like the important Λ-Σ conversion process are naturally included. It is important to distinguish such iterated two-body interactions, from irreducible three-baryon forces, as exemplified in **Figure 4**.

Predictions for *S*- and *P*-wave phase shifts δ as a function of p_{lab} for Λp and $\Sigma^+ p$ scattering are shown in **Figure 14**. The ${}^1S_0$ Λp phase shift from the NLO χEFT calculation is closer to the phenomenological Jülich '04 model than the LO result. It points to moderate attraction at low momenta and strong repulsion at higher momenta. At NLO the phase shift has a stronger downward bending at higher momenta compared to LO or the Jülich '04 model. As stated before, more repulsion at higher energies is a welcome feature in view of neutron star matter with Λ-hyperons as additional baryonic degree of freedom. The ${}^3S_1$ Λp phase shift, part of the *S*-matrix for the coupled ${}^3S_1$-${}^3D_1$ system, changes qualitatively from LO to NLO. The ${}^3S_1$ phase shift of the NLO interaction passes through 90° slightly below the ΣN threshold, which indicates the presence of an unstable bound state in the ΣN system. For the LO interaction and the Jülich '04 model no passing through 90° occurs and a cusp is predicted, that is caused by an inelastic virtual state in the ΣN system. These effects are also reflected by a strong increase of the Λp cross section close to the ΣN threshold (see **Figure 13**). The ${}^3S_1$ ΣN phase shift for the NLO interaction is moderately repulsive and comparable to the LO phase shift.

Recently an alternative NLO χEFT potential for *YN* scattering has been presented [34]. In that work a different strategy for fixing the low-energy constants that determine the strength of the contact interactions is adopted. The objective of that exploration was to reduce the number of LECs that need to be fixed in a fit to the ΛN and ΣN data by inferring some of them from the *NN* sector via the underlying SU(3) symmetry (cf. section 3.1). Indeed, correlations between the LO and NLO LECs of the *S*-waves, i.e., between the $\tilde{c}$'s and c's, had been observed already in the initial *YN* study [33] and indicated that a unique determination of them by considering the existing ΛN and ΣN data alone is not possible. It may be not unexpected in view of those correlations, that the variant considered in Haidenbauer et al. [34] yields practically equivalent results for ΛN and ΣN scattering observables. However, it differs considerable in the strength of the $\Lambda N \to \Sigma N$ transition potential and that becomes manifest in applications to few- and many-body systems [34, 176].

There is very little empirical information about baryon-baryon systems with $S = -2$, i.e., about the interaction in the $\Lambda\Lambda$, $\Sigma\Sigma$, $\Lambda\Sigma$, and ΞN channels. Actually, all one can find in the literature [36] are a few values and upper bounds for the $\Xi^- p$ elastic and inelastic cross sections [177, 178]. In addition there are constraints on the strength of the $\Lambda\Lambda$ interaction from the separation energy of the ${}^{\ \ 6}_{\Lambda\Lambda}$He hypernucleus [179]. Furthermore estimates for the $\Lambda\Lambda$ ${}^1S_0$ scattering length exist from analyses of the $\Lambda\Lambda$ invariant mass measured in the reaction ${}^{12}C(K^-, K^+\Lambda\Lambda X)$ [180] and of $\Lambda\Lambda$ correlations measured in relativistic heavy-ion collisions [181].

Despite the rather poor experimental situation, it turned out that SU(3)-symmetry breaking contact terms that arise at NLO (see section 3.1), need to be taken into account when going from strangeness $S = -1$ to $S = -2$ in order to achieve agreement with the available measurements and upper bounds for the $\Lambda\Lambda$ and ΞN cross sections [36]. This concerns, in particular, the LEC c_χ^1 that appears in the ${}^1S_0$ partial wave (cf. Equation 54). Actually, its value can be fixed by considering the pp and $\Sigma^+ p$ systems, as shown in Haidenbauer et al. [35], and then employed in the $\Lambda\Lambda$ system.

Selected results for the strangeness $S = -2$ sector are presented in **Figure 15**. Further results and a detailed description of the interactions can be found in Polinder et al. [30], Haidenbauer et al. [35, 36], and Haidenbauer and Meißner [37]. Interestingly, the results based on the LO interaction from Polinder et al. [30] (green/gray bands) are consistent with all empirical constraints. The cross sections at LO are basically genuine predictions that follow from SU(3) symmetry utilizing LECs fixed from a fit to the ΛN and ΣN data on the LO level. The $\Lambda\Lambda$ ${}^1S_0$ scattering length predicted by the NLO interaction is $a_{\Lambda\Lambda} = -0.70 \cdots -0.62$ fm [36]. These values are well within the range found in the aforementioned analyses which are $a_{\Lambda\Lambda} = (-1.2 \pm 0.6)$ fm [180] and $-1.92 < a_{\Lambda\Lambda} < -0.50$ fm [181], respectively. The values for the $\Xi^0 p$ and $\Xi^0 n$ *S*-wave scattering length are likewise small and typically in the order of $\pm 0.3 \sim \pm 0.6$ fm [36] and indicate that the ΞN interaction has to be relatively weak in order to be in accordance with the available empirical constraints. Indeed, the present results obtained in chiral EFT up to NLO imply that the published values and upper bounds for the $\Xi^- p$ elastic and inelastic cross sections [177, 178] practically rule out a somewhat stronger attractive ΞN force.

Also for ΞN scattering an alternative NLO χEFT potential has been presented recently [37]. Here the aim is to explore the possibility to establish a ΞN interaction that is still in line with all the experimental constraints for $\Lambda\Lambda$ and ΞN scattering, but at the same time is somewhat more attractive. Recent experimental evidence for the

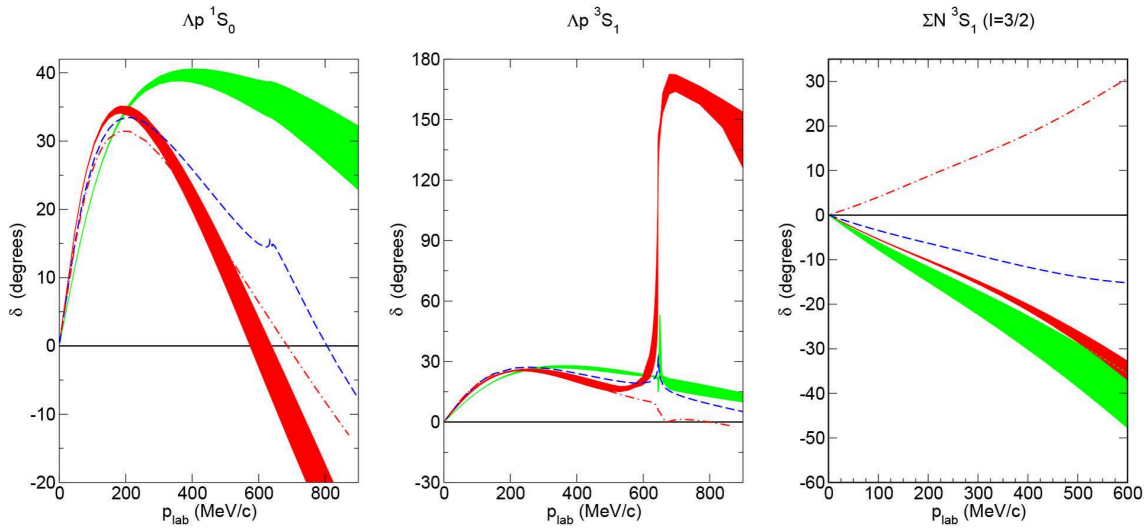


FIGURE 14 | Various *S*- and *P*-wave phase shifts δ as a function of p_{lab} for the Λp and $\Sigma^+ p$ interaction [33]. Same description of curves as in **Figure 13**.

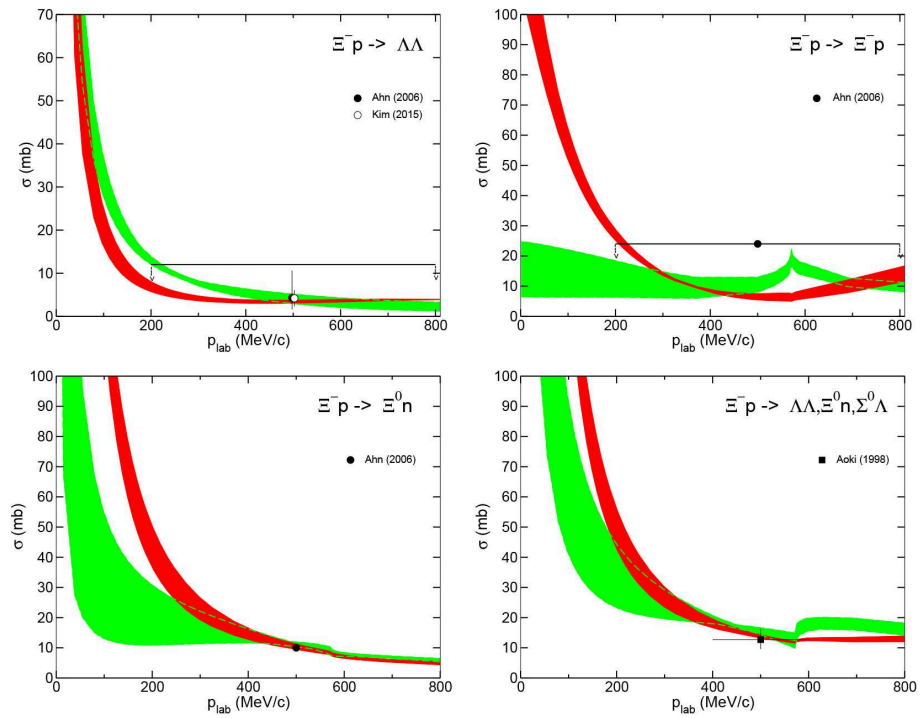


FIGURE 15 | $\Xi^- p$ induced cross sections. The bands represent results at NLO (red/black) [36] and LO (green/gray) [30]. Experiments are from Ahn et al. [178], Kim et al. [unpublished data], and Aoki et al. [177]. Upper limits are indicated by arrows.

existence of Ξ-hypernuclei [182] suggests that the in-medium interaction of the Ξ-hyperon should be moderately attractive [183].

5.2. Hyperons in Nuclear Matter

Experimental investigations of nuclear many-body systems including strange baryons, for instance, the spectroscopy of hypernuclei, provide important constraints on the underlying hyperon-nucleon interaction. The analysis of data for single Λ-hypernuclei over a wide range in mass number leads to the result, that the attractive Λ single-particle potential is about half as deep (≈ -28 MeV) as the one for nucleons [184, 185]. At the same time the Λ-nuclear spin-orbit interaction is found to be exceptionally weak [186, 187]. Recently, the repulsive nature of

the Σ-nuclear potential has been experimentally established in Σ^--formation reactions on heavy nuclei [188]. Baryon-baryon potentials derived within χEFT as presented in section 3 are consistent with these observations [75, 76]. In this section we summarize results of hyperons in infinite homogeneous nuclear matter of Petschauer et al. [76] obtained by employing the interaction potentials from χEFT as microscopic input. The many-body problem is solved within first-order Brueckner theory. A detailed introduction can be found, e.g., in Day [69], Baldo [189], and Fetter and Walecka [190].

Brueckner theory is founded on the so-called *Goldstone expansion*, a linked-cluster perturbation series for the ground state energy of a fermionic many-body system. Let us consider a system of A identical fermions, described by the Hamiltonian

$$H = T + V\,, \tag{99}$$

where T is the kinetic part and V corresponds to the two-body interaction. The goal is to calculate the ground state energy of this interacting A-body system. It is advantageous to introduced a so-called *auxiliary potential*, or single-particle potential, U. The Hamiltonian is then split into two parts

$$H = (T + U) + (V - U) = H_0 + H_1\,, \tag{100}$$

the unperturbed part H_0 and the perturbed part H_1. One expects the perturbed part to be small, if the single particle potential describes well the averaged effect of the medium on the particle. In fact, the proper introduction of the auxiliary potential is crucial for the convergence of Brueckner theory.

Conventional nucleon-nucleon potentials exhibit a strong short-range repulsion that leads to very large matrix elements. Hence, the Goldstone expansion in the form described above will not converge for such hard-core potentials. One way to approach this problem is the introduction of the so-called *Brueckner reaction matrix*, or G-matrix. The idea behind it is illustrated in **Figure 16A**. Instead of only using the simple interaction, an infinite number of diagrams with increasing number of interactions is summed up. This defines the G-matrix interaction, which is, in contrast to the bare potential, weak and of reasonable range. In a mathematical way, the reaction matrix is defined by the *Bethe-Goldstone equation*:

$$G(\omega) = V + V\frac{Q}{\omega - H_0 + \mathrm{i}\epsilon}G(\omega)\,, \tag{101}$$

with the so-called starting energy ω. The Pauli operator Q ensures, that the intermediate states are from outside the Fermi sea. As shown in **Figure 16A**, this equation represents a resummation of the ladder diagrams to all orders. The arising G-matrix interaction is an effective interaction of two particles in the presence of the medium. The medium effects come in solely through the Pauli operator and the energy denominator via the single-particle potentials. If we set the single-particle potentials to zero and omit the Pauli operator ($Q = 1$), we recover the usual Lippmann-Schwinger equation for two-body scattering in vacuum (see also **Figure 2**). This medium effect on the intermediate states is denoted by horizontal double lines in **Figure 16A**. An appropriate expansion using the G-matrix interaction instead of the bare potential is the so-called Brueckner-Bethe-Goldstone expansion, or *hole-line expansion*.

Finally, the form of the auxiliary potential U needs to be chosen. This choice is important for the convergence of the hole-line expansion. Bethe et al. [191] showed for nuclear matter that important higher-order diagrams cancel each other if the auxiliary potential is taken as

$$U_m = \mathrm{Re}\sum_{n\leq A}\langle mn|G(\omega = \omega_{\mathrm{o.s.}})|mn\rangle_{\mathcal{A}}\,, \tag{102}$$

where the Brueckner reaction matrix is evaluated *on-shell*, i.e., the starting energy is equal to the energy of the two particles m, n in the initial state:

$$\begin{aligned}\omega_{\mathrm{o.s.}} &= E_1(k_1) + E_2(k_2)\,,\\ E_{B_i}(k_i) &= M_i + \frac{k_i^2}{2M_i} + \mathrm{Re}\,U_i(k_i)\,.\end{aligned} \tag{103}$$

Pictorially Equation (102) means, that the single-particle potential can be obtained by taking the on-shell G-matrix interaction and by closing one of the baryon lines, as illustrated in **Figure 16B**. Note that this implies a non-trivial self-consistency problem. On the one hand, U is calculated from the G-matrix elements via Equation (102), and on the other hand the starting energy of the G-matrix elements depends on U through the single-particle energies E_i in Equation (103).

At the (leading) level of two hole-lines, called *Brueckner-Hartree-Fock approximation* (BHF), the total energy is given by

$$\begin{aligned}E &= \sum_{n\leq A}\langle n|T|n\rangle + \frac{1}{2}\sum_{m,n\leq A}\langle mn|G|mn\rangle_{\mathcal{A}}\\ &= \sum_{n\leq A}\langle n|T|n\rangle + \frac{1}{2}\sum_{n\leq A}\langle n|U|n\rangle\,,\end{aligned} \tag{104}$$

i.e., the ground-state energy E can be calculated directly after the single-particle potential has been determined.

The definition of U in Equation (102) applies only to occupied states within the Fermi sea. For intermediate-state energies above the Fermi sea, typically two choices for the single-particle potential are employed. In the so-called *gap choice*, the single-particle potential is given by Equation (102) for $k \leq k_F$ and set to zero for $k > k_F$, implying a "gap" (discontinuity) in the single-particle potential. Then only the free particle energies $(M + \vec{p}^{\,2}/2M)$ of the intermediate states appear in the energy denominator of the Bethe-Goldstone equation (Equation 101) since the Pauli-blocking operator is zero for momenta below the Fermi momentum. In the so-called *continuous choice* Equation (102) is used for the *whole* momentum range, hence the single-particle potentials enter also into the energy denominator. In Song et al. [192], the equation of state in symmetric nuclear matter has been considered. It has been shown, that the result including three hole-lines is almost independent of the choice of the auxiliary potential. Furthermore, the two-hole line result with the continuous choice comes out closer to

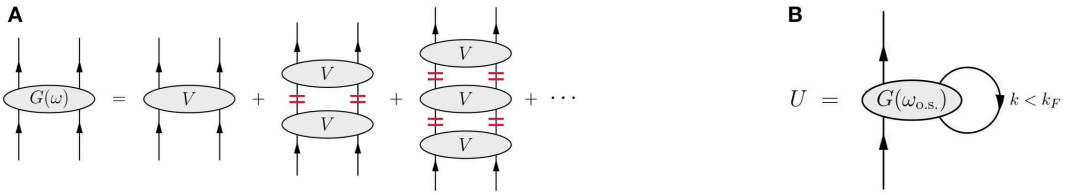


FIGURE 16 | Graphical representation of the determination of the single-particle potential from the G-matrix interaction **(B)** and of the Bethe-Goldstone equation **(A)**. The symbol $\omega_{\text{o.s}}$ denotes the on-shell starting energy.

the three hole-line result, than the two-hole line calculation with the gap choice. Another advantage of the continuous choice for intermediate spectra is that it allows for a reliable determination of the single-particle potentials including their imaginary parts [70]. The results presented here employ the continuous choice.

In the following we present some results of Petschauer et al. [76] for the in-medium properties of hyperons, based on the *YN* interaction derived from SU(3) χEFT at NLO. The same potential V as in the Lippmann-Schwinger equation (Equation 98) for free scattering is used. However, as in Haidenbauer and Meißner [75] the contact term c^{8as} for the antisymmetric spin-orbit force in the *YN* interaction, allowing spin singlet-triplet transitions, has been fitted to the weak Λ-nuclear spin-orbit interaction [193, 194]. Additionally, for the ease of comparison, the *G*-matrix results obtained with two phenomenological *YN* potentials, namely of the Jülich '04 [21] and the Nijmegen NSC97f [20] meson-exchange models, are given. Note that, like the EFT potentials, these phenomenological *YN* interactions produce a bound hypertriton [49]. For more details about derivation and the commonly employed approximations, we refer the reader to Reuber et al. [19], Rijken et al. [20], Kohno et al. [24], Schulze et al. [70], Vidaña et al. [71].

Let us start with the properties of hyperons in symmetric nuclear matter. **Figure 17** shows the momentum dependence of the real parts of the Λ single-particle potential. The values for the depth of the Λ single-particle potential $U_\Lambda(k = 0)$ at saturation density, $k_F = 1.35$ fm^{-1}, at NLO are between 27.0 and 28.3 MeV. In the Brueckner-Hartree-Fock approximation the binding energy of a hyperon in infinite nuclear matter is given by $B_Y(\infty) = -U_Y(k = 0)$. The results of the LO and NLO calculation are consistent with the empirical value of about $U_\Lambda(0) \approx -28$ MeV [184, 185]. The phenomenological models (Jülich '04, Nijmegen NSC97f) lead to more attractive values of $U_\Lambda(0) = (-35 \ldots -50)$ MeV, where the main difference is due to the contribution in the $^3S_1$ partial wave. In contrast to LO, at NLO the Λ single-particle potential at NLO turns to repulsion at fairly low momenta around $k \approx 2$ fm^{-1}, which is also the case for the NSC97f potential.

An important quantity of the interaction of hyperons with heavy nuclei is the strength of the Λ-nuclear spin-orbit coupling. It is experimentally well established [186, 187] that the Λ-nucleus spin-orbit force is very small. For the *YN* interaction of Haidenbauer and Meißner [75] it was indeed possible to tune the strength of the antisymmetric spin-orbit contact interaction (via the constant c^{8as}), generating a spin singlet-triplet mixing ($^1P_1 \leftrightarrow {}^3P_1$), in a way to achieve such a small nuclear spin-orbit potential.

Results for Σ hyperons in isospin-symmetric nuclear matter at saturation density are also displayed in **Figure 17**. Analyses of data on (π^-, K^+) spectra related to Σ^- formation in heavy nuclei lead to the observation, that the Σ-nuclear potential in symmetric nuclear matter is moderately repulsive [188]. The LO as well as the NLO results are consistent with this observation. Meson-exchange models often fail to produce such a repulsive Σ-nuclear potential. The imaginary part of the Σ-nuclear potential at saturation density is consistent with the empirical value of -16 MeV as extracted from Σ^--atom data [195]. The imaginary potential is mainly induced by the ΣN to ΛN conversion in nuclear matter. The bands representing the cutoff dependence of the chiral potentials, become smaller when going to higher order in the chiral expansion.

In **Figure 18**, the density dependence of the depth of the nuclear mean-field of Λ or Σ hyperons at rest ($k = 0$). In order to see the influence of the composition nuclear matter on the single-particle potentials, results for isospin-symmetric nuclear matter, asymmetric nuclear matter with $\rho_p = 0.25\rho$ and pure neutron matter are shown. The single-particle potential of the Λ hyperon is almost independent of the composition of the nuclear medium, because of its isosinglet nature. Furthermore, it is attractive over the whole considered range of density $0.5 \leq \rho/\rho_0 \leq 1.5$. In symmetric nuclear matter, the three Σ hyperons behave almost identical (up to small differences from the mass splittings). When introducing isospin asymmetry in the nuclear medium a splitting of the single-particle potentials occurs due to the strong isospin dependence of the ΣN interaction. The splittings among the Σ^+, Σ^0, and Σ^- potentials have a non-linear dependence on the isospin asymmetry which goes beyond the usual (linear) parametrization in terms of an isovector Lane potential [196].

Recently the in-medium properties of the Ξ have been investigated for ΞN potentials from χEFT [37]. For a more extensive discussion and further applications see Kohno [197].

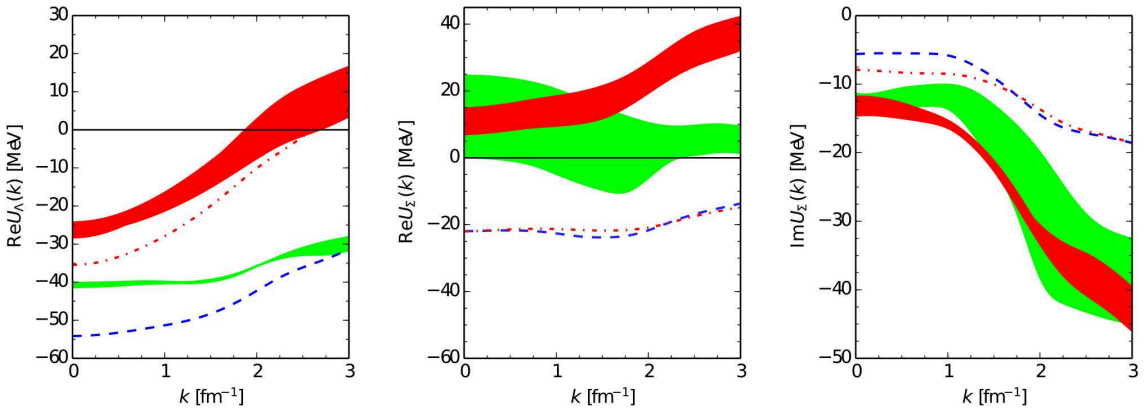


FIGURE 17 | Momentum dependence of the real part of the single-particle potential of a Λ hyperon and of the real and imaginary parts of the single-particle potential of a Σ hyperon in isospin-symmetric nuclear matter at saturation density, $k_F = 1.35$ fm^{-1} [76]. The red band, green band, blue dashed curve, and red dash-dotted curve are for χEFT NLO, χEFT LO, the Jülich '04 model and the NSC97f model, respectively.

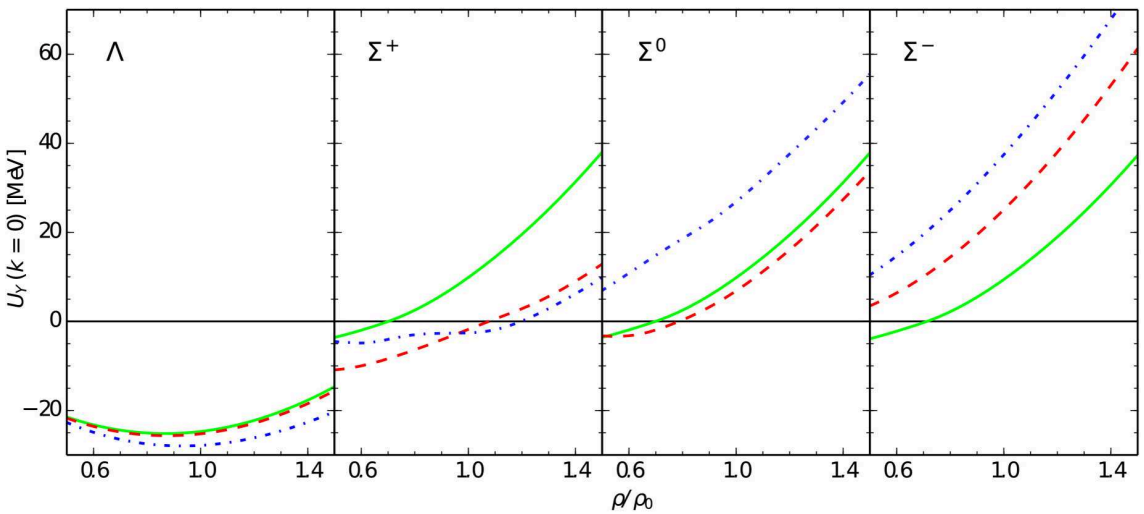


FIGURE 18 | Density dependence of the hyperon single-particle potentials at $k = 0$ with different compositions of the nuclear matter, calculated in χEFT at NLO with a cutoff $\Lambda = 600$ MeV [76]. The green solid, red dashed and blue dash-dotted curves are for $\rho_p = 0.5\rho$, $\rho_p = 0.25\rho$, and $\rho_p = 0$, respectively.

5.3. Hypernuclei and Hyperons in Neutron Stars

The density-dependent single-particle potentials of hyperons interacting with nucleons in nuclear and neutron matter find their applications in several areas of high current interest: the physics of hypernuclei and the role played by hyperons in dense baryonic matter as it is realized in the core of neutron stars.

From hypernuclear spectroscopy, the deduced attractive strength of the phenomenological Λ-nuclear Woods-Saxon potential is $U_0 \simeq -30$ MeV at the nuclear center [183]. This provides an important constraint for $U_\Lambda(k = 0)$ at $\rho = \rho_0$. The non-existence of bound Σ-hypernuclei, on the other hand, is consistent with the repulsive nature of the Σ-nuclear potential as shown in **Figure 18**. In this context effects of *YNN* three-body forces are a key issue. While their contributions at normal nuclear densities characteristic of hypernuclei are significant but modest, they play an increasingly important role when extrapolating to high baryon densities in neutron stars.

First calculations of hyperon-nuclear potentials based on chiral $SU(3)$ EFT and using Brueckner theory have been reported in Haidenbauer et al. [176] and Kohno [122]. Further investigations of (finite) Λ hypernuclei utilizing the EFT interactions can be found in Haidenbauer and Vidana [198], based on the formalism described in Vidaña [199]. For even lighter hypernuclei, the interactions are also currently studied [200, 201]. Examples of three- and four-body results can be found in Haidenbauer et al. [34, 202] and Nogga [49, 175].

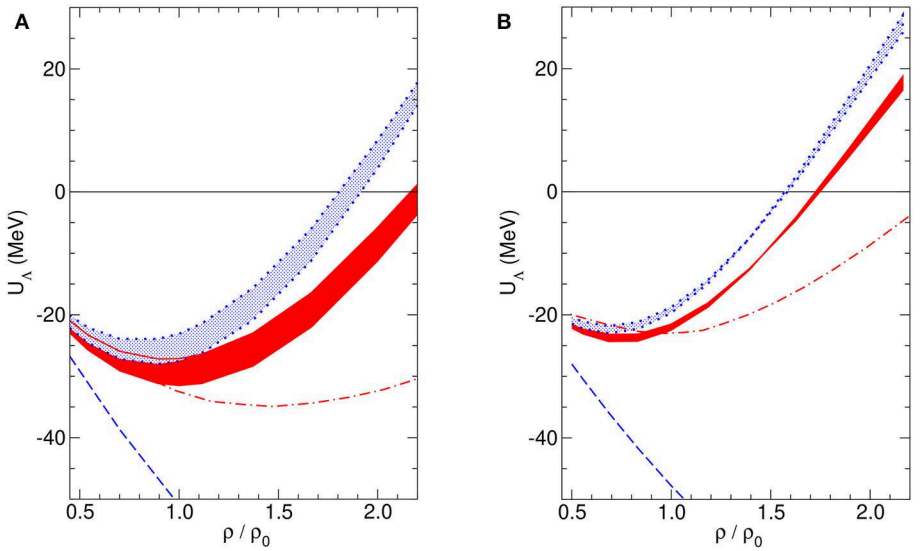


FIGURE 19 | The Λ single-particle potential $U_\Lambda(p_\Lambda = 0, \rho)$ as a function of ρ/ρ_0 in symmetric nuclear matter **(A)** and in neutron matter **(B)**. The solid (red) band shows the chiral EFT results at NLO for cutoff variations $\Lambda = 450-500$ MeV. The dotted (blue) band includes the density-dependent ΛN-interaction derived from the ΛNN three-body force. The dashed curve is the result of the Jülich '04 meson-exchange model [21], the dash-dotted curve that of the Nijmegen NSC97f potential [20], taken from Yamamoto et al. [204].

Here we give a brief survey of Λ-nuclear interactions for hypernuclei and extrapolations to high densities relevant to neutron stars, with special focus on the role of the (a priori unknown) contact terms of the ΛNN three-body force. Details can be found in Haidenbauer et al. [176]. Further extended work including explicit 3-body coupled channels ($\Lambda NN \leftrightarrow \Sigma NN$) in the Brueckner-Bethe-Goldstone equation is proceeding [203].

Results for the density dependence of the Λ single-particle potential are presented in **Figure 19** for symmetric nuclear matter (**Figure 19A**) and for neutron matter (**Figure 19B**). Predictions from the chiral SU(3) EFT interactions (bands) are shown in comparison with those for meson-exchange YN models constructed by the Jülich [21] (dashed line) and Nijmegen [20] (dash-dotted line) groups. One observes an onset of repulsive effects around the saturation density of nuclear matter, i.e., $\rho = \rho_0$. The repulsion increases strongly as the density increases. Already around $\rho \approx 2\rho_0$, $U_\Lambda(0, \rho)$ turns over to net repulsion.

Let us discuss possible implications for neutron stars. It should be clear that it is mandatory to include the ΛN–ΣN coupling in the pertinent calculations. This represents a challenging task since standard microscopic calculations without this coupling are already quite complex. However, without the ΛN–ΣN coupling, which has such a strong influence on the in-medium properties of hyperons, it will be difficult if not impossible to draw reliable conclusions.

The majority of YN-interactions employed so far in microscopic calculations of neutron stars have properties similar to those of the Jülich '04 model. In such calculations, hyperons start appearing in the core of neutron stars typically at relatively low densities around $(2-3)\rho_0$ [113, 119]. This causes the so-called hyperon puzzle: a strong softening of the equation-of-state, such that the maximum neutron star mass falls far below the constraint provided by the existence of several neutron stars with masses around $2M_\odot$. Assume now that nature favors a scenario with a weak diagonal ΛN-interaction and a strong ΛN–ΣN coupling as predicted by SU(3) chiral EFT. The present study demonstrates that, in this case, the Λ single-particle potential $U_\Lambda(k = 0, \rho)$ based on chiral EFT two-body interactions is already repulsive at densities $\rho \sim (2-3)\rho_0$. The one of the Σ-hyperon is likewise repulsive [35]. We thus expect that the appearance of hyperons in neutron stars will be shifted to much higher densities. In addition there is a repulsive density-dependent effective ΛN-interaction that arises within the same chiral EFT framework from the leading chiral YNN three-baryon forces. This enhances the aforementioned repulsive effect further. It makes the appearance of Λ-hyperons in neutron star matter energetically unfavorable. In summary, all these aspects taken together may well point to a solution of the hyperon puzzle in neutron stars without resorting to exotic mechanisms.

6. CONCLUSIONS

In this review we have presented the basics to derive the forces between octet baryons (N, Λ, Σ, Ξ) at next-to-leading order in SU(3) chiral effective field theory. The connection of SU(3) χEFT to quantum chromodynamics via the chiral symmetry and its symmetry breaking patterns, and the change of the degrees of freedom has been shown. The construction principles of the chiral effective Lagrangian and the external-field method have been presented and the Weinberg power-counting scheme has been introduced.

Within SU(3) χEFT the baryon-baryon interaction potentials have been considered at NLO. The effective baryon-baryon

potentials include contributions from pure four-baryon contact terms, one-meson-exchange diagrams, and two-meson-exchange diagrams at one-loop level. The leading three-baryon forces, which formally start to contribute at NNLO, consist of a three-baryon contact interaction, a one-meson exchange and a two-meson exchange component. We have presented explicitly potentials for the ΛNN interaction in the spin and isospin basis. The emerging low-energy constants can be estimated via decuplet saturation, which leads to a promotion of some parts of the three-baryon forces to NLO. The expressions of the corresponding effective two-body potential in the nuclear medium has been presented.

In the second part of this review we have presented selected applications of these potentials. An excellent description of the available *YN* data has been achieved with χEFT, comparable to the most advanced phenomenological models. Furthermore, in studies of the properties of hyperons in isospin symmetric and asymmetric infinite nuclear matter, the chiral baryon-baryon potentials at NLO are consistent with the empirical knowledge about hyperon-nuclear single-particle potentials. The exceptionally weak Λ-nuclear spin-orbit force is found to be related to the contact term responsible for an antisymmetric spin-orbit interaction. Concerning hypernuclei and neutron stars promising results have been obtained and could point to a solution of the hyperon puzzle in neutron stars.

In summary, χEFT is an appropriate tool for constructing the interaction among baryons in a systematic way. It sets the framework for many promising applications in strangeness-nuclear physics.

AUTHOR CONTRIBUTIONS

All authors listed have made a substantial, direct and intellectual contribution to the work, and approved it for publication.

FUNDING

This work was supported in part by the Deutsche Forschungsgemeinschaft (DFG) through the funds provided to the Sino-German Collaborative Research Center Symmetries and the Emergence of Structure in QCD (Grant No. TRR110), by the CAS President's International Fellowship Initiative (PIFI) (Grant No. 2018DM0034), and by the VolkswagenStiftung (Grant No. 93562).

REFERENCES

1. Aoki S, Doi T, Hatsuda T, Ikeda Y, Inoue T, Ishii N, et al. Lattice quantum chromodynamical approach to nuclear physics. *Prog Theor Exp Phys*. (2012) **2012**:01A105. doi: 10.1093/ptep/pts010
2. Beane SR, Detmold W, Orginos K, Savage MJ. Nuclear physics from lattice QCD. *Prog Part Nuclear Phys*. (2011) **66**:1–40. doi: 10.1016/j.ppnp.2010.08.002
3. Beane SR, Chang E, Cohen SD, Detmold W, Lin HW, Luu TC, et al. Hyperon-nucleon interactions from quantum chromodynamics and the composition of dense nuclear matter. *Phys Rev Lett*. (2012) **109**:172001. doi: 10.1103/PhysRevLett.109.172001
4. Nemura H, Aoki S, Doi T, Gongyo S, Hatsuda T, Ikeda Y, et al. Baryon interactions from lattice QCD with physical masses—strangeness $S = -1$ sector —. *EPJ Web Conf*. (2018) **175**:05030. doi: 10.1051/epjconf/201817505030
5. Weinberg S. Nonlinear realizations of chiral symmetry. *Phys Rev*. (1968) **166**:1568–77. doi: 10.1103/PhysRev.166.1568
6. Weinberg S. Phenomenological lagrangians. *Physica*. (1979) **96A**:327–40. doi: 10.1016/0378-4371(79)90223-1
7. Gasser J, Leutwyler H. Chiral perturbation theory to one loop. *Ann Phys*. (1984) **158**:142–210. doi: 10.1016/0003-4916(84)90242-2
8. Gasser J, Sainio ME, Svarc A. Nucleons with chiral loops. *Nucl Phys B*. (1988) **307**:779–853. doi: 10.1016/0550-3213(88)90108-3
9. Bernard V, Kaiser N, Meißner UG. Chiral dynamics in nucleons and nuclei. *Int J Modern Phys E*. (1995) **4**:193–344. doi: 10.1142/S0218301395000092
10. Stoks VGJ, Klomp RAM, Terheggen CPF, de Swart JJ. Construction of high-quality NN potential models. *Phys Rev C*. (1994) **49**:2950–62. doi: 10.1103/PhysRevC.49.2950
11. Wiringa RB, Stoks VGJ, Schiavilla R. Accurate nucleon-nucleon potential with charge-independence breaking. *Phys Rev C*. (1995) **51**:38–51. doi: 10.1103/PhysRevC.51.38
12. Machleidt R. High-precision, charge-dependent Bonn nucleon-nucleon potential. *Phys Rev C*. (2001) **63**:024001. doi: 10.1103/PhysRevC.63.024001
13. Epelbaum E, Hammer HW, Meißner UG. Modern theory of nuclear forces. *Rev Modern Phys*. (2009) **81**:1773–825. doi: 10.1103/RevModPhys.81.1773
14. Machleidt R, Entem DR. Chiral effective field theory and nuclear forces. *Phys Rep*. (2011) **503**:1–75. doi: 10.1016/j.physrep.2011.02.001
15. Kaplan DB, Savage MJ, Wise MB. A new expansion for nucleon-nucleon interactions. *Phys Lett*. (1998) **B424**:390–6. doi: 10.1016/S0370-2693(98)00210-X
16. Nogga A, Timmermans R, van Kolck U. Renormalization of one-pion exchange and power counting. *Phys Rev*. (2005) **C72**:054006. doi: 10.1103/PhysRevC.72.054006
17. Epelbaum E, Meißner UG. On the renormalization of the one-pion exchange potential and the consistency of Weinberg's power counting. *Few Body Syst*. (2013) **54**:2175–90. doi: 10.1007/s00601-012-0492-1
18. Holzenkamp B, Holinde K, Speth J. A meson exchange model for the hyperon-nucleon interaction. *Nucl Phys A*. (1989) **500**:485–528. doi: 10.1016/0375-9474(89)90223-6
19. Reuber AG, Holinde K, Speth J. Meson-exchange hyperon-nucleon interactions in free scattering and nuclear matter. *Nucl Phys A*. (1994) **570**:543–79. doi: 10.1016/0375-9474(94)90073-6
20. Rijken TA, Stoks VGJ, Yamamoto Y. Soft-core hyperon-nucleon potentials. *Phys Rev C*. (1999) **59**:21–40. doi: 10.1103/PhysRevC.59.21
21. Haidenbauer J, Meißner UG. Jülich hyperon-nucleon model revisited. *Phys Rev C*. (2005) **72**:044005. doi: 10.1103/PhysRevC.72.044005
22. Rijken TA, Nagels MM, Yamamoto Y. Baryon-Baryon interactions. *Prog Theor Phys Suppl*. (2010) **185**:14–71. doi: 10.1143/PTPS.185.14
23. Nagels MM, Rijken TA, Yamamoto Y. Extended-soft-core baryon-baryon model ESC16. II. Hyperon-nucleon interactions. *Phys Rev*. (2019) **C99**:044003. doi: 10.1103/PhysRevC.99.044003
24. Kohno M, Fujiwara Y, Fujita T, Nakamoto C, Suzuki Y. Hyperon single-particle potentials calculated from quark-model baryon-baryon interactions. *Nucl Phys A*. (2000) **674**:229–45. doi: 10.1016/S0375-9474(00)00164-0
25. Fujiwara Y, Suzuki Y, Nakamoto C. Baryon-baryon interactions in the SU(6) quark model and their applications to light nuclear systems. *Prog Part Nucl Phys*. (2007) **58**:439–520. doi: 10.1016/j.ppnp.2006.08.001
26. Garcilazo H, Fernandez-Carames T, Valcarce A. Lambda NN and sigma NN systems at threshold. *Phys Rev*. (2007) **C75**:034002. doi: 10.1103/PhysRevC.75.034002
27. Savage MJ, Wise MB. Hyperon masses in nuclear matter. *Phys Rev D*. (1996) **53**:349–54. doi: 10.1103/PhysRevD.53.349
28. Korpa C, Dieperink A, Timmermans R. Hyperon-nucleon scattering and hyperon masses in the nuclear medium. *Phys Rev*. (2002) **C65**:015208. doi: 10.1103/PhysRevC.65.015208

29. Polinder H, Haidenbauer J, Meißner UG. Hyperon-nucleon interactions - a chiral effective field theory approach. *Nucl Phys A*. (2006) **779**:244–66. doi: 10.1016/j.nuclphysa.2006.09.006
30. Polinder H, Haidenbauer J, Meißner UG. Strangeness S=-2 baryon-baryon interactions using chiral effective field theory. *Phys Lett B*. (2007) **653**:29–37. doi: 10.1016/j.physletb.2007.07.045
31. Haidenbauer J, Meißner UG. Predictions for the strangeness S=-3 and S=-4 baryon-baryon interactions in chiral effective field theory. *Phys Lett B*. (2010) **684**:275–80. doi: 10.1016/j.physletb.2010.01.031
32. Petschauer S, Kaiser N. Relativistic SU(3) chiral baryon-baryon Lagrangian up to order q**2. *Nucl Phys A*. (2013) **916**:1–29. doi: 10.1016/j.nuclphysa.2013.07.010
33. Haidenbauer J, Petschauer S, Kaiser N, Meißner UG, Nogga A, Weise W. Hyperon-nucleon interaction at next-to-leading order in chiral effective field theory. *Nucl Phys A*. (2013) **915**:24–58. doi: 10.1016/j.nuclphysa.2013.06.008
34. Haidenbauer J, Meißner U-G, Nogga A. Hyperon-nucleon interaction within chiral effective field theory revisited. *arxiv:1906.11681* (2019).
35. Haidenbauer J, Meißner UG, Petschauer S. Do Xi-Xi bound states exist? *Eur Phys J A*. (2015) **51**:17. doi: 10.1140/epja/i2015-15017-0
36. Haidenbauer J, Meißner UG, Petschauer S. Strangeness S=-2 baryon-baryon interaction at next-to-leading order in chiral effective field theory. *Nucl Phys A*. (2016) **954**:273–93. doi: 10.1016/j.nuclphysa.2016.01.006
37. Haidenbauer J, Meißner UG. In-medium properties of a XiN interaction derived from chiral effective field theory. *Eur Phys J A*. (2019) **55**:23. doi: 10.1140/epja/i2019-12689-2
38. Haidenbauer J, Petschauer S, Kaiser N, Meißner UG, Weise W. Scattering of decuplet baryons in chiral effective field theory. *Eur Phys J C*. (2017) **77**:760. doi: 10.1140/epjc/s10052-017-5309-4
39. Li KW, Ren XL, Geng LS, Long B. Strangeness S=-1 hyperon-nucleon scattering in covariant chiral effective field theory. *Phys Rev D*. (2016) **94**:014029. doi: 10.1103/PhysRevD.94.014029
40. Ren XL, Li KW, Geng LS, Long B, Ring P, Meng J. Leading order relativistic chiral nucleon-nucleon interaction. *Chinese Phys C*. (2018) **42**:014103. doi: 10.1088/1674-1137/42/1/014103
41. Li KW, Ren XL, Geng LS, Long BW. Leading order relativistic hyperon-nucleon interactions in chiral effective field theory. *Chinese Phys C*. (2018) **42**:014105. doi: 10.1088/1674-1137/42/1/014105
42. Song J, Li KW, Geng LS. Strangeness S=-1 hyperon-nucleon interactions: chiral effective field theory versus lattice QCD. *Phys Rev C*. (2018) **97**:065201. doi: 10.1103/PhysRevC.97.065201
43. Li K-W, Hyodo T, Geng L-S. Strangeness $S = -2$ baryon-baryon interactions in relativistic chiral effective field theory. *Phys Rev*. (2018) C98:065203. doi: 10.1103/PhysRevC.98.065203
44. Ren XL, Epelbaum E, Gegelia J. Lambda-nucleon scattering in baryon chiral perturbation theory. *arXiv:1911.05616* (2019).
45. Bernard V, Kaiser N, Meißner UG, Schmidt A. Aspects of nucleon Compton scattering. *Z Phys*. (1994) **A348**:317. doi: 10.1007/BF01305891
46. Miyagawa K, Glöckle W. Hypertriton calculation with meson theoretical nucleon-nucleon and hyperon nucleon interactions. *Phys Rev*. (1993) **C48**:2576–84. doi: 10.1103/PhysRevC.48.2576
47. Miyagawa K, Kamada H, Glöckle W, Stoks VGJ. Properties of the bound Lambda (Sigma) N N system and hyperon nucleon interactions. *Phys Rev*. (1995) **C51**:2905–13. doi: 10.1103/PhysRevC.51.2905
48. Nogga A, Kamada H, Glöckle W. The hypernuclei ${}^{4}_{\Lambda}He$ and ${}^{4}_{\Lambda}H$: challenges for modern hyperon-nucleon forces. *Phys Rev Lett*. (2002) **88**:172501. doi: 10.1103/PhysRevLett.88.172501
49. Nogga A. Light hypernuclei based on chiral interactions at next-to-leading order. *Few Body Syst*. (2014) **55**:757–60. doi: 10.1007/s00601-014-0873-8
50. Bogner SK, Furnstahl RJ, Schwenk A. From low-momentum interactions to nuclear structure. *Prog Part Nucl Phys*. (2010) **65**:94–147. doi: 10.1016/j.ppnp.2010.03.001
51. Wirth R, Gazda D, Navratil P, Calci A, Langhammer J, Roth R. *Ab initio* description of p-shell hypernuclei. *Phys Rev Lett*. (2014) **113**:192502. doi: 10.1103/PhysRevLett.113.192502
52. Wirth R, Roth R. Induced hyperon-nucleon-nucleon interactions and the hyperon puzzle. *Phys Rev Lett*. (2016) **117**:182501. doi: 10.1103/PhysRevLett.117.182501
53. Wirth R, Gazda D, Navritil P, Roth R. Hypernuclear no-core shell model. *Phys Rev C*. (2018) **97**:064315. doi: 10.1103/PhysRevC.97.064315
54. Gazda D, Gal A. Ab initio Calculations of charge symmetry breaking in the $A = 4$ hypernuclei. *Phys Rev Lett*. (2016) 116:122501. doi: 10.1103/PhysRevLett.116.122501
55. Gazda D, Gal A. Charge symmetry breaking in the A = 4 hypernuclei. *Nucl Phys*. (2016) A954:161–75. doi: 10.1016/j.nuclphysa.2016.05.015
56. Gandolfi S, Pederiva F, Fantoni S, Schmidt KE. Quantum Monte Carlo calculations of symmetric nuclear matter. *Phys Rev Lett*. (2007) **98**:102503. doi: 10.1103/PHYSREVLETT.98.102503
57. Gandolfi S, Illarionov AY, Schmidt KE, Pederiva F, Fantoni S. Quantum Monte Carlo calculation of the equation of state of neutron matter. *Phys Rev Lett*. (2009) **79**:054005. doi: 10.1103/PhysRevC.79.054005
58. Lonardoni D, Pederiva F, Gandolfi S. Accurate determination of the interaction between Lambda hyperons and nucleons from auxiliary field diffusion Monte Carlo calculations. *Phys Rev C*. (2014) **89**:014314. doi: 10.1103/PhysRevC.89.014314
59. Borasoy B, Epelbaum E, Krebs H, Lee D, Meißner UG. Lattice simulations for light nuclei: chiral effective field theory at leading order. *Eur Phys J A*. (2007) **31**:105–23. doi: 10.1140/epja/i2006-10154-1
60. Epelbaum E, Krebs H, Lee D, Meißner UG. Ab initio calculation of the Hoyle state. *Phys Rev Lett*. (2011) **106**:192501. doi: 10.1103/PhysRevLett.106.192501
61. Lähde TA, Meißner UG. Nuclear lattice effective field theory. *Lect Notes Phys*. (2019) **957**:1–396. doi: 10.1007/978-3-030-14189-9
62. Holt JW, Kaiser N, Weise W. Nuclear chiral dynamics and thermodynamics. *Prog Part Nucl Phys*. (2013) **73**:35–83. doi: 10.1016/j.ppnp.2013.08.001
63. Coraggio L, Holt JW, Itaco N, Machleidt R, Marcucci LE, Sammarruca F. Nuclear-matter equation of state with consistent two- and three-body perturbative chiral interactions. *Phys Rev C*. (2014) **89**:044321. doi: 10.1103/PhysRevC.89.044321
64. Sammarruca F, Coraggio L, Holt JW, Itaco N, Machleidt R, Marcucci LE. Toward order-by-order calculations of the nuclear and neutron matter equations of state in chiral effective field theory. *Phys Rev C*. (2015) **91**:054311. doi: 10.1103/PhysRevC.91.054311
65. Kaiser N, Weise W. Chiral SU(3) dynamics and Lambda hyperons in the nuclear medium. *Phys Rev C*. (2005) **71**:015203. doi: 10.1103/PhysRevC.71.015203
66. Kaiser N. Chiral dynamics of Sigma hyperons in the nuclear medium. *Phys Rev C*. (2005) **71**:068201. doi: 10.1103/PhysRevC.71.068201
67. Brueckner K, Levinson CA, Mahmoud H. Two-body forces and nuclear saturation. I. Central forces. *Phys Rev*. (1954) **95**:217–28. doi: 10.1103/PhysRev.95.217
68. Brueckner K, Levinson CA. Approximate reduction of the many-body problem for strongly interacting particles to a problem of self-consistent fields. *Phys Rev*. (1955) **97**:1344–52. doi: 10.1103/PhysRev.97.1344
69. Day BD. Elements of the Brueckner-Goldstone theory of nuclear matter. *Rev Modern Phys*. (1967) **39**:719–44. doi: 10.1103/RevModPhys.39.719
70. Schulze HJ, Baldo M, Lombardo U, Cugnon J, Lejeune A. Hyperonic nuclear matter in Brueckner theory. *Phys Rev C*. (1998) **57**:704–13. doi: 10.1103/PhysRevC.57.704
71. Vidaña I, Polls A, Ramos A, Hjorth-Jensen M, Stoks VGJ. Strange nuclear matter within Brueckner-Hartree-Fock theory. *Phys Rev C*. (2000) **61**:025802. doi: 10.1103/PhysRevC.61.025802
72. Baldo M, Burgio GF, Schulze HJ. Hyperon stars in the Brueckner-Bethe-Goldstone theory. *Phys Rev C*. (2000) **61**:055801. doi: 10.1103/PhysRevC.61.055801
73. Schulze HJ, Polls A, Ramos A, Vidaña I. Maximum mass of neutron stars. *Phys Rev C*. (2006) **73**:058801. doi: 10.1103/PhysRevC.73.058801
74. Schulze HJ, Rijken TA. Maximum mass of hyperon stars with the Nijmegen ESC08 model. *Phys Rev C*. (2011) **84**:035801. doi: 10.1103/PHYSREVC.84.035801
75. Haidenbauer J, Meißner UG. A study of hyperons in nuclear matter based on chiral effective field theory. *Nucl Phys A*. (2015) **936**:29–44. doi: 10.1016/j.nuclphysa.2015.01.005

76. Petschauer S, Haidenbauer J, Kaiser N, Meißner UG, Weise W. Hyperons in nuclear matter from SU(3) chiral effective field theory. *Eur Phys J A*. (2016) **52**:15. doi: 10.1140/epja/i2016-16015-4
77. Pieper SC, Wiringa RB. Quantum Monte Carlo calculations of light nuclei. *Annu Rev Nucl Part Sci*. (2001) **51**:53–90. doi: 10.1146/annurev.nucl.51.101701.132506
78. Epelbaum E, Nogga A, Glöckle W, Kamada H, Meißner UG, Witala H. Three-nucleon forces from chiral effective field theory. *Phys Rev C*. (2002) **66**:064001. doi: 10.1103/PhysRevC.66.064001
79. Kalantar-Nayestanaki N, Epelbaum E, Messchendorp JG, Nogga A. Signatures of three-nucleon interactions in few-nucleon systems. *Rept Prog Phys*. (2012) **75**:016301. doi: 10.1088/0034-4885/75/1/016301
80. Hammer HW, Nogga A, Schwenk A. Three-body forces: from cold atoms to nuclei. *Rev Mod Phys*. (2013) **85**:197. doi: 10.1103/RevModPhys.85.197
81. McKellar BHJ, Rajaraman R. Three-body forces in nuclear matter. *Phys Rev Lett*. (1968) **21**:450–3. doi: 10.1103/PhysRevLett.21.450
82. Coon SA, Scadron MD, Barrett BR. The three-body force, off-shell πN scattering and binding energies in nuclear matter. *Nucl Phys A*. (1975) **242**:467–80. doi: 10.1016/0375-9474(75)90109-8
83. Coelho HT, Das TK, Robilotta MR. Two-pion-exchange three-nucleon force and the 3H and 3He nuclei. *Phys Rev C*. (1983) **28**:1812–28. doi: 10.1103/PhysRevC.28.1812
84. Pudliner BS, Pandharipande VR, Carlson J, Pieper SC, Wiringa RB. Quantum Monte Carlo calculations of nuclei with $A \leq 7$. *Phys Rev C*. (1997) **56**:1720–50. doi: 10.1103/PhysRevC.56.1720
85. Pieper SC, Pandharipande VR, Wiringa RB, Carlson J. Realistic models of pion-exchange three-nucleon interactions. *Phys Rev C*. (2001) **64**:014001. doi: 10.1103/PhysRevC.64.014001
86. Weinberg S. Nuclear forces from chiral lagrangians. *Phys Lett B*. (1990) **251**:288–92. doi: 10.1016/0370-2693(90)90938-3
87. Weinberg S. Effective chiral lagrangians for nucleon-pion interactions and nuclear forces. *Nucl Phys B*. (1991) **363**:3–18. doi: 10.1016/0550-3213(91)90231-L
88. Weinberg S. Three-body interactions among nucleons and pions. *Phys Lett B*. (1992) **295**:114–21. doi: 10.1016/0370-2693(92)90099-P
89. van Kolck U. Few-nucleon forces from chiral Lagrangians. *Phys Rev C*. (1994) **49**:2932–41. doi: 10.1103/PhysRevC.49.2932
90. Ishikawa S, Robilotta MR. Two-pion exchange three-nucleon potential: O(q**4) chiral expansion. *Phys Rev C*. (2007) **76**:014006. doi: 10.1103/PhysRevC.76.014006
91. Bernard V, Epelbaum E, Krebs H, Meißner UG. Subleading contributions to the chiral three-nucleon force: Long-range terms. *Phys Rev C*. (2008) **77**:064004. doi: 10.1103/PhysRevC.77.064004
92. Bernard V, Epelbaum E, Krebs H, Meißner UG. Subleading contributions to the chiral three-nucleon force. II. Short-range terms and relativistic corrections. *Phys Rev C*. (2011) **84**:054001. doi: 10.1103/PhysRevC.84.054001
93. Krebs H, Gasparyan A, Epelbaum E. Chiral three-nucleon force at N^4LO: longest-range contributions. *Phys Rev C*. (2012) **85**:054006. doi: 10.1103/PhysRevC.85.054006
94. Krebs H, Gasparyan A, Epelbaum E. Chiral three-nucleon force at N^4LO. II. Intermediate-range contributions. *Phys Rev C*. (2013) **87**:054007. doi: 10.1103/PhysRevC.87.054007
95. Bhaduri RK, Loiseau BA, Nogami Y. Effect of three-body ΛNN long-range potential in nuclear matter. *Nucl Phys B*. (1967) **3**:380–6. doi: 10.1016/0550-3213(67)90007-7
96. Bhaduri RK, Loiseau BA, Nogami Y. Effects of three-body ΛNN forces in light hypernuclei. *Ann Phys*. (1967) **44**:57–73. doi: 10.1016/0003-4916(67)90264-3
97. Gal A, Soper JM, Dalitz RH. A shell-model analysis of Λ binding energies for the p-shell hypernuclei. I. Basic formulas and matrix elements for ΛN and ΛNN forces. *Ann Phys*. (1971) **63**:53–126. doi: 10.1016/0003-4916(71)90297-1
98. Gal A, Soper JM, Dalitz RH. A shell-model analysis of Λ binding energies for the p-shell hypernuclei II. Numerical fitting, interpretation, and hypernuclear predictions. *Ann Phys*. (1972) **72**:445–88. doi: 10.1016/0003-4916(72)90222-9
99. Gal A, Soper JM, Dalitz RH. A shell-model analysis of Λ binding energies for the p-shell hypernuclei III. Further analysis and predictions. *Ann Phys*. (1978) **113**:79–97. doi: 10.1016/0003-4916(78)90250-6
100. Bodmer AR, Usmani QN. Binding energies of the s-shell hypernuclei and the Λ well depth. *Nucl Phys A*. (1988) **477**:621–51. doi: 10.1016/0375-9474(88)90410-1
101. Usmani AA. Three-baryon Lambda N N potential. *Phys Rev C*. (1995) **52**:1773–7. doi: 10.1103/PhysRevC.52.1773
102. Lonardoni D, Gandolfi S, Pederiva F. Effects of the two-body and three-body hyperon-nucleon interactions in Λ hypernuclei. *Phys Rev C*. (2013) **87**:041303. doi: 10.1103/PhysRevC.87.041303
103. Logoteta D, Vidana I, Bombaci I. Impact of chiral hyperonic three-body forces on neutron stars. *Eur Phys J*. (2019) **A55**:207. doi: 10.1140/epja/i2019-12909-9
104. Demorest PB, Pennucci TT, Ransom SM, Roberts MSE, Hessels JWT. A two-solar-mass neutron star measured using Shapiro delay. *Nature*. (2010) **467**:1081–3. doi: 10.1038/nature09466
105. Antoniadis J, Freire PCC, Wex N, Tauris TM, Lynch RS, van Kerkwijk MH, et al. A massive pulsar in a compact relativistic binary. *Science*. (2013) **340**:1233232. doi: 10.1126/science.1233232
106. Hebeler K, Lattimer JM, Pethick CJ, Schwenk A. Constraints on neutron star radii based on chiral effective field theory interactions. *Phys Rev Lett*. (2010) **105**:161102. doi: 10.1103/PhysRevLett.105.161102
107. Hell T, Weise W. Dense baryonic matter: constraints from recent neutron star observations. *Phys Rev C*. (2014) **90**:045801. doi: 10.1103/PhysRevC.90.045801
108. Steiner AW, Lattimer JM, Brown EF. Neutron star radii, universal relations, and the role of prior distributions. *arXiv:151007515* (2015). doi: 10.1140/epja/i2016-16018-1
109. Vidaña I. Hyperons in neutron stars. *J Phys Conf Ser*. (2016) **668**:012031. doi: 10.1088/1742-6596/668/1/012031
110. Vidaña I. Hyperons: the strange ingredients of the nuclear equation of state. *Proc R Soc Lond*. (2018) **A474**:0145. doi: 10.1098/rspa.2018.0145
111. Abbott BP, Abbott R, Abbott TD, Acernese F, Ackley K, Adams C, et al. GW170817: observation of gravitational waves from a binary neutron star inspiral. *Phys Rev Lett*. (2017) **119**:161101. doi: 10.1103/PhysRevLett.119.161101
112. Abbott BP, Abbott R, Abbott TD, Acernese F, Ackley K, Adams T, et al. Multi-messenger observations of a binary neutron star merger. *Astrophys J*. (2017) **848**:L12. doi: 10.3847/2041-8213/aa91c9
113. Djapo H, Schaefer BJ, Wambach J. Appearance of hyperons in neutron stars. *Phys Rev C*. (2010) **81**:035803. doi: 10.1103/PhysRevC.81.035803
114. Weissenborn S, Chatterjee D, Schaffner-Bielich J. Hyperons and massive neutron stars: the role of hyperon potentials. *Nucl Phys A*. (2012) **881**:62–77. doi: 10.1016/j.nuclphysa.2012.02.012
115. Weissenborn S, Chatterjee D, Schaffner-Bielich J. Hyperons and massive neutron stars: vector repulsion and SU(3) symmetry. *Phys Rev C*. (2012) **85**:065802. doi: 10.1103/PhysRevC.85.065802
116. Yamamoto Y, Furumoto T, Yasutake N, Rijken TA. Hyperon mixing and universal many-body repulsion in neutron stars. *Phys Rev C*. (2014) **90**:045805. doi: 10.1103/PhysRevC.90.045805
117. Takatsuka T, Nishizaki S, Tamagaki R. Three-body force as an "Extra Repulsion" suggested from hyperon-mixed neutron stars. *Prog Theor Phys Suppl*. (2008) **174**:80–3. doi: 10.1143/PTPS.174.80
118. Vidaña I, Logoteta D, Providência C, Polls A, Bombaci I. Estimation of the effect of hyperonic three-body forces on the maximum mass of neutron stars. *Europhys Lett*. (2011) **94**:11002. doi: 10.1209/0295-5075/94/11002
119. Lonardoni D, Lovato A, Gandolfi S, Pederiva F. Hyperon puzzle: hints from quantum Monte Carlo calculations. *Phys Rev Lett*. (2015) **114**:092301. doi: 10.1103/PhysRevLett.114.092301

120. Petschauer S, Kaiser N, Haidenbauer J, Meißner UG, Weise W. Leading three-baryon forces from SU(3) chiral effective field theory. *Phys Rev C*. (2016) **93**:014001. doi: 10.1103/PhysRevC.93.014001
121. Petschauer S, Haidenbauer J, Kaiser N, Meißner UG, Weise W. Density-dependent effective baryon-baryon interaction from chiral three-baryon forces. *Nucl Phys A*. (2017) **957**:347–78. doi: 10.1016/j.nuclphysa.2016.09.010
122. Kohno M. Single-particle potential of the Lambda hyperon in nuclear matter with chiral effective field theory NLO interactions including effects of YNN three-baryon interactions. *Phys Rev C*. (2018) **97**:035206. doi: 10.1103/PhysRevC.97.035206
123. Adler SL, Dashen RF. *Current Algebras and Applications to Particle Physics*. New York, NY: Benjamin (1968). Available online at: http://books.google.com/books?id=8OBEAAAAIAAJ
124. Coleman S, Wess J, Zumino B. Structure of phenomenological lagrangians. I. *Phys Rev*. (1969) **177**:2239–47. doi: 10.1103/PhysRev.177.2239
125. Callan CG, Coleman S, Wess J, Zumino B. Structure of phenomenological lagrangians. II. *Phys Rev*. (1969) **177**:2247–50. doi: 10.1103/PhysRev.177.2247
126. Gasser J, Leutwyler H. Chiral perturbation theory: expansions in the mass of the strange quark. *Nucl Phys B*. (1985) **250**:465–516. doi: 10.1016/0550-3213(85)90492-4
127. Jenkins E, Manohar AV. Baryon chiral perturbation theory using a heavy fermion lagrangian. *Phys Lett B*. (1991) **255**:558–62. doi: 10.1016/0370-2693(91)90266-S
128. Bernard V, Kaiser N, Kambor J, Meißner UG. Chiral structure of the nucleon. *Nucl Phys.* (1992) **B388**:315–45. doi: 10.1016/0550-3213(92)90615-I
129. Thomas AW, Weise W. *The Structure of the Nucleon*. Berlin: Wiley-VCH Verlag (2001). Available online at: http://www.wiley-vch.de/publish/en/books/bySubjectPH00/ISBN3-527-40297-7/
130. Scherer S, Schindler M. A primer for chiral perturbation theory. *Lect Notes Phys*. (2012) **830**:1–338. doi: 10.1007/978-3-642-19254-8
131. Petschauer S. *Baryonic forces and hyperons in nuclear matter from SU(3) chiral effective field theory*. Dissertation. Technische Universität München, München, Germany. (2016).
132. Adler SL. Axial-vector vertex in spinor electrodynamics. *Phys Rev*. (1969) **177**:2426–38. doi: 10.1103/PhysRev.177.2426
133. Bell JS, Jackiw R. A PCAC puzzle: $\pi^0 \to \gamma\gamma$ in the σ-model. *IL Nuovo Cimento A*. (1969) **60**:47–61. doi: 10.1007/BF02823296
134. Leutwyler H. On the foundations of chiral perturbation theory. *Ann Phys*. (1994) **235**:165–203. doi: 10.1006/aphy.1994.1094
135. Georgi H. *Weak Interactions and Modern Particle Theory*. Reading, MA: Benjamin; Cummings (1984).
136. Fearing HW, Scherer S. Extension of the chiral perturbation theory meson Lagrangian to order p**6. *Phys Rev D*. (1996) **53**:315–48. doi: 10.1103/PhysRevD.53.315
137. Bijnens J, Colangelo G, Ecker G. The mesonic chiral lagrangian of order p**6. *J High Energy Phys*. (1999) **1999**:020. doi: 10.1088/1126-6708/1999/02/020
138. Fettes N, Meißner UG, Mojzis M, Steininger S. The chiral effective pion-nucleon lagrangian of order p**4. *Ann Phys*. (2000) **283**:273–307. doi: 10.1006/aphy.2000.6059
139. Krause A. Baryon matrix elements of the vector current in chiral perturbation theory. *Helv Phys Acta*. (1990) **63**:3–70.
140. Oller JA, Verbeni M, Prades J. Meson-baryon effective chiral Lagrangians to O(q**3). *J High Energy Phys*. (2006) **2006**:079. doi: 10.1088/1126-6708/2006/09/079
141. Frink M, Meißner UG. On the chiral effective meson-baryon Lagrangian at third order. *Eur Phys J A*. (2006) **29**:255–60. doi: 10.1140/epja/i2006-10105-x
142. Girlanda L, Pastore S, Schiavilla R, Viviani M. Relativity constraints on the two-nucleon contact interaction. *Phys Rev C*. (2010) **81**:034005. doi: 10.1103/PhysRevC.81.034005
143. Borasoy B. Baryon axial vector currents. *Phys Rev D*. (1999) **59**:054021. doi: 10.1103/PhysRevD.59.054021
144. Iwao S. Baryon-baryon interactions and unitary symmetry. *IL Nuovo Cimento*. (1964) **34**:1167–83. doi: 10.1007/BF02748845
145. Dover CB, Feshbach H. Unitary symmetry in baryon-baryon scattering. *Ann Phys*. (1990) **198**:321–57. doi: 10.1016/0003-4916(90)90254-L
146. Dover CB, Feshbach H. Unitary symmetry in baryon-baryon scattering, II. *Ann Phys*. (1992) **217**:51–65. doi: 10.1016/0003-4916(92)90338-M
147. Epelbaum E, Glöckle W, Meißner UG. The two-nucleon system at next-to-next-to-next-to-leading order. *Nucl Phys A*. (2005) **747**:362–424. doi: 10.1016/j.nuclphysa.2004.09.107
148. Kaiser N, Brockmann R, Weise W. Peripheral nucleon-nucleon phase shifts and chiral symmetry. *Nucl Phys A*. (1997) **625**:758–88. doi: 10.1016/S0375-9474(97)00586-1
149. Epelbaum E, Glöckle W, Meißner UG. Nuclear forces from chiral Lagrangians using the method of unitary transformation (I): formalism. *Nucl Phys A*. (1998) **637**:107–34. doi: 10.1016/S0375-9474(98)00220-6
150. Epelbaum E, Glöckle W, Meißner UG. Nuclear forces from chiral Lagrangians using the method of unitary transformation II: the two-nucleon system. *Nucl Phys A*. (2000) **671**:295–331. doi: 10.1016/S0375-9474(99)00821-0
151. Entem DR, Machleidt R. Accurate charge-dependent nucleon-nucleon potential at fourth order of chiral perturbation theory. *Phys Rev C*. (2003) **68**:041001. doi: 10.1103/PhysRevC.68.041001
152. Tominaga K, Ueda T, Yamaguchi M, Kijima N, Okamoto D, Miyagawa K, et al. A one-boson-exchange potential for Lambda N, Lambda Lambda and Xi N systems and hypernuclei. *Nucl Phys*. (1998) **A642**:483–505. doi: 10.1016/S0375-9474(98)00485-0
153. Tominaga K, Ueda T. Effective one-boson-exchange potential for Lambda N and Sigma N systems and hypertriton. *Nucl Phys*. (2001) **A693**:731–54. doi: 10.1016/S0375-9474(01)00882-X
154. Reuber A, Holinde K, Kim HC, Speth J. Correlated pi pi and K anti-K exchange in the baryon baryon interaction. *Nucl Phys*. (1996) **A608**:243–304. doi: 10.1016/0375-9474(96)00256-4
155. Frink M, Meißner UG. Chiral extrapolations of baryon masses for unquenched three-flavor lattice simulations. *J High Energy Phys*. (2004) **407**:28. doi: 10.1088/1126-6708/2004/07/028
156. Mai M, Bruns P, Kubis B, Meißner UG. Aspects of meson-baryon scattering in three- and two-flavor chiral perturbation theory. *Phys Rev D*. (2009) **80**:094006. doi: 10.1103/PhysRevD.80.094006
157. Bernard V, Kaiser N, Meißner UG. Aspects of chiral pion-nucleon physics. *Nucl Phys A*. (1997) **615**:483–500. doi: 10.1016/S0375-9474(97)00021-3
158. Kaiser N, Gerstendörfer S, Weise W. Peripheral NN-scattering: role of delta-excitation, correlated two-pion and vector meson exchange. *Nucl Phys*. (1998) **A637**:395–420. doi: 10.1016/S0375-9474(98)00234-6
159. Krebs H, Epelbaum E, Meißner UG. Nuclear forces with Δ excitations up to next-to-next-to-leading order, part I: peripheral nucleon-nucleon waves. *Eur Phys J A*. (2007) **32**:127–37. doi: 10.1140/epja/i2007-10372-y
160. Epelbaum E, Krebs H, Meißner UG. Δ-excitations and the three-nucleon force. *Nucl Phys A*. (2008) **806**:65–78. doi: 10.1016/j.nuclphysa.2008.02.305
161. Sasaki K, Oset E, Vacas M. Scalar ΛN and $\Lambda\Lambda$ interaction in a chiral unitary approach. *Phys Rev C*. (2006) **74**:064002. doi: 10.1103/PhysRevC.74.064002
162. Ericson TEO, Weise W. *Pions and Nuclei*. Oxford: Clarendon Press (1988).
163. Holt JW, Kaiser N, Weise W. Density-dependent effective nucleon-nucleon interaction from chiral three-nucleon forces. *Phys Rev C*. (2010) **81**:024002. doi: 10.1103/PhysRevC.81.024002
164. Vincent CM, Phatak S. Accurate momentum-space method for scattering by nuclear and Coulomb potentials. *Phys Rev C*. (1974) **10**:391–4. doi: 10.1103/PhysRevC.10.391
165. Furnstahl RJ, Phillips DR, Wesolowski S. A recipe for EFT uncertainty quantification in nuclear physics. *J Phys G*. (2015) **42**:034028. doi: 10.1088/0954-3899/42/3/034028
166. Epelbaum E, Krebs H, Meißner UG. Improved chiral nucleon-nucleon potential up to next-to-next-to-next-to-leading order. *Eur Phys J A*. (2015) **51**:53. doi: 10.1140/epja/i2015-15053-8
167. Furnstahl RJ, Klco N, Phillips DR, Wesolowski S. Quantifying truncation errors in effective field theory. *Phys Rev C*. (2015) **92**:024005. doi: 10.1103/PhysRevC.92.024005
168. Binder S, Calci A, Epelbaum E, Furnstahl RJ, Golak J, Hebeler K, et al. Few-nucleon systems with state-of-the-art chiral nucleon-nucleon forces. *Phys Rev C*. (2016) **93**:044002. doi: 10.1103/PhysRevC.93.044002

169. Sechi-Zorn B, Kehoe B, Twitty J, Burnstein RA. Low-energy lambda-proton elastic scattering. *Phys Rev*. (1968) **175**:1735–40. doi: 10.1103/PhysRev.175.1735
170. Alexander G, Karshon U, Shapira A, Yekutieli G, Engelmann R, Filthuth H, et al. Study of the lambda-N system in low-energy lambda-p elastic scattering. *Phys Rev*. (1968) **173**:1452–60. doi: 10.1103/PhysRev.173.1452
171. Engelmann R, Filthuth H, Hepp V, Kluge E. Inelastic $\Sigma^- p$-interactions at low momenta. *Phys Lett*. (1966) **21**:587–9. doi: 10.1016/0031-9163(66)91310-2
172. Eisele F, Filthuth H, Föhlisch W, Hepp V, Zech G. Elastic $\Sigma^{\pm} p$ scattering at low energies. *Phys Lett B*. (1971) **37**:204–6. doi: 10.1016/0370-2693(71)90053-0
173. Hepp V, Schleich H. A new determination of the capture ratio $r_c = (\Sigma^- p \to \Sigma^0 n)/((\Sigma^- p \to \Sigma^0 n) + (\Sigma^- p \to \Lambda^0 n))$, the Λ^0-lifetime and $\Sigma^- \Lambda^0$ mass difference. *Z Phys*. (1968) **214**:71–7. doi: 10.1007/BF01380085
174. Stephen D. Ph.D. thesis, University of Massachsetts, unpublished (1970).
175. Nogga A. Light hypernuclei based on chiral and phenomenological interactions. *Nucl Phys A*. (2013) **914**:140–50. doi: 10.1016/j.nuclphysa.2013.02.053
176. Haidenbauer J, Meißner UG, Kaiser N, Weise W. Lambda-nuclear interactions and hyperon puzzle in neutron stars. *Eur Phys J A*. (2017) **53**:121. doi: 10.1140/epja/i2017-12316-4
177. Aoki S, Asai S, Bahk SY, Chung SH, Funahashi H, Hahn CH, et al. Quasifree p(K-,K+)Xi- reaction in nuclear emulsion. *Nucl Phys*. (1998) **A644**:365–85. doi: 10.1016/S0375-9474(98)00596-X
178. Ahn JK, Aoki S, Chung KS, Chung MS, Enyo H, Fukuda T, et al. Measurement of the Xi-p scattering cross sections at low energy. *Phys Lett*. (2006) **B633**:214–8.
179. Takahashi H, Ahn JK, Akikawa H, Aoki S, Arai K, Bahk SY, et al. Observation of a (Lambda Lambda)He-6 double hypernucleus. *Phys Rev Lett*. (2001) 87:212502. doi: 10.1103/PhysRevLett.87.212502
180. Gasparyan AM, Haidenbauer J, Hanhart C. Scattering lengths of strangeness S=-2 baryon-baryon interactions. *Phys Rev*. (2012) **C85**:015204. doi: 10.1103/PhysRevC.85.015204
181. Ohnishi A, Morita K, Miyahara K, Hyodo T. Hadron? Hadron correlation and interaction from heavy? Ion collisions. *Nucl Phys*. (2016) **A954**:294–307. doi: 10.1016/j.nuclphysa.2016.05.010
182. Nakazawa K, Endo Y, Fukunaga S, Hoshino K, Hwang SH, Imai K, et al. The first evidence of a deeply bound state of Xi--14N system. *Prog Theor Exp Phys*. (2015) **2015**:033D02. doi: 10.1093/ptep/ptv008
183. Gal A, Hungerford EV, Millener DJ. Strangeness in nuclear physics. *Rev Mod Phys*. (2016) **88**:035004. doi: 10.1103/RevModPhys.88.035004
184. Millener DJ, Dover CB, Gal A. Lambda-nucleus single-particle potentials. *Phys Rev C*. (1988) **38**:2700–8. doi: 10.1103/PhysRevC.38.2700
185. Yamamoto Y, Bandō H, Zofka J. On the Lambda-hypernuclear single particle energies. *Prog Theor Phys*. (1988) **80**:757–61. doi: 10.1143/PTP.80.757
186. Ajimura S, Hayakawa H, Kishimoto T, Kohri H, Matsuoka K, Minami S, et al. Observation of spin-orbit splitting in lambda single-particle states. *Phys Rev Lett*. (2001) **86**:4255–8. doi: 10.1103/PhysRevLett.86.4255
187. Akikawa H, Ajimura S, Chrien RE, Eugenio PM, Franklin GB, Franz J, et al. Hypernuclear fine structure in (Lambda*)Be-9. *Phys Rev Lett*. (2002) **88**:082501. doi: 10.1103/PhysRevLett.88.082501
188. Friedman E, Gal A. In-medium nuclear interactions of low-energy hadrons. *Phys Rep*. (2007) **452**:89–153. doi: 10.1016/j.physrep.2007.08.002
189. Baldo M. *Nuclear Methods and the Nuclear Equation of State, Vol. 8 of International Review of Nuclear Physics*. World Scientific Publishing Co. Pte. Ltd. (1999). Available online at: http://ebooks.worldscinet.com/ISBN/9789812817501/9789812817501.html
190. Fetter AL, Walecka JD. *Quantum Theory of Many-Particle Systems*. Dover Books on Physics. New York, NY: Dover Publications (2003).
191. Bethe HA, Brandow BH, Petschek AG. Reference spectrum method for nuclear matter. *Phys Rev*. (1963) **129**:225–64. doi: 10.1103/PhysRev.129.225
192. Song HQ, Baldo M, Giansiracusa G, Lombardo U. Bethe-Brueckner-goldstone expansion in nuclear matter. *Phys Rev Lett*. (1998) **81**:1584–7. doi: 10.1103/PhysRevLett.81.1584
193. Gal A. Strangeness nuclear physics - 2010. *Prog Theor Phys Suppl*. (2010) **186**:270–81. doi: 10.1143/PTPS.186.270
194. Botta E, Bressani T, Garbarino G. Strangeness nuclear physics: a critical review on selected topics. *Eur Phys J A*. (2012) **48**:41. doi: 10.1140/epja/i2012-12041-6
195. Dover CB, Millener DJ, Gal A. On the production and spectroscopy of Sigma hypernuclei. *Phys Rep*. (1989) **184**:1–97. doi: 10.1016/0370-1573(89)90105-1
196. Dabrowski J. Isospin dependence of the single-particle potential of the Sigma hyperon in nuclear matter. *Phys Rev C*. (1999) **60**:025205. doi: 10.1103/PhysRevC.60.025205
197. Kohno M. Xi hyperons in the nuclear medium described by chiral NLO interactions. *Phys Rev C*. (2019) **100**:024313. doi: 10.1103/PhysRevC.100.024313
198. Haidenbauer J, Vidana I. Structure of single-Λ hypernuclei with chiral hyperon-nucleon potentials. *arXiv: 1910.02695* (2019). doi: 10.1140/epja/s10050-020-00055-6
199. Vidaña I. Single-particle spectral function of the Λ hyperon in finite nuclei. *Nucl Phys*. (2017) **A958**:48–70. doi: 10.1016/j.nuclphysa.2016.11.002
200. Nogga A. Charge-symmetry breaking in light hypernuclei based on chiral and similarity renormalization group-evolved interactions. *AIP Conf Proc*. (2019) **2130**:030004. doi: 10.1063/1.5118394
201. Le H, Haidenbauer J, Meißner U-G, Nogga A. Implications of an increased Λ-separation energy of the hypertriton. *Phys LettB*. (2020) **801**:135189. doi: 10.1016/j.physletb.2019.135189
202. Haidenbauer J, Meißner UG, Nogga A, Polinder H. The hyperon-nucleon interaction: conventional versus effective field theory approach. *Lect Notes Phys*. (2007) **724**:113–40. doi: 10.1007/978-3-540-72039-3_4
203. Gerstung D, Kaiser N, Weise W. Hyperon-nucleon three-body forces and strangeness in neutron stars. *arXiv: 2001.10563*. (2020).
204. Yamamoto Y, Nishizaki S, Takatsuka T. Single-particle potentials and effective masses of hyperons in hyperonic nuclear systems. *Prog Theor Phys*. (2000) **103**:981–1000. doi: 10.1143/PTP.103.981

Conflict of Interest: SP is employed by the company TNG Technology Consulting GmbH.

The remaining authors declare that the research was conducted in the absence of any commercial or financial relationships that could be construed as a potential conflict of interest.

Copyright © 2020 Petschauer, Haidenbauer, Kaiser, Meißner and Weise. This is an open-access article distributed under the terms of the Creative Commons Attribution License (CC BY). The use, distribution or reproduction in other forums is permitted, provided the original author(s) and the copyright owner(s) are credited and that the original publication in this journal is cited, in accordance with accepted academic practice. No use, distribution or reproduction is permitted which does not comply with these terms.

frontiers in Physics

REVIEW
published: 21 July 2020
doi: 10.3389/fphy.2020.00218

Parity- and Time-Reversal-Violating Nuclear Forces

Jordy de Vries[1,2], *Evgeny Epelbaum*[3], *Luca Girlanda*[4,5], *Alex Gnech*[6], *Emanuele Mereghetti*[7] *and Michele Viviani*[8]*

[1] Amherst Center for Fundamental Interactions, Department of Physics, University of Massachusetts, Amherst, MA, United States, [2] RIKEN BNL Research Center, Brookhaven National Laboratory, Upton, New York, NY, United States, [3] Institut für Theoretische Physik II, Fakultät für Physik und Astronomie, Ruhr-Universität Bochum, Bochum, Germany, [4] Department of Mathematics and Physics, University of Salento, Lecce, Italy, [5] Istituto Nazionale di Fisica Nucleare (INFN), Sezione di Lecce, Lecce, Italy, [6] Gran Sasso Science Institute, L'Aquila, Italy, [7] Theoretical Division, Los Alamos National Laboratory, Los Alamos, NM, United States, [8] Istituto Nazionale di Fisica Nucleare, Sezione di Pisa, Pisa, Italy

Parity-violating and time-reversal conserving (PVTC) and parity-violating and time-reversal-violating (PVTV) forces in nuclei form only a tiny component of the total interaction between nucleons. The study of these tiny forces can nevertheless be of extreme interest because they allow one to obtain information on fundamental symmetries using nuclear systems. The PVTC interaction derives from the weak interaction between the quarks inside nucleons and nuclei, therefore the study of PVTC effects opens a window on the quark-quark weak interaction. The PVTV interaction is sensitive to more exotic interactions at the fundamental level, in particular to strong CP violation in the Standard Model Lagrangian, or even to exotic phenomena predicted in various beyond-the-Standard-Model scenarios. The presence of these interactions can be revealed either by studying various asymmetries in polarized scattering of nuclear systems, or by measuring the presence of non-vanishing permanent electric dipole moments of nucleons, nuclei and diamagnetic atoms and molecules. In this contribution, we review the derivation of the nuclear PVTC and PVTV interactions within various frameworks. We focus in particular on the application of chiral effective field theory, which allows for a more strict connection with the fundamental interactions at the quark level. We investigate PVTC and PVTV effects induced by these potentials on several few-nucleon observables, such as the longitudinal asymmetries in proton-proton scattering and the $^3\mathrm{He}(\vec{n},p)^3\mathrm{H}$ reaction, the radiative neutron-proton capture, and the electric dipole moments of the deuteron and the trinucleon system.

Keywords: fundamental symmetries in nuclei, nuclear forces, effective field theory, chiral perturbation theory, few-body systems

OPEN ACCESS

Edited by:
Nunzio Itaco,
University of Campania Luigi Vanvitelli, Italy

Reviewed by:
Barry R. Holstein,
University of Massachusetts Amherst, United States
Rimantas Lazauskas,
UMR7178 Institut Pluridisciplinaire Hubert Curien (IPHC), France

***Correspondence:**
Michele Viviani
michele.viviani@pi.infn.it

Specialty section:
This article was submitted to Nuclear Physics, a section of the journal Frontiers in Physics

Received: *21 January 2020*
Accepted: *22 May 2020*
Published: *21 July 2020*

Citation:
de Vries J, Epelbaum E, Girlanda L, Gnech A, Mereghetti E and Viviani M (2020) Parity- and Time-Reversal-Violating Nuclear Forces. Front. Phys. 8:218. doi: 10.3389/fphy.2020.00218

1. INTRODUCTION

The interaction between nucleons is at the heart of nuclear physics and has been a subject of great scientific interest for many decades. The strong nuclear forces have their origin in the residual interaction between quarks and gluons inside colorless nucleons and are described by quantum chromodynamics (QCD). The resulting parity-conserving, time-reversal-conserving (PCTC) nuclear interactions are known to exhibit a complicated pattern, involving a delicate interplay of strongly state-dependent repulsive and attractive pieces. While the nucleon-nucleon

(NN) scattering data below the pion production threshold can nowadays be accurately described by modern NN potentials, the (weaker) three-nucleon (3N) forces and the electromagnetic interactions (EM) between the nucleons, known to play an important role in the nuclear structure and dynamics, are not so well-understood and represent a subject of active research. The current status of PCTC nuclear forces is reviewed in other contributions to this topical issue.

In addition to the bulk PCTC interactions mentioned above, nuclear forces also feature much tinier components, which originate from the weak forces between quarks and/or physics beyond the standard model (BSM) and whose strength is smaller than that of the strong and EM interactions by many orders of magnitude. These tiny components are, nevertheless, extremely interesting since investigation of their effects may shed new light on fundamental symmetries and BSM physics. While effects of such exotic PCTC components are, of course, completely overwhelmed by the strong and EM nuclear forces, parity- (P) violating and/or time-reversal- (T) violating nuclear interactions can be determined by measuring specific observables which would vanish if these symmetries were conserved. In this contribution, we review the theory of parity-violating, time-reversal-conserving (PVTC) and parity-violating, time-reversal-violating (PVTV) nuclear forces and discuss selected applications.

Starting from 1950s, a wide variety of phenomenological models have been developed to describe nuclear forces, the most prominent utilizing the one-boson exchange picture, see Machleidt [1] and references therein. More recently, the development of chiral effective field theory (χEFT) [2] has given a new impetus to the derivation of nuclear interactions [3–5]. The χEFT approach utilizes the spontaneously broken approximate $SU(2)_L \times SU(2)_R$ chiral symmetry of QCD[1] in order to describe the low-energy dynamics of pions, the (pseudo-) Goldstone bosons of the spontaneously broken axial generators, in a systematic and model-independent fashion within the framework of the effective chiral Lagrangian [6–11], see [12–14] for review articles. Owing to the derivative nature of the Goldstone boson interactions, the scattering amplitude in the pion- and single-baryon sectors can be calculated via a perturbative expansion in powers of Q/Λ_χ, where Q refers to momenta of the order of the pion mass m_π and $\Lambda_\chi \sim m_\rho \sim 1$ GeV denotes the chiral symmetry breaking scale, with m_ρ the ρ-meson mass. The effective Lagrangian involves (an infinite number of) all possible hadronic interactions compatible with the symmetries of QCD, which are naturally organized according to the number of derivatives and/or quark or pion mass insertions[2]. Every term in the effective Lagrangian is multiplied by a coefficient, whose strength is not fixed by the symmetry. These so-called low-energy constants (LECs) can be determined by fits to experimental data and/or obtained from lattice QCD simulations, see [13, 14] and references therein. At every order in the Q/Λ_χ-expansion, only a finite number of terms from the effective Lagrangian contributes to the scattering amplitude. The resulting framework, commonly referred to as chiral perturbation theory (χPT), is nowadays widely applied to analyze low-energy processes in the Goldstone boson and single-nucleon sectors. It has also been generalized to study few- and many-nucleon systems, where certain resummations beyond perturbation theory are necessary in order to dynamically generate the ultrasoft scale associated with nuclear binding. According to Weinberg [2], the breakdown of the perturbative expansion for the NN scattering amplitude is traced back to enhanced contributions of ladder diagrams, i.e., Feynman diagrams that become infrared divergent in the static limit of infinitely heavy nucleons. The simplest and natural way to resum enhanced ladder diagrams is provided by solving the nuclear Schrödinger equation. The framework therefore essentially reduces to the conventional quantum mechanical A-body problem. The corresponding nuclear forces and current operators are defined in terms of non-iterative parts of the scattering amplitude, which are free from the above mentioned enhancement. They can be derived from the effective chiral Lagrangian in a systematically improvable way via a perturbative expansion in powers of Q/Λ_χ [4, 5]. Assuming the scaling of few-nucleon contact operators according to naive dimensional analysis[3], the PCTC interactions are dominated by the pairwise NN force, which receives its dominant contribution at order $(Q/\Lambda_\chi)^\nu$ with $\nu = 0$, defined to be the leading order (LO). Parity conservation forbids the appearance of nuclear forces at order $\nu = 1$, so that the next-to-leading order (NLO) contribution to the PCTC NN potential appears at order $\nu = 2$. Next-to-next-to-leading order (N^2LO) has $\nu = 3$ and so on. PCTC three- and four-nucleon forces are suppressed and start contributing at orders $\nu = 3$ (N^2LO) and $\nu = 4$ (N^3LO), respectively. Presently, the chiral expansion of the PCTC NN force has been pushed to order $\nu = 5$ (N^4LO) [16–19], while many-nucleon interactions have been worked out up through N^3LO, see [4, 5] and references therein. We further emphasize that a number of alternative formulations of χEFT for nuclear systems have been proposed [20–25], see also [26–31] for a related discussion.

Another framework to analyze nuclear systems at very low energies is based on the so-called pionless formulation of EFT, see [31–33] for review articles. It is valid at momenta well below the pion mass, at which the pionic degrees of freedom can be integrated out. In the resulting picture, nucleons interact with each other solely through short-range contact two- and many-body forces. This formulation is considerably simpler than χEFT both at the conceptual and practical levels, and has been successfully applied to study e.g., Efimov physics and universality in few-body systems near the unitary limit, low-energy properties

[1] Here and in what follows, we restrict ourselves to the two-flavor case of the light up and down quarks unless specified otherwise.

[2] In the isospin limit, the quark and pion masses are related to each other via $m_\pi^2 = 2Bm_q + \mathcal{O}(m_q^2)$, where B is a constant proportional to the quark condensate $\langle 0|\bar{u}u|0\rangle = \langle 0|\bar{d}d|0\rangle$.

[3] Notice that for systems near the unitary limit corresponding to the infinitely large scattering length (such as e.g., the NN systems in the S-waves), the scattering amplitude exhibits a certain amount of fine tuning beyond naive dimensional analysis. The expansion of the scattering amplitude does, therefore, not necessarily coincide with the expansion of nuclear potentials [15].

of halo-nuclei and reactions of astrophysical relevance, see [31–33] and references therein.

In this paper we focus on the PVTC and PVTV interactions in the frameworks of χEFT and pionless EFT. We also outline various meson-exchange models frequently adopted to analyze the results for some PVTC and PVTV observables. In the subsections below, we briefly discuss the origin of the PVTC and PVTV interactions and summarize the current experimental and theoretical status of research along these lines.

1.1. The PVTC Interaction

The PVTC component of the nuclear force is governed by the weak interaction between the quarks inside the nucleons (and pions). Studying such effects, therefore, opens a window on the so-called "pure" hadronic weak interaction (HWI) [34–38]. This part of the weak interaction is far less known experimentally.

A number of experiments aimed at studying PVTC in low-energy processes involving few-nucleon systems have been completed/are being planned at cold-neutron facilities, such as the Los Alamos Neutron Science Center (LANSCE), the National Institute of Standards and Technology (NIST) Center for Neutron Research, the Spallation Neutron Source (SNS) at Oak Ridge National Laboratory, and the European Spallation Source (ESS) in Lund. The primary objective of this experimental program is to determine the LECs which appear in the PVTC nuclear potentials. For a recent review of the current status of experiments along this line and the impact of anticipated results, see ([39]).

PVTC nuclear forces have already been analyzed in the framework of χEFT [40–42]. The LO PVTC NN force is driven by the one-pion-exchange term with $\nu = -1$, while the NLO terms with $\nu = 1$ emerge from two-pion-exchange diagrams and NN contact interactions[4]. In Girlanda [44], it was shown that the PVTC NN potential involves only five independent contact operators at this order corresponding to five S-P transition amplitudes at low energies [45]. Including the PVTC pion-nucleon coupling constant h_π^1, the NN potential at NLO thus contains six LECs which need to be determined from experimental data. At N^{2}LO one has to take into account five additional LECs, which determine the strength of the subleading PVTC pion-nucleon interactions [46].

In pionless EFT, the LO PVTC NN potential is completely described in terms of the already mentioned five contact terms [36, 47]. The large-N_c scaling of PVTC NN contact interactions was analyzed in Phillips et al. [48] and Schindler et al. [47]. These studies suggest that three out of five PVTC contact interactions are suppressed by a factor of $(1/N_c)^2$ or by the factor $(1/N_c)\sin^2\theta_W \approx 0.08$, see also a related discussion in Vanasse [49]. If the large-N_c scaling persists to the physically relevant case of $N_c = 3$, the pionless potential at LO should be dominated by only 2 LECs [39]. Unfortunately, the currently available experimental data do not allow one to draw definitive conclusions on whether the suggested large-N_c hierarchy of PVTC contact interactions is indeed realized in Nature.

[4]Notice that PVTC hadronic interactions involve a typical suppression factor of $\sim G_F M_\pi^2 \sim 10^{-7}$ as compared to PCTC vertices [43].

Regarding the various meson-exchange models developed to describe the PVTC interaction, we will mainly discuss the model proposed by Desplanques, Donoghue, and Holstein (DDH) [50] which includes pion and vector-meson exchanges with seven unknown meson-nucleon PVTC coupling constants.

1.2. The PVTV Interaction

PVTV nuclear forces originate from more exotic sources at the fundamental level, which include the so-called θ-term in the Standard Model (SM) Lagrangian [51], or even BSM interactions [52]. Due to the CPT theorem, any PVTV interaction also violates the CP symmetry, where C refers to charge conjugation. CP violation is a key ingredient for the dynamical generation of a matter-antimatter asymmetry in the Universe [53]. The SM with three generations of quarks has a natural source of CP-violation in the phase of the Cabibbo-Kobayashi-Maskawa (CKM) quark mixing matrix. This mechanism is however not sufficient to explain the observed asymmetry [54].

The phase of the CKM matrix also does not contribute sizably to the nuclear PVTV interaction. For example, let us consider the electric dipole moment (EDM) of a system of particles. A non-zero permanent EDM of a particle or a system of particles necessarily involves the breaking of both parity and time-reflection symmetries. EDMs of the electron, nucleons and nuclei are mostly sensitive to P- and T-violating flavor-diagonal interactions. To induce a non-zero EDM, on the other hand, the phase of the CKM requires contributions from all three generations of quarks, including heavy quarks, leading to a large suppression [52, 55–57]. For example, the expected size of the nucleon EDM based on the CKM mechanism in the SM is $|d_N^{\rm CKM}| \sim 10^{-18}$ e fm [58, 59]. Therefore, any observed permanent EDM of an atomic or nuclear system larger in magnitude than the expected size within the SM would highlight PVTV effects beyond the CKM mixing matrix. The present experimental upper bounds on the EDMs of neutron and proton are $|d_n| < 1.2 \cdot 10^{-13}$ e fm [60, 61] and $|d_p| < 2.0 \cdot 10^{-12}$ e fm, where the proton EDM has been inferred from a measurement of the diamagnetic ^{199}Hg atom [62] using a calculation of the nuclear Schiff moment [63]. For the electron, the most recent upper bound is $|d_e| < 1.1 \cdot 10^{-16}$ e fm [64], derived from the EDM of the ThO molecule. In all cases, the current experimental sensitivities are orders of magnitude away from the CKM predictions.

χEFT allows one to derive PVTV nuclear forces in a systematic and model independent way. To this aim, the PCTC effective chiral Lagrangian has to be extended to include all possible PVTV terms classified according to their chiral dimension. Some of these terms are induced, at the microscopic level, by the SM mechanisms discussed above. The effective chiral Lagrangian induced by the θ-term is discussed in Mereghetti et al. [65] and Bsaisou et al. [66]. BSM theories such as supersymmetry, multi-Higgs scenarios, left-right symmetric models, etc. would give rise to additional PVTV sources of dimension six (and higher) in the quark-gluon Lagrangian [67]. The χEFT Lagrangians originating from these sources were derived in de Vries et al. [68] and Bsaisou et al. [69]. Various

terms in the resulting effective chiral Lagrangian possess different scaling with respect to the underlying microscopic PVTV sources. χEFT can thus be used to establish relations between the fundamental PVTV mechanisms and specific terms in the nuclear potentials and, accordingly, specific patterns in the corresponding nuclear observables [65, 68, 69]. In principle, this offers the possibility of identifying the fundamental sources of time-reversal violation and to shed light on some of the BSM scenarios, provided the corresponding LECs in the effective Lagrangian can be determined from Lattice QCD calculations or experimental data [70, 71].

In the framework of χEFT, the PVTV NN potential was derived up to N^{2}LO including one- and two-pion exchange contributions and the corresponding contact interactions [72, 73]. Subsequent works showed the presence in the PVTV Lagrangian of a three-pion term [68], which was for the first time included in the calculations in Bsaisou et al. [66]. This term also generates a PVTV 3N force at NLO, which contributes to the ^{3}H and ^{3}He EDM. The calculation reported in Bsaisou et al. [66] was also the first one carried out using solely the interactions derived in χEFT. More precisely, the PVTV potential at NLO was used in combination with the N^{2}LO PCTC potentials from Epelbaum et al. [74]. Finally, in Gnech and Viviani [75], the EDMs of deuteron and trinucleons were studied using the χEFT PVTV potential up to N^{2}LO along with the N^{4}LO PCTC potential of Entem et al. [18]. In this paper, it was also shown that the N^{2}LO contribution to the PVTV 3N force generated by the three-pion interaction vanishes. The LO χEFT PVTV potential has also been applied in combination with many-body methods to calculate Schiff moments of heavy nuclei [76].

Currently, no direct limits on EDMs of light nuclei have been established. However, experiments are planned to measure the EDM of protons and light nuclei in dedicated storage rings [77–82]. This new approach could reach a precision of $\sim 10^{-16}$ e fm, although this goal has to be established in practice. If successful, these experiments would lead to a great improvement in the hadronic sector of EDM searches. A measurement of a non-vanishing EDM of this magnitude would provide evidence of a PVTV source beyond the CKM mechanism. However, a single measurement would be insufficient to identify the specific source of PVTV. For this reason, experiments with various light nuclei such as ^{2}H, ^{3}H and ^{3}He are planned. Such measurements would provide the complementary information needed to impose constraints on PVTV sources at the fundamental level.

A brief discussion of the PVTV potentials derived in the framework of the one-meson exchange model and in the pionless EFT approach will also be reported in this review.

1.3. Outline of the Article

Our paper is organized as follow. In section 2, we discuss the origins of PVTC and PVTV interactions at the fundamental level and list the relevant terms in the quark-gluon Lagrangian. In section 3, we give the corresponding terms in the effective chiral Lagrangian and discuss the derivation of the PVTC and PVTV potentials in χEFT. In section 4, we specifically focus on the contact few-nucleon interactions which enter the potentials in both the chiral and pionless EFT formulations. We also discuss the expected hierarchy of the corresponding LECs as suggested by the large-N_c analysis. Next, in section 5, the various meson-exchange models developed to describe the PVTC and PVTV interactions will be summarized. Then, in section 6, we report on a selected set of results for PVTC and PVTV observables in light nuclei up to $A = 4$. Finally, the main conclusions of this paper and future perspectives are summarized in section 7.

2. PARITY VIOLATION AND TIME-REVERSAL VIOLATION AT THE MICROSCOPIC LEVEL

Parity is violated in the SM of particle physics because of the different gauge interactions of left- and right-handed fermion fields. Only left-handed particles interact via $SU(2)_L$ gauge interactions such that this part of the SM violates parity maximally. The remaining color and electromagnetic interactions conserve parity modulo the QCD vacuum angle which is discussed below. Parity violation was first observed in semileptonic charged current interactions in 1957 [83]. Twenty years later, in the late '70s, PVTC was observed in neutral current electron-nucleus scattering [84], providing a strong confirmation of the SM. Subsequent PVTC electron scattering experiments have quantitatively confirmed the SM picture [85]. In addition to PVTC in β decays and semileptonic neutral current processes, the SM predicts PVTC in weak interactions between quarks. At energies smaller than the masses of the W and Z bosons, such interactions can be represented by four-fermion operators. Just below the electroweak (EW) scale, and limiting ourselves to the lightest u and d quarks, the four-fermion Lagrangian is

$$\begin{aligned}\mathcal{L}_W = &-\frac{G_F}{\sqrt{2}}\left\{\left(1-\frac{2}{3}s_w^2\right)\bar{q}_L\gamma^\mu\tau_a q_L\,\bar{q}_L\gamma_\mu\tau_a q_L\right.\\ &-\frac{2s_w^2}{3}\bar{q}_L\gamma^\mu\tau_3 q_L\,(\bar{q}_L\gamma_\mu q_L+\bar{q}_R\gamma_\mu q_R)\\ &-2s_w^2\big(\bar{q}_L\gamma^\mu\tau_3 q_L\,\bar{q}_L\gamma_\mu\tau_3 q_L\\ &\left.-\frac{1}{3}\bar{q}_L\gamma^\mu\tau_a q_L\,\bar{q}_L\gamma_\mu\tau_a q_L\right)+\ldots\Big\}\,, \end{aligned} \tag{1}$$

where G_F is the Fermi coupling constant and $s_w^2 \equiv \sin^2\theta_W \simeq 0.231$, with θ_W the Weinberg mixing angle. q_L and q_R denote the left-handed and right-handed doublets $q_L^T = (u_L, d_L)$ and $q_R^T = (u_R, d_R)$, and the dots denote terms that conserve parity[5]. Equation (1) was obtained assuming the CKM matrix to be the identity, that is $V_{ud} = 1$. The three operators in Equation (1) all break parity, but have different transformation properties under chiral symmetry and isospin. We note that the isovector and isotensor terms (the second and third operators) given in Equation (1) are suppressed by a factor s_w^2 with respect to the isoscalar one.

The operators in Equation (1) need to be evolved using the renormalization group equations (RGE) from the EW scale down to the QCD scale, and in this process they mix with

[5]Here u and d denote the u- and d-quark Dirac fields, respectively. Moreover $u_{R,L} = \frac{1\pm\gamma^5}{2}u$, etc.

additional PVTC operators [86]. After the RGE evolution, the PVTC Lagrangian assumes the form

$$\begin{aligned}\mathcal{L}^{\rm SM}_{\rm PVTC} = -\frac{G_F}{\sqrt{2}}\Big\{ & C_1^{\rm SM}\,\bar{q}_L\gamma^\mu\tau_a q_L\,\bar{q}_L\gamma_\mu\tau_a q_L \\ & + C_2^{\rm SM}\,\bar{q}_L\gamma^\mu q_L\,\bar{q}_L\gamma_\mu q_L + C_3^{\rm SM}\,\bar{q}_L\gamma^\mu\tau_3 q_L\,\bar{q}_L\gamma_\mu q_L \\ & + C_4^{\rm SM}\left(\bar{q}_L\gamma^\mu\tau_3 q_L\,\bar{q}_R\gamma_\mu q_R - \bar{q}_L\gamma^\mu q_L\,\bar{q}_R\gamma_\mu\tau_3 q_R\right) \\ & + C_5^{\rm SM}\left(\bar{q}_L^\alpha\gamma^\mu\tau_3 q_L^\beta\,\bar{q}_R^\beta\gamma_\mu q_R^\alpha - \bar{q}_L^\alpha\gamma^\mu q_L^\beta\,\bar{q}_R^\beta\gamma_\mu\tau_3 q_R^\alpha\right) \\ & + C_6^{\rm SM}\left(\bar{q}_L\gamma^\mu\tau_3 q_L\,\bar{q}_L\gamma_\mu\tau_3 q_L - \frac{1}{3}\bar{q}_L\gamma^\mu\tau_a q_L\,\bar{q}_L\gamma_\mu\tau_a q_L\right) \\ & - (L\leftrightarrow R)\Big\}\,, \end{aligned} \tag{2}$$

where in the SM, the coefficients $C_i^{\rm SM}$ are known functions of SM parameters as s_w, the strong coupling constant g_s, etc. Greek indices α and β appearing as superscripts in some of the quark fields in Equation (2) specify color indices. They are only shown for cases where the color contractions are not obvious. Notice that the QCD evolution does not remedy the s_w^2 suppression of the isospin-one and -two operators [86]. BSM physics that arises at scales well above the EW can be represented at the EW scale via gauge-invariant higher-dimensional operators [67, 87]. This framework is usually called the SM Effective Field Theory (SM-EFT). SM-EFT operators can induce new PVTC couplings of the W and Z bosons to left- and right-handed quarks, and new PVTC four-fermion operators. After evolving the effective operators from the EW to the QCD scale, the net effect of BSM PVTC SM-EFT operators is to modify the coefficients $C_i^{\rm SM}$ in Equation (2) with respect to their SM values, namely in Equation (2) one substitutes $C_i^{\rm SM} \to C_i^{\rm SM+BSM}$. We have focused so far on operators involving only the u and d quarks. Flavor-conserving ($\Delta F = 0$) operators involving the s quark can also generate interesting contributions to hadronic P violation [86, 88], such as contributions to isospin-one operators that are not suppressed by s_w^2.

While P and C are maximally broken by the $V-A$ structure of the SM, the breaking of CP is much more delicate. In the SM with three generations of quarks, CP is broken by the phase of the CKM matrix, which explains all the observed CP violation in the kaon [89–91], and B meson systems [92, 93]. Theoretical uncertainties are at the moment too large to definitively conclude whether the recently discovered CP violation in D decays [94] is compatible with the SM. The phase of CKM gives, on the other hand, unobservable contributions to flavor-diagonal CP violation, in particular to the neutron [55, 59, 95] and electron EDMs [96–98].

The second source of CP violation in the SM is the QCD θ term [51, 99, 100]

$$\mathcal{L}^{\theta}_{PVTV} = -\theta\frac{g_s^2}{64\pi^2}\varepsilon^{\mu\nu\alpha\beta}\,G^a_{\mu\nu}G^a_{\alpha\beta}\,, \tag{3}$$

where g_s is the strong coupling constant and $G^a_{\mu\nu}$ the gluon field tensors (a is a color index). The θ term is a total derivative, but it contributes to physical processes through extended, spacetime-dependent field configurations known as instantons. CP violation from the QCD θ term is intimately related to the quark masses. All phases of the quark mass matrix can be eliminated through non-anomalous $SU(2)$ vector and axial rotations, except for a common phase ρ. The mass plus QCD θ terms which are left are

$$\mathcal{L}^{\rm mass+\theta}_{PVTV} = -\left(e^{i\rho}\bar{q}_L\mathcal{M}q_R + e^{-i\rho}\,\bar{q}_R\mathcal{M}q_L\right) - \theta\frac{g_s^2}{64\pi^2}\varepsilon^{\mu\nu\alpha\beta}\,G^a_{\mu\nu}G^a_{\alpha\beta}\,, \tag{4}$$

where $\mathcal{M} = \mathrm{diag}(m_u, m_d)$. The parameters ρ and θ are not independent. In χEFT, it is convenient to rotate $\mathcal{L}^{\rm mass+\theta}_{PVTV}$ into a complex mass term with an anomalous $U(1)_A$ rotation, obtaining, after vacuum alignment [101],

$$\mathcal{L}^{\rm mass+\theta}_{PVTV} = m_*\bar{\theta}\,\bar{q}i\gamma_5 q\,, \tag{5}$$

where

$$\bar{\theta} = \theta + n_f\rho\,, \qquad m_* = \frac{m_u m_d}{m_u+m_d} = \frac{\bar{m}(1-\epsilon^2)}{2}\,. \tag{6}$$

$n_f = 2$ is the number of light flavors, and the combinations of light quarks masses $\bar{m}$ and ϵ are $2\bar{m} = m_u + m_d$, $\epsilon = (m_d - m_u)/(m_d+m_u)$. Equations (5) and (6) can be easily generalized to include strangeness. $\bar{\theta}$ is a free parameter in the QCD Lagrangian, and one would expect $\bar{\theta} = \mathcal{O}(1)$. This would however lead to a large neutron EDM $|d_n| \sim 10^{-3}\bar{\theta}$ e fm [102, 103], ten orders of magnitude larger than the current limits, $d_n < 3.0\cdot 10^{-13}$ e fm [61]. Therefore $\bar{\theta} \lesssim 10^{-10}$, which represents the so-called strong CP problem.

The phase of the CKM matrix and the QCD $\bar{\theta}$ term are the only CP-violating parameters in the SM Lagrangian. They are however not sufficient to explain the observed matter-antimatter asymmetry of the Universe [104–107], and it is therefore natural to think about CP-violating sources induced by BSM physics. The low-energy CP-violating operators relevant for EDMs have been cataloged in several works (e.g., [52, 108–110]). de Vries et al. [68] considered all the low-energy operators that are induced by SM-EFT operators at tree level, retaining the two lightest quarks. Generalization to three flavors are given, for example, in Jenkins et al. [111] and Mereghetti [112]. The most relevant $SU(3)_c\times U(1)_{\rm em}$-invariant purely hadronic operators induced by dimension-six SM-EFT operators are

$$\begin{aligned}\mathcal{L}^{\rm 6,hadr}_{PVTV} = & \frac{g_s\tilde{C}_G}{6v^2}f^{abc}\epsilon^{\mu\nu\alpha\beta}G^a_{\alpha\beta}G^b_{\mu\rho}G^{c\,\rho}_{\nu} \\ & - \frac{1}{2v^2}\left(\bar{q}\left[d_E\right]i\sigma^{\mu\nu}\gamma_5 q\; eF_{\mu\nu} + \bar{q}[d_{CE}]i\sigma^{\mu\nu}\; g_sG_{\mu\nu}\gamma_5 q\right) \\ & - \frac{4G_F}{\sqrt{2}}\Big\{\Sigma_1^{(ud)}(\bar{d}_L u_R\bar{u}_L d_R - \bar{u}_L u_R\bar{d}_L d_R) \\ & \qquad + \Sigma_2^{(ud)}(\bar{d}_L^\alpha u_R^\beta\,\bar{u}_L^\beta d_R^\alpha - \bar{u}_L^\alpha u_R^\beta\,\bar{d}_L^\beta d_R^\alpha)\Big\} \\ & - \frac{4G_F}{\sqrt{2}}\left\{\Xi_1^{(ud)}\,\bar{d}_L\gamma^\mu u_L\,\bar{u}_R\gamma_\mu d_R + \Xi_2^{(ud)}\,\bar{d}_L^\alpha\gamma^\mu u_L^\beta\,\bar{u}_R^\beta\gamma_\mu d_R^\alpha\right\}, \end{aligned} \tag{7}$$

where f^{abc} are the structure constants of the Lie algebra of the color $SU(3)$ group, $[d_E]$ and $[d_{CE}]$ are matrices in flavor space,

$[d_E] = \mathrm{diag}(m_u\tilde{c}_\gamma^{(u)}, m_d\tilde{c}_\gamma^{(d)})$ and $[d_{CE}] = \mathrm{diag}(m_u\tilde{c}_g^{(u)}, m_d\tilde{c}_g^{(d)})$. The coefficients $\tilde{C}_G$, $\tilde{c}_{\gamma,g}^{(q)}$, $\Sigma_{1,2}^{(ud)}$ and $\Xi_{1,2}^{(ud)}$ are dimensionless and scale as $(v/\Lambda_X)^2$, where $v = 246$ GeV is the Higgs vacuum expectation value, and Λ_X is the scale of new physics. The Weinberg three-gluon, the quark EDM (qEDM), and the chromo-EDM (qCEDM) operators (the first, second, and third term given in Equation (7), respectively) have received the most attention in the literature [52, 113]. They can be written directly in terms of $SU(3)_c \times SU(2)_L \times U(1)_Y$-invariant operators at the EW scale, and receive corrections by a variety of CP-violating operators in the SM-EFT, involving heavy SM fields. The four-quark operators, given in the third and fourth lines of (7), can also be expressed in terms of gauge-invariant operators at the EW scale, and they arise, for example, in leptoquark models, see [114, 115]. The four-quark operators, given in the last line of Equation (7), are on the other hand induced by right-handed couplings of quarks to the W boson [68, 116], and are generated, for example, in left-right symmetric models.

While all operators in Equations (5) and (7) violate P and CP symmetry, they transform differently under isospin and chiral rotations. As such, the operators induce different χEFT Lagrangians at lower energies, and different hierarchies of CP-violating hadronic and nuclear observables such as EDMs or scattering observables.

3. PVTC AND PVTV CHIRAL POTENTIALS

In this section, we discuss the derivation of the PVTC and PVTV NN and 3N potentials within the framework of χEFT. In the first and second subsections we briefly review the properties of the PVTC and PVTV chiral Lagrangians. In section 3.3, we present briefly two methods used to derive the potentials starting from a Lagrangian. Finally, in the last two subsections, we present the PVTC and PVTV chiral potentials, respectively.

In order to discuss hadronic observables such as nuclear EDMs or PVTC asymmetries in pp scattering, the quark-level PVTC and PVTV Lagrangians of Equations (2) and (7) need to be matched onto nuclear EFTs, such as chiral EFT and pionless EFT. Due to the non-perturbative nature of QCD at low energy, this matching cannot be done in perturbation theory. Nevertheless, the approximate chiral and isospin symmetries of the QCD Lagrangian provide an organizing principle for low-energy interactions, see [12–14] for review articles.

Let us first introduce the nucleon and pion fields. The (relativistic) nucleon field $N(x)$ is considered to be an isospin doublet

$$N(x) = \begin{pmatrix} p(x) \\ n(x) \end{pmatrix}, \tag{8}$$

where $p(x)$ ($n(x)$) is the proton (neutron) field. The pion fields are given in "Cartesian" coordinates π_a, $a = 1, 2, 3$, where

$$\pi_1(x) = \frac{\pi^{(+)}(x) + \pi^{(-)}(x)}{\sqrt{2}}, \quad \pi_2(x) = \frac{i\left(\pi^{(+)}(x) - \pi^{(-)}(x)\right)}{\sqrt{2}},$$
$$\pi_3(x) = \pi^{(0)}(x), \tag{9}$$

$\pi^{(+)}(x)$, $\pi^{(-)}(x)$, and $\pi^{(0)}(x)$ being the fields associated to the three charge states of the pion. The pion fields in Cartesian coordinates are collectively denoted by $\vec{\pi}(x)$. We use the 2×2 matrices τ_a, $a = 0, \ldots, 3$, where τ_0 is the identity matrix, while τ_a, $a = 1, \ldots, 3$ are the Pauli matrices acting on the isospin degrees of freedom (often indicated cumulatively as $\vec{\tau}$). For example, $\vec{\tau} \cdot \vec{\pi}(x) = \sum_{a=1}^{3} \tau_a \pi_a(x)$. Sometimes the $a = 3$ component will be denoted as the "z" component, i.e., $\pi_3 \equiv \pi_z$, etc., in our notation. Finally, we denote the nucleon (pion) mass by M (m_π).

In some cases, we will perform a non-relativistic reduction of the nucleon field $N(x)$ and use $N_s(x)$

$$N_s(x) = \begin{pmatrix} p_s(x) \\ n_s(x) \end{pmatrix}, \tag{10}$$

where $p_s(x)$ ($n_s(x)$) is the two component Pauli spinor representing the static proton (neutron) field. Effects of the anti-nucleon degrees of freedom are taken into account in the form of $1/M$ relativistic corrections to the vertices. The coefficient of the annihilation operator reduces to $\chi_m \exp(i\boldsymbol{p} \cdot \boldsymbol{x})$, where χ_m is a spinor describing a spin state with z-projection $m = \pm\frac{1}{2}$.

The main "building block" to construct the chiral Lagrangian is the SU(2) pionic matrix field $U(x)$, often written as (but its definition is not unique) [12]

$$U(x) = e^{\frac{i}{f_\pi}\vec{\pi}(x)\cdot\vec{\tau}}, \tag{11}$$

where $f_\pi \approx 92.4$ MeV is the pion decay constant. Another low energy constant frequently entering the chiral Lagrangian is the axial coupling constant $g_A \approx 1.29$. Following the standard convention, we give here the effective value that takes into account the Goldberger-Treiman discrepancy and is extracted from the empirical value of the pion-nucleon coupling constant. The effective chiral Lagrangian is constructed in terms of $N(x)$ and $U(x)$ and therefore contains vertices with arbitrary number of pion fields. In the following, we will retain explicitly only relevant terms with the minimum number of pion fields, obtained by expanding $U(x)$ in powers of the pion field. Additional terms with a larger number of pion fields will only contribute to the PVTC and PVTV potential at higher orders in the chiral expansion. For an introduction to the chiral Lagrangians and their building blocks, the reader is referred to Bernard et al. [12], Bernard [13], and Bijnens and Ecker [14] and references therein.

Each term of the chiral Lagrangian will be classified by the so-called "chiral order". Each four-gradient of the pion matrix field or a multiplication by a pion mass increases the order of the term by one. Four-gradients acting on nucleon fields are

more difficult to classify, since the time derivative brings down a factor proportional to the nucleon mass. An easier counting is obtained using the non-relativistic heavy baryon perturbation theory [12, 117], which was used in the derivation of the PVTC potential in de Vries et al. [46] and of the PVTV potential in Maekawa et al. [72]. In the following, we will use both the relativistic and non-relativistic nucleon fields.

For the sake of completeness, we report first of all the terms of the PCTC Lagrangian that contribute to the PVTC and PVTV potentials up to the order we are interested in. In $SU(2)$ χPT, the PCTC Lagrangian can be conveniently organized in sectors with different numbers of pions and nucleons (below we give the explict expression for the relevant terms in the πN Lagrangian only).

$$\mathcal{L}_{PCTC} = \mathcal{L}_{PCTC,\pi N} + \mathcal{L}_{PCTC,NN} + \mathcal{L}_{PCTC,\pi\pi} + \cdots , \tag{12}$$

$$\begin{aligned}\mathcal{L}_{PCTC,\pi N} = \overline{N}\Big[&-\frac{1}{4f_\pi^2}(\vec{\tau}\times\vec{\pi})\cdot\partial_\mu\vec{\pi}\,\gamma^\mu - \frac{g_A}{2f_\pi}(\vec{\tau}\cdot\partial_\mu\vec{\pi})\,\gamma^\mu\gamma^5 \\ &+4\,c_1\,m_\pi^2\left(1-\frac{\vec{\pi}^{\,2}}{2f_\pi^2}\right)+\frac{c_2}{f_\pi^2}\left(\partial_0\vec{\pi}\cdot\partial_0\vec{\pi}+\frac{1}{M}\partial_0\vec{\pi}\cdot\partial_i\vec{\pi}\,\gamma^0\,i\overleftrightarrow{\partial}^i\right) \\ &+\frac{c_3}{f_\pi^2}\,\partial_\mu\vec{\pi}\cdot\partial^\mu\vec{\pi} - \frac{c_4}{2f_\pi^2}\,(\vec{\tau}\cdot\partial_\mu\vec{\pi}\times\partial_\nu\vec{\pi})\,\sigma^{\mu\nu}+\cdots\Big]N\end{aligned} \tag{13}$$

where "$\cdots$" in the previous expression denotes terms of higher order and/or more pions fields of no interest here. Above $\overleftrightarrow{\partial}^\mu \equiv \overrightarrow{\partial}^\mu - \overleftarrow{\partial}^\mu$ and $\sigma^{\mu\nu} = \frac{i}{2}[\gamma^\mu,\gamma^\nu]$. The parameters $c_{i=1-4}$ are LECs appearing in the Lagrangian of order Q^2. They have dimension of mass^{-1}. For a complete discussion of the terms appearing in the Lagrangians $\mathcal{L}_{PCTC,\pi N}$, $\mathcal{L}_{PCTC,NN}$, and $\mathcal{L}_{PCTC,\pi\pi}$, etc., see [12, 118].

3.1. The PVTC Chiral Lagrangian

The effective chiral Lagrangian that involves contributions from the weak sector of the SM was first discussed in the seminal paper by Kaplan and Savage [88] and subsequently revisited in Kaplan et al. [119], Zhu et al. [40], de Vries et al. [46], and Viviani et al. [42]. Also the PVTC Lagrangian can be conveniently organized in sectors with different numbers of pions and nucleons, explictly

$$\mathcal{L}_{PVTC} = \mathcal{L}_{PVTC,\pi N} + \mathcal{L}_{PVTC,NN} + \mathcal{L}_{PVTC,\pi\pi\pi} + \cdots , \tag{14}$$

$$\mathcal{L}_{PVTC,\pi N} = \mathcal{L}^{(0)}_{PVTC,\pi N} + \mathcal{L}^{(1)}_{PVTC,\pi N} + \cdots , \tag{15}$$

$$\mathcal{L}_{PVTC,NN} = \mathcal{L}^{(1)}_{PVTC,NN} + \mathcal{L}^{(3)}_{PVTC,NN} + \cdots , \tag{16}$$

$$\mathcal{L}_{PVTC,\pi\pi\pi} = \mathcal{L}^{(2)}_{PVTC,\pi\pi\pi} + \cdots , \tag{17}$$

where the superscript (n) denotes the chiral order of each piece. The pion-nucleon interaction terms are collected in $\mathcal{L}_{PVTC,\pi N}$ and those entering the PVTC potential up to Q^1 are the following [46, 88]

$$\mathcal{L}^{(0)}_{PVTC,\pi N} = \frac{h^1_\pi}{\sqrt{2}}\overline{N}(\vec{\pi}\times\vec{\tau})_z N\,, \tag{18}$$

$$\begin{aligned}\mathcal{L}^{(1)}_{PVTC,\pi N} = &-\frac{h^0_V}{2f_\pi}\overline{N}\gamma^\mu\partial_\mu(\vec{\tau}\cdot\vec{\pi})N - \frac{h^1_V}{f_\pi}\overline{N}\gamma^\mu N\partial_\mu\pi_z \\ &-\frac{2h^2_V}{f_\pi}\sum_{a,b}\mathcal{I}_{ab}\partial_\mu\pi_a\,\overline{N}\gamma^\mu\tau_b N - \frac{h^1_A}{f_\pi^2}\overline{N}\gamma^\mu\gamma^5 N(\vec{\pi}\times\partial_\mu\vec{\pi})_z \\ &+\frac{h^2_A}{f_\pi^2}\sum_{a,b=1}^{3}\mathcal{I}_{ab}\overline{N}\Big((\vec{\pi}\times\partial_\mu\vec{\pi})_a\tau_b + \partial_\mu\pi_a(\vec{\pi}\times\vec{\tau})_b\Big)\gamma^\mu\gamma^5 N\,,\end{aligned} \tag{19}$$

where

$$\mathcal{I}_{ab} = \begin{pmatrix} -1 & 0 & 0 \\ 0 & -1 & 0 \\ 0 & 0 & +2 \end{pmatrix}. \tag{20}$$

The parameters h^1_π and $h^{\Delta I}_{V,A}$ are unknown LECs. The superscript ΔI labels the rank of the corresponding isospin tensor. The LECs can be estimated by naive dimensional analysis (NDA) [40, 42, 46, 88]

$$h^1_\pi \sim G_F f_\pi \Lambda_\chi \sim 10^{-6}\,, \qquad h^{\Delta I}_{V,A} \sim \frac{f_\pi}{\Lambda_\chi}h^1_\pi \sim 10^{-7}\,, \tag{21}$$

where $\Lambda_\chi = 4\pi f_\pi \sim 1.2$ GeV is the typical scale of the strong interaction. Equation (21) shows the order-of-magnitude estimates of the PVTC interactions. These estimates do not take into account factors of s^2_w and N_c that could modify the expected scaling of the LECs.

The contact terms entering the Lagrangian $\mathcal{L}_{PVTC,NN}$ are products of a pair of bilinears of nucleon fields that are odd under P and even under CP. The most general bilinear product reads

$$\widetilde{O}_{AB} = \sum_{a,b=0}^{3} F_{ab}(\overline{N}\,\tau_a\Gamma_A\,N)\,(\overline{N}\,\tau_b\Gamma_B\,N)\,, \tag{22}$$

where Γ_A and Γ_B are elements of the Clifford algebra with the possible addition of 4-gradients and F_{ab} are unknown parameters. To violate P but conserve CP, at least one 4-gradient is required. We must build isoscalar, isovector and isotensor terms as discussed in section 2. The operators moreover have to conserve the electric charge and thus commute with the third component of the isospin operator. The terms with only one gradient operator are collected in $\mathcal{L}^{(1)}_{PVTC,NN}$ (i.e., of chiral order 1). Only five independent terms can be written [44], corresponding to the five possible $S \leftrightarrow P$ transitions in NN scattering [45]. It is more convenient to give the Lagrangian using

the non-relativistic reduction of the nucleon fields N_s:

$$\begin{aligned}\mathcal{L}^{(1)}_{PVTC,NN} = \frac{1}{\Lambda_\chi^2 f_\pi}\Bigg[&\frac{C_1}{2}\boldsymbol{\nabla}\times(N_s^\dagger\boldsymbol{\sigma}N_s)\cdot N_s^\dagger\boldsymbol{\sigma}N_s\\ &+\frac{C_2}{2}\boldsymbol{\nabla}\times(N_s^\dagger\boldsymbol{\sigma}\tau_a N_s)\cdot N_s^\dagger\boldsymbol{\sigma}\tau_a N_s\\ &+C_3\epsilon_{ab3}\boldsymbol{\nabla}\cdot(N_s^\dagger\boldsymbol{\sigma}\tau_a N_s)N_s^\dagger\tau_b N_s\\ &+C_4\boldsymbol{\nabla}\times(N_s^\dagger\boldsymbol{\sigma}\tau_3 N_s)\cdot N_s^\dagger\boldsymbol{\sigma}N_s\\ &+\frac{C_5}{2}\mathcal{I}_{ab}\boldsymbol{\nabla}\times(N_s^\dagger\boldsymbol{\sigma}\tau_a N_s)\cdot N_s^\dagger\boldsymbol{\sigma}\tau_b N_s\Bigg]. \quad (23)\end{aligned}$$

The factor $\frac{1}{\Lambda_\chi^2 f_\pi}$ has been chosen to ensure that the C_i are dimensionless and for convenience in the power counting. The construction of Equation (23) and the elimination of redundancies will be discussed in more details in section 4. The operators multiplying the LECs $C_{1,2}$ are isoscalar, those multiplying $C_{3,4}$ change isospin by one unit, while that multiplying C_5 is an isotensor. The scaling of the LECs from naive dimensional analysis [120] is given by

$$C_i \sim G_F \Lambda_\chi f_\pi\,, \quad (24)$$

which once again does not take into account the suppression by s_w^2 affecting, for example, the isovector operators. The operators in Equation (23) contribute to the PVTC potential at NLO (suppressed by $(Q/\Lambda_\chi)^2$ with respect to LO), and we will give the potential derived from them in Equation (60). The terms appearing in $\mathcal{L}^{(3)}_{PVTC,NN}$ contain two additional gradients and contribute to the PVTC potential at higher order. They have not been considered so far.

Finally, there are some terms with 3π vertices appearing in $\mathcal{L}^{(2)}_{PVTC,\pi\pi\pi}$ as discussed in Viviani et al. [42]. These terms would contribute to the Q^2 PVTC potential, but their contributions at the end vanishes as discussed in section 3.4.

3.1.1. Connection to the Underlying PVTC Sources

Attempts to estimate the values of the coupling constants were performed mainly in the framework of the meson exchange models (which will be discussed in section 5). However, since in both χEFT and meson exchange frameworks the lowest order pion-nucleon Lagrangian term is the same as given in Equation (18), we can report here the values for h^1_π estimated from the underlying fundamental theory also before the advent of χEFT [121–127]. One of the most comprehensive calculation including all previous results was performed in 1980 by Desplanques, Donoghue, and Holstein (DDH) [50] using the valence quark model. Additional calculations have been performed subsequently [128–130], using similar or other methods and finding qualitatively similar results. These estimates, however, are based on a series of rather uncertain assumptions (see, for example, [131]). For example, DDH presented not a single value for h^1_π but rather a *range* inside of which it was extremely likely that this parameter would be found [50]. In addition they presented also a single number called the "best value" but this is described simply as an educated guess in view of all the uncertainties. The values of h^1_π were [50]

$$\begin{aligned}\text{DDH:}\quad h^1_\pi &= 4.56\times10^{-7}\quad(\text{"best value"})\,,\\ h^1_\pi &= 0-11.4\times10^{-7}\quad(\text{"reasonable range"})\,. \quad (25)\end{aligned}$$

Some years ago, a lattice QCD calculation of h^1_π was also made [132], resulting in the estimate

$$\text{Lattice:}\quad h^1_\pi = (1.1\pm0.5)\times10^{-7}\,, \quad (26)$$

where the theoretical uncertainty is related to the statistical Monte Carlo error. While the systematic errors are expected to be within the quoted statistical uncertainty [132], we stress that the calculation was performed at a heavy pion mass and not extrapolated to the physical point, disconnected diagrams were not included, and operator renormalization was neglected.

Regarding the other LECs entering the contact Lagrangian given in Equation (23), no direct estimates have been reported in literature. These LECs were estimated by comparing the expression of contact potential with the potential developed using the exchanges of heavy mesons, as for example, in the DDH potential [42, 46] (this issue will be considered in more detail in section 5). However, since also the DDH estimates are rather uncertain, we will not discuss this issue further.

3.2. The PVTV Lagrangian

The PVTV chiral Lagrangian taking into account the QCD $\bar\theta$ term was first considered in the seminal paper by Crewther, di Vecchia, Veneziano and Witten [102], and consequently revisited in Cheng [133], Pich and de Rafael [134], Cho [135], Borasoy [136], and Ottnad et al. [137]. Subleading terms in the chiral expansion were systematically constructed in Mereghetti et al. [65] and Bsaisou et al. [69]. The chiral Lagrangian induced by the dimension-six operators in Equation (7) were derived in de Vries et al. [68] and Bsaisou et al. [69].

As before, in $SU(2)$ χPT, the PVTV Lagrangian can be organized in sectors with different numbers of pions and nucleons

$$\begin{aligned}\mathcal{L}_{PVTV} &= \mathcal{L}_{PVTV,\pi N}+\mathcal{L}_{PVTV,NN}+\mathcal{L}_{PVTV,\pi\pi\pi}+\cdots\,, \quad (27)\\ \mathcal{L}_{PVTV,\pi N} &= \mathcal{L}^{(0)}_{PVTV,\pi N}+\mathcal{L}^{(1)}_{PVTV,\pi N}+\cdots\,, \quad (28)\\ \mathcal{L}_{PVTV,NN} &= \mathcal{L}^{(1)}_{PVTV,NN}+\mathcal{L}^{(3)}_{PVTV,NN}+\cdots\,, \quad (29)\\ \mathcal{L}_{PVTV,\pi\pi\pi} &= \mathcal{L}^{(0)}_{PVTV,\pi\pi\pi}+\cdots\,. \quad (30)\end{aligned}$$

As in the previous subsection, we report here only the most important interactions for each sector, focusing on the terms with the minimum number of pion fields entering in the final expression of the potential. Terms with additional pions are not universal for the different PVTV sources at the quark level, but instead depend on their chiral-symmetry breaking pattern. These differences only enter at higher order in the potentials than we consider here.

In the PVTV case, the simultaneous violation of P, T, and isospin symmetry allows for a pion tadpole linear in the pion field

$\sim \pi_3$ with a corresponding LEC proportional to the symmetry-violating source terms at the quark level. Such tadpoles can always be removed by appropriate field redefinitions of the pion and nucleon fields [65, 68, 69]. At LO in the chiral expansion, the tadpole removal is the same as the vacuum alignment procedure at the quark level [101]. While tadpoles can be removed, the corresponding field redefinitions affect other couplings in the chiral Lagrangian. In particular, for chiral-symmetry-breaking CP sources that do not transform as a quark mass term, a PVTV three-pion vertex of chiral order Q^0 is left behind [68, 69].

$$\mathcal{L}^{(0)}_{PVTV,\pi\pi\pi} = M\bar{\Delta}\pi_3\vec{\pi}^2\,, \tag{31}$$

where $\bar{\Delta}$ is a LEC. Other three-pion vertices will appear at N^{2}LO, but they will contribute to high orders of the PVTV potential.

Arguably the most important interactions appear in the pion-nucleon sector. Simultaneous violation of P, T, and chiral symmetry allows for non-derivative single-pion-nucleon interactions, something which is not possible in the PCTC Lagrangian. In principle, three different interactions can be written

$$\mathcal{L}^{(0)}_{PVTV,\pi N} = \bar{g}_0\overline{N}\vec{\pi}\cdot\vec{\tau}N + \bar{g}_1\overline{N}\pi_3 N + \bar{g}_2\overline{N}\pi_3\tau_3 N\,, \tag{32}$$

corresponding, respectively, to an isospin singlet, vector, and tensor interaction. As discussed below, the relative size of the LECs $\bar{g}_{0,1,2}$ strongly depends on the quark-level PVTV source under consideration. In the case of CP-violation from chiral invariant operators, such as the three gluon term, $\bar{g}_i$ are suppressed by powers of the pion masses, and the pion-nucleon Lagrangian contains chiral-invariant, derivative couplings as important as those in Equation (32) [68]. These can however always be absorbed into a shift of $\bar{g}_0$ and of the $\Delta I = 0$ NN operators discussed below.

The NLO Lagrangian contains several two-pion two-nucleon PVTV interactions [65, 68, 69, 75], but, for all CP-violating sources, they contribute to the two- and three-body PVTV potentials at N^{3}LO and N^{2}LO, respectively. We therefore ignore these couplings. Isospin-breaking sources also generate a single-pion-nucleon NLO coupling. The coupling involves a time derivative of the pion field, thus inducing a relativistic correction in the $\mathcal{O}(Q)$ PVTV potential. At N^{2}LO the number of interactions proliferates significantly and there are also new pure pionic interactions. These contributions can either be absorbed into LO LECs or appear at high orders in the PVTV potential considered here.

Apart from pionic and pion-nucleon interactions, there appear PVTV NN contact interactions. As in the PVTC case, at least one gradient is required such that these operators start at order Q. Terms with three or more gradients have not been considered so far. At order Q, only five independent interactions of this kind can be written, corresponding to the five possible $S \leftrightarrow P$ transitions (see section 4 for a general discussion of this kind of interaction terms). Neglecting terms with multiple pions, the Lagrangian reads (again, it is convenient to write it in terms of the non-relativistic nucleon field N_s)

$$\begin{aligned}\mathcal{L}^{(1)}_{PVTV,NN} = \frac{1}{\Lambda_\chi^2 f_\pi}\Big[&\bar{C}_1\boldsymbol{\nabla}\cdot(N_s^\dagger\boldsymbol{\sigma}N_s)\,N_s^\dagger N_s \\ &+ \bar{C}_2\boldsymbol{\nabla}\cdot(N_s^\dagger\boldsymbol{\sigma}\tau_a N_s)\,N_s^\dagger\tau_a N_s \\ &+ \bar{C}_3\boldsymbol{\nabla}\cdot(N_s^\dagger\boldsymbol{\sigma}\tau_3 N_s)N_s^\dagger N_s + \bar{C}_4\boldsymbol{\nabla}\cdot(N_s^\dagger\boldsymbol{\sigma}N_s)N_s^\dagger\tau_3 N_s \\ &+ \bar{C}_5\mathcal{I}_{ab}\boldsymbol{\nabla}\cdot(N_s^\dagger\boldsymbol{\sigma}\tau_a N_s)\,N_s^\dagger\tau_b N_s\Big]\,.\end{aligned} \tag{33}$$

As suggested by the factor of Λ_χ^2 which we pulled out of the definition of the LECs, in χEFT these operators contribute in general at N^{2}LO and are suppressed with respect to the PVTV one-pion exchange (OPE) potential. The only exception, as discussed in section 3.2.1, are quark-level operators that do not break chiral symmetry, for which $\bar{C}_{1,2}$ are as important as the contributions from $\bar{g}_{0,1}$.

Finally, the calculation of EDMs or other PVTV electromagnetic moments requires the inclusion of electromagnetic currents. Nucleon EDMs are induced by pion loops involving the interactions in $\mathcal{L}^{(0,1)}_{PVTV,\pi N}$. The renormalization of these loops requires the inclusion of short-distance counter terms contributing to the nucleon EDMs. Such counter terms indeed appear in the chiral Lagrangian

$$\mathcal{L}_{PVTV,N\gamma} = \frac{1}{4}\overline{N}\left(\bar{d}_0 + \bar{d}_1\tau_3\right)\epsilon^{\mu\nu\alpha\beta}\sigma_{\mu\nu}N F_{\alpha\beta}\,, \tag{34}$$

where $F_{\alpha\beta}$ is the electromagnetic field strength and $\bar{d}_0$ and $\bar{d}_1$ are LECs related to the proton and neutron EDMs, respectively. The above interactions are sufficient for calculations of hadronic and nuclear PVTV scattering observables and EDMs up to NLO in the chiral expansion. Calculations of higher PVTV moments, such as magnetic quadrupole moments, can depend on additional LECs [138].

3.2.1. Connection to the Underlying PVTV Sources

In the previous section we listed the PVTV hadronic interactions relevant for observables of experimental interest. However, for a given PVTV source at the quark-gluon level, a specific hierarchy among the various interactions appear. The relative importance of the LECs in Equations (31), (32), (33), and (34) for the different microscopic sources of CP violation is summarized in **Table 1**. These estimates are based on NDA [120]. NDA is valid in the regime in which the strong coupling g_s is non-perturbative, and, as done for NDA estimates of the chiral-invariant PCTC interactions, we will take $g_s \simeq 4\pi$. In addition, for dimension-six sources, we assumed that a Peccei-Quinn mechanism [139] relaxes $\bar{\theta}$ to an induced $\bar{\theta}_{\rm ind}$, which depends on the coefficients and vacuum matrix elements of the operators in Equation (7) [52, 140, 141]. The scaling of the couplings without this assumption can be found in deVries et al. [68]. To make the power counting explicit, we introduced three ratios of scales

$$\epsilon_\nu \equiv \frac{\Lambda_\chi^2}{v^2}, \qquad \epsilon_{m_\pi} \equiv \frac{m_\pi^2}{\Lambda_\chi^2}, \qquad \epsilon_\chi \equiv \frac{f_\pi^2}{\Lambda_\chi^2} = \frac{1}{(4\pi)^2}\,. \tag{35}$$

TABLE 1 | Scaling of the LECs in the chiral Lagrangian in dependence of the microscopic CP violation sources.

	$(4\pi\epsilon_{m_\pi})\,\bar{\theta}$	$(4\pi\epsilon_{m_\pi})\epsilon_v\tilde{c}_g^{(u,d)}$	$(4\pi\epsilon_{m_\pi})\,\epsilon_v\tilde{c}_\gamma^{(u,d)}$	$4\pi\epsilon_v\tilde{C}_G$	$\epsilon_v\Xi_{1,2}^{(ud)}/(4\pi)$	$\epsilon_v\Sigma_{1,2}^{(ud)}/(4\pi)$
$\bar{\Delta}$	ϵ_{m_π}	ϵ_{m_π}	–	$\varepsilon\epsilon_{m_\pi}^2$	1	ϵ_{m_π}
$\bar{g}_0$	1	1	–	ϵ_{m_π}	$\varepsilon\epsilon_{m_\pi}$	ϵ_{m_π}
$\bar{g}_1$	$\varepsilon\epsilon_{m_\pi}$	1	–	$\varepsilon\epsilon_{m_\pi}$	1	$\varepsilon\epsilon_{m_\pi}$
$\bar{g}_2$	$\varepsilon^2\epsilon_{m_\pi}^2$	$\varepsilon\epsilon_{m_\pi}$	–	$\varepsilon^2\epsilon_{m_\pi}^2$	$\varepsilon\epsilon_{m_\pi}$	$\varepsilon^2\epsilon_{m_\pi}^2$
$\bar{d}_{0,1}f_\pi$	$e\,\epsilon_\chi$	$e\,\epsilon_\chi$	$e\,\epsilon_\chi$	$e\,\epsilon_\chi$	$e\,\epsilon_\chi$	$e\,\epsilon_\chi$
$\bar{C}_{1,2}$	1	1	–	1	$\varepsilon\epsilon_{m_\pi}$	1
$\bar{C}_{3,4}$	$\varepsilon\epsilon_{m_\pi}$	1	–	$\varepsilon\epsilon_{m_\pi}$	1	$\varepsilon\epsilon_{m_\pi}$
$\bar{C}_5$	$\varepsilon^2\epsilon_{m_\pi}^2$	$\varepsilon\epsilon_{m_\pi}$	–	$\varepsilon^2\epsilon_{m_\pi}^2$	$\varepsilon\epsilon_{m_\pi}$	$\varepsilon^2\epsilon_{m_\pi}^2$

We introduced the counting parameters $\epsilon_v \equiv \Lambda_\chi^2/v^2$, $\epsilon_{m_\pi} \equiv m_\pi^2/\Lambda_\chi^2$, $\epsilon_\chi \equiv f_\pi^2/\Lambda_\chi^2$. With $\epsilon_{m_\pi} \sim \epsilon_\chi$, we introduced two different parameters to explicitly track insertions of the light quark masses from the QCD Lagrangian. ε is the isospin breaking parameter $\varepsilon = (m_d - m_u)/(m_d + m_u) \simeq 1/3$. The scaling of the LECs induced by dimension-six sources assume a Peccei-Quinn mechanism. A "–" implies the interaction is only induced at higher order than considered here. The parameters $\bar{C}_{1,2}$, $\bar{C}_{3,4}$, and $\bar{C}_5$ are the LECs entering the contact PVTV potential, respectively of isoscalar, isovector, and isotensor type.

Numerically, $\epsilon_\chi \sim \epsilon_{m_\pi}$, but we define two different parameters to track the dependence of the LECs on the quark masses. To assess the size of the contribution of different CP violating sources to the nucleon and nuclear EDMs, the scaling of the LECs in **Table 1** can be combined with a naive estimate of these observables. As we will discuss in detail in sections 3.2.2 and 6.5, the nucleon EDM receives tree level contributions from $\bar{d}_{0,1}$ and loop contributions by $\bar{g}_0$ and $\bar{g}_1$, leading to

$$d_{n,p} \sim \frac{\bar{d}_0 \mp \bar{d}_1}{2} + \frac{e}{f_\pi}\epsilon_\chi\left(\alpha_0\bar{g}_0 + \alpha_1\bar{g}_1\epsilon_{m_\pi}^{1/2} + \ldots\right), \quad (36)$$

where e is the electric charge and the coefficients of the loops $\alpha_{0,1}$ will be given explicitly in section 3.2.2. The additional suppression of $\bar{g}_1$ is due to the fact that this coupling only involves neutral pions, which do not interact with a single photon at LO. Nuclear EDMs, on the other hand, receive tree level contributions from the single nucleon EDM, and from pion-nucleon and nucleon-nucleon couplings,

$$d_A = a_n d_n + a_p d_p + e\left(a_\Delta\bar{\Delta} + \sum_{i=0}^{2} a_i\bar{g}_i + \epsilon_\chi\sum_{i=1}^{5} A_i\bar{C}_i\right). \quad (37)$$

The coefficients $a_{n,p}$, $a_{\Delta,0,1,2}$ and $A_{1,\ldots,5}$ depend on the nucleus under consideration, and in section 6.5 we will present results for their calculation in chiral EFT for the deuteron, ^{3}H and ^{3}He. By power counting, they are expected to be $\mathcal{O}(1)$ (measured in units of fm in the case of the dimensionful $a_{\Delta,0,1,2}$ and $A_{1,\ldots,5}$), barring isospin selection rules, which for example suppress the contributions of the isoscalar operators $\bar{g}_0$ and $\bar{C}_{1,2}$ in nuclei with $N = Z$, such as the deuteron [142, 143] [6].

The reader should be aware that the dimensionless Wilson coefficients of the dimension-six operators, $\tilde{c}_g^{(u,d)}$, $\tilde{c}_\gamma^{(u,d)}$, $\tilde{C}_G$, $\Xi_{1,2}^{(ud)}$, and $\Sigma_{1,2}^{(ud)}$ also come with intrinsic suppression factors. These arise from the typical loop and chiral factors that appear in BSM models. For example, quark and gluon dipole operators are typically induced at the one-loop level, and the quark EDM and chromo-EDM coefficients come with explicit factors of the quark mass (already included in Equation 7). This implies that one can expect $\{\tilde{c}_g^{(u,d)}, \tilde{c}_\gamma^{(u,d)}, \tilde{C}_G\} = \mathcal{O}(\epsilon_\Lambda/(4\pi)^2)$, where $\epsilon_\Lambda = v^2/\Lambda_X^2$. Of course this is just an estimate and certainly models exist where these operators appear only at the two- or higher-loop level. On the other hand, the four-quark operators Ξ and Σ can be induced at tree level, so that $\{\Xi, \Sigma\} = \mathcal{O}(\epsilon_\Lambda)$. Once the matching coefficients are calculated in a given model, **Table 1** and Equations (36)-(37) allow identification of the dominant low-energy operator and to get a rough idea of the EDM constraints.

Table 1 highlights the feature that the chiral and isospin properties of the quark-level CP-violating sources induce very specific hierarchies between different low-energy couplings. These hierarchies in turn imply different relations between the EDMs of the nucleon, deuteron, and three-nucleon systems, which, if observed, would allow disentanglement of the various CP-violating sources. From **Table 1**, we see that chiral-symmetry-breaking sources, such as $\bar{\theta}$, $\tilde{c}_g^{(u,d)}$, and $\Xi_{1,2}^{(u,d)}$, induce relatively large PVTV pion-nucleon couplings. These couplings appear in the table with entry 1, indicating no further suppression. In particular, the isoscalar $\bar{\theta}$ term and isovector $\Xi^{(u,d)}$ predominantly induce, respectively, $\bar{g}_0$ and $\bar{g}_1$, while a qCEDM would yield both couplings with similar strengths. The consequence is that for these sources light nuclear EDMs are enhanced with respect to the nucleon EDM. For these chiral-symmetry-breaking sources, the contact nucleon interactions proportional to $\bar{C}_i$ are suppressed in the chiral expansion because these operators involve an explicit derivative. The suppression can be explicitly seen combining the scaling in **Table 1** with the explicit factor of ϵ_χ in Equations (33) and (37).

Chiral invariant sources such as the Weinberg operator $\tilde{C}_G$ and the four-quark operators $\Sigma_{1,2}^{(u,d)}$, on the other hand, require additional chiral-symmetry breaking to generate $\bar{g}_{0,1}$, as indicated by extra powers of ϵ_{m_π}. In this case, EDMs of light-nuclei are expected to be of similar size as the nucleon EDM. Furthermore, the contact nucleon operators proportional to $\bar{C}_{1,2}$ now contribute to the PVTV potential at the same order as $\bar{g}_{0,1}$.

[6] $\bar{g}_0$ and $\bar{C}_{1,2}$ contribute to the deuteron EDM in conjunction with isospin breaking in the strong interaction, or via the spin-orbit coupling of the photon to the nucleons [143]. Both contributions are beyond the accuracy we work at in this paper.

Finally, the qEDM mostly induces $\bar{d}_{0,1}$, all other couplings being suppressed by $\mathcal{O}(\alpha_{\rm em})$, where $\alpha_{\rm em}$ is the fine structure constant $\sim 1/137$. In this case one expects nuclear EDMs to be dominated by the constituent nucleon EDMs.

While most statements are source-dependent, there is an important general message hidden in **Table 1**. There is no PVTV source for which the couplings $\bar{g}_2$ and $\bar{C}_{3,4,5}$ appear at LO. For all sources they appear with a relative suppression of $\varepsilon\epsilon_{m_\pi}$ or ϵ_χ compared to other PVTV interactions. For most calculations one can simply neglect the associated interactions, reducing the number of LECs entering the expression of hadronic and nuclear observables. The suppression of the LECs $\bar{g}_2$ and $\bar{C}_{3,4,5}$ ultimately is a consequence of imposing gauge invariance on the dimension-six PVTV sources.

Table 1 relies on NDA estimates for hadronic matrix elements [120]. A more quantitative assessment of the discriminating power of EDM experiments necessitates to replace the NDA estimates in **Table 1** with solid non-perturbative calculations of the LECs. At the moment, there exist controlled estimates only of a few LECs. The pion-nucleon couplings $\bar{g}_0$ induced by the QCD $\bar{\theta}$ term is related by chiral symmetry to modifications in the baryon spectrum [102]. In particular, in $SU(2)$ χPT $\bar{g}_0$ is related to the quark mass contribution to the nucleon mass splitting [65, 144], up to N^{2}LO corrections. Using Lattice QCD evaluations of the nucleon mass splitting [145, 146], one finds

$$\bar{g}_0(\bar{\theta}) = (15.5 \pm 2.6) \times 10^{-3}\,\bar{\theta}\,, \tag{38}$$

where the 15% error includes both the Lattice QCD error on $m_n - m_p$, and an estimate of the error from N^{2}LO chiral corrections. Unfortunately, chiral-symmetry-based relations do not allow to extract $\bar{g}_1$ and $\bar{d}_{0,1}$. $\bar{g}_1$ has been estimated with resonance saturation leading to $\bar{g}_1(\bar{\theta})/\bar{g}_0(\bar{\theta}) \simeq -0.2$, somewhat larger than expected from NDA [73]. The LECs $\bar{d}_{0,1}$ are usually estimated by naturalness arguments and considered to be of similar size to non-analytic contributions to the isoscalar and isovector nucleon EDM, see the section 3.2.2.

The relation between PVTV pion-nucleon couplings and corrections to the nucleon and pion masses is not specific to the QCD $\bar{\theta}$ term, but can be generalized to all chiral-symmetry-breaking sources, such as for example the qCEDM [68, 147] and $\Xi^{(ud)}_{1,2}$ [141, 148]. Since corrections to spectroscopic quantities should be easier to compute on the lattice, these chiral relations allow a calculation of $\bar{g}_{0,1}$ in Lattice QCD. While promising, this strategy has yet to lead to controlled results. The best estimate of $\bar{g}_{0,1}$ induced by the qCEDM comes from QCD sum rules [52, 149]

$$\begin{aligned}\bar{g}_0 &= (0.1 \pm 0.2)\left(0.7\tilde{c}_g^{(u)} - 1.5\tilde{c}_g^{(d)}\right) \times 10^{-6},\\ \bar{g}_1 &= \left(0.4^{+0.8}_{-0.2}\right)\left(0.7\tilde{c}_g^{(u)} - 1.5\tilde{c}_g^{(d)}\right) \times 10^{-6}.\end{aligned} \tag{39}$$

These estimates agree with NDA, especially for $\bar{g}_1$. However, $\bar{g}_0$ seems to be slightly suppressed, in agreement with large-N_c expectations [150].

Only for the four quark operators proportional to $\Xi^{(ud)}_{1,2}$ of Equation (7) does the three-pion vertex with LEC $\bar{\Delta}$ appear at LO in the chiral Lagrangian. For this case, the LEC $\bar{\Delta}$ is related by $SU(3)$ symmetry to $K \to \pi\pi$ matrix elements and $K - \bar{K}$ matrix elements that have been calculated on the lattice. We obtain

$$\bar{\Delta} = \frac{f_\pi}{Mv^2}\left(\mathcal{A}_{1\,LR}\,\mathrm{Im}\,\Xi^{(ud)}_1 + \mathcal{A}_{2\,LR}\,\mathrm{Im}\,\Xi^{(ud)}_2\right), \tag{40}$$

with

$$\begin{aligned}\mathcal{A}_{1\,LR}(\mu = 3\,\mathrm{GeV}) &= (2.2 \pm 0.13)\ \mathrm{GeV}^2,\\ \mathcal{A}_{2\,LR}(\mu = 3\,\mathrm{GeV}) &= (10.1 \pm 0.6)\,\mathrm{GeV}^2\,.\end{aligned} \tag{41}$$

The matrix elements in Equation (41) are in good agreement with NDA. The value of $\bar{\Delta}$ also determines the tadpole component of $\bar{g}_1$, which again is in line with NDA.

Most of the remaining LECs are undetermined at present. The focus of the Lattice QCD community has been on the matrix elements connecting the nucleon EDMs to the $\bar{\theta}$ term [103, 151, 152], the qEDMs [153, 154], the qCEDMs [152, 155], and the Weinberg operator [156]. Some results are given in next subsection.

3.2.2. The Nucleon EDM in Chiral Perturbation Theory

The PVTV LECs defined in the previous section can be used to calculate the nucleon PVTV electric dipole form factor (EDFF). At zero momentum transfer, the EDFFs are identified with the nucleon EDMs. In dimensional regularization with modified minimal subtraction up to NLO in the chiral expansion, the EDMs are given by [137, 157]

$$d_n = \bar{d}_0(\mu) - \bar{d}_1(\mu) + \frac{eg_A\bar{g}_0}{(4\pi)^2 f_\pi}\left(\log\frac{m_\pi^2}{\mu^2} - \frac{\pi m_\pi}{2M}\right), \tag{42}$$

$$\begin{aligned}d_p &= \bar{d}_0(\mu) + \bar{d}_1(\mu)\\ &\quad - \frac{eg_A\bar{g}_0}{(4\pi)^2 f_\pi}\left[\left(\log\frac{m_\pi^2}{\mu^2} - \frac{2\pi m_\pi}{M}\right) - \frac{\bar{g}_1}{\bar{g}_0}\frac{\pi m_\pi}{2M}\right],\end{aligned} \tag{43}$$

where μ is the dimensional regularization scale. The leading loops proportional to $\bar{g}_0$ are divergent and renormalized by the μ-dependent LECs $\bar{d}_{0,1}$. The NLO corrections proportional to m_π/M are finite. The LEC $\bar{\Delta}$ does not contribute at this order for any of the PVTV sources. As standard in χPT, the loops are associated to inverse powers of $(4\pi f_\pi)^2 = \Lambda_\chi^2$. Combined with the scaling of the LECs in **Table 1**, we conclude that for the $\bar{\theta}$ term and the qCEDMs the leading loop proportional to $\bar{g}_0$ and the counter terms $\bar{d}_{0,1}$ appear at the same order. For all other PVTV sources, the short-range counter terms $\bar{d}_{0,1}$ are expected to dominate the nucleon EDMs. In no scenario can the EDMs be calculated solely from the pion-nucleon LECs $\bar{g}_{0,1}$ as is often assumed in the literature. Estimates for the nucleon EDMs are often obtained by setting $\mu = M$ and $\bar{d}_{0,1}(\mu = M) = 0$ such that EDMs depend on the value of $\bar{g}_{0,1}$, which for some PVTV sources is better known.

The separation between the short-range and loop contributions is scheme dependent and therefore not physical. Lattice QCD calculations can therefore only calculate the total nucleon EDMs d_n and d_p. In recent years, significant efforts have been made toward calculating the nucleon EDMs in terms of the underlying PVTV sources. Most efforts have focused on the

QCD $\bar{\theta}$ term and the qEDM. The most recent results for the $\bar{\theta}$ term [103] give

$$\begin{aligned} d_n &= -(1.5 \pm 0.7) \times 10^{-3}\, \bar{\theta}\, e\,\mathrm{fm}\,, \\ d_p &= (1.1 \pm 1.0) \times 10^{-3}\, \bar{\theta}\, e\,\mathrm{fm}\,, \end{aligned} \tag{44}$$

in good agreement, but with sizeable uncertainties, with expectations from the chiral logarithm in Equation (42) using Equation (38). In the case of the qEDM, the nucleon EDM is related to the tensor charges, which have been computed with good accuracy [153, 154]. Using the FLAG average [154], we get

$$\begin{aligned} d_n &= g_T^d \frac{Q_u m_u}{v^2} \tilde{c}_\gamma^{(u)} + g_T^u \frac{Q_d m_d}{v^2} \tilde{c}_\gamma^{(d)} \\ &= \left(-(0.96 \pm 0.22) \tilde{c}_\gamma^{(u)} - (4.0 \pm 0.4) \tilde{c}_\gamma^{(d)} \right) \times 10^{-9} e\,\mathrm{fm}\,, \\ d_p &= g_T^u \frac{Q_u m_u}{v^2} \tilde{c}_\gamma^{(u)} + g_T^d \frac{Q_d m_d}{v^2} \tilde{c}_\gamma^{(d)} \\ &= \left((3.7 \pm 0.8) \tilde{c}_\gamma^{(u)} + (1.0 \pm 0.1) \tilde{c}_\gamma^{(d)} \right) \times 10^{-9} e\,\mathrm{fm}\,, \end{aligned} \tag{45}$$

where $Q_{u,d}$ are the u and d-quark charges in units of the electric charge, and $g_T^{u,d}$ the u and d-quark tensor charges of the proton, and the error on the r.h.s. of Equation(45) is dominated by the uncertainty on the light quark masses.

On a longer time-scale, calculations of the qCEDMs and the Weinberg operator are also targeted. For now, the best results come from calculations using QCD sum rules [52, 158].

3.3. From the Lagrangian to the Potential

In this subsection, we briefly present two methods that have been used to derive nucleon-nucleon potentials starting from a Lagrangian. We first introduce the notation used here and in the next subsections.

The process under consideration is the scattering of two nucleons from an initial state $|\boldsymbol{p}_1 \boldsymbol{p}_2\rangle$ to the final state $|\boldsymbol{p}_1' \boldsymbol{p}_2'\rangle$ (hereafter the dependence on the spin-isospin quantum numbers is understood). It is convenient to define the momenta

$$\boldsymbol{K}_j = \frac{\boldsymbol{p}_j' + \boldsymbol{p}_j}{2}\,, \quad \boldsymbol{k}_j = \boldsymbol{p}_j' - \boldsymbol{p}_j\,, \tag{46}$$

where $\boldsymbol{p}_j$ and $\boldsymbol{p}_j'$ are the initial and the final momenta of the nucleon j. Furthermore it is useful to define

$$\boldsymbol{\sigma}_j \equiv (\boldsymbol{\sigma})_{s_j', s_j} \equiv \left\langle \frac{1}{2} s_j' | \boldsymbol{\sigma} | \frac{1}{2} s_j \right\rangle\,, \quad \vec{\tau}_j \equiv (\vec{\tau})_{t_j', t_j} \equiv \left\langle \frac{1}{2} t_j' | \vec{\tau} | \frac{1}{2} t_j \right\rangle\,, \tag{47}$$

which are the spin (isospin) matrix element between the final state s_j' (t_j') and the initial state s_j (t_j) of the nucleon j.

Because $\boldsymbol{k}_1 = -\boldsymbol{k}_2 \equiv \boldsymbol{k}$ from the overall momentum conservation $\boldsymbol{p}_1 + \boldsymbol{p}_2 = \boldsymbol{p}_1' + \boldsymbol{p}_2'$, the momentum-space potential V is a function of the momentum variables $\boldsymbol{k}$, $\boldsymbol{K}_1$ and $\boldsymbol{K}_2$, namely

$$\langle \boldsymbol{p}_1' \boldsymbol{p}_2' | V | \boldsymbol{p}_1 \boldsymbol{p}_2 \rangle = V(\boldsymbol{k}, \boldsymbol{K}_1, \boldsymbol{K}_2) (2\pi)^3 \delta(\boldsymbol{p}_1 + \boldsymbol{p}_2 - \boldsymbol{p}_1' - \boldsymbol{p}_2')\,. \tag{48}$$

Moreover, we can write in general

$$V(\boldsymbol{k}, \boldsymbol{K}_1, \boldsymbol{K}_2) = V^{(\mathrm{CM})}(\boldsymbol{k}, \boldsymbol{K}) + V^{(\boldsymbol{P})}(\boldsymbol{k}, \boldsymbol{K})\,, \tag{49}$$

where $\boldsymbol{K} = (\boldsymbol{K}_1 - \boldsymbol{K}_2)/2$, $\boldsymbol{P} = \boldsymbol{p}_1 + \boldsymbol{p}_2 = \boldsymbol{K}_1 + \boldsymbol{K}_2$, and the term $V^{(\boldsymbol{P})}(\boldsymbol{k}, \boldsymbol{K})$ represents a boost correction to $V^{(\mathrm{CM})}(\boldsymbol{k}, \boldsymbol{K})$, the potential in the center-of-mass frame (CM). Below we will ignore the boost correction and provide expressions for $V^{(\mathrm{CM})}(\boldsymbol{k}, \boldsymbol{K})$ only. Note that in the CM we define also $\boldsymbol{p}_1 = -\boldsymbol{p}_2 \equiv \boldsymbol{p}$ and $\boldsymbol{p}_1' = -\boldsymbol{p}_2' \equiv \boldsymbol{p}'$. So we have $\boldsymbol{k} = \boldsymbol{p}' - \boldsymbol{p}$ and $\boldsymbol{K} = (\boldsymbol{p}' + \boldsymbol{p})/2$, so in the following we also write $V^{(\mathrm{CM})}$ as $V^{(\mathrm{CM})}(\boldsymbol{p}, \boldsymbol{p}')$. From now on, we will suppress the superscript "(CM)" for simplicity.

In order to derive the potential, two methods have been frequently used, the method of unitarity transformation (UT), and the method of the time-ordered perturbation theory (TOPT). They are briefly introduced below.

The time-ordered perturbation theory method. Let us consider the matrix element of the T-matrix, $T_{fi} = \langle \boldsymbol{p}_1' \boldsymbol{p}_2' | T | \boldsymbol{p}_1 \boldsymbol{p}_2 \rangle$, the "amplitude" of a process of scattering of two nucleons. Its square modulus $|T_{fi}|^2$ is directly related to the cross section of the process. The conventional perturbative expansion for this matrix element is given as

$$T_{fi} = \langle \boldsymbol{p}_1' \boldsymbol{p}_2' |\, H_I \sum_{n=1}^{\infty} \left(\frac{1}{E_i - H_0 + i\epsilon} H_I \right)^{n-1} | \boldsymbol{p}_1 \boldsymbol{p}_2 \rangle\,, \tag{50}$$

where E_i is the energy of the initial state, H_0 is the Hamiltonian describing free pions and nucleons, and H_I is the Hamiltonian describing interactions among these particles. These operators are defined to be in the Schrödinger picture and they can be derived from the Lagrangian constructed in terms of pions and nucleons as described, for example, in Epelbaum et al. [159] and Baroni et al.[118]. The evaluation of T_{fi} is carried out in practice by inserting complete sets of H_0 eigenstates between successive H_I factors. Power counting is then used to organize the expansion in powers of $Q/\Lambda_\chi \ll 1$, where Q stands for either an external momenta or the pion mass. We will use the "naive" Weinberg counting rules [2], namely, we will count simply the powers of both the external momenta and pion mass insertions (we will consider low energy processes only). Each term will be of some order $(Q/\Lambda_\chi)^\nu$. The terms with the lowest power of ν will be the LO, and so on.

In the perturbative series given in Equation (50), a generic contribution will be characterized by a certain number of vertices coming from the interaction Hamiltonian H_I and energy denominators, and it can be visualized also as a diagram (hereafter referred to as a TOPT diagram). Each vertex will give a "vertex function" and a δ conservation of the momenta of the particles involved in the vertex. The vertex functions are the results of the matrix elements of terms appearing in H_I and are given as products of Dirac four-spinors, momenta, etc. A sum over the momenta of the particles entering the intermediate states is also present. When a diagram includes one or more loops, the δ's are not sufficient to eliminate all the sums over the momenta of the intermediate states. The energy denominators come from the factors $1/(E_i - E_\alpha + i\epsilon)$, where E_α is the (kinetic) energy of a specific intermediate state entering the calculation. The chiral order of each diagram can be calculated as follows. One needs to consider:

1. The chiral order of the vertex functions, which can be calculated from the non-relativistic (NR) expansion of the nucleon Dirac four-spinors ($1/M$ expansion), and from various other factors. Typically, the powers of p/M coming from the NR expansion of the nucleon Dirac four-spinors are counted as $\sim Q^2$ [2, 4, 160]. In other approaches however they are considered to be of order Q [20, 161, 162]. In this paper, we will follow the first prescription.
2. The energy denominators. We note that typical momenta $\boldsymbol{p}$ of the nucleons are much smaller than the mass of the nucleons, so we can treat them non-relativistically. Namely $\sqrt{p^2+M^2} \simeq M + \frac{p^2}{2M} \sim O(Q^0) + O(Q^2)$. Regarding the pion energies, $\omega_{\mathbf{k}} = \sqrt{m_\pi^2 + k^2} \sim O(Q)$. Usually in the energy denominator all the nucleon masses M cancel out and therefore we have two cases:
   - If there are no pions in the intermediate state, the energy denominator has only nucleon energy terms so it results of order $1/Q^2$.
   - If there are pions in the intermediate states, the energy denominator reads

$$\frac{1}{\Delta E - \omega_k} \sim -\frac{1}{\omega_k}\left(1 + \frac{\Delta E}{\omega_k} + \cdots\right), \tag{51}$$

     where the term $\Delta E = E_1 + E_2 + \cdots - E_i$ where $E_1, \ldots$ are the energies of the nucleons in the intermediate state and E_i is the initial scattering energy. In the Taylor expansion the first term is of order Q^{-1}, while the other terms are usually called "recoil corrections". For the sake of consistency with the choice discussed above regarding the NR expansion of the Dirac 4-spinors, here we will count the p/M terms coming from recoil corrections as Q^2 as well.
3. The number of loops, or better the number of the sums over the intermediate state momenta that remain after using the conservation δ's. Each loop at the end will give a contribution of order Q^3.
4. The number of disconnected parts of the diagram. For each of these parts, a δ factor expressing the momentum conservation of each part is present. Then, if there are N_D disconnected parts, one of the δ simply gives the total momentum conservation, a factor common to all diagrams and therefore not relevant. Each of the remaining $N_D - 1$ δ's at the end will "block" a sum over an external three-momentum, each one therefore reducing the chiral order by 3 units.

Once the T-matrix has been calculated, one would obtain in general

$$T_{fi} = \sum_{n=n_{\min}} T_{fi}^{(n)}, \tag{52}$$

where $T_{fi}^{(n)} \sim Q^n$. In all cases the sum starts from a minimum value $n_{\min}$, $n_{\min} = 0$ for the PCTC and $n_{\min} = -1$ for the PVTC and PVTV amplitudes. The idea now is to "define" the potential acting between the two nucleons so that it can reproduce the same amplitude T_{fi}, namely, so that (for more details, see [118])

$$T_V = V + V\frac{1}{E_i - H_0^{(NN)} + i\epsilon}T_V \equiv T_{fi}, \tag{53}$$

where $H_0^{(NN)}$ is the non-interacting Hamiltonian of two nucleons. Clearly, this procedure is not unique, since usually one imposes the relation $T_V = T_{fi}$ to hold "on shell," namely by requiring the conservation of the energy between initial and final states. This induces an ambiguity, as discussed for example in Pastore et al. [162]. However, the obtained potentials are expected to be equivalent by means of a unitary or at least a similarity transformation [163].

Finally, to invert Equation (53), one assumes that V has the same Q expansion as the T matrix,

$$V = \sum_{n=n_{\min}} V^{(n)}, \qquad V^{(n)} \sim Q^n, \tag{54}$$

and Equation (53) can be solved for $V^{(n)}$ order-by-order (see, for example, Baroni et al. [118] for more details). This procedure can be generalized to the $A = 3$ case to define a three-nucleon potential and so on.

The method of unitarity transformation. The method of unitary transformation (MUT) has been pioneered in the 1950s to derive nuclear potentials in the framework of pion field theory [164, 165]. In the context of chiral EFT, this approach was formulated in Epelbaum et al. [166] and Epelbaum [167]. Similarly to TOPT, the MUT is applied to the pion-nucleon Hamiltonian which can be obtained from the effective Lagrangian in a straightforward way using the standard canonical formalism. Let η and λ denote the projection operators on the purely nucleonic subspace and the rest of the Fock space involving pion states with the usual properties $\eta^2 = \eta$, $\lambda^2 = \lambda$, $\eta\lambda = \lambda\eta = 0$ and $\eta + \lambda = 1$. To derive nuclear forces and/or current operators, the Hamiltonian needs to be brought into block-diagonal form with no coupling between the η- and λ-subspaces, which can be achieved via a suitably chosen unitary transformation U. Following Okubo, a unitary operator can be conveniently parametrized in terms of the operator $A = \lambda A \eta$ that mixes the two subspaces via

$$U = \begin{pmatrix} \eta(1 + A^\dagger A)^{-1/2} & -A^\dagger(1 + AA^\dagger)^{-1/2} \\ A(1 + A^\dagger A)^{-1/2} & \lambda(1 + AA^\dagger)^{-1/2} \end{pmatrix}. \tag{55}$$

One then obtains the non-linear decoupling equation for the operator A:

$$\tilde{H} \equiv U^\dagger H U \stackrel{!}{=} \begin{pmatrix} \eta\tilde{H}\eta & 0 \\ 0 & \lambda\tilde{H}\lambda \end{pmatrix} \Longrightarrow \lambda\,(H - [A,\, H] - AHA)\,\eta = 0\,. \tag{56}$$

The solution of the decoupling equation together with the calculation of the unitary operator U and the nuclear potential $\eta\tilde{H}\eta$ is carried out in perturbation theory by employing the standard chiral expansion. The resulting expressions for the operators A, U and $\eta\tilde{H}\eta$ have a form of a sequence of vertices from the pion-nucleon Hamiltonian H and energy denominators

involving the kinetic energies of particles in the intermediate states with one or more virtual pions. They are thus similar to the expressions emerging in the context of TOPT, see e.g., the operator in Equation (50), and the corresponding matrix elements can also be interpreted in terms of TOPT-like diagrams. Notice that contrary to Equation (50), the expressions in the MUT do, per construction, not involve energy denominators that vanish in the static limit of infinitely heavy nucleons and correspond to iterative contributions to the scattering amplitude. As explained in Epelbaum [167], in order to implement the chiral power counting in the algebraic approach outlined above it is convenient to rewrite it in terms of different variables. Using the rules given in the description of the TOPT approach and counting the powers of the soft scale Q for a given irreducible (i.e., of non-iterative type) connected N-nucleon TOPT-like diagram without external sources, one obtains for the chiral order n [2, 167]

$$n = -4 + 2N + 2L + \sum_i V_i \Delta_i \,, \tag{57}$$

where L is the number of loops, V_i is the number of vertices of type i. Further, the vertex dimension Δ_i is given by $\Delta_i = d_i + 1/2 n_i - 2$ with d_i and n_i being the number of derivatives and/or m_π-insertions and the number of nucleon fields, respectively. The above expression is convenient to use for estimating the chiral dimension of TOPT-like diagrams. For the MUT, it is, however, advantageous to rewrite it in the equivalent form

$$n = -2 + \sum_i V_i \kappa_i \,, \qquad \kappa_i = d_i + \frac{3}{2} n_i + p_i - 4 \,, \tag{58}$$

where p_i is the number of pionic fields. The parameter κ_i obviously corresponds to the inverse overall mass dimension of the coupling constant(s) accompanying a vertex of type i. In this form, the chiral expansion becomes formally equivalent to the expansion in powers of the coupling constants, and it is straightforward to employ perturbation theory for solving the decoupling equation (56) and deriving the nuclear potentials $\eta \tilde{H} \eta$.

One non-trivial issue that emerges when applying chiral EFT to nuclear potentials concerns their renormalization. While on-shell scattering amplitudes, calculated in chiral EFT, can always be made finite by including the counterterms from the effective Lagrangian (provided one uses a chiral-symmetry preserving regularization scheme such as dimensional regularization), nuclear potentials represent scheme-dependent quantities, which correspond to non-iterative parts of the scattering amplitude. There is no a priori reason to expect all ultraviolet divergences emerging from TOPT-like diagrams, which give rise to nuclear forces, to be absorbable into a redefinition of the LECs. Indeed, it was found that the static PCTC three-nucleon force at order Q^4 of the two-pion-one-pion exchange type cannot be renormalized if one uses the unitary transformation given in Equation (55) [168]. On the other hand, the employed parametrization of the operator U is clearly not the most general one and represents just one possible choice. The freedom to change the off-shell behavior of the nuclear potentials, already mentioned in the context of TOPT, has been exploited in a systematic way in the PCTC sector in order to enforce renormalizability of nuclear forces (using dimensional regularization) [167, 169–172]. The MUT has also been successfully applied to the effective Lagrangian in the presence of external classical sources in order to derive the corresponding nuclear current operators, see [160] and references therein.

3.4. The PVTC Potential Up to Order Q^2

In this subsection we will discuss in detail the derivation of the PVTC potential up to N^{2}LO using the TOPT approach. We consider diagrams contributing to the T-matrix with one vertex coming from the PVTC Lagrangian, with all other vertices coming from the PCTC interaction. Diagrams with two or more PVTC vertices can be safely neglected.

The TOPT diagrams contributing to the PVTC T-matrix up to N^{2}LO are shown in **Figure 1**.

The one pion exchange diagram (a) gives a contribution to the T-matrix of order Q^{-1} (that will be our LO). The diagram (b) represents a PVTC contact interaction of order Q; also the diagrams (c) and (d) with the PCTC contact vertex and one pion exchange are of order Q. The triangle diagram (e) with a PCTC $\pi\pi NN$ vertex is of order Q, while if we consider the PVTC $\pi\pi NN$ vertex as in panel (l) the diagram is of order Q^2. The box diagrams (f) and (g) includes contribution of order Q^0 and Q; the contribution of order Q^0 is exactly canceled when inverting Equation (53). Finally, the "bubble" diagram (h), the three-pion vertex diagram (i), the box diagram (j) with the πNN vertex coming from the subleading PVTC Lagrangian terms proportionals to the LECs h_V^i, and also the diagram (k) with the $\pi\pi NN$ vertex coming from the subleading PCTC Lagrangian terms proportionals to the LECs c_i, are of order Q^2. These latter diagrams were considered for the first time in de Vries et al. [173] using the MUT, and using TOPT in [174].

Contributions proportional to $1/M$ coming from the NR expansion of the vertex functions or from recoil corrections in this work are considered to be at least of order N^{3}LO.

Other types of diagrams like those shown in **Figure 2**(1–3) simply contribute to a renormalization of the coupling constants and masses, see Viviani et al. [42] for more details. In the following, we will disregard these diagrams, but it should be taken into account that the formulas below are given in terms of the renormalized (physical) LECs and masses. The contribution of diagram (4) is canceled when inverting Equation (53).

Let us now consider each kind of diagram separately:

- *One pion exchange (OPE) diagram.* Diagram (a) of **Figure 1** gives the LO contribution (Q^{-1}) to the potential

$$V_{PVTC}^{(-1)}(a) = \frac{g_A h_\pi^1}{2\sqrt{2} f_\pi} (\vec{\tau}_1 \times \vec{\tau}_2)_z \frac{i\boldsymbol{k} \cdot (\boldsymbol{\sigma}_1 + \boldsymbol{\sigma}_2)}{\omega_k^2} \,, \tag{59}$$

  where $\omega_k = \sqrt{k^2 + m_\pi^2}$ and arises directly from the LO expansion of the vertices and energy denominators. Derived from the same diagram, there are terms coming from the NR expansion of the vertices, the first correction being of order $(p/M)^2$. However, as discussed previously, they are counted

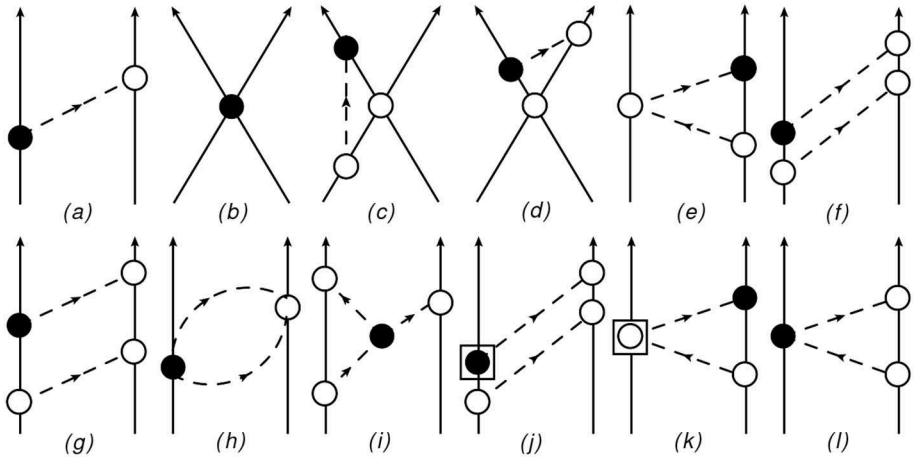


FIGURE 1 | TOPT diagrams contributing up to N^{2}LO to the PVTC amplitude. Nucleons and pions are denoted by solid and dashed lines, respectively. The open (solid) circles represent LO PCTC (PVTC) vertices. The vertex depicted by a square sourrounding a solid circle denotes the contribution of the subleading PVTC πNN terms coming from the Lagrangian given in Equation (19). The vertex depicted by a square surrounding an open circle denotes the contribution of the subleading PCTC $\pi\pi NN$ (PVTC πNN) terms coming from the Lagrangian given in Equation (13).

to be of order Q^4, and thus the corresponding terms are considered to be suppressed by four orders with respect to $V^{(-1)}_{PVTC}$.

- *Contact terms (CT) diagrams.* The diagrams (b) depicted in **Figure 1** derive from the interaction terms appearing in $\mathcal{L}^{(1)}_{PVTC,NN}$. They give a contribution to the potential of order Q^1. As discussed in Chapter 4, this contribution can be written in various equivalent forms due to the Fierz identities [44]. We have chosen to write this part as follows [42]

$$\begin{aligned} V^{(1)}_{PVTC}(b) \;=\; & \frac{1}{\Lambda_\chi^2 f_\pi}[C_1 i(\boldsymbol{\sigma}_1\times\boldsymbol{\sigma}_2)\cdot\boldsymbol{k} + C_2(\vec{\tau}_1\cdot\vec{\tau}_2) i(\boldsymbol{\sigma}_1\times\boldsymbol{\sigma}_2)\cdot\boldsymbol{k} \\ & + C_3(\vec{\tau}_1\times\vec{\tau}_2)_z i(\boldsymbol{\sigma}_1+\boldsymbol{\sigma}_2)\cdot\boldsymbol{k} \\ & + C_4(\tau_{1z}+\tau_{2z}) i(\boldsymbol{\sigma}_1\times\boldsymbol{\sigma}_2)\cdot\boldsymbol{k} \\ & + C_5 \mathcal{I}_{ab}\tau_{1a}\tau_{2b} i(\boldsymbol{\sigma}_1\times\boldsymbol{\sigma}_2)\cdot\boldsymbol{k}]\,. \end{aligned} \tag{60}$$

where $\Lambda_\chi = 4\pi f_\pi \approx 1.2$ GeV. The parameters $C_i, i = 1,\ldots,5$ are LECs. Different (but equivalent) forms of this part were used in de Vries et al. [41] and de Vries et al. [173].

- *Contact plus OPE diagrams.* The diagrams (c) and (d) in **Figure 1** are representative of diagrams containing a contact term and an OPE. However all these diagrams vanish after the integration over the loop variable.
- *NLO two pions exchange: triangle diagrams.* There are 6 different time-orderings of diagrams (e) given in **Figure 1**. After summing them, the total contribution from these diagrams results to be [40, 175]

$$\begin{aligned} V^{(1)}_{PVTC}(e) \;=\; & \frac{g_A h^1_\pi}{8\sqrt{2} f_\pi^3}(\vec{\tau}_1\times\vec{\tau}_2)_z i\boldsymbol{k}\cdot(\boldsymbol{\sigma}_1+\boldsymbol{\sigma}_2) \\ & \int \frac{d^3q}{(2\pi)^3}\frac{1}{\omega_+\omega_-(\omega_+ + \omega_-)}\,, \end{aligned} \tag{61}$$

where $\omega_\pm = \sqrt{(\boldsymbol{q}\pm\boldsymbol{k})^2 + 4m_\pi^2}$. The integral is singular and must be somehow regularized. We will discuss this issue later.

- *NLO two pions exchange: box diagrams.* There are 48 diagrams represented by the diagrams of type (f) and (g) of **Figure 1** when we consider all possible time orderings. The final contribution is [40, 175]

$$\begin{aligned} V^{(1)}_{PVTC}(f,g) = & \frac{h^1_\pi g_A^3}{8\sqrt{2} f_\pi^3}\int\frac{d^3q}{(2\pi)^3}\frac{\omega_+^2+\omega_+\omega_- + \omega_-^2}{\omega_+^3\omega_-^3\,(\omega_+ + \omega_-)} \\ & \{-2i\,(\tau_{1z}+\tau_{2z})\,[\boldsymbol{q}\cdot\boldsymbol{\sigma}_1(\boldsymbol{q}\times\boldsymbol{k})\cdot\boldsymbol{\sigma}_2 - \boldsymbol{q}\cdot\boldsymbol{\sigma}_2(\boldsymbol{q}\times\boldsymbol{k})\cdot\boldsymbol{\sigma}_1] \\ & -2i\,(\tau_{1z}-\tau_{2z})\,[\boldsymbol{q}\cdot\boldsymbol{\sigma}_2(\boldsymbol{q}\times\boldsymbol{k})\cdot\boldsymbol{\sigma}_1 + \boldsymbol{q}\cdot\boldsymbol{\sigma}_1(\boldsymbol{q}\times\boldsymbol{k})\cdot\boldsymbol{\sigma}_2] \\ & + i\,(\vec{\tau}_1\times\vec{\tau}_2)_z\left(k^2-q^2\right)\boldsymbol{k}\cdot(\boldsymbol{\sigma}_1+\boldsymbol{\sigma}_2)\}\,, \end{aligned} \tag{62}$$

and is of order Q^1. Again the integral is singular. In this case, in the amplitude T_{fi} there appears a term of order Q^0 coming from diagram (g), but it cancels out when inverting Equation (53).

- *Bubble diagrams.* We now turn to the diagrams contributing at order Q^2, that is at N^{2}LO. The sum of "bubble" diagrams (h) depicted in **Figure 1** mutually cancel and these diagrams do not give any contribution to the PVTC potential.
- *Diagrams with three pion vertices.* The expansion of the PVTC Lagrangian in terms of pions gives rise to two terms proportional to $(\vec{\pi})^3$ which would contribute to T_{fi} via the diagram (i) depicted in **Figure 1**. However, after summing over all possible time orderings, the corresponding final contribution vanishes.
- *N^{2}LO two pion exchanges: box diagrams.* The box diagrams (j) contributes also at N^{2}LO, where the PVTC vertex comes from the subleading Lagrangian terms proportional to the LECs h_0^V,

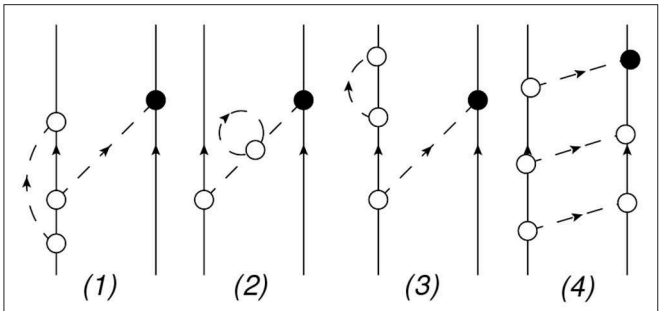


FIGURE 2 | Other diagrams that would contribute at NLO. These diagrams contribute to the renormalization of the LECs (1–3) or give a vanishing contribution to the potential (4) due to the inversion of Equation (53). Notation as in **Figure 1**.

h_1^V, and h_2^V in Equation (19). We have [75, 173]

$$
\begin{aligned}
V_{PVTC}^{(2)}(j) = \frac{g_A^3}{32 f_\pi^4}\Big[\Big(h_V^0(3+2\vec{\tau}_2\cdot\vec{\tau}_1) \\
-\frac{4}{3}h_V^2\mathcal{I}_{ab}\tau_{1b}\tau_{2b}\Big)i\int\frac{d^3q}{(2\pi)^3}\frac{1}{\omega_+^2\omega_-^2}[(\boldsymbol{q}\cdot\boldsymbol{\sigma}_1(\boldsymbol{q}\times\boldsymbol{k})\cdot\boldsymbol{\sigma}_2) \\
-(\boldsymbol{q}\cdot\boldsymbol{\sigma}_2(\boldsymbol{q}\times\boldsymbol{k})\cdot\boldsymbol{\sigma}_1)] \\
-2ih_V^1\int\frac{d^3q}{(2\pi)^3}\frac{1}{\omega_+^2\omega_-^2}[(\boldsymbol{q}\cdot\boldsymbol{\sigma}_1(\boldsymbol{q}\times\boldsymbol{k})\cdot\boldsymbol{\sigma}_2)\tau_{1z} \\
-(\boldsymbol{q}\cdot\boldsymbol{\sigma}_2(\boldsymbol{q}\times\boldsymbol{k})\cdot\boldsymbol{\sigma}_1)\tau_{2z}] \\
+ih_V^1(\vec{\tau}_1\times\vec{\tau}_2)_z\boldsymbol{k}\cdot(\boldsymbol{\sigma}_1+\boldsymbol{\sigma}_2)\int\frac{d^3q}{(2\pi)^3}\frac{q^2-k^2}{\omega_+^2\omega_-^2}\Big]. \qquad (63)
\end{aligned}
$$

- *N^2LO two pion exchanges: triangle diagrams.* The diagram depicted in panel (k) derives from subleading $\pi\pi NN$ vertices in the PCTC Lagrangians [75, 173], see Equation (13),

$$
\begin{aligned}
V_{PVTC}^{(2)}(k) = -i\frac{c_4 h_\pi^1 g_A}{2\sqrt{2}f_\pi^3}\int\frac{d^3q}{(2\pi)^3}\frac{1}{\omega_+^2\omega_-^2}\times \qquad (64) \\
[(\boldsymbol{q}\cdot\boldsymbol{\sigma}_1(\boldsymbol{q}\times\boldsymbol{k})\cdot\boldsymbol{\sigma}_2)\tau_{2z}-(\boldsymbol{q}\cdot\boldsymbol{\sigma}_2(\boldsymbol{q}\times\boldsymbol{k})\cdot\boldsymbol{\sigma}_1)\tau_{1z}].
\end{aligned}
$$

  Note in Equation (64) the presence of the LEC c_4, which belong to the PCTC sector [12].

  The expression for the diagrams (l) comes from the LO PCTC and PVTC vertex functions. The final result is [75, 173]

$$
\begin{aligned}
V_{PVTC}^{(2)}(l) = -\frac{g_A^2}{8f_\pi^4}\int\frac{d^3q}{(2\pi)^3}\frac{1}{\omega_+^2\omega_-^2} \qquad (65) \\
\times\{2h_A^1[(\boldsymbol{q}\cdot\boldsymbol{\sigma}_1(\boldsymbol{q}\times\boldsymbol{k})\cdot\boldsymbol{\sigma}_2)\tau_{2z}-(\boldsymbol{q}\cdot\boldsymbol{\sigma}_2(\boldsymbol{q}\times\boldsymbol{k})\cdot\boldsymbol{\sigma}_1)\tau_{1z}] \\
+h_A^2\mathcal{I}_{ab}\tau_{1a}\tau_{2b}[(\boldsymbol{q}\cdot\boldsymbol{\sigma}_1(\boldsymbol{q}\times\boldsymbol{k})\cdot\boldsymbol{\sigma}_2)-(\boldsymbol{q}\cdot\boldsymbol{\sigma}_2(\boldsymbol{q}\times\boldsymbol{k})\cdot\boldsymbol{\sigma}_1)]\},
\end{aligned}
$$

  where h_A^1 and h_A^2 are two of the LECs that appear in the Lagrangian terms given in Equation (19).

Finally, we conclude this section by mentioning that at N^2LO, one should also include PVTC 3N forces. Examples of diagrams contributing to this 3N force are shown in **Figure 3**. The chiral order of diagrams with more than two nucleons is discussed in detail in Epelbaum [167]. The diagram depicted in panel (a) with a LO PCTC $\pi\pi NN$ vertex would contribute at NLO, but vanishes when summed over all time orderings. The other three diagrams (the one in panel (b) has a subleading PCTC $\pi\pi NN$ vertex proportional to c_i, $i = 1,\ldots,4$ [12]) are N^2LO and therefore they must be considered in order to perform fully consistent calculations in $A \geq 3$ systems. However, these kind of diagrams have not yet been considered in literature. Note that diagrams with a 3N PVTC contact vertex are highly suppressed, so no new LEC needs to be introduced.

3.4.1. Regularization of the PVTC Potential

In this section we deal with the divergences in the loop diagrams. We will briefly present three methods frequently used in literature, namely the dimensional regularization (DR) method used e.g., in [161], the spectral function regularization (SFR) [176], and the novel (semi-)local momentum-space regularization approach of Reinert et al. [19].

- *Dimensional regularization method.* This technique is well-known for dealing with divergences of loop integrals present in Feynman diagrams, where the integration is performed over four-momenta. In case of time-ordered diagrams, the loops involve integration over three-momenta. To deal with the singularities, the integrals are re-defined in d dimensions and successively one takes the limit $d \to 3$. The singular part is singled out by terms $\sim 1/(3-d)$, which then can be reabsorbed in some of the LECs. As usual, we define $\epsilon = 3-d$, and we assume that $\epsilon \to 0$. When we use the DR, it is better to "rescale" all the dimensional quantities with an energy scale μ. Therefore we define $q = \tilde{q}\mu$, $m = \tilde{m}\mu$, etc., where the "tilde" quantities are dimensionless. We can now go to d dimensions and manipulate the integrals as discussed in detail in Pastore et al. [161], see also Friar [177]. Here we limit ourselves to listing the results needed to regularize the loop integrals we have encountered. Regarding the loop integrals appearing at NLO in Equations (61) and (62), we have

$$
\int\frac{d^3q}{(2\pi)^3}\,\frac{1}{\omega_+\,\omega_-\,(\omega_+ + \omega_-)} = -\frac{1}{4\pi^2}\Big(L(k) - d_\epsilon + 2\Big), \qquad (66)
$$

$$
\int\frac{d^3q}{(2\pi)^3}\,\frac{\omega_+^2 + \omega_+\,\omega_- + \omega_-^2}{\omega_+^3\,\omega_-^3(\omega_+ + \omega_-)} = \frac{1}{16\pi^2}\,\frac{H(k)}{m_\pi^2}, \qquad (67)
$$

  where

$$
\begin{aligned}
L(k) = \frac{1}{2}\frac{s}{k}\ln\frac{s+k}{s-k}, \qquad H(k) = \frac{4m_\pi^2}{s^2}L(k), \\
s = \sqrt{4\,m_\pi^2 + k^2}, \qquad (68)
\end{aligned}
$$

  and

$$
d_\epsilon = \frac{2}{\epsilon} - \gamma + \ln\pi - \ln\frac{m_\pi^2}{\mu^2}, \qquad (69)
$$

  which contains the divergent part, where γ is the Euler–Mascheroni constant.

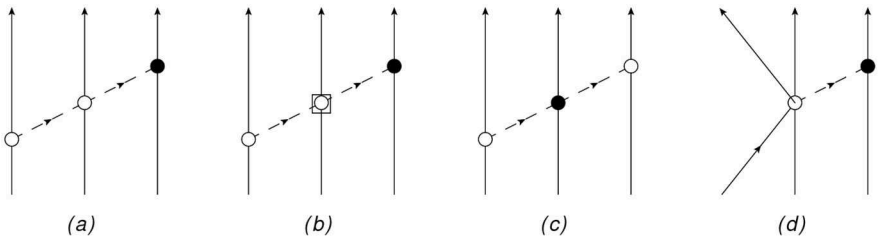


FIGURE 3 | TOPT diagrams that would contribute to the PVTC 3N force For the notation see **Figure 1**.

The loop integrals appearing in the N^{2}LO diagrams as in Equations (64) and (65) are of the form

$$\int \frac{d^3q}{(2\pi)^3} \frac{1}{\omega_+^2 \omega_-^2}\,, \tag{70}$$

$$\int \frac{d^3q}{(2\pi)^3} \frac{1}{\omega_+^2 \omega_-^2} q_i q_j\,, \tag{71}$$

The first integral is finite, but the second integrand diverges linearly as $q \to \infty$. The finite contribution can be obtained using the DR method. Alternatively, one can impose an ultraviolet cut-off Λ_C on the integrals. The integrals then yield divergent pieces as $\Lambda_C \to \infty$, which can be again reabsorbed in some LECs, finite parts independent on Λ_C that are exactly the same as obtained using the DR method, and a number of other terms which can be expressed in terms of a power series of Q/Λ_C, where Q is either k or m_π. Taking the limit Λ_C to infinity these latter parts would disappear. Since, in general we must fix Λ_C at a value greater than the typical energies of the χEFT, then these additional terms carry at least an additional power of Q which means they give contributions at N^{3}LO (or beyond) to the potential. Therefore, for the integral in Equation (71), we have followed the prescription to absorb the divergent parts in some LEC's, to disregard the parts depending on Q/Λ_C, and to retain the finite parts as given by the DR method. Explicitly, the two integrals are given by

$$\int \frac{d^3q}{(2\pi)^3}\ \frac{1}{\omega_+^2\,\omega_-^2} = \frac{A(k)}{4\pi}\,, \tag{72}$$

$$\int \frac{d^3q}{(2\pi)^3}\ \frac{1}{\omega_+^2\,\omega_-^2} q_i q_j \Rightarrow \Big(-\frac{s^2 A(k)}{8\pi} - \frac{m_\pi}{8\pi}\Big)\delta_{ij} + \Big(\frac{s^2 A(k)}{8\pi} - \frac{m_\pi}{8\pi}\Big)\frac{k_i\,k_j}{k^2}\,, \tag{73}$$

where

$$A(k) = \frac{1}{2k} \arctan\Big(\frac{k}{2m_\pi}\Big)\,. \tag{74}$$

- *Spectral function regularization method.* Pion loop integrals appearing in the two-pion exchange contributions discussed in the previous subsection can be generally expressed using a dispersive representation. Writing the momentum-space potentials in the general form $V = \sum_i O_i W_i(k)$ with O_i being spin-isospin-momentum operators and W_i the corresponding structure functions that depend only on the momentum transfer $k \equiv |\boldsymbol{k}|$, the unsubtracted dispersion relations for the functions $W_i(k)$ have the form [178]

$$W_i(k) = \frac{2}{\pi} \int_{2m_\pi}^{\infty} d\mu\, \mu \frac{\rho_i(\mu)}{\mu^2 + k^2}\,, \tag{75}$$

where the spectral functions $\rho_i(\mu)$ are given by $\rho_i = \Im\big(W_i(0^+ - i\mu)\big)$. Notice that the spectral integrals in Equation (75) do not converge for potentials derived in chiral EFT since $\rho_i(\mu)$ generally grow with μ, and must be subtracted the appropriate number of times. The subtractions introduce terms which are polynomial in k^2 and can be absorbed into the corresponding contact interactions. It was shown in Epelbaum et al. [176] that even at fairly large internucleon distances, the potentials receive significant contributions from the spectral function in the region of $\mu \gtrsim \Lambda_\chi$, where the chiral expansion cannot be trusted. It was, therefore, proposed in that paper to employ an ultraviolet cutoff Λ in the spectral integrals. This can be shown to be equivalent to introducing a particular ultraviolet cutoff in the loop integrals over the momentum q. Using a sharp cutoff Λ in the spectral integrals over μ leads to the following modification of the loop functions $L(k)$ and $A(k)$:

$$L^\Lambda(k) = \theta(\Lambda - 2m_\pi)\,\frac{s}{2k}\,\ln\frac{\Lambda^2 s^2 + k^2 l^2 + 2\Lambda k s l}{4m_\pi^2(\Lambda^2 + k^2)}\,,$$
$$A^\Lambda(k) = \theta(\Lambda - 2m_\pi)\,\frac{1}{2k}\,\arctan\frac{k(\Lambda - 2m_\pi)}{k^2 + 2\Lambda m_\pi}\,, \tag{76}$$

where we have introduced $l = \sqrt{\Lambda^2 - 4m_\pi^2}$. The resulting approach is referred to as the spectral function regularization. The limit of an infinitely large cutoff Λ corresponds to the previously considered case of dimensional regularization with $L^\infty(k) = L(k)$ and $A^\infty(k) = A(k)$. The spectral function regularization approach with a finite value of Λ was employed in the PCTC potentials of Epelbaum et al. [74] and the more recent work [18], as well as in the derivation of the N^{2}LO PVTC potential in de Vries et al. [46].

- *Local regularization in momentum space.* The previously introduced spectral function regularization approach has the unpleasant feature of inducing *long-range* finite-Λ artifacts as can be seen by expanding the functions $L^\Lambda(k)$ and $A^\Lambda(k)$ in inverse powers of Λ. This feature may affect the applicability of

chiral EFT for softer cutoff choices. Recently, local regulators in coordinate [17, 179] and momentum space [19] were introduced, which do not affect the analytic structure of the pion-exchange interactions and thus maintain the long-range part of the nuclear force. The approach of Reinert et al. [19] amounts to replacing the static propagators of pions exchanged between different nucleons via

$$\frac{1}{q^2+m_\pi^2} \quad \longrightarrow \quad \frac{1}{q^2+m_\pi^2}\,\exp\left(-\frac{q^2+m_\pi^2}{\Lambda^2}\right), \tag{77}$$

with $q \equiv |\boldsymbol{q}|$. Such a regulator obviously does not induce any long-range artifacts at any order in the $1/\Lambda$-expansion. This regularization approach can be easily implemented for two-pion exchange NN potentials with no need to recalculate the various loop integrals. Using the feature that the regulator does not affect long-range interactions, it is easy to show that the regularization of a generic two-pion exchange contribution simply amounts to introducing a specific cutoff in the dispersive representation (modulo short-range interactions), namely [19]

$$\begin{aligned}&\frac{2}{\pi}\int_{2m_\pi}^{\infty} d\mu\,\mu\,\frac{\rho_i(\mu)}{\mu^2+k^2}\\ &\longrightarrow \quad \frac{2}{\pi}\int_{2m_\pi}^{\infty} d\mu\,\mu\,\frac{\rho_i(\mu)}{\mu^2+k^2}\,\exp\left(-\frac{\mu^2+k^2}{2\Lambda^2}\right).\end{aligned} \tag{78}$$

In Reinert et al. [19], the regularized two-pion exchange contributions were defined using the requirement (i.e., a convention) that the corresponding potentials in coordinate space and derivatives thereof vanish at the origin. This is achieved by adding to the right-hand side of Equation (78) a specific combination of (locally regularized) contact interactions allowed by the power counting. For more details and explicit expressions see Reinert et al. [19]. This local regularization scheme has not been used for PVTC or PVTV nuclear potentials.

3.4.2. The Regularized PVTC Potential

Once the loop integrals have been manipulated as discussed previously, we can now write the PVTC potential up to N^{2}LO derived from χEFT. In the following, some of the LEC's have been further redefined to absorb the singular parts coming from the loop integrals. If one has chosen to regularize the loop integral using the SFR method, then the functions $L(k)$ and $A(k)$ below have to be substituted with $L^\Lambda(k)$ and $A^\Lambda(k)$, the spectral regularized functions, see Equation (76). In summary,

$$\begin{aligned}V_{PVTC} \;=\; & V_{PVTC}^{(-1)}(\mathrm{OPE}) + V_{PVTC}^{(1)}(\mathrm{CT}) + V_{PVTC}^{(1)}(\mathrm{TPE})\\ & + V_{PVTC}^{(2)}(\mathrm{TPE}),\end{aligned} \tag{79}$$

where

$$V_{PVTC}^{(-1)}(\mathrm{OPE}) \;=\; \frac{g_A h_\pi^1}{2\sqrt{2}f_\pi}\,(\vec\tau_1\times\vec\tau_2)_z\,\frac{i\boldsymbol{k}\cdot(\boldsymbol{\sigma}_1+\boldsymbol{\sigma}_2)}{\omega_k^2}, \tag{80}$$

$$\begin{aligned}V_{PVTC}^{(1)}(\mathrm{CT}) \;=\; & \frac{1}{\Lambda_\chi^2 f_\pi}[C_1 i(\boldsymbol{\sigma}_1\times\boldsymbol{\sigma}_2)\cdot\boldsymbol{k}\\ & + C_2(\vec\tau_1\cdot\vec\tau_2) i(\boldsymbol{\sigma}_1\times\boldsymbol{\sigma}_2)\cdot\boldsymbol{k}\\ & + C_3(\vec\tau_1\times\vec\tau_2)_z i(\boldsymbol{\sigma}_1+\boldsymbol{\sigma}_2)\cdot\boldsymbol{k}\\ & + C_4(\tau_{1z}+\tau_{2z}) i(\boldsymbol{\sigma}_1\times\boldsymbol{\sigma}_2)\cdot\boldsymbol{k}\\ & + C_5\mathcal{I}_{ab}\tau_{1a}\tau_{2b} i(\boldsymbol{\sigma}_1\times\boldsymbol{\sigma}_2)\cdot\boldsymbol{k}],\end{aligned} \tag{81}$$

$$\begin{aligned}V_{PVTC}^{(1)}(\mathrm{TPE}) \;=\; & -\frac{g_A h_\pi^1}{2\sqrt{2}f_\pi}\frac{1}{\Lambda_\chi^2}(\vec\tau_1\times\vec\tau_2)_z i\boldsymbol{k}\cdot(\boldsymbol{\sigma}_1+\boldsymbol{\sigma}_2)L(k)\\ & - \frac{g_A^3 h_\pi^1}{2\sqrt{2}f_\pi}\frac{1}{\Lambda_\chi^2}\Big[4(\tau_{1z}+\tau_{2z})\; i\boldsymbol{k}\cdot(\boldsymbol{\sigma}_1\times\boldsymbol{\sigma}_2)\;L(k)\\ & + (\vec\tau_1\times\vec\tau_2)_z i\boldsymbol{k}\cdot(\boldsymbol{\sigma}_1+\boldsymbol{\sigma}_2)\Big(H(k)-3L(k)\Big)\Big],\end{aligned} \tag{82}$$

$$\begin{aligned}V_{PVTC}^{(2)}(\mathrm{TPE}) \;=\; & -\frac{c_4 h_\pi^1 g_A}{\sqrt{2}f_\pi}\frac{\pi}{\Lambda_\chi^2} i\boldsymbol{k}\cdot(\boldsymbol{\sigma}_1\times\boldsymbol{\sigma}_2)(\tau_{1z}+\tau_{2z})s^2A(k)\\ & + \frac{g_A^2}{2f_\pi^2}\frac{\pi}{\Lambda_\chi^2}\Big\{\Big[\frac{3g_A h_V^0}{4}+\frac{g_A h_V^0}{2}\vec\tau_1\cdot\vec\tau_2\\ & + \Big(\frac{g_A h_V^1}{4}-h_A^1\Big)(\tau_{1z}+\tau_{2z})\\ & - \Big(h_A^2+\frac{g_A h_V^2}{3}\Big)\mathcal{I}_{ab}\tau_{1b}\tau_{2b}\Big] i\boldsymbol{k}\cdot(\boldsymbol{\sigma}_1\times\boldsymbol{\sigma}_2)\\ & - \frac{g_A h_V^1}{2}(\vec\tau_1\times\vec\tau_2)_z i\boldsymbol{k}\cdot(\boldsymbol{\sigma}_1+\boldsymbol{\sigma}_2)\Big(1-\frac{2m_\pi^2}{s^2}\Big)\Big\}s^2A(k).\end{aligned} \tag{83}$$

The NLO term $V_{PVTC}^{(1)}$(TPE) derives from the regularized parts of $V_{PVTC}^{(1)}(e)$ and $V_{PVTC}^{(1)}(f,g)$, while the N^{2}LO term $V_{PVTC}^{(2)}$(TPE) from $V_{PVTC}^{(1)}(j)$, $V_{PVTC}^{(1)}(k)$, and $V_{PVTC}^{(1)}(l)$. Let us note that we have in total 11 LECs that must be determined from the experimental data: one in the LO term, five in the subleading order and five at N^{2}LO. This potential is the same as the one derived using the MUT in de Vries et al. [173].

Finally, the potential to be used in calculation of PVTC observables has to be regularized for large values of $\boldsymbol{p}$, $\boldsymbol{p}'$. The frequently used procedure is to multiply by a cutoff function containing a parameter Λ_C

$$V_{PVTC}(\boldsymbol{p},\boldsymbol{p}') \to f_{\Lambda_C}(\boldsymbol{p},\boldsymbol{p}')V_{PVTC}(\boldsymbol{p},\boldsymbol{p}'). \tag{84}$$

Typical choices for f_{Λ_C} are [74]

$$f_{\Lambda_C}(\boldsymbol{p},\boldsymbol{p}') = \exp\left[-\left(\frac{p}{\Lambda_C}\right)^n-\left(\frac{p'}{\Lambda_C}\right)^n\right], \tag{85}$$

where usually $n = 6$, adopted for example in de Vries et al. [173], or

$$f_{\Lambda_C}(\boldsymbol{p},\boldsymbol{p}') = \exp\left[-\left(\frac{|\boldsymbol{p}-\boldsymbol{p}'|}{\Lambda_C}\right)^4\right], \tag{86}$$

adopted in Viviani et al. [42]. The value of the cutoff Λ_C is chosen to be around 400–600 MeV, and consistent with the analogous parameter used to regularize the PCTC potential.

The currently most accurate and precise PCTC NN potentials of Reinert et al. [19] employ the local momentum-space regularization approach for pion-exchange contributions as described in section 3.4.1 in combination with a non-local Gaussian regulator given in Equation (85) with $n = 2$ and $\Lambda_C = \Lambda$ for contact interactions [Λ is the cutoff used in the local regulator in Equations (77), (78)]. The superior performance of the momentum-space regulator in Equation (78), as compared with both the spectral-function regularization and a local multiplicative regularization as defined in Equation (86), manifests itself in exponentially small distortions at large distances as visualized in Figure 5 of [19].

Last but not least, we emphasize that using *different* regulators when calculating loop integrals in the nuclear potentials/currents and solving the Schrödinger equation to compute observables is generally incorrect. This issue becomes relevant at the chiral order, at which one encounters the first loop contributions to the 3N potentials and to the NN exchange current operators (i.e., at order Q^4 or N^{3}LO in the PCTC sector) [180, 181], which is beyond the accuracy of the calculations described in this review article. For more details and a discussion of a possible solution to this problem see [182].

3.4.3. Relevant PCTC and PVTC Electromagnetic Currents

Electromagnetic currents can be calculated in the χEFT expansion. For our purposes we require currents for the longitudinal asymmetry in radiative neutron capture on a proton target at thermal energies. As we deal with a real outgoing photon, the LO PCTC current is induced by the nucleon magnetic moment. At NLO there are contributions from the convection currents and one-pion-exchange currents proportional to g_A^2. At NLO the relevant currents become

$$\begin{aligned}\boldsymbol{J}_{PCTC} = &\sum_{j=1}^{A}\frac{e}{4M}\left\{-\left[(1+\kappa_0)+(1+\kappa_1)\tau_{jz}\right]i(\boldsymbol{\sigma}_j\times\boldsymbol{q})\right.\\ &\left.+(1+\tau_{jz})(\boldsymbol{p}_j+\boldsymbol{p}_j')\right\}\delta_{\boldsymbol{p}_j-\boldsymbol{p}_j',\boldsymbol{q}}\\ &+\frac{eg_A^2}{4f_\pi^2}\sum_{j<k}^{A} i\left(\vec{\tau}_j\times\vec{\tau}_k\right)_z\left\{2\boldsymbol{k}\,\frac{\boldsymbol{\sigma}_j\cdot(\boldsymbol{k}+\boldsymbol{q}/2)}{(\boldsymbol{k}+\boldsymbol{q}/2)^2+m_\pi^2}\,\frac{\boldsymbol{\sigma}_k\cdot(\boldsymbol{k}-\boldsymbol{q}/2)}{(\boldsymbol{k}-\boldsymbol{q}/2)^2+m_\pi^2}\right.\\ &\left.-\boldsymbol{\sigma}_j\,\frac{\boldsymbol{\sigma}_k\cdot(\boldsymbol{k}-\boldsymbol{q}/2)}{(\boldsymbol{k}-\boldsymbol{q}/2)^2+m_\pi^2}-\boldsymbol{\sigma}_k\,\frac{\boldsymbol{\sigma}_j\cdot(\boldsymbol{k}+\boldsymbol{q}/2)}{(\boldsymbol{k}+\boldsymbol{q}/2)^2+m_\pi^2}\right\},\end{aligned}\tag{87}$$

where $\kappa_0 = -0.12$ and $\mu_v = 3.71$ are the isoscalar and isovector anomalous nucleon magnetic moments. $\boldsymbol{p}_j$ and $\boldsymbol{p}_j'$ denote the incoming and outgoing momenta of nucleon j interacting with a photon of outgoing momentum $\boldsymbol{q}$. The intermediate pions carry momenta $\boldsymbol{k}+\boldsymbol{q}/2 = \boldsymbol{p}_j-\boldsymbol{p}_j'$ or $\boldsymbol{k}-\boldsymbol{q}/2 = \boldsymbol{p}_k'-\boldsymbol{p}_k$. de Vries et al. [173] used these currents in combination with N^{3}LO χEFT potentials from Epelbaum et al. [17] to calculate the total $np \to d\gamma$ capture cross section. Using just the LO currents gives a cross section of 305 ± 4 mb, which grows to 319 ± 5 at NLO. The remaining 4% discrepancy to the experimental cross section 334.2 ± 0.5, indicates that N^{2}LO currents should probably be included.

A consistent calculation of PVTC observables such as the photon asymmetry in the $\vec{n}p \to d\gamma$ radiative capture also requires the inclusion of PVTC currents. There is no one-body current in this case, as the anapole moment vanishes for on-shell photons [183]. As such, the leading PVTC currents arises from one-pion-exchange currents

$$\begin{aligned}\boldsymbol{J}_{PVTC} = &\frac{eg_Ah_\pi^1}{2\sqrt{2}f_\pi}\sum_{j<k}^{A}\left(\vec{\tau}_j\cdot\vec{\tau}_k-\tau_{jz}\tau_{kz}\right)\\ &\left\{2\boldsymbol{k}\frac{\boldsymbol{\sigma}_j\cdot(\boldsymbol{k}+\boldsymbol{q}/2)+\boldsymbol{\sigma}_k\cdot(\boldsymbol{k}-\boldsymbol{q}/2)}{[(\boldsymbol{k}+\boldsymbol{q}/2)^2+m_\pi^2][(\boldsymbol{k}-\boldsymbol{q}/2)^2+m_\pi^2]}\right.\\ &\left.-\frac{\boldsymbol{\sigma}_j}{(\boldsymbol{k}-\boldsymbol{q}/2)^2+m_\pi^2}-\frac{\boldsymbol{\sigma}_k}{(\boldsymbol{k}+\boldsymbol{q}/2)^2+m_\pi^2}\right\},\end{aligned}\tag{88}$$

where we stress the dependence on the PVTC pion-nucleon LEC h_π^1. Higher-order PVTC currents have not been developed.

3.5. The PVTV Potential Up to Order *Q*

In this section, we discuss the derivation of the PVTV NN and 3N potentials at N^{2}LO. The final expressions are given in terms of a sum of diagrams, which can be obtained either using the MUT [4, 166, 184], standard dimensional regularization [72] or the TOPT method [75]. In the following, we briefly report the derivation of the PVTV potential in the framework of TOPT approach.

The TOPT diagrams that give contribution to the NN PVTV potential up to N^{2}LO (order Q^1) are shown in **Figure 4**. We do not consider diagrams which give contributions only to the renormalization of the LECs. In this section we write the final expression of the NN PVTV potential V_{PVTV} having already taken into account the singular parts coming from loops. Note that for the PVTV potential the LO term is of order Q^{-1} as for the PVTC case. However, now there will be terms of order Q^0, which will be denoted as NLO terms, etc. We have

$$\begin{aligned}V_{PVTV}(\boldsymbol{p},\boldsymbol{p}') = &\,V_{PVTV}^{(-1)}(\mathrm{OPE})+V_{PVTV}^{(1)}(\mathrm{CT})+V_{PVTV}^{(1)}(\mathrm{TPE})\\ &+V_{PVTV}^{(0)}(3\pi)+V_{PVTV}^{(1)}(3\pi),\end{aligned}\tag{89}$$

namely coming from OPE diagrams at LO, TPE at N^{2}LO, three-pion vertices (3π) at NLO and at N^{2}LO, and contact contributions (CT). From now on we define $\bar{g}_0^* = \bar{g}_0 + \bar{g}_2/3$. In this case, we report here the final form of the potential, namely, the LECs appearing in the expressions below are the physical ones, having reabsorbed the various infinities generated by loops and diagrams like those shown in **Figure 2**(1–3).

- *One pion exchange diagram.* The OPE term, depicted in diagram (a) of **Figure 4**, gives a contribution at LO, namely

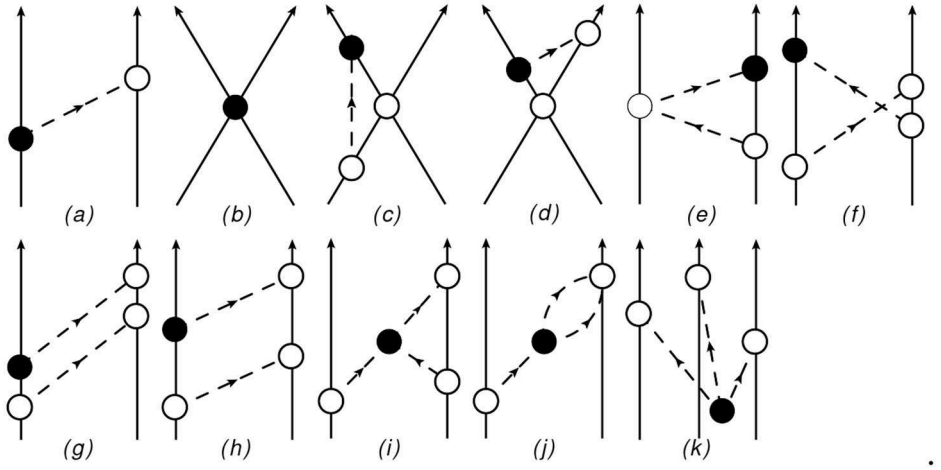


FIGURE 4 | Time-ordered diagrams contributing to the PVTV potential (only a single time ordering is shown). Nucleons and pions are denoted by solid and dashed lines, respectively. The open (solid) circle represents a PCTC (PVTV) vertex.

of order Q^{-1}, coming from the NR expansion of the vertices

$$V^{(-1)}_{PVTV}(\text{OPE}) = \frac{g_A \bar{g}^*_0}{2f_\pi}(\vec{\tau}_1 \cdot \vec{\tau}_2)\frac{i\boldsymbol{k}\cdot(\boldsymbol{\sigma}_1-\boldsymbol{\sigma}_2)}{\omega_k^2} + \frac{g_A \bar{g}_2}{6f_\pi}(3\tau_{1z}\tau_{2z}-\vec{\tau}_1\cdot\vec{\tau}_2)\frac{i\boldsymbol{k}\cdot(\boldsymbol{\sigma}_1-\boldsymbol{\sigma}_2)}{\omega_k^2} + \frac{g_A \bar{g}_1}{4f_\pi}\Big[(\tau_{1z}+\tau_{2z})\frac{i\boldsymbol{k}\cdot(\boldsymbol{\sigma}_1-\boldsymbol{\sigma}_2)}{\omega_k^2} + (\tau_{z1}+\tau_{z2})\frac{i\boldsymbol{k}\cdot(\boldsymbol{\sigma}_1+\boldsymbol{\sigma}_2)}{\omega_k^2}\Big], \quad (90)$$

where there are an isoscalar, an isovector and an isotensor components. Contributions coming from the $1/M$ expansion are considered to be suppressed at least by four orders with respect to $V^{(-1)}_{PVTV}(\text{OPE})$.

- *Contact term diagrams.* The potential $V^{(1)}_{PVTV}(\text{CT})$, derived from the NN contact diagrams (b) of **Figure 4**, reads

$$V^{(1)}_{PVTV}(\text{CT}) = \frac{1}{\Lambda_\chi^2 f_\pi}\Big\{\bar{C}_1\, i\boldsymbol{k}\cdot(\boldsymbol{\sigma}_1-\boldsymbol{\sigma}_2) + \bar{C}_2\, i\boldsymbol{k}\cdot(\boldsymbol{\sigma}_1-\boldsymbol{\sigma}_2)\,\vec{\tau}_1\cdot\vec{\tau}_2 + \frac{\bar{C}_3}{2}\left[i\boldsymbol{k}\cdot(\boldsymbol{\sigma}_1-\boldsymbol{\sigma}_2)(\tau_{1z}+\tau_{2z}) + i\boldsymbol{k}\cdot(\boldsymbol{\sigma}_1+\boldsymbol{\sigma}_2)(\tau_{1z}-\tau_{2z})\right] + \frac{\bar{C}_4}{2}\left[i\boldsymbol{k}\cdot(\boldsymbol{\sigma}_1-\boldsymbol{\sigma}_2)(\tau_{1z}+\tau_{2z}) - i\boldsymbol{k}\cdot(\boldsymbol{\sigma}_1+\boldsymbol{\sigma}_2)(\tau_{1z}-\tau_{2z})\right] + \bar{C}_5\, i\boldsymbol{k}\cdot(\boldsymbol{\sigma}_1-\boldsymbol{\sigma}_2)(3\tau_{1z}\tau_{2z}-\vec{\tau}_1\cdot\vec{\tau}_2)\Big\}. \quad (91)$$

Notice that the above LECs $\bar{C}_1$, $\bar{C}_2$, $\bar{C}_3$, $\bar{C}_4$, and $\bar{C}_5$ have been redefined to absorb various singular terms coming from the TPE and 3π diagrams. It is possible to write ten operators which can enter $V^{(1)}_{PVTV}(\text{CT})$ at order Q but only five of them are independent as discussed in Chapter 4. In this work we have chosen to write the operators in terms of $\boldsymbol{k}$, so that the r-space version of $V^{(1)}_{PVTV}(\text{CT})$ will assume a simple local form with no gradients.

- *Contact terms with an OPE.* Diagrams like (c) and (d) of **Figure 4** vanish directly due to the integration over the loop momentum.
- *Two pions exchange diagrams*. The TPE term comes from the non-singular contributions of diagrams (e-h) in **Figure 4**. This term has no isovector component, as shown for the first time in Bsaisou et al. [73]. It reads

$$V^{(1)}_{PVTV}(\text{TPE}) = \frac{g_A \bar{g}^*_0}{f_\pi \Lambda_\chi^2}\vec{\tau}_1\cdot\vec{\tau}_2\; i\boldsymbol{k}\cdot(\boldsymbol{\sigma}_1-\boldsymbol{\sigma}_2)\,L(k) + \frac{g_A^3 \bar{g}^*_0}{f_\pi \Lambda_\chi^2}\vec{\tau}_1\cdot\vec{\tau}_2\; i\boldsymbol{k}\cdot(\boldsymbol{\sigma}_1-\boldsymbol{\sigma}_2)\,(H(k)-3L(k)) - \frac{g_A \bar{g}_2}{3f_\pi \Lambda_\chi^2}(3\tau_{1z}\tau_{2z}-\vec{\tau}_1\cdot\vec{\tau}_2)\; i\boldsymbol{k}\cdot(\boldsymbol{\sigma}_1-\boldsymbol{\sigma}_2)\,L(k) - \frac{g_A^3 \bar{g}_2}{3f_\pi \Lambda_\chi^2}(3\tau_{1z}\tau_{2z}-\vec{\tau}_1\cdot\vec{\tau}_2) i\boldsymbol{k}\cdot(\boldsymbol{\sigma}_1-\boldsymbol{\sigma}_2)\,(H(k)-3L(k)), \quad (92)$$

where the loop functions $L(k)$ and $H(k)$ are defined in Equation (68).

- *Diagrams with three pion vertices* The 3π-exchange term gives a NLO contribution through the diagram (i) of **Figure 4**,

$$V^{(0)}_{PVTV}(3\pi) = -\frac{5g_A^3\bar{\Delta}M}{4f_\pi\Lambda_\chi^2}\pi\Big[(\tau_{1z}+\tau_{2z})\frac{i\boldsymbol{k}\cdot(\boldsymbol{\sigma}_1-\boldsymbol{\sigma}_2)}{\omega_k^2} + (\tau_{1z}-\tau_{2z})\frac{i\boldsymbol{k}\cdot(\boldsymbol{\sigma}_1+\boldsymbol{\sigma}_2)}{\omega_k^2}\Big] \times\Big((1-\frac{2m_\pi^2}{s^2})s^2A(k)+m_\pi\Big), \quad (93)$$

where $A(k)$ is given in Equation (74). Additional contributions coming from diagram (i) deriving from the $1/M$ expansion

of the energy denominators and vertex functions are here neglected since they are counted as N^{3}LO.

The diagram (j) in **Figure 4** contributes to $V_{PVTV}^{(3\pi)}$ at N^{2}LO,

$$
\begin{aligned}
V_{PVTV}^{(1)}(3\pi) = &\frac{5g_A\bar{\Delta}Mc_1}{2f_\pi\Lambda_\chi^2}\Big[(\tau_{1z}+\tau_{2z})i\boldsymbol{k}\cdot(\boldsymbol{\sigma}_1-\boldsymbol{\sigma}_2)\\
&+(\tau_{1z}-\tau_{2z})i\boldsymbol{k}\cdot(\boldsymbol{\sigma}_1+\boldsymbol{\sigma}_2)\Big]\,4\frac{m_\pi^2}{\omega_k^2}L(k)\\
&-\frac{5g_A\bar{\Delta}Mc_2}{6f_\pi\Lambda_\chi^2}\Big[(\tau_{1z}+\tau_{2z})i\boldsymbol{k}\cdot(\boldsymbol{\sigma}_1-\boldsymbol{\sigma}_2)\\
&+(\tau_{1z}-\tau_{2z})i\boldsymbol{k}\cdot(\boldsymbol{\sigma}_1+\boldsymbol{\sigma}_2)\Big]\Big(2L(k)+6\frac{m_\pi^2}{\omega_k^2}L(k)\Big)\\
&-\frac{5g_A\bar{\Delta}Mc_3}{4f_\pi\Lambda_\chi^2}\Big[(\tau_{1z}+\tau_{2z})i\boldsymbol{k}\cdot(\boldsymbol{\sigma}_1-\boldsymbol{\sigma}_2)\\
&+(\tau_{1z}-\tau_{2z})i\boldsymbol{k}\cdot(\boldsymbol{\sigma}_1+\boldsymbol{\sigma}_2)\Big]\Big(3L(k)+5\frac{m_\pi^2}{\omega_k^2}L(k)\Big)\,.
\end{aligned}
\tag{94}
$$

Note in Equation (94) the presence of the c_1, c_2, and c_3 LECs, which belong to the PCTC Lagrangian given in Equation (13). In Equations (93) and (94), $\bar{\Delta}$ is a renormalized LEC.

The 3π PVTV vertex gives rise to a three body interaction through the diagram (k) in **Figure 4**. The lowest contribution appears at NLO while at N^{2}LO the various time orderings cancel out [75]. The final expression for the NLO of the 3N PVTV potential is,

$$
\begin{aligned}
V_{PVTV}^{(0)}(3\mathrm{N}) = &\frac{\bar{\Delta}g_A^3M}{4f_\pi^3}(\vec{\tau}_1\cdot\vec{\tau}_2\,\tau_{3z}+\vec{\tau}_1\cdot\vec{\tau}_3\,\tau_{2z}+\vec{\tau}_2\cdot\vec{\tau}_3\,\tau_{1z})\\
&\times\frac{(i\boldsymbol{k}_1\cdot\boldsymbol{\sigma}_1)\,(i\boldsymbol{k}_2\cdot\boldsymbol{\sigma}_2)\,(i\boldsymbol{k}_3\cdot\boldsymbol{\sigma}_3)}{\omega_{k_1}^2\omega_{k_2}^2\omega_{k_3}^2}\,,
\end{aligned}
\tag{95}
$$

where $\boldsymbol{k}_i=\boldsymbol{p}_i'-\boldsymbol{p}$. This expression is in agreement with that reported in deVries et al. [68] and Bsaisou et al. [69].

3.5.1. The PVTV Current

The PVTV current up to now has been considered to arise from the LO one-body contribution

$$
\boldsymbol{J}_{PVTV}=-\sum_{j=1}^{A}\left[d_p\frac{1+\tau_{jz}}{2}+d_n\frac{1-\tau_{jz}}{2}\right]i(\boldsymbol{\sigma}_j\cdot\boldsymbol{q})\,,
\tag{96}
$$

where d_p (d_n) is the proton (neutron) EDM. In nuclear physics applications, it is customary to consider d_p and d_n as unknown parameters, although they in principle can be estimated in terms of the LECs entering the χEFT, as we have seen in section 3.2.2. The complete derivation of PVTV two-body currents has not been completed, though partial results have been given in de Vries et al. [143] and Bsaisou et al. [73].

4. PVTC AND PVTV POTENTIALS IN PIONLESS EFT

In this section, we specifically focus on the few-nucleon contact interactions which enter the potentials in both chiral and pionless EFT formulations. We also discuss the expected hierarchy of the corresponding LECs as suggested by the large-N_c analysis.

4.1. Effective Lagrangians

At distances much larger than the range of the interactions mediated by pions, the pionic degrees of freedom can be integrated out of the effective theory, and the relevant effective Lagrangian can be written in terms of nucleon fields only, interacting through contact vertices.

At leading order these vertices involve a single spatial derivative of fields, responsible for parity violation. Time derivatives can be eliminated recursively, using the equations of motion order by order in the low-energy expansion. This reflects our freedom in choosing the nucleon interpolating field, and amounts to a definite choice of the off-shell behavior of amplitudes. The theory can be formulated in terms of non-relativistic nucleon fields represented by two-component Pauli spinors $N_s(x)$. The relativistic $1/M$ corrections, which can in principle be worked out (see e.g., [185]) will be of no interest here. Relativistic covariance requires that the interactions depend on the relative momenta only (momentum-dependent "drift" corrections, which vanish in the center-of-mass frame of two nucleon systems, are part of the above mentioned relativistic corrections). Thus, gradients of nucleon fields in two-nucleon contact operators may only enter in the combinations

$$
\begin{aligned}
&\boldsymbol{\nabla}(N_s^\dagger O_1 N_s)N_s^\dagger O_2 N_s,\\
&[(N_s^\dagger i\overleftrightarrow{\boldsymbol{\nabla}}O_1N_s)N_s^\dagger O_2N_s - N_s^\dagger O_1N_s(N_s^\dagger i\overleftrightarrow{\boldsymbol{\nabla}}O_2N_s)]\,,
\end{aligned}
\tag{97}
$$

where $(ai\overleftrightarrow{\boldsymbol{\nabla}}b)\equiv a(i\boldsymbol{\nabla}b)-(i\boldsymbol{\nabla}a)b$ and the factor i, meant to ensure the hermiticity, makes it odd under time-reversal.

Since the underlying mechanism of parity violation in the SM may induce $\Delta I=0,1,2$ transitions (at least to order G_F^2), the effective Lagrangian will contain contact operators which transform as isoscalars or the neutral components of isovector and isotensors. In the two-nucleon case all these flavor structures are real, and therefore unaffected by the time-reversal operation, except for $(\vec{\tau}_1\times\vec{\tau}_2)_z$, which changes sign.

4.2. PVTC Lagrangian

Following the general considerations outlined above, there are ten possible structures entering the two-nucleon contact

Lagrangian in the PVTC case,

$$\Delta I=0\ \begin{cases} O_1^{PVTC}=\boldsymbol{\nabla}\times(N_s^\dagger\boldsymbol{\sigma}N_s)\cdot N_s^\dagger\boldsymbol{\sigma}N_s\,,\\ O_2^{PVTC}=\boldsymbol{\nabla}\times(N_s^\dagger\boldsymbol{\sigma}\tau^aN_s)\cdot N_s^\dagger\boldsymbol{\sigma}\tau^aN_s\,,\\ O_{1'}^{PVTC}=(N_s^\dagger i\overleftrightarrow{\boldsymbol{\nabla}}\cdot\boldsymbol{\sigma}N_s)N_s^\dagger N_s-N_s^\dagger\boldsymbol{\sigma}N_s\cdot(N_s^\dagger i\overleftrightarrow{\boldsymbol{\nabla}}N_s)\,,\\ O_{2'}^{PVTC}=(N_s^\dagger i\overleftrightarrow{\boldsymbol{\nabla}}\cdot\boldsymbol{\sigma}\tau^aN_s)N_s^\dagger\tau^aN_s\\ -N_s^\dagger\boldsymbol{\sigma}\tau^aN_s\cdot(N_s^\dagger i\overleftrightarrow{\boldsymbol{\nabla}}\tau^aN_s)\,, \end{cases}$$

$$\Delta I=1\ \begin{cases} O_3^{PVTC}=\epsilon^{ab3}\boldsymbol{\nabla}\cdot(N_s^\dagger\boldsymbol{\sigma}\tau^aN_s)N_s^\dagger\tau^bN_s\,,\\ O_4^{PVTC}=\boldsymbol{\nabla}\times(N_s^\dagger\boldsymbol{\sigma}\tau^3N_s)\cdot N_s^\dagger\boldsymbol{\sigma}N_s\,,\\ O_{3'}^{PVTC}=(N_s^\dagger i\overleftrightarrow{\boldsymbol{\nabla}}\cdot\boldsymbol{\sigma}\tau^3N_s)N_s^\dagger N_s\\ -N_s^\dagger\boldsymbol{\sigma}\tau^3N_s\cdot(N_s^\dagger i\overleftrightarrow{\boldsymbol{\nabla}}N_s)\,,\\ O_{4'}^{PVTC}=(N_s^\dagger i\overleftrightarrow{\boldsymbol{\nabla}}\cdot\boldsymbol{\sigma}N_s)N_s^\dagger\tau^3N_s\\ -N_s^\dagger\boldsymbol{\sigma}N_s\cdot(N_s^\dagger i\overleftrightarrow{\boldsymbol{\nabla}}\tau^3N_s)\,, \end{cases}$$

$$\Delta I=2\ \begin{cases} O_5^{PVTC}=\mathcal{I}_{ab}\boldsymbol{\nabla}\times(N_s^\dagger\boldsymbol{\sigma}\tau^aN_s)\cdot N_s^\dagger\boldsymbol{\sigma}\tau^bN_s\,,\\ O_{5'}^{PVTC}=\mathcal{I}_{ab}\Big[(N_s^\dagger i\overleftrightarrow{\boldsymbol{\nabla}}\cdot\boldsymbol{\sigma}\tau^aN_s)N_s^\dagger\tau^bN_s\\ -N_s^\dagger\boldsymbol{\sigma}\tau^aN_s\cdot(N_s^\dagger i\overleftrightarrow{\boldsymbol{\nabla}}\tau^bN_s)\Big]. \end{cases} \tag{98}$$

The Fermi statistics of nucleon fields, together with Fierz's reshuffling of spin-isospin indices allow to establish linear relations between primed and unprimed operators,

$$\begin{aligned} O_{1'}^{PVTC}&=\tfrac{1}{2}\left(O_1^{PVTC}+O_2^{PVTC}\right),\\ O_{2'}^{PVTC}&=\tfrac{1}{2}\left(3O_1^{PVTC}-O_2^{PVTC}\right),\\ O_{3'}^{PVTC}&=O_3^{PVTC}+O_4^{PVTC},\\ O_{4'}^{PVTC}&=-O_3^{PVTC}+O_4^{PVTC},\\ O_{5'}^{PVTC}&=O_5^{PVTC}, \end{aligned} \tag{99}$$

thus reducing the number of independent operators to five, so that the effective Lagrangian can be written as

$$\begin{aligned} \mathcal{L}^{(1)}_{PVTC,NN}=&\frac{1}{\Lambda_\chi^2 f_\pi}\Big[\frac{1}{2}C_1O_1^{PVTC}+\frac{1}{2}C_2O_2^{PVTC}+C_3O_3^{PVTC}\\ &+C_4O_4^{PVTC}+\frac{1}{2}C_5O_5^{PVTC}\Big], \end{aligned} \tag{100}$$

where C_i are LECs. This Lagrangian is identical to that reported in Equation (23). From this Lagrangian, one can derive the potential given in Equation (60).

The five LECs are in a one-to-one correspondence with the possible S-P transitions in two-nucleon systems [45], namely ^{1}S$_0$-^{3}P$_0$ ($\Delta I=0,1,2$), ^{3}S$_1$-^{1}P$_1$ ($\Delta I=0$) and ^{3}S$_1$-^{3}P$_1$ ($\Delta I=1$). This may be shown explicitly by using the spin-isospin projection operators [45, 186–188]

$$\begin{aligned} P_{0,0}&=\frac{1}{\sqrt{8}}\sigma_2\tau_2\,,\quad P_{0,a}=\frac{1}{\sqrt{8}}\sigma_2\tau_2\tau_a\,,\quad P_{i,0}=\frac{1}{\sqrt{8}}\sigma_2\sigma_i\tau_2\,,\\ P_{i,a}&=\frac{1}{\sqrt{8}}\sigma_2\sigma_i\tau_2\tau_a\,, \end{aligned} \tag{101}$$

normalized according to

$$\begin{aligned} \mathrm{Tr}P_{\mu,\alpha}P^\dagger_{\nu,\beta}&=\frac{1}{2}\delta_{\mu\nu}\delta_{\alpha\beta},\quad \mu(\nu)=0,i(j)\,,\\ \alpha(\beta)&=0,a(b)\,, \end{aligned} \tag{102}$$

such that the operator $(N_s^TP_{\mu,\alpha}N_s)^\dagger$ creates a correctly normalized two-nucleon state with the appropriate spin-isospin quantum numbers. The relevant operators [188]

$$\begin{aligned} O_{\Delta I=0}^{(^1\mathrm{S}_0-^3\mathrm{P}_0)}&=(N_s^T\sigma^2\tau^2\tau^aN_s)^\dagger(N_s^Ti\overleftrightarrow{\boldsymbol{\nabla}}\cdot\sigma^2\boldsymbol{\sigma}\tau^2\tau^aN_s)+\mathrm{h.c.}\,,\\ O_{\Delta I=1}^{(^1\mathrm{S}_0-^3\mathrm{P}_0)}&=-i\epsilon^{ab3}(N_s^T\sigma^2\tau^2\tau^aN_s)^\dagger(N_s^Ti\overleftrightarrow{\boldsymbol{\nabla}}\cdot\sigma^2\boldsymbol{\sigma}\tau^2\tau^bN_s)+\mathrm{h.c.}\,,\\ O_{\Delta I=2}^{(^1\mathrm{S}_0-^3\mathrm{P}_0)}&=\mathcal{I}_{ab}(N_s^T\sigma^2\tau^2\tau^aN_s)^\dagger(N_s^Ti\overleftrightarrow{\boldsymbol{\nabla}}\cdot\sigma^2\boldsymbol{\sigma}\tau^2\tau^bN_s)+\mathrm{h.c.}\,,\\ O_{\Delta I=0}^{(^3\mathrm{S}_1-^1\mathrm{P}_1)}&=(N_s^T\sigma^2\boldsymbol{\sigma}\tau^2N_s)^\dagger\cdot(N_s^Ti\overleftrightarrow{\boldsymbol{\nabla}}\sigma^2\tau^2N_s)+\mathrm{h.c.}\,,\\ O_{\Delta I=1}^{(^3\mathrm{S}_1-^3\mathrm{P}_1)}&=(N_s^T\sigma^2\boldsymbol{\sigma}\tau^2N_s)^\dagger\cdot(N_s^T\overleftrightarrow{\boldsymbol{\nabla}}\times\sigma^2\boldsymbol{\sigma}\tau^2\tau^3N_s)+\mathrm{h.c.}\,, \end{aligned} \tag{103}$$

are related to the original basis via Fierz's transformations as follows,

$$\begin{aligned} O_{\Delta I=0}^{(^1\mathrm{S}_0-^3\mathrm{P}_0)}&=3O_1^{PVTC}+O_2^{PVTC}\,,\\ O_{\Delta I=1}^{(^1\mathrm{S}_0-^3\mathrm{P}_0)}&=4O_4^{PVTC}\,,\\ O_{\Delta I=2}^{(^1\mathrm{S}_0-^3\mathrm{P}_0)}&=-2O_5^{PVTC}\,,\\ O_{\Delta I=0}^{(^3\mathrm{S}_1-^1\mathrm{P}_1)}&=-O_1^{PVTC}+O_2^{PVTC}\,,\\ O_{\Delta I=1}^{(^3\mathrm{S}_1-^3\mathrm{P}_1)}&=-4O_3^{PVTC}\,, \end{aligned} \tag{104}$$

whence one can read the relation between the partial-waves projected LECs and the C_i. The potential derived from the operators given in Equation (103) has been often used in studies of PVTC observables. It is given explicitly as [37, 39]

$$\begin{aligned} V^{(1)}_{PVTC}(GHH)=&\frac{1}{2Mm_\rho^2}\Big\{\Lambda_{\Delta I=0}^{(^1\mathrm{S}_0-^3\mathrm{P}_0)}\Big[2(\boldsymbol{\sigma}_1-\boldsymbol{\sigma}_2)\cdot\boldsymbol{K}\\ &+i(\boldsymbol{\sigma}_1\times\boldsymbol{\sigma}_2)\cdot\boldsymbol{k}\Big]\\ &+\Lambda_{\Delta I=0}^{(^3\mathrm{S}_1-^1\mathrm{P}_1)}\Big[2(\boldsymbol{\sigma}_1-\boldsymbol{\sigma}_2)\cdot\boldsymbol{K}-i(\boldsymbol{\sigma}_1\times\boldsymbol{\sigma}_2)\cdot\boldsymbol{k}\Big]\\ &+\Lambda_{\Delta I=1}^{(^1\mathrm{S}_0-^3\mathrm{P}_0)}(\tau_{1z}+\tau_{2z})2(\boldsymbol{\sigma}_1-\boldsymbol{\sigma}_2)\cdot\boldsymbol{K}\\ &+\Lambda_{\Delta I=1}^{(^3\mathrm{S}_1-^3\mathrm{P}_1)}(\tau_{1z}-\tau_{2z})2(\boldsymbol{\sigma}_1+\boldsymbol{\sigma}_2)\cdot\boldsymbol{K}\\ &+\Lambda_{\Delta I=2}^{(^1\mathrm{S}_0-^3\mathrm{P}_0)}I^{ab}\tau_{1a}\tau_{2b}\frac{2}{\sqrt{6}}(\boldsymbol{\sigma}_1-\boldsymbol{\sigma}_2)\cdot\boldsymbol{K}\Big\}, \end{aligned} \tag{105}$$

where the five LECs $\Lambda_{\Delta I}^{(\ldots)}$ are in one-to-one correspondence with C_{1-5}. Explicitly

$$\begin{aligned} \Lambda_{\Delta I=0}^{(^1\mathrm{S}_0-^3\mathrm{P}_0)}&=\frac{\kappa}{2}(C_1+C_2)\,,\\ \Lambda_{\Delta I=0}^{(^3\mathrm{S}_1-^1\mathrm{P}_1)}&=\frac{\kappa}{2}(3C_2-C_1)\,,\\ \Lambda_{\Delta I=1}^{(^1\mathrm{S}_0-^3\mathrm{P}_0)}&=\kappa C_4\,,\\ \Lambda_{\Delta I=1}^{(^1\mathrm{S}_1-^3\mathrm{P}_1)}&=\kappa C_3\,,\\ \Lambda_{\Delta I=2}^{(^1\mathrm{S}_0-^3\mathrm{P}_0)}&=\sqrt{6}\kappa C_5\,, \end{aligned} \tag{106}$$

where $\kappa=2Mm_\rho^2/f_\pi\Lambda_\chi^2$.

4.3. PVTV Lagrangian

The T-odd sector is very similar (see also [189]): one starts with a list of 10 redundant operators,

$$\Delta I=0\begin{cases} O_1^{PVTV}=\boldsymbol{\nabla}\cdot(N_s^\dagger\boldsymbol{\sigma}N_s)N_s^\dagger N_s\,,\\ O_2^{PVTV}=\boldsymbol{\nabla}\cdot(N_s^\dagger\boldsymbol{\sigma}\tau^a N_s)N_s^\dagger\tau^a N_s\,,\\ O_{1'}^{PVTV}=(N_s^\dagger i\overleftrightarrow{\boldsymbol{\nabla}}\times\boldsymbol{\sigma}N_s)\cdot N_s^\dagger\boldsymbol{\sigma}N_s\,,\\ O_{2'}^{PVTV}=(N_s^\dagger i\overleftrightarrow{\boldsymbol{\nabla}}\times\boldsymbol{\sigma}\tau^a N_s)\cdot N_s^\dagger\boldsymbol{\sigma}\tau^a N_s\,,\end{cases}$$

$$\Delta I=1\begin{cases} O_3^{PVTV}=\boldsymbol{\nabla}\cdot(N_s^\dagger\boldsymbol{\sigma}\tau^3 N_s)N_s^\dagger N_s\,,\\ O_4^{PVTV}=\boldsymbol{\nabla}\cdot(N_s^\dagger\boldsymbol{\sigma}N_s)N_s^\dagger\tau^3 N_s\,,\\ O_{3'}^{PVTV}=(N_s^\dagger i\overleftrightarrow{\boldsymbol{\nabla}}\times\boldsymbol{\sigma}\tau^3 N_s)\cdot N_s^\dagger\boldsymbol{\sigma}N_s\\ +(N_s^\dagger i\overleftrightarrow{\boldsymbol{\nabla}}\times\boldsymbol{\sigma}N_s)\cdot N_s^\dagger\boldsymbol{\sigma}\tau^3 N_s\,,\\ O_{4'}^{PVTV}=\epsilon^{ab3}\Big[(N_s^\dagger i\overleftrightarrow{\boldsymbol{\nabla}}\cdot\boldsymbol{\sigma}\tau^a N_s)N_s^\dagger\tau^b N_s\\ +(N_s^\dagger i\overleftrightarrow{\boldsymbol{\nabla}}\tau^a N_s)\cdot N_s^\dagger\boldsymbol{\sigma}\tau^b N_s\Big]\,,\end{cases}$$

$$\Delta I=2\begin{cases} O_5^{PVTV}=\mathcal{I}_{ab}\boldsymbol{\nabla}\cdot(N_s^\dagger\boldsymbol{\sigma}\tau^a N_s)N_s^\dagger\tau^b N_s\,,\\ O_{5'}^{PVTV}=\mathcal{I}_{ab}(N_s^\dagger i\overleftrightarrow{\boldsymbol{\nabla}}\times\boldsymbol{\sigma}\tau^a N_s)\cdot N_s^\dagger\boldsymbol{\sigma}\tau^b N_s\,,\end{cases} \tag{107}$$

and uses Fierz's identities to establish the linear relations,

$$\begin{aligned} O_{1'}^{PVTV}&=-O_1^{PVTV}-O_2^{PVTV}\,,\\ O_{2'}^{PVTV}&=-3O_1^{PVTV}+O_2^{PVTV}\,,\\ O_{3'}^{PVTV}&=-2O_3^{PVTV}-2O_4^{PVTV}\,,\\ O_{4'}^{PVTV}&=-2O_3^{PVTV}+2O_4^{PVTV}\,,\\ O_{5'}^{PVTV}&=-2O_5^{PVTV}\,,\end{aligned} \tag{108}$$

so that the Lagrangian only depends on five LECs,

$$\mathcal{L}^{(1)}_{PVTV,NN}=\frac{1}{\Lambda_\chi^2 f_\pi}\sum_{i=1}^{5}\bar{C}_i O_i^{PVTV}, \tag{109}$$

from which one can derive the potential given in Equation (91).

The five S-P transition operators only differ from the T-even case by a factor i,

$$\begin{aligned} \bar{O}^{(^1S_0-^3P_0)}_{\Delta I=0}&=(N_s^T\sigma^2\tau^2\tau^a N_s)^\dagger(N_s^T\overleftrightarrow{\boldsymbol{\nabla}}\cdot\sigma^2\boldsymbol{\sigma}\tau^2\tau^a N_s)+\text{h.c.}\,,\\ \bar{O}^{(^1S_0-^3P_0)}_{\Delta I=1}&=\epsilon^{ab3}(N_s^T\sigma^2\tau^2\tau^a N_s)^\dagger(N_s^T i\overleftrightarrow{\boldsymbol{\nabla}}\cdot\sigma^2\boldsymbol{\sigma}\tau^2\tau^b N_s)+\text{h.c.}\,,\\ \bar{O}^{(^1S_0-^3P_0)}_{\Delta I=2}&=\mathcal{I}_{ab}(N_s^T\sigma^2\tau^2\tau^a N_s)^\dagger(N_s^T\overleftrightarrow{\boldsymbol{\nabla}}\cdot\sigma^2\boldsymbol{\sigma}\tau^2\tau^b N_s)+\text{h.c.}\,,\\ \bar{O}^{(^3S_1-^1P_1)}_{\Delta I=0}&=(N_s^T\sigma^2\boldsymbol{\sigma}\tau^2 N_s)^\dagger\cdot(N_s^T\overleftrightarrow{\boldsymbol{\nabla}}\sigma^2\tau^2 N_s)+\text{h.c.}\,,\\ \bar{O}^{(^3S_1-^1P_1)}_{\Delta I=1}&=(N_s^T\sigma^2\boldsymbol{\sigma}\tau^2 N_s)^\dagger\cdot(N_s^T i\overleftrightarrow{\boldsymbol{\nabla}}\times\sigma^2\boldsymbol{\sigma}\tau^2\tau^3 N_s)+\text{h.c.}\,,\end{aligned} \tag{110}$$

related to the original basis as follows,

$$\begin{aligned} \bar{O}^{(^1S_0-^3P_0)}_{\Delta I=0}&=6O_1^{PVTV}+2O_2^{PVTV}\,,\\ \bar{O}^{(^1S_0-^3P_0)}_{\Delta I=1}&=-4O_3^{PVTV}-4O_4^{PVTV}\,,\\ \bar{O}^{(^1S_0-^3P_0)}_{\Delta I=2}&=-4O_5^{PVTV}\,,\\ \bar{O}^{(^3S_1-^1P_1)}_{\Delta I=0}&=2O_1^{PVTV}-2O_2^{PVTV}\,,\\ \bar{O}^{(^3S_1-^3P_1)}_{\Delta I=1}&=4O_3^{PVTV}-4O_4^{PVTV}\,.\end{aligned} \tag{111}$$

4.4. Constraints From the Large-N_c Limit

In 1974 't Hooft combined the large-N_c and the small coupling limit, with $g_s^2N_c$ fixed [190], and showed that QCD considerably simplifies, while maintaining many of the features of the actual theory, becoming a theory of stable hadrons. The baryons emerge as dense systems of many quarks, subjected to a mean field potential [191]. Nucleon-nucleon interactions exhibit in this limit a spin-flavor symmetry [192–194]. Indeed, due to the fact that nucleons carry definite spin and isospin of $O(1)$, interactions inducing a change in either spin or isospin are suppressed relative to the dominant $O(N_c)$ ones, that are either spin-isospin independent ($\sim\mathbf{1}$) or dependent on both ($\sim\sigma\tau$). The large-N_c counting of momenta follows from the observation that the nucleon-nucleon scattering amplitude is in this limit a sum of meson exchange poles, each one depending only on the relative momentum transfer. The average relative momenta can only appear as relativistic corrections, which are suppressed by inverse powers of $M\sim O(N_c)$.

Apparently the resulting scaling laws do not conform with the operator identities (99) and (108) and seem to imply a dependence on the choice of operator basis. However, one can start with the redundant set of operators, pertinent to a theory of distinguishable nucleons, since the large-N_c arguments outlined above are completely general and do not rely on the statistics of the interacting baryons (the only assumption is that they both carry spin and isospin of $O(1)$). As a result one obtains the large-N_c scaling of the LECs in the PVTV contact potential,

$$\begin{aligned} &C_2\sim C_5\sim O(1)\,,\\ &C_3\sim C_4\sim C_{3'}\sim O(1/N_c)\,,\\ &C_1\sim C_{1'}\sim C_{2'}\sim C_{5'}\sim O(1/N_c^2)\,,\\ &C_{4'}\sim O(1/N_c^3)\,,\end{aligned} \tag{112}$$

and in the PVTV one,

$$\begin{aligned} &\bar{C}_3\sim O(1)\,,\\ &\bar{C}_1\sim\bar{C}_2\sim\bar{C}_{2'}\sim\bar{C}_5\sim\bar{C}_{5'}\sim O(1/N_c)\,,\\ &\bar{C}_4\sim\bar{C}_{3'}\sim\bar{C}_{4'}\sim O(1/N_c^2)\,,\\ &\bar{C}_{1'}\sim O(1/N_c^3).\end{aligned} \tag{113}$$

Therefore we have only two leading LECs in the PVTC potential (C_2 and C_5 corresponding to $\Delta I=0,2$ respectively) and only one in the PVTV potential ($\bar{C}_3$ with $\Delta I=1$) [47, 150]. This feature largely increases the predictive power for low-energy hadronic parity violation, and allows one to put more severe constraints on the forthcoming experimental results. Notice however that the above results are obtained by simply projecting the Hartree Hamiltonian in the nucleon-nucleon sector. A consistent treatment would require consideration of the induced effect on NN contact vertices of Δ exchanges, since the latter are enhanced, in the large-N_c limit, due to the degeneracy between nucleon and delta masses implied by the spin-flavor symmetry.

Moreover, for the PVTV case, this picture is obscured by the fact that the magnitude of the five contact LECs depends strongly on the particular type of the CP-violating source at the quark level. For example, the QCD $\bar{\theta}$ term conserves isospin symmetry such that $\bar{C}_{3,4,5}$ are suppressed by powers of $\varepsilon\epsilon_{m_\pi}$ compared to

$\bar{C}_{1,2}$ (see **Table 1**). Despite the possible $1/N_c$ suppression of $\bar{C}_{1,2}$ compared to $\bar{C}_3$ the former are still expected to dominate.

5. ONE-MESON EXCHANGE MODELS

In the past, a simple and rather efficient description of the strong PCTC NN interaction was obtained in terms of a sum of single meson exchanges [195, 196]. These models began to be popular on account of the discovery of various meson resonances during the sixties. The potentials were generally constructed taking into account the exchanges of pions ($J^P = 0^-$, $m_\pi = 138$ MeV), η-mesons ($J^P = 0^-$, $m_\eta = 550$ MeV), and ρ- and ω-mesons ($J^P = 1^-$, $m_{\rho,\omega} = 770, 780$ MeV), but clearly, the number of mesons to be included is somewhat arbitrary. This picture has been extended also to describe PVTC and PVTV interactions, simply considering single meson exchanges where one vertex is strong and PCTC, while the other violates P and conserves T or violates both P and T. Then, all the dynamics of such interactions is contained in a number of PVTC and PVTC nucleon-nucleon-meson (NNM) coupling constants.

One starts by writing the Lagrangian consistent of Yukawa-like NNM vertices, invariant under the proper Lorentz transformations, and either conserving or violating the discrete P, C, T symmetries. The building blocks of the Lagrangian are therefore nucleon bilinears multiplied by a meson field arranged so that Lorentz symmetry is satisfied. For the construction of the PCTC Lagrangian, one usually includes only isospin-conserving terms. However, for the PVTC and PVTV Lagrangians, isospin-changing terms must be included since the underlying operators at the quark level are not necessarily isospin symmetric. A summary of the transformation properties of nucleon bilinears with different elements of the Clifford algebra and the various meson fields under hermitian conjugation (H), parity P, and charge conjugation C are reported in **Table 2**.

Using these properties it is not difficult to write the Lagrangians. For example, the strong $\mathcal{L}_{\rm PCTC}$ Lagrangian constructed with these mesons is given by (here we list only isospin -conserving terms)

$$\begin{aligned}\mathcal{L}_{\rm PCTC} &= g_\pi \bar{N} i\gamma_5 \vec{\tau}\cdot\vec{\pi} N + g_\eta \bar{N} i\gamma_5 \eta N \\ &- g_\rho \bar{N}\left(\gamma^\mu - i\frac{\chi_V}{2M}\sigma^{\mu\nu}q_\nu\right)\vec{\tau}\cdot\vec{\rho}_\mu N \\ &- g_\omega \bar{N}\left(\gamma^\mu - i\frac{\chi_S}{2M}\sigma^{\mu\nu}q_\nu\right)\omega_\mu N\,, \end{aligned} \tag{114}$$

where q^μ is the meson momentum[7], π_a, ρ_a^μ, η, and ω^μ are meson fields and g_π, ... PCTC coupling constants. Above, χ_V and χ_S are the ratios of the tensor to vector coupling constant for ρ and ω, respectively. Assuming vector-meson dominance [197], they can be related to the iso-vector and iso-scalar magnetic moments of a nucleon ($\chi_V = 3.70$ and $\chi_S = -0.12$). Note that the pion and rho-meson are isospin triplets, therefore the fields have the isospin index $a = 1, \ldots, 3$. Moreover, the rho- and omega-mesons have spin 1, and their fields correspondingly are vector fields with index $\mu = 0, \ldots, 3$.

Let us now consider the PVTC Lagrangian constructed in terms of the same mesons. In this case one has to take into account Barton's theorem [198], which asserts that exchange of neutral and spinless mesons between on-shell nucleons is forbidden by CP invariance, and therefore they cannot enter in a PVTC Lagrangian. Therefore only $\pi^\pm$, ρ, and ω vertices need to be considered and the form of the PVTC effective Lagrangian is [131]

$$\begin{aligned}\mathcal{L}_{\rm PVTC} &= \frac{h_\pi^1}{\sqrt{2}}\bar{N}(\vec{\pi}\times\vec{\tau})_3 N \\ &+\bar{N}\left(h_\rho^0\vec{\tau}\cdot(\vec{\rho})^\mu + h_\rho^1\rho_3^\mu + \frac{h_\rho^2}{2\sqrt{6}}(3\tau_3\rho_3^\mu - \vec{\tau}\cdot(\vec{\rho})^\mu)\right)\gamma_\mu\gamma_5 N \\ &+\bar{N}(h_\omega^0\omega^\mu + h_\omega^1\tau_3\omega^\mu)\gamma_\mu\gamma_5 N - h_\rho^{\prime 1}\bar{N}(\vec{\tau}\times(\vec{\rho})^\mu)_3\frac{\sigma_{\mu\nu}q^\nu}{2M}\gamma_5 N\,, \end{aligned} \tag{115}$$

where h_π^1, ... are PVTC coupling constants to be determined. As discussed also in section 3, where we focused in particular on the pion-nucleon PVTC constant h_π^1, attempts to estimate the magnitude of these couplings from the fundamental theory were reported in several papers [121–127]. In particular, in the DDH paper [50], the authors presented *reasonable ranges* inside of which these parameters were extremely likely to be found, together with a set of "best values" (see **Table 3**). Clearly, these values have to be considered as educated guesses in view of all the uncertainties of their evaluation. Of the seven unknown weak couplings $h_\pi^1, h_\rho^0, \ldots$, there are estimates that indicate that $h_\rho^{\prime 1}$ is quite small [199] and this term was generally omitted, leaving PVTC observables to be described in terms of six constants. Notice further that the DDH parameters were also considered using a soliton description of the nucleon in [200] and [130].

In the same manner, we can write the PVTV Lagrangian composed of NNM vertices [142, 201]

$$\begin{aligned}\mathcal{L}_{\rm PVTV} &= \bar{N}[\bar{g}_\pi^0\vec{\tau}\cdot\vec{\pi} + \bar{g}_\pi^1\pi_3 + \bar{g}_\pi^2(3\tau_3\pi_3 - \vec{\tau}\cdot\vec{\pi})]N \\ &+ \bar{N}[\bar{g}_\eta^0\eta + \bar{g}_\eta^1\tau_3\eta]N \\ &+ \bar{N}\frac{1}{2M}[\bar{g}_\rho^0\vec{\tau}\cdot(\vec{\rho})^\mu + \bar{g}_\rho^1\rho_3^\mu \\ &+ \bar{g}_\rho^2(3\tau_3\rho_3^\mu - \vec{\tau}\cdot(\vec{\rho})^\mu)]\sigma_{\mu\nu}q^\nu\gamma_5 N \\ &+ \bar{N}\frac{1}{2M}[\bar{g}_\omega^0\omega_\mu + \bar{g}_\omega^1\tau_3\omega_\mu]\sigma^{\mu\nu}q_\nu\gamma_5 N\,, \end{aligned} \tag{116}$$

where $\bar{g}_\alpha^i$, $i = 0, 1, 2$, are PVTV meson-nucleon coupling constants. In this case, there were no attempts to obtain the values of these coupling constants from the fundamental theory, as also the magnitude of the parameters entering the underlying theory is unknown.

From these Lagrangians, the PVTC and PVTV interactions are obtained as a sum of single-meson exchange diagrams.

[7] More appropriately, these Lagrangian terms should be written in terms of four-gradients. For example

$$\bar{N} i\frac{\chi_V}{2M}\sigma^{\mu\nu}q_\nu\vec{\tau}\cdot\vec{\rho}_\mu N \to -\bar{N}\frac{\chi_V}{2M}\left[\partial_\nu\,,\,\sigma^{\mu\nu}\vec{\tau}\cdot\vec{\rho}_\mu\right]N\,.$$

where [,] denotes the commutator.

TABLE 2 | Transformation properties of fermion bilinears with different elements of the Clifford algebra and various meson fields under hermitian conjugation (H), parity (P), and charge conjugation (C).

	$\bar{N}N$	$\bar{N}i\gamma_5 N$	$\bar{N}\gamma_\mu N$	$\bar{N}\gamma_\mu\gamma_5 N$	$\bar{N}\sigma_{\mu\nu}N$	π_a	ρ_a	η	ω
H	+	+	+	+	+	+	+	+	+
P	+	−	+	−	+	−	+	−	+
C	+	+	−	+	−	$(-)^{a+1}$	$-(-)^{a+1}$	+	−

Note that the pion and rho-meson fields are isospin triplets, $a = 1, 2, 3$.

TABLE 3 | Weak NNM couplings as estimated in Desplanques et al. [50].

Coupling	DDH [50] Reasonable range	DDH [50] "Best" value
h^1_π	$0 \to 30$	12
h^0_ρ	$30 \to -81$	−30
h^1_ρ	$-1 \to 0$	−0.5
h^2_ρ	$-20 \to -29$	−25
h^0_ω	$15 \to -27$	−5
h^1_ω	$-5 \to -2$	−3

All numbers are quoted in units of the value 3.8×10^{-8}.

Regarding PVTC, below we report the potential in the form obtained by DDH [50]

$$
\begin{aligned}
V_{\rm PVTC} \;=\; & -\frac{g_\pi h^1_\pi}{2\sqrt{2}M} i(\vec{\tau}_1 \times \vec{\tau}_2)_z \frac{(\boldsymbol{\sigma}_1 + \boldsymbol{\sigma}_2)\cdot \boldsymbol{k}}{k^2 + m_\pi^2} \\
& - \frac{g_\rho}{M}\left[\vec{\tau}_1\cdot\vec{\tau}_2\, h^0_\rho + \frac{(\tau_{1z}+\tau_{2z})}{2} h^1_\rho + \frac{3\tau_{1z}\tau_{2z} - \vec{\tau}_1\cdot\vec{\tau}_2}{2\sqrt{6}} h^2_\rho\right] \\
& \times \left[\frac{2(\boldsymbol{\sigma}_1 - \boldsymbol{\sigma}_2)\cdot \boldsymbol{K} + (1+\chi_V) i(\boldsymbol{\sigma}_1 \times \boldsymbol{\sigma}_2)\cdot \boldsymbol{k}}{k^2 + m_\rho^2}\right] \\
& - \frac{g_\omega}{M}\left[h^0_\omega + \frac{(\tau_{1z}+\tau_{2z})}{2} h^1_\omega\right] \\
& \times \left[\frac{2(\boldsymbol{\sigma}_1 - \boldsymbol{\sigma}_2)\cdot \boldsymbol{K} + (1+\chi_S) i(\boldsymbol{\sigma}_1 \times \boldsymbol{\sigma}_2)\cdot \boldsymbol{k}}{k^2 + m_\omega^2}\right] \\
& + \left[\frac{g_\rho h^1_\rho}{M}\frac{(\tau_{1z}-\tau_{2z})(\boldsymbol{\sigma}_1 + \boldsymbol{\sigma}_2)\cdot \boldsymbol{K}}{k^2 + m_\rho^2}\right] \\
& - \left[\frac{g_\omega h^1_\omega}{M}\frac{(\tau_{1z}-\tau_{2z})(\boldsymbol{\sigma}_1 + \boldsymbol{\sigma}_2)\cdot \boldsymbol{K}}{k^2 + m_\omega^2}\right] \\
& - \left[\frac{g_\rho h^{1\prime}_\rho}{2M}\frac{i(\vec{\tau}_1 \times \vec{\tau}_2)_z(\boldsymbol{\sigma}_1 + \boldsymbol{\sigma}_2)\cdot \boldsymbol{k}}{k^2 + m_\rho^2}\right],
\end{aligned}
\tag{117}
$$

where $\boldsymbol{k}$ and $\boldsymbol{K}$ are defined in Equation (46). Often the potential is regularized for large values of k, modifying the meson propagators so that $1/(k^2 + m_x^2) \to f_{\Lambda_x}(k^2)/(k^2 + m_x^2)$, where $x = \pi$, ρ, and ω. For example, in Schiavilla et al. [202] the following regularization was chosen

$$
\frac{1}{k^2 + m_x^2} \to \frac{1}{k^2 + m_x^2}\left(\frac{\Lambda_x^2 - m_x^2}{\Lambda_x^2 + k^2}\right)^2, \tag{118}
$$

For example, the parameters Λ_π, Λ_ρ, and Λ_ω were chosen to have the same value 2.4 GeV in Schiavilla et al. [203] and Schiavilla et al. [202]. However, the cutoff functions $f_{\Lambda_x}(k^2)$ were not always applied and also their form can vary.

Several PVTC observables have been studied using the DDH potential, with the aim to identify the values of the six or seven coupling constants, see for example [34, 36, 37]. Up to now the lack of accurate experimental values has prevented the completion of this task.

Usually, the experiments are analyzed in terms of the DDH parameters. In the next Section, we will present a discussion of the experimental values within the χEFT framework. In order to make contact between the two approaches, we briefly discuss the relation between DDH and χEFT PVTC potentials. The OPE term is clearly the same, while in the DDH approach all the TPE terms are missing. They can be considered effectively included via the heavy-meson exchanges, however the ρ and ω masses are larger than $2m_\pi$, which is the range of the TPE contributions. More precisely, the heavy meson exchange terms should be considered as equivalent to the five contact terms in the chiral potential multiplied by the LECs C_i. Keeping this in mind, we can match the components of the DDH potential mediated by ρ and ω exchanges to those of $V^{(1)}_{PVTC}$(CT), and obtain in the limit $k \ll m_\rho, m_\omega$ [42, 46]

$$
C_1^{(\rm DDH)} = -\frac{3}{2}h^0_\rho D_\rho - h^0_\omega\left(\frac{3}{2} + \chi_S\right) D_\omega\,, \tag{119}
$$

$$
C_2^{(\rm DDH)} = -h^0_\rho\left(\frac{1}{2} + \chi_V\right) D_\rho - \frac{1}{2}h^0_\omega D_\omega\,, \tag{120}
$$

$$
C_3^{(\rm DDH)} = -\frac{1}{2}(h^{1\prime}_\rho - h^1_\rho) D_\rho - \frac{1}{2}h^1_\omega D_\omega, \tag{121}
$$

$$
C_4^{(\rm DDH)} = -\frac{1}{2}h^1_\rho(2+\chi_V) D_\rho - \frac{1}{2}h^1_\omega(2+\chi_S) D_\omega\,, \tag{122}
$$

$$
C_5^{(\rm DDH)} = -\frac{1}{2\sqrt{6}}h^2_\rho(2+\chi_V) D_\rho\,, \tag{123}
$$

where

$$
D_\rho = g_\rho \frac{\Lambda_\chi^2}{m_\rho^2}\frac{f_\pi}{M}\left(1 - \frac{m_\rho^2}{\Lambda_\rho^2}\right)^2, \tag{124}
$$

$$
D_\omega = g_\omega \frac{\Lambda_\chi^2}{m_\omega^2}\frac{f_\pi}{M}\left(1 - \frac{m_\omega^2}{\Lambda_\omega^2}\right)^2. \tag{125}
$$

Using the "best" values for the DDH parameters given in **Table 3** (the other coupling constants and parameters have been taken from Schiavilla et al. [203]), we obtain, for example, the following estimates (in units of 10^{-7}):

$$C_1^{(\mathrm{DDH})} \approx 17\,, \quad C_2^{(\mathrm{DDH})} \approx 30\,, \quad C_3^{(\mathrm{DDH})} \approx 1\,,$$
$$C_4^{(\mathrm{DDH})} \approx 5\,, \quad C_5^{(\mathrm{DDH})} \approx 7\,. \tag{126}$$

The large value of $C_2^{(\mathrm{DDH})}$ is due to the tensor coupling constant $\chi_V \simeq 3.7$ of the ρ-meson to the nucleon. Clearly, these values should be taken only as indicative, since terms in the DDH vector-meson potential implicitly also account for TPE components, which in the χEFT PVTC potential are included explicitly. Relations where the TPE contributions are subtracted from the results above and the estimations of the LECs C_i within the soliton picture of the nucleon are given in de Vries et al. [46].

The PVTV potential was derived in Haxton and Henley [204], Gudkov et al. [205], Towner and Hayes [206], and Liu and Timmermans [142]. The momentum space version reads

$$\begin{aligned}
V_{\mathrm{PVTV}} \;=\; & +\frac{g_\pi}{2M}\left[\bar{g}_\pi^0\,\vec{\tau}_1\cdot\vec{\tau}_2+\bar{g}_\pi^1\,\frac{(\tau_{1z}+\tau_{2z})}{2}\right.\\
& \left.+\,\bar{g}_\pi^2(3\tau_{1z}\tau_{2z}-\vec{\tau}_1\cdot\vec{\tau}_2)\right]\frac{i(\boldsymbol{\sigma}_1-\boldsymbol{\sigma}_2)\cdot\boldsymbol{k}}{m_\pi^2+k^2}\\
& -\frac{g_\rho}{2M}\left[\bar{g}_\rho^0\,\vec{\tau}_1\cdot\vec{\tau}_2+\bar{g}_\rho^1\,\frac{(\tau_{1z}+\tau_{2z})}{2}\right.\\
& \left.+\,\bar{g}_\rho^2(3\tau_{1z}\tau_{2z}-\vec{\tau}_1\cdot\vec{\tau}_2)\right]\frac{i(\boldsymbol{\sigma}_1-\boldsymbol{\sigma}_2)\cdot\boldsymbol{k}}{m_\rho^2+k^2}\\
& +\frac{g_\eta}{2M}\left[\bar{g}_\eta^0+\bar{g}_\eta^1\,\frac{(\tau_{1z}+\tau_{2z})}{2}\right]\frac{i(\boldsymbol{\sigma}_1-\boldsymbol{\sigma}_2)\cdot\boldsymbol{k}}{m_\eta^2+k^2}\\
& -\frac{g_\omega}{2M}\left[\bar{g}_\omega^0+\bar{g}_\omega^1\,\frac{(\tau_{1z}+\tau_{2z})}{2}\right]\frac{i(\boldsymbol{\sigma}_1-\boldsymbol{\sigma}_2)\cdot\boldsymbol{k}}{m_\omega^2+k^2}\\
& +\left[\frac{g_\pi\bar{g}_\pi^1}{4M}\,\frac{(\tau_{1z}-\tau_{2z})i(\boldsymbol{\sigma}_1+\boldsymbol{\sigma}_2)\cdot\boldsymbol{k}}{k^2+m_\pi^2}\right]\\
& +\left[\frac{g_\rho\bar{g}_\rho^1}{4M}\,\frac{(\tau_{1z}-\tau_{2z})i(\boldsymbol{\sigma}_1+\boldsymbol{\sigma}_2)\cdot\boldsymbol{k}}{k^2+m_\rho^2}\right]\\
& -\left[\frac{g_\eta\bar{g}_\eta^1}{4M}\,\frac{(\tau_{1z}-\tau_{2z})i(\boldsymbol{\sigma}_1+\boldsymbol{\sigma}_2)\cdot\boldsymbol{k}}{k^2+m_\eta^2}\right]\\
& -\left[\frac{g_\omega\bar{g}_\omega^1}{4M}\,\frac{(\tau_{1z}-\tau_{2z})i(\boldsymbol{\sigma}_1+\boldsymbol{\sigma}_2)\cdot\boldsymbol{k}}{k^2+m_\omega^2}\right].
\end{aligned} \tag{127}$$

Also in this case, cut off functions can be applied in order to regularize the large k behavior of V_{PVTV}. It is worthwhile to stress that the PVTV meson-exchange potential involves significantly more parameters than the LO PVTV chiral potential which depends in principle only on 4 LECs $\bar{g}_{0,1}$ and $\bar{C}_{1,2}$, with $\bar{g}_2$, $\bar{\Delta}$, and $\bar{C}_{3,4,5}$ appearing at subleading orders. While the meson-exchange potential can be mapped onto the short-distance $\bar{C}_i$ operators, the dynamics from the 3-pion $\bar{\Delta}$ interaction is not captured in this way.

6. SELECTED RESULTS FOR VARIOUS PVTC AND PVTV OBSERVABLES

In this section we present a selection of results obtained with the chiral EFT potentials and currents described in section 3 for various PVTC and PVTV observables. We will discuss first in the next four subsections the parity violation in (i) the radiative neutron capture on the proton, (ii) the longitudinal asymmetry in $\vec{p}p$ scattering, (iii) the longitudinal asymmetry in the $^3\mathrm{He}(\vec{n},p)^3\mathrm{H}$ reaction, and (iv) the $\vec{n}$-p and $\vec{n}$-d spin rotations, respectively. Finally, in the last subsection, we present some results for the EDM of light nuclei. Our motivation to include these results in the review is mainly to establish benchmarks to help future applications. We include also a "minimum" analysis how the current experimental data constrain some of the values of the LECs entering the χEFT interactions.

Results obtained using the pionless EFT can be found, for example, in Schindler and Springer [36], Haxton and Holstein [37], and Gardner et al. [39]. The meson-exchange potentials (in particular the DDH model) were used to analyze the results of several experiments of PVTC observables also in medium and heavy nuclei. For a summary of the obtained results, see, for example, [34, 39, 131]. Calculations of the EDM of light nuclei using the meson exchange potential were performed in Liu and Timmermans [142], Song et al. [207], and Yamanaka [208].

6.1. Parity Violation in Radiative Neutron Capture on the Proton

The radiative neutron capture on the proton $\vec{n}p \to d\gamma$, where d denotes the deuteron and $\vec{n}$ a longitudinally polarized neutron, represents a very interesting process wherein to study PVTC effects in nuclear physics. The longitudinal analyzing power for this process is defined as

$$A_\gamma(\theta) \;=\; \frac{d\sigma_+(\theta)-d\sigma_-(\theta)}{d\sigma_+(\theta)+d\sigma_-(\theta)} = a_\gamma\,\cos\theta\,, \tag{128}$$

where $d\sigma_\pm(\theta)$ is the differential cross section for positive/negative helicity neutrons, and θ is defined as the angle between the neutron spin and the outgoing photon momentum. a_γ has been measured by several experiments during the past decades. The first non-zero signal was reported last year for incoming neutrons of thermal energies [209],

$$a_\gamma = (-3.0 \pm 1.4 \pm 0.2)\cdot 10^{-8}\,. \tag{129}$$

although this number is only two standard deviations away from a null result.

The theoretical asymmetry is given by

$$\begin{aligned}
a_\gamma \;=\; & \left(-\sqrt{2}\,\mathrm{Re}\left[M_1^*(^1\mathrm{S}_0)E_1(^3\mathrm{S}_1)+E_1^*(^1\mathrm{S}_0)M_1(^3\mathrm{S}_1)\right]\right.\\
& \left.+\mathrm{Re}\left[E_1^*(^3\mathrm{S}_1)M_1(^3\mathrm{S}_1)\right]\right)\\
& \times\left(|M_1(^1\mathrm{S}_0)|^2+|E_1(^1\mathrm{S}_0)|^2+|M_1(^3\mathrm{S}_1)|^2+|E_1(^3\mathrm{S}_1)|^2\right)^{-1},
\end{aligned} \tag{130}$$

where $X_\ell(^{2S+1}S_J)$ are reduced matrix elements (RMEs) either of electric ($X = E$) or magnetic ($X = M$) type, of multipolarity ℓ, and describing the EM transition from the $n - p$ system in the scattering state $^{2S+1}S_J$ [203].

Compared to the PVTC longitudinal analyzing power in proton-proton scattering discussed later, a_γ carries a significant advantage. The initial neutron-proton system can be in the $^3S_1$ state, so that the process is sensitive to the $^3S_1 \leftrightarrow {}^3P_1$ transition and thus depends on the LO PVTC NN potential. In chiral EFT, the LO potential depends only on the LEC h_π^1, meaning that measurements of a_γ provide a unique chance to pin down the value of this LEC – something that is much more difficult to achieve in proton-proton scattering, where the contribution of the LO potential vanishes. The disadvantage is that $\vec{n}p \to d\gamma$ is an electromagnetic process and therefore depends on P-conserving and P-violating electromagnetic currents.

As can be seen from Equation (130), a non-zero value of a_γ requires interference between electric and magnetic dipole currents. As such, including only the leading magnetic moment current in the presence of the LO PVTC NN potential leads to a vanishing result and NLO currents are necessary. There are then three relevant contributions that consist of interference between the isovector nucleon magnetic moment and

1. The one-body convection current in combination with the PVTC NN potential,
2. The two-body PCTC currents in combination with the PVTC NN potential,
3. The two-body PVTC currents.

Each of these contributions is sizeable: $a_\gamma^1 = (-0.27 \pm 0.03)h_\pi^1$, $a_\gamma^2 = (-0.53 \pm 0.02)h_\pi^1$, and $a_\gamma^3 = (0.72 \pm 0.03)h_\pi^1$ where the theoretical error bands are obtained from cut-off variations in the strong NN potential and do not reflect uncertainties from higher-order contributions [173]. While these uncertainties are small on the individual contributions, they lead to a sizeable uncertainty in the total analyzing power [173]

$$a_\gamma = a_\gamma^1 + a_\gamma^2 + a_\gamma^3 = (-0.11 \pm 0.05)h_\pi^1 \,. \tag{131}$$

The cancellations between the different contributions are related to gauge invariance [173, 203, 210] and this explains the relatively large total theoretical uncertainty. While the electromagnetic currents given above are explicitly gauge invariant as they result from the gauge-invariant χEFT Lagrangian, explicit gauge invariance is lost due to applied regulator when solving the NN scattering and bound-state equations. Future calculations can probably reduce the uncertainty by using regulators that do not violate explicit gauge invariance, but such schemes have not been applied to PVTC processes. Alternatively, it is possible to apply the Siegert theorem to relate part of the electric dipole currents to the one-body charge density. Schiavilla et al. [211] applied the Siegert theorem in combination with phenomenological strong potentials to calculate a_γ finding a result in good agreement with the central value in Equation (131). Such calculations however do not include an uncertainty estimate, for instance from missing transverse currents that are not included when applying the Siegert theorem. In this light, Equation (131) can be interpreted as a conservative result. It would be interesting to redo the calculation of a_γ in an updated framework to reduce the theoretical uncertainty.

The contribution to a_γ from the short range components of the potential is considered to be negligible. For example, using the meson-exchange model, the calculations have shown that a_γ is essentially unaffected by short-range contributions [203, 212–214], represented in this case by ρ and ω exchanges. Within χEFT, a resonance saturation estimate of the short-distance LECs contributing to the asymmetry led to short-distance contributions to a_γ of roughly $5 \cdot 10^{-9}$ and is thus very small [173]. Therefore, considering the theoretical expression given in Equation (130) and the experimental value given in Equation (129), we obtain an estimate for the LEC h_π^1

$$h_\pi^1 = (2.7 \pm 1.8) \times 10^{-7} \,. \tag{132}$$

Note that the large experimental error and the large theoretical uncertainty only allow one to establish the positive sign and that the magnitude of this LEC is consistent with the preliminary Lattice QCD evaluation reported in Equation (26) [132].

6.2. Parity Violation in $\vec{p}p$ Scattering

PVTC effects in proton-proton scattering can be studied by looking at the longitudinal analyzing power $A_z(E, \theta)$ defined as,

$$A_z(E,\theta) = \frac{\sigma_+(\theta,E) - \sigma_-(\theta,E)}{\sigma_+(\theta,E) + \sigma_-(\theta,E)} \,, \tag{133}$$

where θ is the scattering angle and E the energy of the protons in the laboratory frame, and $\sigma_+(\theta, E)(\sigma_-(\theta, E))$ the cross section when the polarization of the incoming proton is parallel (anti-parallel) to the beam direction. Actually the experiments detect the particles scattered in angular range $[\theta_1, \theta_2]$ and the measured quantity is an "average" of the asymmetry over the total cross-section in this range, explicitly

$$\overline{A}_z(E) = \frac{\int_{\theta_1 \le \theta \le \theta_2} d\cos\theta \; A_z(\theta,E)\sigma(\theta,E)}{\int_{\theta_1 \le \theta \le \theta_2} d\cos\theta \; \sigma(\theta,E)} \,, \tag{134}$$

where

$$\sigma(\theta,E) = \frac{1}{2}\left(\sigma_+(\theta,E) + \sigma_-(\theta,E)\right) \tag{135}$$

is the unpolarized differential cross-section for the process. There exist several measurements of the angle-averaged $\vec{p}p$ longitudinal asymmetry $\overline{A}_z(E)$, see Equation (134), obtained at different laboratory energies E [215–218]. The measurements and the angle ranges included in our analysis are reported in **Table 4**. The other "non-zero" measurement reported in the literature but not included in our analysis was performed at $E = 15$ MeV, with the result $\overline{A}_z = -1.7 \pm 0.8$ [216].

The isospin state of two proton system is $|pp\rangle \equiv |T = 1, T_z = 1\rangle$, implying that the LO contribution that comes from the OPE vanishes and the LEC h_π^1 will contribute to the observable only via the TPE box diagrams that appear at NLO and N^{2}LO. Taking into account the isospin selection rules, the longitudinal asymmetry can be written as

$$\overline{A}_z = h_\pi^1 \, a_0^{(pp)} + C \, a_1^{(pp)} + \tilde{h} \, a_2^{(pp)} \,, \tag{136}$$

TABLE 4 | Values of $\overline{A}_z$ and angle ranges for the three measurements of the $\vec{p}p$ longitudinal analyzing power [215, 217, 218].

E (MeV)	$\overline{A}_z$ (10^{-7})	(θ_1, θ_2)
13.6	-0.97 ± 0.20	(20°, 78°)
45	-1.53 ± 0.21	(23°, 52°)
221	$+0.84 \pm 0.34$	(5°, 90°)

TABLE 5 | Values of the coefficients $a_i^{(pp)}$ calculated with the χEFT N^{2}LO PVTC potential described in section 3.4 and the N^{4}LO PCTC potential derived in Entem et al. [18] at three energies corresponding to the experimental data points.

E [MeV]	$a_0^{(pp)}$(NLO)	$a_0^{(pp)}$(N^{2}LO)	$a_0^{(pp)}$(TOT)	$a_1^{(pp)}$	$a_2^{(pp)}$
13.6	0.289	0.160	0.449	−0.044	−0.215
45	0.595	0.355	0.950	−0.084	−0.475
221	−0.281	−0.187	−0.468	0.036	0.251

The PVTC potential has been regularized as in Equation (86) adopting the value $\Lambda_C = 500$ MeV for the cutoff parameter. The PCTC potential has been regularized with the same value of the cutoff parameter. For the coefficient $a_0^{(pp)}$ we give separately the contributions of the NLO and N^{2}LO terms only and then their sum, see Equation (139).

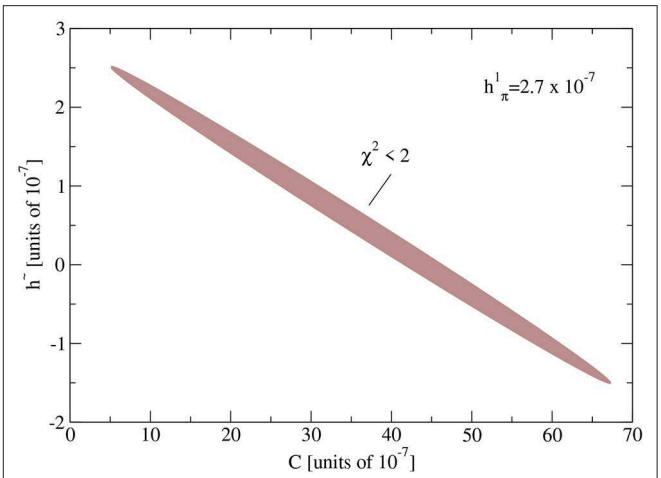


FIGURE 5 | Region of C and $\tilde{h}$ values for which $\chi^2 \leq 2$ for the $\vec{p}$-p longitudinal asymmetry. The calculation is based on the coefficients $a_0^{(pp)}$, $a_1^{(pp)}$, and $a_2^{(pp)}$ reported in **Table 5** assuming the value $h_\pi^1 = 2.7 \times 10^{-7}$.

where the first two terms are NLO contributions and the third term enters at N^{2}LO. We have defined

$$C = C_1 + C_2 + 2\,(C_4 + C_5)\,, \tag{137}$$

$$\tilde{h} = \frac{5g_A}{4} h_V^0 + 2\Big(\frac{g_A}{4} h_V^1 - h_A^1\Big) - 2\Big(\frac{g_A}{3} h_V^2 + h_A^2\Big)\,, \tag{138}$$

and $a_0^{(pp)}$, $a_1^{(pp)}$, $a_2^{(pp)}$ are numerical coefficients independent of the LEC values (but depending on the energy). The values of the coefficients $a_0^{(pp)}$, $a_1^{(pp)}$, and $a_2^{(pp)}$ calculated with the χEFT N^{2}LO PVTC potential described in section 3.4 and the N^{4}LO PCTC potential derived in Entem et al. [18] are reported in **Table 5**. The only coefficient which receives contributions from both the NLO and N^{2}LO potentials is $a_0^{(pp)}$. In the table, we report separately the two contributions and also the total contribution, given simply as

$$\begin{aligned} a_0^{(pp)}(\text{TOT}) &= a_0^{(pp)}(\text{NLO}) + a_0^{(pp)}(\text{N}^2\text{LO})\,, \\ a_0^{(pp)}(\text{N}^2\text{LO}) &= c_4 a_0^{(pp)}(4)\,. \end{aligned} \tag{139}$$

The value of $a_0^{(pp)}$(N^{2}LO) has been obtained assuming a value $c_4 = 3.56$ GeV^{-1} [219]. This correction to $a_0^{(pp)}$ is of the order of $\sim$ 50% with respect to the NLO value, somewhat larger than expected. This is related by the unnaturally large value of the πNN LEC c_4 appearing in the PCTC Lagrangian (13). This value has been obtained from the Roy-Steiner analysis of πN scattering data at N^{2}LO performed in Hoferichter et al. [219].

Unfortunately, of the performed measurements, the two at the lowest energy do not give independent information. In fact, the observable $\overline{A}_z$ at low energy scales as $\sqrt{E}$, since its energy dependence in this energy range is driven solely by that of the S-wave (strong interaction) phase shift [220]. Because of this scaling, it is not possible to fit from these data all three LECs h_π^1, C, and $\tilde{h}$ at the same time. If we fix the value $h_\pi^1 = 2.7 \times 10^{-7}$ from the central value as extracted from the $\vec{n}p \to d\gamma$ observable, see Equation (132), then we can perform a χ^2 analysis of the three data points listed in **Table 4** in order to fix the values of C and $\tilde{h}$. Note that this value of h_π^1 was obtained from the $\vec{n}p \to d\gamma$ calculation performed in de Vries et al. [173] using a different PCTC potential than that one used compute the $a_i^{(pp)}$ coefficients. However, since the $\vec{n}p \to d\gamma$ experiment depends mainly on the peripheral regions of the process, the value of a_γ is not very sensitive to the PCTC interaction (see also the calculations reported in [221]).

First of all, if we restrict ourselves to an NLO analysis, using $h_\pi^1 = 2.7 \times 10^{-7}$ we would obtain $C = (49 \pm 2) \cdot 10^{-7}$. If we take into account also the N^{2}LO LEC, we report in **Figure 5** the C and $\tilde{h}$ values for which $\chi^2 \leq 2$, which form an elliptic region. As can be seen, there appears to be a strong correlation between C and $\tilde{h}$ and the range of allowed values of the LECs is rather large $5 \times 10^{-7} < C < 67 \times 10^{-7}$ and $-1.5 \times 10^{-7} < \tilde{h} < 2.5 \times 10^{-7}$. Note that the ellipse is rather narrow and almost coincides with a straight line. See also de Vries et al. [46], Viviani et al. [42] for a similar analysis performed at NLO for the LECs h_π^1 and C only.

The previous discussion did not take into account the large uncertainty of the h_π^1 coupling constant after the fit of the $\vec{n}$-p radiative capture asymmetry. In **Table 6**, we report representative values of C and $\tilde{h}$ giving the minimum value of χ^2 corresponding to range of values for h_π^1 as given in Equation (132). In the fourth column we report values for C if we neglect the N^{2}LO contributions (setting $\tilde{h} = 0$). We conclude that the combination of the $\vec{p}p$ and $\vec{n}p \to d\gamma$ asymmetries allows for a rough extraction of the LO and NLO LECs h_π^1 and C, but is insufficient to also pinpoint the N^{2}LO LEC $\tilde{h}$. The uncertainty of the extractions of h_π^1 and C is dominated by theoretical and experimental

TABLE 6 | Values for C and $\tilde{h}$ corresponding to different values of h_π^1 (all LECs are given in units of 10^{-7}) giving the minimum value of the χ^2 in the fit of the three experimental $\vec{p}$-p data points.

h_π^1	C	$\tilde{h}$	$C(\tilde{h}=0)$
0.9	27.7	0.11	28 ± 2
2.7	34.5	0.97	49 ± 2
4.5	41.2	1.84	69 ± 3

For example, for $h_\pi^1 = 2.7 \times 10^{-7}$, the C, $\tilde{h}$ values are those lying in the center of the elliptical contour shown in ***Figure 5****. The fourth column corresponds to an analysis where we ignore the N^{2}LO contributions and thus set $\tilde{h} = 0$.*

uncertainties related to the PVTC asymmetry in the radiative neutron capture process.

6.3. The ^{3}He$(\vec{n},p)^3$H Longitudinal Asymmetry

Very recently, a measurement of the longitudinal asymmetry $A_z^{(nh)}$ for the reaction $^3\mathrm{He}(\vec{n},p)^3\mathrm{H}$ induced by ultracold neutrons was successfully completed at ORNL [222]. This quantity is given by $A_z^{(nh)} = a_z \cos\theta$ [223], where θ is the angle between the outgoing proton momentum and the neutron beam direction. The measured value for a_z is given by $a_z = (1.58 \pm 0.97\ (\mathrm{stat}) \pm 0.24\ (\mathrm{sys})) \times 10^{-8}$ [224].

So far, this observable has been calculated using the NLO χEFT PVTC potential [42] (and also the DDH potential in [223]). The expression for the coefficient a_z is given as usual as

$$a_z = h_\pi^1 a_0^{(nh)} + C_1 a_1^{(nh)} + C_2 a_2^{(nh)} + C_3 a_3^{(nh)} + C_4 a_4^{(nh)} + C_5 a_5^{(nh)}, \tag{140}$$

where the various coefficients $a_i^{(nh)}$ are given as products of T-matrix elements involving three PCTC and three PVTC transitions [see [223] for details]. These T-matrix elements have been calculated by means of the HH method [225]. The resulting coefficients $a_i^{(nh)}$ are listed in **Table 7**.

First of all, if we restrict ourselves to LO (namely, setting all $C_i = 0$), using $h_\pi^1 = (2.7 \pm 1.8) \times 10^{-7}$, one obtains $a_z = -(3.2 \pm 2.1) \times 10^{-8}$, a value that is not compatible with the reported experimental value. Therefore, large contributions from NLO terms are expected. The values of $a_0^{(nh)}$ become more negative at NLO. At present, we only have the combination $C_1 + C_2 + 2(C_4 + C_5) = (49 \pm 2) \cdot 10^{-7}$, therefore we cannot proceed any further. Assuming, for example, $C_2 = 10 \times 10^{-7}$, we would obtain a contribution to a_z from this term of $\approx +2.26 \times 10^{-8}$. Therefore, this observable is very sensitive to the LECs C_i, and can be used to fit a linear combination of C_i that is independent of the combination appearing in $\vec{p}p$ scattering. Calculations at N^{2}LO are planned. However, we recall that one should also include the PVTC 3N interaction terms for completeness.

6.4. The $\vec{n}$-p and $\vec{n}$-d Spin Rotation

The spin rotation of neutron traversing a slab of matter in a plane transverse to the beam direction induced by the PVTC potential is given by

$$\frac{\mathrm{d}\phi^{(nX)}}{\mathrm{d}z} = \frac{2\pi\rho}{(2S_X+1)\, v_{\mathrm{rel}}} \mathrm{Re} \sum_{m_n m_X} \epsilon_{m_n}{}^{(-)} \langle p\hat{\mathbf{z}};\, m_n, m_X | V_{PVTC} | p\hat{\mathbf{z}};\, m_n, m_X \rangle^{(+)}, \tag{141}$$

where ρ is the density of hydrogen or deuterium nuclei for $X = p$ or d, $|p\hat{\mathbf{z}};\, m_n, m_X\rangle^{(\pm)}$ are the n-X scattering states with outgoing-wave $(+)$ and incoming-wave $(-)$ boundary conditions and relative momentum $\mathbf{p} = p\,\hat{\mathbf{z}}$ taken along the spin-quantization axis (the $\hat{\mathbf{z}}$-axis), S_X is the X spin, and $v_{\mathrm{rel}} = p/\mu$ is the magnitude of the relative velocity, μ being the n-X reduced mass. The expression above is averaged over the spin projections m_X; however, the phase factor $\epsilon_{m_n} = (-)^{1/2-m_n}$ is ± 1 depending on whether the neutron has $m_n = \pm 1/2$. We consider the n-p and n-d spin rotations for vanishing incident neutron energy (measurements of this observable are performed using ultracold neutron beams). In the following, we assume $\rho = 0.4 \times 10^{23}$ cm^{-3}. The rotation angle depends linearly on the PVTC LECs, as higher-order weak corrections are negligible. We write

$$\begin{aligned}\frac{\mathrm{d}\phi^{(nX)}}{\mathrm{d}z} &= h_\pi^1\, a_0^{(nX)} + C_1\, a_1^{(nX)} + C_2\, a_2^{(nX)} + C_3\, a_3^{(nX)} + C_4\, a_4^{(nX)} \\ &\quad + C_5\, a_5^{(nX)} + h_V^0\, b_1^{(nX)} + h_V^1\, b_2^{(nX)} + h_V^2\, b_3^{(nX)} \\ &\quad + h_A^1\, b_4^{(nX)} + h_A^2\, b_5^{(nX)},\end{aligned} \tag{142}$$

where the $a_i^{(nX)}$ for $i = 0, \ldots, 5$ and $b_i^{(nX)}$ for $i = 1, \ldots, 5$ are numerical coefficients. The coefficient $a_0^{(nX)}$ receives contributions from different chiral orders, in particular

$$a_0^{(nX)} = a_0^{(nX)}(\mathrm{LO}) + a_0^{(nX)}(\mathrm{NLO}) + a_0^{(nX)}(\mathrm{N^2LO}). \tag{143}$$

The values of these coefficients for the n-p case and the cut-off value $\Lambda = 500$ MeV are listed in **Table 8**. From that table, it is possible to appreciate the chiral convergence for the coefficients $a_0^{(np)}$. The NLO correction is $\sim 10\%$ of the LO result. In this case, the N^{2}LO contribution vanishes since the LEC h_π^1 in $V_{PVTC}^{(2)}(\mathrm{TPE})$ multiplies the operator $(\tau_{1z} + \tau_{2z})$. The $\vec{n}$-p spin rotation is sensitive to all the LECs except for the LECs C_4 and h_A^1 multiplying again the isospin term $(\tau_{1z} + \tau_{2z})$; in particular, there is a large sensitivity to C_5 and h_A^2, which multiply the isotensor terms of the PVTC potential.

Regarding the $\vec{n}$-d spin rotation, the coefficients, as reported in **Table 9**, are calculated by using only the NLO PVTC potential. We note the large sensitivity to h_π^1 (this fact is well-known [202, 226]), and to the LEC's C_2 and C_3.

At present there are no measurements of these quantities, however their experimental knowledge could be very useful in isolating certain combinations of LECs.

6.5. EDM of Light Nuclei

The EDM operator $\hat{\boldsymbol{D}}$ is composed by two parts,

$$\hat{\boldsymbol{D}} = \hat{\boldsymbol{D}}_{\mathrm{PCTC}} + \hat{\boldsymbol{D}}_{\mathrm{PVTV}}. \tag{144}$$

TABLE 7 | Values of the coefficients $a_i^{(nh)}$ entering the ^{3}He$(\vec{n},p)^3$H longitudinal asymmetry calculated for the χEFT NLO PVTC potential described in section 3.4 and the N^{3}LO PCTC potential derived in Machleidt and Entem [5] at vanishing neutron beam energy.

$a_0^{(nh)}$(LO)	$a_0^{(nh)}$(TOT)	$a_1^{(nh)}$	$a_2^{(nh)}$	$a_3^{(nh)}$	$a_4^{(nh)}$	$a_5^{(nh)}$
−0.1178	−0.1444	0.0061	0.0226	−0.0199	−0.0174	−0.0005

The PVTC potential has been regularized as in Equation (86) adopting the value $\Lambda_C = 500$ MeV for the cutoff parameter. The PCTC potential has been regularized with the same value of the cutoff parameter. For $a_0^{(nh)}$ we give explicitly its cumulative value at LO and at NLO in the first and second column, respectively.

TABLE 8 | Values of the coefficients entering the expression of the $\vec{n}$ -p spin rotation in units of Rad m^{-1} calculated for the χEFT N^{2}LO PVTC potential described in section 3.4 and the N^{4}LO PCTC potential derived in Entem et al. [18] at vanishing neutron beam energy.

$a_0^{(np)}(LO)$	1.227	$a_1^{(np)}$	0.257	$b_1^{(np)}$	1.653
$a_0^{(np)}(NLO)$	0.137	$a_2^{(np)}$	0.178	$b_2^{(np)}$	−0.181
$a_0^{(np)}(N^2LO)$	0.000	$a_3^{(np)}$	0.106	$b_3^{(np)}$	1.882
$a_0^{(np)}(TOT)$	1.364	$a_4^{(np)}$	0.000	$b_4^{(np)}$	0.000
		$a_5^{(np)}$	−0.949	$b_5^{(np)}$	4.456

The PVTC potential has been regularized as in Equation (86) adopting the value $\Lambda_C = 500$ MeV for the cutoff parameter. The PCTC potential has been regularized with the same value of the cutoff parameter. For $a_0^{(np)}$ we give explicitly the contribution of the different orders, the sum of the three contributions is given in fourth row.

TABLE 9 | The same as in **Table 8** but for the $\vec{n}$ -d spin rotation and using the χEFT NLO PVTC potential and the N^{3}LO PCTC potential derived in Machleidt and Entem [5].

$a_0^{(nd)}$	2.179
$a_1^{(nd)}$	−0.010
$a_2^{(nd)}$	−0.160
$a_3^{(nd)}$	0.191
$a_4^{(nd)}$	0.064
$a_5^{(nd)}$	0.000

$\hat{\boldsymbol{D}}_{\rm PCTC}$ is the electric dipole operator derived from the current $\boldsymbol{J}_{PCTC}$ given in Equation (87), after using the long wavelength approximation and the continuity equation [227], explicitly

$$\hat{\boldsymbol{D}}_{\rm PCTC} = e\sum_i \frac{1+\tau_z(i)}{2}\boldsymbol{r}_i\,, \tag{145}$$

where $e > 0$ is the electric unit charge, $\tau_z(i)$ and $\boldsymbol{r}_i$ are the z component of the isospin and the position of the i-th particle. This operator implicitly takes into account also the main part of the two-body PCTC currents. The $\hat{\boldsymbol{D}}_{\rm PVTV}$ contribution comes from the PVTV current at LO given in Equation (96) and it reads

$$\hat{\boldsymbol{D}}_{\rm PVTV} = \frac{1}{2}\sum_i \left[(d_p+d_n)+(d_p-d_n)\tau_z(i)\right]\boldsymbol{\sigma}_i\,, \tag{146}$$

where d_p and d_n are the EDM of proton and neutron, respectively and $\boldsymbol{\sigma}_i$ is the spin operator which act on the i-th particle. As discussed in section 3.5.1 and in de Vries et al. [143] and Bsaisou et al. [73] the $\hat{\boldsymbol{D}}_{\rm PVTV}$ should also include contributions from transition currents at N^{2}LO. These are not considered in this review.

The EDM of an A nucleus can be expressed as

$$\begin{aligned} d^A &= \langle\psi_+^A|\hat{D}_{\rm PVTV}|\psi_+^A\rangle + 2\,\langle\psi_+^A|\hat{D}_{\rm PCTC}|\psi_-^A\rangle \\ &\equiv d^A_{\rm PVTV} + e\,d^A_{\rm PCTC}\,, \end{aligned} \tag{147}$$

where $|\psi_+^A\rangle$ ($|\psi_-^A\rangle$) is defined to be the even-parity (odd-parity) component of the wave function. In general, due to the smallness of the LECs, the EDM depends linearly on the PVTV LECs

$$d^A_{\rm PVTV} = d_p a_p + d_n a_n \tag{148}$$

$$\begin{aligned} d^A_{\rm PCTC} &= \bar{g}_0 a_0 + \bar{g}_1 a_1 + \bar{g}_2 a_2 \\ &+ \bar{C}_1 A_1 + \bar{C}_2 A_2 + \bar{C}_3 A_3 + \bar{C}_4 A_4 + \bar{C}_5 A_5 + \bar{\Delta} a_\Delta\,, \end{aligned} \tag{149}$$

where the a_i for $i = 0,1,2$, A_i for $i = 1,\ldots,5$, a_Δ, and a_p, a_n are coefficients independent on the LEC values (all coefficients except a_p and a_n have the unit of a length). For the deuteron, $d^2_{\rm PVTV}$ is dominated by one-body components, proportional to the neutron and proton EDM. The coefficients a_p and a_n multiplying the intrinsic neutron and proton EDM, as already pointed out first in Yamanaka and Hiyama [228] and then in Bsaisou et al. [66], are given by,

$$a_n = a_p = \left(1 - \frac{3}{2}P_D\right), \tag{150}$$

where P_D is the percentage of D-wave present in the deuteron wave function. $d^2_{\rm PCTC}$, in the case of the deuteron, receives contribution only from the LECs $\bar{g}_1$, $\bar{\Delta}$, $\bar{C}_3$, and $\bar{C}_4$. The coefficients calculated with the χEFT N^{2}LO PVTV potential described in section 3.5 and the N^{4}LO PCTC potential derived in Entem et al. [18] are reported in **Table 10**. The cutoff for both the PCTC and PVTV potentials has been chosen to be $\Lambda_C = 500$ MeV. The coefficients a_1, A_3, and A_4 agree well with the power counting expectation in Equation (37). The slight suppression of a_1 compared with the naive estimate $a_1 \sim 1$ is in very good agreement with the perturbative pion

TABLE 10 | Values of the coefficients entering the expression of the deuteron EDM calculated for the χEFT N^{2}LO PVTV potential described in section 3.5 and the N^{4}LO PCTC potential derived in Entem et al. [18].

$a_n(a_p)$	0.939
a_1 [fm]	0.200
A_3 [fm]	0.013
A_4 [fm]	−0.013
a_Δ(NLO) [fm]	−0.894
a_Δ(N^{2}LO) [fm]	+0.590
a_Δ(TOT) [fm]	−0.304

The PVTC potential has been regularized as in Equation (86) adopting the value $\Lambda_C = 500$ MeV for the cutoff parameter. The PCTC potential has been regularized with the same value of the cutoff parameter. For a_Δ we give explicitly the contribution of the different orders, the sum of the two contributions is given in the last row.

TABLE 11 | The same as in **Table 10** but for the ^{3}H and ^{3}He EDM.

	^{3}H	^{3}He
a_n	−0.033	0.908
a_p	0.909	−0.033
a_0 [fm]	−0.053	0.054
a_1 [fm]	0.158	0.158
a_2 [fm]	−0.119	0.119
A_1 [fm]	0.006	−0.006
A_2 [fm]	−0.010	0.010
A_3 [fm]	−0.008	−0.008
A_4 [fm]	0.013	0.013
A_5 [fm]	−0.022	0.022
a_Δ(NLO) [fm]	−0.941	−0.929
a_Δ(N^{2}LO) [fm]	+0.598	+0.591
a_Δ(TOT) [fm]	−0.343	−0.339

power counting [70]. The LO perturbative pion calculation of a_1 agrees with the value in **Table 10** at the 20% level [70]. Results obtained in chiral EFT with N^{2}LO PCTC potentials [66], and with "hybrid" approaches [143, 228] based on chiral PVTV and phenomenological PCTC potentials, also agree well with the results reported in **Table 10**. The contribution of the three-pion coupling a_Δ is a bit more problematic. We find in this case that the contribution of the N^{2}LO term is of the order of $\sim$ 60% of the NLO term. We will discuss the issue of these large N^{2}LO corrections more in detail below.

Depending on the source of CP violation at the quark level, the deuteron EDM can be dominated by different LECs. For sources such as quark chromo-EDMs and four-quark operators Ξ, for which $\bar{g}_1$ is induced without any chiral suppression, the pion-exchange contribution proportional to $\bar{g}_1$ is expected to dominate the deuteron EDM. For sources such as quark EDMs or the Weinberg operator, however, the deuteron EDM is well-approximated by the sum of the nucleon EDMs. For the θ-term, the pion-exchange contributions are expected to be minor as well. Given measurements of the deuteron and nucleon EDMs, one can, therefore, identify the underlying source of CP violation [70, 229].

As regarding the ^{3}H and ^{3}He EDMs, the results are summarized in **Table 11**. The coefficients a_0 and a_1 are again a bit smaller than the $\mathcal{O}(1)$ expectation. Note that the value for a_0 reported in **Table 10** is approximately 50% smaller than that reported in Bsaisou et al. [66]. This difference can be traced back to the contribution of the TPE, which was not included in that work. Performing the calculations at LO, namely including only the OPE term, the a_0 coefficient results to agree with that reported in Bsaisou et al. [66]. The values of the numerical coefficients are mostly equal in modulus between ^{3}H and ^{3}He except a_p and a_n. The coefficients associated to isovector terms have the same sign while all the others are opposite. Again the contribution of the N^{2}LO potential term to a_Δ is significant, about 60%. This issue is discussed below.

Let us now consider in more detail the issue of the NLO and N^{2}LO contributions to a_Δ. We have seen that in all cases the N^{2}LO correction to a_Δ is of the order of 60%, a bit larger than expected. Explicitly, the coefficient a_Δ can be written as [75]

$$a_\Delta = a_\Delta(\mathrm{NLO}) + a_\Delta(\mathrm{N^2LO}), \quad (151)$$

$$a_\Delta(\mathrm{NLO}) = a_\Delta(0) + a_\Delta(3\mathrm{N}), \quad (152)$$

$$a_\Delta(\mathrm{N^2LO}) = c_1 a_\Delta(1) + c_2 a_\Delta(2) + c_3 a_\Delta(3), \quad (153)$$

where $a_\Delta(0)$ comes from the NLO potential $V^{(0)}_{PVTV}(3\pi)$ given in Equation (93) and $a_\Delta(3N)$ from the 3N potential given in Equation (95). The N^{2}LO terms come from $V^{(1)}_{PVTV}(3\pi)$, where the LECs c_1, c_2 and c_3 appear. The values for the various components of coefficient a_Δ for different nuclei are reported in **Table 12**. To calculate the values reported in **Tables 10**, **11**, the following values were adopted: $c_1 = -1.10$ GeV^{-1}, $c_2 = +3.57$ GeV^{-1}, and $c_3 = -5.54$ GeV^{-1} as reported in Hoferichter et al. [219] and Hoferichter et al. [230]. The large N^{2}LO corrections are caused by the large values of these LECs[8]. For more detail, see [75]. For the trinucleon systems, the values of $a_\Delta(3\mathrm{N})$ give a correction to a_Δ(NLO) of the order of $\sim$ 25%, which is in line with the chiral perturbation theory prediction because these contributions appear at the same order.

Similarly to the deuteron EDM, the trinucleon EDMs can be dominated by different terms. As the isoscalar interaction proportional to $\bar{g}_0$ and $\bar{C}_{1,2}$ now gives a sizable contribution, the trinucleon EDMs are noticeably different from the nucleon EDMs for the QCD θ-term, the quark chromo-EDMs, the four-quark operators Ξ, and potentially the Weinberg operator and the four-quark operators Σ. These EDMs therefore provide complementary information to the deuteron and nucleon EDMs. Combined measurements of all these EDMs would allow one to unravel various BSM models of new CP violation [71].

[8]Notice that the values of the LECs c_i obtained from the pion-nucleon amplitude at NLO, which would be appropriate for $V^{(1)}_{PVTV}$, are considerably smaller in magnitude. We, however, decided to adopt the larger values to be consistent with the employed PCTC potential.

TABLE 12 | Values of the various components of coefficient a_Δ as given in Equation (151) in units of e fm for the different nuclei.

	^{2}H	^{3}H	^{3}He
$a_\Delta(0)$ [fm]	−0.894	−0.751	−0.749
$a_\Delta(3N)$ [fm]	–	−0.190	−0.180
$a_\Delta(1)$ [fm GeV]	0.120	0.098	0.098
$a_\Delta(2)$ [fm GeV]	−0.119	−0.110	−0.109
$a_\Delta(3)$ [fm GeV]	−0.207	−0.198	−0.196

The coefficients have been evaluated using the N^{4}LO PC potential derived in Entem et al. [18] and using a cutoff parameter of value $\Lambda_C = 500$ MeV.

7. CONCLUSIONS AND PERSPECTIVES

In this paper we have discussed the current status of the PVTC and PVTV nuclear interactions using the traditional approach based on phenomenological boson exchange models and as well as utilizing the modern frameworks of pionless and chiral EFT. The study of PVTC signals in nuclei is interesting since it derives from the non-leptonic weak interactions between quarks. Furthermore, a solid understanding of the manifestation of PVTC interactions at the nuclear level would give us confidence in the analysis of the more exotic PVTV case and other BSM nuclear observables. In fact, PVTV observables provide very valuable information since they are sensitive to interactions originating from the θ-term in the SM and even to more exotic mechanisms appearing in BSM theories.

As discussed in this review, the theoretical understanding of the PVTC and PVTV interactions is already rather advanced. Interactions in χEFT have been developed up to N^{2}LO. The convergence of the χEFT appears to be problematic only for the contributions proportional to the $\pi\pi NN$ LECs c_i, due to the large values of those coefficients as measured in πN scattering [219]. Given that the LECs $c_{2,3,4}$ are largely driven by the $\Delta(1232)$ [231], one may expect a better convergence in a formulation of chiral EFT that includes the Δ as an explicit degree of freedom. Furthermore, large N_c analysis may help in reducing the number of contact LECs. Also Lattice QCD calculations start to give valuable information [132, 232].

We have also reported the results of the theoretical calculations of several observables performed using the potentials derived within the χEFT framework. The PVTC observables considered include (i) the longitudinal asymmetry in $\vec{n}$-p radiative capture, (ii) the longitudinal asymmetry in proton-proton elastic scattering, (iii) the longitudinal asymmetry in the ^{3}He$(\vec{n},p)^3$H reaction, and (iv) the spin rotation of a neutron beam passing through a hydrogen and deuterium gas. As an example of a PVTV observable, we have studied the EDMs of some light nuclei. The main motivation to study these observables is that for such light systems, the theoretical analysis can be carried out without invoking any uncontrolled approximations. Thus, comparison with the experimental data can be performed unambiguously. The analyses of PVTC and PVTV observables using meson exchange models can be found in other review articles [34, 39, 131] and are not reported here.

As discussed previously, there exists a first measurement of the parameter a_γ of the radiative neutron capture on the proton $\vec{n}p \rightarrow d\gamma$. The large error derives from the smallness of this parameter which makes this measurement very challenging [209]. This observable is directly connected to the LO pion-nucleon PVTC coupling constant $a_\gamma \sim h_\pi^1$. However, as we have seen, the theoretical estimate of the proportionality coefficient has been obtained with a relatively large theoretical uncertainty due to sizeable cancellations between different contributions. Therefore, to infer information from this observable, it will be necessary to make progress in both the experimental and theoretical analyses.

Other important information is brought forth by the three measurements at different energies of the $\vec{p}$-p longitudinal asymmetry. This observable is sensitive to h_π^1 via the TPE component of the PVTC potential and also to other LECs. In fact, owing to the isospin quantum numbers $T = 1$, $T_z = 1$ of the p-p system, the LO contribution vanishes. Moreover, at NLO (N^{2}LO), this observable depends on two (three) combinations of the LECs. Unfortunately, only two of the performed measurements give independent information. These two data have not been obtained with enough accuracy, so the constraints to the (combinations of) LECs which can be obtained are not so stringent [42, 46], as discussed in section 6.2. For this observable the wave functions are easily obtained. However, the vanishing of the LO contribution makes the χPT convergence more uncertain. On the other hand, it would be very useful to have more accurate experimental measurements.

Very recently, a measurement of the $\vec{n}$-^{3}He longitudinal asymmetry at the SNS facility was reported [222]. For this $A = 4$ system it is possible to perform accurate calculations of the wave functions, and therefore this observable can give valuable information in particular on the LECs C_i. A complete calculation, however, should also include the PVTC 3N interaction terms.

Regarding the spin rotation observables, no experiments to measure the $\vec{n}$-p and $\vec{n}$-d spin rotation angles, which could provide useful information on some of the contact term LECs, are planned at present. The experimental detection of a non-vanishing $\vec{n}$-p spin rotation would be rather important for two reasons: *i)* the theoretical treatment of the two-nucleon system does not present any difficulty numerically, while *ii)* this observable is sensitive to the LO term and therefore the chiral expansion of the potential is well under control, as discussed in section 6.4. Regarding the $\vec{n}$-d spin rotation, the same is not completely true since, as discussed in section 3.4 one has to include also the PVTC 3N interaction terms which start to appear at N^{2}LO. This is an interesting extension of χEFT which will be considered in the future. From the experimental point of view, we note that there is an existing experiment trying to measure the $\vec{n}$-^{4}He spin rotation at NIST [233]. Some years ago there was a measurement of the longitudinal asymmetry in $\vec{p}$-^{4}He scattering, but this experiment was performed at a rather high energy of the proton beam (46 MeV) [234] and this makes the theoretical treatment very difficult and impossible without some approximations. From the theoretical point of view, recently there has been a rapid progress in solving accurately the $A = 5$

nuclear problem. In particular, the solution of $A = 5$ Faddeev-Yakubovsky equations [235, 236] has allowed a first study of the $\vec{n}$-^{4}He spin rotation [237]. Also accurate applications using the so called "No-Core-Shell-Model with Continuum" technique have been reported [238, 239]. Therefore, we expect that, once the experimental value for the $\vec{n}$-^{4}He spin rotation becomes available, it can be readily analyzed in the χEFT, pionless, and DDH frameworks.

To have the possibility to pin down all the LECs (6 LECs at NLO and 5 more at N^{2}LO) more experimental information will be necessary in any case. In particular, an interesting possibility would be to measure PVTC observables in the $A = 3$ system, such as the longitudinal asymmetry of $\vec{p}$-d elastic scattering and the photon asymmetry in $\vec{n}$-d radiative capture. For both reactions, the theoretical treatment would be straightforward, once the PVTC 3N force has been taken into account. Experimental activities for the $A = 3$ systems were already attempted some years ago [240] (see also [39]). After the success of the recent PVTC observable measurements in $A = 2$ and $A = 4$ systems discussed previously, a successful experimental investigation of $A = 3$ observables appears to be possible. Actually, the measurement of the longitudinal photon asymmetry in $\vec{n}$-d radiative capture is currently being planned [241]. Therefore, a new campaign of measurements of PVTC observables in the $A = 3$ systems, in addition to the measure of the $\vec{n}$-^{4}He spin rotation, would furnish enough information to fix (at least, some of) the LECs of the potentials in the different frameworks.

It would be clearly very interesting to take into account also PVTC measurements in medium-mass and heavy-systems. In particular, it is worth to mention that there exist fairly accurate measurements of the gamma angular asymmetry in ^{19}F gamma decay and the gamma circular polarization in ^{18}F gamma decay [242–244]. The mixing induced by the PVTC interaction in the matrix elements can be calibrated by the corresponding analog β decays of Ne isotopes [242]. Despite the large number of nucleons involved, the theoretical analysis can still be reliably performed. Calculations for these transitions have been performed only using the DDH interaction [37, 245].

Regarding the PVTV observables, the measurement of EDMs of particles is the most promising observable for studying CP violation beyond CKM mixing matrix effects. Currently, there are proposals for the direct measurement of EDMs of electrons, single nucleons and light nuclei in dedicated storage rings [77, 78, 81, 82, 246]. This new approach plans to reach an accuracy of $\sim 10^{-16}$ e fm, improving the sensitivity in particular in the hadronic sector. Any measurement of a non-vanishing EDM of this magnitude would provide evidence of PVTV beyond CKM effects [52, 55–57]. However, a single measurement will be insufficient to identify the source of PVTV, only the availability of the measurement of EDM of various light nuclei such as ^{2}H, ^{3}H, and ^{3}He can impose constrains on all the LECs. Other light nuclear EDMs have been discussed in Yamanaka [208] and Yamanaka et al. [247]. EDMs of heavy diamagnetic systems provide very important information as well, but such systems are too large for chiral EFT calculations.

Other observables sensitive to PVTV effects are the transmission of polarized neutrons through a polarized target [248, 249]. In particular, for heavy nuclei the PVTV effects can be enhanced by factors as large as 10^6 [250, 251], see also [252]. In order to exploit this enhancement, some experiments are being planned, such as the NOPTREX experiment at RIKEN [253, 254]. Also polarized nucleon—polarized deuteron scattering has been proposed as a way to detect PVTV signals [226, 255]. Finally, searching for large P- and T-violations in polarized β-decay of ^{8}Li via measurement of the triple vector correlation is under consideration [256]. Clearly, it would be important to be able to detect a non-zero PVTV signal in all these experiments in order to pin down the values of all the LECs.

From the theoretical point of view, calculations of the EDM of ^{2}H, ^{3}H, and ^{3}He can be performed very accurately, including taking into account the contributions of the PVTV 3N force. The robustness of the calculation has been checked by evaluating the EDMs of the nuclei to different chiral orders in the PCTC potential. The discrepancy between the use of the N^{2}LO and the N^{4}LO PCTC potential has been found to be approximately 5% [75].

Currently, the only missing ingredient is the two-body PVTV N^{2}LO currents [73, 143]. Once this problem is solved, one can achieve a fully consistent calculation of the EDM of light nuclei up to N^{2}LO. There are also plans to perform theoretical studies of PVTV observables in $\vec{n}$-$\vec{p}$ and $\vec{n}$-$\vec{d}$ scattering in order to have independent and complementary information about PVTV effects.

The PVTV χEFT interaction developed in the previous sections depends on 11 coupling constants that need to be determined by comparing with experimental data. As already pointed out by many authors [65, 68, 69] and discussed in section 3.2.1, the LECs $\bar{g}_2$, $\bar{C}_3$, $\bar{C}_4$, and $\bar{C}_5$ are suppressed for all CP-violation sources. However, for certain sources, this suppression is not too severe. For example, in Bsaisou et al. [66], an analysis of the nuclear EDM in the minimal left-right scenario is presented in which the Lagrangian terms with LECs $\bar{C}_3$ and $\bar{C}_4$ appear at N^{2}LO. In any case, since the CP-violation sources are not known, the only way to determine them is to fit all possible LECs and compare the results with predictions for various scenarios.

Most of the observables discussed so far were obtained (or they are planned to be studied) at low energies, where also the pionless EFT framework is valid. The advantage of this framework is related to the fact that the resulting potentials depends on only five LECs. Then, assuming the validity of the large N_c analysis [47, 49], the number of dominant LECs could be further reduced. This new paradigm is advocated for the PVTC case in Gardner et al. [39]. For this case, only two LECs are expected to be dominant, the other three demoted to be subleading. Unfortunately, the photon asymmetry of $\vec{n}p \to d\gamma$ depends on the subleading LECs (this could explain its relative smallness) and therefore cannot be used to give information on the two leading LECs. Moreover, only the low energy $\vec{p}$-p longitudinal asymmetry measurement may be

used to test if this hierarchy is realized in Nature (the other measurement is taken at too high energy to be used in the pionless EFT framework). The other observable which can give valuable information is the $\vec{n}$-^{3}He longitudinal asymmetry, for which the experimental result was just published. However, no theoretical calculations of this observable performed in the framework of pionless EFT are available at present. Additional information could be obtained by calculations of these LECs using Lattice QCD, presently in progress. Regarding the PVTV observables in pionless EFT, here the large N_c analysis predicts that only one of the LECs should be dominant, the other four being suppressed. However, this picture is partially obscured by the fact that the magnitude of the five contact LECs would depend very much on the particular type of the CP-violating source.

In conclusions, the study of PVTC and PVTV observables is an active area of research that provide important tests of the SM and hopefully future evidence for BSM physics.

AUTHOR CONTRIBUTIONS

All authors listed have made a substantial, direct and intellectual contribution to the work, and approved it for publication.

FUNDING

JV was supported by the RHIC Physics Fellow Program of the RIKEN BNL Research Center. EE was supported by BMBF (Grant No. 05P18PCFP1) and by DFG through funds provided to the Sino-German CRC 110 Symmetries and the Emergence of Structure in QCD (Grant No. TRR110). EM was supported in part by the LDRD program at Los Alamos National Laboratory, the DOE topical collaboration on Nuclear Theory for Double-Beta Decay and Fundamental Symmetries, the US DOE, Office of Science, Office of Nuclear Physics, under award numbers DE-AC52-06NA25396. LG, AG, and MV were supported by INFN through the National Initiative FBS.

REFERENCES

1. Machleidt R. Historical perspective and future prospects for nuclear interactions. *Int J Mod Phys E*. (2017) **26**:1730005. doi: 10.1142/S0218301317300053
2. Weinberg S. Nuclear forces from chiral Lagrangians. *Phys Lett B*. (1990) **251**:288–92. doi: 10.1016/0370-2693(90)90938-3
3. Ordonez C, Ray L, van Kolck U. The Two nucleon potential from chiral Lagrangians. *Phys Rev C*. (1996) **53**:2086–105. doi: 10.1103/PhysRevC.53.2086
4. Epelbaum E, Hammer HW, Meißner UG. Modern theory of nuclear forces. *Rev Mod Phys*. (2009) **81**:1773–825. doi: 10.1103/RevModPhys.81.1773
5. Machleidt R, Entem DR. Chiral effective field theory and nuclear forces. *Phys Rept*. (2011) **503**:1–75. doi: 10.1016/j.physrep.2011.02.001
6. Weinberg S. Pion scattering lengths. *Phys Rev Lett*. (1966) **17**:616–21. doi: 10.1103/PhysRevLett.17.616
7. Weinberg S. Nonlinear realizations of chiral symmetry. *Phys Rev*. (1968) **166**:1568–77. doi: 10.1103/PhysRev.166.1568
8. Weinberg S. Phenomenological Lagrangians. *Physica A*. (1979) **96**:327–40. doi: 10.1016/0378-4371(79)90223-1
9. Coleman SR, Wess J, Zumino B. Structure of phenomenological Lagrangians. 1. *Phys Rev*. (1969) **177**:2239–47. doi: 10.1103/PhysRev.177.2239
10. Callan CG Jr., Coleman SR, Wess J, Zumino B. Structure of phenomenological Lagrangians. 2. *Phys Rev*. (1969) **177**:2247–50. doi: 10.1103/PhysRev.177.2247
11. Gasser J, Leutwyler H. Chiral perturbation theory to one loop. *Ann Phys*. (1984) **158**:142. doi: 10.1016/0003-4916(84)90242-2
12. Bernard V, Kaiser N, Meißner UG. Chiral dynamics in nucleons and nuclei. *Int J Mod Phys E*. (1995) **4**:193–346. doi: 10.1142/S0218301395000092
13. Bernard V. Chiral perturbation theory and baryon properties. *Prog Part Nucl Phys*. (2008) **60**:82–60. doi: 10.1016/j.ppnp.2007.07.001
14. Bijnens J, Ecker G. Mesonic low-energy constants. *Ann Rev Nucl Sci*. (2014) **64**:149–74. doi: 10.1146/annurev-nucl-102313-025528
15. Epelbaum E, Gegelia J, Meißner UG. Wilsonian renormalization group versus subtractive renormalization in effective field theories for nucleon–nucleon scattering. *Nucl Phys*. (2017) **B925**:161–85. doi: 10.1016/j.nuclphysb.2017.10.008
16. Entem DR, Kaiser N, Machleidt R, Nosyk Y. Peripheral nucleon-nucleon scattering at fifth order of chiral perturbation theory. *Phys Rev C*. (2015) **91**:014002. doi: 10.1103/PhysRevC.91.014002
17. Epelbaum E, Krebs H, Meißner UG. Precision nucleon-nucleon potential at fifth order in the chiral expansion. *Phys Rev Lett*. (2015) **115**:122301. doi: 10.1103/PhysRevLett.115.122301
18. Entem DR, Machleidt R, Nosyk Y. High-quality two-nucleon potentials up to fifth order of the chiral expansion. *Phys Rev C*. (2017) **96**:024004. doi: 10.1103/PhysRevC.96.024004
19. Reinert P, Krebs H, Epelbaum E. Semilocal momentum-space regularized chiral two-nucleon potentials up to fifth order. *Eur Phys J A*. (2018) **54**:86. doi: 10.1140/epja/i2018-12516-4
20. Kaplan DB, Savage MJ, Wise MB. A New expansion for nucleon-nucleon interactions. *Phys Lett B*. (1998) **424**:390–6. doi: 10.1016/S0370-2693(98)00210-X
21. Nogga A, Timmermans RGE, van Kolck U. Renormalization of one-pion exchange and power counting. *Phys Rev C*. (2005) **72**:054006. doi: 10.1103/PhysRevC.72.054006
22. Birse MC. Power counting with one-pion exchange. *Phys Rev C*. (2006) **74**:014003. doi: 10.1103/PhysRevC.74.014003
23. Valderrama MP. Perturbative renormalizability of chiral two pion exchange in nucleon-nucleon scattering. *Phys Rev C*. (2011) **83**:024003. doi: 10.1103/PhysRevC.83.024003
24. Long B, Yang CJ. Short-range nuclear forces in singlet channels. *Phys Rev C*. (2012) **86**:024001. doi: 10.1103/PhysRevC.86.024001
25. Epelbaum E, Gegelia J. Weinberg′s approach to nucleon–nucleon scattering revisited. Phys Lett B. (2012) **716**:338–44. doi: 10.1016/j.physletb.2012.08.025
26. Lepage GP. How to renormalize the Schrodinger equation. In: Nuclear Physics. *Proceedings, 8th Jorge Andre Swieca Summer School, Sao Jose dos Campos, Campos do Jordao*. Brazil (1997). p. 135–80.
27. Epelbaum E, Meißner UG. On the renormalization of the one-pion exchange potential and the consistency of Weinberg's power counting. *Few Body Syst*. (2013) **54**:2175–90. doi: 10.1007/s00601-012-0492-1
28. Epelbaum E, Gegelia J. Regularization, renormalization and 'peratization' in effective field theory for two nucleons. *Eur Phys J*. (2009) A41:341–54. doi: 10.1140/epja/i2009-10833-3
29. Valderrama MP. Power counting and Wilsonian Renormalization in Nuclear Effective Field Theory. *Int J Mod Phys E*. (2016) **25**:1641007. doi: 10.1142/S021830131641007X
30. Epelbaum E, Gasparyan AM, Gegelia J, Meißner UG. How (not) to renormalize integral equations with singular potentials in effective field theory. *Eur Phys J A*. (2018) **54**:186. doi: 10.1140/epja/i2018-12632-1
31. Hammer HW, König S, van Kolck U. Nuclear effective field theory: status and perspectives. *arXiv:1906 [Preprint]*.12122 (2019).

32. Bedaque PF, van Kolck U. Effective field theory for few nucleon systems. *Ann Rev Nucl Sci*. (2002) **52**:339–96. doi: 10.1146/annurev.nucl.52.050102.090637
33. Hammer HW, Platter L. Efimov States in Nuclear and Particle Physics. *Ann Rev Nucl Sci*. (2010) **60**:207–36. doi: 10.1146/annurev.nucl.012809.104439
34. Ramsey-Musolf MJ, Page SA. Hadronic parity violation: a new view through the looking glass. *Ann Rev Nucl Sci*. (2006) **56**:1–52. doi: 10.1146/annurev.nucl.54.070103.181255
35. Hertzog D, Ramsey-Musolf MJ. Parity- and time-reversal tests in nuclear physics. In: Henley EM, Ellis SD, editors. 100 *Years of Subatomic Physics*. Singapore: World Scientific (2013) p. 155–70. doi: 10.1142/9789814425810_0006
36. Schindler MR, Springer RP. The theory of parity violation in few-nucleon systems. *Prog Part Nucl Phys*. (2013) **72**:1–43. doi: 10.1016/j.ppnp.2013.05.002
37. Haxton WC, Holstein BR. Hadronic parity violation. *Prog Part Nucl Phys*. (2013) **71**:185–203. doi: 10.1016/j.ppnp.2013.03.009
38. de Vries J, Meißner UG. Violations of discrete space–time symmetries in chiral effective field theory. *Int J Mod Phys E*. (2016) **25**:1641008. doi: 10.1142/S0218301316410081
39. Gardner S, Haxton WC, Holstein BR. A new paradigm for hadronic parity nonconservation and its experimental implications. *Ann Rev Nucl Sci*. (2017) **67**:69–95. doi: 10.1146/annurev-nucl-041917-033231
40. Zhu SL, Maekawa CM, Holstein BR, Ramsey-Musolf MJ, van Kolck U. Nuclear parity-violation in effective field theory. *Nucl Phys A*. (2005) **748**:435–98. doi: 10.1016/j.nuclphysa.2004.10.032
41. de Vries J, Meißner UG, Epelbaum E, Kaiser N. Parity violation in proton-proton scattering from chiral effective field theory. *Eur Phys J*. (2013) A49:149. doi: 10.1140/epja/i2013-13149-9
42. Viviani M, Baroni A, Girlanda L, Kievsky A, Marcucci LE, Schiavilla R. Chiral effective field theory analysis of hadronic parity violation in few-nucleon systems. *Phys Rev C*. (2014) **89**:064004. doi: 10.1103/PhysRevC.89.064004
43. Adelberger EG, Haxton WC. Parity violation in the nucleon-nucleon interaction. *Ann Rev Nucl Part Sci*. (1985) **35**:501–58. doi: 10.1146/annurev.ns.35.120185.002441
44. Girlanda L. On a redundancy in the parity-violating 2-nucleon contact Lagrangian. *Phys Rev*. (2008) C77:067001. doi: 10.1103/PhysRevC.77.067001
45. Danilov GS. Circular polarization of γ quanta in absorption of neutrons by protons and isotopic structure of weak interactions. *Phys Lett*. (1965) **18**:40–41. doi: 10.1016/0031-9163(65)90024-7
46. de Vries J, Li N, Meißner UG, Kaiser N, Liu XH, Zhu SL. A study of the parity-odd nucleon-nucleon potential. *Eur Phys J A*. (2014) **50**:108. doi: 10.1140/epja/i2014-14108-8
47. Schindler MR, Springer RP, Vanasse J. Large-N_c limit reduces the number of independent few-body parity-violating low-energy constants in pionless effective field theory. *Phys Rev C*. (2016) **93**:025502. doi: 10.1103/PhysRevC.93.025502
48. Phillips DR, Samart D, Schat C. Parity-violating nucleon-nucleon force in the $1/N_c$ expansion. *Phys Rev Lett*. (2015) **114**:062301. doi: 10.1103/PhysRevLett.114.062301
49. Vanasse J. Parity-violating three-nucleon interactions at low energies and large N_C. *Phys Rev C*. (2019) **99**:054001. doi: 10.1103/PhysRevC.99.054001
50. Desplanques B, Donoghue JF, Holstein BR. Unified treatment of the parity violating nuclear force. *Annals Phys*. (1980) **124**:449. doi: 10.1016/0003-4916(80)90217-1
51. 't Hooft G. Symmetry breaking through Bell-Jackiw anomalies. *Phys Rev Lett*. (1976) **37**:8–11. doi: 10.1103/PhysRevLett.37.8
52. Pospelov M, Ritz A. Electric dipole moments as probes of new physics. *Ann Phys*. (2005) **318**:119–69. doi: 10.1016/j.aop.2005.04.002
53. Sakharov AD. Violation of CP Invariance, C asymmetry, and baryon asymmetry of the universe. *Pisma Zh Eksp Teor Fiz*. (1967) **5**:32–5.
54. Cohen AG, Kaplan DB, Nelson AE. Progress in electroweak baryogenesis. *Ann Rev Nucl Sci*. (1993) **43**:27–70. doi: 10.1146/annurev.ns.43.120193.000331
55. Czarnecki A, Krause B. Neutron electric dipole moment in the standard model: valence quark contributions. *Phys Rev Lett*. (1997) **78**:4339–42. doi: 10.1103/PhysRevLett.78.4339
56. Mannel T, Uraltsev N. Loop-less electric dipole moment of the nucleon in the standard model. *Phys Rev D*. (2012) **85**:096002. doi: 10.1103/PhysRevD.85.096002
57. Mannel T, Uraltsev N. Charm CP Violation and the electric dipole moments from the charm scale. *J High Energy Phys*. (2013) **03**:64. doi: 10.1007/JHEP03(2013)064
58. Wirzba A, Bsaisou J, Nogga A. Permanent electric dipole moments of single-, two-, and three-nucleon systems. *Int J Mod Phys E*. (2017) **26**:1740031. doi: 10.1142/S0218301317400316
59. Seng CY. Reexamination of the standard model nucleon electric dipole moment. *Phys Rev C*. (2015) **91**:025502. doi: 10.1103/PhysRevC.91.025502
60. Baker CA, Doyle DD, Geltenbort P, Green K, van der Grinten MGD, Harris PG, et al. An improved experimental limit on the electric dipole moment of the neutron. *Phys Rev Lett*. (2006) **97**:131801. doi: 10.1103/PhysRevLett.97.131801
61. Pendlebury JM, Afach S, Ayres NJ, Baker CA, Ban G, Bison G, et al. Revised experimental upper limit on the electric dipole moment of the neutron. *Phys Rev D*. (2015) **92**:092003. doi: 10.1103/PhysRevD.92.092003
62. Graner B, Chen Y, Lindahl EG, Heckel BR. Reduced limit on the permanent electric dipole moment of Hg199. *Phys Rev Lett*. (2016) **116**:161601. doi: 10.1103/PhysRevLett.116.161601
63. Dmitriev VF, Sen'kov RA. Schiff moment of the mercury nucleus and the proton dipole moment. *Phys Rev Lett*. (2003) **91**:212303. doi: 10.1103/PhysRevLett.91.212303
64. Andreev V, Ang DG, DeMille D, Doyle JM, Gabrielse G, Haefner J, et al. Improved limit on the electric dipole moment of the electron. *Nature*. (2018) **562**:355–60. doi: 10.1038/s41586-018-0599-8
65. Mereghetti E, Hockings WH, van Kolck U. The effective chiral Lagrangian from the theta term. *Ann Phys*. (2010) **325**:2363–409. doi: 10.1016/j.aop.2010.03.005
66. Bsaisou J, de Vries J, Hanhart C, Liebig S, Meißner UG, Minossi D, et al. Nuclear electric dipole moments in chiral effective field theory. *J High Energy Phys*. (2015) **03**:104. doi: 10.1007/JHEP05(2015)083
67. Grzadkowski B, Iskrzynski M, Misiak M, Rosiek J. Dimension-six terms in the standard model Lagrangian. *J High Energy Phys*. (2010) **10**:085. doi: 10.1007/JHEP10(2010)085
68. de Vries J, Mereghetti E, Timmermans RGE, van Kolck U. The effective chiral Lagrangian from dimension-six parity and time-reversal violation. *Annals Phys*. (2013) **338**:50–96. doi: 10.1016/j.aop.2013.05.022
69. Bsaisou J, Meißner UG, Nogga A, Wirzba A. P- and T-violating Lagrangians in chiral effective field theory and nuclear electric dipole moments. *Ann Phys*. (2015) **359**:317–70. doi: 10.1016/j.aop.2015.04.031
70. de Vries J, Mereghetti E, Timmermans RGE, van Kolck U. Parity- and time-reversal-violating form factors of the deuteron. *Phys Rev Lett*. (2011) **107**:091804. doi: 10.1103/PhysRevLett.107.091804
71. Dekens W, de Vries J, Bsaisou J, Bernreuther W, Hanhart C, Meißner UG, et al. Unraveling models of CP violation through electric dipole moments of light nuclei. *J High Energy Phys*. (2014) **07**: 69. doi: 10.1007/JHEP07(2014)069
72. Maekawa CM, Mereghetti E, de Vries J, van Kolck U. The time-reversal- and parity-violating nuclear potential in chiral effective theory. *Nucl Phys A*. (2011) **872**:117–60. doi: 10.1016/j.nuclphysa.2011.09.020
73. Bsaisou J, Hanhart C, Liebig S, Meißner UG, Nogga A, Wirzba A. The electric dipole moment of the deuteron from the QCD θ-term. *Eur Phys J A*. (2013) **49**:31. doi: 10.1140/epja/i2013-13031-x
74. Epelbaum E, Glockle W, Meißner UG. The Two-nucleon system at next-to-next-to-next-to-leading order. *Nucl Phys A*. (2005) **747**:362–424. doi: 10.1016/j.nuclphysa.2004.09.107
75. Gnech A, Viviani M. Time reversal violation in light nuclei. *Phys Rev C*. (2020) **101**:024004 doi: 10.1103/PhysRevC.101.024004
76. Dobaczewski J, Engel J, Kortelainen M, Becker P. Correlating Schiff moments in the light actinides with octupole moments. *Phys Rev Lett*. (2018) **121**:232501. doi: 10.1103/PhysRevLett.121.232501
77. Orlov YF, Morse WM, Semertzidis YK. Resonance method of electric-dipole-moment measurements in storage rings. *Phys Rev Lett*. (2006) **96**:214802. doi: 10.1103/PhysRevLett.96.214802
78. Semertzidis YK. A storage ring proton electric dipole moment experiment: most sensitive experiment to CP-violation beyond the standard model. In:

Particles and Fields. Proceedings, Meeting of the Division of the American Physical Society, DPF 2011. Providence, RI (2011).
79. Lehrach A, Lorentz B, Morse W, Nikolaev N, Rathmann F. Precursor experiments to search for permanent electric dipole moments (EDMs) of protons and deuterons at COSY. *arXiv preprint arXiv:1201*.5773 (2012).
80. Pretz J. Measurement of permanent electric dipole moments of charged hadrons in storage rings. *Hyperfine Interact*. (2013) **214**:111–117. doi: 10.1007/s10751-013-0799-4
81. Rathmann F, Saleev A, Nikolaev NN. The search for electric dipole moments of light ions in storage rings. *J Phys Conf Ser*. (2013) **447**:012011. doi: 10.1088/1742-6596/447/1/012011
82. Abusaif F, Aggarwal A, Aksentev A, Alberdi-Esuain B, Atanasov A, Barion L, et al. Storage ring to search for electric dipole moments of charged particles-feasibility study. *arXiv preprint arXiv:1912*.07881 (2019).
83. Wu CS, Ambler E, Hayward RW, Hoppes DD, Hudson RP. Experimental test of parity conservation in beta decay. *Phys Rev*. (1957) **105**:1413–4. doi: 10.1103/PhysRev.105.1413
84. Prescott CY, Atwood WB, Leslie Cottrell R, DeStaebler HC, Garwin EL, Gonidec A, et al. Parity nonconservation in inelastic electron scattering. *Phys Lett B*. (1978) **77**:347–52. doi: 10.2172/5786614
85. Androić D, Armstrong DS, Asaturyan A, Averett T, Balewski J, Bartlett K, et al. Precision measurement of the weak charge of the proton. *Nature*. (2018) **557**:207–11. doi: 10.1038/s41586-018-0096-0
86. Tiburzi BC. Hadronic parity violation at next-to-leading order. *Phys Rev D*. (2012) **85**:054020. doi: 10.1103/PhysRevD.85.054020
87. Buchmuller W, Wyler D. Effective lagrangian analysis of new interactions and flavor conservation. *Nucl Phys B*. (1986) **268**:621–53. doi: 10.1016/0550-3213(86)90262-2
88. Kaplan DB, Savage MJ. An analysis of parity violating pion - nucleon couplings. *Nucl Phys A*. (1993) **556**:653–71. doi: 10.1016/0375-9474(93)90475-D
89. Christenson JH, Cronin JW, Fitch VL, Turlay R. Evidence for the 2π decay of the K_2^0 meson. *Phys Rev Lett*. (1964) **13**:138–40. doi: 10.1103/PhysRevLett.13.138
90. Abouzaid E, Arenton M, Barker AR, Barrio M, Bellantoni L, Blucher E, et al. Precise measurements of direct CP violation, CPT symmetry, and other parameters in the neutral kaon system. *Phys Rev D*. (2011) **83**:092001. doi: 10.1103/PhysRevD.83.092001
91. Batley JR, Dosanjh RS, Gershon TJ, Kalmus GE, Lazzeroni C, Munday DJ, et al. A Precision measurement of direct CP violation in the decay of neutral kaons into two pions. *Phys Lett B*. (2002) **544**:97–112. doi: 10.1016/S0370-2693(02)02416-4
92. Aubert B, Boutigny D, Gaillard JM, Hicheur A, Karyotakis Y, Lees JP, et al. Observation of CP violation in the B^0 meson system. *Phys Rev Lett*. (2001) **87**:091801. doi: 10.1103/PhysRevLett.87.091801
93. Abe K, Abe K, Abe R, Adachi I, Ahn BS, Aihara H, et al. Observation of large CP violation in the neutral *B* meson system. *Phys Rev Lett*. (2001) **87**:091802. doi: 10.1103/PhysRevLett.87.091802
94. Aaij R, Abellan Beteta C, Adeva B, Adinolfi M, Aidala CA, Ajaltouni Z, et al. Observation of *CP* violation in charm decays. *Phys Rev Lett*. (2019) **122**:211803. doi: 10.1103/PhysRevLett.122.211803
95. Khriplovich IB, Zhitnitsky AR. What is the value of the neutron electric dipole moment in the Kobayashi-Maskawa model? *Phys Lett B*. (1982) **109**:490–2. doi: 10.1016/0370-2693(82)91121-2
96. Pospelov ME, Khriplovich IB. Electric dipole moment of the W Boson and the electron in the Kobayashi-Maskawa model. *Sov J Nucl Phys*. (1991) **53**:638–40.
97. Booth MJ. The Electric dipole moment of the W and electron in the Standard Model. *arXiv preprint* arXiv:hep-ph/9301293 (1993).
98. Pospelov M, Ritz A. CKM benchmarks for electron electric dipole moment experiments. *Phys Rev D*. (2014) **89**:056006. doi: 10.1103/PhysRevD.89.056006
99. Callan CG Jr., Dashen RF, Gross DJ. The structure of the gauge theory vacuum. *Phys Lett B*. (1976) **63**:334–40. doi: 10.1016/0370-2693(76)90277-X
100. 't Hooft G. Computation of the quantum effects due to a four-dimensional pseudoparticle. *Phys Rev D*. (1976) **14**:3432–50. doi: 10.1103/PhysRevD.14.3432
101. Baluni V. CP Violating effects in QCD. *Phys Rev D*. (1979) **19**:2227–30. doi: 10.1103/PhysRevD.19.2227
102. Crewther RJ, Di Vecchia P, Veneziano G, Witten E. Chiral estimate of the electric dipole moment of the neutron in quantum chromodynamics. *Phys Lett B*. (1979) **88**:123. doi: 10.1016/0370-2693(79)90128-X
103. Dragos J, Luu T, Shindler A, de Vries J, Yousif A. Confirming the existence of the strong CP problem in lattice QCD with the gradient flow. *arXiv preprint arXiv:1902*.03254 (2019).
104. Gavela MB, Hernandez P, Orloff J, Pene O. Standard model CP violation and baryon asymmetry. *Mod Phys Lett A*. (1994) **9**:795–810. doi: 10.1142/S0217732394000629
105. Gavela MB, Lozano M, Orloff J, Pene O. Standard model CP violation and baryon asymmetry. Part 1: Zero temperature. *Nucl Phys B*. (1994) **430**:345–81. doi: 10.1016/0550-3213(94)00409-9
106. Gavela MB, Hernandez P, Orloff J, Pene O, Quimbay C. Standard model CP violation and baryon asymmetry. Part 2: Finite temperature. *Nucl Phys B*. (1994) **430**:382–426. doi: 10.1016/0550-3213(94)00410-2
107. Huet P, Sather E. Electroweak baryogenesis and standard model CP violation. *Phys Rev D*. (1995) **51**:379–94. doi: 10.1103/PhysRevD.51.379
108. Khriplovich IB, Lamoreaux SK. *CP Violation Without Strangeness: Electric Dipole Moments of Particles, Atoms, and Molecules*. Berlin: Springer. (1997). doi: 10.1007/978-3-642-60838-4
109. Dekens W, de Vries J. Renormalization group running of dimension-six sources of parity and time-reversal violation. *J High Energy Phys*. (2013) **05**:149. doi: 10.1007/JHEP05(2013)149
110. Engel J, Ramsey-Musolf MJ, van Kolck U. Electric dipole moments of nucleons, nuclei, and atoms: the standard model and beyond. *Prog Part Nucl Phys*. (2013) **71**:21–74. doi: 10.1016/j.ppnp.2013.03.003
111. Jenkins EE, Manohar AV, Stoffer P. Low-energy effective field theory below the electroweak scale: operators and matching. *J High Energy Phys*. (2018) **03**:016. doi: 10.1007/JHEP03(2018)016
112. Mereghetti E. Electric dipole moments: a theory overview. In: 13*th Conference on the Intersections of Particle and Nuclear Physics (CIPANP 2018)*. Palm Springs, CA (2018).
113. Weinberg S. Larger Higgs exchange terms in the neutron electric dipole moment. *Phys Rev Lett*. (1989) **63**:2333. doi: 10.1103/PhysRevLett.63.2333
114. Fuyuto K, Ramsey-Musolf M, Shen T. Electric dipole moments from CP-violating scalar Leptoquark interactions. *Phys Lett B*. (2019) **788**:52–7. doi: 10.1016/j.physletb.2018.11.016
115. Dekens W, de Vries J, Jung M, Vos KK. The phenomenology of electric dipole moments in models of scalar leptoquarks. *J High Energy Phys*. (2019) **01**:69. doi: 10.1007/JHEP01(2019)069
116. Ng J, Tulin S. D versus d: CP violation in beta decay and electric dipole moments. *Phys Rev D*. (2012) **85**:033001. doi: 10.1103/PhysRevD.85.033001
117. Jenkins EE, Manohar AV. Baryon chiral perturbation theory using a heavy fermion Lagrangian. *Phys Lett B*. (1991) **255**:558–62. doi: 10.1016/0370-2693(91)90266-S
118. Baroni A, Girlanda L, Pastore S, Schiavilla R, Viviani M. Nuclear axial currents in chiral effective field theory. *Phys Rev C*. (2016) **93**:015501. doi: 10.1103/PhysRevC.93.015501
119. Kaplan DB, Savage MJ, Springer RP, Wise MB. An Effective field theory calculation of the parity violating asymmetry in $\vec{n} + p \to d + \gamma$. *Phys Lett B*. (1999) **449**:1–5. doi: 10.1016/S0370-2693(99)00032-5
120. Manohar A, Georgi H. Chiral quarks and the nonrelativistic quark model. *Nucl Phys B*. (1984) **234**:189–212. doi: 10.1016/0550-3213(84)90231-1
121. Michel FC. Parity Nonconservation in nuclei. *Phys Rev*. (1964) **133**:B329-B349. doi: 10.1103/PhysRev.133.B329
122. Donoghue JF, Golowich E, Holstein BR. Dynamics of the standard model. *Camb Monogr Part Phys Nucl Phys Cosmol*. (1992) **2**:1–540.
123. McKellar BHJ. The one pion exchange contribution to the weak parity violating nucleon-nucleon potential. *Phys Lett B*. (1967) **26**:107–8. doi: 10.1016/0370-2693(67)90561-8
124. Fischbach E. Application of current algebra and partially conserved axial-vector current to the weak BBpi vertex. *Phys Rev*. (1968) **170**:1398–400. doi: 10.1103/PhysRev.170.1398
125. Tadic D. Weak parity-nonconserving potentials. *Phys Rev*. (1968) **174**:1694–703. doi: 10.1103/PhysRev.174.1694

126. Kummer W, Schweda M. An SU(6) estimate of the effective nonleptonic parity-violating coupling in strangeness-conserving weak processes. *Acta Phys Austriaca*. (1968) **28**:303–8.
127. Mckellar BHJ, Pick P. Pion-pole dominance of the divergence of the weak parity-nonconserving NN rho amplitude. *Phys Rev D*. (1972) **6**:2184–8. doi: 10.1103/PhysRevD.6.2184
128. Dubovik VM, Zenkin SV. Formation of parity nonconserving nuclear forces in the standard model SU(2)(l) X U(1) X SU(3)(c). *Ann Phys*. (1986) **172**:100–35. doi: 10.1016/0003-4916(86)90021-7
129. Feldman GB, Crawford GA, Dubach J, Holstein BR. Delta contributions to the parity violating nuclear interaction. *Phys Rev C*. (1991) **43**:863–74. doi: 10.1103/PhysRevC.43.863
130. Meißner UG, Weigel H. The Parity violating pion nucleon coupling constant from a realistic three flavor Skyrme model. *Phys Lett B*. (1999) **447**:1–7. doi: 10.1016/S0370-2693(98)01569-X
131. Haeberli W, Holstein BR. Parity violation and the nucleon-nucleon system. arXiv preprint arXiv:nucl-th/9510062 (1995). doi: 10.1142/9789812831446_0002
132. Wasem J. Lattice QCD calculation of nuclear parity violation. *Phys Rev C*. (2012) **85**:022501. doi: 10.1103/PhysRevC.85.022501
133. Cheng HY. Reanalysis of strong CP violating effects in chiral perturbation theory. *Phys Rev D*. (1991) **44**:166–74. doi: 10.1103/PhysRevD.44.166
134. Pich A, de Rafael E. Strong CP violation in an effective chiral Lagrangian approach. *Nucl Phys B*. (1991) **367**:313–33. doi: 10.1016/0550-3213(91)90019-T
135. Cho PL. Chiral estimates of strong CP violation revisited. *Phys Rev D*. (1993) **48**:3304–9. doi: 10.1103/PhysRevD.48.3304
136. Borasoy B. The Electric dipole moment of the neutron in chiral perturbation theory. *Phys Rev D*. (2000) **61**:114017. doi: 10.1103/PhysRevD.61.114017
137. Ottnad K, Kubis B, Meißner UG, Guo FK. New insights into the neutron electric dipole moment. *Phys Lett B*. (2010) **687**:42–7. doi: 10.1016/j.physletb.2010.03.005
138. Liu CP, de Vries J, Mereghetti E, Timmermans RGE, van Kolck U. Deuteron magnetic quadrupole moment from chiral effective field theory. *Phys Lett B*. (2012) **713**:447–52. doi: 10.1016/j.physletb.2012.06.024
139. Peccei RD, Quinn HR. CP conservation in the presence of instantons. *Phys Rev Lett*. (1977) **38**:1440–3. doi: 10.1103/PhysRevLett.38.1440
140. Mereghetti E, van Kolck U. Effective field theory and time-reversal violation in light nuclei. *Ann Rev Nucl Sci*. (2015) **65**:215–43. doi: 10.1146/annurev-nucl-102014-022344
141. Cirigliano V, Dekens W, de Vries J, Mereghetti E. An ϵ' improvement from right-handed currents. *Phys Lett B*. (2017) **767**:1–9. doi: 10.1016/j.physletb.2017.01.037
142. Liu CP, Timmermans RGE. P- and T-odd two-nucleon interaction and the deuteron electric dipole moment. *Phys Rev C*. (2004) **70**:055501. doi: 10.1103/PhysRevC.70.055501
143. de Vries J, Higa R, Liu CP, Mereghetti E, Stetcu I, Timmermans RGE, et al. Electric dipole moments of light nuclei from chiral effective field theory. *Phys Rev C*. (2011) **84**:065501. doi: 10.1103/PhysRevC.84.065501
144. de Vries J, Mereghetti E, Walker-Loud A. Baryon mass splittings and strong CP violation in SU(3) chiral perturbation theory. *Phys Rev C*. (2015) **92**:045201. doi: 10.1103/PhysRevC.92.045201
145. Borsanyi S, Durr S, Fodor Z, Hoelbling C, Katz SD, Krieg S, et al. Ab initio calculation of the neutron-proton mass difference. *Science*. (2015) **347**:1452–5. doi: 10.1126/science.1257050
146. Brantley DA, Joo B, Mastropas EV, Mereghetti E, Monge-Camacho H, Tiburzi BC, et al. Strong isospin violation and chiral logarithms in the baryon spectrum. *arXiv preprint arXiv:*1612.07733 (2016).
147. de Vries J, Mereghetti E, Seng CY, Walker-Loud A. Lattice QCD spectroscopy for hadronic CP violation. *Phys Lett B*. (2017) **766**:254–62. doi: 10.1016/j.physletb.2017.01.017
148. Seng CY, Ramsey-Musolf M. Parity-violating and time-reversal-violating pion-nucleon couplings: Higher order chiral matching relations. *Phys Rev C*. (2017) **96**:065204. doi: 10.1103/PhysRevC.96.065204
149. Pospelov M, Ritz A. Neutron EDM from electric and chromoelectric dipole moments of quarks. Phys Rev *D*. (2001) **63**:073015. doi: 10.1103/PhysRevD.63.073015
150. Samart D, Schat C, Schindler MR, Phillips DR. Time-reversal-invariance-violating nucleon-nucleon potential in the $1/N_c$ expansion. *Phys Rev C*. (2016) **94**:024001. doi: 10.1103/PhysRevC.94.024001
151. Guo FK, Horsley R, Meißner UG, Nakamura Y, Perlt H, Rakow PEL, et al. The electric dipole moment of the neutron from 2+1 flavor lattice QCD. *Phys Rev Lett*. (2015) **115**:062001. doi: 10.1103/PhysRevLett.115.062001
152. Abramczyk M, Aoki S, Blum T, Izubuchi T, Ohki H, Syritsyn S. Lattice calculation of electric dipole moments and form factors of the nucleon. *Phys Rev D*. (2017) **96**:014501. doi: 10.1103/PhysRevD.96.014501
153. Gupta R, Jang YC, Yoon B, Lin HW, Cirigliano V, Bhattacharya T. Isovector charges of the nucleon from 2+1+1-flavor Lattice QCD. *Phys Rev D*. (2018) **98**:034503. doi: 10.1103/PhysRevD.98.034503
154. Aoki S, Aoki Y, Bečirevic D, Blum T, Colangelo G, Collins S, et al. FLAG review 2019: Flavour lattice averaging group (FLAG). *Eur. Phys. J. C*. (2020) **80**:113. doi: 10.1140/epjc/s10052-019-7354-7
155. Kim J, Dragos J, Shindler A, Luu T, de Vries J. Towards a determination of the nucleon EDM from the quark chromo-EDM operator with the gradient flow. *PoS LATTICE2018*. (2019) 260. doi: 10.22323/1.334.0260
156. Rizik M, Monahan C, Shindler A. Renormalization of CP-Violating Pure Gauge Operators in Perturbative QCD Using the Gradient Flow. PoS LATTICE2018 (2018) 215. doi: 10.22323/1.334.0215
157. Mereghetti E, de Vries J, Hockings WH, Maekawa CM, van Kolck U. The electric dipole form factor of the nucleon in chiral perturbation theory to sub-leading order. *Phys Lett B*. (2011) **696**:97–102. doi: 10.1016/j.physletb.2010.12.018
158. Haisch U, Hala A. Sum rules for CP-violating operators of Weinberg type. *arXiv preprint arXiv:1909*.08955 (2019). doi: 10.1007/JHEP11(2019)154
159. Epelbaum E, Meißner UG, Glöckle W. Nuclear forces in the chiral limit. *Nucl Phys A*. (2003) **714**:535–74. doi: 10.1016/S0375-9474(02)01393-3
160. Krebs H, Epelbaum E, Meißner UG. Nuclear axial current operators to fourth order in chiral effective field theory. *Ann Phys*. (2017) **378**:317–95. doi: 10.1016/j.aop.2017.01.021
161. Pastore S, Schiavilla R, Goity JL. Electromagnetic two-body currents of one- and two-pion range. *Phys Rev C*. (2008) **78**:064002. doi: 10.1103/PhysRevC.78.064002
162. Pastore S, Girlanda L, Schiavilla R, Viviani M. The two-nucleon electromagnetic charge operator in chiral effective field theory (χEFT) up to one loop. *Phys Rev C*. (2011) **84**:024001. doi: 10.1103/PhysRevC.84.024001
163. Krebs H, Epelbaum E, Meißner UG. Box diagram contribution to the axial two-nucleon current. *arXiv preprint arXiv: 2001*.03904 (2020). doi: 10.1103/PhysRevC.101.055502
164. Fukuda N, Sawada K, Taketani M. On the construction of potential in field theory. *Prog Theor Phys*. (1954) **12**:156. doi: 10.1143/PTP.12.156
165. Okubo S. Diagonalization of Hamiltonian and Tamm-Dancoff equation. *Prog Theor Phys*. (1954) **12**:603. doi: 10.1143/PTP.12.603
166. Epelbaum E, Glöckle W, Meißner UG. Nuclear forces from chiral Lagrangians using the method of unitary transformation. 1. Formalism. *Nucl Phys A*. (1998) **637**:107–34. doi: 10.1016/S0375-9474(98)00220-6
167. Epelbaum E. Four-nucleon force using the method of unitary transformation. *Eur Phys J A*. (2007) **34**:197–214. doi: 10.1140/epja/i2007-10496-0
168. Epelbaum E. Four-nucleon force in chiral effective field theory. *Phys Lett B*. (2006) **639**:456–61. doi: 10.1016/j.physletb.2006.06.046
169. Bernard V, Epelbaum E, Krebs H, Meißner UG. Subleading contributions to the chiral three-nucleon force. I. Long-range terms. *Phys Rev C*. (2008) **77**:064004. doi: 10.1103/PhysRevC.77.064004
170. Bernard V, Epelbaum E, Krebs H, Meißner UG. Subleading contributions to the chiral three-nucleon force II: short-range terms and relativistic corrections. *Phys Rev C*. (2011) **84**:054001. doi: 10.1103/PhysRevC.84.054001
171. Krebs H, Gasparyan A, Epelbaum E. Chiral three-nucleon force at N^{4}LO I: longest-range contributions. *Phys Rev C*. (2012) **85**:054006. doi: 10.1103/PhysRevC.85.054006
172. Krebs H, Gasparyan A, Epelbaum E. Chiral three-nucleon force at N^{4}LO II: intermediate-range contributions. *Phys Rev C*. (2013) **87**:054007. doi: 10.1103/PhysRevC.87.054007
173. de Vries J, Li N, Meißner UG, Nogga A, Epelbaum E, Kaiser N. Parity violation in neutron capture on the proton: Determining

the weak pion–nucleon coupling. *Phys Lett B*. (2015) **747**:299–304. doi: 10.1016/j.physletb.2015.05.074
174. Gnech A. Parity and Time Reversal Violation in Two Nucleons Systems. University of Pisa, Pisa. (2016).
175. Kaiser N. Parity-violating two-pion exchange nucleon-nucleon interaction. *Phys Rev C*. (2007) **76**:047001. doi: 10.1103/PhysRevC.76.047001
176. Epelbaum E, Glöckle W, Meißner UG. Improving the convergence of the chiral expansion for nuclear forces. 1. Peripheral phases. *Eur Phys J A*. (2004). 19:125–37. doi: 10.1140/epja/i2003-10096-0
177. Friar JL. Dimensional regularization and nuclear potentials. *Mod Phys Lett A*. (1996) **11**:3043–8. doi: 10.1142/S0217732396003027
178. Kaiser N, Brockmann R, Weise W. Peripheral nucleon-nucleon phase shifts and chiral symmetry. *Nucl Phys A*. (1997) **625**:758–88. doi: 10.1016/S0375-9474(97)00586-1
179. Epelbaum E, Krebs H, Meißner UG. Improved chiral nucleon-nucleon potential up to next-to-next-to-next-to-leading order. *Eur Phys J A*. (2015) **51**:53. doi: 10.1140/epja/i2015-15053-8
180. Krebs H. Electroweak current operators in chiral effective field theory. In: *9th International Workshop on Chiral Dynamics (CD18)*. Durham, NC (2019). doi: 10.22323/1.317.0098
181. Epelbaum E. Towards high-precision nuclear forces from chiral effective field theory. In: *6th International Conference Nuclear Theory in the Supercomputing Era (NTSE-2018)*. Daejeon (2019).
182. Epelbaum E, Krebs H, Reinert P. High-precision nuclear forces from chiral EFT: State-of-the-art, challenges and outlook. *Front Phys*. (2020) **8**:98. doi: 10.3389/fphy.2020.00098
183. Maekawa CM, Veiga JS, van Kolck U. The Nucleon anapole form-factor in chiral perturbation theory to subleading order. *Phys Lett B*. (2000) **488**:167–74. doi: 10.1016/S0370-2693(00)00851-0
184. Epelbaum E, Glöckle W, Meißner UG. Nuclear forces from chiral Lagrangians using the method of unitary transformation. 2. The two nucleon system. Nucl Phys A. (2000) **671**:295–331. doi: 10.1016/S0375-9474(99)00821-0
185. Girlanda L, Pastore S, Schiavilla R, Viviani M. Relativity constraints on the two-nucleon contact interaction. *Phys Rev C*. (2010) **81**:034005. doi: 10.1103/PhysRevC.81.034005
186. Kaplan DB, Savage MJ, Wise MB. A Perturbative calculation of the electromagnetic form-factors of the deuteron. *Phys Rev C*. (1999) **59**:617–29. doi: 10.1103/PhysRevC.59.617
187. Savage MJ, Springer RP. Parity violation in effective field theory and the deuteron anapole moment. *Nucl Phys A*. (1998) **644**:235–44. doi: 10.1016/S0375-9474(98)80013-4
188. Phillips DR, Schindler MR, Springer RP. An Effective-field-theory analysis of low-energy parity-violation in nucleon-nucleon scattering. *Nucl Phys A*. (2009) **822**:1–19. doi: 10.1016/j.nuclphysa.2009.02.011
189. Vanasse J, David A. Time-reversal-invariance violation in the *Nd* system and large-N_C. *arXiv preprint arXiv:1910*.03133 (2019).
190. 't Hooft G. A planar diagram theory for strong interactions. *Nucl Phys B*. (1974) **72**:461. doi: 10.1016/0550-3213(74)90154-0
191. Witten E. Baryons in the 1/n Expansion. *Nucl Phys B*. (1979) **160**:57–115. doi: 10.1016/0550-3213(79)90232-3
192. Dashen RF, Jenkins EE, Manohar AV. Spin flavor structure of large N(c) baryons. *Phys Rev D*. (1995) **51**:3697–727. doi: 10.1103/PhysRevD.51.3697
193. Kaplan DB, Savage MJ. The Spin flavor dependence of nuclear forces from large n QCD. *Phys Lett B*. (1996) **365**:244–51. doi: 10.1016/0370-2693(95)01277-X
194. Kaplan DB, Manohar AV. The Nucleon-nucleon potential in the 1/N(c) expansion. *Phys Rev C*. (1997) **56**:76–83. doi: 10.1103/PhysRevC.56.76
195. Nagels MM, Rijken TA, de Swart JJ. Baryon Baryon scattering in an OBEP approach. 1. Nucleon-nucleon scattering. Phys Rev D. (1975) **12**:744. doi: 10.1103/PhysRevD.12.744
196. Nagels MM, Rijken TA, de Swart JJ. Baryon Baryon scattering in a one boson exchange potential approach. 2. Hyperon-nucleon scattering. *Phys Rev D*. (1977) **15**:2547. doi: 10.1103/PhysRevD.15.2547
197. Sakurai JJ. Theory of strong interactions. *Ann Phys*. (1960) **11**:1–48. doi: 10.1016/0003-4916(60)90126-3
198. Barton G. Notes on the static parity nonconserving internucleon potential. *Nuovo Cim*. (1961) **19**:512–27. doi: 10.1007/BF02733247
199. Holstein BR. Nuclear parity violation parameter $h_\rho^{(}1)^\prime$. *Phys Rev D*. (1981) **23**:1618–23. doi: 10.1103/PhysRevD.23.1618
200. Kaiser N, Meissner UG. The Weak Pion - nucleon vertex revisited. *Nucl Phys A*. (1988) **489**:671–82. doi: 10.1016/0375-9474(88)90115-7
201. Herczeg P. T violating effects in neutron physics and CP violation in gauge models. In: *Workshop on Time Reversal Invariance in Neutron Physics*. Chapel Hill, NC (1987).
202. Schiavilla R, Viviani M, Girlanda L, Kievsky A, Marcucci LE. Neutron spin rotation in n-polarized - d scattering. *Phys Rev C*. (2008) **78**:014002. doi: 10.1103/PhysRevC.78.014002
203. Schiavilla R, Carlson J, Paris MW. Parity violating interaction effects in the NP system. *Phys Rev C*. (2004) **70**:044007. doi: 10.1103/PhysRevC.70.044007
204. Haxton WC, Henley EM. Enhanced T violating nuclear moments. *Phys Rev Lett*. (1983) **51**:1937. doi: 10.1103/PhysRevLett.51.1937
205. Gudkov VP, He XG, McKellar BHJ. On the CP odd nucleon potential. *Phys Rev*. (1993) C47:2365-2368. doi: 10.1103/PhysRevC.47.2365
206. Towner IS, Hayes AC. P, T violating nuclear matrix elements in the one meson exchange approximation. *Phys Rev C*. (1994) **49**:2391–7. doi: 10.1103/PhysRevC.49.2391
207. Song YH, Lazauskas R, Gudkov V. Nuclear electric dipole moment of three-body systems. *Phys Rev C*. (2013) **87**:015501. doi: 10.1103/PhysRevC.87.015501
208. Yamanaka N. Review of the electric dipole moment of light nuclei. *Int J Mod Phys E*. (2017) **26**:1730002. doi: 10.1142/S0218301317300028
209. Blyth D, Fry J, Fomin N, Alarcon R, Alonzi L, Askanazi E, et al. First observation of *P*-odd γ asymmetry in polarized neutron capture on hydrogen. *Phys Rev Lett*. (2018) **121**:242002. doi: 10.1103/PhysRevLett.121.242002
210. Hyun CH, Park TS, Min DP. Asymmetry in polarized n + p –> d + gamma. *Phys Lett B*. (2001) **516**:321–6. doi: 10.1016/S0370-2693(01)00917-0
211. Schiavilla R, Carlson J, Paris MW. Parity violating interactions and currents in the deuteron. *Phys Rev C*. (2003) **67**:032501. doi: 10.1103/PhysRevC.67.032501
212. Desplanques B. Study of parity-violating effects in the neutron capture $n + p \rightarrow d + \gamma$. *Nucl Phys A*. (1975) **242**:423–8. doi: 10.1016/0375-9474(75)90105-0
213. McKellar BHJ. Parity Nonconservation in the low-energy nucleon-nucleon system: evidence for an isotensor weak interaction? *Nucl Phys A*. (1975) **254**:349–52. doi: 10.1016/0375-9474(75)90221-3
214. Desplanques B. Parity nonconserving nuclear forces. *Nucl Phys A*. (1980) **335**:147–67. doi: 10.1016/0375-9474(80)90174-8
215. Eversheim PD, Schmitt W, Kuhn S, Hinterberger F, von Rossen P, Chlebek J, et al. Parity violation in proton proton scattering at 13.6-MeV. *Phys Lett B*. (1991) **256**:11–4. doi: 10.1016/0370-2693(91)90209-9
216. Nagle DE, Bowman JD, Hoffman C, McKibben J, Mischke R, Potter JM, et al. Parity violation in the scattering of 15 MeV protons by hydrogen. *AIP Conf Proc*. (1979) **51**:224–30. doi: 10.1063/1.31768
217. Kistryn S, Lang J, Liechti J, Maier T, Muller R, Nessi-Tedaldi F, et al. Precision measurement of parity violation in proton proton scattering at 45-MeV. *Phys Rev Lett*. (1987) **58**:1616. doi: 10.1103/PhysRevLett.58.1616
218. Berdoz AR, Birchall J, Bland JB, Bowman JD, Campbell JR, Coombes GH, et al. Parity violation in proton proton scattering at 221-MeV. *Phys Rev C*. (2003) **68**:034004. doi: 10.1103/PhysRevC.68.034004
219. Hoferichter M, Ruiz de Elvira J, Kubis B, Meißner UG. Matching pion-nucleon Roy-Steiner equations to chiral perturbation theory. *Phys Rev Lett*. (2015) **115**:192301. doi: 10.1103/PhysRevLett.115.192301
220. Carlson J, Schiavilla R, Brown VR, Gibson BF. Parity violating interaction effects 1: the Longitudinal asymmetry in pp elastic scattering. *Phys Rev C*. (2002) **65**:035502. doi: 10.1103/PhysRevC.65.035502
221. Desplanques B. About the parity nonconserving asymmetry in $n+p \rightarrow d+\gamma$. *Phys Lett B*. (2001) **512**:305–13. doi: 10.1016/S0370-2693(01)00713-4
222. McCrea M, Kabir ML, Birge N, Coppola CE, Hayes C, Plemons E, et al. The n^3He experiment: parity violation in polarized neutron capture on ^{3}He. *arXiv preprint arXiv:2004*.10889 (2020).

223. Viviani M, Schiavilla R, Girlanda L, Kievsky A, Marcucci LE. The Parity-violating asymmetry in the $^3He(n,p)^3H$ reaction. *Phys Rev C*. (2010) **82**:044001. doi: 10.1103/PhysRevC.82.044001
224. Gericke MT, Baeßler S, Barrón-Palos L, Birge N, Bowman JD, Britton C Jr., et al. First precision measurement of the parity violating asymmetry in cold neutron capture on ^{3}He. arXiv preprint *arXiv:2004*.11535 (2020).
225. Kievsky A, Rosati S, Viviani M, Marcucci LE, Girlanda L. A High-precision variational approach to three- and four-nucleon bound and zero-energy scattering states. *J Phys G*. (2008) **35**:063101. doi: 10.1088/0954-3899/35/6/063101
226. Song YH, Lazauskas R, Gudkov V. Parity violation in low energy neutron deuteron scattering. *Phys Rev C*. (2011) **83**:015501. doi: 10.1103/PhysRevC.83.015501
227. Walecka JD. *Theoretical Nuclear and Subnuclear Physics*. Vol. 16. Cambridge, UK: Cambridge University Press (1995).
228. Yamanaka N, Hiyama E. Enhancement of the CP-odd effect in the nuclear electric dipole moment of ^{6}Li. *Phys Rev C*. (2015) **91**:054005. doi: 10.1103/PhysRevC.91.054005
229. Lebedev O, Olive KA, Pospelov M, Ritz A. Probing CP violation with the deuteron electric dipole moment. *Phys Rev D*. (2004) **70**:016003. doi: 10.1103/PhysRevD.70.016003
230. Hoferichter M, Ruiz de Elvira J, Kubis B, Meißner UG. Roy-Steiner-equation analysis of pion–nucleon scattering. *Phys Rep*. (2016) **625**:1–88. doi: 10.1016/j.physrep.2016.02.002
231. Siemens D, Ruiz de Elvira J, Epelbaum E, Hoferichter M, Krebs H, Kubis B, et al. Reconciling threshold and subthreshold expansions for pion-nucleon scattering. *Phys Lett B*. (2017) **770**:27–34. doi: 10.1016/j.physletb.2017.04.039
232. Guo FK, Seng CY. Effective field theory in the study of long range nuclear parity violation on lattice. *Eur Phys J C*. (2019) **79**:22. doi: 10.1140/epjc/s10052-018-6529-y
233. Bass CD, Bass TD, Heckel BR, Huffer CR, Luo D, Markoff DM, et al. A Liquid helium target system for a measurement of parity violation in neutron spin rotation. Nucl Instrum Methods A. (2009) **612**:69–82. doi: 10.1016/j.nima.2009.10.055
234. Lang J, Maier T, Muller R, Nessi-Tedaldi F, Roser T, Simonius M, et al. Parity nonconservation in elastic p alpha scattering and the determination of the weak meson - nucleon coupling constants. *Phys Rev Lett*. (1985) **54**:170–3. doi: 10.1103/PhysRevLett.54.170
235. Lazauskas R. Solution of the $n-^4$He elastic scattering problem using the Faddeev-Yakubovsky equations. *Phys Rev C*. (2018) **97**:044002. doi: 10.1103/PhysRevC.97.044002
236. Lazauskas R, Carbonell J. Description of four- and five-nucleon systems by solving Faddeev-Yakubovsky equations in configuration space. *Front Phys*. (2020) **7**:251. doi: 10.3389/fphy.2019.00251
237. Lazauskas R, Song YH. Parity-violating neutron spin rotation in ^{4}He. *Phys Rev C*. (2019) **99**:054002. doi: 10.1103/PhysRevC.99.054002
238. Hupin G, Quaglioni S, Navratil P. Ab initio predictions for polarized deuterium-tritium thermonuclear fusion. *Nat Commun*. (2019) **10**:351. doi: 10.1038/s41467-018-08052-6
239. Kravvaris K, Quinlan KR, Quaglioni S, Wendt KA, Navratil P. Quantifying uncertainties in neutron-alpha scattering with chiral nucleon-nucleon and three-nucleon forces. (2020).
240. Avenier M, Cavaignac JF, Koang DH, Vignon B, Hart R, Wilson R. Parity violation in n d capture. *Phys Lett B*. (1984) **137**:125–128. doi: 10.1016/0370-2693(84)91119-5
241. Crawford CB. Private Communication (2020).
242. Adelberger EG, Hindi MM, Hoyle CD, Swanson HE, Von Lintig RD, Haxton WC. Beta decays of Ne-18 and Ne-19 and their relation to parity mixing in F-18 and F-19. *Phys Rev C*. (1983) **27**:2833–56. doi: 10.1103/PhysRevC.27.2833
243. Elsener K, Grubler W, Konig V, Schmelzbach PA, Ulbricht J, Singy D, et al. Constraints on weak meson nucleon coupling from parity nonconservation in F-19. *Phys Rev Lett*. (1984) **52**:1476–9. doi: 10.1103/PhysRevLett.52.1476
244. Elsener K, Grubler W, Konig V, Schmelzbach PA, Ulbricht J, Vuaridel B, et al. Parity nonconservation in ^{1}9F nuclei. *Nucl Phys A*. (1987) **461**:579–602. doi: 10.1016/0375-9474(87)90411-8
245. Haxton WC. Parity Nonconservation in ^{1}8F and meson exchange contributions to the axial charge operator. *Phys Rev Lett*. (1981) **46**:698. doi: 10.1103/PhysRevLett.46.698
246. Guidoboni G, Stephenson E, Andrianov S, Augustyniak W, Bagdasarian Z, Bai M, et al. How to reach a thousand-second in-plane polarization lifetime with 0.97-GeV/c deuterons in a storage ring. *Phys Rev Lett*. (2016) **117**:054801. doi: 10.1103/PhysRevLett.117.054801
247. Yamanaka N, Yamada T, Funaki Y. Nuclear electric dipole moment in the cluster model with a triton: ^{7}Li and ^{1}1B. *Phys Rev C*. (2019) **100**:055501. doi: 10.1103/PhysRevC.100.055501
248. Kabir PK. Test of *T* invariance in neutron optics. *Phys Rev D*. (1982) **25**:2013. doi: 10.1103/PhysRevD.25.2013
249. Stodolsky L. Parity violation in threshold neutron scattering. *Nucl Phys B*. (1982) **197**:213–27. doi: 10.1016/0550-3213(82)90287-5
250. Bunakov VE, Gudkov VP. Parity violation and related effects in neutron induced reactions. *Nucl Phys A*. (1983) **401**:93–116. doi: 10.1016/0375-9474(83)90338-X
251. Gudkov VP. On CP violation in nuclear reactions. *Phys Rept*. (1992) **212**:77–105. doi: 10.1016/0370-1573(92)90121-F
252. Bowman JD, Gudkov V. Search for time reversal invariance violation in neutron transmission. *Phys Rev C*. (2014) **90**:065503. doi: 10.1103/PhysRevC.90.065503
253. Shimizu H, Gudkov V, Curole J, Harada H, Hautle P, Hino M, et al. Discrete symmetry tests in neutron-induced compound states. *PoS INPC2016*. (2017) 187. doi: 10.22323/1.281.0187
254. Gudkov V, Shimizu HM. Nuclear spin dependence of time reversal invariance violating effects in neutron scattering. *Phys Rev C*. (2018) **97**:065502. doi: 10.1103/PhysRevC.97.065502
255. Uzikov YN, Haidenbauer J. Polarized proton-deuteron scattering as a test of time-reversal invariance. *Phys Rev C*. (2016) **94**:035501. doi: 10.1103/PhysRevC.94.035501
256. Murata J, Baba H, Behr JA, Goto F, Inaba S, Kawamura H, et al. The MTV Experiment: from T-violation to Lorentz-violation. *PoS INPC2016*. (2017) 185. doi: 10.22323/1.281.0185

Conflict of Interest: The authors declare that the research was conducted in the absence of any commercial or financial relationships that could be construed as a potential conflict of interest.

The reviewer BH declared a shared affiliation, with no collaboration, with one of the authors, JV, to the handling editor at time of review.

Copyright © 2020 de Vries, Epelbaum, Girlanda, Gnech, Mereghetti and Viviani. This is an open-access article distributed under the terms of the Creative Commons Attribution License (CC BY). The use, distribution or reproduction in other forums is permitted, provided the original author(s) and the copyright owner(s) are credited and that the original publication in this journal is cited, in accordance with accepted academic practice. No use, distribution or reproduction is permitted which does not comply with these terms.

frontiers in Physics

REVIEW
published: 23 January 2020
doi: 10.3389/fphy.2019.00233

Quark Models of the Nucleon–Nucleon Interaction

Francisco Fernández[1]*, *Pablo G. Ortega*[1,2] *and David R. Entem*[1,2]

[1] *Instituto de Física Fundamental y Matemáticas (IUFFyM), Universidad de Salamanca, Salamanca, Spain,* [2] *Departamento de Física Fundamental, Universidad de Salamanca, Salamanca, Spain*

The present paper aims to provide a review of the relevance of quark degrees of freedom in the description of the nucleon-nucleon and, in general, of the baryon-baryon interaction. After a historical introduction, the second section of the paper will be dedicated to the first attempts to describe the short-range part of the NN potential in the so-called quark potential models. Here the importance of the symmetries of the 6-quark system will be emphasized. Then, we will discuss the concept of the constituent quark mass as originated by the breakdown of the chiral symmetry, in line with the articles of Manohar and Georgi [1] and the Instanton Liquid Model of Diakonov [2], and its consequences on the quark-quark interaction due to the presence of the Goldstone boson exchanges. Once the full quark-quark interaction is established, the description of the bound states (deuteron), the scattering states of the NN system, and nuclear matter in constituent quark models will be addressed. In this section, a discussion of the influence of $N\Delta$, $\Delta\Delta$ or NN^* components will be included. The rest of the paper will be devoted to the extension of the model to another baryon-baryon system, namely the triton, hyperon-hyperon, and nucleon-antinucleon systems and references to other possible descriptions of the NN interaction in terms of quark degrees of freedom (bag models). The chapter will end with a concluding remark, and the success and limitations of the model described above will be summarized.

Keywords: nucleon-nucleon interaction, nucleon-nucleon interactions (including antinucleons, deuterons, etc.), quark model, quark model baryon-baryon interaction, constituent quark cluster model

OPEN ACCESS

Edited by:
Laura Elisa Marcucci,
University of Pisa, Italy

Reviewed by:
Roelof Bijker,
National Autonomous University of Mexico, Mexico
Artur Polls,
University of Barcelona, Spain

***Correspondence:**
Francisco Fernández
fdz@usal.es

Specialty section:
This article was submitted to Nuclear Physics, a section of the journal Frontiers in Physics

Received: *26 September 2019*
Accepted: *12 December 2019*
Published: *23 January 2020*

Citation:
Fernández F, Ortega PG and Entem DR (2020) Quark Models of the Nucleon–Nucleon Interaction. Front. Phys. 7:233. doi: 10.3389/fphy.2019.00233

1. A HISTORICAL INTERLUDE

Upon the discovery of the compound nature of the nucleon it was suspected that the quark degrees of freedom had to be responsible for the properties of nucleon-nucleon interaction, at least of their short-range parts. However, due to the complexity of QCD (the underlying theory of the quark model), the implementation of these ideas was not straightforward. Although the deep inelastic scattering suggests that quarks are massless particles confined within the nucleons, the magnetic moments of the protons and neutrons could be explained by assuming an effective mass around 300 MeV for the quarks.

The apparent duality of the properties of the quarks gave rise to two types of models: the bags model (relativistic massless quarks confined within a cavity) and the potential model (no relativistic massive quarks confined within a potential). In both models, attempts were made to explain the properties of the short range of nuclear forces.

In 1975, Fairley and Squires [3, 4] tried to describe the deuteron using the MIT bag model. In the same year, Neudatchin et al. [5] proposed an explanation for the short-range repulsion due to

the Pauli Exclusion Principle. Two years later, Neudatchin et al. [6] gave an algebraic reasoning to explain the hard core of nuclear forces in terms of six quarks states, assuming that the quark-quark interaction mixes the [6] and the [42] symmetries of the six-quark system, producing the node of the [42] state phase shifts and showing "hard-core like" behavior. More quantitative attempts were made by Liberman [7] (in a potential model) and [8] (in a bag model), though both calculations based on the Born-Oppenheimer approach [9] do not appear to be useful at the present time.

In 1980, three calculations appeared that used a more sophisticated scheme, the Resonant Group Method (RGM) [10, 11], which has been widely used in the treatment of the interaction between composite particles. The method allows you to make non-relativistic multichannel calculations and obtain phase shifts in a simple way. Within this framework, Oka and Yazaki [12] calculated the phase shifts for the $^3S_1$ and $^1S_0$ states of two nucleons, including the $\Delta\Delta$ channel, thereby showing the presence of a strong repulsive force at short distance. This feature is due to an interplay between the Pauli principle and a spin-spin interaction between quarks. Similar calculations were performed by Ribeiro [13] and Toki [14], using, for the quark-quark interaction, a quadratic confinement plus a spin-spin force more or less related to the one-gluon exchange interaction derived by De Rújula [15]. They found a rather soft core (Toki) or hard core (Ribeiro) depending on the functional form of the spin-spin interaction and the election of the parameters, which, in these first stages of the calculation, are not clearly established.

The hope of being able to describe the short-range part of the nuclear forces in terms of the degrees of freedom of quarks suffered a heavy blow with the publication of the article of Harvey [16]. Harvey performed a similar calculation of the Liberman paper but did so using a quark-quark interaction similar to the one-gluon exchange, taking into account, besides the $\Delta\Delta$ states, hidden color states, namely two three-quark color states coupled to color singlet's, in the two-nucleon system as required by completeness. The inclusion of these new states had dramatic effects: the repulsive core was transformed into a weak attraction. Although the use of the Born-oppenheimer approximation may be questionable, the need to include the configuration mixing remained very much in force. The situation was restored by the papers of Faessler et al. [17], which returned to the previous results that showed that obtaining a hard core, even if the hidden color states were included in the calculation provided, meant that the different parameters appearing in the calculation were chosen in a consistent way, as we will see later.

Once the question of the origin of the hard core was settled, the next objective was to achieve a description consistent with the quark degrees of freedom of all pieces of the nuclear forces. Two different ways have been used in the past to address this problem. The first one introduced an effective meson exchange potential (EMEP) into the Resonating Group Method equation [18–20]. The second one coupled the pion directly to the $q\bar{q}$ pairs [21, 22]. The difference between the two approaches is that the last one allowed for the study of the influence of the quark antisymmetrization on the one-pion exchange potential, which seems to be relevant in certain cases [23].

Although these methods succeeded to describe the *NN* and *NY* phase shift or the properties of the deuteron, its phenomenological nature leaves too many free parameters unconstrained by the theory, and the interplay between mesonic and quark degrees of freedom is worked out in a rather inconsistent way.

These problems have been partially solved by the introduction of the chiral (or constituent) quark models. These models are founded on the idea that the constituent (dynamical) quark mass is a consequence of the spontaneous breaking of the chiral symmetry of the QCD lagrangian. This $SU(3)_L \times SU(3)_R$ chiral symmetry is spontaneously broken to an $SU(3)_V$ symmetry at the scale $\Lambda_{\chi SB}$, which is different from the confinement scale Λ_{QCD}. The Goldstone theorem implies that there must exist an octet of Goldstone bosons coupled to the quark fields. There is no reason for these two scales to be the same. In fact, Manohar and Georgi [1] argued that $\Lambda_{\chi SB}$ is in fact greater than Λ_{QCD}, which allows them to develop a field theory effective in the intermediate region, which includes quarks, gluons, and Goldstone boson fields.

A realistic mechanism for the chiral symmetry breaking is provided by instantons. Diakonov [2] showed that the light quarks in the liquid instanton vacuum acquired a momentum-dependent effective mass that breaks down the chiral symmetry of QCD spontaneously. This author ended up with an effective chiral Lagrangian, within which QCD was reduced at low energy, with quarks and Goldstone bosons fields. Based on this approach to QCD at low energy, in Fernandez et al. [24], the authors developed an improved quark-quark interaction that was suggested by instanton models that included π and σ exchanges as non-perturbative components and the one-gluon exchange as a perturbative one. The nucleon-nucleon potential derived from this model presents short-range repulsion and medium-range attraction besides the usual pion tail. The authors used this interaction to calculate the nucleon-nucleon phase shifts within the resonating group method, and a large number of observables were related to the N-N interaction. The results agreed reasonably well with experimental values. A similar approach has been pursued by the group of Beijing [25]. Further references of this period can be found in Myhrer and Wroldsen [26].

From the end of the twentieth century, the progress in the description of the nucleon-nucleon interaction based on quark degrees of freedom slowed down, and this was mainly due to the appearance of the effective field theories applied to the nucleon-nucleon interaction.

These theories are based on the Weinberg idea [27] that one has to write down the most general Lagrangian consistent with the symmetries of QCD, particularly the (spontaneously broken) chiral symmetry. Thus, in this formulation, which is seen as more fundamental than constituent quark models, the effective degrees of freedom, rather than quarks and gluons, are the Goldstone bosons of the broken symmetry and the nucleons. A detailed description of the progress of these theories in the last years can be found in the section dedicated to the nucleon-nucleon description in the framework of the effective field theories.

In these last years, there has nevertheless been progress in the field of the constituent quark models, which deserves

a mention. Thus, several calculations have been done within the framework of the extended quark-delocalization color-screening model (QDCSM) [28], addressing problems with the intermediate range attraction (σ-exchange) [29] and the spin-orbit interaction [30]. On the other hand, Huang and Wang performed a calculation using the chiral SU(3) model in which the parameters of the nucleon-nucleon interaction are chosen consistently with the mass of octet and decuplet baryon ground states [31]. An improvement in the description of the nucleon-nucleon-meson vertices is achieved through the so-called Oxford potential [32], which uses the $^3P_0$ model to calculate the form factors of these vertices, thus achieving a good description of the nucleon-nucleon phenomenology. Finally, during these years there has been impressive experimental progress in the discovery of the heavy baryons. This fact has produced a revival of the previous hyperon-nucleon calculations, thus extending the field to charmed and bottom baryon-nucleon interaction [33, 34].

2. THE QUARK ANTISYMMETRY AND THE HARD CORE OF THE N-N INTERACTION

By analogy with the short-range repulsion between two α particles, the short-range repulsion in the nucleon-nucleon interaction was naively expected to originate from the Pauli principle between quarks. In the case of the $\alpha - \alpha$ scattering, the Pauli principle forbids eight particles to be in the $0S$ state. Therefore, one must put at least four particles in the $1P$ state, so the relative wave function between two α particles in a state with zero relative angular momentum must have a radial node inside the range of the nuclear forces. This node plays a role that is equivalent to a hard core.

However, the situation in the case of the nucleon-nucleon interaction is slightly different. Due to of the color degree of freedom, it is possible to have the six quarks in the lowest $0S$ so that the relative wave function between the two nucleons does not necessarily exhibit a node in the wave function.

Neudatchin et al. [6] was the first study to point out that the hard-core behavior can be still recovered in the quark model provided that the quark-quark interaction mixed the lowest 6-quark state with the first excited state. The relative wave function between the two nucleons would then be strongly suppressed in the inner region due to the node of the excited state, and the corresponding phase shifts would show 'hard-core like' behavior. In this sense, the validty of the analogy with the Pauli principle effects on the $\alpha - \alpha$ system would be totally dependent on the character of the quark-quar interaction.

An interaction that can perform this task is the color magnetic part $-g(r)(\lambda_i\lambda_j)(\sigma_i\sigma_j)$ of the one-gluon exchange interaction, as shown by De Rújula [15]. The expectation values of the operators $\sigma_i\sigma_j$ and $\lambda_i\lambda_j$ are positive (negative) for spatially symmetric (antisymmetric) qq pair states [15]. Then, the color magnetic part is attractive (due to the global minus sign of the interaction) for qq pairs, which are symmetric in color-spin space, and repulsive for qq pairs, which are antisymmetric.

The product wave function of two nucleons, each with a spatially symmetric three-quark state, gives the following $S_3 \otimes S_3 \longrightarrow S_6$ representations of the S_6 symmetry group:

$$[3]_X \otimes [3]_X = [6]_X + [51]_X + [42]_X + [33]_X \tag{1}$$

The $[6]_X$ and $[42]_X$ ($[51]_X$, and $[33]_X$) are symmetric (antisymmetric) for the whole exchange of the two nucleons. For the different spatial symmetries of the two nucleon states with $l = 0$ and isospin T = 0 ($[33]_T$) or T = 1 ($[42]_T$), the Pauli Principle requests the following color-space symmetries:

$$\begin{aligned}
[6]_X \times [2^3]_{CS} \times [33]_{T=0} &= [1^6], \quad (3s, 6a) \\
[42]_X \times [42]_{CS} \times [33]_{T=0} &= [1^6], \quad (7s, 2a) \\
[42]_X \times [321]_{CS} \times [33]_{T=0} &= [1^6], \quad (4s, 4a) \\
[42]_X \times [2^3]_{CS} \times [33]_{T=0} &= [1^6], \quad (3s, 6a) \\
[42]_X \times [31^3]_{CS} \times [33]_{T=0} &= [1^6], \quad (3s, 6a) \\
[42]_X \times [21^4]_{CS} \times [33]_{T=0} &= [1^6], \quad (1s, 10a)
\end{aligned} \tag{2}$$

$$\begin{aligned}
[6]_X \times [2^2 1^2]_{CS} \times [42]_{T=1} &= [1^6], \quad (2s, 6a) \\
[42]_X \times [33]_{CS} \times [42]_{T=1} &= [1^6], \quad (6s, 3a) \\
[42]_X \times [41^2]_{CS} \times [42]_{T=1} &= [1^6], \quad (6s, 3a) \\
[42]_X \times [2^2 1^2]_{CS} \times [42]_{T=1} &= [1^6], \quad (2s, 6a) \\
[42]_X \times [1^6]_{CS} \times [42]_{T=1} &= [1^6], \quad (0s, 14a)
\end{aligned} \tag{3}$$

From these two equations one can see that, in both isospin cases, the state with spatial symmetry [6] have, in the color spin state, more antisymmetric than symmetric pairs, and they are therefore pushed up by the quark-quark color-magnetic interaction. However, the state with spatial symmetry $[42]_X$ has, in the color spin space, components with more symmetric than antisymmetric states, namely the $[42]_{CS}$ for the isospin $T = 0$ and the $[33]_{CS}$ and $[41^2]_{CS}$ for the isospin $T = 1$. These states must be lowered by the color-magnetic interaction and can be mixed with the $[6]_X$ spatial symmetry.

Three important conclusions can be made from this kind of analysis. The first one is that the hard-core part of the nucleon-nucleon interaction is related to the node of the spatial $[42]_X$ component of the six-quark system. The second one is that the mixing of the $[42]_X$ and $[6]_X$ components is controlled by the strength parameter of the color-magnetic interaction. Finally, colorless objects, like nucleons, cannot exchange colored particles, like gluons, unless a quark is also exchanged. Therefore, the mechanism described above only works when the two nucleons overlap through a genuine short-range mechanism.

The effect of quark antisymmetrization also appears in other processes, such as the one-pion exchange process. Let assume for a moment that we can couple pions to qq pairs (we will come back to this point later on). The typical $(\sigma \cdot \sigma)(\tau \cdot \tau)$ spin-isospin dependence of the one-pion exchange potential gets modified by the quark antisymmetrization operator $A = 1 - \sum_{i=1}^{3}\sum_{j=4}^{6} P_{ij}$, where P_{ij} is the quark exchange operator, which

is the product of the orbital exchange $P_{ij}^{(0)}$, the spin-isospin exchange $P_{ij}^{(\sigma\tau)}$, and the color exchange $P_{ij}^{(c)}$. As a consequence of the application of the antisymmetrization, it results in as a spin-isopin independent term, a $(\sigma \cdot \sigma)$, and a $(\tau \cdot \tau)$ term, besides the original $(\sigma \cdot \sigma)(\tau \cdot \tau)$ term [22]. In the latter reference, following the model of Tegen and Weise [35], the author assumes that each nucleon consists of three massless quarks confined in a scalar potential $M(r) = cr^2$. The NN potential was generated from a Born-Oppenheimer approximation using the quark wave functions obtained as a solution for the Dirac equation. The pions have been included in the model as a consequence of quark confinement that necessarily implies a breaking of the original chiral symmetry of the QCD Lagrangian of a free quark with zero mass. In this situation, the axial current of massless quarks confined by $M(r)$ is not conserved.

$$\partial^{\mu}[\bar{\psi}(x)\gamma_{\mu}\gamma_5\frac{\vec{\tau}}{2}\psi(x)] = M(r)\bar{\psi}(x)i\gamma_5\ \vec{\tau}\ \psi(x) \tag{4}$$

To restore the chiral symmetry, one introduces a pseudoscalar, isovector field $\pi_{\lambda}(x)$ so that the generalized axial current:

$$A_{\lambda}^{\mu}(x) = \bar{\psi}(x)\gamma^{\mu}\gamma_5\frac{\tau}{2}\psi(x) - C\partial^{\mu}\pi_{\lambda}(x) \tag{5}$$

is a conserved quantity.

Imposing PCAC, the later equation implies a Klein-Gordon equation for the pion field:

$$(\partial^{\mu}\partial_{\mu} + m_{\pi}^2)\pi_{\lambda}(x) = i\sum M(r)f_{\pi}^{-1}\bar{\psi}(x)\gamma_5\tau\psi(x) \tag{6}$$

where f_{π} is the pion decay constant, and the summation runs over all quarks.

This last equation tells us that the πqq coupling is given by:

$$H_{\pi qq} = iM(r)f_{\pi}^{-1}\bar{\psi}(x)\gamma_5\tau\psi(x)\pi_{\lambda}(x) \tag{7}$$

By employing this πqq one can calculate the one-pion exchange potential between nucleons using the Born-Oppenheimer approximation. The results of Shimizu [22] show that the effect of the quark antisymetrization on the one-pion is very large at short distances, producing a spin-isospin independent short-range repulsion that can be as important as the one generated by the color-magnetic piece of the one-gluon exchange potential. Besides the usual, part of the one-pion exchange potential with $(\sigma \cdot \sigma)(\tau \cdot \tau)$ dependence becomes very weak. These results can be obtained with other models of the quark-pion coupling [21, 36].

The quark antisymmetrization can have an effect on the one-pion exchange interaction that is an observable consequence of the pion-dominated processes. One example is the confusing situation that arises with the interpretation of the $p(n,p)n$ and $p(p,\Delta^{++})n$ charge-exchange reactions at intermediate energies in the forward direction using a meson-exchange model. A thorough study of the $p(p,\Delta^{++})n$ and $p(n,p)n$ reactions has been done by Jain and Santra [37] from threshold to 5.5 GeV/c beam momentum. These authors use a one-boson exchange model for the transition potential in the framework of the distorted wave Born approximation (DWBA). The $p(p,\Delta^{++})n$ experimental data for the forward cross section in the considered energy region agree remarkably well with the theoretical results when only the one-pion exchange is included in the calculation. However the results for the $p(n,p)n$ reaction greatly underestimate the experimental data.

The situation changes completely if the ρ-exchange is included in the transition potential. In this case, the $p(n,p)n$ calculated cross section comes close to the experimental values. On the other hand, the inclusion of the ρ-exchange destroyed the former agreement in the $p(p,\Delta^{++})n$ independently of the choice of parameters.

These results can be understood in the following way. The $p(p,\Delta^{++})n$ reaction is dominated by the tensor terms of the transition potential due to the spin flip involved in the reaction, whereas the $p(n,p)n$ process is dominated by the central potential. The central part of the OPE Born amplitude behaves like $t/(t-m)$ $(t=-q^2)$, which gives a vanishing cross section in the forward direction. The finite value of the $p(n,p)n$ cross section appears due to the modification of this behavior by the distortions in the DWBA treatment. The inclusion of the ρ-exchange in the transition potential contributes to enhancing the cross section in the $p(n,p)n$ reaction but also reduces the tensor potential and destroy the agreement in the case of the $p(p,\Delta^{++})n$ reaction.

The solution to this conundrum can be found in the modification of the $(\sigma \cdot \sigma)(\tau \cdot \tau)$ dependence of the one-pion exchange potential by the quark antisymmetrization [38]. As showed by Shimizu [22], quark antisymmetrization produces a sizable modification of the behavior of the central piece of the OPE potential but keeps the tensor piece almost unchanged. This fact explains simultaneously the $p(p,\Delta^{++})n$ reaction and the non-vanishing forward $p(n,p)n$ cross section task that obviously cannot be done by the meson exchange models because the required modification of the central part of the interaction has, as a consequence, inconvenient changes in the tensor interaction.

The same mechanism provides a natural justification for the OPE-δ or *poor's mans* absorption procedure used to explain the behavior of the double-spin-flip helicity amplitudes for elastic nucleon-nucleon scattering. More details can be found in Fernández and Oset [39].

3. THE NUCLEON-NUCLEON INTERACTION IN THE RESONATING GROUP METHOD

Two different approaches have been used in the literature to study the nucleon-nucleon interaction in the framework of the quark model. We have already referred to the first, namely, the Born-Oppenheimer approximation. In this approach, the distance between two nucleons is taken as a parameter, and one calculates the energy of the six-quark system from different distances. If the relative kinetic energy between the nucleons is subtracted, the remaining energy is identified with the nucleon-nucleon potential. However, as mentioned before, because of the color nature of the one-gluon exchange interaction, only those

terms that include an additional quark exchange contribute to the nucleon-nucleon potential because it is not possible to exchange a colored object between two colorless objects. Then, the gluon exchange is only possible when the two nucleons overlap. This fact makes the potential highly non-local. Since the potential produced by the Born-Oppenheimer approximation is essentially local, it is difficult to admit that this potential is suitable to describe the short-range part of the N-N interaction.

The second approach, which has been widely used to describe the scattering problem of two composite objects and therefore seems to be the most appropriate method to incorporate the non-local effects, is the Resonating Group Method (RGM). This method was originally formulated by Wheeler [10] and applied to nuclear physics by Wildermuth and Tang [11]. The phase shifts of the two-nucleon interaction are usually calculated in the scheme developed by Kamimura [40].

The RGM assumes the wave function for two-nucleon (six quark) system can be written as:

$$\psi(\xi_A, \xi_B, R_{AB}) = \mathcal{A}\left\{[\phi_A(\xi_A) \times \phi_B(\xi_B)]_{ST}\chi_N(R_{AB})\right\} \quad (8)$$

The coordinates $\xi_A = (\xi_1, \xi_2)$ and $\xi_B = (\xi_3, \xi_4)$ are internal coordinates of the 19 three-quark clusters A and B in the Jacobi coordinate system [11]. R_{AB} is the relative coordinate between the two nucleons. The internal nucleon wave function ϕ_N includes the color, spin, isospin, and orbital degrees of freedom. Once the quark-quark interaction is fixed, one should get ϕ_N as a solution of the three-body system. However, it is usually assumed that the internal orbital function is the 0*S* harmonic oscillator function with oscillator length *b*. The spin and isospin of each nucleon are coupled to total *S* and *T*.

The relative wave function $\chi_N(R_{AB})$, which is the only unknown of the problem, is calculated by solving the RGM equation:

$$\int \phi(\xi_A,)^+\phi(\xi_B)^+(H-E)\psi(\xi_A, \xi_B, R_{AB})d\xi_A d\xi_B = 0 \quad (9)$$

where H is the total Hamiltonian of the six-quark system. It is usual to introduce the RGM Hamiltonian and normalization kernels in the following way:

$$\begin{aligned}\mathcal{L}(R', R) &= \int \phi(\xi_A,)^+\phi(\xi_B)^+\delta(R' - R_{AB})(H-E)\mathcal{A} \\ &\quad \times \left\{[\phi_A(\xi_A) \times \phi_B(\xi_B)\delta(R - R_{AB})]_{ST}d\xi_A d\xi_B dR_{AB}\right\} \\ &= H(R', R) - EN(R', R) \end{aligned} \quad (10)$$

Using this expression, Equation (9) can be written as:

$$\int \mathcal{L}(R', R)\chi(R')dR' = 0 \quad (11)$$

which is usually referred to as the RGM equation.

From the asymptotic behavior of the relative wave function, one can easily calculate the corresponding phase shifts [40]. In the case of an S-wave, the phase shift can convert into an equivalent hard-core radius parameter r_0 through the equation:

$$\delta_0(k) = -r_0 k \quad (12)$$

Another advantage of this formulation is that one can incorporate the modification of the nucleon wave function over short distances through standard coupling channel techniques. In this case, Equation (11) becomes a coupled-channel equation:

$$\begin{aligned}&\sum_\beta \int \mathcal{L}(R', R)_{\alpha\beta}\chi_\beta(R)dR \\ &= \sum_\beta \int \left\{H_{\alpha\beta}(R', R) - EN_{\alpha\beta}(R', R)\right\}\chi_\beta(R)dR = 0 \end{aligned} \quad (13)$$

Ribeiro [13], Toki [14], Oka and Yazaki [12] and Faessler et al. [17] have employed the previous RGM method to describe the dispersion of N-N in terms of quark degrees of freedom using a coupled-channel calculation. However, for the sake of clarity, we will first discuss the short-range part of the N-N interaction in the channel approximation following [17], although the conclusion of the other calculation is very similar.

At short distances, the interaction between quarks is mediated by the exchange of gluons. However, gluons can interact with each other, which make the quark-quark interaction rather complicated to describe in an exact way. Usually, one assumes that the quark-quark potential V consist of two terms: the one-gluon exchange potential V^{OGEP}, which describes the interaction at high momentum transfer, and the confining potential V^{CONF}, which modelizes the multigluon interaction. In the one-channel approximation, V^{CONF} does not contribute to the N-N interaction because nucleons are color singlets; however the stabilization of each nucleon should be taken into account, as we will see later.

Then, a typical Hamiltonian used in this kind of calculation is given by:

$$\begin{aligned}H &= \sum_i \frac{p_i^2}{2m_q} - K_G + V \\ V &= \sum_{i>j}(V_{ij}^{CONF} + V_{ij}^{OGEP}) \end{aligned} \quad (14)$$

where m is the quark mass, p_i is a momentum of the *i*th quark, and K_G is the center of mass kinetic energy.

A detailed reduction for the OGE amplitude can be found in several textbooks, e.g., Berestetskii et al. [41], and we shall therefore only give the final expressions. One can start with the quark-gluon interaction Lagrangian:

$$\mathcal{L} = \frac{1}{2}g\bar{\psi}(x)\lambda_i\gamma^\mu\psi(x)G_\mu^i(x) \quad (15)$$

where $\psi(x)$ is the quark field, $G_\mu^i(x)$ $(i = 1, \ldots 8)$ are the eight gluon fields, λ_i the $SU(3)$ generators, and g the quark gluon

coupling constant. From this Lagrangian, one arrives, in the one-gluon approximation and the static limit, at a potential between quarks of the form:

$$V_{ij}^{OGEP} = \frac{1}{4}(\lambda_i \cdot \lambda_j)\alpha_s \left(\frac{1}{rij} - \frac{2}{3}\pi \frac{\sigma_i \cdot \sigma_j}{m_q^2}\delta(r_{ij}) - \frac{\pi}{m_q^2}\delta(r_{ij}) \right) \quad (16)$$

where $\alpha_s = g/4\pi$ and σ_i is the spin operator of the i-th quark.

There are no prescriptions to obtain an expression for the confining potential. Usually, this V^{CONF} is chosen as:

$$V_{ij}^{CONF} = -a_c(\lambda_i \lambda_j) r_{ij} \quad (17)$$

where a_c is the strength of the confining potential, λ_i the color $SU(3)$ generator for the i-th quark, and, as before, r_{ij} is the distance between the i-th and the j-th quarks.

The orbital part of the quark wave function is assumed to be of Gaussian form:

$$\psi(r_i) = \frac{1}{\sqrt{\pi} b} e^{r_i^2/2b^2} \quad (18)$$

where b is the size parameter related to the root mean square charge radius (rms-radius) of the proton through $\sqrt{< r^2 >_p} = b$ [17]. The model described above contains four parameters a, α_s, m_q, and b. In Faessler et al. [17], the parameter values are chosen so that they give reasonable values for the rms-radius of the proton, the magnetic moment of the proton, and the mass difference between the nucleon and the Δ. Although the rms-radius of the proton is around 0.8 fm, b is chosen as $b = 0.5 - 0.6$, taking into account the possible effect of the pion cloud. The quark mass is fixed in this calculation as $m_q = 336$ MeV/c^2 to be consistent with the observed proton and neutron magnetic moments. Once the quark mass and size parameter are fixed, the coupling constant α_s is determined so that the nucleon and Δ mass difference comes out to be 294 MeV. However, this way of choosing the value of the parameters does not guarantee that we are describing the nucleon. In fact, one must satisfy the stability condition of the nucleon mass in terms of the size parameter:

$$\frac{\partial}{\partial b}\langle N|H|N\rangle = 0 \quad (19)$$

This condition is used to determine the value of the remaining unfixed parameter, namely the strength of the confining potential a, to be 61.6 MeV/fm.

Figure 1 shows the result for the triplet S and the singlet S phase shifts for a value $b = 0.6$ fm. The behavior of the phase shifts corresponds with a hard-core potential of 0.45 fm for the triplet case and 0.52 fm for the singlet one. As b is actually a free parameter, **Figure 2** shows the behavior of the hard-core radius calculated for several potentials available in the literature with different values of the parameter b. The common feature of all these potentials is that the coupling constant α_s is readjusted for each value of b to reproduce the experimental $N\Delta$ mass difference.

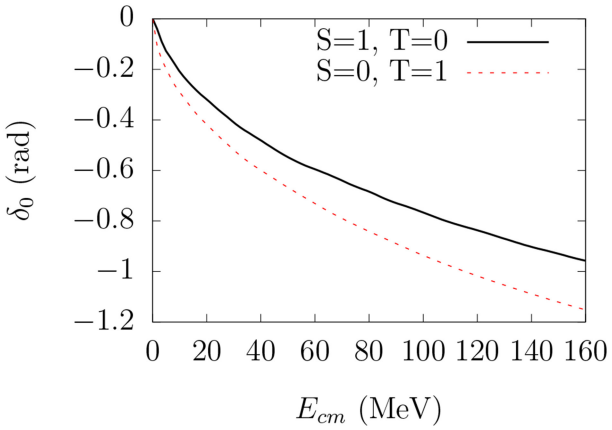


FIGURE 1 | Singlet S and triplet S phase shifts as a function of the two-nucleon center of mas energy for the *NN* channel. The parameters of the quark-quark interaction are given in the text.

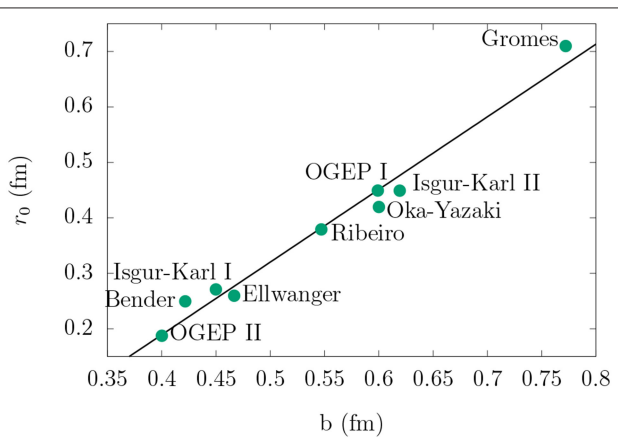


FIGURE 2 | Hard-core radius r_0 as a function of the oscillator length b for different quark-quark forces. The potentials are from ref OGEP I and OGEP II [17], Bender [42], Isgur-Karl I [43], Isgur-Karl II [44] Ellwanger [45], Ribeiro [13], Oka-Yazaki [12], and Gromes [46].

The general trend for all these calculations is an increasing of the hard-core radius with the oscillator length b. This fact agrees with the previous conclusions that the size of the hard core is related to the node at $r = b$ in the [42] orbital configuration of the six-quark system.

So far, one has implicitly assumed that the nucleons remain unchangeable in their mutual interaction. However, this may not be the reality as different six-quark structures can come up when the two nucleons overlap. A possible candidate that might appear is the $\Delta(1232)$ resonance, which belongs together with the nucleon to the lowest orbital configuration of the three-quark system. The inclusion of the $\Delta\Delta$ channel in a coupled-channel RGM calculation was done in Oka and Yazaki [12] and Faessler et al. [17]. They conclude that the $\Delta\Delta$ channel does not appreciably modify the results.

More important could be the contribution of the so-called hidden color channels (*CC*). These channels are those in which the three-quark color wave function belongs to the color octet, rather than to the color singlet as the physical nucleon, even though the full six-quark system remains colorless. These three-quarks clusters are now sensitive to the confining force, and their dynamics are therefore different from the colorless cluster dynamics. The first calculation in which hidden color states were taken into account was made by Harvey [16] in the framework of the Born-Oppenheimer approximation. Harvey found that the three channels *NN*, $\Delta\Delta$, and *CC* coupled with each other rather strongly, and, as a result of the configuration mixing, the hard-core behavior of the *NN* potential disappeared. However, Faessler et al. [17, 47] showed, in an RGM coupled-channel calculation, that the inclusion of the CC channels does not produce a significant modification of the behavior of the S-wave phase shifts, the repulsion being only slightly weaker than in the case of only *NN* and $\Delta\Delta$ were included.

The reason for this disagreement must be sought after in the treatment of the confinement parameter a_c. The *CC* channel is the only channel sensible to the confining force; therefore, the election of the confinement strength is crucial to determining the final results. As we mentioned before in the Faessler's calculation, the confinement strength is adjusted to the minimum of the nucleon mass at a given rms-radius. Otherwise, Harvey chose the oscillator length b (fitted to the proton rms-radius) and the confinement strength (fitted to the baryon spectrum) independently. If we release the condition $dM/db = 0$ and allow the parameter a_c to vary freely for a fixed value of b, the configuration mixing increases dramatically and the hard core even disappears when the value of a_c is far enough from that which corresponds to the minimum condition (see **Figure 3**). This result is very understandable if one thinks of releasing the $dM/db = 0$ condition; we are not describing the physical nucleon anymore but some excited state of that couples strongly with the *CC* channels. Therefore, it is very important to choose the quark-quark interaction and the quark wave function in a self-consistent way in order to avoid unphysical coupling with the hidden color states.

The RGM calculations based on quark degrees of freedom that showed until now allowed for the understanding of the origin of the hard core of the nucleon-nucleon interaction, though it they are too naive to provide a quantitative description of the experimental phase shifts.

To go forward in the description of the experimental data one needs to include, in the RGM, Hamiltonian terms, which take care of the medium range attraction as well as the one-pion tail. Obviously, these terms should be related with a meson cloud surrounding the quark core and without any explicit assumption made about the coupling of mesons with the quark core. The most direct way is the introduction of effective meson exchange potentials (EMEP) in the renormalized RGM equations [18, 48, 49]. In this way, the so-called hybrid models appear.

The RGM equation can be symbolically written as:

$$(E\hat{N} - \hat{H})\chi = 0 \tag{20}$$

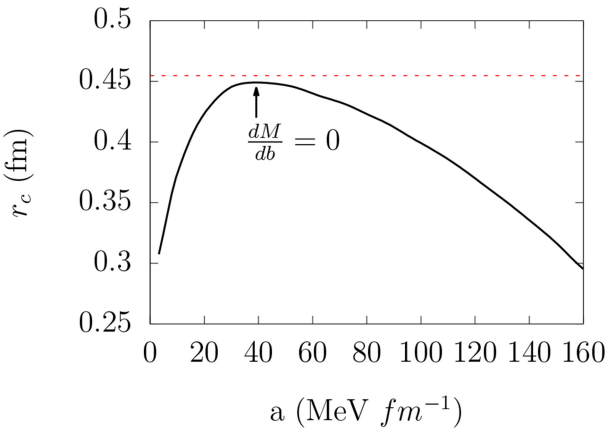


FIGURE 3 | Triplet S hard-core radius r_0 as a function of the confinement parameter *a* for one channel *NN* (dashed line) and three channels *NN*, $\Delta\Delta$, and *CC* (solid line) calculation. In the one channel case the hard-core radius is independent of *a*. The dependence with *a* in the three-channel calculation appears through the coupling with de hidden color states. The arrow shows the value of *a* which minimize the nucleon mass with respect to *b*.

This equation differs from the usual Schrödinger-type equation due to the presence of the normalization kernel $\hat{N}$. This term can be eliminated by the renormalization of χ, i.e.,

$$\chi_r = \hat{N}^{1/2}\chi \tag{21}$$

The equation for χ_r now can be written as:

$$(E - \hat{N}^{-1/2}\hat{H}\hat{N}^{-1/2})\chi_r = 0 \tag{22}$$

This equation is called the renormalization RGM equation and is adequate to introduce the effective meson exchange potential V^{EMEP}:

$$(E - \hat{N}^{-1/2}\hat{H}\hat{N}^{-1/2} - V^{EMEP})\chi_r = 0 \tag{23}$$

The description of the NN phase shifts with this modified RGM equation depends on the shape and the number of parameters included in the different V^{EMEP}. Examples can be seen in the literature cited above.

4. THE CONSTITUENT QUARK MASS AND THE CONSTITUENT QUARK MODEL

In the last paragraph we argued that the chiral symmetry of the massless QCD Lagrangian is spontaneously broken by the bag surface in the bag model, thereby providing a scheme to couple quarks and pions. However, the spontaneous breaking of the chiral symmetry is not a characteristic of the bag model but a more general property of the QCD Lagrangian. In fact, if this symmetry were exact, we would observe degeneracy between states with opposite parity but with the same quantum numbers. For example, the ρ (1^-, 775) meson would be degenerated with the axial a_1 (1^+, 1260) meson, the nucleon ($1/2^+$, 940) would

be degenerated with the $(1/2^-, 1535)$ resonance, etc. Since it is not the case, we conclude that the $SU(3)_L \times SU(3)_R$ symmetry is spontaneously broken. In a seminal article, Manohar and Georgi [1] argued that the chiral symmetry, spontaneously broken to an $SU(3)_v$ symmetry at same $\Lambda_{\chi SB}$ scale, does not necessarily have to match with the confinement scale Λ_{CONF}. Therefore, one can develop an effective field theory in the intermediate region whose Lagrangian includes quarks and gluons fields and Goldstone bosons coupled to the quarks.

How the spontaneous breaking of the chiral symmetry comes about is still a topic of discussion. Diakonov and Petrov [50] suggested a theory of the light quarks in the instanton vacuum, which explained the spontaneous breakdown of chiral symmetry as being due to the delocalization of the would-be zero fermion modes in the field of individual instantons and allows for an effective chiral Lagrangian. The rationale of the model is that the quark propagator in the instanton vacuum develops a momentum-dependent dynamical mass (which we prefer to call constituent mass) that is related to the instanton density, N/V, and the average instanton size, $\bar{\rho}$, as:

$$M(p^2) = \sqrt{\frac{\pi^2 N \bar{\rho}^2}{VN_c}} F(p\bar{\rho}) \tag{24}$$

so that the quark propagator has the form of a massive propagator:

$$S(p) = \frac{\gamma^\mu p_\mu + iM(p^2)}{p^2 + M^2(p^2)} \tag{25}$$

where $F(z)$ is a combination of the modified Bessel functions, which is equal to 1 at $z = 0$ and decreases rapidly with the momentum measured in units of the inverse of instanton size. Diakonov [51] estimated that the value of the dynamical mass at zero momentum is around 350 MeV/c^2, which is in concordance with the values used in the non-relativistic quark model. Starting from these ideas, Diakonov [51] deduced an effective partition function:

$$Z = \int \mathcal{D}\pi^A \int \mathcal{D}\psi^+ \mathcal{D}\psi \exp\left\{ \int d^4x\, \psi^+(x) \Big[i\gamma^\mu \partial_\mu + iMe^{i\gamma_5 \vec{\tau}\cdot\vec{\phi}/f_\pi} \Big] \psi(x) \right\} \tag{26}$$

from which an effective Lagrangian, invariant under chiral rotations (meaning, therefore, that it must contain chiral fields), can be expressed as:

$$\mathcal{L} = \overline{\psi}(i\partial\!\!\!/ - M(q^2)U^{\gamma_5})\,\psi \tag{27}$$

where ψ is the quark spinor, $U^{\gamma_5} = e^{i\frac{\lambda_a}{f_\pi}\phi^a\gamma_5}$ is the Goldstone boson fields matrix, and $M(q^2)$ is the dynamical (constituent) mass that vanishes at large momenta and is frozen at low momenta for a value around 300 MeV.

The appearance of the constituent quark mass (or dynamical quark mass) related to the chiral symmetry justified, at least qualitatively, the non-relativistic quark model. Moreover, the Goldstone boson fields provide a natural coupling for quarks and pions.

5. CONSTITUENT QUARK MODEL DESCRIPTION OF THE NUCLEON-NUCLEON INTERACTION

The conclusions of the former section open the door to a complete description of the N-N interaction. They not only provide a justification for the constituent quark mass, as claimed by the phenomenology, but also explain how to include an important piece of the N-N interaction, namely the pion exchange.

Based on these ideas, a constituent quark model of the nucleon-nucleon interaction has been developed by the groups of Tubingen [24] and Salamanca [52, 53].

The starting point of the model is a non-relativistic reduction of the Lagrangian of Equation (27). Although the momentum dependence of the dynamical mass can be provided by the theory, it is more practical to simulate this behavior by parameterizing the dynamical mass as $M(q^2) = m_q F(q^2)$, where $m_q \simeq 300$ MeV, and

$$F(q^2) = \left[\frac{\Lambda_\chi^2}{\Lambda_\chi^2 + q^2} \right]^{\frac{1}{2}}. \tag{28}$$

The cut-off Λ_χ fixes the chiral symmetry breaking scale.

The Goldstone boson field matrix U^{γ_5} can be expanded in terms of boson fields,

$$U^{\gamma_5} = 1 + \frac{i}{f_\pi}\gamma^5\lambda^a\pi^a - \frac{1}{2f_\pi^2}\pi^a\pi^a + ... \tag{29}$$

The first term of the expansion generates the constituent quark mass while the second one gives rise to a one-pion exchange interaction between quarks. The main contribution of the third term comes from the two-pion exchange, which, in Fernandez et al. [24], has been simulated by means of a scalar $\sigma-$exchange potential.

Now it is straightforward to write the non-relativistic potentials generated in the static approximation in the following way,

$$V_{ij}^{PS}(\vec{q}) = -\frac{1}{(2\pi)^3}\frac{g_{ch}^2}{4m_q^2}\frac{\Lambda_{\chi SB}^2}{\Lambda_{\chi SB}^2 + q^2}\frac{(\vec{\sigma}_i\cdot\vec{q})(\vec{\sigma}_j\cdot\vec{q})}{m_{PS}^2 + q^2}(\vec{\tau}_i\cdot\vec{\tau}_j) \tag{30}$$

$$V_{ij}^{S}(\vec{q}) = -\frac{g_{ch}^2}{(2\pi)^3}\frac{\Lambda_{\chi SB}^2}{\Lambda_{\chi SB}^2 + q^2}\frac{1}{m_S^2 + q^2} \tag{31}$$

where $\vec{q}$ is the three-momentum transfer, the σ's (τ's) are the spin (isospin) Pauli matrices, and m_q, m_{PS}, and m_S are the masses

of the quark, pseudoscalar, and scalar bosons, respectively. The momentum states are normalized to 1.

It is well known that the long-range piece of the *NN* interaction is due to the one-pion exchange. Therefore, to reproduce accurately the long-range tail of the *NN* interaction, one need to identify the mass of the pseudoscalar field with the physical pion mass. Once the mass of the pseudoscalar field is fixed, the mass of the scalar field is obtained by the chiral relation [54].

$$\begin{aligned} m_{PS}^2 &= m_\pi^2 \\ m_S^2 &= m_{PS}^2 + 4m_q^2 \end{aligned} \tag{32}$$

In an early version of the model [24], the chiral Langrangian was linearized using the definitions

$$\pi = \vec{\phi} f_\pi sin(\phi/f_\pi), \tag{33}$$

$$\sigma = f_\pi \left[cos(\phi/f_\pi) - 1\right] \tag{34}$$

giving rise to the Hamiltonian:

$$H = g_{ch} F(q^2) \overline{\psi}(\sigma + i\gamma_5 \vec{\tau} \cdot \vec{\pi})\psi \tag{35}$$

The results of the two formulations are equivalent.

Below the chiral symmetry breaking scale, quarks still interact through gluon exchanges described by the Lagrangian:

$$\mathcal{L}_{gqq} = i\sqrt{4\pi\alpha_s}\ \overline{\psi}\gamma_\mu G_c^\mu \lambda_c \psi\ , \tag{36}$$

where λ_c are the SU(3) color generators and G_c^μ the gluon field.

The corresponding non-relativistic reduction produces the one-gluon exchange potential:

$$V_{ij}^{OGE}(\vec{q}) = \frac{1}{(2\pi)^3}\frac{1}{4}(\vec{\lambda}_i \cdot \vec{\lambda}_j)\, 4\pi\alpha_s \left\{ \frac{1}{q^2} - \frac{1}{4m_q^2}\left(1 + \frac{2}{3}(\vec{\sigma}_i \cdot \vec{\sigma}_j)\right) + \right.$$
$$\left. + \frac{1}{4m_q^2}\frac{1}{q^2}\left[\vec{q} \otimes \vec{q}\right]^2 \cdot \left[\vec{\sigma}_i \otimes \vec{\sigma}_j\right]^2 \right\} \tag{37}$$

where the λ's are the color Gell-Mann matrices and α_s is the strong coupling constant.

Finally, the other QCD non-perturbative effect corresponds to confinement. This effect does not contribute to the N-N interaction because, taking into account the conclusion of the former sections, the model only includes color singlet three-quarks states.

As we will see below, the formulation of a realistic interaction of NN in terms of quark degrees of freedom has the advantage that nucleons and their resonances can be described in a unified way; only the wave function changes and the underlying interaction stays the same.

The works described above presented solutions of the RGM equations in coordinate space. However, it is more convenient to work in momentum space because, in this way, one avoids the problem of the rapid oscillations that the relative wave function exhibits in coordinate space at high energy. Moreover, the parametrization of the width of nucleon resonances is more naturally introduced, which simplified the equations in multichannel calculations.

With this approach, the usual ansatz for the quark radial wave function is:

$$\psi(\vec{p}_i) = \prod_{i=1}^{3} \left[\frac{b^2}{\pi}\right]^{\frac{3}{4}} e^{-\frac{b^2 p_i^2}{2}} \tag{38}$$

where b fixes the size of the nucleon.

One could argue that the wave function of the three-quark clusters should be obtained consistently with the quark-quark interaction as the solution of the Schrödinger equation for the three-quark system. This calculation was carried out in Valcarce et al. [55] showing that the *NN* potential obtained in the Born-Oppenheimer approximation using the wave function coming from the full calculation were very similar to the one obtained with a Gaussian wave function for a certain value of the parameter b. This result legitimizes the use of Gaussian wave function to calculate RGM kernels The baryon total wave function, including the spin, isospin, and color degrees of freedom, can be written as,

$$\begin{aligned} \psi_B &= \phi_B(\vec{p}_{\xi_1}, \vec{p}_{\xi_2})\chi_B \xi_c[1^3]; \\ \phi_B(\vec{p}_{\xi_1}, \vec{p}_{\xi_2}) &= \left[\frac{2b^2}{\pi}\right]^{\frac{3}{4}} e^{-b^2 p_{\xi_1}^2} \left[\frac{3b^2}{2\pi}\right]^{\frac{3}{4}} e^{-\frac{3b^2}{4} p_{\xi_2}^2} \end{aligned} \tag{39}$$

where $\phi_B(\vec{p}_{\xi_1}, \vec{p}_{\xi_2})$ takes into account the internal spatial baryon degrees of freedom and is obtained from Equation (38) by removing the center of the mass wave function. Also, χ_B labels the totally symmetric spin-isospin wave function coupled to the quantum numbers of the baryon B, and $\xi_c[1^3]$ is the color-singlet wave function. Built in this way, ψ_B is totally antisymmetric in quark exchanges.

From this expression, it easily to write the two-baryon wave function:

$$\begin{aligned} \psi_{B_1 B_2} &= \mathcal{A}\left[\chi(\vec{P})\psi_{B_1 B_2}^{ST}\right] \\ &= \mathcal{A}\left[\phi_{B_1}(\vec{p}_{\xi_{B_1}})\phi_{B_2}(\vec{p}_{\xi_{B_2}})\chi(\vec{P})\chi_{B_1 B_2}^{ST}\xi_c[2^3]\right] \end{aligned} \tag{40}$$

where, $\mathcal{A}$ is the antisymmetrizer of the six-quark system, $\phi_{B_i}(\vec{p}_{\xi_{B_i}})$ is the internal spatial wave function defined in Equation (39), $\chi_{B_1 B_2}^{ST}$ denotes the spin-isospin wave function of baryons B_1 and B_2 coupled to a total spin-isospin ST, and $\xi_c[2^3]$ is the product of the two color singlets.

The dynamics of the system is governed by the projection equation:

$$(\mathcal{H} - E_T)\,|\,\psi\,\rangle = 0 \quad \Rightarrow \quad \langle\,\delta\psi\,|\,(\mathcal{H} - E_T)\,|\,\psi\,\rangle = 0 \tag{41}$$

where,

$$\mathcal{H} = \sum_{i=1}^{N} \frac{\vec{p}_i^{\,2}}{2m_q} + \sum_{i<j} V_{ij} - T_{CM} \tag{42}$$

with T_{CM} being the center of mass kinetic energy, V_{ij} the interaction described in the previous section, and m_q the constituent quark mass.

In Equation (41) the variations are performed on the relative wave function $\chi(\vec{P})$. Then, integrating all the internal degrees of freedom, the projected Schrödinger equation for the relative wave function adopts the expression:

$$\left(\frac{\vec{P}'^{\,2}}{2\mu} - E\right)\chi(\vec{P}') + \int \left({}^{\rm RGM}V_D(\vec{P}',\vec{P}_i) + {}^{\rm RGM}K(\vec{P}',\vec{P}_i)\right)\chi(\vec{P}_i)d\vec{P}_i = 0 \quad (43)$$

where $E = E_T - E_A - E_B$ is the relative energy of the clusters, and ${}^{\rm RGM}V_D(\vec{P}',\vec{P}_i)$ and ${}^{\rm RGM}K(\vec{P}',\vec{P}_i)$ are the direct potential and the exchange kernel, respectively given by,

$${}^{\rm RGM}V_D(\vec{P}',\vec{P}_i) = \sum_{i\in A,\, j\in B}\int \phi_A^*(\vec{p}_{\xi_A'})\phi_B^*(\vec{p}_{\xi_B'})V_{ij}(\vec{P}',\vec{P}_i)\phi_A(\vec{p}_{\xi_A})\phi_B(\vec{p}_{\xi_B})d\vec{p}_{\xi_A'}d\vec{p}_{\xi_B'}d\vec{p}_{\xi_A}d\vec{p}_{\xi_B} \quad (44)$$

and

$${}^{\rm RGM}K(\vec{P}',\vec{P}_i) = {}^{\rm RGM}H_E(\vec{P}',\vec{P}_i) - E_T\,{}^{\rm RGM}N_E(\vec{P}',\vec{P}_i) \quad (45)$$

with

$${}^{\rm RGM}H_E(\vec{P}',\vec{P}_i) = -9\int d\vec{p}_{\xi_A'}d\vec{p}_{\xi_B'}d\vec{p}_{\xi_A}d\vec{p}_{\xi_B}d\vec{P}\;\phi_A^*(\vec{p}_{\xi_A'})\phi_B^*(\vec{p}_{\xi_B'})\mathcal{H}\,P_{36}\left[\phi_A(\vec{p}_{\xi_A})\phi_B(\vec{p}_{\xi_B})\,\delta^3(\vec{P}-\vec{P}_i)\right] \quad (46)$$

A similar expression can be found for the normalization exchange kernel, replacing $\mathcal{H}$ with the identity operator. Equation (43) is readily generalized to a coupled-channel equation, starting from a sum of wave functions of the type of Equation (40) for the different baryon channels considered.

The solution of coupled-channel RGM equations is derived from Equation (43), a set of coupled Lippmann-Schwinger equations of the form:

$$T_\alpha^{\alpha'}(z;p',p) = V_\alpha^{\alpha'}(p',p) + \sum_{\alpha''}\int dp''\,p''^2\,V_{\alpha''}^{\alpha'}(p',p'')\frac{1}{z-E_{\alpha''}(p'')}T_\alpha^{\alpha''}(z;p'',p) \quad (47)$$

where α labels the group of quantum numbers B_1B_2JLST, which defines a certain partial wave, $V_\alpha^{\alpha'}(p,'p)$ is the projected potential that contains the direct potential and the RGM exchange kernels, and $E_{\alpha''}(p'')$ is the energy corresponding to a momentum p'', written as (in the non-relativistic case):

$$E_\alpha(p) = \frac{p^2}{2\mu_\alpha} + \Delta M_\alpha \quad (48)$$

Here, μ_α is the reduced mass of the B_1B_2 system corresponding to the channel α, and ΔM_α is the difference between the threshold of the B_1B_2 system and the one used as a reference, the NN system. The mass difference ΔM_α is obtained from the interaction terms for quarks belonging to the same baryon, which relate to the total energy of the system E_T and to the relative energy between clusters E.

The coupled-channel Lippmann-Schwinger equation is solved by a generalized version of the matrix inversion method of Machleidt [56] in order to include channels with different thresholds. Once the T matrix is calculated, the scattering matrix S is obtained for non-relativistic kinematics from the relationship:

$$S_\alpha^{\alpha'} = 1 - 2\pi i\sqrt{\mu_\alpha\mu_{\alpha'}k_\alpha k_{\alpha'}}\;T_\alpha^{\alpha'}(E+i0^+;k_{\alpha'},k_\alpha) \quad (49)$$

with k_α defined by:

$$k_\alpha^2 = 2\mu_\alpha(E-\Delta M_\alpha) \quad (50)$$

so that, for channels above the threshold, $k_\alpha^2 > 0$.

For bound states, the integral equations do not have poles, and the problem is simplified. In this case, a discretized Schrödinger equation can be written in the form:

$$\sum_j\left[E_i(p_i)\delta_{ij} + V_{ij} - E\delta_{ij}\right]\psi_j = 0 \quad (51)$$

where i and j label the discretization of the integral and the quantum numbers of the different channels included in the calculation, and ψ_j is the value of the wave function in the channel and momentum corresponding to the index j.

Details of the calculation of the RGM Kernels and the solution of the equations for both bound and scattering states can be found in Entem et al. [52].

If the pseudoscalar field is to be identified with the one-pion exchange (OPE), a way to obtain the value of the coupling constant g_{ch} is to require that the pseudoscalar interaction should reproduce at long range the well-established OPE Yukawa potential. If the two nucleons are well separated, the central part of the pseudoscalar interaction between quarks given by Equation (30) generates an interaction between nucleons of the form,

$$V_c^{PS}(r) = \frac{1}{3}\frac{g_{ch}^2}{4\pi}\frac{m_\pi^2}{4m_q^2}\tilde{\rho}(im_\pi)^2\;\frac{e^{-m_\pi r}}{r}\left(\frac{5}{3}\right)^2(\vec{\sigma}_N\cdot\vec{\sigma}_N)(\vec{\tau}_N\cdot\vec{\tau}_N) \quad (52)$$

where $\tilde{\rho}(q)$ is the quark density Fourier transform of each nucleon normalized to $\tilde{\rho}(q=0)=1$. Compared with the standard OPE Yukawa potential,

$$V_c^{OPE}(r) = \frac{1}{3}\frac{f_{\pi NN}^2}{4\pi}\frac{e^{-m_\pi r}}{r}(\vec{\sigma}_N\cdot\vec{\sigma}_N)(\vec{\tau}_N\cdot\vec{\tau}_N) \quad (53)$$

and using $\tilde{\rho}(q) = e^{-\frac{b^2q^2}{6}}$, one finally obtains:

$$\frac{g_{ch}^2}{4\pi} = \left(\frac{3}{5}\right)^2\frac{f_{\pi NN}^2}{4\pi}\frac{4m_q^2}{m_\pi^2}\;e^{-\frac{b^2m_\pi^2}{3}} \quad (54)$$

This gives the chiral coupling constant g_{ch} in terms of the πNN coupling constant, taken to be $\frac{f^2_{\pi NN}}{4\pi} = 0.0749$ [57].

As discussed above, the parameter b describe the radius of the nucleon quark content, which is different from the nucleon charge radius and therefore cannot be directly measured. A value for this Gaussian parameter is determined by comparing the N-N potential obtained in a Born-Oppenheimer approximation using the nucleon wave function solution of Schrödinger equation, with the full quark-quark interaction and the one calculated with a single Gaussian of parameter b [55].

$\Lambda_{\chi SB}$ acts in the model as a cut-off for the pion interaction. Therefore, its value controls the NN tensor force, which is mainly due to the one-pion exchange. Then, the more clear way to determine the $\Lambda_{\chi SB}$ value is to resort to processes dominated by the one-pion tensor term. As discussed above, one such processes is the $p(p, \Delta^{++})n$ reaction. Fitting the missing mass spectrum of this reaction [58] estimated a value close to 4.2 fm $^{-1}$ for $\Lambda_{\chi SB}$.

Finally, the value of α_s is estimated by means of the $N\Delta$ mass difference. It is worth noticing that, in this model, the pseudoscalar piece of the interaction contributes to approximately half of the total mass difference. The rest is attributed to the OGE, and the value of α_s is adjusted to this value.

TABLE 1 | Model parameters from Entem et al. [52].

***b*(fm)**	**0.518**
***m*$_q$(MeV)**	**313**
$\Lambda_{\chi SB}$(fm^{-1})	4.2997
m_{PS}(fm^{-1})	0.7
g^2_{ch}	6.6608
α_s	0.4977
m_S(fm^{-1})	3.513

The values of the parameters determined, as explained above, are given in **Table 1**.

Once the model is completely defined, one can solve the scattering problem, obtaining the NN phase shifts and the bound state problem, namely the deuteron. The phase shifts calculation will include couplings to a $\Delta\Delta$ channel for the isosinglet ($T = 0$) partial waves and to $\Delta\Delta$ and $N\Delta$ channels for isotriplet ($T = 1$) partial waves. One of the great advantages of the description in

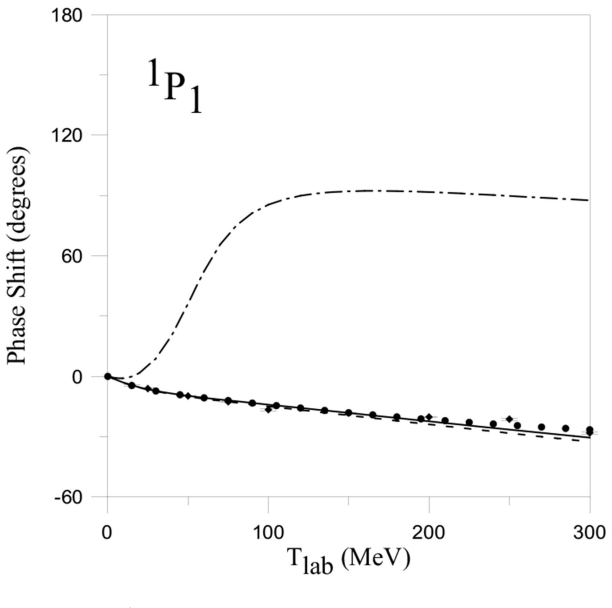


FIGURE 5 | *NN* $^1P_1$ phase-shift. Dashed and solid lines have the same meanings as in **Figure 4B**. Dashed-dotted line shows the effect of antisymmetry, corresponding to the result when all the exchange kernels are removed. Reprinted figure with permission from Entem et al. [52] Copyright (2000) by the American Physical Society.

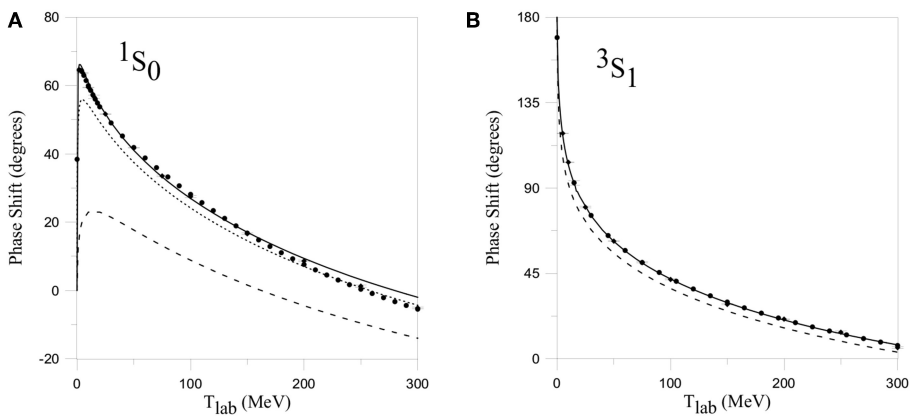


FIGURE 4 | *NN S* wave phase-shifts for $T = 1$ **(A)** and $T = 0$ **(B)**. Experimental points with and without error bars correspond to the energy independent and energy dependent solutions of Arndt et al. [59], respectively. The phase shifts are shown and the analysis correspond to neutron-proton. **(A)** Dashed line represents the calculation including *NN* channels only, dotted line includes also $N\Delta$ components, and solid line is the full calculation with *NN*, $N\Delta$, and $\Delta\Delta$ channels. **(B)** Dashed line is the calculation with *NN* only, and the solid line is the full calculation including *NN* and $\Delta\Delta$ channels. Reprinted figure with permission from Entem et al. [52] Copyright (2000) by the American Physical Society.

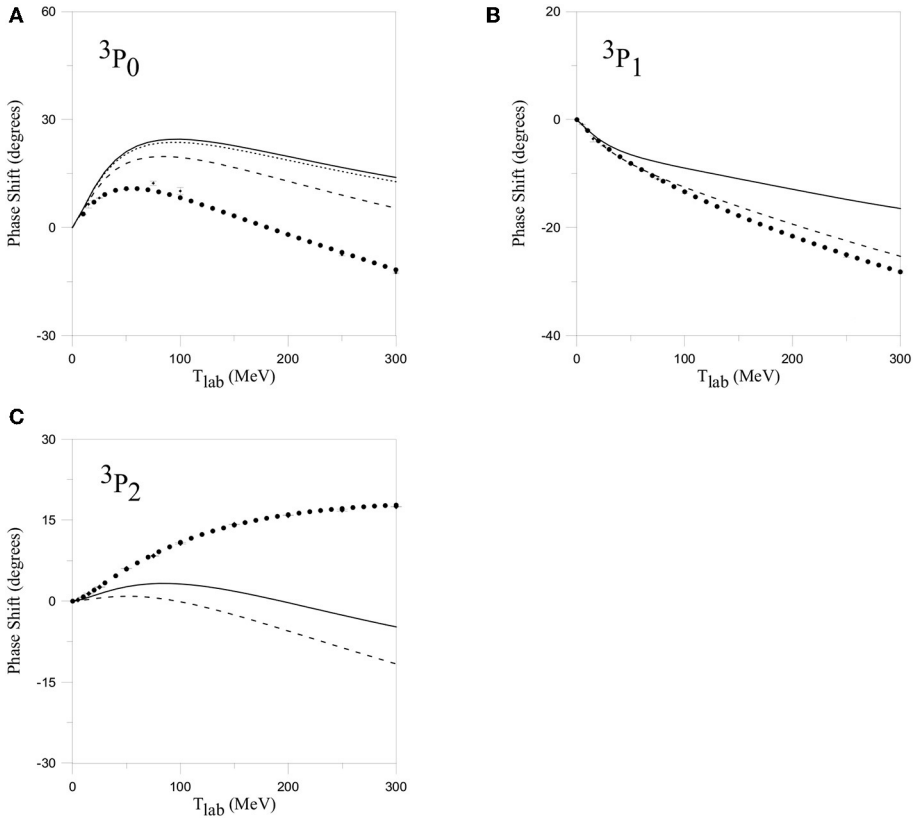


FIGURE 6 | *NN* ^3P_J phase-shifts. **(A)** Same meaning as in **Figure 4A**. **(B,C)** Dashed line corresponds to the result with *NN* channels only, and the solid line includes *NN* and *N*Δ channels. Reprinted figure with permission from Entem et al. [52] Copyright (2000) by the American Physical Society.

terms of quark degrees of freedom is that this scheme allows us to treat the nucleon an its resonances Δ, N^* in a single framework without having to increase the number of parameters. In **Figures 4–10**, one can see the comparison between the results of the model and the experimental data of Arndt et al. [59].

The first aspect that is interesting to remark upon is the result for the $^1S_0^{NN}$ partial wave. This channel cannot be coupled to other *NN* channels by angular momentum selection rules, and it is therefore an ideal candidate to test the quark-quark interaction. As seen in **Figure 4**, the one channel *NN* calculation does not show enough attraction to reproduce the experimental data. A possible solution is to increase the strength of the σ exchange. However, in this model, the σ-quark coupling is related with the π-quark coupling by chiral symmetry and, hence, there is not freedom to fit the data. The required attraction is supplied by the coupling to the $^5D_0^{N\Delta}$ channel (dotted line) [60]. A complete agreement with the experimental data is obtained when the coupling to ΔΔ channels is included (solid line). For the isotriplet $^3S_1^{NN}$ partial waves, the effect of the coupling to ΔΔ channels is very small, as shown here and as will be also seen for higher angular momentum partial waves.

The short-range repulsion of the potential is reproduced very well and without introducing any additional parameters. Although the presence of a pseudoscalar interaction reduces the value of α_s in the OGE (the interaction usually advocated an explanation of the short-range repulsion of the *NN* potential), the strong spin-isospin independent repulsion produced by the effect of the quark antisymmetry on the one-pion exchange potential compensates for the lack of the OGE repulsion.

Table 2 shows the result for the low-energy scattering parameters. The agreement with the experimental results and other theoretical calculations is good, with the exception of the a_{np}. One must be aware that the scattering length in the $^1S_0$, due to the existence of an almost bound state in this partial wave, is extremely sensitive to small changes in the strength of the force. Moreover, the results of **Table 2** have been calculated with the same set of parameters for the $T = 0$ and $T = 1$ channels. A non-significant change of the scalar boson mass in the $T = 1$ channel will drive the results to the experimental value. Further discussions of the scattering length problem in this model can be found in Entem et al. [66].

The $^1P_1$ wave is the only one that is not affected by the spin-orbit term of the interaction. This partial wave provides another example of the importance of the quark antisymmetrization in the model. In **Figure 5** one can see that, if one removes the terms coming from the antisymmetrization, the interaction is attractive and, consequently, the phase shifts are positive. The one-gluon exchange interaction does not contribute due

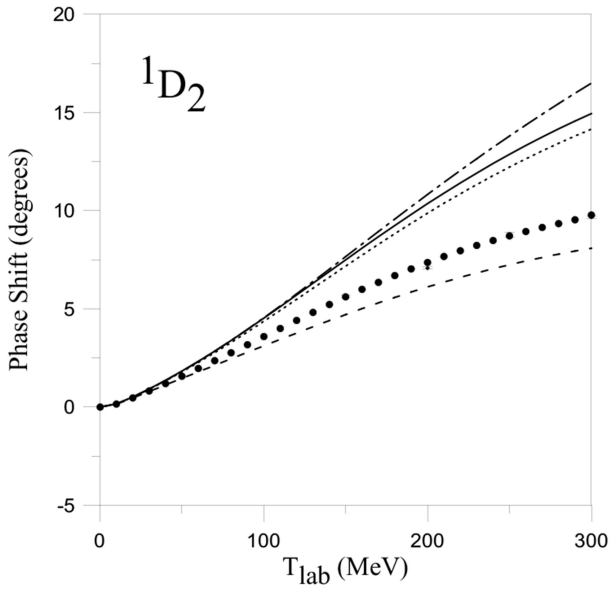


FIGURE 7 | *NN* $^1D_2$ phase-shift. Solid, dashed, and dotted lines have the same meanings as in **Figure 4A**. Dashed-dotted line represents the result without exchange kernels. Reprinted figure with permission from Entem et al. [52] Copyright (2000) by the American Physical Society.

to its δ-like character, and the direct pseudoscalar is attractive for the $^1P_1$ due to sign of the spin-isospin matrix elements. Only the repulsion coming from the quark antisymmetrization term of the one-pion exchange potential reproduces the correct experimental behavior.

As a general trend, the agreement between theory and experiment is reasonable for phase shifts with $L > 1$, although, as explained in Entem et al. [52], the interaction shows a lack of spin-orbit interaction.

The problem of the origin of the spin-orbit interaction in the constituent quark model is a long-standing problem that is rooted in the fact that the Galilei-invariant term of the spin-orbit piece, which comes from the one-gluon exchange interaction and is the best one founded for the description of the *NN* interaction, severely disturbs the description of the negative parity baryon spectrum [67].

Besides the one-gluon exchange, they are several possible sources of the spin-orbit term of the quark-quark interaction. Valcarce et al. [68] studied the spin-orbit terms generated by the one sigma exchange together with the Galilei-invariant spin-orbit terms coming from the one-gluon exchange. They found that the combination of scalar-meson-exchange interaction between quarks and the one-gluon exchange leads to a satisfactory description of the P-wave NN phase shifts and the baryon spectrum. A similar conclusion can be found in Takeuchi [69]. Another source of spin-orbit interaction is one arising as a relativistic effect from the confinement potential (the so-called Thomas term). In Koike [70], this interaction is studied using a particular model of confinement (flip-flop model). The spin-orbit force generated by one-gluon exchange and by a flip-flop model for confinement gives results that are qualitatively similar to those reported by Valcarce et al. [68].

Recent attempts to overcome this problem have been made by Chen et al. using an extension of the quark delocalization color screening model (QDCSM) [71], which includes a one-pion exchange with a short-range cutoff in the QDCSM Hamiltonian [28]. The quark delocalization is achieved by writing the wave function of each nucleon as a linear combination of left and right Gaussians in a two-center cluster model approximation where the mixing parameter ϵ is determined by the six quark dynamics. They obtain similar results as the Salamanca version of the constituent quark model [52] but replacing the σ-meson exchange by the quark delocalization and color-screening mechanism [29]. However, this new mechanism does not contribute to solving the spin-orbit problem [30].

One must conclude, therefore, that the situation of the spin-orbit force in quark potential models is still quite controversial. To remove the remaining uncertainties, a better understanding of the quark confinement is clearly needed (see also the discussion of this issue in Myhrer and Wroldsen [26]).

Besides the problem of the spin-orbit interaction, the constituent quark model description of the nucleon-nucleon interaction still has room for improvement. Although the Gaussian ansatz for the wave function is a reasonable and useful approximation, one may wonder what the result would be if a more accurate wave function was used. This has been done by Huang and Wang [31] in the framework of the SU(3) chiral model [72]. The authors constrained the adjustable parameters of the model by minimizing the masses of the octet and decuplet baryon ground states. These masses were calculated by using Gaussian trial wave functions where the size parameters are determined by a variational method, which guarantees that all baryons correspond to minimum states of the Hamiltonian model. The *NN* scattering phase shifts are in satisfactory agreement with the experimental data describing in a consistently unified way the single baryon properties and the baryon-baryon dynamics.

A still controversial and challenging problem is the inclusion of the vector-meson exchanges into the model. In a schematic model, Yazaki showed that the pseudo-scalar (π, η) and scalar (σ) meson exchange terms can be simply added to the quark exchange term without the risk of double counting, but the vector-meson (ρ, ω) exchange needs some care because it plays a role similar to the one-gluon exchange [48]. The same conclusion is obtained in Huang and Zhang [73]. These authors show, in a kaon-nucleon interaction in the extended chiral SU(3) quark model that includes vector-meson exchanges, that the role of the gluon is now nearly replaced by the vector-meson exchange. For heavy quarks, meson exchanges are questionable Because, in this sector, the chiral symmetry is explicitly broken by the quark masses. Hence, it seems that the one-gluon exchange should be a piece of the quark-quark interaction. However, which mechanism is the right one for describing the short-range quark-quark interactions is still an open question.

The quark scheme is also very suited to describing the nucleon-nucleon bound states and their possible baryon-baryon components. The deuteron has been traditionally described as an

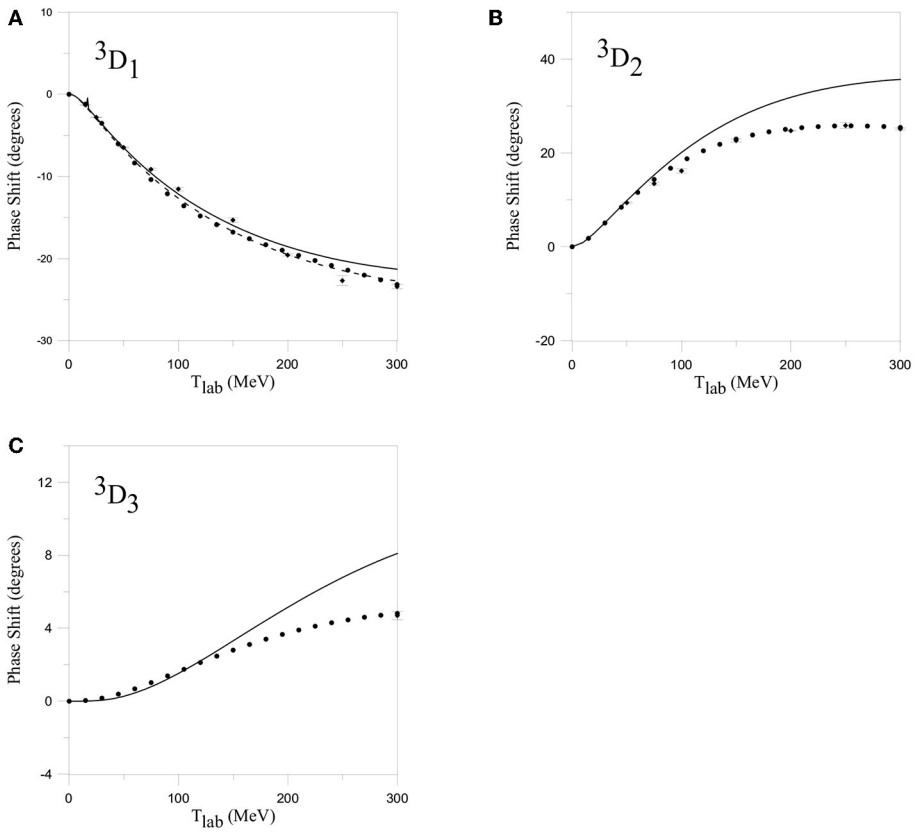


FIGURE 8 | *NN* ^3D_J phase-shifts. **(A)** Lines are labeled as in **Figure 4B**. **(B,C)** Solid line corresponds to the result with *NN* channels only. Reprinted figure with permission from Entem et al. [52] Copyright (2000) by the American Physical Society.

isospin singlet $J^\pi = 1^+$ two-nucleon system in even partial waves (i.e., $^3S_1$ and $^3D_1$). However, its structure could also be explained as a linear combination of pairs of baryonic resonances, provided they have the adequate total quantum numbers.

The usual way to treat the contribution of these resonances is to include them explicitly in a coupled-channel calculation. When this is done at the baryonic level, two problems immediately arise. If one uses for the nucleon-nucleon channel an effective potential that is fitted to the nucleon-nucleon scattering, it will already include contributions from the resonance intermediates N^* or Δ. Therefore, one has to modify the normal nucleon-nucleon potential in order to account for the additional attraction coming from the channel coupling. Such procedures usually introduce an unwanted model dependence on the results obtained and are sometimes not fully consistent.

Examples of these concerns are the calculation of Haapakoski and Saarela [74] ($\Delta\Delta$ components) and Rost [75] (NN^* components). Both used a Reid Soft core potential for the *NN* channel and one-pion exchange potential for the NN^* or $\Delta\Delta$ channel. Rost realized that when NN^* configurations are included, the *NN* potential must be modified because part of the attraction is produced by NN^* components. It implicitly appears in the fit to the experimental data, and, now that the NN^* are explicitly included in the coupled-channels calculation, it must be subtracted out to avoid double counting. This is done by modifying the values of the parameters responsible for the intermediate range attraction in the Reid potential. A similar problem appears in Haapakoski and Saarela [74] in their $\Delta\Delta$ calculation. A second problem is that there is no guidance to construct the specific transition potential to the N^* resonances, and one thus resorts to scaling some pieces (for example the one-pion exchange) of the nucleon-nucleon interaction, As shown by Juliá-Díaz et al. [76], however, the NN^* interaction, due to quark antisymetrization, shows significant differences with respect to those obtained by a direct scaling of the nucleon-nucleon interaction.

These two difficulties are overcome in calculations based on quark degrees of freedom as the one performed in Entem et al. [52]. These authors assume that the deuteron can be described as a combination of different configurations, with two clusters of three quarks being the most important, in order of increasing mass, $N(939)N(939)$, $N(939)N^*(1440)$, and $\Delta(1232)\Delta(1232)$. **Table 3** displays the different configurations and partial waves included in the calculation. The results of the calculation are shown in **Table 4**. In all cases, the deuteron binding energy is correctly reproduced, being $E_d = -2.2246$ MeV. There are a number of conclusions that can be drawn from this table. The first one is that the probability of the $NN^*(1440)$ components are

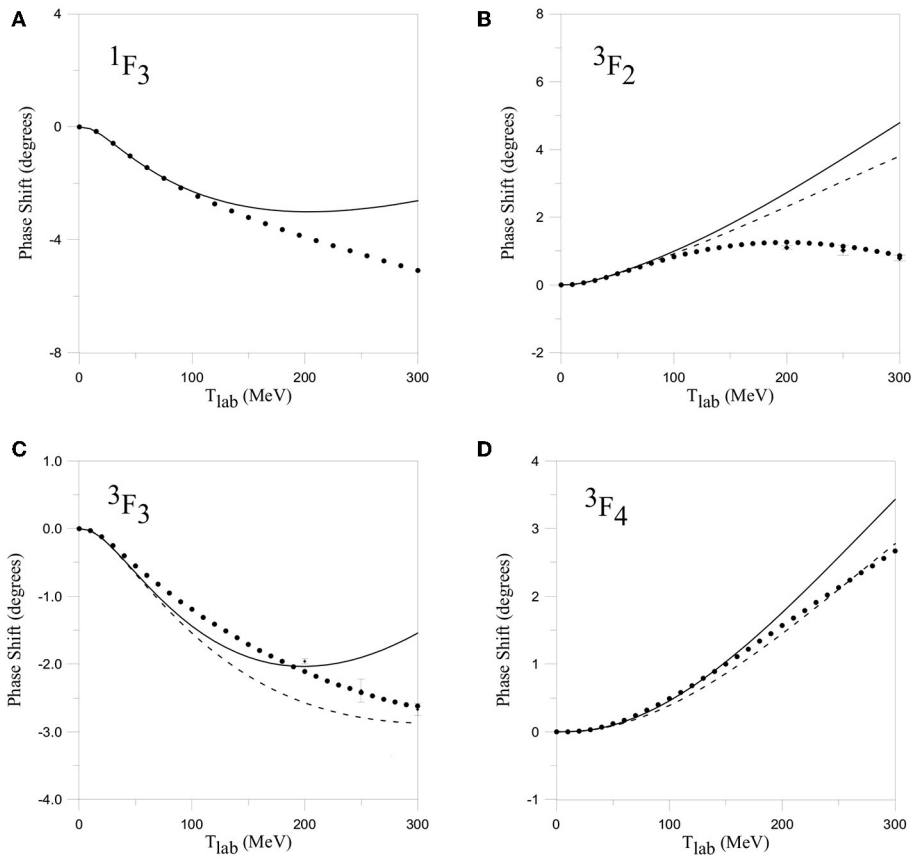


FIGURE 9 | *NN F* phase-shifts. In the $T = 0$ sector **(A)**, the solid line includes *NN* channels only. In the $T = 1$ sector **(B,C,D)**, the dashed line corresponds to including *NN* channels only, and the solid line considers also $N\Delta$ channels. Reprinted figure with permission from Entem et al. [52] Copyright (2000) by the American Physical Society.

significantly smaller than the $\Delta\Delta$ ones, which is in agreement with the indirect estimations of Dorodnykh et al. [78]. As a consequence, the influence of these components on the value of the observables, such as the root mean square radius or A_S, is negligible. Finally, the probability of the $\Delta\Delta$ components (around 0.25%) agree with the upper limit established by Allasia et al. [79].

6. OTHER BARYONIC SYSTEMS

The nucleon-nucleon interaction described above can be applied to other systems, in the same way that they do other nucleon-nucleon potentials likes the ones based in boson exchanges. The most obvious system to extend the application of the quark model-based nucleon-nucleon interaction is the triton.

The interest of this calculation lies in the fact that the NN potential derived from the quark-quark interaction is non-local. This potential is generated using the Resonating Group Method so that the non-localities resulting from the internal structure of nucleons is persevered. These non-localities can produce off-shell behavior different to the quark model-based potential.

In Juliá-Díaz et al. [76], the triton binding energy was obtained from a Fadeev calculation, including only $^1S_0$ and $^3S_1 - {}^3D_1$ NN partial waves, used for the NN interaction of the direct and exchange potential obtained in a fully RGM-based nucleon-nucleon calculation. The results for the triton observables are shown in **Table 5** together with those obtained for conventional NN potentials. One can see that they are no significant differences between the three calculations, and so the quark model-based NN interaction can provide a realistic description of triton. A more complete calculation, which includes up to 50 channels in the Fadeev calculation and uses a different scheme for the quark-quark interaction, was developed by Fujiwara et al. [83], and it obtained a binding energy of $E_b = -8.52$ MeV.

Particularly attractive are those processes in which the quark model description involves completely different physics from the conventional one. One of these systems is the hyperon production process $p\bar{p} \to \Lambda\bar{\Lambda}$.

The experimental data shows two characteristic features of this production process. The first one is that the $p\bar{p} \to \Lambda\bar{\Lambda}$ process that occurs predominately in a spin-triplet state. The second feature refers to the energy dependence of the cross section immediately after the threshold, which needs the inclusion of the calculation of partial waves higher than $L = 0$.

In the quark level description, the $\Lambda\bar{\Lambda}$ pair is produced from the $p\bar{p}$ state via the annihilation of a $u\bar{u}$ pair and the subsequent

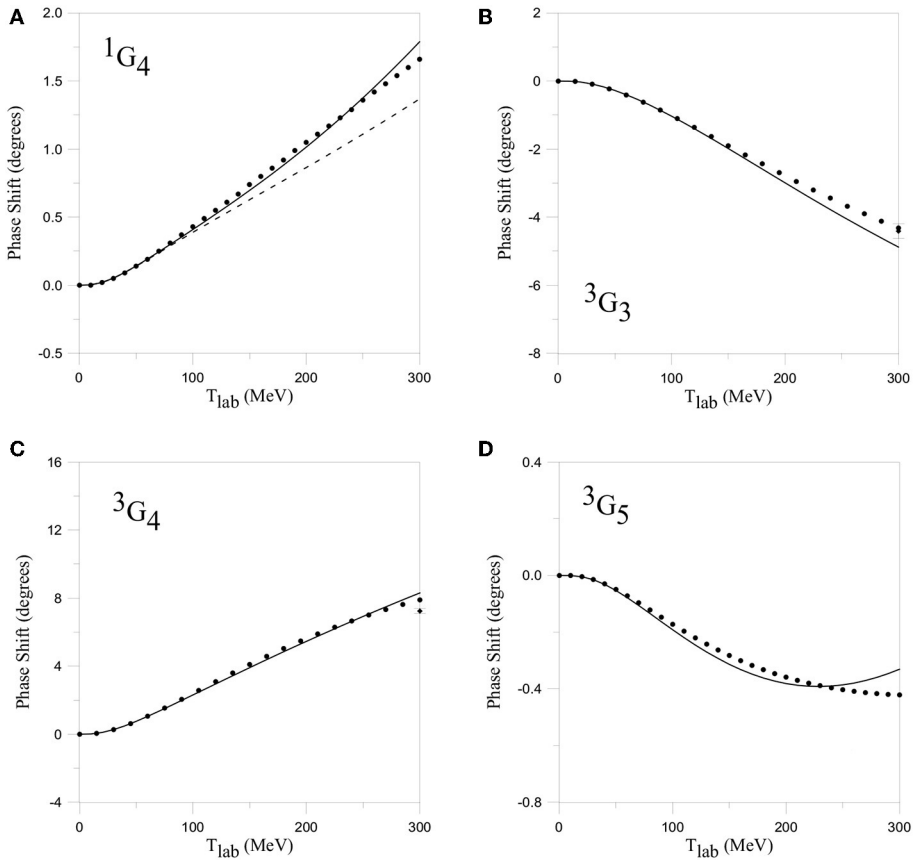


FIGURE 10 | *NN G* phase shifts in the $T = 0$ **(B,C,D)** and $T = 1$ **(A)** sectors. Lines have the same meanings as in **Figure 9**. Reprinted figure with permission from Entem et al. [52] Copyright (2000) by the American Physical Society.

creation of an $s\bar{s}$ pair by s-channel exchanges. In a conventional description, meanwhile, this production relies on the t-channel meson exchanges, where at least kaon exchanges are needed. Examples of this different point of view can be found in Ortega et al. [84], Haidenbauer et al. [85] and references therein.

The two types of models involve completely different physics. Thus, the triplet-state dominance can easily be understood in quark models because the $s\bar{s}$ pair, which carry the $\Lambda\bar{\Lambda}$ spin, is produced by effective vector exchanges (gluons and Goldstone bosons), which gives rise to a spin 1 for the $\Lambda\bar{\Lambda}$ state. In meson exchange models, the tensor pieces of the K and K^* mesons must be combined to produce the spin-triplet dominance, which may introduce a model dependence.

For the real part of the $p\bar{p}$ ($\Lambda\bar{\Lambda}$) interaction, both type of models use a G-parity transformation of some nucleon-nucleon (hyperon-nucleon) potential. The model of Haidenbauer et al. [85] is based in the OBEPF version of the one-boson exchange potential of Haidenbauer et al. [86] for the $p\bar{p}$, whereas the corresponding interaction for the $\Lambda\bar{\Lambda}$ channel is derived from the hyperon-nucleon potential of Holzenkamp et al. [87]. The transition potential $p\bar{p} \rightarrow \Lambda\bar{\Lambda}$ includes K and K^* meson exchanges.

TABLE 2 | Low-energy scattering parameters from Entem et al. [52].

	Quark	OBEP	Paris	Exp.
a_{np} (fm)	–27.010	–23.750	–17.612	–23.748(10)
r_{np} (fm)	2.64	2.71	2.88	2.75(5)
a_t (fm)	5.437	5.424	5.427	5.419(7)
r_t (fm)	1.779	1.761	1.766	1.754(8)

The result of the OBEP and Paris potential are from [61] and [62], respectively. Experimental data are from [63–65].

TABLE 3 | Different channels and partial waves considered in the calculation of the deuteron properties from Juliá-Díaz et al. [77].

NN	$^3S_1$ - $^3D_1$
*NN**	$^3S_1$ - $^3D_1$
$\Delta\Delta$	$^3S_1$ - $^3D_1$ - $^7D_1$ - $^7G_1$

The quark-quark interaction used by Ortega et al. [84] is a generalization of the quark-quark interaction of Entem et al. [52]. It includes the exchange of $\pi, K, \eta, \sigma, \kappa$, and gluons in the t-channel and π, κ, η, and gluons in the annihilation s-channel.

TABLE 4 | Different components in (%) of the deuteron wave function.

NN		*NN**		ΔΔ						
$^3S_1$	$^3D_1$	$^3S_1$	$^3D_1$	$^3S_1$	$^3D_1$	$^7D_1$	$^7G_1$	r_m(fm)	A_S(fm$^{-1/2}$)	η
95.38	4.62	–	–	–	–	–	–	1.976	0.8895	0.0251
95.20	4.56	–	–	0.11	0.0035	0.12	0.0063	1.985	0.8941	0.0250
95.17	4.53	*0.0027*	0.024	0.13	0.0036	0.12	0.0062	1.986	0.8944	0.0250
95.19	*4.54*	*0.0022*	*0.015*	*0.12*	*0.0036*	*0.12*	*0.0063*	*1.985*	*0.8941*	*0.0250*

TABLE 5 | Comparison of triton properties from Juliá-Díaz et al. [80].

	Quark	NijmII	Bonn B
E_B (*MeV*)	−7.72	−7.65	−8.17
P_S (%)	91.49	90.33	91.35
$P_{S'}$ (%)	1.430	1.339	1.368
P_P (%)	0.044	0.064	0.049
P_P (%)	7.033	8.267	7.235

The results of NijmII are from Stoks et al. [81], whereas the results of Bonn B are from Schadow et al. [82].

Initial and final state interactions are automatically included by the diagonal channel interactions.

Besides the interaction described above, both the $p\bar{p}$ and $\Lambda\bar{\Lambda}$ annihilate into mesons. These processes are very difficult to describe, and they are usually parameterized in both models by a complex potential, including spin- and isospin-dependent terms. The parameters of this potential are fitted to the $p\bar{p} \rightarrow p\bar{p}$ cross sections (total, elastic, and charge exchange) and $p\bar{p} \rightarrow \Lambda\bar{\Lambda}$ total cross section. Although both models reproduce the total and differential cross section with reasonable accuracy, completely different patters appear in the description of polarization observables, such as the depolarization observable D_{nn}, the K_{nn} spin transfer, and the $C_{i,j}$ spin correlation coefficients. The calculation of Haidenbauer et al. [85] concluded that the quark model seemed to be in better agreement with the $C_{i,j}$ spin correlation coefficients data. There was no comparison with experimental data of D_{nn}, and the K_{nn} spin transfer was performed, but the results show significant differences between the prediction of the two models. In Ortega et al. [84], the authors compared the results of the quark model calculation with a set of data on a different energy, concluding that the model seemed to show a reasonable agreement with the data. However, the scarcity and inaccuracy of existing data prevents us from forming any definitive conclusion.

The same scheme used to describe the nucleon-nucleon interaction in terms of degrees of quark freedom can be used to study the hyperon-nucleon interaction and the hyperon-hyperon interaction. Technically, this means extending the $SU(2)$ flavor model to the $SU(3)$ flavor model (or $SU(6)$ spin flavor). Most of the parameters of the extended model are obtained from the nucleon-nucleon interaction and the rest from the low-energy cross section data of the hyperon-nucleon interaction.

Among the different works done in this line [88], we will refer to two of them, which use different approaches: the one develop by the Beijing group [89] and the one developed by the Kyoto group [49].

The model of Zhang et al. was an extension of the low-momentum effective Lagrangian coming from the instanton liquid picture of the QCD vacuum Equation (27) of Fernandez et al. [24] to a $SU(3)$ model by the inclusion of an s-quark in the system. As a consequence, aside from the usual π and σ exchanges, K, η, and η' exchanges appeared in a natural way. The 12 parameters of the model were fixed in the same way of Fernandez et al. [24], but the oscillator parameter b_s was obtained by scaling the parameter b_u as $b_s = \sqrt{m_u/m_s}b_u$, were m_u and m_s are the constituent masses of the light and strange quark, respectively. The one-gluon exchange coupling constant for the light and strange quark were determined from the mass splitting of ΔN and ΛN, respectively. Finally, the strength of the confinements were obtained from the stability condition of nucleon Λ and Ξ.

Using this interaction, Zhang et al. [72, 89] studied the binding energy of the deuteron, the NN scattering phase shifts, and the hyperon-nucleon cross section in the framework of the RGM, obtaining results reasonably consistent with experiment.

The model of the Kyoto group follows the philosophy of the hybrids models. The effective qq interaction of the model consist of the one-gluon exchange Fermi-Breit interaction, a quark-confining potential, and other terms generated effective meson-exchange potentials (EMEP) from various meson-exchange mechanisms. They are various version of the model depending of the mesons included in the (EMEP). All of these versions can be found in the extensive review of Fujiwara et al. [88]. We will only mention the most recent version named *fss2* [49], which, besides the scalar and pseudo-scalar meson exchanges, includes the vector meson exchanges as well. This potential reproduces the existing data of the NN and YN interactions quite well and, therefore, can predict all the interactions in the strangeness S = −2, −3, and −4 sectors without adding any extra parameters.

In the last years, the experimental progress in the phenomenology of heavy hadrons has increased the interest in the hadron-hadron interaction involving heavy flavors as well as the bound nuclear systems with heavy mesons. Due to the lack of experimental results, most works are devoted to looking for bound states or resonances or comparing phase shifts with lattice calculations, e.g., Miyamoto et al. [90, 91]. Thus, Huang et al. [33] the $N\Lambda_c$, $N\Lambda_b$, $N\Sigma_c$, and $N\Sigma_b$ are investigated in the quark delocalization color screening model. The authors have shown that, although the interaction $N\Lambda_c$ is attractive, it is not strong enough to form bound states. That is not the case of the

$N\Sigma_c$ interaction, which is able to form bound sates that become resonances with the coupling with the $N\Lambda_c$. The corresponding bottom states have similar properties.

A comparative study of charmed baryon-nucleon interaction is performed in Garcilazo et al. [34] based on different theoretical approaches and comparing them with a lattice calculation, forming a general qualitative agreement among the different approaches. However, more experimental efforts are necessary in this field to be able to drawn quantitative conclusions.

Finally, a *NN* interaction based on quark degrees of freedom has been applied to the description of the nuclear matter saturation point in Fukukawa et al. [92]. These authors derive the equation of states (EOS) of nuclear matter in the framework of the Bethe-Brueckner-Goldstone approach using the *fss2* interaction of Fujiwara et al. [49]. The results showed that the nuclear matter saturation curves can be reproduced at the same level of the best *NN* interactions but without the need of the introduction of three-body forces or parameters different from the one used to reproduce the *NN* phase shifts and the deuteron properties. These results may be an indication that the effects of the three-body forces used in more traditional interactions are, to a large extend, automatically included when the quark degrees of freedom are explicitly introduced in the calculation.

7. OTHER QUARK APPROACHES TO THE NUCLEON-NUCLEON INTERACTION

Although the constituent quarks model, in its different versions, has been the most popular model to use to study the nucleon-nucleon interaction, there have been attempts to use other models for the same purpose, as the bag model is the most important. As we said in the introduction, the first attempts to describe this interaction using degrees of freedom from quarks were made by Fairley using the MIT bag model [93]. The ingredients of the model are very simple: relativistic quarks of three colors and two, three, or four flavors interacting through an octet of colored vector gluons. Quarks and gluons are confined to a finite volume by a uniform pressure. Non-strange quarks are massless, satisfying all quarks the Dirac equation inside the cavity.

The first serious effort to use the MIT bag model to describe the nucleon-nucleon interaction was carried out by DeTar [8]. In this model, the nucleon-nucleon interaction is obtained from the adiabatic deformation of a bag containing six quarks into two color singlet bags containing three each. The energy of the two three-quark bags is minimized with respect to two collective variables: a parameter that measures the separation of the three-quark subsystems and a second parameter related to the baryonic quadrupole moment that, in certain ways, takes into account the deformation of the three-quark bags in their mutual interaction. The obtained potential shows a soft core of about 300 MeV at short distances and it is attractive in the intermediate range. The soft core can be easily understood, as explained below.

In the MIT bag model, the color magnetic energy of n-quarks coupled to a color singlet and located in the same orbit is DeGrand et al. [94]:

$$E_n = \frac{1}{2} M_{00} \left[n(n-6) + J(J+1) + 3I(I+1) \right] \tag{55}$$

where J is the angular momentum of the state and I the isospin. M_{00} is a model parameter that take the value 50 MeV in order to reproduce the $\Delta(1230)$-nucleon mass difference. In the case $J = 1$ and $I = 0$ (calculated by DeTar), the color magnetic interaction when the two nucleons completely overlap was only 50 MeV, whereas each nucleon had a color magnetic energy of 150 MeV. This 250 MeV difference between the energy of two separated and merged nucleons accounted for the repulsion found by DeTar. The intermediate-range attraction obtained by DeTar could not have been predicted without a quantitative calculation and should be related with the strong color electrostatic attraction within the quark triplets [8].

The calculations in this model are sufficiently complex not to be able to advance much more in the calculation of the *NN* interaction. Moreover, the center of mass energy of the two bags is difficult to subtract, which can lead to double counting problems when calculating the nucleon-nucleon phase shifts. In order to solve the scattering problem of two bags, Jaffe and Low proposed the use of the P-matrix formalism [95]. These authors suggested that the energy of multiquarks states appears as poles of the P matrix, that is the logarithmic derivative of the hadronic wave function:

$$P(k,b) = \left| \frac{u'(k,r)}{u(k,r)} \right|_{r=b} \tag{56}$$

provided that the matching radius b is chosen to be consistent with that of the multiquark state. In this way, P-matrix poles are obtained from the experimental phase sifts and compared with the predictions of the bag model to form the multiquark states.

The Jaffe-Low hypothesis was tested for the *NN* system [96, 97], finding a qualitative explanation for the origin of the repulsive core and an overall agreement with the experimental data with an accuracy up to $10 - 15\%$. Possible improvements to the model include a better determination of the relationship between the bags parameter and the matching radius and the possibility of allowing for deformed bag shapes. This last point is technically complicated, although some advances have been made by expanding the wave function in an harmonic oscillator basis [98].

Bags models have also been used to generate boson-exchange interactions through a Fierz transformation of the gluon exchange between two bags, being that the form factors appearing in the OBE are defined as matrix elements of the vertex invariants with quark wave functions taken from the MIT bag model [99].

8. CONCLUDING REMARKS

Throughout this chapter we have presented the achievements of the description of the nucleon-nucleon interaction in terms of quark degrees of freedom. At the scale of nuclear phenomena or

low-energy hadron physics, the QCD running coupling constant is large, and, in this strong-coupling regime, non-perturbative methods are indispensable. But, so far, not much success has been achieved in this respect. Then, if one wants to explicitly keep the fundamental constituents in QCD, i.e., quarks and gluons, one is then led to the model non-perturbative QCD using 'QCD-inspired' models. One of these models, the constituent quark model, is experiencing a resurgence because of the recent studies of the *NN* interaction from first-principles lattice-QCD simulations near the physical quark masses that indicate that their behavior at short distances are qualitatively consistent with the constituent quark model [100, 101]. In particular, when a compact six-quark state is Pauli blocked, the baryon interaction is highly repulsive. However, when the channel is Pauli allowed, the interaction can be either attractive or repulsive, as predicted by the constituent quark model [102].

Leaving aside the fact that these models are not derived from the fundamental theory, the use of quark and gluon degrees of freedom allows us to better understand the physics underlying some phenomena, such as the hard core of the nuclear force or the role played by the quark antisymmetry, which in other models can be hidden in the parameters used. On the other hand, these models represent a complexity added to the calculations that make them less flexible in reproducing certain phenomenology.

The main advantages of these models is that they can describe a huge variety of phenomena, baryon and meson spectrum, baryon-baryon interactions, and few nucleons system (deuteron, triton,…), within an unified (and sometimes reduced) set of parameters with a quality comparable with the other models.

However, these models present the same caveats, such as their non-relativistic character; the way to set the values of the model parameters make it difficult to determine errors of the calculated observables and impossible to improving the model order by order.

AUTHOR CONTRIBUTIONS

All authors listed have made a substantial, direct and intellectual contribution to the work, and approved it for publication.

FUNDING

This work has been funded by Ministerio de Economía, Industria y Competitividad under Contract No. FPA2016-77177-C2-2-P and by the EU STRONG-2020 project under the program H2020-INFRAIA-2018-1, grant agreement no. 824093.

REFERENCES

1. Manohar A, Georgi H. Chiral quarks and the non-relativistic quark model. *Nuclear Phys B*. (1984) **234**:189–212.
2. Diakonov D. Instantons at work. *Prog Part Nucl Phys*. (2003) **51**:173–222. doi: 10.1016/S0146-6410(03)90014-7
3. Fairley GT, Squires EJ. The deuteron in a bag model of hadrons. *Nucl Phys*. (1975) **B93**:56–60.
4. Fairley GT, Squires EJ. Nuclear forces and the quantization of M.I.T. bags. *Acta Phys Polon*. (1975) **B6**:893.
5. Neudatchin VG, Obukhovsky IT, Kukulin VI, Golovanova NF. Attractive potential with forbidden states for the $N-N$ interaction. *Phys Rev C*. (1975) **11**:128–36.
6. Neudatchin VG, Smirnov YF, Tamagaki R. An explanation of N-N "Repulsive Core" in terms of forbidden states based on the quark model. *Progress Theor Phys*. (1977) **58**:1072–4.
7. Liberman DA. Short-range part of the nuclear force. *Phys Rev D*. (1977) **16**:1542–4.
8. DeTar C. Hadronic deformation energy. II. Two-nucleon interaction. *Phys Rev D*. (1978) **17**:323–39.
9. Born M, Oppenheimer R. Zur Quantentheorie der Molekeln. *Annalen der Physik*. (1927) **389**:457–84.
10. Wheeler JA. Molecular viewpoints in nuclear structure. *Phys Rev*. (1937) **52**:1083–106.
11. Wildermuth K, Tang YC. *A Unified Theory of the Nucleus*. New York, NY; San Francisco, CA; London: Academic Press (1977).
12. Oka M, Yazaki K. Nuclear force in a quark model. *Phys Lett B*. (1980) **90**:41–4.
13. Ribeiro JEFT. Microscopic calculation of the repulsive core in the elastic nucleon-nucleon scattering. *Zeitschrift für Physik C Particles Fields*. (1980) **5**:27–35.
14. Toki H. Short range behaviour of the N-N potential within the quark model. *Zeitschrift für Physik A Atoms Nuclei*. (1980) **294**:173–81.
15. De Rújula A, Georgi H, Glashow SL. Hadron masses in a gauge theory. *Phys Rev D*. (1975) **12**:147–62.
16. Harvey M. Effective nuclear forces in the quark model with delta and hidden-color channel coupling. *Nuclear Phys A*. (1981) **352**:326–42.
17. Faessler A, Fernandez F, Lübeck G, Shimizu K. The quark model and the nature of the repulsive core of the nucleon-nucleon interaction. *Phys Lett B*. (1982) **112**:201–5.
18. Makato O, Koichi Y. Short-range part of the nuclear force and the deuteron in a quark model. *Nuclear Phys A*. (1983) **402**:477–90.
19. Maltman K, Isgur N. Nuclear physics and the quark model: six quarks with chromodynamics. *Phys Rev D*. (1984) **29**:952–77.
20. Fujiwara Y, Kohno M, Nakamoto C, Suzuki Y. Interactions between octet baryons in the SU_6 quark model. *Phys Rev C*. (2001) **64**:054001. doi: 10.1103/PhysRevC.64.054001
21. Faessler A, Fernandez F. The quark model and the nucleon-nucleon interaction. *Phys Lett B*. (1983) **124**:145–8.
22. Shimizu K. One-pion exchange potential based on a quark model. *Phys Lett B*. (1984) **148**:418–22.
23. Fernández F. Neutron-proton charge exchange scattering in a one-pion-exchange model with quark exchange. *Phys Lett B*. (1987) **188**:314–6.
24. Fernandez F, Valcarce A, Straub U, Faessler A. The nucleon-nucleon interaction in terms of quark degrees of freedom. *J Phys G Nuclear Part Phys*. (1993) **19**:2013–26.
25. Yu YW, Zhang ZY, Shen PN, Dai LR. Quark-quark potential from chiral symmetry. *Phys Rev C*. (1995) **52**:3393–8.
26. Myhrer F, Wroldsen J. The nucleon-nucleon force and the quark degrees of freedom. *Rev Mod Phys*. (1988) **60**:629–61.
27. Weinberg S. Phenomenological lagrangians. *Phys A Statist Mechan Appl*. (1979) **96**:327 –340.
28. Lu XF, Ping JL, Wang F. The NN phase shifts in the extended quark-delocalization, color-screening model. *Chin Phys Lett*. (2003) **20**:42–5. doi: 10.1088/0256-307X/20/1/313
29. Chen L, Pang H, Huang H, Ping J, Wang F. An Alternative approach to the sigma-meson-exchange in nucleon-nucleon interaction. *Phys Rev*. (2007) **C76**:014001. doi: 10.1103/PhysRevC.76.014001
30. Huang HX, Ping JL, Chen LZ, Wang F, Pang HR. Influence of spin-orbit force on nucleon-nucleon scattering in the quark delocalization colour screening model. *Chin Phys Lett*. (2008) **25**:1617–20. doi: 10.1088/0256-307X/25/5/026
31. Huang F, Wang WL. Nucleon-nucleon interaction in a chiral SU(3) quark model revisited. *Phys Rev*. (2018) **D98**:074018. doi: 10.1103/PhysRevD.98.074018

32. Downum C, Stone J, Barnes T, Swanson E, Vidana I. Nucleon-nucleon interactions from the quark model. *AIP Conf Proc*. (2010) **1257**:538–42. doi: 10.1063/1.3483388
33. Huang H, Ping J, Wang F. $N\Sigma_c$c and $N\Sigma_b$b resonances in the quark-delocalization color-screening model. *Phys Rev C*. (2013) **87**:034002. doi: 10.1103/PhysRevC.87.034002
34. Garcilazo H, Valcarce A, Caramés TF. Charmed baryon-nucleon interaction. *Eur Phys J*. (2019) **C79**:598. doi: 10.1140/epjc/s10052-019-7110-z
35. Tegen R, Weise W. The nucleon axial form factor and the pion-nucleon vertex function. *Zeitschrift für Physik A Atoms Nuclei*. (1983) **314**:357–64.
36. Bräuer K, Faessler A, Fernandez F, Shimizu K. Nucleon-nucleon interaction in a quark model with pions. *Nuclear Phys A*. (1990) **507**:599–610.
37. Jain BK, Santra AB. Study of the $p(p,n)\Delta^{++}$ reaction in nuclei. *Nuclear Phys A*. (1990) **519**:697–720.
38. Fernandez F, Valcarce A, Gonzalez P, Vento V. $p(n,p)n$ and $p(p,\Delta^{++})n$ charge-exchange reactions in a constituent quark model. *Phys Lett B*. (1992) **287**:35–9.
39. Fernández F, Oset E. A model of the double-spin-flip NN amplitude based on a one-pion exchange potential with quark exchange. *Nuclear Phys A*. (1986) **455**:720–36.
40. Kamimura M. Chapter V. A coupled channel variational method for microscopic study of reactions between complex nuclei. *Progress Theor Phys Suppl*. (1977) **62**:236–94.
41. Berestetskii VB, Pitaevskii LP, Lifshitz EM. *Quantum Electrodynamics*. v. 4. Oxford, UK: Elsevier Science (2012).
42. Bender I, Dosch HG. *NN* Potentials in QCD - motivated quark models. *Fortsch Phys*. (1982) **30**:633.
43. Isgur N, Karl G. P wave baryons in the quark model. *Phys Rev*. (1978) **D18**:4187.
44. Isgur N, Karl G. Ground state baryons in a quark model with hyperfine interactions. *Phys Rev*. (1979) **D20**:1191–4.
45. Ellwanger U. Baryon mass splitting by the strong hyperfine interaction and SU(3) breaking. *Nucl Phys*. (1978) **B139**: 422–32.
46. Gromes D. On the effective quark potential in the baryons. *Nucl Phys*. (1977) **B130**:18.
47. Faessler A, Fernandez F, Lübeck G, Shimizu K. The nucleon-nucleon interaction and the role of the [42] orbital six-quark symmetry. *Nuclear Phys A*. (1983) **402**:555–68.
48. Yazaki K. Quark versus mesons in nuclear force and nuclear currents. *Progress Part Nuclear Phys*. (1990) **24**:353–61.
49. Fujiwara Y, Fujita T, Kohno M, Nakamoto C, Suzuki Y. Resonating-group study of baryon-baryon interactions for the complete baryon octet: NN interaction. *Phys Rev C*. (2001) **65**:014002. doi: 10.1103/PhysRevC.65.014002
50. Diakonov DI, Petrov VY. A theory of light quarks in the instanton vacuum. *Nuclear Phys B*. (1986) **272**:457–89.
51. Diakonov D. Foundations of the constitutent quark model. *Progress Part Nuclear Phys*. (1996) **36**:1–17.
52. Entem DR, Fernández F, Valcarce A. Chiral quark model of theNNsystem within a Lippmann-Schwinger resonating group method. *Phys Rev C*. (2000) **62**. doi: 10.1103/PhysRevC.62.034002
53. Valcarce A, Garcilazo H, Fernandez F, Gonzalez P. Quark-model study of few-baryon systems. *Rept Prog Phys*. (2005) **68**:965–1042. doi: 10.1088/0034-4885/68/5/R01
54. Scadron MD. SU(2) linear sigma model: its dynamical generation and phenomenological applications. *Phys Atom Nucl*. (1993) **56**:1595–603.
55. Valcarce A, González P, Fernández F, Vento V. A consistent study of the low energy baryon spectrum and the nucleon-nucleon interaction within the chiral quark model. *Phys Lett B*. (1996) **367**:35–9.
56. Machleidt R. One-boson-exchange potentials and nucleon-nucleon scattering. In: Langanke K, Maruhn JA, Koonin SE, editors. *Computational Nuclear Physics 2: Nuclear Reactions*. Berlin: Springer-Verlag (1993). p. 1–29.
57. Bergervoet JR, van Campen PC, Klomp RAM, de Kok JL, Rijken TA, Stoks VGJ, et al. Phase shift analysis of all proton-proton scattering data below $T_{\rm lab}$=350 MeV. *Phys Rev C*. (1990) **41**:1435–52.
58. Fernández F, Valcarce A, González P, Vento V. A quark-model description of the Δ-production in proton-proton collisions. *Nuclear Phys A*. (1994) **567**:741–60.
59. Arndt RA, Heon Oh C, Strakovsky II, Workman RL, Dohrmann F. Nucleon-nucleon elastic scattering analysis to 2.5 GeV. *Phys Rev C*. (1997) **56**:3005–13.
60. Valcarce A, Faessler A, Fernández F. Influence of the 5D0 nucleon-Δ channel on the 1S0 nucleon-nucleon phase shift in a quark model. *Phys Lett B*. (1995) **345**:367–71.
61. Machleidt R. The Meson theory of nuclear forces and nuclear structure. *Adv Nucl Phys*. (1989) **19**:189–376.
62. Lacombe M, Loiseau B, Richard JM, Vinh Mau R, Cote J, Pires P, et al. Parametrization of the Paris n n Potential. *Phys Rev*. (1980) **C21**:861–73.
63. Houk TL. Neutron-proton scattering cross section at a few electron volts and charge independence. *Phys Rev*. (1971) **C3**:1886–903.
64. Dilg W. Measurement of the neutron-proton total cross section at 132 eV. *Phys Rev*. (1975) **C11**:103–9.
65. Klarsfeld S, Martorell J, Sprung DWL. Deuteron properties and the nucleon nucleon interaction. *J Phys*. (1984) **G10**:165–79.
66. Entem DR, Fernández F, Valcarce A. Charge dependence and charge asymmetry of nuclear forces in chiral quark cluster models. *Phys Lett B*. (1999) **463**:153–8.
67. Isgur N, Karl G. *P*-wave baryons in the quark model. *Phys Rev D*. (1978) **18**:4187–205.
68. Valcarce A, Buchmann A, Fernández F, Faessler A. Spin-orbit force in a quark model based nucleon-nucleon potential. *Phys Rev C*. (1995) **51**:1480–7.
69. Takeuchi S. Effects of instantons on *P*-wave multiquark systems. *Phys Rev Lett*. (1994) **73**:2173–5.
70. Koike Y. Nucleon-nucleon interaction with a flip-flop model for quark confinement. *Nuclear Phys A*. (1986) **454**:509–26.
71. Wang F, Wu Gh, Teng Lj, Goldman JT. Quark delocalization, color screening, and nuclear intermediate range attraction. *Phys Rev Lett*. (1992) **69**:2901–4.
72. Zhang ZY, Yu YW, Shen PN, Dai LR, Faessler A, Straub U. Hyperon-nucleon interactions in a chiral SU(3) quark model. *Nuclear Phys A*. (1997) **625**:59–70.
73. Huang F, Zhang ZY. Kaon-nucleon interaction in the extended chiral SU(3) quark model. *Phys Rev*. (2005) **C72**:024003.
74. Haapakoski P, Saarela M. The double Δ(1236)-resonance in the deuteron. *Phys Lett B*. (1974) **53**:333–6.
75. Rost E. Baryon resonance components in the deuteron. *Nuclear Phys A*. (1975) **249**:510–22.
76. Juliá-Díaz B, Valcarce A, González P, Fernández F. Microscopic $NN \rightarrow NN^*(1440)$ transition potential: determination of $\pi NN^*(1440)$ and $\sigma NN^*(1440)$ coupling constants. *Phys Rev C*. (2002) **66**:024005. doi: 10.1103/PhysRevC.66.024005
77. Juliá-Díaz B, Entem DR, Valcarce A, Fernández F. Deuteron NN*(1440) components from a chiral quark model. *Phys Rev C*. (2002) **66**:047002. doi: 10.1103/PhysRevC.66.047002
78. Dorodnykh YL, Lykasov GI, Rzjanin MV, Cassing W. Probing the deuteron structure at small NN distances by subthreshold antiproton production. *Phys Lett B*. (1995) **346**:227–32.
79. Allasia D, Angelini C, Baldini A, Bobisut F, Borg A, Capillupi P, et al. Search for a Δ(1236)-Δ(1236) structure of the deuteron. *Phys Lett B*. (1986) **174**:450–2.
80. Juliá-Díaz B, Haidenbauer J, Valcarce A, Fernández F. Quark-model based study of the triton binding energy. *Phys Rev C*. (2002) **65**:034001. doi: 10.1103/PhysRevC.65.034001
81. Stoks VGJ, Klomp RAM, Terheggen CPF, de Swart JJ. Construction of high quality N N potential models. *Phys Rev*. (1994) **C49**:2950–62.
82. Schadow W, Sandhas W, Haidenbauer J, Nogga A. Comparison of triton bound state properties using different separable representations of realistic potentials. *Few Body Syst*. (2000) **28**:241–58. doi: 10.1007/s006010070023
83. Fujiwara Y, Miyagawa K, Suzuki Y, Kohno M, Nemura H. Three-nucleon bound state in the SU6 quark model for the baryon-baryon interaction. *Nuclear Phys A*. (2003) **721**:C983–6. doi: 10.1016/S0375-9474(03)01265-X
84. Ortega PG, Entem DR, Fernández F. $p\bar{p} \rightarrow \Lambda\bar{\Lambda}$ depolarization and spin transfer in a constituent quark model. *Phys Lett B*. (2011) **696**:352–8. doi: 10.1016/j.physletb.2010.12.034
85. Haidenbauer J, Holinde K, Mull V, Speth J. Meson-exchange and quark-gluon transitions in the $\bar{p}p \rightarrow \bar{\Lambda}\Lambda$ process. *Phys Rev C*. (1992) **46**:2158–71.

86. Haidenbauer J, Holinde K, Johnson MB. Folded diagram nucleon-nucleon potential for application to the many body problem. *Phys Rev*. (1992) **C45**:2055–67.
87. Holzenkamp B, Holinde K, Speth J. A meson exchange model for the hyperon nucleon interaction. *Nucl Phys*. (1989) **A500**:485–528.
88. Fujiwara Y, Suzuki Y, Nakamoto C. Baryon-baryon interactions in the SU6 quark model and their applications to light nuclear systems. *Progress Part Nucl Phys*. (2007) 58:439–520.
89. Zhang ZY, Faessler A, Straub U, Glozman LYa. The Baryon baryon interaction in a modified quark model. *Nucl Phys*. (1994) **A578**:573–85.
90. Miyamoto T, Aoki S, Doi T, Gongyo S, Hatsuda T, Ikeda Y, et al. $\Lambda_c N$ interaction from lattice QCD and its application to Λ_c hypernuclei. *Nucl Phys*. (2018) **A971**:113–29. doi: 10.1016/j.nuclphysa.2018.01.015
91. Miyamoto T. Coupled-channel $\Lambda_c N - \Sigma_c N$ interaction from lattice QCD. PoS. (2018) Hadron2017:146. doi: 10.22323/1.310.0146
92. Fukukawa K, Baldo M, Burgio GF, Monaco LL, Schulze HJ. Nuclear matter equation of state from a quark-model nucleon-nucleon interaction. *Phys Rev C*. (2015) **92**:065802. doi: 10.1103/PhysRevC.92.065802
93. Chodos A, Jaffe RL, Johnson K, Thorn CB, Weisskopf VF. New extended model of hadrons. *Phys Rev D*. (1974) **9**:3471–95.
94. DeGrand T, Jaffe RL, Johnson K, Kiskis J. Masses and other parameters of the light hadrons. *Phys Rev D*. (1975) **12**:2060–76.
95. Jaffe RL, Low FE. Connection between quark-model eigenstates and low-energy scattering. *Phys Rev D*. (1979) **19**:2105–18.
96. Simonov YA. The quark compound bag model and the Jaffe-low P-matrix. *Phys Lett B*. (1981) **107**:1–4.
97. Mulders PJ. Quark bags and the NN interaction. *Phys Rev D*. (1983) **28**:443–9.
98. Furui S, Faessler A. Nucleon-nucleon scattering in the two-center MIT bag model with nonlocality and removal of the spurious relative motion. *Nucl Phys A*. (1983) **397**:413–46.
99. Bakker BLG, Bozoian M, Maslow JN, Weber HJ. NN interaction from bag-model quark interchange. *Phys Rev C*. (1982) **25**:1134–51.
100. Hatsuda T. Lattice quantum chromodynamics and baryon-baryon interactions. *Front Phys*. (2018) **13**:132105. doi: 10.1007/s11467-018-0829-4
101. Park A, Lee SH, Inoue T, Hatsuda T. Baryon-baryon interactions at short distances–constituent quark model meets lattice QCD. *arXiv:1907.06351*. (2019).
102. Valcarce A, Fernández F, González P, Vento V. Microscopic description of the nucleon-Δ interaction in the quark cluster model. *Phys Rev C*. (1995) **52**:38–48.

Conflict of Interest: The authors declare that the research was conducted in the absence of any commercial or financial relationships that could be construed as a potential conflict of interest.

Copyright © 2020 Fernández, Ortega and Entem. This is an open-access article distributed under the terms of the Creative Commons Attribution License (CC BY). The use, distribution or reproduction in other forums is permitted, provided the original author(s) and the copyright owner(s) are credited and that the original publication in this journal is cited, in accordance with accepted academic practice. No use, distribution or reproduction is permitted which does not comply with these terms.

frontiers in Physics

HYPOTHESIS AND THEORY
published: 14 August 2020
doi: 10.3389/fphy.2020.00307

Lattice QCD and Baryon-Baryon Interactions: HAL QCD Method

Sinya Aoki[1,2]* *and Takumi Doi*[2,3]

[1] Center for Gravitational Physics, Yukawa Institute for Theoretical Physics, Kyoto University, Kyoto, Japan, [2] Quantum Hadron Physics Laboratory, RIKEN Nishina Center, Wako, Japan, [3] Interdisciplinary Theoretical and Mathematical Sciences Program (iTHEMS), RIKEN, Wako, Japan

In this article, we review the HAL QCD method to investigate baryon-baryon interactions, such as nuclear forces in lattice QCD. We first explain our strategy in detail to investigate baryon-baryon interactions by defining potentials in field theories, such as QCD. We introduce the Nambu-Bethe-Salpeter (NBS) wave functions in QCD for two baryons below the inelastic threshold. We then define the potential from NBS wave functions in terms of the derivative expansion, which is shown to reproduce the scattering phase shifts correctly below the inelastic threshold. Using this definition, we formulate a method to extract the potential in lattice QCD. Secondly, we discuss pros and cons of the HAL QCD method, by comparing it with the conventional method, where one directly extracts the scattering phase shifts from the finite volume energies through the Lüscher's formula. We give several theoretical and numerical evidences that the conventional method combined with the naive plateau fitting for the finite volume energies in the literature so far fails to work on baryon-baryon interactions due to contaminations of elastic excited states. On the other hand, we show that such a serious problem can be avoided in the HAL QCD method by defining the potential in an energy-independent way. We also discuss systematics of the HAL QCD method, in particular errors associated with a truncation of the derivative expansion. Thirdly, we present several results obtained from the HAL QCD method, which include (central) nuclear force, tensor force, spin-orbital force, and three nucleon force. We finally show the latest results calculated at the nearly physical pion mass, $m_\pi \simeq 146$ MeV, including hyperon forces which lead to form $\Omega\Omega$ and $N\Omega$ dibaryons.

Keywords: lattice QCD, nuclear forces, baryon-baryon interactions, dibaryons, equation of state, neutron stars

OPEN ACCESS

Edited by:
Laura Elisa Marcucci, University of Pisa, Italy

Reviewed by:
Fiorella Burgio, National Institute of Nuclear Physics, Italy
Raul A. Briceno, Old Dominion University, United States

***Correspondence:**
Sinya Aoki
saoki@yukawa.kyoto-u.ac.jp

Specialty section:
This article was submitted to Nuclear Physics, a section of the journal Frontiers in Physics

Received: *13 January 2020*
Accepted: *03 July 2020*
Published: *14 August 2020*

Citation:
Aoki S and Doi T (2020) Lattice QCD and Baryon-Baryon Interactions: HAL QCD Method. Front. Phys. 8:307. doi: 10.3389/fphy.2020.00307

1. INTRODUCTION

How do nuclear many-body systems emerge from the fundamental degrees of freedom, quarks and gluons? It has been a long-standing problem to establish a connection between nuclear physics and the fundamental theory of strong interaction, quantum chromodynamics (QCD). In particular, nuclear forces serve as one of the most basic constituents in nuclear physics, which are yet to be understood from QCD. While so-called realistic nuclear forces [1–3] have been established with a good precision, they are constructed phenomenologically based on scattering data experimentally obtained. Recent development in effective field theory (EFT) provides a more systematic approach for nuclear forces

from a viewpoint of chiral symmetry in QCD [4–8], whose unknown low-energy constants, however, cannot be determined within its framework but are obtained only by the fit to the experimental data. Under these circumstances, it is most desirable to determine nuclear forces as well as general baryon-baryon interactions from first-principles calculations of QCD, the lattice QCD method. Once baryon forces are extracted from QCD, we can solve finite nuclei, hypernuclei and nuclear/hyperonic matter by employing various many-body techniques developed in nuclear physics. The outcome is expected to make a significant impact on our understanding of nuclear astrophysical phenomena, such as supernovae, binary neutron star merges and nucleosynthesis.

In this paper, we review the HAL QCD method to determine baryon-baryon interactions in lattice QCD. In this method, integral kernels, or so-called "potentials," are first extracted from lattice QCD, and physical observables, such as scattering phase shifts and binding energies are calculated by solving the Schrödinger equation with obtained potentials in the infinite volume. We show that the notion of potential can be rigorously introduced as a representation of the S-matrix in quantum field theories as QCD. The essential point is that the potentials are defined through the Nambu-Bethe-Salpeter (NBS) wave functions, in which the information of phase shifts are encoded in their asymptotic behaviors. We employ a non-local and energy-independent potential where the non-locality is defined through the derivative expansion. In particular, energy-independence of the potential is useful since one can extract the potential from the ground state as well as elastic excited states simultaneously. This enables us to avoid the notorious signal-to-noise issue for multi-baryon systems in lattice QCD (or the ground state saturation problem), and to make a reliable determination of baryon-baryon interactions.

In lattice QCD, there also exists a conventional method, in which phase shifts are obtained from finite volume energies through the Lüscher's formula. For meson-meson systems, a number of works have been performed based on the Lüscher's formula [9], where finite volume energies are extracted utilizing the variational method [10]. The Lüscher's formula has been generalized for various systems, such as boosted systems [11], arbitrary spin/partial waves [12, 13], and three-particle systems [14, 15]. While theoretical bases are well-established for both conventional method and HAL QCD method, numerical results for baryon-baryon systems at heavy pion masses have shown inconsistencies with each other. In this paper, we make a detailed comparison between two methods, scrutinizing possible sources of systematic errors. In particular, we examine whether the systematic errors associated with excited state contaminations are controlled or not in the procedure of the conventional method in the literature ("the direct method"), namely, simple plateau fitting for the ground state at early Euclidean times. We also examine systematic errors in the HAL QCD method, in particular, the truncation error of the derivative expansion. We show theoretical and numerical evidences that the inconsistency between two methods originates from excited state contaminations in the direct method. We also demonstrate that the inconsistency can be actually resolved if and only if finite energy spectra are properly obtained with an improved method rather than the naive plateau fitting in the conventional method.

After establishing the reliability of the HAL QCD method, we present the numerical results of nuclear forces from the HAL QCD method at various lattice QCD setups. The results at heavy pion masses for central and tensor forces are shown and their quark mass dependence as well as physical implications are discussed. The calculations of spin-orbit forces and three-nucleon forces are also given. Once nuclear forces are obtained, one can solve nuclear many-body systems with the obtained potentials. We study finite nuclei, nuclear equation of state and structure of neutron stars based on lattice nuclear forces at heavy pion masses. Finally, the latest results of nuclear forces near the physical pion mass are presented, as well as hyperon forces, which are shown to generate $\Omega\Omega$ and $N\Omega$ dibaryons.

This paper is organized as follows. In section 2, we discuss methods to study baryon-baryon interactions from lattice QCD. After briefly introducing the conventional method and its actual practice, called the "direct method," we describe the detailed theoretical formulation as well as its practical demonstration for the newly developed method, the HAL QCD method. In section 3, we discuss pros and cons of these two methods, and compare the numerical results at heavy pion masses. We present evidences that the results from the direct method suffer from uncontrolled systematic errors associated with the excited state contaminations. In section 4, we summarize results on nuclear potentials in the HAL QCD method. After reviewing the results obtained at heavy pion masses for central and tensor forces in the parity-even channel as well as spin-orbit forces and three-nucleon forces, we present nuclear many-body calculations based on lattice nuclear forces for double-magic nuclei, equation of state and the structure of neutron stars. Latest results for nuclear forces near the physical pion mass are also given. In section 5, we present hyperon forces near the physical pion mass, which lead to $\Omega\Omega$ and $N\Omega$ dibaryons. Section 6 is devoted to the summary and concluding remarks.

2. TWO BARYON SYSTEMS IN LATTICE QCD

In lattice QCD, the 2-pt function for a hadron H, created by $O_H^\dagger$ and annihilated by O_H, is expressed as

$$\langle 0|O_H(\vec{p},t)O_H^\dagger(\vec{p},0)|0\rangle = \sum_{n=0}^{\infty} Z_n(\vec{p})e^{-E_n(\vec{p})t} + \cdots,$$
$$Z_n(\vec{p}) = |\langle 0|O_H(\vec{p},0)|n,E_n(\vec{p})\rangle|^2, \qquad (1)$$

where $|n,E_n(\vec{p})\rangle$ is the n-th one-particle state with a mass m_n, a momentum $\vec{p}$ and an energy $E_n(\vec{p}) = \sqrt{m_n^2+\vec{p}^2}$, and ellipses represent contributions from multi particle states. We here assume $m_0 < m_{n>0}$, so that m_0 is the hadron mass for the ground state, which can be extracted from the asymptotic behavior of the 2-pt function in the large t as

$$\langle 0|O_H(\vec{p},t)O_H^\dagger(\vec{p},0)|0\rangle \simeq Z_0(\vec{p})e^{-E_0(\vec{p})t} + O\left(e^{-E_{n>0}(\vec{p})t}\right),$$
$$t \to \infty, \qquad (2)$$

where finite volume artifact is exponentially suppressed and can be eliminated by an infinite volume extrapolation.

So far, this method in lattice QCD (and the extension to lattice QCD + QED) has successfully reproduced light hadron spectra [16] including the proton–neutron mass splitting [17]. A simple application of the method, however, does not work well for an investigation of hadron interactions. For example, the 2-pt function of two baryons in the center of mass system behaves in the large t as

$$\langle 0|O_{BB}(\vec{0},t)O_{BB}(\vec{0},0)^{\dagger}|0\rangle \simeq Z_{BB}e^{-E_{BB}t}+\cdots, \qquad (3)$$

where we obtain the lowest energy E_{BB}. In the infinite volume limit, E_{BB} behaves as $E_{BB} = 2m_B$ or $E_{BB} = 2m_B - \Delta E$ depending on an absence or presence of bound state. Here m_B is the corresponding baryon mass and $\Delta E > 0$ is the binding energy of the lowest bound state. Only the binding energy of the bound state can be extracted by this simple method and thus more sophisticated methods are required. Currently there are two methods to investigate hadron interactions in lattice QCD, the direct method (or finite volume method) and the HAL QCD method, which are explained in this section.

2.1. Direct Method

The method most widely used to investigate hadron interactions in lattice QCD is to extract scattering phase shifts from energy eigenvalues in 3-dimensional finite boxes through the Lüscher's finite volume formula [18]. For example, in the case of the S-wave scattering phase shift, $\delta_0(k)$, the formula reads

$$k\cot\delta_0(k)=\frac{1}{\pi L}\sum_{\vec{n}\in\mathbf{Z}^3}\frac{1}{\vec{n}^2-q^2}, \qquad q=\frac{kL}{2\pi}, \qquad (4)$$

where k is determined through $E_{BB}(L) = 2\sqrt{k^2+m_B^2}$ with $E_{BB}(L)$ being the energy of the two baryon measured in lattice QCD on a finite box with the spatial extension L as in Equation (3). We here neglect the partial wave mixing in the cubic group and spin degrees of freedom, for simplicity. Only the discrete sets of point $(k^2, k\cot\delta_0(k))$, which satisfies Equation (4), are realized on a given volume L^3. Thus, the scattering phase shift $\delta_0(k)$ at the corresponding k can be extracted in lattice QCD, simply by measuring the finite volume energy, $E_{BB}(L)$. Note that the formula assumes that the hadron interaction is accommodated within the lattice box and is not distorted by the finite volume artifact, which condition should be examined numerically to be satisfied in actual calculations.

In **Figure 1**, we illustrate how scattering phase shifts and the bound state energy can be extracted by this method in the case of the NN scatterings. In the figure, the red solid line represents the effective range expansion (ERE) for $k\cot\delta_0(k)/m_\pi$ at the Next-to-Leading order (NLO) as

$$\frac{k}{m_\pi}\cot\delta_0(k) = \frac{1}{a_0 m_\pi}+\frac{r_0 m_\pi}{2}\frac{k^2}{m_\pi^2} \qquad (5)$$

where the scattering length a_0 and the effective range r_0 are taken to be $a_0 m_\pi = 16.8$, $r_0 m_\pi = 1.9$ for $NN(^1S_0)$ (Left) or $a_0 m_\pi = -3.8$, $r_0 m_\pi = 1.3$ for $NN(^3S_1)$ (Right) with $m_\pi = 140$ MeV, while colored dashed lines represent the Lüscher's finite volume formula, Equation (4) on $L = 10, 12, 14, 18$ fm. Discrete points which satisfy both the Lüscher's finite volume formula and the ERE are realized on each volume, as shown by the open squares, up/down triangles and diamonds.

A distribution of the allowed k^2 for $k^2 > 0$ becomes denser as the volume increases, so as to be continuous in the infinite volume limit, while a sequence of discrete points for $k^2 < 0$ leads to an accumulation point, which corresponds to the scattering state at $k^2 = 0$ in the left figure or the bound state pole, denoted by the black solid circle in the right figure. It is noted here that the bound state pole appears as the intersection between the ERE and the bound state condition, $-\sqrt{-(k/m_\pi)^2}$ (black solid line). To see this, we first write

$$k\cot\delta_0(k) = ik\cdot\frac{S(k)+1}{S(k)-1}, \qquad S(k)=e^{2i\delta_0(k)}, \qquad (6)$$

where $S(k)$ is the S-matrix for the NN elastic scattering. The bound state energy κ_b can be extracted from the pole of this S-matrix as

$$S(k\sim i\kappa_b)\simeq\frac{-i\beta_b^2}{k-i\kappa_b}, \qquad (7)$$

where β_b^2 is real and positive for physical poles [20]. Thus at $k^2\simeq-\kappa_b^2$, we have

$$k\cot\delta_0(k)\big|_{k=i\kappa_b} = -\kappa_b = -\sqrt{-k^2}\Big|_{k=i\kappa_b}, \qquad (8)$$

which means that the binding momentum $k = i\kappa_b$ is given by an intersection between $k\cot\delta_0(k)$ and $-\sqrt{-k^2}$. Moreover, since

$$\frac{d}{dk^2}\left[k\cot\delta_0(k)-(-\sqrt{-k^2})\right]\Big|_{k^2=-\kappa_b^2} = -\frac{1}{\beta_b^2}<0, \qquad (9)$$

the slope of $k\cot\delta_0(k)$ must be smaller than that of $-\sqrt{-k^2}$ as a function of k^2 at the bound state pole, as in the case of **Figure 1** (right). The finite volume analysis thus provides not only an infinite volume extrapolation of the binding energy but also a novel way to examine the normality of the result in the direct method [19].

2.2. HAL QCD Method

2.2.1. Formulation

The HAL QCD method, another method to investigate hadron interactions in lattice QCD, employs the equal time Nambu-Bethe-Salpeter (NBS) wave function, defined by

$$\phi_{\mathbf{k}}(\mathbf{r})e^{-W_{\mathbf{k}}t} \equiv \langle 0|N(\mathbf{x}+\mathbf{r},t)N(\mathbf{x},t)|NN,W_k\rangle, \qquad (10)$$

where $|NN,W_k\rangle$ is the NN eigenstate in QCD with the center of mass energy $W_k = 2\sqrt{\mathbf{k}^2+m_N^2}$ and the nucleon mass m_N, and $N(\mathbf{x},t)$ is a nucleon (annihilation) operator, made of quarks.

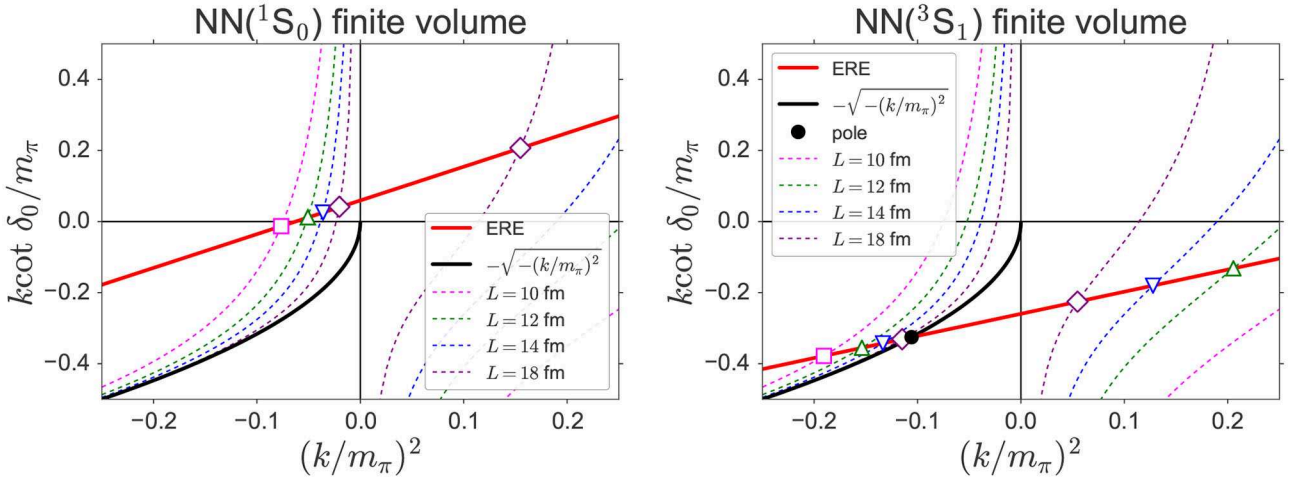


FIGURE 1 | A determination of $k\cot\delta_0(k)/m_\pi$ from energies of the two nucleon state in the finite volume. Taken from Iritani et al. [19].

Other quantum numbers, such as spin/isospin of two nucleons are suppressed for simplicity. We mainly use

$$N_\alpha(x) = \varepsilon^{abc}\left(u^{a\,T}(x)C\gamma_5 d^b(x)\right)q^c_\alpha(x), \qquad x \equiv (\mathbf{x}, t), \quad (11)$$

where $C = \gamma_2\gamma_4$ is the charge conjugation matrix, $q = u(d)$ for proton (neutron). Other choices, such as smeared quarks are possible here, and such arbitrariness is considered to be a choice of the scheme for the definition of the NBS wave function or the potential (see [21] for such an example). Throughout this paper, we consider the *NN* elastic scattering, so that $W_k < W_{\rm th} \equiv 2m_N + m_\pi$, where m_π is the pion mass. Note that this condition is also necessary for the finite volume method in the previous subsection.

Since interactions among hadrons are all short-ranged in QCD, there exists some length scale R, beyond which (i.e., $r \equiv |\mathbf{r}| > R$) the NBS wave function satisfies the Helmholtz equation as

$$(k^2 + \nabla^2)\phi_{\mathbf{k}}(\mathbf{r}) \simeq 0, \qquad k = |\mathbf{k}|. \quad (12)$$

Furthermore, it behaves for large $r > R$ as

$$\phi_{\mathbf{k}}(\mathbf{r}) \simeq \sum_{l,m} Z_{l,m}\frac{\sin(kr - l\pi/2 + \delta_l(k))}{kr}Y_{lm}(\Omega_{\mathbf{r}}), \quad (13)$$

where Y_{lm} is the spherical harmonic function for the solid angle $\Omega_{\mathbf{r}}$ of $\mathbf{r}$, and we ignore spins of nucleon for simplicity[1]. Here it is important to note that the NBS wave function contains information of the phase $\delta_l(k)$ of the S-matrix for the orbital angular momentum l, which is a consequence of the unitarity of the S-matrix in QCD [24, 25].

[1]The formula becomes more complicated if the nucleon spins are considered [22, 23].

In the HAL QCD method, the non-local but energy-independent potential is defined from the NBS wave function through the following equation,

$$(E_k - H_0)\phi_{\mathbf{k}}(\mathbf{r}) = \int d^3\,r' U(\mathbf{r}, \mathbf{r}')\phi_{\mathbf{k}}(\mathbf{r}'), \quad E_k = \frac{k^2}{2m}, \quad H_0 = -\frac{\nabla^2}{2m}, \quad m = \frac{m_N}{2}, \quad (14)$$

for $W_k < W_{\rm th}$, and Equation (12) implies $U(\mathbf{r}, \mathbf{r}') = 0$ for $r > R$. While an existence of $U(\mathbf{r}, \mathbf{r}')$ has been shown in Ishii et al. [26] and Aoki et al. [23, 27], the non-local potential which satisfies Equation (14) is not unique. Thus we have to define the potential uniquely, by specifying how to extract it. For this purpose, we introduce the derivative expansion, $U(\mathbf{r}, \mathbf{r}') = V(\mathbf{r}, \nabla)\delta^{(3)}(\mathbf{r} - \mathbf{r}')$, whose lowest few orders for the *NN* with a given isospin channel are written as

$$V(\mathbf{r}, \nabla) = \underbrace{V_0(r) + V_\sigma(r)(\sigma_1 \cdot \sigma_2) + V_T(r)S_{12}}_{\rm LO} + \underbrace{V_{\rm LS}(r)\mathbf{L}\cdot\mathbf{S}}_{\rm NLO} + O(\nabla^2), \quad (15)$$

where $V_0(r)$ is the central potential, $V_\sigma(r)$ is the spin dependent potential with σ_i being the Pauli matrix acting on the spinor index of the i-th nucleon, $V_T(r)$ is the tensor potential with the tensor operator $S_{12} = 3(\hat{\mathbf{r}}\cdot\sigma_1)(\hat{\mathbf{r}}\cdot\sigma_2) - (\sigma_1\cdot\sigma_2)$ ($\hat{\mathbf{r}} \equiv \mathbf{r}/r$), and $V_{\rm LS}(r)$ is the spin-orbit (LS) potential with the angular momentum $\mathbf{L} = \mathbf{r} \times \mathbf{p}$ and the total spin $\mathbf{S} = (\sigma_1 + \sigma_2)/2$. It is noted that an expansion of the non-local potential is not unique. For example, we may improve the convergence of the expansion by modifying the ∇ operator [28].

Once we obtain the approximated potential at lowest few orders, we can calculate the scattering phase shifts or the binding energies of possible bound states by solving the Schrödinger equation with this potential in the infinite volume. As is the case

for the finite volume method, it is necessary that the potential is not distorted by the finite volume artifact, but this can be checked easily since the potential itself is explicitly obtained. We can also check how good the approximated potential is, by increasing the order of the expansion. Needless to say, the approximated potential depends on momenta of input wave functions. As pointed out in Aoki et al. [29], these dependences of the approximated potentials have been misidentified with those of the non-local potential in the literature [30]. In the next subsection, we will explicitly demonstrate how this procedure works.

2.2.2. Demonstration

In order to see how the scattering phase shifts can be obtained by the HAL QCD method, we consider the quantum mechanics for a spinless system with a separable potential, defined by

$$U(\mathbf{r},\mathbf{r}') = \omega v(\mathbf{r})v(\mathbf{r}'), \quad v(\mathbf{r}) \equiv e^{-\mu r}. \tag{16}$$

The S-wave solution of the Schrödinger equation with this potential is given exactly by

$$\phi_k^0(r) = \frac{e^{i\delta_0(k)}}{kr}\left[\sin\{kr+\delta_0(k)\} - \sin\delta_0(k) e^{-\mu r}\left(1+\frac{r(\mu^2+k^2)}{2\mu}\right)\right], \tag{17}$$

where

$$k\cot\delta_0(k) = -\frac{1}{4\mu^2}\left[2\mu(\mu^2-k^2) - \frac{3\mu^2+k^2}{4\mu^3}(\mu^2+k^2)^2 + \frac{(\mu^2+k^2)^4}{8\pi m\omega}\right], \tag{18}$$

which is the 4-th order polynomials in k^2. In order to make the scattering phase shift a more complicated function of k^2, we artificially modify the wave function from $\phi_k^0(r)$ to $\phi_k(r)$ which is defined by

$$\phi_k(r) = \begin{cases} \phi_k^0(r) & (r \le R) \\ C(k)\dfrac{e^{i\delta_R(k)}}{kr}\sin\{kr+\delta_R(k)\} & (r > R), \end{cases} \tag{19}$$

where R is an infrared cutoff, and it is understood that the potential is modified accordingly. The continuity of $\phi_k(r)$ and $\phi_k'(r)$ at $r = R$ gives

$$k\cot\delta_R(k) = k\frac{Y\cot(kR)+X}{X\cot(kR)-Y}, \quad X = \phi_k^0(R), \quad Y = \frac{d}{dr}[r\phi_k^0(r)]\Big|_{r=R}, \tag{20}$$

as well as $C(k) = X/\sin(kR+\delta_R(k))$. Hereafter, we study how the scattering phase shifts are obtained in the HAL QCD method.

The derivative expansion for the S-wave scatterings leads to

$$V(\mathbf{r},\nabla) = V_0(r) + V_1(r)\nabla^2 + O(\nabla^2), \tag{21}$$

and we consider to determine the potential in each order from $\phi_k(r)$.

The leading order (LO) potential is given by

$$V^{\rm LO}(\mathbf{r},\nabla) = V_0^{\rm LO}(r;k) = \frac{(E_k - H_0)\phi_k(r)}{\phi_k(r)}, \tag{22}$$

while the next-to-leading order (NLO) potential is extracted as

$$V^{\rm NLO}(\mathbf{r},\nabla) = V_0^{\rm NLO}(r;k_1,k_2) + V_1^{\rm NLO}(r;k_1,k_2)\nabla^2, \tag{23}$$

where

$$\begin{pmatrix} V_0^{\rm NLO}(r;k_1,k_2) \\ V_1^{\rm NLO}(r;k_1,k_2) \end{pmatrix} = \frac{1}{D(r;k_1,k_2)}\begin{pmatrix} 2m\left[V_0^{\rm LO}(r;k_2)E_{k_1} - V_0^{\rm LO}(r;k_1)E_{k_2}\right] \\ V_0^{\rm LO}(r;k_2) - V_0^{\rm LO}(r;k_1) \end{pmatrix},$$
$$D(r;k_1,k_2) = 2m\left[V_0^{\rm LO}(r;k_2) - V_0^{\rm LO}(r;k_1) - (E_{k_2} - E_{k_1})\right]. \tag{24}$$

Note that the potential in each order in the derivative expansion $\{V_0(r), V_1(r), \cdots\}$ are defined to be k-independent, while the potentials approximately obtained in each LO/NLO analysis, $\{V_0^{\rm LO}(r;k)\}$ and $\{V_0^{\rm NLO}(r;k_1,k_2), V_1^{\rm NLO}(r;k_1,k_2)\}$, have implicit k-dependence due to the truncation error in the derivative expansion [29].

We calculate S-wave scattering phase shifts corresponding to these approximated potentials, and compare them with the exact phase shifts, $\delta_R(k)$. Considering μ as a typical inelastic threshold energy in this model, we take $k = 0$ and/or $k = \mu$ for the following analysis. **Figure 2** shows the S-wave scattering phase shift $\delta(k)$ (Left) and $k\cot\delta(k)$ (Right) as a function of k^2, where all (dimensionful) quantities are measured in units of μ. In this example, we take $\omega = -0.017\mu^4$, $m = 3.30\mu$, and $R = 2.5/\mu$. In the figures, the exact phase shift $\delta_R(k)$(Left) or $k\cot\delta_R(k)$ (Right) is given by the blue solid line, while the LO approximations at $k = 0$ or $k = \mu$ are represented by orange and green solid lines, respectively. As seen from the figures, the LO approximation at $k = 0$ (orange), exact at $k^2 = 0$ by construction, gives a reasonable approximation at low energies ($k^2 \simeq 0$) but deviates from the exact one at high energies near $k^2 \simeq \mu^2$. On the other hand, the LO approximation at $k = \mu$ (green) becomes accurate at higher energies near $k^2 \simeq \mu^2$ but inaccurate at low energies near $k^2 \simeq 0$. Combining two NBS wave functions, $\phi_{k_1=0}(r)$ and $\phi_{k_2=\mu}(r)$, one can determine the approximated potential at the NLO, $V^{\rm NLO}(\mathbf{r},\nabla)$, whose scattering phase shifts are represented by the red solid lines in the figures. The phase shifts at the NLO (red lines) gives reasonable approximations of the exact results (blue solid lines) in the whole range ($0 \le k^2 \le \mu^2$), as they are exact at $k^2 = 0$ and $k^2 = \mu^2$ by construction. If we increase the order of the expansion more and more, the approximation becomes better and better[2].

Using this model, let us compare the direct method and the HAL QCD method. At the LO, the direct method gives either

[2]A similar attempt to represent an arbitrary potential in terms of a separable potential is given in Ernst et al. [31, 32].

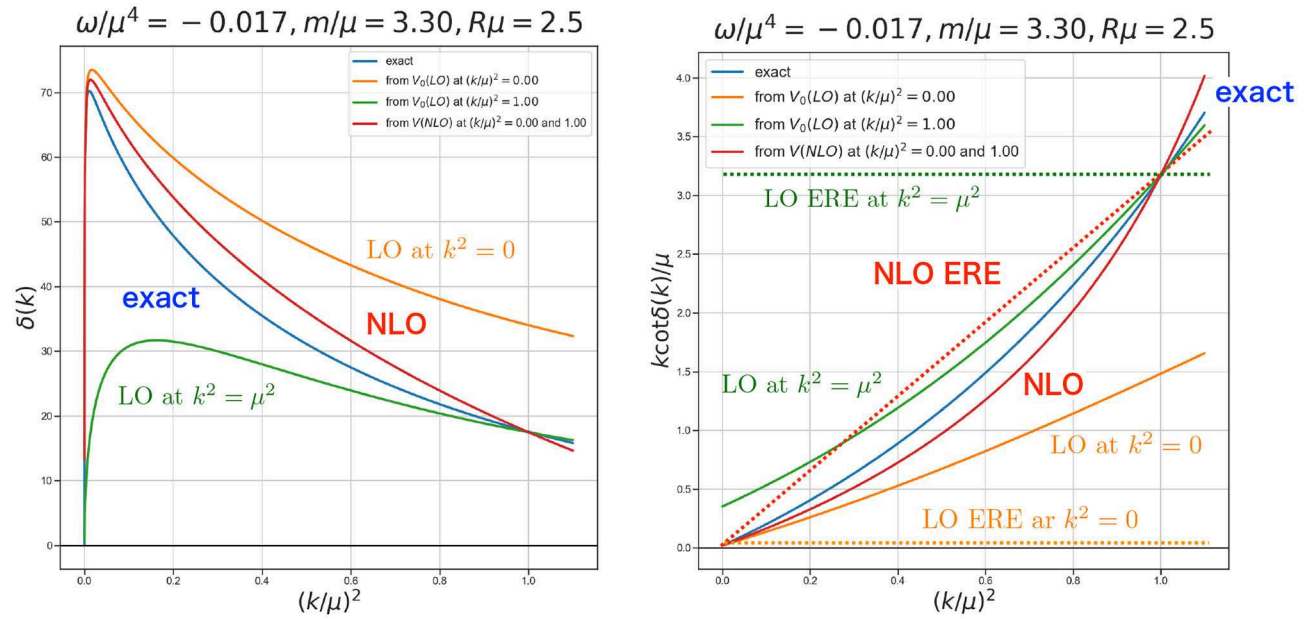


FIGURE 2 | The scattering phase shifts $\delta(k)$ and $k\cot\delta(k)$ as a function of k^2. See the main text for more details.

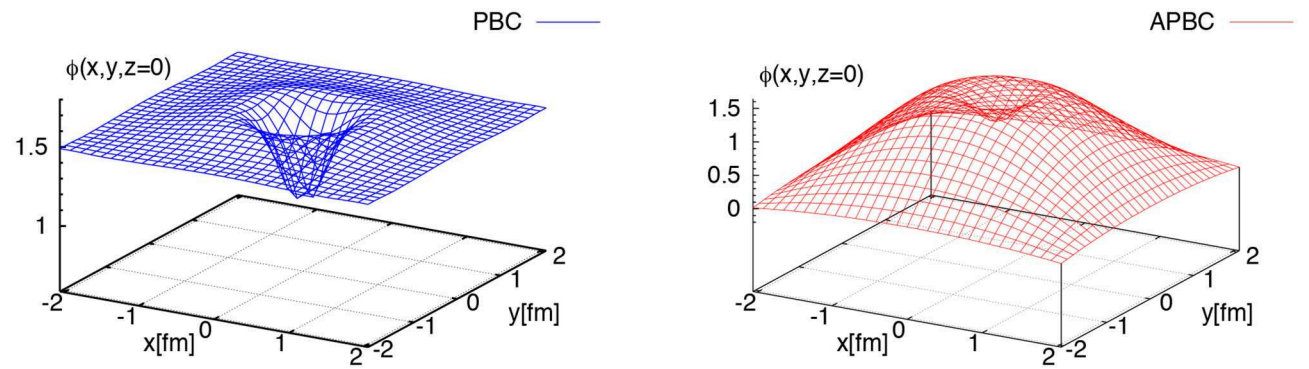


FIGURE 3 | The NBS wave function for $NN(^1S_0)$ at $E_k \simeq 0$ MeV with the PBC (left) and at $E_k \simeq 45$ MeV with the APBC (right). Both are normalized to unity at $r = 1$ fm. Taken from Murano et al. [33].

$k\cot\delta(k)$ at $k^2 = 0$ or $k^2 = \mu^2$ without any information about the effective range, which only gives the LO ERE (an orange dashed line or a green dashed line in the right figure). Thus the LO potentials approximate the exact $k\cot\delta(k)$ much better (the orange solid line or the green solid line). In the direct method, the ERE at NLO is obtained by combining the data at $k^2 = 0$ and $k^2 = \mu^2$ as

$$k\cot\delta(k) = \frac{1}{a_0} + \frac{r_{\rm eff}}{2}k^2, \quad \frac{1}{a_0} = \lim_{k\to 0} k\cot\delta(k),$$
$$\frac{r_{\rm eff}}{2} = \frac{\cot\delta(\mu)}{\mu} - \frac{1}{\mu^2 a_0}, \tag{25}$$

which is given by a red dashed line in the right figure. By comparing the HAL QCD method with potentials at NLO (the red solid line) and the direct method with NLO ERE (the red dashed line), the former leads to a better approximation of the exact result than the latter, since higher order effects in ERE in terms of k^2 are included in the former. Note, however, that sufficiently precise data in the direct method can also evaluate higher order ERE terms than NLO, in principle.

2.2.3. Dependence of the LO *NN* Potential on Energy and Partial Waves

In this subsection, we consider effects of higher order terms in the derivative expansion for the *NN* in QCD.

Figure 3 shows three dimensional plots of the NBS wave functions $\phi_{\mathbf{k}}(x, y, z = 0)$ for $NN(^1S_0)$ with the periodic boundary condition (PBC) at $E_k \simeq 0$ MeV (Left) and with the anti-periodic boundary condition (APBC) at $E_k \simeq 45$ MeV (Right), in quenched lattice QCD at $a \simeq 0.137$ fm on $L \simeq 4.4$ fm with

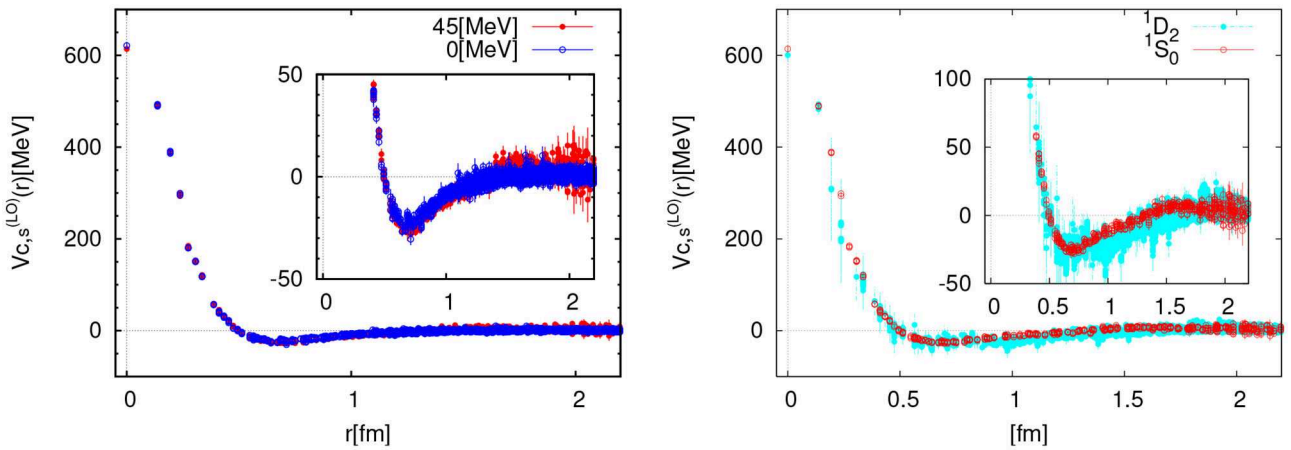


FIGURE 4 | (Left) The LO potential for $NN(^1S_0)$ as a function of r at $E_k \simeq 45$ MeV (red solid circles) and at $E_k \simeq 0$ MeV (blue open circles). (Right) The LO potential as a function of r at $E_k \simeq 45$ MeV for $NN(^1S_0)$ (red open circles) and for $NN(^1D_2)$ (cyan solid circles). Taken from Murano et al. [33].

$m_\pi \simeq 530$ MeV [33]. As seen from the figure, two NBS wave functions look very different from each other. In particular, the right one vanishes on the boundary due to the APBC constraint.

Figure 4 (Left) compares the LO potentials for $NN(^1S_0)$ obtained from the corresponding NBS wave functions in **Figure 3**. While the NBS wave functions at different energies have different spatial structures, the potentials look very similar. This suggests that the higher order terms in the derivative expansion of the potential have negligible contributions at this energy interval, $0 \le E_k \le 45$ MeV.

Figure 4 (Right) compares the LO potential for $NN(^1S_0)$ (red open circles) with the one for $NN(^1D_2)$ (cyan solid circles) at $E_k \simeq 45$ MeV. Although statistical fluctuations are larger for the latter, they look similar, suggesting that $\mathbf{L}^2$ dependence of the potential is also small in this setup. If more accurate data show a difference of potentials between $NN(^1S_0)$ and $NN(^1D_2)$, one may determine the $\mathbf{L}^2$ dependent term of the potential in the spin-singlet channel.

2.2.4. Time-Dependent HAL QCD Method

In order to extract the NBS wave functions on the finite volume in lattice QCD, we consider the 4-pt function given by

$$F^J(\mathbf{r}, t-t_0) = \langle 0|N(\mathbf{x}+\mathbf{r}, t)N(\mathbf{x}, t)\bar{J}_{NN}(t_0)|0\rangle = \sum_n A_n^J \phi_{\mathbf{k}_n}(\mathbf{r}) e^{-W_{k_n}(t-t_0)} + \cdots, \quad (26)$$

where $\bar{J}_{NN}(t_0)$ is an operator which creates two nucleon states at time t_0, $A_n^J \equiv \langle NN, W_{k_n}|\bar{J}_{NN}(0)|0\rangle$, and ellipses represent inelastic contributions, which become negligible at $W_{\rm th}(t-t_0) \gg 1$. Like the direct method, one can extract the NBS wave function for the ground state from the above 4-pt function as

$$F^J(\mathbf{r}, t) \simeq A_0^J \phi_{\mathbf{k}_0}(\mathbf{r}) e^{-W_{k_0} t} \quad (27)$$

for $(W_{k_1} - W_{k_0})t \gg 1$, where W_{k_0} (W_{k_1}) is the lowest (second-lowest) energy on the finite volume. The LO potential from the NBS wave function for the ground state is then extracted from $F^J(\mathbf{r}, t)$ at large t. As will be discussed in the next section, however, it is numerically very difficult to determine $F^J(\mathbf{r}, t)$ for two nucleons at such large t due to the bad signal-to-noise (S/N) ratio.

Fortunately, an alternative extraction is available for the HAL QCD method [34]. Let us consider the ratio of 4-pt function to the 2-pt function squared as

$$R^J(\mathbf{r}, t) \equiv \frac{F^J(\mathbf{r}, t)}{G_N(t)^2}, \quad G_N(t) = \sum_{\mathbf{x}} \langle 0|N(\mathbf{x}, t)N(\mathbf{0}, 0)|0\rangle \simeq Z_N e^{-m_N t} + \cdots, \quad (28)$$

which behaves

$$R^J(\mathbf{r}, t) = \sum_n \tilde{A}_n^J \phi_{\mathbf{k}_n}(\mathbf{r}) e^{-\Delta W_{k_n} t}, \quad \tilde{A}_n^J \equiv \frac{A_n^J}{Z_N^2}, \quad \Delta W_k \equiv W_k - 2m_N, \quad (29)$$

for $W_{\rm th} t \gg 1$, where inelastic contributions can be neglected. Noticing that

$$\Delta W_k = \frac{k^2}{m_N} - \frac{(\Delta W_k)^2}{4m_N}, \quad \left(\frac{k^2}{m_N} - H_0\right)\phi_{\mathbf{k}}(\mathbf{r}) = V(\mathbf{r}, \nabla)\phi_{\mathbf{k}}(\mathbf{r}), \quad (30)$$

we obtain

$$\left\{-H_0 - \frac{\partial}{\partial t} + \frac{1}{4m_N}\frac{\partial^2}{\partial t^2}\right\} R^J(\mathbf{r}, t) = V(\mathbf{r}, \nabla) R^J(\mathbf{r}, t). \quad (31)$$

We can approximately extract $V(\mathbf{r}, \nabla)$ from $R^J(\mathbf{r}, t)$ for (different) J's, as long as t satisfies the condition that $W_{\rm th}\, t \gg 1$ (elastic state saturation), which is much easier than to achieve $(W_{k_1} - W_{k_0})t \gg 1$ (ground state saturation). We call this alternative extraction the time-dependent HAL QCD method.

3. A COMPARISON OF THE TWO METHODS AT HEAVIER PION MASSES

It is interesting to ask whether the attractions of the nuclear forces at low energies would become weaker or stronger if the pion mass were larger than the value in Nature. In principle, such a question can be answered by employing either the direct method or the HAL QCD method in lattice QCD. There exists, however, a qualitative discrepancy between the two methods on the answer to this question. As summarized in **Table 1**, the direct method tends to indicate that attractions between two nucleons become stronger as the pion mass increases, so that both deuteron and di-neutron form bound states, while the HAL QCD method suggests that the attractions become weaker and the bound deuteron does not exist at heavier pion masses. Note that the results from the direct method in the flavor SU(3) limit ($N_f = 3$ in the table), NPL2013/NPL2017, CalLat2017, and Mainz2018, exhibit discrepancies with each other [19]. In addition, while both methods lead to the bound H-dibaryon at heavier pion masses, in particular, in the flavor SU(3) limit, the predicted binding energies differ even within the direct method: NPL2013 [40] gives 75(5) MeV at $m_\pi = 810$ MeV, which is much larger than 19(10) MeV at $m_\pi = 960$ MeV by Mainz2018 [43]. On the other hand, HAL2012 [44] gives 38(5) MeV at $m_\pi = 837$ MeV from the HAL QCD method. These deviations seem to be too large to be explained by lattice artifacts.

In order to understand origins of these discrepancies, we have performed extensive investigations, whose results have been published in a series of papers [19, 46–48], which will be explained in the following subsections.

3.1. Operator Dependence in the Direct Method

In the direct method, reliable extractions of the two nucleon ground state energies are crucially important. As long as $(W_{k_1} - W_{k_0})t \gg 1$, the two nucleon correlation function is dominated by the ground state as

$$G_{NN}(t) = \langle 0|J_{NN}(t)\bar{J}'_{NN}(0)|0\rangle \simeq Z^J_{k_0}\bar{Z}^{J'}_{k_0}e^{-W_{k_0}t},$$
$$Z^{J(J')}_{k_0} \equiv \langle 0|J_{NN}(J'_{NN})|NN, W_{k_0}\rangle, \quad (32)$$

so that the extracted ground state energy W_{k_0} depends neither the source operator $\bar{J}'_{NN}$ nor the sink operator J_{NN}, while magnitudes of contaminations from excited states are affected by the choices of these operators. Since $W_{k_1} - W_{k_0} \simeq (2\pi/L)^2/m_N$ on the finite box with the spacial extension L, $t \gg 4$ fm is required, for example, for $L \simeq 4$ fm and $m_N \simeq 2$ GeV at heavier pion masses. Due to the bad S/N ratio at such large t, however, authors in previous literature extracted the ground state energies at much smaller t, $t \sim 1$ fm, by tuning the source operators $\bar{J}'_{NN}$ in order to achieve

TABLE 1 | Summary of binding energies [MeV] for $NN(^1S_0)$, $NN(^3S_1)$, and H-dibaryon in lattice QCD.

Collaboration	References	N_f	m_π	$-\Delta E(^1S_0)$	$-\Delta E(^3S_1)$	$-\Delta E(H)$
The direct method						
YKU2011	[35]	0	800	4.4 (1.2)	7.5 (1.0)	—
YIKU2012	[36]	2+1	510	7.4 (1.4)	11.5 (1.3)	—
NPL2015	[37]	2+1	450	12.5 $(^{+3.0}_{-5.0})$	14.4 $(^{+3.2}_{-2.6})$	—
NPL2012	[38]	2+1	390	7.1 (9.0)	11 (13)	13.2 (4.4)
YIKU2015	[39]	2+1	300	8.5 $(^{+1.7}_{-0.9})$	14.5 $(^{+2.5}_{-1.1})$	—
NPL2013	[40]	3	810	15.9 (3.8)	19.5 (4.8)	74.6 (4.7)
NPL2017	[41]	3	810	20.6 $(^{+3.3}_{-2.9})$	27.9 $(^{+3.8}_{-2.7})$	—
CalLat2017	[42]	3	810	21.8 $(^{+3.3}_{-5.8})$	30.7 $(^{+2.5}_{-3.0})$	—
		3		8.35 (1.1)*	3.3 $(^{+1.2}_{-0.9})$	—
Mainz2018	[43]	3†	960	0	—	19 (10)
		2+1†	440	—	—	18.8 (5.5)*
The HAL QCD method						
IAH2007	[26]	0	530	0	0	—
AHI2009	[23]	0	380, 530, 730	0	0	—
HAL2012	[44]	3	1171	0	0	49.1(6.5)
		3	1015	0	0	37.2(4.4)
		3	837	0	0	37.8(5.2)
		3	672	0	0	33.6(5.9)
		3	469	0	0	26.0(6.5)
HAL2012a	[34]	2+1	701	0	—	—
HAL2013	[45]	2+1	411, 570, 701	0	—	—

NPL2013, NPL2017, and CalLat2017 employed the same set of gauge configurations. CalLat2017 found two states in each channel. In Mainz2018, dynamical 2-flavor with quenched strange quark configurations are employed and N_f in the table (with † symbol) denotes the information in the valence quark sector. All values of ΔE correspond to those in the infinite volume limit except ones with $*$, which are values on the finite volumes. The number 0 in ΔE indicates the system is unbound in this channel.

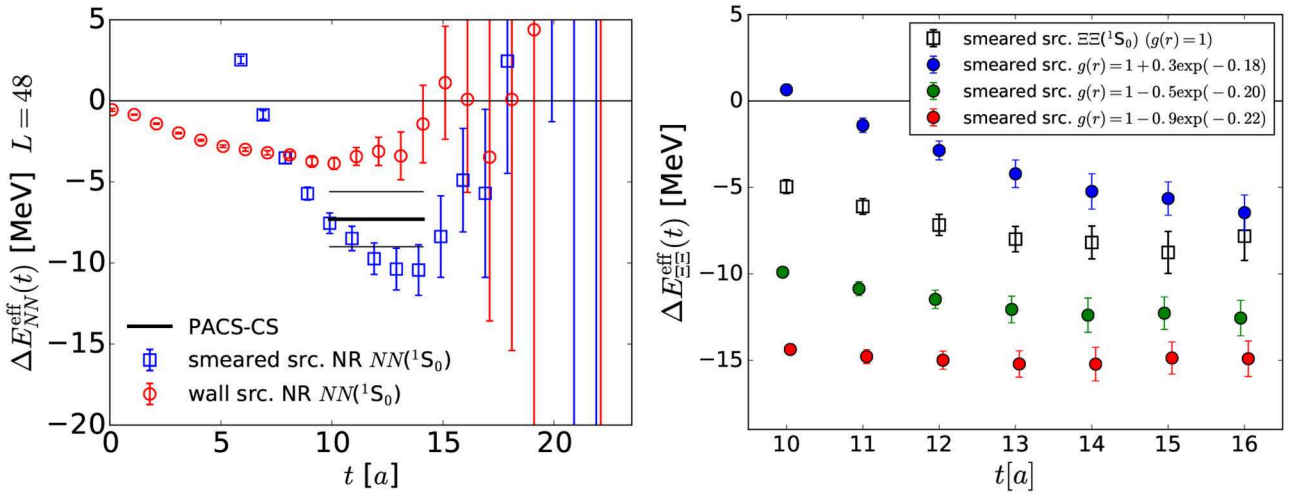


FIGURE 5 | (Left) The effective energy shift $\Delta E^{\rm eff}_{NN}(t)$ for $NN(^1S_0)$ from the wall source (red circles) and the smeared source (blue squares) on $L = 48a \simeq 4.3$ fm at $m_\pi = 0.51$ GeV, $m_N = 1.32$ GeV and $m_\Xi = 1.46$ GeV [46]. (Right) The effective energy shift $\Delta E^{\rm eff}_{\Xi\Xi}(t)$ for $\Xi\Xi(^1S_0)$ from the smeared source with different sink operators on the same gauge configurations [46].

a plateau of the effective energy shift $\Delta E^{\rm eff}_{NN}(t)$ at such a small t, where

$$\Delta E^{\rm eff}_{NN}(t) = -\frac{1}{a}\log\frac{R_{NN}(t+a)}{R_{NN}(t)}, \quad R_{NN}(t) \equiv \frac{G_{NN}(t)}{G_N(t)^2}, \quad (33)$$

Unfortunately, such a naive plateau fitting at earlier t may not be reliable due to contaminations from nearby excited states, which may easily produce (incorrect) plateau-like behaviors in effective energies. It was indeed demonstrated that plateau-like behaviors in effective energy shifts at small t can depend not only on the source operator but also on the sink operator: Plateaux disagree between the wall source (red circle) and the smeared source (blue square) in the left of **Figure 5**, while plateaux depend on sink operators for the same smeared source in the right figure.

In order to see how easily contaminations from elastic-excited states can produce plateau-like behaviors at earlier t, let us consider the effective energy shift from the mockup data for $R_{NN}(t)$, given by

$$R^{\rm mockup}_{NN}(t) = e^{-\Delta E_{NN} t}\left(1 + b_1 e^{-\delta E_{\rm el.} t} + c_0 e^{-\delta E_{\rm inel.} t}\right), \quad (34)$$

where we take $\delta E_{\rm el.} = 50$ MeV for the typical lowest elastic excitation energy on $L \simeq 4$ fm at $m_N \simeq 1.5$ GeV, and $\delta E_{\rm inel.} \simeq m_\pi \simeq 500$ MeV for the lowest inelastic energy. Naively, it is expected that the correct plateau at ΔE_{NN} for the ground state appears at $t \gg 1/\delta E_{\rm el.} \simeq 4$ fm, which however is too large to have good signals for two baryons, such as NN. By tuning the source operator, one may reduce coefficients b_1 and c_0. Since the NN operator does not strongly couple to $NN\pi$ state, we expect small c_0 and take $c_0 = 0.01$. On the other hand, NN operators easily couple to both ground and 1st elastic excited states as they become almost identical to each other in the infinite volume limit. We therefore take $b_1 = 0.01$ (the highly tuned operator), $b_1 = \pm 0.1$ (the tuned ones) as well as $b_1 = 0.5$ (the untuned one). **Figure 6** (Left) shows $\Delta E^{\rm eff}_{NN}(t)$ for these 4 examples with $c_0 = 0.01$, where random fluctuations and errors whose magnitude increase exponentially in t are assigned to $R^{\rm mockup}_{NN}(t)$. All examples show plateau-like behaviors at $t \simeq 1$ fm, but these four plateaux disagree with each other. As $|b_1|$ increases, the deviation between the values of these "pseudo plateaux" and the true value becomes larger. Contaminations of the elastic excited states can easily produce the plateau-like behavior at earlier t, and the t dependence of data alone cannot tell us which plateau is correct, or in other words, cannot tell which tuning is good.

Contaminations from inelastic states seem unimportant to produce the plateau-like behavior, as shown in **Figure 6** (Right), where the effective energy shift for $c_0 = 0.01, 0.05, 0.1$ with $b_1 = -0.1$ is plotted. All cases converge to almost the same pseudo plateau, while a pseudo plateau starts at later t for larger c_0. It is noted that the multi-exponential fit does not work in this case at $t \simeq 1.0$ fm, which is much smaller than the necessary $t \gg 1/\delta E_{\rm el.}$. The multi-exponential fit at such small t only separates the pseudo plateau from the inelastic contributions but is difficult to distinguish the ground state and the 1st excited state for the elastic states.

3.2. Normality Check in the Direct Method

While the check through operator dependence is useful, it requires extra calculations. We find that the finite volume formula in Equation (4) provides a simpler test, which tells us whether the ground state energies extracted by the plateau fitting give a reasonable ERE or not without extra calculations. We call this test a normality check [19]. **Figure 7** (Left) shows $k\cot\delta_0(k)/m_\pi$ in YIKU2012 [36] as a function of k^2/m_π^2 for $NN(^1S_0)$, where the solid red line represents the NLO ERE fit in Equation (5), and the light red bands shows statistical and

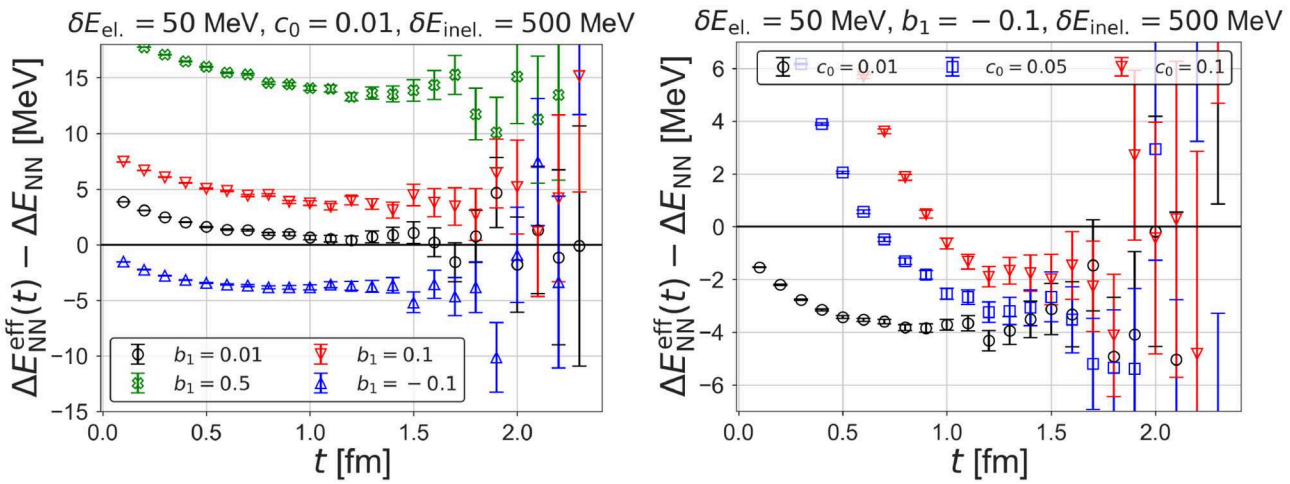


FIGURE 6 | $\Delta E^{\rm eff}_{NN}(t) - \Delta E_{NN}$ from the mockup data $R^{\rm mockup}_{NN}(t)$ with fluctuations and errors as a function of t. (Left) $b_1 = 0.01, \pm 0.1, 0.5$ and $c_0 = 0.01$. (Right) $c_0 = 0.01, 0.05, 0.1$ and $b_1 = -0.1$.

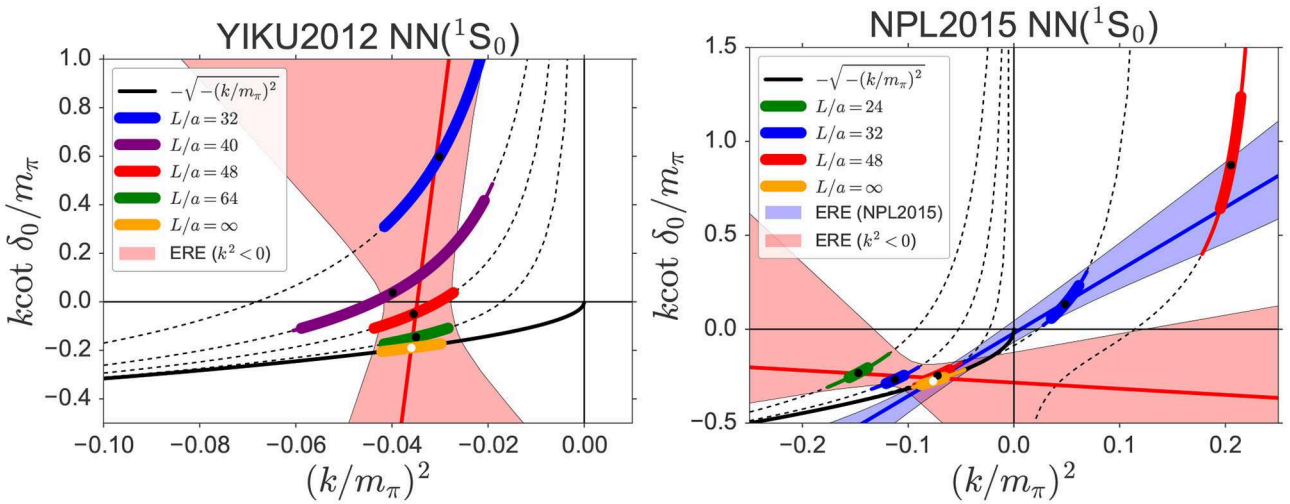


FIGURE 7 | (Left) $k\cot\delta_0(k)/m_\pi$ in YIKU2012 [36] for $NN(^1S_0)$ as a function of $(k/m_\pi)^2$. The solid red line and light red band represent the ERE fit and the corresponding error (statistical and systematic added in quadrature), respectively. The dashed lines are the finite volume formula for the corresponding volume. (Right) $k\cot\delta_0(k)/m_\pi$ in NPL2015 [37] for $NN(^1S_0)$ as a function of $(k/m_\pi)^2$. Two ERE fits are performed depending on the lattice data to be used for the fit. The red line with the band represents the fit made by the authors in Iritani et al. [19], while the blue line with the band is plotted by the authors in Iritani et al. [19] using the fit result of NPL2015. Both figures are taken from Iritani et al. [19].

systematic errors added in quadrature [19]. Contrary to a naive expectation from non-singular ERE behaviors, data align almost vertically, since ΔE_{NN} is almost independent of the volume. In other words, according to the finite volume formula, the claimed "binding energy" (open circle) is too shallow to have such volume independent ΔE. Not only the central value of the NLO ERE fit gives singular parameters as $((a_0 m_\pi)^{-1}, r_0 m_\pi) = (5.27, 303.6)$ but also it violates the physical pole condition, Equation (9), at the crossing point (open circle). The singular and unphysical behaviors, in addition to the operator dependence of these data, strongly indicate that the naive plateau fitting employed in the direct method is unreliable. Another example is shown in **Figure 7** (Right) for $NN(^1S_0)$ from NPL2015 [37]. In this case, two different NLO ERE fits (red line/band and blue line/band) are performed depending on the lattice data to be used for the fit. It turns out that two ERE are inconsistent with each other, indicating that their lattice data themselves are "self-inconsistent." In addition, one of ERE (blue line/band) is found to violate the physical pole condition, Equation (9), at the crossing point (open circle). Similar symptoms are observed for all other

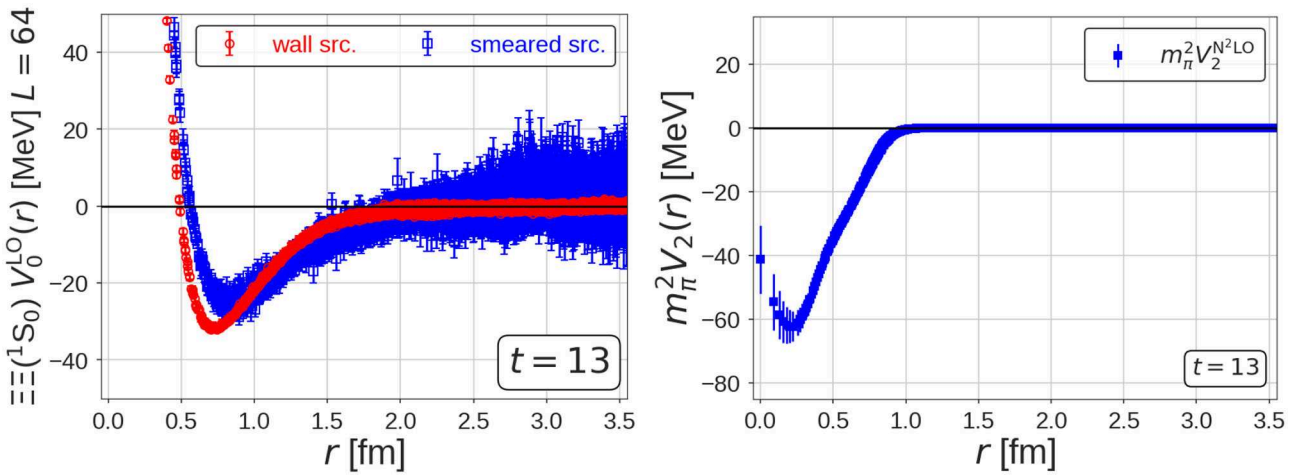


FIGURE 8 | (Left) The LO potential, $V_0^{LO}(r)$, for $\Xi\Xi(^1S_0)$ from the wall source (red open circles) and the smeared source (blue open square). (Right) The second order term, $V_2^{N^2LO}(r)$ (blue solid squares), in the N^{2}LO potential $V^{N^2LO}(r, \nabla) = V_0^{N^2LO}(r) + V_2^{N^2LO}(r)\nabla^2$ for $\Xi\Xi(^1S_0)$. Both are taken from Iritani et al. [47].

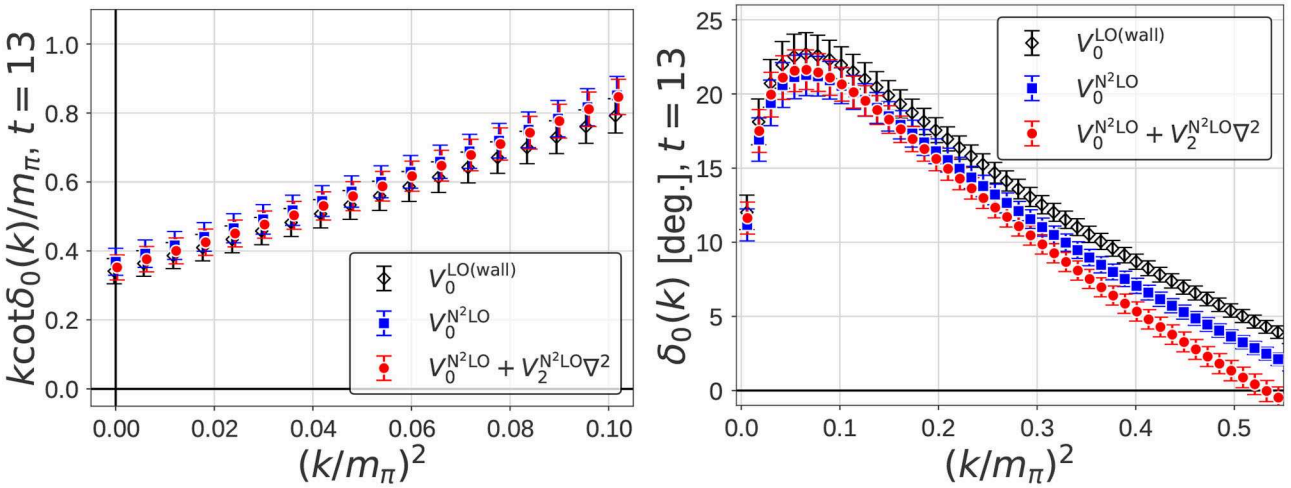


FIGURE 9 | (Left) $k\cot\delta_0(k)/m_\pi$ as a function of $(k/m_\pi)^2$ at low energies, where $\delta_0(k)$ is the scattering phase shift for $\Xi\Xi(^1S_0)$, calculated from $V^{N^2LO}(r, \nabla)$ (red solid circles), $V_0^{N^2LO}(r)$ (blue solid squares) and $V_0^{LO(wall)}(r)$ (black open diamond). (Right) The corresponding $\delta_0(k)$. Both are taken from Iritani et al. [47].

data in the direct method claiming the existence of *NN* bound states at heavy quark masses [19][3].

3.3. The Source Dependence and the Derivative Expansion in the HAL QCD Method

The source operator dependence of the HAL QCD potential has been investigated in Iritani et al. [47]. **Figure 8** (Left) compares the LO potentials, $V_0^{LO}(r)$, for $\Xi\Xi(^1S_0)$ between the wall source (red open circles) and the smeared source (blue open squares). We observe a small difference at short distances, from which one can determine the N^{2}LO potential, $V^{N^2LO}(\mathbf{r}, \nabla) = V_0^{N^2LO}(r) + V_2^{N^2LO}(r)\nabla^2$. Note that the NLO term, $V_1^{N^2LO}(r)\nabla = V_{LS}^{N^2LO}(r)\mathbf{L}\cdot\mathbf{S}$ is absent in the $^1S_0$ channel. **Figure 8** (Right) shows $V_2^{N^2LO}(r)$, which is non-zero only at $r < 1.0$ fm, where two LO potentials differ. We then extract the scattering phase shifts, using this N^{2}LO potential.

The N^{2}LO corrections turn out to be negligible at low energies, as shown in **Figure 9** (Left), where $k\cot\delta_0(k)$ is almost identical between $V^{N^2LO}(\mathbf{r}, \nabla)$ (red solid circles) and $V_0^{N^2LO}(r)$ (blue solid squares). Furthermore, even the LO analysis for the wall source, $V_0^{LO(wall)}(r)$ (black open diamond), is sufficiently good at low energies. As energy increases, the N^{2}LO corrections become visible as seen in **Figure 9** (Right), where $(k/m_\pi)^2 = 0.5$ corresponds to $\Delta E \simeq 90$ MeV for the energy shift from the threshold. It is noted that $V_0^{N^2LO}(r)$ (blue solid squares) gives a little closer results to N^{2}LO results (red solid circles) than $V_0^{LO(wall)}(r)$ (black open diamond) does.

[3]After these problems were pointed out in Iritani et al. [19], revised data of NPL2013 have been presented in Wagman et al. [41], whose EREs are still marginal to satisfy/violate the physical pole condition.

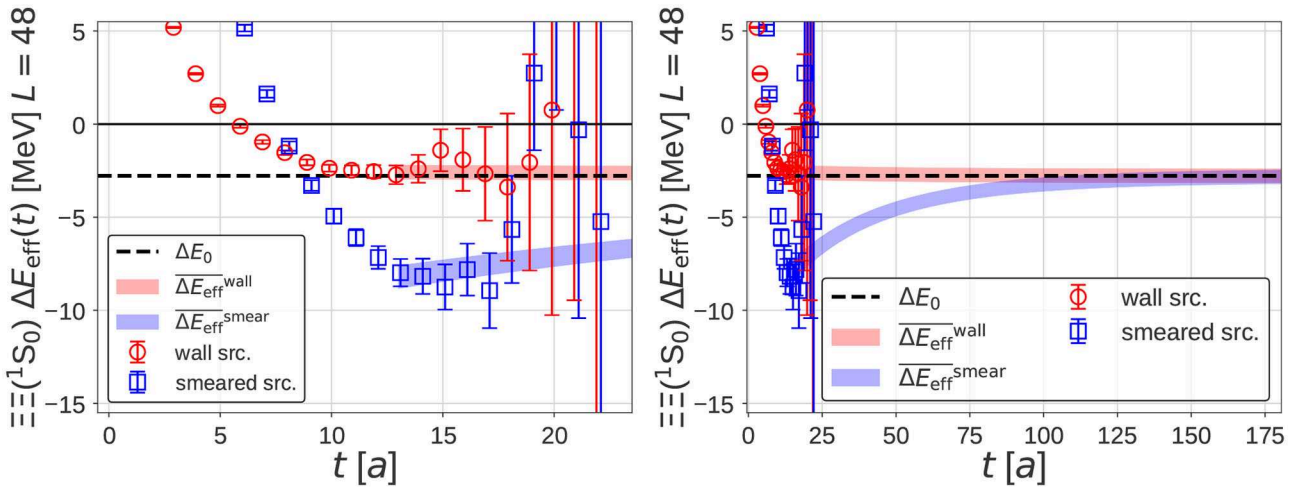


FIGURE 10 | The reconstructed effective energy shift $\overline{\Delta E}^J_{\rm eff}(t, t_0 = 13a)$ for the wall source (red bands) and the smeared source (blue bands) on $L = 48a$, while the effective energy shifts directly from $R^J_{\Xi\Xi}(t)$ are shown for $J =$ wall (red open circles) and $J =$ smear (blue open squares). The black dashed lines are the energy shifts for the ground state of H in the finite box. (Left) $0 \le t/a \le 24$. (Right) $0 \le t/a \le 175$. Taken from Iritani et al. [48].

3.4. Understanding Pseudo Plateaux

In this subsection, we explain why the wall source and the smeared source give inconsistent plateau behaviors, in the case of $\Xi\Xi$ correlation functions as an example.

To this end, we consider the Hamiltonian $H = H_0 + V_0^{\rm LO(wall)}$, where we employ $V_0^{\rm LO(wall)}(r)$, the LO potential from the wall source, since it works rather well at low energies as shown in the previous subsection. We first decompose $R^J_{\Xi\Xi}(\mathbf{r}, t)$ for $J =$ wall/smear in terms of finite volume eigenfunctions of H as

$$R^J_{\Xi\Xi}(\mathbf{r}, t) = \sum_n a^J_n(t)\Psi_n(\mathbf{r})e^{-\Delta E_n t},$$
$$a^J_n(t) = \sum_{\mathbf{r}} \Psi^\dagger_n(\mathbf{r})R^J_{\Xi\Xi}(\mathbf{r}, t)e^{\Delta E_n t}. \quad (35)$$

where $\Psi_n(\mathbf{r})$ and ΔE_n are normalized-eigenfunction and eigenenergy in the finite volume, respectively, and $a^J_n(t)$ is the overlapping coefficient extracted at t.

Then the correlation function for the source J in the direct method is given by

$$R^J_{\Xi\Xi}(t) = \sum_{\mathbf{r}} R^J_{\Xi\Xi}(\mathbf{r}, t) = \sum_n b^J_n(t)e^{-\Delta E_n t}$$
$$b^J_n(t) = a^J_n(t)\sum_{\mathbf{r}} \Psi_n(\mathbf{r}). \quad (36)$$

Finally, approximating a sum over n by the lowest few orders, we reconstruct the behavior of the effective energy shift as a function of t as

$$\overline{\Delta E}^J_{\rm eff}(t, t_0) = \frac{1}{a}\log\left(\frac{R^J(t, t_0)}{R^J(t + a, t_0)}\right),$$
$$R^J(t, t_0) = \sum_{n=0}^{n_{\rm max}} b^J_n(t_0)e^{-\Delta E_n t}, \quad (37)$$

where we fix the overlapping coefficient $b^J_n(t_0)$ at $t = t_0$, and $n_{\rm max}$ is a number of excited states used in the approximation.

In **Figure 10**, we show reconstructed effective energy shift $\overline{\Delta E}^J_{\rm eff}(t, t_0 = 13a)$ on $L = 48a$ with $n_{\rm max} = 4$, together with the effective energy shifts from $R^J_{\Xi\Xi}(t)$, for the wall source (red bands and red open circles) and the smeared source (blue bands and blue open squares). The black dashed line represents the energy shift for the ground state of $H = H_0 + V_0^{\rm LO(wall)}$ on $L = 48a$.

We find that the plateau-like structures in the direct method around $t/a = 15$ are well-reproduced by $\overline{\Delta E}^J_{\rm eff}(t, t_0 = 13a)$ for both sources in **Figure 10** (Left). This indicates that the plateau-like structures in the direct method at this time interval are explained by the contributions from several low-lying states.

These plateau-like structures of course do not necessarily correspond to the true energy shift of the ground state. The fate of these structures is shown in **Figure 10** (Right), where we plot $\overline{\Delta E}^J_{\rm eff}(t, t_0 = 13a)$ at asymptotically large t. While the plateau-like structure for the wall source is almost unchanged, $\overline{\Delta E}^J_{\rm eff}(t, t_0 = 13a)$ for the smeared source gradually increases and reaches to the true value at $t/a \sim 100$.

The above results clearly reveal that the plateau-like structures at $t/a \sim 15$ for the smeared source are pseudo-plateaux caused by the contaminations of the excited states. Large contaminations from excited states in the case of the smeared source are not caused by the smearing, but are indeed implied by putting two baryon operators on the same space-time point as

$$\frac{1}{L^3}\sum_{\mathbf{x}} B(\mathbf{x}, t)B(\mathbf{x}, t) = \sum_{\mathbf{p}} \tilde{B}(\mathbf{p}, t)\tilde{B}(-\mathbf{p}, t),$$

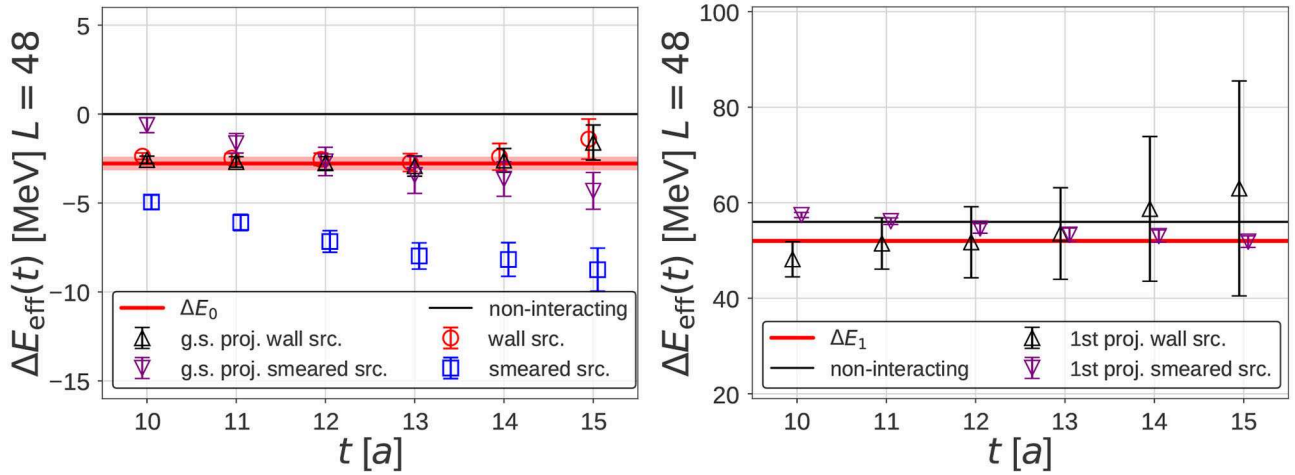


FIGURE 11 | The effective energy shift $\Delta E^{J,n}_{\rm eff}(t)$ from $R^{J,n}_{\Xi\Xi}(t)$, the correlation function projected to the n-th eigenstate at the sink on $L = 48a$, for $J =$ wall (black open up-triangles) and $J =$ smear (purple open down-triangle). Red bands represent the energy shifts from the eigenvalues of H in the finite box, while black lines denote those of a free Hamiltonian H_0. (Left) The projection to the ground state ($n = 0$), together with the effective energy shift in the direct method without projection for the wall source (red open circles) and the smeared source (blue open squares). (Right) The projection to the 1st excited state ($n = 1$). Taken from Iritani et al. [48].

$$\tilde{B}(\mathbf{p}, t) \equiv \sum_{\mathbf{x}} B(\mathbf{x}, t) e^{-i\mathbf{p}\cdot\mathbf{x}}, \tag{38}$$

where the above source operator couples to all momentum modes with almost equal weight. Since almost all previous studies on NN interactions in the direct method employed this type of the source operator, their conclusions on the existences of both deuteron and di-neutron are not valid due to large contaminations[4].

3.5. Consistency Between the Two Methods

Once eigenmodes of H in the finite box are obtained, we can construct an improved sink operator for a particular eigenstate, whose correlation function with the J source is given by

$$R^{J,n}_{BB}(t) = \sum_{\mathbf{r}} \Psi^{\dagger}_n(\mathbf{r}) R^{J}_{BB}(\mathbf{r}, t). \tag{39}$$

Figure 11 shows the effective energy shift $\Delta E^{J,n}_{\rm eff}(t)$ calculated from $R^{J,n}_{\Xi\Xi}(t)$ on $L = 48a$ with $J =$ wall (black open up-triangles) and $J =$ smear (purple open down-triangle), for the ground state (Left) and the 1st excited state (Right), together with ΔE_0 or ΔE_1, eigenvalues of H in the finite box (red bands) as well as those of H_0 (black lines). For the ground state in **Figure 11** (Left), the effective energy shift in the direct method without projection are also plotted for the wall source (red open circles) and the smeared source (blue open squares).

After the sink projection, the effective energy shifts agree well between wall and smeared sources around $t/a \sim 13$, not only for the ground state but also for the 1st excited state. while the effective energy shifts for the ground state in the direct method without projection disagree between two sources. In particular, an agreement between two sources with sink projection for the 1st excited state is rather remarkable, since variational methods, usually mandatory for excited states in lattice QCD, are not used here. Furthermore, the plateaux of the effective energy shifts after the sink projection also agree with $\Delta E_{0,1}$ of H (red bands). Note that the effective energy shift for the 1st excited state, $\Delta E^{\rm wall,1}_{\rm eff}(t)$, has larger errors since the contribution of the 1st excited state in $R^{\rm wall}_{\Xi\Xi}(t)$ is much smaller.

Although the sink operator projection utilizes the information of the HAL QCD potential to construct eigenfunctions, agreements in the effective energy shifts for the ground state as well as the 1st excited state provide a non-trivial consistency check between the HAL QCD method and the Lüscher's finite volume formula (with proper projections to extract the finite volume spectra). We thus conclude from **Figure 11** not only that the HAL QCD potential correctly describes the energy shifts of two baryons in the finite box for both ground and excited states but also that these energy shifts can be extracted even for baryon-baryon systems if and only if the sink/source operators are highly improved. We emphasize that improvement of operators has to be performed not by the tuning of the plateau-like structures but by a sophisticated method, such as the variational method [10][5] (or a method presented here). See Francis et al. [43] for a recent study toward such a direction.

4. NUCLEAR POTENTIAL

In this section, we summarize results on nuclear potentials in the HAL QCD method.

[4]Note that Mainz2018 employed a source operator as $\tilde{B}(\mathbf{p} = \mathbf{0}, t)\tilde{B}(-\mathbf{p} = \mathbf{0}, t)$ and they reported that "In the 27-plet (dineutron) sector, the finite volume analysis suggests that the existence of a bound state is unlikely."

[5]In lattice QCD studies for the meson-meson scatterings [9], serious systematics from the excited state contaminations in the simple plateau fitting have been widely recognized and the variational method has been utilized to obtain the finite volume spectra rather reliably, which can be combined with the Lüscher's finite volume formula to extract phase shifts.

4.1. Parity-Even Channel With LO Analysis at Heavy Pion Masses

We first show the results of nuclear forces in the parity-even channel ($^1S_0$ and $^3S_1$-$^3D_1$ channels) at heavy quark masses obtained by the LO analysis for the derivative expansion of the potential. Since the statistical fluctuations are smaller at heavier quark masses in lattice QCD, this study is a good starting point to grasp the nature of lattice QCD nuclear forces. In addition, quark mass dependence of nuclear forces is of fundamental importance from a point of view of, e.g., anthropic principle, which cannot be studied by experiments.

In the case of $^1S_0$ channel, we obtain the LO central force following Equation (31). In the case of $^3S_1$-$^3D_1$ channel, the LO potentials consist of the central and tensor forces, which can be obtained from the coupled channel analysis between the *S*- and *D*-wave components as

$$\left\{-H_0 - \frac{\partial}{\partial t} + \frac{1}{4m_N}\frac{\partial^2}{\partial t^2}\right\} R^J(\mathbf{r},t) = \left[V_C(r) + V_T(r)S_{12} + \cdots\right] R^J(\mathbf{r},t), \quad (40)$$

where ellipses represent higher order terms in the derivative expansion. Using the projection to the A_1^+ representation of the cubic group (*S*-wave projection), $\mathcal{P}^{A_1^+}$, and the orthogonal one (*D* wave projection), $(1-\mathcal{P}^{A_1^+})$, the above equation reduces to two independent equations, from which $V_C(r)$ and $V_T(r)$ can be obtained [23]. Since the A_1^+ representation couples to the angular momentum $l = 0, 4, 6, \cdots$, these projections are expected to serve as the relevant partial wave decomposition at low energies. We find that the NBS correlation functions after $\mathcal{P}^{A_1^+}$ and $(1-\mathcal{P}^{A_1^+})$ are dominated by *S*-wave and *D*-wave components, respectively, indicating that the contaminations from $l \geq 4$ components are indeed small. For a more advanced partial wave decomposition, see Miyamoto et al. [49].

We perform the calculations in quenched [23, 26], dynamical 2-flavor [50], dynamical 3-flavor [44, 51, 52], and dynamical (2+1)-flavor [34, 45, 47, 53] lattice QCD with various quark masses. We here present the results obtained in 3-flavor lattice QCD at $(M_{\rm ps}, M_{\rm oct})$=(1171, 2274), (1015, 2031), (837, 1749), (672, 1484), (469, 1161) MeV [44, 51, 52][6]. In the case of $(M_{\rm ps}, M_{\rm oct}) = (837, 1749)$, the value of quark masses $m_u = m_d = m_s$ nearly correspond to the physical strange quark mass. We generate gauge configurations with the RG-improved Iwasaki gauge action and non-perturbatively $\mathcal{O}(a)$-improved Wilson quark action on a $L^3 \times T = 32^3 \times 32$ lattice. The lattice spacing is $a = 0.121(2)$ fm and hence lattice size L is 3.87 fm. In the calculation of the NBS correlation function, parity-even states are created by a two-baryon operator with a wall quark source, while a point operator is employed for each baryon at the sink.

Shown in **Figure 12** (Upper) are the lattice QCD results for the potentials. We find that the results are insensitive to the Euclidean time t, at which the NBS correlation function is evaluated, indicating that the derivative expansion is well-converged. The obtained potentials are found to reproduce the qualitative features of the phenomenological *NN* potentials, namely, attractive wells at long and medium distances, central repulsive cores at short distance and strong tensor force with a negative sign. We also find intriguing features in the quark mass dependence of the potentials. At long distances, it is observed that the ranges of the tail structures in the central and tensor forces become longer at lighter quark masses. Such a behavior can be understood from the viewpoint of one-boson-exchange potential. At short distances, the repulsive cores in the central forces are found to be enhanced at lighter quark masses. This could be explained by the short-range repulsion due to the one-gluon-exchange in the quark model, whose strength is proportional to the inverse of the (constituent) quark mass. In fact, our systematic studies including hyperon forces with the same lattice setup revealed that the nature of repulsive core is well-described by the quark Pauli blocking effect together with the one-gluon-exchange effect [44, 51, 54].

As noted before, the potentials themselves are not physical observables and quantitative lattice QCD predictions shall be given in terms of scattering observables. Shown in **Figure 12** (Lower) are the scattering phase shifts (and mixing angles) obtained from lattice nuclear forces. We find that *NN* systems do not bound at these pseudoscalar masses as discussed in section 3. Behaviors of phase shifts are qualitatively similar to the experimental ones, while the strength of the attraction is weaker due to the heavy quark masses in this calculation. It is also observed that quark mass dependence of phase shifts is quite non-trivial. In fact, if we decrease the quark masses, there appear competing effects in the interaction: the long-range attraction becomes stronger and the short-range repulsive core also becomes stronger. We also note that lighter quark masses correspond to lighter nucleon mass, which leads to larger kinetic energies.

We also present the results obtained in (2+1)-flavor lattice QCD at quark masses corresponding to $(m_\pi, m_N) \simeq$(701, 1584), (570, 1412), and (411, 1215) MeV [45]. Note that only up and down quark masses are varied with a strange quark mass being fixed to the physical value in this study. We employ the gauge configurations generated by the PACS-CS Collaboration with the RG-improved Iwasaki gauge action and non-perturbatively $\mathcal{O}(a)$-improved Wilson quark action on a $L^3 \times T = 32^3 \times 64$ lattice. The lattice spacing is $a \simeq 0.091$ fm ($a^{-1} = 2.16(31)$GeV), which leads to the spatial extension $L \simeq 2.9$ fm.

In **Figure 13**, we show the lattice QCD results for the potentials in the $^1S_0$ and $^3S_1$-$^3D_1$ channels, together with the corresponding phase shifts in the $^1S_0$ channel. Qualitative features are similar to those in 3-flavor case: (i) the central forces have repulsive cores at short distance and attractive wells at long and medium distances, both of which are enhanced at lighter quark masses (ii) the tensor force is strong with a negative sign, which increases at lighter quark masses.

4.2. More Structures: Spin-Orbit Forces in the Parity-Odd Channel and Three Nucleon Forces

If we consider an interaction at higher order terms in the derivative expansion, there appear more structures in the

[6] $M_{\rm ps} = m_\pi = m_K$ and $M_{\rm oct} = m_N = m_\Lambda = m_\Sigma = m_\Xi$ in 3-flavor QCD.

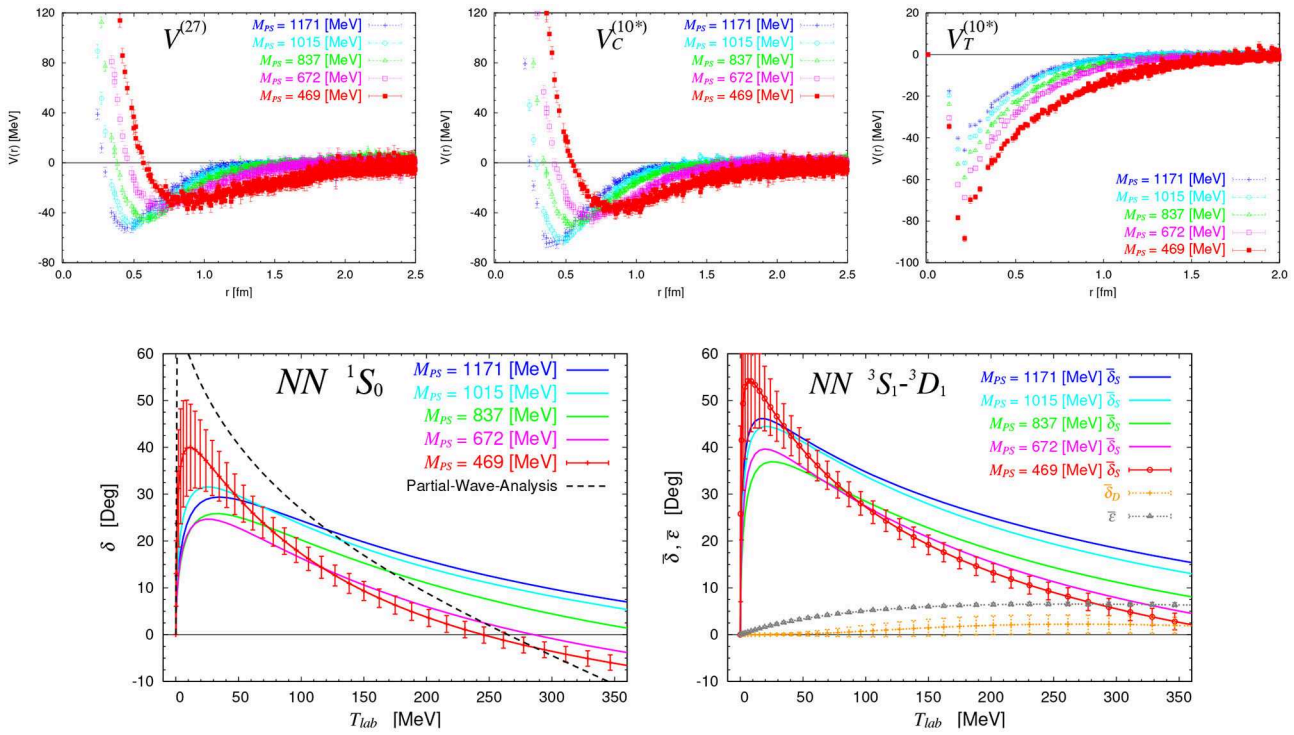


FIGURE 12 | (Upper) Nuclear forces obtained from 3-flavor lattice QCD at $M_{\rm ps} = 469$–1171 MeV. (Left) Central force in the $^1S_0$ channel (27-plet in SU(3)$_f$ representation). (Middle) Central force in the $^3S_1$-$^3D_1$ channel (10*-plet in SU(3)$_f$ representation). (Right) Tensor force in the $^3S_1$-$^3D_1$ channel. (Lower) *NN* scattering phase shifts as a function of energy in the laboratory frame (colored solid lines), obtained from 3-flavor lattice QCD at $M_{\rm ps} = 469$-1171 MeV, together with those from experiments (black dashed lines). (Left) Results in the $^1S_0$ channel. (Right) Results in the $^3S_1$-$^3D_1$ channel (with Stapp's convention). Figures are taken from Inoue et al. [44].

potentials. In particular, the extension from LO analysis to NLO analysis enables us to determine the spin-orbit (LS) force. The LS force is known to play an important role in the LS-splittings of nuclear spectra and the nuclear magic numbers. In addition, the LS force in the $^3P_2$-$^3F_2$ channel attracts great interest in nuclear astrophysics, since it could lead to the *P*-wave superfluidity in the neutron stars and affect the cooling process of neutron stars.

We here present the calculation in parity-odd channels ($^1P_1$, $^3P_0$, $^3P_1$, $^3P_2$-$^3F_2$ channels) at heavy quark masses and show the results of LS forces as well as central/tensor forces [50]. In order to construct the source operator which couples to parity-odd states, we employ the two nucleon operators as

$$\mathcal{J}_{\alpha\beta}(f_i) \equiv N_\alpha(f^{(i)})N_\beta(f^{(i)*}) \quad \text{for } i = \pm1, \pm2, \pm3 \qquad (41)$$

where N denotes a nucleon operator with a momentum,

$$N_\alpha(f^{(i)}) = \sum_{\vec{x}_1,\vec{x}_2,\vec{x}_3} \epsilon_{abc} \left(u_a^T(\vec{x}_1)C\gamma_5 d_b(\vec{x}_2)\right) q_{c,\alpha}(\vec{x}_3) f^{(i)}(\vec{x}_3) \quad (42)$$

with $f^{(\pm j)}(\vec{x}) \equiv \exp\left(\pm 2\pi i x_j/L\right)$. A cubic group analysis shows that this source operator contains the orbital contribution $T_1^- \oplus A_1^+ \oplus E^+$, whose dominant components have $l = 1, 0, 2$, respectively, and thus covers all the two-nucleon channels with $J \leq 2$. Combined with the spin degrees of freedom, we consider the T_1^- representation in the spin singlet channel and the A_1^-, T_1^-, $(E^- \oplus T_2^-)$ representations in the spin triplet channel. At low energies, these representations correspond to the $^1P_1$ channel and the $^3P_0$, $^3P_1$, and $^3P_2$-$^3F_2$ channels, respectively, from which we extract the central force in the spin singlet channel ($V^{I=0}_{C,S=0}(r)$), and the central, tensor and LS forces ($V^{I=1}_{C,S=1}(r)$, $V^{I=1}_{T}(r)$, $V^{I=1}_{LS}(r)$) in the spin triplet channel.

Calculations are performed in 2-flavor lattice QCD at quark masses corresponding to $(m_\pi, m_N) \simeq (1133, 2158)$ MeV [50]. We employ the gauge configurations generated by the CP-PACS Collaboration with the RG-improved Iwasaki gauge action and a mean field $\mathcal{O}(a)$-improved Wilson quark action on a $16^3 \times 32$ lattice. The lattice spacing $a = 0.156(2)$ fm leads to the spatial extension $L \simeq 2.5$ fm.

Shown in **Figure 14** (Upper-Left) are the lattice QCD results for the potential, $V^{I=0}_{C,S=0}(r)$, $V^{I=1}_{C,S=1}(r)$, $V^{I=1}_{T}(r)$, $V^{I=1}_{LS}(r)$. We find that (i) the central forces $V^{I=0}_{C,S=0}(r)$ and $V^{I=1}_{C;S=1}(r)$ are repulsive, (ii) the tensor force $V^{I=1}_{\rm T}(r)$ is positive and weak compared to $V^{I=1}_{\rm C;S=1}(r)$ and $V^{I=1}_{\rm LS}(r)$, and (iii) the LS force $V^{I=1}_{\rm LS}(r)$ is negative and strong. These features are qualitatively in line well with those of the phenomenological potential. One can also see these properties in terms of the potential in each channel. In **Figure 14** (Upper-Right), we plot the potentials in the $^1P_1$, $^3P_0$, $^3P_1$ and $^3P_2$ channels, which are defined by $V(r;\ ^1P_1) = V^{I=0}_{C,S=0}(r)$,

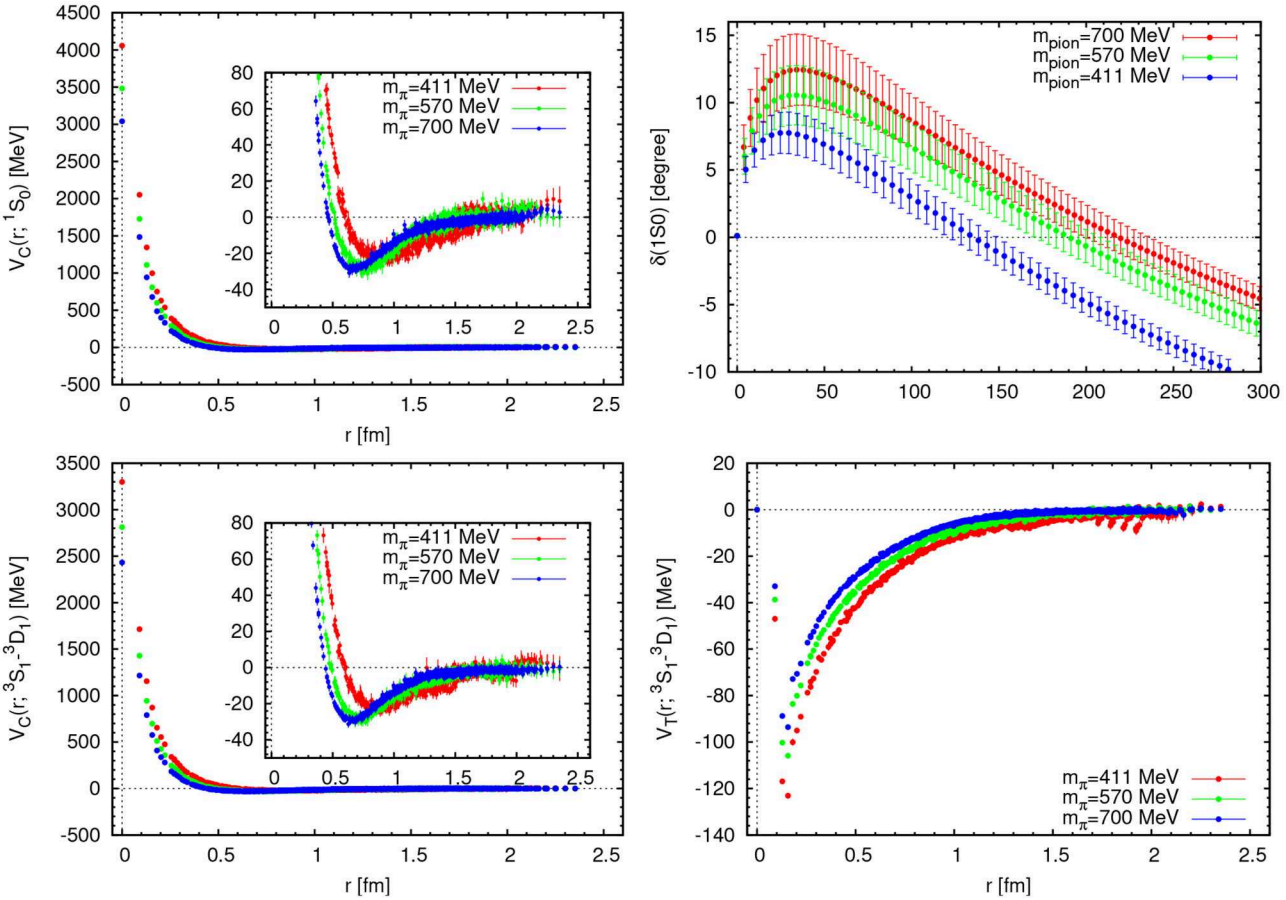


FIGURE 13 | Nuclear forces obtained from (2+1)-flavor lattice QCD at $m_\pi \simeq 411$ (red), 570 (green), 701 (blue) MeV: (Upper-Left) Central forces in the $^1S_0$ channel (Lower) Central forces (left) and tensor forces (right) in the $^3S_1$-$^3D_1$ channel. (Upper-Right) The scattering phase shifts in the $^1S_0$ channel at $m_\pi \simeq 411$ (blue), 570 (green), 701 (red) MeV. Figures are taken from Ishii [45].

$V(r;\ ^3P_0) = V^{I=1}_{\mathrm{C},S=1}(r) - 4V^{I=1}_{\mathrm{T}}(r) - 2V^{I=1}_{\mathrm{LS}}(r)$, $V(r;\ ^3P_1) = V^{I=1}_{\mathrm{C},S=1}(r) + 2V^{I=1}_{\mathrm{T}}(r) - V^{I=1}_{\mathrm{LS}}(r)$, $V(r;\ ^3P_2) = V^{I=1}_{\mathrm{C},S=1}(r) - \frac{2}{5}V^{I=1}_{\mathrm{T}}(r) + V^{I=1}_{\mathrm{LS}}(r)$.

To obtain the scattering observables, we fit the potentials and solve the Schrödinger equation in the infinite volume. In **Figure 14** (Lower), we show the results for the scattering phase shifts. Compared with the experimental phase shifts, we find that behaviors of phase shifts are generally well-reproduced, while the magnitudes are smaller due to the heavier pion mass in lattice QCD calculations. In the $^3P_0$ channel, we observe that the attraction is missing compared with the experimental one, which however is also likely due to the weak tensor force V_{T} caused by the heavier pion mass. Among others, the most interesting feature is the attraction in the $^3P_2$ channel as shown in **Figure 14** (Lower-Right), originated from the strong (and negative) LS forces. As noted before, it is this interaction which is relevant to the paring correlation of the neutrons and possible P-wave superfluidity in the neutron stars.

We now turn to the study of three-nucleon forces. Determination of three-nucleon forces is one of the most challenging problems in nuclear physics: Three-nucleon forces are known to play important role in nuclear spectra/structures, such as the binding energies of (light) nuclei and properties of neutron-rich nuclei. They are also essential ingredients to understand properties of nuclear matters, such as the equation of state (EoS) at high density, which is relevant to the structures of neutron stars and nucleosynthesis at the binary neutron star mergers. While there have been many studies to construct three-nucleon forces by phenomenological approaches [55, 56] or by chiral EFT approaches [6–8, 57], it is most desirable to carry out the direct determination from QCD.

To study three-nucleon forces in lattice QCD, we consider the NBS wave function for a $n(\geq 3)$-particle system, $|\alpha\rangle$,

$$\Psi^n_\alpha([\boldsymbol{x}])e^{-W_\alpha t} = \langle 0|N(\boldsymbol{x}_1,t)N(\boldsymbol{x}_2,t)\cdots N(\boldsymbol{x}_n,t)|\alpha\rangle,$$
$$[\boldsymbol{x}] = \boldsymbol{x}_1,\boldsymbol{x}_2,\cdots,\boldsymbol{x}_n \tag{43}$$

where W_α is the center of mass energy of the system and we ignore the spins of nucleon for simplicity. In Aoki et al. [58, 59] and Gongyo and Aoki [60], we show that the asymptotic behavior

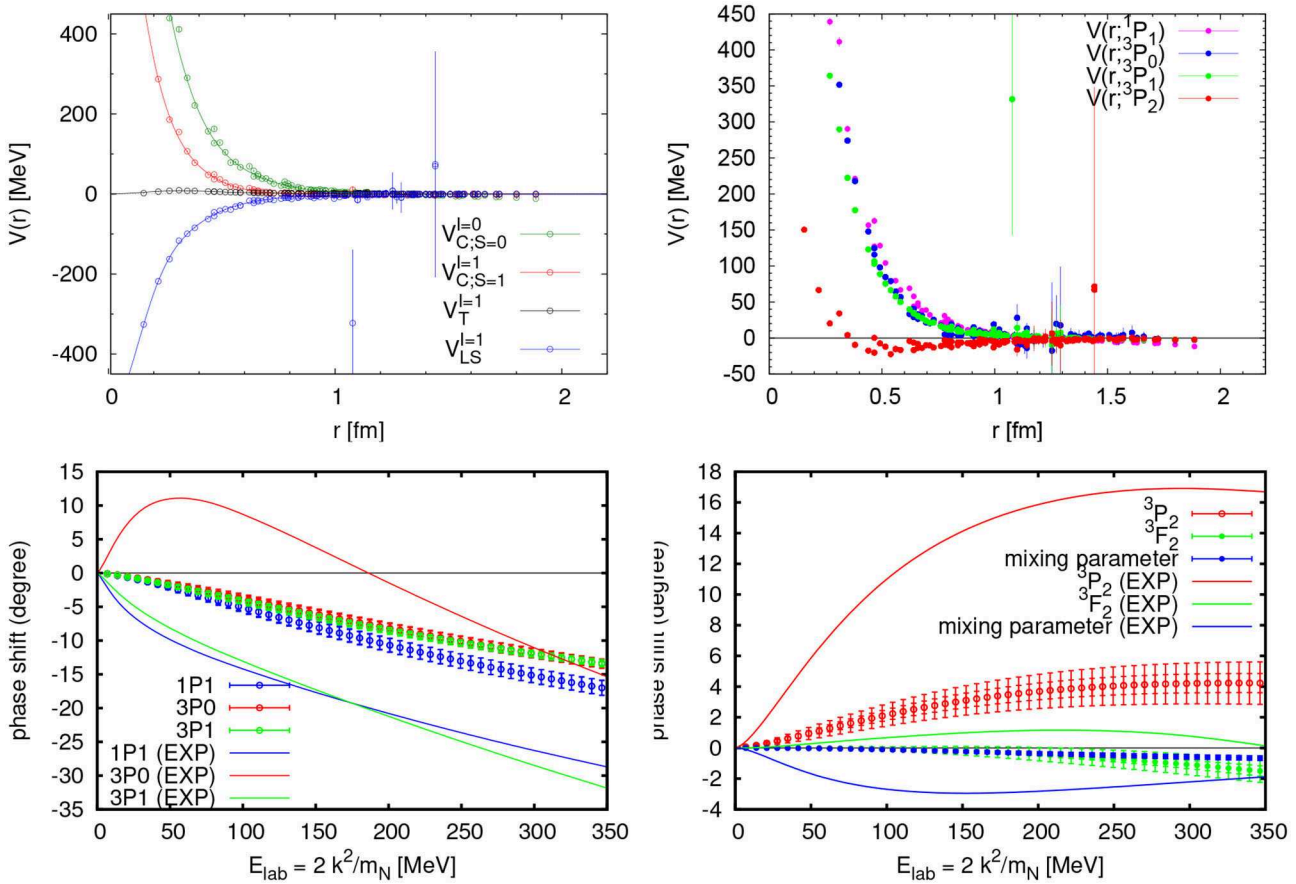


FIGURE 14 | (Upper-Left) Central ($S = 0$ and 1), tensor and spin-orbit potentials in parity-odd channels obtained by 2-flavor lattice QCD at $m_\pi \simeq 1133$ MeV. (Upper-Right) The potentials for the $^1P_1$, $^3P_0$, $^3P_1$, and $^3P_2$ channels. (Lower-Left) Phase shifts in the $^1P_1$, $^3P_0$, and $^3P_1$ channels, together with the experimental ones for comparisons. (Lower-Right) Phase shifts and mixing parameter (with Stapp's convention) in the $^3P_2$–$^3F_2$ channel, together with the experimental ones. Figures are taken from Murano et al. [50].

of the NBS wave function with the non-relativistic approximation can be written as

$$\Psi^n_{[L],[K]}(R,Q) \propto \sum_{[N]} U_{[L][N]}(Q) e^{i\delta_{[N]}(Q)} \frac{\sin\left(QR - \Delta_L + \delta_{[N]}(Q)\right)}{(QR)^{\frac{D-1}{2}}} U^\dagger_{[N][K]}(Q) \tag{44}$$

where $D = 3(n-1)$ is the dimension of a n-particle system, $\Delta_L = (2L + D - 3)\pi/4$, $\Psi^n_{[L],[K]}(R,Q)$ is the radial component of the NBS wave function in D-dimension with R and Q being the hyper radius and momentum, respectively, and $[L],[K]$ denotes the quantum numbers of the angular momentum in D-dimension. $\delta_{[N]}(Q)$ is the generalized "phase shift" for a n-particle system and $U_{[L][N]}(Q)$ is a unitary matrix, which parameterize the T-matrix as

$$T_{[L][K]}(Q,Q) = \sum_{[N]} U_{[L][N]}(Q) T_{[N]}(Q) U^\dagger_{[N][K]}(Q), \tag{45}$$

$$T_{[N]}(Q) = -\frac{2n^{3/2}}{m_N Q^{3n-5}} e^{i\delta_{[N]}(Q)} \sin\delta_{[N]}(Q). \tag{46}$$

Therefore, as in the case of $n = 2$ system (see section 2.2.1), the information of T-matrix is encoded in the asymptotic behavior of the NBS wave function. Based on this property, we can define the energy-independent non-local potential for a n-particle system, which can be extracted from the (time-dependent) HAL QCD method.

We calculate the six-point correlation function divided by two-point correlation function cubed,

$$R_{3N}(\vec{r},\vec{\rho},t-t_0) \equiv G_{3N}(\vec{r},\vec{\rho},t-t_0)/\{G_N(t-t_0)\}^3 \tag{47}$$

$$G_{3N}(\vec{r},\vec{\rho},t-t_0) \equiv \frac{1}{L^3}\sum_{\vec{R}} \langle 0|(N(\vec{x}_1)N(\vec{x}_2)N(\vec{x}_3))(t)\,\overline{(N'N'N')}(t_0)|0\rangle \tag{48}$$

where $\vec{R} \equiv (\vec{x}_1 + \vec{x}_2 + \vec{x}_3)/3$, $\vec{r} \equiv \vec{x}_1 - \vec{x}_2$, $\vec{\rho} \equiv \vec{x}_3 - (\vec{x}_1 + \vec{x}_2)/2$ are the Jacobi coordinates. In the time-dependent HAL QCD method at the LO analysis for the derivative expansion and with the non-relativistic approximation, we can extract the three-nucleon forces $V_{3NF}(\vec{r},\vec{\rho})$ through the following

Schrödinger equation,

$$\left[-\frac{1}{2\mu_r}\nabla_r^2 - \frac{1}{2\mu_\rho}\nabla_\rho^2 + \sum_{i<j} V_{2N}(\vec{r}_{ij}) + V_{3NF}(\vec{r},\vec{\rho})\right] R_{3N}(\vec{r},\vec{\rho},t) = -\frac{\partial}{\partial t} R_{3N}(\vec{r},\vec{\rho},t), \quad (49)$$

where $V_{2N}(\vec{r}_{ij})$ with $\vec{r}_{ij} \equiv \vec{x}_i - \vec{x}_j$ denotes two-nucleon forces between (i,j)-pair, $\mu_r = m_N/2$, $\mu_\rho = 2m_N/3$ the reduced masses.

In our first study of three-nucleon forces, we consider the total 3N quantum numbers of $(I, J^P) = (1/2, 1/2^+)$, the triton channel. We also consider a particular spacial geometry of the 3N, i.e., the "linear setup" ($\vec{\rho} = \vec{0}$), where 3N are aligned linearly with equal spacing of $r_2 \equiv |\vec{r}|/2$. This setup makes the analysis much simpler. In addition, we consider the following channel, $\psi_S \equiv \frac{1}{\sqrt{6}}\Big[-p_\uparrow n_\uparrow n_\downarrow + p_\uparrow n_\downarrow n_\uparrow - n_\uparrow n_\downarrow p_\uparrow + n_\downarrow n_\uparrow p_\uparrow + n_\uparrow p_\uparrow n_\downarrow - n_\downarrow p_\uparrow n_\uparrow\Big]$, and calculate the corresponding matrix element of V_{3NF}, so that we can suppress the statistical fluctuations in subtracting the contribution from V_{2N}.

One of the biggest challenges in the lattice QCD study of three-nucleon forces is the enormous computational cost required for the calculation of correlation functions. In fact, in terms of a mass number A, the cost grows with the multiplication of two factors, one of which scales factorially in A due to the Wick contraction (permutation of quarks), and the other of which scales exponentially in A due to the color/spinor contractions. On this point, we have developed a novel computational algorithm, called the unified contraction algorithm (UCA), in which two contractions are unified and redundant calculations are eliminated systematically [61]. In particular, the computation becomes faster by a factor of 192 for a calculation of three-nucleon forces.

We perform the calculation in 2-flavor lattice QCD at $(m_\pi, m_N) = (0.76, 1.81), (0.93, 1.85), (1.13, 2.15)$ GeV [62]. We employ the gauge configurations generated by CP-PACS Collaboration with mean field $\mathcal{O}(a)$-improved Wilson fermion and RG-improved Iwasaki gauge action on a $L^3 \times T = 16^3 \times 32$ lattice. The lattice spacing is $a = 0.1555(17)$ fm and thus $L = 2.5$ fm. Shown in **Figure 15** (Left) are the lattice QCD results for the three-nucleon forces. We find a repulsive interaction at short-distances, $r_2 \simeq 0.2$–0.4 fm (results at $r_2 \lesssim 0.2$ fm would suffer from lattice discretization error). Note that a repulsive short-range three-nucleon force is phenomenologically required to explain the properties of high density matter. On the other hand, three nucleon forces are found to be suppressed at long distances. This is in accordance with the suppression of two-pion-exchange due to the heavier pion masses.

Shown in **Figure 15** (Right) is the latest preliminary result obtained at $m_\pi = 510$ MeV. In this calculation, we employ (2+1)-flavor lattice QCD gauge configurations generated in Yamazaki et al. [36] with the RG-improved Iwasaki gauge action and non-perturbatively $\mathcal{O}(a)$-improved Wilson quark action on a $L^3 \times T = 64^3 \times 64$ lattice (work in progress). The lattice spacing is $a = 0.090$ fm and $L = 5.8$ fm. Avoiding the very short-distance region where lattice discretization error could affect the results, we again find the short-range repulsive three-nucleon forces at $r_2 \simeq 0.2$–0.7 fm. We find that, while the pion mass dependence of three-nucleon forces is not significant at $m_\pi = 0.76$–1.13 GeV, the range of repulsive three-nucleon forces tend to be enlarged at $m_\pi = 0.51$ GeV. It is important to pursue the study at lighter pion masses toward the physical pion mass.

4.3. Applications to Nuclei, Nuclear Equation of State, and Structure of Neutron Stars

Once nuclear potentials are obtained by lattice QCD, we can use them to study various phenomena in nuclear physics and astrophysics. We here present the study of nuclear spectra/structures and Equation of State (EoS) of dense matter relevant to neutron star physics. Potentials used in this subsection are of the leading order only, and therefore are all hermitian. We can make non-hermitian higher order potentials in the HAL QCD method hermitian in the derivative expansion [63], which may be used for future applications in nuclear many body calculations.

In McIlroy et al. [64], binding energies and structures of doubly magic nuclei, ^{4}He, ^{16}O, ^{40}Ca, are studied by an ab initio nuclear many-body calculation based on lattice nuclear forces. We employ the nuclear forces obtained in 3-flavor lattice QCD at $M_{\rm ps} = 469$ MeV (see **Figure 12**). We consider two-body nuclear forces in $^1S_0$, $^3S_1$, and $^3D_1$ channels, while nuclear forces in other channels and spin-orbit forces as well as three-nucleon forces are neglected. For simplicity, the Coulomb force between protons is not taken into account, either. As the ab initio many-body calculation, we employ self-consistent Green's function (SCGF) method, in which the single-particle propagator (Green's function) and the self-energy is solved self-consistently in a non-perturbative manner. In a practical calculation, the self-energy is calculated by Algebraic Diagrammatic Construction (ADC) formalism at third order for the so-called (low-momentum) P-space and Bethe-Goldstone equation (BGE) for the $Q = 1 - P$ space. (see [64] for details.)

In **Table 2**, we summarize the results for the ground state energies, together with the results from Brueckner Hartree-Fock (BHF) calculation [65] and exact stochastic variational calculation [66] using the same lattice nuclear forces. For the results from SCGF, the first parentheses show the errors associated with the infrared (IR) extrapolation in the SCGF calculation. We also estimate the errors from many-body truncations using ^{4}He as a benchmark. Since the SCGF result deviates from the exact solution by $<$10% for ^{4}He, and the SCGF approach is size extensive, we take a conservative estimate of 10% error for ^{16}O and ^{40}Ca, which are quoted in the second parentheses. The BHF results are sensibly more bound than the SCGF results, and we interpret this as a limitation of BHF theory. For the results shown in **Table 2**, there exist additional errors associated with the statistical fluctuations in the input lattice nuclear forces, which are estimated to be $\sim$10% [65]. Note that statistical fluctuations are correlated among nuclei, so we expect our observations described below are rather robust against statistical errors.

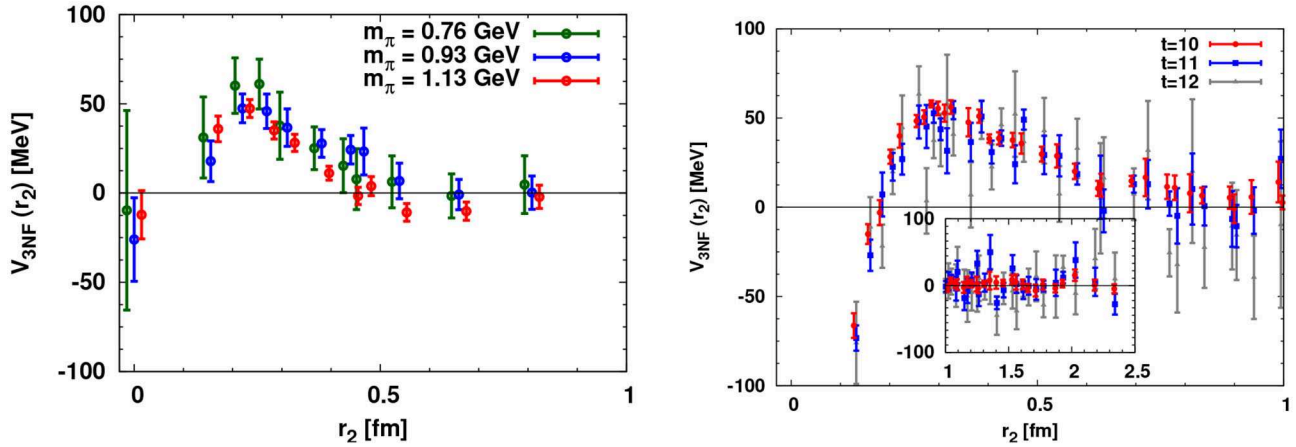


FIGURE 15 | Three-nucleon forces in the triton channel with the linear setup. (Left) Results from 2-flavor lattice QCD at $m_\pi = 0.76$–1.13 GeV. (Right) Results from (2+1)-flavor lattice QCD at $m_\pi = 0.51$ GeV.

TABLE 2 | Ground state energies of ^{4}He, ^{16}O, and ^{40}Ca calculated by self-consistent Green's function (SCGF) method using nuclear forces at M_{PS} = 469 MeV obtained from 3-flavor lattice QCD with the HAL QCD method.

E_0^A [MeV]	^{4}He	^{16}O	^{40}Ca
SCGF	−4.80(0.03)	−17.9 (0.3) (1.8)	−75.4 (6.7) (7.5)
BHF	−8.2	−34.7	−112.7
Exact calc.	−5.09	–	–
Experiment	−28.3	−127.7	−342.0
Separation into ^{4}He clusters		−2.46 (0.3) (1.8)	24.5 (6.7) (7.5)

Comparison is given with those obtained with BHF [65] and the exact calculation [66]. The last line is the breakup energy for splitting the system in ^{4}He clusters (of total energy A/4×5.09 MeV). Taken from McIlroy et al. [64].

TABLE 3 | Matter and charge radii of ^{4}He, ^{16}O, and ^{40}Ca at M_{PS} = 469 MeV computed by the SCGF method, which are compared with those by BHF [65], by Hartree-Fock (HF) and by experiments [67, 68].

		^{4}He	^{16}O	^{40}Ca
$r_{pt-matter}$[fm]:	SCGF	1.67	2.64	2.97
	BHF	2.09	2.35	2.78
	HF	1.62	2.39	2.78
r_{charge}[fm]:	SCGF	1.89	2.79	3.10
	Experiment	1.67	2.73	3.48

For charge radii, we assumed the physical charge distributions of the nucleons. Taken from McIlroy et al. [64].

We find that at $M_{ps} = 469$ MeV in the SU(3) limit of QCD, both ^{4}He and ^{40}Ca have bound ground states while the deuteron is unbound. ^{16}O is likely to decay into four separate alpha particles, though it is already close to become bound. Moreover, we find that asymmetric isotopes, like ^{28}O, are strongly unbound systems. These results suggest that, when lowering the pion mass toward its physical value, closed shell isotopes are created at first around the traditional magic numbers and the region of $M_{ps} \sim 500$ MeV marks a transition between an unbound nuclear chart and the emergence of bound isotopes.

We calculate the root mean square radii, which are given in **Table 3**, where we show only the central values. Although the total binding energies are 15–20% of the experimental value (**Table 2**), the computed charge radii are about the same as the experiment. We also find that the calculated one-nucleon spectral distributions are qualitatively close to those of real nuclei even for $M_{ps} = 469$ MeV considered here. This is due to the fact that the heavy nucleon mass ($m_N = 1161.1$ MeV) used here reduces the motion of the nucleons inside the nuclei and counterbalances the effect of weak attraction of the lattice nuclear forces at this pion mass.

We next present the study of properties of dense matter, namely, Equation of State (EoS) of nuclear matter. We again employ the nuclear forces in $^1S_0$, $^3S_1$, and $^3D_1$ channels obtained in 3-flavor lattice QCD. To study the quark mass dependence, we use lattice results for all five quark masses, at $M_{\rm ps}$ = 469, 672, 837, 1015, 1171 MeV, which are shown in **Figure 12**. As a method for a many-body calculation, we employ the Brueckner-Hartree-Fock (BHF) theory [69], which is known to be quantitative enough to give the essential underlying physics for infinite matter.

In **Figure 16** (Upper), we show the results of the ground state energy per nucleon (E/A) as a function of the Fermi momentum k_F for the symmetric nuclear matter and the pure neutron matter. Shown together are the so-called APR EoS [70], which are obtained by the variational chain summation method from phenomenological nuclear forces with (APR(Full)) and without (APR(AV18)) three-nucleon forces. In **Figure 16** (Upper-Left), we find that the symmetric nuclear matter becomes a self-bound system with a saturation point $(k_F, E/A) \simeq (1.83(16)\ \mathrm{fm}^{-1}, -5.4(5)\ \mathrm{MeV})$ at the lightest quark mass ($M_{\rm ps} = 469$ MeV). This is the first time that the saturation in the symmetric nuclear matter is obtained through first-principles lattice QCD simulations. The saturation point, however, deviates

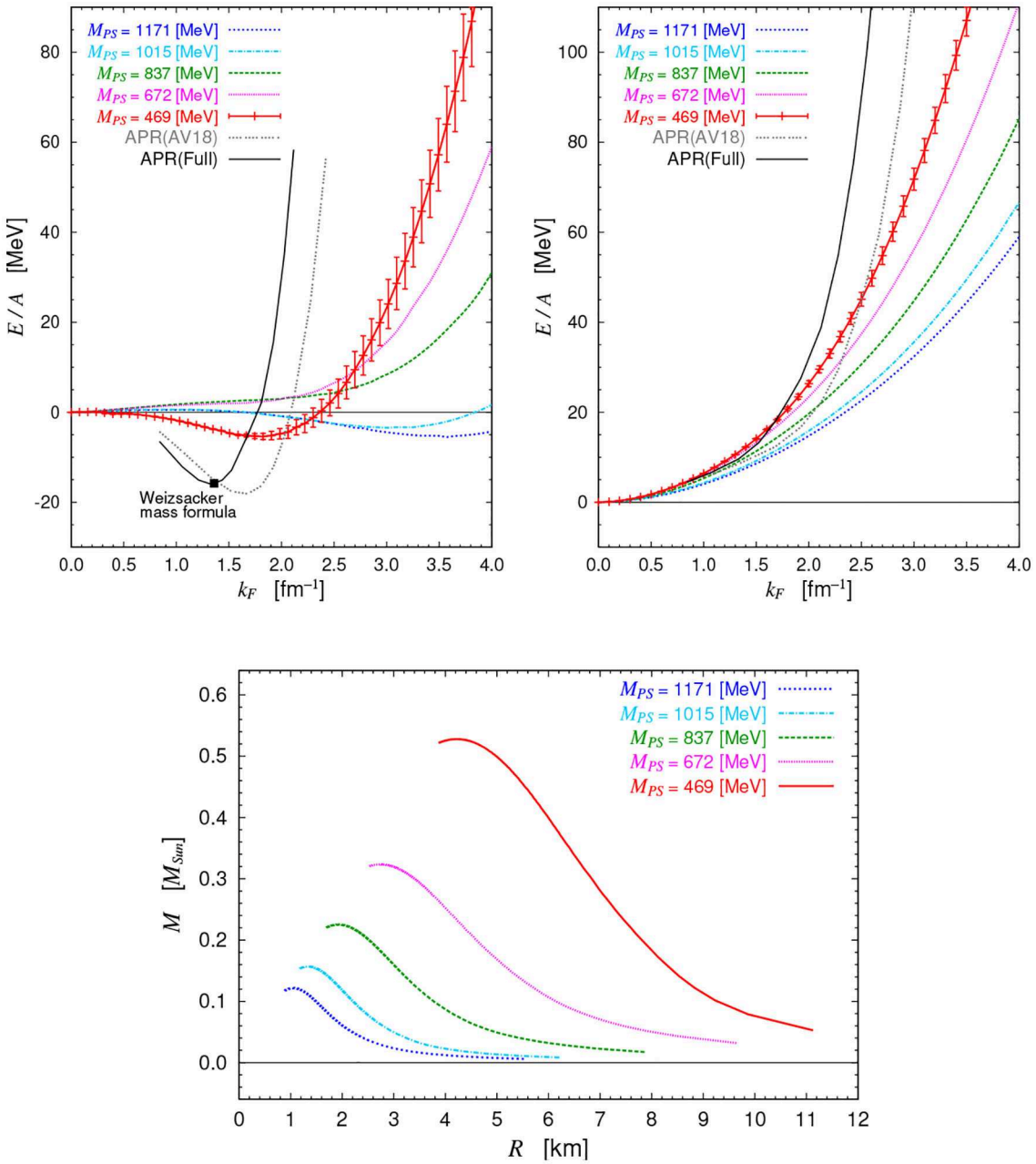


FIGURE 16 | (Upper) Ground state energy per nucleon (E/A) as a function of the Fermi momentum k_F by the BHF theory with nuclear forces from 3-flavor lattice QCD at $M_{\rm ps}$ = 469–1,171 MeV, together with that from APR [70] with and without phenomenological three-nucleon forces. (Left) Results for the symmetric nuclear matter. filled square indicates the empirical saturation point. (Right) Results for the pure neutron matter. (Lower) Mass-radius relation of the neutron star based on EoS obtained by the BHF theory with nuclear forces from 3-flavor lattice QCD at $M_{\rm ps}$ = 469–1,171 MeV. Figures are taken from Inoue et al. [69].

from the empirical point primarily due to heavy pion (pseudo-scalar meson) mass in lattice simulation and the lack of three-nucleon forces in BHF calculation.

We also find a non-trivial $M_{\rm ps}$ dependence of the EoS: the saturation disappears at intermediate pion masses ($M_{\rm ps}$ = 672, 837 MeV) and possibly appears again at the heavy pion mass region ($M_{\rm ps}$ = 1015, 1171 MeV). This implies that the saturation originates from a subtle balance between short-range repulsion and the intermediate attraction of the nuclear force, which have different m_q dependence [44]. A similar non-trivial $M_{\rm ps}$ dependence originated from the balance between repulsion and attraction is also observed for NN scattering phase shifts, as was discussed in section 4.1.

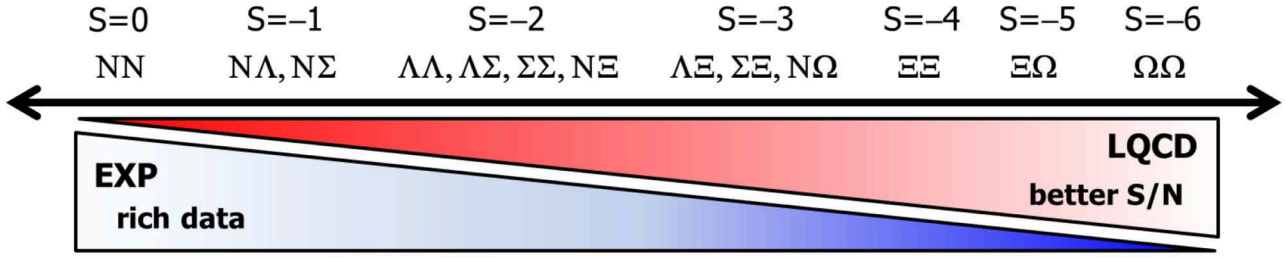


FIGURE 17 | An illustration of the complementary role of lattice QCD and experiments in the determination of baryon forces.

In **Figure 16** (Upper-Right), we find that neutron matter is not self-bound due to large Fermi energy. If we decrease the pion mass, EoS is found to become stiffer. To further study the impact on phenomena in nuclear astrophysics, we calculate the mass (M) vs. the radius (R) relation of neutron stars at each pion mass. Here, we solve the Tolman-Oppenheimer-Volkoff (TOV) equation by using the EoS of the neutron-star matter with neutron, proton, electron and muon under the charge neutrality and beta equilibrium, where we use the standard parabolic approximation for asymmetric nuclear matters.

Shown in **Figure 16** (Lower) is the M-R relation of the neutron star for different pion masses. As $M_{\rm ps}$ decreases, the M-R curve shifts to the upper right direction, due to the stiffening of the EoS. While the maximum mass of the neutron star ($M_{\rm max}$) in this calculation is much smaller than the recent observations, $M_{\rm max} \simeq 2M_\odot$, the deviation is most likely due to the heavy pion masses and lack of interactions as three-nucleon forces. A naive extrapolation of $M_{\rm max}$ and the corresponding radius to $M_{\rm ps} = 137$ MeV would give $M_{\rm max} \sim 2.2M_\odot$ and $R \sim 12$ km, which are encouraging for more quantitative studies in future. Another hottest topic in the context of neutron star physics is the effect of hyperon on the EoS at high density (so-called "hyperon puzzle"). Lattice QCD can play an unique role to study this effect by determining the hyperon forces which suffer from large uncertainties in experiments to date. For the on-going study in this direction, see Inoue [71].

4.4. Challenge: Nuclear Forces Near the Physical Pion Mass

While the results of nuclear forces at heavy pion masses are very intriguing and useful to extract the physical picture of nuclear forces, the quantitative results require the study at the physical pion mass. Note that the pion mass dependence of nuclear forces is quite non-trivial as discussed in sections 4.1 and 4.3, so the direct calculation near the physical point is desirable.

To this end, we have recently performed the first calculation of nuclear forces near the physical up, down and strange quark masses. Actually, our aim is to calculate not only nucleon forces but also hyperon forces, hereby achieve the comprehensive determination of two-baryon interactions from the strangeness $S = 0$ to -6 in parity-even channels (S- and D-waves). As mentioned before, the statistical fluctuations in lattice QCD are smaller (larger) for larger (smaller) quark masses, and thus the results have better precision in sectors involving more number of strange quarks (larger strangeness $|S|$). On the other hand, experiments in such larger $|S|$ sectors are more difficult due to the short life time of hyperons. Therefore, lattice QCD studies and experiments are complementary with each other in the determination of baryon forces (see **Figure 17**).

(2+1)-flavor gauge configurations are generated on a $L^3 \times T = 96^3 \times 96$ lattice with the RG-improved Iwasaki gauge action and non-perturbatively $\mathcal{O}(a)$-improved Wilson quark action and APE stout smearing. The lattice spacing is $a \simeq 0.0846$ fm ($a^{-1} \simeq 2.333$ GeV), so that spatial extent, $L = 8.1$ fm, is sufficiently large to accommodate two baryons in a box. Quark masses are tuned so as to be near the physical point, and the hadron masses are found to be $(m_\pi, m_K, m_N) \simeq (146, 525, 955)$ MeV. NBS correlation functions for two-baryon systems are calculated for 55 channels in total and we extract the central and tensor forces in parity-even channel at the LO analysis for the derivative expansion (work in progress, and see also [72]). In order to make this first calculation a reality, "trinity" of state-of-the-art developments was crucial: (a) time-dependent HAL QCD method (theory), (b) unified contraction algorithm (software) and (c) K-computer, HOKUSAI and HA-PACS supercomputers (hardware).

Shown in **Figure 18** are the results for the central force in the $^1S_0$ channel (Left), and the central force (Middle) and tensor force (Right) in the $^3S_1$-$^3D_1$ channel. As noted above, nuclear forces are the most challenging interactions in lattice QCD calculation, and one can see that the results suffer from large statistical fluctuations. Nevertheless, the obtained results exhibit several interesting properties.

First of all, the repulsive core at short-range is clearly observed in central forces. In order to clarify the physical picture for the repulsive core, it is useful to compare them with hyperon forces obtained in the same lattice setup. We find that the strength of repulsive core (or attractive core) highly depends on the flavor SU(3) ($SU(3)_f$) classification, in a consistent way with the quark Pauli blocking effect. In addition, if we compare interactions which belong to the same $SU(3)_f$ classification, such as $NN(^1S_0)$ and $\Xi\Xi(^1S_0)$ both of which belong to 27-plet, we find that the strength differs in a way which can be understood from the viewpoint of one-gluon-exchange (e.g., repulsive core in $NN(^1S_0)$ is stronger than that in $\Xi\Xi(^1S_0)$). These observations confirm

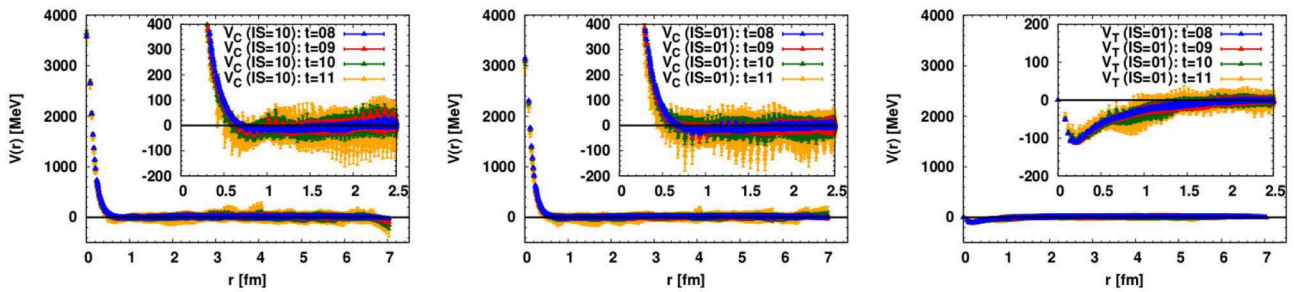


FIGURE 18 | Nuclear forces from (2+1)-flavor lattice QCD near the physical point, $m_\pi = 146$ MeV. The central force in the $^1S_0$ channel (Left). The central force (Middle) and the tensor force (Right) in the $^3S_1$-$^3D_1$ channel.

the physical picture for the repulsive core obtained in the 3-flavor lattice QCD (section 4.1), the quark Pauli blocking effect and the one-gluon-exchange, is relevant even at physical quark masses. See also Park et al. [73] for a more detailed study on this point.

At middle and long distances, while statistical errors are quite large, we observe that the central force is attractive, resembling the phenomenological potential as one-pion-exchange potential (OPEP). The tensor force has relatively smaller statistical errors than the central forces, showing that the tensor force becomes stronger (with a negative sign) and has a longer tail, as compared with the tensor forces at heavier pion masses (section 4.1). This property can be understood by the picture of OPEP. These results are encouraging and serve as the first step to establish a direct connection between QCD and nuclear physics. At the same time, statistical errors remain to be large and there also exist systematic errors associated with inelastic state contaminations. The studies to resolve these issues are in progress, and the second generation calculation is planned on the forthcoming Exascale computer, "Fugaku" (see https://postk-web.r-ccs.riken.jp/).

5. DIBARYONS

Before closing this review, we present our latest results on dibaryon searches in lattice QCD near the physical pion mass [72]. A dibaryon, a bound-state (or a resonance) with a baryon number $B = 2$ in QCD, can be classified in the SU(3)$_f$ as

$$\mathbf{8} \otimes \mathbf{8} = \mathbf{27} \oplus \mathbf{8_s} \oplus \mathbf{1} \oplus \overline{\mathbf{10}} \oplus \mathbf{10} \oplus \mathbf{8_a} \tag{50}$$

for the octet-octet system, where the deuteron, the only stable dibaryon observed in nature so far, appears in the $\overline{\mathbf{10}}$ representation while H dibaryon has been predicted in the **1** representation [74] and actively investigated in lattice QCD [43, 44, 51, 52, 75]. For the decuplet-octet system, the classification leads to

$$\mathbf{10} \otimes \mathbf{8} = \mathbf{35} \oplus \mathbf{8} \oplus \mathbf{10} \oplus \mathbf{27} \tag{51}$$

and $N\Omega$ ($N\Delta$) dibaryon has been predicted in the **8** (**27**) representation [76–78], and

$$\mathbf{10} \otimes \mathbf{10} = \mathbf{28} \oplus \mathbf{27} \oplus \mathbf{35} \oplus \overline{\mathbf{10}} \tag{52}$$

for the decuplet-decuplet system, where $\Omega\Omega$ dibaryon has been predicted in the **28** representation [79] while $\Delta\Delta$ has been predicted in the $\overline{\mathbf{10}}$ [78, 80] and the corresponding $d^*(2380)$ was indeed observed [81]. Note that among decuplet baryons, only Ω is stable against strong decays.

5.1. The Most Strange Dibaryon

We first consider the $\Omega\Omega$ system in the **28** representation of SU(3)$_f$ in the $^1S_0$ channel [82].

Figure 19 (Upper-Left) shows $\Omega\Omega$ potentials at $t/a = 16, 17, 18$, which has qualitative features similar to the central potentials for NN but whose repulsion is weaker and attraction is shorter-ranged. This potential predicts an existence of one shallow bound state, whose binding energy is plotted in **Figure 19** (Upper-Right) as a function of the root-mean-square distance, with (red) and without (blue) Coulomb repulsion between $\Omega\Omega$. We may call this $\Omega\Omega$ bound state "*the most strange dibaryon*." Such a system can be best searched experimentally by two-particle correlations in relativistic heavy-ion collisions [84].

5.2. $N\Omega$ Dibaryon

We next consider the $N\Omega$ system with $S = -3$ in the **8** representation in the $^5S_2$ channel [83]. Near the physical point, $N\Omega(^5S_2)$ may couple to D-wave octet-octet channels below the $N\Omega$ threshold ($\Lambda\Xi$ and $\Sigma\Xi$), but such couplings are assumed to be small in this calculation.

Figure 19 (Lower-Left) shows the $N\Omega$ potential at $t/a = 11$–14, which is attractive at all distances without repulsive core, so that one bound state appears in this channel. In **Figure 19** (Lower-Right), the binding energy (vertical) and the the root-mean-square distance (horizontal) are plotted for $n\Omega^-$ with no Coulomb interaction (red) and $p\Omega^-$ with Coulomb attraction (blue). These binding energies are much smaller than $B = 18.9(5.0)(^{+12.1}_{-1.8})$ MeV at heavy pion mass $m_\pi = 875$ MeV [85]. Such a $N\Omega$ state can be searched through two-particle correlations in relativistic nucleus-nucleus collisions [84] and an experimental indication was also reported [86].

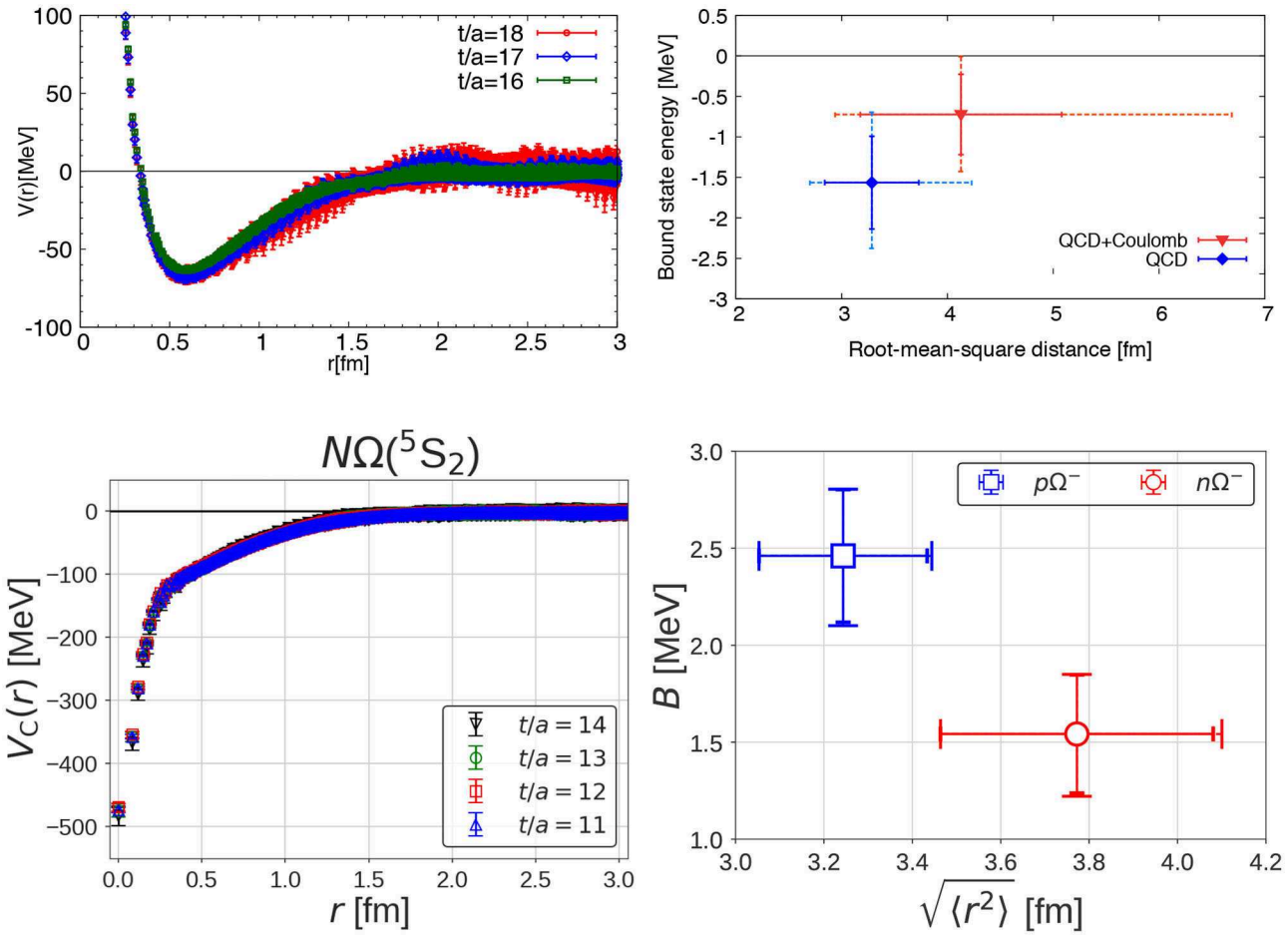


FIGURE 19 | (Upper) The ΩΩ system in the $^1S_0$ channel in 2 + 1 flavor QCD at $m_\pi \simeq 146$ MeV and $a \simeq 0.0846$ fm on a (8.1 fm)^3 box. (Left) The ΩΩ potential $V(r)$ at $t/a = 16, 17, 18$. (Right) The binding energy of the ΩΩ system and the root-mean-square distance between two Ω's are shown by blue solid diamond (red solid triangle), calculated from the ΩΩ potential $V(r)$ at $t/a = 17$ without (with) the Coulomb repulsion. Taken from Gongyo et al. [82]. (Lower) The $N\Omega$ system in the $^5S_2$ channel with the same lattice setup for ΩΩ. (Left) The $N\Omega$ potential $V_C(r)$ at $t/a = 11, 12, 13, 14$. (Right) The binding energy and the root-mean-square distance for the $n\Omega^-$ (red open circle) and $p\Omega^-$ (blue open square). Taken from Iritani et al. [83].

5.3. Comparison Among Dibaryons

Let us consider the scattering length a_0 and the effective range $r_{\rm eff}$ for $\Omega\Omega(^1S_0)$ and $N\Omega(^5S_2)$. In **Figure 20**, the ratio $r_{\rm eff}/a_0$ as a function of $r_{\rm eff}$ are plotted for $\Omega\Omega(^1S_0)$ and $N\Omega(^5S_2)$ obtained in lattice QCD near the physical pion mass, together with the experimental values for $NN(^3S_1)$ (deuteron) and $NN(^1S_0)$ (di-neutron). Small values of $|r_{\rm eff}/a_0|$ in all cases indicate that these systems are located close to the unitary limit.

6. CONCLUSIONS

In this paper, we have reviewed the recent progress in lattice QCD study of baryon-baryon interactions by the HAL QCD method. We first presented the detailed account on how to define the potentials in quantum field theories, such as QCD. The key observation is that the Nambu-Bethe-Salpeter (NBS) wave functions contain the information of scattering phase shifts below inelastic threshold in their asymptotic behaviors outside the range of the interactions. The potentials at the interaction region can then be defined through the NBS wave functions so as to be faithful to the phase shifts by construction, where the non-locality of the potential is defined by the derivative expansion. In addition, by constructing the potentials in energy-independent way, the potentials can be extracted from two-baryon correlation functions without the requirement of the ground state saturation.

We then made a detailed comparison between the HAL QCD method and the conventional method, in which phase shifts are obtained from the finite volume energies through the Lüscher's formula. We pointed out that, while the validity of the latter method relies on the ground state saturation of the correlation function, its practical procedure for multi-baryon systems ("direct method") so far has utilized only the plateau-like structures of the effective energies at Euclidean times much earlier than the inverse of the lowest excitation

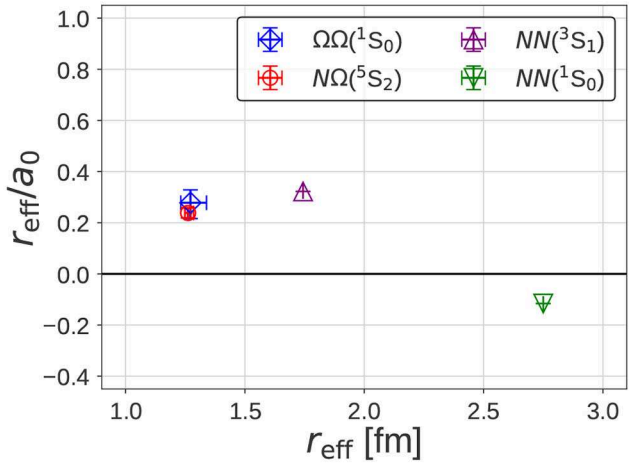


FIGURE 20 | The ratio of the effective range and the scattering length r_{eff}/a_0 as a function of r_{eff} for $\Omega\Omega(^1S_0)$ (blue open diamond) and $N\Omega(^5S_2)$ (red open circle) obtained in lattice QCD, as well as for $NN(^3S_1)$ (purple open up-triangle) and $NN(^1S_0)$ (green open down-triangle) in experiments. Taken from Iritani et al. [83]. The sign convention for the scattering length is opposite to Eq. (5) in this figure.

energy. We showed theoretical and numerical evidences that such a procedure generally leads to unreliable results due to the contaminations from the elastic excited states: For instance, the results were found to be dependent on the operators and unphysical behaviors were exposed by the normality check. This invalidates the claim of the literature in the direct method that *NN* bound states exist for pion masses heavier than 300 MeV.

On the other hand, HAL QCD method is free from such a serious problem since the signal of potentials can be extracted from not only the ground state but also elastic excited states. While there instead exists the truncation error of the derivative expansion of the potential, the calculation of the higher order term in the derivative expansion showed that the convergence of the expansion is sufficiently good at low energies. Furthermore, utilizing the finite volume eigenmodes of the HAL QCD Hamiltonian, the excited state contaminations in the direct method were explicitly quantified. It turns out that the plateau-like structures of effective energies at early time slices are indeed pseudo-plateaux contaminated by elastic excited states and that the plateau for the ground state is realized only at a much larger time corresponding to the inverse of the lowest excitation energy gap. We also showed that, by employing an optimized operator utilizing the finite volume eigenmodes, the effective energies from the correlation functions give consistent results with those from the HAL QCD potential. Thus the long-standing issue on the consistency between the conventional method based on the Lüscher's formula and the HAL QCD method was positively resolved.

After establishing the reliability of the HAL QCD method, we presented the numerical results of nuclear forces from the HAL QCD method at various lattice QCD setups. At heavy pion masses, where good signal-to-noise ratio can be achieved in lattice QCD, we observed that the obtained *NN* potentials in the parity-even channel ($^1S_0$, $^3S_1$-$^3D_1$) reproduce the qualitative features of the phenomenological potentials, namely, attractive wells at long and medium distances, accompanied with repulsive cores at short distance in the central potentials and the strong tensor force. The net interactions were found to be attractive, which however are not strong enough to form a bound *NN* state, probably due to the heavy pion masses. We observed that the tail structures are enhanced at lighter pion masses, which can be understood from the viewpoint of one-pion exchange contributions. We also found the repulsive cores are enhanced at lighter pion masses. Combined with our systematic studies including hyperon forces, the nature of repulsive cores was found to be well-described by the quark Pauli blocking effect together with the one-gluon-exchange contribution.

The HAL QCD method can be extended to determine more complicated nuclear forces, such as spin-orbit forces and three-nucleon forces. In this paper, we considered two-nucleon systems in the parity-odd channels ($^1P_1$, $^3P_0$, $^3P_1$, $^3P_2$-$^3F_2$ channels) and calculated spin-orbit forces as well as central and tensor forces. We found that qualitative features of experimental results are generally well-reproduced, while the magnitudes differ due to the heavy pion mass. In particular, we observed the strong (and negative) spin-orbit forces, which lead to the attraction in the $^3P_2$ channel. Three-nucleon forces were studied in the triton channel, $(I, J^P) = (1/2, 1/2^+)$, thank to the unified contraction algorithm (UCA), which can enormously speed up calculations of multi-baryon correlation functions. It was found that there exists a repulsive three-nucleon forces at short distances. These observations are of interest in the context of not only the structures of nuclei but also those of neutron stars, e.g., *P*-wave superfluidity and the maximum mass of neutron stars.

We carried out the applications to nuclei, nuclear equation of state (EoS) and structure of neutron stars based on lattice nuclear forces at heavy quark masses. We performed ab initio self-consistent Green's function (SCGF) calculations for closed shell nuclei with nuclear forces at M_{ps}=469 MeV in the SU(3) limit of QCD. We found that ^{4}He, ^{40}Ca nuclei are bound, and ^{16}O is close to become bound, while asymmetric isotopes are strongly unbound. The results suggest that, when lowering the pion mass toward its physical value, islands of stability appear at first around the traditional doubly magic numbers. The nuclear EoS was also studied by the BHF theory with nuclear forces in the flavor SU(3) limit. We found that the saturation property appears in the symmetric nuclear matter at M_{ps} = 469 MeV. A mass-radius relation of the neutron star was also studied based on the EoS obtained from lattice nuclear forces and we observed a tendency that the maximum mass of a neutron star increases as the pion mass decreases.

Finally, we presented the first lattice QCD study of baryon forces near the physical pion mass in the parity-even channel. The computation is quite challenging particularly for nuclear forces due to bad signal-to-noise ratio near the physical point.

Nevertheless, we observed prominent characteristics of nuclear forces, such as repulsive cores at short distances as well as attractive interactions at mid and long distances in central forces, and a strong (and negative) tensor force. We also presented the results for the hyperon forces obtained near the physical point. We found that both $\Omega\Omega(^1S_0)$ and $N\Omega(^5S_2)$ systems have strong attractions, and (quasi) bound dibaryons are formed near the unitary limit. These systems could be searched experimentally through two-particle correlations in relativistic nucleus-nucleus collisions.

Present results shown in this paper already indicate a clear pathway which connects nuclear physics with its underlying theory of the strong interaction, QCD. While there remain many challenges to accomplish researches in this direction, there is no doubt that successive theoretical developments together with next-generation supercomputers will further deepen the connection between the two. The outcome is also expected to play a crucial role to understand the nuclear astrophysical phenomena, such as supernova explosions and mergers of binary neutron stars, as well as the nucleosynthesis associated with these explosive phenomena.

DATA AVAILABILITY STATEMENT

The original contributions presented in the study are included in the article/supplementary materials, further inquiries can be directed to the corresponding author/s.

AUTHOR CONTRIBUTIONS

All authors listed have made a substantial, direct and intellectual contribution to the work, and approved it for publication.

FUNDING

This work was supported in part by the Grant-in-Aid of the Japanese Ministry of Education, Sciences and Technology, Sports and Culture (MEXT) for Scientific Research (Nos. JP16H03978, JP18H05236, JP18H05407, and JP19K03879), by HPCI programs (hp120281, hp130023, hp140209, hp150223, hp150262, hp150085, hp160211, hp160093, hp170230, hp170170, hp180179, hp180117, hp190160, and hp190103), by a priority issue (Elucidation of the fundamental laws and evolution of the universe) to be tackled by using Post K Computer, and by Joint Institute for Computational Fundamental Science (JICFuS).

ACKNOWLEDGMENTS

The authors thank members of the HAL QCD Collaboration for providing lattice QCD results and for fruitful collaborations based on which this paper was prepared. **Figure 12** was reprinted from Inoue et al. [44] with permission from Elsevier. **Figure 14** was taken from Murano et al. [50], and **Figures 19**, **20** were taken from Iritani et al. [83], under the term of the https://creativecommons.org/licenses/by/3.0/.

REFERENCES

1. Stoks VGJ, Klomp RAM, Terheggen CPF, de Swart JJ. Construction of high quality N N potential models. *Phys Rev C.* (1994) **49**:2950–62. doi: 10.1103/PhysRevC.49.2950
2. Wiringa RB, Stoks VGJ, Schiavilla R. An Accurate nucleon-nucleon potential with charge independence breaking. *Phys Rev C.* (1995) **51**:38–51. doi: 10.1103/PhysRevC.51.38
3. Machleidt R. The High precision, charge dependent Bonn nucleon-nucleon potential (CD-Bonn). *Phys Rev C.* (2001) **63**:024001. doi: 10.1103/PhysRevC.63.024001
4. Weinberg S. Nuclear forces from chiral Lagrangians. *Phys Lett B.* (1990) **251**:288–92. doi: 10.1016/0370-2693(90)90938-3
5. Weinberg S. Effective chiral Lagrangians for nucleon–pion interactions and nuclear forces. *Nucl Phys B.* (1991) **363**:3–18. doi: 10.1016/0550-3213(91)90231-L
6. Epelbaum E, Hammer HW, Meissner UG. Modern theory of nuclear forces. *Rev Mod Phys.* (2009) **81**:1773–825. doi: 10.1103/RevModPhys.81.1773
7. Machleidt R, Entem DR. Chiral effective field theory and nuclear forces. *Phys Rept.* (2011) **503**:1–75. doi: 10.1016/j.physrep.2011.02.001
8. Hammer HW, Koenig S, van Kolck U. Nuclear effective field theory: status and perspectives. *Rev Mod Phys.* (2019) **92**:025004. doi: 10.1103/RevModPhys.92.025004
9. Briceno RA, Dudek JJ, Young RD. Scattering processes and resonances from lattice QCD. *Rev Mod Phys.* (2018) **90**:025001. doi: 10.1103/RevModPhys.90.025001
10. Luscher M, Wolff U. How to calculate the elastic scattering matrix in two-dimensional quantum field theories by numerical simulation. *Nucl Phys B.* (1990) **339**:222–52. doi: 10.1016/0550-3213(90)90540-T
11. Rummukainen K, Gottlieb SA. Resonance scattering phase shifts on a nonrest frame lattice. *Nucl Phys B.* (1995) **450**:397–436. doi: 10.1016/0550-3213(95)00313-H
12. Briceno RA, Davoudi Z, Luu TC. Two-nucleon systems in a finite volume: (I) quantization conditions. *Phys Rev D.* (2013) **88**:034502. doi: 10.1103/PhysRevD.88.034502
13. Briceno RA. Two-particle multichannel systems in a finite volume with arbitrary spin. *Phys Rev D.* (2014) **89**:074507. doi: 10.1103/PhysRevD.89.074507
14. Hansen MT, Sharpe SR. Relativistic, model-independent, three-particle quantization condition. *Phys Rev D.* (2014) **90**:116003. doi: 10.1103/PhysRevD.90.116003
15. Hansen MT, Sharpe SR. Lattice QCD and three-particle decays of resonances. *Ann Rev Nucl Part Sci.* (2019) **69**:65–107. doi: 10.1146/annurev-nucl-101918-023723
16. Durr S, Fodor Z, Frison J, Hoelbling C, Hoffmann R, Katz SD, et al. *Ab-initio* determination of light hadron masses. *Science.* (2008) **322**:1224–7. doi: 10.1126/science.1163233
17. Borsanyi S, Durr S, Fodor Z, Hoelbling C, Katz SD, Krieg S, et al. *Ab initio* calculation of the neutron-proton mass difference. *Science.* (2015) **347**:1452–5. doi: 10.1126/science.1257050
18. Luscher M. Two particle states on a torus and their relation to the scattering matrix. *Nucl Phys B.* (1991) **354**:531–78. doi: 10.1016/0550-3213(91)90366-6
19. Iritani T, Aoki S, Doi T, Hatsuda T, Ikeda Y, Inoue T, et al. Are two nucleons bound in lattice QCD for heavy quark masses? Consistency check with Lüscher's finite volume formula. *Phys Rev D.* (2017) **96**:034521. doi: 10.1103/PhysRevD.96.034521
20. Sitenko AG. *Lectures in Scattering Theory*. New York, NY: Pergamon Press Oxford (1971).
21. Kawai D, Aoki S, Doi T, Ikeda Y, Inoue T, Iritani T, et al. $I = 2\,\pi\pi$ scattering phase shift from the HAL QCD method with the LapH smearing. *PTEP.* (2018) **2018**:043B04. doi: 10.1093/ptep/pty032
22. Ishizuka N. Derivation of Luscher's finite size formula for N pi and NN system. *PoS LAT.* (2009) **2009**:119. doi: 10.22323/1.091.0119

23. Aoki S, Hatsuda T, Ishii N. Theoretical foundation of the nuclear force in QCD and its applications to central and tensor forces in quenched lattice QCD simulations. *Prog Theor Phys.* (2010) **123**:89–128. doi: 10.1143/PTP.123.89
24. Lin CJD, Martinelli G, Sachrajda CT, Testa M. $K \to \pi\pi$ decays in a finite volume. *Nucl Phys B.* (2001) **619**:467–98. doi: 10.1016/S0550-3213(01)00495-3
25. Aoki S, Fukugita M, Ishikawa KI, Ishizuka N, Iwasaki Y, Kanaya K, et al. I=2 pion scattering length from two-pion wave functions. *Phys Rev D.* (2005) **71**:094504. doi: 10.1103/PhysRevD.71.094504
26. Ishii N, Aoki S, Hatsuda T. The nuclear force from lattice QCD. *Phys Rev Lett.* (2007) **99**:022001. doi: 10.1103/PhysRevLett.99.022001
27. Aoki S, Doi T, Hatsuda T, Ikeda Y, Inoue T, Ishii N, et al. Lattice QCD approach to nuclear physics. *PTEP.* (2012) **2012**:01A105. doi: 10.1093/ptep/pts010
28. Sugiura T, Ishii N, Oka M. Derivative expansion of wave function equivalent potentials. *Phys Rev D.* (2017) **95**:074514. doi: 10.1103/PhysRevD.95.074514
29. Aoki S, Doi T, Hatsuda T, Ishii N. Comment on "Relation between scattering amplitude and Bethe-Salpeter wave function in quantum field theory". *Phys Rev D.* (2018) **98**:038501. doi: 10.1103/PhysRevD.98.038501
30. Yamazaki T, Kuramashi Y. Relation between scattering amplitude and Bethe-Salpeter wave function in quantum field theory. *Phys Rev D.* (2017) **96**:114511. doi: 10.1103/PhysRevD.96.114511
31. Ernst DJ, Shakin CM, Thaler RM. Separable representations of two-body interactions. *Phys Rev C.* (1973) **8**:46–52. doi: 10.1103/PhysRevC.8.46
32. Ernst DJ, Shakin CM, Thaler RM. Separable representations of T matrices valid in the vicinity of off-shell points. *Phys Rev C.* (1974) **9**:1780–3. doi: 10.1103/PhysRevC.9.1780
33. Murano K, Ishii N, Aoki S, Hatsuda T. Nucleon-nucleon potential and its non-locality in lattice QCD. *Prog Theor Phys.* (2011) **125**:1225–40. doi: 10.1143/PTP.125.1225
34. Ishii N, Aoki S, Doi T, Hatsuda T, Ikeda Y, Inoue T, et al. Hadron-hadron interactions from imaginary-time Nambu-Bethe-Salpeter wave function on the lattice. *Phys Lett B.* (2012) **712**:437–41. doi: 10.1016/j.physletb.2012.04.076
35. Yamazaki T, Kuramashi Y, Ukawa A. Two-nucleon bound states in quenched lattice QCD. *Phys Rev D.* (2011) **84**:054506. doi: 10.1103/PhysRevD.84.054506
36. Yamazaki T, Ishikawa Ki, Kuramashi Y, Ukawa A. Helium nuclei, deuteron and dineutron in 2+1 flavor lattice QCD. *Phys Rev D.* (2012) **86**:074514. doi: 10.1103/PhysRevD.86.074514
37. Orginos K, Parreno A, Savage MJ, Beane SR, Chang E, Detmold W. Two nucleon systems at $m_\pi \sim$ 450MeV from lattice QCD. *Phys Rev D.* (2015) **92**:114512. doi: 10.1103/PhysRevD.92.114512
38. Beane SR, Chang E, Detmold W, Lin HW, Luu TC, Orginos K, et al. The deuteron and exotic two-body bound states from lattice QCD. *Phys Rev D.* (2012) **85**:054511. doi: 10.1103/PhysRevD.85.054511
39. Yamazaki T, Ishikawa Ki, Kuramashi Y, Ukawa A. Study of quark mass dependence of binding energy for light nuclei in 2+1 flavor lattice QCD. *Phys Rev D.* (2015) **92**:014501. doi: 10.1103/PhysRevD.92.014501
40. Beane SR, Chang E, Cohen SD, Detmold W, Lin HW, Luu TC, et al. Light nuclei and hypernuclei from quantum chromodynamics in the limit of SU(3) flavor symmetry. *Phys Rev D.* (2013) **87**:034506. doi: 10.1103/PhysRevD.87.034506
41. Wagman ML, Winter F, Chang E, Davoudi Z, Detmold W, Orginos K, et al. Baryon-Baryon interactions and spin-flavor symmetry from lattice quantum chromodynamics. *Phys Rev D.* (2017) **96**:114510. doi: 10.1103/PhysRevD.96.114510
42. Berkowitz E, Kurth T, Nicholson A, Joo B, Rinaldi E, Strother M, et al. Two-nucleon higher partial-wave scattering from lattice QCD. *Phys Lett B.* (2017) **765**:285–92. doi: 10.1016/j.physletb.2016.12.024
43. Francis A, Green JR, Junnarkar PM, Miao C, Rae TD, Wittig H. Lattice QCD study of the H dibaryon using hexaquark and two-baryon interpolators. *Phys Rev D.* (2019) **99**:074505. doi: 10.1103/PhysRevD.99.074505
44. Inoue T, Aoki S, Doi T, Hatsuda T, Ikeda Y, Ishii N, et al. Two-Baryon potentials and H-dibaryon from 3-flavor lattice QCD simulations. *Nucl Phys A.* (2012) **881**:28–43. doi: 10.1016/j.nuclphysa.2012.02.008
45. Ishii N. Baryon-baryon interactions from lattice QCD. *PoS CD.* (2013) **12**:025. doi: 10.22323/1.172.0025
46. Iritani T, Doi T, Aoki S, Gongyo S, Hatsuda T, Ikeda Y, et al. Mirage in temporal correlation functions for Baryon-Baryon interactions in lattice QCD. *JHEP.* (2016) **10**:101. doi: 10.1007/JHEP10(2016)101
47. Iritani T, Aoki S, Doi T, Gongyo S, Hatsuda T, Ikeda Y, et al. Systematics of the HAL QCD potential at low energies in lattice QCD. *Phys Rev D.* (2019) **99**:014514. doi: 10.1103/PhysRevD.99.014514
48. Iritani T, Aoki S, Doi T, Hatsuda T, Ikeda Y, Inoue T, et al. Consistency between Lüscher's finite volume method and HAL QCD method for two-baryon systems in lattice QCD. *JHEP.* (2019) **3**:007. doi: 10.1007/JHEP03(2019)007
49. Miyamoto T, Akahoshi Y, Aoki S, Aoyama T, Doi T, Gongyo S, et al. Partial wave decomposition on the lattice and its applications to the HAL QCD method. *Phys Rev D.* (2019) **101**:074514. doi: 10.1103/PhysRevD.101.074514
50. Murano K, Ishii N, Aoki S, Doi T, Hatsuda T, Ikeda Y, et al. Spin-orbit force from lattice QCD. *Phys Lett B.* (2014) **735**:19–24. doi: 10.1016/j.physletb.2014.05.061
51. Inoue T, Ishii N, Aoki S, Doi T, Hatsuda T, Ikeda Y, et al. Baryon-Baryon interactions in the flavor SU(3) limit from full QCD simulations on the lattice. *Prog Theor Phys.* (2010) **124**:591–603. doi: 10.1143/PTP.124.591
52. Inoue T, Ishii N, Aoki S, Doi T, Hatsuda T, Ikeda Y, et al. Bound H-dibaryon in flavor SU(3) limit of lattice QCD. *Phys Rev Lett.* (2011) **106**:162002. doi: 10.1103/PhysRevLett.106.162002
53. Ishii N, Aoki S, Hatsuda T. Nuclear forces from quenched and 2+1 flavor lattice QCD using the PACS-CS gauge configurations. *PoS Lattice.* (2008) **2008**:155. doi: 10.22323/1.066.0155
54. Oka M, Shimizu K, Yazaki K. Quark cluster model of baryon baryon interaction. *Prog Theor Phys Suppl.* (2000) **137**:1–20. doi: 10.1143/PTPS.137.1
55. Coon SA, Han HK. Reworking the Tucson-Melbourne three nucleon potential. *Few Body Syst.* (2001) **30**:131–41. doi: 10.1007/s006010170022
56. Pieper SC, Pandharipande VR, Wiringa RB, Carlson J. Realistic models of pion exchange three nucleon interactions. *Phys Rev C.* (2001) **64**:014001. doi: 10.1103/PhysRevC.64.014001
57. Weinberg S. Three body interactions among nucleons and pions. *Phys Lett B.* (1992) **295**:114–21. doi: 10.1016/0370-2693(92)90099-P
58. Aoki S, Charron B, Doi T, Hatsuda T, Inoue T, Ishii N. Construction of energy-independent potentials above inelastic thresholds in quantum field theories. *Phys Rev D.* (2013) **87**:034512. doi: 10.1103/PhysRevD.87.034512
59. Aoki S, Ishii N, Doi T, Ikeda Y, Inoue T. Asymptotic behavior of Nambu-Bethe-Salpeter wave functions for multiparticles in quantum field theories. *Phys Rev D.* (2013) **88**:014036. doi: 10.1103/PhysRevD.88.014036
60. Gongyo S, Aoki S. Asymptotic behavior of Nambu-Bethe-Salpeter wave functions for scalar systems with a bound state. *PTEP.* (2018) **2018**:093B03. doi: 10.1093/ptep/pty097
61. Doi T, Endres MG. Unified contraction algorithm for multi-baryon correlators on the lattice. *Comput Phys Commun.* (2013) **184**:117. doi: 10.1016/j.cpc.2012.09.004
62. Doi T, Aoki S, Hatsuda T, Ikeda Y, Inoue T, Ishii N, et al. Exploring three-nucleon forces in lattice QCD. *Prog Theor Phys.* (2012) **127**:723–38. doi: 10.1143/PTP.127.723
63. Aoki S, Iritani T, Yazaki K. Hermitizing the HAL QCD potential in the derivative expansion. *PTEP.* (2020) **2**:023. doi: 10.1093/ptep/ptz166
64. McIlroy C, Barbieri C, Inoue T, Doi T, Hatsuda T. Doubly magic nuclei from lattice QCD forces at M_PS =469 MeV/c^2. *Phys Rev C.* (2018) **97**:021303. doi: 10.1103/PhysRevC.97.021303
65. Inoue T, Aoki S, Charron B, Doi T, Hatsuda T, Ikeda Y, et al. Medium-heavy nuclei from nucleon-nucleon interactions in lattice QCD. *Phys Rev C.* (2015) **91**:011001. doi: 10.1103/PhysRevC.91.011001
66. Nemura H. Recent developments on LQCD studies of nuclear force. *Int J Mod Phys E.* (2014) **23**:1461006. doi: 10.1142/S0218301314610060
67. De Vries H, De Jager CW, De Vries C. Nuclear charge and magnetization density distribution parameters from elastic electron scattering. *Atom Data Nucl Data Tabl.* (1987) **36**:495–536. doi: 10.1016/0092-640X(87)90013-1
68. Angeli I, Marinova KP. Table of experimental nuclear ground state charge radii: an update. *Atom Data Nucl Data Tabl.* (2013) **99**:69–95. doi: 10.1016/j.adt.2011.12.006
69. Inoue T, Aoki S, Doi T, Hatsuda T, Ikeda Y, Ishii N, et al. Equation of state for nucleonic matter and its quark mass dependence from

the nuclear force in lattice QCD. *Phys Rev Lett.* (2013) **111**:112503. doi: 10.1103/PhysRevLett.111.112503
70. Akmal A, Pandharipande VR, Ravenhall DG. The equation of state of nucleon matter and neutron star structure. *Phys Rev C.* (1998) **58**:1804–28. doi: 10.1103/PhysRevC.58.1804
71. Inoue T. Strange nuclear physics from QCD on lattice. *AIP Conf Proc.* (2019) **2130**:020002. doi: 10.1063/1.5118370
72. Doi T, Iritani T, Aoki S, Gongyo S, Hatsuda T, Ikeda Y, et al. Baryon interactions from lattice QCD with physical quark masses-Nuclear forces and ΞΞ forces. *EPJ Web Conf.* (2018) **175**:05009. doi: 10.1051/epjconf/201817505009
73. Park A, Lee SH, Inoue T, Hatsuda T. Baryon-baryon interactions at short distances-constituent quark model meets lattice QCD. *Eur Phys J A.* (2019) **56**:93. doi: 10.1140/epja/s10050-020-00078-z
74. Jaffe RL. Perhaps a stable dihyperon. *Phys Rev Lett.* (1977) **38**:195–8. doi: 10.1103/PhysRevLett.38.195
75. Beane SR, Chang E, Detmold W, Joo B, Lin HW, Luu TC, et al. Evidence for a bound H-dibaryon from lattice QCD. *Phys Rev Lett.* (2011) **106**:162001. doi: 10.1103/PhysRevLett.106.162001
76. Goldman JT, Maltman K, Stephenson GJ Jr., Schmidt KE, Wang F. Strangeness-3 dibaryons. *Phys Rev Lett.* (1987) **59**:627. doi: 10.1103/PhysRevLett.59.627
77. Oka M. Flavor octet dibaryons in the Quark model. *Phys Rev D.* (1988) **38**:298. doi: 10.1103/PhysRevD.38.298
78. Dyson F, Xuong NH. Y=2 states in Su(6) theory. *Phys Rev Lett.* (1964) **13**:815–7. doi: 10.1103/PhysRevLett.13.815
79. Zhang ZY, Yu YW, Shen PN, Dai LR, Faessler A, Straub U. Hyperon nucleon interactions in a chiral SU(3) quark model. *Nucl Phys A.* (1997) **625**:59–70. doi: 10.1016/S0375-9474(97)00033-X
80. Kamae T, Fujita T. Possible existence of a deeply bound delta-delta system. *Phys Rev Lett.* (1977) **38**:471–5. doi: 10.1103/PhysRevLett.38.471
81. Adlarson P, Adolph C, Augustyniak W, Baru V, Bashkanov M, Bergmann FS, et al. ABC effect in basic double-pionic fusion–observation of a new resonance? *Phys Rev Lett.* (2011) **106**:242302. doi: 10.1103/PhysRevLett.106.242302
82. Gongyo S, Sasaki K, Aoki S, Doi T, Hatsuda T, Ikeda Y, et al. Most strange dibaryon from lattice QCD. *Phys Rev Lett.* (2018) **120**:212001. doi: 10.1103/PhysRevLett.120.212001
83. Iritani T, Aoki S, Doi T, Etminan F, Gongyo S, Hatsuda T, et al. $N\Omega$ dibaryon from lattice QCD near the physical point. *Phys Lett B.* (2019) **792**:284–9. doi: 10.1016/j.physletb.2019.03.050
84. Morita K, Gongyo S, Hatsuda T, Hyodo T, Kamiya Y, Ohnishi A. Probing ΩΩ and $p\Omega$ dibaryons with femtoscopic correlations in relativistic heavy-ion collisions. *Phys Rev C.* (2020) **101**:015201. doi: 10.1103/PhysRevC.101.015201
85. Etminan F, Nemura H, Aoki S, Doi T, Hatsuda T, Ikeda Y, et al. Spin-2 $N\Omega$ dibaryon from lattice QCD. *Nucl Phys A.* (2014) **928**:89–98. doi: 10.1016/j.nuclphysa.2014.05.014
86. Adam J, Adamczyk L, Adams J, Adkins K, Agakishiev G, Aggarwal M, et al. The Proton-Ω correlation function in Au+Au collisions at $\sqrt{s_{NN}}$ = 200 GeV. *Phys Lett B.* (2019) **790**:490–7. doi: 10.1016/j.physletb.2019.01.055

Conflict of Interest: The authors declare that the research was conducted in the absence of any commercial or financial relationships that could be construed as a potential conflict of interest.

Copyright © 2020 Aoki and Doi. This is an open-access article distributed under the terms of the Creative Commons Attribution License (CC BY). The use, distribution or reproduction in other forums is permitted, provided the original author(s) and the copyright owner(s) are credited and that the original publication in this journal is cited, in accordance with accepted academic practice. No use, distribution or reproduction is permitted which does not comply with these terms.

frontiers in Physics

ORIGINAL RESEARCH
published: 14 February 2020
doi: 10.3389/fphy.2019.00251

Description of Four- and Five-Nucleon Systems by Solving Faddeev-Yakubovsky Equations in Configuration Space

Rimantas Lazauskas[1]* *and Jaume Carbonell*[2]

[1] IPHC, IN2P3-CNRS/Université de Strasbourg BP 28, Strasbourg, France, [2] Université Paris-Saclay, CNRS/IN2P3, IJCLab, Orsay, France

The Faddeev-Yakubovsky equations constitute a rigorous formulation of the quantum mechanical N-body problem in the framework of non-relativistic dynamics. They allow the exact solutions of the Schrödinger equation for bound and scattering states to be obtained. In this review, we will present the general formalism as well as the numerical tools we use to solve Faddeev-Yakubovsky equations in configuration space. We will consider in detail the description of the four- and five-nucleon systems based on modern realistic nuclear Hamiltonians. Recent achievements in this domain will be summarized. Some of the still controversial issues related with the nuclear Hamiltonians as well as the numerical methods traditionally employed to solve few-nucleon problems will be highlighted.

Keywords: Faddeev-Yakubovsky equations, four-nucleon system, five-nucleon systems, few-body collisions, scattering observables

OPEN ACCESS

Edited by:
Laura Elisa Marcucci,
University of Pisa, Italy

Reviewed by:
Sonia Bacca,
Johannes Gutenberg University Mainz, Germany
Hiroyuki Kamada,
Kyushu Institute of Technology, Japan

***Correspondence:**
Rimantas Lazauskas
rimantas.lazauskas@iphc.cnrs.fr

Specialty section:
This article was submitted to Nuclear Physics, a section of the journal Frontiers in Physics

Received: *25 October 2019*
Accepted: *24 December 2019*
Published: *14 February 2020*

Citation:
Lazauskas R and Carbonell J (2020) Description of Four- and Five-Nucleon Systems by Solving Faddeev-Yakubovsky Equations in Configuration Space. Front. Phys. 7:251. doi: 10.3389/fphy.2019.00251

1. INTRODUCTION

The solution of the Faddeev-Yakubovsky (FY) equations is an extremely challenging task from both the intellectual and technical points of view. The fast growth in the complexity of this problem with the number of interacting nucleons (A) makes progress in solving these equations relatively slow [1]. During the last twenty years, we have witnessed the emergence of the full solution—bound and scattering states—of the four-nucleon problem [2, 3] and only very recently have the first solutions for A = 5 [4–6] been published.

Although the four-boson bound problem was already formulated—and solved with S-wave interaction—in [2], the first converged result employing realistic NN interactions for the A = 4 bound state (^{4}He) took another 10 years to achieve [3].

The first solution of the scattering problem for the elastic 1+3, 2+2, and 1+3→ 2+3 rearrangement channels within the isospin approximation and S-wave interactions dated from 1998 [7], and it took twenty years more to obtain a full solution of the four-nucleon scattering problem with (i) realistic interactions [8–10] (ii) including charge-dependent (CD) and non local terms [11], (iii) Coulomb effects [12–15], (iv) three- and four-body breakup amplitudes [13, 16–18], and (v) a proper *ab-initio* determination of the 4N resonant states (e.g., 4n or ^{4}H) as S-matrix poles in the complex energy plane [6, 19–23]. There remains only the computation and analysis of the three- and four-body breakup differential cross-sections, since only the integrated cross-sections are nowadays available.

The A = 4 schematic chart is displayed in the left panel of **Figure 1**. It comprises five different charge states (Z = 0, 1, 2, 3, 4), including a single bound state (^{4}He) as well as five two-cluster scattering channels (n-^{3}H, n-^{3}He, p-^{3}H, ^{2}H-^{2}H, p-^{3}He denoted in an olive color), several three-body (in blue) and four-body (in black) break-up thresholds, and numerous—well-identified or questioned—low-energy resonances. The A = 4 sector presents the simplest case, revealing in practice all the phenomena of the theoretical nuclear physics: the presence of several thresholds and resonances. As an example, the continuum of the ^{4}He nucleus contains almost degenerate n-^{3}He and p-^{3}H thresholds, with an ^{4}He resonant state situated in between whose position must be accurately determined since it strongly modifies the scattering in both channels and thus constitutes a serious challenge for all realistic NN interaction models [8, 26]. Although still far from the intricacy of heavy nuclei, one can say that, in some sense, the nuclear complexity really starts at A = 4.

Solving the A = 5 problem represents a redoubtable technical and numerical difficulty with respect to the A = 4 case. However, the A = 5 chart is simpler than the A = 4 one due to the absence of the A = 5 bound state and of ^{3,5}Li and/or ^{4}Be targets: the number of charge states effectively investigated is limited to three (Z = 1, 2, 3) since the experimentally inaccessible 5n and 4p states raise less interest. There are four two-body scattering channels (n-^{4}He, ^{2}H-^{3}H, ^{2}H-^{3}He, and p-^{4}He, also denoted in olive), some of them, like the ^{2}H+^{3}H $\rightarrow$ n+^{4}He fusion reaction, of paramount importance in nuclear physics and in the stellar nucleosynthesis cycle. In contrast, the number of three- and four-body breakup thresholds (in blue) is sensibly larger. This is illustrated in the right panel of **Figure 1**, where the "nuclear chart" corresponding to A = 5 is displayed. The FY solutions for A = 5 are at present limited to low energy (S- and P-waves) n-^{4}He elastic scattering [4, 5] and in computing the lowest resonant states of ^{5}H [6], in both cases using realistic interactions. Some disagreements with the R-matrix analysis were found in both systems. The fusion reaction ^{2}H+^{3}H $\rightarrow$ n+^{4}He has not yet been solved within the FY framework, but a recent pioneering result has been achieved within the NCSMC approach [27].

We would like to point out from the very beginning that other rigorous schemes were proposed for solving the *ab initio* N-body problem. One of the most relevant is that provided by the AGS equations [28], which is strictly equivalent to the FY formalism and has produced very accurate results for the three- and four-nucleon problem, always in momentum space [29, 30]. We also emphasize that such rigorous mathematical schemes are not necessary when dealing with bound states or simple $1 + (N - 1)$ elastic scattering processes and that the Schrödinger equation can then be directly solved by several methods.

It is worth also mentioning that, aside from FY solutions in configuration space, on which we report, there are several competing approaches to solving the A = 4 and A = 5 problems that have produced very interesting and, in some cases, pioneering results. Any attempt at an exhaustive reference list is beyond our capabilities. However, we would like to point out among them the GFMC [31, 32], variational approaches with Hyperspherical Harmonics [33, 34] or a Gaussian basis [35], RGM [36], NCSM and NCSMC [27, 37], and Lorentz Integral Transform [38], which can produce very accurate results, in some cases well beyond the technical capabilities of the Faddev-Yakubovsky approach. However, the Faddeev-Yakubovsky partition of the wave function is interesting for increasing the numerical convergence of the results or is even unavoidable for an appropriate implementation of the boundary conditions [35, 39]. The interested reader can find a more thorough bibliography in some devoted reviews [40].

In this contribution, we will concentrate on some particular issues that our previous works had not treated with the required detail. We will mostly present results related to the four-nucleon scattering problem, obtained by solving the Faddeev-Yakubovsky equations in configuration space, and will add some recent results on the five-nucleon n-^{4}He low-energy scattering. In section 2, we will detail the theoretical aspects of the four-body equations. section 3 is devoted to the discussion of 4N scattering results with different realistic models. Some concluding remarks are collected in the Conclusions.

2. THEORETICAL DESCRIPTION

In what follows, we will present the general formalism as well as the numerical methods relevant to the solution of the four-body problem in configuration space. Some results related with neutron scattering on ^{4}He that we obtained by solving five-body FY equations will also be discussed; however, and due to its complexity, the five-body formalism will not be presented here. For this particular case, a interested reader may refer to Sasakawa [41], Lazauskas [4, 5], and Lazauskas and Song [42].

2.1. The Four-Body FY Equations

The derivation of the four-body Faddeev-Yakubovsky equations starts by defining the three-body-like Faddeev components (FC) ψ_{ij}, which are associated to each interacting pair of particles (ij):

$$\psi_{ij} = G_0 V_{ij} \Psi \;\; (i < j). \tag{1}$$

Here, $G_0 = (E - H_0)^{-1}$ denotes the free four-body Green's function, associated with the four-body kinetic energy operator H_0 and the four-body energy E, while V_{ij} denotes the two-body potential between the particles i and j. Naturally, for a four-body system, there exist six different three-body-like Faddeev components. In terms of these, one can define two types of the so-called Faddeev-Yakubovsky component (FYCs), denoted, respectively type-K and type-H components, by the relations:

$$\begin{aligned} \mathcal{K}^l_{ij,k} &= G_{ij} V_{ij} (\psi_{jk} + \psi_{ik}) \qquad (i < j); \\ \mathcal{H}^{kl}_{ij} &= G_{ij} V_{ij} \psi_{kl} \qquad (i < j; \quad k < l). \end{aligned} \tag{2}$$

In this equation, $G_{ij} = (E - H_0 - V_{ij})^{-1}$ denotes the interacting four-body Green's function associated with the interaction term between particles i and j. By permuting particle indexes, one may construct 12 independent components of type-K as well as six independent components of type-H. The asymptotes

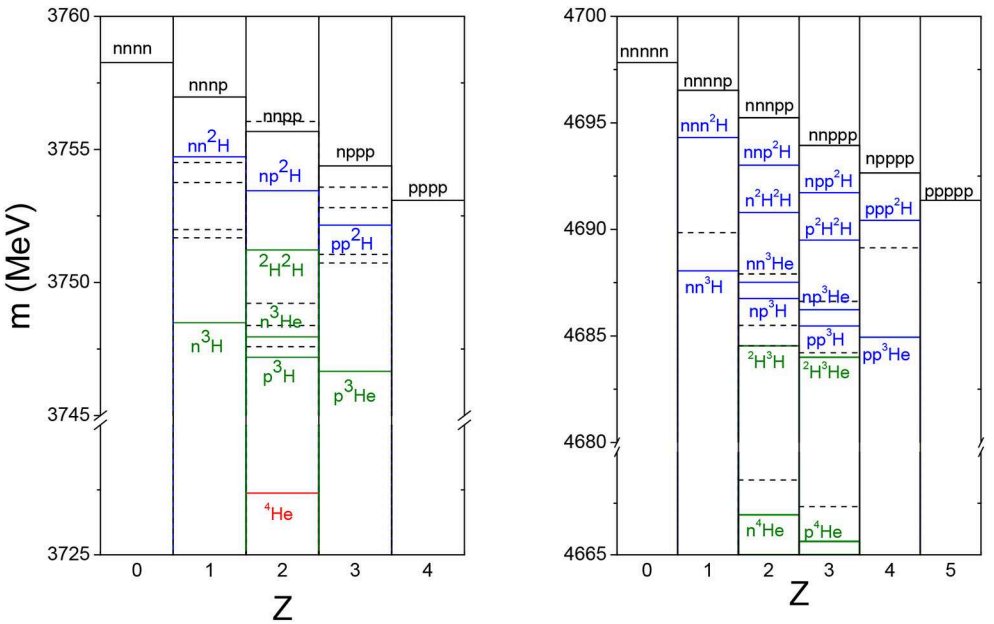


FIGURE 1 | Schematic nuclear chart for A = 4 **(left)** and A = 5 **(right)** systems displaying the different thresholds (full lines). The two-cluster thresholds are depicted in an olive color, many-cluster thresholds in blue and black. Some selected resonant states are depicted by dashed lines, indicating approximate positions of their centroids, as predicted by R-matrix analysis by Tilley et al. [24] and Tilley et al. [25]. The widths of the resonant states are disregarded.

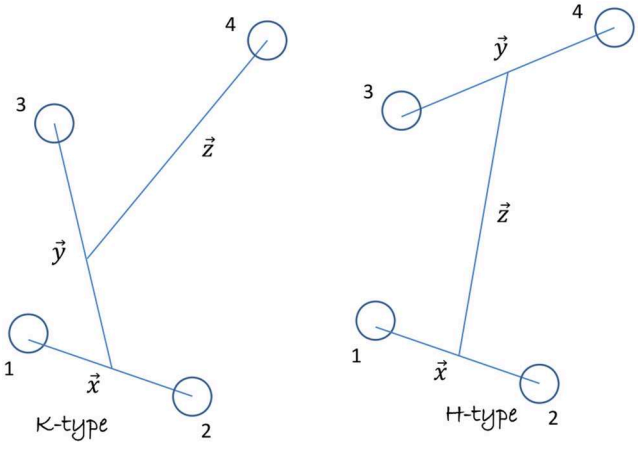


FIGURE 2 | Four-particle partitions $\mathcal{K}^4_{12,3}$ and $\mathcal{H}^{34}_{12}$, together with the associated Jacobi coordinate sets.

of the components $\mathcal{K}^l_{ij,k}$ and $\mathcal{H}^{kl}_{ij}$ incorporate all the possible 3+1 and the 2+2 particle channels, respectively, as illustrated in **Figure 2**. Here, we are interested in nuclear problems, involving protons and neutrons. Within the isospin formalism, neutrons and protons are treated as isospin-degenerate states of the same particle: the nucleon. Then, the FY components, which differ by the order of the particle indexing, are related due to the symmetry of particle permutation. There remain only two independent FYCs, which are further denoted $\mathcal{K} \equiv \mathcal{K}^4_{12,3}$ and $\mathcal{H} \equiv \mathcal{H}^{34}_{12}$ by omitting their particle indexes. For FY equations for a case of four identical particles (see [11, 43]):

$$\begin{aligned}(E - H_0 - V_{12})\,\mathcal{K} &= V_{12}(P^+ + P^-)\left[(1+Q)\mathcal{K} + \mathcal{H}\right],\\ (E - H_0 - V_{12})\,\mathcal{H} &= V_{12}\tilde{P}\left[(1+Q)\mathcal{K} + \mathcal{H}\right],\end{aligned} \tag{3}$$

Each FY component $\mathcal{F} = (\mathcal{K}, \mathcal{H})$ has its natural expression in its proper set of Jacobi coordinates, as depicted in **Figure 2**. However, they may be as well-considered as a function of any set of Jacobi coordinates and converted for one coordinate set into another one by using the particle permutation operators, which are summarized as follows:

$$\begin{aligned}P^+ &= (P^-)^{-1} \equiv P_{23}P_{12},\\ Q &\equiv -P_{34},\\ \tilde{P} &\equiv P_{13}P_{24} = P_{24}P_{13},\end{aligned}$$

where P_{ij} indicates the operator permuting particles i and j.

In terms of the FYCs, the total wave function of an $A = 4$ system is given by:

$$\begin{aligned}\Psi = &\left[1 + (1 + P^+ + P^-)Q\right](1 + P^+ + P^-)\mathcal{K}\\ &+ (1 + P^+ + P^-)(1 + \tilde{P})\mathcal{H}.\end{aligned} \tag{4}$$

Each FY component $\mathcal{F} = (\mathcal{K}, \mathcal{H})$ is considered as a function, described in its proper set of Jacobi coordinates, as depicted in **Figure 2**.

The angular, spin, and isospin dependence of these components are described using the tripolar harmonics $\mathcal{Y}_\alpha(\hat{x}, \hat{y}, \hat{z})$, i.e.,:

$$\langle \vec{x}\vec{y}\vec{z}|\mathcal{F}\rangle = \sum_\alpha \frac{\mathcal{F}_\alpha(xyz)}{xyz}\,\mathcal{Y}_\alpha(\hat{x}, \hat{y}, \hat{z}). \tag{5}$$

The quantities $\mathcal{F}_\alpha(xyz)$ are called the regularized radial FY amplitudes, where the label α holds for a set of 10 intermediate quantum numbers describing a given four-nucleon quantum state $(J^\pi, T, \mathcal{T}_z)$. By using the LS-coupling scheme, the tripolar harmonics are defined for components of K and H type, respectively, by

$$\mathcal{Y}_{\alpha_\mathcal{K}} \equiv \left\{\left[\left(l_x l_y\right)_{l_{xy}} l_z\right]_L \left[\left((s_1 s_2)_{s_x}\, s_3\right)_{S_3}\, s_4\right]_S\right\}_{J^\pi \mathcal{M}} \otimes \left[\left((t_1 t_2)_{t_x}\, t_3\right)_{T_3}\, t_4\right]_{T\mathcal{T}_z}, \quad (6)$$

$$\mathcal{Y}_{\alpha_\mathcal{H}} \equiv \left\{\left[\left(l_x l_y\right)_{l_{xy}} l_z\right]_L \left[(s_1 s_2)_{s_x}\, (s_3 s_4)_{s_y}\right]_S\right\}_{J^\pi \mathcal{M}} \otimes \left[(t_1 t_2)_{t_x}\, (t_3 t_4)_{t_y}\right]_{T\mathcal{T}_z}. \quad (7)$$

The FY equations were originally derived to treat systems of particles interacting by pairwise short-range interactions. Nevertheless, these equations can be modified with relative ease to include three-body forces (3BF). This has been achieved for the first time in the work of the Bochum group [44]. In implementing three-nucleon forces, we have followed quite a similar but nevertheless slightly optimized strategy [43]. It is worth noticing a recent work by Kamada [45] presenting a systematic derivation of the four-body FY equations by including three-body forces.

2.2. Treatment of the Coulomb Interaction

One of the more delicate issues in solving few-particle scattering problems is the proper treatment of the Coulomb interaction. Due to the long-range nature of Coulomb potential in coordinate space, or, equivalently, due to its singular behavior in momentum space, the standard approach of the scattering theory based on expansion in free waves in the asymptote region is not appropriate. Indeed, the FY equations, as presented in the previous section, are formulated for short-range interactions and are not appropriate for handling scattering problems including Coulomb interaction.

For a three-body system, the proper mathematical formalism to include Coulomb interactions was proposed by Merkuriev [46]. This formalism is valid both for attractive and for repulsive Coulomb forces. The problem becomes considerably simpler if only one repulsive Coulomb interaction is present (only two out of three particles are charged by equal sign charges) like for a proton-deuteron scattering. For this particular case, there are several alternative prescriptions to handle Coulomb interaction force [47–52]. They are based on inserting, fully or partially, the Coulomb potential $V_C(x, y)$, in the left-hand side of the Faddeev equation

$$[E - H_0 - V(x) - V_C(x, y)]\Psi(x, y) = (V(x) - V_c^l(x, y))(P^+ + P^-)\Psi(x, y). \quad (8)$$

In this way, the long-range part of the Coulomb interaction $V_c^l(x, y)$ is subtracted on the right-hand side of the Faddeev equation and is appropriately compensated by the term $V_C(x, y)$ on the left-hand side, thus accounting for the Coulomb asymptotic wave function in the scattering channel.

On the contrary, for an N>3 case, no such modifications of FY equations existed prior to our work. Only in the work of Filikhin and Yakovlev [53] has this problem been partly addressed by being limited to S-wave approximation.

2.2.1. Formulation, *à la* Merkuriev [46]

In this work, we present two alternatives for how to treat Coulomb interaction for N>3 systems: following the strategy of Merkuriev, and following the method proposed by Sasakawa and Sawada [48]. It is worth mentioning that many alternative treatments of the repulsive Coulomb interaction, corresponding to the three-body approaches of Noble [47] and Chen et al. [50], may be formally spanned under Merkuriev's approach by considering different forms of splitting the Coulomb interaction into short- and long-range parts.

In this section, we propose a generalization of the four-body FY equations following Merkurievs approach to the three-body system [46]. We start by splitting the Coulomb potential V_{ij}^C into two parts: short-range V_{ij}^s and long-range V_{ij}^l, such that $V_{ij}^C = V_{ij}^s + V_{ij}^l$. This is realized by means of appropriate cut-off functions $\chi^{s_a}(x_{ij}, y_a, z_a)$, depending on the radial parts of Jacobi coordinates as they are depicted in **Figure 2**:

$$V_{ij}^{s_a} = \chi_a^s(x_{ij}, y_a, z_a) V^C(x_{ij}). \quad (9)$$

We introduce three different forms of splitting

$$V_{ij}^C(x_{ij}) = V_{ij}^{l_K}(x_{ij}, y_{ij,k}) + V_{ij}^{s_K}(x_{ij}, y_{ij,k}), \quad (10)$$

$$V_{ij}^C(x_{ij}) = V_{ij}^{l_H}(x_{ij}, y_{lk}) + V_{ij}^{s_H}(x_{ij}, y_{lk}), \quad (11)$$

$$V_{ij}^C(x_{ij}) = V_{ij}^{l_\rho}(x_{ij}, \rho_{ij}) + V_{ij}^{s_\rho}(x_{ij}, \rho_{ij}), \quad (12)$$

and, following the steps leading to three-body Merkuriev equations, we reformulate the four-body equations as follows:

$$(E - H_0 - V_{12} - V_{13}^{l_K} - V_{23}^{l_\mathcal{K}} - V_{14}^{l_\rho} - V_{24}^{l_\rho} - V_{34}^{l_\rho})\mathcal{K}_{12,3}^4 = V_{12}^{s_K}(\mathcal{K}_{23,1}^4 + \mathcal{K}_{31,2}^4) + V_{12}^{s_\rho}(\mathcal{K}_{23,4}^1 + \mathcal{K}_{31,4}^2 + \mathcal{H}_{23}^{14} + \mathcal{H}_{31}^{24}), \quad (13)$$

$$(E - H_0 - V_{12} - V_{34}^{l_H} - V_{13}^{l_\rho} - V_{23}^{l_\rho} - V_{14}^{l_\rho} - V_{24}^{l_\rho})\mathcal{H}_{12}^{34} = V_{12}^{s_H}\mathcal{H}_{34}^{12} + V_{12}^{s_\rho}(\mathcal{K}_{34,1}^2 + \mathcal{K}_{34,2}^1). \quad (14)$$

One may easily verify that, by summing these equations, one obtains Schrödingers equation for the total wave function of the system : $\Psi = \sum \mathcal{K}_{ij,k}^l + \sum \mathcal{H}_{ij}^{lk}$. On the other hand, the asymptotes of the different binary channels become perfectly separated. To demonstrate this feature, let us investigate the FY component $\mathcal{K}_{12,3}^4$ associated with Equation (13). This component is meant to incorporate the asymptote of the (123)+4 particle channel and is directly coupled with the components $\mathcal{K}_{23,4}^1$, $\mathcal{K}_{31,4}^2$, $\mathcal{H}_{23}^{14}$, and $\mathcal{H}_{31}^{24}$, which are not proper to the (123)+4 particle channel. Nevertheless, in Equation (13) this coupling is ensured only by the short-range interaction $V_{12}^{s_\rho}$. It remains coupled with the components $\mathcal{K}_{23,1}^4$ and $\mathcal{K}_{31,2}^4$ by the long-range interaction terms, but all these components belong to the same (123)+4

particle channel. Very similar behavior is preserved by the component $\mathcal{H}^{34}_{12}$, associated with Equation (14). This component contributes to the asymptote of the (12)+(34) particle channel and is coupled by a long-range interaction term only with the component $\mathcal{H}^{12}_{34}$ belonging to the same binary channel. Therefore, the modified FY Equations (13)-(14) uncouple the asymptotes belonging to different binary scattering channels even when the Coulomb interaction is present. Their uncoupling properties are in this way similar to the original FY equations involving only short-range interactions.

2.2.2. Alternative Formulation, *à la* Sasakawa and Sawada [48]

For each FYC, one introduces an auxiliary long-range potential in their asymptote describing an effective Coulomb repulsion between the fragments of the associated binary channel $V^l_{z_\alpha}(z_\alpha)$, such that:

$$V^l_{z_\alpha}(z_\alpha \to \infty) = \frac{C_\alpha}{z_\alpha}, \tag{15}$$

where, for a type-K component, defined by the particle ordering $\alpha = (^4_{12,3})$:

$$C^4_{12,3} \equiv C_4 = \sqrt{\frac{2m_4(M-m_4)}{Mm}}; \tag{16}$$

and for type-H component with $\alpha = (^{34}_{12})$,

$$C^{34}_{12} \equiv C^{12}_{34} = \sqrt{\frac{2(m_1+m_2)(m_3+m_4)}{Mm}}. \tag{17}$$

We denote by m_i the mass of nucleon i, and by $M = \sum_i m_i$, the total mass of the system. FY equations are reformulated by subtracting this long-range potential in their left-hand side. These auxiliary potential terms are compensated by introducing appropriate terms in the right-hand side of FY equations:

$$\begin{aligned}
&(E - H_0 - V_{12} - q_4(q_1+q_2+q_3)V^l_{z_4})\mathcal{K}^4_{12,3} \\
&\quad = V_{12}(\mathcal{K}^4_{23,1} + \mathcal{K}^4_{31,2} + \mathcal{K}^1_{23,4} + \mathcal{K}^2_{31,4} + \mathcal{H}^1_{23,4} + \mathcal{H}^2_{31,4}), \\
&\quad -q_1q_2(V^l_{z_1}\mathcal{K}^1_{23,4} + V^l_{z_2}\mathcal{K}^2_{31,4} + V^l_{z^{14}_{23}}\mathcal{H}^{14}_{23} + V^l_{z^{24}_{13}}\mathcal{H}^{24}_{13})
\end{aligned} \tag{18}$$

$$\begin{aligned}
&(E - H_0 - V_{12} - (q_1+q_2)(q_3+q_4)V^l_{z^4_{12,3}})\mathcal{H}^{34}_{12} \\
&\quad = V_{12}(\mathcal{K}^{12}_{34} + \mathcal{K}^2_{34,1} + \mathcal{K}^1_{34,2}) - q_1q_2(V^l_{z_2}\mathcal{K}^2_{34,1} + V^l_{z_1}\mathcal{K}^1_{34,2}),
\end{aligned} \tag{19}$$

where q_i is the charge of particle i. The auxiliary potential terms $V^l_{z_\alpha}(z_\alpha)$ in the left- and right-hand sides of equations are balanced in such a way that they compensate each other once all 18 FY equations are added to recover Schrödingers equation.

Further, we are interested in uncoupling of the wave components describing different two-cluster scattering channels. To see how well these components uncouple in their asymptotes, let us analyze the first equation associated with a component $\mathcal{K}^4_{12,3}$. In the right-hand side of this equation, components $\mathcal{K}^1_{23,4}, \mathcal{K}^2_{31,4}, \mathcal{H}^{14}_{23}$, and $\mathcal{H}^{24}_{13}$ are present, which are not proper to the (123) + 4 elastic channel of the component $\mathcal{K}^4_{12,3}$. As an example, component $\mathcal{K}^1_{23,4}$, associated with the (234) + 1 scattering channel, is coupled with the $\mathcal{K}^4_{12,3}$ in this equation by the potential term

$$V_{12} - q_1q_2V^l_{z_1} = q_1q_2\left(\frac{1}{x_{12}} - \frac{\sqrt{\frac{2m_1(M-m_1)}{Mm}}}{z_1}\right), \tag{20}$$

which behaves as $O((z_1)^{-3})$ in the $z_1 >> \max(x_{23}, y^4_{23})$ region, which defines the asymptote of the (234) + 1 scattering channel. One may reach the same conclusion relative to the coupling between the components of types $\mathcal{K}$ and $\mathcal{H}$. Thus, the asymptotic coupling between the components belonging to different binary channels is realized by the effective potential terms decaying as $O((z_1)^{-3})$ and thus is strongly suppressed relative to the original Coulomb potential. One should mention, however, that such uncoupling is not ensured for the case when breakup in three (or four) clusters is energetically allowed.

By comparing the approach of Equations (13)–(14) to the one following Equations (18)–(19), one may readily conclude that, in the first approach, the FY components are more properly uncoupled by the exponentially decaying potential terms. Nevertheless, the second formalism requires less effort implement numerically. In the following section, we will present some results demonstrating that these two approaches work equally well for the nuclear problem, where only repulsive Coulomb interactions are present.

3. RESULTS

3.1. Models

The results presented in this study are obtained using realistic nuclear Hamiltonians. The realistic nucleon-nucleon (NN) potentials contain several adjustable parameters, which are tuned in order to reproduce experimental NN scattering data and the properties of a deuteron with very high accuracy. Three different NN potentials, Argonne v_{18} (AV18) [54], INOY04 [55], and Idaho N3LO (I-N3LO) [56], are used in this work. The AV18 model is a phenomenological potential, which is defined in configuration space and is local. The longest-range part of the AV18 potential is determined by one-pion exchange and electromagnetic NN interaction terms, but its short-range part is fully phenomenological.

The locality of the NN force assumed in the pioneering high-accuracy NN interaction models was due to numerical convenience. Nevertheless, it was soon realized that such models suffer from the underbinding problem when describing $A > 2$ nuclei [57–59]. The inclusion of non-local interaction terms allows the off-shell structure of the potential to change and may strongly affect the description of the $A > 2$ sector. This feature has been explored by Doleschall [55, 60, 61], who constructed a set of phenomenological potentials. The internal parts of these potentials are built by employing highly non-local form factors (the INOY04 model non-locality range is approximately 2 fm), whereas their outside parts are local and are defined by the Yukawa potential representing one-pion exchange. The NN interaction models of Doleschall et al., and in particular INOY04, were able to overcome the lack of binding energy in

TABLE 1 | Parameters of the local N2LO 3BF employed in this work.

Λ (MeV)	c_D	c_E	c_1	c_3	c_4	References
350	−0.2	0.205	−0.81	−3.2	5.4	[72]
400	−0.2	0.098	−0.81	−3.2	5.4	[72]
450	−0.2	−0.016	−0.81	−3.2	5.4	[72]
500	−0.0411	0.945	−0.81	−3.2	5.4	[71]
500	−0.2	−0.205	−0.81	−3.2	5.4	[70]

In the last column, a reference to the original work where the values of the parameters c_D and c_E were established is provided.

TABLE 2 | Comparison of the p-^{3}He singlet ($J^\pi = 0$) and triplet ($J^\pi = 1$) scattering lengths calculated by the approach of Equations (13)–(14) to those obtained by solving Equations (18)–(19).

J^π	0^+	1^+
Equations (13)–(14)	11.92	9.346
Equations (18)–(19)	11.86	9.302

Scattering lengths are provided in units of fm.

the three-nucleon sector, namely ^{3}H and ^{3}He, without explicitly using three-nucleon forces and still accurately reproduce NN observables [11, 55].

From the early 2000s, inspired by the works of Weinberg [62], a new generation of nuclear forces appeared based on chiral effective field theory [63, 64]. Chiral effective field theory provides a powerful framework with which to link the NN potentials with the pion-nucleon ones but, at the same time, construct systematically, order by order, an improvable scheme to build consistent multinucleon forces as well as control the uncertainties in their determination. The chiral NN interaction model developed up to next-to-next-to-next-to-leading order by the Idaho group [56], denoted here as I-N3LO, remains one of the most successful descriptions of the NN interaction.

Realistic nucleon-nucleon interaction models are nowadays able to describe all the available scattering data in the two nucleon sector almost perfectly. Studies of heavier nuclei are therefore required in order to test and validate these interaction models. However, calculations of the trinucleon binding energies already reveal an underbinding problem: most of the nucleon-nucleon potentials fail to reproduce binding energies of triton and ^{3}He. A single exception is provided by the INOY potentials, which, employing non-local form factors, are adjusted at NN level to also reproduce the binding energy of ^{3}H. Nevertheless, these models turn out to be too soft, compressing, and overbinding ^{4}He [11, 65], leading to high saturation density of the nuclear matter [66] as well as severe overbinding of heavier nuclei [67]. The natural remedy is the introduction of three-nucleon forces, which appear in any theoretically motivated nuclear interaction model. It should be noted that only models based on effective-field theory provide a systematic hierarchy between two-nucleon and multi-nucleon forces. Regardless of the three-nucleon interaction model, these forces have some adjustable parameters.

There are several different three-nucleon force models that can be used in conjunction with AV18 and the chiral effective field potentials of Epelbaum et al. [63] or Machleidt and Entem [64]. Notably, with AV18 NN potential, we will employ the Urbanna IX (UIX) three-nucleon interaction model of Pudliner et al. [68], adjusted in order to improve description of the three-nucleon binding energies as well as the nuclear matter saturation density.

In Navratil [69], a three-nucleon force employing local momentum-space regulators, and developed up to next-to-next-to-leading order was proposed. In Gazit et al. [70], two unknown coupling constants, c_D and c_E, of this 3BF were adjusted to reproduce triton binding energy and β-decay half-life simultaneously. In a recent work [71], it was found that the relation between the low-energy constants (LECs) c_D and c_E, determining the three-nucleon contact interaction and the two-nucleon contact axial current, was given erroneously. A new parametrization of the last force was also provided. In our work, we will essentially use the last parametrization of the force of Marcucci et al. [71] using cutoff $\Lambda = 500$ MeV (see **Table 1**). It is worth mentioning that the two parameterizations, one of Gazit et al. [70] and one of Marcucci et al. [71], provide almost identical predictions for all the nuclear observables considered here.

An alternative strategy to fix c_D and c_E coupling constants was followed by Roth et al. [72]. Those authors noticed that heavier nuclei are overbound when 3BF of Gazit et al. [70] is used. A new set of three-nucleon forces were proposed using lower cutoff values, $\Lambda = 350$, 400, and 450 MeV, which describe the binding energies of the medium mass nuclei along the dripline better.

For convenience, the different parameterizations of 3BF used in what follows in conjunction with I-N3LO NN interaction will be referred to by the cutoff value Λ regularizing this force. In **Table 1**, we provide the parameters of the different 3BFs tested in this work.

3.2. Coulomb Phaseshifts

As described in section 2.2, the implementation of the Coulomb interactions represents a real challenge for the few-nucleon scattering problem. Two different methods have been proposed to implement the Coulomb force in nucleon-trinucleon scattering. We present in **Tables 2**, **3** a comparison among these two approaches. One may see that, regardless of the fact that the method based on Equations (13)–(14) is formally more appropriate, in Practice, the two methods provide almost identical results. Even for p-^{3}He scattering length calculations, where the effect of Coulomb repulsion should be the most appreciable, the two methods provide indistinguishable results within the numerical accuracy. A small discrepancy might be still observed in calculating negative parity phaseshifts (see **Table 3** corresponding to $E_p = 2.25$ MeV), which might be related to the importance of the triton polarizations terms, while these terms are partly screened in the approach based on Equations (18)–(19).

3.3. Description of the Four-Nucleon Scattering

The main goal of theoretical nuclear physics is to construct a reliable model describing the nuclear structure and reactions.

TABLE 3 | The same as in **Table 2** but for the scattering phase shifts ($^{2s+1}L_J$) and mixing angles (ϵ^{J^π}) at $E_p = 2.25$ MeV, both presented in degrees.

	$^1S_0$	$^3S_1$	$^3D_1$	ϵ^{1^+}	$^3P_0$	$^1P_1$	$^3P_1$	ϵ^{1^-}	$^3P_2$
Equations (13)–(14)	−41.57	−35.49	−0.28	−0.58	7.74	17.75	10.84	8.43	16.41
Equations (18)–(19)	−41.50	−35.42	−0.28	−0.57	8.15	17.72	11.25	8.55	16.66

Realistic nucleon-nucleon interaction models are built to reproduce available data in two-nucleon sectors. In addition, three-nucleon forces are usually introduced and adjusted to reproduce the ground state binding energies of triton (^{3}H), ^{3}He, and ^{4}He. Nevertheless, the binding energies of the stable nuclei, appearing along the dripline, are strongly correlated and thus provide only limited insight into nuclear forces. Scattering experiments, allowing unbound structures far from the stability to be accessed, remain the richest tool to study the properties of the underlying nuclear interaction.

Three-nucleon systems have been extensively studied throughout the last two decades [73]. Realistic nuclear Hamiltonians provide a satisfactory description of the uttermost part of the trinucleon data. Still, there remain some discrepancies, like in the description of the analyzing powers (A_y-puzzle) and some breakup observables (space-star anomaly) [74, 75], which have not yet been addressed by any NN+3BF model. It is noteworthy that these problematic observables are relatively small, representing only a few percentiles of the total scattering cross-section.

Three-nucleon systems remain relatively simple, due to the absence of any thresholds (apart from the three-particle breakup one) or resonant structures in the continuum. The two experimentally accessible systems, ^{3}H and ^{3}He, are mirror systems and thus exhibit very similar properties. Four- and five-nucleon systems, accommodating several resonant states and a rich threshold structure in the continuum, therefore present interesting theoretical laboratories for testing the nuclear interactions.

The elastic neutron scattering on ^{3}H, being a process free from Coulomb interaction, is the simplest four-nucleon reaction to describe theoretically. Unfortunately, due to nuclear safety regulations, experiments with tritium are scarce. Nevertheless, some successful measurements were realized in the 1970s. In particular, very accurate measurement of the total neutron-tritium cross-section was realized by Phillips et al. [76].

In **Figure 3**, we compare our calculated results with the ones of this measurement. There are two important energy regions for the elastic neutron scattering on ^{3}H: the zero energy region (S-waves) and the region of P-wave resonances.

At very low energies, the process is dominated by neutron scattering in S-waves relative to the target. These waves are governed by the Pauli repulsion between the neutron projectile and those present in the tritium target. Due to this repulsion, the scattering process is mostly peripheral, and therefore the calculated scattering lengths strongly correlate with the size of the target nucleus and consequently with the predicted tritium binding energy. Thus, the nuclear interaction models that tend to underbind the triton overestimate the n-^{3}H cross-section at low energy. By adjusting the triton binding energy, either by means of three-nucleon force or by the presence of non-locality in NN interaction (INOY models), the agreement with the experimental n-^{3}H cross-section significantly improves in the zero-energy limit. It is worth noticing that some minor differences still remain between the models, i.e., the predictions of INOY04 or I-N3LO+3BF($\Lambda = 500$ MeV) agree with a lower bound of the zero-energy cross-section, whereas AV18+UIX agrees with an upper one. These differences could be resolved by comparing the calculated spin-dependent (a_0 and a_1) scattering lengths. Unfortunately, there is quite a large discrepancy between the measured coherent scattering lengths a_c, defined as $a_c = \frac{a_0}{4} + \frac{3a_1}{4}$, and the inferred spin-dependent values. The measurement of the coherent scattering length a_c constrains the values of a_1 and a_0 to a linear band, while the measurement of the total n-^{3}H cross-section constrains them in an elliptic one. The spin-dependent values a_i result from the intersection of these two bands, but their practical determination is not free of ambiguities due to experimental errors. This is illustrated in **Figure 4**, together with the predictions of the nuclear models considered.

The total neutron-triton cross-section peaks at around 3 MeV. This peak results from the interference of four broad negative parity resonant states present in the ^{4}H nucleus. The accurate description of the n-^{3}H cross-section in this resonance region turns out to be a very challenging problem for nuclear interaction models. Most of these models fail to provide sufficient attraction for negative parity states (essentially P-waves), providing a very flat structure. In this context, the role of 3BF is quite essential and far from trivial. First, by adding a 3BF that reproduces the triton binding energy, one automatically reduces the contribution of the partial cross-sections in the positive parity states $J^\pi = 0^+$ and 1^+. Then, the required increase in negative parity cross-section should fill the existing gap in the resonance region and compensate for the reduction from the positive parity state contribution.

Among the models described in **Figure 3**, UIX fails to boost the contribution from the negative parity states in the total cross-section. Therefore, the net effect is a reduction of the total cross-section in the resonance region. Of the three NN interaction models considered, I-N3LO provides the most attraction in the negative parity states. The three-nucleon interaction model with a cutoff $\Lambda = 500$ MeV further improves the agreement between the calculated and measured cross-sections, describing almost ideally the experimental data of Phillips et al. [76]. Notice, however, that the parameterizations of the same 3BF employing lower cutoff values from Roth et al. [72] are not so successful, underpredicting the total cross-section. It is also worth noting that the discrepancy in the resonance region is increased by reducing the value of the cutoff Λ. Very similar consequences are observed when calculating the binding energies of the P-shell nuclei [72].

The proton scattering on ^{3}He is a nuclear mirror process to neutron scattering on ^{3}H. The presence of Coulomb interaction makes the proton scattering on the ^{3}He cross-section diverge at small angles, so one is not able to study the cross-section of this process with the same ease as for the n-^{3}H case. Nevertheless, experimental differential cross-sections are much more abundant for the p-^{3}He case since they are easier to measure.

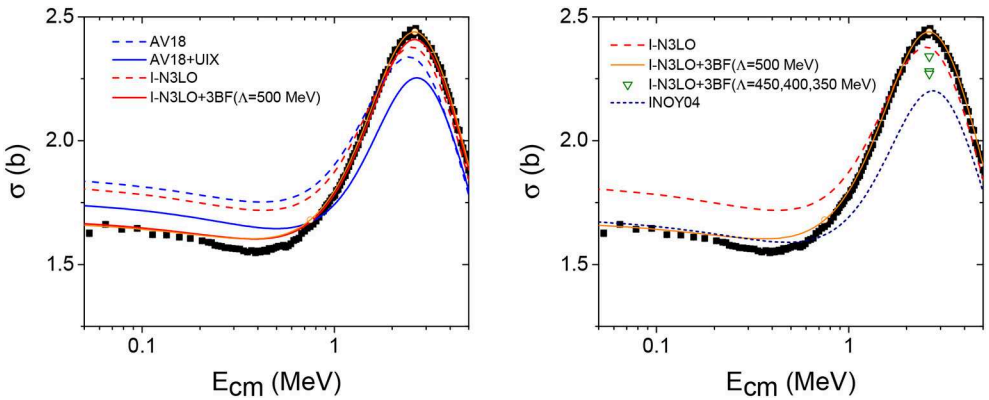


FIGURE 3 | Elastic neutron-^{3}H scattering cross-sections calculated using different combinations of *NN* and *NNN* interaction models. Theoretical results are compared with the experimental values of Phillips et al. [76].

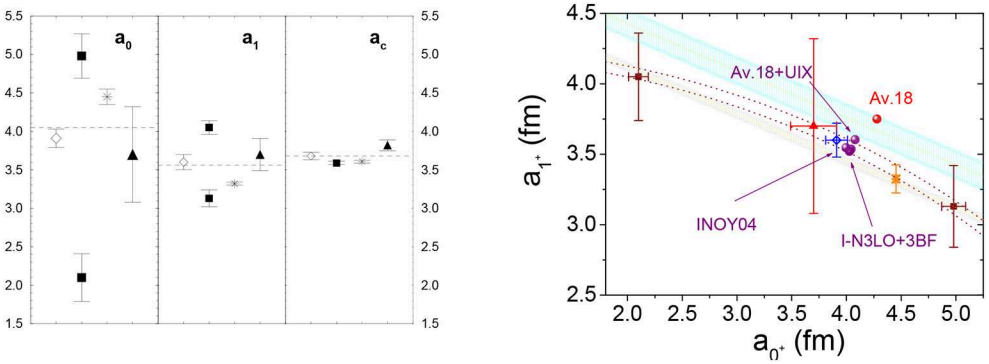


FIGURE 4 | (Left) Experimentally deduced singlet (a_0), triplet (a_1), and coherent (a_c) n-^{3}H scattering lengths. Diamonds from Seagrave et al. [77], up-triangles from Hammerschmied et al. [78], squares from Rauch et al. [79], and stars from Hale et al. [80]. **(Right)** Comparison of the spin-dependent scattering lengths a_i, with some theoretical predictions. The measurement of the total cross-section [76] constrains the allowed $a_1(a_0)$ values to the elliptic band region between the doted curves. The coherent scattering length measurements constrain $a_1(a_0)$ to a linear band region given by $4a_c = a_0 + 3a_1$. Notice that two coherent scattering length measurements, the upper band [78] and the lower band [79], are incompatible within their error bars, whereas Hammerschmied et al. [78] is also incompatible with the cross-section measurement of Phillips et al. [76].

We have displayed in **Figure 5** the calculated p-^{3}He scattering observables for an incident energy of 4.05 MeV. The same observables for protons of 5.54 MeV are displayed in **Figure 6**. Calculated results arrived at by employing Equations (13)–(14) to take Coulomb into account are compared with the available experimental data from McDonald et al. [81], Alley and Knutson [82], Fisher et al. [83], and Daniels et al. [84]. The energy region considered is still marked by the important contribution of the negative parity ^{4}Li resonances. Notably, due to the presence of the repulsive Coulomb interaction, these resonances manifest at slightly higher energies for the p-^{3}He case relative to the n-^{3}H one. In **Figure 5**, relevant for 4.05 MeV protons, the theoretical values corresponding to all the aforementioned nuclear interaction models are displayed.

By studying the angular differential cross-section, one may observe quite similar properties as previously outlined for the n-^{3}H total cross-section at the resonance peak. The I-N3LO NN interaction model provides the most accurate description of the data if used in conjunction with a 3BF with a cut-off parameter of $\Lambda = 500$ MeV. Other models tend to underestimate the scattering cross-section, while the net differences are quite small. The most relevant observable for studying the model dependence remains the analyzing power A_{y0}. At the maximum of A_{y0}, one observes an up to 30% spread between the different model predictions. Once again, I-N3LO+3BF($\Lambda = 500$ MeV) turns to be the most successful in describing experimental data and sits almost on top of it. Nevertheless, the deviation relative to the experimental data is approximately 2% of the absolute cross-section values, which is comparable to the discrepancy present in the three-nucleon sector (Ay-puzzle). The analyzing powers are simply much weaker, in absolute values, in nucleon-deuteron scattering, and therefore discrepancies seem to be much more substantial.

When comparing the effect of different the 3BFs employed in conjunction with I-N3LO NN interaction in a similar way as outlined for the n-^{3}H cross-section case, the description of p-^{3}He deteriorates when the cutoff Λ is reduced from its original

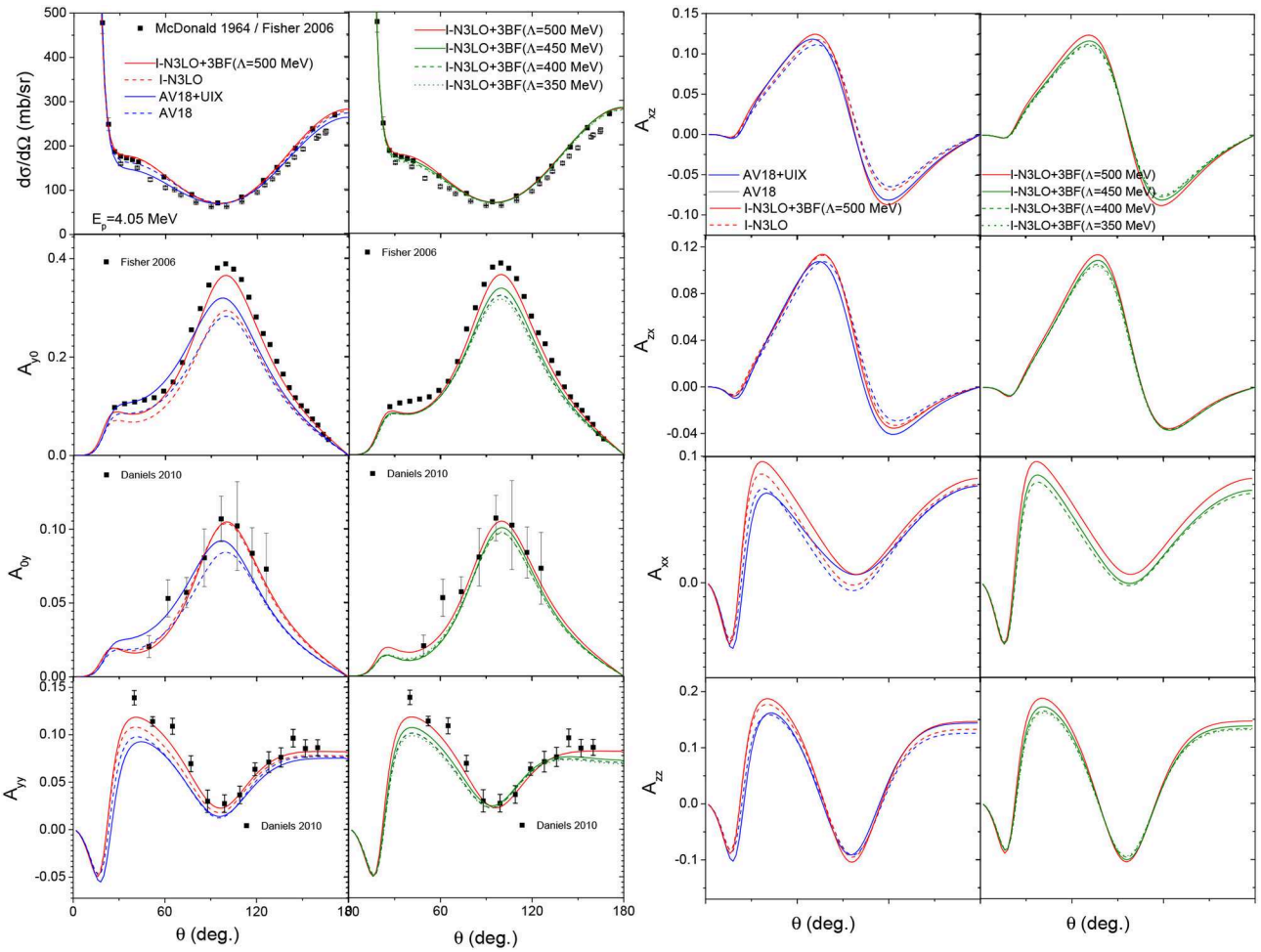


FIGURE 5 | Several differential observables calculated for proton scattering on ^{3}He at 4.05 MeV.

value, 500 MeV. This feature does not seem to be related to the importance of reproducing the tritium beta decay half-life, as only the Marcucci et al. [71] model accounts for it. The 3BF model of Gazit et al. [70] provides almost identical results to those obtained using the 3BF from Marcucci et al. [71], both using the value $\Lambda = 500$ MeV. Another quite straightforward answer would be the importance of maintaining consistency between the regulators in NN and three-nucleon interaction. Nevertheless, while the I-N3LO interaction is regulated by employing the same cutoff value of $\Lambda = 500$ MeV, the expressions of these regulators are quite different for NN and 3BF.

In order to consider scattering at even higher energies—for $E_n \gtrsim 8$ MeV neutrons or $E_p \gtrsim 7$ MeV protons—one should take the presence of the three- (or/and even four-) particle breakup channels into account. The description of such processes is far beyond the reach of the standard techniques based on imposing proper boundary conditions in configuration space (or treating singularities in a multidimensional kernel of integral equations formulated in momentum space). Nevertheless, one may avoid these complications by employing complex scaling or complex energy methods, as has been successfully demonstrated in Carbonell et al. [85]. The scattering in n-^{3}H and p-^{3}He systems has been accurately described above d+N+N and also above 4N thresholds in recent work [17, 86, 87]. In particular, it has been found that description of the analyzing power improves in these systems once energy is increased. This fact is clearly demonstrated in **Figure 7**. The interplay of the 3BF has not yet been explored in studying four-nucleon scattering above the three-particle breakup threshold. Nevertheless, some indications are present that the calculated total elastic and breakup cross-sections correlate with the predicted binding energy of the target nucleus, as illustrated in **Figure 8**. This feature is attributed to the importance of correctly positioning the thresholds in describing low-energy scattering cross-sections. In the vicinity of a threshold, and due to the kinematic form factor, the breakup cross-section increases with the available kinetic energy. Conversely, the elastic cross-sections tend to decrease with energy. For the models reproducing tri-nucleon binding energies properly, the obtained n-^{3}H and p-^{3}He cross-sections are successfully described in the intermediate energy region.

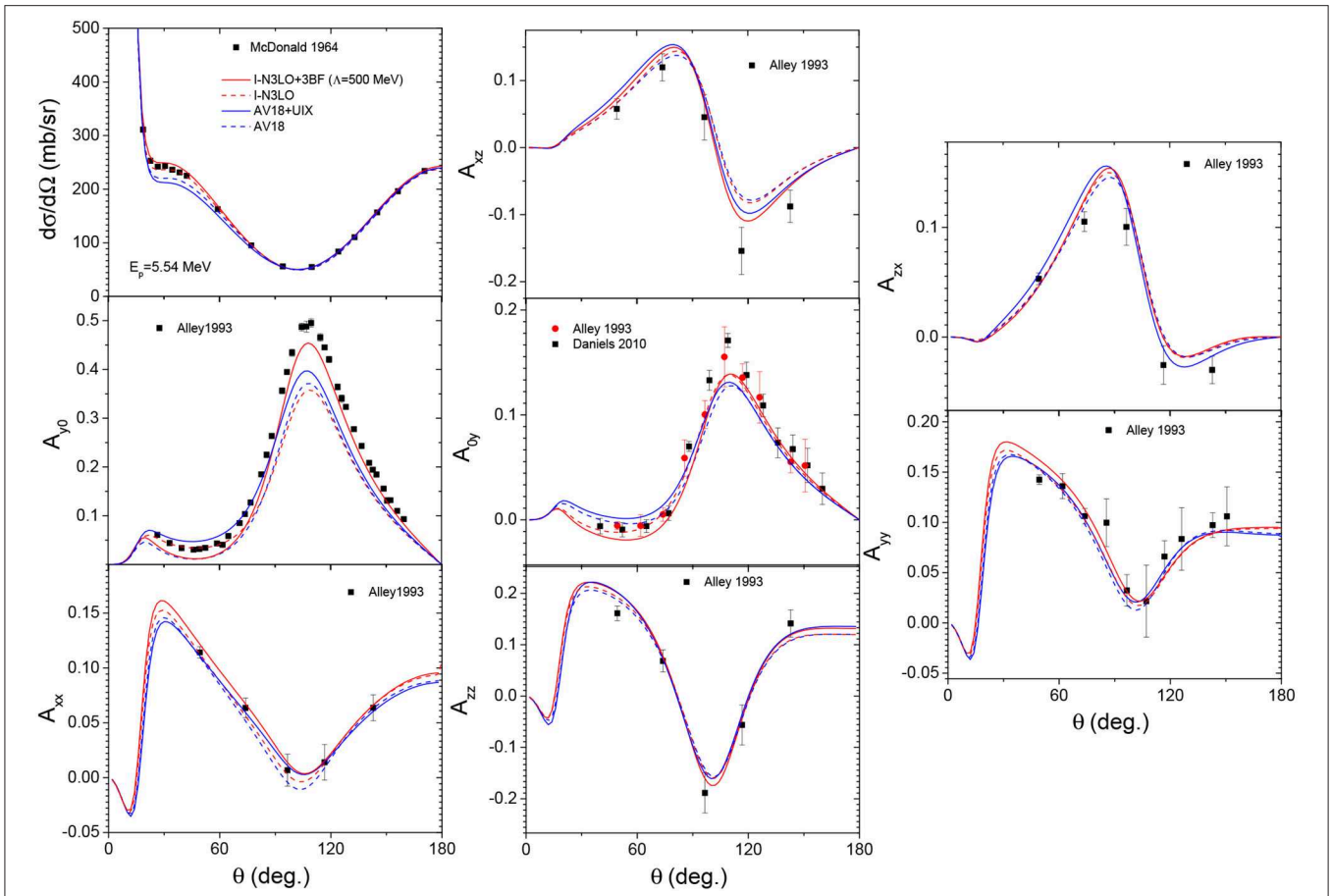


FIGURE 6 | Various differential observables calculated for proton scattering on ^{3}He at 5.54 MeV.

When considering elastic differential cross-sections, some discrepancies have been found when studying 22.1 MeV neutron scattering on ^{3}H, in particular at the cross-section minima (see **Figure 7**). The theoretical values are sizeably larger than the measured ones, and furthermore, this discrepancy is the largest for the models describing tritium binding energy well. On the other hand, as demonstrated in Deltuva and Fonseca [86], the calculated cross-sections for 18 MeV neutrons lie in the middle between the data sets of Seagrave et al. [88] and Debertin et al. [89]. One might thus expect a lack of reliability for the data from Seagrave et al. [88]. As this disagreement is only manifested in the vicinity of the cross-section minima, one is tempted to attribute the discrepancy to a simple underestimation of the experimental error-bars. New precise measurements are required to resolve this issue.

The description of the scattering in the continuum of the ^{4}He nucleus, involving three experimentally accessible processes p-^{3}H/n-^{3}He/^{2}H+^{2}H, is the most complicated four-nucleon problem. Nevertheless, an accurate description of this system has been achieved by three different groups, successfully benchmarking their results [15]. The Vilnius-Lisbon group has studied this system extensively in a broad energy region, as well as employing different interaction models [29, 30, 90–92]. One may single out two very challenging energy regions in this system. The first is related to the presence of a $J^\pi = 0^+$ resonant state embedded between the p-^{3}H and n-^{3}He thresholds (see **Figure 1**). Small modifications in the nuclear Hamiltonian affecting the position of this resonant state have huge effects on the calculated cross-sections between the two thresholds. As demonstrated in Lazauskas [93], the majority of the nuclear Hamiltonians fail in this enterprise. Another challenging case is the description of the ^{4}He continuum just above the n+^{3}He threshold. In this window, not only the analyzing powers but also elastic n+^{3}He as well as transfer $n + {}^3He \rightarrow p + {}^3H$ cross-sections are purely reproduced [29, 92]. This feature is determined by the difficulty of describing two relatively narrow ($J^\pi = 0^-$ and $J^\pi = 2^-$) resonant states (see **Figure 1**). One should still explore whether the 3BF models may provide any improvement in describing this region. When increasing energy and moving above the three- and four-nucleon breakup thresholds, in close similarity with p+^{3}He and n+^{3}H systems, description of the scattering cross-sections but also the analyzing powers tends to improve [30, 92].

3.4. Five-Nucleon Systems

As mentioned above, the description of a five-nucleon system based on the solution of the Faddeev-Yakubovsky

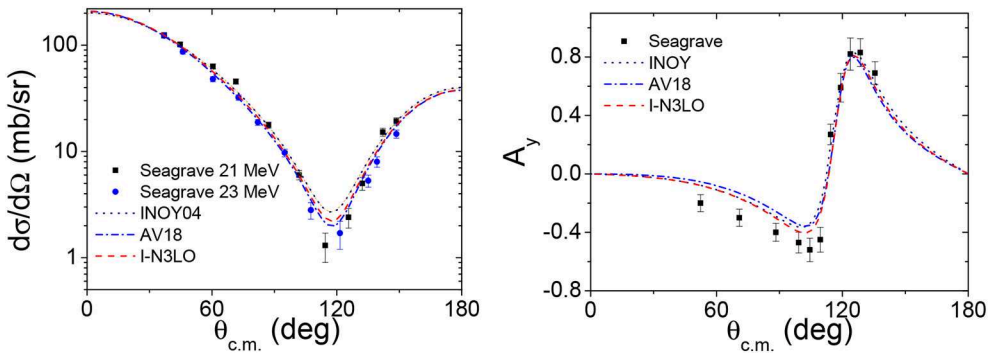


FIGURE 7 | Calculated n-^{3} H elastic differential cross-sections **(left)** and analyzing power A_y **(right)** for neutrons of laboratory energy 22.1 MeV compared with the experimental results of Seagrave et al. [88].

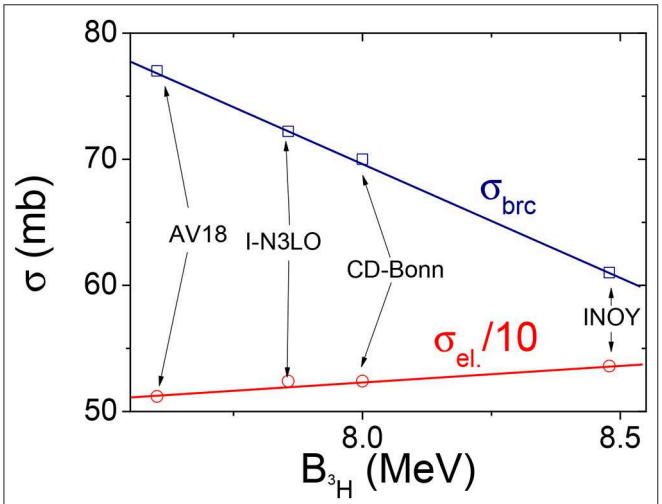


FIGURE 8 | Dependence of the calculated n-^{3}H total elastic and inelastic (breakup) cross-sections on the triton binding energy for different nuclear models. Calculations have been performed for neutrons with laboratory energy of 22.1 MeV.

equations represents a considerable technical challenge. Nevertheless, during the last few years, we have achieved a converged solution of the elastic neutron scattering on ^{4}He as well as being able to determine the ^{5}H resonance position in the complex energy plane. In both cases, the results were based on realistic NN and three-nucleon interaction models.

Our results on n-^{4}He were in good agreement with some previous calculations based on NCMC techniques [37]. Ideally, one should compare the calculated observables directly with the experimentally available data. However, due to the limited accuracy of the calculations (of order 5% for the phase shifts) and the fact that very accurate phase shift analysis has been carried out on the experimental data for this system, it is practical to analyze the obtained results by comparing the phase shifts.

We present in **Figure 9** our calculated S- and P-wave phaseshifts in the energy region up to 8 MeV. One may see quite a nice description of the scattering observables in the relative S-wave, which also demonstrates a remarkable model independence. In close analogy to the n-^{3}H scattering case, this partial wave is dominated by Pauli repulsion between the neutron projectile and the ones present within the ^{4}He target. We would like to note, however, that some model dependence is observed even in S-waves if one compares the phase shifts at very low energy and, in particular, the calculated scattering length. Significant differences are observed between the different theoretical predictions [95] but also between the experimentally measured [96–98] as well as adopted [25, 99, 100] scattering length values. In particular, our calculated values are in conflict with those obtained using GFMC techniques [32], where a scattering length $a(^2S_{1/2}) = 2.4$ fm was found, the same value for AV18 or AV18 supplemented with UIX (or IL2) 3N forces, while our calculations with AV18 give $a(^2S_{1/2}) = 2.96(5)$ fm, whereas for AV18+UIX, we get $a(^2S_{1/2}) = 2.71(7)$. We believe that this difference may be attributable to the lack of accuracy in Nollett et al. [32], as their calculations are not able to reveal any difference in calculated scattering length for AV18 and AV18+UIX Hamiltonians. In contrast, our calculations indicate the presence of a strong correlation between the calculated scattering length and ^{4}He binding energy, displayed in **Figure 10**. Therefore, it should be expected that AV18 and AV18+UIX models sizeably differing in predicted ^{4}He binding energies should also provide different n-^{4}He scattering lengths.

Even more problematic is description of the resonant n-^{4}He P-waves. Realistic NN interaction models fail to provide sufficient splitting between the quartet and the doublet P-waves. For the INOY04 model, the situation is even worse: this model significantly lacks attraction in both P-waves. The addition of the UIX 3BF to the AV18 model does not improve description of the n-^{4}He P-wave phaseshifts, as was the case for the n-^{3}H and p-^{3}He systems. In contrast, the I-N3LO model, when used in conjunction with the 3BF ($\Lambda = 500$ MeV) from Marcucci et al. [71], turns out to be quite successful in describing both P-waves. The phase shifts of the strongly resonant $^{3/2}$P channel are reproduced quite well, with only a slight lack of attraction, whereas the $^{1/2}$P phase shifts are described ideally. The comparison of the results from different

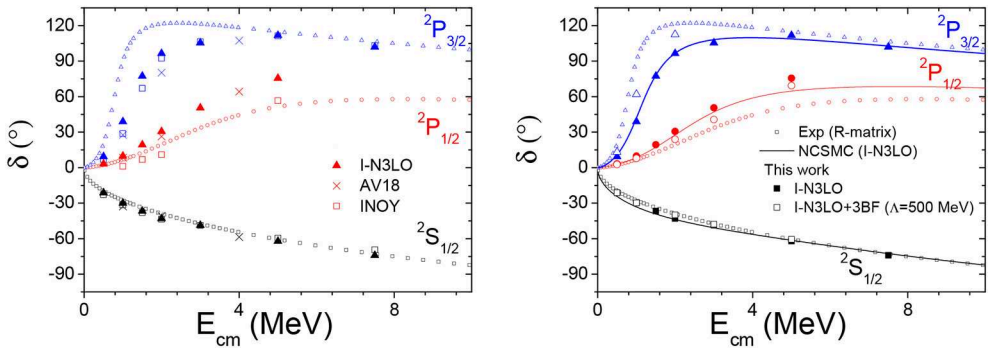


FIGURE 9 | Comparison between the theoretical predictions of the n-^{4}He, S- and P-waves, phaseshifts, and the results of a partial wave analysis of the experimental data by Hale [94]. In the left panel, the results corresponding to different NN interactions are indicated respectively by triangles (I-N3LO), × (AV18), or squares (INOY), and the dotted curves correspond to R-matrix analysis. In the right panel, our calculated values for the I-N3LO model—with (empty symbols) and without (full symbols) three-body forces (3BF)—are also compared with the results obtained by NCSMC calculations (solid lines) of Navrátil et al. [37].

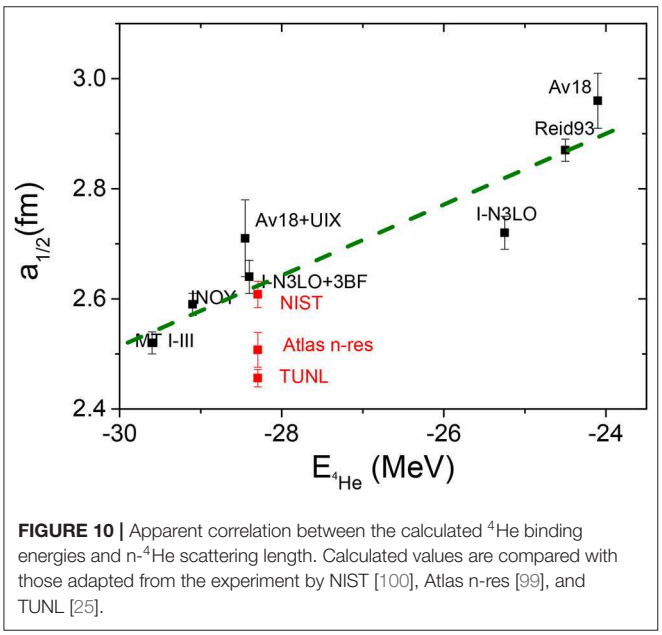


FIGURE 10 | Apparent correlation between the calculated ^{4}He binding energies and n-^{4}He scattering length. Calculated values are compared with those adapted from the experiment by NIST [100], Atlas n-res [99], and TUNL [25].

interaction models suggests the presence of strong similarities in the n-^{3}H and n-^{4}He scattering. There is an apparent correlation between the positions of P-wave resonant states in ^{4}H and ^{5}He nuclei.

The ^{5}H resonance parameters were first computed ab-initio in Lazauskas et al. [6] with phenomenological and realistic NN interactions. We used two independent methods to locate the resonance positions in the complex energy plane: a variant of the smooth exterior complex scaling method, and the analytic continuation on the coupling constant. The results show remarkable stability with respect to the different tested interactions and support recent experimental findings [101, 102]. The resonance parameters of the $J^\pi = 2^-, 0^-, 1^-$ states in ^{4}H, which dominate the low-energy n-^{3}H elastic cross-section, have also been computed and found to be slightly wider than those for ^{5}H ($\Gamma_{^4H} \approx 4$ MeV for $\Gamma_{^5H} \approx 2.5$ MeV), advocating for the presence of additional attraction of the 4n with respect to the 3n system. In view of this, any attempt to reproduce the experimental finding of a ^{7}H narrow state would be of the highest interest.

4. CONCLUSIONS

We have presented some recent results related to the solutions of the Faddeev-Yakubovsky equations in configuration space for nuclei with four or five nucleons obtained with several modern realistic NN and NNN interactions.

Two independent methods to include the Coulomb interaction in the A = 4 scattering states, namely in the p-^{3}He low-energy elastic cross-section, have been compared.

We have discussed in detail the n+^{3}H elastic cross-section in the resonance peak, which constitutes a stumbling block for all realistic NN and 3BF models, even those that most successfully describe the binding energy of A = 3, 4 nuclei.

The mirror reaction p+^{3}He was also presented by computing several observables such as differential cross-sections and analyzing power at $E_p \approx 5$ MeV.

The first results for the five-nucleon system have been considered. They concern the n-^{4}He elastic scattering at low energy and the resonance position of ^{5}H in the complex energy plane. The n-^{4}H scattering displays severe discrepancies in terms of scattering length, both between models and with experimental data. The resonance parameters of ^{5}H show great stability with respect to the NN interactions used and are compatible with some of the experimental analyses.

The general conclusion concerning the nuclear interactions is that the I-N3LO NN model used in conjunction with 3BF with a cut-off parameter Λ = 500 MeV provides the most accurate description of the data.

DATA AVAILABILITY STATEMENT

The raw data supporting the conclusions of this article will be made available by the authors, without undue reservation, to any qualified researcher.

AUTHOR CONTRIBUTIONS

All authors listed have made a substantial, direct and intellectual contribution to the work, and approved it for publication.

FUNDING

This work was supported by IN2P3 for the master project Neutron-rich light unstable nuclei.

ACKNOWLEDGMENTS

We were granted access to the HPC resources of TGCC/IDRIS under the allocation 2018-A0030506006 made by GENCI (Grand Equipement National de Calcul Intensif).

REFERENCES

1. Lazauskas R, Carbonell J. The Faddeev-Yakubovsky symphony. *arXiv preprint* arXiv:190804861 (2019). doi: 10.1007/s00601-019-1529-5
2. Merkuriev S, Yakovlev S, Gignoux C. Four-body Yakubovsky differential equations for identical particles. *Nuclear Phys A*. (1984) **431**:125–38. doi: 10.1016/0375-9474(84)90057-5
3. Glöckle W, Kamada H. Alpha-particle binding energies for realistic nucleon-nucleon interactions. *Phys Rev Lett*. (1993) **71**:971–4. doi: 10.1103/PhysRevLett.71.971
4. Lazauskas R. Description of five-nucleon systems using Faddeev-Yakubovsky equations. *Few-Body Syst*. (2018) **59**:13. doi: 10.1007/s00601-018-1333-7
5. Lazauskas R. Solution of the n- He4 elastic scattering problem using the Faddeev-Yakubovsky equations. *Phys Rev C*. (2018) **97**:044002. doi: 10.1103/PhysRevC.97.044002
6. Lazauskas R, Hiyama E, Carbonell J. *Ab initio* calculations of 5H resonant states. *Phys Lett B*. (2019) **791**:335–41. doi: 10.1016/j.physletb.2019.02.047
7. Ciesielski F, Carbonell J, Gignoux C. Low energy n+ t scattering and the NN forces. *Phys Lett B*. (1999) **447**:199–208. doi: 10.1016/S0370-2693(98)01501-9
8. Carbonell J. The continuum spectrum of the 4N system. Results and challenges. *arXiv preprint nucl-th/0103041*. (2001). doi: 10.1016/S0375-9474(01)00417-1
9. Lazauskas R, Carbonell J. *Ab-initio* calculations of four-nucleon elastic scattering. *Few-Body Syst*. (2004) **34**:105–11. doi: 10.1007/s00601-004-0049-z
10. Deltuva A, Fonseca AC, Kievsky A, Rosati S, Sauer PU, Viviani M. Benchmark calculation for proton-deuteron elastic scattering observables including the Coulomb interaction. *Phys Rev C*. (2005) **71**:064003. doi: 10.1103/PhysRevC.71.064003
11. Lazauskas R, Carbonell J. Testing nonlocal nucleon-nucleon interactions in four-nucleon systems. *Phys Rev C*. (2004) **70**:044002. doi: 10.1103/PhysRevC.70.044002
12. Lazauskas R, Carbonell J. Coulomb effects in four nucleon continuum states. In: *Contribution to 17th International IUPAP Conference on Few-Body Problems in Physics, June 5–10, 2003*. Durham, NC (2004).
13. Lazauskas R. Modern nuclear force predictions for $n-^3$H scattering above the three- and four-nucleon breakup thresholds. *Phys Rev C*. (2015) **91**:041001. doi: 10.1103/PhysRevC.91.041001
14. Viviani M, Deltuva A, Lazauskas R, Carbonell J, Fonseca AC, Kievsky A, et al. Benchmark calculation of n-^{3}H and p-^{3}He scattering. *Phys Rev C*. (2011) **84**:054010. doi: 10.1103/PhysRevC.84.054010
15. Viviani M, Deltuva A, Lazauskas R, Fonseca A, Kievsky A, Marcucci L. Benchmark calculation of p- H 3 and n- He 3 scattering. *Phys Rev C*. (2017) **95**:034003. doi: 10.1103/PhysRevC.95.034003
16. Lazauskas R, Carbonell J. Application of the complex-scaling method to few-body scattering. *Phys Rev C*. (2011) **84**:034002. doi: 10.1103/PhysRevC.84.034002
17. Lazauskas R. Application of the complex-scaling method to four-nucleon scattering above break-up threshold. *Phys Rev C*. (2012) **86**:044002. doi: 10.1103/PhysRevC.86.044002
18. Lazauskas R, Carbonell J. Complex scaling method for three-and four-body scattering above the break-up thresholds. *Few-Body Syst*. (2013) **54**:967–72. doi: 10.1007/s00601-012-0531-y
19. Lazauskas R, Carbonell J. Three-neutron resonance trajectories for realistic interaction models. *Phys Rev C*. (2005) **71**:044004. doi: 10.1103/PhysRevC.71.044004
20. Lazauskas R, Carbonell J. Is a physically observable tetraneutron resonance compatible with realistic nuclear interactions? *Phys Rev C*. (2005) **72**:034003. doi: 10.1103/PhysRevC.72.034003
21. Hiyama E, Lazauskas R, Carbonell J, Kamimura M. Possibility of generating a 4-neutron resonance with a $T = 3/2$ isospin 3-neutron force. *Phys Rev C*. (2016) **93**:044004. doi: 10.1103/PhysRevC.93.044004
22. Lazauskas R, Carbonell J, Hiyama E. Modeling the double charge exchange response function for a tetraneutron system. *Prog Theor Exp Phys*. (2017) **2017**:073D03. doi: 10.1093/ptep/ptx078
23. Deltuva A, Lazauskas R. Comment on: is a trineutron resonance lower in energy than a tetraneutron resonance? *Phys Rev Lett*. (2019) **123**:069201. doi: 10.1103/PhysRevLett.123.069201
24. Tilley DR, Weller H, Hale GM. A=4 energy levels. *Nucl Phys*. (1992) **A541**:1. doi: 10.1016/0375-9474(92)90635-W
25. Tilley TR, Cheves CM, Godwin JL, Hale GM, Hofmann HM, Kelley JH, et al. Energy levels of light nuclei A=5, 6, 7. *Nucl Phys A*. (2002). **708**:23. doi: 10.1016/S0375-9474(02)00597-3
26. Carbonell J. Solutions of Faddeev-Yakubovsky equations in configuration space for the 4N scattering states. In: *Few-Body Problems in Physics 99*. Vienna: Springer (2000). p. 439–44.
27. Hupin G, Quaglioni S, Navrátil P. Ab initio predictions for polarized deuterium-tritium thermonuclear fusion. *Nat Commun*. (2019) **10**:351. doi: 10.1038/s41467-018-08052-6
28. Alt E, Grassberger P, Sandhas W. Reduction of the three-particle collision problem to multi-channel two-particle Lippmann-Schwinger equations. *Nuclear Phys B*. (1967) **2**:167–80. doi: 10.1016/0550-3213(67)90016-8
29. Deltuva A, Fonseca A. Ab initio four-body calculation of n-He 3, p-H 3, and d-d scattering. *Phys Rev C*. (2007) **76**:021001. doi: 10.1103/PhysRevC.76.021001
30. Deltuva A, Fonseca A. Four-body calculation of H 2 (d, p) H 3 and H 2 (d, n) He 3 reactions above breakup threshold. *Phys Rev C*. (2017) **95**:024003. doi: 10.1103/PhysRevC.95.024003
31. Pudliner B, Pandharipande V, Carlson J, Pieper SC, Wiringa RB. Quantum Monte Carlo calculations of nuclei with A<˜ 7. *Phys Rev C*. (1997) **56**:1720. doi: 10.1103/PhysRevC.56.1720
32. Nollett KM, Pieper SC, Wiringa RB, Carlson J, Hale GM. Quantum Monte Carlo calculations of neutron-α scattering. *Phys Rev Lett*. (2007) **99**:022502. doi: 10.1103/PhysRevLett.99.022502
33. Gattobigio M, Kievsky A, Viviani M. Six-bodies calculations using the Hyperspherical Harmonics method. *Few-Body Syst*. (2013) **54**:657–66. doi: 10.1007/s00601-012-0460-9
34. Kievsky A, Rosati S, Viviani M, Marcucci LE, Girlanda L. A high-precision variational approach to three-and four-nucleon bound and zero-energy scattering states. *J Phys G*. (2008) **35**:063101. doi: 10.1088/0954-3899/35/6/063101
35. Hiyama E, Kino Y, Kamimura M. Gaussian expansion method for few-body systems. *Prog Part Nuclear Phys*. (2003) **51**:223–307. doi: 10.1016/S0146-6410(03)90015-9

36. Hofmann H, Hale G. Microscopic calculation of the spin-dependent neutron scattering lengths on 3 He. *Phys Rev C*. (2003) **68**:021002. doi: 10.1103/PhysRevC.68.021002
37. Navrátil P, Quaglioni S, Hupin G, Romero-Redondo C, Calci A. Unified ab initio approaches to nuclear structure and reactions. *Phys Scripta*. (2016) **91**:053002. doi: 10.1088/0031-8949/91/5/053002
38. Efros VD, Leidemann W, Orlandini G. Response functions from integral transforms with a Lorentz kernel. *Phys Lett B*. (1994) **338**:130–3. doi: 10.1016/0370-2693(94)91355-2
39. Kievsky A, Viviani M, Rosati S. Study of bound and scattering states in three-nucleon systems. *Nuclear Phys A*. (1994) **577**:511–27. doi: 10.1016/0375-9474(94)90931-8
40. Orlandini G. Ab initio methods for nuclear structure and reactions: from few to many nucleons. In: *An Advanced Course in Computational Nuclear Physics*. Cham; Vancouver, BC: Springer (2017). p. 263–92. doi: 10.1007/978-3-319-53336-0_7
41. Sasakawa T. Five-body equation. *Prog Theor Phys Suppl*. (1977) **61**:149–60. doi: 10.1143/PTPS.61.149
42. Lazauskas R, Song YH. Parity-violating neutron spin rotation in He 4. *Phys Rev C*. (2019) **99**:054002. doi: 10.1103/PhysRevC.99.054002
43. Lazauskas R. *Scattering of Heavy Charged Particles in Atomic and Nuclear Systems*. Grenoble: Université Joseph Fourier (2003). Available online at: http://tel.ccsd.cnrs.fr/documents/archives0/00/00/41/78/
44. Hüber D, Witała H, Nogga A, Glöckle W, Kamada H. A new look into the partial-wave decomposition of three-nucleon forces. *Few-Body Syst*. (1997) **22**:107–35.
45. Kamada H. Four-body scattering equations including a three-body force in the Faddeev–Yakubovsky theory. *Few-Body Syst*. (2019) **60**:33. doi: 10.1007/s00601-019-1501-4
46. Merkuriev SP. On the three-body Coulomb scattering problem. *Ann Phys*. (1980) **130**:395–426.
47. Noble JV. Three-body problem with charged particles. *Phys Rev*. (1967) **161**:945. doi: 10.1103/PhysRev.161.945
48. Sasakawa T, Sawada T. Treatment of charged three-body problems. *Phys Rev C*. (1979) **20**:1954. doi: 10.1103/PhysRevC.20.1954
49. Friar JL, Gibson B, Payne G. Configuration space Faddeev continuum calculations: pd s-wave scattering length. *Phys Rev C*. (1983) **28**:983. doi: 10.1103/PhysRevC.28.983
50. Chen C, Payne G, Friar JL, Gibson BF. Nd zero-energy scattering. *Phys Rev C*. (1991) **44**:50. doi: 10.1103/PhysRevC.44.50
51. Kievsky A, Viviani M, Rosati S. Variational calculations for scattering states in three-nucleon systems. In: *Few-Body Problems in Physics 1993*. Vienna: Springer (1994). p. 278–81.
52. Ishikawa S. Low-energy proton-deuteron scattering with a Coulomb-modified Faddeev equation. *Few-Body Syst*. (2003) **32**:229–48. doi: 10.1007/s00601-003-0001-7
53. Filikhin I, Yakovlev S. Solving the differential Yakubovsky equations for p 3 He scattering by the cluster-reduction method. *Phys Atom Nuclei*. (2000) **63**:69–75. doi: 10.1134/1.855607
54. Wiringa RB, Stoks VGJ, Schiavilla R. Accurate nucleon-nucleon potential with charge-independence breaking. *Phys Rev C*. (1995) **51**:38–51. doi: 10.1103/PhysRevC.51.38
55. Doleschall P. Influence of the short range nonlocal nucleon-nucleon interaction on the elastic $n-d$ scattering: below 30 MeV. *Phys Rev C*. (2004) **69**:054001. doi: 10.1103/PhysRevC.69.054001
56. Entem DR, Machleidt R. Accurate charge-dependent nucleon-nucleon potential at fourth order of chiral perturbation theory. *Phys Rev C*. (2003) **68**:041001(R). doi: 10.1103/PhysRevC.68.041001
57. Friar JL, Gibson BF, Payne G. H 3 and He 3 solutions for momentum-dependent potentials. *Phys Rev C*. (1988) **37**:2869–72. doi: 10.1103/PhysRevC.37.2869
58. Wu Y, Ishikawa S, Sasakawa T. Three-nucleon bound states: detailed calculations of 3 H and 3 He. *Few-Body Syst*. (1993) **15**:145–88. doi: 10.1007/BF01076246
59. Nogga A, Kamada H, Gloeckle W, Barrett BR. The α particle based on modern nuclear forces. *Phys Rev C*. (2002) **65**:054003. doi: 10.1103/PhysRevC.65.054003
60. Doleschall P. Phenomenological non-local NN interactions and the triton binding energy. *Nuclear Phys A*. (1996) **602**:60–76. doi: 10.1016/0375-9474(96)00116-9
61. Doleschall P. Three-nucleon observables and the low-energy behavior of triplet P-wave nucleon-nucleon interactions. *Phys Rev C*. (2008) **77**:034002. doi: 10.1103/PhysRevC.77.034002
62. Weinberg S. Effective chiral Lagrangians for nucleon-pion interactions and nuclear forces. *Nuclear Phys B*. (1991) **363**:3–18. doi: 10.1016/0550-3213(91)90231-L
63. Epelbaum E, Hammer HW, Meißner UG. Modern theory of nuclear forces. *Rev Modern Phys*. (2009) **81**:1773–825. doi: 10.1103/RevModPhys.81.1773
64. Machleidt R, Entem DR. Chiral effective field theory and nuclear forces. *Phys Rep*. (2011) **503**:1–75. doi: 10.1016/j.physrep.2011.02.001
65. Caurier E, Navrátil P. Proton radii of He 4, 6, 8 isotopes from high-precision nucleon-nucleon interactions. *Phys Rev C*. (2006) **73**:021302. doi: 10.1103/PhysRevC.73.021302
66. Baldo M, Maieron C. Equation of state of nuclear matter at high baryon density. *J Phys G*. (2007) **34**:R243. doi: 10.1088/0954-3899/34/5/R01
67. Forssén C, Caurier E, Navrátil P. Charge radii and electromagnetic moments of Li and Be isotopes from the ab initio no-core shell model. *Phys Rev C*. (2009) **79**:021303. doi: 10.1103/PhysRevC.79.021303
68. Pudliner BS, Pandharipande VR, Carlson J, Pieper SC, Wiringa RB. Urb IX. *Phys Rev C*. (1997) **56**:1720.
69. Navratil P. Local three-nucleon interaction from chiral effective field theory. *Few-Body Syst*. (2007) **41**:117–40. doi: 10.1007/s00601-007-0193-3
70. Gazit D, Quaglioni S, Navrátil P. Three-nucleon low-energy constants from the consistency of interactions and currents in chiral effective field theory. *Phys Rev Lett*. (2009) **103**:102502. doi: 10.1103/PhysRevLett.103.102502
71. Marcucci LE, Kievsky A, Rosati S, Schiavilla R, Viviani M. Erratum: chiral effective field theory predictions for muon capture on deuteron and ^{3}He [Phys. Rev. Lett. 108, 052502 (2012)]. *Phys Rev Lett*. (2018) **121**:049901(E). doi: 10.1103/PhysRevLett.121.049901
72. Roth R, Calci A, Langhammer J, Binder S. Evolved chiral N N+ 3 N Hamiltonians for ab initio nuclear structure calculations. *Phys Rev C*. (2014) **90**:024325. doi: 10.1103/PhysRevC.90.024325
73. Glöckle W, Witala H, Hüber D, Kamada H, Golak J. The three-nucleon continuum: achievements, challenges and applications. *Phys Rep*. (1996) **274**:107–285. doi: 10.1016/0370-1573(95)00085-2
74. Setze H, Howell C, Tornow W, Braun R, Glöckle W, Hussein A, et al. Verification of the space-star anomaly in nd breakup. *Phys Lett B*. (1996) **388**:229–34. doi: 10.1016/S0370-2693(96)01069-6
75. Deltuva A. Momentum-space calculation of proton-deuteron scattering including Coulomb and irreducible three-nucleon forces. *Phys Rev C*. (2009) **80**:064002. doi: 10.1103/PhysRevC.80.064002
76. Phillips TW, Berman BL, Seagrave JD. Neutron total cross section for tritium. *Phys Rev C*. (1980) **22**:384–96. doi: 10.1103/PhysRevC.22.384
77. Seagrave J, Berman B, Phillips T. The neutron zero-energy total cross section and scattering lengths for tritium. *Phys Lett B*. (1980) **91**:200–202. doi: 10.1016/0370-2693(80)90430-X
78. Hammerschmied S, Rauch H, Clerc H, Kischko U. Measurements of the coherent neutron-tritium scattering length and its relation to the four nucleon problem. *Z Phys A Atoms Nuclei*. (1981) **302**:323–8. doi: 10.1007/BF01414263
79. Rauch H, Tuppinger D, Wölwitsch H, Wroblewski T. Re-measurement of the neutron-tritium scattering length. *Phys Lett B*. (1985) **165**:39–42. doi: 10.1016/0370-2693(85)90686-0
80. Hale G, Dodder D, Seagrave J, Berman B, Phillips T. Neutron-triton cross sections and scattering lengths obtained from p- 3 He scattering. *Phys Rev C*. (1990) **42**:438. doi: 10.1103/PhysRevC.42.438
81. McDonald D, Haeberli W, Morrow L. Polarization and Cross Section of Protons Scattered by He 3 from 4 to 13 MeV. *Phys Rev*. (1964) **133**:B1178. doi: 10.1103/PhysRev.133.B1178
82. Alley M, Knutson L. Effective range parametrization of phase shifts for p-3 He elastic scattering between 0 and 12 MeV. *Phys Rev C*. (1993) **48**:1901. doi: 10.1103/PhysRevC.48.1901

83. Fisher B, Brune C, Karwowski H, Leonard D, Ludwig E, Black TC, et al. Proton-He 3 elastic scattering at low energies. *Phys Rev C*. (2006) **74**:034001. doi: 10.1103/PhysRevC.74.034001
84. Daniels TV, Arnold C, Cesaratto J, Clegg T, Couture A, Karwowski H, et al. Spin-correlation coefficients and phase-shift analysis for p+ He 3 elastic scattering. *Phys Rev C*. (2010) **82**:034002. doi: 10.1103/PhysRevC.82.034002
85. Carbonell J, Deltuva A, Fonseca AC, Lazauskas R. Bound state techniques to solve the multiparticle scattering problem. *Prog Part Nuclear Phys*. (2014) **74**:55–80. doi: 10.1016/j.ppnp.2013.10.003
86. Deltuva A, Fonseca AC. Neutron-^{3}H scattering above the four-nucleon breakup threshold. *Phys Rev C*. (2012) **86**:011001. doi: 10.1103/PhysRevC.86.011001
87. Deltuva A, Fonseca A. Calculation of proton-3 He elastic scattering between 7 and 35 MeV. *Phys Rev C*. (2013) **87**:054002. doi: 10.1103/PhysRevC.87.054002
88. Seagrave J, Hopkins J, Dixon D, Kerr NA Jr, Sherman R, Walter R. Elastic scattering and polarization of fast neutrons by liquid deuterium and tritium. *Ann Phys*. (1972) **74**:250–299. doi: 10.1016/0003-4916(72)90263-1
89. Debertin K, Roessle E, Schott J. *EXFOR Database NNDC*. Brookhaven (1967).
90. Deltuva A, Fonseca A. Polarization observables and spin-aligned fusion rates in H 2 (d, p) H 3 and H 2 (d, n) He 3 reactions. *Phys Rev C*. (2010) **81**:054002. doi: 10.1103/PhysRevC.81.054002
91. Deltuva A, Fonseca A. Calculation of neutron-He 3 scattering up to 30 MeV. *Phys Rev C*. (2014) **90**:044002. doi: 10.1103/PhysRevC.90.044002
92. Deltuva A, Fonseca A. Four-body calculation of elastic deuteron-deuteron scattering. *Phys Rev C*. (2015) **92**:024001. doi: 10.1103/PhysRevC.92.024001
93. Lazauskas R. Elastic proton scattering on tritium below the n- He 3 threshold. *Phys Rev C*. (2009) **79**:054007. doi: 10.1103/PhysRevC.79.054007
94. Hale G. Low-energy proton-deuteron scattering with a Coulomb-modified Faddeev equation. Private communication (2008).
95. Lazauskas R. Recent developments in solving the few-particle scattering problem by the solution of the faddeev-yakubovsky equations. In: *Proceedings of the FB22 Conference*. Cham: Springer (2018).
96. Kaiser H, Rauch H, Badurek G, Bauspiess W, Bonse U. Measurement of coherent neutron scattering lengths of gases. *Z Phys A Atoms Nuclei*. (1979) **291**:231–8. doi: 10.1007/BF01409188
97. Serebrov AP, Geltenbort P, Zherebtsov OM, Sbitnev S, Varlamov V, Vassiljev A, et al. Measurement of the total cross sections of ultracold neutrons with noble gases and search for long-range forces. *JETP Lett*. (2013) **97**:676–80. doi: 10.1134/S0021364013120114
98. Haddock CC, Hiromoto M, Hirota K, Ino T, Kitaguchi M, Mishima K, et al. Measurement of the total neutron scattering cross section ratios of natural isotopic mixtures of noble gas atoms using a pulsed neutron beam. *arXiv preprint* arXiv:190608223 (2019). doi: 10.1103/PhysRevC.100.064002
99. Mughabghab SF. *Atlas of Neutron Resonances: Resonance Parameters and Thermal Cross Sections. Z= 1-100*. Vancouver, BC: Elsevier Science (2006).
100. Varley FS. Neutron scattering lengths and cross sectioirn. *Neutron News*. (1992) **3**:29–37. doi: 10.1080/10448639208218770
101. Korsheninnikov A, Golovkov M, Tanihata I, Rodin A, Fomichev A, Sidorchuk S, et al. Superheavy hydrogen H 5. *Phys Rev Lett*. (2001) **87**:092501. doi: 10.1103/PhysRevLett.87.092501
102. Wuosmaa A, Bedoor S, Brown K, Buhro W, Chajecki Z, Charity R, et al. Ground-state properties of H 5 from the He 6 (d, He 3) H 5 reaction. *Phys Rev C*. (2017) **95**:014310. doi: 10.1103/PhysRevC.95.014310

Conflict of Interest: The authors declare that the research was conducted in the absence of any commercial or financial relationships that could be construed as a potential conflict of interest.

Copyright © 2020 Lazauskas and Carbonell. This is an open-access article distributed under the terms of the Creative Commons Attribution License (CC BY). The use, distribution or reproduction in other forums is permitted, provided the original author(s) and the copyright owner(s) are credited and that the original publication in this journal is cited, in accordance with accepted academic practice. No use, distribution or reproduction is permitted which does not comply with these terms.

frontiers in Physics

REVIEW
published: 07 April 2020
doi: 10.3389/fphy.2020.00069

The Hyperspherical Harmonics Method: A Tool for Testing and Improving Nuclear Interaction Models

Laura E. Marcucci[1,2]*, *Jérémy Dohet-Eraly*[3], *Luca Girlanda*[4,5], *Alex Gnech*[2,6], *Alejandro Kievsky*[1,2] *and Michele Viviani*[1,2]

[1] Department of Physics "E. Fermi", University of Pisa, Pisa, Italy, [2] Istituto Nazionale di Fisica Nucleare, Sezione di Pisa, Pisa, Italy, [3] Physique Quantique, and Physique Nucléaire Théorique et Physique Mathématique, Université libre de Bruxelles, Brussels, Belgium, [4] Department of Mathematics and Physics "E. De Giorgi", University of Salento, Lecce, Italy, [5] Istituto Nazionale di Fisica Nucleare, Sezione di Lecce, Lecce, Italy, [6] Gran Sasso Science Institute, L'Aquila, Italy

The Hyperspherical Harmonics (HH) method is one of the most accurate techniques to solve the quantum mechanical problem for nuclear systems with a number of nucleons $A \leq 4$. In particular, by applying the Rayleigh-Ritz or Kohn variational principle, both bound and scattering states can be addressed, using either local or non-local interactions. Thanks to this versatility, the method can be used to test the two- and three-nucleon components of the nuclear interaction. In the present review we introduce the formalism of the HH method, both for bound and scattering states. In particular, we describe the implementation of the method to study the $A = 3$ and 4 scattering problems. Second, we present a selected choice of results of the last decade, most representative of the latest achievements. Finally, we conclude with a discussion of what we believe will be the most significant developments within the HH method for the next 5–10 years.

Keywords: hyperspherical harmonics method, ab initio methods, nuclear interactions, few-nucleon systems, light nuclei, $A = 3, 4$ scattering

OPEN ACCESS

Edited by:
Nunzio Itaco,
University of Campania Luigi Vanvitelli, Italy

Reviewed by:
Sonia Bacca,
Johannes Gutenberg University Mainz, Germany
Andreas Nogga,
Julich Research Centre, Germany
Winfried Leidemann,
University of Trento, Italy

***Correspondence:**
Laura E. Marcucci
laura.elisa.marcucci@unipi.it

Specialty section:
This article was submitted to Nuclear Physics, a section of the journal Frontiers in Physics

Received: *29 November 2019*
Accepted: *28 February 2020*
Published: *07 April 2020*

Citation:
Marcucci LE, Dohet-Eraly J, Girlanda L, Gnech A, Kievsky A and Viviani M (2020) The Hyperspherical Harmonics Method: A Tool for Testing and Improving Nuclear Interaction Models. Front. Phys. 8:69. doi: 10.3389/fphy.2020.00069

1. INTRODUCTION

The "standard" picture of a nucleus sees it as a system of A nucleons, protons or neutrons, interacting among themselves and eventually with external electroweak probes. The interaction between nucleons, i.e., the nuclear interaction, is the subject of the Research Topic of which this contribution is part. Using the nucleon as the relevant degree of freedom, the system is described by the nuclear Hamiltonian, written as

$$H = \sum_{i=1}^{A} \frac{p_i^2}{2m_i} + \sum_{j>i=1}^{A} V_{ij} + \sum_{k>j>i=1}^{A} V_{ijk} + \cdots , \tag{1}$$

where the first term is the (non-relativistic) kinetic energy (in the center-of-mass reference frame), m_i being the ith nucleon mass, V_{ij} and V_{ijk} are, respectively, the two- and three-nucleon interactions, i.e., the interaction between each ij pair or ijk triple. It has been shown in several studies (for recent ones see references [1, 2]) that even the nuclear systems with medium-large values of A can be at least qualitatively described including V_{ij} and V_{ijk} only: essentially, it seems

to be little room [3] for four- or more-nucleon interactions [the dots of Equation (1)]. Therefore, we will neglect from now on the contributions beyond three-nucleon interaction.

There exists a large variety of realistic models for V_{ij} and V_{ijk}. The most important ones are presented in this Research Topic. These models are very different among themselves, as they can be local, or minimally non-local and expressed in coordinate space, or non-local and expressed in momentum space. Some older models were derived phenomenologically or in a meson-theoretical approach, as the Argonne v_{18} [4] or the CDBonn [5] potentials, but, since the seminal work of Weinberg [6], the preferred framework to derive the nuclear interaction is chiral effective field theory. Since the presentation of the different models is assigned to this Research Topic, here we only mention that all the models have a common characteristic: the V_{ij} and V_{ijk} interactions have an intricate operatorial structure. As a consequence, the solution of the Schrödinger equation for $A > 2$ becomes a challenging problem. The methods which are able to solve the A-body quantum mechanical problem without approximations, or with approximations which can be maintained under control, are the so-called *ab initio* methods[1]. They are clearly essential in order to test a given model for the nuclear interaction against experiment. It is fundamental for these methods to be sufficiently accurate to capture the small details introduced by the complexity of the interaction. As an example, we can quote the case of the triton binding energy. It is nowadays well-known that the triton binding energy calculated just retaining V_{ij} in Equation (1) is underestimated by $0.5 - 1$ MeV, depending of the considered model. It is straightforward that the required accuracy of the *ab initio* method to catch this disagreement must be better that 500 keV. Nowadays, the methods for the $A = 3$ bound systems have reached a much higher accuracy, of the order of 1 keV, or even better. And therefore, the presence of V_{ijk} is not anymore under discussion. To be noted that (i) all models for the two-nucleon interaction are phase-equivalent, and (ii) each model for V_{ijk} is built in conjunction with a given model for V_{ij}, and therefore two- and three-nucleon interactions are linked to each other and cannot be uniquely defined.

There are several *ab initio* methods which can solve the A-body quantum mechanical problem in different regions of the nuclear chart. A recent review is given in reference [7]. Here we limit ourselves to mention the methods based on Monte Carlo techniques, as the variational Monte Carlo (VMC) or the Green's function Monte Carlo (GFMC) methods (see reference [8], and references therein). There are then the methods linked to the shell model, as the no-core shell model (NCSM) or the realistic shell model (RSM) (see references [9–11]), respectively. All these methods are quite powerful to study medium-mass nuclear bound states, but less accurate, apart from the GFMC and NCSM, for very light nuclei, as those with $A = 3, 4$. Furthermore, their extension to the scattering systems is not so trivial, and, in some cases, still not at reach.

[1]The expression "*ab initio* method" has been quite widely used in the literature, with a somewhat less strict definition, than the one used here. Here we follow the definition of reference [7].

Restricting ourselves to the $A = 3, 4$ nuclear systems, both bound and scattering states, we have at hand very few accurate *ab initio* methods, i.e., the Faddeev (Faddeev-Yakubovsky for $A = 4$) equations (FE) technique, solved in coordinate- or in momentum-space, the method based on the Alt-Grassberger-Sandhas (AGS) equations solved in momentum space, and the Hyperspherical Harmonics (HH) method presented here. We refer the reader to references [12, 13] for the FE method in coordinate space, to references [14, 15] for the FE method in momentum space, to references [16, 17] for recent reviews on the AGS method. Clearly, each method has advantages and drawbacks. For instance, the FE method in momentum space can be applied to $A = 3, 4$ bound and scattering states in a wide energy range. However, the inclusion of the Coulomb interaction for charged particle scattering states is quite problematic. The FE method in coordinate space can handle the Coulomb interaction, but it has not yet been applied to scattering problems at very low-energy, and it has been applied only recently to study systems with larger A values [18]. It is though a method with in principle great possibilities of extension [13]. The AGS method, although working in momentum space, can handle the Coulomb interaction and can be applied to a large variety of $A = 3, 4$ scattering states, in a wide energy range. However, the very low energy range, that of interest to nuclear astrophysics, i.e., below about 100 keV, is still not accessible with the AGS method. The method has also not been applied for $A > 4$ yet.

The HH method has a long history, summarized in the introduction of reference [19]. We will concentrate here on the latest developments, essentially those obtained since 2008, year of publication of reference [19]. However, to fully appreciate the major developments of this last decade, it is necessary to briefly outline the state-of-the-art of the HH method at that time. The HH method in 2008 was extensively used by two groups, one formed by some of the present authors, and referred to as the Pisa group, and the other one including, among others, N. Barnea, W. Leidemann, and G. Orlandini. The latter has developed over the years the so-called effective interaction HH method (EIHH), which uses the Suzuki-Lee approach [20–22] to significantly reduce the number of the basis functions needed in the expansion. The method has been applied to study the $A \leq 4$ nuclear bound systems in references [23, 24] using local realistic interactions, and had been pushed to work up to $A = 6$ with central potential models [23]. In the last decade, the EIHH method has been updated in order to work also with the most recent non-local potential models [25]. Furthermore, the EIHH method has been extensively used in testing the nuclear interaction models, using reactions between light nuclei and electromagnetic probes. For example, a test of the interaction models has been performed studying the 0^+ resonance of ^{4}He in $^4\mathrm{He}(e, e')$, where a large potential model dependence has been found [26, 27]. In this review, however, we have decided to leave out the large body of results for the electromagnetic reactions on light nuclei, which would deserve a review all by itself (see reference [28]).

The HH method as developed by the Pisa group existed in 2008 in two flavors: the correlated HH method, including a pair-correlation function (pair-correlated HH method—PHH)

or with a Jastrow type factor (correlated HH method—CHH), and the "pure" HH method. The correlation factor was introduced to describe correlations induced by the strong repulsion of the interaction at short range. The correlation factor describes the particular configuration in which two particles are close to each other and goes to unity for large pair relative distances. Therefore the HH expansion has to take care of reconstructing the wave function outside this range, making the convergence of the expansion much faster. The drawbacks of the PHH and CHH methods are (i) the necessity of performing numerical integrations, which would be instead analytical without correlation factors, reducing the accuracy of the method in the $A = 4$ case; (ii) the not simple extension of the PHH method to work in momentum space. Therefore, it is difficult to apply the PHH method with the non-local potentials mentioned above. This has motivated our group, together with the continuous increasing of computing power, to return to the "pure" HH method. Up to the year 2008, this had been developed and applied to study with great accuracy the $A = 3, 4$ bound states, with both local potentials, expressed in coordinate space, or non-local ones, given in momentum-space. In fact, while the local interactions had been at reach for the HH method from the very beginning [29], the non-local ones were a recent achievement at that time [30]. In 2008, the zero-energy $A = 3, 4$ scattering states were also calculated with both local and non-local interactions [19]. The higher energy scattering states, still below the breakup threshold of the target nucleus, had been studied for both $A = 3$ and 4 systems only with local interactions, in a variety of contributions extensively mentioned in reference [19]. What was still missing in 2008 was the study of the $A = 3, 4$ scattering states, still below the target breakup threshold, with non-local potentials. This has been obtained in references [31–35] for both $A = 3$ and 4, and it is in fact one of the main achievements of the HH method in the last decade. The HH method, in its PHH version, has been applied, including the full electromagnetic interaction, to describe elastic scattering observables in $A = 3$ above the deuteron breakup threshold [36] and in wide energy region [37]. Preliminary studies of the method to treat the breakup channels, as for instance to the process $n + d \rightarrow n + n + p$, can be found in references [38–40]. The application of the method using the Hamiltonian defined in Equation (1) is in progress. In progress is also the further development of the method toward $A > 4$. This has been performed within the so-called non-symmetrized HH method [41] with central potentials, or, as mentioned above, by the EIHH method. The first steps to use the HH method without the Suzuki-Lee procedure have been shown in references [42, 43], and intense research activity is currently underway. The formalism which is presented here is in fact quite general, and can be applied also to the $A = 5, 6$ nuclear systems.

Before concluding this section with the outline of this contribution, we would like to make few remarks: (i) the HH method is extremely powerful, and its application to systems up to $A \sim 7, 8$ is limited essentially by computing power. (ii) The accuracy of the HH method has been tested in a number of benchmark calculations. In particular we quote the benchmark on the $A = 3$ [44] and $A = 4$ [45] bound states, on the *nd* and *pd* scattering phase shifts [46, 47], and, in the last decade, on the $A = 4$ scattering states [34, 48]. (iii) Compared with the other *ab initio* methods, the HH technique seems to be one of the best choices to study low-energy scattering states, in order to obtain accurate predictions for nuclear reactions of astrophysical interest [49, 50].

The present review is organized as follows: in section 2 we discuss the HH formalism, both for bound and scattering states. We will try to keep a somewhat "pedagogical" level, in order to allow the interested reader to perform his/her own algebraic steps and eventually reproduce the already existing results. In section 3 we discuss the most important results obtained within the HH method since the year 2008. In particular, we will show that the HH method has reached such a degree of accuracy for both bound and scattering states, that it has been used in order to construct an accurate model for the three-nucleon interaction, with a procedure similar, in principle, to the one used to derive the nowadays very accurate two-nucleon interaction models. Finally, in section 4 we will give some concluding remarks and an outlook.

2. THE HH FORMALISM

We review in this section the HH formalism, focusing in particular on the three- and four-body systems, both bound and scattering states. The approach described below can be used in conjunction with both local and non-local two-nucleon interactions. At present, the method works with only local three-nucleon interactions, but its extension to the non-local case presents no conceptual difficulties.

2.1. Hyperspherical Harmonic Functions

Let us consider a system of A particles with masses $m_1, \ldots, m_A$ and spatial coordinates $\boldsymbol{r}_1, \ldots, \boldsymbol{r}_A$, respectively. For separating the internal and center-of-mass (c.m.) motion, it is convenient to introduce another set of coordinates made of $N = A - 1$ internal Jacobi coordinates $\boldsymbol{x}_1, \ldots, \boldsymbol{x}_N$ and the c.m. coordinate $\boldsymbol{X}$ defined by

$$\boldsymbol{X} = \frac{1}{M} \sum_{i=1}^{A} m_i \boldsymbol{r}_i \tag{2}$$

where $M = \sum_{i=1}^{A} m_i$ is the total mass of the system. There are several definitions of the Jacobi coordinates, but a convenient one which will be used through this work is the following

$$\boldsymbol{x}_{N-j+1} = \sqrt{\frac{2m_{j+1}M_j}{M_{j+1}m}} \left(\boldsymbol{r}_{j+1} - \frac{1}{M_j} \sum_{i=1}^{j} m_i \boldsymbol{r}_i \right), \tag{3}$$

where m is a reference mass, $M_j = \sum_{i=1}^{j} m_i$, and $j = 1, \ldots, N$. In the case where all the particles have the same mass m, Equation (3) reduces to

$$\boldsymbol{x}_{N-j+1} = \sqrt{\frac{2j}{j+1}} \left(\boldsymbol{r}_{j+1} - \frac{1}{j} \sum_{i=1}^{j} \boldsymbol{r}_i \right). \tag{4}$$

From a given choice of the Jacobi vectors, the hyperspherical coordinates (ρ, Ω_N) can be introduced. The hyperradius ρ is defined by

$$\rho = \sqrt{\sum_{i=1}^{N} x_i^2} = \sqrt{\frac{2}{A}\sum_{j>i=1}^{A}(\boldsymbol{r}_i - \boldsymbol{r}_j)^2} = \sqrt{2\sum_{i=1}^{A}(\boldsymbol{r}_i - \boldsymbol{X})^2}, \quad (5)$$

where x_i is the modulus of the Jacobi vector $\boldsymbol{x}_i$. The hyperradius ρ is symmetric with respect to particle exchanges and does not depend on the particular choice of Jacobi coordinates. The set Ω_N of hyperangular coordinates,

$$\Omega_N = \{\hat{\boldsymbol{x}}_1, \ldots, \hat{\boldsymbol{x}}_N, \varphi_2, \ldots, \varphi_N\}, \quad (6)$$

is made of the angular parts $\hat{\boldsymbol{x}}_i = (\theta_i, \phi_i)$ of the spherical components of the Jacobi vectors $\boldsymbol{x}_i$, with $i = 1, \ldots N$, and of the hyperangles φ_j, defined by

$$\cos\varphi_j = \frac{x_j}{\sqrt{x_1^2 + \ldots + x_j^2}}, \quad (7)$$

where $0 \leq \varphi_j \leq \pi/2$ and $j = 2, \ldots, N$.

The advantage of using the hyperspherical coordinates can be appreciated noting that the internal kinetic energy operator of the A-body system can be decomposed as

$$T = -\frac{\hbar^2}{m}\sum_{i=1}^{N}\Delta_{\mathbf{x}_i} = -\frac{\hbar^2}{m}\left(\frac{\partial^2}{\partial\rho^2} + \frac{3N-1}{\rho}\frac{\partial}{\partial\rho} - \frac{\Lambda_N^2(\Omega_N)}{\rho^2}\right), \quad (8)$$

where the operator $\Lambda_N^2(\Omega_N)$ is the so-called grand-angular momentum operator. Its explicit expression can be found, for instance, in references [19, 51], but it is not essential for our purposes. More important are the eigenfunctions of the grand-angular momentum $\Lambda_N^2(\Omega_N)$, the so-called hyperspherical harmonics (HH). They can be defined as

$$\mathcal{Y}_{[K]}^{KLM_L}(\Omega_N) = [[\ldots[Y_{l_1}(\hat{\boldsymbol{x}}_1)Y_{l_2}(\hat{\boldsymbol{x}}_2)]_{L_2}\ldots Y_{l_{N-1}}(\hat{\boldsymbol{x}}_{N-1})]_{L_{N-1}} Y_{l_N}(\hat{\boldsymbol{x}}_N)]_{LM_L}\prod_{j=2}^{N}{}^{(j)}\mathcal{P}_{n_j}^{K_{j-1},l_j}(\varphi_j). \quad (9)$$

Here $Y_{l_i}(\hat{\boldsymbol{x}}_i)$ is a spherical harmonic function for $i = 1, \ldots, N$, L is the total orbital angular momentum, M_L its projection on the z axis, and

$$K_j = \sum_{i=1}^{j}(l_i + 2n_i) \quad (10)$$

with $n_1 = 0, j = 1, \ldots, N$, and $K_N \equiv K$ is the so-called grand-angular momentum. The notation $[K]$ stands for the collection of all the quantum numbers $[l_1, \ldots, l_N, L_2, \ldots, L_{N-1}, n_2, \ldots, n_N]$. The functions ${}^{(j)}\mathcal{P}_{n_j}^{K_{j-1},l_j}(\varphi_j)$ in Equation (9) are defined by

$${}^{(j)}\mathcal{P}_{n_j}^{K_{j-1},l_j} = \mathcal{N}_{n_j}^{l_j,\nu_j}(\cos\varphi_j)^{l_j}(\sin\varphi_j)^{K_{j-1}}P_{n_j}^{\nu_{j-1},l_j+1/2}(\cos 2\varphi_j), \quad (11)$$

where $P_{n_j}^{\nu_{j-1},l_j+1/2}(\cos 2\varphi_j)$ are Jacobi polynomials [52], with

$$\nu_j = K_j + \frac{3}{2}j - 1, \quad (12)$$

and the normalization factors $\mathcal{N}_n^{l,\nu}$ are given by

$$\mathcal{N}_n^{l,\nu} = \sqrt{\frac{2\nu\Gamma(\nu-n)\Gamma(n+1)}{\Gamma(\nu-n-l-1/2)\Gamma(n+l+3/2)}}, \quad (13)$$

with Γ indicating the standard Gamma function [52]. To be noticed that for $A = 3$, $j = 1, 2$, and since $n_1 = 0$, there is only one index $n_2 \equiv n$. In this case, $K = l_1 + l_2 + 2n$. For the convergence on n or alternatively K, see the discussion in section 3. With the definition of Equation (9), the HH functions are eigenvectors of the grand-angular momentum operator $\Lambda_N^2(\Omega_N)$, the square of the total orbital angular momentum $\boldsymbol{L}$, its z component $\boldsymbol{L}_z$, and the parity operator Π. Therefore we have

$$\Lambda_N^2(\Omega_N)\mathcal{Y}_{[K]}^{KLM_L}(\Omega_N) = K(K+3N-2)\mathcal{Y}_{[K]}^{KLM_L}(\Omega_N), \quad (14)$$

$$L^2\mathcal{Y}_{[K]}^{KLM_L}(\Omega_N) = \hbar^2 L(L+1)\mathcal{Y}_{[K]}^{KLM_L}(\Omega_N), \quad (15)$$

$$L_z\mathcal{Y}_{[K]}^{KLM_L}(\Omega_N) = \hbar M_L\mathcal{Y}_{[K]}^{KLM_L}(\Omega_N), \quad (16)$$

$$\Pi\mathcal{Y}_{[K]}^{KLM_L}(\Omega_N) = (-1)^K\mathcal{Y}_{[K]}^{KLM_L}(\Omega_N). \quad (17)$$

We remark here two useful properties of the HH functions. First of all, the HH functions are orthonormal with respect to the volume element $d\Omega_N$, i.e.,

$$\int d\Omega_N\,[\mathcal{Y}_{[K']}^{K'L'M'_L}(\Omega_N)]^*\,\mathcal{Y}_{[K]}^{KLM_L}(\Omega_N) = \delta_{[K][K']}\delta_{KK'}\delta_{LL'}\delta_{M_LM'_L}, \quad (18)$$

with

$$d\boldsymbol{x}_1\cdots d\boldsymbol{x}_N = \rho^{3N-1}d\rho\,d\Omega_N \quad (19)$$

and

$$d\Omega_N = \sin\theta_1 d\theta_1 d\phi_1\prod_{j=2}^{N}\sin\theta_j d\theta_j d\phi_j\,(\cos\varphi_j)^2\,(\sin\varphi_j)^{3j-4}d\varphi_j. \quad (20)$$

Therefore, the number of HH functions for a given K increases fast with K, but is always finite. In fact, according with Equation (10), $K = \sum_{i=1,N}(l_i + 2n_i)$. Furthermore, independently of the specific choice of Jacobi coordinates used to define the hyperspherical ones or of the order of the coupling of the spherical harmonics in Equation (9), the HH functions constitute a complete basis.

Secondly, in order to evaluate matrix elements of a given many-body operator between HH functions, it is often useful to determine the effect of a particles permutation on an HH function. Since the grand-angular and the total orbital angular momenta are fully symmetric, and since the HH functions constitute a complete basis, the permuted HH functions $\mathcal{Y}_{[K]}^{KLM_L}(\Omega_N^p)$ can be written as linear combinations of unpermuted

HH functions $\mathcal{Y}^{KLM_L}_{[K']}(\Omega_N)$ with same K, L, and M_L values. Therefore, we can write

$$\mathcal{Y}^{KLM_L}_{[K]}(\Omega^p_N) = \sum_{[K']} a^{KL,p}_{[K];[K']} \mathcal{Y}^{KLM_L}_{[K']}(\Omega_N). \quad (21)$$

The transformation coefficients $a^{KL,p}_{[K];[K']}$ do not depend on the quantum number M_L. For $A = 3$, they are called the Raynal-Revai coefficients [53]. To be remarked that $[K'] \equiv [l'_1, \dots, l'_N, L'_2, \dots, L'_{N-1}, n'_2, \dots, n'_N]$, but such that $K' = K$. Note that L is conserved. For $A > 3$, see references [42, 54].

Let us consider more specifically a system of A nucleons described within the isospin formalism. The A-nucleon wave function contains spatial, spin, and isospin parts. We can define the spin functions $\chi^{SM_S}_{[S]}$ with total spin S and total spin projection M_S and the isospin functions $\xi^{TM_T}_{[T]}$ with total isospin T and total isospin projection M_T by coupling the individual spin functions $\chi_{1/2,\pm 1/2}$ or isospin functions $\xi_{1/2,\pm 1/2}$, respectively, of each nucleon, as

$$\chi^{SM_S}_{[S]} = [[\dots[\chi_{1/2}(1)\chi_{1/2}(2)]_{S_2} \dots \chi_{1/2}(N-1)]_{S_{N-1}} \chi_{1/2}(N)]_{SM_S}, \quad (22)$$

$$\xi^{TM_T}_{[T]} = [[\dots[\xi_{1/2}(1)\xi_{1/2}(2)]_{T_2} \dots \xi_{1/2}(N-1)]_{T_{N-1}} \xi_{1/2}(N)]_{TM_T}. \quad (23)$$

So now $[S]$ stands for $[S_2, \dots, S_{N-1}]$ and $[T]$ for $[T_2, \dots, T_{N-1}]$.

Including the spin and isospin functions, the HH basis functions read

$$\mathbb{Y}^{KLSJJ_zTM_T}_{[KST]}(\Omega_N) = [\mathcal{Y}^{KL}_{[K]}(\Omega_N)\chi^{S}_{[S]}]_{JJ_z}\xi^{TM_T}_{[T]}, \quad (24)$$

where J is the total angular momentum, J_z its projection, and $[KST]$ stands for $[K][S][T]$. To be noticed that also the spin-isospin part of $\mathbb{Y}^{KLSJJ_zTM_T}_{[KST]}(\Omega_N)$ constructed with a given ordering of the particles, can be rewritten in terms of a different permutation, using the Wigner 6j coefficients [55].

We conclude by noting that the HH functions can also be built in momentum space instead of configuration space. They can be obtained by replacing the hyperspherical coordinates (ρ, Ω_N) associated with the Jacobi coordinates $\{\boldsymbol{x}_i\}_{i=1,\dots,N}$ by the hyperspherical coordinates $(Q, \Omega^{(q)}_N)$ associated with the N Jacobi conjugate momenta $\{\boldsymbol{q}_i\}_{i=1,\dots,N}$. The rest of the formalism remains unchanged. For more details, see references [19, 30, 56].

2.2. The HH Method for $A = 3$ and 4

We discuss in some detail the method for systems with $A = 3, 4$ nucleons within the isospin formalism for both bound and scattering states in sections 2.2.1 and 2.2.2, respectively. The extension to $A > 4$ is straightforward, but leads to more lengthy expressions.

2.2.1. The $A = 3$ and 4 Bound States

The wave function of an A-body bound state, with $A = 3, 4$, having total angular momentum J, J_z and parity π, and third component of the total isospin M_T, can be decomposed as a sum of Faddeev-like amplitudes as:

$$\Psi_A = \sum_{p=1}^{N_p} \psi(\boldsymbol{x}^{(p)}_1, \cdots, \boldsymbol{x}^{(p)}_N). \quad (25)$$

Here the sum on p runs up to $N_p = 3$ or 12 even permutations of the A particles, with $A = 3$ or 4, respectively, and the coordinates $\boldsymbol{x}^{(p)}_1, \cdots, \boldsymbol{x}^{(p)}_N$ are the Jacobi coordinates as defined in Equation (3), but here we show explicitly the dependence on the permutation p. To be noticed that, increasing the number of particles, different arrangements of them in sub-clusters allow for different definitions of the Jacobi coordinates. For example, in $A = 4$ two different sets exist corresponding to have a 3+1 or a 2+2 asymptotic configuration. However in the sub-space defined by the grand-angular momentum K, HH functions defined in different sets of Jacobi coordinates result to be linearly dependent. In the following we always refer to the set defined in Equation (3).

The coordinate-space hyperspherical coordinates are given in Equations (5)–(7), and the hyperangular variables are φ_2 for $A = 3$ and φ_2, φ_3 for $A = 4$.

We rewrite here the HH basis of Equation (24) for the $A = 3$ and 4 cases. Historically, the angular, spin and isospin quantum numbers have been collected in the so-called channels α, defined explicitly by

$$[\alpha] = [l_{1\alpha}, l_{2\alpha}, L_\alpha, S_{a\alpha}, S_\alpha, T_{a\alpha}, T_\alpha]; \quad A = 3 \quad (26)$$

$$[\alpha] = [l_{1\alpha}, l_{2\alpha}, l_{3\alpha}, L_{2\alpha}, L_\alpha, S_{a\alpha}, S_{b\alpha}, S_\alpha, T_{a\alpha}, T_{b\alpha}, T_\alpha]; \quad A = 4 \quad (27)$$

so that we can write

$$\mathbb{Y}^{K}_{[\alpha]n_2}(\Omega_N) = \left[[Y_{l_{1\alpha}}(\hat{\boldsymbol{x}}_1)\, Y_{l_{2\alpha}}(\hat{\boldsymbol{x}}_2)]_{L_\alpha} \left[[\chi_{1/2}(1)\, \chi_{1/2}(2)]_{S_{a\alpha}}\, \chi_{1/2}(3) \right]_{S_\alpha} \right]_{JJ_z} \left[[\xi_{1/2}(1)\, \xi_{1/2}(2)]_{T_{a\alpha}}\, \xi_{1/2}(3) \right]_{T_\alpha M_T} {}^{(2)}\mathcal{P}^{l_{1\alpha},l_{2\alpha}}_{n_2}(\varphi_2), \quad (28)$$

for $A = 3$, and

$$\mathbb{Y}^{K}_{[\alpha]n_2n_3}(\Omega_N) = \left[\left[[Y_{l_{1\alpha}}(\hat{\boldsymbol{x}}_1)\, Y_{l_{2\alpha}}(\hat{\boldsymbol{x}}_2)]_{L_{2\alpha}} Y_{l_{3\alpha}}(\hat{\boldsymbol{x}}_3) \right]_{L_\alpha} \left[\left[[\chi_{1/2}(1)\, \chi_{1/2}(2)]_{S_{a\alpha}}\, \chi_{1/2}(3) \right]_{S_{b\alpha}} \chi_{1/2}(4) \right]_{S_\alpha} \right]_{JJ_z} \left[\left[[\xi_{1/2}(1)\, \xi_{1/2}(2)]_{T_{a\alpha}}\, \xi_{1/2}(3) \right]_{T_{b\alpha}} \xi_{1/2}(4) \right]_{T_\alpha M_T} {}^{(2)}\mathcal{P}^{l_{1\alpha},l_{2\alpha}}_{n_2}(\varphi_2)\, {}^{(3)}\mathcal{P}^{2n_2+l_{1\alpha}+l_{2\alpha},l_{3\alpha}}_{n_3}(\varphi_3), \quad (29)$$

for $A = 4$. To be noticed that, in order to ensure the antisymmetry of the wave function, the Faddeev-like amplitudes have to change sign under exchange of particle 1 and 2. Therefore, the sum $l_{2\alpha} + S_{a\alpha} + T_{a\alpha}$ for $A = 3$ and $l_{3\alpha} + S_{a\alpha} + T_{a\alpha}$ for $A = 4$ must be odd. Furthermore, $l_{1\alpha} + l_{2\alpha}$ for $A = 3$ and $l_{1\alpha} + l_{2\alpha} + l_{3\alpha}$ for $A = 4$ must be an even or odd number in correspondence to a positive or negative parity state. Even with these restrictions, there is an infinite number of channels. However, the contributions of the channels with higher and higher values for $l_{1\alpha} + l_{2\alpha}$ for $A = 3$ and $l_{1\alpha} + l_{2\alpha} + l_{3\alpha}$ for $A = 4$ should become less and less important, due to the centrifugal barrier. Therefore, it is found that the number of channels with a significant contribution is relatively small for bound and low-energy scattering states. The most important ones for $A = 3$ and for $A = 4$ are listed, respectively, in Tables 1, 2 of reference [19].

By using Equations (28) and (29), the A-body wave function Ψ_A of Equation (25) can be written in coordinate-space as

$$\Psi_A = \sum_{\alpha,n_2} u_{\alpha n_2}(\rho) \sum_{p=1}^{N_p} \mathbb{Y}^K_{[\alpha]n_2}(\Omega_2^{(p)}), \tag{30}$$

for $A = 3$, and

$$\Psi_A = \sum_{\alpha,n_2,n_3} u_{\alpha n_2 n_3}(\rho) \sum_{p=1}^{N_p} \mathbb{Y}^K_{[\alpha]n_2 n_3}(\Omega_3^{(p)}), \tag{31}$$

for $A = 4$. The sum over n_2 in Equation (30) and n_2, n_3 in Equation (31) is restricted to independent states, see below. The hyperradial functions $u_{\alpha n_2}(\rho)$ ($u_{\alpha n_2 n_3}(\rho)$ for $A = 4$) are themselves expanded in terms of known functions. It is common to use Laguerre polynomials multiplied by an exponential function, as they have been found to give a nice convergence of this expansion. Therefore,

$$u_{\alpha n_2/\alpha n_2 n_3}(\rho) = \sum_{m=0}^{N_L} c_{\alpha n_2/\alpha n_2 n_3;m} f_m(\rho), \tag{32}$$

where the sum is truncated at N_L, and the functions $f_m(\rho)$ are written as

$$f_m(\rho) = \gamma^{D/2} \sqrt{\frac{m!}{(m+D-1)!}}\, L_m^{(D-1)}(\gamma\rho)\ \mathrm{e}^{-\gamma\rho/2}. \tag{33}$$

Here $D \equiv 3N-1$, $L_m^{(D-1)}(\gamma\rho)$ is a Laguerre polynomial [52], and γ is a non-linear parameter, to be variationally optimized. The exponential factor $\mathrm{e}^{-\gamma\rho/2}$ ensures that $f_m(\rho) \to 0$ for $\rho \to \infty$. The optimal value of γ depends on the potential model, and it is typically in the interval 2.5–4.5 fm^{-1} for local and 4–8 fm^{-1} for non-local potentials. Also N_L depends on the potential models, but typically with $N_L \sim 20-30$ a convergence at the 1 keV (10 keV) level for the $A = 3$ ($A = 4$) binding energies is achieved.

When working in momentum space, the A-body wave function Ψ_A is written as in Equations (30) and (31), with $u_{\alpha n_2}(\rho)$ and $u_{\alpha n_2 n_3}(\rho)$ replaced with $w_{\alpha n_2}(Q)$ and $w_{\alpha n_2 n_3}(Q)$, i.e., functions of the hypermomentum Q, while the HH functions are expressed in terms of conjugate Jacobi momenta. The w-functions are related to the u-functions as

$$w_{\alpha n_2/\alpha n_2 n_3}(Q) = (-i)^K \int_0^\infty d\rho \frac{\rho^{D-1}}{(Q\rho)^{D/2-1}} J_{K+\frac{D}{2}-1}(Q\rho)\, u_{\alpha n_2/\alpha n_2 n_3}(\rho), \tag{34}$$

where $J_{K+\frac{D}{2}-1}(Q\rho)$ are Bessel functions of the first kind [19], and K is again the grand-angular momentum.

At the end, the A-body wave function of Equations (30)–(34) can be cast in the form

$$\Psi_A = \sum_{K,m} c_{K;m} |K,m\rangle, \tag{35}$$

where

$$|K,m\rangle \equiv f_m(\rho) \sum_{p=1}^{N_p} \mathbb{Y}^K_{[\alpha]n_2/[\alpha]n_2 n_3}(\Omega_N^{(p)}) \tag{36}$$

in coordinate-space (a similar expression holds in momentum-space). The decomposition proposed in Equation (25) ensures the complete antisymmetrization of the state through the sum on the permutations as indicated in Equation (36). Indeed, the hyperangular-spin-isospin basis state $|K,m\rangle$ is completely antisymmetric. However, the sum over the permutations for fixed values of K produces linear dependent states that have to be individuated and eliminated from the basis set [42, 54, 57]. This procedure could be delicate from a numerical point of view as the number of K increases. In such a case, one needs a robust orthonormal procedure capable to deal with the presence of large numerical cancellations. However, if one is successful in this step, at the end one can work with a basis of independent antisymmetrical states, whose number is noticeably less than the degeneracy of the full HH basis. Attempts to use the HH basis without symmetrization has been recently proposed [41]. The idea is then to use the complete HH basis in which all symmetries are represented to describe a particular state. The diagonalization of the Hamiltonian produces eigenvectors with well-defined permutation properties reflecting the symmetries in it. Different applications followed this procedure for bosons as well as for fermions (see references [41, 58–61]). The advantage of eliminating the orthonormalization of the states has to be balanced by the fact that in this case one has to work with the full basis of HH functions, whose degeneracy rapidly increases with K and the number of particles A.

Once the antisymmetric state $|K,m\rangle$ is constructed, what is left is to obtain the unknown coefficients $c_{K;m}$ of the expansion. In order to do so, we apply the Rayleigh-Ritz variational principle, which states that the quantity $\langle\Psi_A|H-E|\Psi_A\rangle$ is stationary with respect to the variation of any unknown coefficient. Here H is the nuclear Hamiltonian and $E = -B$ the energy of the state, which, in the case of a bound state, is negative and opposite to the binding energy B.

When differentiating respect to $c_{K;m}$ we obtain the following equation

$$\sum_{K',m'} \langle K,m|H|K',m'\rangle c_{K';m'} = E \sum_{K',m'} \langle K,m|\mathbb{1}|K',m'\rangle c_{K';m'}, \tag{37}$$

where the matrix elements of the Hamiltonian H and of the identity operator $\mathbb{1}$ can be calculated with standard numerical techniques (see reference [19] for more details). Equation (37) represents a generalized eigenvalue-eigenvector problem, which can be solved with a variety of numerical algorithms. Widely used within the HH method is the Lanczos algorithm [62], since the HH basis can become quite large (up to about 10,000 terms for $A = 3$ and about one order of magnitude larger for $A = 4$ are used in practice).

The results obtained solving Equation (37) for a variety of nuclear interaction models will be presented in section 3.

2.2.2. The $A = 3$ and 4 Scattering States

The HH method has been also applied to the scattering problem. In particular, the method can study the elastic $N + Y \to N + Y$ process, where N is a nucleon and Y a bound system ($A_Y + 1 \equiv A = 3, 4$), both below and above the Y nucleus breakup

threshold. The extension of the HH method to the full breakup problem, i.e., for $A = 3$ the process $n + d \rightarrow n + n + p$, is currently underway and will not be discussed here.

The wave function $\Psi_{NY}^{LSJJ_z}$ describing the $N + Y$ scattering state with incoming orbital angular momentum L, channel spin $\vec{S} \equiv \vec{\frac{1}{2}} + \vec{S}_Y$, parity $\pi = (-1)^L$, and total angular momentum J, J_z, is written as

$$\Psi_{NY}^{LSJJ_z} = \Psi_C^{LSJJ_z} + \Psi_A^{LSJJ_z}. \tag{38}$$

Here we have introduced $\Psi_C^{LSJJ_z}$, which is the so-called "core" wave function, describing the system in the region where all the particles are close to each other and their mutual interaction is strong, and $\Psi_A^{LSJJ_z}$, which is the so-called "asymptotic" wave function, describing the relative motion between nucleon N and nucleus Y in the asymptotic region, where the $N - Y$ interaction is negligible or reduces to the Coulomb interaction in the case of $N \equiv p$. The core function $\Psi_C^{LSJJ_z}$ has to vanish at large $N - Y$ distances, and can be expanded in terms of the HH basis as for the bound state. Therefore, using Equation (35), we can write

$$\Psi_C^{LSJJ_z} = \sum_{K,m} c_{K;m} |K, m\rangle. \tag{39}$$

The asymptotic wave function $\Psi_A^{LSJJ_z}$ is the solution of the Schrödinger equation of the relative $N + Y$ motion. It is written as a linear combination of the following functions

$$\Omega_{LSJJ_z}^{\lambda} = \frac{\mathcal{C}}{\sqrt{N_p}} \sum_{p=1}^{N_p} [[\chi_{1/2}(N)\, \phi_{S_Y}(Y)]_S\, Y_L(\hat{\boldsymbol{y}}_p)]_{JJ_z} R_L^{\lambda}(y_p). \tag{40}$$

Here we have indicated with $\mathcal{C}$ a normalization factor [to be explained below, see Equation (49)]. The sum runs over the N_p even permutations of the A nucleons necessary to antisymmetrize the function $\Omega_{LSJJ_z}^{\lambda}$, $\chi_{1/2}(N)$ and $\phi_{S_Y}(Y)$ are the nucleon N and nucleus Y wave functions, respectively, and $\boldsymbol{y}_p$ is the relative distance between N and the c.m. of nucleus Y and is proportional to $\boldsymbol{x}_{N-j+1}$ of Equation (3). Furthermore, $Y_L(\hat{\boldsymbol{y}}_p)$ is the standard spherical harmonic function, and the functions $R_L^{\lambda}(y_p)$ for $\lambda = R, I$ are respectively the regular and irregular solutions of the two-body $N + Y$ Schrödinger equation without the nuclear interaction. They are explicitly written as [19, 31]

$$R_L^R(y_p) = \frac{1}{(2L+1)!! q^L C_L(\eta)} \frac{F_L(\eta, qy_p)}{qy_p}, \tag{41}$$

$$R_L^I(y_p) = (2L+1)!! q^{L+1} C_L(\eta) f(b, y_p) \frac{G_L(\eta, qy_p)}{qy_p}, \tag{42}$$

where q is the modulus of the $N - Y$ relative momentum, such that the total kinetic energy in the c.m. frame is $T_{c.m.} = q^2/2\mu$, μ being the $N - Y$ reduced mass, $\eta = Z_N Z_Y \mu e^2/q$ is the Coulomb parameter, where Z_N and Z_Y are the charge numbers of N and Y, and $F_L(\eta, qy_p)$ and $G_L(\eta, qy_p)$ are the regular and irregular Coulomb functions defined in the standard way [52]. The factor $C_L(\eta)$ is defined in reference [52] as

$$C_L(\eta) = \frac{2^L e^{-\frac{\pi\eta}{2}} |\Gamma(L + 1 + i\eta)|}{\Gamma(2L+2)}. \tag{43}$$

The factor $(2L+1)!! q^L C_L(\eta)$ has been introduced so that the functions $R_L^R(y_p)$ and $R_L^I(y_p)$ have a finite limit for $q \rightarrow 0$. Finally, the function $f(b, y_p)$ in Equation (42) is given by

$$f(b, y_p) = [1 - e^{-by_p}]^{2L+1}, \tag{44}$$

so that the divergent behavior of $G_L(\eta, qy_p)$ for small values of y_p is cured, and $R_L^I(y_p)$ is well-defined also in this limit. The trial parameter b is determined by requiring $f(b, y_p) \rightarrow 1$ for large values of y_p, leaving therefore unchanged the asymptotic behavior of the scattering wave function. A value of $b \sim 0.25$ fm^{-1} has been found appropriate in all the considered cases. The non-Coulomb case of Equations (41) and (42) is obtained if either Z_N or $Z_Y = 0$, so that the functions $F_L(\eta, qy_p)/(qy_p)$ and $G_L(\eta, qy_p)/(qy_p)$ are replaced by the regular and irregular Riccati-Bessel functions $j_L(qy_p)$ and $n_L(qy_p)$ as defined in reference [52], and the factor $(2L+1)!! C_L(\eta)$ reduces to 1 for $\eta \rightarrow 0$ [52].

With these definitions, $\Psi_A^{LSJJ_z}$ can be cast in the form

$$\Psi_A^{LSJJ_z} = \sum_{L'S'} \left[\delta_{LL'} \delta_{SS'} \Omega_{L'S'JJ_z}^R + \mathcal{R}_{LS,L'S'}^J(q) \Omega_{L'S'JJ_z}^I \right], \tag{45}$$

where the parameters $\mathcal{R}_{LS,L'S'}^J(q)$ give the relative weight between the regular and irregular components of the wave function. These parameters can be written in terms of the reactance matrix ($\mathcal{K}$-matrix) elements as [19, 31]

$$\mathcal{K}_{LS,L'S'}^J(q) = (2L+1)!!(2L'+1)!! q^{L+L'+1} C_L(\eta) C_{L'}(\eta) \mathcal{R}_{LS,L'S'}^J(q). \tag{46}$$

The $\mathcal{K}$-matrix, by definition, is such that its eigenvalues are $\tan\delta_{LSJ}$, δ_{LSJ} being the phase shifts. The sum over L' and S' in Equation (45) is over all values compatible with a given J and parity π, and therefore the sum over L' is limited to include either even or odd values since $(-1)^{L'} = \pi$.

Using Equations (39) and (45), the full scattering wave functions is written as

$$\Psi_{NY}^{LSJJ_z} = \sum_{K,m} c_{K;m} |K, m\rangle + \sum_{L'S'} \left[\delta_{LL'} \delta_{SS'} \Omega_{L'S'JJ_z}^R + \mathcal{R}_{LS,L'S'}^J(q) \Omega_{L'S'JJ_z}^I \right], \tag{47}$$

where the unknown quantities are the coefficients $c_{K;m}$ and $\mathcal{R}_{LS,L'S'}^J(q)$. In order to determine their values, we use the Kohn variational principle [63], which states that the functional

$$[\mathcal{R}_{LS,L'S'}^J(q)] = \mathcal{R}_{LS,L'S'}^J(q) - \left\langle \Psi_{NY}^{L'S'JJ_z} | H - E | \Psi_{NY}^{LSJJ_z} \right\rangle, \tag{48}$$

has to be stationary with respect to variations of the trial parameters $c_{K;m}$ and $\mathcal{R}_{LS,L'S'}^J(q)$ in $\Psi_{NY}^{LSJJ_z}$. Here E is the total energy of the system, and the normalization coefficients $\mathcal{C}$ of the asymptotic functions $\Omega_{LSJJ_z}^{\lambda}$ in Equation (40) are chosen so that

$$\langle \Omega_{LSJJ_z}^R | H - E | \Omega_{LSJJ_z}^I \rangle - \langle \Omega_{LSJJ_z}^I | H - E | \Omega_{LSJJ_z}^R \rangle = 1. \tag{49}$$

The variation of the diagonal functionals of Equation (48) with respect to the linear parameters $c_{K;m}$ leads to a system of linear inhomogeneous equations,

$$\sum_{K',m'} \langle K,m|H-E|K',m'\rangle c^{\lambda}_{K';m'} = -D^{\lambda,LSJJ_z}_{K,m}, \tag{50}$$

where the two terms D^{λ} corresponding to $\lambda \equiv R, I$ are defined as

$$D^{\lambda,LSJJ_z}_{K,m} = \langle K,m|H-E|\Omega^{\lambda}_{LSJJ_z}\rangle. \tag{51}$$

Therefore, two sets of the coefficients $c^{\lambda}_{K;m}$ are obtained, depending on $\lambda \equiv R, I$, and consequently, we can introduce two core functions, defined as

$$\Psi_C^{LSJJ_z,\lambda} = \sum_{K,m} c^{\lambda}_{K;m}|K,m\rangle. \tag{52}$$

The matrix elements $\mathcal{R}^J_{LS,L'S'}(q)$ are obtained varying the diagonal functionals of Equation (48) with respect to them. This leads to the following set of algebraic equations

$$\sum_{L''S''} \mathcal{R}^J_{LS,L''S''}(q) X_{L'S',L''S''} = Y_{LS,L'S'}, \tag{53}$$

with the coefficients X and Y defined as

$$\begin{aligned} X_{LS,L'S'} &= \langle \Omega^I_{LSJJ_z} + \Psi_C^{LSJJ_z,I}|H-E|\Omega^I_{L'S'JJ_z}\rangle, \\ Y_{LS,L'S'} &= -\langle \Omega^R_{LSJJ_z} + \Psi_C^{LSJJ_z,R}|H-E|\Omega^I_{L'S'JJ_z}\rangle. \end{aligned} \tag{54}$$

The solution of Equation (53) provides a first-order estimate of the matrix elements $\mathcal{R}^J_{LS,L'S'}(q)$. A second-order estimate of $\mathcal{R}^J_{LS,L'S'}(q)$, and consequently of $\mathcal{K}^J_{LS,L'S'}(q)$, is given by the quantities $[\mathcal{R}^J_{LS,L'S'}(q)]$, obtained by substituting in Equation (48) the first order results of Equations (50) and (53). Such second-order calculation provides then a symmetric $\mathcal{K}$-matrix. This condition is not imposed *a priori*, and therefore it is a useful test of the numerical accuracy reached by the method.

The Kohn variational principle as explained so far is particularly useful in the case of $q = 0$ (zero-energy scattering). For $q = 0$ the scattering can occur only in the $L = 0$ channel, and the observables of interest are the scattering lengths. Within the present approach, they can be easily obtained from the relation

$${}^{(2J+1)}a_{NY} = -\lim_{q\to 0} \mathcal{R}^J_{0J,0J}(q), \tag{55}$$

from which

$$\Psi_A^{0JJJ_z} = \left[\Omega^R_{0JJJ_z} - {}^{(2J+1)}a_{NY}\Omega^I_{0JJJ_z}\right]. \tag{56}$$

An alternative version of the Kohn variational principle is the so-called complex Kohn variational principle for the $\mathcal{S}$-matrix, quite convenient when $q \neq 0$ and especially above the Y nucleus breakup threshold, as explained in reference [64]. In this case, the Kohn variational principle of Equation (48) becomes

$$[\mathcal{S}^J_{LS,L'S'}(q)] = \mathcal{S}^J_{LS,L'S'}(q) + i\langle \Psi^{+,L'S'JJ_z}_{NY}|H-E|\Psi^{+,LSJJ_z}_{NY}\rangle, \tag{57}$$

where

$$\Psi^{+,LSJJ_z}_{NY} = \Psi_C^{LSJJ_z} + \Psi_A^{+,LSJJ_z}, \tag{58}$$

$\Psi_C^{LSJJ_z}$ being expanded as in Equation (39) and

$$\begin{aligned} \Psi_A^{+,LSJJ_z} &= [\, i\Omega^R_{LSJJ_z} - \Omega^I_{LSJJ_z}\,] \\ &+ \sum_{L'S'} \mathcal{S}^J_{LS,L'S'}(q)[\, i\Omega^R_{L'S'JJ_z} + \Omega^I_{L'S'JJ_z}\,]. \end{aligned} \tag{59}$$

The functions $\Omega^{\lambda}_{LSJJ_z}$ have been given in Equation (40). Note that, with the above definition, the reactance $\mathcal{K}$-matrix elements can be related to the $\mathcal{S}$-matrix elements as

$$\begin{aligned} \mathcal{K}^J_{LS,L'S'}(q) &= (-i)[\mathcal{S}^J_{LS,L'S'}(q) - \delta_{LL'}\delta_{SS'}] \\ &\quad [\mathcal{S}^J_{LS,L'S'}(q) + \delta_{LL'}\delta_{SS'}]^{-1}. \end{aligned} \tag{60}$$

The differentiation of the complex Kohn variational principle of Equation (57) leads to a set of equations for $c_{K;m}$ and $\mathcal{S}^J_{LS,L'S'}(q)$ similar to those given in Equations (50) and (53), where now λ stands for $\lambda = +, -$.

We conclude this section with the following remarks: (i) the calculation of the matrix elements between the core functions $\Psi_C^{LSJJ_z}$ can be performed with the HH expansion either in coordinate- or in momentum-space, depending on what is more convenient. Therefore, regarding this part, we can apply the method with any potential model, both local or non-local. (ii) Some difficulties arise with the calculations of the potential matrix elements which involve $\Omega^{\lambda}_{LSJJ_z}$, i.e., $\langle K,m|V|\Omega^{\lambda}_{LSJJ_z}\rangle$ present in Equation (51), and $\langle \Omega^{\lambda'}_{L'S'JJ_z} + \Psi_C^{L'S'JJ_Z,\lambda'}|V|\Omega^{\lambda}_{LSJJ_z}\rangle$ of Equation (54), with $\lambda, \lambda' = R, I$. In particular, we note that, being $\Omega^{\lambda}_{LSJJ_z}$ given in coordinate-space, which is particularly suitable when the Coulomb interaction is considered, as for $p-d$ scattering, the non-local potential expressed in momentum-space is Fourier transformed to work in coordinate-space. The consequent integration on the momentum transfer are easily performed for the recent chiral and V_{low-k} potential models, but not for the non-local meson-theoretic CDBonn potential model, which has a high-momentum tail. Therefore, the CDBonn potential model has not been used in the study of the scattering processes presented here. We further refer to reference [31] for all technical details. (iii) The three-nucleon interaction models which at the moment have been implemented with the HH method are only the local ones, like the Urbana IX potential (UIX) of reference [65] and the N2LO model of reference [66]. The models used so far, besides being local, have a well-defined operatorial structure. In this case, the projection procedure as used for the two-nucleon interaction is not needed and the approach follows well-established footsteps, as explained in references [67, 68].

3. SELECTED RESULTS

We present in this section selected results obtained with the HH method described above. The method has been applied widely

since many years, and therefore a selection is mandatory. We have followed these criteria: (i) we focus on the results obtained after 2008, year of the publication of the review of reference [19] on the same method. (ii) We restrict ourselves to the potential models, mostly discussed in the Research Topic of which this contribution is part. They are the most widely used models. (iii) We concentrate on the results obtained for the $A = 3, 4$ elastic scattering observables, but we present briefly also the corresponding bound state results.

The aim of this section is two-fold: first of all we wish to show the effectiveness of the HH method for few-nucleon systems; secondly, we want to emphasize that the HH method, as well as any *ab initio* method, is an essential tool for testing and eventually improving nuclear interaction models.

All the results presented here are obtained at convergence, i.e., the HH expansion and the expansion on the Laguerre polynomials [see Equations (32) and (33)] has been pushed so that an accuracy of 1 keV (10 keV) is reached for the $A = 3$ ($A = 4$) binding energies, and the numerical accuracy on the scattering lengths is of the order of 0.001 fm. For a discussion on the convergence of the expansion see, for instance, references [30, 31].

The potentials which will appear in the following subsections include both two- and three-nucleon interactions. They are the phenomenological two-nucleon interaction Argonne v_{18} (AV18) [4], augmented by the three-nucleon Urbana IX (UIX) model [65], the meson-theoretic CDBonn potential [5] (CDB), together with the three-nucleon Tucson-Melbourne [69, 70] (TM) model, and the V_{low-k} potential [71], obtained from the AV18 with $\Lambda = 2.2$ fm^{-1}, so that the triton binding energy is reproduced. We consider in addition also chiral potentials, in particular the two-nucleon interaction models of the Idaho group of reference [72], obtained at next-to-next-to-next-to-leading order (N3LO), and here labeled with N3LO-I, and the more recent models derived by the same group in reference [73], here labeled according to the chiral order, i.e., from leading order (LO) up to next-to-next-to-next-to-next-to leading order (N4LO). All these two-nucleon models have been augmented with a (local) three-nucleon interaction derived up to N2LO as in reference [66]. The momentum-cutoff value is set equal to $\Lambda = 500$ MeV, unless differently specified. Note that the low-energy constants (LECs) c_D and c_E are those of reference [66] when the N2LO three-nucleon interaction is used in conjunction with the N3LO-I two-nucleon potential, while the LECs are those of reference [74] when the N2LO three-nucleon interaction is used in conjunction with the N2LO, N3LO, and N4LO two-nucleon interactions of reference [73] (no three-nucleon interaction is present at lower chiral order). To be remarked that the LECs c_D and c_E, and more generally the parameters entering the three-nucleon interaction model, depend on which two-nucleon interaction is used, as well as on which set of observables is used for their determination. This is why, for instance, the N2LO three-nucleon interaction in conjunction with the N2LO two-nucleon interaction has different values for the LECs compared to those present in the same three-nucleon interaction considered together with the N3LO or N4LO two-nucleon interaction. Finally, we will present results obtained also with the minimally non-local chiral potentials of the Norfolk group, as derived in reference [75] for the two-nucleon, and in references [1, 76] for the three-nucleon interaction. The two-nucleon models are labeled NVIa, NVIIa, NVIb, and NVIIb depending on the cutoff value and the maximum laboratory energy of the considered *NN* database. When the three-nucleon interaction are included, we will refer to NV2+3/Ia, NV2+3/IIa, and so on, corresponding to the fitting procedure of reference [1], and NV2+3/Ia*, NV2+3/IIa*, and so on, corresponding to the fitting procedure of reference [76]. We discuss in more details these fitting procedures below, and we refer the reader to the original references, or to the contributions present in this Research Topic. To be noticed that when the HH method is

TABLE 1 | The binding energies in MeV for ^{3}H, ^{3}He, and ^{4}He, calculated with the HH technique using different Hamiltonian models.

Interaction	^{3}H	^{3}He	^{4}He
AV18	7.624	6.925	24.21
AV18/UIX	8.479	7.750	28.46
CDB	7.998	7.263	26.13
CDB/TM	8.474	7.720	29.00
N3LO-I	7.854	7.128	25.38
N3LO-I/N2LO	8.474	7.733	28.36
LO	11.091	10.409	40.09
NLO	8.307	7.597	27.55
N2LO	8.206	7.460	27.23
N3LO	8.092	7.343	26.68
N4LO	8.080	7.337	26.58
N2LO/N2LO	8.474	7.729	27.92
N3LO/N2LO	8.477	7.728	27.97
N4LO/N2LO	8.477	7.728	28.15
NVIa	7.818	7.090	25.15
NVIIa	7.949	7.213	25.80
NVIb	7.599	6.885	23.96
NVIIb	7.866	7.133	25.28
NV2+3/Ia	8.475	7.735	28.33
NV2+3/IIa	8.475	7.730	28.16
NV2+3/Ib	8.475	7.737	28.30
NV2+3/IIb	8.475	7.727	28.15
NV2+3/Ia*	8.477	7.727	28.30
NV2+3/IIa*	8.474	7.725	28.18
NV2+3/Ib*	8.469	7.724	28.21
NV2+3/IIb*	8.474	7.724	28.11
Experiment	8.475	7.725	28.30

The underlined values are used in the LECs fitting procedure. In the last row, we show the ^{3}H (^{3}He) experimental binding energy of 8.482 MeV (7.718 MeV), lowered (increased) by 7 keV in order to take into account the $n - p$ mass difference. See text for more details. All the results presented here are in very good agreement with the values reported in the literature. The experimental binding energies are taken from reference [78]. The experimental uncertainty is well below the 1 keV level, and therefore it is not quoted in the table.

used to study the bound states, the local AV18, AV18/UIX, NV, and NV2+3 potentials have been all augmented by the full electromagnetic interaction, which includes corrections up to α^2 (α is the fine-structure constant) [77]. On the other hand, the non-local CDB, CDB/TM, and all the non-local chiral potentials retain only the point-Coulomb interaction. The point-Coulomb interaction, and not the full electromagnetic one, is also used when studying the scattering states presented below.

3.1. $A = 3, 4$ Bound States

The results for the trinucleon and ^{4}He binding energies, obtained using all the above mentioned potentials, are given in **Table 1**. To be noticed that in many cases, the experimental trinucleon binding energy is used for the LECs fitting procedure performed applying the HH method. When this occurs, the corresponding HH results is underlined in the table. The results not underlined are obtained using the "original" two- and three-nucleon interactions, whose parameters are usually fitted to the triton binding energy and other observables, applying *ab initio* methods different than the HH method. The HH results are therefore not necessarily in perfect agreement with the experimental data.

We briefly outline the fitting procedure for the LECs c_D and c_E in order to better understand the results, and we refer to references [1, 76, 79] for more details. The ^{3}H and ^{3}He ground state wave functions are calculated using a given two- and three-nucleon potential, and the corresponding LECs c_D and c_E are determined by fitting the $A = 3$ experimental binding energies, corrected for a small contribution (+7 keV in ^{3}H and −7 keV in ^{3}He), due to the $n - p$ mass difference [44], since in the present HH method this effect is neglected. This procedure generates two trajectories, one for ^{3}H and one for ^{3}He, in the $\{c_D, c_E\}$ plane, so that each point of the trajectory corresponds to the correct binding energy. The two trajectories are typically extremely close to each other and the average can be safely considered, since the points of the average trajectory typically lead to $A = 3$ binding energies within 10 keV of the experimental values. A second observable is needed in the fitting procedure. In reference [1] the $n - d$ doublet scattering length $^2a_{nd}$ has been used, which leads in the $\{c_D, c_E\}$ plane to another trajectory, which is very close to the one corresponding to the ^{3}H binding energy, but not exactly overlapping. This is a well-known fact, that the ^{3}H binding energy and $^2a_{nd}$ are correlated observables. However, it is possible to find an intersection point of the two trajectories, which allows to determine the LECs. This procedure has been used for the NV2+3/Ia, NV2+3/Ib, NV2+3/IIa, and NV2+3/IIb potential models. The corresponding $\{c_D, c_E\}$ values, as given in Table 1 of reference [1], are $\{3.666, -1.638\}$, $\{-2.061, -0.982\}$, $\{1.278, -1.029\}$, $\{-4.480, -0.412\}$, respectively. Alternatively we can choose as the second observable the Gamow-Teller matrix element of tritium β-decay, to take advantage of the fact that the LEC c_D enters also in the two-nucleon axial current operator at N2LO [76, 79–81]. This second procedure has been used for

TABLE 2 | $n - d$ and $p - d$ doublet and quartet scattering lengths in fm calculated with the HH technique using different Hamiltonian models.

Interaction	$^2a_{nd}$	$^4a_{nd}$	$^2a_{pd}$	$^4a_{pd}$
AV18	1.275	6.325	1.185	13.588
AV18/UIX	0.610	6.323	-0.035	13.588
V_{low-k}	0.572	6.321	-0.001	13.571
N3LO-I	1.099	6.342	0.876	13.646
N3LO-I/N2LO	0.675	6.342	0.072	13.647
NVIa	1.119	6.326	0.959	13.596
NVIb	1.307	6.327	1.294	13.597
NV2+3/Ia*	0.638	6.326	0.070	13.596
NV2+3/Ib*	0.650	6.327	0.070	13.597
Experiment	0.645±0.003 ± 0.007	6.35±0.02	−0.13 ± 0.04	14.7 ± 2.3

The experimental value for $^2a_{nd}$ is from reference [82], that for $^4a_{nd}$ is from reference [83], while those for $^2a_{pd}$ and $^4a_{pd}$ are from reference [84].

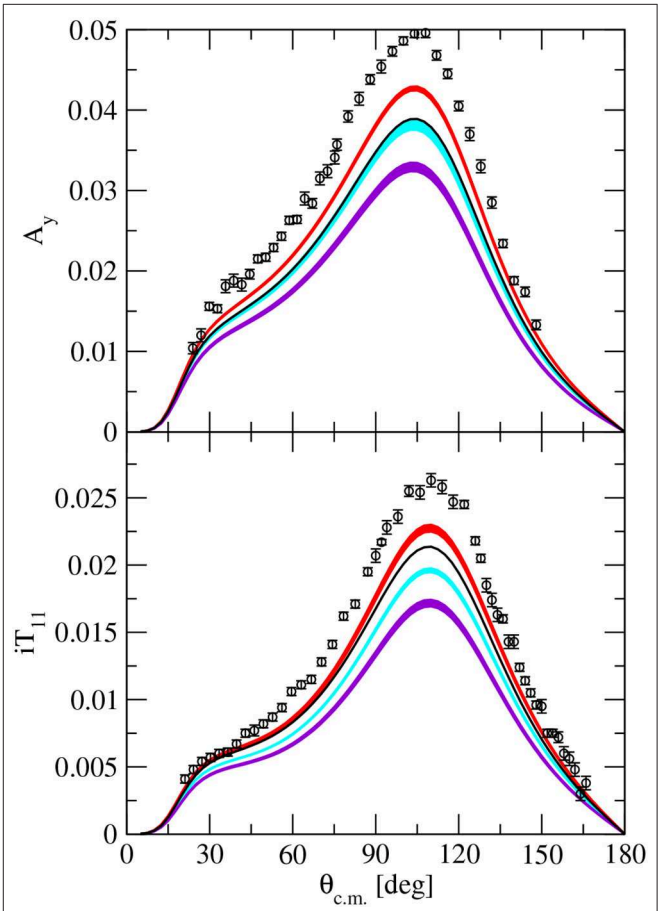


FIGURE 1 | The vector analyzing powers A_y and iT_{11} for $p - d$ elastic scattering at center-of-mass energy $E_{c.m.} = 2$ MeV, using models in the AV18/TM class (cyan bands), AV18/UIX (violet bands), and AV18/N2LO (red bands). The predictions of the original AV18/UIX model (solid lines) and the experimental points from reference [86] are also shown.

the N2LO/N2LO, N3LO/N2LO, and N4LO/N2LO potentials of reference [74], and the NV2+3/Ia*, NV2+3/Ib*, NV2+3/IIa*, and NV2+3/IIb* potential models of reference [76]. In this last case, we report the corresponding $\{c_D, c_E\}$ values for completeness, which are $\{-0.635, -0.090\}$, $\{-4.710, 0.550\}$, $\{-0.610, -0.350\}$, $\{-5.250, 0.050\}$, respectively.

We can now proceed with some comments regarding the binding energies results of **Table 1**. (i) The large variety of models for the nuclear interaction which the HH method can handle is an indication of how strong and reliable this method has become. Furthermore, we should mention that the theoretical uncertainty is of 1 keV (10 keV) for the $A = 3$ (^{4}He) binding energies. The HH method is therefore extremely accurate. Furthermore, all the HH results are in very good agreement with the values reported in the literature, when available. (ii) In order to reproduce the experimental binding energies the inclusion of three-nucleon force is essential. In all cases, the triton binding energy is well-reproduced, within few keV. On the other hand, the ^{4}He binding energies can differ from the experimental value of even up to 700 keV (in the CDB/TM case). (iii) In the case of the NV2+3 potential models, when the observables used to fit the LECs are the triton binding energy and $^2a_{nd}$, we notice a systematic overestimation of the ^{3}He binding energy. (iv) All the results for the $A = 3$ ($A = 4$) binding energies obtained with any model for the two- and three-nucleon interaction are within 10 (400) keV from the experimental values. Therefore we can conclude that any of the constructed model is essentially able to reproduce these very light nuclei.

3.2. $N - d$ Scattering

One of the remarkable features of the HH method resides in its capability of dealing with local as well as with non-local potentials, formulated in either coordinate or momentum space, not only for the bound states, as we have seen above, but also for $N - d$ scattering observables. This has been demonstrated in reference [31], in which the local AV18 and the non-local chiral N3LO-I potential models were used to calculate the $N - d$ elastic scattering observables below the deuteron breakup threshold. Here we present results with a subset of all the potential models mentioned above, and in particular with the AV18, AV18/UIX, the N3LO-I, N3LO-I/N2LO, and some of the NV and NV2+3 models. A further class of nuclear interactions that has been tested using the HH method is represented by the so-called V_{low-k} potential obtained from the AV18 with $\Lambda = 2.2$ fm^{-1}, so chosen to reproduce the triton binding energy when the complete electromagnetic interaction is used [71]. We do not report here detailed investigations on the convergence of the HH expansion, but we can mentioned that this convergence is faster for the non-local potentials as compared to the local ones, due to the much softer behavior at small distances. For instance, for $N - d$ elastic scattering in the channel $J^\pi = 1/2^+$, the HH basis can be of the order of 12000 (7000) elements with the NV (N3LO-I) potential to get convergence.

We first consider the converged results for the $n - d$ and $p - d$ doublet and quartet scattering lengths, which are given in **Table 2**, together with the very precise experimental result

TABLE 4 | χ^2/datum of the two-parameter fit to $p - d$ elastic scattering data at $E_{c.m.} = 2$ MeV, obtained neglecting in Equation (61) all the subleading operators except the leading contact term proportional to the LEC E_0, and the tensor S_{ij} and spin-orbit $(L \cdot S)_{ij}$ operators, proportional to the LECs E_5 and E_7, considered on top of the AV18/UIX potential model.

Λ (MeV)	**200**	**300**	**400**	**500**
χ^2/datum	2.0	2.0	2.1	2.1
e_0	−0.074	−0.037	0.053	0.451
e_5	−0.212	−0.248	−0.403	−0.799
e_7	1.104	1.195	1.686	2.598
$\langle AV18 \rangle$ (MeV)	−7.353	−7.373	−7.394	−7.343
$\langle UIX \rangle$ (MeV)	−1.118	−1.095	−1.058	−1.031
$\langle E_0 \rangle$ (MeV)	−0.057	−0.069	0.125	0.841
$\langle E_5 S_{ij} \rangle$ (MeV)	−0.032	−0.182	−0.609	−1.553
$\langle E_7 (L \cdot S)_{ij} \rangle$ (MeV)	0.079	0.237	0.454	0.605
$^2a_{nd}$ (fm)	0.611	0.618	0.626	0.638
$^4a_{nd}$ (fm)	6.32	6.32	6.32	6.32

The LECs e_0, e_5, e_7 are defined in terms of E_0, E_5, E_7 as $E_0 = e_0/(F_\pi^4 \Lambda)$, $E_i = e_i/(F_\pi^4 \Lambda^3)$, $i = 5, 7$, $F_\pi = 92.4$ MeV being the pion decay constant, so that $e_0 \sim e_i \sim O(1)$ if natural. Also shown are the mean values in the triton state of the one- plus two-body Hamiltonian (labeled as $\langle AV18 \rangle$), of the UIX three-body potential (labeled as $\langle UIX \rangle$), and of individual contributions from the short-distance three-body potential. The calculated values of $^2a_{nd}$ and $^4a_{nd}$ are also given.

TABLE 3 | χ^2/datum of the $p - d$ elastic scattering observables at center-of-mass energies $E_{c.m.} = 0.666, 1.33, 1.66$ and 2.0 MeV, calculated with the N3LO-I or AV18 two-nucleon only, and the N3LO-I/N2LO or AV18/UIX two- and three-nucleon Hamiltonian models.

	0.666 MeV					**1.33 MeV**	**1.66 MeV**					**2.0 MeV**				
	A_y	iT_{11}	T_{20}	T_{21}	T_{22}	A_y	A_y	iT_{11}	T_{20}	T_{21}	T_{22}	A_y	iT_{11}	T_{20}	T_{21}	T_{22}
N	7	8	24	24	24	38	44	50	50	50	50	38	51	51	51	51
AV18	283.3	113.4	6.9	4.7	2.8	186.0	267.6	121.3	1.9	3.2	6.6	237.1	148.8	3.7	5.1	12.5
AV18/UIX	205.2	67.0	3.2	3.5	1.1	112.4	264.7	110.1	4.2	7.2	2.1	202.4	115.0	6.4	14.3	2.2
N3LO-I	197.7	68.7	4.0	2.6	1.5	108.4	227.9	92.6	1.0	2.2	2.7	186.0	108.3	1.9	2.8	4.4
N3LO-I/N2LO	139.9	49.5	2.7	2.5	0.9	70.0	159.4	84.3	2.1	4.0	2.8	114.0	85.8	3.6	8.3	1.6

The different number N of experimental data is also indicated. The data are from references [89, 90] at $E_{c.m.} = 0.666$ MeV, and from reference [86] at $E_{c.m.} = 1.33, 1.66$, and 2.0 MeV.

from reference [82] for ${}^2a_{nd}$, and the older experimental results from reference [83] for ${}^4a_{nd}$. Though no experimental data are available for ${}^2a_{pd}$ and ${}^4a_{pd}$, the results of the energy-dependent phase-shift analysis of reference [84], using very low $p-d$ data, is reported. All the results are obtained using the pure Coulomb electromagnetic interaction. When the full electromagnetic interaction is used, ${}^4a_{nd}$ remains practically unchanged, while ${}^2a_{nd}$ becomes smaller. For the NVIa and NVIb potentials, for instance, ${}^2a_{nd} = 1.103$ fm and 1.293 fm, respectively, with the full electromagnetic interaction. As it is clear from inspection of **Table 2**, while ${}^4a_{nd}$ is very little model-dependent and in good agreement with experiment, the same is not true for ${}^2a_{nd}$. In particular, the inclusion of a three-nucleon force appears necessary to bring the results closer to the experimental datum. However, not every model agrees with the experiment. The disagreement is more pronounced for the V_{low-k} interaction, showing that this observable cannot be simply reproduced by increasing the attraction of the two-nucleon interaction, as is done in this case by choosing the right value for Λ to describe the triton; instead, a subtle balance between attraction and repulsion in the three-nucleon system has to be reached. Indeed, being the zero-energy $n-d$ scattering state orthogonal to the triton, the associated wave function presents a node in the relative distance, whose precise position, which is related to the scattering length, depends on the interplay between attraction and repulsion. The results of the $p-d$ phase-shift analysis given in reference [84] are a first tentative to determine the $p-d$ scattering lengths from $p-d$ data. Very few experimental data exist for center-of-mass energies below

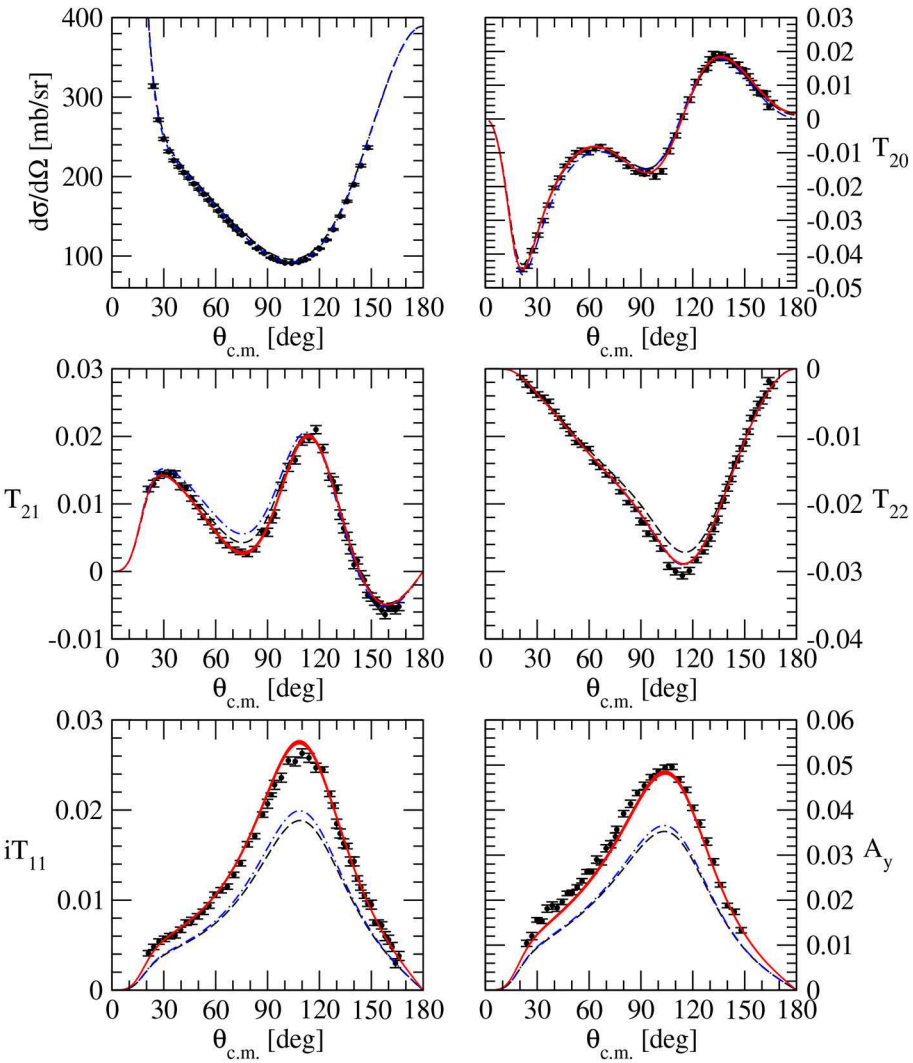


FIGURE 2 | Curves obtained including only the tensor and spin-orbit subleading contact operator on the top of the AV18/UIX interaction, fitted to a set of cross section and polarization observables in $p-d$ elastic scattering at 2 MeV center-of-mass energy [86], for $\Lambda = 200-500$ MeV (red bands), are compared to the purely two-body AV18 interaction (dashed black lines) and to the AV18/UIX two- and three-nucleon interaction (dashed-dotted blue lines).

500 keV, introducing large uncertainties in the quartet case. In the case of the doublet scattering length, difficulties arise from the particular pole structure of the doublet $p-d$ effective range expansion close to threshold (see, for example, Figure 1 of reference [84]).

With the purpose of investigating the capability of some widely used models of three-nucleon interaction to reproduce ${}^2a_{nd}$, a sensitivity study was conducted in reference [85] taking the AV18 as the reference two-nucleon interaction. Three different models of the three-nucleon interactions were considered: the UIX, the TM and the chiral N2LO of reference [66]. Their parameters were adjusted, constraining them to reproduce simultaneously ${}^2a_{nd}$ and the triton binding energy, and the resulting value for the ^{4}He binding energy was calculated. For the UIX model, a reasonable description of these three observables was possible, at the cost of a sizable increase of the repulsive term, as compared to the original parameterization. A similar conclusion held for the TM model, where a repulsive short-range term was found to be necessary. Finally, for the N2LO three-nucleon interaction, the relative importance of the parameters involving the P-wave pion rescattering had to be changed. This is not surprising, due to the mismatch between the physics underlying the adopted models for two- and three-nucleon interactions. Also in this case, a repulsive short-range interaction was preferred. Then, a set of polarization observables on elastic $p-d$ scattering were computed using the AV18 augmented by the modified versions of the three-nucleon interactions models as described above. These led to three classes of interaction models. As an interesting result, all models within a given class led to very similar predictions, but for some observables, namely the proton A_y and the deuteron iT_{11}. These predictions were different from class to class, and all in

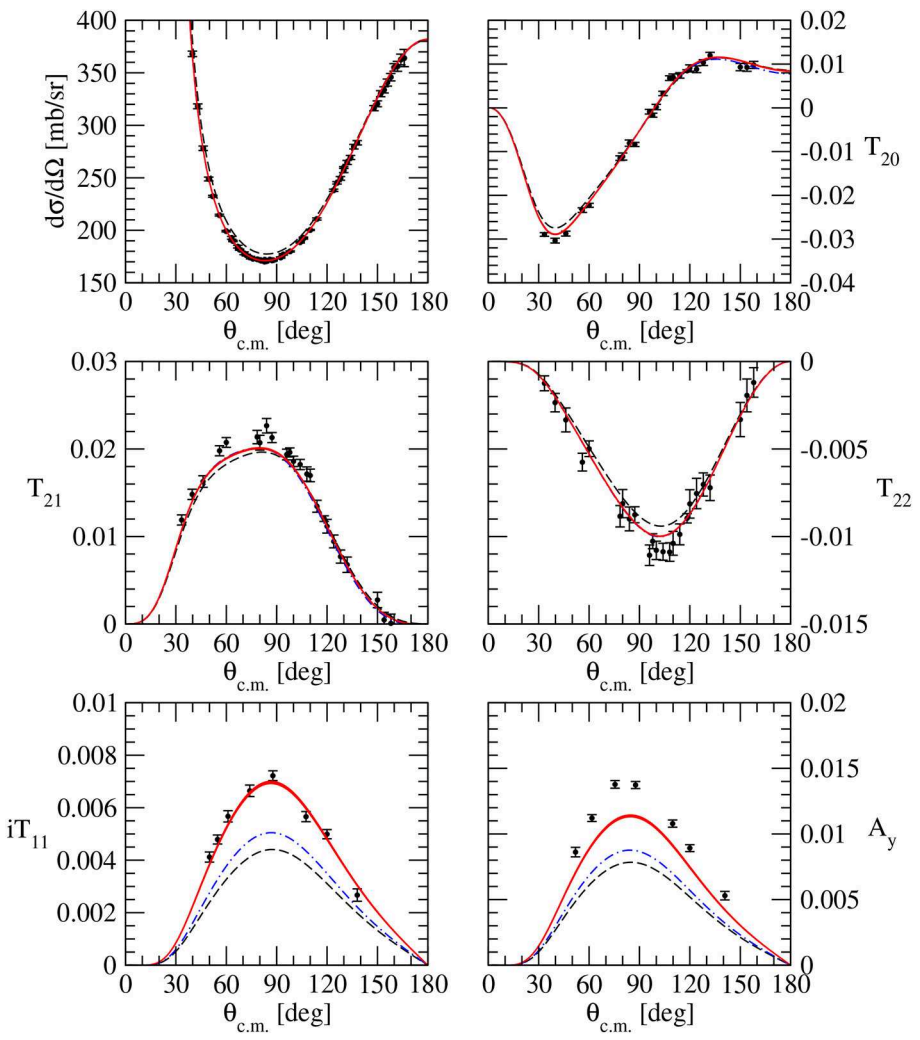


FIGURE 3 | Predictions obtained with the three-nucleon interaction models discussed in the text with $\Lambda = 200-500$ MeV (red bands) for a set of cross section and polarization $p-d$ observables at 0.666 MeV center-of-mass energy, as compared to the purely two-body AV18 interaction (dashed black lines), to the AV18/UIX two- and three-nucleon interaction (dashed-dotted blue lines), and to the experimental data of reference [90].

disagreement with the data. This is shown in **Figure 1**. Since the three classes of models mostly differ in their short-distance behavior, it follows that an improvement in this component of the three-nucleon interaction is needed to explain the data. Indeed, no sensible improvement was obtained as compared to the original AV18/UIX model.

In order to be more quantitative, as to the accuracy of the existing models of two- and three-nucleon interaction, we show in **Table 2** the χ^2/datum for all $p-d$ elastic scattering observables at different center-of-mass energies, as obtained with the AV18 and N3LO-I two-body interactions, without or with the inclusion of the UIX and N2LO three-nucleon interaction models [31]. It is clear that all considered models fail to give a satisfactory description of all polarization observables, especially for A_y and iT_{11}. From the previous discussion, there are strong hints that the improvement should come from a more accurate modeling of the short distance structure of the three-nucleon interaction. Therefore, in reference [87] all the possible short-distance (contact) structures for the three-nucleon interaction have been classified up to the subleading order of a systematic low-energy expansion. It has been found that the short-distance component of the three-nucleon interaction can be parameterized by ten LECs, denoted by E_i with $i = 1, ..., 10$. The corresponding three-nucleon potential in configuration space can be written as

$$
\begin{aligned}
V_{3Ncont} = & \sum_{i\neq j\neq k} E_0 Z_0(r_{ij};\Lambda) Z_0(r_{ik};\Lambda) \\
& + (E_1 + E_2 \boldsymbol{\tau}_i\cdot\boldsymbol{\tau}_j + E_3 \boldsymbol{\sigma}_i\cdot\boldsymbol{\sigma}_j + E_4 \boldsymbol{\tau}_i\cdot\boldsymbol{\tau}_j \boldsymbol{\sigma}_i\cdot\boldsymbol{\sigma}_j) \\
& \left[Z_0''(r_{ij};\Lambda) + 2\frac{Z_0'(r_{ij};\Lambda)}{r_{ij}} \right] Z_0(r_{ik};\Lambda) \\
& + (E_5 + E_6 \boldsymbol{\tau}_i\cdot\boldsymbol{\tau}_j) S_{ij} \left[Z_0''(r_{ij};\Lambda) - \frac{Z_0'(r_{ij};\Lambda)}{r_{ij}} \right] Z_0(r_{ik};\Lambda) \\
& + (E_7 + E_8 \boldsymbol{\tau}_i\cdot\boldsymbol{\tau}_k)(\mathbf{L}\cdot\boldsymbol{S})_{ij} \frac{Z_0'(r_{ij};\Lambda)}{r_{ij}} Z_0(r_{ik};\Lambda) \\
& + (E_9 + E_{10} \boldsymbol{\tau}_j\cdot\boldsymbol{\tau}_k) \boldsymbol{\sigma}_j\cdot\hat{\mathbf{r}}_{ij} \boldsymbol{\sigma}_k\cdot\hat{\mathbf{r}}_{ik} Z_0'(r_{ij};\Lambda) Z_0'(r_{ik};\Lambda), \quad (61)
\end{aligned}
$$

where $\boldsymbol{\sigma}_i$ ($\boldsymbol{\tau}_i$) are the Pauli spin (isospin) matrices of particle i, $\mathbf{r}_{ij}$ is the relative distance between particles i and j, and S_{ij} and $(\mathbf{L}\cdot\boldsymbol{S})_{ij}$ are, respectively, the tensor and spin-orbit operators. The profile functions $Z_0(r;\Lambda)$ are written as

$$
Z_0(r;\Lambda) = \int \frac{d\mathbf{k}}{(2\pi)^3} e^{i\mathbf{k}\cdot\mathbf{r}} F(\mathbf{k}^2;\Lambda), \quad (62)
$$

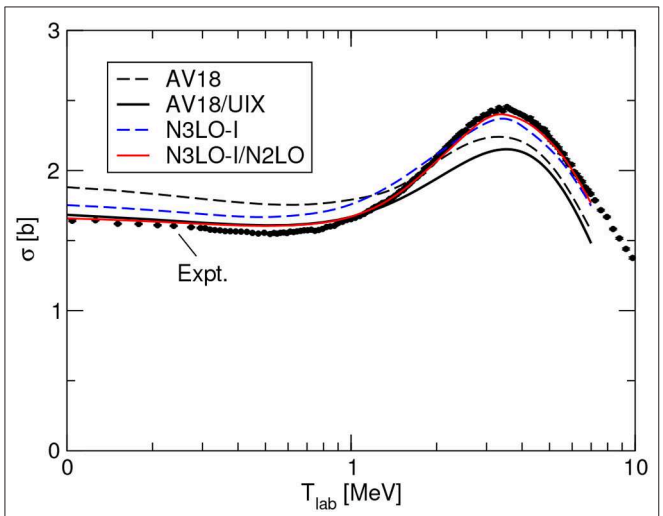


FIGURE 4 | $n-{}^3$H total cross sections calculated with the AV18 (dashed black line), AV18/UIX (solid black line), N3LO-I (dashed blue line), and the N3LO-I/N2LO (solid red line) potential models as function of the incident neutron laboratory energy E_n. The experimental data are from reference [91].

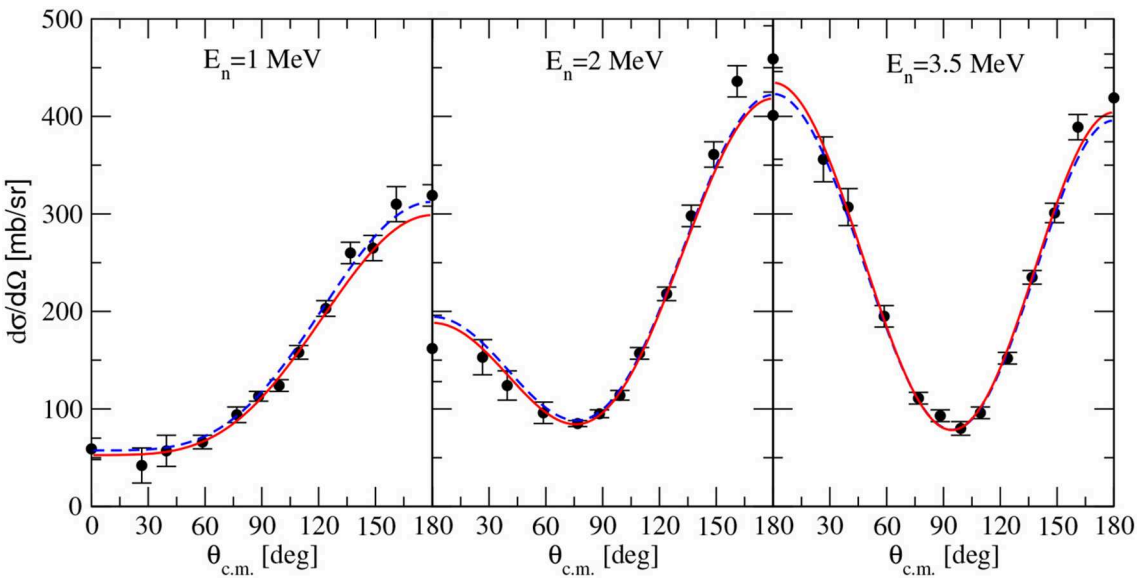


FIGURE 5 | $n-{}^3$H differential cross sections calculated with the N3LO-I (dashed blue lines) and the N3LO-I/N2LO (solid red lines) interaction models for three different incident neutron energies. The experimental data are from reference [92].

with $F(\mathbf{k}^2;\Lambda)$ a suitable cutoff function which suppresses the momentum transfers $\mathbf{k}$ above a given short-distance cutoff Λ. In Equation (61), the basis of operators has been chosen so that most terms in the potential can be viewed as an ordinary interaction of particles ij with a further dependence on the coordinate of the third particle k. In reference [88], elastic $p-d$ scattering data at $E_{c.m.} = 2$ MeV center-of-mass energy have been used to fit the E_i LECs, when the subleading three-nucleon interaction given in Equation (61) is considered in addition to the AV18/UIX interaction. Also ${}^2a_{nd}$ and ${}^4a_{nd}$ and the triton binding energy have been included in the fit.

The results of reference [88] can be summarized as follows. First of all, we noticed that the operators which play a leading role in reducing the large χ^2/datum of **Table 3** are the spin-orbit and tensor interactions, which depend on the LECs E_5 and E_7. We present in **Table 4** the results of a fit where only the terms proportional to E_0, E_5, and E_7 are kept. The LEC E_0 is used to fix the triton binding energy. Then the experimental data for the doublet and quartet $n-d$ scattering lengths of references [82, 83], and those of several $p-d$ scattering observables at 2 MeV center-of-mass energy of reference [86] are used for the determinations of the LECs. As it is shown in **Table 4**, the χ^2/datum is drastically reduced to ~ 2 for the short distance cutoff Λ of Equation (62) between 200 and 500 MeV. More sophisticated fits, including all the involved LECs, lead to only slightly better χ^2/datum ~ 1.6. In **Figure 2** we show the corresponding fitted curves compared to the AV18 and AV18/UIX predictions. It is clear that a very accurate description can be obtained with only the spin-orbit and tensor subleading operators. We also note that the values of the LECs e_0, e_5, e_7, defined in terms of E_0, E_5, E_7 as $E_0 = e_0/(F_\pi^4\Lambda)$, $E_i = e_i(F_\pi^4\Lambda^3)$, $i = 5, 7$, $F_\pi = 92.4$ MeV being the pion decay constant, are of order 1 as expected.

With the interaction fitted using the $E_{c.m.} = 2$ MeV data of reference [86], we can perform a study at lower energies, where experimental data exist. As a representative example we show in **Figure 3** the results corresponding to $E_{c.m.} = 0.666$ MeV, from which we can observe that the adopted interaction captures quite nicely the energy dependence of the data. In reference [88], a fit including all the subleading operators of Equation (61) leads to predictions in even better agreement with the data. However, in order to obtain further improvements, a global fit at multiple energies should be performed.

3.3. $p-{}^3$He and $n-{}^3$H Scattering

The study of $N-d$ scattering to constrain the three-nucleon force has the limitation of being mostly restricted to the isospin $T = 1/2$ channel. From this perspective, $A = 4$ systems open new possibilities, besides being of direct relevance for the role they play in many reactions of astrophysical and cosmological interest. The HH method has been used in this context to address first of all the $n-{}^3$H [32] and $p-{}^3$He [33, 35] elastic scattering at low energies. The HH method applied to these systems has been benchmarked in reference [34] with the only two other *ab initio* methods which can study low-energy scattering states, with full inclusion of the Coulomb interaction. They are the AGS equations solved in momentum space (see for a review references [16, 17] and references therein), and the FE method in configuration space (see reference [13]. This topic is also covered in the present Research Topic). All these methods differ by <1%, which is smaller than the experimental uncertainties of the available data. The agreement found using softer potentials of the V_{low-k}-type is even better.

The $n-{}^3$H elastic scattering total cross section is shown in **Figure 4**. From inspection of the figure, we can see a sizable dependence on the three-nucleon interaction, both in the very low-energy region and in the peak region (for neutron laboratory energy $E_n \sim 3.5$ MeV). Indeed, at very low energies, it is crucial to have a correct description of the triton binding energy in order to reproduce the data, whereas in the peak region there is more model dependence. The HH calculations of **Figure 4** have been performed using the non-local chiral N3LO-I two-nucleon potential, also supplemented by the chiral N2LO three-nucleon interaction of reference [66] with the LECs fixed to reproduce the $A = 3, 4$ binding energies. This leads to a remarkable agreement with the available experimental data in the low-energy region. The chiral N3LO-I model seems to perform better than the AV18 one also in the peak region.

In **Figure 5** we show the $n-{}^3$H differential cross section compared to the experimental data at three different neutron laboratory energies. As it is clear from inspection of the figure, the N3LO-I/N2LO results are in nice agreement with the data. A further study of convergence with respect to chiral orders and of cutoff dependence would be highly desirable, and it is currently underway.

Much more accurate data are available for $p-{}^3$He elastic scattering, whose polarization observables have also been accurately measured [93]. Similarly to the $p-d$ case, there is a strong discrepancy between theory and experiment for the proton analyzing power A_y. In reference [35] the HH method has been applied with the N3LO-I/N2LO chiral potential model, in this case obtained with two different values of the momentum cutoff $\Lambda = 500, 600$ MeV [94], and two different procedures to fix the LECs entering the three-nucleon interaction, i.e., either reproducing the $A = 3, 4$ binding energies [66], or reproducing the triton binding energy and Gamow-Teller matrix element in tritium β-decay [79]. We show in **Figure 6** the corresponding results for proton laboratory energy of 5.54 MeV, compared to experimental data. The two bands reflect the cutoff dependence and the model dependence introduced by the LECs determinations. As it is clear, the A_y discrepancy is largely reduced down to the 8–10% level. Note that these asymmetries are 10 times larger in the $A = 4$ systems than for $p-d$ and $n-d$. The remaining discrepancy, although it appears small, is of the order of 0.05, the size of A_y for $p-d$. Therefore, we expect that the subleading components of the three-nucleon interactions discussed in section 3.2 could give a correction of the necessary order of magnitude to solve the remaining discrepancy. Work is in progress in this direction.

3.4. $p-{}^3$H and $n-{}^3$He Scattering

The treatment of $p-{}^3$H and $n-{}^3$He scattering, even below the $d+d$ threshold, is more challenging due to the coupling between these two channels and to the presence of both isospin 0 and 1 states. Also in this case, recently, in reference [48], a benchmark calculation has been performed with the HH, AGS and FE methods, using the N3LO-I interaction. Good

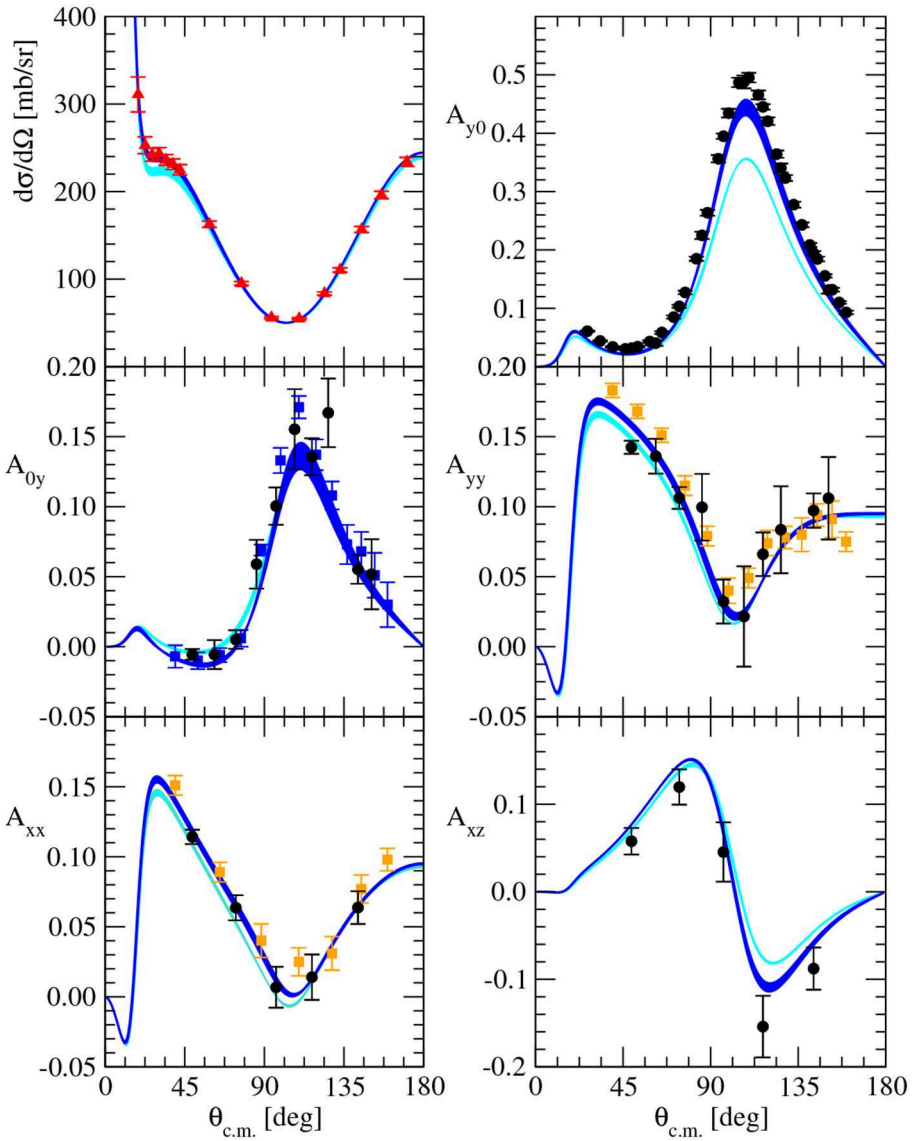


FIGURE 6 | $p-^3$He differential cross section, analyzing powers and various spin correlation coefficients at proton laboratory energy $E_p = 5.54$ MeV, calculated with only the two-nucleon N3LO-I (light cyan band) or with two- and three-nucleon interaction N3LO-I/N2LO (darker blue band). The experimental data are from references [95–97]. See text for more details.

agreement among the three methods has been found, with discrepancies smaller than the uncertainties in the experimental data. In references [98, 99], we have studied with the HH method the effect of the inclusion of the N2LO three-nucleon interaction, with the LECs fixed from the triton binding energy and the Gamow-Teller matrix element in the tritium β-decay [79]. We show in **Figure 7** the $p-^3$H differential cross section, for which, only at very low energies, below the opening of the $n-^3$He channel, some sizable effects are visible. Otherwise, the three-nucleon interaction contributions are found very small. The $p-^3$H analyzing power at three values of the laboratory beam energy are shown in **Figure 8**. Also for this observable, the three-nucleon interaction effect is found too small to improve the agreement with the available experimental data.

We conclude showing in **Figure 9** the HH results for the differential cross section and proton analyzing power of the charge-exchange reaction $p+^3\mathrm{H} \rightarrow n+^3\mathrm{He}$ at three different proton laboratory energies, compared with the experimental data. By inspection of the figure, we can see that also in this case the effects of the three-nucleon interaction are quite small, and sometimes go in the wrong direction as compared to the experimental data, as for the analyzing power A_{y0}. It is important to notice that this observable is mostly sensitive to the two-nucleon interaction. Therefore, it could be used for a more stringent test of the two-nucleon force.

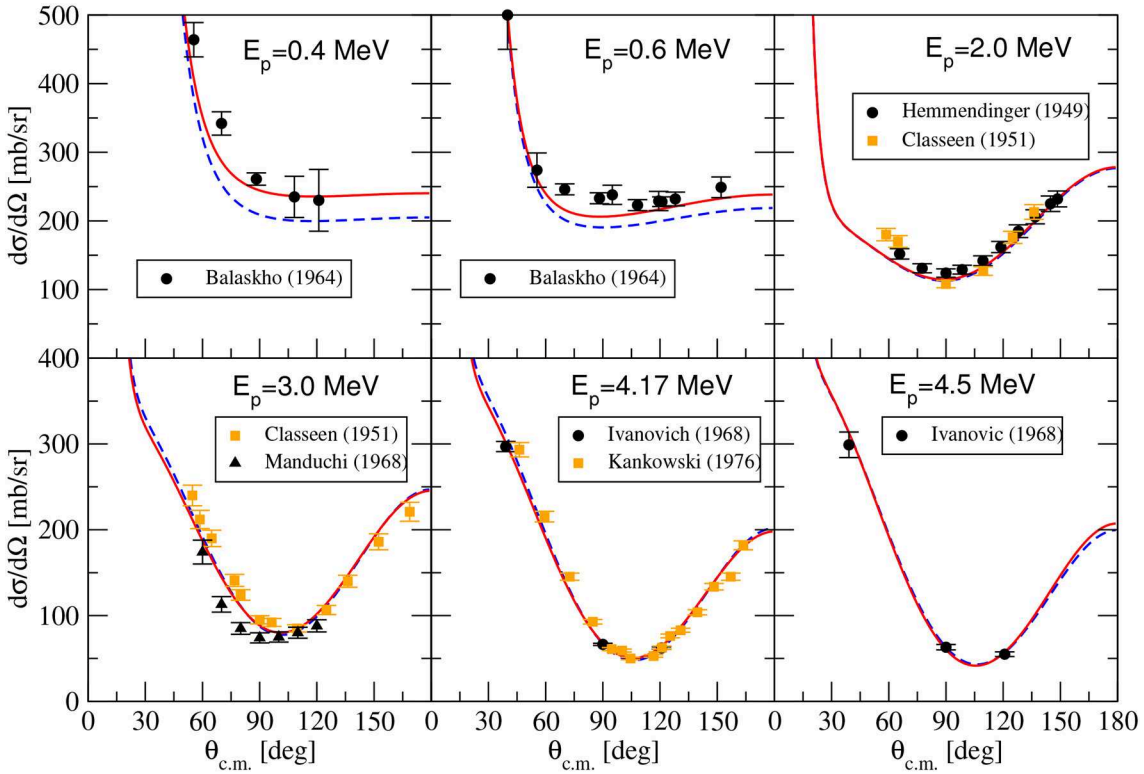


FIGURE 7 | $p-^3$H differential cross section at several values of the proton laboratory beam energy E_p, calculated with the N3LO-I (dashed blue lines) and with the N3LO-I/N2LO (solid red lines) interactions. The experimental data are from references [100–105].

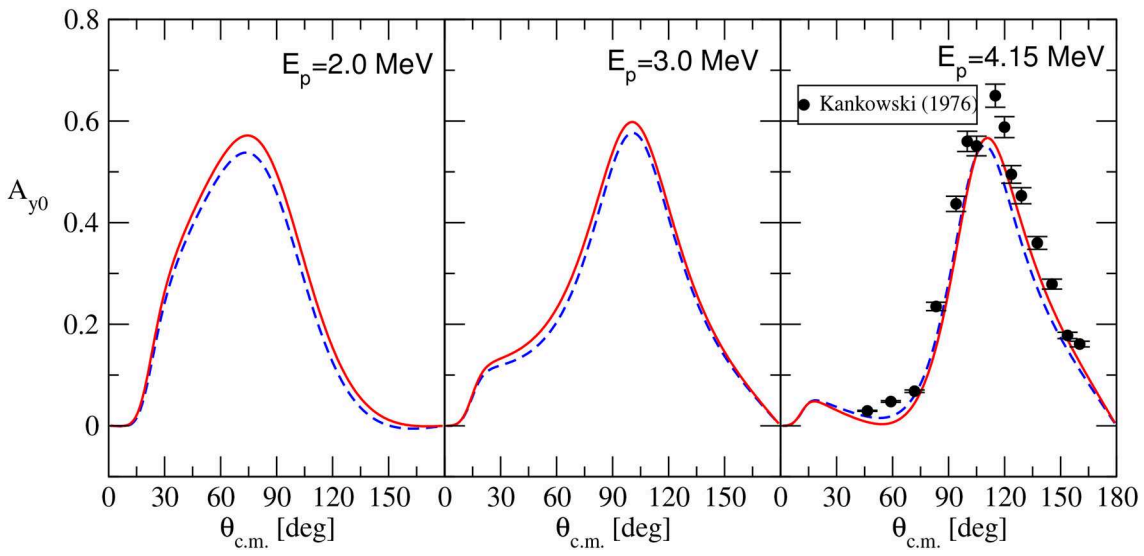


FIGURE 8 | $p-^3$H proton analyzing power at three values of the proton laboratory beam energy E_p calculated with the N3LO-I (dashed blue lines) and with the N3LO-I/N2LO (solid red lines) interactions. The experimental data are from reference [105].

4. CONCLUSIONS AND OUTLOOK

In this work we have presented a review of the HH method, focusing on the most significant achievements after the year 2008, when the previous review on the HH method [19] was published. We have also included a presentation of the HH formalism with some detail, in order to make the reader appreciate the main concepts of the method and to provide him/her the instruments

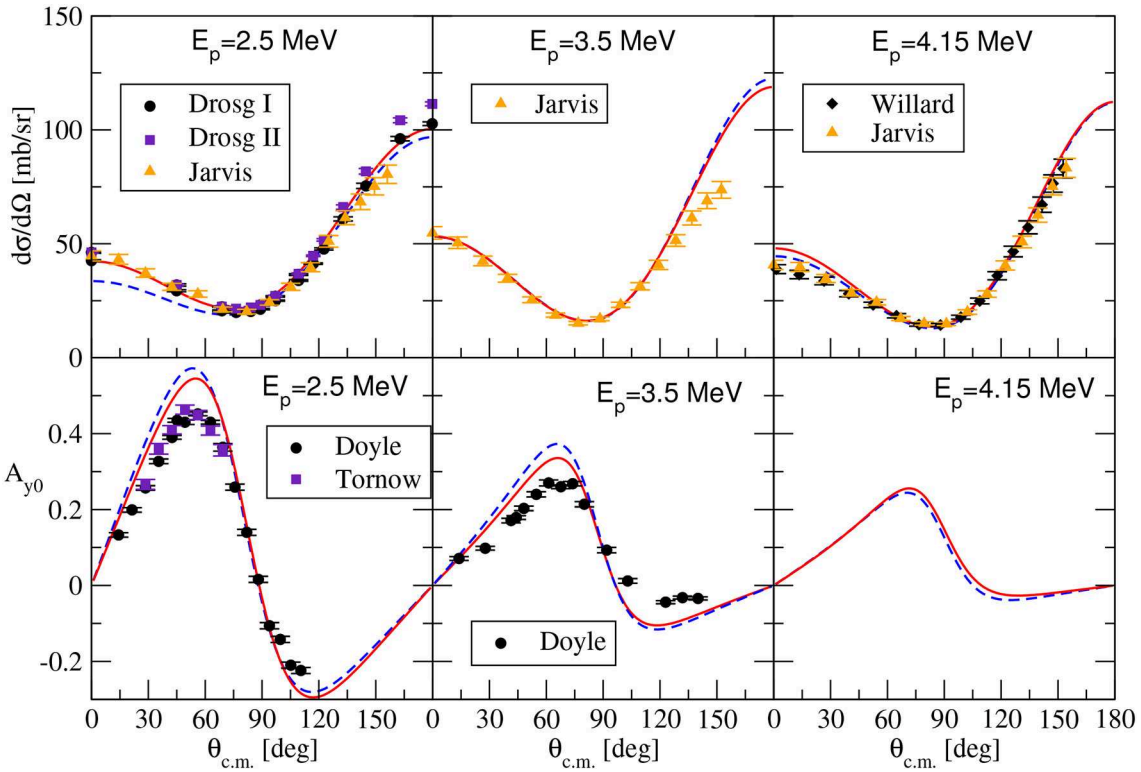


FIGURE 9 | p+^{3}H $\rightarrow$ n+^{3}He differential cross section and proton analyzing power at three values of the proton laboratory beam energy E_p calculated with the N3LO-I (dashed blue lines) and with the N3LO-I/N2LO (solid red lines) interactions. The experimental data are from references [106–110].

needed to implement the method by him/herself. We have then focused on the latest results obtained within the HH method. We can summarize the situation as follows: the HH method can solve the three- and four-body bound-state problem with great accuracy and with essentially any (local and non-local) model for the two-nucleon interaction available in the literature. The three-nucleon interaction models used so far are however only local. The $A = 3, 4$ scattering states have been studied with several local and non-local potentials below the target nucleus breakup threshold. Using local potentials, also the elastic channel above the breakup threshold have been investigated. The HH method has then a wide range of applications: it has been used not only to test the models for the two- and three-nucleon interactions, but also to determine the parameters entering in the subleading three-nucleon contact interaction, derived in reference [87]. This has allowed one to construct a model for the three-nucleon interaction able to solve, at least within the (preliminary) hybrid framework of reference [88], some long-standing puzzles, as the A_y-puzzle. Furthermore, the HH method has been widely used in the study of nuclear reactions of astrophysical interest, as well as the electroweak structure of light nuclei [50, 111, 112].

The HH method has still a lot of potentialities, which will be explored in the near future. First of all, we will implement the method to the case of a non-local three-nucleon interaction. This is widely requested, in order to have consistency in the two- and three-nucleon cutoff functions which appear in the models derived within chiral effective field theory, for instance in references [72, 73]. Once the LECs c_D and c_E will be determined using the non-local three-nucleon interaction with the same procedure outlined in section 3, they will be used in *fully consistent* studies of other systems, as nuclear and neutron matter.

Secondly, we can mention only preliminary applications of the HH method to describe breakup reactions in $A = 3$ [40]. Work on the implementation of the HH method to the breakup channels in $A = 3, 4$ is currently underway. It does not require significant modifications of the method, but still it has not been performed yet. Once done, the three- and four-body nuclear systems will be completely covered by the method.

As mentioned above, the extension of the method to the $A = 5, 6$ nuclear systems has been investigated and the first results obtained using a V_{low-k} interaction will appear soon and are indeed very promising. This is a major step for the HH method, as it will allow us to tackle a large number of interesting subjects, and especially a large number of nuclear reactions of astrophysical interest. From a first investigation, the further extension of the method to even larger values of A, i.e., $A = 7, 8$, seems feasible.

Finally, in order to have access to higher mass nuclear systems, both bound and scattering states, we could take advantage of the strong clusterization present in some of them, as, for instance, in ^{9}Be, which can be studied as a $\alpha - \alpha - n$ system. In order to do so, the HH method must then be extended to the case of

non-equal mass systems. And this, in turn, will allow to study also more exotic systems, as hypernuclei, where one nucleon is replaced with an hyperon. Works along this line have started in reference [61], and are conducted also by other groups [113, 114].

In conclusion, the HH method has quite a "glorious" history, and has fulfilled its service in the continuous test of the nuclear interaction models. However, this service is not yet at an end, and we expect to see the HH method playing a protagonist role also in the next years.

AUTHOR CONTRIBUTIONS

All the authors have contributed essentially equally to this work, read, and corrected the whole manuscript. In particular, JD-E, AG, AK, and LM have worked in writing the section on the formalism. LG, AK, LM, and MV have taken care of collecting the presented results. AK and LM have taken care of writing the introductory and concluding sections.

FUNDING

This work of JD-E was supported by the Fonds de la Recherche Scientifique (FNRS) under Grant Number 4.45.10.08.

ACKNOWLEDGMENTS

The computational resources of the Istituto Nazionale di Fisica Nucleare (INFN), Sezione di Pisa, were gratefully acknowledged.

REFERENCES

1. Piarulli M, Baroni A, Girlanda L, Kievsky A, Lovato A, Lusk E, et al. Light-nuclei spectra from chiral dynamics. *Phys Rev Lett*. (2018) **120**:052503. doi: 10.1103/PhysRevLett.120.052503
2. Epelbaum E, Golak J, Hebeler K, Hüther T, Kamada H, Krebs H, et al. Few- and many-nucleon systems with semilocal coordinate-space regularized chiral two- and three-body forces. *Phys Rev C*. (2019) **99**:024313. doi: 10.1103/PhysRevC.99.024313
3. Rozpedzik D, Golak J, Skibinski R, Witala H, Glöckle W, Epelbaum E, et al. A first estimation of chiral four-nucleon force effects in ^{4}He. *Acta Phys Polon B*. (2006) **37**:2889.
4. Wiringa RB, Stoks VGJ, Schiavilla R. Accurate nucleon-nucleon potential with charge-independence breaking. *Phys Rev C*. (1995) **51**:38. doi: 10.1103/PhysRevC.51.38
5. Machleidt R. High-precision, charge-dependent Bonn nucleon-nucleon potential. *Phys Rev C*. (2001) **63**:024001. doi: 10.1103/PhysRevC.63.024001
6. Weinberg S. Nuclear forces from chiral lagrangians. *Phys Lett B*. (1990) **251**:288. doi: 10.1016/0370-2693(90)90938-3
7. Leidemann W, Orlandini G. Modern *ab initio* approaches and applications in few-nucleon physics with $A \geq 4$. *Prog Part Nucl Phys*. (2013) **68**:158. doi: 10.1016/j.ppnp.2012.09.001
8. Carlson J, Gandolfi S, Pederiva F, Pieper SC, Schiavilla R, Schmidt KE, et al. Quantum Monte Carlo methods for nuclear physics. *Rev Mod Phys*. (2015) **87**:1067. doi: 10.1103/RevModPhys.87.1067
9. Barrett BR, Navrátil P, Vary JP. *Ab initio* no core shell model. *Prog Part Nucl Phys*. (2013) **69**:131. doi: 10.1016/j.ppnp.2012.10.003
10. Fukui T, De Angelis L, Ma YZ, Coraggio L, Gargano A, Itaco N, et al. Realistic shell-model calculations for *p*-shell nuclei including contributions of a chiral three-body force. *Phys Rev C*. (2018) **98**:044305. doi: 10.1103/PhysRevC.98.044305
11. Coraggio L, Covello A, Gargano A, Itaco N, Kuo TTS. Effective shell-model hamiltonians from realistic nucleon-nucleon potentials within a perturbative approach. *Ann Phys*. (2012) **327**:2125. doi: 10.1016/j.aop.2012.04.013
12. Lazauskas R, Carbonell J. Testing nonlocal nucleon-nucleon interactions in four-nucleon systems. *Phys Rev C*. (2004) **70**:044002. doi: 10.1103/PhysRevC.70.044002
13. Lazauskas R, Carbonell J. The Faddeev-Yakubovsky Symphony. *Few Body Syst*. (2019) **60**:62. doi: 10.1007/s00601-019-1529-5
14. Glöckle W, Witala H, Hüber D, Kamada H, Golak J. The three-nucleon continuum: achievements, challenges and applications. *Phys Rep*. (1996) **274**:107. doi: 10.1016/0370-1573(95)00085-2
15. Nogga A, Hüber D, Kamada H, Glöckle W. Triton binding energies for modern NN forces and the $\pi - \pi$ exchange three-nucleon force. *Phys Lett B*. (1997) **409**:19. doi: 10.1016/S0370-2693(97)00841-1
16. Fonseca AC, Deltuva A. Numerical exact *ab initio* four-nucleon scattering calculations: from dream to reality. *Few Body Syst*. (2017) **58**:46. doi: 10.1007/s00601-017-1211-8
17. Deltuva A, Fonseca AC, Sauer PU. Coulomb force effects in few-nucleon systems. *Few Body Syst*. (2019) **60**:29. doi: 10.1007/s00601-019-1496-x
18. Lazauskas R. Solution of the $n-^4$ He elastic scattering problem using the Faddeev-Yakubovsky equations. *Phys Rev C*. (2018) **97**:044002. doi: 10.1103/PhysRevC.97.044002
19. Kievsky A, Rosati S, Viviani M, Marcucci LE, Girlanda L. A High-precision variational approach to three- and four-nucleon bound and zero-energy scattering states. *J Phys G Nucl Part Phys*. (2008) **35**:063101. doi: 10.1088/0954-3899/35/6/063101
20. Okubo S. Diagonalization of Hamiltonian and Tamm-Dancoff equation. *Progr Theor Phys*. (1954) **12**:603. doi: 10.1143/PTP.12.603
21. Suzuki K. Construction of Hermitian effective interaction in nuclei: general relation between Hermitian and non-Hermitian forms. *Progr Theor Phys*. (1982) **68**:246. doi: 10.1143/PTP.68.246
22. Suzuki K, Okamoto R. Degenerate perturbation theory in quantum mechanics. *Progr Theor Phys*. (1983) **70**:439. doi: 10.1143/PTP.70.439
23. Barnea N, Leidemann W, Orlandini G. State dependent effective interaction for the hyperspherical formalism. *Phys Rev C*. (2000) **61**:054001. doi: 10.1103/PhysRevC.61.054001
24. Barnea N, Leidemann W, Orlandini G. State-dependent effective interaction for the hyperspherical formalism with noncentral forces. *Nucl Phys A*. (2001) **693**:565. doi: 10.1016/S0375-9474(01)00794-1
25. Barnea N, Leidemann W, Orlandini G. Hyperspherical effective interaction for nonlocal potentials. *Phys Rev C*. (2010) **81**:064001. doi: 10.1103/PhysRevC.81.064001
26. Bacca S, Barnea N, Leidemann W, Orlandini G. Isoscalar monopole resonance of the alpha particle: a prism to nuclear Hamiltonians. *Phys Rev Lett*. (2013) **110**:042503. doi: 10.1103/PhysRevLett.110.042503
27. Bacca S, Barnea N, Leidemann W, Orlandini G. Examination of the first excited state of ^{4} He as a potential breathing mode. *Phys Rev C*. (2015) **91**:024303. doi: 10.1103/PhysRevC.91.024303
28. Bacca S, Pastore S. Electromagnetic reactions on light nuclei. *J Phys G Nucl Part Phys*. (2014) **41**:123002. doi: 10.1088/0954-3899/41/12/123002
29. Kievsky A, Marcucci LE, Rosati S, Viviani M. High-precision calculation of the triton ground state within the hyperspherical-harmonics method. *Few Body Syst*. (1997) **22**:1. doi: 10.1007/s006010050049
30. Viviani M, Marcucci LE, Rosati S, Kievsky A, Girlanda L. Variational calculation on $A = 3$ and 4 nuclei with non-local potentials. *Few Body Syst*. (2006) **39**:159. doi: 10.1007/s00601-006-0158-y
31. Marcucci LE, Kievsky A, Girlanda L, Rosati S, Viviani M. *N-d* elastic scattering using the hyperspherical harmonics approach with realistic local and nonlocal interactions. *Phys Rev C*. (2009) **80**:034003. doi: 10.1103/PhysRevC.80.034003
32. Viviani M, Kievsky A, Girlanda L, Marcucci LE. Neutron-triton elastic scattering. *Few Body Syst*. (2009) **45**:119. doi: 10.1007/s00601-009-0036-5
33. Viviani M, Girlanda L, Kievsky A, Marcucci LE, Rosati S. Proton-^{3}He elastic scattering at low energies and the 'A_y Puzzle'. *EPJ Web Conf*. (2010) **3**:05011. doi: 10.1051/epjconf/20100305011

34. Viviani M, Deltuva A, Lazauskas R, Carbonell J, Fonseca AC, Kievsky A, et al. Benchmark calculation of n-^{3}H and p-^{3}He scattering. *Phys Rev C*. (2011) **84**:054010. doi: 10.1103/PhysRevC.84.054010
35. Viviani M, Girlanda L, Kievsky A, Marcucci LE. Effect of three-nucleon interaction in $p-^3$He elastic scattering. *Phys Rev Lett*. (2013) **111**:172302. doi: 10.1103/PhysRevLett.111.172302
36. Kievsky A, Viviani M, Rosati S. Polarization observables in $p - d$ scattering below 30 MeV. *Phys Rev C*. (2001) **64**:024002. doi: 10.1103/PhysRevC.64.024002
37. Kievsky A, Viviani M, Marcucci LE. *N-d* scattering including electromagnetic forces. *Phys Rev C*. (2004) **69**:014002. doi: 10.1103/PhysRevC.69.014002
38. Kievsky A, Rosati S, Viviani M. Proton-deuteron elastic scattering above the deuteron breakup. *Phys Rev Lett*. (1999) **82**:3759. doi: 10.1103/PhysRevLett.82.3759
39. Viviani M, Kievsky A, Rosati S. The Kohn variational principle for elastic proton deuteron scattering above deuteron breakup threshold. *Few Body Syst*. (2001) **30**:39. doi: 10.1007/s006010170017
40. Garrido E, Kievsky A, Viviani M. Breakup of three particles within the adiabatic expansion method. *Phys Rev C*. (2014) **90**:014607. doi: 10.1103/PhysRevC.90.014607
41. Gattobigio M, Kievsky A, Viviani M. Nonsymmetrized hyperspherical harmonic basis for an *A*-body system. *Phys Rev C*. (2011) **83**:024001. doi: 10.1103/PhysRevC.83.024001
42. Dohet-Eraly J, Viviani M. Computing an orthonormal basis of symmetric or antisymmetric hyperspherical harmonics. *Comp Phys Comm*. (2020) 107183. doi: 10.1016/j.cpc.2020.107183
43. Dohet-Eraly J, Viviani M, Kievsky A, Marcucci LE, Gnech A. Five-nucleon systems with an hyperspherical harmonic method. In: Orr NA, Ploszajczak M, Marqués FM, Carbonell J, editors. *Recent Progress in Few-Body Physics*. Cham: Springer International Publishing (2020). p. 163–7. doi: 10.1007/978-3-030-32357-8_29
44. Nogga A, Kievsky A, Kamada H, Glöckle W, Marcucci LE, Rosati S, et al. Three-nucleon bound states using realistic potential models. *Phys Rev C*. (2003) **67**:034004. doi: 10.1103/PhysRevC.67.034004
45. Kamada H, Nogga A, Glöckle W, Hiyama E, Kamimura M, Varga K, et al. Benchmark test calculation of a four nucleon bound state. *Phys Rev C*. (2001) **64**:044001. doi: 10.1103/PhysRevC.64.044001
46. Kievsky A, Viviani M, Rosati S, Hüber D, Glöckle W, Kamada H, et al. Benchmark calculations for polarization observables in three nucleon scattering. *Phys Rev C*. (1998) **58**:3085. doi: 10.1103/PhysRevC.58.3085
47. Deltuva A, Fonseca AC, Kievsky A, Rosati S, Sauer PU, Viviani M. Benchmark calculation for proton-deuteron elastic scattering observables including Coulomb. *Phys Rev C*. (2005) **71**:064003. doi: 10.1103/PhysRevC.71.064003
48. Viviani M, Deltuva A, Lazauskas R, Fonseca AC, Kievsky A, Marcucci LE. Benchmark calculation of $p-^3$H and $n-^3$He scattering. *Phys Rev C*. (2017) **95**:034003. doi: 10.1103/PhysRevC.95.034003
49. Marcucci LE, Nollett KM, Schiavilla R, Wiringa RB. Modern theories of low-energy astrophysical reactions. *Nucl Phys A*. (2006) **777**:111. doi: 10.1016/j.nuclphysa.2004.09.008
50. Marcucci LE, Mangano G, Kievsky A, Viviani M. Implication of the proton-deuteron radiative capture for Big Bang nucleosynthesis. *Phys Rev Lett*. (2016) **116**:102501. [Erratum: (2016) Phys. Rev. Lett. 117, 049901]. doi: 10.1103/PhysRevLett.116.102501
51. Fabre de la Ripelle M. The potential harmonic expansion method. *Ann Phys*. (1983) **147**:281. doi: 10.1016/0003-4916(83)90212-9
52. Abramowitz M, Stegun IA. *Handbook of Mathematical Functions*. New York, NY: Dover Publications (1964).
53. Raynal J, Revai J. Transformation coefficients in the hyperspherical approach to the three-body problem. *Nuovo Cim A*. (1970) **68**:612. doi: 10.1007/BF02756127
54. Viviani M. Transformation coefficients of hyperspherical harmonic functions of an *A*-body system. *Few Body Syst*. (1998) **25**:177. doi: 10.1007/s006010050101
55. Edmonds AR. *Angular Momentum in Quantum Mechanics*. Princeton, NJ: Princeton University Press (1954).
56. Rosati S. The hyperspherical harmonic method: a review and some recent developments. *Ser Adv Quant Many Body Theor*. (2002) **7**:339. doi: 10.1142/9789812777072_0009
57. Viviani M, Kievsky A, Rosati S. Calculation of the α-particle ground state within the hyperspherical harmonic basis. *Phys Rev C*. (2005) **71**:024006. doi: 10.1103/PhysRevC.71.024006
58. Gattobigio M, Kievsky A, Viviani M, Barletta P. Harmonic hyperspherical basis for identical particles without permutational symmetry. *Phys Rev A*. (2009) **79**:032513. doi: 10.1103/PhysRevA.79.032513
59. Gattobigio M, Kievsky A, Viviani M. Spectra of helium clusters with up to six atoms using soft-core potentials. *Phys Rev A*. (2011) **84**:052503. doi: 10.1103/PhysRevA.84.052503
60. Deflorian S, Barnea N, Leidemann W, Orlandini G. Nonsymmetrized hyperspherical harmonics with realistic NN potentials. *Few Body Syst*. (2013) **54**:1879. doi: 10.1007/s00601-013-0717-y
61. Nannini A, Marcucci LE. Non-symmetrized hyperspherical harmonics method for non-equal mass three-body systems. *Front Phys*. (2018) **6**:122. doi: 10.3389/fphy.2018.00122
62. Chen CR, Payne GL, Friar JL, Gibson BF. Faddeev calculations of the $2\pi-3N$ force contribution to the ^3H binding energy. *Phys Rev C*. (1986) **33**:1740. doi: 10.1103/PhysRevC.33.1740
63. Kohn W. Variational methods in nuclear collision problems. *Phys Rev*. (1948) **74**:1763. doi: 10.1103/PhysRev.74.1763
64. Kievsky A. The complex Kohn variational method applied to $N-d$ scattering. *Nucl Phys A*. (1997) **624**:125. doi: 10.1016/S0375-9474(97)81832-5
65. Pudliner BS, Pandharipande VR, Carlson J, Wiringa RB. Quantum Monte Carlo calculations of $A \leq 6$ nuclei. *Phys Rev Lett*. (1995) **74**:4396. doi: 10.1103/PhysRevLett.74.4396
66. Navrátil P. Local three-nucleon interaction from chiral effective field theory. *Few Body Syst*. (2007) **41**:117. doi: 10.1007/s00601-007-0193-3
67. Kievsky A, Viviani M, Rosati S. Study of bound and scattering states in three-nucleon systems. *Nucl Phys A*. (1994) **577**:511. doi: 10.1016/0375-9474(94)90931-8
68. Kievsky A, Rosati S, Tornow W, Viviani M. Critical comparison of experimental data and theoretical predictions for N-d scattering below the breakup threshold. *Nucl Phys A*. (1996) **607**:402. doi: 10.1016/0375-9474(96)00240-0
69. Coon SA, Glöckle W. The two pion exchange three nucleon potential: partial wave analysis in momentum space. *Phys Rev C*. (1981) **23**:1790. doi: 10.1103/PhysRevC.23.1790
70. Coon SA, Han HK. Reworking the Tucson-Melbourne three-nucleon potential. *Few Body Syst*. (2001) **30**:131. doi: 10.1007/s006010170022
71. Bogner SK, Furnstahl RJ, Ramanan S, Schwenk A. Low-momentum interactions with smooth cutoffs. *Nucl Phys A*. (2007) **784**:79. doi: 10.1016/j.nuclphysa.2006.11.123
72. Entem DR, Machleidt R. Accurate charge-dependent nucleon-nucleon potential at fourth order of chiral perturbation theory. *Phys Rev C*. (2003) 68:041001. doi: 10.1103/PhysRevC.68.041001
73. Entem DR, Machleidt R, Nosyk Y. High-quality two-nucleon potentials up to fifth order of the chiral expansion. *Phys Rev C*. (2017) **96**:024004. doi: 10.1103/PhysRevC.96.024004
74. Marcucci LE, Sammarruca F, Viviani M, Machleidt R. Momentum distributions and short-range correlations in the deuteron and ^{3}He with modern chiral potentials. *Phys Rev C*. (2019) **99**:034003. doi: 10.1103/PhysRevC.99.034003
75. Piarulli M, Girlanda L, Schiavilla R, Pérez RN, Amaro JE, Arriola ER. Minimally nonlocal nucleon-nucleon potentials with chiral two-pion exchange including Δ-resonances. *Phys Rev C*. (2015) **91**:024003. doi: 10.1103/PhysRevC.91.024003
76. Baroni A, Schiavilla R, Marcucci LE, Girlanda L, Kievsky A, Lovato A, et al. Local chiral interactions, the tritium Gamow-Teller matrix element, and the three-nucleon contact term. *Phys Rev C*. (2018) **98**:044003. doi: 10.1103/PhysRevC.98.044003
77. Stoks VGJ, de Swart JJ. Magnetic moment interaction in nucleon-nucleon phase-shift analyses. *Phys Rev C*. (1990) **42**:1235. doi: 10.1103/PhysRevC.42.1235

78. Wang M, Audi G, Wapstra AH, Kondev FG, MacCormick M, Xu X, et al. The Ame2012 atomic mass evaluation. *Chin Phys C*. (2012) **36**:1603. doi: 10.1088/1674-1137/36/12/003
79. Marcucci LE, Kievsky A, Rosati S, Schiavilla R, Viviani M. Chiral effective field theory predictions for muon capture on deuteron and ^{3}He. *Phys Rev Lett*. (2012) **108**:052502. [Erratum: (2018) Phys. Rev. Lett. 121, 049901]. doi: 10.1103/PhysRevLett.108.052502
80. Gårdestig A, Phillips DR. How low-energy weak reactions can constrain three-nucleon forces and the neutron-neutron scattering length. *Phys Rev Lett*. (2006) **96**:232301. doi: 10.1103/PhysRevLett.96.232301
81. Gazit D, Quaglioni S, Navrátil P. Three-nucleon low-energy constants from the consistency of interactions and currents in chiral effective field theory. *Phys Rev Lett*. (2009) **103**:102502. [Erratum: (2019) Phys. Rev. Lett. 122, 029901]. doi: 10.1103/PhysRevLett.103.102502
82. Schoen K, Jacobson DL, Arif M, Huffman PR, Black TC, Snow WM, et al. Precision neutron interferometric measurements and updated evaluations of the $n-p$ and $n-d$ coherent neutron scattering lengths. *Phys Rev C*. (2003) **67**:044005. doi: 10.1103/PhysRevC.67.044005
83. Dilg W, Koester L, Nistler W. The neutron-deuteron scattering lengths. *Phys Lett B*. (1971) **36**:208. doi: 10.1016/0370-2693(71)90070-0
84. Black TC, Karwowski HJ, Ludwig EJ, Kievsky A, Rosati S, Viviani M. Determination of proton-deuteron scattering lengths. *Phys Lett B*. (1999) **471**:103. doi: 10.1016/S0370-2693(99)01366-0
85. Kievsky A, Viviani M, Girlanda L, Marcucci LE. Comparative study of three-nucleon force models in $A = 3, 4$ systems. *Phys Rev C*. (2010) **81**:044003. doi: 10.1103/PhysRevC.81.044003
86. Shimizu S, Sagara K, Nakamura H, Maeda K, Miwa T, Nishimori N, et al. Analyzing powers of $p + d$ scattering below the deuteron breakup threshold. *Phys Rev C*. (1995) **52**:1193. doi: 10.1103/PhysRevC.52.1193
87. Girlanda L, Kievsky A, Viviani M. Subleading contributions to the three-nucleon contact interaction. *Phys Rev C*. (2011) **84**:014001. doi: 10.1103/PhysRevC.84.014001
88. Girlanda L, Kievsky A, Viviani M, Marcucci LE. Short-range three-nucleon interaction from A=3 data and its hierarchical structure. *Phys Rev C*. (2019) **99**:054003. doi: 10.1103/PhysRevC.99.054003
89. Kievsky A, Wood MH, Brune CR, Fisher BM, Karwowski HJ, Leonard DS, et al. Evidence for three nucleon force effects in proton–deuteron elastic scattering. *Phys Rev C*. (2001) **63**:024005. doi: 10.1103/PhysRevC.63.024005
90. Wood MH, Brune CR, Fisher BM, Karwowski HJ, Leonard DS, Ludwig EJ, et al. Low-energy $p - d$ scattering: High precision data, comparisons with theory, and phase shift analyses. *Phys Rev C*. (2002) **65**:034002. doi: 10.1103/PhysRevC.65.034002
91. Phillips TW, Berman BL, Seagrave JD. Neutron total cross section for tritium. *Phys Rev C*. (1980) **22**:384. doi: 10.1103/PhysRevC.22.384
92. Seagrave JD, Cranberg L, Simmons JE. Elastic scattering of fast neutrons by tritium and he^3. *Phys Rev*. (1960) **119**:1981. doi: 10.1103/PhysRev.119.1981
93. Daniels TV, Arnold CW, Cesaratto JM, Clegg TB, Couture AH, Karwowski HJ, et al. Spin-correlation coefficients and phase-shift analysis for p+^{3}He elastic scattering. *Phys Rev C*. (2010) **82**:034002. doi: 10.1103/PhysRevC.82.034002
94. Machleidt R, Entem DR. Chiral effective field theory and nuclear forces. *Phys Rep*. (2011) **503**:1. doi: 10.1016/j.physrep.2011.02.001
95. Fisher BM, Brune CR, Karwowski HJ, Leonard DS, Ludwig EJ, Black TC, et al. Proton-He^3 elastic scattering at low energies. *Phys Rev C*. (2006) **74**:034001. doi: 10.1103/PhysRevC.74.034001
96. Alley MT, Knutson LD. Spin correlation measurements for p-^{3}He elastic scattering between 4.0 and 10.0 MeV. *Phys Rev C*. (1993) **48**:1890. doi: 10.1103/PhysRevC.48.1890
97. Viviani M, Kievsky A, Rosati S, George EA, Knutson LD. The Ay problem for p-^{3}He elastic scattering. *Phys Rev Lett*. (2001) **86**:3739. doi: 10.1103/PhysRevLett.86.3739
98. Viviani M, Girlanda L, Kievsky A, Marcucci LE. Three-nucleon force effects in $\vec{p}$ $-^3$ H and $\vec{n}-^3$ He scattering. *Few Body Syst*. (2017) **58**:110. doi: 10.1007/s00601-017-1264-8
99. Viviani M, Girlanda L, Kievsky A, Marcucci LE, Dohet-Eraly J. Three-nucleon force effects in $A = 4$ scattering. *Few Body Syst*. (2018) **59**:73. doi: 10.1007/s00601-018-1379-6
100. Hemmendinger A, Jarvis GA, Taschek RF. Scattering of protons by tritons. *Phys Rev*. (1949) **76**:1137. doi: 10.1103/PhysRev.76.1137
101. Claassen RS, Brown RJS, Freier GD, Stratton WR. The scattering of protons by tritons. *Phys Rev*. (1951) **82**:589. doi: 10.1103/PhysRev.82.589
102. Balashko YG, Barit IY, Dulkova LS, Kurepin AB. Elastic scattering protons on the tritium by energy below (p,n) reactions. *Bull Russ Acad Sci Phys*. (1965) **28**:1028.
103. Manduchi C, Moschini G, Tornielli G, Zannoni G. Experimental study on low-energy levels of ^{4}He. *Nuovo Cim B*. (1968) **57**:340. doi: 10.1007/BF02710206
104. Ivanovich M, Young PG, Ohlsen GG. Elastic scattering of several hydrogen and helium isotopes from tritium. *Nucl Phys A*. (1968) **110**:441. doi: 10.1016/0375-9474(68)90552-6
105. Kankowsky R, Fritz JC, Kilian K, Neufert A, Fick D. Elastic scattering of polarized protons on tritons between 4 and 12 MeV. *Nucl Phys A*. (1976) **263**:29. doi: 10.1016/0375-9474(76)90181-0
106. Willard HB, Bair JK, Kington JD. The reactions T(p,n)He^3 and T(p,γ)He^4. *Phys Rev*. (1953) **90**:865. doi: 10.1103/PhysRev.90.865
107. Jarvis GA. Charged particle cross sections, the reaction T(p,n)He^3. *Los Alamos Sci Rep*. (1956) **2014**:35.
108. Drosg M. The ^{3}H$(p,n)^3$He differential cross sections below 5 MeV and the $n-^3$He cross section. *Los Alamos Sci Rep*. (1980) **1980**:8215. doi: 10.2172/5207437
109. Doyle MA, Clark HW, Dries LJ, Regner JL, Donoghue TR, Hale GM. Comparison of analyzing power and polarization in the reaction ^{3}H$(p,n)^3$He. *Nucl Phys A*. (1981) **371**:225. doi: 10.1016/0375-9474(81)90065-8
110. Tornow W, Byrd RC, Lisowski PW, Walter RL, Donoghue TR. Comparison of analyzing power and polarization in the reaction ^{3}H$(p,n)^3$ He. *Nucl Phys A*. (1981) **371**:235. doi: 10.1016/0375-9474(81)90066-X
111. Marcucci LE, Viviani M, Schiavilla R, Kievsky A, Rosati S. Electromagnetic structure of $A = 2$ and 3 nuclei and the nuclear current operator. *Phys Rev C*. (2005) **72**:014001. doi: 10.1103/PhysRevC.72.014001
112. Marcucci LE, Gross F, Peña MT, Piarulli M, Schiavilla R, Sick I, et al. Electromagnetic structure of few-nucleon ground states. *J Phys G Nucl Part Phys*. (2016) **43**:023002. doi: 10.1088/0954-3899/43/2/023002
113. Theeten M, Matsumura H, Orabi M, Baye D, Descouvemont P, Fujiwara Y, et al. Three-body model of light nuclei with microscopic nonlocal interactions. *Phys Rev C*. (2007) **76**:054003. doi: 10.1103/PhysRevC.76.054003
114. Ferrari Ruffino F, Lonardoni D, Barnea N, Deflorian S, Leidemann W, Orlandini G, et al. Benchmark results for few-body hypernuclei. *Few Body Syst*. (2017) **58**:113. doi: 10.1007/s00601-017-1273-7

Conflict of Interest: The authors declare that the research was conducted in the absence of any commercial or financial relationships that could be construed as a potential conflict of interest.

Copyright © 2020 Marcucci, Dohet-Eraly, Girlanda, Gnech, Kievsky and Viviani. This is an open-access article distributed under the terms of the Creative Commons Attribution License (CC BY). The use, distribution or reproduction in other forums is permitted, provided the original author(s) and the copyright owner(s) are credited and that the original publication in this journal is cited, in accordance with accepted academic practice. No use, distribution or reproduction is permitted which does not comply with these terms.

frontiers in Physics

REVIEW
published: 10 December 2019
doi: 10.3389/fphy.2019.00213

Nuclear Forces in the Medium: Insight From the Equation of State

Francesca Sammarruca and Randy Millerson*

Physics Department, University of Idaho, Moscow, ID, United States

In this review, we concentrate on recent efforts of our group aimed at investigating the nuclear equation of state of symmetric nuclear matter (equal concentrations of protons and neutrons) and the one of pure neutron matter. Although idealized, these systems are suitable "laboratories" to probe nuclear forces in the many-body system. The energy per particle as a function of density can reveal rich information about the nature of nuclear forces in the medium and how they impact observable properties. For instance, the pressure in neutron-rich matter has been found to have profound impact on very diverse systems, ranging from the thickness of the neutron skin in a heavy nucleus to the properties of compact stars. The current trend in nuclear physics is to build few-nucleon forces according to the prescription of chiral effective field theory. We open by reviewing in depth how we develop equations of state based on state-of-the-art chiral interactions. We then highlight some applications in neutron-rich nuclei and neutron stars.

Keywords: nuclear forces, chiral effective field theory, symmetry energy, neutron skin thickness, neutron stars

OPEN ACCESS

Edited by:
Laura Elisa Marcucci,
University of Pisa, Italy

Reviewed by:
Constança Providência,
University of Coimbra, Portugal
Fiorella Burgio,
National Institute of Nuclear Physics (INFN), Italy

****Correspondence:***
Francesca Sammarruca
fsammarr@uidaho.edu

Specialty section:
This article was submitted to Nuclear Physics, a section of the journal Frontiers in Physics

Received: *29 September 2019*
Accepted: *21 November 2019*
Published: *10 December 2019*

Citation:
Sammarruca F and Millerson R (2019) Nuclear Forces in the Medium: Insight From the Equation of State. Front. Phys. 7:213. doi: 10.3389/fphy.2019.00213

1. INTRODUCTION

Understanding the interaction of hadrons in nuclei is a most fundamental problem in nuclear physics. Our present knowledge of the nuclear force in vacuum is still incomplete, although decades of efforts have been devoted to this problem. The study of nuclear forces in many-body systems is, of course, much more challenging because additional aspects are involved beyond those which can be constrained by free-space nucleon-nucleon (*NN*) scattering. Predictive power with respect to the properties of nuclei is the true test for a successful microscopic theory.

The system known as "nuclear matter" is a suitable, although idealized, theoretical "test bench" for many-body theories. Nuclear matter is defined as an infinite system of nucleons interacting *via* strong forces in the absence of electromagnetic interactions. Nuclear matter's "signature" is its energy per particle as a function of density and potentially additional "variables" (for instance, isospin polarization or temperature). The nuclear matter equation of state (EoS) is precisely the energy per particle as a function of density and other appropriate quantities. Naturally, the idealized nature of this system, which implies translational invariance, simplifies theoretical calculations. Furthermore, within the "local density approximation" (LDA), one can utilize the EoS directly in calculations of actual nuclei. (We recall that LDA amounts to the assumption that the properties at a point with density ρ in a nucleus are the same as they would be in infinite nuclear matter at the same density).

When the densities of protons and neutrons are equal, we speak of isospin-symmetric nuclear matter. The latter has been studied since the earlier works by Brueckner and others [1–4], who introduced what became known as the Brueckner-Hartree-Fock (BHF) theory. The BHF theory seeks to find the ground state energy of a many-body system [1–6] as a linked-cluster perturbation expansion. The main point was the realization that regrouping the linked-cluster diagrams by the number of hole lines allowed the series to converge.

Other approaches to the development of the EoS were also pursued, one of them being the variational method [7, 8]. The latter yielded predictions in close agreement with those from Brueckner theory if realistic *NN* potentials were adopted [9].

The BHF theory, or "conventional approach," was followed by the Dirac-Brueckner-Hartree-Fock (DBHF) approach [10–13], developed during the 1980's. The novel, and most striking feature of the DBHF theory was its ability to describe the saturation properties (both energy and density) of nuclear matter, a fundamental aspect which reflects the saturating nature of the nuclear force. The DBHF method contains important relativistic features through the description of the nuclear mean field in terms of a scalar and a vector components, strong and of opposite sign. In their combination, they provide an explanation for the binding of nucleons and the spin-orbit splitting in nuclear states. The reader is referred to Muether et al. [14] for a relatively recent review of the DBHF method and a variety of applications to both nuclear matter and nuclei.

Irrespective of the many-body framework, a quantitative *NN* potential must be part of its input. Presently, forces based on nuclear chiral effective field theory (χEFT) [15–18] are the most popular. Chiral effective field theory respects the symmetries of quantum chromodynamics (QCD) but, at the same time, makes use of the degrees of freedom typical of low-energy nuclear physics, nucleons, and pions. Furthermore, it provides a clear systematics to determine the few- and many-body diagrams which must be present at each order of the perturbation.

Deriving nuclear forces directly from QCD is problematic. For starters, each nucleon is, itself, a complicated many-body system consisting of quarks, quark-antiquark pairs, and gluons, thus rendering the two-nucleon problem an even more complex many-body problem. Second, the interaction among quarks, which is due to the exchange of gluons, is very strong at the low energies involved in nuclear physics processes. For this reason, it is difficult to find converging perturbative solutions. Therefore, the first attempts to incorporate QCD in nuclear physics consisted mostly of QCD-inspired quark models. On the positive side, these models sought to explain nucleon structure (which consists of three quarks) and nucleon-nucleon processes (involving six-quarks) in an internally consistent manner. Some global features of the two-nucleon force, like the "hard core," could be explained by these quark models. On the other hand, quark-based approaches are, in fact, models rather than a theory. From an entirely different point of view, one may confront the six-quark problem by putting this system on a four dimensional discrete lattice representing three dimensions in space and one in time. This method is known as lattice QCD. Although progress in lattice QCD goes on, such calculations are computationally very demanding and thus the approach is not (currently) feasible as a standard tool to make predictions of nuclear properties.

A new era for the theory of nuclear forces started when Steven Weinberg worked out an effective field theory (EFT) for low-energy QCD [16, 19]. He argued that all one needs to do is to write the most general Lagrangian consistent with all the properties of low-energy QCD, as this action would render the theory equivalent to low-energy QCD. A crucially important property for this discussion is $SU(2)_R \times SU(2)_L$ symmetry, or chiral symmetry, which is "spontaneously" broken, as briefly reviewed next. Massless spin-$\frac{1}{2}$ fermions have their spin and momentum either parallel to each other ("right-handed") or anti-parallel ("left-handed"), a property which is referred to as having definite chirality. Since nucleons are made of "up" and "down" quarks, which have nearly zero mass, chiral symmetry holds approximately. As a consequence of this symmetry, one might expect to find in nature mesons of the same mass but opposite parity. However, such parity "doublets" are not observed, which amounts to a "spontaneous" breaking of the symmetry. According to a theorem first proven by Goldstone, the spontaneous symmetry breaking implies the existence of a pseudoscalar meson, the pion. Thus, the pion plays an outstanding role in generating the nuclear force. Pions and nucleons interact weakly at low energies as compared to the gluons and quarks. Therefore, calculations of pion-nucleon processes pose no problems. Moreover, in EFT one makes use of expansions in powers of momentum over an appropriate "scale," which is the "chiral symmetry breaking scale," close to 1 GeV. In short, this is the essence chiral perturbation theory or ChPT, and the reason why it allows to calculate the various contributions to the potential systematically order by order, where each order refers to a particular power of the momentum. Furthermore, χEFT can generate not only the force between two nucleons, but also many-nucleon forces in a consistent manner [17]. The χEFT approach continues to gain popularity and is applied with great success in contemporary theoretical nuclear physics [18, 20–22].

However, it is important to keep in mind that a low-momentum expansion has a limited range of applicability. For that reason, interactions derived from chiral perturbation theory are not meant for applications to high energy processes or in dense matter, where high Fermi momenta are involved, as is the case in the interior of compact stars. In such situations, strategies to extend chiral predictions must be adopted, and we will discuss some instances where extensions become necessary.

Mean-field models, both relativistic and non-relativistic (see, for instance [23, 24]) are still a popular, although non-microscopic alternative to methods based on the in-medium reaction matrix. They continue to be utilized frequently in the development of the EoS and related predictions.

Describing the properties of (dense) systems from elementary forces and including all required contributions is an extremely challenging program, whose completion is not in sight. However, χEFT provides a path on which to proceed systematically toward that goal. We share the point of view that χEFT is currently the most fundamental approach due to its strong link with QCD. At the same time, the degrees of freedom of the theory make calculations of low-energy observables a manageable task.

Our main objective in this article is to provide a self-contained review of the recent work with isospin symmetric and asymmetric matter done systematically by our group and based mainly on chiral interactions, comparing with empirical constraints when available. We will place particular emphasis on neutron-rich matter, which is currently the focus of numerous empirical investigations both in terrestrial laboratories (especially through experiments aimed at constraining the thickness of

neutron skins), or through astrophysical observations of neutron stars and related phenomena.

This article is organized as follows. After these opening remarks, in section 2 we describe in detail the calculations of the EoS, starting with the two-nucleon forces (2NF) and the three-nucleon forces (3NF) which we apply (see sections 2.2.1 and 2.2.2, respectively). In section 2.3, we review and discuss some of our results of the energy per particle in both symmetric and neutron matter [25]. In section 3, we focus specifically on the symmetry energy and the chief role its density dependence plays for neutron-rich systems. We then develop a discussion on the EoS in neutron stars (see section 4). We conclude with a summary and an outlook in section 5.

2. NUCLEAR MATTER AND THE EQUATION OF STATE

2.1. The G-Matrix and the Energy per Particle

In the previous section, we mentioned the linked-cluster perturbation series for the energy of a many-body system [1–6]. To facilitate convergence (otherwise problematic in view of the strong repulsive core of the *NN* force), the linked-cluster expansion for the energy per particle in nuclear matter [3] is written in terms of the reaction matrix or "*G*-matrix," which itself is solution of the Bethe-Goldstone equation. Schematically, the Bethe-Goldstone equation can be written as

$$G(E_0) = V + V\frac{Q}{E - E_0}G(E_0)\ , \tag{1}$$

where V is the *NN* potential, Q is the Pauli operator, and E_0 the starting energy of the two nucleons. The second term on the RHS of Equation (1) represents the infinite ladder sum which builds short-range correlations (SRC) into the wave function. The correlated (ψ) and the uncorrelated (ϕ) wave functions satisfy

$$G\phi = V\psi\ , \tag{2}$$

from which one can write

$$\psi = \phi + V\frac{Q}{E - E_0}G\phi\ . \tag{3}$$

At large distances, the correlated wave function is expected to approach the uncorrelated one (a behavior known as the "healing" property), whereas the two can be very different at short range. Hence, the difference between the correlated and the uncorrelated wave functions, or "defect function" $f = \psi - \phi$, can be associated to the degree of SRC.

Usually, its momentum-dependent Bessel transform is considered instead, so as to bring out the dependence on specific partial waves. For each angular momentum state [5], we then have

$$f^{JST}_{LL'}(k) = \frac{k\ \bar{Q}(k_F, k, P^{c.m.}_{avg})G^{JST}_{LL'}(P^{c.m.}_{avg}, k, k_0)}{E_0 - E}\ , \tag{4}$$

where the angle-averaging has been applied to the Pauli operator, $\bar{Q}$. Equation (4) is related to the probability of exciting two nucleons having relative momentum k_0 and relative orbital angular momentum L to a state with relative momentum k and relative orbital angular momentum L'. The integral of the probability amplitude squared is known as the "wound integral" and defined, for each partial wave at some density ρ, as

$$\kappa^{JST}_{LL'} = \rho\int_0^\infty |f^{JST}_{LL'}(k)|^2 dk\ . \tag{5}$$

Thus, both f and κ contain information on correlations present in the wave function and the *G*-matrix. The degree of SRC has been traditionally associated with the "strength" of a given potential, as indicated, for instance, by the deuteron D-state probability [26].

The topic of SRC deserves a review by itself and will not be covered here. However, we have taken the opportunity to recall how one may obtain, through Equations (4–5), some information about SRC in nuclear matter. The latter is complementary to studies of SRC in nuclei, which are currently the object of intense experimental investigations through high momentum-transfer (inclusive or exclusive) electron scattering measurements. (For a review on this topic, see [27] and references therein). Two-nucleon dynamics at short distances is mostly determined by the presence of short-range repulsion in the two-nucleon force, which is one of the reasons why a mean-field picture of the nucleus has strong limitations. Short-range correlations, particularly two-nucleon correlations, are therefore fundamentally important and open intriguing questions concerning momentum distributions in nuclei as a tool to probe the off-shell nature of the *NN* potential. For a recent work of our group on SRC in A=2,3 nuclei see [28].

Back to Equation (1), we solve it self-consistently to obtain the *G*-matrix together with the single-particle potential, which we define for (anti-symmetrized) states below and above the Fermi level according to the so-called "continuous choice":

$$U(p) = Re\sum_{q\le k_F} < pq|G(E_0)|pq - qp > \ . \tag{6}$$

The starting energy is written as

$$E_0 = e(q) + e(p) \tag{7}$$

in terms of on-shell single-particle energies

$$e(p) = T(p) + U(p)\ , \tag{8}$$

where T is the kinetic energy. The average energy per particle in nuclear matter is then obtained from

$$E/A = \frac{1}{A}\sum_{p\le k_F} T(p) + \frac{1}{2A}\sum_{p\le k_F} U(p)\ . \tag{9}$$

Equation (9) as a function of density is the nuclear EoS. Next, we will address how the *NN* potential V in Equation (1) is constructed.

2.2. The Equation of State From Chiral Forces

It is our philosophy that constructing the EoS microscopically from state-of-the-art few-body interactions is the right way to gain insight into effective nuclear forces in the medium. High-precision meson-theoretic interactions [29–31] are often utilized in contemporary calculations of nuclear matter, structure, and reactions. However, in the meson-theoretic approach it is difficult, if not impossible, to maintain a strong connection between the 3NF, or more generally the A-nucleon forces with $A > 2$, and the associated 2NF [32]. On the other hand, χEFT [18, 20, 22] provides a systematic way to construct nuclear many-body forces consistently [17] with two-body forces, as well as to assess theoretical uncertainties through a systematic expansion controlled by a counting scheme [15]. Furthermore, and perhaps most importantly, χEFT maintains consistency with the symmetries and symmetry breaking pattern of the fundamental theory of strong interactions, QCD.

Because of the strengths described above, χEFT has become the authoritative approach for developing nuclear forces. Applications include few-nucleon reactions [33–38], nuclear structure, especially of light- and medium-mass nuclei [39–55], cold infinite matter [22, 53, 56–64], infinite matter at finite temperature [65, 66], and various aspects of nuclear dynamics [67–73].

In regard to the connection between nuclear matter properties and finite nuclei, it is interesting to point out a persistent problem encountered in structure calculations and related to the bulk properties of medium-mass nuclei. Typically charge radii are underpredicted [74] while the opposite is true for binding energies [75]. Including the desired properties of medium-mass nuclei directly into the fitting protocol for the low-energy constants (LECs) which parametrize short-distance physics in chiral nuclear forces has resulted in improved predictions [76]. However, for a truly microscopic approach the 2NF should be constrained by two-nucleon data and the 3NF by three-nucleon data, without additional adjustments. Applications to $A > 3$ systems would then be actual predictions, although they may carry substantial uncertainties.

Two recent studies [54, 55] provide indications for how the overbinding problem may be overcome. In these studies, a rather soft nucleon-nucleon (NN) potential (due to renormalization group evolution) along with 3NFs fitted to the binding energy of ^{3}H and the charge radius of ^{4}He were employed to calculate the ground-state properties of closed shell nuclei from ^{4}He to the light Tin isotopes [54, 55]. Predictions of the ground-state energies were accurate, whereas the radii were somewhat underpredicted, although still in fairly good agreement with experiment. These features can be linked to the good nuclear matter saturation properties of the employed 2NF + 3NF combination [57]. In the above example, the 2NF was soft and alone would lead to substantial overbinding in nuclear matter, whereas the addition of a repulsive 3NF contribution leads to a much better description of the nuclear matter saturation point [57]. As we mentioned earlier, the first quantitative explanation of nuclear matter saturation was achieved in this way within the framework of Dirac-Brueckner-Hartree-Fock theory [12, 14, 77–79]. As an alternative, one could begin with a relatively repulsive 2NF and then add an attractive, density-dependent 3NF contribution. An example of such combination is provided by the Argonne v_{18} (AV18) 2NF [31] together with the Urbana IX 3NF [80]. However, in this way satisfactory predictions for both the nuclear matter saturation energy and density cannot be obtained [81] and the binding energies of medium-mass nuclei are seriously underpredicted [82]. A similar scenario presents itself when the AV18 2NF is used in combination with the Illinois-7 3NF [82, 83]. Efforts to treat the 3NF microscopically were reported in Zuo et al. [84] and Li et al. [85]. In Li et al. [85], in particular, a 3NF including the Δ, Roper, and nucleon-antinucleon excitations was proposed, based on the Bonn [86] and the Nijmegen [30] one-boson-exchange potentials.

The predictions reviewed in this work are based on the high-quality *soft* chiral NN potentials from leading order to fifth order of the chiral expansion constructed in Entem et al. [87]. More details are provided below.

2.2.1. Two-Nucleon Forces

The NN potentials used in this review go over five orders in the χEFT series, from leading order (LO) to fifth order (N^{4}LO). This set of interactions is more internally consistent as compared to earlier ones [88, 89], in that the same power counting and regularization schemes are used for each order.

Furthermore, the long-range contributions are fixed by the πN LECs provided by the recent analysis of Hoferichter et al. [90, 91], which provided very accurate determinations. The errors in those πN LECs are small enough to be safely ignored in the process of uncertainty quantification. We also recall that, at the fifth (and highest) order, the NN data below pion production threshold are reproduced with the precision of a χ^2/datum equal to 1.15.

Prior to iterating the potential in the Lippmann-Schwinger equation, one must remove high-momentum components, in line with the low-momentum expansion concept of chiral perturbation theory. For the interactions we use, this step is carried out through the application of a non-local regulator function:

$$f(p', p) = \exp[-(p'/\Lambda)^{2n} - (p/\Lambda)^{2n}], \tag{10}$$

where $p' \equiv |\vec{p}\,'|$ and $p \equiv |\vec{p}\,|$ are the final and initial nucleon momenta in their center-of-mass system, respectively. We will consider only values of the cutoff parameter Λ smaller than or equal to 500 MeV, which have been found to have good perturbative properties. The soft nature of the potentials has been confirmed by the Weinberg eigenvalue analysis of Hoppe et al. [92] and in the context of the perturbative calculations of infinite matter of Drischler et al. [93].

2.2.2. Three-Nucleon Forces

Three-nucleon forces contribute for the first time at the third order of the chiral expansion (N^{2}LO), where they contain three

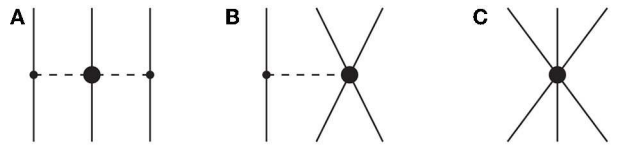


FIGURE 1 | The 3NF at N^{2}LO with **(A)** the 2PE, **(B)** the 1PE, and **(C)** the contact terms.

parts [33]: the two-pion-exchange (2PE) term, which is of long-range nature, the medium-range one-pion exchange (1PE) contribution, and a short-range contact term. These diagrams are shown in **Figure 1**. We apply these 3NFs in the form of the density-dependent effective two-nucleon interactions [94, 95], which can be expressed in terms of the well-known non-relativistic two-body nuclear force operators and thus easily incorporated in the usual *NN* partial wave formalism and subsequently in the computation of the EoS *via* the particle-particle ladder approximation. We recall that the strategy of including the 3NF as an effective density dependent 2NF was first proposed in Baldo et al. [96] within the BHF theory.

The effective density-dependent two-nucleon interactions can be regrouped into six topologies involving one loop. Three of them originate from the 2PE graph of the chiral 3NF (**Figure 1A**), and depend on the LECs $c_{1,3,4}$, which already appear in the 2PE part of the *NN* force. Two one-loop topologies are derived from the 1PE diagram (**Figure 1B**), and contain the LEC c_D. Last, we have the one-loop topology related to the 3NF contact diagram (**Figure 1C**), associated with the LECs c_E. Note that, in pure neutron matter, the contributions proportional to the LECs c_4, c_D, and c_E vanish [56]. In recent nuclear matter calculations [63, 93], progress has been made toward including N^{3}LO three-body interactions in the two-body normal-ordering approximation as well as including the residual three-body normal-ordered force. Our group is in the process of including effective density-dependent 3NF at N^{3}LO as from Kaiser et al. [97, 98]. We have preliminary evidence that the contributions from the short-range terms [97] may be negligibly small.

The LECs c_D and c_E which we use are determined *via* the three-nucleon system. They are constrained to reproduce the $A = 3$ binding energies and the Gamow-Teller matrix element of tritium β-decay through the procedure described in Gardestig and Phillips [99], Gazit et al. [100], and Marcucci et al. [101]. The regulator function applied to the 3NF is

$$f(q) = \exp[(-q/\Lambda)^4]\,, \tag{11}$$

as in Navrátil [102], with $q = |\vec{p}\,' - \vec{p}\,|$ the momentum transfer. Note that this choice makes the 3NF local in coordinate space, which, in turn, facilitates the construction of the $A = 3$ wave functions [103].

The complete 3NF at orders higher than the third (N^{2}LO) is very challenging, both in its development and applications, and, therefore, it is frequently excluded from nuclear structure studies. Note, though, that good progress is being made toward the inclusion of the subleading 3NF at N^{3}LO [63, 93, 97, 98, 104, 105]. However, in Krebs et al. [106] it was shown that the 2PE 3NF has nearly the same analytical structure at the third (N^{2}LO), fourth (N^{3}LO), and fifth (N^{4}LO) orders. Thus, one can parametrize the sum of all the three orders of 3NF contributions in terms of a set of effective LECs. Therefore, at least for this very important component of the 3NF, complete calculations up to N^{4}LO are possible.

In the N^{4}LO rows of **Table 2** we give the effective LECs $c_{1,3,4}$ obtained in Krebs et al. [106]. Concerning the 2PE 3NF at N^{3}LO, Equation (2.8) of Bernard et al. [107] provides the corrections to the c_i. (Note, though, that there is an error in the values given below that equation. The correct values for δc_3 and δc_4 are $\delta c_3 = -\delta c_4 = 0.89$ GeV^{-1}.) With these corrections, we obtain the values given in the N^{3}LO rows of **Table 2**. Then, inserting the c_i of **Table 2** in the expression for the N^{2}LO 3NF, we are able to include the 2PE parts of the 3NF up to N^{3}LO and up to N^{4}LO in a straightforward way, with the LECs c_D and c_E refitted. Their values, also listed in **Table 2**, are different from those listed in **Table 1** but of the same order and with the same sign.

We close this section by highlighting that, of all possible 3NF contributions, the 2PE 3NF is the first to have been calculated [108]. The prescriptions outlined above allow to include this very important 3NF up to the highest order we consider at this time.

TABLE 1 | Values of the LECs $c_{1,3,4}$, c_D, and c_E for different orders of the 2NF in the χEFT expansion, and the 3NF at N^{2}LO, and different values of the momentum-space cutoff Λ.

	Λ (MeV)	n	c_1	c_3	c_4	c_D	c_E
N^{2}LO	450	2	−0.74	−3.61	2.44	0.935 (0.215)	0.12 (0.04)
	500	2	−0.74	−3.61	2.44	0.495 (0.195)	−0.07 (0.04)
N^{3}LO	450	2	−1.07	−5.32	3.56	0.675 (0.205)	0.31 (0.05)
	500	2	−1.07	−5.32	3.56	−0.945 (0.215)	−0.68 (0.04)
N^{4}LO	450	2	−1.10	−5.54	4.17	1.245 (0.225)	0.28 (0.05)
	500	2	−1.10	−5.54	4.17	−0.670 (0.230)	−0.83 (0.03)

The LECs $c_{1,3,4}$ are given in units of GeV^{-1}, while c_D and c_E are dimensionless. The numbers in parentheses indicate the error arising from the fitting procedure. In addition, we also show the value for the exponent n that appears in the regulator function of Equation (10).

TABLE 2 | Same as **Table 1**, but including the 2PE 3NF at N^{3}LO and N^{4}LO.

	Λ (MeV)	n	c_1	c_3	c_4	c_D	c_E
N^{2}LO	450	2	−0.74	−3.61	2.44	0.935 (0.215)	0.12 (0.04)
	500	2	−0.74	−3.61	2.44	0.495 (0.195)	−0.07 (0.04)
N^{3}LO	450	2	−1.20	−4.43	2.67	0.670 (0.210)	0.41 (0.05)
	500	2	−1.20	−4.43	2.67	−0.750 (0.210)	−0.41 (0.04)
N^{4}LO	450	2	−0.73	−3.38	1.69	0.560 (0.220)	0.46 (0.05)
	500	2	−0.73	−3.38	1.69	−0.745 (0.225)	−0.15 (0.04)

*That is, at each order, the 2PE term of the 3NF is included summing up all contributions up to that order. (The N^{2}LO numbers are the same as in **Table 1**).*

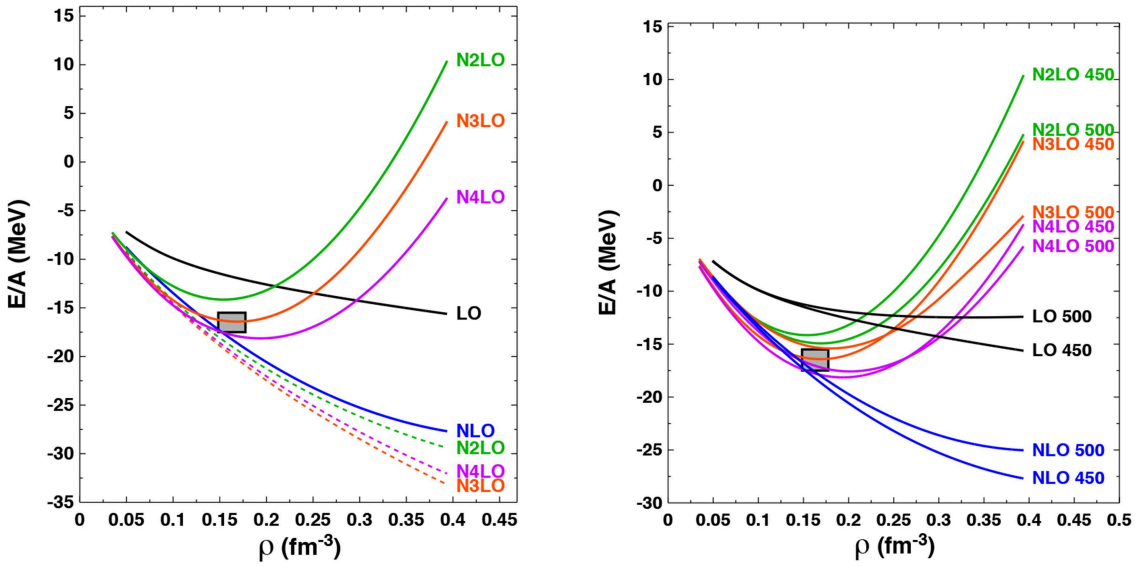


FIGURE 2 | (Left) Ground state energy per particle of SNM as a function of density from the chiral two- and three-body forces with cutoff $\Lambda = 450$ MeV. The three dotted curves show predictions which include only two-body forces. For the 3NF contributions at N^{2}LO and above, the LECs of **Table 2** are used. The shaded box locates the approximate empirical saturation energy and density. **(Right)** Ground state energy per particle of SNM as a function of density at the indicated orders and with varying cutoff parameters. Other details as on the left.

2.3. Predictions for the Equation of State

2.3.1. Symmetric Matter Predictions

We begin with the symmetric nuclear matter (SNM) EoS. This is displayed in **Figure 2**, where, on the left, the momentum-space cutoff is fixed at 450 MeV but the chiral order of the two-body force is varied from leading to fifth order. The 3NFs are chosen with LECs in **Table 2**, which at N^{3}LO and N^{4}LO include the 2PE 3NF at fourth and fifth order, respectively. (We note that, in all that follows, when we refer to predictions obtained with 3NF at N^{3}LO or at N^{4}LO, we mean to say that the 2PE 3NF is included up to those orders). The dashed lines indicate results at N^{2}LO and above with no three-body forces present, while the solid lines include the 3NF when appropriate, that is, at N^{2}LO and up. Formally, we observe a good convergence pattern at the two-body level with this family of *NN* potentials, but naturally we do not expect realistic saturation behavior when soft two-body forces alone are included in the calculation of the EoS. We see that the inclusion of 3NFs is necessary beyond about half nuclear matter saturation density and that for this set of nuclear potentials the total 3NF contribution to the EoS decreases with the chiral order from N^{2}LO to N^{4}LO.

We note that the uncertainty band obtained by varying the chiral order from N^{2}LO to N^{4}LO while keeping Λ fixed to 450 MeV encloses the empirical saturation point. The saturation energy varies in the range $-14\,\text{MeV} \lesssim E_0 \lesssim -18\,\text{MeV}$ while the saturation density varies between $0.155\,\text{fm}^{-3} \lesssim \rho_0 \lesssim 0.195\,\text{fm}^{-3}$. We stress that, once the two- and three-nucleon forces are fixed by the *NN* data and the properties of the three-nucleon system, no parameters are readjusted, making the many-body calculation parameter-free. Since the predicted binding energies and charge radii of intermediate-mass nuclei are closely related to the corresponding saturation point in SNM, we see the possibility that the new class of chiral potentials constructed in Entem et al. [87] and used in this work may lead to more reliable predictions in ab initio calculations of finite nuclei. For densities larger than $\rho \gtrsim 0.20\,\text{fm}^{-3}$, the predictions shown on the LHS of **Figure 2** display a trend that does not suggest satisfactory convergence, since the three (saturating) solid curves are about equally spaced. This is most likely due to the incompleteness of the 3NF at orders above N^{2}LO. It is natural to expect that such trend will be a recurrent theme in later results. As discussed in section 2.2.2, we believe that including the important 2PE contribution consistently across all orders is important and insightful. For instance, our results suggest that the missing 3NF contributions at orders higher than N^{3}LO can be expected to play a substantial role toward a successful convergence.

On the RHS of **Figure 2** we show the dependence of the SNM EoS on the choice of momentum-space cutoff Λ in the two- and three-body forces as well as the order in the chiral expansion. In the present work we consider only the two cases $\Lambda = 450, 500$ MeV, see comments in section 2.2.1. At orders N^{2}LO, N^{3}LO, and N^{4}LO, the cutoff dependence appears to be comparable but generally smaller than the truncation errors.

In **Figure 2**, we show the impact of choosing at fourth (N^{3}LO) and fifth (N^{4}LO) order in the chiral expansion either the N^{2}LO 3NF coupling strengths shown in **Table 1** (labeled "I" in the figure) or those obtained by including the 2PE 3NF contributions at higher order shown in **Table 2** (labeled "II" in the figure). We only show results for potentials with momentum-space cutoff $\Lambda = 450$ MeV, but we expect similar results for the $\Lambda = 500$ MeV cutoff potentials due to the identical change in the important c_i LECs ($i = 1, 3, 4$). We see that at N^{4}LO the impact is rather

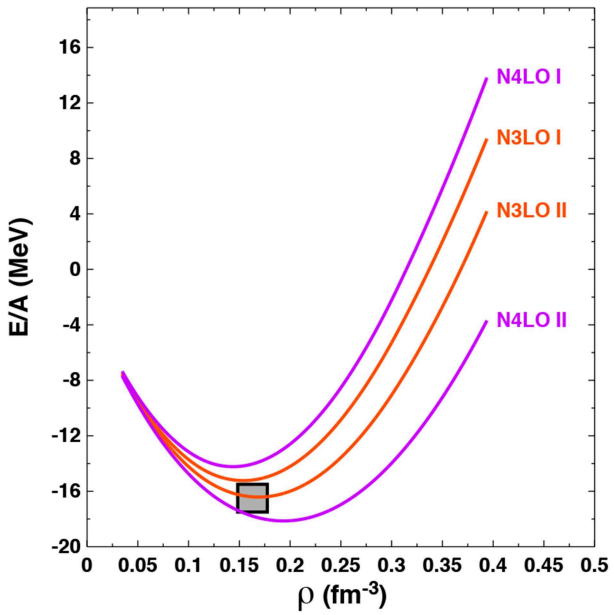


FIGURE 3 | Energy per particle in SNM as a function of density at N^{3}LO and N^{4}LO with a cutoff of $\Lambda = 450$ MeV. For the 3NF contributions, the LECs of either **Table 1** or **Table 2** are applied as indicated by labels "I" or "II", respectively. Case "II" is characterized by including the 2PE 3NF up to the given order. The approximate empirical saturation energy and density are indicated by the gray box.

large and roughly of the same size as variations in the chiral order from N^{2}LO to N^{4}LO. However, the additional theoretical uncertainty resulting from the choice of LECs entering into the 2PE 3NF would extend the overall error band inferred from the RHS of **Figure 2** only moderately and only at the largest densities considered. In other words, **Figure 3** shows that the truncation error (compare N^{3}LO II and N^{4}LO II) can be much smaller than the uncertainty arising from using different sets of LECs (compare N^{4}LO I and N^{4}LO II), indicating the importance of completeness in the 3NF at all orders.

Before closing this section, we summarize the saturation properties of SNM at the various orders and cutoff values. In **Table 3**, we show saturation density, saturation energy, and the isoscalar incompressibility. For the latter, constraints can be obtained from giant monopole resonance energies. In De et al. [109], the authors obtain a range of 211.9 ± 24.5 MeV. Our predictions at N^{3}LO are consistent with this range, whereas the larger values at N^{4}LO reflect the larger saturation density at that order.

Parameters which involve isospin asymmetry will be discussed later.

2.3.2. Neutron Matter Predictions

We next consider the ground state energy of neutron matter (NM) as a function of density, employing the same set of chiral potentials and many-body methods discussed previously in the case of symmetric nuclear matter. The EoS for both SNM and NM are crucial to determine the density-dependent nuclear

TABLE 3 | Saturation properties from N^{2}LO to N^{3}LO and two values of the cutoff.

	Λ (MeV)	ρ_0 (fm^{-3})	$e_0(\rho_0)$ (MeV)	K_0 (MeV)
N^{2}LO	450	0.155 ± 0.015	-14.2 ± 2.3	217.4 ± 3.6
	500	0.170 ± 0.010	-14.9 ± 0.5	214.4 ± 8.0
N^{3}LO	450	0.170 ± 0.025	-16.4 ± 1.7	221.2 ± 51.5
	500	0.180 ± 0.023	-15.4 ± 2.2	206.4 ± 49.2
N^{4}LO	450	0.195 ± 0.012	-18.1 ± 0.8	272.7 ± 24.3
	500	0.203 ± 0.010	-17.6 ± 0.9	255.6 ± 21.2

symmetry energy and to better understand the properties of neutron-rich nuclei and neutron stars, aspects which will be addressed in later sections.

In **Figure 4**, on the LHS, we show the energy per particle of NM as a function of density starting from chiral two- and three-body forces with the same value of the momentum-space cutoff $\Lambda = 450$ MeV but at different orders in the chiral expansion. As in the case of symmetric nuclear matter, we observe good convergence at the level of 2NF alone. When 3NFs are included, we find somewhat smaller truncation errors compared to the case of SNM. This may be due in part to the absence of large, central isospin-0 partial waves in NM, which appear to be more sensitive to differences among interactions. Clearly, the 3NF plays an outstanding role in very neutron-rich systems at and beyond nuclear saturation density, where its contribution to the EoS grows more strongly with the density than the 2NF contributions.

On the RHS of **Figure 4** we display the energy per particle of pure neutron matter as a function of density when varying both the order in the chiral expansion and the momentum-space cutoff Λ from 450 to 500 MeV. We see that, in comparison to the analogous study in symmetric nuclear matter, the pure neutron matter results display a much weaker cutoff dependence, which may again be due to the absence of strong isospin-0 partial waves. Interestingly, even in the case of the relatively large density $\rho = 0.4\,\text{fm}^{-3}$, corresponding to a Fermi momentum of $k_F = 450$ MeV which lies at the effective breakdown scale of the expansion, there is relatively little cutoff dependence.

Once again, we observe that the order-by-order pattern is not satisfactory when moving from N^{3}LO to N^{4}LO. The impact of including the 2PE 3NF up to fourth (N^{3}LO) and fifth (N^{4}LO) order (consistent with the order of the 2NF), compared to including only the third-order (N^{2}LO) contributions, through the adoption of the LECs given in **Table 2**, is demonstrated in **Figure 5**. As in the case of symmetric nuclear matter, the effect at N^{4}LO is much larger than at N^{3}LO due to the larger change $\Delta c_3 = 2.16\,\text{GeV}^{-1}$ vs. $\Delta c_3 = 0.89\,\text{GeV}^{-1}$, respectively, in the c_3 LEC at these two orders in the chiral expansion. Moreover, the choice of LECs entering into the 2PE 3NF contributions again results in a moderate systematic increase in the pure neutron matter energy per particle at the highest densities considered. As we mentioned earlier, the investigation of higher-order 3NF contributions is in progress.

Before closing this section, we take the opportunity to comment on how our SNM and NM EoS compare with those

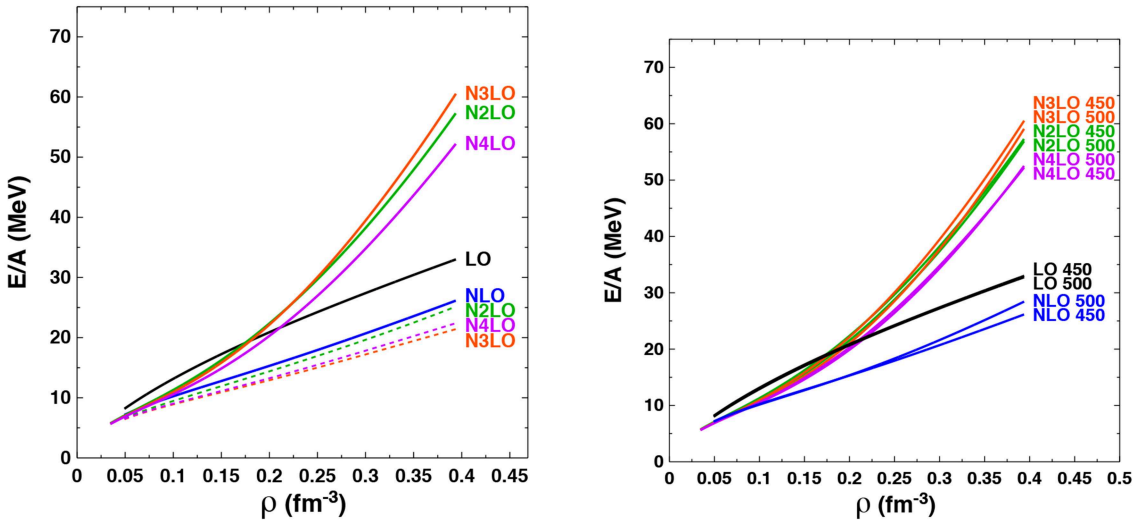


FIGURE 4 | (Left) Ground state energy per particle of NM as a function of density at the indicated orders in the chiral expansion. The three dotted curves show predictions including only the 2NF. The cutoff parameter is fixed at $\Lambda = 450$ MeV and the 3NF LECs from **Table 2** are used. **(Right)** Ground state energy per particle of NM as a function of density at the indicated chiral orders and with varying cutoff. The LECs of **Table 2** are used.

from Drischler et al. [93]. There, chiral interactions including full 3NF and 4NF at N^{3}LO are applied to investigate nuclear saturation. Judging from the RHS of **Figure 4** in Drischler et al. [93], where the EoS for both SNM and NM [63] are displayed, we conclude that our EoS at N^{3}LO are qualitatively comparable with them within the density range covered in **Figure 4** in Drischler et al. [93], namely up to ρ=0.20 fm^{-3}, with ours revealing more attraction. We also point out that, in Drischler et al. [93], the 3NF couplings are fit to triton and to saturation properties, whereas we do not impose any constraints other than those from the two- and the three-nucleon systems. Even so, we find (confirming the conclusion from [93]) that realistic saturation properties are possible at N^{3}LO.

3. THE SYMMETRY ENERGY AND RELATED ASPECTS

3.1. Review of Some Basic Concepts and Definitions

The properties of isospin-polarized matter have relevance for a number of open questions in nuclear physics and nuclear astrophysics. For instance, the existance of the neutron drip lines, the thickness of neutron skins, and the properties of neutron stars all have in common a strong sensitivity to the EoS of neutron-rich matter. The symmetry energy determines to a good approximation the energy per particle in homogeneous nuclear matter with any degree of isospin asymmetry (cf. Equation 14 below). The symmetry energy and its density dependence are therefore a key focus of contemporary theoretical and experimental investigations, and much effort has been devoted to identifying nuclear observables which correlate with this important property of infinite matter [25, 45, 53, 56–64, 110–120].

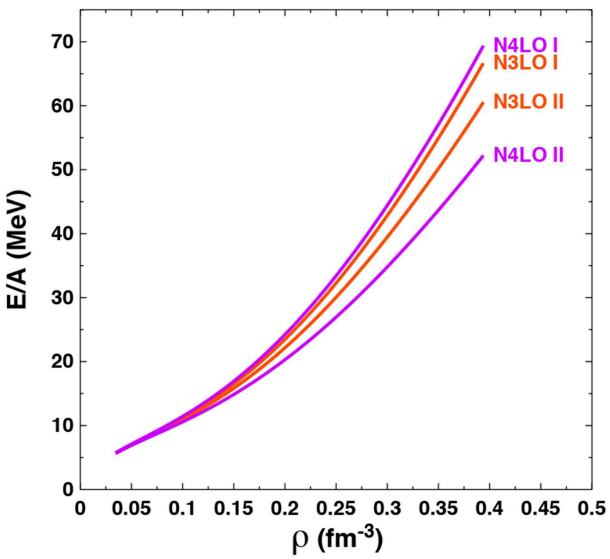


FIGURE 5 | Ground state energy per particle of NM as a function of density at N^{3}LO and N^{4}LO with cutoff equal to 450 MeV. Similar to **Figure 3**, for the 3NF contributions the LECs of either **Table 1** or **Table 2** are applied as indicated by labels "I" or "II," respectively.

The isospin asymmetry parameter is a measure of the relative densities of neutrons and protons and is defined as

$$\alpha = \frac{(\rho_n - \rho_p)}{(\rho_n + \rho_p)}\,, \tag{12}$$

where ρ_n and ρ_p are the neutron and proton densities. It is useful to write the energy per particle in isospin asymmetric matter at

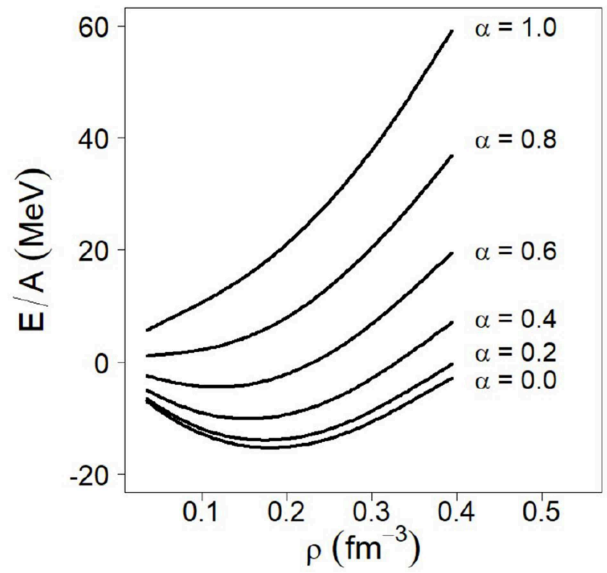


FIGURE 6 | Energy per particle in isospin-asymmetric nuclear matter. In each case, the isospin asymmetry parameter is given. Calculations conducted at N^{3}LO of the 2NF (and the 2PE 3NF included up to N^{3}LO) with cutoff equal to 500 MeV.

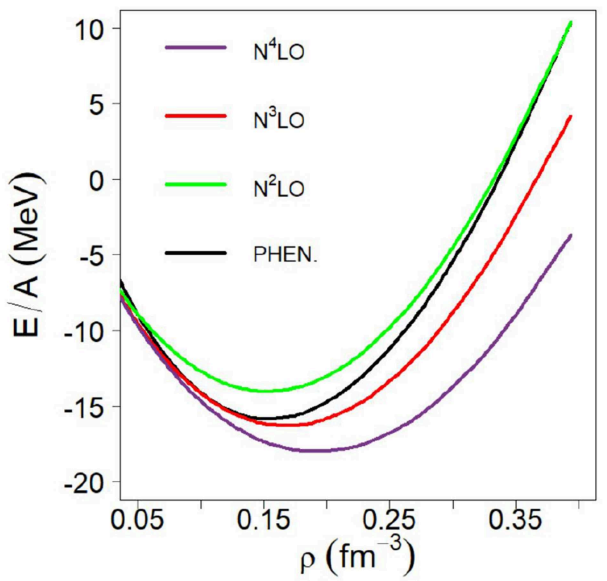


FIGURE 7 | The EoS of SNM at the three chiral orders considered here (cutoff fixed at 450 MeV) compared with the phenomenological EoS of Alam et al. [135].

some density as an expansion with respect to α:

$$e(\rho,\alpha) = e(\rho,\alpha=0) + \frac{1}{2}\left(\frac{\partial^2 e(\rho,\alpha)}{\partial\alpha^2}\right)_{\alpha=0}\alpha^2 + \mathcal{O}(\alpha^4)\,. \quad (13)$$

Frequently, the expansion above is truncated at the term quadratic in α, resulting in the popular parabolic approximation:

$$e(\rho,\alpha) \approx e_0(\rho) + e_{sym}(\rho)\,\alpha^2\,, \quad (14)$$

where $e_0(\rho) = e(\rho,\alpha=0)$. [Equation (14) has been verified to be valid up to fairly high densities [119].] Within the assumption of Equation (14), the symmetry energy, e_{sym}, is the difference between the energy per particle in neutron matter and the one in symmetric matter. We can expand the symmetry energy about the saturation density, ρ_0,

$$e_{sym}(\rho) \approx e_{sym}(\rho_0) + \frac{L}{3}\frac{\rho-\rho_0}{\rho_0} + \frac{K_{sym}}{18}\left(\frac{\rho-\rho_0}{\rho_0}\right)^2 + \ldots\,. \quad (15)$$

The slope parameter, L, is defined as

$$L = 3\rho_0\left(\frac{\partial e_{sym}(\rho)}{\partial\rho}\right)_{\rho_0}\,, \quad (16)$$

and therefore is a measure of the density dependence of the symmetry energy around saturation density. We recall that L is an important quantity because of its significance for the skin thickness in neutron-rich nuclei. Experiments which plan to measure the neutron radius of ^{208}Pb and ^{48}Ca using electroweak probes, such as PREX II [121] and CREX [122], respectively, are expected to provide accurate measurements of the neutron skin. As a consequence, one hopes for reliable constraints on the *symmetry pressure*, clearly related to the slope parameter (see section 3.3.1 below). Also, the radius of the average-mass neutron star is known to be sensitive to the pressure in neutron matter at normal density, P_0^{NM}, which is simply related to L (for fixed ρ_0) due to the vanishing of the density derivative of $e(\rho,\alpha=0)$ at saturation. That is:

$$P_0^{NM} \approx L\,\rho_0/3\,. \quad (17)$$

The reader is referred, for instance, to Sammarruca and Millerson [123] and the comprehensive list of citations therein.

The isovector incompressibility, K_{sym}, is associated with the next higher-order derivative, that is, it measures the curvature of the symmetry energy at saturation density. It is defined as:

$$K_{sym} = 9\rho_0^2\left(\frac{\partial^2 e_{sym}(\rho)}{\partial\rho^2}\right)_{\rho_0}\,. \quad (18)$$

Correlations between L and both K_{sym} and the symmetry energy at saturation, $e_{sym}(\rho_0)$ [124–126] have been examined. Predictions for the isovector incompressibility carry large uncertainty, as is the case for the isoscalar one. Attempts to constrain the second derivative of the symmetry energy (that is, its curvature) are discussed in Vidaña et al. [127], Ducoin et al. [128], and Santos et al. [129].

3.2. Predictions of Symmetry Energy and Related Properties

Figure 6 displays the energy per particle in isospin asymmetric matter as a function of density and for increasing degree

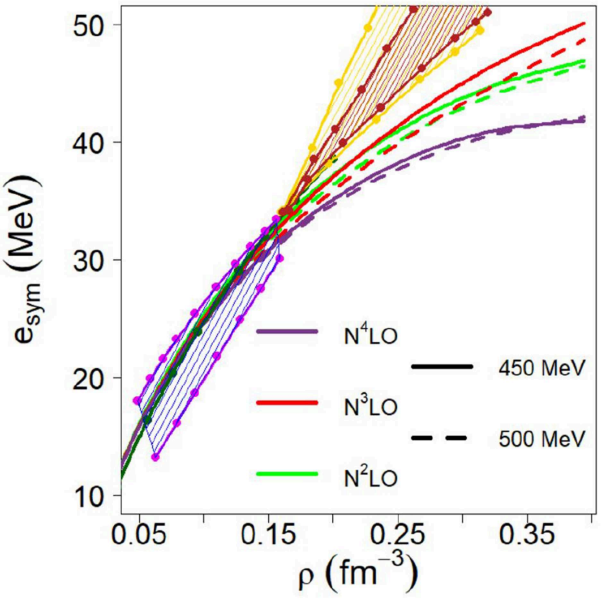


FIGURE 8 | The symmetry energy vs. density. The curves are obtained from the various microscopic EoS for NM at the indicated chiral orders and cutoff values, combined with the phenomenological EoS for SNM [135] as explained in the text. The additional predictions and various constraints are from: Danielewicz and Lee [136], dark green; Tsang et al. [137], magenta contour; Russotto et al. [138, 139], yellow and brown shaded areas. (The data points were extracted from the graphs assuming $\rho_0 = 0.16$ fm^{-3} and using WebPlotDigitizer opensource software, https://automeris.io/WebPlotDigitizer).

TABLE 4 | Predicted values of symmetry energy and related properties at three orders of chiral perturbation theory and two values of the cutoff parameter obtained as explained in the text.

	Λ (MeV)	$e_{sym}(\rho_0)$ (MeV)	L (MeV)	K_{sym} (MeV)
N^{2}LO	450	32.8 ± 0.4	52.2 ± 0.8	-117.6 ± 36.1
	500	32.2 ± 0.5	50.2 ± 1.5	-106.3 ± 31.1
N^{3}LO	450	32.4 ± 1.0	53.0 ± 7.2	-81.5 ± 32.8
	500	31.7 ± 0.6	48.8 ± 4.6	-75.2 ± 32.8
N^{4}LO	450	31.4 ± 0.5	45.8 ± 3.1	-114.3 ± 14.3
	500	31.1 ± 0.2	44.2 ± 1.8	-108.0 ± 12.9

of asymmetry, cf. Equation (14), for one selected order and cutoff [130].

As we already noted in conjunction with **Figure 2**, the saturation properties of the chiral interactions we are considering are different from one another, with the saturation density varying between about 0.16 and 0.20 fm^{-3}. Clearly, this will impact the expansion parameters contained in Equation (15), see definitions in Equations (16–18), differently than if the derivative were evaluated, in all cases, at some common, nominal saturation density ρ_0. On the other hand, analyses of correlations between the symmetry energy, its density slope, and the neutron skin thickness are typically done utilizing families of phenomenological models, such as large sets of Skyrme interactions or relativistic mean-field (RMF) models [131]. These models are constructed so as to have in common good saturation properties (usually by adjusting parameters to empirical properties of nuclei) while differing in the slope of the symmetry energy which, at saturation, is essentially a measure for the pressure in pure neutron matter (see Equation 17). Already almost two decades ago, Brown [132] considered a set of Skyrme interactions whose predictions of the density slope of the NM EoS around normal density differed dramatically and found a linear relation between such derivative and the neutron skin thickness in ^{208}Pb. Similar investigations have been and continue to be done with RMF models, with families of interactions constructed so as to span a large range of L values. For instance, RMF models such as NL3 [133] and IU-FSU [134] give values of L equal to 118.2 and 47.2 MeV, respectively. (Not surprisingly, these models span a large range of both neutron skin values and stellar radii). In Roca-Maza et al. [24], the authors utilize a large set of RMF models all of which describe accurately the nuclear binding energies and charge radii across the periodic table (which should constrain tightly the binding energy and saturation density of SNM). On the other hand, the same models predict very different neutron root-mean-squared (*r.m.s.*) radii, since the isovector channel is poorly constrained [24].

Our EoS are microscopic and parameter-free and we are not in the practice of constructing families of parameterized EoS models to establish phenomenological correlations. Nevertheless, for the purpose of demonstration, next we wish to perform a study meant to highlight the role of neutron matter pressure for the neutron skin thickness once the uncertainty associated with the saturation point in SNM, cf. **Figure 2**, is removed. To that end, we will construct "semi-microscopic" models of asymmetric matter as follows: for the symmetric part, we will use an established phenomenological EoS, such as the one from Alam et al. [135]. For the neutron matter part, currently our focal point, we will continue to use the chiral EoS presented in section 2.3.2. We then proceed treating these six cases (three chiral orders and two cutoffs) as six EoS models differing in their NM components. **Figure 7** shows the phenomenological EoS of SNM in comparison with our chiral predictions with cutoff equal to 450 MeV. **Figure 8** displays the symmetry energy obtained with our microscopic NM EoS combined with SNM EoS represented by the black curve in **Figure 7**. We also include in the figures the results of several analyses and constraints [136–139]. The predictions based on our microscopic NM EoS are considerably softer than those constraints above normal density. **Table 4** contains values for the parameters defined previosly through Equation (15), for the six EoS models which we have constructed as described.

We now proceed to discuss the spread of our values for the symmetry energy, the L parameter, and the isovector incompressibility in the framework of chiral uncertainties of the NM EoS. We recall that one of the strengths of χEFT is the opportunity of order-by-order improvement of the predictions. Naturally, the truncation error at a given order should be a reasonable measure of the uncertainty which arises from omitting the next order contributions. If the value of the observable X has been calculated at order $n+1$, than the truncation error at order

n can be estimated as the difference between the values at order $n+1$ and n:

$$\epsilon_n = |X_{n+1} - X_n| \,, \tag{19}$$

which is a reasonable way to estimate what one is missing by retaining only terms up to order n. On the other hand, if X_{n+1} is not known, then some alternative prescription must be used. We use the definition [87]

$$\epsilon_n \approx |X_n - X_{n-1}| \frac{Q}{\Lambda} \,, \tag{20}$$

where Q is a momentum characteristic for the observable under consideration and Λ is the cutoff. For the fifth (and highest) order, we use Equation (20) and we find it reasonable to define Q as the *r.m.s.* value of the relative momentum of two neutrons in neutron matter at the given density [see [123] and references therein].

We wish to express our final results for the symmetry energy, the slope parameter, and the isovector incompressibility at N^{3}LO. To that end, we average the predictions for the quantity X obtained with the two values of the cutoff separately at N^{3}LO and N^{4}LO, yielding $\bar{X}_4$ and $\bar{X}_5$, respectively. The truncation uncertainty at N^{3}LO can then be estimated as $\Delta_X = |\bar{X}_4 - \bar{X}_5|$. As an alternative, we choose to take the largest of the errors at the two cutoff values.

Applying that prescription, we obtain for the symmetry energy, the slope parameter, and the isovector incompressibility at N^{3}LO (all numbers in MeV):

$$e_{sym} = 32.1 \pm \Delta_{e_{sym}} \qquad \Delta_{e_{sym}} = 1.0 \,, \tag{21}$$

$$L = 50.9 \pm \Delta_L \qquad \Delta_L = 7.2 \,, \tag{22}$$

$$K_{sym} = -78.4 \pm \Delta_{K_{sym}} \qquad \Delta_{K_{sym}} = 32.8 \,. \tag{23}$$

We see that K_{sym} shows large variations, which reflect the extreme sensitivity of the second derivative to the details of the interactions for each of the curves in **Figure 8**. We emphasize that variations among those curves are due entirely to the NM predictions.

A phenomenological study of the EoS based on Skyrme density functionals [135] reports the slope parameter to be $L = 65.4 \pm 13.5$ MeV, whereas the isovector incompressibility is found to be within the range $K_{sym} = -22.9 \pm 73.2$ MeV. Lattimer and Lim [140] determined L to be between 40.5 and 61.9 MeV. For the isovector incompressibility, they suggest a linear relation between K_{sym} and L, that is, $K_{sym} \approx aL - b$, with a, b equal to 3.33 and 281 MeV, respecively [128], or 2.867 and 260 MeV [127]. More recent constraints obtained from tidal deformabilitie inferred from GW170817, report $30 < L < 86$ MeV and $-140 < K_{sym} < 16$ MeV or $40 < L < 62$ MeV and $-112 < K_{sym} < -52$ MeV [141].

Before closing this section, we take the opportunity to address the pressure in neutron matter at saturation density, which, for the EoS of SNM which we have chosen is equal to 0.155 fm^{-3}. Using Equation (17) and the uncertainty on L, we find (in MeV/fm^3):

$$P_0^{NM} = 2.66 \pm \Delta_P \qquad \Delta_P = 0.37 \,. \tag{24}$$

3.3. Symmetry Energy Slope and Neutron Skins

The neutron skin is defined as the difference between the r.m.s. radii of the neutron and proton density distributions:

$$S_n = R_n - R_p \,, \tag{25}$$

where

$$R_i = \sqrt{\frac{1}{T_i} \int_0^\infty \rho_i(r)\, r^2\, d^3r} \,, \tag{26}$$

$i = n, p$ and $T_n,\ T_p = N,\ Z$ respectively.

As mentioned before, the neutron skin thickness, particularly for ^{208}Pb, is of great contemporary interest due to the possibility of constraining the slope of the symmetry energy through skin measurements [24, 142–147].

3.3.1. The Experimental State-of-the-Art

While electron scattering has been very successful in providing accurate information on the proton distributions within the nucleus, mapping neutron densities is a much more challenging task. In particular, measurements which make use of hadronic probes carry large uncertainties due to the model dependence of the nuclear interactions used in the analyses.

On the other hand, parity-violating electron scattering is in principle capable of providing accurate information on the weak charge distribution in the nucleus through the coupling of the neutron to the Z-boson. The typical parity-violating electron scattering experiment measures the difference between the cross sections for scattering of right-handed and left-handed electrons, that is

$$A_{PV} = \frac{\sigma_R - \sigma_L}{\sigma_R + \sigma_L} \,, \tag{27}$$

which is proportional to the ratio of the weak to the charge form factor of the nucleus [110] and thus can be related to coordinate space densities by Fourier transform. The challenging aspects of measuring observables related to parity violation is that they can be etremely small, in the case of A_{PV} between 10^{-4} to 10^{-7} [110].

The first PREX experiment [148, 149] provided a value of 0.33(+0.16, −0.18) fm for the skin of ^{208}Pb, which carries a large experimental error due to technical problems which resulted into poor statistics. However, the planned PREX-II and CREX experiments have a target uncertainty of ±0.06 fm and ±0.02 fm for the neutron skin of ^{208}Pb and ^{48}Ca, respectively [121, 122].

Furthermore, additional constraints are expected from the forthcoming MESA accelerator in Mainz [150], which promises to constraint the neutron skin of ^{208}Pb within ±0.03 fm and the one of ^{48}Ca within ±0.02 fm, same as the target uncertainty of CREX. Note that these two nuclei are both stable, doubly-magic, and with a relatively large neutron to proton asymmetry, which is part of the reasons why investigations have concentrated on them.

For an extensive review of correlation analyses based on a large set of relativistic and non-relativistic nuclear density functionals see [110].

TABLE 5 | Predicted neutron skin of ^{208}Pb and ^{48}Ca.

Nucleus	Order	Λ = 450 MeV (fm)	Λ = 500 MeV (fm)
^{208}Pb	N2LO	0.155 ± 0.005	0.147 ± 0.004
	N3LO	0.150 ± 0.009	0.143 ± 0.004
	N4LO	0.141 ± 0.004	0.139 ± 0.002
^{48}Ca	N2LO	0.150 ± 0.003	0.144 ± 0.002
	N3LO	0.147 ± 0.005	0.142 ± 0.002
	N4LO	0.141 ± 0.003	0.140 ± 0.001

3.3.2. Predictions

We now move to neutron skins, specifically for the ^{208}Pb and ^{48}Ca nuclei, as predicted by the EoS models based on the six chiral interactions in NM as described previously. Using the energy per particle in infinite isospin-asymmetric matter as given in Equation (14), we can establish a simple but direct connection with the energy per nucleon in a spherically symmetric nucleus through the semi-empirical mass formula:

$$E(Z,A) = \int d^3r\, \rho(r)\, e(\rho,\alpha) + \int d^3r\, f_0\, |\nabla\rho|^2 + E_{Coul}\,, \quad (28)$$

where the Coulomb contribution is written as:

$$E_{Coul} = \frac{e^2}{\epsilon_0}\int_0^\infty dr'\,[r'\,\rho_p(r')\int_0^{r'} d^3r\,\rho_p(r)]\,. \quad (29)$$

The parameter f_0 is a fitted constant for which we used a value of 65 MeV fm^5, consistent with the range determined in Oyamatsu et al. [151].

We use the two-parameter Thomas-Fermi distribution function to describe the nucleon density:

$$\rho(r) = \frac{\rho_a}{1+e^{(r-r_b)/c}}\,. \quad (30)$$

The "radius" r_b and the "diffuseness" c are themselves evaluated through minimization of the energy per nucleon, while ρ_a is easily obtained from normalization.

Table 5 shows the values of the neutron skin thickness predictions along with the truncation error for ^{208}Pb and ^{48}Ca. Proceeding as described previously, and taking the largest of the errors at the two cutoff values, we state our final estimates for the neutron skins of ^{208}Pb and ^{48}Ca as

$$S_n(^{208}Pb) = 0.147 \pm \Delta_{S_n} \qquad \Delta_{S_n} = 0.009\,, \quad (31)$$

$$S_n(^{48}Ca) = 0.145 \pm \Delta_{S_n} \qquad \Delta_{S_n} = 0.005\,. \quad (32)$$

Note that the skin depends considerably on the constant f_0 appearing in Equation (28). We have not included that uncertainty in Equations (31–32) as we are focusing on chiral truncation errors. We report, however, that varying f_0 between 60 and 70 MeV fm^5 introduces an uncertainty of 0.01 fm, essentially independent of chiral order or cutoff.

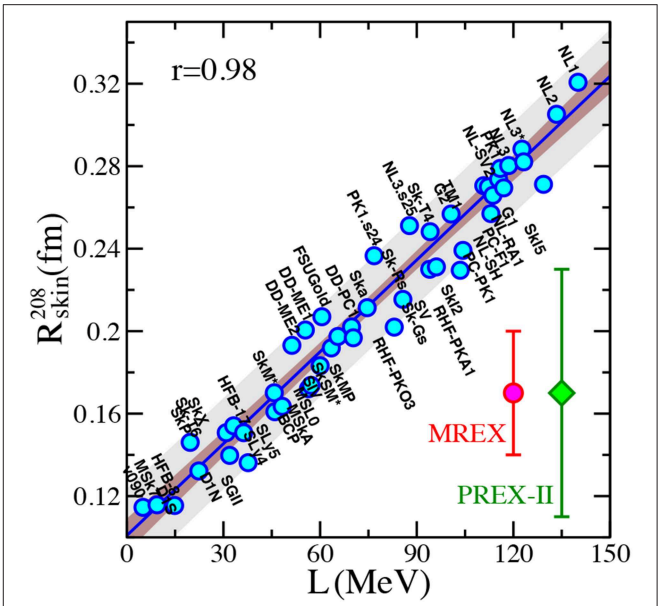


FIGURE 9 | Correlation between the slope parameter (L) and the neutron skin thickness of ^{208}Pb obtained with RMF models. The error bars represent the target precision for the future PREX-II [121] and MREX [150] experiments. Reproduced from Physics Today **72**, 7, 30 (2019) (https://doi.org/10.1063/PT.3.4247) with the permission of the American Institute of Physics.

We close this section by showing in **Figure 9** a typical correlation between L and the thickness of the neutron skin in ^{208}Pb obtained with a large set of successful RMF models. As we discussed previously, the ranges we give in Equations (22) and (31) are relatively small, which is, of course, desirable, since they originate from chiral uncertainties in the NM rather than variations of phenomenological parameterizations. We note that our range of values seem to be located on the low end of the correlation in **Figure 9**, with L approximately between 44 and 58 MeV and the skin between approximately 0.14 and 0.16 fm.

4. THE EQUATION OF STATE AND NEUTRON STARS

4.1. Some General Aspects

It is remarkable that the relation between the mass and the radius of neutron stars is uniquely determined by the EoS together with the star's self-gravity through the Tolman-Oppenheimer-Volkoff (TOV) equations of General Relativity [152]. In fact, although the detailed structure of a neutron star is complex and varies as a function of density, the part of its core mostly composed of a uniform liquid of neutrons, protons, and leptons in β-equilibrium accounts for almost all the mass and the volume. Therefore, these compact systems are intriguing testing grounds for both nuclear physics [153–156] and General Relativity. Extensive effort has been and continue to be devoted to constraining properties of compact stars from astrophysical observations see, for instance [156–160].

The largest possible value for the mass of a neutron star was estimated by Rhoades and Ruffini [161] based on the following assumptions: (1) General Relativity is the appropriate theory of gravitation; (2) the EoS obeys the Le Chatelier's principle ($\partial P/\partial\epsilon \geq 0$) and is consistent with causality, $\partial P/\partial\epsilon \leq c^2$; and (3) the EoS is reliably known below some density. Subject to these conditions, it was determined that the maximum mass of a neutron star cannot exceed 3.2 solar masses. Note that, releasing the causality constraint, the limit can be as high as 5 solar masses [162, 163] due to the increased stiffness of the EoS at supernuclear densities.

While the maximum mass is mostly determined by the stiffness of the EoS at densities greater than a few times saturation density, the star radius is impacted mainly by the slope of the symmetry energy. More precisely, it is closely connected to the internal pressure (that is, the energy gradient) of matter at densities between about $1.5\rho_0$ and $2\text{-}3\rho_0$ [157]. The mass and the radius of the neutron star are predicted by the TOV equation as we review next.

The equations for a perfect fluid in hydrostatic equilibrium allow to determine the pressure and the total mass-energy density as a function of the radial distance from the center of the star. These coupled equations are

$$\frac{dP(r)}{dr} = -\frac{G}{c^2}\frac{(P(r)+\epsilon(r))(M(r)+4\pi r^3 P(r)/c^2)}{r(r-2GM(r)/c^2)}\,, \qquad (33)$$

with

$$\frac{dM(r)}{dr} = 4\pi r^2 \epsilon(r)/c^2\,, \qquad (34)$$

where ϵ is the total mass-energy density. The star *gravitational* mass is

$$M(R) = \int_0^R 4\pi r^2(\epsilon(r)/c^2)dr\,, \qquad (35)$$

with R the value of r where the pressure vanishes. It's worth recalling that no mass limit exists in Newtonian gravitation.

Recently, the LIGO/Virgo [164] detection of gravitational waves originating from two neutron stars spiraling inward and merging, the neutron star merger GW170817, has generated even more interest and excitement around these highly exotic systems.

The dimensionless *tidal deformability* is related to the neutron star response to the tidal field induced by the companion star and is defined as

$$\Lambda = \frac{2}{3}k_2\Big(\frac{R}{M}\Big)^5\,, \qquad (36)$$

where the *Love number* k_2 reflects the quadrupole component of the gravitational potential induced by the companion star at the surface [165]. It depends on the neutron star *compactness*, M/R, and the energy density and pressure profile of the star. The tidal deformability can be obtained by solving the appropriate equations together with the TOV equations which yield the $M(R)$ relation [166]. Hence, the merger detection can provide constraints on the star radius based on the tidal deformabilities of the colliding system [167]. In fact, the August 2017 first direct detection of a binary neutron star merger helped establish new limits on the radius of a 1.4 $M_\odot$ neutron star. Additional references addressing the radius of a 1.4 $M_\odot$ neutron star include [166, 168–172].

The correlation between the neutron skin thickness (discussed in section 3.3) and the radius of a neutron star originates from the sensitivity of the star radius to the *pressure at normal density*. Note that such correlation weakens as the mass increases see, for instance [110], which is why the radii of lighter stars are good candidate to help constrain the neutron skin of ^{208}Pb and, in turn, the slope of the symmetry energy around saturation density. Based on these considerations, an upper limit of 0.25 fm was found for the neutron skin thickness of ^{208}Pb. Additional observations from the LIGO-Virgo collaboration scheduled for 2019 are likely to provide stronger constraints.

In the remainder of this section, after reviewing how the EoS of β-stable matter is obtained from conditions of charge neutrality and energy minimization (section 4.2), we will address (spherical) neutron star properties, with emphasis on the radius of a "typical" neutron star, namely one with a mass approximately equal to 1.4 $M_\odot$. The reasons for this choice have been given in the previous paragraph.

4.2. The EoS of β-Stable Matter

In this section, we review the basic equations which we use to obtain the EoS for stellar matter in β-equilibrium.

The total energy per particle, e_{tot}, related to the total energy density, ϵ_{tot}, by $e_{tot} = \epsilon_{tot}/\rho$, for neutrons and protons in β equilibrium with leptons (electrons and muons) is given by:

$$e_{tot} = e_0 + e_{sym}(Y_n - Y_p)^2 + \sum_{i=n,p} Y_i m_i + e_e + e_\mu\,, \qquad (37)$$

where Y_i, $i = n(p)$, stands for the neutron(proton) fraction. On the right-hand side are the baryon contributions including their rest energies (first three terms), and the relativistic electron and the muon energies per baryon (last two terms). Note that, in the equation above, e_0 and e_{sym} are the EoS of symmetric nuclear matter and the symmetry energy, respectively. All terms are functions of density.

The relativistic energy density for particle species "i" having Fermi momentum $(k_F)_i$ is given by

$$\epsilon_i = \frac{\gamma}{2\pi^2}\int_0^{(k_F)_i}\sqrt{k^2+m_i^2}\,k^2\,dk\,, \qquad (38)$$

where γ is an appropriate degeneracy factor. The partial densities are related to the respective Fermi momenta as

$$\rho_i = \frac{\gamma}{2\pi^2}\int_0^{(k_F)_i} k^2\,dk\,, \qquad (39)$$

which gives, for spin-$\frac{1}{2}$ fermions (γ=2),

$$\rho_i = \frac{(k_F)_i^3}{3\pi^2}\,, \qquad (40)$$

with the corresponding particle fractions given by

$$Y_i = \frac{\rho_i}{\rho} \,. \tag{41}$$

The chemical potential for species "i" is defined as

$$\mu_i = \frac{\partial \epsilon_i}{\partial \rho_i} = \frac{\partial \epsilon_i}{\partial (k_F)_i} \frac{\partial (k_F)_i}{\partial \rho_i} = \sqrt{(k_F)_i^2 + m_i^2} \,, \tag{42}$$

where we have used Equations (38–39) to perform the derivatives with respect to the upper integration limit.

The standard procedure is to minimize the total energy per particle with the constraints of fixed baryon density and global charge neutrality:

$$\rho_p + \rho_n = \rho \;\Rightarrow\; Y_p + Y_n = 1 \tag{43}$$

and

$$\rho_p = \rho_e + \rho_\mu \;\Rightarrow\; Y_p = Y_e + Y_\mu \,. \tag{44}$$

The resulting set of equations allow to solve for the various lepton fractions from which one can easily obtain the corresponding energy densities.

For the purpose of applying the Lagrange multipliers method, we define the functional

$$F = e_{tot} + \lambda_1 \eta_1 + \lambda_2 \eta_2 \,, \tag{45}$$

where

$$\eta_1 = 1 - Y_n - Y_p \tag{46}$$

and

$$\eta_2 = Y_p - Y_e - Y_\mu \,, \tag{47}$$

and set

$$\frac{\partial F}{\partial Y_i} = 0 \,. \tag{48}$$

Equations (45–48) then yield

$$\frac{\partial F}{\partial Y_p} = \frac{\partial e_{tot}}{\partial Y_p} - \lambda_1 + \lambda_2 = 0 \;\Rightarrow \mu_p = \lambda_1 - \lambda_2 \tag{49}$$

$$\frac{\partial F}{\partial Y_n} = \frac{\partial e_{tot}}{\partial Y_n} - \lambda_1 = 0 \;\Rightarrow \mu_n = \lambda_1 \tag{50}$$

$$\frac{\partial F}{\partial Y_e} = \frac{\partial e_{tot}}{\partial Y_e} - \lambda_2 = 0 \;\Rightarrow \mu_e = \lambda_2 \tag{51}$$

$$\frac{\partial F}{\partial Y_\mu} = \frac{\partial e}{\partial Y_\mu} - \lambda_2 = 0 \;\Rightarrow \mu_\mu = \lambda_2 \,. \tag{52}$$

Thus,

$$\mu_\mu = \mu_e \tag{53}$$

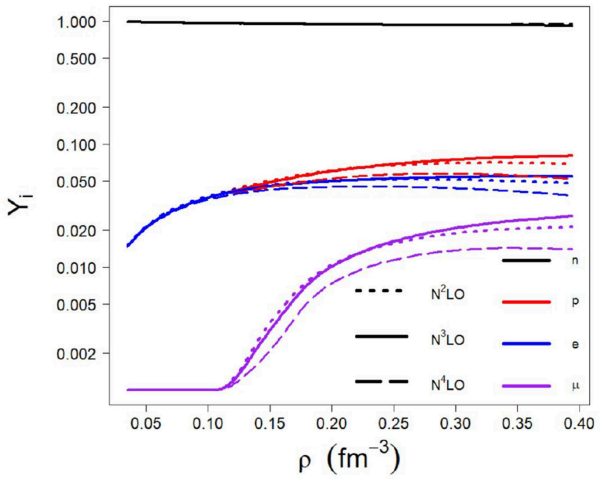


FIGURE 10 | Fractions of neutrons, protons, electrons, and muons as a function of density at the indicated orders for Λ = 450 MeV.

and

$$\mu_p = \mu_n - \mu_e \,. \tag{54}$$

The equations above allow to solve for the various lepton fractions and, through Equation (38), the corresponding energies are easily obtained. For electrons, we find the ultra-relativistic approximation to be appropriate and set their rest energy to zero in Equation (38).

In **Figure 10**, we show the predicted fractions for the various species (neutrons, protons, and leptons) at the three highest orders of χEFT which we consider. We note that the proton fraction goes up to just above 10% at the highest densities being considered. This is a rather low value, most likely related to the relatively soft nature of the symmetry energy displayed in **Figure 8**. It implies that neutron stars (with central densities up to those included in the figure) will not cool down *via* direct Urca processes.

One is now in the position to calculate the pressure in β-stable matter. The pressure is related to the energy density through

$$P(\rho) = \rho^2 \frac{d(e_{tot})}{d\rho} \,. \tag{55}$$

In order to continue the discussion started in section 3.2 and extend it to neutron star radii in a consistent manner, in this section we will use the same interactions constructed in section 3 in terms of an empirical SNM EoS and the microscopic NM chiral EoS. Note, from section 4.2, that the symmetry energy, and thus the EoS of both SNM and NM are needed to obtain the various particle fractions. As mentioned earlier, those fractions tend to be rather small (see **Figure 10**), and thus the results shown in this and the next sections are to a large extent determined by our chiral predictions in NM.

We close this section by showing in **Figure 11** the calculated pressure in β-stable matter at the third, fourth, and fifth orders

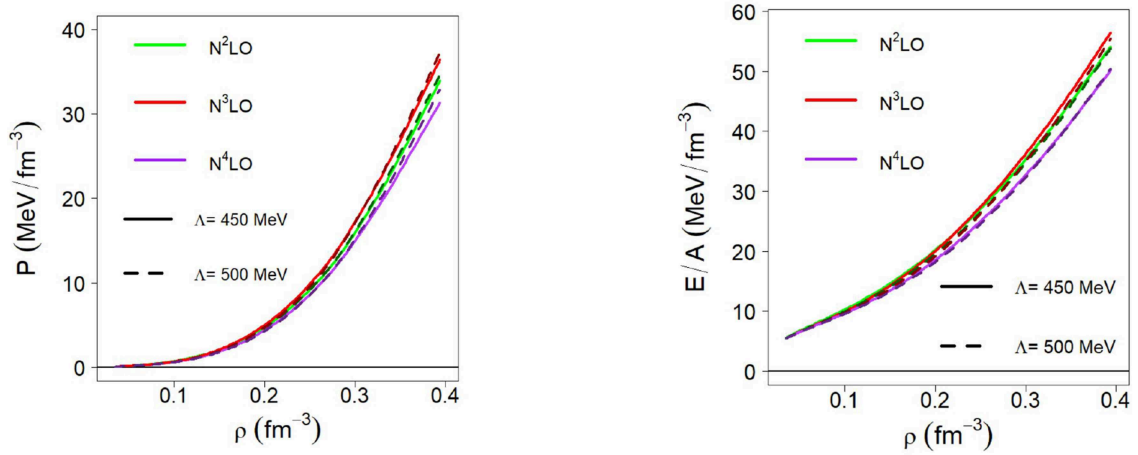


FIGURE 11 | (Left) pressure in β-equilibrated matter *vs.* density at the given chiral orders (of the NM chiral EoS). Predictions with both cutoffs are shown, revealing that the two sets of curves are very similar. **(Right)** the corresponding energy per particle. These are the predictions which we retain up to $2\rho_0$.

of the 2NF together with the 3NF constructed as described in section 2.2.2. Of course we are referring to the chiral 3NF appropriate for NM, where the LECs c_4, c_D, and c_E vanish [56].

The BHF approach to nuclear matter is appropriate for the description of homogeneous matter, such as a homogeneous fluid of nucleons. Below nuclear densities, the chiral EoS are joined with the crustal equations of state from Harrison and Wheeler [173] and Negele and Vautherin [174], performing a smooth interpolation between the two EoS. The crust has crystal-like composition, and contains light [173] or heavy [174] metals together with a gas of electrons.

4.3. Predicting Neutron Star Masses and Radii

We now proceed to discuss specifically neutron star predictions. As mentioned above, we will focus on the radius of a star with mass equal to 1.4 $M_\odot$. We note, in passing, that the increased population of neutron stars observed around the mass range of 1.4 $M_\odot$ may be related to the physics of white dwarfs, atomic stars supported by electron (rather than neutron) degeneracy pressure. Since the Chandrasekhar limit of white dwarfs is approximately 1.4 $M_\odot$ [175], their collapse is likely to generate neutron stars in that mass range.

As stated in section 1, χEFT is a low-energy theory and thus limitations to its domain of applicability must be carefully considered. To begin with, the chiral symmetry breaking scale, $\Lambda_\chi \approx 1$ GeV, imposes clear limitations on the momentum or energy ranges where pions and nucleons can be taken as suitable degrees of freedom [15, 17]. Furthermore, the cutoff parameter Λ appearing in the regulator function (cf. Equation 10), has the purpose to remove high momentum components. Naturally, the strength of the cutoff determines to which degree such high-momentum components are suppressed. On the other hand, central densities of compact astrophysical systems can reach as high as several times the density of normal saturated matter, resulting, of course, in the presence of Fermi momenta which are beyond the reach of χEFT. Therefore, if one wishes to make predictions based, to some extent, on χEFT, methods to extend those predictions must be devised.

It has been observed that the pressure as a function of baryon density (or mass density) for a very large number of existing EoS can be fitted by piecewise polytropes, namely functions of the form $P(\rho) = \alpha\rho^\Gamma$ [176]. (Note that, in our definitions, ρ denotes the baryon density). Guided by this observation, we find it reasonable to extrapolate the pressure predictions obtained from the EoS shown in **Figure 11** using polytropes, as we have done in Sammarruca and Millerson [123]. More precisely, we employ our semi-microscopic predictions up to about $2\rho_0$, where ρ_0 is defined to be 0.16 fm^{-3}, approximately the density of saturated matter. The reason for choosing $2\rho_0$ as a matching density is as follows: since we are dealing with a perturbative expansion in the parameter Q/Λ, we base our arguments on the size of the expansion parameter for typical momenta of the system under consideration. The highest momentum for pure neutron matter around twice normal density is approximately 420 MeV, as obtained from the usual relation $\rho = \frac{k_{F,n}^3}{3\pi^2}$, with $k_{F,n}$ the neutron Fermi momentum. And of course, the highest momentum in β-stable matter is slightly lower due to the presence of a small proton fraction. In conclusion, we are still below (although getting close to) $\Lambda \sim 450 - 500$ MeV. Furthermore, the *r.m.s.* value of the relative momentum for two nucleons in infinite matter is lower than their maximum momentum, and in fact it can be estimated to be about 60% of the Fermi momentum [177]. Thus, on statistical grounds, we should be safe from "cutoff artifacts," even in the presence of smooth regulators.

We then proceed to match polytropes with diverse adiabatic indices, preserving continuity of the pressure. The range of the polytropic index was taken to be between 1.5 and 4.5 [123] (based on guidelines from the literature [176]), and these extensions are calculated up to about $3\rho_0$. At this density, every polytrope is again joined continuously with another set of polytropes spanning the same range in values of Γ. In this way, we

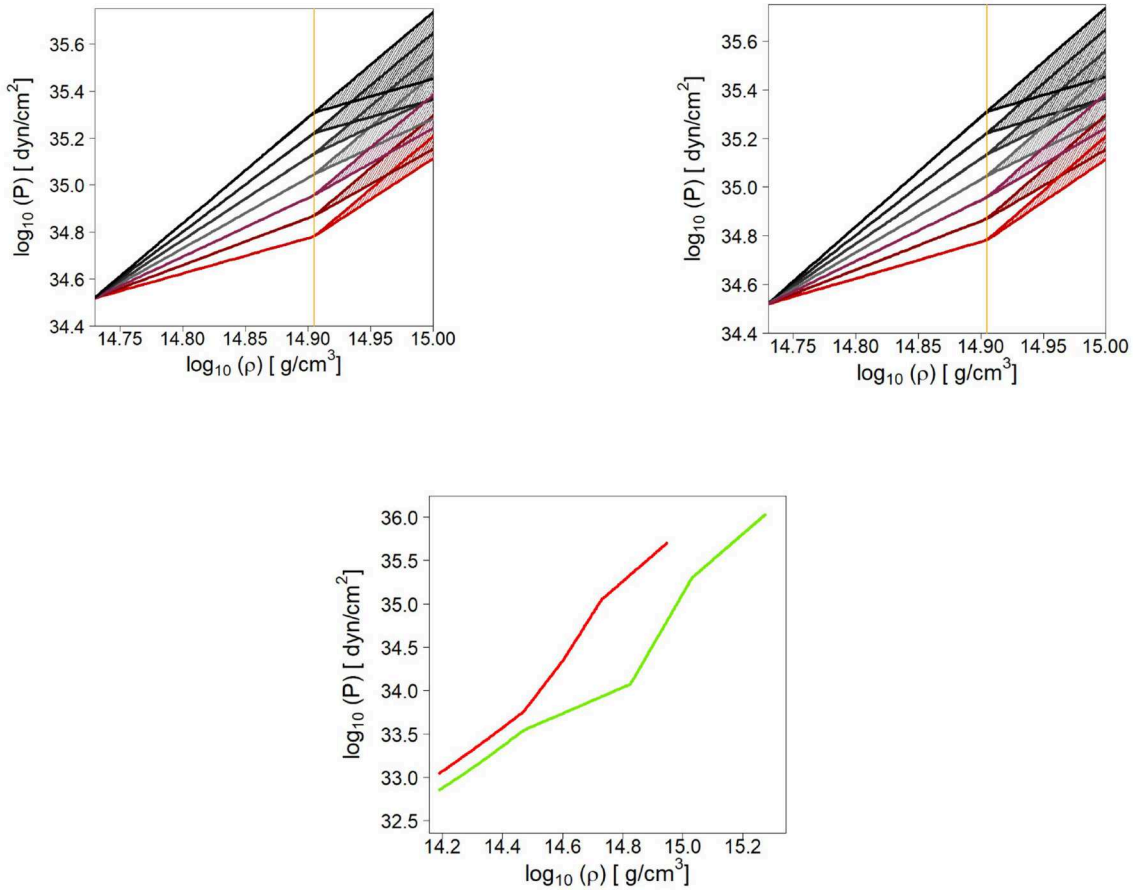


FIGURE 12 | (Top) Pressure in β-equilibrated matter *vs.* density at N^{3}LO for Λ=450 MeV (left) and Λ=500 MeV (right) extended with polytropes as explained in the text. The vertical axis and the vertical yellow line mark the two matching densities (see text for details). **(Bottom)** Vaues of the pressure as a function of density taken from Table 5 of Hebeler et al. [178]. The lower (higher) values correspond to the "soft" ("stiff") predictions shown in that table.

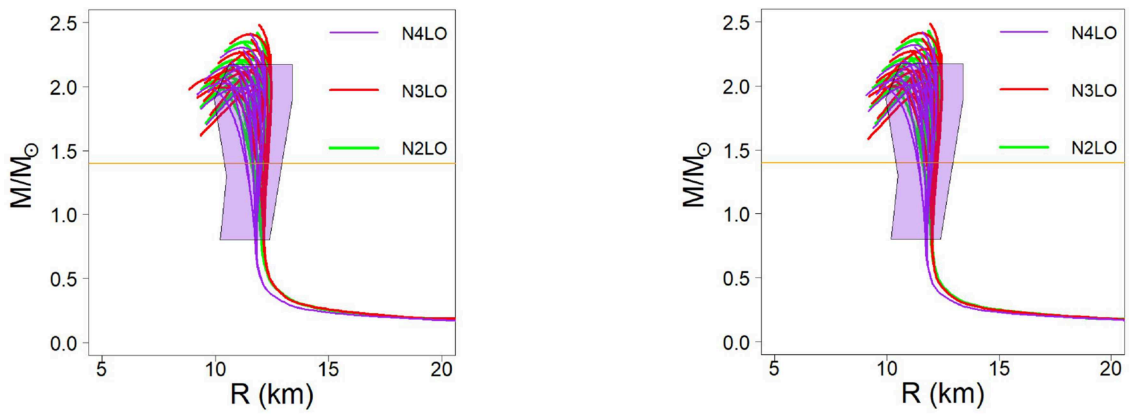


FIGURE 13 | The mass vs. radius relation at the given chiral order. **(Left)** Λ=450 MeV; **(Right)** Λ=500 MeV. The purple curves are the result of extending the predictions at N^{4}LO, while the red and the green curves are obtained extrapolating the predictions at N^{3}LO and at N^{2}LO, respectively. The horizontal yellow lines marks the value of 1.4 $M_\odot$. The shaded area in the background is the constraint taken from Steiner et al. [159].

are able to cover a large set of possible EoS continuations, simulating scenarios where the EoS displays different degrees of "softness" or "stiffness" in different density regions, and thus we can estimate a realistic uncertainty. We stress again that this procedure is a way to simulate the uncertainty arising from reasonable parameterizations of the EoS as determined

by phenomenological studies in the literature, and is not to be understood as a replacement for a theoretical model. A demonstration of this procedure is shown in **Figure 12** (top row) for the case of N^{3}LO with Λ = 450 MeV. (Note that cgs units are adopted in **Figure 12** as those are popular in astronomy and may facilitate comparison by other authors).

In Hebeler et al. [178], the β-equilibrated EoS based on microscopic chiral interactions in neutron matter, is extended to high densities employing a general piecewise polytropic extrapolation, which leads to a very large number of EoS. Applying causality and the requirement that the EoS must be able to support a mass of 1.97 $M_\odot$, the author select a range of possible EoS, ranging from "soft" to "stiff." We show the resulting uncertainty band in the bottom row of **Figure 12**, noting that our uncertainty band from **Figure 12** is consistent with it.

Having built up the EoS at all needed densities, we are now in the position to solve the TOV [152] star structure equations and obtain the mass as a function of the radius for a sequence of stars differing in their central densities, up to several times normal density. The $M(R)$ relations we obtain are shown on the bottom row of **Figure 13**. Note that only combinations of polytropic indices which can support a maximum mass of at least 1.97 $M_\odot$ have been retained for the purpose of **Figure 13**, to account for the observation of a pulsar with a mass of 2.01 $\pm$ 0.04 $M_\odot$ [179]. It is appropriate to point out here that most recent observations [180] are consistent with the even higher value of 2.14 $M_\odot$. In future work, we will apply this new constraint, which will result in a more limited set of acceptable EoS.

The causality constraint imposes limitations and those are applied in **Figure 13**. That is, one must require that the speed of sound in stellar matter is less than the speed of light, a condition which can be expressed as $\frac{dP}{d\epsilon} < 1$, where ϵ is the total energy density.

Table 6 shows the the radius and the central density of the 1.4 $M_\odot$ neutron star when the pressure curves at the fourth and fifth orders from **Figure 11** are extrapolated *via* piecewise polytropes with adiabatic indices Γ_1 and Γ_2 as shown. The speed of sound at central density is also included. Confirming what we found in Sammarruca and Millerson [123], **Table 6** demonstrates quite clearly that the radius is practically insensitive to how the continuation is done. In particular, no changes are observed due to variations of the polytrope attached at $3\rho_0$, and changes by less that one kilometer occurr in response to varying the first polytropic index. Note that the central densities we predict for the canonical-mass star are typically in the order of, and can exceed $3\rho_0$. These densities are at or above those where the spreading of the pressure can be quite large (see **Figure 12**). Evidently, the radius of a star with this kind of mass responds to pressures at much lower than central densities, in line with earlier observations (see, for instance [178, 181]), where the insensitivity of the radius to the higher densities was pointed out. Tables similar to **Table 6** with Λ=500 MeV and at N^{4}LO with changing value of Λ are not included but do lead to very similar observations.

At the same time, the very small spreading of the pressure at normal to moderately high densities (see **Figure 11**), would suggest similarity of the radius in all cases (differing in chiral order and/or cutoff). This is in fact the case. Taking into consideration both the truncation error and the uncertainty from the polytropes, one may state, estimating the error pessimistically, that $R_{N^3LO} \approx 11.8 \pm 1$ km for M=1.4$M_\odot$.

For completeness, in **Figure 13** the full $M(R)$ relation is also displayed. However, we stress that, at the high central densities probed by the heaviest stars, it is not possible to make reliable statements at this time. Predictions are no longer constrained by the chiral theory and are mostly phenomenology.

TABLE 6 | Adiabatic indices, Γ_1 and Γ_2, of the polytropes attached at the two matching densities, followed by the radius and the central density of the 1.4 $M_\odot$ neutron star.

Γ_1	Γ_2	R (km)	ρ (fm^{-3})	$v_s(c)$
1.5	3.5	11.19	0.653	0.718
1.5	4.0	11.28	0.615	0.767
1.5	4.5	11.34	0.589	0.813
2.0	3.0	11.49	0.620	0.642
2.0	3.5	11.56	0.585	0.695
2.0	4.0	11.60	0.564	0.741
2.0	4.5	11.62	0.548	0.786
2.5	3.0	11.83	0.543	0.621
2.5	3.5	11.84	0.529	0.677
2.5	4.0	11.85	0.521	0.734
2.5	4.5	11.86	0.514	0.789
3.0	2.5	12.05	0.488	0.555
3.0	3.0	12.06	0.485	0.615
3.0	3.5	12.06	0.482	0.671
3.0	4.0	12.05	0.479	0.721
3.0	4.5	12.06	0.478	0.766
3.5	1.5	12.19	0.445	0.650
3.5	2.0	12.19	0.445	0.653
3.5	2.5	12.18	0.444	0.660
3.5	3.0	12.18	0.444	0.673
3.5	3.5	12.18	0.444	0.665
3.5	4.0	12.18	0.444	0.671
3.5	4.5	12.18	0.444	0.676
4.0	1.5	12.27	0.420	0.759
4.0	2.0	12.27	0.420	0.744
4.0	2.5	12.27	0.420	0.734
4.0	3.0	12.27	0.419	0.731
4.0	3.5	12.27	0.420	0.726
4.0	4.0	12.27	0.420	0.710
4.0	4.5	12.27	0.420	0.699
4.5	1.5	12.32	0.404	0.792
4.5	2.0	12.32	0.404	0.781
4.5	2.5	12.32	0.403	0.775
4.5	3.0	12.32	0.403	0.772
4.5	3.5	12.32	0.403	0.772
4.5	4.0	12.32	0.403	0.766
4.5	4.5	12.32	0.404	0.750

The speed of sound is also shown, in units of the speed of light. The microscopic part of the NM predictions are obtained at N^{3}LO with Λ=450 MeV.

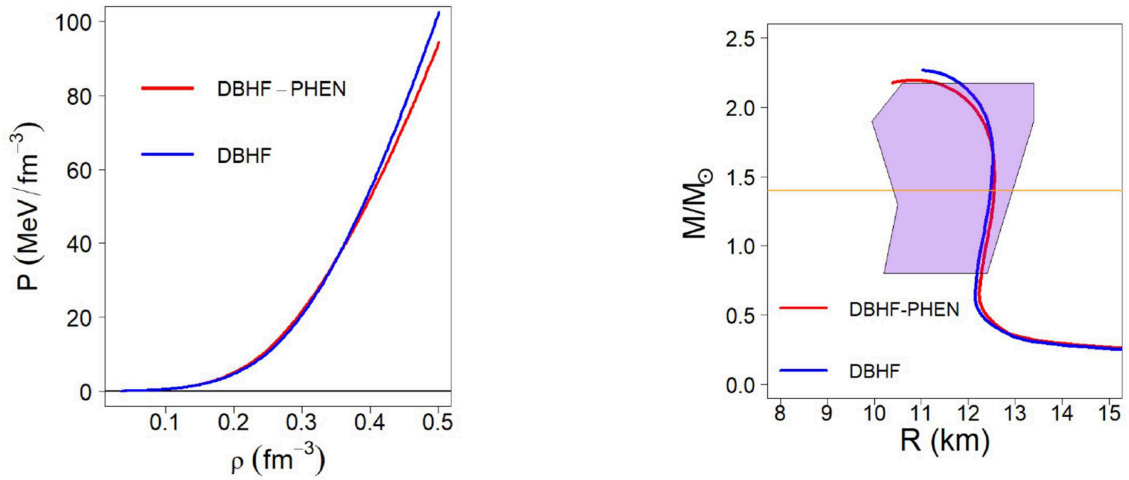


FIGURE 14 | (Left) Pressure in β-stable matter as a function of density obtained with the Bonn B meson-exchange potential and the DBHF approach to nuclear and neutron matter. The blue and the red curves are obtained using the phenomenological EoS for SNM or the microscopic one, respectively. **(Right)** The mass *vs.* radius relation for a neutron star obtained with the DBHF calculations as explained in the text. As before, the lavender shaded area is the constraint from Steiner et al. [159].

To broaden the scopes of this discussion, we will include next a set of predictions obtained in a more "traditional" way rather than with χEFT. In particular, we will use a meson-exchange potential (the Bonn B potential [86]) and the DBHF approach mentioned in the Introduction and used extensively in the past by one of the authors of this review [14]. We recall that the characteristic feature of the DBHF method is its ability to effectively take into account an important class of 3NF generated by the so-called "nucleon-antinucleon Z-diagrams" (see [14] and references therein).

However, one of the problems with the traditional approaches based either on meson-theoretic potentials (such as Bonn B or CD-Bonn [29]) or entirely phenomenological ones (such as AV18 [31]), is the absence of guidelines to select the 3NF contributions to be included (among the infinitely many possibilities). Typically, a particular diagram or set of 3NF diagrams are chosen to accompany the 2NF, but no well-defined link exists between the 2NF and the associated 3NF. On the other hand, the chiral approach, through the order-by-order scheme, prescribes exactly which 2NF, 3NF, and higher-body force must be retained at each order.

In **Figure 14**, we show the pressure in β-stable matter from the DBHF EoS. Comparison between the blue and the red curves demonstrate that choosing a phenomenological SNM EoS (red curve) as compared to the microscopic one (blue curve) has only a minor impact on the EoS for β-stable matter (which is comprised mostly of neutrons), particularly from low to medium densities.

We then proceed to compare the pressure predictions based on the meson-exchange model with the predictions from **Figure 11**. As to be expected, differences become larger with increasing density, with the chiral EoS being substantially softer at the higher densities.

Once again, we place our focus on the radius of the average-mass star, which we find to be approximately equal to 12.5 km for the DBHF calculations. This value is reasonably close to our previous, chirally based predictions, which makes sense based on our earlier discussions and the fact that the DBHF pressure around normal density is not very different from the one in the chirally-based models (see **Figure 15**).

Finally, we employ the DBHF EoS in the TOV equations and calculate the $M(R)$ relation, which is shown on the RHS of **Figure 14**. The blue and red curves correspond to the blue and red curves in **Figure 14**. Differences become noticible for the heavier stars and are consistent with those seen in **Figure 14**. In other words, the model with the larger pressure at the higher densities generates the larger maximum mass.

We end this exercise with an important comment: even if a theory (of nucleons and mesons) can be formally taken to high densities, as we have done with the DBHF predictions, the composition and thus the EoS of stellar matter in the inner core is simply unknown. At densities as high as those typical of compact stars, hyperons are expected to exist on simple energetic grounds. Similarly, other non-nucleonic degrees of freedom, such as quark degrees of freedom, can exist as the result of phase transitions. These possibilities have been explored by several groups (see, for instance [182–185]). Such investigations are not within the scope or the reach of χEFT. The polytropic extrapolations we have performed do indeed simulate a broad set of possible EoS consistent with current constraints but whose specific composition remains unknown.

Of course, we also take note of some other works aimed at incorporating aspects of chiral dynamics in the development of EoS suitable for astrophysical phenomena, such as Rapaj et al. [186]. In the latter reference, the authors calculate neutron star masses and radii with mean-field models whose parameters are made consistent with a chiral EoS at low to

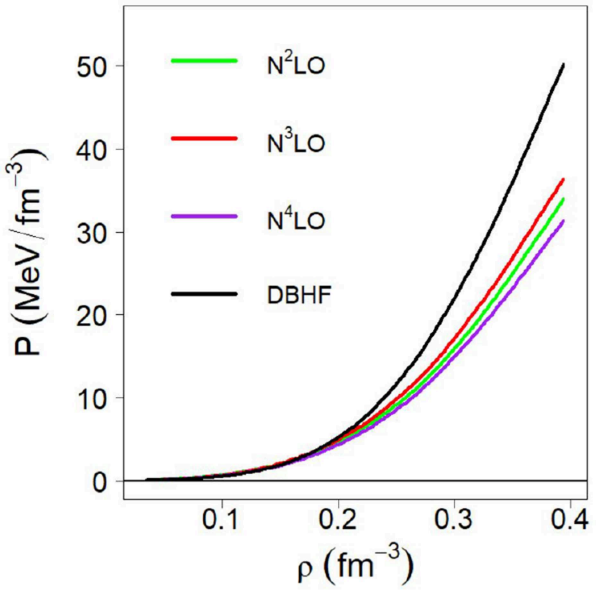


FIGURE 15 | Pressure in β-stable matter from the red curve on the LHS of **Figure 14** compared with the predictions from the LHS of **Figure 11**.

moderate densities. Constraints from χEFT on neutron star tidal deformabilities were investigated in Lim and Holt [166]. General relativistic simulations of neutron star mergers based on the EoS of Bombaci and Logoteta [111] have been reported in Endrizzi et al. [187].

We close this section with a few final remarks addressing predictions *vs.* constraints. Masses of neutron stars can be and have been measured with high precision. However, simultaneous measurements of radii are much more problematic. Some techniques do exist, such as those based on photospheric radius expansion [188]. Current observations have begun to determine the $M(R)$ relation. In Steiner et al. [159], the authors determine the radius of a 1.4 $M_\odot$ neutron star to be between 10.4 and 12.9 km. Furthermore, from their Bayesian analysis of several EoS parameterized so as to be consistent with a baseline data set (see [159] and references therein), they are able to determine the $M(R)$ relation within a range of masses. Our predictions fall within those constraints, shown in **Figure 13** as the shaded purple area. Recent LIGO/Virgo measurements have constrained the radius of a 1.4 $M_\odot$ neutron star to be between 11.1 and 13.4 km [164, 167]. The predictions from our group are well within these new constraints.

5. SUMMARY AND CONCLUSIONS

In this review, we have stressed the importance of the nuclear EoS toward understanding of nuclear interactions in the medium. First, we presented a detailed review of our most recent EoS based on state-of-the-art chiral *NN* potentials. We operate within the framework of chiral effective field theory. Our approach is microscopic in that chiral two-nucleon forces are fitted to two-nucleon data and never readjusted in the medium. To render the nuclear matter calculations manageable, the leading chiral 3NF is included as an effectively two-body density-dependent potential. The relevant LECs, c_D and c_E, are obtained from accurate fittings within the three-nucleon sector. Actually, we go beyond the leading 3NF by effectively including the 2PE 3NF up to the highest order we consider at this time. This is possible because the 2PE 3NF has essentially the same analytical structure at N^{2}LO, N^{3}LO, and N^{4}LO. Thus, one can add the three orders of 3NF contributions and parameterize the result in terms of effective LECs.

The contribution from the 3NF is remarkable, although somewhat weaker in NM, due to the fact that some of the leading 3NF contributions vanish in a system of only neutrons. Therefore, the lack of full order consistency between the 2NF and the 3NF sectors is likely to impact the EoS of NM to a lesser degree as compared to the the case of SNM. In fact, we find that the NM EoS is under better control with regard to the order-by-order pattern.

In view of the considerations above, in discussions of some observables sensitive to the EoS of neutron-rich matter, we have chosen to emphasize the role of the NM EoS by constraining the SNM EoS to be an empirical one. This allowed us to better scrutinize the role of neutron matter pressure on the neutron skin thickness.

A contemporary discussion of neutron-rich matter must include some of the most exotic and intriguing (neutron-rich) systems in the universe—neutron stars. We reviewed the outstanding role of the EoS in calculations of neutron star structure.

We discussed the limitations of χEFT as a low-energy theory. The high Fermi momenta involved in the core of neutron stars cannot be probed with χEFT. This is also the case for average-mass stars, where typical central densities can be as high as three times normal nuclear density. Therefore, we extend our EoS to high densities *via* polytropes with a broad range of adiabatic indices.

Although extrapolation with polytropes, or any other continuation method one may choose, should in no way be seen as a replacement for true predictions, it gave us the opportunity to explore the sensitivity of specific predictions to the behavior of the EoS at the high densities unreachable to χEFT. In fact, we were able to confirm what has been observed previously with other methods. Namely, the radius of the typical-mass neutron star is essentially insensitive to the pressure in the high-density regime. Instead, it is mostly controlled by the pressure in NM at normal densities. Therefore, we feel confident that our χEFT-based predictions of neutron-rich matter are on solid ground for lighter stars, including those with the "canonical" mass of 1.4 $M_\odot$.

At this point, to broaden the scopes of the discussion, we included a set of predictions based on a very different, and more traditional philosophy. We calculated the NM EoS from the Bonn B meson-theoretic potential and the DBHF approach to neutron matter. The purpose of this comparison

was, mostly, to highlight the different philosophy of the "single-shot" calculation as compared to the chiral approach, where order-by-order and other uncertainty considerations play a major role in the extraction and interpretation of the result.

In line with the observed sensitivity of the radius to, mainly, the pressure in NM at normal density, and the fact that the meson-theoretic and the chiral EoS are similar up to moderate densities, the value we obtained for the radius of the $M = 1.4M\odot$ neutron star was close to those from the chirally-based calculations.

Of course, the complete chiral 3NF at N^{3}LO must be included, as done in Drischler et al. [93]. Our approach to fitting the c_D and c_E LECs is different, as the authors of Drischler et al. [93] include nuclear matter saturation properties in their fitting protocol, whereas we fit those constants within the three-nucleon sector. We are presently calculating the various contributions of the 3NF at N^{3}LO in the form of density-dependent effective interactions [97, 98] and noticed that the short-range terms [97] tend to be very small. It will be interesting to see how the full contribution impacts our calculations of the NM EoS and related observables.

AUTHOR CONTRIBUTIONS

As the senior member of the team, FS coordinated the conceptual design and development of the paper. Both authors contributed to the production of the results being shown.

FUNDING

This work was supported by the U.S. Department of Energy, Office of Science, Office of Basic Energy Sciences, under Award Number DE-FG02-03ER41270.

ACKNOWLEDGMENTS

FS wishes to acknowledge L. E. Marcucci, L. Coraggio, J. W. Holt, N. Itaco, and R. Machleidt, for their contributions to the development of the equations of state reviewed in this article.

REFERENCES

1. Brueckner KA, Levinson CA, Mahmoud HM. Two-body forces and nuclear saturation. I. Central forces. *Phys Rev.* (1954) **95**:217–28. doi: 10.1103/PhysRev.95.217
2. Bethe HA. Nuclear many-body problem. *Phys Rev.* (1956) **103**:1353–90. doi: 10.1063/1.2915762
3. Goldstone J. Derivation of the Brueckner many-body theory. *Proc R Soc.* (1957) **A239**:267–79. doi: 10.1098/rspa.1957.0037
4. Bethe HA. Theory of nuclear matter. *Annu Rev Nucl Sci.* (1971) **21**:93–214. doi: 10.1146/annurev.ns.21.120171.000521
5. Haftel MI, Tabakin F. Nuclear saturation and the smoothness of nucleon-nucleon potentials. *Nucl Phys.* (1970) **A158**:1–42. doi: 10.1016/0375-9474(70)90047-3
6. Sprung DWL. Nuclear matter calculations. *Adv Nucl Phys.* (1972) **5**:225–343. doi: 10.1007/978-1-4615-8231-1_2
7. Pandharipande VR, Wiringa RB. Variations on a theme of nuclear matter. *Rev Mod Phys.* (1979) **51**:821–59. doi: 10.1103/RevModPhys.51.821
8. Lagaris IE, Pandharipande VR. Variational calculations of realistic models of nuclear matter. *Nucl Phys.* (1981) **A359**:349–64. doi: 10.1016/0375-9474(81)90241-4
9. Day BD, Wiringa RB. Brueckner-Bethe and variational calculations of nuclear matter. *Phys Rev C.* (1985) **32**:1057–62. doi: 10.1103/PhysRevC.32.1057
10. Anastasio MR, Celenza LS, Pong WS, Shakin CM. Relativistic nuclear structure physics. *Phys Rep.* (1983) **100**:327–92. doi: 10.1016/0370-1573(83)90060-1
11. Horowitz CJ, Serot BD. Two-nucleon correlations in a relativistic theory of nuclear matter. *Phys Lett.* (1984) **137B**:287–93. The relativistic two-nucleon problem in nuclear matter, Nucl. Phys. **A464**, 613-699 (1987).
12. Brockmann R, Machleidt R. Nuclear saturation in a relativistic Bruckner-hartree-fock Approach. *Phys Lett.* (1984) **149B**:283–7.
13. Brockmann R, Machleidt R. Relativistic nuclear structure. I: Nuclear matter. *Phys Rev C.* (1990) **42**:1965.
14. Muether H, Sammarruca F, Ma Z. Relativistic effects and three-nucleon forces in nuclear matter and nuclei. *Int J Mod Phys E.* (2017) **26**:1730001. doi: 10.1142/S0218301317300016
15. Weinberg S. Nuclear forces from chiral Lagrangians. *Phys Lett B.* (1990) **251**:288–92. doi: 10.1016/0370-2693(90)90938-3
16. Weinberg S. Effective chiral lagrangians for nucleon-pion interactions and nuclear forces. *Nucl Phys B.* (1991) **363**:3–18. doi: 10.1016/0550-3213(91)90231-L
17. Weinberg S. Three-body interactions among nucleons and pions. *Phys Lett B.* (1992) **295**:114–21. doi: 10.1016/0370-2693(92)90099-P
18. Machleidt R, Entem DR. Chiral effective field theory and nuclear force. *Phys Rep.* (2011) **503**:1–75. doi: 10.1016/j.physrep.2011.02.001
19. Weinberg S. Phenomenological lagrangians. *Physica.* (1979) **96A**:327–40.
20. Epelbaum E. Hammer HW, Meissner UG. Modern theory of nuclear forces. *Rev Mod Phys.* (2009) **81**:1773–825. doi: 10.1103/RevModPhys.81.1773
21. Meißner UG. The long and winding road from chiral effective Lagrangians to nuclear structure. *Phys Scr.* (2016) **91**:033005. doi: 10.1088/0031-8949/91/3/033005
22. Machleidt R, Sammarruca F. Chiral EFT based nuclear forces: achievements and challenges. *Phys Scr.* (2016) **91**:083007. doi: 10.1088/0031-8949/91/8/083007
23. Fattoyev FJ, Piekarewicz J. Accurate calibration of relativistic mean-field models: correlating observables and providing meaningful theoretical uncertainties. *Phys Rev C.* (2011) **84**:064302. doi: 10.1103/PhysRevC.84.064302
24. Roca-Maza X, Centelles M, Viñas X, Warda M. Neutron skin of ^{208}Pb, nuclear symmetry energy, and the parity radius experiment. *Phys Rev Lett.* (2011) **106**:252501. doi: 10.1103/PhysRevLett.106.252501
25. Sammarruca F, Marcucci LE, Coraggio L, Holt JW, Itaco N, Machleidt R. Nuclear and neutron matter equations of state from high-quality potentials up to fifth order of the chiral expansion. *arXiv:1807.06640* (2018).
26. Sammarruca F. Short-range correlations in the deuteron: chiral effective field theory, meson-exchange, and phenomenology. *Phys Rev C.* (2015) **92**:044003. doi: 10.1103/PhysRevC.92.044003
27. Hen O, Miller GA, Piasetzky E, Weinstein LB. Nucleon-nucleon correlations, short-lived excitations, and the quarks within. *Rev Mod Phys.* (2017) **89**:045002. doi: 10.1103/RevModPhys.89.045002
28. Marcucci LE, Sammarruca F, Viviani M, Machleidt R. Momentum distributions and short-range correlations in the deuteron and

^{3}He with modern chiral potentials. *Phys Rev C.* (2019) **99**:034003. doi: 10.1103/PhysRevC.99.034003

29. Machleidt R. High-precision, charge-dependent Bonn nucleon-nucleon potential. *Phys Rev C.* (2001) **63**:024001. doi: 10.1103/PhysRevC.63.024001
30. Stoks VGJ, Klomp RAM, Terheggen CPF, de Swart JJ. Construction of high-quality NN potential models. *Phys Rev C.* (1994) **49**:2950–63. doi: 10.1103/PhysRevC.49.2950
31. Wiringa RB, Stoks VGJ, Schiavilla R. Accurate nucleon-nucleon potential with charge-independence breaking. *Phys Rev C.* (1995) **51**:38–51. doi: 10.1103/PhysRevC.51.38
32. Machleidt R. Historical perspective and future prospects for nuclear interactions. *Int J Mod Phys E.* (2017) **26**:1730005. doi: 10.1142/S0218301317300053
33. Epelbaum E, Nogga A, Glˈockle W, Kamada H, Meißner UG, Witala H. Three nucleon forces from chiral effective field theory. *Phys Rev C.* (2002) **66**:064001. doi: 10.1103/PhysRevC.66.064001
34. Navratil P, Roth R, Quaglioni S. *Ab initio* many-body calculations of nucleon scattering on ^{4}He, ^{7}Li, ^{7}Be, ^{12}C and ^{16}O. *Phys Rev C.* (2010) **82**:034609. doi: 10.1103/PhysRevC.82.034609
35. Viviani M, Girlanda L, Kievsky A, Marcucci LE. Effect of three-nucleon interaction in p-3He elastic scattering. *Phys Rev Lett.* (2013) **111**:172302. doi: 10.1103/PhysRevLett.111.172302
36. Golak J, Skibiński R, Topolnicki K, Witala H, Epelbaum E, Krebs H, et al. Low-energy neutron-deuteron reactions with N^{3}LO chiral forces. *Eur Phys J A.* (2014) **50**:177–89. doi: 10.1140/epja/i2014-14177-7
37. Kalantar-Nayestanaki N, Epelbaum E, Messchendorp JG, Nogga A. Signatures of three-nucleon interactions in few-nucleon systems. *Rept Prog Phys.* (2012) **75**:016301. doi: 10.1088/0034-4885/75/1/016301
38. Navratil P, Quaglioni S, Hupin G, Romero-Redondo C, Calci A. Unified ab initio approaches to nuclear structure and reactions. *Phys Scr.* (2016) **91**:053002. doi: 10.1088/0031-8949/91/5/053002
39. Coraggio L, Covello A, Gargano A, Itaco N, Kuo TTS, Entem DR, et al. Low-momentum nucleon-nucleon interactions and shell-model calculations. *Phys Rev C.* (2007) **75**:024311. doi: 10.1103/PhysRevC.75.024311
40. Coraggio L, Covello A, Gargano A, Itaco N. Shell-model calculations for neutron-rich carbon isotopes with a chiral nucleon-nucleon potential. *Phys Rev C.* (2010) **81**:064303. doi: 10.1103/PhysRevC.81.064303
41. Coraggio L, Covello A, Gargano A, Itaco N, Kuo TTS. Effective shell-model hamiltonians from realistic nucleon-nucleon potentials within a perturbative approach. *Ann Phys.* (2012) **327**:2125–51. doi: 10.1016/j.aop.2012.04.013
42. Hagen H, Hjorth-Jensen M, Jansen GR, Machleidt R, Papenbrock T. Continuum effects and three-nucleon forces in neutron-rich oxygen isotopes. *Phys Rev Lett.* (2012) **108**:242501. doi: 10.1103/PhysRevLett.108.242501
43. Hagen H, Hjorth-Jensen M, Jansen GR, Machleidt R, Papenbrock T. Evolution of shell structure in neutron-rich calcium isotopes. *Phys Rev Lett.* (2012) **109**:032502. doi: 10.1103/PhysRevLett.109.032502
44. Barrett BR, Navratil P, Vary JP. Ab initio no core shell model. *Prog Part Nucl Phys.* (2013) **69**:131–81. doi: 10.1016/j.ppnp.2012.10.003
45. Gezerlis A, Tews I, Epelbaum E, Gandolfi S, Hebeler K, Nogga A, et al. Quantum Monte Carlo calculations with chiral effective field theory interactions. *Phys Rev Lett.* (2013) **111**:032501. doi: 10.1103/PhysRevLett.111.032501
46. Hergert H, Bogner SK, Binder S, Calci A, Langhammer J, Roth R, Schwenk A. In-medium similarity renormalization group with chiral two- plus three-nucleon interactions. *Phys Rev C.* (2013) **87**:034307. doi: 10.1103/PhysRevC.87.034307
47. Hagen G, Papenbrock T, Hjorth-Jensen M, Dean DJ. Coupled-cluster computations of atomic nuclei. *Rept Prog Phys.* (2014) **77**:096302. doi: 10.1088/0034-4885/77/9/096302
48. Somà V, Cipollone A, Barbieri C, Navratil P, Duget T. Chiral two- and three-nucleon forces along medium-mass isotope chains. *Phys Rev C.* (2014) **89**:061301(R). doi: 10.1103/PhysRevC.89.061301
49. Hebeler K, Holt JD, Menéndez J, Schwenk A. Nuclear forces and their impact on neutron-rich nuclei and neutron-rich matter. *Annu Rev Nucl Part Sci.* (2015) **65**:457–84. doi: 10.1146/annurev-nucl-102313-025446
50. Hagen G, Ekström A, Forssén C, Jansen GR, Nazarewicz W, Papenbrock T, et al. Neutron and weak-charge distributions of the ^{48}Ca nucleus. *Nat Phys.* (2015) **12**:186–90. doi: 10.1038/nphys3529
51. Carlson J, Gandolfi S, Pederiva F, Pieper SC, Schiavilla R, Schmidt KE, Wiringa RB. Quantum Monte Carlo methods for nuclear physics. *Rev Mod Phys.* (2015) **87**:1067–118. doi: 10.1103/RevModPhys.87.1067
52. Hergert H, Bogner SK, Morris TD, Schwenk A, Tsukiyama K. The in-medium similarity renormalization group: a novel *ab initio* method for nuclei. *Phys Rep.* (2016) **621**:165–222. doi: 10.1016/j.physrep.2015.12.007
53. Holt J W, Kaiser N. Equation of state of nuclear and neutron matter at third-order in perturbation theory from chiral effective field theory. *Phys Rev C.* (2017) **95**:034326. doi: 10.1103/PhysRevC.95.034326
54. Simonis J, Stroberg SR, Hebeler K, Holt JD, Schwenk A. Saturation with chiral interactions and consequences for finite nuclei. *Phys Rev C.* (2017) **96**:014303. doi: 10.1103/PhysRevC.96.014303
55. Morris TD, Simonis J, Stroberg SR, Stumpf C, Hagen G, Holt JD, et al. Structure of the lightest Tin isotopes. *arXiv:1709.02786 [nucl-th]* (2017). doi: 10.1103/PhysRevLett.120.152503
56. Hebeler K, Schwenk A. Chiral three-nucleon forces and neutron matter. *Phys Rev C.* (2010) **82**:014314. doi: 10.1103/PhysRevC.82.014314
57. Hebeler K, Bogner SK, Furnstahl RJ, Nogga A, Schwenk A. Improved nuclear matter calculations from chiral low-momentum interactions. *Phys Rev C.* (2011) **83**:031301(R). doi: 10.1103/PhysRevC.83.031301
58. Baardsen G, Ekström A, Hagen G, Hjorth-Jensen M. Coupled-cluster studies of infinite nuclear matter. *Phys Rev C.* (2013) **88**:054312. doi: 10.1103/PhysRevC.88.054312
59. Hagen G, Papenbrock T, Ekström A, Wendt KA, Baardsen G, Gandolfi S, et al. Coupled-cluster calculations of nucleonic matter. *Phys Rev C.* (2014) **89**:014319. doi: 10.1103/PhysRevC.89.014319
60. Coraggio L, Holt JW, Itaco N, Machleidt R, Sammarruca F. Reduced regulator dependence of neutron-matter predictions with perturbative chiral interactions. *Phys Rev C.* (2013) **87**:014322. doi: 10.1103/PhysRevC.87.014322
61. Coraggio L, Holt JW, Itaco N, Machleidt R, Marcucci LE, Sammarruca F. Nuclear-matter equation of state with consistent two- and three-body perturbative chiral interactions. *Phys Rev C.* (2014) **89**:044321. doi: 10.1103/PhysRevC.89.044321
62. Sammarruca F, Coraggio L, Holt JW, Itaco N, Machleidt R, Marcucci LE. Toward order-by-order calculations of the nuclear and neutron matter equations of state in chiral effective field theory. *Phys Rev C.* (2015) **91**:054311. doi: 10.1103/PhysRevC.91.054311
63. Drischler C, Carbone A, Hebeler K, Schwenk A. Neutron matter from chiral two- and three-nucleon calculations up to N^{3}LO. *Phys Rev C.* (2016) **94**:054307. doi: 10.1103/PhysRevC.94.054307
64. Tews I, Gandolfi S, Gezerlis A, Schwenk A. Quantum Monte Carlo calculations of neutron matter with chiral three-body forces. *Phys Rev C.* (2016) **93**:024305. doi: 10.1103/PhysRevC.93.024305
65. Wellenhofer C, Holt JW, Kaiser N, Weise W. Nuclear thermodynamics from chiral low-momentum interactions. *Phys Rev C.* (2014) **89**:064009. doi: 10.1103/PhysRevC.89.064009
66. Wellenhofer C, Holt JW, Kaiser N. Thermodynamics of isospin-asymmetric nuclear matter from chiral effective field theory. *Phys Rev C.* (2015) **92**:015801. doi: 10.1103/PhysRevC.92.015801
67. Bacca S, Hally K, Pethick CJ, Schwenk A. Chiral effective field theory calculations of neutrino processes in dense matter. *Phys Rev C.* (2009) **80**:032802. doi: 10.1103/PhysRevC.80.032802
68. Bartl A, Pethick CJ, Schwenk A. Supernova matter at subnuclear densities as a resonant fermi gas: enhancement of neutrino rates. *Phys Rev Lett.* (2014) **113**:081101. doi: 10.1103/PhysRevLett.113.081101
69. Rapaj E, Holt JW, Bartl A, Reddy S, Schwenk A. Charged-current reactions in the supernova neutrino-sphere. *Phys Rev C.* (2015) **91**:035806. doi: 10.1103/PhysRevC.91.035806
70. Buraczynski M, Gezerlis A. Static response of neutron matter. *Phys Rev Lett.* (2016) **116**:152501. doi: 10.1103/PhysRevLett.116.152501
71. Holt JW, Kaiser N, Miller GA. Microscopic optical potential for exotic isotopes from chiral effective field theory. *Phys Rev C.* (2016) **93**:064603. doi: 10.1103/PhysRevC.93.064603

72. Birkhan J, Miorelli M, Bacca S, Bassauer S, Bertulani CA, Hagen C, et al. Electric dipole polarizability of ^{48}Ca and implications for the neutron skin. *Phys Rev Lett.* (2017) **118**:252501. doi: 10.1103/PhysRevLett.118.252501
73. Rotureau J, Danielewicz P, Hagen G, Nunes F, Papenbrock T. Optical potential from first principles. *Phys Rev C.* (2017) **95**:024315. doi: 10.1103/PhysRevC.95.024315
74. Lapoux V, Somà V, Barbieri C, Hergert H, Holt JD, Stroberg SR. Radii and binding energies in oxygen isotopes: a challenge for nuclear forces. *Phys Rev Lett.* (2016) **117**:052501. doi: 10.1103/PhysRevLett.117.052501
75. Binder S, Langhammer J, Calci A, Roth R. *Ab initio* path to heavy nuclei. *Phys Lett B.* (2014) **736**:119–23. doi: 10.1016/j.physletb.2014.07.010
76. Ekström A, Jansen GR, Wendt KA, Hagen G, Papenbrock T, Carlsson BD, et al. Accurate nuclear radii and binding energies from a chiral interaction. *Phys Rev C.* (2015) **91**:051301. doi: 10.1103/PhysRevC.91.051301
77. Alonso D, Sammarruca F. A Microscopic calculation of asymmetric nuclear matter properties. *Phys Rev C.* (2003) **67**:054301. doi: 10.1103/PhysRevC.67.054301
78. Sammarruca F. The '*Ab initio*' approach to the nuclear equation of state: review and discussion. *arXiv:0807.0263 [nucl-th]* (2008).
79. Sammarruca F, Chen B, Coraggio L, Itaco N, Machleidt R. Dirac-Brueckner-Hartree-Fock versus chiral effective field theory. *Phys Rev C.* (2012) **86**:054317. doi: 10.1103/PhysRevC.86.054317
80. Pudliner BS, Pandharipande VR, Carlson J, Wiringa RB. Quantum Monte Carlo calculations of $A \leq 6$ nuclei. *Phys Rev Lett.* (1995) **74**:4396–9. doi: 10.1103/PhysRevLett.74.4396
81. Akmal A, Pandharipande VR, Ravenhall DG. The Equation of state of nucleon matter and neutron star structure. *Phys Rev C.* (1998) **58**:1804–28. doi: 10.1103/PhysRevC.58.1804
82. Lonardoni D, Lovato A, Pieper SC, Wiringa RB. Variational calculation of the ground state of closed-shell nuclei up to $A = 40$. *Phys Rev C.* (2017) **96**:024326. doi: 10.1103/PhysRevC.96.024326
83. Pieper SC. The Illinois extension to the Fujita-Miyazawa three-nucleon force. *AIP Conf Proc.* (2008) **1011**:143–52. doi: 10.1063/1.2932280
84. Zuo W, Lejeune A, Lombardo U, Mathiot JF. Microscopic three-body force for asymmetric nuclear matter. *Eur Phys J A.* (2002) **14**:469–75. doi: 10.1140/epja/i2002-10031-y
85. Li ZH, Lombardo U, Schulze HJ, Zuo W. Consistent nucleon-nucleon potentials and three-body forces. *Phys Rev C.* (2008) **77**:034316. doi: 10.1103/PhysRevC.77.034316
86. Machleidt R. The meson theory of nuclear forces and nuclear structure. *Adv Nucl Phys.* (1989) **19**:189–376. doi: 10.1007/978-1-4613-9907-0_2
87. Entem DR, Machleidt R, Nosyk Y. High-quality two-nucleon potentials up to fifth order of the chiral expansion. *Phys Rev C.* (2017) **96**:024004. doi: 10.1103/PhysRevC.96.024004
88. Entem DR, Machleidt R. Accurate charge-dependent nucleon-nucleon potential at fourth order of chiral perturbation theory. *Phys Rev C.* (2003) **68**:041001. doi: 10.1103/PhysRevC.68.041001
89. Marji E, Canul A, MacPherson Q, Winzer R, Zeoli C, Entem DR, et al. Nonperturbative renormalization of the chiral nucleon-nucleon interaction up to next-to-next-to-leading order. *Phys Rev C.* (2013) **88**:054002. doi: 10.1103/PhysRevC.88.054002
90. Hoferichter M, de Elvira RJ, Kubis B, Meissner UG. Matching pion-nucleon roy-steiner equations to chiral perturbation theory. *Phys Rev Lett.* (2015) **115**:192301. doi: 10.1103/PhysRevLett.115.192301
91. Hoferichter M, de Elvira RJ, Kubis B, Meissner UG. Roy-Steiner-equation analysis of pion-nucleon scattering. *Phys Rep.* (2016) **625**:1–88. doi: 10.1016/j.physrep.2016.02.002
92. Hoppe J, Drischler C, Furnstahl RJ, Hebeler K, Schwenk A. Weinberg eigenvalues for chiral nucleon-nucleon interactions. *Phys Rev C.* (2017) **96**:054002. doi: 10.1103/PhysRevC.96.054002
93. Drischler C, Hebeler K, Schwenk A. Chiral interactions up to N^{3}LO and nuclear saturation. *Phys Rev Lett.* (2019) **122**:042501. doi: 10.1103/PhysRevLett.122.042501
94. Holt JW, Kaiser N, Weise W. Chiral three-nucleon interaction and the ^{14}C-dating β decay. *Phys Rev C.* (2009) **79**:054331. doi: 10.1103/PhysRevC.79.054331
95. Holt JW, Kaiser N, Weise W. Density-dependent effective nucleon-nucleon interaction from chiral three-nucleon forces. *Phys Rev C.* (2010) **81**:024002. doi: 10.1103/PhysRevC.81.024002
96. Baldo M, Bombaci I, Burgio GF. Microscopic nuclear equation of state with three-body forces and neutron star structure. *Astron Astrophys.* (1997) **328**:274–84.
97. Kaiser N, Niessner V. Density-dependent NN interaction from subleading chiral 3N forces: short-range terms and relativistic corrections. *Phys Rev C.* (2018) **98**:054002. doi: 10.1103/PhysRevC.98.054002
98. Kaiser N, Singh B. Density-dependent NN interaction from subleading chiral three-nucleon forces: long-range terms. *Phys Rev C.* (2019) **100**:014002. doi: 10.1103/PhysRevC.100.014002
99. Gardestig A, Phillips DR. How low-energy weak reactions can constrain three-nucleon forces and the neutron-neutron scattering length. *Phys Rev Lett.* (2006) **96**:232301. doi: 10.1103/PhysRevLett.96.232301
100. Gazit D, Quaglioni S, Navrátil P. Three-nucleon low-energy constants from the consistency of interactions and currents in chiral effective field theory. *Phys Rev Lett.* (2009) **103**:102502. doi: 10.1103/PhysRevLett.103.102502
101. Marcucci LE, Kievsky A, Rosati S, Schiavilla R, Viviani M. Chiral effective field theory predictions for muon Capture on Deuteron and ^{3}He, *Phys Rev Lett.* (2012) **108**:052502; Erratum: Chiral effective field theory predictions for muon capture on deuteron and ^{3}He. (2018) **121**:049901(E). doi: 10.1103/PhysRevLett.108.052502
102. Navrátil P. Local three-nucleon interaction from chiral effective field theory. *Few-Body Syst.* (2007) **41**:117–40. doi: 10.1007/s00601-007-0193-3
103. Kievsky A, Rosati S, Marcucci LE, Girlanda L. A high-precision variational approach to three- and four-nucleon bound and zero-energy scattering states. *J Phys G.* (2008) **35**:063101. doi: 10.1088/0954-3899/35/6/063101
104. Tews I, Krüger T, Hebeler K, Schwenk A. Neutron matter at next-to-next-to-next-to-leading order in chiral effective field theory. *Phys Rev Lett.* (2013) **110**:032504. doi: 10.1103/PhysRevLett.110.032504
105. Hebeler K, Krebs H, Epelbaum E, Golak J, Skibinski R. Efficient calculation of chiral three-nucleon forces up to N^{3}LO for ab initio studies. *Phys Rev C.* (2015) **91**:044001. doi: 10.1103/PhysRevC.91.044001
106. Krebs H, Gasparyan A, Epelbaum E. Chiral three-nucleon force at N^{4}LO: longest-range contributions. *Phys Rev C.* (2012) **85**:054006. doi: 10.1103/PhysRevC.85.054006
107. Bernard V, Epelbaum E, Krebs H, Meißner UG. Subleading contributions to the chiral three-nucleon force: long-range terms. *Phys Rev C.* (2008) **77**:064004. doi: 10.1103/PhysRevC.77.064004
108. Fujita JI, Miyazawa H. Pion theory of three-body forces. *Prog Theor Phys.* (1957) **17**:360–5. doi: 10.1143/PTP.17.360
109. De JN, Samadar SK, Agrawal BK. Reassessing nuclear matter incompressibility and its density dependence. *Phys Rev C.* (2015) **92**:014304. doi: 10.1103/PhysRevC.92.014304
110. Thiel M, Sfienti C, Piekarewicz J, Horowitz CJ, Vanderhaeghen M. Neutron skins of atomic nuclei: per aspera ad astra. *arXiv:1904.12269* (2019). doi: 10.1088/1361-6471/ab2c6d
111. Bombaci I, Logoteta D. Equation of state of dense nuclear matter and neutron star structure from nuclear chiral interactions. *Astron Astrophys.* (2018) **609**:A128. doi: 10.1051/0004-6361/201731604
112. Oertel M, Hempel M, Klahn T, Typel S. Equations of state for supernovae and compact stars. *Rev Mod Phys.* (2017) **89**:015007. doi: 10.1103/RevModPhys.89.015007
113. Baldo M, Burgio GF. The nuclear symmetry energy. *Prog Part Nucl Phys.* (2016) **91**:101016. doi: 10.1016/j.ppnp.2016.06.006
114. Le Fevre A, Leifels Y, Reisdorf W, Aichelin J, Hartnack Ch. Constraining the nuclear matter equation of state around twice saturation density. *Nucl Phys A.* (2016) **945**:112–3. doi: 10.1016/j.nuclphysa.2015.09.015
115. Horowitz CJ, Brown EF, Kim Y, Lynch WG, Michaels R, Ono A, et al. A way forward in the study of the symmetry energy:

experiment, theory, and observation. *J Phys G.* (2014) **41**:093001. doi: 10.1088/0954-3899/41/9/093001
116. Verde G. Probing the nuclear equation-of-state and the symmetry energy with heavy-ion collisions. *EPJ Web Conf.* (2014) **66**:01018. doi: 10.1051/epjconf/20146601018
117. Trautmann W, Wolter HH. Elliptic flow and the symmetry energy at supra-saturation density. *Int J Mod Phys E.* (2012) **21**:1230003. doi: 10.1142/S0218301312300032
118. Steiner AW, Prakash M, Lattimer JM, Ellis PJ. Isospin asymmetry in nuclei and neutron stars. *Phys Rep.* (2005) **411**:325–75. doi: 10.1016/j.physrep.2005.02.004
119. Bombaci I, Lombardo U. Asymmetric nuclear matter equation of state. *Phys Rev C.* (1991) **44**:1892–900. doi: 10.1103/PhysRevC.44.1892
120. Sammarruca F. Recent advances in microscopic approaches to nuclear matter and symmetry energy. *Symmetry.* (2014) **6**:851–79. doi: 10.3390/sym6040851
121. Paschke K, Kumar K, Michael R, Souder PA, Urciuoli GM. *PREX-II: Precision Parity-Violating Measurement of the Neutron Skin of Lead*. Available online at: http://hallaweb.jlab.org/parity/prex/prexII.pdf
122. Mammei J, McNulty D, Michaels R, Paschke K, Riordan S, Souder P. C-REX: parity-violating measurement of the weak charge of 48Ca to an accuracy of 0.02 fm. Available online at: http://hallaweb.jlab.org/parity/prex/c-rex2013_v7.pdf
123. Sammarruca F, Millerson R. The radius of the canonical-mass neutron star and chiral effective field theory. *J Phys G.* (2019) **46**:024001. doi: 10.1088/1361-6471/aafbcd
124. Santos BM, Dutra M, Lourenco O, Delfino A. Correlations between bulk parameters in relativistic and nonrelativistic hadronic mean-field models. *Phys Rev C.* (2015) **92**:015210. doi: 10.1103/PhysRevC.92.0152
125. Tong H, Ren XL, Ring P, Shen SH, Wang SB, Meng J. Relativistic Brueckner-Hartree-Fock theory in nuclear matter without the average momentum approximation. *Phys Rev C.* (2018) **98**:054302. doi: 10.1103/PhysRevC.98.054302
126. Holt JW, Lim Y. Universal correlations in the nuclear symmetry energy, slope parameter, and curvature. *Phys Lett.* (2018) **B784**:77–81. doi: 10.1016/j.physletb.2018.07.038
127. Vidaña I, Providencia C, Polls A, Rios A. Density dependence of the nuclear symmetry energy: a microscopic perspective. *Phys Rev C.* (2009) **80**:045806. doi: 10.1103/PhysRevC.80.045806
128. Ducoin C, Margueron J, Providencia CMC, Vidaña I. Core-crust transition in neutron stars: predictivity of density developments. *Phys Rev C.* (2011) **83**:045810. doi: 10.1103/PhysRevC.83.045810
129. Santos BM, Dutra M, Lourenco O, Delfino A. Correlations between the nuclear matter symmetry energy, its slope, and curvature from a nonrelativistic solvable approach and beyond. *Phys Rev C.* (2014) **90**:035203. doi: 10.1103/PhysRevC.90.035203
130. Millerson R, Sammarruca F. Properties of isospin asymmetric matter derived from chiral effective field theory. *arXiv:1906.02905 [nucl-th]* (2019).
131. Piekarewicz J, Fattoyev FJ. Neutron rich matter in heaven and on Earth. *arXiv:1907.02561 [nucl-th]*.
132. Brown BA. Neutron radii in nuclei and the neutron equation of state. *Phys Rev Lett.* (2000) **85**:5296–9. doi: 10.1103/PhysRevLett.85.5296
133. Lalazissis GA, Konig J, Ring P. New parametrization for the Lagrangian density of relativistic mean field theory. *Phys Rev C.* (1997) **55**:540–3. doi: 10.1103/PhysRevC.55.540
134. Fattoyev FJ, Horowitz CJ, Piekarewicz J, Shen G. Relativistic effective interaction for nuclei, giant resonances, and neutron stars. *Phys Rev C.* (2010) **82**:055803. doi: 10.1103/PhysRevC.82.055803
135. Alam N, Agrawal BK, De JN, Samaddar SK, Colo G. Equation of state of nuclear matter from empirical constraints. *Phys Rev C.* (2014) **90**:054317. doi: 10.1103/PhysRevC.90.054317
136. Danielewicz P, Lee J. Symmetry energy II: isobaric analog states. *Nucl Phys A.* (2014) **922**:1–70. doi: 10.1016/j.nuclphysa.2013.11.005
137. Tsang MB, Zhang Y, Danielewicz P, Famiano M, Li Z, Lynch WG, et al. Constraints on the density dependence of the symmetry energy. *Phys Rev Lett.* (2009) **102**:122701. doi: 10.1103/PhysRevLett.102.122701
138. Russotto P, Gannon S, Kupny S, Lasko P, Acosta L, Adamczyk M, et al. Results of the ASY-EOS experiment at GSI: the symmetry energy at suprasaturation density. *Phys Rev C.* (2016) **94**:034608. doi: 10.1103/PhysRevC.94.034608
139. Russotto P, Wu PZ, Zoric M, Chartier M, Leifels Y, Lemmon RC, et al. Symmetry energy from elliptic flow in ^{197}Au + ^{197}Au. *Phys Lett B.* (2011) **697**:471–6. doi: 10.1016/j.physletb.2011.02.033
140. Lattimer JM, Lim Y. Constraining the symmetry parameters of the nuclear interaction. *Astrophys J.* (2013) **771**:51–65. doi: 10.1088/0004-637X/771/1/51
141. Malik T, Alam N, Fortin M, Providencia C, Agrawal BK, Jha TK, et al. GW170817: constraining the nuclear matter equation of state from the neutron star tidal deformability. *Phys Rev C.* (2018) **98**:035804. doi: 10.1103/PhysRevC.98.035804
142. Sammarruca F. Proton skins, neutron skins, and proton radii of mirror nuclei. *Front Phys.* (2018) **6**:90–8. doi: 10.3389/fphy.2018.00090
143. Sammarruca F. Investigation of constraints on few-neutron forces in neutron matter by empirical information on the neutron skin of ^{4}8Ca and ^{2}08Pb. *Phys Rev C.* (2016) **94**:054317. doi: 10.1103/PhysRevC.94.054317
144. Inakura T, Nakada N. Constraining the slope parameter of the symmetry energy from nuclear structure. *Phys Rev C.* (2015) **92**:064302. doi: 10.1103/PhysRevC.92.064302
145. Warda M., Viñas X, Roca-Maza X, Centelles M. Neutron skin thickness in the droplet model with surface width dependence: indications of softness of the nuclear symmetry energy. *Phys Rev C.* (2009) **80**:024316. doi: 10.1103/PhysRevC.80.024316
146. Xu C, Li B, Chen L, Ko CM. Analytical relations between nuclear symmetry energy and single-nucleon potentials in isospin asymmetric nuclear matter. *Nucl Phys A.* (2011) **865**:1–16. doi: 10.1016/j.nuclphysa.2011.06.027
147. Roca-Maza X, Brenna M, Agrawal BK, Bortignon PF, Colo G, Cao LG, et al. Giant quadrupole resonances in ^{2}08Pb, the nuclear symmetry energy, and the neutron skin thickness. *Phys Rev C.* (2013) **87**:034301. doi: 10.1103/PhysRevC.87.034301
148. Abrahamyan S, Ahmed Z, Albataineh H, Aniol K, Armstrong DS, Armstrong W, et al. Measurement of the neutron radius of ^{208}Pb through parity violation in electron scattering. *Phys Rev Lett.* (2012) **108**:112502. doi: 10.1103/PhysRevLett.108.112502
149. Mammei J (for the PREX Collaboration). The Pb radius experiment (PREX). *AIP Conf Proc.* (2013) **1560**:620–3. doi: 10.1063/1.4826855
150. Becker D, Bucoveanu R, Grzesik C, Imai K, Kempf R, Molitor M, et al. The P2 experiment. *Eur Phys J.* (2018) **A54**:208–69. doi: 10.1140/epja/i2018-12611-6
151. Oyamatsu K, Iida K, Koura H. Neutron drip line and the equation of state of nuclear matter. *Phys Rev C.* (2010) **82**:027301. doi: 10.1103/PhysRevC.82.027301
152. Oppenheimer JR, Volkoff GM. On massive neutron cores. *Phys Rev C.* (1939) **55**:374–80. doi: 10.1103/PhysRev.55.374
153. Weber F. *Pulsar as Astrophysical Laboratories for Nuclear and Particle Physics*. Bristol; Philadelphia, PA: IOP (1999).
154. Glendenning NK. *Compact Stars*. 2nd Edn. New York, NY: Springer (2000).
155. Özel F, Freire P. Masses, radii, and the equation of state of neutron stars. *Annu Rev Astron Astrophys.* (2016) **54**:401–40. doi: 10.1146/annurev-astro-081915-023322
156. Lattimer JM, Prakash M. The physics of neutron stars. *Science.* (2004) **304**:536–42. doi: 10.1126/science.1090720
157. Lattimer JM, Prakash M. Neutron star observations: prognosis for equation of state constraints. *Phys Rep.* (2007) **442**:109–65. doi: 10.1016/j.physrep.2007.02.003
158. Lattimer JM, Prakash M. The equation of state of hot, dense matter and neutron stars. *Phys Rep.* (2016) **621**:127–64. doi: 10.1016/j.physrep.2015.12.005
159. Steiner AW, Lattimer JM, Brown E.F. The neutron star mass-radius relation and the equation of state of dense matter. *Astrophys J.* (2013) **765**:L5. doi: 10.1088/2041-8205/765/1/L5
160. Özel F. Surface emission from neutron stars and implications for the physics of their interiors. *Rep Prog Phys.* (2013) **76**:016901. doi: 10.1088/0034-4885/76/1/016901
161. Rhoades CD, Ruffini R. Maximum mass of a neutron star. *Phys Rev Lett.* (1974) **32**:324–7. doi: 10.1103/PhysRevLett.32.324

162. Sabbadini AG, Hartle JB. Bounds on the moment of inertia of nonrotating neutron stars. *Ann Phys NY.* (1977) **104**:95–113. doi: 10.1016/0003-4916(77)90047-1
163. Hartle JB. Bounds on the mass and moment of inertia of non-rotating neutron stars. *Phys Rep.* (1978) **46**:201–47. doi: 10.1016/0370-1573(78)90140-0
164. Abbott BP, [LIGO Scientific and Virgo Collaborations]. GW170817: Observation of gravitational waves from a binary neutron star inspiral. *Phys Rev Lett.* (2017) **119**:161101. doi: 10.1103/PhysRevLett.119.161101
165. Hinderer T, Lackey BD, Lang RN, Read JS. Tidal deformability of neutron stars with realistic equations of state and their gravitational wave signatures in binary inspiral. *Phys Rev D.* (2010) **81**:123016. doi: 10.1103/PhysRevD.81.123016
166. Lim Y, Holt JW. Neutron star tidal deformabilities constrained by nuclear theory and experiment. *Phys Rev Lett.* (2018) **121**:062701. doi: 10.1103/PhysRevLett.121.062701
167. Annala E, Gorda T, Kurkela A, Vuorinen A. Gravitational-wave constraints on the neutron-star-matter equation of state. *Phys Rev Lett.* (2018) **120**:172703. doi: 10.1103/PhysRevLett.120.172703
168. Fattoyev FJ, Piekarewicz J, Horowitz CJ. Neutron skins and neutron stars in the multimessenger era. *Phys Rev Lett.* (2018) **120**:172702. doi: 10.1103/PhysRevLett.120.172702
169. Most ER, Weih LR, Rezzolla L, Schffner-Bielich J. New constraints on radii and tidal deformabilities of neutron stars from GW170817. *Phys Rev Lett.* (2018) **120**:261103. doi: 10.1103/PhysRevLett.120.261103
170. Raithel CA, Ozel F, Psaltis D. Tidal Deformability from GW170817 as a direct probe of the neutron star radius. *Astrophys J.* (2018) **857**:L23. doi: 10.3847/2041-8213/aabcbf
171. Nandi R, Char P, Pal S. Constraining the relativistic mean-field model equations of state with gravitational wave observations. *Phys Rev C.* (2019) **99**:052802. doi: 10.1103/PhysRevC.99.052802
172. Burgio GF, Drago A, Pagliara G, Schulze HJ, Wei JB. Are small radii of compact stars ruled out by GW170817/AT2017gfo?. *Astrophys J.* (2018) **860**:139-144. doi: 10.3847/1538-4357/aac6ee
173. Harrison BK, Wheeler JA. *Gravitation Theory and Gravitational Collapse*. Chicago, IL: University of Chicago Press (1965).
174. Negele JW, Vautherin D. Neutron star matter at sub-nuclear densities. *Nucl Phys.* (1973) **A207**:298–320. doi: 10.1016/0375-9474(73)90349-7
175. Liebert J. White dwarf stars. *Annu Rev Astron Astrophys.* (1980) **18**:363–98. doi: 10.1146/annurev.aa.18.090180.002051
176. Read JS, Lackey BD, Owen BJ, Friedman JL. Constraints on a phenomenologically parametrized neutron-star equation of state. *Phys Rev D.* (2009) **79**:124032. doi: 10.1103/PhysRevD.79.124032
177. Sammarruca F. Short-range correlations in isospin symmetric and asymmetric nuclear matter: a microscopic perspective. *Phys Rev C.* (2014) **90**:064312. doi: 10.1103/PhysRevC.90.064312
178. Hebeler K, Lattimer JM, Pethick CJ, Schwenk A. Equation of state and neutron star properties constrained by nuclear physics and observation. *ApJ.* (2013) **773**:11–25. doi: 10.1088/0004-637X/773/1/11
179. Antoniadis J, Freire PCC, Wex N, Tauris TM, Lynch RS, van Kerkwijk MH, et al. A massive pulsar in a compact relativistic binary. *Science.* (2013) **340**:6131. doi: 10.1126/science.1233232
180. Cromartie HT, Fonseca E, Ransom SM, Demorest PB, Arzoumanian Z, Blumer H, et al. Relativistic Shapiro delay measurements of an extremely massive millisecond pulsar. *Nat Astron.* (2019). doi: 10.1038/s41550-019-0880-2
181. Lattimer JM, Prakash M. Neutron star structure and the equation of state. *ApJ.* (2001) **550**:426–42. doi: 10.1086/319702
182. Miyatsu T, Saito K, Cheoun MK. Equation of state for neutron stars with hyperons and quarks in the relativistic hartree - fock approximation. *Astrophys J.* (2015) **813**:2–15. doi: 10.1088/0004-637X/813/2/135
183. Mishra RN, Sahoo HS, Panda PK, Barik N, Frederico T. Hyperon stars in a modified quark meson coupling model. *Phys Rev C.* (2016) **94**:035805. doi: 10.1103/PhysRevC.94.035805
184. Bombaci I. The hyperon puzzle in neutron stars. *arXiv:1601.05339 [nucl-th].*
185. Vidana I. Hyperons in neutron stars. *J Phys Conf Ser.* (2016) **668**:012031. doi: 10.1088/1742-6596/668/1/012031
186. Rapaj E, Roggero A, Holt JW. Microscopically constrained mean-field models from chiral nuclear thermodynamics. *Phys Rev C.* (2016) **93**:065801. doi: 10.1103/PhysRevC.93.065801
187. Endrizzi A, Logoteta D, Giacomazzo B, Bombaci I, Kastaun W, Ciolfi R. Effects of chiral effective field theory equation of state on binary neutron star mergers. *arXiv:1806.09832 [astro-ph.HE]* (2018). doi: 10.1103/PhysRevD.98.043015
188. van Paradijs J. Possible observation constraints on the Mass-Radius relation of neutron stars. *Astrophys J.* (1979) **234**:609–11. doi: 10.1086/157535

Conflict of Interest: The authors declare that the research was conducted in the absence of any commercial or financial relationships that could be construed as a potential conflict of interest.

Copyright © 2019 Sammarruca and Millerson. This is an open-access article distributed under the terms of the Creative Commons Attribution License (CC BY). The use, distribution or reproduction in other forums is permitted, provided the original author(s) and the copyright owner(s) are credited and that the original publication in this journal is cited, in accordance with accepted academic practice. No use, distribution or reproduction is permitted which does not comply with these terms.

frontiers in Physics

ORIGINAL RESEARCH
published: 24 April 2020
doi: 10.3389/fphy.2020.00100

Implementing Chiral Three-Body Forces in Terms of Medium-Dependent Two-Body Forces

Jeremy W. Holt[1,2]*, *Mamiya Kawaguchi*[3,4] *and Norbert Kaiser*[5]

[1] Department of Physics and Astronomy, Texas A&M University, College Station, TX, United States, [2] Cyclotron Institute, Texas A&M University, College Station, TX, United States, [3] Department of Physics, Nagoya University, Nagoya, Japan, [4] Department of Physics, Center for Particle Physics and Field Theory, Fudan University, Shanghai, China, [5] Physik-Department, Technische Universität München, Garching, Germany

Three-nucleon (3N) forces are an indispensable ingredient for accurate few-body and many-body nuclear structure and reaction theory calculations. While the direct implementation of chiral 3N forces can be technically very challenging, a simpler approach is given by employing instead a medium-dependent NN interaction $V_{\rm med}$ that reflects the physics of three-body forces at the two-body normal-ordered approximation. We review the derivation and construction of $V_{\rm med}$ from the chiral 3N interaction at next-to-next-to-leading order (N2LO), consisting of a long-range 2π-exchange term, a mid-range 1π-exchange component, and a short-range contact-term. Several applications of $V_{\rm med}$ to the equation of state of cold nuclear and neutron matter, the nucleon single-particle potential in nuclear matter, and the nuclear quasiparticle interaction are discussed. We also explore differences in using local vs. non-local regulating functions on 3N forces and make direct comparisons to exact results at low order in perturbation theory expansions for the equation of state and single-particle potential. We end with a discussion and numerical calculation of the in-medium NN potential $V_{\rm med}$ from the next-to-next-to-next-to-leading order (N3LO) chiral 3N force, which consists of a series of long-range and short-range terms.

Keywords: chiral effective field theory, three-body forces, nuclear matter, equation of state, nuclear reaction theory

OPEN ACCESS

Edited by:
Laura Elisa Marcucci, University of Pisa, Italy

Reviewed by:
Maria Colonna, Laboratori Nazionali del Sud (INFN), Italy
Arnau Rios Huguet, University of Surrey, United Kingdom

***Correspondence:**
Jeremy W. Holt
holt@physics.tamu.edu

Specialty section:
This article was submitted to Nuclear Physics, a section of the journal Frontiers in Physics

Received: *17 December 2019*
Accepted: *18 March 2020*
Published: *24 April 2020*

Citation:
Holt JW, Kawaguchi M and Kaiser N (2020) Implementing Chiral Three-Body Forces in Terms of Medium-Dependent Two-Body Forces. Front. Phys. 8:100. doi: 10.3389/fphy.2020.00100

1. INTRODUCTION

Three-nucleon forces are essential to any microscopic description of nuclear many-body systems, from the structure and reactions of finite nuclei [1–4] to the equation of state and transport properties of dense matter encountered in core-collapse supernovae and neutron stars [2, 5–13]. Three-body forces have been shown to dramatically improve the saturation properties of nuclear matter [6, 7, 14], though there are still large uncertainties compared to the empirical saturation energy and density. Three-nucleon forces are now also routinely implemented in a number of ab initio many-body methods such as the no-core shell model [15], coupled-cluster theory [16, 17], self-consistent Green's function theory [18], the similarity renormalization group [19, 20], and quantum Monte Carlo [3] to study nuclear ground-state and excited states up to medium-mass nuclei. In particular, three-body forces have been shown to be especially relevant for understanding the properties of neutron-rich nuclei out to the drip line [16, 18, 21, 22].

In the past, it has been challenging [5] to obtain nuclear two- and three-body forces that simultaneously fit well the properties of finite nuclei and nuclear matter, but in recent years, much progress has been achieved within the framework of chiral effective field theory [23–27] to construct three-body forces consistent with the employed two-body force, all within a systematic power series expansion involving the ratio of the physical scale Q to the chiral symmetry breaking scale $\Lambda_\chi \sim 1$ GeV. In chiral effective field theory with explicit nucleon and pion degrees of freedom only, three-nucleon forces appear first at third order in the chiral expansion $(Q/\Lambda_\chi)^3$, or next-to-next-to-leading (N2LO) order. These leading contributions to the chiral three-nucleon force (3NF) are now routinely employed in nuclear structure and reaction theory calculations, but many-body contributions at N3LO [28–31] are expected to be important.

In the present work, we will review how to implement three-nucleon forces via medium-dependent two-body interactions [6, 7, 32] in nuclear many-body calculations of the equation of state, single-particle potential, and quasiparticle interaction. We will show that this approach provides an excellent approximation at first order in many-body perturbation theory by comparing to exact results from three-body forces. At higher orders in perturbation theory, the use of medium-dependent NN interactions fail to reproduce all topologies, however, residual three-body interactions have been shown [33] to give relatively small contributions ($\sim$ 1 MeV) to the nuclear equation of state at saturation density up to second order in perturbation theory. We also consider several commonly used high-momentum regulating functions for three-body forces and study their impact on the density-dependent interaction $V_{\rm med}$. In particular, we find that local regulators introduce large artifacts compared to nonlocal regulators when the same value of the cutoff scale Λ is used in both cases.

2. FROM THREE-BODY FORCES TO MEDIUM-DEPENDENT TWO-BODY FORCES

2.1. Chiral Three-Body Force at Next-to-Next-to-Leading Order

The nuclear Hamiltonian can generically be written in the form

$$H = \sum_i \frac{\vec{p}_i^{\,2}}{2M} + \frac{1}{2}\sum_{ij} V_{ij} + \frac{1}{6}\sum_{ijk} V_{ijk} + \cdots , \qquad (1)$$

where $\vec{p}_i$ is the momentum of nucleon i, V_{ij} represents the two-body interaction between particles i and j, and V_{ijk} represents the three-body interaction between particles i, j, k. Three-body forces emerge first at N2LO in the chiral expansion and comprise three different topologies represented diagrammatically in **Figure 1**. The two-pion-exchange three-body force (**Figure 1A**), consists of three terms proportional to the low-energy constants c_1, c_3, and c_4:

$$V_{3N}^{(2\pi)} = \sum_{i\neq j\neq k} \frac{g_A^2}{8f_\pi^4} \frac{\vec{\sigma}_i\cdot\vec{q}_i\,\vec{\sigma}_j\cdot\vec{q}_j}{(\vec{q}_i^{\,2}+m_\pi^2)(\vec{q}_j^{\,2}+m_\pi^2)} F_{ijk}^{\alpha\beta}\tau_i^\alpha\tau_j^\beta , \qquad (2)$$

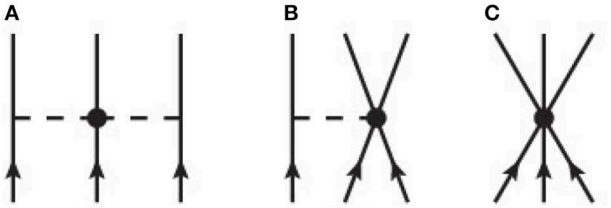


FIGURE 1 | Diagrammatic contributions to the chiral three-nucleon force at next-to-next-to-leading order (N2LO) in the chiral expansion: **(A)** two-pion-exchange interaction, **(B)** one-pion-exchange interaction, and **(C)** contact interaction.

where $g_A = 1.29$ is the axial coupling constant, $m_\pi = 138$ MeV is the average pion mass, $f_\pi = 92.2$ MeV is the pion decay constant, $\vec{q}_i = \vec{k}_i' - \vec{k}_i$ is the change in momentum of nucleon i (i.e., the momentum transfer), and the isospin tensor $F_{ijk}^{\alpha\beta}$ is defined by

$$F_{ijk}^{\alpha\beta} = \delta^{\alpha\beta}\left(-4c_1 m_\pi^2 + 2c_3\,\vec{q}_i\cdot\vec{q}_j\right) + c_4\,\epsilon^{\alpha\beta\gamma}\tau_k^\gamma\,\vec{\sigma}_k\cdot\left(\vec{q}_i\times\vec{q}_j\right). \qquad (3)$$

The three low-energy constants c_1, c_3, and c_4 can be fitted to empirical pion-nucleon [34, 35] or nucleon-nucleon [36, 37] scattering data.

The one-pion exchange term (**Figure 1B**), proportional to the low-energy constant c_D, has the form

$$V_{3N}^{(1\pi)} = -\sum_{i\neq j\neq k} \frac{g_A c_D}{8f_\pi^4\,\Lambda_\chi} \frac{\vec{\sigma}_j\cdot\vec{q}_j}{\vec{q}_j^{\,2}+m_\pi^2}\,\vec{\sigma}_i\cdot\vec{q}_j\,\vec{\tau}_i\cdot\vec{\tau}_j , \qquad (4)$$

where the high-momentum scale is typically taken as $\Lambda_\chi = 700$ MeV. The three-nucleon contact force (**Figure 1C**), proportional to c_E reads:

$$V_{3N}^{(\rm ct)} = \sum_{i\neq j\neq k} \frac{c_E}{2f_\pi^4\,\Lambda_\chi}\,\vec{\tau}_i\cdot\vec{\tau}_j . \qquad (5)$$

There are several different experimental observables commonly used for fitting the low-energy constants c_D and c_E. Most approaches fit the binding energies of $A = 3$ nuclei together with one of the following observables: (a) the neutron-deuteron doublet scattering length [38, 39], (b) the radius of ^{4}He [40], (c) the properties of light and medium-mass nuclei [41, 42], and (d) the triton lifetime [43, 44].

Since the three-nucleon force V_{3N} is symmetric under the interchange of particle labels, there are only three independent terms from the i, j, k permutations, which allows us to write $V_{3N} = W_1 + W_2 + W_3$. For instance, $W_1^{(\rm ct)} = \frac{c_E}{f_\pi^4\Lambda}\,\vec{\tau}_2\cdot\vec{\tau}_3$. The antisymmetrized three-body interaction $\bar{V}_{3N}$ can be written in terms of two-body antisymmetrization operators P_{ij} as follows:

$$\bar{V}_{3N} = (1-P_{12})(1-P_{13}-P_{23})V_{3N}, \qquad (6)$$

where

$$P_{ij} = \left(\frac{1+\vec{\sigma}_i\cdot\vec{\sigma}_j}{2}\right)\left(\frac{1+\vec{\tau}_i\cdot\vec{\tau}_j}{2}\right), \quad \vec{k}_i \longleftrightarrow \vec{k}_j . \qquad (7)$$

2.2. Density-Dependent NN Interaction at Order N2LO

In second quantization, a three-body force V_{3N} can be written as

$$V_{3N} = \frac{1}{36}\sum_{123456}\langle 123|\bar{V}_{3N}|456\rangle \hat{a}_1^\dagger \hat{a}_2^\dagger \hat{a}_3^\dagger \hat{a}_6 \hat{a}_5 \hat{a}_4 \tag{8}$$

where $\bar{V}_{3N}$ denotes the antisymmetrized three-body matrix element, and $a_i^\dagger$ (a_i) are the usual creation (annihilation) operators associated with state $|i\rangle$. A medium-dependent two-body interaction can then be constructed by normal ordering the three-body force with respect to a convenient reference state, such as the ground state of the noninteracting many-body system, rather than the true vacuum as in Equation (8). Normal ordering with respect to the noninteracting ground state then produces a three-body force of the form

$$\begin{aligned} V_{3N} &= \frac{1}{6}\sum_{ijk}\langle ijk|\bar{V}_{3N}|ijk\rangle + \frac{1}{2}\sum_{ij14}\langle ij1|\bar{V}_{3N}|ij4\rangle :\hat{a}_1^\dagger \hat{a}_4: \\ &+ \frac{1}{4}\sum_{i1245}\langle i12|\bar{V}_{3N}|i45\rangle :\hat{a}_1^\dagger \hat{a}_2^\dagger \hat{a}_5 \hat{a}_4: \\ &+ \frac{1}{36}\sum_{123456}\langle 123|\bar{V}_{3N}|456\rangle :\hat{a}_1^\dagger \hat{a}_2^\dagger \hat{a}_3^\dagger \hat{a}_6 \hat{a}_5 \hat{a}_4:, \end{aligned} \tag{9}$$

where $:\hat{\mathcal{O}}:$ denotes normal ordering of operator $\hat{\mathcal{O}}$. In practice the construction of the medium-dependent two-body force

$$\frac{1}{4}\sum_{i1245}\langle i12|\bar{V}_{3N}|i45\rangle :\hat{a}_1^\dagger \hat{a}_2^\dagger \hat{a}_5 \hat{a}_4: \tag{10}$$

then amounts to summing the third particle over the filled states in the noninteracting Fermi sea, involving spin and isospin summations as well as momentum integration:

$$\bar{V}_{\rm med} = \sum_{s_3 t_3}\int \frac{d^3k_3}{(2\pi)^3}\theta(k_f - k_3)(1 - P_{13} - P_{23})V_{3N}, \tag{11}$$

where k_f is the Fermi momentum and we have absorbed the particle exchange operator $(1 - P_{12})$ into the definition of the antisymmetrized medium-dependent NN interaction $\bar{V}_{\rm med}$. In general, there are nine different diagrams that need to be evaluated independently: $(1 - P_{13} - P_{23})(W_1 + W_2 + W_3)$, which correspond to different closings of one incoming and outgoing particle line.

As a simple example, we compute the density-dependent NN interaction arising from the three-body contact term at N2LO shown diagrammatically in **Figure 2** (*f*). We begin by evaluating the spin and isospin traces in Equation (11):

$$\begin{aligned} & Tr_{\sigma_3\tau_3}\left[(1 - P_{13} - P_{23})(\vec{\tau}_2\cdot\vec{\tau}_3 + \vec{\tau}_1\cdot\vec{\tau}_3 + \vec{\tau}_1\cdot\vec{\tau}_2)\right] \\ &= Tr_{\sigma_3\tau_3}(\vec{\tau}_2\cdot\vec{\tau}_3 + \vec{\tau}_1\cdot\vec{\tau}_3 + \vec{\tau}_1\cdot\vec{\tau}_2) - Tr_{\sigma_3\tau_3} \\ &\quad\left[\left(\frac{1+\vec{\sigma}_1\cdot\vec{\sigma}_3}{2}\frac{1+\vec{\tau}_1\cdot\vec{\tau}_3}{2}\right)(\vec{\tau}_2\cdot\vec{\tau}_3 + \vec{\tau}_1\cdot\vec{\tau}_3 + \vec{\tau}_1\cdot\vec{\tau}_2)\right] \\ &- Tr_{\sigma_3\tau_3}\left[\left(\frac{1+\vec{\sigma}_2\cdot\vec{\sigma}_3}{2}\frac{1+\vec{\tau}_2\cdot\vec{\tau}_3}{2}\right)(\vec{\tau}_2\cdot\vec{\tau}_3 + \vec{\tau}_1\cdot\vec{\tau}_3 + \vec{\tau}_1\cdot\vec{\tau}_2)\right] \end{aligned} \tag{12}$$

$$\begin{aligned} &= 4\vec{\tau}_1\cdot\vec{\tau}_2 - \frac{1}{4}Tr_{\sigma_3\tau_3}(\vec{\tau}_1\cdot\vec{\tau}_2 + (\vec{\tau}_1\cdot\vec{\tau}_3)(\vec{\tau}_2\cdot\vec{\tau}_3) + (\vec{\tau}_1\cdot\vec{\tau}_3)(\vec{\tau}_1\cdot\vec{\tau}_3)) \\ &- \frac{1}{4}Tr_{\sigma_3\tau_3}(\vec{\tau}_1\cdot\vec{\tau}_2 + (\vec{\tau}_2\cdot\vec{\tau}_3)(\vec{\tau}_2\cdot\vec{\tau}_3) + (\vec{\tau}_2\cdot\vec{\tau}_3)(\vec{\tau}_1\cdot\vec{\tau}_3)) \\ &= 2\vec{\tau}_1\cdot\vec{\tau}_2 - \frac{1}{2}(4\vec{\tau}_1\cdot\vec{\tau}_2 + 12) = -6, \end{aligned}$$

where we have used the well known properties of Pauli matrices: $Tr\vec{\sigma} = 0$, $Tr1 = 2$, $Tr_3(\vec{\tau}_i\cdot\vec{\tau}_3)(\vec{\tau}_j\cdot\vec{\tau}_3) = 2\vec{\tau}_i\cdot\vec{\tau}_j$, and $\vec{\tau}_i\cdot\vec{\tau}_i = 3$. The integration over filled momentum states is trivial:

$$\int \frac{d^3k_3}{(2\pi)^3}\theta(k_f - k_3)\frac{c_E}{f_\pi^4\Lambda_\chi} = \frac{1}{2\pi^2}\frac{k_f^3}{3}\frac{c_E}{f_\pi^4\Lambda_\chi}, \tag{13}$$

which gives a final result of

$$V_{\rm med}^{\rm (ct)} = -\frac{c_E k_f^3}{\pi^2 f_\pi^4 \Lambda_\chi}. \tag{14}$$

This particularly simple three-body contact interaction gives rise to a momentum-independent effective two-body interaction. For the more complicated 1π- and 2π-exchange topologies, it is convenient to consider the on-shell scattering ($|\vec{p}\,| = |\vec{p}\,'|$) of two nucleons in the center-of-mass frame: $N_1(\vec{p}\,) + N_2(-\vec{p}\,) \to N_1(\vec{p}\,') + N_2(-\vec{p}\,')$. This assumption results in a medium-dependent 2N interaction with the same isospin and spin structures as the free-space 2N potential, which allows for a simple decomposition of $V_{\rm med}$ into partial-wave matrix elements as we show in section 4.1. In the more general case $N_1(\vec{p}_1) + N_2(\vec{p}_2) \to N_1(\vec{p}_3) + N_2(\vec{p}_4)$, the in-medium 2N interaction will contain operator structures depending on the center-of-mass momentum $\vec{P} = \vec{p}_1 + \vec{p}_2 = \vec{p}_3 + \vec{p}_4$. Such contributions have been shown to be small in practice [45]. In the applications discussed below, higher-order perturbative contributions to the ground state energy and single-particle energies involve also off-shell matrix elements of the interaction $\langle\vec{p}\,'|V|\vec{p}\,\rangle$, where $|\vec{p}\,| \neq |\vec{p}\,'|$. In such cases we use as an approximation the substitution $p^2 \to \frac{1}{2}(p^2 + p'^2)$ in the formulas derived below. The resulting interaction can then be straightfowardly implemented into modern nuclear structure codes. We will explicitly test some of the approximations noted above by comparing exact results at low order in perturbation theory using the full three-body force to the results using instead the medium-dependent 2N interaction.

Note that in the above derivation of the density-dependent 2N interaction associated with $V_{3N}^{\rm (ct)}$, we have not applied a high-momentum regulator, which would be necessary to eliminate the components of the nuclear interaction that lie beyond the breakdown scale of the effective field theory. In the case of nucleon-nucleon potentials, the cutoff scale is typically chosen $\Lambda \lesssim 700\,\text{MeV}$, beyond which the introduction of a new dynamical degree of freedom (the ρ meson with mass $m_\rho = 770\,\text{MeV}$) would be required. On the other hand, in order to fit empirical nucleon-nucleon scattering phase shift data up to laboratory energies of $E_{\rm lab} = 350\,\text{MeV}$, the cutoff is normally chosen $\Lambda \gtrsim 414\,\text{MeV}$ (the relative momentum in the center-of-mass frame corresponding to $E_{\rm lab} = 350\,\text{MeV}$). In practice,

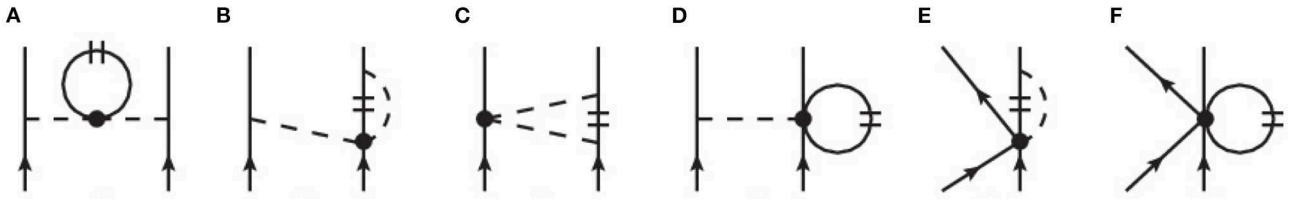


FIGURE 2 | Diagrammatic contributions to the density-dependent NN interaction derived from the N2LO chiral three-nucleon force: **(A)** one-pion-exchange propagator correction, **(B)** one-pion-exchange vertex correction, **(C)** Pauli-blocked two-pion exchange correction, **(D)** short-range one-pion-exchange vertex correction, **(E)** contact interaction vertex correction, and **(F)** two-body contact interaction.

it is found that relatively low values of the momentum-space cutoff $\Lambda \lesssim 500\,\mathrm{MeV}$ lead to perturbative nucleon-nucleon potentials, which are suitable for a wide range of methods to solve the quantum many-body problem. Such low-cutoff potentials, however, exhibit larger artifacts in calculations of the density-dependent ground state energy of nuclear matter and single-particle potential as we will discuss explicitly below. While the choice of cutoff scale is well motivated, the regulating function can take various forms. Traditionally, an exponential regulator in the incoming and outgoing relative momenta is chosen:

$$f(p', p) = \exp[-(p'/\Lambda)^{2n} - (p/\Lambda)^{2n}], \tag{15}$$

where $\vec{p} = \frac{1}{2}(\vec{p}_1 - \vec{p}_2)$ and $\vec{p}\,' = \frac{1}{2}(\vec{p}_3 - \vec{p}_4)$ for the general two-body scattering process $N(\vec{p}_1) + N(\vec{p}_2) \rightarrow N(\vec{p}_3) + N(\vec{p}_4)$, and n is an integer chosen such that the regulator affects only high powers in the chiral expansion. More recently [27, 46], the pion-exchange components of the nucleon-nucleon interaction have been regularized in coordinate space according to

$$V_\pi(\vec{r}\,)\left[1 - e^{-r^2/R^2}\right], \tag{16}$$

where $0.8\,\mathrm{fm} \leq R \leq 1.2\,\mathrm{fm}$, while the contact terms in the nuclear potential were regularized according to Equation (15) above. In previous calculations [47, 48] of the medium-dependent 2N force V_{med}, we have imposed the nonlocal regulating function above only after the momentum-space integration over k_3 is performed. This choice led to simplified analytical expressions for the density-dependent NN interaction in cold nuclear matter. A three-body regulator that treats all particles symmetrically can be defined by [49]

$$W_3 \longrightarrow W_3 F(q_1, q_2) = W_3 \exp[-(q_1/\Lambda)^4 - (q_2/\Lambda)^4], \tag{17}$$

where $\vec{q}_1 = \vec{p}\,'_1 - \vec{p}_1$ and $\vec{q}_2 = \vec{p}\,'_2 - \vec{p}_2$ are the momentum transfers for particles 1 and 2 in W_3. Analogous expressions hold for the contributions $W_1 \longrightarrow W_1 F(q_2, q_3)$ and $W_2 \longrightarrow W_2 F(q_1, q_3)$. This choice of regulating function leads to more complicated expressions for the density-dependent 2N interaction since now the regulator in general can involve the momentum k_3 over which we integrate. More importantly, the local regulator in Equation (17) leads to much stronger cutoff artifacts for the same choice of scale ($\Lambda_{\mathrm{loc}} = \Lambda_{\mathrm{nonloc}}$) as we will demonstrate in the following. Additional discussion regarding the role of cutoff artifacts on nuclear many-body calculations can be found in Dyhdalo et al. [50].

To start, when we employ the local regulator in Equation (17), we now find for the density-dependent NN interaction in isospin-symmetric nuclear matter:

$$V_{\mathrm{med}}^{(\mathrm{ct})} = \frac{c_E}{2\pi^2 f_\pi^4 \Lambda_\chi}\Big[\frac{4}{3}k_f^3\,\vec{\tau}_1\cdot\vec{\tau}_2 F^2(q^2,\Lambda) - 2\vec{\tau}_1\cdot\vec{\tau}_2 F(q^2,\Lambda)\tilde{\Gamma}_4(p) - 3\Gamma'_4(p,q)\Big], \tag{18}$$

where

$$F(q^2, \Lambda) = e^{-q^4/\Lambda^4}, \tag{19}$$

$$\tilde{\Gamma}_4(p) = \int_0^{k_f} dk \int_{-1}^{1} dx\, k^2\, F(p^2 + k^2 + 2pkx, \Lambda), \tag{20}$$

$$\Gamma'_4(p,q) = \int_0^{k_f} dk \int_{-1}^{1} dx \int_0^{2\pi} d\phi\, \frac{k^2}{2\pi} F(p^2 + k^2 + kx\sqrt{4p^2 - q^2} + qk\sqrt{1-x^2}\cos\phi, \Lambda) \times F(p^2 + k^2 + kx\sqrt{4p^2 - q^2} - qk\sqrt{1-x^2}\cos\phi, \Lambda). \tag{21}$$

In the limit of large Λ we find that $F(q^2, \Lambda) \rightarrow 1$, $\tilde{\Gamma}_4(p) \rightarrow \frac{2k_f^3}{3}$, and $\Gamma'_4(p,q) \rightarrow \frac{2k_f^3}{3}$. Thus, in this limit we clearly recover Equation (14).

Previously, for the in-medium pion self-energy correction (**Figure 2A**), with no regulator we found

$$V_{NN}^{\mathrm{med},1} = \frac{g_A^2 k_f^3}{3\pi^2 f_\pi^4}\vec{\tau}_1\cdot\vec{\tau}_2\frac{\vec{\sigma}_1\cdot\vec{q}\,\vec{\sigma}_2\cdot\vec{q}}{(m_\pi^2 + q^2)^2}\left(2c_1 m_\pi^2 + c_3 q^2\right). \tag{22}$$

With the local regulator in Equation (17) we now find

$$V_{NN}^{\mathrm{med},1} = \frac{g_A^2 k_f^3}{3\pi^2 f_\pi^4}\vec{\tau}_1\cdot\vec{\tau}_2\frac{\vec{\sigma}_1\cdot\vec{q}\,\vec{\sigma}_2\cdot\vec{q}}{(m_\pi^2 + q^2)^2}\left(2c_1 m_\pi^2 + c_3 q^2\right) F^2(q^2, \Lambda). \tag{23}$$

Previously, for the Pauli-blocked vertex correction (**Figure 2B**), we found

$$V_{NN}^{\mathrm{med},2} = \frac{g_A^2}{8\pi^2 f_\pi^4}\vec{\tau}_1\cdot\vec{\tau}_2\frac{\vec{\sigma}_1\cdot\vec{q}\,\vec{\sigma}_2\cdot\vec{q}}{m_\pi^2 + q^2} \Big(-4c_1 m_\pi^2[\Gamma_0 + \Gamma_1] - (c_3 + c_4)[q^2(\Gamma_0 + 2\Gamma_1 + \Gamma_3) + 4\Gamma_2]$$

$$+4c_4\Big[\frac{2}{3}k_f^3 - m_\pi^2\Gamma_0\Big]\Big). \quad (24)$$

When the local regulators are employed, we now find that the p-dependent auxiliary functions Γ_i must be replaced by

$$\tilde{\Gamma}_0(p) = \int_0^{k_f} dk \int_{-1}^{1} dx \, \frac{k^2}{m_\pi^2 + p^2 + k^2 + 2pkx} F(p^2 + k^2 + 2pkx, \Lambda), \quad (25)$$

$$\tilde{\Gamma}_1(p) = \int_0^{k_f} dk \int_{-1}^{1} dx \, \frac{k^3\, x/p}{m_\pi^2 + p^2 + k^2 + 2pkx} F(p^2 + k^2 + 2pkx, \Lambda), \quad (26)$$

$$\tilde{\Gamma}_2(p) = \int_0^{k_f} dk \int_{-1}^{1} dx \, \frac{k^4(1-x^2)/2}{m_\pi^2 + p^2 + k^2 + 2pkx} F(p^2 + k^2 + 2pkx, \Lambda), \quad (27)$$

$$\tilde{\Gamma}_3(p) = \int_0^{k_f} dk \int_{-1}^{1} dx \, \frac{k^4(3x^2-1)/(2p^2)}{m_\pi^2 + p^2 + k^2 + 2pkx} F(p^2 + k^2 + 2pkx, \Lambda), \quad (28)$$

where the versions of these functions without the superscript tildes in Equation (24) can be obtained by setting $\Lambda \to \infty$. In addition, the term $4c_4\left[\frac{2k_f^3}{3}\right]$ in $V_{NN}^{\rm med,2}$ must be replaced with the quantity

$$4c_4\left[\frac{2k_f^3}{3}\right] \longrightarrow 4c_4 \int_0^{k_f} dk \int_{-1}^{1} dx\, k^2\, F(p^2 + k^2 + 2pkx, \Lambda)$$
$$\equiv 4c_4 \tilde{\Gamma}_4(p). \quad (29)$$

Then the revised Pauli-blocked vertex correction has the form

$$V_{NN}^{\rm med,2} = \frac{g_A^2}{8\pi^2 f_\pi^4}\vec{\tau}_1\cdot\vec{\tau}_2 \frac{\vec{\sigma}_1\cdot\vec{q}\,\vec{\sigma}_2\cdot\vec{q}}{m_\pi^2+q^2}\Big(-4c_1 m_\pi^2[\tilde{\Gamma}_0+\tilde{\Gamma}_1]$$
$$-(c_3+c_4)[q^2(\tilde{\Gamma}_0+2\tilde{\Gamma}_1+\tilde{\Gamma}_3)+4\tilde{\Gamma}_2]$$
$$+4c_4\Big[\tilde{\Gamma}_4 - m_\pi^2\tilde{\Gamma}_0\Big]\Big)F(q^2,\Lambda). \quad (30)$$

Previously, we found for the Pauli-blocked two-pion-exchange interaction (**Figure 2C**),

$$V_{NN}^{\rm med,3} = \frac{g_A^2}{16\pi^2 f_\pi^4}\{-12c_1 m_\pi^2\left[2\Gamma_0 - (2m_\pi^2+q^2)G_0\right]$$
$$-\ c_3[8k_f^3 - 12(2m_\pi^2+q^2)\Gamma_0 - 6q^2\Gamma_1 + 3(2m_\pi^2+q^2)^2 G_0]$$
$$+4c_4\vec{\tau}_1\cdot\vec{\tau}_2(\vec{\sigma}_1\cdot\vec{\sigma}_2 q^2 - \vec{\sigma}_1\cdot\vec{q}\,\vec{\sigma}_2\cdot\vec{q})G_2$$
$$-\ (3c_3 + c_4\vec{\tau}_1\cdot\vec{\tau}_2)i(\vec{\sigma}_1+\vec{\sigma}_2)\cdot(\vec{q}\times\vec{p})$$
$$\times[2\Gamma_0 + 2\Gamma_1 - (2m_\pi^2+q^2)(G_0+2G_1)]$$
$$-12c_1 m_\pi^2 i(\vec{\sigma}_1+\vec{\sigma}_2)\cdot(\vec{q}\times\vec{p})[G_0+2G_1]$$
$$+4c_4\vec{\tau}_1\cdot\vec{\tau}_2\vec{\sigma}_1\cdot(\vec{q}\times\vec{p})\vec{\sigma}_2\cdot(\vec{q}\times\vec{p})[G_0+4G_1+4G_3]\}. \quad (31)$$

When substituting in the local regulator functions we obtain

$$V_{NN}^{\rm med,3} = \frac{g_A^2}{16\pi^2 f_\pi^4}\{-12c_1 m_\pi^2\left[2\Gamma_0' - (2m_\pi^2+q^2)G_0'\right]$$
$$-c_3[12\,\Gamma_4' - 12(2m_\pi^2+q^2)\Gamma_0' - 6q^2\Gamma_1'$$
$$+3(2m_\pi^2+q^2)^2 G_0'] + 4c_4\vec{\tau}_1\cdot\vec{\tau}_2(\vec{\sigma}_1\cdot\vec{\sigma}_2 q^2 - \vec{\sigma}_1\cdot\vec{q}\,\vec{\sigma}_2\cdot\vec{q})G_2'$$
$$-(3c_3 + c_4\vec{\tau}_1\cdot\vec{\tau}_2)i(\vec{\sigma}_1+\vec{\sigma}_2)\cdot(\vec{q}\times\vec{p})$$
$$[2\Gamma_0' + 2\Gamma_1' - (2m_\pi^2+q^2)(G_0'+2G_1')]$$
$$-12c_1 m_\pi^2 i(\vec{\sigma}_1+\vec{\sigma}_2)\cdot(\vec{q}\times\vec{p})[G_0'+2G_1']$$
$$+4c_4\vec{\tau}_1\cdot\vec{\tau}_2\vec{\sigma}_1\cdot(\vec{q}\times\vec{p})\vec{\sigma}_2\cdot(\vec{q}\times\vec{p})[G_0'+4G_1'+4G_3']\}. \quad (32)$$

In the above expressions we encounter the p- and q-dependent functions

$$G_{0,*,**}'(p,q) = \int_0^{k_f} dk \int_{-1}^{1} dx \int_0^{2\pi} d\phi \, \frac{\{k^2,k^4,k^6\}/(2\pi)}{A^2 - B^2\cos^2\phi}$$
$$F(p^2+k^2+kx\sqrt{4p^2-q^2}+qk\sqrt{1-x^2}\cos\phi,\Lambda)$$
$$F(p^2+k^2+kx\sqrt{4p^2-q^2}$$
$$-\ qk\sqrt{1-x^2}\cos\phi,\Lambda), \quad (33)$$

where $A = m_\pi^2 + p^2 + k^2 + kx\sqrt{4p^2-q^2}$ and $B = qk\sqrt{1-x^2}$. In Equation (33), the functions $G_{0,*,**}(p,q)$ are obtained from Equation (33) by substituting $\Lambda \to \infty$. In addition we encounter the following p- and q-dependent functions

$$G_1'(p,q) = \frac{\Gamma_0' - (m_\pi^2+p^2)G_0' - G_*'}{4p^2-q^2}, \quad (34)$$

$$G_{1*}'(p,q) = \frac{3\Gamma_2' + p^2\Gamma_3' - (m_\pi^2+p^2)G_*' - G_{**}'}{4p^2-q^2}, \quad (35)$$

$$G_2'(p,q) = (m_\pi^2+p^2)G_1' + G_*' + G_{1*}', \quad (36)$$

$$G_3'(p,q) = \frac{\frac{1}{2}\Gamma_1' - 2(m_\pi^2+p^2)G_1' - 2G_{1*}' - G_*'}{4p^2-q^2}, \quad (37)$$

where

$$\Gamma_0'(p,q) = \int_0^{k_f} dk \int_{-1}^{1} dx \int_0^{2\pi} d\phi$$
$$\frac{k^2/(2\pi)}{m_\pi^2+p^2+k^2+kx\sqrt{4p^2-q^2}+qk\sqrt{1-x^2}\cos\phi}$$
$$\times F(p^2+k^2+kx\sqrt{4p^2-q^2}+qk\sqrt{1-x^2}\cos\phi,\Lambda)$$
$$\times F(p^2+k^2+kx\sqrt{4p^2-q^2}-qk\sqrt{1-x^2}\cos\phi,\Lambda), \quad (38)$$

$$\Gamma_1'(p,q) = \int_0^{k_f} dk \int_{-1}^{1} dx \int_0^{2\pi} d\phi$$
$$\frac{k^3[x\sqrt{4p^2-q^2}+q\sqrt{1-x^2}\cos\phi]/(4\pi p^2)}{m_\pi^2+p^2+k^2+kx\sqrt{4p^2-q^2}+qk\sqrt{1-x^2}\cos\phi}$$
$$\times F(p^2+k^2+kx\sqrt{4p^2-q^2}+qk\sqrt{1-x^2}\cos\phi,\Lambda)$$
$$\times F(p^2+k^2+kx\sqrt{4p^2-q^2}-qk\sqrt{1-x^2}\cos\phi,\Lambda), \quad (39)$$

$$\Gamma_2'(p,q) = \int_0^{k_f} dk \int_{-1}^{1} dx \int_0^{2\pi} d\phi \; \frac{k^4 \left[4p^2 - \left(x\sqrt{4p^2-q^2} + q\sqrt{1-x^2}\cos\phi\right)^2\right]/(16\pi p^2)}{m_\pi^2 + p^2 + k^2 + kx\sqrt{4p^2-q^2} + qk\sqrt{1-x^2}\cos\phi} \times F(p^2+k^2+kx\sqrt{4p^2-q^2}+qk\sqrt{1-x^2}\cos\phi,\Lambda) \times F(p^2+k^2+kx\sqrt{4p^2-q^2}-qk\sqrt{1-x^2}\cos\phi,\Lambda), \quad (40)$$

$$\Gamma_3'(p,q) = \int_0^{k_f} dk \int_{-1}^{1} dx \int_0^{2\pi} d\phi \; \frac{k^4 \left[3\left(x\sqrt{4p^2-q^2} + q\sqrt{1-x^2}\cos\phi\right)^2 - 4p^2\right]/(16\pi p^4)}{m_\pi^2 + p^2 + k^2 + kx\sqrt{4p^2-q^2} + qk\sqrt{1-x^2}\cos\phi} \times F(p^2+k^2+kx\sqrt{4p^2-q^2}+qk\sqrt{1-x^2}\cos\phi,\Lambda) \times F(p^2+k^2+kx\sqrt{4p^2-q^2}-qk\sqrt{1-x^2}\cos\phi,\Lambda), \quad (41)$$

Additionally, we have replaced the quantity $8k_f^3$ in Equation (21) with $12\Gamma_4'$ defined in Equation (31). The term $8k_f^3$ in Equation (31) as well as all unprimed Γ and G functions can be obtained by setting $\Lambda \to \infty$. For the c_D vertex correction to one-pion exchange (**Figure 2D**), we previously had

$$V_{NN}^{\text{med},4} = -\frac{g_A c_D k_f^3}{12\pi^2 f_\pi^4 \Lambda_\chi} \frac{\vec{\sigma}_1\cdot\vec{q}\,\vec{\sigma}_2\cdot\vec{q}}{m_\pi^2+q^2}\vec{\tau}_1\cdot\vec{\tau}_2. \quad (42)$$

Including the local regulators we find

$$V_{NN}^{\text{med},4} = -\frac{g_A c_D}{8\pi^2 f_\pi^4 \Lambda_\chi} \frac{\vec{\sigma}_1\cdot\vec{q}\,\vec{\sigma}_2\cdot\vec{q}}{m_\pi^2+q^2}\vec{\tau}_1\cdot\vec{\tau}_2 \left(\frac{4}{3}k_f^3 F(q^2,\Lambda) - \Gamma_4'\right). \quad (43)$$

For the c_D vertex correction to the $2N$ contact term (**Figure 2E**), we previously had

$$V_{NN}^{\text{med},5} = \frac{g_A c_D}{16\pi^2 f_\pi^4 \Lambda_\chi}\Big\{\vec{\tau}_1\cdot\vec{\tau}_2\Big[2\vec{\sigma}_1\cdot\vec{\sigma}_2\Gamma_2 + \Big(\vec{\sigma}_1\cdot\vec{\sigma}_2\Big(2p^2 - \frac{q^2}{2}\Big) + \vec{\sigma}_1\cdot\vec{q}\,\vec{\sigma}_2\cdot\vec{q}\Big(1-\frac{2p^2}{q^2}\Big) - \frac{2}{q^2}\vec{\sigma}_1\cdot(\vec{q}\times\vec{p})\vec{\sigma}_2\cdot(\vec{q}\times\vec{p})\Big) (\Gamma_0 + 2\Gamma_1 + \Gamma_3)\Big] + 4k_f^3 - 6m_\pi^2\Gamma_0\Big\}. \quad (44)$$

Including the local regulators we obtain

$$V_{NN}^{\text{med},5} = \frac{g_A c_D}{16\pi^2 f_\pi^4 \Lambda_\chi}\left\{\vec{\tau}_1\cdot\vec{\tau}_2\left[2\vec{\sigma}_1\cdot\vec{\sigma}_2\tilde{\Gamma}_2 + \left(\vec{\sigma}_1\cdot\vec{\sigma}_2\left(2p^2-\frac{q^2}{2}\right) + \vec{\sigma}_1\cdot\vec{q}\,\vec{\sigma}_2\cdot\vec{q}\Big(1-\frac{2p^2}{q^2}\Big) - \frac{2}{q^2}\vec{\sigma}_1\cdot(\vec{q}\times\vec{p})\vec{\sigma}_2\cdot(\vec{q}\times\vec{p})\right)(\tilde{\Gamma}_0 + 2\tilde{\Gamma}_1 + \tilde{\Gamma}_3)\right] + 6\tilde{\Gamma}_4 - 6m_\pi^2\tilde{\Gamma}_0\right\}F(q^2,\Lambda). \quad (45)$$

We reiterate that the above expressions are obtained in the center-of-mass frame assuming on-shell scattering conditions. In all cases, the expressions for the in-medium 2N interaction above are well-behaved (no poles) and involve only elementary integrations.

3. APPLICATIONS OF DENSITY-DEPENDENT 2N INTERACTIONS TO NUCLEAR MANY-BODY SYSTEMS

3.1. Equation of State of Cold Nuclear Matter

The equation of state of nuclear matter gives important insights into many properties of finite nuclei, including the volume and symmetry energy contributions to the binding energy in the semi-empirical mass formula, the saturated central density of medium-mass and heavy nuclei, as well as nuclear collective excitation modes and giant resonances. The equation of state is also essential for modeling neutron stars [51–59], including their birth in core-collapse supernovae, their radii as a function of mass, their tidal deformabilities in the presence of compact binary companions, and their moments of inertia. For relatively soft equations of state, the central densities of typical neutron stars with mass $M \simeq 1.4\,M_\odot$ reach $n \simeq 3n_0$ [60], where $n_0 = 0.16\,\text{fm}^{-3}$ is the nucleon number density in the saturated interior of heavy nuclei. At such densities, three-body forces give a large contribution to the pressure and are therefore critical for understanding neutron star structure.

The first-order perturbative contribution (Hartree-Fock approximation) to the ground state energy of isospin-symmetric nuclear matter is given by

$$E_{2N}^{(1)} = \frac{1}{2}\sum_{12}\langle 12|\bar{V}_{2N}|12\rangle n_1 n_2, \quad (46)$$

for the antisymmetrized two-body force $\bar{V}_{2N}$ and

$$E_{3N}^{(1)} = \frac{1}{6}\sum_{123}\langle 123|\bar{V}_{3N}|123\rangle n_1 n_2 n_3, \quad (47)$$

for the antisymmetrized three-body force $\bar{V}_{3N}$. In the above equations, $n_i = \theta(k_f - |\vec{k}_i|)$ is the zero-temperature Fermi-Dirac distribution function with Fermi momentum k_f, and the sum is taken over the momentum, spin, and isospin of the occupied states in the Fermi sea.

In **Figure 3**, we show the density-dependence of the Hartree-Fock contribution to the ground state energy of isospin-symmetric nuclear matter from the N2LO chiral three-nucleon force in different approximations. As a representative example, we consider the low-energy constants $c_1 = -0.81\,\text{GeV}^{-1}$, $c_3 = -3.4\,\text{GeV}^{-1}$, $c_4 = 3.4\,\text{GeV}^{-1}$, $c_D = -0.24$, and $c_E = -0.106$ obtained in Coraggio et al. [61] and associated with the N3LO NN chiral interaction with cutoff scale $\Lambda = 450\,\text{MeV}$. We see that in all cases the first-order perturbative contribution from three-body forces in isospin-symmetric matter is strongly repulsive. The exact treatment of the Hartree-Fock

contribution to the ground state energy arising from the N2LO three-nucleon force is shown in **Figure 3** as the thick black line labeled "$V^{\Lambda\to\infty}_{3N,\,\mathrm{exact}}$." Employing instead the density-dependent NN interaction V_{med} with $\Lambda \to \infty$ we obtain the contribution shown with the thin blue line and labeled "$V^{\Lambda\to\infty}_{\mathrm{med}}$." Note that in order to avoid triple-counting when the density-dependent NN interaction V_{med} is used in Equation (46), we must replace $\bar{V}_{2N} \to \frac{1}{3}\bar{V}_{\mathrm{med}}$. From **Figure 3**, we observe that at the Hartree-Fock level the density-dependent NN interaction accurately reflects the physics encoded in the full three-body force. This is not a trivial observation since several approximations were employed to derive the density-dependent NN interaction from V_{3N}. In **Figure 3**, we see that the largest deviation in the two curves is only 1 MeV (or $\simeq 3\%$) at $n = 0.32\,\mathrm{fm}^{-3}$.

Imposing the nonlocal regulator in Equation (15) leads to the red dot-dashed line labeled "$V^{\Lambda}_{\mathrm{med,\,nonloc}}$." As expected, the presence of the momentum-space cutoff reduces the Hartree-Fock contribution to the ground-state energy, particularly at high densities. However, the cutoff artifacts introduced are rather small and amount to only 0.8 MeV (or $\simeq 2\%$) relative to the result from $V^{\Lambda\to\infty}_{\mathrm{med}}$ at $n = 0.32\,\mathrm{fm}^{-3}$. We note that since the Hartree-Fock contribution to the ground state energy E/A is always finite and probes only the characteristic physical energy scale of the system, the differences between $V^{\Lambda\to\infty}_{\mathrm{med}}$ and $V^{\Lambda}_{\mathrm{med,\,nonloc}}$ are true regulator artifacts. We next impose the local regulator in Equation (17), which is shown as the dotted green line in **Figure 3** and labeled "$V^{\Lambda}_{\mathrm{med,\,loc}}$." For this choice of regulator we find severe cutoff artifacts, even at low densities where one would expect the role of the regulating function to be minimal. For example, at $n = 0.10\,\mathrm{fm}^{-3}$, there is a 19% relative error between $V^{\Lambda\to\infty}_{\mathrm{med}}$ and $V^{\Lambda}_{\mathrm{med,\,loc}}$. From Equation (17), we expect the regulator to introduce corrections at order $(Q/\Lambda)^4 \sim (k_f/\Lambda)^4$. The Fermi momentum at this density is $k_f = 225\,\mathrm{MeV}$, which for the $\Lambda = 450\,\mathrm{MeV}$ chiral potential implies an error of $(k_f/\Lambda)^4 \simeq 6\%$. One key difference between the non-local and local regulators of Equations (15) and (17) is that the relative momentum ranges from $0 < k < k_f$ while the momentum transfer ranges from $0 < q < 2k_f$. Therefore, one naturally expects larger cutoff artifacts for the local regulating function in Equation (17). Indeed, when the value of the momentum-space cutoff is increased to 2Λ, as can be seen from the dashed green curve of **Figure 3**, the results from employing the local regulator are now comparable to those using the non-local regulator.

In **Figure 4**, we show the density-dependence of the Hartree-Fock contribution to the ground state energy of pure neutron matter from the N2LO chiral three-nucleon force in different approximations. Again we consider the low-energy constants $c_1 = -0.81\,\mathrm{GeV}^{-1}$, $c_3 = -3.4\,\mathrm{GeV}^{-1}$, $c_4 = 3.4\,\mathrm{GeV}^{-1}$, $c_D = -0.24$, and $c_E = -0.106$ associated with the N3LO NN chiral interaction with cutoff scale $\Lambda = 450\,\mathrm{MeV}$. However, in pure neutron matter the Hartree-Fock contribution from three-body forces is independent of c_4, c_D, and c_E. We show as the thick black line labeled "$V^{\Lambda\to\infty}_{3N,\,\mathrm{exact}}$" in **Figure 4**, the Hartree-Fock contribution to the ground-state energy of pure neutron matter. Employing the density-dependent NN interaction V_{med} with $\Lambda \to \infty$ we obtain the contribution shown with the thin blue line

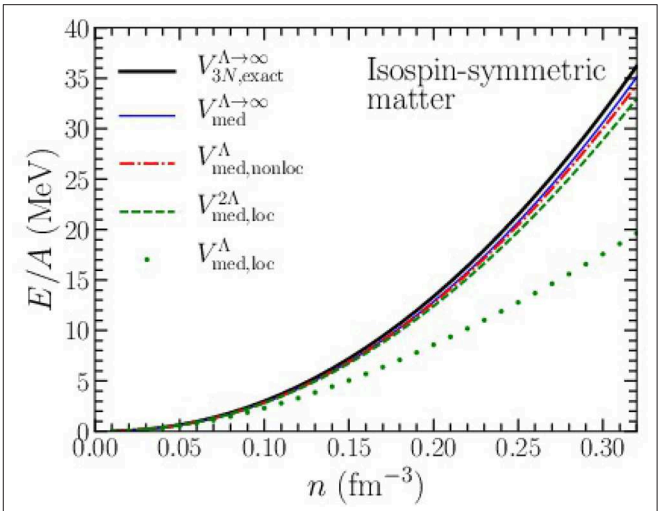


FIGURE 3 | Hartree-Fock contribution to the ground-state energy of isospin-symmetric nuclear matter as a function of density due to the N2LO chiral three-nucleon force with cutoff scale $\Lambda = 450\,\mathrm{MeV}$.

labeled "$V^{\Lambda\to\infty}_{\mathrm{med}}$." Again, at the Hartree-Fock level the density-dependent NN interaction very accurately reproduces the result from the full three-body force.

Inserting the nonlocal regulator in Equation (15) we find the red dot-dashed line labeled "$V^{\Lambda}_{\mathrm{med,\,nonloc}}$." The non-local regulator preserves the property that none of the three-body force terms proportional to c_4, c_D, and c_E contribute to the ground-state energy of pure neutron matter. We find that the momentum-space cutoff reduces the Hartree-Fock contribution to the ground-state energy even more than that in isospin-symmetric nuclear matter. This is due to the larger neutron Fermi momentum (compared to the nucleon Fermi momentum in isospin-symmetric nuclear matter at the same density). The cutoff artifacts introduced are nevertheless relatively small and amount to 2 MeV at $n = 0.32\,\mathrm{fm}^{-3}$. Finally, we impose the local regulator in Equation (17) to obtain the dotted green line labeled "$V^{\Lambda}_{\mathrm{med,\,loc}}$" in **Figure 4**. Again, the cutoff artifacts are very large. For example, at $n = 0.10\,\mathrm{fm}^{-3}$, there is now a 34% relative error between $V^{\Lambda\to\infty}_{\mathrm{med}}$ and $V_{\mathrm{med,\,loc}}$. At this density, the maximum momentum transfer is $q = 2k_f \simeq 570\,\mathrm{MeV}$, which is clearly problematic for the chosen cutoff $\Lambda = 450\,\mathrm{MeV}$. In addition to larger artifacts, the local regulator also induces contributions to the density-dependent NN interaction in pure neutron matter that now depend on the low-energy constants c_4, c_D, and c_E. In the case of pure neutron matter, diagrams (*d*), (*e*), and (*f*) in **Figure 2** produce $V^{\mathrm{med},4}_{NN} = V^{\mathrm{med},5}_{NN} = V^{\mathrm{med},6}_{NN} = 0$ with either the nonlocal regulator or no regulator at all. Instead, for the local regulator we find

$$V^{\mathrm{med},4}_{NN} = -\frac{g_A c_D}{8\pi^2 f_\pi^4 \Lambda_\chi}\frac{\vec{\sigma}_1\cdot\vec{q}\,\vec{\sigma}_2\cdot\vec{q}}{m_\pi^2+q^2}\left(\frac{2}{3}k_f^3 F(q^2,\Lambda)-\Gamma_4'\right), \quad (48)$$

which indeed vanishes when the local regulators are replaced by 1. For the c_D vertex correction to the $2N$ contact term with local

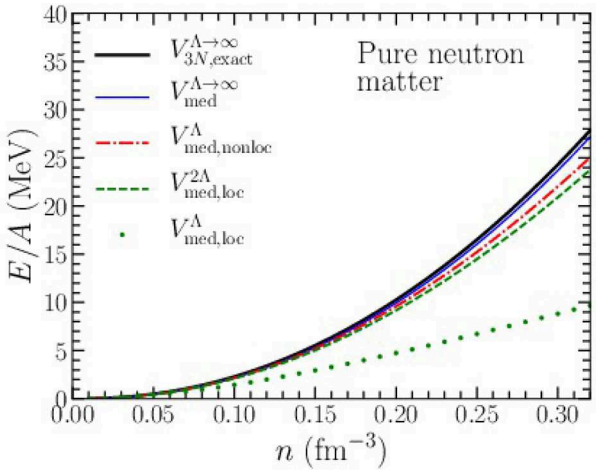


FIGURE 4 | Hartree-Fock contribution to the ground-state energy of pure neutron matter as a function of density due to the N2LO chiral three-nucleon force with cutoff scale $\Lambda = 450$ MeV.

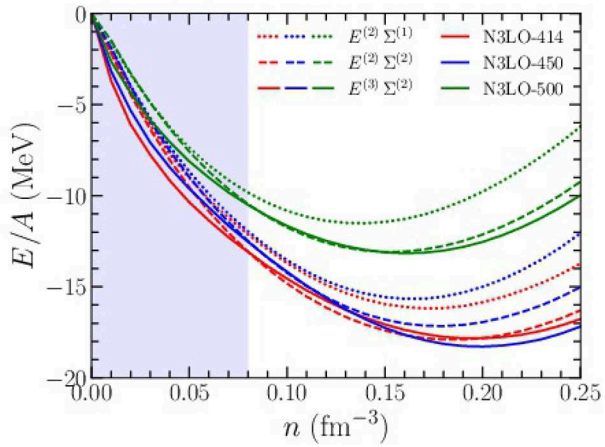


FIGURE 5 | Equation of state of isospin-symmetric nuclear matter from chiral two- and three-body forces with different choices of the momentum-space cutoff Λ and at different orders in many-body perturbation theory. The label $E^{(i)}$ denotes the i-th order in perturbation theory, and $\Sigma^{(n)}$ denotes the n-th order treatment of the self-energy. The shaded region below $n = 0.08\,\mathrm{fm}^{-3}$ represents the approximate location of the spinodal instability.

regulators we obtain

$$V_{NN}^{\mathrm{med},5} = \frac{g_A c_D}{16\pi^2 f_\pi^4 \Lambda_\chi}\Bigg\{2\vec{\sigma}_1\cdot\vec{\sigma}_2\tilde{\Gamma}_2 + \Bigg(\vec{\sigma}_1\cdot\vec{\sigma}_2\Bigg(2p^2 - \frac{q^2}{2}\Bigg) + \vec{\sigma}_1\cdot\vec{q}\,\vec{\sigma}_2\cdot\vec{q}\Bigg(1 - \frac{2p^2}{q^2}\Bigg) - \frac{2}{q^2}\vec{\sigma}_1\cdot(\vec{q}\times\vec{p})\vec{\sigma}_2\cdot(\vec{q}\times\vec{p})\Bigg)(\tilde{\Gamma}_0 + 2\tilde{\Gamma}_1 + \tilde{\Gamma}_3) + 2\tilde{\Gamma}_4 - 2m_\pi^2\tilde{\Gamma}_0\Bigg\}F(q^2,\Lambda), \tag{49}$$

where $\tilde{\Gamma}_4(p)$ is defined in Equation (20). Finally, the three-body contact term with the local regulator leads to

$$V_{NN}^{\mathrm{med},6} = \frac{c_E}{2\pi^2 f_\pi^4 \Lambda_\chi}\left[\frac{2}{3}k_f^3 F^2(q^2,\Lambda) - 2F(q^2,\Lambda)\tilde{\Gamma}_4(p) - \Gamma_4'(p,q) + \frac{4}{3}k_f^3 F(q^2,\Lambda)\right]. \tag{50}$$

Again, this term vanishes when the regulating functions are set to 1. These additional terms have been included in the present calculation of the dotted green line in **Figure 4**. Substituting $\Lambda \to 2\Lambda$ into the nonlocal regulator again reduces the cutoff artifacts, as seen in the dashed green curve of **Figure 4**.

The inclusion of three-body forces in the nuclear equation of state beyond the Hartree-Fock approximation remains challenging. While several recent works [33, 62] have computed the exact second-order contribution to the equation of state from three-body forces, the use of derived density-dependent two-body interactions allows for an approximate treatment up to third order in perturbation theory [61, 63]:

$$E^{(2)} = -\frac{1}{4}\sum_{1234}\left|\langle 12\left|\bar{V}_{\mathrm{eff}}\right|34\rangle\right|^2 \frac{n_1 n_2 \bar{n}_3 \bar{n}_4}{e_3 + e_4 - e_1 - e_2}, \tag{51}$$

$$E_{pp}^{(3)} = \frac{1}{8}\sum_{123456}\langle 12\left|\bar{V}_{\mathrm{eff}}\right|34\rangle\langle 34\left|\bar{V}_{\mathrm{eff}}\right|56\rangle\langle 56\left|\bar{V}_{\mathrm{eff}}\right|12\rangle \frac{n_1 n_2 \bar{n}_3 \bar{n}_4 \bar{n}_5 \bar{n}_6}{(e_3 + e_4 - e_1 - e_2)(e_5 + e_6 - e_1 - e_2)}, \tag{52}$$

$$E_{hh}^{(3)} = \frac{1}{8}\sum_{123456}\langle 12\left|\bar{V}_{\mathrm{eff}}\right|34\rangle\langle 34\left|\bar{V}_{\mathrm{eff}}\right|56\rangle\langle 56\left|\bar{V}_{\mathrm{eff}}\right|12\rangle \frac{\bar{n}_1 \bar{n}_2 n_3 n_4 n_5 n_6}{(e_1 + e_2 - e_3 - e_4)(e_1 + e_2 - e_5 - e_6)}, \tag{53}$$

$$E_{ph}^{(3)} = -\sum_{123456}\langle 12\left|\bar{V}_{\mathrm{eff}}\right|34\rangle\langle 54\left|\bar{V}_{\mathrm{eff}}\right|16\rangle\langle 36\left|\bar{V}_{\mathrm{eff}}\right|52\rangle \frac{n_1 n_2 \bar{n}_3 \bar{n}_4 n_5 \bar{n}_6}{(e_3 + e_4 - e_1 - e_2)(e_3 + e_6 - e_2 - e_5)}, \tag{54}$$

where $\bar{n}_j = 1 - n_j$ and $V_{\mathrm{eff}} = V_{2N} + V_{\mathrm{med}}$. The intermediate-state single-particle energies e_i in Equations (51)–(54) can be treated in several different approximations. In the simplest case, they are taken as the free-space energies: $e(k) = k^2/2M$. More generally, they can be dressed with interaction lines [64] in which case $e(k) = k^2/2M + \Re\Sigma(e(k),k)$, where $\Sigma(e(k),k)$ is the self-consistent energy- and momentum-dependent nucleon self energy.

Third-order diagrams [61] and fourth-order diagrams [33] are found to give rather small contributions (~ 2 MeV) to the equation of state up to $n = 1.5n_0$ for potentials with momentum-space cutoffs $\Lambda \simeq 400 - 500$ MeV. However, the intermediate-state energies in Equations (51)–(54) should be treated at least to second order [63] in a perturbative expansion of the self-energy. In **Figure 5**, we plot the equation of state of isospin-symmetric nuclear matter for several different choices of the cutoff scale $\Lambda = 414, 450, 500$ MeV (represented by red, blue, and green colors, respectively) and orders in many-body perturbation

theory (denoted by the symbol). In all cases we employ an N3LO chiral nucleon-nucleon interaction with only the N2LO chiral three-body force with low-energy constants fitted to the binding energies of ^{3}H and ^{3}He as well as the beta-decay lifetime of ^{3}H. For the density-dependent three-body force we use the nonlocal regulator in Equation (15). From **Figures 3**, **4**, we see that the local regulator in Equation (17) would be highly constraining and only allow for a meaningful calculation of the nuclear equation of state below saturation density. In **Figure 5**, the dotted lines denote the inclusion of second-order ground-state energy diagrams ($E^{(2)}$) with first-order self energies ($\Sigma^{(1)}$) for the intermediate-state propagators. The dashed lines denote the inclusion of second-order ground-state energy diagrams ($E^{(2)}$) with second-order self energies ($\Sigma^{(2)}$) for the intermediate-state propagators. From **Figure 5**, we see that the second-order self energy diagrams contribute $2-3$ MeV to the ground state energy per particle for densities $n \geq 0.16\,\mathrm{fm}^{-3}$. Finally, the solid lines denote the inclusion of third-order ground-state energy diagrams [$E^{(3)}$] with second-order self energies [$\Sigma^{(2)}$] for the intermediate-state propagators. In general, the sum of all third-order diagrams gives a relatively small contribution to the equation of state around saturation density. However, below the critical density for the spinodal instability ($n_c \simeq 0.08\,\mathrm{fm}^{-3}$) [65], denoted by the blue shaded region in **Figure 5**, the third-order diagrams give somewhat large effects due to the breakdown of perturbation theory. Nevertheless, the saturation of nuclear matter is robust and both the empirical saturation density and energy are within the uncertainties predicted from chiral nuclear forces. We note that the ground state energy from the N3LO-414 and N3LO-450 chiral potentials are very similar in all approximations. Both potentials are known to converge very rapidly in perturbation theory compared to the N3LO-500 potential [63], which may partly explain the similarity of their results.

3.2. Nucleon-Nucleus Optical Potentials

The theoretical description of nucleon-nucleus scattering and reactions can be greatly simplified through the introduction of optical model potentials, which replace the complicated two- and many-body interactions between projectile and target with an average one-body potential. In many-body perturbation theory, the optical potential can be identified as the nucleon self-energy, which in general is complex, non-local, and energy dependent:

$$V(\vec{r},\vec{r}\,';E) = U(\vec{r},\vec{r}\,';E) + iW(\vec{r},\vec{r}\,';E). \tag{55}$$

While phenomenological optical potentials [66] are fitted to a great amount of differential elastic scattering, total cross section, and analyzing power data, microscopic optical potentials can be constructed from high-precision two-nucleon and three-nucleon forces [67–71]. In chiral effective field theory, three-nucleon forces in particular have been shown [64, 72] to give rise to an overall repulsive single-particle potential at all projectile energies that increases strongly with the density of the medium. Three-nucleon forces are therefore essential for an accurate description of nucleon-nucleus scattering at moderate energies where the projectile penetrates the target nucleus.

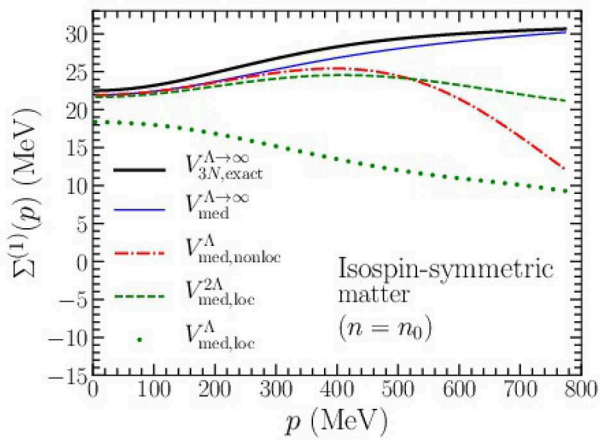


FIGURE 6 | Hartree-Fock contribution to the nucleon self energy in symmetric nuclear matter at saturation density n_0 from the N2LO chiral three-nucleon force with cutoff scale $\Lambda = 450$ MeV. Results are shown for an exact treatment as well as from the density-dependent interaction V_{med} with different choices of regulating function (see text).

In the Hartree-Fock approximation, the contribution to the non-local (but energy-independent) nucleon self energy is given by

$$\Sigma^{(1)}_{2N}(q) = \sum_1 \langle \vec{q}\,\vec{h}_1 s s_1 t t_1 | \bar{V}_{2N} | \vec{q}\,\vec{h}_1 s s_1 t t_1 \rangle n_1, \tag{56}$$

where $\bar{V}_{2N}$ denotes the antisymmetrized NN potential, $n_1 = \theta(k_f - |\vec{h}_1|)$ is the zero-temperature Fermi-Dirac distribution function, and the sum is taken over the momentum, spin, and isospin of the intermediate hole state $|\vec{h}_1, s_1, t_1\rangle$. The Hartree-Fock contribution from three-body forces is given by

$$\Sigma^{(1)}_{3N}(q) = \frac{1}{2}\sum_{12} \langle \vec{q}\,\vec{h}_1\vec{h}_2; s s_1 s_2; t t_1 t_2 | \bar{V}_{3N} | \vec{q}\,\vec{h}_1\vec{h}_2; s s_1 s_2; t t_1 t_2 \rangle n_1 n_2, \tag{57}$$

where $\bar{V}_{3N}$ is the fully-antisymmetrized three-body interaction. We have computed the Hartree-Fock contribution to the single-particle energy exactly [64] from Equation (57) as well as from Equation (56) using the density-dependent NN interaction V_{med}. Note that in order to avoid double-counting we must replace $\bar{V}_{2N} \to \frac{1}{2}\bar{V}_{\mathrm{med}}$ in Equation (56).

In **Figure 6**, we demonstrate the accuracy of using the density-dependent NN interaction in place of the full three-body force when computing the Hartree-Fock contribution to the nucleon self energy. Specifically, we plot the momentum-dependent nucleon self-energy (note that both the 2N and 3N Hartree-Fock contributions are real and energy independent) in isospin-symmetric nuclear matter at saturation density n_0. The thick black curve labeled "$V^{\Lambda}_{3N,\mathrm{exact}}$" is the exact result without a high-momentum regulator. The thin blue curve labeled "$V^{\Lambda\to\infty}_{\mathrm{med}}$" is obtained from the density-dependent NN interaction without regulator. We see that there is a systematic difference of $1-2$ MeV (or about 5%) between the two results across all momenta. This

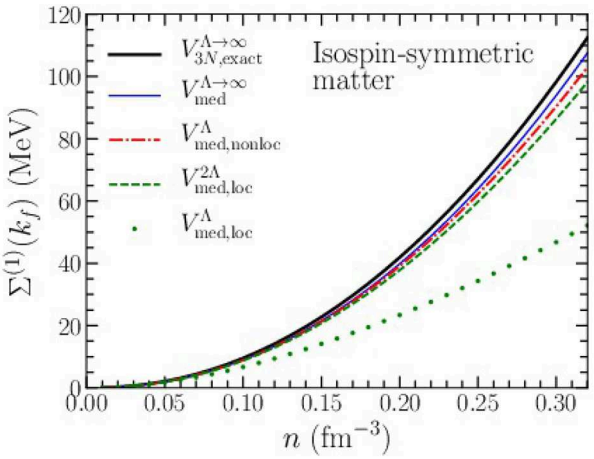


FIGURE 7 | Hartree-Fock contribution to the nucleon self energy at the Fermi momentum ($p = k_f$) in symmetric nuclear matter as a function of density from the N2LO chiral three-nucleon force with cutoff scale $\Lambda = 450$ MeV. Results are shown for an exact treatment as well as from the density-dependent interaction V_{med} with different choices of regulating function (see text).

difference represents the inherent error introduced through the approximations employed in constructing the density-dependent NN interaction. Except for this systematic reduction in the nucleon self energy, we see that overall V_{med} faithfully reproduces the exact Hartree-Fock self-energy across all momenta.

Introducing the non-local regulator in Equation (15) results in the red dash-dotted line of **Figure 6**. The artifacts associated with the nonlocal regulator grow rapidly for momenta beyond $p \simeq 400$ MeV and by $p \simeq 600$ MeV the three-nucleon force contribution to the self energy is reduced by $\sim$ 25%. This corresponds to a lab energy of about $E_{\mathrm{lab}} \simeq 175$ MeV [72] beyond which a description of nucleon-nucleus scattering in terms of chiral optical potentials becomes highly questionable. Introducing the local regulator in Equation (17) leads to the dotted green curve in **Figure 6**. We see that this regulator generates artifacts (of at least 15%) even for low-momentum particles in isospin-symmetric nuclear matter at saturation density. This is due to the already large nucleon Fermi momentum ($k_f \simeq 270$ MeV) in nuclear matter at this density. Finally, if we double the value of the momentum-space cutoff in the local regulating function, we find the results given by the dashed green curve in **Figure 6**. Again, this choice of cutoff leads to artifacts that are on par with those from the nonlocal regulator but which are noticeably smaller at the largest momenta considered.

In **Figure 7**, we plot the value of the Hartree-Fock single-particle potential at the Fermi momentum ($p = k_f$) from chiral three-body forces for densities up to $n \simeq 2n_0$. This contribution to the single-particle energy from the chiral 3NF grows approximately quadratically with the density. Again we find that the density-dependent NN interaction from the leading chiral three-nucleon force reproduces well the exact Hartree-Fock result. The artifacts introduced through the nonlocal regulator in Equation (15), the local regulator in Equation (17), and the local regulator with $\Lambda_{\mathrm{loc}} = 2\Lambda_{\mathrm{nonloc}}$ follow the same trends already observed in the Hartree-Fock contribution to the equation of state.

Recently, several works [64, 72] have included the second-order contributions to the nucleon self energy (both in isospin-symmetric and asymmetric nuclear matter):

$$\Sigma_{2N}^{(2a)}(q,\omega) = \frac{1}{2}\sum_{123}\frac{|\langle \vec{p}_1\vec{p}_3 s_1 s_3 t_1 t_3|\bar{V}_{\mathrm{eff}}|\vec{q}\,\vec{h}_2 s s_2 t t_2\rangle|^2}{\omega + e_2 - e_1 - e_3 + i\eta}\bar{n}_1 n_2 \bar{n}_3 \tag{58}$$

and

$$\Sigma_{2N}^{(2b)}(q,\omega) = \frac{1}{2}\sum_{123}\frac{|\langle \vec{h}_1\vec{h}_3 s_1 s_3 t_1 t_3|\bar{V}_{\mathrm{eff}}|\vec{q}\,\vec{p}_2 s s_2 t t_2\rangle|^2}{\omega + e_2 - e_1 - e_3 - i\eta} n_1 \bar{n}_2 n_3, \tag{59}$$

with the antisymmetrized potential $\bar{V}_{\mathrm{eff}} = \bar{V}_{2N} + \bar{V}_{\mathrm{med}}$ that includes the density-dependent interaction from the N2LO chiral three-body force. The single-particle energies in Equations (58) and (59) are computed self-consistently according to

$$e(q) = \frac{q^2}{2M} + \mathcal{R}\Sigma(e(q), q). \tag{60}$$

Generically, Equations (58) and (59) give rise to complex and energy-dependent single-particle potentials. This allows for the construction of nucleon-nucleus optical potentials that have been shown [73] to reproduce well differential elastic scattering cross sections for proton projectiles on a range of calcium targets up to about $E = 150$ MeV.

The general form of phenomenological optical potentials for nucleon-nucleus scattering is given by

$$\begin{aligned} U(r,E) \;=\; & V_V(r,E) + iW_V(r,E) + iW_D(r,E) + V_{SO}(r,E)\vec{\ell}\cdot\vec{s} \\ & + iW_{SO}(r,E)\vec{\ell}\cdot\vec{s} + V_C(r), \end{aligned} \tag{61}$$

consisting of a real volume term, an imaginary volume term, an imaginary surface term, a real spin-orbit term, an imaginary spin-orbit term, and finally a central Coulomb interaction. In Equation (61), $\vec{\ell}$ and $\vec{s}$ are the single-particle orbital angular momentum and spin angular momentum, respectively. To construct a microscopic nucleon-nucleus optical potential from the nuclear matter approach, one can employ the local density approximation (LDA):

$$V(E;r) + iW(E;r) = V(E;k_f^p(r),k_f^n(r)) + iW(E;k_f^p(r),k_f^n(r)), \tag{62}$$

where $k_f^p(r)$ and $k_f^n(r)$ are the local proton and neutron Fermi momenta. This approach can be improved by taking account of the finite range of the nuclear force through the improved local density approximation (ILDA):

$$V(E;r)_{ILDA} = \frac{1}{(t\sqrt{\pi})^3}\int V(E;r')e^{\frac{-|\vec{r}-\vec{r}'|^2}{t^2}}d^3r', \tag{63}$$

which introduces an adjustable length scale t taken to be the typical range of the nuclear force. In previous works [73, 74], this

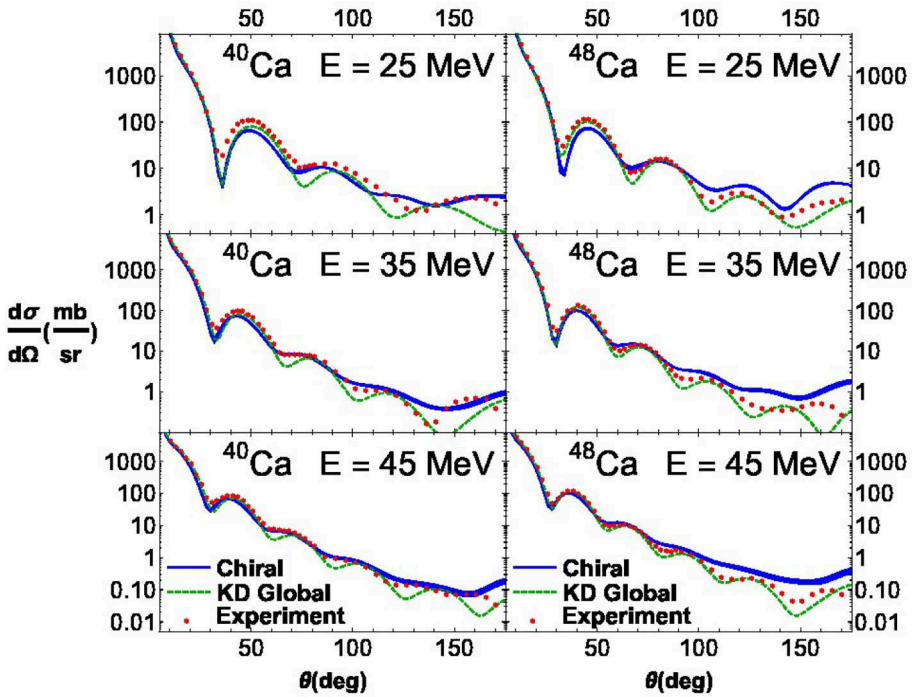


FIGURE 8 | Differential elastic scattering cross sections for proton projectiles on ^{40}Ca and ^{48}Ca targets at the energies $E = 25, 35, 45$ MeV. The cross sections computed from microscopic chiral optical potentials including two- and three-body forces are shown as the blue band. The cross sections from the Koning-Delaroche "KD" phenomenological optical potential are given by the green dashed curves, and experimental data are shown by red circles.

Guassian smearing factor was chosen to be $t \simeq 1.2$ fm and varied in order to estimate the introduced theoretical uncertainties.

The ILDA approach starts by defining the isoscalar and isovector density distributions for a given target nucleus. In our previous works [73, 75], we have employed for this purpose Skyrme energy density functionals fitted to the equation of state of isospin-asymmetric nuclear matter [76] calculated from the same chiral two- and three-body forces used to compute the nucleon self energy in Equations (56)−(59). The Gaussian smearing factor t in the ILDA was chosen in the range $1.15\,\text{fm} \leq t \leq 1.25\,\text{fm}$. The real part of the optical potential is found [73] to be in excellent agreement with that from phenomenological optical potentials [66], however, the microscopic imaginary part exhibits a surface peak that is too small and a volume contribution that grows too strongly with energy. This leads to larger total reaction cross sections [73] compared to phenomenology and experiment. This is in fact a general feature of the microscopic nuclear matter approach [77, 78] independent of the choice of nuclear potential, and previous works [74, 79] have attempted to mitigate this deficiency by introducing scaling factors for the imaginary part.

In **Figure 8**, we plot the differential elastic scattering cross sections for proton projectiles on ^{40}Ca and ^{48}Ca isotopes from microscopic optical potentials derived in chiral effective field theory. In this study we employ the N3LO nucleon-nucleon potential with momentum-space cutoff $\Lambda = 450\,\text{MeV}$ together with the density-dependent NN interaction using the nonlocal regulator in Equation (15). From **Figure 8**, we see that the predictions from chiral effective field theory (shown in blue) reproduce well the elastic scattering cross section data (red dots) from $E = 25$ to 45 MeV. The small uncertainty band associated with the blue curve is due entirely to variations in the ILDA Gaussian smearing factor. In some cases, the results from chiral nuclear optical potentials give better agreement with experiment than the Koning-Delaroche phenomenological optical potential (shown as the green dashed line in **Figure 8**). In contrast to semi-microscopic approaches [74, 79] that introduce energy-dependent scaling factors for the real and imaginary parts of the optical potential, our calculations are not fitted in any way to scattering data. Qualitatively similar results have been found [73] for proton energies as low as $E \simeq 2\,\text{MeV}$ and as high as $E \simeq 160\,\text{MeV}$. Moreover, the construction of *neutron*-nucleus optical potentials is in progress [75] and preliminary results for differential elastic scattering cross sections are found to be of similar quality to the case of proton-nucleus scattering.

3.3. Quasiparticle Interaction in Nuclear Matter

Landau's theory of normal Fermi liquids [80, 81] remains a valuable theoretical framework for understanding the excitations, response, and transport coefficients of nuclear many-body systems [82, 83]. Fermi liquid theory is based on the concept of quasiparticles, i.e., dressed single-particle excitations of a (potentially) strongly-interacting many-body system that retain key properties of the bare particles in the analogous non-interacting system. In this way, Fermi liquid theory allows for

a convenient description of the low-energy excitations of the interacting system and in the context of the nuclear many-body problem helps justify the nuclear shell model and the independent-particle description of nuclei and nuclear matter. The theory is made quantitative through the introduction of the quasiparticle interaction $\mathcal{F}$, defined as the second functional derivative of the energy with respect to the quasiparticle distribution function $n(\vec{p}\,)$:

$$E = E_0 + \sum_1 e_{\vec{p}_1}\,\delta n_{\vec{p}_1 s_1 t_1} + \frac{1}{2\Omega}\sum_{12}\mathcal{F}(\vec{p}_1 s_1 t_1;\vec{p}_2 s_2 t_2)\delta n_{\vec{p}_1 s_1 t_1}\delta n_{\vec{p}_2 s_2 t_2}, \tag{64}$$

where E_0 is the ground state energy, Ω is a normalization volume, and $\delta n_{\vec{p}_i s_i t_i}$ is the change in occupation number of state i. In Equation (64), the quasiparticle interaction $\mathcal{F}$ in momentum space has units fm^2, s_i labels the spin quantum number of quasiparticle i, and t_i labels the isospin quantum number. Enforcing the symmetries of the strong interaction and assuming that the quasiparticles lie exactly on the Fermi surface leads to the general form of the quasiparticle interaction:

$$\mathcal{F}(\vec{p}_1,\vec{p}_2\,) = \mathcal{A}(\vec{p}_1,\vec{p}_2\,) + \mathcal{A}'(\vec{p}_1,\vec{p}_2\,)\vec{\tau}_1\cdot\vec{\tau}_2, \tag{65}$$

where [84]

$$\begin{aligned}\mathcal{A}(\vec{p}_1,\vec{p}_2\,) &= f(\vec{p}_1,\vec{p}_2\,) + g(\vec{p}_1,\vec{p}_2\,)\vec{\sigma}_1\cdot\vec{\sigma}_2 + h(\vec{p}_1,\vec{p}_2\,)S_{12}(\hat{p})\\ &+k(\vec{p}_1,\vec{p}_2\,)S_{12}(\hat{P}) + \ell(\vec{p}_1,\vec{p}_2\,)(\vec{\sigma}_1\times\vec{\sigma}_2)\cdot(\hat{p}\times\hat{P}),\end{aligned} \tag{66}$$

and likewise for $\mathcal{A}'$ except with the replacement $\{f,g,h,k,\ell\}\longrightarrow\{f',g',h',k',\ell'\}$. The relative momentum is given by $\vec{p}=\vec{p}_1-\vec{p}_2$, the center-of-mass momentum is defined by $\vec{P}=\vec{p}_1+\vec{p}_2$, and the tensor operator has the form $S_{12}(\hat{v}) = 3\vec{\sigma}_1\cdot\hat{v}\,\vec{\sigma}_2\cdot\hat{v}-\vec{\sigma}_1\cdot\vec{\sigma}_2$.

For two quasiparticle momenta on the Fermi surface ($|\vec{p}_1| = |\vec{p}_2| = k_f$), the scalar functions $\{f,g,h,k,\ell,f',g',h',k',\ell'\}$ depend only the angle θ between and $\vec{p}_1$ and $\vec{p}_2$. The quasiparticle interaction can therefore be written in terms of Legendre polynomials:

$$\begin{aligned} f(\vec{p}_1,\vec{p}_2) &= \sum_{L=0}^{\infty} f_L(k_f)P_L(\cos\theta),\\ f'(\vec{p}_1,\vec{p}_2) &= \sum_{L=0}^{\infty} f'_L(k_f)P_L(\cos\theta),\\ &\cdots\end{aligned} \tag{67}$$

where $\cos\theta = \hat{p}_1\cdot\hat{p}_2$, $q = 2k_f\sin(\theta/2)$, and $P = 2k_f\cos(\theta/2)$. The coefficients $f_L, f'_L, \ldots$ are referred to as the Fermi liquid parameters. Dimensionless Fermi liquid parameters $F_L, F'_L, \ldots$ can be defined by multiplying $f_L, f'_L, \ldots$ by the density of states, e.g., for symmetric nuclear matter:

$$N_0 = 2M^* k_f/\pi^2, \tag{68}$$

where M^* the effective nucleon mass.

Originally, Fermi liquid theory was treated as a phenomenological model [82] in which the lowest-order Fermi liquid parameters would be constrained by select experimental data. From the Brueckner-Goldstone linked diagram expansion for the ground-state energy [see e.g., Equations (46)−(54)], a diagrammatic expansion for the quasiparticle interaction in terms of the nuclear potential can be obtained [85] by performing functional derivatives with respect to the occupation probabilities. Up to second order in perturbation theory one obtains for a general two-body interaction V_{2N}:

$$\mathcal{F}^{(1)}_{2N}(\vec{p}_1 s_1 t_1;\vec{p}_2 s_2 t_2) = \langle 12|\bar{V}_{2N}|12\rangle \tag{69}$$

$$\mathcal{F}^{(2pp)}_{2N}(\vec{p}_1 s_1 t_1;\vec{p}_2 s_2 t_2) = \frac{1}{2}\sum_{mn}\frac{|\langle 12|\bar{V}_{2N}|mn\rangle|^2\bar{n}_m\bar{n}_n}{e_1+e_2-e_m-e_n} \tag{70}$$

$$\mathcal{F}^{(2hh)}_{2N}(\vec{p}_1 s_1 t_1;\vec{p}_2 s_2 t_2) = \frac{1}{2}\sum_{ij}\frac{|\langle ij|\bar{V}_{2N}|12\rangle|^2 n_i n_j}{e_i+e_j-e_1-e_2} \tag{71}$$

$$\mathcal{F}^{(2ph)}_{2N}(\vec{p}_1 s_1 t_1;\vec{p}_2 s_2 t_2) = -2\sum_{jn}\frac{|\langle 1j|\bar{V}_{2N}|2n\rangle|^2 n_j\bar{n}_n}{e_1+e_j-e_2-e_n}, \tag{72}$$

which correspond, respectively to **Figures 9A–D**. The first-order contribution in Equation (69) is just the antisymmetrized two-body potential for two nucleons restricted to the Fermi surface. It contains only the four central terms f, f', g, g' as well as the two relative momentum tensor interactions h, h'. The second-order contributions in Equations (70)−(72) give rise generically to the center-of-mass tensor interactions k, k', but only the particle-hole term Equation (72) can generate the cross-vector interactions l, l' through the interference of a spin-orbit interaction with any other nonspin-orbit component in the bare nucleon-nucleon potential [86].

The expressions in Equations (69)−(72) can be decomposed into partial wave matrix elements of the bare nucleon-nucleon potential or the derived medium-dependent 2N interaction. In section 4.1 below, we give explicit expressions for the partial-wave matrix elements of the density-dependent 2N interaction derived from the N2LO [47] and N3LO [87, 88] chiral three-body force. To date, the contributions from the N2LO chiral three-body force have been included [86, 89, 90] exactly in the calculation of the quasiparticle interaction in isospin-symmetric nuclear matter and pure neutron matter. At first order in perturbation theory, the second functional derivative of Equation (47) leads to

$$\mathcal{F}^{(1)}_{3N}(\vec{p}_1 s_1 t_1,\vec{p}_2 s_2 t_2) = \sum_i n_i\langle i12|\bar{V}_{3N}|i12\rangle, \tag{73}$$

where $\bar{V}_{3N}$ is the fully antisymmetrized three-body force. This is equivalent to the definition of the density-dependent NN interaction in Equation (11) but restricted by the kinematics of quasiparticles lying on the Fermi surface. Moreover, the use of the in-medium 2N interaction constructed assuming on-shell scattering in the center-of-mass frame is not appropriate [in particular, it would give no center-of-mass

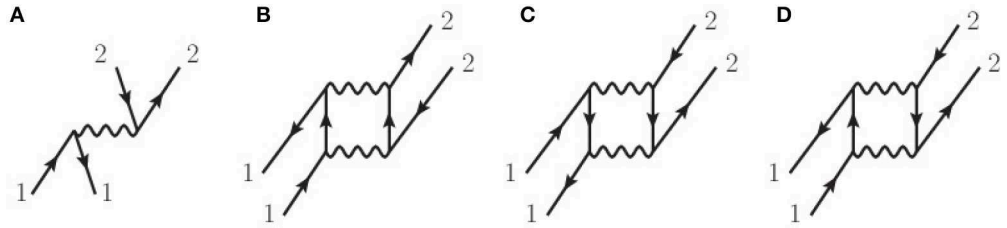


FIGURE 9 | Diagrammatic contributions to the quasiparticle interaction up to second order in perturbation theory: **(A)** first-order contribution, **(B)** second-order particle-particle contribution, **(C)** second-order hole-hole contribution, and **(D)** second-order particle-hole contribution. Wavy lines denote the antisymmetrized nuclear interaction.

dependence at leading order in Equation (73)]. Explicit and exact expressions (in the absence of a momentum-space cutoff) for the Landau Fermi liquid parameters in Equations (65)−(67) from the N2LO chiral three-nucleon force have therefore been derived in Holt and Kaiser [90]. Only the higher-order perturbative contributions to the quasiparticle interaction (where medium effects are included through normal Pauli blocking of intermediate states) utilize the in-medium 2N interaction derived in the center-of-mass frame. In the following we highlight their qualitative significance on the different terms of the quasiparticle interaction.

In **Figure 10**, we plot the dimensionless Fermi liquid parameters associated with the $L = 0, 1$ Legendre polynomials (black and red dotted lines, respectively) in isospin-symmetric nuclear matter from the N2LO chiral three-body force as a function of the nucleon density (up to $n = 0.4\,\mathrm{fm}^{-3}$). Although one may be skeptical of results from chiral effective field theory beyond $n \simeq 2n_0$, the Landau parameters must obey stability inequalities, e.g.,

$$Q_L > -(2L+1), \tag{74}$$

where $Q \in \{F, F', G, G'\}$, for the central components of the quasiparticle interaction. Therefore, we find it informative to speculate on the high-density behavior of the Landau parameters, since they might give hints toward possible instability mechanisms in dense matter. We note that complete stability conditions involving all spin-dependent interactions H, K, L (and H', K', L') that couple to G (and G') have not yet been worked out. To date only the effect of the relative tensor quasiparticle interaction has been considered [91]. We have found that in the presence of such Pomeranchuk instabilities, perturbation theory itself can be poorly behaved. For instance, in symmetric nuclear matter with density $n \lesssim n_0/2$ (where $F_0 < -1$ and nuclear matter is unstable to density fluctuations), we have computed also the third-order particle-particle contributions to the Fermi liquid parameters and found that F_0 is of comparable size to the second-order particle-particle diagrams. For other Fermi liquid parameters, however, the third-order particle-particle contributions are generally small at low densities.

The dotted lines in **Figure 10** are obtained from only the leading contribution due to three-body forces in Equation (73). The solid lines represent the Fermi liquid parameters obtained from the sum of two- and three-body forces up to second order in perturbation theory. For the second-order contributions in Equations (70)−(72) we have replaced the two-body interaction V_{2N} with $V_{2N} + V_{\mathrm{med}}$, where V_{2N} is the N3LO-450 potential and V_{med} is the consistent density-dependent interaction constructed from the N2LO three-body force with nonlocal regulator. For several Fermi liquid parameters, we see that three-body forces provide the dominant contribution at high density. For instance, the strong increase in the F_0 Landau parameter (top left panel of **Figure 10**) as a function of density is a direct result of the first-order contribution from three-body forces. The nuclear matter incompressibility $\mathcal{K} = 9\partial P/\partial\rho$, where $P = \rho^2 \frac{\partial(E/A)}{\partial\rho}$, is related to the F_0 Landau parameter through

$$\mathcal{K} = \frac{3k_f^2}{M^*}\,(1 + F_0)\,, \tag{75}$$

where M^* is the nucleon effective mass, and therefore three-body forces play a central role in the saturation mechanism [7] of nuclear matter with chiral nuclear forces. On the other hand, in some cases three-body forces play only a minor role, such as for the Landau parameters F_1 and F_0'. The former is related to the nucleon effective mass through

$$\frac{M^*}{M} = 1 + \frac{F_1}{3}, \tag{76}$$

and the latter is related to the nuclear isospin-asymmetry energy through

$$S_2 = \frac{k_f^2}{6M^*}\left(1 + F_0'\right), \tag{77}$$

where S_2 is defined as the first term in a power series expansion of the nuclear equation of state about the isospin-symmetric configuration:

$$\frac{E}{A}(n, \delta_{np}) = \frac{E}{A}(n, 0) + S_2(n)\delta_{np}^2 + \cdots \tag{78}$$

with $\delta_{np} = \frac{n_n - n_p}{n_n + n_p}$.

In general, we see from **Figure 10**, that the noncentral components K and L of the quasiparticle interaction that depend explicitly on the center-of-mass momentum $\vec{P}$ are small at nuclear saturation density. However, several of the associated Fermi liquid parameters, such as K_0', L_0, and L_1' begin to grow

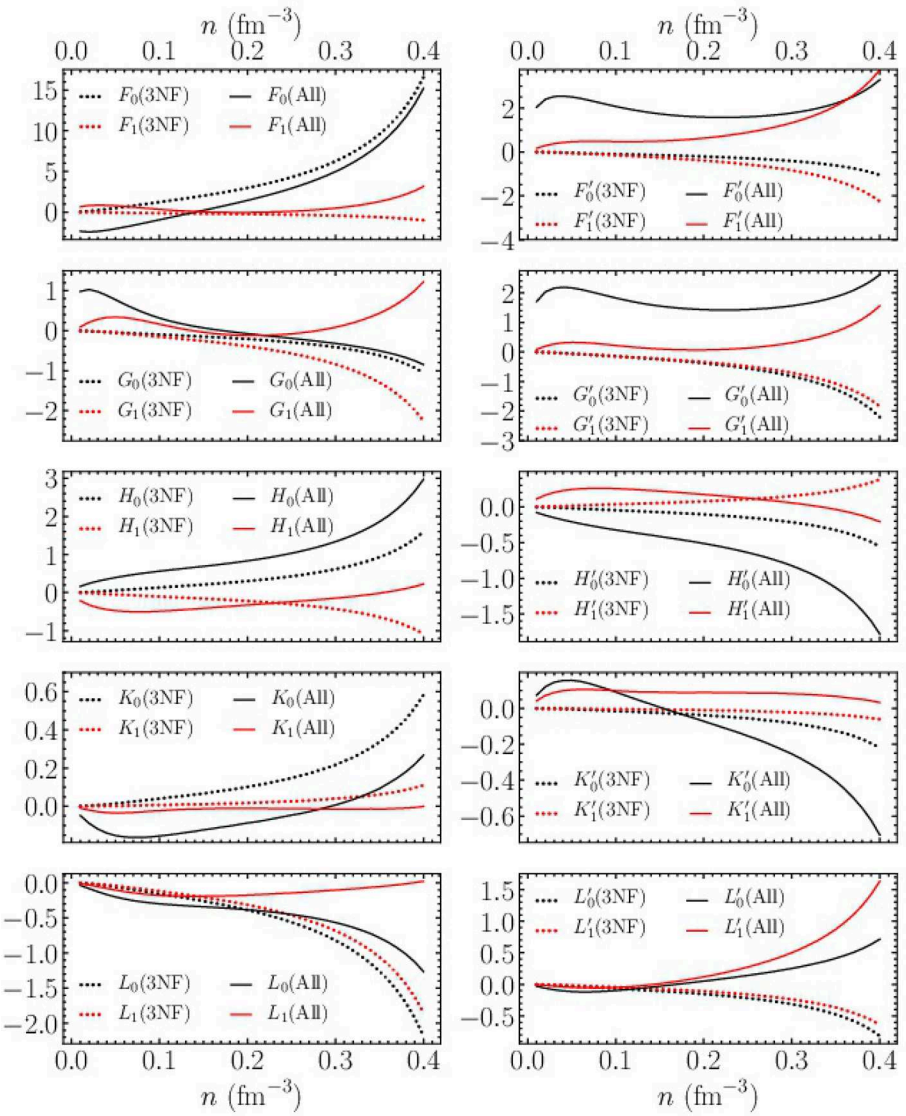


FIGURE 10 | Density-dependent dimensionless Fermi liquid parameters in isospin-symmetric nuclear matter. Dotted lines symbolize the first-order perturbative contribution from three-body forces, while solid lines represent the sum of all second-order contributions including two- and three-body forces.

rapidly for higher densities. Therefore, even though there has been little motivation to include such terms in modern energy density functionals fitted to the properties of finite nuclei, such novel interactions may become more relevant in applications related to neutron star physics. The full quasiparticle interaction in pure neutron matter has already been computed [86] with modern chiral two- and three-nucleon forces. One finds again an enhanced role of three-body forces on the incompressibility of pure neutron matter and therefore the stability of neutron stars against gravitational collapse. The more general case of the quasiparticle interaction in nuclear matter at arbitrary isospin-asymmetry is in progress.

4. CHIRAL THREE-NUCLEON FORCE AT NEXT-TO-NEXT-TO-NEXT-TO-LEADING ORDER

Up to now we have considered only the chiral three-body force at N2LO. At order N3LO in the chiral power counting, additional three- and four-nucleon forces arise without any additional undetermined low-energy constants. However, except in the case of pure neutron matter, the inclusion of the N3LO three-body contributions requires a refitting of the three-body low-energy constants c_D and c_E. The N3LO three-body force is written schematically as

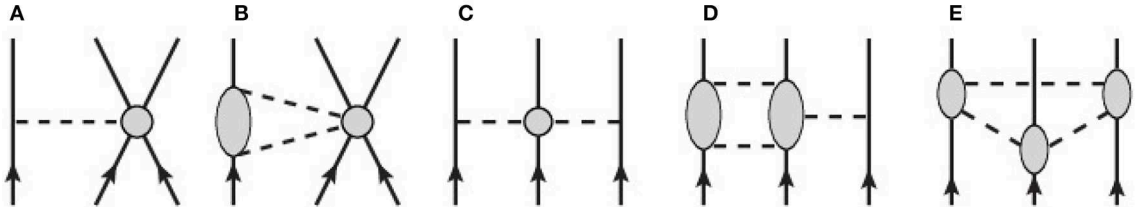


FIGURE 11 | Schematic representation of the diagrammatic contributions to the chiral three-nucleon force at next-to-next-to-next-to-leading order (N3LO): **(A)** 1π-contact interaction, **(B)** 2π-contact interaction, **(C)** 2π interaction, **(D)** 2π-1π interaction, and **(E)** ring interaction.

$$V_{3N}^{(4)} = V_{1\pi-\text{cont.}}^{(4)} + V_{2\pi-\text{cont.}}^{(4)} + V_{1/M}^{(4)} + V_{2\pi}^{(4)} + V_{2\pi-1\pi}^{(4)} + V_{\text{ring}}^{(4)}, \tag{79}$$

corresponding to the $1\pi-$contact, $2\pi-$contact, relativistic $1/M$, 2π, $2\pi-1\pi$, and ring topologies, respectively. All contributions have been worked out and presented in Ishikawa and Robilotta [28] and Bernard et al. [29, 30]. Although we will not consider their specific effects in the present work, we note that the leading four-nucleon forces have been calculated in Epelbaum [31]. In deriving the density-dependent 2N interaction at N3LO, we take the expressions from Bernard et al. [29, 30] based on the method of unitary transformations.

The density-dependent 2N interaction from the short-range terms and relativistic corrections, shown diagrammatically in **Figures 11A,B**, was computed first in Kaiser and Niessner [87]. Results were derived in the absence of a regulating function depending explicitly on the value of the intermediate-state momentum k_3 in Equation (11). The resulting expressions for V_{med} obtained from the N3LO 3N force could therefore be simplified to analytical expressions involving at most a one-dimensional integration. In Kaiser and Niessner [87], it was found that the 1π-exchange contact topology proportional to the 2N low-energy constant C_T gives rise to a vanishing contribution to V_{med} in isospin-symmetric nuclear matter. The density-dependent 2N interaction derived from the long-range contributions to the N3LO three-body force, shown diagrammatically in **Figures 11C–E**, was calculated in Kaiser and Singh [88]. Again, the integration over the three-dimensional filled Fermi sphere could be performed up to at most one remaining integration. The formulas for the density-dependent NN interaction from the N3LO three-body force are quite lengthy, and we refer the reader to Kaiser and Niessner [87] and Kaiser and Singh [88] for additional details.

4.1. Partial-Wave Decomposition

The analytical expressions for the medium-dependent 2N potential V_{med} obtained from the N3LO chiral three-body force [87, 88] can be conveniently understood by examining their attractive or repulsive effects in various partial waves. For comparison we will show also the lowest-order partial-wave contributions from the N2LO chiral three-body force, however, we note that the values of the three-body contact terms will need to be refitted in order to make a consistent comparison. In all cases, we choose the values $c_1 = -0.81\,\text{GeV}^{-1}$, $c_3 = -3.4\,\text{GeV}^{-1}$, $c_4 = 3.4\,\text{GeV}^{-1}$, $c_D = -0.24$, and $c_E = -0.106$, which have been used in other calculations presented in this work. We recall that the low-energy constants c_D and c_E of the N2LO chiral 3N force are fitted (including the N3LO chiral 2N interaction with cutoff scale $\Lambda = 450\,\text{MeV}$) to the binding energies of ^{3}H and ^{3}He as well as the beta-decay lifetime of ^{3}H. Comparing to the values of c_D and c_E fitted in combination with the N2LO two-body force [see Table II of [12]], we do not expect qualitative differences in the results below coming from these two different choices in the chiral order. For the leading-order (LO) contact term C_T that appears in the 1π- and 2π-contact topologies, we use the value $C_T = -2.46491\,\text{GeV}^{-2}$ from the N3LO-450 2N potential.

We follow the description in Erkelenz et al. [92] to obtain the diagonal momentum-space partial-wave matrix elements of the density-dependent NN interaction. With start with the form of a general nucleon-nucleon potential:

$$\begin{aligned} V(\vec{p},\vec{q}\,) &= V_C + \vec{\tau}_1\cdot\vec{\tau}_2\, W_C + \left[V_S + \vec{\tau}_1\cdot\vec{\tau}_2\, W_S\right]\vec{\sigma}_1\cdot\vec{\sigma}_2 \\ &+ \left[V_T + \vec{\tau}_1\cdot\vec{\tau}_2\, W_T\right]\vec{\sigma}_1\cdot\vec{q}\,\vec{\sigma}_2\cdot\vec{q} \\ &+ \left[V_{SO} + \vec{\tau}_1\cdot\vec{\tau}_2\, W_{SO}\right] i(\vec{\sigma}_1+\vec{\sigma}_2)\cdot(\vec{q}\times\vec{p}\,) \\ &+ \left[V_Q + \vec{\tau}_1\cdot\vec{\tau}_2\, W_Q\right]\vec{\sigma}_1\cdot(\vec{q}\times\vec{p}\,)\,\vec{\sigma}_2\cdot(\vec{q}\times\vec{p}\,), \end{aligned} \tag{80}$$

where the subscripts refer to the central (C), spin-spin (S), tensor (T), spin-orbit (SO), and quadratic spin orbit (Q) components, each with an isoscalar (V) and isovector (W) version. The diagonal (in momentum space) partial-wave matrix elements for different spin and orbital angular momentum channels are then given in terms of the functions $U_K = V_K + (4I-3)W_K$, where $K \in \{C, S, T, SO, Q\}$ and the total isospin quantum number takes the values $I = 0, 1$. Explicit expressions can be found in Holt et al. [47].

In **Figure 12**, we show the $^1S_0$, $^3S_1$, $^3D_1$, $^3S_1 - {}^3D_1$ diagonal momentum-space matrix elements of V_{med} from the N2LO (blue circles) and N3LO (red diamonds) chiral three-nucleon force in isospin-symmetric nuclear matter at the density $n = n_0$. Note that we have multiplied the matrix elements by the nucleon mass M to obtain dimensions of [fm]. Interestingly, we observe that the total N3LO three-body force in these partial-wave channels is roughly equal in magnitude but opposite in sign compared to the N2LO three-body force. Whereas, the N2LO three-body force is largely repulsive in symmetric nuclear matter at saturation density, the N3LO three-body force is strongly attractive, except in the case of the coupled $^3S_1 - {}^3D_1$ tensor channel. One should keep in mind, however, that the low-energy constants c_D and c_E must be refitted after the introduction of the N3LO three-body force. One might expect

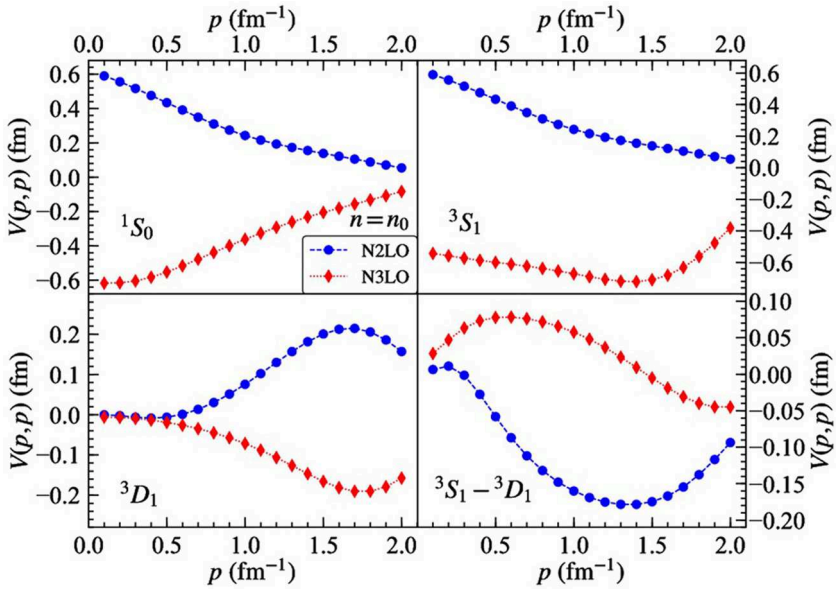


FIGURE 12 | Diagonal momentum-space matrix elements of $V_{\rm med}$ associated with the total N2LO and N3LO three-body force in the $^1S_0$ and $^3S_1 - {}^3D_1$ partial-wave channels at $n = n_0$ in isospin-symmetric nuclear matter.

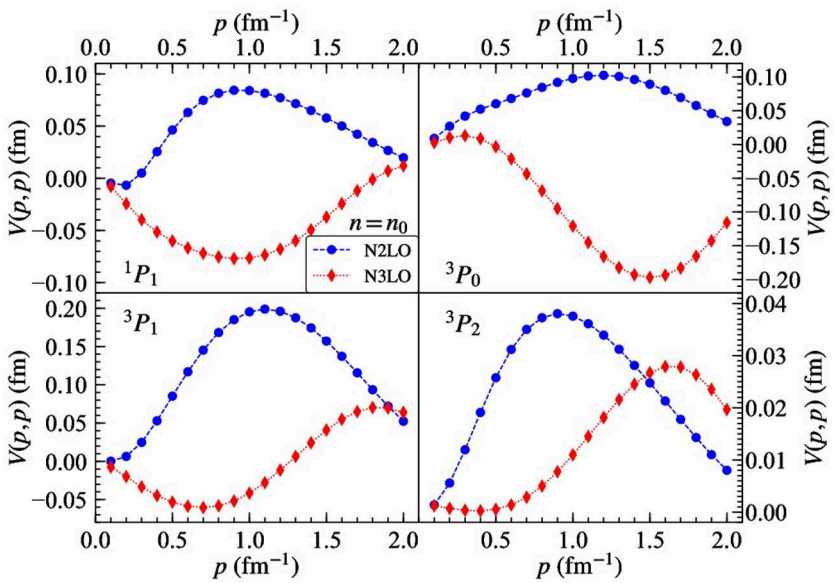


FIGURE 13 | Diagonal momentum-space matrix elements of $V_{\rm med}$ associated with the total N2LO and N3LO three-body force in the $^1P_1$, $^3P_0$, $^3P_1$, and $^3P_2$ partial-wave channels at $n = n_0$ in isospin-symmetric nuclear matter.

from the above observations that the N2LO three-body force would be enhanced in order to offset the opposite behavior introduced from the N3LO three-body force in the lowest partial-wave channels.

In **Figure 13**, we show the $^1P_1$, $^3P_0$, $^3P_1$, and $^3P_2$ diagonal momentum-space matrix elements of $V_{\rm med}$ from the N2LO (blue circles) and N3LO (red diamonds) chiral three-nucleon force in isospin-symmetric nuclear matter at the density $n = n_0$. In both the $^1P_1$ and $^3P_0$ channels, the N2LO and N3LO contributions are approximately equal in magnitude but opposite in sign. In the $^3P_1$ channel, which is repulsive in the bare 2N potential, we see that the combination of N2LO and N3LO contributions enhances the repulsion. The $^3P_2$ channel, which is attractive in the free-space 2N potential, also receives repulsive contributions from the N2LO and N3LO in-medium interaction $V_{\rm med}$. The feature that N3LO loop corrections are not small compared to N2LO tree contributions has been seen in several instances, e.g., in pion-nucleon scattering [93] as well as the three-nucleon force

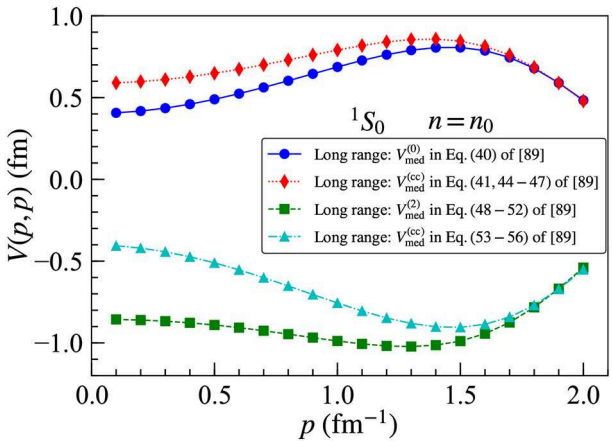


FIGURE 14 | Diagonal momentum-space matrix elements of the N3LO three-body force for selected topologies in the $^1S_0$ partial-wave channel at saturation density n_0 in isospin-symmetric nuclear matter.

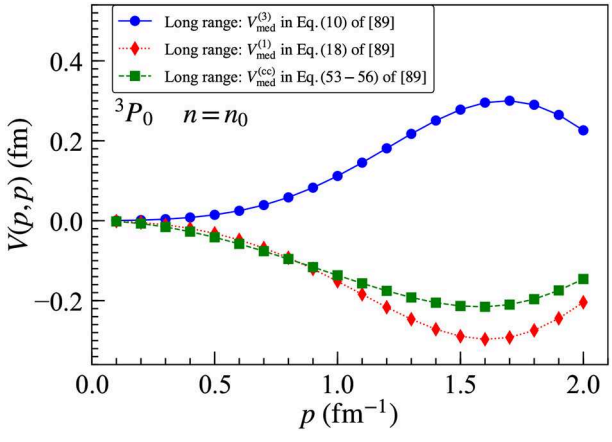


FIGURE 15 | Diagonal momentum-space matrix elements of the N3LO three-body force for selected topologies in the $^3P_0$ partial-wave channel at saturation density n_0 in isospin-symmetric nuclear matter.

derivation [29] and its application [94]. The results presented in **Figures 12**, **13** are state of the art and may change if the effects of sub-sub-leading chiral 3N forces are included. For the $2\pi - 1\pi$ and ring topologies, the N4LO corrections are sizable and dominate in most cases over the nominally leading N3LO terms [95].

The long-range parts of the N3LO chiral three-body force are expected [96] to give larger contributions to the equation of state than the relativistic $1/M$ corrections and the $2\pi-$contact topologies. Due to the large number of contributions to $V_{\rm med}$ at N3LO, we only show selected results for individual topologies. In **Figure 14**, we plot several of the dominant pion-ring contributions to the $^1S_0$ partial-wave matrix elements for the density-dependent NN interaction derived from the N3LO chiral three-body force. We see that individual long-range contributions are large, but sizable cancelations lead to an overall reduced attractive $^1S_0$ partial-wave channel at low momenta. In **Figure 15**, we plot several of the important 2π, 2π-1π, and ring topology contributions to the $^3P_0$ partial-wave matrix elements of the density-dependent NN interaction derived from the N3LO chiral three-body force. We again find large cancelations among individual terms, but the sum produces significant attraction in this partial-wave channel.

5. SUMMARY AND CONCLUSIONS

We have reviewed the construction and implementation of density-dependent two-body interactions from three-body forces at N2LO and N3LO in the chiral expansion. We showed that at leading order in many-body perturbation theory, the in-medium 2N interaction reproduces very well the exact contributions to the nuclear equation of state and nucleon self energy from the complete three-body force. The standard nonlocal high-momentum regulator used in our previous works leads to simpler analytical expressions for the density-dependent 2N interaction, consistency with the bare 2N potential, and relatively small artifacts in both the equation of state up to twice saturation density and the single-particle potential up to $p \simeq 400-500$ MeV at nuclear matter saturation density. Local 3N regulators with the same value of the cutoff, $\Lambda_{\rm loc} = \Lambda_{\rm nonloc}$, have been commonly used in previous studies of nuclear few-body systems, but these are shown to produce very large artifacts, even in the nuclear equation of state at saturation density. This could be remedied by choosing a local regulating function with $\Lambda_{\rm loc} = 2\Lambda_{\rm nonloc}$, which is well-motivated since the momentum transfer q can reach values twice as large as the relative momentum for two particles on the Fermi surface.

The use of medium-dependent two-body interactions has been shown to facilitate the implementation of three-body forces in higher-order perturbative calculations of the nuclear equation of state, single-particle potential, and quasiparticle interaction. In particular, nuclear matter was shown to saturate at the correct binding energy and density within theoretical uncertainties when computed up to third-order in perturbation theory. Moreover, microscopic nucleon-nucleus optical potentials derived from chiral two- and three-body forces have been shown to accurately predict proton elastic scattering cross sections on calcium isotopes up to projectile energies of $E \simeq 150$ MeV. The use of medium-dependent NN potentials derived from the N3LO chiral three-body force for calculations of the nuclear equation of state, single-particle potential, and quasiparticle interaction remain a topic of future research. As a first step, we have performed a partial-wave decomposition of $V_{\rm med}$ at N3LO in the chiral expansion and shown that the effective interaction is expected to be attractive in symmetric nuclear matter around saturation density.

DATA AVAILABILITY STATEMENT

The datasets generated for this study are available on request to the corresponding author.

AUTHOR CONTRIBUTIONS

JH was primarily responsible for the preparation of the manuscript. JH, MK, and NK contributed to analytical derivations and their numerical implementation.

FUNDING

Work of JH was supported by the National Science Foundation under Grant No. PHY1652199 and by the U.S. Department of Energy National Nuclear Security Administration under Grant No. DE-NA0003841. The work of MK was supported in part by JSPS Grant-in-Aid for JSPS Research Fellow No. 18J15329. The work of NK has been supported in part by DFG and NSFC (CRC110).

ACKNOWLEDGMENTS

Portions of this research were conducted with the advanced computing resources provided by Texas A&M High Performance Research Computing. This manuscript has been released as a Pre-Print at [97].

REFERENCES

1. Hergert H, Bogner SK, Binder S, Calci A, Langhammer J, Roth R, et al. In-medium similarity renormalization group with chiral two- plus three-nucleon interactions. *Phys Rev C.* (2013) **87**:034307. doi: 10.1103/PhysRevC.87.034307
2. Hebeler K, Holt JD, Menendez J, Schwenk A. Nuclear forces and their impact on neutron-rich nuclei and neutron-rich matter. *Annu Rev Nucl Part Sci.* (2015) **65**:457. doi: 10.1146/annurev-nucl-102313-025446
3. Carlson J, Gandolfi S, Pederiva F, Pieper SC, Schiavilla R, Schmidt KE, et al. Quantum Monte Carlo methods for nuclear physics. *Rev Mod Phys.* (2015) **87**:1067. doi: 10.1103/RevModPhys.87.1067
4. Navratil P, Quaglioni S, Hupin G, Romero-Redondo C, Calci A. Unified ab initio approaches to nuclear structure and reactions. *Phys Scripta.* (2016) **91**:053002. doi: 10.1088/0031-8949/91/5/053002
5. Wiringa RB, Fiks V, Fabrocini A. Equation of state for dense nucleon matter. *Phys Rev C.* (1988) **38**:1010. doi: 10.1103/PhysRevC.38.1010
6. Baldo M, Bombaci I, Burgio GF. Microscopic nuclear equation of state with three-body forces and neutron star structure. *Astron Astrophys.* (1997) **328**:274.
7. Bogner SK, Schwenk A, Furnstahl RJ, Nogga A. Is nuclear matter perturbative with low-momentum interactions? *Nucl Phys.* (2005) **A763**:59. doi: 10.1016/j.nuclphysa.2005.08.024
8. Coraggio L, Holt JW, Itaco N, Machleidt R, Sammarruca F. Reduced regulator dependence of neutron-matter predictions with perturbative chiral interactions. *Phys Rev C.* (2013) **87**:014322. doi: 10.1103/PhysRevC.87.014322
9. Gezerlis A, Tews I, Epelbaum E, Gandolfi S, Hebeler K, Nogga A, et al. Quantum Monte Carlo calculations with chiral effective field theory interactions. *Phys Rev Lett.* (2013) **111**:032501. doi: 10.1103/PhysRevLett.111.032501
10. Baardsen G, Ekström A, Hagen G, Hjorth-Jensen M. Coupled-Cluster studies of infinite nuclear matter. *Phys Rev C.* (2013) **88**:054312. doi: 10.1103/PhysRevC.88.054312
11. Carbone A, Rios A, Polls A. Correlated density-dependent chiral forces for infinite-matter calculations within the Green's function approach. *Phys Rev C.* (2014) **90**:054322. doi: 10.1103/PhysRevC.90.054322
12. Sammarruca F, Coraggio L, Holt JW, Itaco N, Machleidt R, Marcucci LE. Toward order-by-order calculations of the nuclear and neutron matter equations of state in chiral effective field theory. *Phys Rev C.* (2015) **91**:054311. doi: 10.1103/PhysRevC.91.054311
13. Drischler C, Carbone A, Hebeler K, Schwenk A. Neutron matter from chiral two- and three-nucleon calculations up to N3LO. *Phys Rev C.* (2016) **94**:054307. doi: 10.1103/PhysRevC.94.054307
14. Akmal A, Pandharipande VR, Ravenhall DG. Equation of state of nucleon matter and neutron star structure. *Phys Rev C.* (1998) **58**:1804. doi: 10.1103/PhysRevC.58.1804
15. Barrett BR, Navrátil P, Vary JP. Ab initio no core shell model. *Prog Part Nucl Phys.* (2013) **69**:131. doi: 10.1016/j.ppnp.2012.10.003
16. Hagen G, Hjorth-Jensen M, Jansen GR, Machleidt R, Papenbrock T. Evolution of shell structure in neutron-rich calcium isotopes. *Phys Rev Lett.* (2012) **109**:032502. doi: 10.1103/PhysRevLett.109.032502
17. Hagen G, Papenbrock T, Hjorth-Jensen M, Dean DJ. Coupled-cluster computations of atomic nuclei. *Rept Prog Phys.* (2014) **77**:096302. doi: 10.1088/0034-4885/77/9/096302
18. Somà V, Barbieri C, Duguet T. Ab-initio Gorkov-Green's function calculations of open-shell nuclei. *Phys Rev C.* (2013) **87**:011303. doi: 10.1103/PhysRevC.87.011303
19. Roth R, Langhammer J, Calci A, Binder S, Navrátil P. Similarity-transformed chiral NN+3N interactions for the ab initio description of 12-C and 16-O. *Phys Rev Lett.* (2011) **107**:072501. doi: 10.1103/PhysRevLett.107.072501
20. Stroberg SR, Bogner SK, Hergert H, Holt JD. Nonempirical interactions for the nuclear shell model: an update. *Annu Rev Nucl Part Sci.* (2019) **69**:307. doi: 10.1146/annurev-nucl-101917-021120
21. Otsuka T, Suzuki T, Holt JD, Schwenk A, Akaishi Y. Three-body forces and the limit of oxygen isotopes. *Phys Rev Lett.* (2010) **105**:032501. doi: 10.1103/PhysRevLett.105.032501
22. Hagen G, Hjorth-Jensen M, Jansen GR, Machleidt R, Papenbrock T. Continuum effects and three-nucleon forces in neutron-rich oxygen isotopes. *Phys Rev Lett.* (2012) **108**:242501. doi: 10.1103/PhysRevLett.108.242501
23. Weinberg S. Phenomenological lagrangians. *Phys A.* (1979) **96**:327. doi: 10.1016/0378-4371(79)90223-1
24. Epelbaum E, Hammer HW, Meißner UG. Modern theory of nuclear forces. *Rev Mod Phys.* (2009) **81**:1773. doi: 10.1103/RevModPhys.81.1773
25. Machleidt R, Entem DR. Chiral effective field theory and nuclear forces. *Phys Rept.* (2011) **503**:1. doi: 10.1016/j.physrep.2011.02.001
26. Entem DR, Machleidt R, Nosyk Y. High-quality two-nucleon potentials up to fifth order of the chiral expansion. *Phys Rev C.* (2017) **96**:024004. doi: 10.1103/PhysRevC.96.024004
27. Reinert P, Krebs H, Epelbaum E. Semilocal momentum-space regularized chiral two-nucleon potentials up to fifth order. *Eur Phys J A.* (2018) **54**:86. doi: 10.1140/epja/i2018-12516-4
28. Ishikawa S, Robilotta MR. Two-pion exchange three-nucleon potential: $O(q^4)$ chiral expansion. *Phys Rev C.* (2007) **76**:102502. doi: 10.1103/PhysRevC.76.014006
29. Bernard V, Epelbaum E, Krebs H, Meissner UG. Subleading contributions to the chiral three-nucleon force. I. Long-range terms. *Phys Rev C.* (2008) **77**:064004. doi: 10.1103/PhysRevC.77.064004
30. Bernard V, Epelbaum E, Krebs H, Meissner UG. Subleading contributions to the chiral three-nucleon force II: Short-range terms and relativistic corrections. *Phys Rev C.* (2011) **84**:054001. doi: 10.1103/PhysRevC.84.054001
31. Epelbaum E. Four-nucleon force in chiral effective field theory. *Phys Lett.* (2006) **B639**:456. doi: 10.1016/j.physletb.2006.06.046
32. Hagen G, Papenbrock T, Dean DJ, Schwenk A, Nogga A, Włoch M, et al. Coupled-cluster theory for three-body Hamiltonians. *Phys Rev C.* (2007) **76**:034302. doi: 10.1103/PhysRevC.76.034302
33. Drischler C, Hebeler K, Schwenk A. Chiral interactions up to next-to-next-to-next-to-leading order and nuclear saturation. *Phys Rev Lett.* (2019) **122**:042501. doi: 10.1103/PhysRevLett.122.042501
34. Büttiker P, Meissner UG. Pion nucleon scattering inside the Mandelstam triangle. *Nucl Phys.* (2000) **A668**:97. doi: 10.1016/S0375-9474(99)00813-1
35. Hoferichter M, Ruiz de Elvira J, Kubis B, Meißner UG. Matching pion-nucleon Roy-Steiner equations to chiral perturbation theory. *Phys Rev Lett.* (2015) **115**:192301. doi: 10.1103/PhysRevLett.115.192301

36. Rentmeester MCM, Timmermans RGE, de Swart JJ. Determination of the chiral coupling constants c(3) and c(4) in new pp and np partial wave analyses. *Phys Rev C.* (2003) **67**:044001. doi: 10.1103/PhysRevC.67.044001
37. Entem DR, Machleidt R. Accurate charge dependent nucleon nucleon potential at fourth order of chiral perturbation theory. *Phys Rev C.* (2003) **68**:041001. doi: 10.1103/PhysRevC.68.041001
38. Epelbaum E, Nogga A, Glöckle W, Kamada H, Meißner UG, Witała H. Three nucleon forces from chiral effective field theory. *Phys Rev C.* (2002) **66**:064001. doi: 10.1103/PhysRevC.66.064001
39. Piarulli M, Baroni A, Girlanda L, Kievsky A, Lovato A, Lusk E, et al. Light-nuclei spectra from chiral dynamics. *Phys Rev Lett.* (2018) **120**:052503. doi: 10.1103/PhysRevLett.120.052503
40. Hebeler K, Bogner SK, Furnstahl RJ, Nogga A, Schwenk A. Improved nuclear matter calculations from chiral low-momentum interactions. *Phys Rev C.* (2011) **83**:031301. doi: 10.1103/PhysRevC.83.031301
41. Navrátil P, Gueorguiev VG, Vary JP, Ormand WE, Nogga A. Structure of A=10-13 nuclei with two plus three-nucleon interactions from chiral effective field theory. *Phys Rev Lett.* (2007) **99**:042501. doi: 10.1103/PhysRevLett.99.042501
42. Ekström A, Jansen GR, Wendt KA, Hagen G, Papenbrock T, Carlsson BD, et al. Accurate nuclear radii and binding energies from a chiral interaction. *Phys Rev C.* (2015) **91**:051301. doi: 10.1103/PhysRevC.91.051301
43. Gardestig A, Phillips DR. How low-energy weak reactions can constrain three-nucleon forces and the neutron-neutron scattering length. *Phys Rev Lett.* (2006) **96**:232301. doi: 10.1103/PhysRevLett.96.232301
44. Gazit D, Quaglioni S, Navrátil P. Three-nucleon low-energy constants from the consistency of interactions and currents in chiral effective field theory. *Phys Rev Lett.* (2009) **103**:102502. doi: 10.1103/PhysRevLett.103.102502
45. Hebeler K, Schwenk A. Chiral three-nucleon forces and neutron matter. *Phys Rev C.* (2010) **82**:014314. doi: 10.1103/PhysRevC.82.014314
46. Epelbaum E, Krebs H, Meißner UG. Improved chiral nucleon-nucleon potential up to next-to-next-to-next-to-leading order. *Eur Phys J A.* (2015) **51**:53. doi: 10.1140/epja/i2015-15053-8
47. Holt JW, Kaiser N, Weise W. Density-dependent effective nucleon-nucleon interaction from chiral three-nucleon forces. *Phys Rev C.* (2010) **81**:024002. doi: 10.1103/PhysRevC.81.024002
48. Wellenhofer C, Holt JW, Kaiser N, Weise W. Nuclear thermodynamics from chiral low-momentum interactions. *Phys Rev C.* (2014) **89**:064009. doi: 10.1103/PhysRevC.89.064009
49. Navrátil P. Local three-nucleon interaction from chiral effective field theory. *Few Body Syst.* (2007) **41**:117. doi: 10.1007/s00601-007-0193-3
50. Dyhdalo A, Furnstahl RJ, Hebeler K, Tews I. Regulator artifacts in uniform matter for chiral interactions. *Phys Rev C.* (2016) **94**:034001. doi: 10.1103/PhysRevC.94.034001
51. Lattimer JM, Prakash M. Nuclear matter and its role in supernovae, neutron stars and compact object binary mergers. *Phys Rept.* (2000) **121**:333–4. doi: 10.1016/S0370-1573(00)00019-3
52. Steiner AW, Prakash M, Lattimer JM, Ellis PJ. Isospin asymmetry in nuclei and neutron stars. *Phys Rept.* (2005) **411**:325–75. doi: 10.1016/j.physrep.2005.02.004
53. Lattimer JM, Prakash M. Neutron star observations: prognosis for equation of state constraints. *Phys Rept.* (2007) **442**:109–65. doi: 10.1016/j.physrep.2007.02.003
54. Hebeler K, Lattimer JM, Pethick CJ, Schwenk A. Constraints on neutron star radii based on chiral effective field theory interactions. *Phys Rev Lett.* (2010) **105**:161102. doi: 10.1103/PhysRevLett.105.161102
55. Annala E, Gorda T, Kurkela A, Vuorinen A. Gravitational-wave constraints on the neutron-star-matter equation of state. *Phys Rev Lett.* (2018) **120**:172703. doi: 10.1103/PhysRevLett.120.172703
56. Most ER, Weih LR, Rezzolla L, Schaffner-Bielich J. New constraints on radii and tidal deformabilities of neutron stars from GW170817. *Phys Rev Lett.* (2018) **120**:261103. doi: 10.1103/PhysRevLett.120.261103
57. Lim Y, Holt JW. Neutron star tidal deformabilities constrained by nuclear theory and experiment. *Phys Rev Lett.* (2018) **121**:062701. doi: 10.1103/PhysRevLett.121.062701
58. Landry P, Kumar B. Constraints on the moment of inertia of PSR J0737-3039A from GW170817. *Astrophys J.* (2018) **868**:L22. doi: 10.3847/2041-8213/aaee76
59. Lim Y, Holt JW, Stahulak RJ. Predicting the moment of inertia of pulsar J0737-3039A from Bayesian modeling of the nuclear equation of state. *Phys Rev C.* (2019) **100**:035802. doi: 10.1103/PhysRevC.100.035802
60. Lim Y, Holt JW. Bayesian modeling of the nuclear equation of state for neutron star tidal deformabilities and GW170817. *Eur Phys J A.* (2019) **55**:209. doi: 10.1140/epja/i2019-12917-9
61. Coraggio L, Holt JW, Itaco N, Machleidt R, Marcucci LE, Sammarruca F. Nuclear-matter equation of state with consistent two- and three-body perturbative chiral interactions. *Phys Rev C.* (2014) **89**:044321. doi: 10.1103/PhysRevC.89.044321
62. Kaiser N. Exact calculation of three-body contact interaction to second order. *Eur J Phys A.* (2012) **48**:58. doi: 10.1140/epja/i2012-12058-9
63. Holt JW, Kaiser N. Equation of state of nuclear and neutron matter at third-order in perturbation theory from chiral effective field theory. *Phys Rev C.* (2017) **95**:034326. doi: 10.1103/PhysRevC.95.034326
64. Holt JW, Kaiser N, Miller GA, Weise W. Microscopic optical potential from chiral nuclear forces. *Phys Rev C.* (2013) **88**:024614. doi: 10.1103/PhysRevC.88.024614
65. Wellenhofer C, Holt JW, Kaiser N. Thermodynamics of isospin-asymmetric nuclear matter from chiral effective field theory. *Phys Rev C.* (2015) **92**:015801. doi: 10.1103/PhysRevC.92.015801
66. Koning AJ, Delaroche JP. Local and global nucleon optical models from 1 keV to 200 MeV. *Nucl Phys.* (2003) **A713**:231. doi: 10.1016/S0375-9474(02)01321-0
67. Jeukenne JP, Lejeune A, Mahaux C. Optical-model potential in finite nuclei from Reid's hard core interaction. *Phys Rev C.* (1977) **16**:80. doi: 10.1103/PhysRevC.16.80
68. Toyokawa M, Minomo K, Kohno M, Yahiro M. Roles of chiral three-nucleon forces in nucleon-nucleus scattering. *J Phys G.* (2015) **42**:025104. doi: 10.1088/0954-3899/42/2/025104
69. Vorabbi M, Finelli P, Giusti C. Theoretical optical potential derived from nucleon-nucleon chiral potentials. *Phys Rev C.* (2016) **93**:034619. doi: 10.1103/PhysRevC.93.034619
70. Rotureau J, Danielewicz P, Hagen G, Jansen GR, Nunes FM. Microscopic optical potentials for calcium isotopes. *Phys Rev C.* (2018) **98**:044625. doi: 10.1103/PhysRevC.98.044625
71. Idini A, Barbieri C, Navrátil P. Ab initio optical potentials and nucleon scattering on medium mass nuclei. *Phys Rev Lett.* (2019) **123**:092501. doi: 10.1103/PhysRevLett.123.092501
72. Holt JW, Kaiser N, Miller GA. Microscopic optical potential for exotic isotopes from chiral effective field theory. *Phys Rev C.* (2016) **93**:064603. doi: 10.1103/PhysRevC.93.064603
73. Whitehead TR, Lim Y, Holt JW. Proton elastic scattering on calcium isotopes from chiral nuclear optical potentials. *Phys Rev C.* (2019) **100**:014601.
74. Bauge E, Delaroche JP, Girod M. Semi-microscopic nucleon-nucleus spherical optical model for nuclei with $A < 40$ at energies up to 200 MeV. *Phys Rev C.* (1998) **58**:1118. doi: 10.1103/PhysRevC.58.1118
75. Whitehead TR, Lim Y, Holt JW. Neutron elastic scattering on calcium isotopes from chiral nuclear optical potentials. *arXiv: 1912.10043* (2019).
76. Lim Y, Holt JW. Structure of neutron star crusts from new Skyrme effective interactions constrained by chiral effective field theory. *Phys Rev C.* (2017) **95**:065805. doi: 10.1103/PhysRevC.95.065805
77. Lagrange C, Lejeune A. Phenomenological and microscopic optical model analyses of the interaction of low-energy nucleons with Nb-93. *Phys Rev C.* (1982) **25**:2278. doi: 10.1103/PhysRevC.25.2278
78. Kohno M, Sprung DWL, Nagata S, Yamaguchi N. Incident energy dependence of the effective interaction and radius of the optical model potential. *Phys Lett.* (1984) **B137**:10–4. doi: 10.1016/0370-2693(84)91095-5
79. Goriely S, Delaroche JP. The isovector imaginary neutron potential: a key ingredient for the r-process nucleosynthesis. *Phys Lett.* (2007) **B653**:178. doi: 10.1016/j.physletb.2007.07.046
80. Landau LD. The theory of a Fermi liquid. *Sov Phys JETP.* (1957) **3**:920.
81. Landau LD. On the theory of the Fermi liquid. *Sov Phys JETP.* (1959) **8**:70.
82. Migdal AB, Larkin AI. A phenomenological approach to the theory of the nucleus. *Sov Phys JETP.* (1964) **18**:717.

83. Migdal AB. *Theory of Finite Fermi Systems and Properties of Atomic Nuclei*. New York, NY: Interscience (1967).
84. Schwenk A, Friman B. Polarization contributions to the spin dependence of the effective interaction in neutron matter. *Phys Rev Lett.* (2004) **92**:082501. doi: 10.1103/PhysRevLett.92.082501
85. Brown GE. Landau, brueckner-bethe, and migdal theories of fermi systems. *Rev Mod Phys.* (1971) **43**:1. doi: 10.1103/RevModPhys.43.1
86. Holt JW, Kaiser N, Weise W. Chiral Fermi liquid approach to neutron matter. *Phys Rev C.* (2013) **87**:014338. doi: 10.1103/PhysRevC.87.014338
87. Kaiser N, Niessner V. Density-dependent NN interaction from subleading chiral 3N forces: short-range terms and relativistic corrections. *Phys Rev C.* (2018) **98**:054002. doi: 10.1103/PhysRevC.98.054002
88. Kaiser N, Singh B. Density-dependent NN interaction from subleading chiral three-nucleon forces: long-range terms. *Phys Rev C.* (2019) **100**:014002. doi: 10.1103/PhysRevC.100.014002
89. Holt JW, Kaiser N, Weise W. Quasiparticle interaction in nuclear matter with chiral three-nucleon forces. *Nucl Phys.* (2012) **A876**:61. doi: 10.1016/j.nuclphysa.2011.12.001
90. Holt JW, Kaiser N, Whitehead TR. Tensor Fermi liquid parameters in nuclear matter from chiral effective field theory. *Phys Rev C.* (2018) **97**:054325. doi: 10.1103/PhysRevC.97.054325
91. Bäckman SO, Sjöberg O, Jackson AD. The role of tensor forces in Fermi liquid theory. *Nucl Phys.* (1979) **A321**:10. doi: 10.1016/0375-9474(79)90682-1
92. Erkelenz K, Alzetta R, Holinde K. Momentum space calculations and helicity formalism in nuclear physics. *Nucl Phys.* (1971) **A176**:413. doi: 10.1016/0375-9474(71)90279-X
93. Bernard V, Kaiser N, Meissner UG. Aspects of chiral pion-nucleon physics. *Nucl Phys.* (1997) **A615**:483. doi: 10.1016/S0375-9474(97)00021-3
94. Golak J, Skibinski J, Topolnicki K, Witala H, Epelbaum E, Krebs H, et al. Low-energy neutron-deuteron reactions with N3LO chiral forces. *Eur Phys J A.* (2014) **50**:177.
95. Krebs H, Gasparyan A, Epelbaum E. Chiral three-nucleon force at N4LO II: intermediate-range contributions. *Phys Rev C.* (2013) **87**:054007. doi: 10.1103/PhysRevC.87.054007
96. Tews I, Krüger T, Hebeler K, Schwenk A. Neutron matter at next-to-next-to-next-to-leading order in chiral effective field theory. *Phys Rev Lett.* (2013) **110**:032504. doi: 10.1103/PhysRevLett.110.032504
97. Holt JW, Kawaguchi M, Kaiser N. Implementing chiral three-body forces in terms of medium-dependent two-body forces. *arXiv:1912.06055.* (2019).

Conflict of Interest: The authors declare that the research was conducted in the absence of any commercial or financial relationships that could be construed as a potential conflict of interest.

Copyright © 2020 Holt, Kawaguchi and Kaiser. This is an open-access article distributed under the terms of the Creative Commons Attribution License (CC BY). The use, distribution or reproduction in other forums is permitted, provided the original author(s) and the copyright owner(s) are credited and that the original publication in this journal is cited, in accordance with accepted academic practice. No use, distribution or reproduction is permitted which does not comply with these terms.

frontiers in Physics

REVIEW
published: 28 January 2020
doi: 10.3389/fphy.2020.00006

Antiproton Physics

*Jean-Marc Richard**

Institut de Physique des 2 Infinis de Lyon, Université de Lyon, UCBL & CNRS-IN2P3, Villeurbanne, France

We review the physics of low-energy antiprotons, and its link with the nuclear forces. This includes: antinucleon scattering on nucleons and nuclei, antiprotonic atoms, and antinucleon-nucleon annihilation into mesons.

Keywords: antiproton, antimatter, strong interactions, fundamental symmetries, antinucleon-nucleus

1. A BRIEF HISTORY

In 1932, the positron, the antiparticle of the electron, was discovered in cosmic rays and confirmed in the β^+ decay of some radioactive nuclei (see e.g., the Nobel lecture by Anderson [1]). It was then reasonably anticipated that the proton also has an antiparticle, the *antiproton*[1]. It was also suspected that the antiproton would be more difficult to produce and detect than positrons in cosmic rays. The Bevatron project (BeV, i.e., billion of electron-volts, was then a standard denomination for what is now GeV) was launched at Berkeley to reach an energy high-enough to produce antiprotons through the reaction

$$p + A \to p + A + \bar{p} + p, \tag{1}$$

where A denotes the target nucleus. For $A = p$, this is a standard exercise in relativistic kinematics to demonstrate that the kinetic energy of the incoming proton should be higher than $6\,m$, where m is the proton mass, and $c = 1$. This threshold decreases if the target A is more massive. The Bevatron was completed in 1954, and the antiproton was discovered in 1955 by a team lead by Chamberlain and Segrè, who were awarded the Nobel prize in 1959[2].

Shortly after the antiproton, the antineutron, $\bar{n}$, was also discovered at Berkeley, and up to now, for any new elementary particle, the corresponding antiparticle has also been found. The discovery of the first anti-atom was well-advertised [2], but this was not the case for the earlier observation of the first antinucleus, antideuterium, because of a controversy between an European team [3] and its US competitors [4]. In experiments at very high energy, in particular collisions of heavy ions at STAR (Brookhaven) and ALICE (CERN), one routinely produces light antinuclei and even anti-hypernuclei (in which an antinucleon is replaced by an antihyperon $\bar{\Lambda}$) [5–7].

The matter-antimatter symmetry is almost perfect, except for a slight violation in the sector of weak interactions, which is nearly exactly compensated by a simultaneous violation of the left-right symmetry, i.e., the product PC of parity P and charge-conjugation C is only very marginally violated. Up to now, there is no indication of any violation of the product CPT, where T is the time-reversal operator: this implies that the proton and antiproton have the same mass, a property now checked to $< 10^{-9}$ [8].

[1]The only doubt came from the magnetic moment of the proton, which is not what is expected for a particle obeying the Dirac equation.

[2]The other collaborators were acknowledged in the Nobel lectures, but nevertheless Piccioni sued Chamberlain and Segrè in a court of California, which dismissed the suit on procedural grounds.

OPEN ACCESS

Edited by:
Laura Elisa Marcucci,
University of Pisa, Italy

Reviewed by:
Johann Haidenbauer,
Julich Research Centre, Germany
Matteo Vorabbi,
National Nuclear Data Center,
Brookhaven National Laboratory,
United States

***Correspondence:**
Jean-Marc Richard
j-m.richard@ipnl.in2p3.fr

Specialty section:
This article was submitted to Nuclear Physics, a section of the journal Frontiers in Physics

Received: *17 October 2019*
Accepted: *08 January 2020*
Published: *28 January 2020*

Citation:
Richard J-M (2020) Antiproton Physics. Front. Phys. 8:6. doi: 10.3389/fphy.2020.00006

Many experiments have been carried out with low energy antiprotons, in particular at Brookhaven and CERN in the 60s and 70s, with interesting results, in particular for the physics of the mesons produced by annihilation. However, in these early experiments, the antiprotons were part of secondary beams containing many negatively-charged pions and kaons, and with a wide momentum spread.

In the 70s, Simon van der Meer, and his colleagues at CERN and elsewhere imagined and developed the method of *stochastic cooling* [9], which produces antiproton beams of high purity, sharp momentum resolution, and much higher intensity than in the previous devices. CERN transformed the fixed-target accelerator SpS into a proton-antiproton collider, Sp$\bar{\text{p}}$S, with the striking achievement of the discovery of the $W^{\pm}$ and Z^0, the intermediate bosons of the electro-weak interaction. A similar scheme was later adopted at Fermilab with higher energy and intensity, leading to many results, among which the discovery of the top quark.

As a side product of the experiments at the Sp$\bar{\text{p}}$S program, CERN built a low-energy facility, LEAR (Low-Energy Antiproton Ring) which operated from 1982 to 1996, and hosted several experiments on which we shall come back later. Today, the antiproton source of CERN is mainly devoted to experiments dealing with atomic physics and fundamental symmetries. In spite of several interesting proposals, no low-energy extension of the antiproton program was built at Fermilab.

As for the intermediate energies, at the beginning of the CERN cooled-antiproton program, a $\bar{p}$ beam was sent in the ISR accelerator to hit a thin hydrogen target. The experiment R704 got sharp peaks corresponding to some charmonium states, and in particular a first indication of the—then missing—P-wave singlet state h_c [10]. But ISR was to be closed, and in spite of a few more days of run, R704 was interrupted. The team moved to Fermilab, and charmonium physics with antiprotons was resumed with antiproton-proton collisions arranged in the accumulation device (experiments E760-E835) [11].

Today, the techniques of production of sharp antiproton beams is well-undercontrol. There are projects to perform strong-interaction physics with antiprotons at FAIR (Darmstadt) [12] and JPARC in Japan [13]. In the 80s, an ambitious extension of LEAR at higher energies, SuperLEAR [14], was proposed by Montanet et al., but was not approved by the CERN management. A major focus of SuperLEAR was charm physics. But more than 30 years later, this physics has been largely unveiled by beauty factories and high-energy hadron colliders.

Presently, the only running source of cooled antiprotons is the very low energy AD at CERN (Antiproton Decelerator) and its extension ELENA (Extra Low ENergy Antiproton) with the purpose of doing atomic-physics and high-precision tests of fundamental symmetries. Some further decelerating devices are envisaged for the gravitation experiments [15]. Of course, standard secondary antiproton beams are routinely produced, e.g., at KEK in Japan.

Note also that in devices making antiproton beams, a non-negligible fraction of antideuterium is produced, which could be cooled and stored. The intensity would be sufficient to perform strong-interaction measurements, but there is not yet any proposal for an experiment with an antideuterium beam.

We shall discuss along this review many results obtained at LEAR and elsewhere. Already the measurements made at Berkeley during the weeks following the discovery of the antiproton were remarkable. After more than 60 years, we realize today that they gave keys to the modern understanding of hadrons, but the correct interpretation was too far from the current wisdom of the 50s. Indeed, from the work by Fermi and Yang, on which more later, it was realized that one-pion exchange constitutes the long-range part of the antinucleon-nucleon interaction. The simplest model, just before the discovery of the antiproton, would be one-pion exchange supplemented by a very short-range annihilation. This would imply for the charge-exchange ($\bar{p}p \to \bar{n}n$), elastic ($\bar{p}p \to \bar{p}p$) and annihilation ($\bar{p}p \to$ mesons) cross-sections a hierarchy

$$\sigma_{\text{ce}} > \sigma_{\text{el}} > \sigma_{\text{an}}, \tag{2}$$

the first inequality resulting from straightforward isospin algebra. What was observed at Berkeley is just the opposite! And it took us years to admit and understand this pattern, which is a consequence of the composite character of the nucleon and antinucleon.

The era of LEAR and Sp$\bar{\text{p}}$S at CERN, and then the large $\bar{p}p$ collider of Fermilab will certainly be reminded as the culmination of antiproton physics. At very high energy, the trend is now more on pp rather than $\bar{p}p$ collision, due to the higher intensity of proton beams. Certainly very-low energy experiments will remain on the floor to probe the fundamental symmetries with higher and higher precision. The question is open on whether antiproton beams will be used for hadron physics, a field where electron beams and flavor factories already provide much information.

Of course, the role of antimatter in astrophysics is of the highest importance. Antiprotons and even antinuclei are seen in high-energy cosmic rays. The question is to estimate how many antinuclei are expected to be produced by standard cosmic rays, to estimate the rate of primary antinuclei (see e.g., [16, 17]). Some years ago, cosmological models were built [18] in which the same amount of matter and antimatter was created, with a separation of zones of matter and zones of antimatter. In modern cosmology, it is assumed that an asymmetry prevailed, so that, after annihilation, some matter survived.

This review is mainly devoted to the low-energy experiments with antinucleons. Needless to say that the literature is abundant, starting with dedicated workshops [19–24] and schools [25–28].

Because of the lack of space, some important subjects will not be discussed, in particular the ones related to fundamental symmetry: the inertial mass of the antiproton, its charge and magnetic moment, in comparison with the values for the proton; the detailed comparison of hydrogen and antihydrogen atoms; the gravitational properties of neutral atoms, such as antihydrogen, etc. We will mention only very briefly, in the section on antiprotonic atoms, the dramatically precise atomic physics made with the antiprotonic Helium.

2. FROM THE NUCLEON-NUCLEON TO THE ANTINUCLEON-NUCLEON INTERACTION

In this section we outline the general theoretical framework: how to extrapolate our information on the nuclear forces to the antinucleon-nucleon system. We present the basics of the well-known *G*-parity rule, with a remark about the definition of antiparticle states.

2.1. The *G*-Parity Rule

In QED, the $e^-e^- \to e^-e^-$ and $e^+e^- \to e^+e^-$ amplitudes are related by crossing, but there is a long way from the region $\{s > 4\,m_e^2, t < 0\}$ to the one with $\{s < 0, t > 4\,m_e^2$ to attempt a reliable analytic extrapolation. Here, m_e is the electron mass and s and t the usual Mandelstam variables[3]. A more useful approach consists of comparing both reactions for the same values of s and t. The $e^-e^- \to e^-e^-$ amplitude can be decomposed into a even and odd part according to the C-conjugation in the t-channel, say

$$\mathcal{M}(e^-e^- \to e^-e^-) = \mathcal{M}_{\rm even} + \mathcal{M}_{\rm odd}, \tag{3}$$

and the $e^+e^- \to e^+e^-$ amplitude for the same energy and transfer is given by

$$\mathcal{M}(e^+e^- \to e^+e^-) = \mathcal{M}_{\rm even} - \mathcal{M}_{\rm odd}. \tag{4}$$

The first term contains the exchange of an even number of photons, and the last one the exchange of an odd number. At lowest order, one retrieves the sign flip of the Coulomb potential. This rule remains valid to link $pp \to pp$ and $\bar{p}\bar{p} \to \bar{p}\bar{p}$ amplitudes: the exchange of a π^0 with charge conjugation $C = +1$, is the same for both reactions, while the exchange of an ω meson ($C = -1$) flips sign.

Fermi and Yang [29] astutely combined this C-conjugation rule with isospin symmetry, allowing to include the exchange of charged mesons, as in the charge-exchange processes. Instead of comparing $pp \to pp$ to $\bar{p}p \to \bar{p}p$ or $np \to np$ to $\bar{n}p \to \bar{n}p$, the G-parity rule relates amplitudes of given isospin I. More precisely, if the nucleon-nucleon amplitude is decomposed as

$$\mathcal{M}^I(NN) = \mathcal{M}_{\rm G=+1} + \mathcal{M}_{\rm G=-1}, \tag{5}$$

according to the G-odd (pion, omega, …) or G-even (ρ, …) in the t-channel, then its $\bar{N}N$ counterpart reads

$$\mathcal{M}^I(\bar{N}N) = \mathcal{M}_{\rm G=+1} - \mathcal{M}_{\rm G=-1}. \tag{6}$$

Note that there is sometimes some confusion between the C-conjugation and the G-parity rules, especially because there are two ways of defining the isospin doublet $\{\bar{n}, \bar{p}\}$ (see Appendix: Isospin Conventions).

In current models of NN, the pion-exchange tail, the attraction due to isoscalar two-pion exchange, and the spin-dependent part of the ρ exchange are rather well-identified, and thus can be rather safely transcribed in the $\bar{N}N$ sector. Other terms, such as the central repulsion attributed to ω-exchange, might contain contributions carrying the opposite G-parity, hidden in the effective adjustment of the couplings. Thus, the translation toward $\bar{N}N$ might be biased.

2.2. Properties of the Long-Range Interaction

Some important consequences of the G-parity rule have been identified. First, the moderate attraction observed in NN, due to a partial cancellation of σ (or, say, the scalar-isoscalar part of two-pion exchange) and ω-exchanges, becomes a coherent attraction once ω-exchange flips sign. This led Fermi and Yang to question whether the mesons could be interpreted as bound states of a nucleon and an antinucleon. This idea has been regularly revisited, in particular at the time of bootstrap [30]. As stressed, e.g., in Ball et al. [31], this approach hardly accounts for the observed degeneracy of $I = 0$ and $I = 1$ mesons (for instance ω and ρ having about the same mass).

In the 70s, Shapiro et al., and others, suggested that baryon-antibaryon bound states were associated with new types of hadrons, with the name *baryonium*, or *quasi-deuteron* [32–34]. Similar speculations were made later for other hadron-hadron systems, for instance $D\bar{D}^*$, where D is a charmed meson ($\bar{c}q$) of spin 0 and $\bar{D}^*$ an anticharmed meson ($\bar{c}q$) of spin 1 [35]. Some candidates for baryonium were found in the late 70s, interpreted either as quasi-nuclear $\bar{N}N$ states à la Shapiro, or as exotic states in the quark model, and motivated the construction of the LEAR facility at CERN. Unfortunately, the baryonium states were not confirmed.

Another consequence of the G-parity rule is a dramatic change of the spin dependence of the interaction. At very low energy, the nucleon-nucleon interaction is dominated by the spin-spin and tensor contributions of the one-pion exchange. However, when the energy increases, or, equivalently, when one explores shorter distances, the main pattern is a pronounced spin-orbit interaction. It results from a coherent sum of the contributions of vector mesons and scalar mesons[4]. The tensor component of the NN interaction is known to play a crucial role: in most models, the $^1S_0$ potential is stronger than the $^3S_1$ one, but in this latter partial wave[5], the attraction is reinforced by S-D mixing. However, the effect of the tensor force remains moderate, with a percentage of D wave of about 5% for the deuteron.

In the case of the $\bar{N}N$ interaction, the most striking coherence occurs in the tensor potential, especially in the case of isospin $I = 0$ [36]. A scenario with dominant tensor forces is somewhat unusual, and leads to unexpected consequences, in particular a relaxation of the familiar hierarchy based on the hight of the centrifugal barrier. For instance, if one calculates the spectrum of bound states from the real part of the $\bar{N}N$ interaction, the

[3]For a reaction $1 + 2 \to 3 + 4$, the Mandestam variables are given in terms of the energy-momentum quadrivectors as $s = (\tilde{p}_1 + \tilde{p}_2)^2$, $t = (\tilde{p}_3 - \tilde{p}_1)^2$ and $u = (\tilde{p}_4 - \tilde{p}_1)^2$.

[4]The origin is different, for vector mesons, this is a genuine spin-orbit effect, for scalar mesons, this is a consequence of Thomas precession, but the effect is the same in practice.

[5]The notation is $^{2S+1}L_J$, as there is a single choice of isospin, and it will become $^{2I+1,2S+1}L_J$ for $\bar{N}N$.

ground-state is $^{1,3}P_0$, and next a coherent superposition of $^{1,3}S_1$ and $^{1,3}D_1$, and so on. In a scattering process, there is no polarization if the tensor component is treated to first order, but polarization shows up at higher order. Thus, one needs more than polarization measurements[6] to distinguish the dynamics with a moderate spin-orbit component from the dynamics with a very strong tensor component.

2.3. Appendix: Isospin Conventions

There are two possible conventions for writing the isospin states of antinucleons [37].

The natural choice is based on the charge conjugation operator C, namely $|\bar{p}\rangle_c = C|p\rangle$ and $|\bar{n}\rangle_c = C|n\rangle$. However, it transforms the two representation of SU(2) into a $\bar{2}$ which does not couple with the usual Clebsch-Gordan coefficients. For instance, the isospin $I = 0$ state of $\bar{N}N$ reads in this convention

$$|I = 0\rangle = \frac{|\bar{p}p\rangle_c + |\bar{n}n\rangle_c}{\sqrt{2}}, \tag{7}$$

which anticipates the formula for an SU(3) singlet,

$$|0\rangle = \frac{|\bar{u}u\rangle + |\bar{d}d\rangle + |\bar{s}s\rangle}{\sqrt{3}}, \tag{8}$$

However, the $\bar{2}$ representation of SU(2) is equivalent to the 2 one, and it turns out convenient to perform the corresponding rotation, that is to say, define the states by the G-parity operator, namely (without subscript) $|\bar{p}\rangle = G|n\rangle$ and $|\bar{n}\rangle = G|p\rangle$. With this convention, the isospin singlet is written as.

$$|I = 0\rangle = \frac{|\bar{n}n\rangle - |\bar{p}p\rangle}{\sqrt{2}}, \tag{9}$$

3. BARYONIUM

The occurrence of baryonium candidates in antiproton-induced reactions was a major subject of discussion in the late 70s and in the 80s and the main motivation to build new antiprotons beams and new detectors. The name "baryonium" suggests a baryon-antibaryon structure, as in the quasi-nuclear models. More generally "baryonium" denotes mesons that are preferentially coupled to the baryon-antibaryon channel, independently of any prejudice about their internal structure.

Nowadays, baryonium is almost dead, but interestingly, some of the innovative concepts and some unjustified approximations developed for baryonium are re-used in the current discussions about the new hidden-charm mesons *XYZ* and other exotic hadrons [38].

3.1. Experimental Candidates for Baryonium

For an early review on baryonium (see [39]). For an update, see the Particle Data Group [40]. In short: peaks have been seen in the integrated cross sections, or in the angular distribution (differential cross section) at given angle, or in some specific annihilation rates as a function of the energy. The most famous candidate was the S(1932), seen in several experiments [39]. The most striking candidate was the peak of mass 2.95 GeV/c^2 seen in $\bar{p}p\pi^-$ [41], with some weaker evidence for peaks at 2.0 and 2.2 GeV/c^2 in the $\bar{p}p$ subsystem, suggesting a sequential decay $\mathcal{B}^- \to \mathcal{B} + \pi^-$, where $\mathcal{B}$ denotes a baryonium. Peaks were also seen in the inclusive photon and pion spectra of the annihilations $\bar{p}p \to \gamma X$ and $\bar{p}p \to \pi X$ at rest.

None of the experiments carried out at LEAR confirmed the existence of such peaks. However, some enhancements have been seen more recently in the $\bar{p}p$ mass distribution of the decay of heavy particles, such as $J/\psi \to \gamma\bar{p}p$, $B \to K\bar{p}p$, or $B \to D\bar{p}p$, see Ablikim et al. [42] and the notice on non $\bar{q}q$ mesons in Tanabashi et al. [40]. There is a debate about whether they correspond a baryonium states or just reveal a strong $\bar{p}p$ interaction in the final state (see e.g., the discussion in [43–45]). Also, as stressed by Amsler [46], the $f_2(1565)$ is seen only in annihilation experiments, and thus could be a type of baryonium, $^{1,3}P_2 - {}^{1,3}F_2$ in the quasi-nuclear models. See the review on $f_2(1565)$ in Tanabashi et al. [40].

3.2. The Quasi-Nuclear Model

Today, it is named "molecular" approach. The observation that the real part of the $\bar{N}N$ interaction is more attractive than its NN counterpart led Shapiro et al. [32], Dover et al. [33], and others, to predict the existence of deuteron-like $\bar{N}N$ bound states and resonances. Due to the pronounced spin-isospin dependence of the $\bar{N}N$ interaction, states with isospin $I = 0$ and natural parity were privileged in the predictions. The least one should say is that the role of annihilation was underestimated in most early studies. Attempts to include annihilation in the spectral problem have shown, indeed, that most structures created by the real potential are washed out when the absorptive part is switched on [47].

3.3. Duality

Duality is a very interesting concept developed in the 60s. For our purpose, the most important aspect is that in a hadronic reaction $a + b \to c + d$, there is an equivalence between the t-channel dynamics, i.e., the exchanges schematically summarized as $\sum_i a + \bar{c} \to X_i \to \bar{b} + d$, and the low-energy resonances $\sum_j a + b \to Y_j \to c + d$. In practice, one approach is usually more efficient than the other, but a warning was set by duality against empirical superpositions of t-channel and s-channel contributions. For instance, $\bar{K}N$ scattering with strangeness $S = -1$ benefits the hyperons as s-channel resonances, and one also observes a coherent effect of the exchanged mesons. On the other hand, KN is exotic, and, indeed, has a much smaller cross-section. In KN, there should be destructive interferences among the t-channel exchanges.

Though invented before the quark model, duality is now better explained with the help of quark diagrams. Underneath is the Zweig rule, that suppresses the disconnected diagrams. See e.g., [48, 49] for an introduction to the Zweig rule, and refs. there. The case of $\bar{K}N$, or any other non-exotic meson-baryon scattering is shown in **Figure 1**. For the exotic KN channel the incoming

[6] Actually more than spin measurements along the normal $\hat{n}$ to the scattering plane, such as the analyzing power A_n or the transfer D_{nn} or normal polarization.

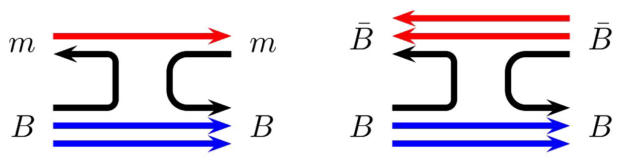


FIGURE 1 | Duality diagram for non-exotic meson-baryon **(left)** and baryon-antibaryon **(right)** scattering.

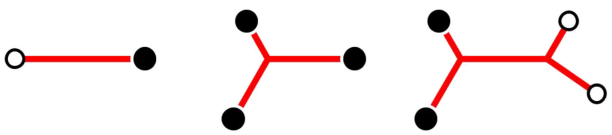


FIGURE 2 | String picture of a meson **(left)**, a baryon **(center)**, and a baryonium **(right)**.

antiquark is $\bar{s}$, and it cannot annihilate. So there is no possibility of forming a quark-antiquark meson in the *t* channel, nor a three-quark state in the *s*-channel. In a famous paper [50], Rosner pointed out that as meson-exchanges are permitted in nucleon-antinucleon scattering (or any baryon-antibaryon system with at least one quark matching an antiquark), there should be resonances in the *s*-channel: baryonium was born, and more generally a new family of hadrons. The corresponding quark diagram is shown in **Figure 1**. As stressed by Roy [49], duality suggests higher exotics.

3.4. Baryonium in the Hadronic-String Picture

This concept of duality is illustrated in the hadronic-string picture, which, in turn, is supported by the strong-coupling limit of QCD (see e.g., the contribution by Rossi and Veneziano in [39]). A meson is described as a string linking a quark to an antiquark. A baryon contains three strings linking each of the three quarks to a junction, which acts as a sort of fourth component and tags the baryon number. The baryonium has a junction linked to the two quarks, and another junction linked to the two antiquarks (see **Figure 2**). The decay happens by string breaking and $q\bar{q}$, leading either to another baryonium and a meson, or to baryon-antibaryon pair. The decay into two mesons proceeds via the internal annihilation of the two junctions, and is suppressed.

The baryonium of Jaffe was somewhat similar, with the string realized by the cigar-shape limit of the bag model [51]. Note that the suppression of the decay into mesons is due in this model to a centrifugal barrier, rather than to a topological selection rule. The orbitally excited mesons consist of a quark and an antiquark linked by a string, the excited baryons are the analogs with a quark and a diquark, and the baryonia involve a diquark and an antidiquark.

3.5. Color Chemistry

Chan et al. [52] pushed the speculations a little further in their "color chemistry." They have baryonia with color $\bar{3}$ diquarks, which decay preferentially into a baryon-antibaryon pair rather than into mesons, also more exotic baryonia in which the diquark has color sextet. Then even the baryon-antibaryon decay is suppressed, and the state is expected to be rather narrow. This was a remarkable occurrence of the color degree of freedom in spectroscopy. However, there was no indication on how and why such diquark-antidiquark structure arises from the four-body dynamics.

3.6. Other Exotics?

The baryonium story is just an episode in the long saga of exotics, which includes the strangeness $S = +1$ "Z" baryons in the 60s, their revival under the name "light pentaquark" [40]. The so-called "molecular approach" hadrons was illustrated by the picture of the Δ resonance as πN by Chew and Low [53], and of the $\Lambda(1405)$ as $\bar{K}N$ by Dalitz and Yan [54], with many further discussions and refinements.

As reminded, e.g., in Rossi and Veneziano [55], there is some analogy between the baryonium of the 70s and 80s and the recent *XYZ* spectroscopy. The *XYZ* are mesons with hidden heavy flavor that do not fit in the ordinary quarkonium spectroscopy [38]. One can replace "quasi-nuclear" by "molecular," "baryon number" by "heavy flavor," etc., to translate the concepts introduced for baryonium for use in the discussions about *XYZ*. The diquark clustering in the light sector is now replaced by an even more delicate assumption, namely cq or $\bar{c}\bar{q}$ clustering. While the $X(3872)$ is very well-established, some other states either await confirmation or could be interpreted as mere threshold effects. Before the *XYZ* wave, it was suggested that baryon-antibaryon states could exist with strange or charmed hyperons. This spectroscopy is regularly revisited (see e.g., [56] and references therein).

4. ANTINUCLEON-NUCLEON SCATTERING

In this section, we give a brief survey of measurements of antinucleon-nucleon scattering and their interpretation, for some final states: $\bar{N}N$, $\bar{\Lambda}\Lambda$, and two pseudoscalars. Some emphasis is put on spin observables. It is stressed in other chapters of this book how useful were the measurements done with polarized targets and/or beams for our understanding of the *NN* interaction, leading to an almost unambiguous reconstruction of the *NN* amplitude. The interest in $\bar{N}N$ spin observables came at workshops held to prepare the LEAR experiments [19, 20, 22], and at the spin Conference held at Lausanne in 1980 [57]. A particular attention was paid to $p\bar{p} \rightarrow \bar{\Lambda}\Lambda$, but all the theoreticians failed in providing valuable guidance for the last measurements using a polarized target, as discussed below in section 4.7. However, *Felix Culpa*[7], we learned how to better deal with the relationships and constraints among spin observables.

[7] "For God judged it better to bring good out of evil than not to permit any evil to exist," Augustinus.

4.1. Integrated Cross Sections

As already mentioned, the integrated cross sections have been measured first at Berkeley, shortly after the discovery of the antiproton. More data have been taken in many experiments, mainly at the Brookhaven National Laboratory (BNL) and CERN, at various energies. The high-energy part, together with its proton-proton counter part, probes the Pomerantchuk theorem, Froissart bound and the possible onset of the odderon (see e.g., [58] and references therein).

As for the low-energy part, some values of the total cross section are shown in **Figure 3**, as measured by the PS172 collaboration [59]. It can be contrasted to the annihilation cross section of **Figure 3**, due to the PS173 collaboration [60]. When one compares the values at the same energy, one sees that annihilation is more than half the total cross section. Meanwhile, the integrated charge-exchange cross section is rather small (just a few mb).

Let us stress once more that the hierarchy $\sigma_{\rm ann} > \sigma_{\rm el}$ of the annihilation and elastic cross-sections is remarkable. One needs more than a full absorptive core. Somehow, the long-range attraction pulls the wave function toward the inner regions where annihilation takes place [61, 62].

4.2. Angular Distribution for Elastic and Charge-Exchange Reactions

The elastic scattering has been studied in several experiments, most recently at LEAR, in the experiments PS172, PS173, PS198, ... An example of differential distribution is shown in **Figure 4**.

The charge exchange scattering has been studied by the PS199-206 collaboration at LEAR. As discussed in one of the workshops on low-energy antiproton physics [19], charge exchange gives the opportunity to study the interplay between the long-range and short-range physics. An example of differential cross-section is shown in **Figure 5**, published in Ahmidouch et al. [65]. Clearly the distribution is far from flat. This illustrates the role of high partial waves. The amplitude for charge exchange corresponds to the isospin combination

$$\mathcal{M}(\bar{p}p \to \bar{n}n) \propto \mathcal{M}_0 - \mathcal{M}_1, \tag{10}$$

The smallness of the integrated charge-exchange cross-section is due to a large cancellation in the low-partial waves. But in the high partial waves, there is a coherent superposition. In particular the one-pion exchange gets an isospin factor $+1$ for $\mathcal{M}_1$, and a factor -3 for $\mathcal{M}_0$.

4.3. Antineutron Scattering

To access to pure isospin $I = 1$ scattering, data have been taken with antiproton beams and deuterium targets, but the subtraction of the $\bar{p}p$ contribution and accounting for the internal motion and shadowing effects is somewhat delicate. The OBELIX collaboration at CERN has done direct measurements with antineutrons [66]. For instance, the total $\bar{n}p$ cross-section has been measured between $p_{\rm lab} = 50$ and 480 MeV/c [67]. The data are shown in **Figure 6** together with a comparison with the $\bar{p}p$ analogs. There is obviously no pronounced isospin dependence. The same conclusion can be drawn for the $\bar{p}p$ and $\bar{n}p$ annihilation cross sections [68].

4.4. Spin Effects in Elastic and Charge-Exchange Scattering

A few measurements of spin effects in $\bar{N}N \to \bar{N}N$ were done before LEAR, mainly dealing with the analyzing power. Some further measurements were done at LEAR, with higher statistics and a wider angular range. An example of measurement by PS172 is shown in **Figure 7**: the analyzing power of $\bar{p}p \to \bar{p}p$ at 679 MeV/c [69]. One can see that the value of A_n is sizable,

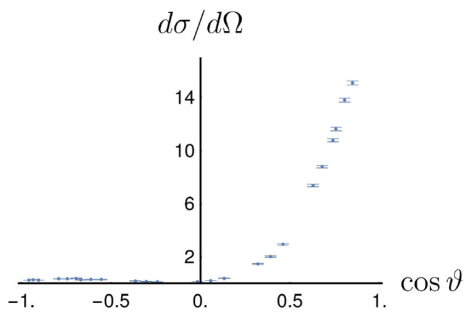


FIGURE 4 | Angular distribution in elastic $\bar{p}p \to \bar{p}p$ scattering at 0.697 GeV/c, as measured by the PS198 collaboration [63].

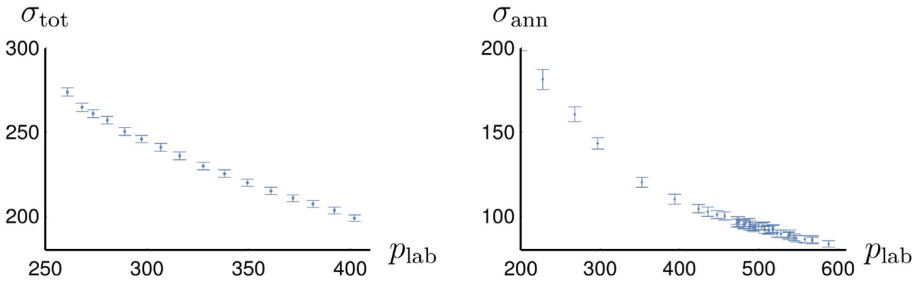


FIGURE 3 | (Left) Total $\bar{p}p$ cross section (in mb), as measured by the PS172 collaboration at LEAR.lation. **(Right)** Annihilation $\bar{p}p$ cross section (in mb), as measured by the PS173 collaboration.

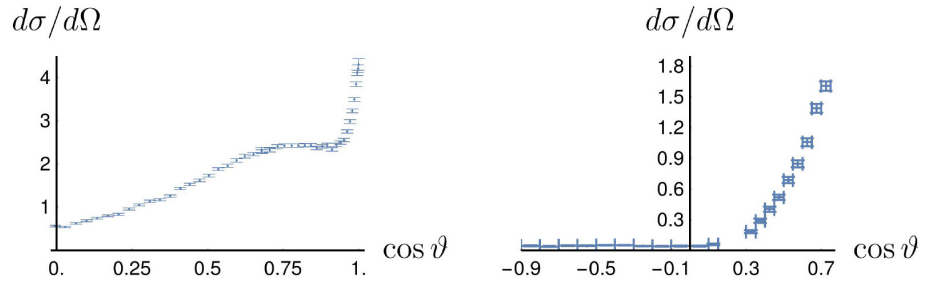


FIGURE 5 | Angular distribution for the charge-exchange reaction $\bar{p}p \to \bar{n}n$ at incident momentum 0.601 Gev/c (left) and 1.083 GeV/c in the target frame [64]. Only the statistical error is shown here. Large systematic errors have to be added.

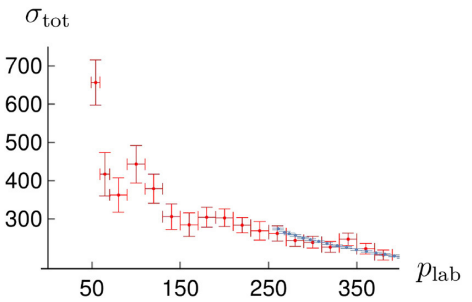


FIGURE 6 | Total $\bar{n}p$ cross section (red), as measured by the PS201 collaboration, and comparison with the $\bar{p}p$ total cross-section (blue).

but not very large. It is compatible with either a moderate spin-orbit component of the interaction, or a rather strong tensor force acting at second order. PS172 also measured the depolarization parameter D_{nn} in $\bar{p}p \to \bar{p}p$. This parameter D_{nn} expresses the fraction of recoiling-proton polarization along the normal direction that is due to the polarization of the target. Thus, $D_{nn} = 1$ in absence of spin forces. PS172 obtained the interesting result $D_{nn} = -0.169 \pm 0.465$ at $\cos\vartheta = -0.169$ for the momentum $p_{\rm lab} = 0.679\,\text{GeV}/c$ [70]. The effect persists at higher momentum, as seen in **Figure 8**.

The charge-exchange reaction has been studied by the PS199-206 collaborations at LEAR (see e.g., [71, 72]). In **Figure 8** is shown the depolarization parameter D_{nn}. The effect is clearly large. It is predicted that $D_{\ell\ell}$ is even more pronounced, and interestingly, also $K_{\ell\ell}$, the transfer of polarization from the target to the antineutron. This means that one can produce polarized antineutrons by scattering antiprotons on a longitudinally polarized proton target.

4.5. Amplitude Analysis?

Decades of efforts have been necessary to achieve a reliable knowledge of the NN interaction at low energy, with experiments involving both a polarized beam and a polarized target. In the case of $\bar{N}N$, the task is more delicate, as the phase-shifts are complex even at very low energy, and there is no Pauli principle to remove every second partial wave. So, as we have much less observables available for $\bar{N}N$ than for NN, it is impossible to reconstruct the phase-shifts or the amplitudes: there are unavoidably several solutions with about the same χ^2, and one flips from one solution to another one when one adds or removes a set of data. This is why the fits by Timmermans et al. [73, 74] have been received with some skepticism [75, 76].

Clearly the measurements of analyzing power and depolarization at LEAR should have been pursued, as was proposed by some collaborations, but unfortunately not approved by the CERN management. Now, we badly miss the information that would be needed to reconstruct the $\bar{N}N$ interaction unambiguously, and estimate the possible ways to polarize antiprotons (spin filter, spin transfer).

4.6. Potential Models

For the use in studies of the protonium and antinucleon-nucleus systems, it is convenient to summarize the information about the "elementary" $\bar{N}N$ interaction in the form of an effective $\bar{N}N$ potential. Early attempts were made by Gourdin et al. [77], Bryan and Phillips [78] among others, and more recently by Kohno and Weise [79], and the Bonn-Jülich group [80–82]. Dover, Richard, and Sainio [62, 83, 84] used as long range potential $V_{\rm LR}$ the G-parity transformed of the Paris NN potential, regularized in a square-well manner, i.e., $V_{\rm LR}(r < r_0) = V_{\rm LR}(r_0)$ with $r_0 = 0.8$ fm, supplemented by a complex core to account for unknown short-range forces and for annihilation,

$$V_{\rm SR}(r) = -\frac{V_0 + i\,W_0}{1 + \exp(-(r-R)/a)}. \tag{11}$$

The short-range interaction was taken as spin and isospin independent, for simplicity. A good fit of the data was achieved with two sets of parameters

$$\begin{aligned} &\text{model DR1} \quad R = 0\,\text{fm}, \quad a = 0.2\,\text{fm}, \quad V_0 = 21\,\text{GeV}, \\ &\qquad\qquad W_0 = 20\,\text{GeV}, \\ &\text{model DR2} \quad R = 0.8\,\text{fm}, \quad a = 0.2\,\text{fm}, \quad V_0 = 0.5\,\text{GeV}, \\ &\qquad\qquad W_0 = 0.5\,\text{GeV}. \end{aligned} \tag{12}$$

In Timmers et al. [85], the annihilation part is not described by an optical model, but by two effective meson-meson channels. This probably gives a more realistic energy dependence. In some other models, the core contains some spin and isospin-dependent

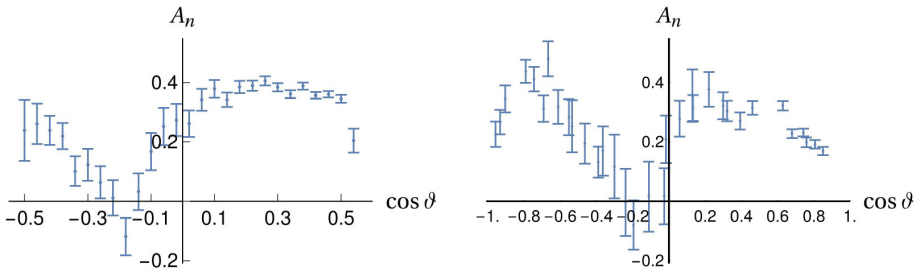


FIGURE 7 | Analyzing power of $\bar{p}p \to \bar{p}p$ **(left)** at 672 MeV/c, as measured at LEAR by the PS172 collaboration [69], **(right)** at 697 MeV/c by the PS198 collaboration [63].

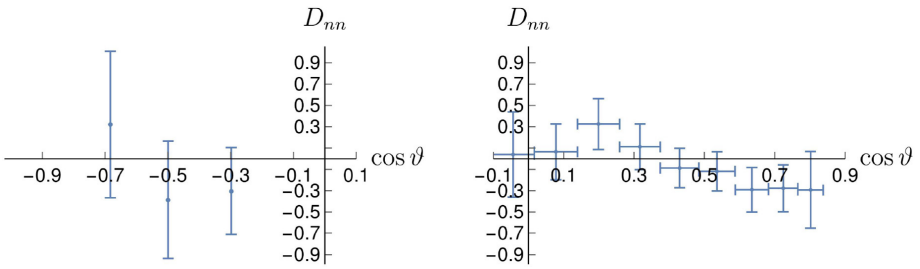


FIGURE 8 | Transfer of polarization D_{nn}, in elastic $\bar{p}p$ scattering at $p_{\text{lab}} = 1.089$ GeV/c [70] (right) and in the charge exchange reaction at 0.875 GeV/c [72].

terms, but there are not enough data to constrain the fit. Some examples are given by the Paris group in El-Bennich et al. [86], and earlier attempts cited there. In Klempt et al. [87], a comparison is made of the successive versions of such a $\bar{N}N$ potential: the parameters change dramatically when the fit is adjusted to include a new measurement. The same pattern is observed for the latest iteration [86].

More recent models will be mentioned in section 8 devoted to the modern perspectives, namely an attempt to combine the quark model and meson-exchanges, or potentials derived in the framework of chiral effective theories.

4.7. Hyperon-Pair Production

The PS185 collaboration has measured in detail the reactions of the type $\bar{p}p \to \bar{Y}Y'$, where Y or Y' is an hyperon. We shall concentrate here on the $\bar{\Lambda}\Lambda$ channel, which was commented on by many theorists (see e.g., [88]). In the last runs, a polarized hydrogen target was used. Thus, $\bar{p}p \to \bar{\Lambda}\Lambda$ interaction at low energy is known in great detail, and motivated new studies on the correlations among the spin observables, which are briefly summarized in Appendix: Constraints on Spin Observables.

The weak decay of the Λ (and $\bar{\Lambda}$) gives access to its polarization in the final state, and thus many results came from the first runs: the polarization $P(\Lambda)$ and $P(\bar{\Lambda})$ (which were checked to be equal), and various spin correlations of the final state C_{ij}, where i or j denotes transverse, longitudinal, etc.[8] In particular the combination of observables

$$F_0 = \frac{1}{4}(1 + C_{xx} - C_{nn} + C_{\ell\ell}), \tag{13}$$

corresponds to the percentage of spin singlet, and was found to be compatible with zero within the error bars. Unfortunately, at least two explanations came:

- According to the quark model, the spin of Λ is carried by the s quark, with the light pair ud being in a state spin and isospin zero. The vanishing of the spin singlet fraction is due to the creation of the $s\bar{s}$ pair in a spin triplet to match the gluon in perturbative QCD or the prescription of the $^3P_0$ model, in which the created quark-antiquark pair has the quantum number 0^{++}.
- In the nuclear-physics type of approach, the reaction is mediated by K and K^* exchanges. This produces a coherence in some spin-triple amplitude, analogous to the strong tensor force in the isospin $I = 0$ of $\bar{N}N$. Hence, the triplet is favored.

It was then proposed to repeat the measurements on a polarized hydrogen target. This suggestion got support and was approved. In spite of a warning that longitudinal polarization might give larger effect, a transverse polarization was considered as an obvious choice, as it gives access to more observables. A detailed analysis of the latest PS185 are published in Bassalleck et al. and Paschke et al. [90, 91].

[8]The data have been analyzed with the value of the decay parameter α of that time. The parameter α is defined, e.g., in the note "Baryon decay parameters" of Tanabashi et al. [40]. A recent measurement by the BESIII collaboration in Beijing gives a larger value of α [89]. This means that the Λ polarization would be about 17 % smaller.

What retained attention was the somewhat emblematic D_{nn} which measures the transfer of normal polarization from p to Λ (in absence of spin effects, $D_{nn} = 1$). It was claimed that the transfer observable D_{nn} could distinguish among the different scenarios for the dynamics [92], with quark models favoring D_{nn} positive (except models making use of a polarized $s\bar{s}$ sea [93]), and meson-exchange $D_{nn} < 0$. When the result came with $D_{nn} \sim 0$, this was somewhat a disappointment. But in fact, it was realized [94, 95] that $D_{nn} \sim 0$ was a *consequence* of the earlier data! As reminded briefly in Appendix: Constraints on Spin Observables, there are indeed many constraints among the various spin observables of a given reaction. For instance, one can show that

$$C_{\ell\ell}^2 + D_{nn}^2 \leq 1. \tag{14}$$

This inequality, and other similar constraints, implied that D_{nn} had be small, just from data taken with an unpolarized target, while $D_{\ell\ell}$ had a wider permitted range.

A sample of the PS185 results can be found in **Figure 9**.

4.8. Spin Effects in Annihilation Into Two Pseudoscalar Mesons

The reactions $\bar{p}p \to \pi^+\pi^-$ (and to a lesser extent $\pi^0\pi^0$) and K^+K^- were measured before LEAR. For instance, some results can be read in the proceedings of the Strasbourg conference in 1978 [96]. However, some adventurous analyses concluded to the existence of unnatural-parity broad resonances, the large-width sector of baryonium. Needless to say that such analyses with few or no spin observables, were flawed from the very beginning. The same methods, and sometimes the same authors, were responsible for the misleading indication in favor of the so-called Z baryons with strangeness $S = +1$, the ancestor of the late light pentaquark $\theta(1540)$.

The LEAR experiment PS172 remeasured these reactions with a polarized target. This gives access to the analyzing power A_n, the analog of the polarization in the crossed reactions, such as $\pi^- p \to \pi^- p$. Remarkably, A_n is very large, in some wide ranges of energy and angle (see **Figures 10**, **11**). There is a choice of amplitudes, actually the transversity amplitudes, such that

$$A_n = \frac{|f]^2 - |g|^2}{|f]^2 + |g|^2}, \tag{15}$$

In this notation, $|A_n| \sim 1$ requires one amplitude f or g to be dominant. This was understood from the coupled channel effects [97, 98]. Alternatively, one can argue that the initial state is made of partial waves ${}^3(J-1)_J$ and ${}^3(J+1)_J$ coupled by tensor forces. The amplitudes f and g correspond to the eigenstates of the tensor operator S_{12} (see section 2), and the amplitude in which the tensor operator is strongly attractive tends to become dominant [99].

4.9. Appendix: Constraints on Spin Observables

A typical spin observable X is usually normalized such that $-1 \leq X \leq +1$. But if one considers two normalized observables X and Y of the same reaction, several scenarios can occur:

- The entire square $-1 \leq X, Y \leq +1$ is allowed. Then the knowledge of X does not constrain Y.
- $\{X, Y\}$ is restricted to a subdomain of the square. One often encounters the unit circle $X^2 + Y^2 \leq 1$. In such case a large X implies a vanishing Y. This is what happens for D_{nn} vs. some of C_{ij} in $\bar{p}p \to \bar{\Lambda}\Lambda$. Another possibility is a triangle (see **Figure 12**).

For instance, in the simplest case of $\pi N \to \pi N$ (or its cross reaction as in Equation 15), there is a set of amplitudes such that the polarization (or the analyzing power), and the two independent transfer of polarization) are given by

$$X = \frac{|f]^2 - |g|^2}{|f]^2 + |g|^2}, \quad Y = \frac{2\ \mathrm{Re}(f^* g)}{|f]^2 + |g|^2}, \quad Z = \frac{2\ \mathrm{Im}(f^* g)}{|f]^2 + |g|^2}, \tag{16}$$

such that $X^2 + Y^2 + Z^2 = 1$ and thus $X^2 + Y^2 \leq 1$. For reactions with two spin-1/2 particles, the algebra is somewhat more intricate [95].

At about the same time as the analysis of the PS172 and PS185 data, similar inequalities were derived for the spin-dependent parton distributions, in particular by the late Jacques Soffer, starting from the requirement of positivity. An unified presentation of the inequalities in the hadron-hadron and quark distribution sectors can be found in Artru et al. [95]. The domain allowed for three normalized observables X, Y, Z can be found in this reference, with sometimes rather amazing shapes for the frontier.

Perhaps a new strategy could emerge. Instead of either disregarding all spin measurements, or to cumulate all possible spin measurements in view of an elusive full reconstruction, one could advocate a stage by stage approach: measure first a few observables and look for which of the remaining are less constrained, i.e., keep the largest potential of non-redundant information.

5. PROTONIUM

Exotic atoms provide a subtle investigation of the hadron-nucleon and hadron-nucleus interaction at zero energy. For a comprehensive review, see Deloff [100]. Let us consider (h^-, A), where h^- is a negatively charged hadron, such as π^- or K^-, and A a nucleus of charge $+Z$. One can calculate the energy levels $E_{n,\ell}^{(0)}$ by standard QED techniques, including finite volume, vacuum polarization, etc. The levels are shifted and broadened by the strong interactions, and it can be shown (most simply in potential models, but also in effective theories), that the complex shift is given by

$$\delta E_{n,\ell} = E_{n,\ell} - E_{n,\ell}^{(0)} \simeq C_{n,\ell}\, a_\ell, \tag{17}$$

where a_ℓ is the scattering length for $\ell = 0$, volume for $\ell = 1$, ...of the strong hA interaction. $C_{n,\ell}$ is a know constant involving the reduced mass and the ℓ^{th} derivative of the radial wave function at the origin of the pure Coulomb problem. Experiments on protonium have been carried out before and after LEAR. For a summary, see e.g., Klempt et al. [68]. The latest results are:

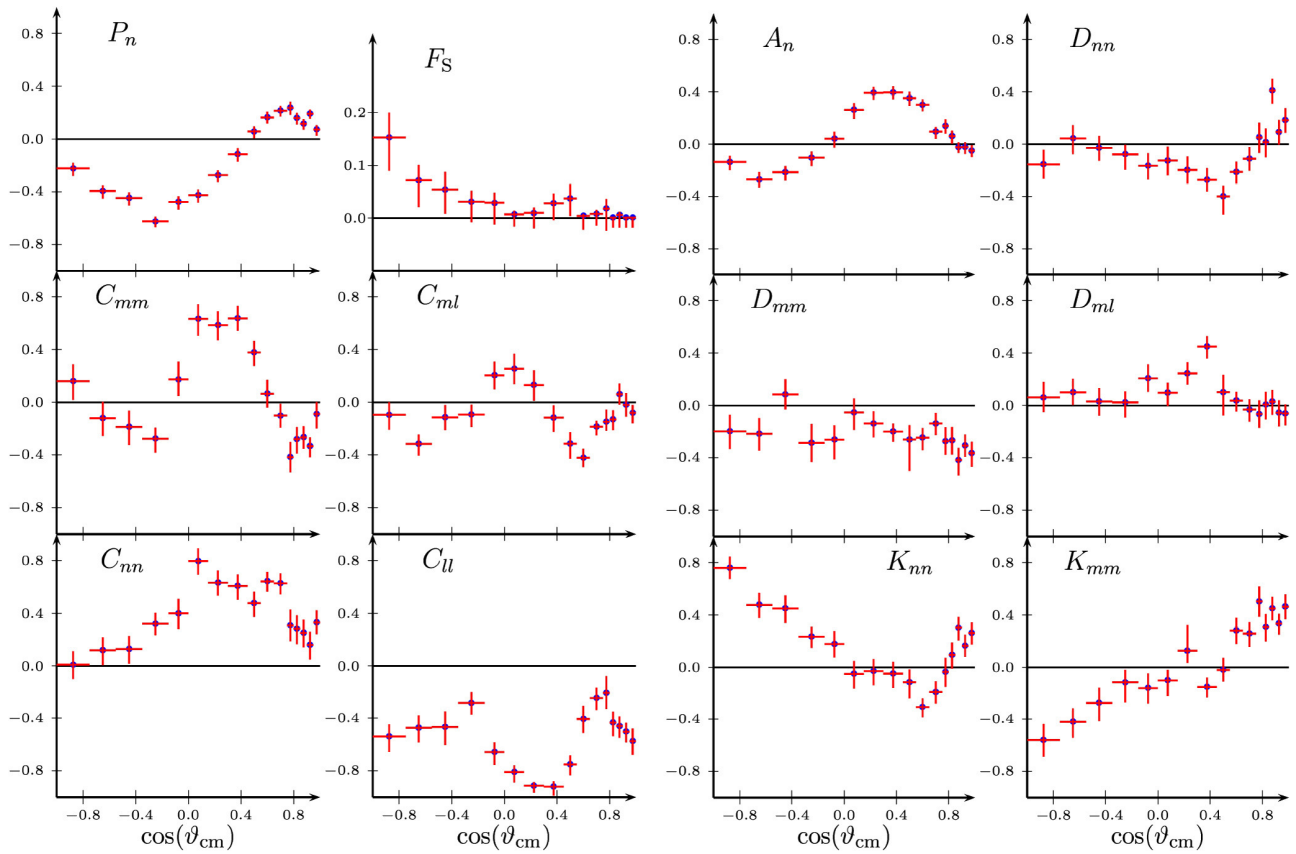


FIGURE 9 | Some spin observables of the reaction $\bar{p}p \to \bar{\Lambda}\Lambda$. Reproduced from Artru et al. [95] with the permission from Physics Reports.

- For the 1S level, the average shift and width are [101] $\delta E(1S) = 712.5 \pm 20.3$ eV (to be compared with the Bohr energy $E(1S) \simeq -12.5$ keV), and $\Gamma(1S) = 1054 \pm 65$ eV, with a tentative separation of the hyperfine level as $\delta E(^3S_1) = 785 \pm 35$ eV, $\Gamma(^3S_1) = 940 \pm 80$ eV, and $\delta E(^1S_0) = 440 \pm 75$ eV, $\Gamma(^1S_0) = 1200 \pm 250$ eV. The repulsive character is a consequence of the strong annihilation.
- For the 2P level, one can not distinguish among $^1P_1$, $SLJ3P1$ and $^3P_2$, but this set of levels is clearly separated from the $^3P_0$ which receives a larger attractive shift, as predicted in potential models (see e.g., [84, 102]) and a larger width. More precisely [103], $\delta E[2(^3P_2, ^3 1_P 1, ^3P_1)] \simeq 0$, $\Gamma[2(^3P_2, ^3 1_P 1, ^3P_1)] = 38 \pm 9$ meV, and $\delta E[2^3P_0] \simeq -139 \pm 28$ mEV, $\Gamma[2^3P_0] = 489 \pm 30$ meV. For the latter, the admixture of the $\bar{n}n$ component is crucial in the calculation, and the wave function at short distances is dominated by it isospin $I = 0$ component [104].

5.1. Quantum Mechanics of Exotic Atoms

Perturbation theory is valid if the energy shift is small as compared to the level spacing. However, a small shift does not mean that perturbation theory is applicable. For instance, a hard core of radius a added to the Coulomb interaction gives a small upward shift to the levels, as long as the core radius a remains small as compared to the Bohr radius R, but a naive application of ordinary perturbation theory will give an infinite correction! For a long-range interaction modified by a strong short-range term, the expansion parameters is the ratio of the ranges, instead of the coupling constant. At leading order, the energy shift is given by the formula of Deser et al. [105], and Trueman [106], which reads

$$\delta E \simeq 4\,\pi\,|\phi_{n\ell}(0)|^2\,a_0, \tag{18}$$

where a_0 is the scattering length in the short-range potential alone, and $\phi_{n\ell}(0)$ the unperturbed wave function at zero separation. For a simple proof, see e.g., Klempt et al. [68]. The formula (18) and its generalization (17) look perturbative, because of the occurrence of the unperturbed wavefunction, but it is not, as the scattering length (volume, ...) a_ℓ implies iterations of the short-range potential.

There are several improvements and generalizations to any superposition of a short-range and a long-range potential, the latter not necessarily Coulombic (see e.g., [107]). For instance, in the physics of cold atoms, one often considers systems experiencing some harmonic confinement and a short-range pairwise interaction.

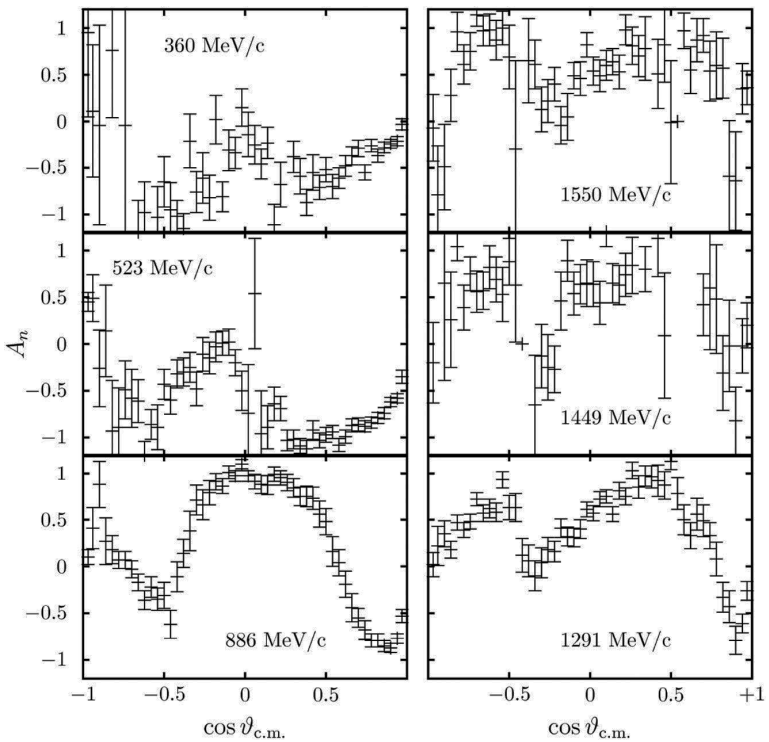


FIGURE 10 | Some results on $\bar{p}p \to \pi\pi$ polarization at LEAR. Reproduced from Artru et al. [95] with the permission from Physics Reports.

5.2. Level Rearrangement

The approximation (18) implies that the scattering length a remains small as compared to the Bohr radius (or, say, the typical size of the unperturbed wave function). Zel'dovich [108], Shapiro [32], and others have studied what happens, when the attractive short-range potential becomes large enough to support a bound state on its own. Let the short-range attractive interaction be $\lambda\, V_{\rm SR}$, with $\lambda > 0$. When λ approaches and passes the critical value λ_0 for the first occurrence of binding in this potential, the whole Coulomb spectrum moves rapidly. The 1S state drops from the keV to the MeV range, the 2S level decreases rapidly and stabilizes in the region of the former 1S, etc. (see for instance, **Figure 13**). Other examples are given in Deloff and Combescure et al. [100, 107].

It was then suggested that a weakly bound quasi-nuclear $\bar{N}N$ state will be revealed by large shifts in the atomic spectrum of protonium [32]. However, this rearrangement scenario holds for a single-channel real potential $V_{\rm SR}$. In practice, the potential is complex, and the Coulomb spectrum is in the $\bar{p}p$ channel, and the putative baryonium in a state of pure isospin $I = 0$ or $I = 1$. Hence, the rearrangement pattern is more intricate.

5.3. Isospin Mixing

In many experiments dealing with "annihilation at rest," protonium is the initial state before the transition $N\bar{N} \to$ mesons. Hence the phenomenological analysis include parameters describing the protonium: S-wave vs. P-wave probability and isospin mixing. Consider, e.g., protonium in the $^1S_0$ state. In a potential model, its dynamics is given by

$$\begin{aligned} -u''(r)/m + V_{11}\,u(r) + V_{12}\,v(r) - \frac{e^2}{r}\,u(r) &= E_{1,0}\,u(r), \\ -v''(r)/m + V_{22}\,v(r) + V_{21}\,u(r) + 2\,\delta m\,u(r) &= E_{1,0}\,v(r), \end{aligned} \tag{19}$$

where δm is the mass difference between the proton and the neutron, and the strong (complex) potentials are the isospin combinations

$$V_{11} = V_{22} = \frac{1}{2}(V_{I=0} + V_{I=1}), \quad V_{12} = V_{21} = \frac{1}{2}(V_{I=0} - V_{I=1}). \tag{20}$$

The energy shift is well-approximated by neglecting the neutron-antineutron component, i.e., $v(r) = 0$. But at short distance, this component is crucial. In most current models, one isospin component is dominant, so that the protonium wave function is dominantly either $I = 0$ or $I = 1$ at short distances, where annihilation takes place. This influences much the pattern of branching ratios. For instance, Dover et al. [104] found in a typical potential model that the $^3P_0$ level consists of 95 % of isospin $I = 0$ in the annihilation region. For $^3P_1$, the $I = 1$ dominates, with 87 %. See references [104, 109, 110] for a detailed study of the role of the $\bar{n}n$ channel on the protonium levels and their annihilation.

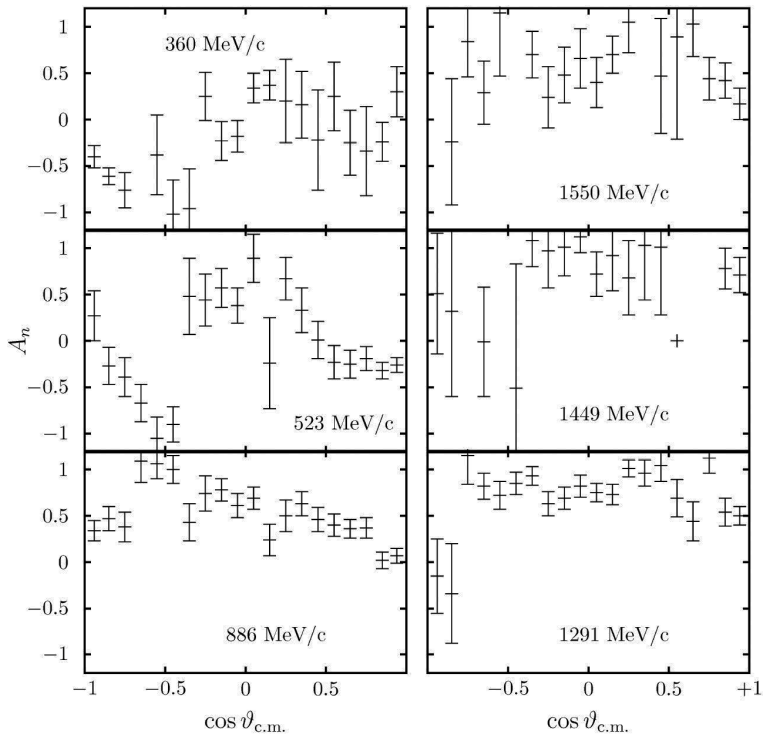


FIGURE 11 | Some results on $\bar{p}p \to \bar{K}K$ polarization at LEAR. Reproduced from Artru et al. [95] with the permission from Physics Reports.

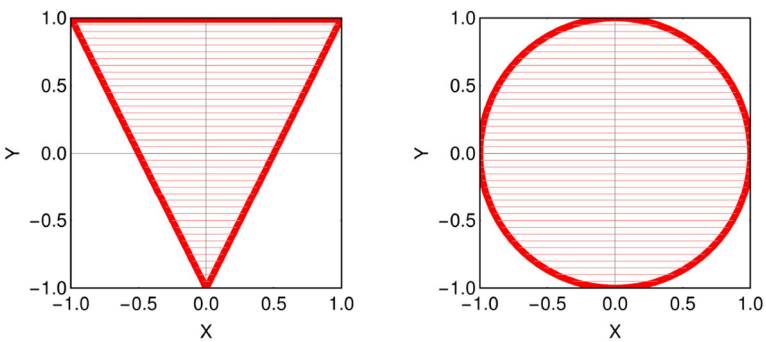


FIGURE 12 | Examples of constraints among spin observables: only the colored area is permitted.

5.4. Day-Snow-Sucher Effect

When a low-energy antiproton is sent on a gaseous or liquid hydrogen target, it is further slowed down by electromagnetic interaction, and is captured in a high orbit of the antiproton-proton system. The electrons are usually expelled during the capture and the subsequent decay of the antiproton toward lower orbits. The sequence favors circular orbits with $\ell = n - 1$, in the usual notation. Annihilation is negligible for the high orbits, and becomes about 1% in 2P and, of course, 100% in 1*S*. This was already predicted in the classic paper by Kaufmann and Pilkuhn [111].

In a dense target, however, the compact $\bar{p}p$ atom travels inside the orbits of the ordinary atoms constituting the target, and experiences there an electric field which, by Stark effect, mixes the $(\ell = n - 1, n)$ level with states of same principal quantum number n and lower orbital momentum. Annihilation occurs from the states with the lowest ℓ. This is known as the Day-Snow-Sucher effect [112]. In practice, to extract the branching ratios and distinguish *S*-wave from *P*-wave annihilation, one studies the rates as a function of the target density.

5.5. Protonium Ion and Protonium Molecule

So far, the physics of hadronic atoms has been restricted to 2-body systems, such as $\bar{p}p$ or K^-A. In fact, if one forgets about the experimental feasibility, there are many other possibilities.

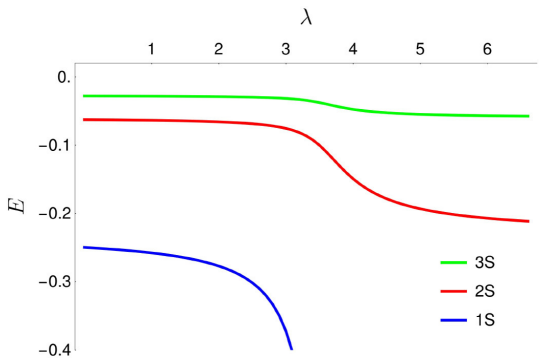


FIGURE 13 | Rearrangement of levels: first three levels of the radial equation $-u''(r) + V(r)\,u(r) = E\,u(r)$ with $V(r) = -1/r + \lambda\, a^2 \exp(-a\,r)$, here with $a = 100$ and λ variable.

If one takes only the long-range Coulomb interaction, without electromagnetic annihilation nor strong interaction, many stable configurations exist, such as $\bar{p}pp$, the protonium ion, or $\bar{p}\bar{p}pp$, the heavy analog of the positronium molecule. Identifying these states and measuring the shift and width of the lowest level would be most interesting. Today this looks as science fiction, as it was the case when $Ps_2 = e^+e^+e^-e^-$ was suggested by Wheeler in 1945. But Ps_2 was eventually detected, in 2007.

6. THE ANTINUCLEON-NUCLEUS INTERACTION

6.1. Antinucleon-Nucleus Elastic Scattering

At the very beginning of LEAR, Garreta et al. [113, 114] measured the angular distribution of $\bar{p}$-A scattering, where A was ^{12}C, ^{40}Ca or ^{208}Pb. Some of their results are reproduced in **Figure 14**[9]. More energies and targets were later measured.

The results have been analyzed by Lemaire et al. in terms of phenomenological optical models [115], which were in turn derived by folding the elementary $\bar{N}N$ amplitudes with the nuclear density (see e.g., [116–118]).

In particular, a comparison of ^{16}O and ^{18}O isotopes (see **Figure 14**), reveals that there is very little isospin dependence of the $\bar{p}N$ interaction, when averaged on spins.

Other interesting measurements of the antinucleon-nucleus interaction have been carried out and analyzed by the PS179 and OBELIX (PS201) collaborations, with more nuanced conclusions about the isospin dependence of the interaction at very low energy (see, for instance [119, 120]).

6.2. Inelastic Scattering

It has been stressed that the inelastic scattering $\bar{p}A \to \bar{p}A^*$, where A is a known excitation of the nucleus A, could provide very valuable information on the spin-isospin dependence of the elementary $\bar{N}N$ amplitude, as the transfer of quantum numbers is identified. One can also envisage the charge-exchange reaction $\bar{p}A \to \bar{n}B^{(*)}$ (see, for instance [121]).

Some measurements were done by PS184, on ^{12}C and ^{18}O [122]. The angular distribution for $\bar{p} + {}^{12}\mathrm{C} \to \bar{p} + {}^{12}\mathrm{C}^*$ is given in **Figure 15** for the case where ^{12}C is the 3^- level at 9.6 MeV. In their analysis, the authors were able to distinguish among models that were equivalent for the $\bar{N}N$ data, but have some differences in the treatment of the short-range part of the interaction. This is confirmed by the analysis in references [121, 123]. Unfortunately, this program of inelastic antiproton-nucleus scattering was not thoroughly carried out.

6.3. Antiprotonic Atoms

The physics is nearly the same as for protonium. A low energy antiproton sent toward a target consisting of atoms of nucleus ^A_ZX, is decelerated by the electromagnetic interaction and captured in a high atomic orbit, and cascades down toward lower orbits. During this process, the electrons are expelled. The difference is that annihilation occurs before reaching the S or P levels, actually when the size of the orbit becomes comparable to the size of the nucleus. Again, the Day-Snow-Sucher mechanism can induce some Stark effect. Thus, precocious annihilation can happen, depending on the density of the target.

A review of the experimental data is provided in Batty et al. and Gotta [124, 125], where a comparison is made with pionic and kaonic atoms. The models developed to describe antiproton-nucleus scattering (see section 6.1) have been applied, and account rather well for the observed shifts. As for the purely phenomenological optical potentials V_{opt}, the most common parametrization is of the form

$$2\,\mu\,V_{\mathrm{opt}} = -4\,\pi\left(1+\frac{\mu}{m}\right)(b_{\mathrm{R}} + i\,b_{\mathrm{I}})\varrho(r), \tag{21}$$

where μ is the reduced mass of $\bar{p}$-A, m the mass of the nucleon, $\varrho(r)$ the nuclear density and $b_{\mathrm{R}} + i\,b_{\mathrm{i}}$ an effective scattering length.

More refined models, aiming at describing simultaneously the data on a variety of nuclei, are written as [124]

$$\begin{aligned} 2\,\mu\,V_{\mathrm{opt}} = -4\,\pi\left(1+\frac{\mu}{m}\right)\big(b_0[\varrho_n(r)+\varrho_p(r)] \\ +b_1[\varrho_n(r)-\varrho_p(r)]\big)\,, \end{aligned} \tag{22}$$

where the complex $b_{0,1}$ are the isospin-independent and isospin-dependent effective scattering lengths, respectively. Further refinements introduce in (22) a "P-wave" term $\boldsymbol{\nabla}.\alpha(r)\,\boldsymbol{\nabla}$, or terms proportional to the square of the density. Typical values are [124]

$$\begin{aligned} b_0 &= (2.7 \pm 0.3) + i\,(3.1 \pm +0.4)\ \mathrm{fm}, \\ b_1 &= (1.2 \pm 1.6) + i\,(1.6 \pm +1.3)\ \mathrm{fm}, \end{aligned} \tag{23}$$

so that there is no firm evidence for a strong isospin dependence.

It is important to stress that the potential V_{opt} is probed mainly at the surface. Its value inside the nucleus hardly matters. The same property is seen in the low-energy heavy-ion collisions: what is important is the interaction at the point where the two ions come in contact.

[9]I thank Matteo Vorabbi for making available his retrieving of the data in a convenient electronic form.

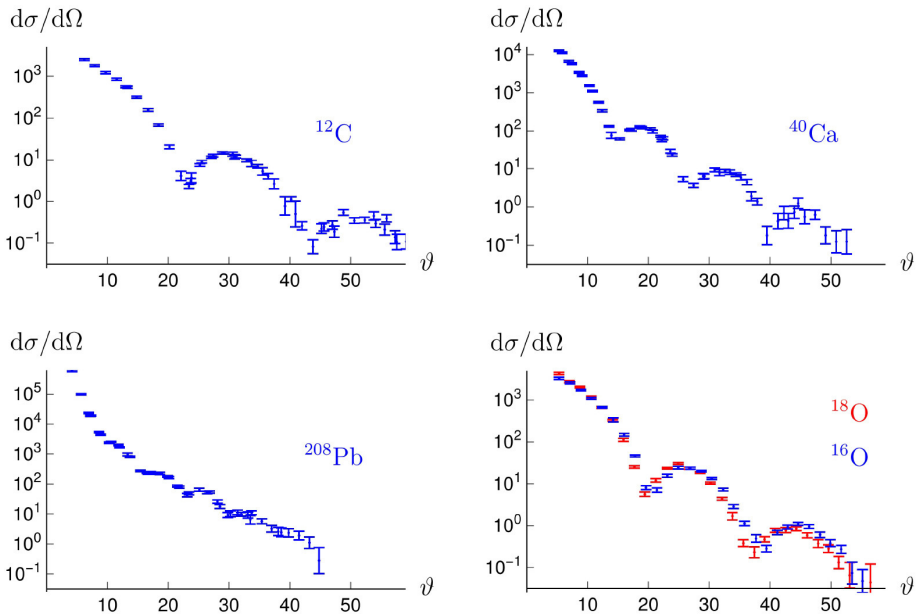


FIGURE 14 | Angular distribution for $\bar{p}$ scattering on the nuclei ^{12}C, ^{40}Ca, and ^{208}Pb at kinetic energy $T_{\bar{p}} = 180$ MeV, and on the two isotopes ^{16}O and ^{16}O [113, 114].

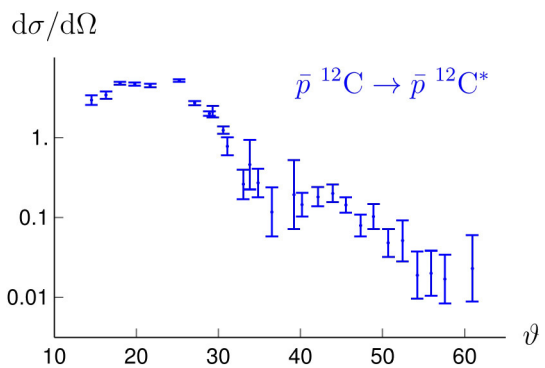


FIGURE 15 | Angular distribution of the $^{12}C(\bar{p},\bar{p})^{12}C^*$ reaction for the 3^- excited state at 9.6 MeV [122]. The incident $\bar{p}$ has an energy of 179.7 MeV.

6.4. Antiproton-Nucleus Dynamics

Modeling the antiproton-nucleus interaction has been done with various degrees of sophistication. We have seen in the last section that phenomenological (complex) potentials proportional to the nuclear density account for a wide body of data on antiprotonic atoms. A relativistic mean-field approach was attempted years ago by Bouyssy and Marcos [126] and revisited more recently [127]. Meanwhile, a Glauber approach has been formulated [128] and applied to the elastic and inelastic scattering of relativistic antiprotons.

There is a persisting interest in the domain of very low energies and possible bound states. For instance, Friedman et al. [129] analyzed the subtle interplay between the $\bar{N}N$ S- and P-waves when constructing the antiproton-nucleus potential. There has been also speculations about possible $\bar{p} - A$ states, in line with the studies on the molecular $\bar{N}N$ baryonium. For a recent update, see e.g., Hrtánková and Mareš [130].

One could also envisage to use antiprotons to probe the tail of the nuclear density for neutron-rich nuclei with a halo structure. For early references, see Bradamante et al. [27]. Recently, the PUMA proposal suggests an investigation by low-energy antiprotons of some unstable isotopes, for which the conventional probes have limitations [131].

6.5. Neutron-Antineutron Oscillations

In some theories of grand unification, the proton decay is suppressed, and one expects neutron-to-antineutron oscillations. An experimental search using free neutrons has been performed at Grenoble [132], with a limit of about $\tau_{n\bar{n}} \gtrsim 10^{-8}$ s for the oscillation period. Any new neutron source motivates new proposals of the same vein (see e.g., [133]).

An alternative is to use the bound neutrons of nuclei. The stability of, say, ^{16}O, reflects as well the absence of decay of its protons as the lack of $n \to \bar{n}$ conversion with subsequent annihilation of the antineutron. It has been sometimes argued [134] that the phenomenon could be obscured in nuclei by uncontrolled medium corrections. However, the analysis shows that the neutrons oscillate mainly outside the nucleus, and the subsequent annihilation takes place at the surface, so that, fortunately, the medium corrections are small.

The peripheral character of the $n\bar{n}$ oscillations in nuclei explains why a simple picture (sometimes called closure approximation) does not work too well, with the neutron and the antineutron in a box feeling an average potential $\langle V_n \rangle$ or $\langle V_{\bar{n}} \rangle$, resulting in a simple 2×2 diagonalization. The true dynamics of

$n\bar{n}$ oscillations relies on the tail of the neutron distribution, where n and $\bar{n}$ are almost free.

There are several approaches, see for instance [135]. The simplest is based on the Sternheimer equation, which gives the first order correction to the wave function without summing over unperturbed states. In a shell model with realistic neutron (reduced) radial wave functions $u_{n\ell J}(r)$ with shell energy $E_{n\ell J}$, the induced $\bar{n}$ component is given by

$$-\frac{w''_{n\ell J}(r)}{\mu}+\frac{\ell(\ell+1)}{\mu\, r^2}+V_{\bar{n}}(r)\, w'_{n\ell J}(r)-E_{n\ell J}\, w'_{n\ell J}(r)=\gamma\, u_{n\ell J}(r), \tag{24}$$

with μ the reduced mass of the $\bar{n}$-$(A-1)$ system, $V_{\bar{n}}$ the complex (optical) $\bar{n}$-$(A-1)$ potential, and $\gamma = 1/\tau_{n\bar{n}}$ the strength of the transition. Once $w_{n\ell J}$ is calculated, one can estimate the second-order correction to the energy, and in particular the width $\Gamma_{n\ell J}$ of this shell

$$\Gamma_{n\ell J} = -2\int_0^\infty \mathrm{Im}\, V_{\bar{n}}\, |w_{n\ell J}(r)|^2\, \mathrm{d}r = -2\,\gamma \int_0^\infty u_{n\ell J}(r)\ \mathrm{Im}\, w_{n\ell J}(r)\, \mathrm{d}r, \tag{25}$$

which scales as

$$\Gamma_{n\ell J} \propto \gamma^2. \tag{26}$$

An averaging over the shells give a width per neutron Γ associated with a lifetime T

$$T = T_r\, \tau_{n\bar{n}}^2, \tag{27}$$

where T_r is named either the "reduced lifetime" (in s^{-1}) or the "nuclear suppression factor." The spatial distribution of the $w_{n\ell J}$ and the integrands in (25), the relative contribution to Γ clearly indicate the peripheral character of the process. See e.g., Barrow et al. [136] for an application to a simulation in the forthcoming DUNE experiment, and refs. there to earlier estimates. Clearly, DUNE will provide the best limit for this phenomenon.

For the deuteron, an early calculation by Dover et al. [137] gave $T_r \simeq 2.5 \times 10^{22}\,\mathrm{s}^{-1}$. Oosterhof et al. [138], in an approach based on effective chiral theory (see section 8), found a value significantly smaller, $T_r \simeq 1.1 \times 10^{22}\,\mathrm{s}^{-1}$. However, their calculation has been revisited by Haidenbauer and Meißner [139], who got almost perfect agreement with Dover et al. For ^{40}Ar relevant for the DUNE experiment, the result of [136] is $T_r \simeq 5.6 \times 10^{22}\,\mathrm{s}^{-1}$.

7. ANTINUCLEON ANNIHILATION

7.1. General Considerations

$N\bar{N}$ annihilation is a rather fascinating process, in which the baryon and antibaryon structures disappear into mesons. The kinematics is favorable, with an initial center-of-mass energy of 2 GeV at rest and more in flight, allowing in principle up to more than a dozen of pions. Of course, the low mass of the pion is a special feature of light-quark physics. We notice, however, that the quark model predicts that $(QQQ) + (\bar{Q}\bar{Q}\bar{Q}) > 3(Q\bar{Q})$ [140], so that annihilation at rest remains possible in the limit where all quarks are heavy. The same quark models suggest that $(\bar{Q}\bar{Q}\bar{Q}) + (qqq) < 3\,(\bar{Q}q)$ if the mass ratio Q/q becomes large, so that, for instance, a triply-charmed antibaryon $(\bar{c}\bar{c}\bar{c})$ would not annihilate on an ordinary baryon.

One should acknowledge at the start of this section that there is no theory, nor even any model, that accounts for the many data accumulated on $\bar{N}N$ annihilation. Actually the literature is scattered across various subtopics, such a the overall strength and range of annihilation, the average multiplicity, the percentage of events with hidden-strangeness, the explanation of specific branching ratios, such as the one for $\bar{p}p \to \rho\,\pi$, the occurrence of new meson resonances, etc. We shall briefly survey each of these research themes.

7.2. Quantum Numbers

An initial $\bar{N}N$ state with isospin I, spin S, orbital momentum L and total angular momentum J has parity $P = -(-1)^L$ and G-parity $G = (-1)^{I+L+S}$. If the system is neutral, its charge conjugation is $C = (-1)^{L+S}$. A summary of the quantum numbers for the S and P states is given in **Table 1**.

So, for a given initial state, some transitions are forbidden or allowed. The result for some important channels is shown in **Table 2**. In particular, producing two identical scalars or pseudoscalars requires an initial P-state.

The algebra of quantum numbers is not always trivial, especially if identical mesons are produced. For instance, the question was raised whether or not the $^1\mathrm{S}_0$ state of protonium with $J^{PC} = 0^{-+}$ and $I^G = 0$ can lead to a final state made of four π^0. An poll among colleagues gave an overwhelming majority of negative answers. But a transition, such as $^1\mathrm{S}_0 \to 4\,\pi^0$ is actually possible at the expense of several internal orbital excitations among the pions. For an elementary proof, see Klempt et al. [87], for a more mathematical analysis [141].

The best known case, already mentioned in section 1, deals with $\pi\pi$. An S-wave $\pi^+\pi^-$ with a flat distribution, or a $\pi^0\pi^0$ system (necessarily with $I = 0$ and J even) requires an initial state $^{1,3}\mathrm{P}_0$. It has been observed to occur even in annihilation at rest on a dilute hydrogen target [142]. This is confirmed by a study of the $J = 0$ vs. $J = 1$ content of the $\pi\pi$ final state as a function of the density of the target, as already mentioned in section 5.4.

7.3. Global Picture of Annihilation

As already stressed, the main feature of annihilation is its large cross-section, which comes together with a suppression of the charge-exchange process. This is reinforced by the observation that even at rest, annihilation is not reduced to an S-wave phenomenon. This is hardly accommodated with a zero-range mechanism, such as baryon exchange. The baryon exchange, for say, annihilation into two mesons is directly inspired by electron exchange in $e^+\,e^- \to \gamma\,\gamma$ (see **Figure 16**). After iteration, the absorptive part of the $\bar{N}N$ interaction, in this old-fashioned picture, would be driven by diagrams, such as the one in **Figure 16**. Other contributions involve more than two mesons and crossed diagrams. As analyzed (e.g., [143, 144]), this corresponds to a very small range, practically a contact interaction. Not surprisingly, it was impossible to follow this

TABLE 1 | Quantum numbers of the S and P partial waves (PW) of the $\bar{N}N$ system. The notation is $^{2I+1,2S+1}L_J$.

PW	$^{1,1}S_0$	$^{3,1}S_0$	$^{1,3}S_1$	$^{3,3}S_1$	$^{1,1}P_1$	$^{3,1}P_1$	$^{1,3}P_0$	$^{3,3}P_0$	$^{1,3}P_1$	$^{3,3}P_1$	$^{1,3}P_2$	$^{3,3}P_2$
J^{PC}	0^{-+}	0^{-+}	1^{--}	1^{--}	1^{+-}	1^{+-}	0^{++}	0^{++}	1^{++}	1^{++}	2^{++}	2^{++}
I^G	0^+	1^-	0^-	1^+	0^-	1^+	0^+	1^-	0^+	1^-	0^+	1^-

TABLE 2 | Allowed decays from S and P-states into some two-meson final states.

FS	$^{1,1}S_0$	$^{3,1}S_0$	$^{1,3}S_1$	$^{3,3}S_1$	$^{1,1}P_1$	$^{3,1}P_1$	$^{1,3}P_0$	$^{3,3}P_0$	$^{1,3}P_1$	$^{3,3}P_1$	$^{1,3}P_2$	$^{3,3}P_2$
$\pi^0\pi^0$							√				√	
$\pi^-\pi^+$				√			√				√	
$\pi^0\eta^{(\prime)}$								√				√
$\eta^{(\prime)}\eta^{(\prime)}$							√				√	
K^-K^+			√	√			√	√			√	√
K_sK_l			√	√								
K_sK_s							√	√			√	√
$\pi^0\omega(\phi)$				√		√						
$\eta^{(\prime)}\omega(\phi)$			√		√							
$\pi^0\rho^0$			√		√							
$\eta^{(\prime)}\rho^0$				√		√						
$\pi^\pm\rho^\mp$		√	√		√					√		√

prescription when building optical models to fit the observed cross-sections. Among the contributions, one may cite [62, 77–79]. Claims, such as Côté et al. [145], that it is possible to fit the cross sections with a short-range annihilation operator, are somewhat flawed by the use of very large strengths, wide form factors, and a momentum dependence of the optical potential that reinforce annihilation in $L > 0$ partial waves.

In the 80s, another point of view started to prevail: annihilation should be understood at the quark level[10]. This picture was hardly accepted by a fraction of the community. An anecdote illustrates how hot was the debate. After a talk at the 1988 Mainz conference on antiproton physics, where I presented the quark rearrangement, Shapiro strongly objected. At this time, the questions and answers were recorded and printed in the proceedings. Here is the verbatim [148]: *I.S. Shapiro (Lebedev) : The value of the annihilation range . . . is not a question for discussion. It is a general statement following from the analytical properties of the amplitudes in quantum field theory . . . . It does not matter how the annihilating objects are constructed from their constituents. It is only important that, in the scattering induced by annihilation, an energy of at least two baryons masses is transferred. J.M. Richard: First of all, for me, this is an important "question for discussion." In fact, we agree completely in the case of "total annihilation," for instance* $\bar{N}N \to \phi\phi$. *The important point is that [baryons and] mesons are composite, so, what we call "annihilation" is, in most cases, nothing but a soft rearrangement of the constituents, which does not have to be short range.*

In the simplest quark scenario, the spatial dependence of "annihilation" comes from that this is not an actual annihilation similar to $e^+e^- \to$ photons, in which the initial constituents disappear, but a mere *rearrangement* of the quarks, similar to the rearrangement of the atoms in some molecular collisions. This corresponds to the diagram of **Figure 17**. The amplitude for this process is $\langle\Psi_f|H|\Psi_i\rangle$, where H is the 6-quark Hamiltonian, Ψ_i the nucleon-antinucleon initial state, and Ψ_f the final state made of three mesons. See, for instance [149–151], for the details about the formalism. One gets already a good insight on the spatial distribution of annihilation within the quark-rearrangement model by considering the mere overlap $\langle\Psi_f|\Psi_i\rangle$ using simple oscillator wave functions. For the initial state, a set of Jacobi coordinates (here normalized to correspond to an unitary transformation)

$$\boldsymbol{x} = \frac{\boldsymbol{r}_2 - \boldsymbol{r}_1}{\sqrt{2}}, \qquad \boldsymbol{y} = \frac{2\,\boldsymbol{r}_3 - \boldsymbol{r}_1 - \boldsymbol{r}_2}{\sqrt{6}}, \qquad \boldsymbol{z} = \frac{\boldsymbol{r}_1 + \boldsymbol{r}_2 + \boldsymbol{r}_3}{\sqrt{3}},$$
$$\boldsymbol{x}' = \frac{\boldsymbol{r}_5 - \boldsymbol{r}_4}{\sqrt{2}}, \qquad \boldsymbol{y}' = \frac{2\,\boldsymbol{r}_6 - \boldsymbol{r}_4 - \boldsymbol{r}_5}{\sqrt{6}}, \qquad \boldsymbol{z}' = \frac{\boldsymbol{r}_4 + \boldsymbol{r}_5 + \boldsymbol{r}_6}{\sqrt{3}}, \tag{28}$$

with the further change

$$\boldsymbol{r} = \frac{\boldsymbol{z}' - \boldsymbol{z}}{\sqrt{2}}, \qquad \boldsymbol{R} = \frac{\boldsymbol{z} + \boldsymbol{z}'}{\sqrt{2}}, \tag{29}$$

which, to a factor, are the $\bar{N}N$ separation and the overall center of mass. The initial-state wave function is thus of

[10] Of course, the rearrangement was introduced much earlier, in particular by Stern, Rubinstein, Caroll, . . . [146, 147], but simply to calculate ratios of branching ratios, without any attempt to estimate the cross sections.

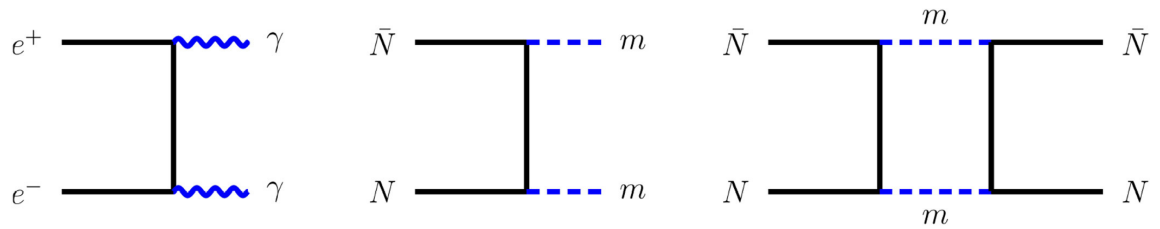


FIGURE 16 | e^+e^- annihilation into two photons (left), $\bar{N}N$ annihilation into two mesons (center) and its iteration contributing to the absorptive part of the $\bar{N}N$ amplitude.

the form

$$\Psi_i = \left(\frac{\alpha}{\pi}\right)^3 \exp\left[-(\alpha/2)(\boldsymbol{x}^2 + \boldsymbol{y}^2 + \boldsymbol{x}'^2 + \boldsymbol{y}'^2)\right] \varphi(\boldsymbol{r}), \quad (30)$$

where φ denotes the $\bar{N}N$ wave function. Similarly for the final state, one can introduce the normalized Jacobi coordinates

$$\begin{aligned}
\boldsymbol{u}_1 &= \frac{\boldsymbol{r}_4 - \boldsymbol{r}_1}{\sqrt{2}}, \quad & \boldsymbol{u}_2 &= \frac{\boldsymbol{r}_5 - \boldsymbol{r}_2}{\sqrt{2}}, \quad & \boldsymbol{u}_3 &= \frac{\boldsymbol{r}_6 - \boldsymbol{r}_3}{\sqrt{2}}, \\
\boldsymbol{v}_1 &= \frac{\boldsymbol{r}_1 + \boldsymbol{r}_4}{\sqrt{2}}, \quad & \boldsymbol{v}_2 &= \frac{\boldsymbol{r}_2 + \boldsymbol{r}_5}{\sqrt{2}}, \quad & \boldsymbol{v}_3 &= \frac{\boldsymbol{r}_3 + \boldsymbol{r}_6}{\sqrt{2}}, \\
\boldsymbol{X} &= \frac{\boldsymbol{v}_2 - \boldsymbol{v}_1}{\sqrt{2}}, \quad & \boldsymbol{Y} &= \frac{2\,\boldsymbol{v}_3 - \boldsymbol{v}_1 - \boldsymbol{v}_2}{\sqrt{6}}, \quad & \boldsymbol{R} &= \frac{\boldsymbol{v}_1 + \boldsymbol{v}_2 + \boldsymbol{v}_3}{\sqrt{3}},
\end{aligned} \quad (31)$$

and the wave function

$$\Psi_f = \left(\frac{\beta}{\pi}\right)^{9/4} \exp\left[-(\beta/2)(\boldsymbol{u}_1^2 + \boldsymbol{u}_2^2 + \boldsymbol{u}_3^2)\right] \Phi(\boldsymbol{X}, \boldsymbol{Y}). \quad (32)$$

Integrating for instance over $\boldsymbol{x}' - \boldsymbol{x}$ and $\boldsymbol{y}' - \boldsymbol{y}$, one ends with

$$\Phi_f^*(\boldsymbol{X}, \boldsymbol{Y}) \exp(-\beta \boldsymbol{r}^2/2) \exp(-\alpha(\boldsymbol{X}^2 + \boldsymbol{Y}^2)/2)\, \varphi(\boldsymbol{r}), \quad (33)$$

and after iteration, one gets a separable operator $v(r)\, v(r')$, where $v(r)$ is proportional to $\exp(-\beta r^2/2)$ and contains some energy-dependent factors [149, 151]. As expected, the operator is not local. There is an amazing exchange of roles: the size of the baryon, through the parameter α, governs the spatial spread of the three mesons, while the size the mesons becomes the range of the separable potential. Schematically speaking, the range of "annihilation" comes from the ability of the mesons to make a bridge, to pick up a quark in the baryon and an antiquark in the antibaryon.

Explicit calculations show that the rearrangement potential has about the required strength to account for the observed annihilation cross-sections. Of course, the model should be improved to include the unavoidable distortion of the initial- and final-state hadrons. Also one needs a certain amount of intrinsic quark-antiquark annihilation and creation to explain the production of strange mesons. This leads us to the discussion about the branching ratios.

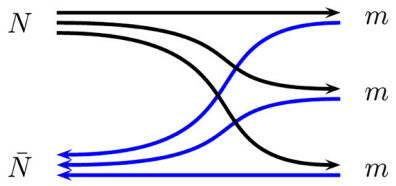


FIGURE 17 | Rearrangement of the quarks and antiquarks from a baryon and an antibaryon to a set of three mesons.

7.4. Branching Ratios: Experimental Results

Dozens of final states are available for $\bar{N}N$ annihilation, even at rest. When the energy increases, some new channels become open. For instance, the $\phi\phi$ channel was used to search for glueballs in the PS202 experiment [152]. However, most measurements have been performed at rest with essentially two complementary motivations. The first one was to detect new multi-pion resonances, and, indeed, several mesons have been either discovered or confirmed thanks to the antiproton-induced reactions. The second motivation was to identify some leading mechanisms for annihilation, and one should confess that the state of the art is not yet very convincing.

Several reviews contain a summary of the available branching ratios and a discussion on their interpretation (see e.g., [87, 153]). We shall not list all available results, but, instead, restrict ourselves to the main features or focus on some intriguing details. For instance:

- The average multiplicity is about 4 or 5. But in many cases, there is a formation of meson resonances, with their subsequent decay. In a rough survey, one can estimate that a very large fraction of the annihilation channels are compatible with the primary formation of two mesons which subsequently decay.
- In the case of a narrow resonance, one can distinguish the formation of a resonance from a background made of uncorrelated pions, e.g., $\omega\pi$ from $\pi\pi\pi\pi$. In the case of broad resonances, e.g., $\rho\pi$ vs. $\pi\pi\pi$, this is much more ambiguous.
- The amount of strangeness, in channels, such as $\bar{K}+K$, $\bar{K}+K^*$, $\bar{K}+K+$ pions, is about 5%.
- Charged states, such as $\bar{p}n$ or $\bar{n}p$ are pure isospin $I = 1$ initial state. In the case of $\bar{p}p$ annihilation at rest, the isospin is not known, except if deduced from the final state, like in the

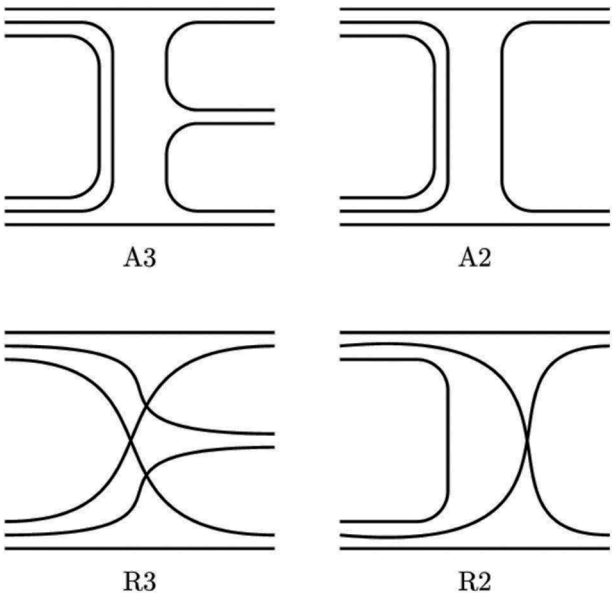


FIGURE 18 | Some quark diagrams describing annihilation.

case of $\pi\eta$. Indeed, $\bar{p}p$ is the combination $(|I = 0\rangle + |I = 1\rangle)/\sqrt{2}$. But, at short distances, one of the components often prevails, at least in model calculations. In the particle basis, there is an admixture of $\bar{n}n$ component, which, depending on its relative sign, tends to make either a dominant $I = 0$, or $I = 1$. For instance, Kudryavtsev [154] analyzed the channels involving two pseudoscalars, and concluded that if protonium annihilation is assumed to originate from an equal mixture of $I = 0$ and $I = 1$, then annihilation is suppressed in one of the isospin channels, while a better understanding is achieved, if $\bar{p}p - \bar{n}n$ is accounted for.

7.5. Branching Ratios: Phenomenology

The simplest model, and most admired, is due to Vandermeulen [155]. It assumes a dominance of 2-body modes, say $\bar{N}N \to a + b$, where a and b are mesons or meson resonances, produced preferentially when the energy is slightly above the threshold $s_{ab}^{1/2} = m_a + m_b$. More precisely, the branching ratios are parameterized as

$$f = C_{ab}\, p(\sqrt{s}, m_a, m_b)\, \exp[-A(s - s_{ab})], \tag{34}$$

where A is an universal parameter, p the center-of-mass momentum and the constant C_{ab} assume only two values: C_0 for non-strange and C_1 for strange.

In the late 80s, following the work by Green and Niskanen [149, 150], and others, there were attempts to provide a detailed picture of the branching ratios, using quark-model wave functions supplemented by operators to create or annihilate quark-antiquark pairs. A precursor was the so-called $^3P_0$ model [156] introduced to describe decays, such as $\Delta \to N + \pi$.

There has been attempts to understand the systematics of branching ratios at the quark level. We already mentioned some early papers [146, 147]. In the late 80s and in the 90s, several papers were published, based on a zoo of quark diagrams. Some of them are reproduced in **Figure 18**. The terminology adopted is A*n* or R*n* for annihilation or rearrangement into *n* mesons. Of course, they are not Feynman diagrams, but just a guidance for a quark model calculation with several assumptions to be specified. On the one had, the R3 diagram comes as the most "natural," as it does not involve any change of the constituents. On the other hand, it was often advocated that planar diagrams should be dominant (see e.g., [157]). This opinion was, however, challenged by Pirner in his re-analysis the $1/N_c$ expansion, where N_c is the number of colors in QCD [158].

A key point is of course strangeness. The R3 diagram hardly produces kaons, except if extended as to include the sea quarks and antiquarks. On the other hand, the A*n* diagrams tend to produce too often kaons, unless a controversial *strangeness suppression factor* is applied: at the vertex where a quark-antiquark pair is created, a factor $f = 1$ is applied for $q = u, d$ and $f \ll 1$ for $q = s$. This is an offending violation of the flavor $SU(3)_F$ symmetry. For instance the decays $J/\psi \to p\bar{p}$ and $J/\psi \to \Lambda\bar{\Lambda}$ are nearly identical, especially once phase-space corrections are applied. The truth is that at low-energy, strangeness is dynamically suppressed by phase-space and a kind of tunneling effect [159]. This could have been implemented more properly in the analyses of the branching ratios. An energy-independent strangeness suppression factor is probably too crude.

Note that a simple phenomenology of quark diagrams is probably elusive. A diagram involving two primary mesons can lead to 4 or 5 pions after rescattering or the decay of a resonance. Also the A*n* diagrams require a better overlap of the initial baryon and antibaryon, and thus are of shorter range than the R*n* diagrams. So the relative importance can vary with the impact parameter and the incident energy.

7.6. Annihilation on Nuclei

There has been several studies of $\bar{N}$-A annihilation. In a typical scenario, a primary annihilation produces mesons, and some of them penetrate the nucleus, giving rise to a variety of phenomenons: pion production, nucleon emission, internal excitation, etc. (see e.g., [160]). Some detailed properties have been studied, for instance whether annihilation on nuclei produces less or more strange particles than annihilation on nucleons [161].

At very low energy, due to the large $\bar{N}N$ cross section, the primary annihilation takes place near the surface. It has been speculated that with medium-energy antiprotons, thanks to the larger momentum and the smaller cross section, the annihilation could sometimes take place near the center of the nucleus. Such rare annihilations with a high energy release (at least 2 GeV) and little pressure, would explore a sector of the properties of the nuclear medium somewhat complementary to the heavy-ion collisions (see e.g., [14, 162–164]).

Note the study of Pontecorvo reactions. In $\bar{N}N$ annihilation, at least two mesons have to be produced, to conserve energy

and momentum. On a nucleus, there is the possibility of primary annihilation into n mesons, with $n-1$ of them being absorbed by the remaining nucleons. An example is $\bar{p}NN \rightarrow \pi N$ or ϕn [165, 166]. This is somewhat related to the pionless decay of Λ in hypernuclei [167].

7.7. Remarkable Channels

Some annihilation channels have retained the attention:

- $p\bar{p} \rightarrow e^+e^-$ led to a measurement of the proton form factor in the time-like region. The reversed reaction $e^+e^- \rightarrow p\bar{p}$ was studied elsewhere, in particular at Frascati. For a general overview, see [168, 169], and for the results of the PS170 collaboration at CERN [170].
- We already mentioned the $\bar{p}p \rightarrow$ charmonium $\rightarrow$ hadrons, leading to a better measurement of the width of some charmonium states, and the first indication for the h_c, the $^1P_1$ level of $c\bar{c}$ [10, 171]. In principle, while $e^+e^- \rightarrow$ charmonium is restricted to the $J^{PC} = 1^{--}$ states, $\bar{p}p$ can match any partial wave. However, perturbative QCD suggests that the production is suppressed for some quantum numbers. It was thus a good surprise that $\eta_c(1S)$ was seen in $\bar{p}p$, but the coupling turns out less favorable for $\eta_c(2S)$ [11, 172].
- The overall amount of hidden-strangeness is about 5 % [87]. This is remarkably small and is hardly accommodated in models where several incoming $q\bar{q}$ pairs are annihilated and several quark-antiquark pairs created. Note that the branching ratio for K^+K^- is significantly larger for an initial S-wave than for P-wave [46]. This confirms the idea that annihilation diagrams are of shorter range than the rearrangement ones.
- $\bar{p}p \rightarrow K^0\bar{K}^0$ in the so-called CPLEAR experiment (PS195) [173] gave the opportunity to measure new parameters of the CP violation in the neutral K systems, a phenomenon first discovered at BNL in 1964 by Christenson, Cronin, Fitch, and Turlay[11]. The CPLEAR experiment found evidence for a direct T-violation (time reversal).
- Precision measurements of the $\bar{p}p \rightarrow \gamma + X$ and $\bar{p}p \rightarrow \pi + X$ in search of bound baryonium, of which some indications were found before LEAR. The results of more intensive searches at LEAR were unfortunately negative (see e.g., [174]). When combined to the negative results of the scattering experiments, this was seen as the death sentence of baryonium. But, as mentioned in section 3, this opinion is now more mitigated, because of the $p\bar{p}$ enhancements observed in the decay of heavy particles.
- $\bar{p}p \rightarrow \rho\pi$ has intriguing properties. Amazingly, the same decay channel is also puzzling in charmonium decay, as the ratio of $\psi(2S) \rightarrow \rho\pi$ to $J/\psi \rightarrow \rho\pi$ differs significantly from its value for the other channels (see e.g., [175] and references therein). In the case of $\bar{p}p$ annihilation, the problem (see e.g., [46]), is that the production from $^{1,3}S_1$ is much larger than from $^{1,3}S_0$. Dover et al., for instance, concluded to the dominance of the A2 type of diagram [176], once the quark-antiquark creation operator is assumed to be given by the $^3P_0$ model [156]. But the A2 diagram tends to produce too often kaons!
- $\bar{p}N \rightarrow \bar{K} + X$, if occurring in a nucleus, monitors the production of heavy hypernuclei. It was a remarkable achievement of the LEAR experiment PS177 by Polikanov et al. to measure the lifetime of heavy hypernuclei (see e.g., [177]).
- $p\bar{p} \rightarrow \pi^+\pi^-$ and $p\bar{p} \rightarrow K^+K^-$ by PS172 revealed striking spin effects (see section 4.8).
- $p\bar{p} \rightarrow \phi\phi$ was used to search for glueballs (Experiment PS 202 "JETSET") [152], with innovative detection techniques.

8. MODERN PERSPECTIVES

So far in this review, the phenomenological interpretation was based either on the conventional meson-exchange picture or on the quark model for annihilation. The former was initiated in the 50s, and the latter in the 80s. Of course, it is not fully satisfactory to combine two different pictures, one for the short-range part, and another for the long-range, as the results are very sensitive to the assumptions for the matching of the two schemes. This is one of the many reasons why the quark-model description of the short-range nucleon-nucleon interaction has been abandoned, though it provided an interesting key for a simultaneous calculation of all baryon-baryon potentials. One way out that was explored consists of exchanging the mesons between quarks. Then the quark wave function generates a form factor. For $N\bar{N}$, a attempt was made by Entem and Fernández [102], with some phenomenological applications. In this paper, the annihilation potential is due to transition $q\bar{q} \rightarrow$ meson $\rightarrow q\bar{q}$ or $q\bar{q} \rightarrow$ gluon $\rightarrow q\bar{q}$. But this remains a rather hybrid picture and it was not further developed.

Somewhat earlier, in the 80s, interesting developments of the bag model have been proposed, where the nucleon is given a pion cloud that restores its interaction with other nucleons. This led to a solitonic picture, e.g., Skyrme-type of models for low-energy hadron physics [178]. A first application to $\bar{N}N$ was proposed by Zahed and Brown [179].

As seen in other chapters of this book, a real breakthrough was provided by the advent of effective chiral theories, with many successes, for instance in the description of the $\pi\pi$ interaction. For a general introduction, see e.g., the textbook by Donnelly et al. [180]. This approach was adopted by a large fraction of the nuclear-physics community, and, in particular, it was applied to the study of nuclear forces and nuclear structures. Chiral effective field theory led to very realistic potentials for the NN interaction, including the three-body forces and higher corrections in a consistent manner [181, 182]. Thus, the meson-exchange have been gradually forsaken.

In such modern NN potentials, one can identify the long-range part due to one-, two- or three-pion exchange, and apply

[11] Happy BNL director, as his laboratory also hosted the experiment in which the Ω^- was discovered, the same year 1964.

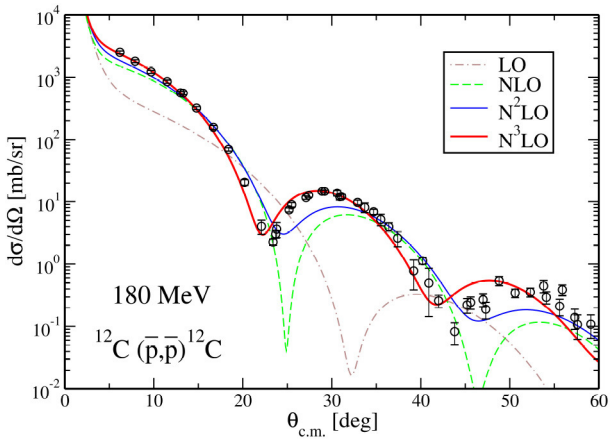


FIGURE 19 | Differential cross-section for elastic $\bar{p}$ scattering on ^{12}C at 180 MeV. The optical potential is computed from successive refinements in the effective theory. Reproduced from Vorabbi et al. [186] with the permission of the authors.

the G-parity rule, to derive the corresponding long-range part of the $\bar{N}N$ potential. The short-range part of the NN interaction is determined empirically, by fixing the strength of a some constant terms which enter the interaction in this approach. This part cannot be translated as such to the $\bar{N}N$ sector. There exists for sure, analogous constant terms that describe the real part of the interaction. As for the annihilation part, there are two options. The first one consists of making the contact terms complex. This is the choice made by Chen et al. [183]. Another option that keeps unitarity more explicit is to introduce a few effective meson channels X_i and iterate, i.e., $\bar{N}N \rightarrow X \rightarrow \bar{N}N$, with the propagator of the mesonic channel X_i properly inserted [184]. Then some empirical constant terms enter now the transition potential $V(\bar{N}N \rightarrow X_i)$. A fit of the available data determines in principle the constants of the model [74]. The question remains whether the fit of the constant terms is unique, given the sparsity of spin observables. For a recent review on chiral effective theories applied to antiproton physics (see [76, 185]). The phenomenology will certainly extent beyond scattering data. One can already notice that the amplitude of Dai et al. [184], when properly folded with the nuclear density, provides with an optical potential that accounts fairly well for the scattering data, as seen in **Figure 19** borrowed from Vorabbi et al. [186].

9. OUTLOOK

The physics of low-energy antiprotons covers a variety of topics: fundamental symmetries, atomic physics, inter-hadronic forces, annihilation mechanisms, nuclear physics, etc.

New experiments are welcome or even needed to refine our understanding of this physics. For instance, a better measurement of the shift and width of the antiprotonic lines, and some more experiments on the scattering of antineutrons off nucleons or nuclei. We also insisted on the need for more measurements on $\bar{p}p$ scattering with a longitudinally or transversally polarized target.

Selected annihilation measurements could also be useful, from zero energy to well above the charm threshold, and again, the interest is 2-fold: access to new sectors of hadron spectroscopy, and test the mechanisms of annihilation. For this latter purpose, a through comparison of $\bar{N}N$- and $\bar{Y}N$-induced channels would be most useful, where Y denotes a hyperon.

The hottest sectors remain these linked to astrophysics: how antiprotons and light antinuclei are produced in high-energy cosmic ray? Is there a possibility in the early Universe of separating matter from antimatter before complete annihilation? Studying these questions require beforehand a good understanding of the antinucleon-nucleon and antinucleon-nucleus interaction.

AUTHOR CONTRIBUTIONS

The author confirms being the sole contributor of this work and has approved it for publication.

ACKNOWLEDGMENTS

I would like to thank many colleagues, in particular my collaborators, for several stimulating and entertaining discussions along the years about the physics of antiprotons, and also the editors of Frontiers in Physics for initiating this review, and their referees for constructive comments. Special acknowledgments are due to M. Asghar for remarks and suggestions.

REFERENCES

1. Brink L, Ekspong G, Lundqvist S. *Nobel Lectures Physics: Including Presentation Speeches and Laureates' Biographies*. Singapore: World Scientific (1967). The first 3 volumes were published by North-Holland, Amsterdam.
2. Baur G, Boero G, Brauksiepe S, Buzzo A, Eyrich W, Geyer R, et al. Production of antihydrogen. *Phys Lett B.* (1996) **368**:251–8. doi: 10.1016/0370-2693(96)00005-6
3. Massam T, Muller T, Righini B, Schneegans M, Zichichi A. Experimental observation of antideuteron production. *Nuovo Cim Ser.* (1965) **39**:10–4. doi: 10.1007/BF02814251
4. Dorfan DE, Eades J, Lederman LM, Lee W, Ting CC. Observation of antideuterons. *Phys Rev Lett.* (1965) **14**:1003–6. doi: 10.1103/PhysRevLett.14.1003
5. Ma YG. Observation of antimatter nuclei at RHIC-STAR. *J Phys Conf Ser.* (2013) **420**:012036. doi: 10.1088/1742-6596/420/1/012036
6. Adam J, Adamczyk L, Adams JR, Adkins JK, Agakishiev G, Aggarwal MM, et al. Precise measurement of the mass difference and the binding energy of hypertriton and antihypertriton. *arXiv [Preprint].* (2019) *arXiv:1904.10520.*
7. Dönigus B. Highlights of the production of (anti-)(hyper-)nuclei and exotica with ALICE at the LHC. *J Phys Conf Ser.* (2019) **1271**:012001. doi: 10.1088/1742-6596/1271/1/012001

8. Hori M, Sótér A, Barna D, Dax A, Hayano R, Friedreich S, et al. Two-photon laser spectroscopy of antiprotonic helium and the antiproton-to-electron mass ratio. *Nature.* (2011) **475**:484–8. doi: 10.1038/nature10260
9. Mohl D. Stochastic cooling of particle beams. *Lect Notes Phys.* (2013) **866**:1–139. doi: 10.1007/978-3-642-34979-9
10. Baglin C, Baird SA, Bassompierre G, Borreani G, Brient JC, Broll C, et al. Charmonium spectroscopy by anti-proton annihilation with protons from an internal H_2 gas jet target. In: Nitti L, Preparata G, editors. *International Europhysics Conference on High-Energy Physics*, Bari, Laterza Bari (1985). p. 609.
11. Patrignani C. E835 at FNAL: charmonium spectroscopy in anti-p p annihilations. *AIP Conf Proc.* (2004) **717**:581–90. doi: 10.1063/1.1799766
12. Augustin I, Gutbrod HH, Kramer D, Langanke K, Stocker H. New physics at the international facility for antiproton and ion research (FAIR) next to GSI. In: *4th International Conference on Fission and Properties of Neutron Rich nuclei (ICFN4)*, Sanibel Island, FL (2008). doi: 10.1142/9789812833433_0016
13. Kumano S. Spin physics at J-PARC. *Int J Mod Phys Conf Ser.* (2016) **40**:1660009. doi: 10.1142/S2010194516600090
14. Dalpiaz P, Klapisch R, Lefevre P, Macri M, Montanet L, Mohl D, et al. Physics at SUPERLEAR. In: *The Elementary Structure of Matter. Proceedings, Workshop*, Les Houches (1987). p. 0414.
15. Husson A, Lunney D. An antiproton deceleration device for the GBAR experiment at CERN. In: *Proceedings, 12th International Conference on Low Energy Antiproton Physics (LEAP2016).* Kanazawa (2019).
16. Chardonnet P, Orloff J, Salati P. The production of antimatter in our galaxy. *Phys Lett B.* (1997) **409**:313–20. doi: 10.1016/S0370-2693(97)00870-8
17. Aguilar M, Ali Cavasonza L, Alpat B, Ambrosi G, Arruda L, Attig N, et al. Antiproton flux, antiproton-to-proton flux ratio, and properties of elementary particle fluxes in primary cosmic rays measured with the alpha magnetic spectrometer on the international space station. *Phys Rev Lett.* (2016) **117**:091103. doi: 10.1103/PhysRevLett.117.091103
18. Aly JJ, Caser S, Omnes R, Puget JL, Valladas G. The amount of matter in a matter-antimatter model of the universe. *Astron Astrophys.* (1974) **35**:271.
19. Gastaldi U, Klapisch R, editors. *Physics at LEAR With Low-Energy Cooled Antiprotons, Proceedings of LEAR Workshop*, Erice. New York, NY: Plenum (1984). doi: 10.1007/978-1-4684-8727-5
20. Gastaldi U, Klapisch R, Richard JM, Trân Thanh Vân J, editors. *Physics With Antiprotons at LEAR in the ACOL Era, Proceedings of 3th LEAR Workshop*, Tignes. Gif-sur-Yvette: Frontières (1985).
21. Charalambous S, Papastefanou C, Pavlopoulos P, editors. *Anti-proton 86. Proceedings, 8th European Symposium on Nucleon Anti-nucleon Interactions*, Thessaloniki. Singapore: World Scientific (1987).
22. Amsler C, Backenstoss G, Klapisch R, Leluc C, Simon D, Tauscher L, editors. *Physics at LEAR With Low Energy Antiprotons Proceedings of LEAR Workshop*, Villars-sur-Ollon. Chur: Harwood (1988).
23. Amsler C, Urner D, editors. *Physics at SuperLEAR, Proceedings of SuperLEAR Workshop*, Zurich. Bristol: IOP (1992).
24. Pinsky LS. A report on the first Fermilab workshop on antimatter physics at low energy. *AIP Conf Proc.* (1986) **150**:515–9. doi: 10.1063/1.36123
25. Bloch P, Pavlopoulos P, Klapisch R, editors. *1st International School of Physics With Low-Energy Antiprotons "Ettore Majorana" Fundamental Symmetries*, Erice. New York, NY: Plenum (1987). doi: 10.1007/978-1-4684-5389-8
26. Gastaldi U, Klapisch R, Close F, editors. *Spectroscopy of Light and Heavy Quarks. Proceedings, 2nd Course of the International School of Physics With Low-Energy Anti-protons*, Erice (1989).
27. Bradamante F, Richard JM, Klapisch R, editors. *Proceedings, 3rd International School of Physics With Low-Energy Antiprotons "Ettore Majorana" Anti-proton–Nucleon and Anti-proton–Nucleus Interactions*. New York, NY: Plenum (1990).
28. Landua R, Klapisch R, Richard JM, editors. *Proceedings, 4th International School of Physics With Low-Energy Antiprotons–Medium-Energy Anti-protons and the Quark–Gluon Structure of Hadrons*. New York, NY: Plenum (1991).
29. Fermi E, Yang CN. Are mesons elementary particles? *Phys Rev.* (1949) **76**:1739–43. doi: 10.1103/PhysRev.76.1739
30. Jacob MRM, Chew GF. *Strong-Interaction Physics: a Lecture Note Volume*. Frontiers in Physics. New York, NY: Benjamin (1964).
31. Ball JS, Scotti A, Wong DY. O boson exchange model of *NN* and $N\bar{N}$ interaction. *Phys Rev.* (1966) **142**:1000–12. doi: 10.1103/PhysRev.142.1000
32. Shapiro IS. The physics of nucleon–antinucleon systems. *Phys Rept.* (1978) **35**:129–85. doi: 10.1016/0370-1573(78)90190-4
33. Buck WW, Dover CB, Richard JM. The interaction of nucleons with anti-nucleons. 1. General features of the $\bar{N}N$ spectrum in potential models. *Ann Phys.* (1979) **121**:47. doi: 10.1016/0003-4916(79)90091-5
34. Dover CB, Richard JM. The interaction of nucleons with anti-nucleons. 2. Narrow mesons near threshold: experiment and theory. *Ann Phys.* (1979) **121**:70. doi: 10.1016/0003-4916(79)90092-7
35. Törnqvist NA. From the deuteron to deusons, an analysis of deuteron–like meson meson bound states. *Z Phys C.* (1994) **61**:525–37. doi: 10.1007/BF01413192
36. Dover CB, Richard JM. Strong tensor forces and the possibility of high spin states in the nucleon-antinucleon system. *Phys Rev D.* (1978) **17**:1770–7. doi: 10.1103/PhysRevD.17.1770
37. Martin AD, Spearman TD. *Elementary-Particle Theory*. Amsterdam: North-Holland (1970).
38. Brambilla N, Eidelman S, Hanhart C, Nefediev A, Shen CP, Thomas CE, et al. The XYZ states: experimental and theoretical status and perspectives. *arXiv [Preprint].* (2019) *arXiv:1907.07583*.
39. Montanet L, Rossi GC, Veneziano G. Baryonium physics. *Phys Rept.* (1980) **63**:149–222. doi: 10.1016/0370-1573(80)90161-1
40. Tanabashi M, Hagiwara K, Hikasa K, Nakamura K, Sumino Y, Takahashi F, et al. Review of particle physics. *Phys Rev D.* (2018) **98**:030001. doi: 10.1103/PhysRevD.98.030001
41. Evangelista C, Ghidini B, Palano A, Picciarelli V, Zitoa G, Mättig P, et al. Evidence for a narrow width boson of mass 2.95-GeV. *Phys Lett B.* (1977) **72**:139–43. doi: 10.1016/0370-2693(77)90081-8
42. Ablikim M, Achasov MN, An ZH, Bai JZ, Ferroli RB, Ban Y, et al. Spin-parity analysis of $p\bar{p}$ mass threshold structure in J/ψ and ψ' radiative decays. *Phys Rev Lett.* (2012) **108**:112003. doi: 10.1103/PhysRevLett.108.112003
43. Loiseau B, Wycech S. Antiproton-proton channels in J/psi decays. *Phys Rev C.* (2005) **72**:011001. doi: 10.1103/PhysRevC.72.011001
44. Wycech S, Dedonder JP, Loiseau B. In search of baryonium. *J Phys Conf Ser.* (2012) **374**:012002. doi: 10.1088/1742-6596/374/1/012002
45. Kang XW, Haidenbauer J, Meißner UG. Near-threshold $\bar{p}p$ invariant mass spectrum measured in J/ψ and ψ' decays. *Phys Rev D.* (2015) **91**:074003. doi: 10.1103/PhysRevD.91.074003
46. Amsler C. Nucleon-antinucleon annihilation at LEAR. In: *Talk at the ECT* Workshop on Antiproton Physics*, Trento (2019).
47. Myhrer F, Thomas A. The influence of absorption on possible nucleon-antinucleon resonances and bound states. *Phys Lett B.* (1976) **64**:59–61. doi: 10.1016/0370-2693(76)90357-9
48. Isgur N, Thacker HB. Origin of the Okubo-Zweig-Iizuka rule in QCD. *Phys Rev D.* (2001) **64**:094507. doi: 10.1103/PhysRevD.64.094507
49. Roy DP. History of exotic meson (four quark) and baryon (five quark) states. *J Phys G.* (2004) **30**:R113. doi: 10.1088/0954-3899/30/3/R02
50. Rosner JL. Possibility of baryon–anti-baryon enhancements with unusual quantum numbers. *Phys Rev Lett.* (1968) **21**:950–2. doi: 10.1103/PhysRevLett.21.950
51. Jaffe RL. $Q^2\bar{Q}^2$ resonances in the baryon–antibaryon system. *Phys Rev D.* (1978) **17**:1444. doi: 10.1103/PhysRevD.17.1444
52. Chan HM, Fukugita M, Hansson TH, Hoffman HJ, Konishi K, Hogaasen H, et al. Color chemistry: a study of metastable multiquark molecules. *Phys Lett B.* (1978) **76**:634–40. doi: 10.1016/0370-2693(78)90872-9
53. Chew GF, Low FE. Effective range approach to the low-energy p wave pion–nucleon interaction. *Phys Rev.* (1956) **101**:1570–9. doi: 10.1103/PhysRev.101.1570
54. Dalitz RH, Tuan SF. The phenomenological description of K-nucleon reaction processes. *Ann Phys.* (1960) **10**:307–51. doi: 10.1016/0003-4916(60)90001-4
55. Rossi G, Veneziano G. The string-junction picture of multiquark states: an update. *JHEP.* (2016) **6**:041. doi: 10.1007/JHEP06(2016)041

56. Maeda S, Yokota A, Hiyama E, Oka M, Liu Yr. Y_cN and Λ_cNN bound states in the potential model. *JPS Conf Proc.* (2017) **17**:112006. doi: 10.7566/JPSCP.17.112006
57. Joseph C, Soffer J, editors. *Proceedings, International Symposium on High-Energy Physics with Polarized Beams and Polarized Targets*, Vol. 38. Birkhaeuser. Basel: Birkhaeuser (1981). doi: 10.1007/978-3-0348-6301-8
58. Martynov E, Nicolescu B. Evidence for maximality of strong interactions from LHC forward data. *Phys Lett B.* (2018) **786**:207–11. doi: 10.1016/j.physletb.2018.09.049
59. Bugg DV, Hall J, Clough AS, Shypit RL, Bos K, Kluyver JC, et al. $\bar{p}p$ Total cross sections below 420 MeV/*c*. *Phys Lett B.* (1987) **194**:563–7. doi: 10.1016/0370-2693(87)90235-8
60. Bruckner W, Cujec B, Döbbeling H, Dworschak K, Güttner F, Kneis H, et al. Measurements of the anti-proton–proton annihilation cross-section in the beam momentum range between 180-MeV/*c* and 600-MeV/*c*. *Z Phys A.* (1990) **335**:217–29.
61. Dalkarov OD, Myhrer F. A simple model for proton-anti-proton scattering at low-energies. *Nuovo Cim A.* (1977) **40**:152. doi: 10.1007/BF02776782
62. Dover CB, Richard JM. Elastic, charge exchange, and inelastic $\bar{p}p$ cross sections in the optical model. *Phys Rev C.* (1980) **21**:1466–71. doi: 10.1103/PhysRevC.21.1466
63. Bertini R, Costa M, Perrot F, Catz H, Chaumeaux A, Faivre JCl, et al. Full angular distribution of the analyzing power in $\bar{p}p$ elastic scattering at 697-MeV/*c*. *Phys Lett B.* (1989) **228**:531–5. doi: 10.1016/0370-2693(89)90988-X
64. Birsa R, Bradamante F, Bressan A, Dalla Torre-Colautti S, Giorgi M, Lamann M, et al. High precision measurement of the $\bar{p}p \rightarrow \bar{n}n$ charge exchange differential cross-section. *Phys Lett B.* (1994) **339**:325–31. doi: 10.1016/S0370-2693(97)00685-0
65. Ahmidouch A, Heer E, Hess R, Lechanoine-Leluc C, Mascarini Ch, Rapin D, et al. Charge exchange$\bar{p}p \rightarrow \bar{n}n$ differential cross-sections between 546 MeV/*c* and 1287 MeV/*c*. *Phys Lett B.* (1995) **364**:116–20. doi: 10.1016/0370-2693(95)01348-7
66. Marcello S. Five years of antineutron physics at LEAR. *Nucl Phys A.* (1999) **655**:107–16. doi: 10.1016/S0375-9474(99)00187-6
67. Iazzi F, Feliciello A, Agnello M, Astrua M, Botta E, Bressani T, et al. Antineutron proton total cross-section from 50 MeV/*c* to 400 MeV/*c*. *Phys Lett B.* (2000) **475**:378–85. doi: 10.1016/S0370-2693(00)00086-1
68. Klempt E, Bradamante F, Martin A, Richard JM. Antinucleon nucleon interaction at low energy: scattering and protonium. *Phys Rept.* (2002) **368**:119–316. doi: 10.1016/S0370-1573(02)00144-8
69. Kunne RA, Beard CI, Birsa R, Bos K, Bradamante F, Bugg DV, et al. Asymmetry in $\bar{p}p$ elastic scattering. *Phys Lett B.* (1988) **206**:557–60. doi: 10.1016/0370-2693(88)91629-2
70. Kunne RA, Beard CI, Birsa R, Bos K, Bradamante F, Bugg D, et al. First measurement of D_{0n0n} in $\bar{p}p$ elastic scattering. *Phys Lett B.* (1991) **261**:191–6. doi: 10.1016/0370-2693(91)91349-Z
71. Birsa R, Bradamante F, Dalla Torre S, Giorgi MA, Lamanna M, Martin A, et al. PS199: $\bar{p}p \rightarrow \bar{n}n$ spin physics at LEAR. In: *Proceedings, 4th International School of Physics With Low-Energy Antiprotons–Medium-Energy Anti-protons and the Quark–Gluon Structure of Hadrons*, Erice (1990). p. 195–201.
72. Birsa R, Bradamante F, Bressan A, Dalla Torre-Colautti S, Giorgi M, Lamanna M, et al. First measurement of the depolarization parameter D_{0n0n} of the $\bar{p}p \rightarrow \bar{n}n$ charge exchange reaction. *Phys Lett B.* (1993) **302**:517–22. doi: 10.1016/0370-2693(93)90436-L
73. Timmermans R, Rijken TA, de Swart JJ. Anti-proton–proton partial wave analysis below 925-MeV/c. *Phys Rev C.* (1994) **50**:48–73. doi: 10.1103/PhysRevC.50.48
74. Zhou D, Timmermans RGE. Energy-dependent partial-wave analysis of all antiproton-proton scattering data below 925 MeV/c. *Phys Rev C.* (2012) **86**:044003. doi: 10.1103/PhysRevC.86.044003
75. Richard JM. Comment on 'Antiproton proton partial wave analysis below 925 MeV/*c*'. *Phys Rev C.* (1995) **52**:1143–4. doi: 10.1103/PhysRevC.52.1143
76. [Dataset] Haidenbauer J, editor. *Talk at the ECT* Workshop on Antiproton Physics*, Trento (2019). Available online at: https://indico.ectstar.eu/event/41/contributions/848/attachments/814/1048/Haidenbauer.pdf (accessed November 2019).
77. Gourdin M, Jancovici B, Verlet L. On the nucleon-antinucleon interactions. *Il Nuovo Cim.* (1958) **8**:485–96. doi: 10.1007/BF02828757
78. Bryan RA, Phillips RJN. Nucleon anti-nucleon potential from single meson exchanges. *Nucl Phys B.* (1968) **5**:201–19. doi: 10.1016/0550-3213(68)90125-9
79. Kohno M, Weise W. Proton–anti-proton scattering and annihilation into two mesons. *Nucl Phys A.* (1986) **454**:429–52. doi: 10.1016/0375-9474(86)90098-9
80. Haidenbauer J, Hippchen T, Holinde K. The Bonn $N\bar{N}$ potential and the range of $N\bar{N}$ annihilation. *Nucl Phys A.* (1990) **508**:329C–34C. doi: 10.1016/0375-9474(90)90493-6
81. Hippchen T, Haidenbauer J, Holinde K, Mull V. Meson–baryon dynamics in the nucleon–antinucleon system. 1. The nucleon–antinucleon interaction. *Phys Rev C.* (1991) **44**:1323–36. doi: 10.1103/PhysRevC.44.1323
82. Mull V, Holinde K. Combined description of $\bar{N}N$ scattering and annihilation with a hadronic model. *Phys Rev C.* (1995) **51**:2360–71. doi: 10.1103/PhysRevC.51.2360
83. Dover CB, Richard JM. Spin observables in low-energy nucleon anti-nucleon scattering. *Phys Rev C.* (1982) **25**:1952–8. doi: 10.1103/PhysRevC.25.1952
84. Richard JM, Sainio ME. Nuclear effects in protonium. *Phys Lett B.* (1982) **110B**:349–52. doi: 10.1016/0370-2693(82)91270-9
85. Timmers PH, van der Sanden WA, de Swart JJ. An antinucleon-nucleon potential. *Phys Rev D.* (1984) **29**:1928. doi: 10.1103/PhysRevD.29.1928
86. El-Bennich B, Lacombe M, Loiseau B, Wycech S. Paris $N\bar{N}$ potential constrained by recent antiprotonic-atom data and antineutron-proton total cross sections. *Phys Rev C.* (2009) **79**:054001. doi: 10.1103/PhysRevC.79.054001
87. Klempt E, Batty C, Richard JM. The antinucleon-nucleon interaction at low energy: annihilation dynamics. *Phys Rept.* (2005) **413**:197–317. doi: 10.1016/j.physrep.2005.03.002
88. Kohno M, Weise W. Anti-hyperon–hyperon production in low-energy anti-proton–proton reactions. *Nucl Phys A.* (1988) **479**:433C–49C. doi: 10.1016/0375-9474(88)90454-X
89. Ablikim M, Achasov MN, Ahmed S, Albrecht M, Alekseev M, Amoroso A, et al. Polarization and entanglement in baryon-antibaryon pair production in electron-positron annihilation. *Nat Phys.* **15** (2019) 631–634. doi: 10.1038/s41567-019-0494-8
90. Bassalleck B, Berdoz A, Bradtke C, Bröders R, Bunker B, Dennert H, et al. Measurement of spin transfer observables in $\bar{p}p \rightarrow \bar{\Lambda}\Lambda$ at 1.637 GeV/*c*. *Phys Rev Lett.* (2002) **89**:212302. doi: 10.1103/PhysRevLett.89.212302
91. Paschke KD, Quinn B, Berdoz A, Franklin GB, Khaustov P, Meyer CA, et al. Experimental determination of the complete spin structure for $\bar{p}p \rightarrow \bar{\Lambda}\Lambda$ at 1.637 GeV/*c*. *Phys Rev C.* (2006) **74**:015206. doi: 10.1103/PhysRevC.74.015206
92. Haidenbauer J, Holinde K, Mull V, Speth J. Can one discriminate between meson exchange and quark–gluon transition mechanisms in the $\bar{p}p \rightarrow \bar{\Lambda}\Lambda$ process? *Phys Lett B.* (1992) **291**:223–7. doi: 10.1016/0370-2693(92)91035-8
93. Alberg MA, Ellis JR, Kharzeev D. The proton spin puzzle and depolarization in $\bar{p}p \rightarrow \bar{\Lambda}\Lambda$. *Phys Lett B.* (1995) **356**:113–7. doi: 10.1016/0370-2693(95)00789-N
94. Richard JM. Remarks about spin measurements in $\bar{p} \rightarrow \bar{\Lambda}\Lambda$. *Phys Lett B.* (1996) **369**:358–61. doi: 10.1016/0370-2693(95)01598-1
95. Artru X, Elchikh M, Richard JM, Soffer J, Teryaev OV. Spin observables and spin structure functions: inequalities and dynamics. *Phys Rep.* (2009) **470**:1–92. doi: 10.1016/j.physrep.2008.09.004
96. Fridman A, editor. *4th Antiproton Symposium, Proceedings of Antiproton Conference*, Barr & Strasbourg. Paris: CNRS (1979).
97. Liu GQ, Tabakin F. Coupled channels study of anti-proton proton reactions. *Phys Rev C.* (1990) **41**:665–79. doi: 10.1103/PhysRevC.41.665
98. Takeuchi S, Myhrer F, Kubodera K. Maximum asymmetry phenomena in $\bar{p}p \rightarrow \pi^-\pi^+$ and $\bar{p}p \rightarrow K^-K^+$ reactions. *Nucl Phys A.* (1993) **556**:601–20. doi: 10.1016/0375-9474(93)90472-A
99. Elchikh M, Richard JM. Meson exchange and nonlocality effects in proton anti-proton annihilation into two pseudoscalar mesons. *Phys Rev C.* (1993) **48**:R17–20. doi: 10.1103/PhysRevC.48.R17
100. Deloff A. *Fundamentals in Hadronic Atom Theory*. River Edge, NJ: World Scientific (2003). p. 352.

101. Augsburger M, Anagnostopoulos D, Borchert G, Chatellard D, Egger JP, El-Khoury P, et al. Measurement of the strong interaction parameters in antiprotonic hydrogen and probable evidence for an interference with inner bremsstrahlung. *Nucl Phys A* (1999) **658**:149–62. doi: 10.1016/S0375-9474(99)00352-8
102. Entem DR, Fernandez F. The $N\bar{N}$ interaction in a constituent quark model: Baryonium states and protonium level shifts. *Phys Rev C.* (2006) **73**:045214. doi: 10.1103/PhysRevC.73.045214
103. Gotta D, Anagnostopoulos D, Augsburger M, Borchert G, Castelli C, Chatellard D, et al. Balmer α transitions in antiprotonic hydrogen and deuterium. *Nucl Phys A.* (1999) **660**:283–321. doi: 10.1016/S0375-9474(99)00385-1
104. Dover CB, Richard JM, Carbonell J. Isospin mixing in protonium and annihilation dynamics. *Phys Rev C.* (1991) **44**:1281–8. doi: 10.1103/PhysRevC.44.1281
105. Deser S, Goldberger ML, Baumann K, Thirring WE. Energy level displacements in pi mesonic atoms. *Phys Rev.* (1954) **96**:774–6. doi: 10.1103/PhysRev.96.774
106. Trueman TL. Energy level shifts in atomic states of strongly-interacting particles. *Nucl Phys.* (1961) **26**:57–67. doi: 10.1016/0029-5582(61)90115-8
107. Combescure M, Khare A, Raina A, Richard JM, Weydert C. Level rearrangement in exotic atoms and quantum dots. *Int J Mod Phys B.* (2007) **21**:3765–81. doi: 10.1142/S0217979207037855
108. Zel'dovich Y. Energy levels in a distorted coulomb field. *Sov Phys Solid State.* (1960) **1**:1497.
109. Carbonell J, Richard JM, Wycech S. On the relation between protonium level shifts and nucleon–anti-nucleon scattering amplitudes. *Z Phys A.* (1992) **343**:325–29.
110. Furui S, Strobel G, Faessler A, Vinh Mau R. The isospin mixing effect in $\bar{p}p$ annihilation at rest into $\pi^+\pi^-$ and $K\bar{K}$. *Nucl Phys A.* (1990) **516**:643–61. doi: 10.1016/0375-9474(90)90132-6
111. Kaufmann WB, Pilkuhn H. Black sphere model for the line widths of p state protonium. *Phys Rev C.* (1978) **17**:215–8. doi: 10.1103/PhysRevC.17.215
112. Day TB, Snow GA, Sucher J. High-orbital S-state capture of π-mesons by protons. *Phys Rev.* (1960) **118**:864–6. doi: 10.1103/PhysRev.118.864
113. Garreta D, Birien P, Bruge G, Chaumeaux A, Drake DM, Janouin S, et al. Elastic scattering of anti-protons from carbon, calcium and lead at 180-MeV. *Phys Lett B.* (1984) **149B**:64–8. doi: 10.1016/0370-2693(84)91552-1
114. Bruge G, Chaumeaux A, Birien P, Drake DM, Garreta D, Janouin S, et al. Comparative study of the elastic scattering of 178.4-MeV anti-protons by the ^{16}O and ^{18}O isotopes. *Phys Lett B.* (1986) **169**:14–6. doi: 10.1016/0370-2693(86)90676-3
115. Janouin S, Lemaire MC, Garreta D, Birien P, Bruge G, Drake DM, et al. Optical model analysis of anti-proton nucleus elastic scattering at 50-MeV and 180-MeV. *Nucl Phys A.* (1986) **451**:541–61. doi: 10.1016/0375-9474(86)90291-5
116. Adachi S, Von Geramb HV. Microscopic analysis of anti-proton–nucleus elastic scattering. *Nucl Phys A.* (1987) **470**:461–76. doi: 10.1016/0375-9474(87)90581-1
117. Suzuki T. Analysis of anti-proton nucleus scattering with the medium corrected optical potential. *Nucl Phys A.* (1985) **444**:659–77. doi: 10.1016/0375-9474(85)90111-3
118. Heiselberg H, Jensen AS, Miranda A, Oades GC, Richard JM. Microscopic calculation of anti-proton nucleus elastic scattering. *Nucl Phys A.* (1986) **451**:562–80. doi: 10.1016/0375-9474(86)90292-7
119. Balestra F, Bossolasco S, Bussa MP, Busso L, Ferrero L, Panzieri D, et al. Evidence of isospin effects in anti-proton–nucleus annihilation. *Nucl Phys A.* (1989) **491**:572–86. doi: 10.1016/0375-9474(89)90518-6
120. Botta E. Antineutron nucleus annihilation. *Nucl Phys A.* (2001) **692**:39–46. doi: 10.1016/S0375-9474(01)01157-5
121. Dover CB, Sainio ME, Walker GE. Antinucleon as a probe of nuclear spin and isospin excitations. *Phys Rev C.* (1983) **28**:2368–73. doi: 10.1103/PhysRevC.28.2368
122. Lemaire MC, Birien P, Bruge G, Drake DM, Garreta D, Janouin S, et al. Inelastic scattering of anti-protons from ^{12}C and ^{18}O at 50-MeV and 180-MeV. *Nucl Phys A.* (1986) **456**:557–76. doi: 10.1016/0375-9474(86)90075-8
123. Dover CB, Franey MA, Love WG, Sainio ME, Walker GE. Antinucleon nucleus inelastic scattering and the spin dependence of the $\bar{N}N$ annihilation potential. *Phys Lett B.* (1984) **143**:45–9. doi: 10.1016/0370-2693(84)90801-3
124. Batty CJ, Friedman E, Gal A. Strong interaction physics from hadronic atoms. *Phys Rept.* (1997) **287**:385–445. doi: 10.1016/S0370-1573(97)00011-2
125. Gotta D. Precision spectroscopy of light exotic atoms. *Prog Part Nucl Phys.* (2004) **52**:133–95. doi: 10.1016/j.ppnp.2003.09.003
126. Bouyssy A, Marcos S. Relativistic mean field approach to the scattering of antinucleons and nucleons by nuclei. *Phys Lett B.* (1982) **114**:397–402. doi: 10.1016/0370-2693(82)90079-X
127. Gaitanos T, Kaskulov M. Toward relativistic mean-field description of $\bar{N}$-nucleus reactions. *Nucl Phys A.* (2015) **940**:181–93. doi: 10.1016/j.nuclphysa.2015.04.006
128. Larionov AB, Lenske H. Elastic scattering, polarization and absorption of relativistic antiprotons on nuclei. *Nucl Phys A.* (2017) **957**:450–76. doi: 10.1016/j.nuclphysa.2016.10.006
129. Friedman E, Gal A, Loiseau B, Wycech S. Antinucleonnucleus interaction near threshold from the Paris $\bar{N}N$ potential. *Nucl Phys A.* (2015) **943**:101–16. doi: 10.1016/j.nuclphysa.2015.08.010
130. Hrtánková J, Mareš J. Calculations of antiprotonnucleus quasi-bound states using the paris $\bar{n}n$ potential. *Nucl Phys A.* (2018) **969**:45–59. doi: 10.1016/j.nuclphysa.2017.09.011
131. Aumann T, Bartmann W, Bouvard A, Boine-Frankenheim O, Broche A, Butin F, et al. *PUMA: Antiprotons and Radioactive Nuclei*. Technical Report CERN-SPSC-2019-033. SPSC-P-361. Geneva: CERN (2019).
132. Baldo-Ceolin M, Benetti P, Bitter T, Bobisut F, Calligarich E, Dolfini R, et al. A new experimental limit on neutron–anti-neutron oscillations. *Z Phys C.* (1994) **63**:409–16. doi: 10.1007/BF01580321
133. Theroine C. A neutron-antineutron oscillation experiment at the European spallation source. *Nucl Part Phys Proc.* (2016) **273–275**:156–61. doi: 10.1016/j.nuclphysbps.2015.09.019
134. Kabir PK. Limits on $n\bar{n}$ oscillations. *Phys Rev Lett.* (1983) **51**:231. doi: 10.1103/PhysRevLett.51.231
135. Alberico WM. Neutron antineutron oscillations: theory. In: *Lepton and Baryon Number Violation in Particle Physics, Astrophysics and Cosmology. Proceedings, 1st International Symposium, Lepton-baryon'98*, Trento (1998). p. 94–108.
136. Barrow JL, Golubeva ES, Paryev E, Richard JM. Progress and simulations for intranuclear neutron–antineutron transformations in $^{40}_{18}$Ar. *arXiv [Preprint]*. (2019) *arXiv:1906.02833*.
137. Dover CB, Gal A, Richard JM. Neutron antineutron oscillations in nuclei. *Phys Rev D.* (1983) **27**:1090–100. doi: 10.1103/PhysRevD.27.1090
138. Oosterhof F, Long B, de Vries J, Timmermans RGE, van Kolck U. Baryon-number violation by two units and the deuteron lifetime. *Phys Rev Lett.* (2019) **122**:172501. doi: 10.1103/PhysRevLett.122.172501
139. Haidenbauer J, Meißner UG. Neutron-antineutron oscillations in the deuteron studied with NN and $\bar{N}N$ interactions based on chiral effective field theory. *arXiv [Preprint]*. (2019) *arXiv:1910.14423*.
140. Nussinov S, Lampert MA. QCD inequalities. *Phys Rept.* (2002) **362**:193–301. doi: 10.1016/S0370-1573(01)00091-6
141. Zupancic C. Decay of a spinless particle into four identical spinless bosons. *Ann Phys.* (1994) **235**:245–317. doi: 10.1006/aphy.1994.1099
142. Devons S, Kozlowski T, Nemethy P, Shapiro S, Horwitz N, Kalogeropoulos T, et al. Observation of $\bar{p}p \rightarrow 2\pi^0$ at rest: evidence concerning s state annihilation. *Phys Rev Lett.* (1971) **27**:1614. doi: 10.1103/PhysRevLett.27.1614
143. Lévy M. Range of proton-antiproton annihilation. *Phys Rev Lett.* (1960) **5**:380–1. doi: 10.1103/PhysRevLett.5.380
144. Martin A. Range of the nucleon-antinucleon annihilation potential. *Phys Rev.* (1961) **124**:614–5. doi: 10.1103/PhysRev.124.614
145. Côté J, Lacombe M, Loiseau B, Moussallam B, Mau RV. Nucleon-antinucleon optical potential. *Phys Rev Lett.* (1982) **48**:1319–22. doi: 10.1103/PhysRevLett.48.1319
146. Rubinstein HR, Stern H. Nucleon–antinucleon annihilation in the quark model. *Phys Lett.* (1966) **21**:447–9. doi: 10.1016/0031-9163(66)90526-9

147. Carroll JP. Extended quark-rearrangement model for proton-antiproton annihilation at rest. *Phys Rev.* (1969) **184**:1793–802. doi: 10.1103/PhysRev.184.1793
148. Kleinknecht K, Klempt E, editors. *Proton Anti-proton Interactions and Fundamental Symmetries. Proceedings, 9th European Symposium*, Vol. 8, Mainz (1989).
149. Green AM, Niskanen JA. From phenomenological to microscopic descriptions of $N\overline{N}$ annihilation. *Int Rev Nucl Phys.* (1984) **1**:569–700. doi: 10.1142/9789814415132_0007
150. Green AM, Niskanen JA. Low-energy anti-proton physics in the early LEAR era. *Prog Part Nucl Phys.* (1987) **18**:93–182. doi: 10.1016/0146-6410(87)90009-3
151. Ihle G, Pirner HJ, Richard JM. *s* Wave nucleon–anti-nucleon interaction in the constituent quark model. *Nucl Phys A.* (1988) **485**:481–508. doi: 10.1016/0375-9474(88)90549-0
152. Eisenstein RA, Armenteros R, Bassi D, Birien P, Bock R, Busso A, et al. The JETSET experiment at LEAR. In: *Proceedings, BNL Workshop on Glueballs, Hybrids, and Exotic Hadrons*. Upton, NY: Brookhaven (1989). p. 636–42. doi: 10.1063/1.38092
153. Amsler C, Myhrer F. Low-energy anti-proton physics. *Ann Rev Nucl Part Sci.* (1991) **41**:219–67. doi: 10.1146/annurev.ns.41.120191.001251
154. Kudryavtsev AE. Some comments on $\bar{n}p$ annihilation branching ratios into $\pi\pi$, $\bar{K}K$ and $\pi\eta$ channels. *Phys Atom Nucl.* (2000) **63**:1969–72. doi: 10.1134/1.1335095
155. Vandermeulen J. $N\bar{N}$ Annihilation creates two mesons. *Z Phys C.* (1988) **37**:563–7. doi: 10.1007/BF01549715
156. Le Yaouanc A, Oliver L, Pène O, Raynal JC. *Hadron Transitions in the Quark Model*. New York, NY: Gordon and Breach (1988).
157. Genz H. The quark line rule in nucleon antinucleon annihilation. *AIP Conf Proc.* (1988) **176**:405–10. doi: 10.1063/1.37745
158. Pirner HJ. $N\bar{N}$ annihilation in the large N_c limit. *Phys Lett B.* (1988) **209**:154–8. doi: 10.1016/0370-2693(88)90923-9
159. Dosch HG, Gromes D. Flavor dependence of spontaneous pair creation. *Z Phys C.* (1987) **34**:139. doi: 10.1007/BF01561125
160. Cugnon J, Jasselette P, Vandermeulen J. Dynamics of the anti-p nucleus annihilation. In: *Proceedings, 4th LEAR Workshop: Physics at LEAR With Low Energy Antiprotons*, Villars (1996). p. 775–8.
161. Cugnon J, Vandermeulen J. Double strangeness production in anti-proton annihilation on nuclei. *Z Phys A.* (1991) **338**:349–56. doi: 10.1007/BF01288199
162. Rafelski J. Deep anti-proton annihilations on nuclei. In: *Proceedings, 3rd International School of Physics With Low-Energy Antiprotons "Ettore Majorana" Anti-proton–Nucleon and Anti-proton–Nucleus Interactions*, Erice (1996). p. 231–9.
163. Koch H. Hadron physics with antiprotons. *Nucl Instrum Meth B.* (2004) **214**:50–5. doi: 10.1016/S0168-583X(03)01771-3
164. Wiedner U. Hadron physics with PANDA. *Hyperfine Interact.* (2009) **194**:219–23. doi: 10.1007/s10751-009-0075-9
165. Chiba M, Fujitani T, Iwahori J, Kawaguti M, Kobayashi M, Kurokawa SI, et al. Pontecorvo reactions in antiproton annihilation at rest in deuterium to $\pi^0 n$, $\pi^0\Delta^0$, ηn and $\eta\Delta^0$. *Phys Rev D.* (1997) **55**:2577–83. doi: 10.1103/PhysRevD.55.2577
166. Gorchakov OE, Cerello P, Ableev VG, Prakhov SN, Rozhdestvensky AM, Sapozhnikov MG, et al. Measurement of the $\bar{p}d \rightarrow \phi n$ Pontecorvo reaction for anti-proton annihilation at rest. *Phys Lett B.* (2002) **528**:34–42. doi: 10.1016/S0370-2693(02)01175-9
167. Alberico WM, Garbarino G. Weak decay of Λ hypernuclei. *Phys Rept.* (2002) **369**:1–109. doi: 10.1016/S0370-1573(02)00199-0
168. Denig A, Salme G. Nucleon electromagnetic form factors in the timelike region. *Prog Part Nucl Phys.* (2013) **68**:113–57. doi: 10.1016/j.ppnp.2012.09.005
169. Pacetti S, Baldini Ferroli R, Tomasi-Gustafsson E. Proton electromagnetic form factors: basic notions, present achievements and future perspectives. *Phys Rept.* (2015) **550–551**:1–103. doi: 10.1016/j.physrep.2014.09.005
170. Bardin G, Burgun G, Calabrese R, Capon G, Carlin R, Dalpiaz P, et al. Measurement of the proton electromagnetic form-factor near threshold in the timelike region. *Phys Lett B.* (1991) **255**:149–54. doi: 10.1016/0370-2693(91)91157-Q
171. Baglin C, Baird S, Bassompierre G, Borreani G, Brient JC, Broll C, et al. Search for the p wave singlet charmonium state in $\bar{p}p$ annihilations at the CERN intersecting storage rings. *Phys Lett B.* (1986) **171**:135–41. doi: 10.1016/0370-2693(86)91013-0
172. Ambrogiani M, Argirò S, Bagnasco S, Baldini W, Bettoni D, Borreani G, et al. Search for the $\eta_c'(2^1S_0)$ charmonium resonance. *Phys Rev D.* (2001) **64**:052003. doi: 10.1103/PhysRevD.64.052003
173. Gabathuler E, Pavlopoulos P. The CPLEAR experiment. *Phys Rept.* (2004) **403–404**:303–21. doi: 10.1016/j.physrep.2004.08.020
174. Hatzifotiadou D, Adiels L, Backenstoss G, Bergstrom I, Carius S, Charalambous S, et al. Some results of experiment PS182 at LEAR. In: *Anti-proton 86. Proceedings, 8th European Symposium on Nucleon Anti-nucleon Interactions*, Thessaloniki (1986). p. 199–204.
175. Wang Q, Li G, Zhao Q. Open charm effects in the explanation of the long-standing '$\rho\pi$ puzzle'. *Phys Rev D.* (2012) **85**:074015. doi: 10.1103/PhysRevD.85.074015
176. Dover CB, Fishbane PM, Furui S. Dynamical selection rules in $N\bar{N}$ annihilation. *Phys Rev Lett.* (1986) **57**:1538–41. doi: 10.1103/PhysRevLett.57.1538
177. Nifenecker H. Fission of heavy hypernuclei. *Prog Part Nucl Phys.* (1993) **30**:407–14. doi: 10.1016/0146-6410(93)90042-E
178. Zahed I, Brown GE. The Skyrme model. *Phys Rept.* (1986) **142**:1–102. doi: 10.1016/0370-1573(86)90142-0
179. Zahed I, Brown GE. A nonperturbative description of $N\bar{N}$ annihilation. *Z Phys A.* Cambridge, (1990) **335**:349–54.
180. Donnelly TW, Formaggio JA, Holstein BR, Milner RG, Surrow B. *Foundations of Nuclear and Particle Physics*. Cambridge, UK: Cambridge University Press (2017).
181. Machleidt R, Entem DR. Chiral effective field theory and nuclear forces. *Phys Rept.* (2011) **503**:1–75. doi: 10.1016/j.physrep.2011.02.001
182. Epelbaum E, Krebs H, Meißner UG. Improved chiral nucleon-nucleon potential up to next-to-next-to-next-to-leading order. *Eur Phys J A.* (2015) **51**:53. doi: 10.1140/epja/i2015-15053-8
183. Chen GY, Ma JP. $N\bar{N}$ scattering at NLO order in an effective theory. *Phys Rev D.* (2011) **83**:094029. doi: 10.1103/PhysRevD.83.094029
184. Dai LY, Haidenbauer J, Meißner UG. Antinucleon-nucleon interaction at next-to-next-to-next-to-leading order in chiral effective field theory. *JHEP.* (2017) **7**:78. doi: 10.1007/JHEP07(2017)078
185. Haidenbauer J. Antinucleon-nucleon interaction in chiral effective field theory. *EPJ Web Conf.* (2018) **181**:01028. doi: 10.1051/epjconf/201818101028
186. Vorabbi M, Gennari M, Finelli P, Giusti C, Navrátil P. Elastic antiproton-nucleus scattering from chiral forces. *arXiv [Preprint]*. (2019) *arXiv:1906.11984*.

Conflict of Interest: The author declares that the research was conducted in the absence of any commercial or financial relationships that could be construed as a potential conflict of interest.

Copyright © 2020 Richard. This is an open-access article distributed under the terms of the Creative Commons Attribution License (CC BY). The use, distribution or reproduction in other forums is permitted, provided the original author(s) and the copyright owner(s) are credited and that the original publication in this journal is cited, in accordance with accepted academic practice. No use, distribution or reproduction is permitted which does not comply with these terms.

Advantages of publishing in Frontiers

OPEN ACCESS
Articles are free to read for greatest visibility and readership

FAST PUBLICATION
Around 90 days from submission to decision

HIGH QUALITY PEER-REVIEW
Rigorous, collaborative, and constructive peer-review

TRANSPARENT PEER-REVIEW
Editors and reviewers acknowledged by name on published articles

Frontiers
Avenue du Tribunal-Fédéral 34
1005 Lausanne | Switzerland

Visit us: www.frontiersin.org
Contact us: frontiersin.org/about/contact

REPRODUCIBILITY OF RESEARCH
Support open data and methods to enhance research reproducibility

DIGITAL PUBLISHING
Articles designed for optimal readership across devices

FOLLOW US
@frontiersin

IMPACT METRICS
Advanced article metrics track visibility across digital media

EXTENSIVE PROMOTION
Marketing and promotion of impactful research

LOOP RESEARCH NETWORK
Our network increases your article's readership